CISET

SAGE
YAYINCILIK REKLAM MATBAACILIK

ISBN 978-605-184-196-0

MERSİN ÜNİVERSİTESİ 1992

CISET

2nd CISET

Cilicia International Symposium on Engineering and Technology

10-12 October 2019 MERSIN/TURKEY

PROCEEDINGS BOOK

ciset.mersin.edu.tr
ciset@mersin.edu.tr

ORGANIZATION BY KEYKUBATCOPY Dijital Yayıncılık - Organizasyon

ciset.mersin.edu.tr
ciset@mersin.edu.tr

2nd CILICIA INTERNATIONAL SYMPOSIUM ON ENGINEERING AND TECHNOLOGY (CISET 2019)

Proceedings Book

October 10-12, 2019

Mersin University Engineering Faculty

Editor
Prof.Dr. Murat YAKAR

Assistant Editor
Assoc.Prof.Dr. Erdinç AVAROĞLU
Assist.Prof.Dr. Çiğdem ACI

2nd CISET

Cilicia International Symposium on Engineering and Technology

10-12 October 2019 MERSIN/TURKEY

E book: ISBN 978-605-184-196-0

Proceedings Book

Editor

Prof.Dr. Murat YAKAR

Assistant Editor

Assoc.Prof.Dr. Erdinç AVAROĞLU

Assist.Prof.Dr. Çiğdem ACI

Yayınevi

SAGE

Yayıncı Sertifika No: 14721

SAGE Matbaacılık Rek.Mat.San.Tic.Ldt.Şti.
Uğurlu İş Merkezi No:97/24 İskitler - Ankara
0 312 341 00 02 - 0 321 341 00 05
bilgi@bizimdijital.com
www.bizimdijitamatbaa.com

6-11-2019

Honor Board

Ali İhsan SU

Governor of Mersin

Vahap SEÇER

Mersin Metropolitan Municipality Mayor

Prof. Dr. Ahmet ÇAMSARI

Mersin University Rector

Organization Committee

Prof. Dr. Murat YAKAR

Symposium Chairman

Executive Committee

Prof. Dr. İlker Fatih KARA (Department of Civil Engineering)
Dean

Prof.Dr. Sedat SAYAR (Department of Food Engineering)

Prof.Dr. Cahit BİLİM (Department of Civil Engineering)

Prof.Dr. Bahadır Kürşad KÖRBAHTİ (Department of Chemical Engineering)

Prof.Dr. Şükrü Dursun (Department of Environmental Engineering)

Assoc.Prof.Dr. Erdinç AVAROĞLU (Department of Computer Engineering)

Assoc.Prof.Dr. Hüseyin ERİŞTİ (Department of Electrical and Electronics Engineering)

Assoc.Prof.Dr. Bahadır SAYINCI (Department of Mechanical Engineering)

Assoc.Prof.Dr. Memduh KARA (Department of Mechanical Engineering)

Assoc.Prof.Dr. Ömer GÜLER (Department of Metallurgical and Materials Engineering)

Assist.Prof.Dr. Çiğdem ACI (Department of Computer Engineering)

Assist.Prof.Dr. Hüdaverdi ASLAN (Department of Environmental Engineering)

Assist.Prof.Dr. Fatma BÜNYAN ÜNEL (Department of Geomatic Engineering)

Assist.Prof.Dr. Lütfiye KUŞAK (Department of Geomatic Engineering)

Assist.Prof.Dr. Hidayet TAĞA (Department of Geological Engineering)

Res.Assist.Dr. Cemile SOLAK (Department of Geological Engineering)

Res.Assist. Yasin ÖZAY (Department of Environmental Engineering)

Res.Assist. Hüseyin YANIK (Department of Electrical and Electronics Engineering)

Res.Assist. Fırat ÇINAR (Department of Food Engineering)

Res.Assist. Mehmet Özgür ÇELİK (Department of Geomatic Engineering)

Res.Assist. Furkan İNAL (Department of Civil Engineering)

Res.Assist. Didem DEMİR KARAKUŞ (Department of Chemical Engineering)

Res.Assist. Alper GÜNÖZ (Department of Mechanical Engineering)

Res.Assist. Öyküm BAŞGÖZ (Department of Metallurgical and Materials Engineering)

Res.Assist. Ayşegül Yaman (Department of Computer Engineering)

Symposium Secretary

Hüseyin KARA

Secretary of Engineering Faculty

Symposium Website Admin

Veli YILDIZ

Engineer

Scientific Committee

Prof.Dr. Reha Metin Alkan	Istanbul Technical University
Prof.Dr. Ahmet Bedri ÖZER	Fırat University
Prof.Dr. Hamza EROL	Mersin University
Prof.Dr. Zeki YETGİN	Mersin University
Prof.Dr. Ali Karcı	İnönü University
Prof.Dr. Caner ÖZDEMİR	Mersin University
Prof.Dr. Ali AKDAĞLI	Mersin University
Prof.Dr. Cemil Cengiz ARCASOY	Toros University
Prof.Dr. Mehmet TÜMAY	Çukurova University
Prof.Dr. Hamit SERBEST	Çukurova University
Prof.Dr. Turgut İKİZ	Çukurova University
Prof.Dr. İlyas EKER	Çukurova University
Prof.Dr. Mustafa GÖK	Çukurova University
Prof.Dr. Ulus ÇEVİK	Çukurova University
Prof.Dr. Erol Özer	Mersin University
Prof.Dr. Fevzi ÖNER	Mersin University
Prof.Dr. Kemal TASLI	Mersin University
Prof.Dr. Cüneyt GÜLER	Mersin University
Prof.Dr. Tolga ÇAN	Çukurova University
Prof.Dr. Arzu Başman	Hacettepe University
Prof.Dr. Haşim Kelebek	Adana Alparslan Türkeş Science and Technology University
Prof.Dr. Hüseyin Erten	Çukurova University
Prof.Dr. İhsan Karabulut	İnönü University
Prof.Dr. Hacı İbrahim Ekiz	Mersin University
Prof.Dr. Tunç Koray Palazoğlu	Mersin University
Prof.Dr. Mahir Turhan	Mersin University
Prof.Dr. Nüzhet İkbal Türker	Mersin University
Prof. Dr. Sedat Sayar	Mersin University
Prof.Dr. Ayla ÖZER	Mersin University
Prof.Dr. Ayten ATEŞ	Cumhuriyet University
Prof.Dr. Bahadır Kürşad KÖRBAHTİ	Mersin University
Prof.Dr. Dilhan M. KALYON	Stevens Institute of Technology
Prof.Dr. Hüseyin KARACA	İnönü University
Prof.Dr. Mahmut BAYRAMOĞLU	Gebze Technical University
Prof.Dr. Mehmet YÜCEER	İnönü University
Prof.Dr. Nahit AKTAŞ	Kyrgyz-Turkish Manas University
Prof.Dr. Satılmış BASAN	Hitit University
Prof.Dr. Tonguç ÖZDEMİR	Mersin University
Prof.Dr. Uğur SALGIN	Cumhuriyet University
Prof. Dr. A. Alper ÖNER	Erciyes University

Prof. Dr. Mustafa ŞAHMARAN	Hacettepe University
Prof.Dr. Emel ORAL	Çukurova University
Prof.Dr. Ertan EVİN	Fırat University
Prof.Dr. Onuralp YÜCEL	İstanbul Technical University
Prof.Dr. Nuran AY	Anadolu University
Prof.Dr. Ali KALKANLI	Orta Doğu Technical University
Prof.Dr. Yoke Khin YAP	Michigan Technological University
Prof.Dr. Adem KURT	Gazi University
Prof.Dr. Şaduman ŞEN	Sakarya University
Prof.Dr. Murat YAKAR	Mersin University
Prof.Dr. Hacı Murat YILMAZ	Aksaray University
Prof.Dr. Bülent BAYRAM	Yıldız Technical University
Prof.Dr. Tayfun ÇAY	Konya Technical University
Prof.Dr. Şükrü Dursun	Konya Technical University
Prof.Dr. Hanlar Reşidoğlu	Mersin University
Prof.Dr. Hamza Menken	Mersin University
Prof.Dr. C. Cengiz Arcasoy	Toros University
Prof.Dr. Selma Erat	Mersin University
Assoc.Prof. Dr Hüseyin ERİŞTİ	Mersin University
Assoc.Prof.Dr. Taner Tuncer	Fırat University
Assoc.Prof. Dr. Kadir ABACI	Mersin University
Assoc.Prof. Dr. Alkan ALKAYA	Mersin University
Assoc.Prof. Dr. Sami ARICA	Çukurova University
Assoc.Prof. Dr. Turgay İBRİKCİ	Çukurova University
Assoc.Prof. Dr. Ahmet TEKE	Çukurova University
Assoc.Prof. Dr. Murat AKSOY	Çukurova University
Assoc.Prof. Dr. Kerem ÜN	Çukurova University
Assoc.Prof. Dr. Mehmet Uğraş CUMA	Çukurova University
Assoc.Prof.Dr. İlkay Şensoy	Middle East Technical University
Assoc.Prof.Dr. Serpil Öztürk	Sakarya University
Assoc.Prof.Dr. Hakan Karaca	Pamukkale University
Assoc.Prof.Dr. Ayşe AYTAÇ	Kocaeli University
Assoc.Prof.Dr. Ayşe KARAKEÇİLİ	Ankara University
Assoc.Prof.Dr. Bora GARİPCAN	Boğaziçi University
Assoc.Prof.Dr. Dilek KILIÇ APAR	Yıldız Technical University
Assoc.Prof.Dr. Elif ÖDEŞ AKBAY	Eskişehir Technical University
Assoc.Prof.Dr. Ferda GÖNEN	Mersin University
Assoc.Prof.Dr. Feridun DEMİR	Osmaniye Korkut Ata University
Assoc.Prof.Dr. Hakan KAYI	Ankara University
Assoc.Prof.Dr. Hilal DEMİR KIVRAK	Van Yüzüncü Yıl University
Assoc.Prof.Dr. M. Oğuzhan ÇAĞLAYAN	Bilecik Şeyh Edebali University
Assoc.Prof.Dr. Nimet KARAGÜLLE	Mersin University
Assoc.Prof.Dr. Rükan GENÇ ALTÜRK	Mersin University
Assoc.Prof.Dr. Ercan ERDİŞ	İskenderun Teknik University
Assoc.Prof.Dr. Erdal UNCUOĞLU	Erciyes University

Assoc.Prof.Dr. Özgür Lütfi ERTUĞRUL	Mersin University
Assoc.Prof.Dr. Kubilay AKÇAÖZOĞLU	Niğde Ömer Halisdemir University
Assoc.Prof.Dr. Bahadır SAYINCI	Mersin University
Assoc.Prof.Dr. İskender ÖZKUL	Mersin University
Assoc.Prof.Dr. Memduh KARA	Mersin University
Assoc.Prof.Dr. Osman ÇULHA	Celal Bayar University
Assoc.Prof.Dr. Serdar ALTIN	İnönü University
Assoc.Prof.Dr. Uğur ÇALIGÜLÜ	Fırat University
Assoc.Prof.Dr. Aykut ÇANAKÇI	Karadeniz Technical University
Assoc.Prof.Dr. Mehmet Deniz Turan	Fırat University
Assc.Prof.Dr. Serkan ISLAK	Kastamonu Ünv.
Assoc.Prof.Dr. Ömer Güler	Mersin University
Assoc. Prof. Dr. İbrahim YILMAZ	Afyon Kocatepe University
Assoc. Prof. Dr. Şinasi KAYA	İstanbul Teknik University
Assoc. Prof. Dr. Serkan DOĞANALP	Konya Teknik University
Assoc. Prof. Dr. Mevlüt YETKİN	İzmir Katip Çelebi University
Assoc. Prof. Dr. Mustafa ZEYBEK	Artvin Çoruh University
Assoc. Prof. Dr. Mehmet Küçükaslan	Mersin University
Assoc. Prof. Dr. Yahya Nural	Mersin University
Assoc. Prof. Dr. Bünyamin Demir	Mersin University
Assist. Prof. Dr. Mehmet ERTAŞ	Konya Technical University
Assist. Prof. Dr. Sertaç Göktaş	Mersin University
Dr. Ali YILDIZ	Mersin University
Dr. Ahmet Naci METE	Mersin University
Dr. Evren DEĞİRMENCİ	Mersin University
Dr. Şevket DEMİRCİ	Mersin University
Dr. Filiz KARAÖMERLİOĞLU	Mersin University
Dr. Betül YILMAZ	Mersin University
Dr. Cevher AK	Toros University
Dr. Adnan TAN	Çukurova University
Dr. Ercan AVŞAR	Çukurova University
Dr. Osman ORHAN	Konya Teknik University
Assist.Prof.Dr. Kevser Kahraman	Abdullah Gül University
Assist.Prof.Dr. Esma Eser	Çanakkale Onsekiz Mart University
Assist. Prof. Serpil Yalım Kaya	Mersin University
Assist.Prof.Dr. Ebru ERÜNAL	Çukurova University
Assist.Prof.Dr. Onur DÖKER	Mersin University
Assist.Prof.Dr. Yeliz GÜRDAL DURĞUN	Adana Alparslan Türkeş Science and Technology University
Assist.Prof. Dr. Murat ÖZEN	Mersin University
Assist.Prof.Dr. Erhan Akkaya	İnönü University
Assist.Prof.Dr. Kemal Adem	Aksaray University

Assist.Prof.Dr. İsmail Koyuncu	Afyon Kocatepe University
Assist.Prof.Dr. Akın Tatoğlu	University of Hartford
Assist.Prof.Dr. İpek ABASIKELEŞ TURGUT	Iskenderun Technical University
Assist.Prof.Dr. Esra SARAÇ EŞSİZ	Adana Alparslan Türkeş Science and Technology University
Assist.Prof.Dr. Abdullah Elewi	Mersin University
Assist.Prof.Dr. Mehmet Acı	Mersin University
Assist.Prof. Dr. Hasan GÜZEL	İskenderun Teknik University
Assist.Prof. Dr. Gökhan ARSLAN	Mersin University
Assist.Prof. Dr. Bengi ŞANLI	Mersin University
Assist.Prof. Dr. İlker SUGÖZÜ	Mersin University
Assist.Prof.Dr. Yakup SAY	Munzur University
Assist.Prof.Dr. Ayşe KALEMTAŞ	Bursa Technical University
Assist.Prof. Dr. Fatih TAKTAK	Uşak University
Assist.Prof. Dr. Osman Sami KIRTILOĞLU	İzmir Katip Çelebi University
Assist.Prof. Dr. Lütfiye KUŞAK	Mersin University
Assist.Prof. Dr. Fatma BÜNYAN ÜNEL	Mersin University
Lecturer Dr. Ali ULVİ	Selçuk University

CISET - 2nd Cilicia International Symposium on Engineering and Technology
10-12 October, 2019, Mersin / TURKEY

APPLICATION OF DISCRETE TIME CONTROLLERS TO A PILOT SCALE PACKED DISTILLATION COLUMN

Semin Altuntaş [*1, 2] and Hale Hapoğlu [1]

[1] Ankara University, Engineering Faculty, Chemical Engineering Department, Ankara, Turkey, seminaltuntas@hotmail.com, hapoglu@eng.ankara.edu.tr

[2] Provincial Directorate of Environment and Urbanization, 55070 Samsun, Turkey, seminaltuntas@hotmail.com

ABSTRACT
The process involved is a pilot scale packed distillation column that separates a mixture of methanol and water. The performances of two discrete time controllers that different parameter tuning techniques were used for each of them were examined in the face of the set point tracking of the overhead product composition. The success of the discrete time controllers were assessed by means of the rise time and integral of the square error (ISE) criteria. A discrete time proportional integral controller with two terms was obtained by using the velocity form of controller law. For this controller, the proportional sensitivity term (K_c) and the other term were determined by creating root locus diagram and replacing the closed loop poles to the appropriate location in unit circle of z-plane. The most successful proposed controller action was obtained with K_c of 0.95 and integral time constant of 2.375 min according to rise time of 3.7 min and ISE criteria of 1.08. The discrete time proportional integral derivative (PID) controller with six parameters as P=0.009185, I=0.01835, D=0, N=100, b=1, c=1 that were tuned by using Simulink control design and 1 min sampling time was applied to the process. The same controller performance with six parameters of P=1.164, I=0.5319, D=-0.01481, N=3.783, b=0.1233, c=0.01017 was investigated by choosing 0.5 min sampling time. By comparing all the performances obtained, it can be said that the discrete time controller with two terms tuned by the suggested approach can easily be applied to obtain the most desired performance.

Keywords: *Discrete time controller, Packed distillation column, Root locus, Closed loop pole placement*

[*] Corresponding Author

1. INTRODUCTION

Discrete time controller accuracy and speed has of importance in industrial applications. A compromise is needed between cost and reliability (Desyatirikova et al., 2019). The corresponding controllers are called digital computers. System models are described in certain discrete time domain, and their parameters are determined by using various methods based on experimental or well-simulated input and output data (Altuntas et al., 2017; Camcioglu et al., 2017). The controlled systems dynamic are determined by the choice of controller parameters which are determined using various methods (Aldemir and Hapoğlu, 2016).

Discrete time controllers are designed to minimize a cost function or to locate closed-loop system poles in the z-plane unit circle. Obtaining a desired closed-loop system response of a controller also minimize indirectly a cost function. A cost effective design based on a closed-loop pole-placement approach was reported for discrete proportional integral (PI) controller (Khan et al., 2018). For two-degrees-of-freedom (2DOF) PI current controller, an analytical discrete-time pole-placement technique was used (Hinkkanen et al., 2016). By separating a closed-loop system poles as a dominant pole pair and other poles and locating them in z-plane unit circle by targeting a certain distance between each set of poles, a discrete PI-proportional derivate (PI-PD) controller was designed by Dincel and Soylemez (2018). This technique is called a dominant pole-placement.

In the present work, two discrete-time controllers were used to track set point of the overhead product composition of a pilot-scale packed distillation column for performance comparison. The two tuning parameters of the proposed discrete PI controller were tuned by observing root locus diagram pole branches for proportional only control and by choosing the three poles location in z-plane according to a performance criteria of the system response with discrete PI controller. The two application performances of discrete-time PID controller (2DOF) that the related six parameters tuned by means of Simulink control design in MATLAB were also examined by choosing the sampling time (T_s) as 1 min and 0.5 min respectively.

2. DISCRETE-TIME CONTROLLERS

Wardle and Hapoglu (1993) proposed a discrete time transfer function of process without control. This transfer function response to a step increase in control signal was compared (Wardle and Hapoglu, 1993) with two-film approach model computer simulation that verified (Wardle and Hapoglu, 1994) by the experimental data (Steiner et al., 1978) obtained from a pilot-scale packed distillation column where methanol water mixture was feed between 1m and 0.9m effective packing height in enriching and stripping sections.

The discrete system transfer function (Wardle and Hapoglu, 1993) without control which relates the deviation form of overhead product molar methanol composition (x_D') and the deviation form of reflux flow rate (L') was given in Eq. (1). Where, the T_s value was used as 1 min. The same system discrete transfer function can be written by using T_s of 0.5 min and zero order hold element in Eq. (2).

$$\frac{x_D'}{L'} = \frac{0.411z + 0.0119}{z^2 - 0.742z + 0.0183} \quad (1)$$

$$\frac{x_D'}{L'} = \frac{0.2122z - 0.01472}{z^2 - 1.006z + 0.1353} \quad (2)$$

The closed loop system with proportional control transfer function which relates overhead product composition in Eq. (1) and set point was given in Eq. (3).

$$\frac{x_D'}{x_{SET}'} = \frac{K_c(0.411z + 0.0119)}{(z^2 - 0.742z + 0.0183) + K_c(0.411z + 0.0119)} \quad (3)$$

Where, x_{SET}' represents the set point value of the overhead product composition in deviation variable form. K_c is the proportional sensitivity (or the gain) of the proportional (P) controller. The characteristic equation of the transfer function given in Eq. (3) was utilized to create root locus diagram data. The K_c value that locates two desired positive poles far from the edge of the unit circle was chosen to apply as a constant value in Eq. (9).

The proposed discrete-time PI controller transfer function can be written as Eq. (4), because the changes of the manipulated variable are determined by varying two terms. Equation (7) is obtained by combining the discrete definition of the coefficients q_0 and q_1 which are given in Eq. (5) and Eq. (6) respectively. The velocity form control algorithm is utilized to create the terms in Eq. (5) and Eq. (6). The tuning parameter, A can be presented in Eq. (8).

$$G_C(z) = \frac{q_0 z - q_1}{z - 1} \quad (4)$$

$$q_0 = K_c + \frac{K_c T_s}{2\tau_I} \quad (5)$$

$$q_1 = \frac{K_c T_s}{2\tau_I} - K_c \quad (6)$$

$$G_C(z) = \frac{(K_c + A)z - (A - K_c)}{z - 1} \quad (7)$$

$$A = \frac{K_c T_s}{2\tau_I} \quad (8)$$

$$G_C(z) = \frac{(0.95 + A)z - (A - 0.95)}{z - 1} \quad (9)$$

Where τ_I is integral time constant which can be varied by using different A values (see Eq. (9)).

$$ISE = 10^4 \sum_{n=0}^{n=N} T_s (x_{SET} - x_D)_n^2 \quad (10)$$

For controller performance comparison, integral of the square error (ISE) criteria given in Eq. (10) can be used in discrete domain, where the error (x_{SET}-x_D) is the deviation of the overhead product composition from the set point. The N value is the total number of sampling time step used to reach the final run time.

$$G_C(z) = P(b * x'_{SET}) + I * T_s \frac{1}{(z-1)}(x'_{SET} - x'_D) + D \frac{N}{1 + N * T_s \frac{1}{(1-z)}}(c * x'_{SET} - x'_D) \quad (11)$$

The second discrete controller can be obtained from Simulink Library in MATLAB. This discrete PID controller (2DOF) can be presented in Eqn. (11). Where P, I, D represent proportional, integral, derivative terms respectively. The parameters of b and c are the set point weights. The symbol of N is filter coefficient. The discrete PID controller block parameters can be tuned by using Simulink Control Design in MATLAB. By replacing D=0 in Eq. (11) the discrete PI controller Simulink block may be obtained.

3. RESULTS AND DISCUSSION

The discrete-time transfer function of the packed distillation column without control (Wardle and Hapoglu, 1993) which relates overhead product molar methanol composition as output and reflux flow rate as inputs was used to capture the closed loop behavior of the process with proportional only control. The proportional sensitivity (Kc) of the closed loop transfer function given in Eq. (3) was varied to determine the poles location in z-plane by using MATLAB (see Table 1). Root locus diagram obtained was presented in Fig. 1. The branches corresponding to the two poles of the proportional only control system begin at the two poles (0.7165 and 0.0255) of the system transfer function without control (These poles are represented by symbols of cross in Fig. 1).

In Table 1, The Kc value was varied by considering the related root locus diagram to determine adequate location for the poles. For non-oscillatory stable case, Kc=0.95 was chosen with two real positive closed loop poles as 0.2119 and 0.1397.

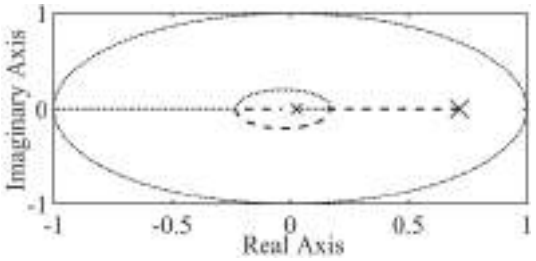

Fig. 1. Root locus diagram generated using MATLAB for the closed loop discrete system with P controller

Table 1. Poles for the closed loop discrete system with P controller

K_c	poles	
1.1	0.1450-0.1019i	0.1450+0.1019i
1.0	0.1655-0.0530i	0.1655+0.0530i
0.98	0.1692-0.0346i	0.1692-0.0346i
(*) 0.95	0.2119	0.1397
0.90	0.2609	0.1112
0.80	0.3285	0.0847
0.009185	0.7124	0.0258

(*) represents the selected poles and K_c

At all set point tracking applications studied in the present work, an initial step change from 0.969 to 0.978 was introduced. For the proposed discrete-time PI controller parameters identification the Kc value selected from Table 1 was used in Eq. (7). The coefficient of A in Eq. (9) was selected based on closed-loop pole placement technique by considering the three poles location and the ISE criteria (Table 2). For this selection, the controlled variable behaviors versus time were also examined (Figs. 2 to 4).

Table 2. Poles for the discrete system with PI controller

A	Three poles	ISE
1.70	0.3222±0.9953i, 0.0086+0.0000i	79.26
0.70	0.5155±0.6143i, 0.0331+0.0000i	1.41
0.40	0.5683±0.4124i, 0.0504+0.0000i	1.10
(*) 0.20	0.5987±0.1466i, 0.0716+0.0000i	1.08
0.18	0.6016±0.0735i, 0.0748+0.0000i	1.10
0.17	0.6527, 0.5529, 0.0764	1.11
0.16	0.7055, 0.5023, 0.0782	1.13
0.15	0.7400, 0.4700, 0.0800	1.14

The symbol (*) represents the selected A value according to ISE criteria. The values of K_c and T_s are 0.95 and 1 min respectively.

In cases studied (Table 2), with the proposed discrete-time PI controller, offset problem was not exist. However, the addition of the integral (I) action with A=1.7 (T_s=1.0 min, τ_I=0.28min) in the discrete controller that includes the previously chosen K_c value of 0.95 caused the oscillatory system response and increased the maximum deviation from the desired value (Fig. 2). The system response to a change in set point may exhibit less oscillatory behavior with tolerable rise time or non-oscillatory behavior with high rise time as A value decreases (τ_I value increases).

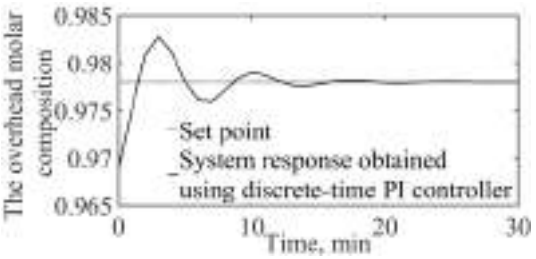

Fig. 2. The control of overhead product composition using the proposed discrete-time PI controller with T_s=1.0 min, Kc=0.95, τ_I=0.28min, A=1.7.

Fig.3 showed that the A value of 0.15 produced an overdamped response with high rise time of 8.8 min. The best response according to minimum ISE criteria and rise time of 3.7 min was shown in Fig. 4.

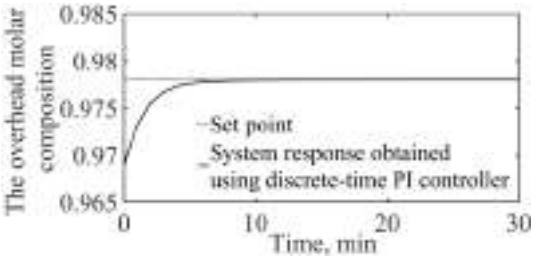

Fig. 3. The control of overhead product composition using the proposed discrete-time PI controller with T_s=1.0 min, K_c=0.95, τ_I=3.17min, A=0.15.

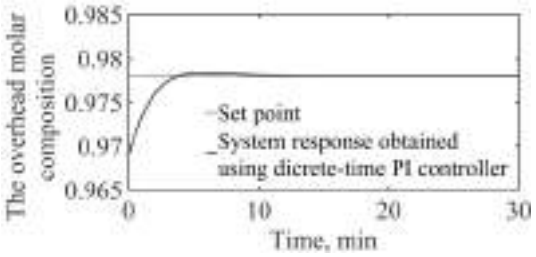

Fig. 4. The control of overhead product composition using the proposed discrete-time PI controller with T_s=1.0 min, K_c=0.95, τ_I=2.375min, A=0.2.

The discrete PID controller (2DOF) which is available in MATLAB/Simulink library was examined when applied to the overhead product composition control of the packed distillation column in the face of a set point change from 0.969 to 0.978. Its six tuning parameters were determined as P=0.009185, I=0.01835, D=0, N=100, b=1, c=1 using Simulink control design by using T_s of 1 min. It was noted that the PID controller given in Eq.(11) converted to the PI control action by substituting zero (D=0) for the last term. The overhead product composition set point tracking with this controller was shown in Fig. 5. This control action performance according to ISE criteria was evaluated as 15.89. This response with 169 min rise time exhibited sluggishness.

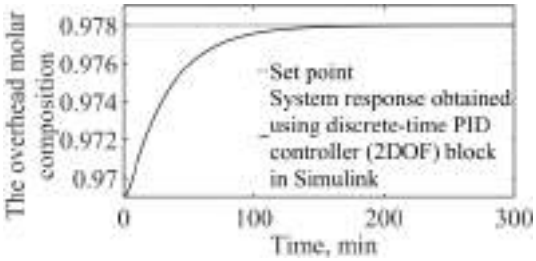

Fig. 5. The closed loop response of overhead product composition with the discrete-time PID controller (2DOF) that is available in MATLAB/ Simulink library.

By using T_s of 0.5 min and the system transfer function in Eq. (2), the discrete PID controller (2DOF) parameters were also determined as P=1.164, I=0.5319, D=-0.01481, N=3.783, b=0.1233, c=0.01017 using Simulink control design. The closed loop system response obtained was illustrated in Fig. 6. This set point tracking response obtained with the discrete PID controller (2DOF) performed with the ISE criteria of 3.68 and the rise time of 8 min. A decrease in T_s from 1 min to 0.5 min revealed 95.27 % and 76.84 % decreases in the ISE and in the rise time values respectively.

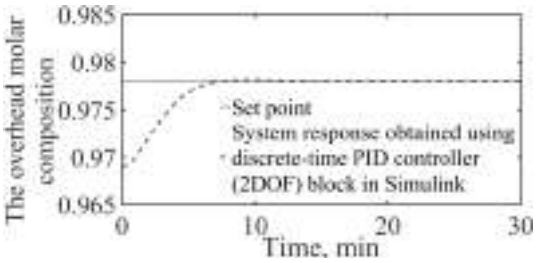

Fig. 6. The control of overhead product composition using the discrete-time PID controller (2DOF) Simulink block that its parameters tuned as P=1.164, I=0.5319, D=-0.01481, N=3.783, b=0.1233, c=0.01017.

4. CONCLUSION

Clearly the proposed discrete PI controller with the technique applied based on root locus search and pole-placement approach has a desired influence upon the set-point tracking performance of the overhead product composition of a packed distillation column. The discrete proposed PI controller exhibited much better performance than the one obtained using the discrete PID (2DOF) controller in MATLAB/Simulink library. This controller can be recommended for relatively high sampling time applications.

REFERENCES

Aldemir A. and Hapoğlu H. (2016). "Comparison of PID tuning methods for wireless temperature control." *Journal of Polytechnic*, Vol. 19, No. 1, pp. 9-19.

Altuntas S., Hapoglu H., Ertunc S., Alpbaz M. (2017). "Experimental Self-Tuning Proportional Integral Derivative pH Control: Application to a Bioprocess." *Acta Physica Polonica A*, Vol. 132, No. 3, pp. 1006-1009.

Camcioglu, S., Ozyurt, B., Dogan, İ. C., Hapoglu, H. (2017). "Application of response surface methodology as a new PID tuning method in an electrocoagulation process control case." *Water Science and Technology*, Vol. 76, No. 12, pp. 3410-3427.

Desyatirikova, E. N., Akimov V. I., Mager V. E., Chernenkaya L. V. (2019). "Selection of controller settings in digital control systems." *IEEE Conference of Russian Young Researchers in Electrical and Electronic Engineering*, EIConRus, IEEE, Saint Petersburg and Moscow, Russia, pp. 474-477.

Dincel, E. and Söylemez, M. T. (2018). "Digital PI-PD controller design for arbitrary order systems: Dominant pole placement approach." *ISA Transactions*, Vol. 79, pp. 189-201.

Hinkkanen, M., Awan, H. A. A., Qu, Z., Tuovinen, T., Briz F. (2016). "Current control for synchronous motor drives: direct discrete-time pole-placement design." *IEEE Transactions on Industry Applications*, Vol. 52, No. 2, pp. 1530-1541.

Khan, P. F., Sengottuvel, S., Patel, R., Gireesan, K., Baskaran, R., Mani, A. (2018). "Design and implementation of a discrete- time proportional integral (PI) controller for the Ttemperature control of a heating pad.", *Society for Laboratory Automation and Screening (SLAS) Technology*, Vol. 23, No. 6, 614-623.

Steiner, L., Barrendrenght H.P. and Harland S. (1978). "Concentration profiles in a packed distillation column." *Chemical Engineering Science*, Vol. 33, pp. 255-262.

Wardle, A. P. and Hapoglu, H. (1994). "On the solution of models of binary and multicomponent packed distillation columns using orthogonal collocation on finite elements." *Chemical Engineering Research and Design*, Vol. 72, pp. 551-564.

Wardle, A. P. and Hapoglu, H. (1993). "The self-tuning control of packed distillation columns." *Proceedings of the Twelfth IASTED International Conference Modelling, Identification and Control*, Acta Press, Zurich, Switzerland, pp. 431-434.

CISET - 2nd Cilicia International Symposium on Engineering and Technology
10-12 October, 2019, Mersin / TURKEY

TREND ANALYSIS AND MAPPING OF THE BLACK SEA REGION

Cavit Berkay YILMAZ[1], Vahdettin DEMİR [*2], and Mehmet Faik SEVİMLİ[3]

[1] KTO Karatay University, Civil Engineering Department, Konya, TURKEY, cavitberkayyilmaz@gmail.com

[2] KTO Karatay University, Civil Engineering Department, Konya, TURKEY, vahdettin.demir@karatay.edu.tr

[3] KTO Karatay University, Civil Engineering Department, Konya, TURKEY, mehmet.faik.sevimli@karatay.edu.tr

ABSTRACT
Black Sea region is the most precipitation region of Turkey. Thus, risk of the flood in region is the highest in all regions. Flood, landslide, extreme rains etc. heavily affects the life and production in the region. In this study 18 stations (Bartın-17020, Zonguldak-17022, Sinop-17026, Samsun-17030, Ordu-17033, Giresun-17034, Trabzon-17037, Rize-17040, Artvin-17045, Bolu-17070, Düzce-17072, Kastamonu-17074, Karabük-17078, Çorum-17084, Amasya-17085, Tokat-17086, Gümüşhane-17088, Bayburt-17089)belonging to Turkish State Meteorological Service. Annual total precipitation height (mm) data were analyzed between 1961 and 2015. As homogeneity test Run homogeneity test and for trend analysis Mann-Kendall Rank Correlation methods were used. Study was performed in 95% confidence interval and the obtained values were compared with critical value (± 1.96). As the results of the study carried out there are increasing trends in the East Black Sea Region except Bayburt station and in the Middle Black Sea Region there are increasing trends in Karabük, Sinop and Tokat stations.

Keywords: *Homogeneity, Mann-Kendall Rank Correlation Test, Run Test, Trend, Precipitation*

[*] vahdettin.demir@karatay.edu.tr

1. INTRODUCTION

Human activities have influenced the environment throughout the history. But before the industrial revolution, this effect was small enough to be neglected in the ecological cycle. After the industrial revolution, the rapid development of technology, increasing production and irregular urbanization has brought serious dangers after increasing expectations and needs. At the beginning of these dangers, depletion and even extinction or vice versa of the limited water resources is of utmost importance for the hydrology field, which is one of the basic building blocks of civil engineering, causing the precipitation to be affected globally and irreversibly on the climate levels. As a result of these changes, droughts and floods are increasing, causing the losses on existing products by affecting the production in the basic necessities of human beings such as agriculture and animal husbandry.

Partal (Partal, 2003), examined precipitation data of 96 stations across Turkey and detected Middle and Eastern Black Sea Region in decreasing trend. Özkoca (Özkoca, 2015), examined the hydrometeorological parameters of the Coastal Provinces of the Central Black Sea Region and found precipitation parameter is in decreasing trend in the inner parts compared to the stations near the sea. Çeribaşı (Çeribaşı, 2015), found in addition to the declining trend in the province of Karabük. Nemli (Nemli, 2017), examined the trend of the biggest precipitation intensities at standard times in his\her thesis which studied 10 meteorological stations in the Eastern Black Sea Region. It has determined the existence of an increasing trend across the region. Demir (Demir, 2018), In his\her thesis study, carried out trend analysis of precipitation data in the Black Sea Region and found an increasing trend in Eastern and Middle Black Sea Region and decreasing trend in Western Black Sea Region. Saplıoğlu (Saplıoğlu, 2013), annual total precipitation data of 80 provinces across Turkey and determined increasing trends in 8 provinces and 10% increase in the near century.

In this study 18 stations have been examined. 2 types of tests were applied these tests are Run Test as homogeneity test and Mann-Kendall Rank Correlation test as trend test. Results of these tests have been compared to critical value of 95% confidence interval (± 1.96)..

2. DATA WORKSPACE

The Black Sea Region is the most precipitation region of Turkey. Most of the precipitation in Autumn season and the least precipitation in the Spring season. The flora of the Black Sea Region is generally composed of forests and alpine meadows are seen above the tree growth border. Maximum annual total precipitation was recorded in Giresun station as “521.60” mm and the minimum annual total precipitation was recorded in Bartın, Zonguldak, Sinop, Samsun, Bolu, Karabük, Çorum, Amasya, Tokat, Gümüşhane and Bayburt stations as “0” mm. Location information for stations is shown in Table 1.

Table 1. Information about stations used in this study.

Station Name	Latitude (°N)	Longitude (°W)	Altitude (m)
Bartın	41.62	32.35	30
Zonguldak	41.45	31.77	1301
Sinop	42.02	35.15	32
Samsun	41.35	36.24	4
Ordu	40.98	37.88	5
Giresun	40.92	38.39	37
Trabzon	41.00	39.78	39
Rize	41.04	40.50	9
Artvin	41.18	41.82	628
Bolu	40.74	31.60	743
Düzce	40.84	31.14	146
Kastamonu	41.37	33.77	800
Karabük	41.20	32.62	259
Çorum	40.54	34.94	776
Amasya	40.65	35.83	412
Tokat	40.30	36.56	608
Gümüşhane	40.46	39.47	1219
Bayburt	40.25	40.43	1584

Fig. 1. Eighteen stations in Black Sea Region

3. METHODS AND APPLICATIONS

There are number of parametric and non-parametric methods have been developed to test the homogeneity and trend status of the time series. In parametric tests, factors such as location and continuity of the data are important. In parametric tests, data is evaluated by its place in time series. In non-parametric methods, the place of data in series and continuity of series are not important. The non-parametric Run Homogeneity Test was used as a homogeneity test. In addition, the Mann-Kendall Rank Correlation Test which is non-parametric test can determine the start of the trend, was used as a trend test.

3.1. Run Homogenity Test

Within the scope of this test, two assumptions can be checked that the data is dependent and independent. As a result of this test, two hypotheses of hypothesis are accepted (H0 hypothesis, H1 hypothesis) (Oliver, 1981). These hypotheses are:

H0 Hypothesis: Assumes that the data is homogeneous and the data group is independent of each other.

H1 Hypothesis: Assumes that the data is not homogeneous and the data is not independent from each other.

When the run test is applied, the median value of the data group is calculated and the size of data is checked according to the median value. The sum of the change between the values that are larger or smaller than the median value is called the run sequence number (Toros, 2011).

$$Z = \frac{r - \frac{2 \cdot N_a \cdot N_b}{(N_a + N_b)}}{\sqrt{\frac{2 \cdot N_a \cdot N_b \cdot (2 \cdot N_a \cdot N_b - N)}{N^2 \cdot (N-1)}}} \quad (1)$$

In this formula Na represents values less than median value, Nb represents values bigger than median value.

3.2. Mann-Kendall Rank Correlation Test

With the help of this test, if there is a trend in the time series, starting year of the trend and increase or decrease due to time can be found with graphs. Instead of the values, ranks of the values and values of u(t) and u'(t) are used. While examining the results of the test ± 1.96 corresponding to 95% confidence interval has been used. "t" refers to sum of ranks before the rank of value. Var(t) refers to the variance of the series. The Mann-Kendall Rank Correlation Test is calculated with the help of the following formula. "n" represents ranks of the values (Büyükyıldız et al., 2004).

$$t = \sum_{i=1}^{n} n_i \quad (2)$$

$$E(t) = \frac{n \cdot (n-1)}{4} \quad (3)$$

$$Var(t) = \frac{n \cdot (n-1) \cdot (2 \cdot n+5)}{72} \quad (4)$$

$$u(t) = \frac{t - E(t)}{\sqrt{Var(t)}} \quad (5)$$

$$u'(t) = \frac{E(t) - t}{\sqrt{Var(t)}} \quad (6)$$

3.3. Application

First Run test has been applied to data then, Mann-Kendall Rank Correlation test is applied and the result of each station checked for the trend. Analysis results are shown in Table 2.

Table 2. Information about stations used in this study.

Station Name	Station No.	Run Test Results "Z"	MK-RC Results "u(t)"
Bartın	17020	1.84	0.28
Zonguldak	17022	1.10	-0.62
Sinop	17026	**-2.04**	**2.11**
Samsun	17030	-1.12	1.20
Ordu	17033	0.14	1.44
Giresun	17034	0.96	**3.01**
Trabzon	17037	0.00	**3.42**
Rize	17040	0.41	**2.04**
Artvin	17045	-0.13	**2.05**
Bolu	17070	1.14	0.31
Düzce	17072	0.86	-1.51
Kastamonu	17074	0.14	1.58
Karabük	17078	-1.19	**2.72**
Çorum	17084	1.49	-0.01
Amasya	17085	-0.16	1.17
Tokat	17086	-0.15	**2.18**
Gümüşhane	17088	0.00	1.62
Bayburt	17089	-1.17	**2.60**

When Table 2 examine maximum increasing trend found in Trabzon as 3.42 and maximum decreasing trend found in Düzce station. According to Run test results only Sinop station was found to be non-homogenic and H0 hypothesis rejected.

4. TREND AND HOMOGENEİTY MAPS

The trend analysis results obtained from Mann-Kendall Rank Correlation test were transferred to ArcGIS software and the results were expressed visually.

According to the annual data, there has been an increasing trend in Karabük, Sinop, Tokat, Giresun, Bayburt, Trabzon, Rize and Artvin stations. More information about the stations is shown at Fig.2 and Fig.3.

Fig. 2. Run Test results on a map plane.

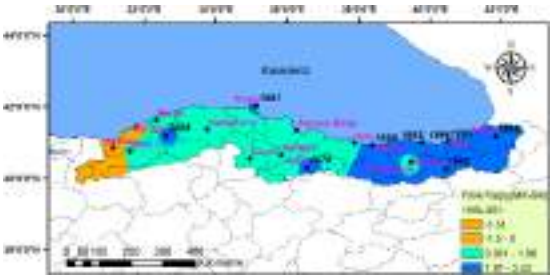

Fig. 3. MK-RC Test results on a map plane.

5. RESULTS

u(t) values obtained from Mann-Kendall Rank Correlation test were transferred to ArcGIS environment and the results were checked for the trend starting points in the time line between 1961-2015 after this control trend starting points for each station were found and transferred to the ArcGIS environment. Trend starting points for each station are in Trabzon 1992 and 1996, in Sinop 1997, in Giresun 1999, in Rize 1995, in Artvin 1986, in Karabük 2008, in Tokat 1978, in Bayburt 1985. In this study the Inverse Distance Weight method (IDW), which is used to map the results of the analysis, is basically referred as Shepard's method and can be calculated with formulas at (7) and (8) (Shephard, 1968).

$$F(x,y) = \sum_{i=1}^{n} w_i f_i \quad (7)$$

$$w_i = \frac{h_i^{-p}}{\sum_{i=1}^{n} h_i^{-p}} \quad (8)$$

In the formulas at (7) and (8) "p" references force parameter, "h_i" references identifies the spatial distance between the pointes of the sample and the interpolated points, "w_i" references weights and sum of the values must be 1.

6. CONCLUSION

In this study 18 stations belonging to Turkish State Meteorological Service were examined. Annual total precipitation height (mm) data were examined between 1961 and 2015. As homogeneity test Run homogeneity test and for trend analysis Mann-Kendall Rank Correlation methods were used. Study was performed in 95% confidence interval and the obtained values were compared with critical value (± 1.96).

When the results were evaluated for the whole region, Run test results indicate that the data found to be 94.44% ((17/18)x100) homogeneous. Only Sinop station was not homogeneous. There are increasing trends in the East Black Sea Region except Bayburt station and in the Middle Black Sea Region there are increasing trends in Karabük, Sinop and Tokat stations. Statistically significant trend was not detected in other stations.

REFERENCES

Büyükyıldız M. and Berktay A. (2004). "Parametrik olmayan testler kullanılarak sakarya havzası yağışlarının trend analizi" Selçuk Üniversitesi Mühendislik Mimarlık Fakültesi Dergisi Vol.19, No. 2, pp. 24-38.

Çeribaşı, G. (2015). Karadeniz ve Sakarya havzalarında yağış-akış-askıda katı madde verilerinin trend analizi ile incelenmesi. PhD Thesis. T.C. Sakarya Üniversitesi. Sakarya, Türkiye.

Demir, V. (2018). Karadeniz Bölgesi yağışlarının trend analizi, PhD Thesis. T.C Ondokuz Mayıs Üniversitesi. Samsun, Türkiye.

Hüseyin Toros. T.C İstanbul Teknik Üniversitesi Meteoroloji Mühendisliği Bölümü. https://web.itu.edu.tr/toros/uygulamalar/. [Erişim Tarihi : 23 Mayıs 2019]

Karadeniz İklimi Nedir? http://karadeniz-iklimi.nedir.org/ [Erişim Tarihi : 23 Mayıs 2019]

Nemli, M. Ö. (2017). Doğu Karadeniz Bölgesi'nde yıllık maksimum yağışların trend analizi, PhD Thesis. T.C Karadeniz Teknik Üniversitesi. Trabzon, Türkiye.

Özkoca, T. (2015). Orta Karadeniz Bölgesi kıyı illerinin hidrometeorolojik parametrelerinin trend analizi, PhD Thesis. T.C. Ondokuz Mayıs Üniversitesi. Samsun, Türkiye.

Oliver, R. L. (1981). "Measurement and evaluation of satisfaction processes in retail settings". *Journal of Retailing*, Vol. 57, No. 3, pp. 25–48.

Partal, T. (2003). Türkiye yağış verilerinin trend analizi, PhD Thesis. T.C İstanbul Teknik Üniversitesi. İstanbul, Türkiye.

Saplıoğlu K. (2013). "Karadeniz bölgesi yağış Serilerinin trend analizi" *VII. Ulusal Hidroloji Kongresi*, Isparta, Türkiye pp. 500-512.

Toros, H. (2011), "Spatio- temporal precipitation change assessments over Turkey." *International Journal of Climatology*, Vol. 32, pp. 1310 – 1325.

Shepard, D. (1968). "A two-dimensional interpolation function for irregularly spaced data." *Proceedings of the 1968 23rd ACM National Conference*, New York, USA pp. 517–524.

CISET - 2nd Cilicia International Symposium on Engineering and Technology
10-12 October, 2019, Mersin / TURKEY

LONG-TERM MONTH TEMPERATURE FORECAST WITH INVERSE DISTANCES WEIGHTED, KRIGING AND ARTIFICIAL NEURAL NETWORKS

Vahdettin DEMİR*[1], Esra Aslı ÇUBUKÇU[2] and Mehmet Faik SEVİMLİ[3]

[1] KTO Karatay University, Engineering Faculty, Department of Civil Engineering, Konya, Turkey, vahdettin.demir@karatay.edu.tr

[2] KTO Karatay University, Engineering Faculty, Department of Civil Engineering, Konya, Turkey, cubukcuasli@gmail.com

[3] KTO Karatay University, Engineering Faculty, Department of Civil Engineering, Konya, Turkey, mehmet.faik.sevimli@karatay.edu.tr

ABSTRACT
In this study, spatial distribution maps of long-term average temperature in Turkey have been prepared with Geographic Information Systems (GIS). Artificial Neural Networks (ANN), Inverse Distances Weighted (IDW), and Kriging interpolation methods were used to obtain the maps. In total, 75% (60 stations) of the 81 provincial central stations were used during the training phase and the remaining 25% (21 stations) were used during the testing phase of the interpolation maps. Accuracy analysis of the maps were performed by using Root Mean Square Error (RMSE), Mean Absolute Error (MAE) and Determination Coefficient (R^2). As a result of the analysis, ANN was found to be more suitable than IDW and Kriging methods. In addition, IDW results better predict long term temperatures than Kriging interpolation method. As a result, spatial distribution of ANN at long term temperature can be used and found to be an alternative method.

Keywords: *Forecast, Temperature, Turkey, Artificial Neural Network, Inverse Distances Weighted, Kriging Interpolation*

* Corresponding Author

1. INTRODUCTION

Human, from the very first moment, has been an entity that influences the natural balance of the world. Although this effect did not show great changes in the balance of the world at first, the industrial revolution, increase in population and the damage caused to the environment by mechanization increase the accumulation of greenhouse gases in the world. With this greenhouse gas accumulation, the atmosphere heats up, global climate change, global environmental interaction and ultraviolet radiation increase, stratospheric ozone decreases. In 1987, the United Nations, (Anonymous, 2019), held a meeting with the World Meteorological Organization on the subject, but how the global climate change and distribution will affect the world is not fully understood (Çelik, et. al., 2008). In the reports prepared at the International Climate Change Conference in 1990 (Anonymous, 2019), countries were advised on global warming and climate change. These advise suggested that the world's average temperature will rise by an average of 3 ° C in 40 years from 1990 onwards. In addition, in the report with the rise in temperature, the glaciers melt and rise in sea level, while sudden and extreme effects (storms, floods) can be seen in weather even (Çelik et al., 2008).

The main causes of climate change are solar reflections, earth's trajectory, atmospheric components, albedo properties of the atmosphere, volcanic ash, cloud cover factors. These factors increase the greenhouse effect together or alone. Nowadays, as a result of this change, climate change process has started and the increase in temperature gradually increases in the long period.

Global climate change has similar results in our country. Sudden and severe rains and consequent floods, collapse of urban infrastructure, and the increase in the frequency of hot weather events have become influential on daily life. General Directorate of Meteorology in 2010 and 2012. 'Assessment of Climate Data in the report' Turkey has also been shown to be affected by this process (Algedik, 2013). The report, which evaluates 2010, reveals that 2010 was 2.38 ° C hotter than 12.81 ° C, which was the 1970-2000 norms. According to the current meteorological data, the report determines that all of the hottest 10 years took place between 1998 and 2010 (Algedik, 2013).

The Kriging method is an interpolation method that estimates the values of data at other points using data from known nearby points. The most important feature that distinguishes Kriging from other interpolation methods is that the variance value can be calculated for each predicted point. The Inverse Distance Weighting (IDW) method is an interpolation method used to determine the values of non-sampled points with the help of values from known sample points. The predicted values are a function of the distance and the size of the neighboring points, and as the distance increases, the importance and effect on the points to be estimated decreases. Artificial Neural Networks (ANN) is an information processing technology inspired by the information processing technique of the human brain. ANN simulates the way the biological nervous system works. The imitated nerve cells contain neurons and these neurons connect to each other in various ways to form the network. These networks have the capacity to reveal the relationship between learning, storing and data (Erkaymaz et. al., 2011). In other words, ANNs provide solutions to problems that require human's natural abilities to think and observe (K. Papik et al., 1998). The main reason why a person can produce solutions to these problems is the ability of the human brain and therefore the ability to learn by experiencing and experiencing. ANNs are mathematical systems consisting of several processing units (neurons) connected to each other in a weighted manner (Tekkanat et al.,, 2015).

In this study Turkey's long-term monthly temperatures was estimated Artificial Neural Networks (ANN), Inverse Distances Weighted (IDW) and Kriging was estimated using interpolation methods. Monthly average temperature data of the measurement stations in the centers of 81 provinces between 1981 and 2010 were used. Latitude, longitude, altitude and periodicity were used as input data. Periodicity only was used ANN.

2. MATERIAL and METHOD

2.1. Material

Turkey, 36 ° - 42 ° north latitude and 26 ° - 45 ° East is situated between meridians. Since our country, which is surrounded by seas on 3 sides, is located in the Eastern Mediterranean Basin, it is among the risky countries that will be heavily affected by global climate change and warming (Yıldırım and Gürkan, 2016). Long-term monthly average temperature data were recorded by the monitoring stations of the General Directorate of Meteorology (GDM). The data was obtained from GDM's https://www.mgm.gov.tr/veridegerlendirme/il-ve-ilceler-istatistik.aspx?k=H website. The locations of the stations used are given in Figure 1 and Figure 2. 25% of the stations were used in the test and 75% were used training phase. The statistical information of the stations is given in Table 1.

Fig. 1. Study area and training stations

Fig. 2. Study area and test stations

Table 1. Summary of the geographical information of the studied weather stations

Station name	Latitude (ºN)	Longitude (ºE)	T(ºC)	Station name	Latitude (ºN)	Longitude (ºE)	T(ºC)
Adana	37.00	35.32	19.2	Konya	37.99	32.56	11.6
Adıyaman	37.76	38.27	17.3	Kütahya	39.42	29.99	10.9
Afyon	38.74	30.55	11.4	Malatya	38.35	38.31	13.9
Ağrı	39.72	43.05	6.4	Manisa	38.61	27.40	17.1
Amasya	40.65	35.83	13.7	K.maraş	37.57	36.91	16.9
Ankara	39.97	32.86	12.1	Mardin	37.31	40.73	16.3
Antalya	36.90	30.79	18.4	Muğla	37.29	28.37	15.1
Artvin	41.18	41.82	12.1	Muş	38.74	41.49	9.9
Aydın	37.84	27.84	17.8	Nevşehir	38.63	34.71	10.7
Balıkesir	39.63	27.92	14.6	Niğde	37.97	34.69	11.3
Bilecik	40.14	29.97	12.6	Ordu	40.98	37.88	14.4
Bingöl	38.88	40.49	11.9	Rize	41.04	40.50	14.4
Bitlis	38.39	42.12	9.6	Sakarya	40.77	30.39	14.6
Bolu	40.74	31.60	10.7	Samsun	41.35	36.24	14.5
Burdur	37.68	30.33	13.3	Siirt	37.93	41.94	16.2
Bursa	40.23	29.01	14.7	Sinop	42.02	35.15	14.2
Çanakkale	40.15	26.41	15.2	Sivas	39.74	37.02	9.2
Çankırı	40.61	33.61	11.3	Tekirdağ	40.99	27.49	14.1
Çorum	40.54	34.94	10.7	Tokat	40.30	36.56	12.5
Denizli	37.76	29.09	16.5	Karabük	41.20	32.62	13.3
Diyarbakır	37.92	40.22	15.7	Kilis	36.72	37.12	17.2
Edirne	41.68	26.56	13.8	Osmaniye	37.10	36.25	18.3
Elazığ	38.67	39.22	13.1	Düzce	40.84	31.15	13.3
Erzincan	39.74	39.50	11	Trabzon*	41.00	39.78	14.7
Erzurum	39.95	41.17	5.2	Tunceli*	39.10	39.55	12.9
Eskişehir	39.78	30.58	10.8	Şanlıurfa*	37.16	38.79	18.5
Gaziantep	37.07	37.39	15.3	Uşak*	38.67	29.40	12.7
Giresun	40.92	38.39	14.5	Van*	38.49	43.39	9.5
Gümüşhane	40.46	39.47	9.6	Yozgat*	39.82	34.81	9.1
Hakkari	37.57	43.75	10.3	Zonguldak*	41.45	31.78	13.6
Hatay	36.36	36.28	18.4	Aksaray*	38.37	34.03	12.2
Isparta	37.76	30.55	12.2	Bayburt*	40.25	40.43	7.1
Mersin	36.80	34.62	19.6	Karaman*	37.17	33.22	12
İstanbul	40.98	28.82	13.9	Kırıkkale*	39.85	33.51	12.7
İzmir	38.41	27.14	18.1	Batman*	37.89	41.12	16.7
Kars	40.59	43.08	5	Şırnak*	37.52	42.45	14.7
Kastamonu	41.37	33.77	9.8	Bartın*	41.62	32.35	12.7
Kayseri	38.72	35.49	10.7	Ardahan*	41.11	42.70	3.9
Kırklareli	41.73	27.21	13.3	Iğdır*	39.92	44.06	12.3
Kırşehir	39.16	34.15	11.5	Yalova*	40.66	29.27	14.8
Kocaeli	40.76	29.91	14.8	-	-	-	-

* Test Stations

2.2. Methods

2.2.1. Radial Based Artificial Neural Networks

Radial-Based ANN (RBANN) concept was introduced into the literature in 1988 by Broomhead and Lave. ANN model and Radial-based functions have been developed by considering the effect-response states of neuron cells in human nervous system (Okkan et al., 2012). It is possible to see the education of RBANN models as a curve fitting approach in multidimensional space (Partal et al.,, 2008; Poggio et al.,, 1990). Thus, the educational performance of the RBANN sample turns into a problem of finding the closest result to the data in the output vector space and thus an interpolation problem (Okkan et al., 2012). RBANN structure generally consists of input layer, hidden layer and output layer similar to ANN structure. However, unlike other ANNs, the data is subjected to radial based activation functions and a nonlinear cluster analysis when passing from the input layer to the hidden layer. The structure between the hidden layer and the output layer functions as in other ANN types and the actual training takes place in this layer. In the RBANN model we used, the problem was solved with purelin function.

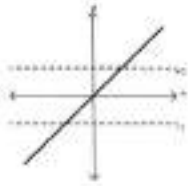

Fig. 2. a = n (Purelin function, Linear Transfer Function)

2.2.2. Inverse Distances Weighted

Inverse Distance Weighted (IDW) is one of the most preferred non-geostatistics methods. This method is an interpolation technique used to determine the cell values of unknown points using the values of known sample points. Since it produces estimates only from neighboring points, it makes a local intermediate value estimation. The method is based on the fact that the nearby points have a greater weight on the surface to be interpolated than the distant points. The cell value is calculated by observing the various points moving away from the cell of interest and depending on the increase in distance. The predicted values are a function of the distance and the size of the points in the neighboring neighborhood, and as the distance increases, the importance and effect on the cell to be estimated decreases (Kazancı et al., 2014, Taylan et al., 2016).

$$F(x,y)=\sum_{i=1}^{n} w_i f_i \qquad (1)$$

$$w_i=\frac{h_i^{-p}}{\sum_{j=1}^{n} h^{-p}{}_i} \qquad (2)$$

The weights used to estimate the function are expressed as any exponent of the distance in inverse proportion to the distance.

In the equations 1-2;
p; known as force parameter and show exponent,
h_i;spatial distance between sample points and interpolated points,
w_i; Weights are doing and the sum of the values must be 1.
f_i= known altitude values

2.2.3. Kriging Method

The kriging method is an interpolation method that estimates the optimum values of data at other points using data from known nearby points. The most important feature that distinguishes Kriging from other methods is that a variance value can be calculated for each estimated point or area. This is a measure of the reliability of the predicted value (Yaprak et al., 2008).

The estimation by the Kriging interpolation method has two stages: (i) adaptation to a model: creation of variograms and covariance functions, this is based on the autocorrelation model and (ii) estimation: estimation of the unknown (Öztürk et al., 2016).

General equality used in kriging;

$$N_p=\sum_{i=1}^{n} P_i * N_i \qquad (3)$$

Where;
n = number of points in the model,
N_i = N_p, The geoid undulation values used in the calculation of
N_p = The required undulation value
P_i = The weight values for each N_i value used in the calculation of N_i.
Kriging technique provides more objective results than other estimation techniques and also gives minimum variance and standard deviation of estimation.

3. APLICATIONS

Root Mean Square Error (RMSE), Mean Absolute Error (MAE) and determination coefficient (R^2) were used as comparison criteria. The formulas of the criteria are given in the equations 4 - 6.

$$RMSE=\sqrt{\frac{1}{N}\sum_{i=1}^{N}(T_o-T_e)^2} \qquad (4)$$

$$MAE=\frac{1}{N}\sum_{i=1}^{N}\left|T_o-T_e\right| \qquad (5)$$

$$R^2=\left(\frac{N*\left(\sum T_o*T_e\right)-\left(\sum T_o\right)*\left(\sum T_e\right)}{\sqrt{\left(N*\sum T_o^2\right)-\left(\sum T_o\right)^2*\left(N*\sum T_e^2\right)-\left(\sum T_e\right)^2}}\right)^2 \qquad (6)$$

In the equations, "T_e" and "T_o" show the estimated and observed temperature values and "N" represents the number of data.

Table 2. Summary of the training and test results of the RBANN, IDW and Kriging models

Model/ criterion	RBANN	IDW	Kriging
RMSE	2.675	2.816	3.098
MAE	1.992	2.275	2.417
R^2	0.910	0.915	0.892

When the table is examined, it is seen that MAE value and RMSE values are higher, although R^2 value is higher in IDW method. therefore, the RBANN method, which has both the highest R^2 value and lower error rates, appears to be the best performing method.

4 different inputs were used in the RBANN method. Latitude and longitude inputs of the stations were used in 2 entrances. When the 2-input application results were examined, R^2 low error values were high. However, when we add the height as the 3th entry and the periodicity as the 4th entry, we see that the results have improved. The most effective input can be said to be periodicity which is the 4th input.

Table 3. RBANN test results

Stations	RBANN		
	RMSE (°C)	*MAE(°C)*	*R^2*
Trabzon	5.31	4.60	0.974
Tunceli	1.45	1.14	0.990
Şanlıurfa	2.25	1.95	0.990
Uşak	1.53	1.30	0.990
Van	0.79	0.69	0.993
Yozgat	4.77	4.72	0.991
Zonguldak	1.38	1.12	0.986
Aksaray	0.94	0.76	0.993
Bayburt	3.30	3.10	0.985
Karaman	4.76	4.65	0.991
Kırıkkale	1.04	0.87	0.991
Batman	2.51	2.15	0.982
Şırnak	3.74	3.60	0.990
Bartın	0.89	0.76	0.990
Ardahan	3.93	3.49	0.973
Iğdır	2.21	1.72	0.966
Yalova	0.84	0.60	0.994
Karabük	0.92	0.75	0.988
Kilis	0.98	0.70	0.992
Osmaniye	2.61	2.25	0.989
Düzce	1.08	0.93	0.994

Table 4. IDW test results

Stations	IDW		
	RMSE (°C)	*MAE(°C)*	*R^2*
Trabzon	3.87	3.40	0.951
Tunceli	1.94	1.08	0.979
Şanlıurfa	3.78	3.56	0.984
Uşak	1.53	1.25	0.970
Van	1.46	1.30	0.981
Yozgat	2.20	2.18	0.977
Zonguldak	2.72	2.21	0.951
Aksaray	1.56	0.89	0.972
Bayburt	3.67	3.50	0.982
Karaman	2.07	1.91	0.981
Kırıkkale	2.16	1.57	0.978
Batman	3.93	3.67	0.980
Şırnak	2.90	2.47	0.975
Bartın	1.85	1.38	0.975
Ardahan	4.31	4.04	0.984
Iğdır	4.81	4.39	0.961
Yalova	1.67	1.28	0.972
Karabük	2.57	2.20	0.970
Kilis	1.97	1.68	0.983
Osmaniye	2.41	2.14	0.978
Düzce	1.96	1.68	0.977

Table 5. Kriging test results

Stations	Kriging		
	RMSE (°C)	*MAE(°C)*	*R^2*
Trabzon	3.81	3.29	0.936
Tunceli	2.15	1.20	0.967
Şanlıurfa	4.19	3.47	0.937
Uşak	1.74	1.47	0.958
Van	1.81	1.50	0.971
Yozgat	2.35	2.32	0.961
Zonguldak	2.84	2.24	0.937
Aksaray	1.40	0.98	0.975
Bayburt	3.82	3.65	0.975
Karaman	2.77	2.59	0.954
Kırıkkale	2.39	1.64	0.960
Batman	4.53	3.90	0.947
Şırnak	3.84	3.05	0.945
Bartın	1.76	1.33	0.945
Ardahan	4.73	4.42	0.978
Iğdır	4.55	4.13	0.964
Yalova	2.15	1.55	0.950
Karabük	2.55	2.16	0.969
Kilis	2.64	1.60	0.932
Osmaniye	3.39	2.71	0.928
Düzce	1.98	1.58	0.968

4. CONCLUSION

Our world is increasingly exposed to climate change and global warming. While our world is being more and more affected by climate change, the importance of accurate weather detection is increasing day by day. More than one-third of the world economy is affected by changes in weather conditions, while the importance of accurate weather detection is increasing. The right temperature detection combined with the right measures prevent both loss of life and ensure that the country's economy survives air disasters with minimum damage.

In this study Turkey's long-term monthly temperatures RBANN, IDW and Kriging was estimated using interpolation methods. Monthly average temperature data of the measurement stations in the centers of 81 provinces between 1981 and 2010 were used. We used latitude, longitude, altitude and periodicity input data in ANN application. In other applications only latitude and longitude data were used. Training and test stations were randomly selected. The training data covers 75% of all data and the test covers 25%.

When the results are examined;

- Estimates of all methods appear to be acceptable accuracy.
- When compare the R^2, the best predicting methods are RBANN, IDW and Kriking, respectively. In addition, the error rates show that RBANN is the best method for both RMSE and MAE.
- The periodicity of the most influential entry in RBANN also appeared in the results.
- As a result, spatial distribution of ANN at long term temperature can be used and found to be an alternative method.

REFERENCES

Algedik, Ö. (2013). ‘‘İklim Değişikliği Eylem Planı Değerlendirme Raporu’’, access address: https://tr.boell.org/sites/default/files/tipig_idep_raporu.pdf (Accessed: 14.05.2019).

Anonymous. (2019). ‘‘Report of the World Commission on Environment and Development: Our Common Future’’ access address : https://sustainabledevelopment.un.org/content/documents/5987our-common-future.pdf (Accessed: 02.08.2019).

Çelik, S., Bacanlı, H., Görgeç, H. (2008). ‘‘Küresel İklim Değişikliği ve İnsan Sağlığına Etkileri’’, access address : https://www.mgm.gov.tr/FILES/genel/saglik/iklimdegisikligi/kureseliklimdegisikligietkileri.pdf (Accessed: 14.05.2019).

Erkaymaz, H., and Yaşar, Ö. (2011). ‘‘Approximation Air Temperature With Artificial Neural Network’’, *International Computer & Instructional Technologies Symposium*. Elazığ, Türkiye.

Okkan, U. and Dalkılıç, H. Y. (2012). ‘‘Radyal Tabanlı Yapay Sinir Ağları ile Kemer Barajı Aylık Akımlarının Modellenmesi’’, *İMO Teknik Dergi*, pp. 5957–5966.

Ozturk, D., and Kılıç, F. (2016). ‘‘Geostatistical Approach for Spatial Interpolation of Meteorological Data. ’’ *Annals of the Brazilian Academy of Sciences,* 88(4), pp. 2121–2136.

Papik, K., Molnar, B., Schaefer, R., Dombovari, Z., Tulassay, Z., & Feher, J. (1998). Application of neural networks in medicine - A review. *Medical Science Monitor*, *4*(3), pp. 538–546.

Papik, K., Molnar, B., Schaefer, R., Dombovari, Z., Tulassay, Z., Feher, J. (1998). ‘‘Application Of Neural Networks In Medicine ’’, *Diagnostics and Medical Technology*, 4(3), pp. 538–546..

Partal, T., Kahya, E., Cığızoğlu, K. (2008). ‘‘Yağış Verilerinin Yapay Sinir Ağları ve Dalgacık Dönüşümü Yöntemleri ile Tahmini’’, *İtü Mühendislik Dergisi,* 7(3), pp. 73–85.

Poggio, T., and Girosi, F. (1990). ‘‘Regularization Algorithms for Learning That Are Equivalent to Multilayer Networks’’, *Science,* 247(4945), pp. 978–982.

Taylan, E. D., and Damçayırı, D. (2016). ‘‘Isparta Bölgesi Yağış Değerlerinin IDW ve Kriging Enterpolasyon Yöntemleri ile Tahmini.’’ *İmo Teknik Dergi*, pp. 7551–7560.

Tekkanat, İ. S., and Sarış, F. (2015). ‘‘Porsuk Çayı Havzasında Akarsu Akımlarında Gözlenen Uzun Dönemli Eğilimler’’, *Türk Coğrafya Dergisi,* 64, pp. 69–83.

Yaprak, S., and Arslan, E. (2008). ‘‘Kriging Yöntemi ve Geoit Yüksekliklerinin Enterpolasyonu’’, *Jeodezi, Jeinformasyon ve Arazi Yönetimi Dergisi*, 1(98) pp. 36–42.

EK-1

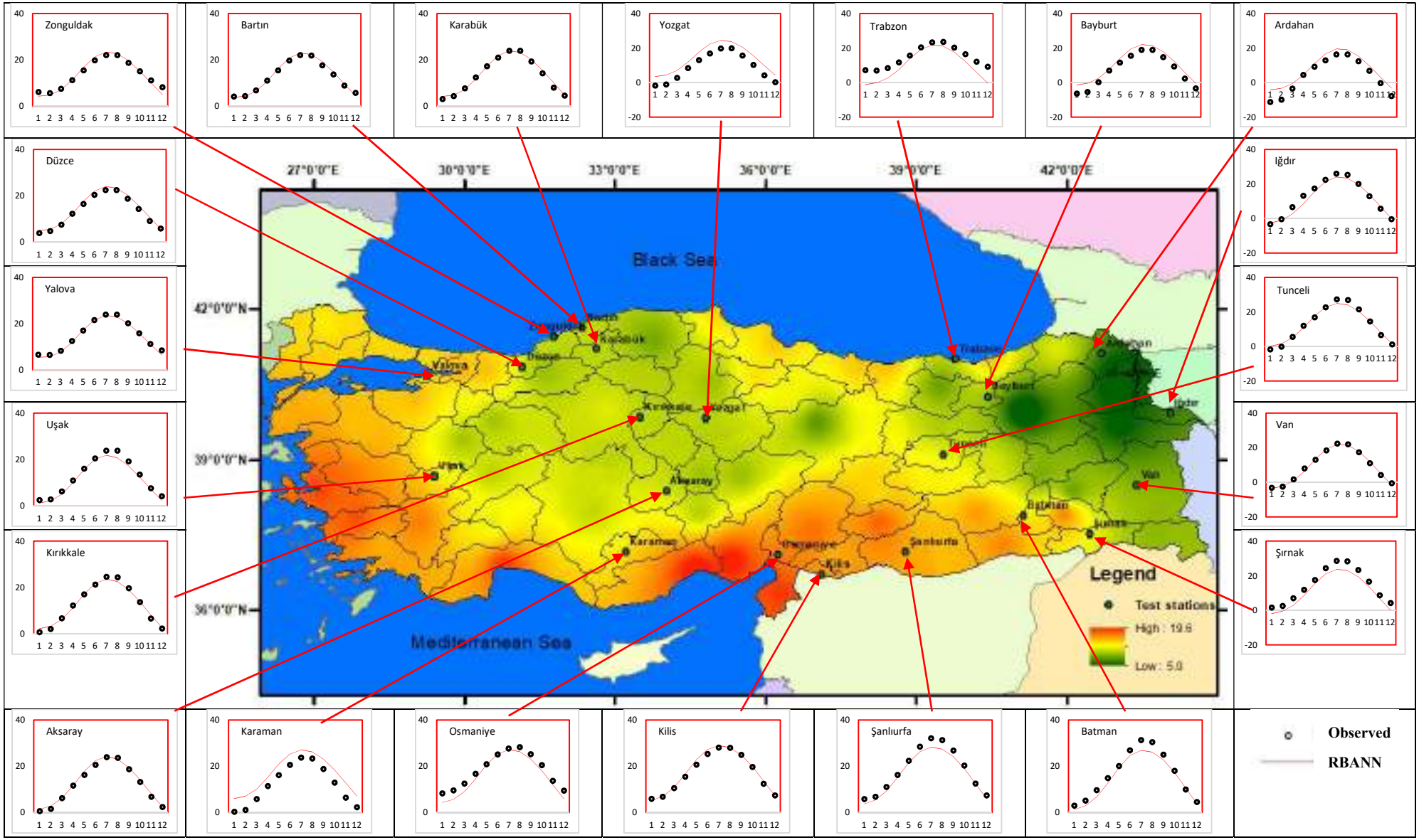
Zonguldak
Bartın
Karabük
Yozgat
Trabzon
Bayburt
Ardahan
Düzce
Iğdır
Yalova
Tunceli
Uşak
Van
Kırıkkale
Şırnak
Aksaray
Karaman
Osmaniye
Kilis
Şanlıurfa
Batman
Observed
RBANN
Black Sea
Mediterranean Sea
Legend
Test stations
High : 19.6
Low : 5.0
27°0'0"E
30°0'0"E
33°0'0"E
36°0'0"E
39°0'0"E
42°0'0"E
42°0'0"N
39°0'0"N
36°0'0"N

ECOSYSTEMS AS RESERVOIRS OF ANTIBIOTIC-RESISTANT BACTERIA

Lyudmyla Symochko[1]*, Hosam E.A.F. Bayoumi Hamuda[2] , Olena Demyanyuk[3], Hysen Mankolli[4], Sukru Dursun[5], Dr.Vitaliy Symochko[1]

[1] Faculty of Biology; SR&E Center of Molecular Microbiology and the Immunology of Mucous Membranes, Uzhhorod National University, Voloshyna Str. 32, 88000, Uzhhorod, Ukraine; Email: lyudmilassem@gmail.com

[2] Obuda University, Budapest, Hungary; Email: bayoumi.hosam@rkk.uni-obuda.hu

[3] Institute of Agroecology and Environmental Management, Kyiv, Ukraine; Email: demolena@ukr.net.

[4]Expert in Ecology, Plainfield, Illinois, USA; Consultant Scientific Earth System Science Interdisciplinary Center (ESSIC), University of Maryland College Park, USA; E-mail: hysenmankolli@yahoo.com;

[5]Head of Environmental Engineering Science Department, Engineering and Natural Science Faculty, Konya Technical University, Konya, Turkey; E-mail: sdursun@ktun.edu.tr;

ABSTRACT
Terrestrial ecosystems may provide an ideal setting for the acquisition and dissemination of antibiotic resistance, because they are frequently impacted by anthropogenic activities. The soil microbiome plays an important role in development and spread of antibiotic resistance in humans. The aim of our study was to detect the antibiotic resistance soil bacteria in different ecosystems: natural ecosystems, agroecosystems and urboecosystems. Were isolated 468 dominanting bacteria, among them 79 antibiotic resistant bacteria. All isolates were multi-drug resistant, of which greater than 74,5% were resistant to 9 antibiotics. A study of soil samples from the primeval forests showed that the microbial community characterized by a low content of antibiotic-resistant microorganisms. Among 78 isolated bacteria only two of them *Bacillus cereus*, and *Pantoea agglomerans* demonstrated high level of resistance to antibiotics. A total 106 strains were isolated from the soil of medicinal plants, 13 of them were antibiotic-resistant. The greatest numbers of antibiotic-resistant bacteria have been isolated from soil of urboecosystems and agroecosystems contaminated by enrofloxacin. Among the 284 tested bacteria 64 were antibiotic resistant. Multi-resistance were such pathogenic and conditionally pathogenic bacteria as: *Enterococcus faecium*, *Acinetobacter baumannii*, *Pseudomonas aeruginosa, Escherichia coli, Bacillus licheniformis, Serratia fonticola, Hafnia alvei*, *Bacillus cereus, Bacillus megaterium* and *Clostridium difficile*.

Keywords: *Ecosystem, Soil, Microbiome, Antibiotic resistance.*

1. INTRODUCTION

Materials of research were soil samples, which had been collected by envelope method from different type of ecosystems: virgin forest, agroecosystems, urboecosystems. Materials of research were soil samples, which had been collected by envelope method from the virgin forests of Uzhanskyi National Nature Park at the deep 0-25cm. Uzhanskyi National Nature Park is located in the western part of Transcarpathia in the basin of the river Uzh and extends from the southwest of the village Zabrod (226 m above sea level) to north-east to Uzhotskyi pass (852 m above sea level). In 2007 primeval beech forests of Uzhanskyi National Nature Park were included into UNESCO World Heritage List "Primeval Beech Forests of the Carpathians and the Ancient Beech Forests of Germany". The Uzhansky NPP is located in the southwest sub-region of the Atlantic-continental climatic region of the temperate zone, in the low-mountainous zone of moderate relative humidity. Absolute temperature maxima occur most often in July and August, and make up + 34 ° C - + 37 ° C, in some years fall on April - May. The absolute minimum temperatures are January-February and are characterized by -28 ° C -32 ° C. The total vegetation period in the region lasts 195 days. The average annual rainfall is 856 - 909 mm. There are mainly brown mountain-forest soils (brown-soils) in the park among them are two subtypes: dark brown and light-brown mountain-forest soils. The reaction of the forest soil is slightly acidic. Humus is dominated by full-fatty acids, which are closely linked to the one and a half oxides of iron and aluminum. Sampling was carried out seasonally at different altitudes from 450 m to 650 m. Studies of soils were carried out at the Scientific Research and Educational Center of Molecular Microbiology and the Immunology of Mucous Membranes (Uzhhorod National University), Research Laboratory Monitoring of Water and Terrestrial Ecosystems of department entomology and biodiversity conservation (Uzhhorod National University) and at Laboratory of Soil microorganisms, (Institute of Agroecology and Environmental Management, Kyiv Agrarian Academy of Sciences of Ukraine). The research was carried out within the framework of the complex theme, Eco-microbiological monitoring of various types ecosystems of the Carpathian region" №0116U003331 (state registration number). following the standard protocol (Shyrobokov, 2011; Goldman, Green, 2015) All soil samples were analyzed within 24 hours. Microbiological study of soil was performed in sterile conditions. The method of serial dilution was used to obtain the suspension where microorganisms titre were 10-3 CFU/ml. - 10-5 CFU/ml. 100 µl of the soil suspension was evenly distributed on the surface of the medium with a sterile spatula. For the study we used the following media: Endos agar, Meat peptone agar, Strepto agar and Entero agar, Agar-Agar, Eshbi agar, Soil agar, Chapek agar, Starch agar in 4 repetitions. Petri dishes with study material were incubated in the thermostat at 37ºC for 48 hours in aerobic conditions.

All isolated microorganisms were identified by applying of appropriate biochemical test-systems LACHEMA according to the instructions. Antibiotic resistance of the identified microorganisms was analysed by Kirby-Bauer method with the aim to find antibiotic resistant strains of pathogenic microorganisms. All isolates from the soil were examined for resistance to 12 antibiotics of the main pharmacological groups: TE_{30} Tetracycline; VA_{30} Vancomycin; L_{10} Lincomycin; CXM_{30} Cefuroxime; AMP_{10} Ampicillin; CIP_5 Ciprofloxacin; GEN_{10} Gentamicin; DO_{30} Doxycycline; AK_{30} Amikacin; AMX_{10} Amoxicillin; E_{15} Erythromycin; OL_{15} Oleandomycin. Anaerobic microbiota were additionally tested to Metronidazole MT_5; Rifampicin RIF_5; Clindamycin CD_2. The amount of enrofloxacin in plants soil was determined in triplicate on each sample by High Performance Liquid Chromatography (HPLC).

Results were expressed as means (±) standard deviation (SD) and (SSD_{05}) smallest significant differences of experiments conducted in quadruplicating. Data were evaluated using the software Statistica 10.0. An assessment of the integrability of soil microbial community in different edaphotops of ecosystems was carried out using correlation-regression analysis.

2. RESULT AND DISCUSSION

Environment surrounding is a huge bacterial reservoir, and antibiotic resistance can be passed between bacteria in the environment, including in the soil. Soil microorganism as a part of forest ecosystems plays an important role in sustainable development of forestry. They are highly sensitive to anthropogenic pressure, so changes of qualitative and quantitative composition of the soil microbiota – is an indicator of the environmental changing. Due to the high sensitivity to changes in environment microorganisms serve as a convenient object of observation. They are in a close contact with habitat and they are characterized by high rate of growth and reproduction. Biocenotic relations of trophic and topical types are decisive in edaphotope shaping of different type of ecosystems [20]. Due to this fact, the purpose of the research was to determine the number of different ecological-functional groups of soil microorganisms. Studies of the soil were taken from primeval ecosystems revealed general regularities of distribution of main ecological- functional groups of microorganisms, their population dynamics in different habitats. The most favourable conditions for the development and functioning of microorganisms were recorded in an edaphotop which was located at an altitude of 450 meters above sea level. It is highly connected to local temperature and water regime, as well as reserves of nutrients (organic origin) in the soil (Table1).

Table 1 Microbial community composition in soils of primeval forest ecosystems (CFU/gr.d.s.)

№	Biotopes, altitude above	Ammonifiers*10^6	Spore forming bacteria *10^6	Micromycetes*10^3	Actinomyces*10^3	Bacteria wich are using mineral forms of nitrogen*10^4	Anaerobic bacteria*10	Aerobic nitrogen fixing bacteria, %	Anaerobic nitrogen fixing bacteria *10^3	Oligotrophic bacteria *10^6	Oligonitrophic bacteria*10^4	Pedotrophic bacteria*10
1	450	5,33	2,35	430	10,78	3,35	35,20	66,51	6,70	3,45	4,45	2,34
2	500	3,89	2,23	540	12,03	3,26	41,22	49,60	9,56	3,97	3,81	2,89
3	650	3,54	3,07	573	16,89	2,67	50,22	40,22	10,67	4,10	3,65	3,44
4	650.1	1,32	4,66	240	32,96	1,24	94,68	17,21	16,25	7,45	1,35	1,89
5	650.2	4,89	3,78	380	20,34	2,66	73,82	29,73	12,78	3,24	2,97	4,78
SSD05		*0,24*	*0,16*	*6,28*	*0,37*	*0,44*	*0,21*	*2,18*	*0,64*	*1,20*	*1,77*	*0,72*

With the creation of favourable conditions for competitive species of microbiota we can see changes in microbial cenoses, owing to the active competition of microorganisms. In edaphotopes that were not changed by direct human impact the dominate type of microorganisms was organotrophic microbiota. It should be noted that their percentage in the structure of groups was reduced by 36% with increasing of the height. At the same time the number of oligotrophes also increased with altitude. Significant negative changes in the structure of microbiocenosis of the soil can be the effect of anthropogenic influence. Violation of the integrity of the phytocenosis as a result of deforestation has led to the increase in the content of oligotrophes and pedotrophes, which indicates disruption of the normal flow of microbiological processes in the soil. It also influenced the decline in biodiversity of soil microorganisms. The most negative changes in the structure of soil microbial community were observed due to compaction. Nearly 80% of the studied ecological-functional groups of microorganisms were oligotrophes, which shows a significant deterioration of the ecological state of the soil. Soil microbial communities are intricately linked to ecosystem functioning because they play important roles in carbon and nitrogen cycling, and feedback to plant communities as mutualists and pathogens (Symochko L. Hamuda H.B., 2015). Although much research has been done to study the impacts of a range of disturbances on soil microbial communities and their functioning (Van der Heijden M.G.A., Bardgett R.D., Van Straalen N.M., 2008), many uncertainties remain about the controls on soil microbial community stability, and the consequences of disturbance-induced changes in microbial communities for their capacity to withstand further disturbances. The influence of biodiversity on ecosystem stability is complex and depends not only on species richness but also on the evenness or composition of the soil microbial community. Resistance and resilience to disturbance might also vary between functional microbial guilds dependent on their levels of functional redundancy.

Our results indicate high stability of the studied soil systems and suggest the existence of functional redundancy among soil microorganisms, leading to ecosystem resistance and resilience (Table 2).

A high level of functional redundancy, within a functional community, that is, a high number species performing the same function, might act as a buffer against the effect of biodiversity loss on functioning.

However, functional redundancy is likely more limited within specialised rather than global processes.

The results of our studies have shown that there are strong correlation relations between the majorities of functional groups of soil microorganisms in non-disturbed edaphotopes (Table 2).

Oligotrophic bacteria and pedotrophic bacteria correlated with micromycetes and actinomyces, a correlation coefficients (CC) were 1,0; 0,79 and 0,95; 0,95.

Aerobic nitrogen fixing bacteria positive correlated with ammonifiers (CC=0,98) and bacteria wich are using mineral forms of nitrogen (CC=0,84). anaerobic bacteria high correlated with spore forming bacteria (CC=0,86), micromycetes (CC=0,91) and actinomyces (CC=0,98).

In general, should be noted a high level integrity of soil microbiome, 46 bonds were identified between different groups of microorganisms, which characterized a high level of correlation (CC > 0,75).

Microbiological soil control is necessary for assessing and predicting the possibility of spreading antibiotic-resistant microorganisms.

As model terrestrial ecosystem of soil resistome we analysed virgin forest. A study of soil samples from the primeval forests showed that the microbial community characterized by a low content of antibiotic-resistant (AR) microorganisms (Table 3).

Table 2. Integrity of soil microbial community in non-disturbed edaphotopes.

	Ammonifiers	Spore forming bacteria	Micromycetes	Actinomyces	Bacteria wich are using mineral forms of nitrogen	Anaerobic bacteria	Aerobic nitrogen fixing bacteria	Anaerobic nitrogen fixing bacteria	Oligotrophic bacteria	Oligonitrophic bacteria	Pedotrophic bacteria
Ammonifiers	–	-0,55	-1,00	-1,00	0,74	-0,90	0,98	-1,00	-1,00	1,00	-0,94
Spore forming bacteria	-0,55	–	0,58	0,95	-0,97	0,86	-0,68	0,62	0,55	-0,55	0,79
Micromycetes	-1,00	0,58	–	0,81	-0,76	0,91	-0,99	1,00	1,00	-1,00	0,95
Actinomyces	-1,00	0,95	0,81	–	-1,00	0,98	-0,88	0,84	0,79	-0,79	0,95
Bacteria wich are using mineral forms of nitrogen	0,74	-0,97	-0,76	-1,00	–	-0,96	0,84	-0,80	-0,74	0,74	-0,92
Anaerobic bacteria	-0,90	0,86	0,91	0,98	-0,96	–	-0,96	0,93	0,90	-0,90	0,99
Aerobic nitrogen fixing bacteria	0,98	-0,68	-0,99	-0,88	0,84	-0,96	–	-1,00	-0,99	0,99	-0,99
Anaerobic nitrogen fixing bacteria	-1,00	0,62	1,00	0,84	-0,80	0,93	-1,00	–	1,00	-1,00	0,97
Oligotrophic bacteria	-1,00	0,55	1,00	0,79	-0,74	0,90	-0,99	1,00	–	-1,00	0,94
Oligonitrophic bacteria	1,00	-0,55	-1,00	-0,79	0,74	-0,90	0,99	-1,00	-1,00	–	-0,94
Pedotrophic bacteria	-0,94	0,79	0,95	0,95	-0,92	0,99	-0,99	0,97	0,94	-0,94	–

Table 3. Persentage of AR bacteria in the different ecosystems.

№	Type of ecosystem	Total number of dominant bacteria with level of AR to tested antibiotics more than 30% (468)	Total number of dominant bacteria with level of AR to tested antibiotics more than 70% (79)
1	Natural ecosystem	78	2
2	Agroecosystem of medicinal plant	106	13
3	Agroecosystem contaminated by antibiotic	148	42
4	Urboecosystem	136	22

The fluoroquinolones are one of the most used classes of antibiotics. Enrofloxacin belongs to the class of fluoroquinolone antibiotics that have been intensively used for the treatment of bacterial infections in veterinary medicine. The effect of enrofloxacin on the function and structure of soil microbial communities were evaluated (Table 4).

It should be noted, the soil with a high concentration of antibiotic was characterized by a low content of nitrogen-fixing microorganisms and a high number of oligotrophic and sporeforming microbiota. Among AR microorganisms were anaerobic bacteria: Clostridium difficile, Clostridium perfringens and aerobic bacteria: Enterococcus faecalis, Yersinia enterocolitica, Enterobacter cloacae. Other dominant bacteria were characterized by a high or moderate level of antibiotic resistance. From the soil, were isolated bacteria resistant to all tested antibiotics. They were representatives of aerobic microbiota: Bacillus licheniformis, Serratia fonticola, Hafnia alvei, Bacillus cereus, Pantoea agglomerans, Bacillus megaterium and one anaerobic bacteria - Clostridium difficile. In natural conditions, from the soil of model ecosystems were isolated mostly bacteria of the genus Bacillus. All of them are antibiotic resistant and are the causative agents of foodborne infections and pose a threat not only to the environment but also to human health.

The level of integration of soil microbiome in contaminated edaphotopes was lower than in etalon ecosystem (Table 3). It was recorded 29 correlation connections between different ecological groups of soil microorganisms with high level of correlation (CC > 0,75). Strong correlation connections have been observed between anaerobic bacteria and micromycetes (CC=0,85); anaerobic bacteria and actinomyces (CC=0,98). Oligotrophic bacteria strong correlated with micromycetes, actinomyces and anaerobic nitrogen fixing bacteria.

The presence of enrofloxacin in the soil, especially in high concentrations, cause negative changes in the microbial community, significantly increasing number of antibiotic-resistant bacteria loses stability and integrity of soil microbiome. Contamination by antibiotics is one of the important factors in the formation of soil resistome. The urban environment the main habitat for human population is a potential harmful substance source, with high risk for resident's health. Indeed, harmful substance concentration and distribution are related to traffic intensity, distance from roads, local topography, and heating. Industrial emissions also contribute to the release of toxic elements. Sustainable management and microbiological control of urban soils and gardens in relation to human health are necessary for estimation and improvement of ecological situation in metabolises. The effects of most trace metals on human health are not yet fully understood. Uncertainty is still prevailing, particularly with non-essential elements that are "suspected" to be harmful to humans, causing serious health problems as intoxication, neurological disturbances and also cancer. Contamination of urban soils causes changes in the structure of soil microbiome, increase the number of antibiotic resistance bacteria (Table 3), most of them are causative agents of foodborne diseases.

Soil microbial communities are heterogeneous entities with distinct components that are each capable of responding differently to environmental characteristics. Microbial composition was shown dynamics and differences in the structure of microbial communities, depending on the level of anthropogenic impact.

One of the important indicators of the ecological and sanitary state of the soil and the whole ecosystem is the presence of conditionally pathogenic and pathogenic microorganisms. Particularly dangerous are the antibiotic-resistant microorganisms, which, together with the bioproduction, can enter to he human and animal organisms from the terrestrial ecosystems.

The structure of microbial communities of the soil is interrelated with the presence of antibiotic-resistant pathogenic microorganisms. In the soil of agroecosystems where the number of pedotrophes and oligotrophes was higher, a greater number of antibiotic-resistant microorganisms were isolated. *Clostridium perfringens* (resistant to erythromycin, clindamycin, tetracycline, rifampicin, amoxicillin, moderately sensitive to metronidazole and vancomycin sensitive), *Clostridium oedematiens* (moderately susceptible to amoxicillin and vancomycin), *Clostridium difficile* (sensitive to metronidazole). Nevertheless, the enrichments of *Clostridium* in soil which was continually treated with manure containing can be dangerous for public health. The enrichment of these bacteria, which are phylogenetically closely related to human pathogens, may improve the chance of transferring antibiotic resistance genes to human pathogens, since horizontal gene transfer is more prevalent between closely related organisms than between those distantly related (Forsberg KJ, Reyes A, Wang B, Selleck EM, Sommer MOA, et al., 2012; Symochko L., 2019).

Soil particles carrying viable bacteria can be transported over long distances and might contribute to the spreading of antibiotic resistant bacteria over wide geographic ranges. A significant number of aerobic microorganisms with multiple antibiotic resistances were isolated from the agroecosystem, all of them are the causative agents of foodborne infections. The soil microbiome plays an important role in the development and spread of antibiotic resistance in humans.

Table 4 Microbial community composition (CFU/gr.d.s.) in soils of agroecosystems contaminated by antibiotic (1000mg*kg-1).

№	Agroecosystems	Ammonifiers*10^6	Spore forming bacteria *10^6	Micromycetes*10^3	Actinomyces*10^3	Bacteria wich are using mineral forms of nitrogen*10^4	Anaerobic bacteria*10^3	Aerobic nitrogen fixing bacteria, %	Anaerobic nitrogen fixing bacteria *10^3	Oligotrophic bacteria *10^6	Oligonitrophic bacteria*10^4	Pedotrophic bacteria*10^6
1	*Mentha piperita*	4,07	3,88	11	7,21	4,32	35,20	19,22	3,77	2,63	4,56	3,68
2	*Calendula officinalis*	8,30	1,88	20	10,33	3,64	41,22	28,56	5,96	1,61	2,17	1,88
3	*Thymus Serpillum*	5,46	4,45	15	14,11	3,22	50,22	22,34	8,22	2,87	3,27	3,52
4	*Anethum graveolens*	7,93	1,74	28	21,22	3,14	94,68	38,23	11,35	1,24	1,68	2,26
5	*Lactuca sativa var. crispa*	8,66	2,23	25	12,38	2,18	73,82	29,67	9,23	1,70	2,95	2,96
	SSD_{05}	*0,48*	*0,23*	*0,36*	*0,37*	*0,32*	*0,21*	*1,12*	*1,34*	*0,41*	0,55	*0,18*

Table 5. Integrity of soil microbial community in edaphotopes of agroecosystem contaminated by antibiotic.

	Ammonifiers	Spore forming bacteria	Micromycetes	Actinomyces	Bacteria wich are using mineral forms of nitrogen	Anaerobic bacteria	Aerobic nitrogen fixing bacteria	Anaerobic nitrogen fixing bacteria	Oligotrophic bacteria	Oligonitrophic bacteria	Pedotrophic bacteria
Ammonifiers	–	-0,58	-1,00	-0,33	0,72	-0,55	0,46	-0,77	-0,25	1,00	-0,92
Spore forming bacteria	-0,58	–	0,55	0,95	-0,97	0,86	-0,68	0,62	0,55	-0,50	0,79
Micromycetes	-1,00	0,55	–	0,81	-0,76	0,85	-0,99	1,00	1,00	-1,00	0,95
Actinomyces	-0,33	0,95	0,81	–	-1,00	0,98	-0,88	0,84	0,79	-0,77	0,35
Bacteria wich are using mineral forms of nitrogen	0,72	-0,97	-0,76	-1,00	–	-0,56	0,84	-0,80	-0,74	0,68	-0,62
Anaerobic bacteria	-0,55	0,86	0,85	0,98	-0,56	–	-0,96	0,34	0,60	-0,90	0,35
Aerobic nitrogen fixing bacteria	0,46	-0,68	-0,99	-0,88	0,84	-0,96	–	-1,00	-0,48	0,99	-0,49
Anaerobic nitrogen fixing bacteria	-0,77	0,62	1,00	0,84	-0,80	0,34	-1,00	–	1,00	-1,00	0,97
Oligotrophic bacteria	-0,25	0,55	1,00	0,79	-0,74	0,60	-0,48	1,00	–	-0,44	0,52
Oligonitrophic bacteria	1,00	-0,50	-1,00	-0,77	0,68	-0,90	0,99	-1,00	-0,44	–	-0,64
Pedotrophic bacteria	-0,92	0,79	0,95	0,35	-0,62	0,35	-0,49	0,97	0,52	-0,64	–

3. CONCLUSION

Structure of soil microbiome of terrestrial ecosystem depends from anthropogenic impact. Forest ecosystems characterized by high functional biodiversity and stability and small number of AR bacteria, humans pathogens. The taxonomic structure of the microbial community has been determined by biochemical markers and showed a significant difference between level of transformation and contamination of ecosystems. The screening of conditionally pathogenic and pathogenic microorganisms of soil microbiome has proved that terrestrial ecosystems are the source of the spread of pathogenic and opportunistic antibiotic-resistant microorganisms. In total from 468 bacteria were isolated 79 which characterized by high level of antibiotic resistance. All of them are pathogenic or conditionally pathogenic for human and can cause foodborne diseases. The risk to antibiotic resistance exposure via produce consumption should best be managed by ensuring that practices designed to protect bioproduction from contamination with pathogenic microorganisms are also protective with respect to exposure to antibiotic-resistant bacteria selected for in the digestive tract of animals or humans.

REFERENCES

Allen, H. K., Donato, J., Wang, H. H., Cloud-Hansen, K. A., Davies, J., & Handelsman, J. (2010). Call of the wild: antibiotic resistance genes in natural environments. *Nature Reviews Microbiology*, 8(4), pp. 251-259. doi: 10.1038/nrmicro2312.

Aminov R. (2007) Evolution and ecology of antibiotic resistance genes. *FEMS Microbiol Lett.*,Vol. 271, pp.147–161.

Boxall, A. B., Johnson, P., Smith, E. J., Sinclair, C. J., Stutt, E., & Levy, L. S. (2006). Uptake of veterinary medicines from soils into plants. *Journal of Agricultural and Food Chemistry*, 54(6), pp. 2288-2297. doi: 10.1021/jf053041t.

Cavigelli, M. A., & Robertson, G. P. (2000) The functional significance of denitrifier community composition in a terrestrial ecosystem. Ecology, Vol.81, no 5, pp. 1402-1414.

Cavigelli, M. A., & Robertson, G. P. (2000). The functional significance of denitrifier community composition in a terrestrial ecosystem.

Ecology, 81(5), pp. 1402-1414. doi: 10.2307/177217.

Chee-Sanford, J. C., Aminov, R. I., Krapac, I. J., Garrigues-Jeanjean, N., & Mackie, R. I. (2001). Occurrence and diversity of tetracycline resistance genes in lagoons and groundwater underlying two swine production facilities. *Applied and environmental microbiology*, 67(4), pp. 1494-1502. doi: 10.1128/aem.67.4.1494-1502.2001.

Christian, T., Schneider, R. J., Färber, H. A., Skutlarek, D., Meyer, M. T., & Goldbach, H. E. (2003). Determination of antibiotic residues in manure, soil, and surface waters. CLEAN–Soil, Air, Water, 31(1),pp. 36-44.

Diao, X., Sun, Y., Sun, Z., & Shen, J. (2004). Effects of Apramycin on microbial activity in different types of soil. *Ecology and Environment,* 13(4), pp. 565-568.

Díaz-Cruz, M. S., de Alda, M. J. L., & Barcelo, D. (2003). Environmental behavior and analysis of veterinary and human drugs in soils, sediments and sludge. TrAC *Trends in Analytical Chemistry*, 22(6), pp. 340-351. doi:10.1016/s0165-9936(03)00603- 4.

Ebert, I., Bachmann, J., Kühnen, U., Küster, A., Kussatz, C., Maletzki, D., & Schlüter, C. (2011). Toxicity of the fluoroquinolone antibiotics enrofloxacin and ciprofloxacin to photoautotrophic aquatic organisms. *Environmental Toxicology and Chemistry,* 30(12), pp. 2786-2792. doi:10.1002/etc.678.

Forsberg KJ, Reyes A, Wang B, Selleck EM, Sommer MOA, et al. (2012) The shared antibiotic resistome of soil bacteria and human pathogens. *Science,* Vol. 337, pp. 1107–1111.

Goldman, E., & Green, L. H. (Eds.). (2015). Practical handbook of microbiology , Third Edition. doi:10.1201/b17871.

Hammesfahr U, Heuer H, Manzke B, Smalla K, Thiele-Bruhn S. (2008) Impact of the antibiotic sulfadiazine and pig manure on the microbial community structure in agricultural soils. *Soil Biol Biochem*, Vol.40, pp.1583–1591.

Heuer H, Schmitt H, Smalla K. (2011) Antibiotic resistance gene spread due to manure application on agricultural fields. *Curr Opin Microbiol,* Vol.14, pp. 236–243.

Heuer H, Smalla K. (2007) Manure and sulfadiazine synergistically increased bacterial antibiotic resistance in soil over at least two months. *Environ Microbiol*, Vol. 9, pp. 657–666.

Keen, P. L., & Patrick, D. M. (2013). Tracking Change: A look at the ecological footprint of antibiotics and antimicrobial resistance.

Antibiotics, 2(2), pp.191-205. doi:10.3390/antibiotics2020191.

Kümmerer, K. (2004). Resistance in the environment *J Antimicrob Chemother* 54 (2): pp. 311–320. doi:10.1093/jac/dkh325.

Lyudmyla Symochko (2019), "Food Safety in Agroecosystems-Soil Resistome", *13th Paris International Conference (PACBES-19)*
Conference Proceedings, Paris, France, pp. 99-102.

Lyudmyla Symochko, Ruslan Mariychuk, Olena Demyanyuk, Vitaliy Symochko (2018). "Ecological effects of antibiotics on microbial community – soil resistome". Abstract Book *International Conference «Smart Bio»* – 3-5 May, Kaunas, Lithuania, P. 43.

Martínez, J. L. (2008). Antibiotics and antibiotic resistance genes in natural environments. *Science,* 321(5887), pp. 365-367. doi:10.1126/science.1159483.

Migliore, L., Civitareale, C., Brambilla, G., & Di Delupis, G. D. (1997). Toxicity of several important agricultural antibiotics to Artemia.

Water Research, 31(7), pp. 1801-1806. doi:10.1016/s0043-1354(96)00412-5.

Mikola, J., & Setälä, H. (1998). No evidence of trophic cascades in an experimental microbial based soil food web. *Ecology*, 79(1), pp.153-164. doi:10.2307/176871.

Murray, B. E. (1996). Antibiotic resistance. *Advances in internal medicine*, 42, pp.339-367.

Pruden, A., Pei, R., Storteboom, H., & Carlson, K. H. (2006). Antibiotic resistance genes as emerging contaminants: studies in northern Colorado. *Environmental Science & Technology*, 40(23), pp.7445-7450. doi:10.1021/es060413l.

Schmitt, H., Van Beelen, P., Tolls, J., & Van Leeuwen, C. L. (2004). Pollution-induced community tolerance of soil microbial communities caused by the antibiotic sulfachloropyridazine. *Environmental science & technology*, 38(4), pp.1148-1153. doi:10.1021/es034685p.

Shyrobokov V. P. (2011) Medical Microbiology, Virology, and Immunologyю. Nova Knyha, Vinnytsia (in Ukrainian).

Symochko L. (2017) Assessment of sorption and toxicity of fluoroquinolone antibiotic in agroecosystems. *Agroecological journal*, (3), pp.147–151.

Symochko L. Hamuda H.B. (2015) Microbial monitoring of soil as additional tools for conservation biology. *Obuda University e- Bulletin*, 5(1), pp.177–185.

Symochko L., Meleshko T., Symochko V., Boyko N. (2018) Microbiological control of soil-borne antibiotic resistance human pathogens in agroecosystems. *International Journal of Ecosystems and Ecology Sciences*, Vol. 8 (3), pp. 591-598. https://doi.org/10.31407/ijees8320.

Thiele-Bruhn, S. (2003). Pharmaceutical antibiotic compounds in soils–a review. *Journal of Plant Nutrition and SoilScience*, 166(2),pp. 145-167.

Torsvik V, Qvreås L.(2002). Microbial diversity and function in soil: from genes to ecosystems. *Curr Opin Microbiol*, Vol.5, pp. 240– 245.

Van der Heijden M.G.A., Bardgett R.D., Van Straalen N.M. (2008) The unseen majority: soil microbes as drivers of plant diversity and productivity in terrestrial ecosystems. *Ecol. Lett.*, 11, pp. 296–310.

Wright, G. D. (2007). The antibiotic resistome: the nexus of chemical and genetic diversity. *Nature Reviews Microbiology*, 5(3), pp. 175- 186. doi:10.1038/nrmicro1614.

Wright, G. D. (2010). The antibiotic resistome. *Expert opinion on drug discovery*, 5(8), 779-788. doi:10.1517/17460441.2010.497535.

DETERMINATION OF SPRAY ANGLE IN SPRAYER NOZZLES USING COMPUTER VISION TECHNIQUE

Ahmet Nusret Toprak[1], Bahadır Sayıncı[*2], Bünyamin Demir[3], Fehim Köylü[1] and Necati Çetin[4]

[1] Computer Engineering, Faculty of Engineering, Erciyes University 38039 Talas-Kayseri/Turkey, antoprak@erciyes.edu.tr

[2] Mechanical Engineering, Faculty of Engineering, Mersin University 33340, Yenişehir-Mersin/Turkey, bsayinci@mersin.edu.tr

[3] Vocational School of Technical Sciences, Department of Mechanical and Metal Technologies, Mersin University, 33340 Yenişehir-Mersin/Turkey, bd@mersin.edu.tr

[4] Biosystem Engineering, Faculty of Agriculture, Erciyes University 38039 Talas-Kayseri/Turkey, necaticetin@erciyes.edu.tr

ABSTRACT
Before the pesticide applications with sprayers, the flow rates of the spray nozzles should be controlled, and the flow rate uniformity of the spraying should be checked in the calibration processes. Irregular flow in the sprayer nozzles causes deterioration of the spray pattern and the volumetric distribution uniformity. Production errors in the orifice geometry of the hydraulic nozzle used in sprayers, wear due to long-term use, tearing or cracking of the nozzle body over time, faulty nozzle connections and sealing problems can be listed as structural factors disrupting spray angle and pattern. The aim of this research is to develop a measurement system and software that controls nozzle spray angle in real time in addition to the measurement and control systems currently used to perform flow controls in sprayer nozzles. The measurement system consists of light apparatus and camera. In the software creation, it is aimed to determine the spray angle online through the real-time flow images. The angle values determined on a standard basis can be viewed on the control screen and various statistics can be obtained from the images taken online with the camera. According to preliminary results, the spray angle measurement system and software can be used efficiently and practically in research, production and development studies, measurement and control laboratories and hydraulic nozzle flow tests.

Keywords: *Hydraulic nozzle, Image processing, Sprayer, Spray pattern*

[*] Corresponding Author

1. INTRODUCTION

The fastest and most effective method against diseases and pests that harm the culture plants is the chemical method, which makes it necessary to use powder or liquid chemicals called pesticides. Most of the applications are carried out with equipment called sprayers equipped with hydraulic pump. The chemicals prepared by diluted in the liquid form in the tank are sprayed under the influence of hydraulic pressure and transmitted to the target in drops. The preparation of a particular concentration prepared in a homogeneous manner during spraying ensures that the effective substance reaches the same dosage to all surfaces and thus increases the expected success of the chemical control. The uniformly transport of the chemical to the target, which is broken into drops, varies depending on the type of hydraulic nozzle, operating pressure, spray height, application speed and meteorological factors (Hoffmann and Salyani, 1996; Panneton *et al*., 2000; Zhu *et al*., 2002; Zhu *et al*., 2004; Bayat and Bozdoğan, 2005).

In order to uniformly transport of the drops set leaving the orifice in a given distribution pattern, it is necessary to provide sufficient coating on the surface by overlapping at a certain height. The coating rate required for this is dependent on the spray height, which is determined by the spray angle of the hydraulic nozzle. For conventional spray applications, the minimum spray heights recommended for 65º, 80º, 110º and 120º nozzles were reported to be 75, 60, 40 and 40 cm, respectively (Teejet®, 2016). Narrow angled spray nozzles are recommended to be used in banded applications for plants planted in rows, but are preferred to increase drop penetration in tall plants (Matthews and Thornhill, 1994; Matthews, 2004). However, increasing the spray height as the spray angle decreases can cause the droplets to evaporate by the effect of temperature and humidity, turbulence with wind speed and reverse air currents, leading to increased pesticide consumption and losses (Dursun *et al*., 2000). As the spray angle varies depending on the design of the outlet orifice in the hydraulic nozzles, at the same spray pressure, the liquid strip leaving the orifice becomes thinner and the resistance to disintegration decreases and finer droplets occurs. As the height of such nozzles increases, the energy of transporting the drug drops to the target decreases and thus drug losses increase due to evaporation and drift. Therefore, in order to reduce drag on nozzles with a wide spray angle, the spray distance must be reduced. For these reasons, there is a general tendency in the choice of nozzle to use sprayer nozzles with a larger spray angle (Matthews, 2004).

Spray pattern and flow uniformity tests related to hydraulic nozzles used in sprayers are carried out on measuring tables called patternators. It was reported that the volumetric distribution was acceptable for the 15% variation and the distribution for the 10% variation was quite homogeneous (Bode *et al*., 1983; Azimi *et al*., 1985; Krishnan *et al*., 1988). The measurements and tests performed on hydraulic nozzles reveal the operating characteristics (height, pressure, mounting range, position angle, etc.) required for uniform pesticide applications. In addition, flow tests reveal production errors in the nozzle orifice geometry, wear caused by long-term use, tearing or cracking of the nozzle body over time, faulty nozzle connections and sealing problems. These factors, which disrupt the flow uniformity, often cause deviations in the spray angle of the hydraulic nozzle. This appears to be detectable with control equipment which measures the spray angle in a practical way.

There is no standard method used in practice for determining the spray angle. In the present case, protractors are used in practice or can be measured by means of image processing software via spray images. However, this process takes time as well as the contours of the angle on the image are determined by the operator's personal preference. Determination of the spray angle on a standard basis is of great importance for the accuracy and practicality of the measurements. The aim of this study is to develop a new measurement system and software that can calculate, record and calculate spray angle values online through flow images of sprayer nozzles in laboratory conditions.

2. MATERIAL AND METHOD

Computer vision is an interdisciplinary field that enables us to evaluate and make useful decisions about the environment through digital images of the environment of interest (Aslantaş and Toprak, 2017). Calculation of the spray angle on the spray images by computer vision techniques will make this process objective by removing the operator's initiative. This section provides details of the system and software developed for calculating the nozzle spray angle in the laboratory using computer vision techniques. In addition, the spray angle calculation method used in the developed software is introduced.

2.1. Image Acquisition System

In order to determine the spray angle variation during spray application, it is aimed to develop an application in which spray angle is calculated instantly in spray nozzles displayed in the laboratory condition. In the system, the images obtained through a camera in the laboratory condition are transferred to the developed software. With the application developed, both the current spray image and the spray angle are presented to the user. The operation of the system designed for calculating the spray angle of the sprayer nozzle is shown in Figure 1.

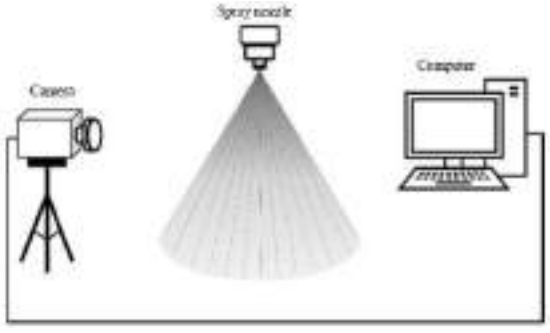

Fig. 1. System diagram for measuring the spray angle of a spray nozzle in a laboratory

The Nikon D300 DSLR camera is used for spraying images. The camera was placed on a tripod to stabilize the images. To achieve high contrast images, a black

background was placed on the background of the spray boom, and two paraflashes are again positioned behind the spray boom. To improve the quality of the spray image, the floor-mounted lighting device is arranged to illuminate the output of the flow beam.

2.2. Application of Spray Angle Measurement

The spray angle measurement application is intended to enable the user to instantly display the spray image and calculated spray angle value of a sprayer nozzle in the laboratory with an easy to use and interactive interface. In the development of the software, Python programming language has been preferred in order to be able to design the interface easily and to perform visual operations with the computer. A spray image and an angle value representation on the interface is shown in Figure 2.

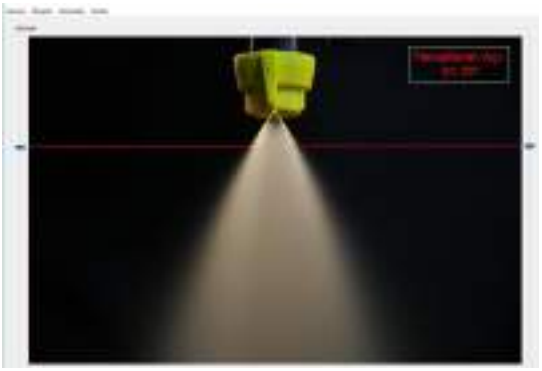

Fig. 2. Interface of spray angle measurement application

The spray angle calculation starts with the acquisition of the spray image from the camera. To do this, the user must first select the start option from the camera drop-down list in the top menu. When the user clicks the start tab, a connection is established between the camera and the software defined in the system and the system is ready to receive the image. The camera drop-down list also includes the pause and stop options for pausing and turning off the camera.

The display tab in the top menu of the main screen also includes the take-up and start analysis tabs, in which the user can perform image acquisition from the camera and calculate the angle value, respectively. When the user clicks on the take image command, the image of the scene displayed by the camera defined in the system is captured and shown to the user on the interface. When the user clicks the start analysis command again under the view menu, the recorded image is analysed in the following section with the method detailed and the spray angle is calculated and presented to the user on the interface.

If the positions of the points used by the operator to calculate the angle in the spray angle calculation process are not selected appropriately, the spray angle may be calculated incorrectly. In order to accurately calculate the spraying angles of sprayer nozzles of different types and pressures, it is expected that the lines where the right and left edge points will be searched on the image will be determined interactively by the user. For this purpose, the user can determine the lines through which the right and left switch points are searched by means of the slider bars on both sides of the spray image received from the camera. The user must specify the process of determining the lines on which the analysis is to be performed before starting the analysis.

Spray images to calculate the spray angle can be refreshed at any time using the take image command. The user should start the process of calculating the angle again with the start analysis command for each image taken from the camera.

2.3. Spray Angle Calculation Method

Three key points, right, left and top, are used to calculate the spray angle on the spray image from the camera. The first step of the spray angle calculation process is to determine the right and left key points on the user-specified lines. The points where the sprayed liquid starts and ends on the user-specified line should be determined as left and right key points. Since the user does not have sufficient information about the constantly changing images, a manual angle calculation will not give the desired result in all cases. Therefore, in the developed application, a method has been proposed which allows the automatic finding of the right and left key points. The proposed method requires user-defined lines to calculate points.

The right and left key points are located on the boundary between the area covered by the sprayed liquid and the background area in the user-specified line. This boundary line corresponds to the points at which the intensity change occurs in the respective lines. From this perspective, if images are divided into spray and background zones, the right and left switch points can be specified as the transition between the background and spray zone. Automatic thresholding methods can be used to determine this transition.

One of the most common and successful automatic thresholding functions is the Otsu method (Otsu, 1979). The herbaceous automatic thresholding method works with the assumption that the image consists of pixels that fall into two classes, foreground and background. Iteratively investigates the minimized threshold value of the in-class variances of the obtained classes and the value is found as the optimal threshold value. In-class variance is found by Eq. (1) as the weighted sum of the variance values of the two classes:

$$\boldsymbol{\sigma_{si}^2 = \omega_0(t)\sigma_0^2(t) + \omega_1(t)\sigma_1^2(t)} \quad (1)$$

here ω_0 and ω_1 are the probability values of the two classes separated by the threshold value t, and σ_0^2 and σ_1^2 are the variance values of these classes. Minimizing in-class variance is equal to maximizing inter-class variance. Since the calculation of variance between classes brings less processing load, Eq. (2) preferred to find the optimum threshold value:

$$\boldsymbol{\sigma_{sa}^2 = \sigma^2 - \sigma_{si}^2(t) = \omega_0(\mu_0 - \mu_T)^2 + \omega_1(\mu_1 - \mu_T)^2} \quad (2)$$

where μ_0 and μ_1 are the means of the two classes, and μ_T is the mean of the entire grey-level image. As given by Eq. (3), the Otsu method determines the threshold value that will maximize the differences between the classes as the optimum threshold value:

$$\boldsymbol{t_{opt} = arg\ max\{\sigma_{sa}^2(t)\}} \quad (3)$$

After applying the Otsu threshold value method to the user-selected lines, the pixel at which the transition from the spray zone to the background on the black and white image of that line is determined as the key point.

After the right and left points obtained by the Otsu threshold determination method, the end point required for the calculation of the spray angle should be determined. This third point is the peak, the starting point of the sprayed liquid. This point cannot be detected directly since it remains essentially within the sprayer nozzle and cannot be imaged. However, it can be estimated approximately using the spray zone. In order to estimate the peak, the curves forming the boundaries of the spray zone need to be known.

In order to find the peak, the spraying image is first replaced by pixels 1 higher than a certain threshold value and pixels with low intensity 0, resulting in a binary (black and white) image. The above mentioned Otsu method is used to find the threshold value. However, the resulting dual image may include the spraying zone as well as the spray nozzle and different objects. Since only the spray zone is needed to locate the peak, only the spray zone must be removed first on the binary image. Therefore, the linked regions are determined by applying component analysis based on binary image. The linked component analysis operator scans the binary image pixel by pixel to identify adjacent pixel regions that share the same intensity value. The largest of the zones obtained as a result of this process is determined as the spray zone.

The peak may be defined as the intersection of two curves forming the edges of the spray zone. The pixels forming the right and left edges of the spray area are found and their horizontal and vertical coordinate values are recorded. The polynomial is best defined by the curve fitting method using the coordinates of the points that make up the left and right sides. Curve fitting is defined as finding an appropriate curve or the right equation to reflect the pattern of the relationship between the two variables (Guest, 2012). Within the scope of the paper, there are two functions of the 3rd order using points expressing the right and left edges. If the polynomials expressing the left and right edges are considered *f(x)* and *p(x)* respectively, the intersection point of these polynomials is found by the exit point of the sprayed liquid, in other words, the peak point (*T*) by Eq. (4):

$$\boldsymbol{T} = \boldsymbol{f}(\boldsymbol{x}) \cap \boldsymbol{p}(\boldsymbol{x}). \tag{4}$$

The spray angle can then be calculated using these three points found after this step. The vertex, left margin and right margin are defined as T, A and B respectively. The vectors between the vertex and edge points are defined in Eq. 5.

$$\begin{aligned} \overrightarrow{\boldsymbol{TA}} &= \boldsymbol{A} - \boldsymbol{T}, \\ \overrightarrow{\boldsymbol{TB}} &= \boldsymbol{B} - \boldsymbol{T}. \end{aligned} \tag{5}$$

In this case, since the points T, A and B are known, the angle (θ) between the two vectors can be calculated by Eq. (6).

$$\boldsymbol{\theta} = \boldsymbol{arccos}\left(\frac{\overrightarrow{\boldsymbol{TA}} \cdot \overrightarrow{\boldsymbol{TB}}}{\|\overrightarrow{\boldsymbol{TA}}\|\|\overrightarrow{\boldsymbol{TB}}\|}\right), \tag{6}$$

here || || refers to the length of the vector.

3. RESULTS

In order to investigate the performance of the proposed method, the spray angle values calculated on the instant spray images were compared with the angle values found by the expert using the image processing methods on the same images. The spray angle at the nozzle orifice outlet was determined by the operator using the angle module of the ImageJ v.1.38x (Wayne Rasband, National Institutes of Health, US) image processing software on the obtained high contrast fixed images (Abràmoff *et al*., 2004). Images were taken at three different spray pressures (200, 400 and 600 kPa) on disc-core type hollow cone nozzles made of stainless steel (Cr-Ni) with orifice diameter 1.0 mm and 1.5 mm. In repetitive studies, five different nozzle discs taken from the same diameter group by chance were used.

Table 1 shows the results from the orifice diameter 1.0 mm nozzle disc. When the results were examined, the average of the angles measured by the operator by image processing technique were measured as 41.77º, 53.77º and 59.83º for 200, 400 and 600 kPa, respectively. The angle values measured by the spray angle calculation software were 40.80º, 57.77º and 62.04º. Accordingly, the spray angle provided very close results in both methods.

Table 1. Spray angle (º) values in hollow cone nozzle with orifice diameter 1.0 mm

Nozzle discs	Image processing technique			Spray angle software		
	Pressure (kPa)			Pressure (kPa)		
	200	400	600	200	400	600
1	43.09	56.17	62.26	42.90	58.49	63.65
2	40.27	55.74	61.67	40.65	60.51	63.36
3	44.70	53.09	56.84	43.50	58.00	59.53
4	40.59	51.20	58.22	40.53	55.67	60.20
5	40.20	52.67	60.16	36.43	56.17	63.44
Mean	41.77	53.77	59.83	40.80	57.77	62.04
SD*	2.03	2.12	2.29	2.78	1.94	2.00

*: standard deviation

The spray angle values determined by image processing technique and spray angle calculation software in hollow cone nozzle disc with orifice diameter 1.5 mm were compared in Table 2. The average spray angle values varied from 69.85º to 84.15º in image processing at 400 kPa spray pressure, and between 69.88º and 78.34º in the software. When the image processing technique and the spray angle calculation software are compared, it is generally found that all spray angle values overlap with each other.

Table 2. Spray angle (º) values in hollow cone nozzle disc with orifice diameter 1.5 mm

Nozzle discs	Image processing technique			Spray angle software		
	Pressure (kPa)			Pressure (kPa)		
	200	400	600	200	400	600
1	67.97	79.95	76.49	67.71	78.51	78.17
2	71.65	84.15	88.84	75.06	78.34	83.45
3	66.15	69.85	68.36	72.16	69.88	74.57
4	65.40	76.06	77.54	64.18	75.32	78.02
5	66.74	72.09	71.52	67.72	74.24	75.39
Mean	67.58	76.42	76.55	69.37	75.26	77.92
SD*	2.46	5.79	7.82	4.26	3.54	3.47

*: standard deviation

The proposed method has 0.1379 seconds processing time for 1072×712 source images on a computer with AMD FX-8350 4Ghz processor and 16GB main memory. This result is much shorter than the time required for an expert to analyse the image, place the dots on the images, and determine the angle.

4. CONCLUSION

Hollow cone nozzle discs with different orifice diameters were used in the study and spray angle changes were compared with two different methods at three different operating pressures. When the measurement method is evaluated, it is observed that the flow contours that allow the determination of the spray angle on the images can vary from user to user, and the time taken in the measurements is higher than the newly developed application. With the developed spray angle detection method, no operator experience is required, it is observed that the spray angle can be determined on a standard basis thanks to the easy-to-use and interactive interface, and the spray angle values can be observed instantly on the control screen depending on time. As a result of the research, it was determined that the spray angle values determined by two different measurement methods matched at a high rate and the developed software showed successful results.

The spray angle calculation method proposed within the scope of this study is able to calculate on single images taken in the laboratory. In future studies, it is planned to introduce a more practical and modular new software that can detect spray angle in real time on continuous images.

ACKNOWLEDGMENT

This study was supported by Mersin University Scientific Research Projects (BAP) Unit with project number 2017-2-AP4-2565.

REFERENCES

Abràmoff, M. D., Magalhães, P. J. and Ram, S. J. (2004). "Image processing with ImageJ," *Biophotonics International*, Vol. 11, No. 7, pp. 36-42.

Aslantas V. and Toprak, A. N., (2017). "Multi-focus image fusion based on optimal defocus estimation." *Computers and Electrical Engineering*, Vol. 62., pp. 302-318.

Azimi, A. H., Carpenter, T. G. and Reichard, D. L. (1985). "Nozzle spray distribution for pesticide application." *Transactions of the ASAE*, Vol. 28, No. 5, pp. 1410-1414.

Bayat, A. and Bozdogan, N. Y. (2005). "An air-assisted spinning disc nozzle and its performance on spray deposition and reduction of drift potential." *Crop Protection*, Vol. 24, pp. 951-960.

Bode, L. E., Butler, B. J., Pearson, S. L. and Bouse, L. F. (1983). "Characteristics of the micromax rotary atomizer." *Transactions of the ASAE*, Vol. 24, No. 4, pp. 999-1004.

Dursun, E., Karahan, Y. ve Çilingir, İ. (2000). "Türkiye'de üretilen konik hüzmeli bazı meme plakalarında delik çapı ve düzgünlüğünün belirlenmesi." *Tarım Bilimleri Dergisi-Journal of Agricultural Sciences*, Vol. 6, No. 3, pp. 135-140. (in Turkish)

Guest, P. G., (2012). Numerical methods of curve fitting. *Cambridge University Press*, p. 438.

Hoffmann, W. C. and Salyani, M. (1996). "Spray deposition on citrus canopies under different meteorological conditions." *Transactions of the ASAE*, Vol. 39, No. 1, pp. 17-32.

Krishnan, P., Williams, T. H. and Kemble, L. J. (1988). "Technical Note: Spray pattern displacement measurement technique for agricultural nozzles using spray table." *Transactions of the ASAE*, Vol. 31, No. 2, pp. 386-389.

Matthews, G. A. (2004). "How was the pesticide applied?" *Crop Protection*, Vol. 23, pp. 651-653.

Matthews, G. A. and Thornhill, E. W. (1994). "Pesticide application equipment for use in Agriculture." Vol. 1. Manually carried equipment. *FAO Agricultural Services Bulletin*, 112/1, ISSN: 1010-1365, Rome-Italy, p. 163.

Otsu, N. (1979). "A threshold selection method from gray-level histograms." *IEEE Transactions on Systems, Man, and Cybernetics*, Vol. 9, No. 1, pp. 62–66.

Panneton, B., Philion, H., Thériault, R. and Khelifi, M. (2000). "Spray chamber evaluation of air-assisted spraying on potato plants." *Transactions of the ASAE*, Vol. 43, No. 3, pp. 529-534.

Teejet®, 2006. "Sprayer Nozzles." http://www.teejet.com [Accessed 06 Dec 2006].

Zhu, H., Dorner, J. W., Rowland, D. L., Derksen, R. C. and Ozkan, H. E. (2004). "Spray penetration into peanut canopies with hydraulic nozzle tips." *Biosystems Engineering*, Vol. 87, No. 3, pp. 275-273.

Zhu, H., Rowland, D. L., Dorner, J. W., Derksen, R. C. and Sorensen, R. B. (2002). "Influence of plant structure, orifice size, and nozzle inclination on spray penetration into peanut canopy." *Transactions of the ASAE*, Vol. 45, No. 5, pp. 1295-1301.

COMPARISON OF GPS-TEC WITH IRI-2007, IRI-2012 AND IRI-2016 TEC PREDICTIONS AT ISTA STATION, TURKEY

Salih Alcay [*1], Gurkan Oztan [1]

[1] Necmettin Erbakan University, Engineering and Architecture Faculty, Geomatics Engineering Department, Konya, Turkey, salcay@erbakan.edu.tr, oztangurkan@gmail.com

ABSTRACT
The International Reference Ionosphere (IRI) is recognized as the international standard for specifying ionospheric parameters. The first version of the IRI was released in 1978 and followed by several improved editions. However the performance of the model needs to be validated. In this study, TEC prediction performance of IRI-2007, IRI-2012 and IRI-2016 was evaluated at ISTA IGS station (Geographic: 41.10º N, 29.02º E). Model derived TEC values were compared with the GPS-TEC data. The period of comparison includes the quiet days during January 2018 and January 2019. The hourly behavior of TEC differences between GPS-TEC and model derived TEC indicates that the improvement in TEC prediction of IRI-2016 is not clear comparing to the previous versions of the model.

Keywords: *IGS, IRI, ISTA, TEC*

[*] Corresponding Author

1. INTRODUCTION

Ionosphere is the part of Earth's atmosphere including ionized molecules and free electrons which affect radio wave propagation. The variation of the ionosphere effects the performance of spaced based applications including navigation, surveillance systems etc. Therefore monitoring the ionosphere and examination of the ionospheric parameters such as Total Electron Content (TEC) are crucial. TEC values are mostly derived using GPS, which are used as reference (Durmaz *et al*, 2010; Nohutcu *et al*., 2010; Alcay *et al*., 2014; Tariku, 2015; Karia *et al*., 2015; Kumar *et al*., 2016; Wang *et al*., 2017; Alcay *et al*., 2017; Tang *et al*., 2018).

Besides GPS-TEC, TEC values can be obtained using IRI model. For a given place, date and time, IRI model provide TEC data. This empirical model is widely used and continuously being improved and modernized with successive improvements from its previous version. The brief history of the IRI model is provided in Bilitza (2018). In this study we have considered the latest three versions of IRI model (IRI-2007, IRI-2012, IRI-2016) to compare their effectiveness with respect to the observed TEC from GPS observables. IRI-2012 is the model after IRI-2007, including new Bottomside Thickness (ABT-2009) and Te Topside (TBT-2012) options. IRI-2016 has the latest improvements in the model after IRI-2012 by introducing two new F-peak height options (AMTB2013 and SHU-2015). Details of the recent version are provided in Bilitza *et al.* (2017). Thus, with this study it would be possible to realize whether the recent version of IRI (IRI-2016) has superiority, compared to the preceding versions (IRI-2012 and IRI-2007) in terms of TEC prediction.

2. DATA AND METHOD OF ANALYSIS

In this study GPS-TEC and model derived TEC values were compared at ISTA IGS station (Geographic: 41.10º N, 29.02º E), Turkey. Location of this station is given in Fig. 1.

Fig. 1. Location of the ISTA station

GPS-TEC data were obtained using ionolabtecv1.31 software (URL-1) covering one month periods from January 1, 2018 to January 31, 2018 and January 1, 2019 to January 31, 2019.

In order to derive model derived TEC values, the IRI web interfaces URL-2, URL-3 and URL-4, were used to obtain the TEC values from IRI-2007, IRI-2012 and IRI-2016, respectively. In all models, NeQuick option for the topside electron density and CCIR option for the F-Peak were used. We selected Bottomside Thickness (B0 Table) in IRI-2007, (ABT-2009) in IRI-2012 and IRI-2016. In addition, TTSA-2000, TBT-2012 and TBT2012+SA options were chosen for Te Topside in IRI-2007, IRI-2012 and IRI-2016, respectively. Moreover, DS95/TTS05 (IRI-2007), RBV03/TTS03 (IRI-2012) and RBV10/TBT15 (IRI-2016) options were used for ion composition. The major improvement in the recent version (IRI-2016) is the inclusion of F-Peak height models of which the AMTB2013 was considered in this study.

3. RESULTS

This study is restricted to quiet geomagnetic and solar conditions. Thus geomagnetic storm (Kp), geomagnetic activity (Dst) and solar activity (F10.7) indices were examined (Figs. 2, 3). According to the index values, there is no activity that can cause TEC anomaly during the first month of 2018 and 2019.

GPS-TEC and model based TEC values during January 01-31, 2018 and January 01-31, 2019 were obtained at 4 hour intervals and given in Figs. 4, 5. Figure 4 shows that models derived TEC values are similar and except few hours underestimate GPS-TEC during January 01-31, 2018. However, it is interesting to note that IRI-2007 and IRI-2012 TEC data exhibit higher values (reaching above 35 TECU) comparing to the IRI-2016 TEC during January 01-31, 2019 (Fig. 5). This may be due to the problems caused by the updates of the previous versions. Moreover, GPS-TEC and IRI-2016 TEC are consistent and differences generally less than 3 TECU.

Besides, in an attempt to further enhance the evaluation, TEC differences were calculated based on GPS-TEC values. Basic statistical values of the differences, including maximum (absolute), minimum (absolute), range, mean and std values are provided in Table 1. According to the Table 1, the statistical values of the differences are of similar magnitude during January, 2018. While mean of the differences are 2.7 TECU, std values, which indicate the repeatability of differences, are ~2 TECU level. In addition GPS-TEC and IRI-2016 TEC values are consistent during January, 2019. Mean and std of the differences are 2.4 TECU and 1.7 TECU, respectively.

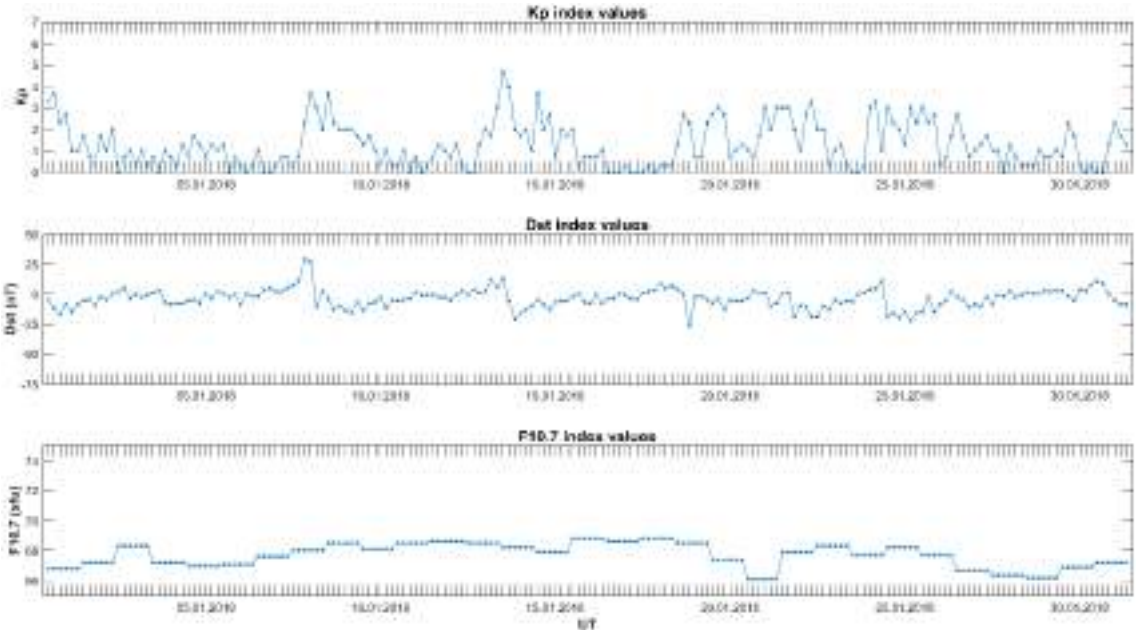

Fig. 2.Kp, Dst and F10.7 index values for January 2018 (URL-5)

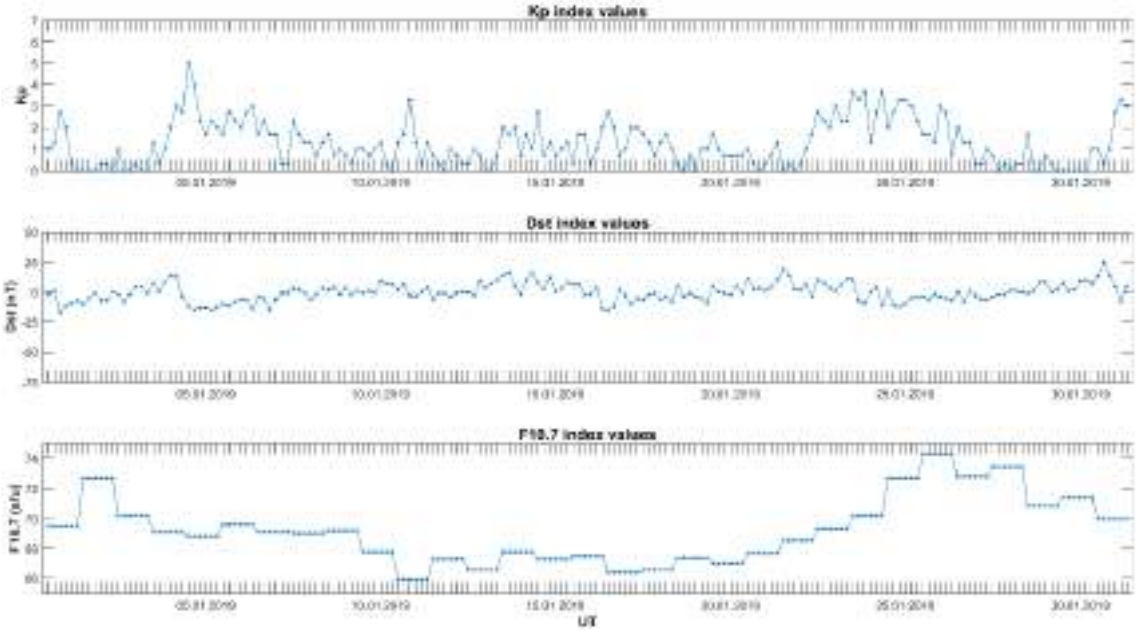

Fig. 3.Kp, Dst and F10.7 index values for January 2019 (URL-5)

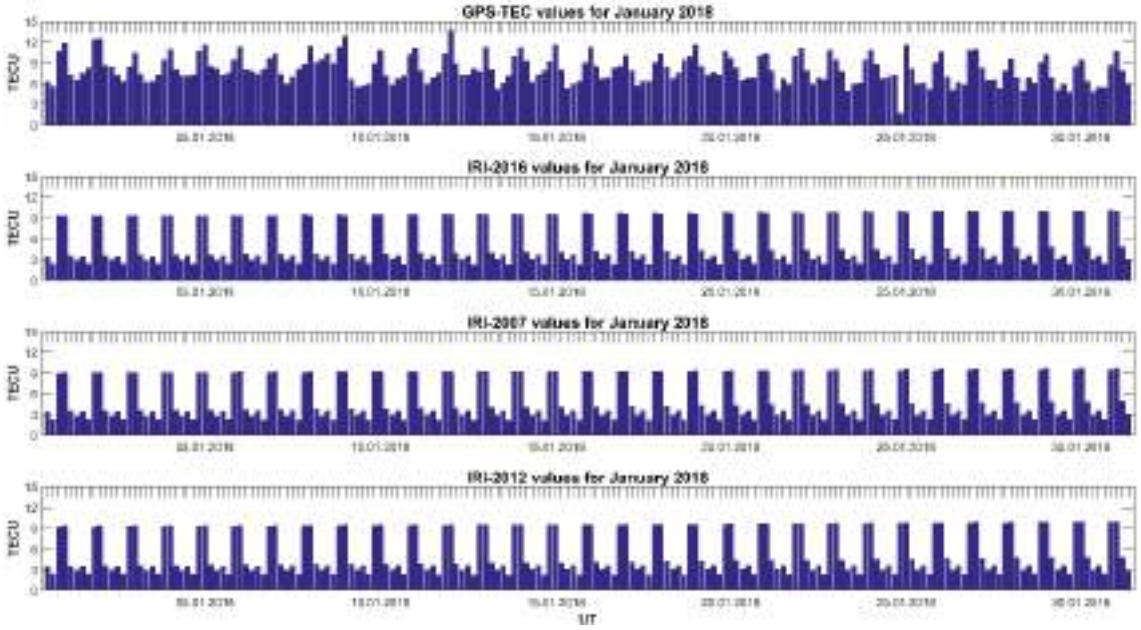

Fig. 4.TEC variation for January 2018 at ISTA IGS station

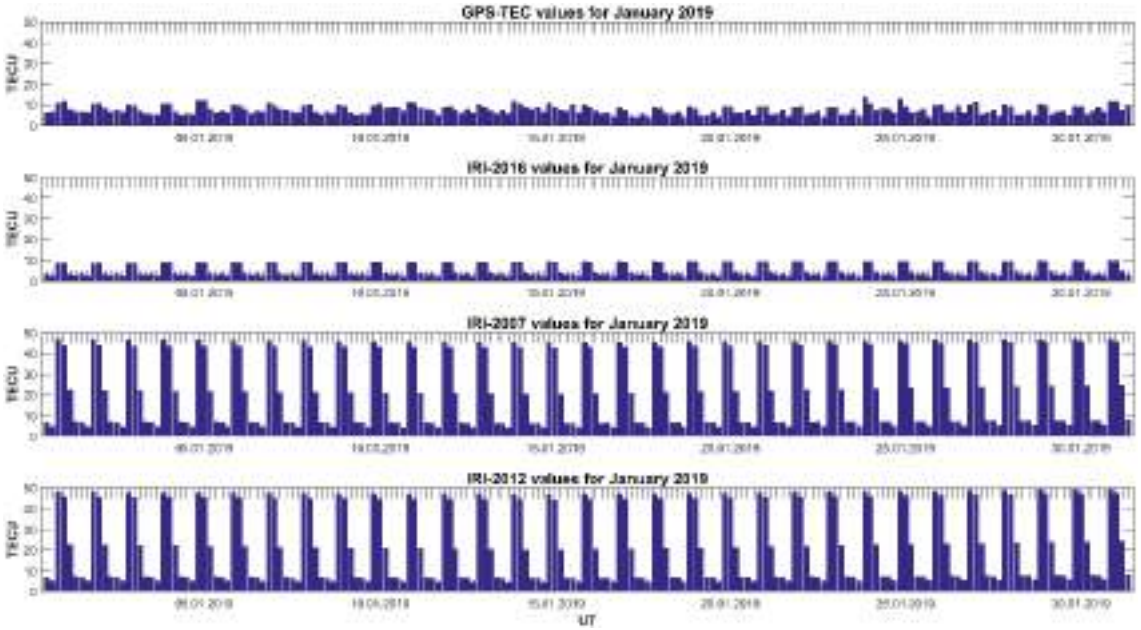

Fig. 5. TEC variation for January 2019 at ISTA IGS station

Table 1. Basic statistical values of the differences

January, 2018			
Statistical Values	**(GPS-TEC) - (IRI-2007)**	**(GPS-TEC) - (IRI-2012)**	**(GPS-TEC) - (IRI-2016)**
Max	7.8	8.2	8.3
Min	0.0	0.1	0.0
Range	15.0	15.4	15.5
Mean	2.8	2.7	2.7
Std	1.9	2.0	2.1
January, 2019			
Max	37.4	39.9	6.5
Min	0.0	0.0	0.1
Range	41.0	43.3	8.3
Mean	-14.1	-14.8	2.4
Std	15.8	16.5	1.7

4. CONCLUSION

In this study TEC prediction performance of IRI-2007, IRI-2012 and IRI-2016 models were tested based on GPS-TEC covering the data for the periods January 01-31, 2018 and January 01-31, 2019. Due to the deficiency of the models in active days, quiet ionospheric periods were chosen. The overall results illustrate that IRI-2007, IRI-2012 and IRI-2016 TEC values are consistent to each other at normal conditions. Models derived TEC values are mostly underestimate the GPS-TEC and mean of the differences are generally at the level of ~2.7 TECU.

ACKNOWLEDGEMENTS

We would like to express our gratitude to the IRI working group for providing IRI-2007, IRI-2012 and IRI-2016 models. The authors would like to thank to IONOLAB group for providing ionolabtecv1.31 software.

REFERENCES

Alcay S., Yigit C.O., Seemala G., Ceylan A. (2014). GPS-Based Ionosphere Modeling: A Brief Review, *Fresenius Environmental Bulletin*, Vol. 23, No. 3a, pp.815-824.

Alcay, S., Oztan, G., Selvi, H.Z. (2017). "Comparison of IRI_PLAS and IRI_2012 model predictions with GPS_TEC measurements in different latitude regions", *Annals of Geophysics*, Vol. 60, No. 5.

Bilitza, D. (2018). "IRI the international standard for the ionosphere", *Advances in Radio Science*, Vol.16, pp. 1-11.

Bilitza, D., Altadill, D., Truhlik, V., Shubin, V., Galkin, I., Reinisch, B., Huang, X. (2017). International Reference Ionosphere 2016: From ionospheric climate to real-time weather predictions, *Space Weather*, 15, No.2, 418-429.

Durmaz, M., Karslioglu, M.O., Nohutcu, M. (2010). "Regional VTEC modeling with multivariate adaptive regression splines", *Advances in Space Research*, Vol. 46, No. 2, pp. 180–189.

Karia, S.P., Patel, N.C., Pathak, K.N. (2015). "Comparison of GPS based TEC measurements with the IRI-2012 model for the period of low to moderate solar activity (2009–2012) at the crest of equatorial anomaly in Indian region", *Advances in Space Research*, Vol. 55, No. 8, pp. 1965–1975.

Kumar, S., Patel, K., Singh, A.K. (2016). "TEC variation over an equatorial and anomaly crest region in India during 2012 and 2013", *GPS Solutions*, Vol. 20, No. 4, pp. 617-626.

Nohutcu, M., Karslioglu M.O., Schmidt, M. (2010). "B-Spline modeling of VTEC over Turkey using GPS observations", *Journal of Atmospheric and Solar-Terrestrial Physics*, Vol.72, No. 7-8, pp. 617-624.

Tang, L., Li, Z., Zhou, B. (2018). "Large-area tsunami signatures in ionosphere observed by GPS TEC after the 2011 Tohoku earthquake", *GPS Solutions,* Vol. 22, No. 93.

Tariku, Y.A. (2015). "Comparison of GPS-TEC with IRI-2012 TEC over African equatorial and low latitude regions during the period of 2012–2013", *Advances in Space Research*, Vol. 56, No. 8, pp. 1677–1685.

Wang, N., Yuan, Y., Li, Z., Ying, L., Huo, X., Min, L. (2017). "An examination of the Galileo NeQuick model: comparison with GPS and JASON TEC", *GPS Solutions*, Vol. 21, No. 2, pp. 605-615.

URL-1 ionolabtecv1.30 software, http://www.ionolab.org/ [Accessed 10 July 2019].

URL-2 web interface of IRI-2007 model, https://ccmc.gsfc.nasa.gov/modelweb/models/iri_vitmo.php [Accessed 12 July 2019].

URL-3 web interface of IRI-2012 model, https://ccmc.gsfc.nasa.gov/modelweb/models/iri2012_vitmo.php [Accessed 12 July 2019].

URL-4 web interface of IRI-2016 model, https://ccmc.gsfc.nasa.gov/modelweb/models/iri2016_vitmo.php [Accessed 12 July 2019].

URL-5 web interface of kp, Dst and F10.7 indices https://omniweb.gsfc.nasa.gov/form/dx1.html [Accessed 10 July 2019]

DYNAMIC PERFORMANCE COMPARISON OF PI AND INTERVAL TYPE-2 TAKAGI-SUGENO-KANG FUZZY CONTROLLER ON POSITIVE OUTPUT LUO CONVERTER

Ö. Fatih Keçecioğlu [1], Ahmet Gani [*2] and Erdal Kılıç [3]

[1] Kahramanmaraş Sütçü İmam University, Faculty of Engineering and Architecture, Department of Electrical and Electronics Engineering, Turkey, Kahramanmaraş, fkececioglu@ksu.edu.tr

[2] Kahramanmaraş Sütçü İmam University, Faculty of Engineering and Architecture, Department of Electrical and Electronics Engineering, Turkey, Kahramanmaraş, agani@ksu.edu.tr

[3] Kahramanmaraş Sütçü İmam University, Faculty of Engineering and Architecture, Department of Electrical and Electronics Engineering, Turkey, Kahramanmaraş, ekilic@ksu.edu.tr

ABSTRACT

Luo converter, a high voltage gain converter, shows a higher voltage gain and a lower output voltage ripple compared to conventional boost DC-DC converters. Luo converters perform voltage gain using a voltage lift method. Voltage gain is adjusted thanks to various circuit topologies using voltage lift method. Unlike linear circuit topologies, it is often difficult to model and control DC-DC converter circuits due to their switched structure. Conventional controllers such as PI, PD and PID remain inefficient in terms of controlling non-linear systems. Therefore, fuzzy logic based modern and intelligent controllers are needed in order to improve the performance of non-linear systems. The present study proposes a PI and an Interval Type-2 Takagi-Sugeno-Kang Fuzzy Controller (IT2TSKFLC) for Luo converter with a positive output self-lift (POSLLC) circuit topology. MATLAB/Simulink was used to analyze the dynamic performance of these controllers.

Keywords: *Fuzzy Control, Luo Converter.*

[*] Ahmet GANİ

1. INTRODUCTION

Luo converters offer several advantages such as higher output voltage, higher power density, higher efficiency and lower output voltage ripples (Luo, 1999). Fuzzy logic (FL) can be defined as a set of rules which can be used to control mathematically undefinable complex systems. FL aims at transferring verbal expressions to the computer on the basis of mathematical expressions thanks to an expert's experience (Acikgoz, 2018). Introduced by L. Zadeh in 1975, Type-2 fuzzy logic controller (T2FLC) has been one of the most popular research topics in recent years (Zadeh, 1965). Because T2FLC shows a better performance in modelling uncertainties compared to Type 1 FLC (T1FLC), it yields betters results in controlling systems. T2FLC provides an efficient and adaptable structure for a high controlling performance against system uncertainties and parameter changes (Kumbasar *et al*., 2012). The present study proposes an IT2TSKFLC, which is a special version of T2FLC, and a PI controller for the robust control of POSLLC. Section 2 POSLLC describes circuit structure and equations. Section 3 and 4 present IT2TSKFLC controlling system and PI controller, respectively. Section 5 discusses simulation studies. The conclusion section presents findings.

2. POSITIVE OUTPUT SELF LİFT LUO CONVERTER

Various circuit topologies using voltage lift technique can be found in the literature such as elementary circuit, self-lift circuit, re-lift circuit, triple-lift and quardruple-lift circuit. Voltage lift technique eliminates effect of the parasitic elements, and thus offers a higher voltage gain and a lower output voltage ripple (Rashid, 2017). Positive output self-lift Luo converter (POSLLC) with a circuit topology is shown in Fig. 1.

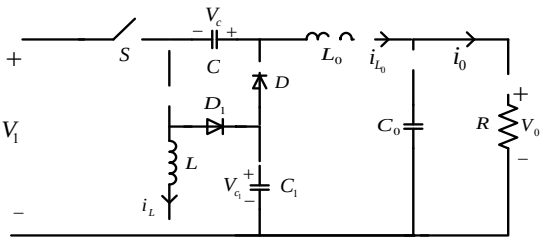

Fig. 1. POSLLC circuit model

When S switch is turned on, D_1 is on whereas D diode is off. At a steady state, inductor voltages are zero for a certain period of time. During switch on period, voltage in C_1 capacitor is equal to source voltage. In this situation, i_L inductor current increases whereas it starts to decrease during switch off period. The equivalent circuit during switch on period is shown in Fig. 2.

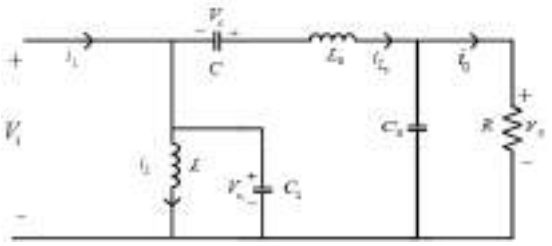

Fig. 2 POSLLC equivalent circuit during switch on period

Eq.1 can be written for the equivalent circuit during switch on period.

$$V_0 = V_c = V_{c_1} = \frac{V_1}{1-k} \tag{1}$$

Because all components are ideal, power loss of circuit elements is neglected. Therefore, it is assumed that output power is considered as equal to the input power.

When S switch is turned off, D is on whereas D_1 diode is off. The equivalent circuit during switch off period is shown in Fig. 3.

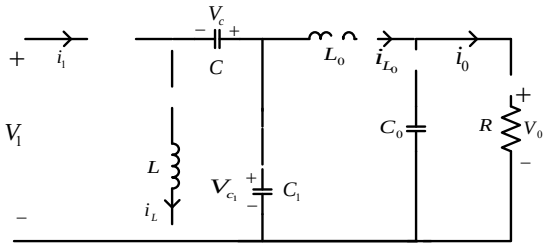

Fig. 3 POSLLC equivalent circuit during switch off period

During switch off period, D diode is forward biased on and C capacitor is charged with input voltage (Chilambarasan *et al.*, 2014). Eqs. 2-3 can be written for the equivalent circuit.

$$I_0 = I_L \tag{2}$$

$$I_1 = \frac{I_0}{1-k} \tag{3}$$

3. INTERVAL TYPE 2 TAKAGI-SUGENO-KANG FUZZY LOGIC CONTROLLER

In the design of T1FLC, the expert has to define the rules and parameters for the membership function. Uncertainties encountered in defining the rules may derive from the expert's linguistic definitions. Problems may occur in defining the crisp values required for the membership function (Karanjkar, 2014). These problems in T1FLCs may cause some instabilities such as measurement errors and changes in operating conditions of the controller. Furthermore, these unstable conditions can be considered as membership function uncertainties in IT2TSKFLCs. IT2TSKFLCs can eliminate adverse effects in instability conditions. IT2TSKFLC consists of four main parts: fuzzifier, a rule base, a fuzzy inference, and a type reducer. The most important difference

between IT2TSKFLC and T1FLC is type reduction. Type-2 information is converted to Type-1 information by means of the type reducer. The output of type-reduction block is called type-reduced set. The type reduced set is used for defuzzification process (Acikgoz, 2018). The internal structure of in IT2TSKFLC is shown in Fig. 4.

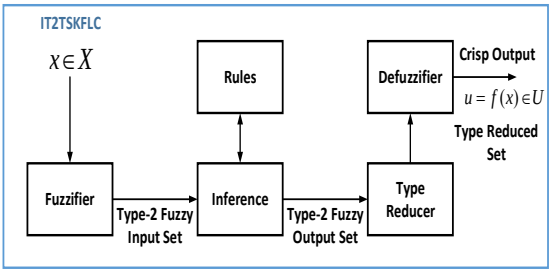

Fig. 4 The internal structure of IT2TSKFLC

Introduced by Takagi, Sugeno and Kang, Takagi-Sugeno-Kang (TSK) is a fuzzy modelling method that comprises high dimensions, non-linearity and complexity (Takagi et al., 1985). An interval type-2 TSK model has a structure with two inputs and single output using rules given in Eq. 4. (Mendel, 2001):

$$R_i: IF\ x_1 \text{ is } \tilde{A}_{1i}\ \text{AND}\ \ldots\ x_n \text{ is } \tilde{A}_{ni}\ \text{THEN}\ y_i^{'} = c_{0i} + c_{1i}x_1 + \ldots + c_{ni}x_n \quad (4)$$

where i = 1…r represents the IF-THEN rules of the fuzzy system; $x_1, \ldots, x_n$ are input variables and $\tilde{A}_{ni}$ is membership function (MF) of IT2TSKFLC for the variable n and rule r; and $y_i^{''}$ is the rule output; and $c_0 + c_1 + \ldots + c_n$ are the consequent parameters. In the present study; Gaussian type MF is preferred as shown in Fig.5. The mathematical equations of Gaussian type MF are expressed in Eqs. 5-6:

$$\bar{\mu}_{ij} = \exp\left\{-\frac{1}{2}\left(\frac{x_i - c_{ij}}{\bar{\sigma}_{ij}}\right)^2\right\} \quad (5)$$

$$\underline{\mu}_{ij} = \exp\left\{-\frac{1}{2}\left(\frac{x_i - c_{ij}}{\underline{\sigma}_{ij}}\right)^2\right\} \quad (6)$$

Where, c_{ij} is the mean value, σ_{ij} is standard deviation, and x_i is the input variable.

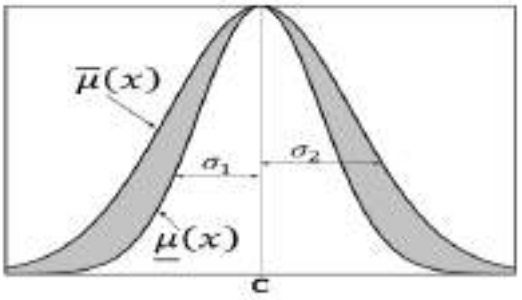

Fig.5. Gaussian type-2 fuzzy set

The t-norm operation is defined in Eq. 7:

$$f_i = \prod_{j=1}^{n} \mu(x_j) \quad (7)$$

A normalized firing strength can be defined in Eq.8:

$$\bar{f}_i = \frac{f_i}{\sum_{k=1}^{r} f_k} \quad (8)$$

$\bar{f}_i$ denotes the normalized firing strength. IT2TSKFLC includes lower and upper membership functions in case of uncertainties (Chang *et al*., 2011). The firing strengths of a fuzzy rule is defined as lower and upper using the t-norm operator in Eqs. 9-10, respectively.

$$\underline{f}_i = \prod_{j=1}^{n} \underline{\mu}(x_j) \quad (9)$$

$$\bar{f}_i = \prod_{j=1}^{n} \bar{\mu}(x_j) \quad (10)$$

Biglarbegian-Melek-Mendel (BMM) method is closed-form type reduction and defuzzification methods used in IT2TSKFLC (Biglarbegian *et al*., 2010). Closed mathematical form of type reduction and defuzzification process for the proposed IT2TSKFLC is calculated using Eq. 11.

$$Y_{BMM} = q\frac{\sum_{i=1}^{r} f_i\, y_i}{\sum_{i=1}^{r} \underline{f}_i} + p\frac{\sum_{i=1}^{r} \bar{f}_i\, y_i}{\sum_{i=1}^{r} \bar{f}_i} \quad (11)$$

4. PI CONTROLLER

PI controller is widely used by researchers due to its easy structure. Generally, the output of a classical PI controller is represented by Eq.12.

$$u(t) = K_p e(t) + K_i \int_0^t e(t)dt \quad (12)$$

In the present study, Ziegler–Nichols method is selected to adjust the parameters of the PI controller because it does not need a mathematical model of the system. The parameters Kp and Ki are designed from plant step response. From Ziegler–Nichols method, the parameters Kp and Ki of the controller are obtained as 0.001 and 5 for the POSLLC converter, respectively.

5. SIMULATION STUDIES

IT2TSKFLC designed in the present study have two inputs and a single output. The inputs are the error (e) and change of error (de).Gaussian membership functions were selected for each input as shown in Fig. 6.

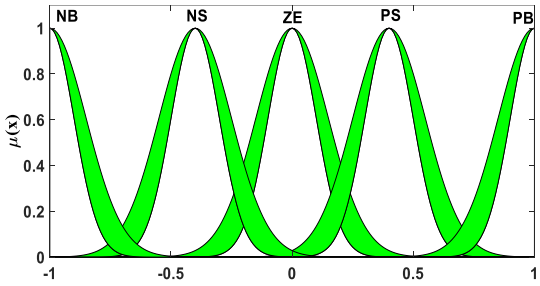

Fig. 6. Gaussian membership functions selected for the error and change of error

A value range of [-1, 1] was set for Gaussian membership functions. Linguistic variables used for the error and change of error in Matlab/Simulink simulation of the designed system were selected as Negative Big (NB), Positive Big (PB), ZE (S), Negative Small (NS), Positive Small (PS). In addition, a rule base of 25 rules consisting of these linguistic variables are presented in Table 1.

Table 1. 5x5 rule base

e \ de	NB	NS	ZE	PS	PB
NB	**NB**	**NB**	**NB**	**NS**	**ZE**
NS	**NB**	**NB**	**NS**	**ZE**	**PS**
ZE	**NB**	**NS**	**ZE**	**PS**	**PB**
PS	**NS**	**ZE**	**PS**	**PB**	**PB**
PB	**ZE**	**PS**	**PB**	**PB**	**PB**

In the analysis of POSLLC, boundary values of proposed converter were calculated using Eqs. 13-17 based on the variation ratios of inductor currents and variation ratios of capacitor voltages.

$$\zeta_1 = \frac{R}{2M^2 fL} \tag{13}$$

$$\zeta_2 = \frac{kR}{2MfL_0} \tag{14}$$

$$\rho = \frac{k}{2fCR} \tag{15}$$

$$\sigma_1 = \frac{M}{2fC_1R} \tag{16}$$

$$\varepsilon = \frac{k}{8Mf^2L_0C_0} \tag{17}$$

Continuous current mode (CCM) is a steady state mode for converter circuits. Voltage gain in POSLLC for CCM is given in Eq. 18.

$$M = \frac{V_0}{V_i} = \frac{1}{1-k} \tag{18}$$

k in Eq. 18 represents the duty cycle of POSLLC. The calculated boundary values for CCM in POSLLC are given in Table 2.

Table 2. Boundary values for POSLLC

V_I	20 V	L	1.1 mH
V_0	60 V	C_0	8 uF
R	100 Ω	C	10.67 uF
k	0.6667	C_1	12 uF
L_0	2.2 mH	f	50 Khz
M	3	ζ_1	0.1
ζ_2	0.1	ρ	0.00625
σ_1	0.025	ε	0.000625

Real converter values should be selected higher than boundary values for CCM. The selected converter parameters for simulation studies are given in Table 3.

Table 3. Selected values for POSLLC

V_I	20 V	L	10 mH
V_0	60 V	C_0	1300 uF
R	100 Ω	C	1300 uF
k	0.6667	C_1	1300 uF
L_0	10 mH	f	50 Khz
M	3	ζ_1	0.1
ζ_2	0.1	ρ	0.00625
σ_1	0.025	ε	0.000625

It can be understood that i_{L0} and i_L current variation ratios and C, C_0, and C_1 voltage variation ratios are low. V_0, which is the output voltage, is an actual DC voltage with slight ripple. In addition, I_0, which is the output current, is an actual DC waveform with slight ripple. The circuit controlling model of POSLLC is shown in Fig. 7.

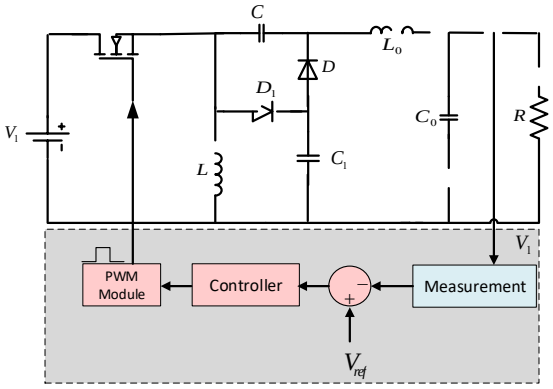

Fig. 7. POSLLC circuit controlling model

The performances of controllers for tracking reference voltage are shown in Fig. 8.

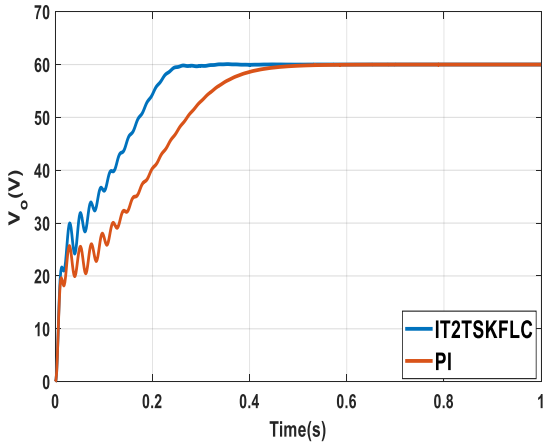

Fig. 8. Dynamic responses of controllers

As shown in Fig. 8, the response of the proposed IT2TSKFLC converter is remarkably faster compared to PI converter, and reached reference voltage in a shorter period of time.

5. CONCLUSION

The present study designed a simulation model using Matlab/Simulink environment in order to analyze the performances of the proposed IT2TSKFLC and PI converters for POSLLC circuit model. The findings of the simulation studies are showed that IT2TSKFLC has more efficient dynamic performance compared to PI controller in terms of parameters such as rise time, settling time and steady state error.

ACKNOWLEDGEMENTS

This work was financially supported by the Kahramanmaras Sutcu Imam University, Scientific Research Projects Unit, the project entitled “Dynamic Performance Comparison Of PI and Interval Type-2 Takagi-Sugeno-Kang Fuzzy Controller On Positive Output Luo Converter” under Project No: 2019/4-40 UKSP.

REFERENCES

Acikgoz, H. (2018). “Speed Control of DC Motor Using Interval Type-2 Fuzzy Logic Controller.” *International Journal of Intelligent Systems and Applications in Engineering*, Vol. 6, No. 3, pp. 197-202.

Biglarbegian, M. Melek, W. W., and. Mendel, J. M.(2010). “On the stability of interval type-2 TSK fuzzy logic control systems,” Systems, Man, and Cybernetics, Part B: Cybernetics, IEEE Transactions on, Vol. 40, No. 3, pp. 798–818.

Chang, C.C. Lin, C.J. (2011). “LIBSVM: A library for support vector machines,” ACM Trans. Intel. Sys. and Tech., Vol. 2, No.3, pp. 1–27.

Chilambarasan, M. Devi, M.L. Babu,M.R. (2014). "Design and Simulation of Self Lift Positive Output Luo Converter Using Incremental Conductance Algorithm for Photovoltaic Applications", Applied Mechanics and Materials, Vol. 622, pp. 51-58.

Karanjkar, D.S. Chatterj, S. Kumar, A. Shimi, S .L. (2014).“Fuzzy Adaptive Proportional-Integral-Derivative Controller with Dynamic Set-Point Adjustment for Maximum Power Point Tracking in Solar Photovoltaic System”, Systems Science & Control Engineering, Vol. 2, No.1, pp.562-582.

Kumbasar, T. et al., (2012). “Type-2 Fuzzy Model Based Controller Design for Neutralization Processes”, ISA Transactions, Vol. 51, No. 2, pp. 277-287.

Luo, F.L. (1999). “Positive Output Luo Converters: Voltage Lift Technique.” *IEE Proc., Electric Power Applications*. Vol.146 No.4, pp.415-432.

Mendel, J.M. (2001). “Uncertain Rule-Based Fuzzy Logic Systems” Introduction and New Directions. Prentice Hall.

Rashid, M. H. (2017). “Power Electronics Handbook”. Academic Press, California, USA.

Takagi, T. Sugeno, M. (1985) “Fuzzy Identification of Systems and Its Applications to Modeling and Control,” IEEE Transactions on Systems, Man, and Cybernetics, Vol. SMC-15, No. 1, pp. 116–132.

Zadeh, L.A. (1965) “Fuzzy Sets”, *Information and Control*, Vol. 8, pp. 335-353.

CISET - 2nd Cilicia International Symposium on Engineering and Technology
10-12 October, 2019, Mersin / TURKEY

Renewable Bio-Based Filler for EPDM Rubber: Indian Laura (*ficus nitida)*

İsmail Kutlugün AKBAY [1] and Ahmet GÜNGÖR *[2]

[1] Mersin University, Engineering Faculty, Chemical Engineering Department, Mersin, TURKEY, akbay@mersin.edu.tr

[2] Mersin University, Engineering Faculty, Chemical Engineering Department, Mersin, TURKEY, ahmet.gungor@mersin.edu.tr

ABSTRACT
Indian Laura is an evergreen tree with a very high amounts of fallen leaf that could be used as an engineering material. Carbon black, which is the leading filler material in rubber industry, is a very harmful and carcinogenic filler. In order to decrease its harmful effects, we aimed to partly replace carbon black with Indian Laura leafs without gave up much properties. Indian Laura leaves was collected and milled to improve the interaction with the rubber matrix. The rheological tests showed that the addition improves the molding conditions positively. The mechanical test results showed that the addition improves the toughness of the material and it can lead to increase the usage scenarios. The gel content and swelling ratio tests indicates that the filler is in well corporate with the EPDM matrix. The results showed that, an unused natural waste could be used as an alternative bio-based filler material.

Keywords: *Indian Laura, Bio-based Filler, EPDM, rubber, waste management*

* Corresponding Author

1. INTRODUCTION

Thermosets, which is a subgroup of polymeric materials, have been used extensively for engineering purposes. Natural rubber had been used without knowing its full potential by native people for several centuries. In 19th century, after finding the sulphur vulcanization, several different rubber types were found (Ninyong *et al.*, 2017).

One of this findings is EPDM rubber. Because of its unsaturated nature, unlike EPM rubber, it can mixture with other types of polymers, and can vulcanized with different types of chemicals. Moreover, EPDM rubber has high resistance to air, ozone, polar liquids, and has high mechanical and thermal strength (Ravishankar, 2012).

Carbon black, which is one of the main fillers of EPDM rubber is extensively used for strengthening filler for rubber production. Also, it is also utilised as a dye in the rubber and plastic industry because of its chemical and thermal properties. Unfortunately, it is tremendously dangerous to the health of the workers in rubber industry. To overwhelmed above-mentioned drawbacks, the recent intention is to practice the bio-based and biodegradable materials within the rubber matrix (Kanking *et al.*, 2012).

Indian Laura (IL) or Benjamin fig is a tree reaching up to 25 metres tall in its natural habitat, which make a very large and leafy tree for parks and urban areas. Unfortunately, Indian Laura, is a very deciduous tree and an evergreen tree. There are many fallen leaf in the planting areas. This tree also has a stick sap for its healing properties, and it's leafs also contain this sap in its matrix. With this way, a valuable product lost in nature can be used as a biodegradable filler (Ali *et al.*, 2016).

There are several studies that have been researched for the probable use of bio-based fillers in rubber studies. Karaağaç has studied procedure of pistachio shells as strengthening filler in NR/SBR rubber composites (Karaağaç, 2014). Botros et al studied a natural rubber based lignin containing composite material and it is enforcing the all properties of the composite after the addition (Botros *et al.*, 2005). Shivamurthy et al. studied jatropha seed cake waste within epoxy and the accumulation of the jatropha seed cake waste amplified the mechanical and wear properties of the composites (Shivamurthy *et al.*, 2014). Menon et al. studied the natural rubber (NR) modified with cashew nut shell liquid with different amounts and the tear strengths and tensile properties are improved (Menon *et al.*, 1998).

Therefore, the fallen Indian Laura could be facilitated for the purpose of a free and useful filler material. The dried leafs was milled with a laboratory type mill and it is used as a filler material within the EPDM rubber. Several analysis were done to understand its interaction with the rubber matrix.

2. MATERIAL & METHOD

Indian Laura leaves were collect in Mersin University campus. Only the fallen leafs are collected. The taken leafs were washed with tap water three times then washed with distilled water three times. The cleaned leaves were dehydrated in a laboratory-type oven at 60°C to fixed weighing. The dried leaves were milled with a laboratory type grounder then sieved with different mesh-sized sieves. Only the <250 μm sized leaves were used in the experiments.

The composites with different amounts of IL leaves were prepared according to formulate that is given in Table 1.

Table 1. Used Materials and their function in the Rubber Matrix (phr: per hundred rubber)

Materials	Function	phr
KELTAN 9650Q	Polymer	100
Carbon Black	Filler	30
Zinc Oxide	Activator	1.5
Mineral Oil	Lubricant	32
Stearic Acid	Activator	1
TAC 50	Coagent	1
Perkadox	Agent	5
Waste Leaves (IL)	Filler	0, 10, 20

EPDM compound with waste leaves (IL) was prepared with a Kneader type closed mixer. After the rubber mixture were reached up to 60°C, the mixing was stopped and the all compound were compressed in a laboratory scale two-roll mill to prepare a 2 mm-shaped compound. The obtained compound was placed into a 2 mm mound and vulcanized in a thermal hydraulic press under 20 MPa pressure at different for moving die rheometer (MDR) specified minutes.

The mechanical properties of prepared EPDM/IL composites samples were obtained according to the ASTM D412 Type C standard. The dogbone shaped samples were prepared using a sample cutter press. The tensile test was done using a universal testing machine with a 20 kN gauge. The crosshead speed was applied at a 50 mm/min rate. Hardness of samples were done with a laboratory type Shore A hardness device.

The gel content of the prepared samples was analysed using Soxhlet extraction method. The gel content of the samples was calculated using Eq. (1) where w_i is initial weight of sample and w_f is final weight of the sample. The solvent used in the experiment was Hexane and the experiments were done at 70 °C. The swelling ratio of the samples was analysed using petri cup using toluene as the swelling medium. The swelling ratio of the samples was calculated using Eq. (2) where w_i is initial weight of sample and w_f is final weight of the sample (Akbay *et al.*, 2017).

$$\%\ Gel\ Content = \frac{W_f}{W_i} x100 \quad (1)$$

$$\%\ Swelling\ Ratio = \frac{W_f - W_i}{W_i} x100 \quad (2)$$

The rheological parameters and the vulcanization kinetics of EPDM/IL samples were analysed according to ASTM D5289 by a laboratory type MDR at temperatures of 180 °C with an oscillating arc of 3° for different contents of EPDM/IL composites. The CRI values calculated as follows in Eq. (3) where t_{s2}, is the scorch time and t_{90}, is the optimum cure time (Güngör *et al.*, 2018).

$$CRI = 100/(t_{90} - t_{s2}) \quad (3)$$

3. RESULTS & DISCUSSION

3.1. MDR test

In order to a comprehensive evaluation of waste leaf addition to the EPDM matrix, vulcanization process should be examined thoroughly. Therefore, we aimed to achieve low t_{s2} and high t_{90} values for better moulding times. Fig. 1 shows the MDR torque results of the prepared composites. The results showed that the addition ground IL particles increased the torque value of the samples. Moreover, the addition has led to reach the aim of low t_{s2} and high t_{90} values. Unfortunately, IL20 sample has bad MDR values for our case, mainly due to discontinuity within the EPDM matrix. Table 2 shows the calculated CRI values. The results showed that the best resulting samples is IL10. This could be interpreted that the optimal IL content is 10 phr. The IL20 sample has high IL content and it reduces the free space within the EPDM matrix which leads to the decreased values of CRI (Leroy *et al.*, 2013).

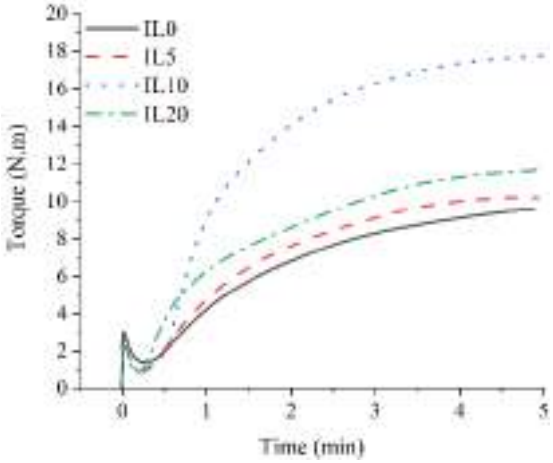

Fig 1. MDR torque curves of the samples

Table 2. MDR tests results

	t_{s2} (min)	t_{90} (min)	CRI
IL0	0.41	4.54	24.21
IL5	0.38	4.31	25.45
IL10	0.55	4.13	27.93
IL20	0.27	4.45	23.92

3.2. Mechanical Tests

Main property of an engineering rubber is mechanical properties. In order to achieve a proper usage, high mechanical results must be achieved. As a result of this thought, gummy nature of IL leafs was utilised as a bio-based filler material. The mechanical tests results of the samples are given in Fig. 1. The results showed that the addition of IL leafs increased both tensile and elongation values of the samples. Unfortunately, the results of the IL20 sample decreased with the addition of IL leafs. To understand this result, hardness values of the samples has examined. The results showed that the IL addition increased the hardness of the samples. So, the filler content of IL20 sample has increased the hardness value of the sample to a point that the material starts to abrasive wearing within the EPDM matrix. Thus, the mechanical properties has a sharp decrease that leads to low values of tensile strength and elongation at break values.

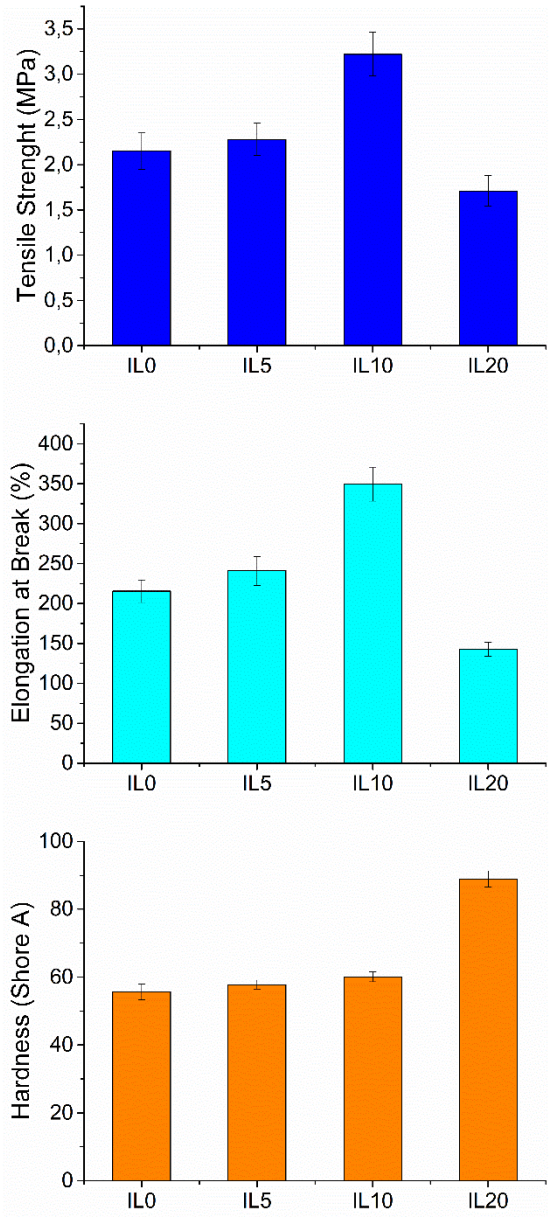

Fig 2. Mechanical tests results of the samples

3.3. Swelling Properties

Swelling ratio and gel content of the prepared samples are given in Fig. 3. As it is well-known that, swelling ratio and gel content are inversely proportional to each other. This is a well-stated in Fig 3. Moreover, IL addition increased the gel content of the samples which is in line with mechanical test results. The further addition on IL10 has decreased the gel content of the samples which could be a sign of low interlayer interaction with the EPDM matrix (Salvatierra *et al.*, 2004).

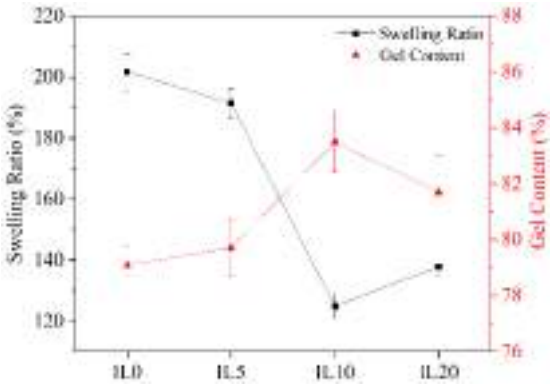

Fig 3. Swelling data of the samples

4. CONCLUSION

In this study, we aimed to use fallen Indian Laura leafs as a bio-based filler within the EPDM rubber. Without using any chemicals or hurting any tree or plant, we manage to improve the properties of a highly used engineering rubber, which is EPDM. The MDR test results showed that the addition of IL leafs increased the t_{s2} values up to 0.55 minutes which is very good for moulding processes. Mechanical properties of samples has increased with the addition of the IL leafs. Moreover, both increase in elongation break and tensile strength values means the toughness of the samples has increased which could increase the usage scenarios of the prepared composite. Swelling analysis were done in order to understand the gel content variation for IL leaf increment. The gel content and swelling ratio results showed that the addition of IL leaf is sufficient to improve its swelling properties. The study, according to the analysis, showed that the best performing sample is IL10. The results are hearting enough to pursue Indian Laura leafs within EPDM and other polymeric and rubber materials as a bio-based filler material against carbon black or other synthetic filler materials.

REFERENCES

Akbay, İ. K., Güngör, A. and Özdemir, T. (2017) 'Optimization of the vulcanization parameters for ethylene–propylene–diene termonomer (EPDM)/ground waste tyre composite using response surface methodology', *Polymer Bulletin*, Vol. 74, No. 12, pp. 5095–5109.

Ali, I. H. and Alrafai, H. A. (2016) 'Kinetic, isotherm and thermodynamic studies on biosorption of chromium(VI) by using activated carbon from leaves of Ficus nitida', *Chemistry Central Journal*, Vol. 10, No. 1, p. 36.

Botros, S., Eid, M. and Nageeb, Z. (2005) 'Thermal Stability and Dielectric Relaxation of NR/Soda Lignin and NR/thiolignin Composites', *Egypt. J. Solids*, Vol. 28, No. 1, pp. 67–83.

Güngör, A. *et al.* (2018) 'Flexible X/Gamma ray shielding composite material of EPDM rubber with bismuth trioxide: Mechanical, thermal investigations and attenuation tests', *Progress in Nuclear Energy*, Vol. 106, pp. 262-269.

Kanking, S. *et al.* (2012) 'Use of bagasse fiber ash as secondary filler in silica or carbon black filled natural rubber compound', *Materials & Design*. Elsevier, Vol. 41, pp. 74–82.

Karaağaç, B. (2014) 'Use of Ground Pistachio Shell as Alternative Filler in Natural Rubber/Styrene–Butadiene Rubber-Based Rubber Compounds', *Polymer Composites*, Vol. 35, No. 2, pp. 245–252.

Leroy, E. *et al.* (2013) 'A knowledge based approach for elastomer cure kinetic parameters estimation', *Polymer Testing*, Vol. 32, pp. 9–14.

Menon, a R. R., Pillai, C. K. S. and Nando, G. B. (1998) 'Physicomechanical properties of filled natural rubber vulcanizates modified with phosphorylated cashew nut shell liquid', *Journal of Applied Polymer Science*, Vol. 68, No. 8, pp. 1303–1311.

Ninyong, K. *et al.* (2017) 'Potential use of NR and wood/NR composites as thermal neutron shielding materials', *Polymer Testing*, Vol. 59, pp. 336–343.

Ravishankar, P. S. (2012) 'Treatise on Epdm', *Rubber Chemistry and Technology*, Vol. 85, No. 3, pp. 327–349.

Salvatierra, L. M. *et al.* (2004) 'Growing of crystalline zones in EPDM irradiated with a low neutron flux', *Nuclear Instruments and Methods in Physics Research Section B: Beam Interactions with Materials and Atoms*, Vol. 225, No. 3, pp. 297–304.

Shivamurthy, B. *et al.* (2014) 'Mechanical properties and sliding wear behavior of jatropha seed cake waste/epoxy composites', *Journal of Material Cycles and Waste Management*, Vol. 17, No. 1, pp. 144–156.

CISET - 2nd Cilicia International Symposium on Engineering and Technology
10-12 October, 2019, Mersin / TURKEY

THE APPLICATION OF WASTE BLUE CRAB SHELL AS A BIO-BASED FILLER IN EPDM RUBBER

Ahmet GÜNGÖR [1], İsmail Kutlugün AKBAY [*2] and Tonguç ÖZDEMİR[3]

[1] Mersin University, Engineering Faculty, Chemical Engineering Department, Mersin, TURKEY, ahmet.gungor@mersin.edu.tr

[2] Mersin University, Engineering Faculty, Chemical Engineering Department, Mersin, TURKEY, akbay@mersin.edu.tr

[3] Mersin University, Engineering Faculty, Chemical Engineering Department, Mersin, TURKEY,

tonguc.ozdemir@mersin.edu.tr

ABSTRACT
Rubber materials are frequently used with different filler materials in order to improve the mechanical, thermal and rheological properties. Carbon black is the most preferred filler material due to the high mechanical and thermal properties. Despite its superior properties, carbon black has a carcinogenic effect and is a problem for both employees and the environment. In recent years, many studies have been done on the use of bio-based filler material within the rubber matrix. Mersin is one of the natural habitats of blue crabs and blue crab is consumed frequently in this region. In this study, waste blue crab shells washed and milled were added in EPDM matrix as bio-based filler material in different amounts and the effect of the material on mechanical, rheological and swelling properties was investigated. Characterization results showed that the addition of blue crab shell was considerably improved the tensile and rheological properties of sample up to 10BCS case. In addition, swelling properties indicates that the BCS is in well corporate with the EPDM matrix. the obtained results indicated that the use of BCS as a filler material is a significant alternative with regards to economic and environmental concerns.

Keywords: *Blue Crab Shell, Bio-based Filler, EPDM, Rubber, Waste Management*

[*] Corresponding Author

1. INTRODUCTION

In the synthesis of rubber material, the blending of rubbers prepares a new composite with a wide array of usages by having the edge on the interesting properties of the mixture component when avoiding the economic and technical uncertainties related to synthesizing new composite materials. Mixing two or more types of rubber or adding new fillers is useful in the preparation of non-blending materials in the rubber (Martinez *et al.*, 2011). Natural rubber and natural rubber based materials are often preferred in rubber applications because of their superior mechanical properties components (Da Maia *et al.*, 2013). However, due to the highly unsaturated polymeric backbone of natural rubber, ozone resistance is very low. Therefore, in recent years, different types of elastomeric materials with high bard strength and high mechanical and thermal properties have been used in rubber production (Nabil *et al.*, 2013)

Ethylene propylene diene terpolymer (EPDM) rubber has excellent properties for application in many industries due to its low cost, low density and excellent mechanical properties compared to other elastomers used in similar applications (Ravishankar, 2012; Özdemir *et al.*, 2016). EPDM has been extensively used for many years in many fields such as rubber contact switches, electromagnetic interference protection, wires for electronic and electrical applications, sports equipment and outdoor electrical insulators (Lourenco *et al.*, 2006; Sarac *et al.*, 2016; Wang *et al.*, 2016). Moreover, low price, good radiation and chemical resistance are the major reasons for its use in different applications (Kim *et al.*, 2015; Moustafa *et al.*, 2015)

Rubber materials are often used with different filler materials in order to improve their properties in accordance with the field of use. Among these fillers, carbon black is the most preferred because it significantly increases the mechanical and rheological properties. Despite its superior properties, carbon black has been found to have a carcinogenic effect as a result of research and is a problem for both employees and the environment (Rausch *et al.*, 2004). Therefore, the choice of biodegradable fillers has been an important subject in the selection of fillers as well as the possibility to improve mechanical, thermal and rheological properties. On order to overcome the foregoing issues, natural materials such as pistachio, walnut, seashell and fish scales could be used as filler material in rubber industry (Karaağaç, 2014) (Akbay *et al.*,2018; Güngör *et al.*, 2019).

Aquaculture wastes are categorized as animal by-products. It can be prepared by different kind of wastes such as shell-fishes, fish bones, skin, and scales (Akbay *et al.*, 2018). With the increasing population in recent years, the production / consumption of aquaculture products has increased, which has led to an increase in aquaculture wastes. Furthermore, aquaculture wastes contain valuable components such as chitin, chitosan, collagen.

Blue crab (BC) lives in the Mediterranean Region, especially in Mersin and is frequently consumed in this region (Laughlin, 1982). Blue crab shells resulting from consumption are not evaluated in any area/application. Inability to usage of aquaculture products that have valuable content causes both environmental problems and extra cost in terms of economic concerns.

Although the use of different aquaculture products as filler material in rubber exists in the literature, with our best knowledge, the blue crab shell (BCS) is not used. In this study, ground blue crab shells with different amount as a filler material was added into EPDM. The mechanical and rheological and swelling properties of the composite material were investigated.

2. MATERIAL & METHODS

Blue crab shell *(Callinectes sapidus)* (BCS) was supplied from a local pub. The blue crab shell was cleaned by tap water five times and the washed material was dried at 45 oC in a laboratory scale oven. After that, washed and cleaned blue crab shell was ground with laboratory type sieve machine. During the study, only particles below 250 microns of the ground blue crab shells were used.

The EPDM with different BCS content were produced with using the chemicals that was summarized in Table 1.

Table 1. The recipe of EPDM/BCS Composite

Materials	Function	phr
KELTAN 9650Q	Rubber	100
Carbon Black	Filler	30
Zinc oxide	Activator	1.5
Mineral Oil	Lubricant	32
Stearic Acid	Activator	1
TAC/50	Coagent	1
Perkadox	Curing Agent	5
Blue Crab Shell	Bio-Based Filler	0, 15, 30

EPDM compound with Blue Crab Shell (BCS) was produced with a Baihong mark ML-132 model Kneader type closed mixer. After the rubber mixture were reached up to 70 °C, the blending was stopped and prepared material were compressed in a Baihong mark HL-66 model laboratory scale two-roll mill to prepare a 2 mm-shaped compound. After that, the prepared material was placed into a 2 mm mound and vulcanized in a thermal hydraulic press under 20 MPa pressure at different for moving die rheometer (MDR) specified minutes (Akbay, *et al.*, 2017).

The tensile properties of EPDM/Blue Crab Shell (BCS) composites were determined in accordance with the ASTM D412 Type C standard. The mechanical test was performed by Shimadzu AGS-X universal testing machine with a 20 kN gauge. The crosshead speed was performed at a 50 mm/min rate according to the ASTM D412 Type C standard. In addition, the hardness values of prepared samples were determined by using laboratory type Shore A testing apparatus (Özdemir *et al.*, 2018).

The gel content of the EPDM/BCS composite was performed via Soxhlet extraction method and was calculated using Eq. (1);

$$Gel\ Content\ (\%) = {}^{w_f}/_{w_i} * 100 \quad (1)$$

where w_i and w_f are represents to the initial and final weight of sample, respectively. The solvent utilized in the experiment was Hexane and the experiments were carried out at 75°C.

The swelling ratio of the EPDM/BCS composite was performed by using petri cup and toluene was used as the swelling medium all the experiments. The swelling ratio

of the samples was calculated using Eq. (2);

$$Swelling\ Ratio\ (\%) = {}^{w_f - w_i}/_{w_i} * 100 \quad (2)$$

where w_i and w_f are represents to the initial and final weight of sample, respectively (Akbay *et al.*, 2018).

Rheological properties of EPDM/BCS samples were done by using Moving Die Rheometer at 180 °C. Cure rate index (CRI) was calculated from MDR data with Eq. (3), where t_{90} is the optimum cure time and t_{s2} is the scorch time (Güngör *et al.*, 2018).

$$CRI = {}^{100}/_{(t_{90} - t_{s2})} * 100 \quad (3)$$

3. RESULTS & DISCUSSIONS

3.1. Rheological Properties

In order to evaluate the vulcanization process and rheological properties of EPDM/BCS composites, MDR test was carried out and torque curves were given in Fig. 1. The maximum torque (M_H) gives information about the mechanical properties of the material and the high torque values indicates that the material has high tensile properties (Güngör *et al.*, 2019). As can be seen in Fig. 1, M_H values of material increases up to 10 BCS case, while the torque decreases at 20 BCS.

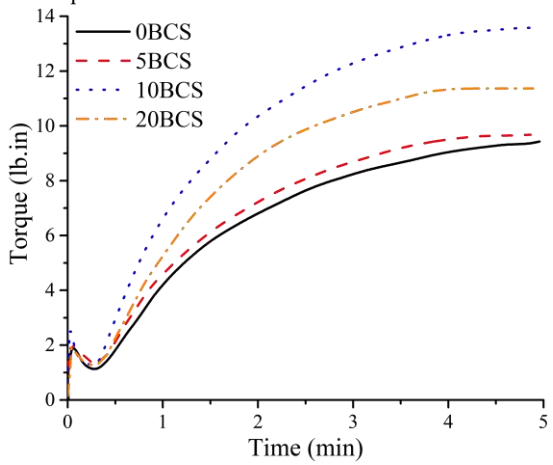

Fig. 1. MDR curves of EPDM/BCS composites

Vulcanization parameters of EPDM/BCS composite was summarized in Table 1. Optimum vulcanization time (t_{90}) and scorch time (t_{s2}) are significant parameters to evaluate the curing process (Güngör *et al.*, 2018). The high t_{s2} value and the low t_{90} value indicate that the material is sufficient in terms of rheological properties. As can be concluded from the Table 1, the optimum amount of blue crab shell is understood to be 10 phr (10BCS sample) when the vulcanization parameters are considered. Moreover, the optimum cure rate index value was obtained in 10BCS sample.

Table 1. Vulcanization parameters of EPDM/BCS composites

Sample	t_{s2} (min)	t_{90} (min)	CRI
0BCS	0,38	4,59	23,75
5BCS	0,39	4,49	24,39
10BCS	0,43	4,06	27,55
20BCS	0,41	4,33	25,51

3.2. Tensile Properties

The tensile properties of EPDM/BCS sample are given in Fig. 2. The mechanical analysis results showed that the addition of blue crab shell (BCS) into the EPDM matrix improved the tensile properties. BCS addition increased both tensile strength and elongation at break values up to 10 BCS cases. However, it is clear that the mechanical properties of the material are decreased compared to the 10BCS sample when 20 phr BCS is added to the EPDM matrix. Due to the excessive amount of filler used, decrement of free spaces has been occurred between the rubber chains, resulting in decreased mechanical properties. In addition, the hardness value of samples decreased with the increase of BCS content in EPDM matrix. Moreover, the mechanical analysis results are compatible with the MDR test results.

3.3. Swelling Properties

The gel content and swelling ratio of EPDM with different blue crab shell content are shown in Figure 3. Gel content and swelling ratio are associated with the crosslink density of EPDM composite (Akbay *et al.*,2018; Güngör *et al.*, 2019). Therefore, it gives information about the mechanical properties of the material. Besides, it is well-known that the gel content and swelling ratio are adversely proportional to each other. As can be concluded from Fig. 3, the addition of BCS into the EPDM matrix has considerably improved the crosslink density of prepared samples. The gel content of prepared samples reached at 86.2% for 10 BCS sample while swelling ratio of samples determined as 101.3% for 10 BCS sample. Consequently, the optimum BCS content determined as 10 phr according to the swelling properties. Also, the obtained results are compatible with the tensile and rheological analysis results.

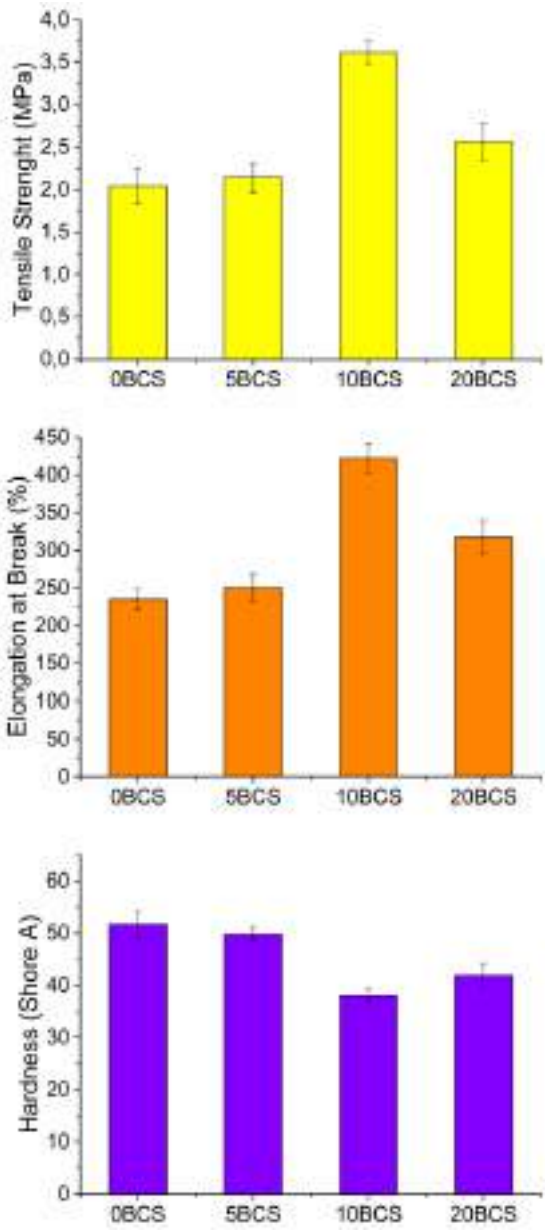

Fig. 2. Mechanical test results of EPDM/BCS composites

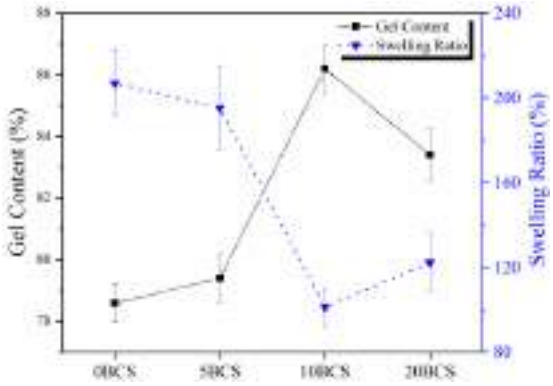

Fig. 3. Gel content and swelling ratio of EPDM/BCS composites

4. CONCLUSION

In this work, the usage of the blue ground shell (BCS) as a biodegradable filler material into the EPDM matrix was studied. For this purpose, EPDM composite with different BCS content was prepared and tensile, rheological and swelling properties of samples were characterized. MDR analysis results showed that the addition of BCS within the EPDM matrix considerably improved the vulcanization process. In addition, mechanical analysis results demonstrated that the tensile strength and elongation at break values of prepared samples increased with the increase of BCS amount up to 10 BCS sample while the hardness values of samples decreased. Moreover, the gel content of prepared samples also increased with the addition of blue crab shell, which this result is consistent with the mechanical and MDR analysis results. The characterization studies shown that optimum filler content determined as 10 phr blue crab shell. Moreover, the obtained results indicated that the use of BCS as a filler material is a significant alternative with regards to economic and environmental concerns.

REFERENCES

Akbay, İ. K., Güngör, A. and Özdemir, T. (2017) 'Optimization of the vulcanization parameters for ethylene–propylene–diene termonomer (EPDM)/ground waste tyre composite using response surface methodology', *Polymer Bulletin*, Vol. 74, No.12, pp.5095-5109.

Akbay, İ. K., Güngör, A. and Özdemir, T. (2018) 'Using fish scales (Sardina pilchardus) within ethylene-propylene-diene ter monomer rubber as bio-based filler', *Journal of Applied Polymer Science*, Vol. 135, No. 39, pp. 1–8.

Güngör, A. *et al.* (2018) 'Flexible X/Gamma ray shielding composite material of EPDM rubber with bismuth trioxide: Mechanical, thermal investigations and attenuation tests', *Progress in Nuclear Energy*, Vol. 106, pp. 262–269.

Güngör, A., Akbay, I. K. and Özdemir, T. (2019) 'Waste walnut shell as an alternative bio-based filler for the EPDM: mechanical, thermal, and kinetic studies', *Journal of Material Cycles and Waste Management*. Springer Japan, Vol. 21, No. 1, pp. 145–155.

Karaağaç, B. (2014) 'Use of Ground Pistachio Shell as Alternative Filler in Natural Rubber/Styrene–Butadiene Rubber-Based Rubber Compounds', *Polymer Composites*, Vol. 35, No. 2, pp. 245–252.

Kim, W. *et al.* (2015) 'Effects of soy-based oils on the tensile behavior of EPDM rubber', *Polymer Testing*. Elsevier Ltd, Vol. 46, pp. 33–40.

Laughlin, R. A. (1982) 'Feeding Habits of The Blue Crab, In The Apalachicola Estuary , Florida The Blue Crab, *Bulletin of Marine Science*, Vol. 32, No. 4, pp. 807–822.

Lourenco, E. and Felisberti, M. (2006) 'Polymer Thermal and mechanical properties of in situ polymerized PS / EPDM blends', *European Polymer Journal*, Vol. 42, No.

10, pp. 2632–2645.

Da Maia, J. V. *et al.* (2013) 'Influence of gas and treatment time on the surface modification of EPDM rubber treated at afterglow microwave plasmas', *Applied Surface Science*. Elsevier B.V., Vol. 285(PARTB), pp. 918–926.

Martinez, L. *et al.* (2011) 'Influence of friction on the surface characteristics of EPDM elastomers with different carbon black contents', *Tribology International*, Vol. 44, No. 9, pp. 996–1003.

Moustafa, H. and Darwish, N. A. (2015) 'Effect of different types and loadings of modified nanoclay on mechanical properties and adhesion strength of EPDM-g-MAH/nylon 66 systems', *International Journal of Adhesion and Adhesives*. Elsevier, Vol. 61, pp. 15–22.

Nabil, H., Ismail, H. and Azura, A. R. (2013) 'Compounding, mechanical and morphological properties of carbon-black-filled natural rubber/recycled ethylene-propylene-diene-monomer (NR/R-EPDM) blends', *Polymer Testing*. Elsevier Ltd, Vol. 32, No. 2, pp. 385–393.

Özdemir, T. *et al.* (2016) 'Neutron shielding of EPDM rubber with boric acid: Mechanical, thermal properties and neutron absorption tests', *Progress in Nuclear Energy*, Vol. 89, pp. 102–109.

Özdemir, T. *et al.* (2018) 'Nano lead oxide and epdm composite for development of polymer based radiation shielding material: Gamma irradiation and attenuation tests', *Radiation Physics and Chemistry*, Vol. 144, pp. 248-255.

Rausch, L. J., Bisinger, E. C. and Sharma, A. (2004) 'Carbon black should not be classified as a human carcinogen based on rodent bioassay data', *Regulatory Toxicology and Pharmacology*, Vol. 40, No. 1, pp. 28–41.

Ravishankar, P. S. (2012) 'Treatise on Epdm', *Rubber Chemistry and Technology*, Vol. 85, No. 3, pp. 327–349.

Sarac, T. *et al.* (2016) 'Influence of ??-irradiation and temperature on the mechanical properties of EPDM cable insulation', *Radiation Physics and Chemistry*, Vol. 125, pp. 151–155.

Wang, H., Ding, Y. and Zhao, S. (2016) *Effects of Co-Agents on the Properties of Peroxide-Cured Ethylene-Propylene Diene Rubber (EPDM)*, *Journal of Macromolecular Science, Part B*, Vol. 55, No. 5, pp. 433-444.

ANALYSIS OF WORTH ASSESSMENT OF INFORMATION SOURCES OF SOME SOCIO-ECONOMIC CHARACTERISTICS OF ARTISANAL FISHERS IN NIGER DELTA

Gbarabe Roland*[1], Simon Letsoalo[1] and Ngodigha Sabina[2]

[1] North-West University, Department of Agricultural Economics and Extension, South Africa

[2] Isaac Jasper Boro College of Education, Department of Agricultural Education, Sagbama, Nigeria

ABSTRACT
Worth assessment of information sources of artisanal fishers in selected coastal areas of Nigeria was carried out in the coastal States of Bayelsa, Rivers and Akwa Ibom. Data for the study was obtained from well-structured questionnaire. Descriptive and inferential statistical analyses were employed. Results showed that income range between ₦11,000 and ₦50,000. The artisans were mostly married people who had fairly large families with an average of two wives. Pressing information needs were: effects of fishing methods, effects of use of explotives to fish, effects of different mesh size, effects of bad fishing practice and water pollution.Others includes: types of materials for boat making, use of safety materials, information on gear maintenance, dangers of rough sea and where to acquire cheap fishing tools. Information on use of different types of fishing gear as well as processing and storage were recorded as not a need. These findings if well managed could make significant contributions to food security, employment generation and multiplier effect on the economy of the Niger Delta.

Keywords: *Assessment, Artisanal, Fishers, Information, Niger Delta, Worth*

* Corresponding Author

1. INTRODUCTION

Agriculture serves as the backbone of Africa's economy. According to Dulle et al., (2014) about 70% of Africans and roughly 80% of the continent's poor, live in rural areas and depend on agriculture for their livelihood. Millions of people depend on fisheries, an aspect of agriculture as a source of employment and living in Nigeria (Simon & Kereke 2013; FAO 2010). Fishery activities are executed through two main methods in Nigeria namely artisanal or capture fishery and fish farming or aquaculture.

Artisanal fishery covers the operations of small scale canoes, fishers operating in the coastal areas, creeks, lagoons, rivers, streams, lakes, inshore water and inland rivers using both traditional and modern fishing gears (Bolarinwa, 2014; Okeowo et al., 2015). It is the most important of fishery production in Nigeria and accounts for 82 to 85% of her fishery domestic production and giving livelihood to 1million artisans and 5.8million fisher folks in the secondary sector (Faturoti, 2010; Akinwumiet al., 2011).

Artisanal fishers could be identified by labor intensiveness, low productivity, low income, low technology and lack of skilful techniques (Annune, 2012). They also make use of fishing nets of various sizes, hooks and lines, dugout canoes, boats (Ngodigha et al., 2013) and above all have access to little information which in most cases is not so relevant.

However, if increased production must be achieved, artisanal fishers will need to avail themselves with information on current practices of fishing which are disseminated through various sources of information communication. Information dissemination is a significant tool for promoting national development and artisanal fishers can only make progress, increase production when needed information on fisheries are disseminated to them as and when due.

The role of information in enhancing agricultural development cannot be over emphasized, to accelerate the pace at which information reaches the artisanal fisher, several approaches have been used. Poor and unreliable information infrastructure, high illiteracy levels, low income, lack of electricity and high cost of ICTs has been identified as factors that have limited accessibility of information services in rural areas (Mtega, 2012). The attributes of good information as identified by Osikabor et al.,(2011) are relevance (significance of the information), timeliness (rightness of the information), credibility/accuracy (integrity and exactness of the information), cost-effectiveness(cheaper but valuable source of information), consistency (steadiness of the information), accessibility (user-friendliness of the information) and usability (ease with which the information is put to use) to mention but few. Nevertheless, all these aforementioned attributes lead to an improved decision making (Ogola, 2015; Osikabor et al., 2011).

The success of these attributes depends on the information access points. These information access points are the channels through which informations are communicated to the artisanal fishers such as newspapers, journals, bulletins, community leaders, extension agents, friends, and radio and farmer groups (Mtega & Benard 2013). Other sources are family members, neighbor farmers, extension services, input providers and mass media (Boz & Ozcatalbas 2010), personal experience, workshops and seminars, training, friends and neighbors, Ministry of agriculture, magazines of agriculture, extension officers, local Government officers, Non-Governmental Organizations and posters (Ogboma 2010).

However, the information been disseminated through the information access points depend on the information needs of the fisher. Which includes: where to obtain loan, how to market fish, fish processing and storage, access to modern fishing facilities, new methods of catching fish, organisation of fishery cooperatives, middlemen exploitation, where to acquire fishing tools at cheaper rates, effects of water pollution and effects of bad fishing practices (Annune 2012).

Similarly the worth of the information is a determinant of the information needs of the artisanal fisher. Information that does not meet the need of the fishers is likely to be scored low on the worth continuum. The worth of the information is a subjective value which is the reflection of the artisans' complete impression of information and the amount the fishers are willing to pay for specific information at a given time. Thus, this study seeks to determine if there is any relationship between some socio-economic characteristics of artisanal fishers and information access points.

2. METHODOLOGY

The study was conducted between April 2018 and March 2019 in three out of the seven states in the coastal region of Nigeria. These states are; Bayelsa, Rivers and Akwa Ibom states. The states cover a landmass of about 18,050 km², of which more than 60% is land, lies between

Longitude 5 ° 00, 6°.45' East and Latitude 5 ° 00,and 6°.30' north. It is bounded in the west by Delta State, the north by Imo and Abia States and east by Cross Rivers State. On the southern flank is the Bight of Benin, which covers about 160 kilometres of the state's coastline. The states have a wide coastal belt inter-lace with rivulets and streams, which form part of the Niger Delta (Michael, 2013).

Fig. 1. Map of Nigeria showing study area (Bayelsa, Rivers and Akwa Ibom States)

The study made use of the quantitative method in its analytical approach. This method was used because set of predetermined questions were used to collect data from the sample size in the study population. The data gathered was quantitative in line with the specific research objective of the study.

Population of the study was all full time artisanal fishers in the selected coastal states of Nigeria. The total

number of registered artisanal fishers per state were 315 in Bayelsa, 304 in Rivers and 201 in Akwa Ibom state, Agricultural Development Projects (ADPs) 2013.

The multi-stage sampling technique was used in the selection of the sample of which it was in three stages. In the first instance, out of seven states, three were purposively selected, because these states were more involved in artisanal fishing. Four local government areas were also purposively selected from each of the three states due to their more riverine nature in the second stage, after which a random sampling was used based on online Rao soft calculation making a sample size of 477 respondents out of 820 artisanal fishers as shown in the table below.

Table 1. Composition of the sampling size.

States	No of LGA	Population	Sample size
Bayelsa	4	315	174
Rivers	4	304	170
Akwa Ibom	4	201	133
Total	12	820	477

The data for this study was obtained from primary sources based on structured questionnaire. It helps in dealing with respondents who are uneducated artisanal fishers. The Statistical Package for Social Sciences (SPSS) version 20 was used to process quantitative data gathered from the structured questionnaire. Descriptive and inferential statistical analyses were employed. Using the analysis, calculations of the measures of central tendency as well as frequencies in percentages were computed. Inferential statistics used was multiple regression analysis.

3. RESULTS AND DISCUSSION

Table 2. Socio economic characteristics of Artisanal Fishers.

Income (₦) at ₦360/$		
N1-10,000	99	22.40
11,000-50,000	243	55.00
51,000-100,000	71	16.10
101,000 and above	29	6.60
Total	442	100
House hold size		
1-2	157	31.00
3-4	205	46.40
5-6	71	16.10
6 and above	29	6.60
Total	442	100
Wives		
1-2	423	95.70
2-4	19	4.30
Total	442	100
Marital Status		
Married	355	80.30
Single	87	19.70
Total	442	100

The respondents were mostly married (80.30%). This could be due to the fact that fishers operate nuclear families (Akinwumi et al., 2011) with majority (205) having 3 – 4 children (46.40%), and 1- 2 wives (95.70%). The larger the family size, the higher the quantity of fish caught (Inoni and Oyaide; 2007), which when sold will meet their financial needs (Ngodigha et al., 2018).

A total of 243 (55%) of artisanal fishers earn monthly income of between ₦11,000 – ₦ 50,000 while 22.40% earn between ₦1 – ₦10,000, 16% earn from ₦51,000 to ₦100,000 and 6.60% earn ₦101,000 and above with a mean of 2.07. This could be due to the fact that most inhabitants of the fishing communities have left the fishing industry for other occupation due to the dwindling fisheries resources (Ngodigha and Abowei 2018; Ngodigha et al.,2018).

Table 3. Worth of the information.

Information type	Timeliness (%)	Adequacy (%)	Relavance (%)
Use of different type of fishing gear	Less timely(15.6)	Less adequate(0)	Less relevant(39.4)
Water trend/movement	Timely(50.4)	Adequate(50.4)	Less relevant(49.3)
Weather trend	Timely(75.6)	Adequate(63.6)	Relevant(69.9)
New methods of catching fish	Timely(50.2)	Adequate(50.7)	Relevant(70.2)
Types of material for boat making	Timely(77.1)	Adequate(91.6)	Relevant(100)
Use of motorized Vessels	Less timely(19.9)	Adequate(79)	Relevant(81)
Brackish/fresh water Fishing	Less timely(49.3)	Adequate(50.2)	Relevant(77.6)
Access to modern fishing facilities	Less timely(10.6)	Adequate(68.1)	Relevant(69)
Use of non-motorized vessel	Timely(50.4	Less adequate(49.8)	Less relevant(49.3)
Effect of fishing method	Timely(95.2)	Adequate(65)	Relevant(70.1)
Use of safety materials	Timely(69.2)	Adequate(64.7)	Relevant(93.2)
Effects of use of explosives	timely(50.4)	adequate(85.8)	relevant(77.4)

Effects of different mesh size	Timely(94.4)	Adequate(85.5)	Relevant(93.4)
Information on gear Maintenance	Timely(50.2)	Adequate(93.5)	Relevant(93.7)
Effects of bad fishing	Timely(78.3)	Adequate(50.2)	Relevant(100)
Modern technique in boat maintenance	Timely(99.3)	Less adequate(27.1)	Relevant(94.6)
Dangers of roughsea/waves	Timely(78.9)	Adequate(50.2)	Relevant(99.1)
Processing/storage	Less timely(49.3)	Less adequate(43)	Less relevant(45.5)
Effects of deforestation	Timely(50.7)	Less adequate(0.9)	Relevant(50.4)
How to obtain loan	Less timely(15.7)	Less adequate(2.5)	Relevant(93.4)
Available government grant and provision of other incentives	Less timely(0.9)	Adequate(50.6)	Relevant(100)
Organization of fishing	Timely(50.4)	Less adequate(32.5)	Relevant(100)
Negative activities of middle-men	Timely(99.4)	Less adequate(49.3)	Relevant(81)
Where to acquire cheap fishing tools	Timely(54)	Adequate(59)	Relevant(93)

As shown in table 3, information on effects of fishing methods, effects of use of explotives to fish, effects of different mesh size, effects of bad fishing practice and water pollution were the pressing needs of fishers in the Niger Delta. Fishers have come to realize the effects of these information types on the depleting fisheries resources (Ngodigha et al.,2018) and so they are very ready to gather new and enough information that will increase harvest and improve their livelihood. Other information types such as: types of materials for boat making, use of safety materials, information on gear maintenance, dangers of rough sea and where to acquire cheap fishing tools and also important to manage and enhance their income were also needful to the fishers.

Information on use of different types of fishing gear observed as not a need to the fishers, could be due to the fact that fishers were taught from birth on how to fish and so they know the particular fishing gear to harvest any fish at any given time. Processing and storage recorded as not a need might be attributed to the fact that fishers are more comfortable with smoke drying their catch with Rhizophora species commonly found in the Niger Delta, that gives the processed catch a particular taste and aroma liked by buyers of their products.

Table 4 shows a regression analysis carried out to determine the relationship between the some socio-economic characteristics of the respondents and their information worth assessment. Information worth assessment is the dependent variable, while the socio-economic variables income, children, wives and marital status were the independent variables.

Table 4. Influence of socio-economic characteristics of artisanal fishers on information worth assessment.

Variables	B	SE	T
Constant	234.309	1.437	163.028
Income	-9.722	5.697	-1.706
Children	-38.336	5.197	-7.376
Wives	53.747	7.837	6.858
Marital Status	10.568	19.712	.536

*Significant at 10%, ** Significant at 5%. R2 = 0.957 n= 442, F-ratio= 1204.669.
Field Survey 2018

Different functional forms were tried and the form that gave the best result was used for interpretation. The selection was based on the value of the R-square, number of significant variables and conformation to the a priori expectations. The semi-log form was found to best explain the relationship; the R-square value indicates that about 95% of the variability in information worth assessment among the respondents was determined by some socio-economic characteristics.

The coefficient for income was negative and significant at 5%. This implies that as the income of the respondent increases their information worth assessment tend to decrease. However, there was a positive significance between the number of wives and information worth assessment. This implies that the information worth assessment of the respondent tend to increase as the number of his wives increases. Marital Status was also positively correlated with the dependent variable as most of the respondents were married. This implies that marriage aids information assessment in the Niger Delta.

Number of children correlated negatively with information worth assessment. The correlation was significant at 5% level. The negative correlation implies that those with less number of children have more information worth than those with high number of children. The implication is that the number of children does not mean more information worth, that the fewer children, the better the information that can be acquired and consequently the higher the productivity (Matovelo, 2008).

4. CONCLUSION

Findings from the study revealed that almost all information items were needs of the artisanal fishers. The regression shows there is significant relationship between some of the socio-economic characteristics of the artisanal fishers and the information worth. Based on the regression analysis, the statement that there is no significant relationship between the socio-economic characteristics of the respondents and their information worth assessment is rejected. In other words, there is significant relationship between some socio-economic

characteristics of respondents and their information worth assessment.

RECOMMENDATIONS

Effective information dissemination methods like packaging and repackaging information should be employed in the study area. This will help the artisanal fishers to improve on their fishing techniques for enhanced fish production. Other intervention agencies providing information on different information needs of the artisanal fishers should complement government efforts in providing valuable information in order to increase their level of production

Worth of the various information types based on the timeliness, adequacy and relevance of information types be provided on time and adequately only on the ones that are relevant to the needs of the fishers. This will be the basis for increased fish production.

REFERENCES

Akinwumi F.O, Akinwumi I.O & Ogundahunsi O.A (2011). Characterization of Artisanal Fishery in the Coastal Area of Ondo State, Nigeria. International Research Journal of Agricultural Science and Soil Science 1(3) 083-089.

Annune E.A (2012). Information needs and information dissemination to artisanal fishermen in selected communities in three local government areas of Benue State, Nigeria: University of Nigeria Nsukka (Master Thesis).

Bolarinwa, J.B(2014).Public relations and extension services in Nigerian Fisheries Industry, International Journal of Agricultural Research, 9(7):327-330.

Boz, I. &Ozcatalbas, O. (2010). Determining information sources used by crop producers: A case study of Gaziantep province in Turkey.African Journal of Agricultural Research, 5 (10): 980-987.

Dulle F, Benard R &Ngalapa H, (2014). Assessment of information needs of rice farmers in Tanzania: A case study of Kilombero Districts, Morogoro. LibraryPhilosophy and Practice. Paper, 1071: 1.

FAO. (2010). State of world Fisheries and Aquaculture Food and Agricultural Organization. Rome (SOFIA).

Faturoti O (2010). Nigeria: Fisheries contribute $US1 billion to economy. 25th Annual Conf. Fish. Soc. Nigeria, Badagry, Lagos, Nigeria. Fish Center, Cairo, Egypt.

Inoni, O.E., and Oyaide, W.J. (2007). Socio-economic analysis of artisanal fishing in the

south agro-ecological zone of Delta State, Nigeria. Agricultura Tropica et Subtropica,40(4),135-149.

Matovalo D.S (2008). Ehancing Farmers access to and use of Agricultural Information for Empowerment and Improved Livelihoods : A case of Morogoro Region Tanzania, A PhD Thesis, University of Dar es salam

Michael Hogan (2013). Niger River in Encyclopaedia of Earth M. Micginly (ed). Washington, DC National Council for Science and Environment.

Mtega, W. P (2012), "Access to and Usage of Information among Rural Communities: a Case Study of Kilosa District Morogoro Region in Tanzania" The Canadian journal of Library and information practice and research. 7(1) https://journal.lib.uoguelph.ca/index.php/perj/article/viewArticle/1646/2462 Retrieved on 22nd January 2013.

Mtega, W. &Benard, R. 2013. The state of rural information and communication services in Tanzania: A meta-analysis. International Journal of Information and Communication Technology Research, 3(2): 64 – 73.

Ngodigha, S.A., Abowei, J.F.N., Gbarabe, R. (2013) Palaemon Fishery in River Nun estuary, Bayelsa State, Niger. African Science and Technology Journal 7(1) 142-149

Ngodigha, S.A., Gbarabe, R and Austin, A (2018) Using fishers knowledge in community based fisheries management in River Nun Estuary, Niger Delta. Tansylvanian Review of Systematical and Ecological Research. Vol.20 (2), 75 – 84. DOI: 10.2478/trser-2018-007. www.stiinte.ulbsibiu.ro>trser

Ogboma, Margaret U. (2010). Access to Agricultural Information by Fish Farmers in Niger Delta Region of Nigeria. Library Philosophy and Practice (e-journal).

Ogola, P.A., (2015). Assessing communication channels and the impact of agricultural information used by farmers in watermelon production in Yimbo east ward, Siaya County. Nairobi: University of Nairobi (PhD Thesis).

Okeowo T. A., Bolarinwa J. B &Dauda I. (2015). Socioeconomic Analysis of Artisanal Fishing and Dominant Fish Species in Lagoon Waters of EPE and Badagry Areas of Lagos State. International Journal of Research in Agriculture and Forestry.3(1), 38-45.

Osikabor, B., Oladele, I.O. &Ogunlade, I. (2011). Worth assessment of information and their access points by small scale cassava farmers in Nigeria. South African Journal of Agricultural Extension, 39(2): 69-78.

Simon A. A. & Kereke F. O. (2013). Innovation and Entrepreneurship.International Journal of Knowledge, 1(2): 41-56.

CISET - 2nd Cilicia International Symposium on Engineering and Technology
10-12 October, 2019, Mersin / TURKEY

LOW VELOCITY IMPACT BEHAVIORS OF BASALT/EPOXY REINFORCED COMPOSITE LAMINATES WITH DIFFERENT FIBER ORIENTATIONS

Özkan Özbek [*1], Ömer Yavuz Bozkurt[1] and Ahmet Erkliğ[1]

[1, 2] Gaziantep University, Faculty of Engineering, Mechanical Engineering Department, Gaziantep, Turkey

ABSTRACT

The current study aims to explore the effects of fiber orientation angle on the low velocity impact behaviors of the basalt fiber reinforced composite laminates fabricated by vacuum assisted resin transfer molding. The beam type samples with four different orientation angles (0°/90°, 15°/-75°, 30°/-60° and 45°/-45°) and eight number of layers are tested on the Charpy impact test machine. Furthermore, the failure modes are discussed to understand fracture mechanisms on the samples subjected to flatwise and edgewise impact loadings. The results show that the fiber orientation angle has a very significant influence on the energy absorption and impact toughness of the samples. Briefly, the higher fiber orientation angle results in increasing of considered parameters and shows less damage. The best values as 3.07 J and 34.82 kJ/m^2 for impact energy and impact toughness, respectively, are obtained from the edgewise-notched samples with the (45°/-45°) fiber orientation angle.

Keywords: *Basalt Fiber, Charpy, Fiber Orientation Angle, Energy Absorption, Impact Toughness*

[*] Corresponding Author: ozkanozbek@gantep.edu.tr

1. INTRODUCTION

With the awareness of industrialization that is growing faster than ever on a global scale, scientists are working in many fields of application to facilitate life and meet the increasing consumption demands of human beings, in terms of economic, productivity and flexibility compared to the materials used. Amongst these fields, materials science has been making great progress by constantly dealing with the development or derivation of new materials. In this context, polymer based composite materials by exhibiting higher specific strength and durability, longer service life and fatigue behavior compared to the classical metallic materials (Zhong *and* Joshi, 2015) have been derived. In addition to the above mentioned advantages, there are also opportunities to provide the ease of production and desired design parameters to obtain them. Polymer based composites generally consist of a reinforcement material (carbon fiber, aramid fiber, glass fiber, basalt fiber, jute fiber etc.) and a matrix system.

In today's world, the use of natural materials increases with the understanding of human being not to harm the nature. Although it is widely used in other fields, it is new to evaluate basalt material that eco-friendly, natural, safe and easy to recycle in polymer based composites (Jamshaid *et al.*, 2017). It is obtained from molten basalt rocks in volcanic areas. Furthermore, basalt fiber reinforcements exhibiting good mechanical strength (Czigany *et al.*, 2005), non-flammable (Wittek and Tanimoto, 2008), high temperature resistance [4], biological stability (Zhang *et al.*, 2012), and high resistance to chemical attacks (Fiore *et al.*, 2011) have been attracted the attention of the researchers. There are several studies relevant the basalt fiber and its applications in the literature (Demirci *et al.*, 2014; Bozkurt *et al.*, 2018; Sim *and* Park, 2005). Demirci *et al.* (2014) investigated the fracture toughness characteristics of the basalt and glass fiber reinforced having arc shaped samples. Charpy impact experiments were conducted to examine the effects of the different notch depth ratios on the energy characteristics of the samples. Increasing in the considered ratios resulted with the decreasing in impact energy and fracture toughness values. Also, basalt fiber reinforced samples showed the better features than glass ones. Bozkurt *et al.* (2016) examined the effects of the different fiber orientation angle on the vibration and damping behaviors of the basalt fiber reinforced composites. They stated that the higher fiber orientation angle resulted in decrease of natural frequency and increase of damping ratios. Subagia *et al.* (2014) conducted a study about the effects of hybridization of basalt and carbon fibers on the flexural characteristics. They pointed out the hybridization process gave the new materials with less cost compared to carbon fiber reinforced samples and comparable flexural strength and improved ductility.

The aim of this work is to investigate the effects of the fiber orientation angle on the energy absorption characteristics of the basalt fiber reinforced composite laminates. The samples having four different orientation angles as ((0°/90°), (15°/-75°), (30°/-60°) and (45°/-45°)) and eight layers was considered and subjected to low velocity impact loading with Charpy impact test method.

2. MATERIALS & METHOD

2.1. Sample Preparation

The bidirectional basalt fiber fabrics with 0.17 mm thickness and 200 g/m^2 areal density procured from Tila Kompozit, Turkey, were used for reinforcement component. For matrix system, epoxy resin (MOMENTIVE MGS L285) and hardener (MOMENTIVE MGS H285) which were supplied from Dost Kimya, Turkey, were mixed with a stoichiometric ratio of 100:40 in weight basis, respectively.

Basalt fiber reinforced composite laminate was fabricated by vacuum assisted resin transfer molding technique (VARTM) seen in Figure 1. Prepared resin was impregnated from outside helping by vacuum process. After whole laminate was wet, the laminate was exposed to 700 mmHg vacuum was applied for 8 hours and curing process was performed at room temperature. The thickness of the laminate was measured as 1.6 mm. The samples by considering the test geometry were cut on the CNC router with different fiber orientation angles.

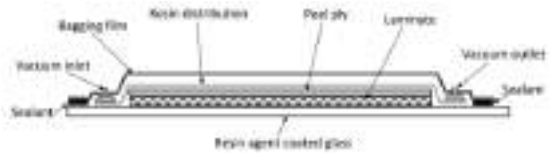

Fig. 1. Vacuum assisted resin transfer molding (VARTM) (Bozkurt *et al.*, 2018)

2.2. Low Velocity Impact Tests

Charpy impact experiments as low velocity impact test were performed to determine the effects of fiber orientation angle on the energy and toughness characteristics of the basalt fiber reinforced composite laminates. ISO 179/92 standard was used for reference guide for the sample preparation and testing procedure. A Köger 3/70 Charpy impact tester with 15.0 J impact energy capacity, shown in Figure 2(a), were employed for the experiments. The samples having 55 mm x 10 mm in length and width were prepared as notched and unnotched configurations subjected to edgewise and flatwise impact loading as seen in Figure 2(b) and 2(c), respectively. At least five number of replicated tests were conducted to ensure experimental reliability.

Fig. 2. a) Köger 3/70 Charpy impact tester, b) edgewise placement, c) flatwise placement

Impact energy, E was directly measured from the dial on the machine using potential energy lost after breaking the sample as shown in Eq. (1).

$$E = E_a - E_b \quad (1)$$

where E_a and E_b represent the pendulum energy before and after impact event, respectively. Impact toughness, a_{cu} which is the absorbed energy per unit area, was calculated from Eq. (2):

$$a_{cu} = E/(bh) \quad (2)$$

where b and h are the thickness and width of the samples. Figure 3 also presents an illustration of Charpy impact test machine.

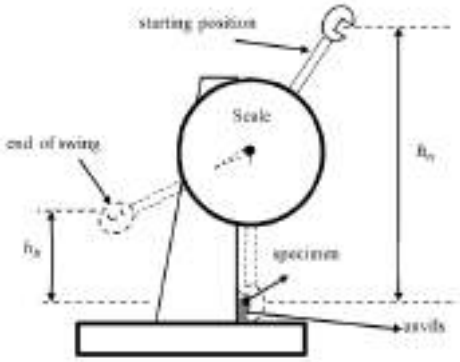

Fig. 3. The schematic illustration of the Charpy impact test

3. RESULTS & DISCUSSIONS

Impact energy and impact toughness values of the samples subjected to flatwise and edgewise loadings were presented in Figure 4 and Figure 5, respectively. Flatwise replacement resulted with the worse response due to more resistance of the samples in edgewise direction. The results showed that the increase in fiber orientation angle improved the amount of absorbed energy and the toughness of the material in general. This can be explained by the easier pull out failure mode (Flasar, 2018) happening in smaller orientations.

For the notched samples, the maximum absorbed energy and impact toughness as 1.73 J and 3.09 kJ/m2 was obtained from the (45°/-45°) fiber orientation angle. When compared to (0°/90°) fiber orientation, 22.7% and 23.1% increase were achieved in energy and toughness values, respectively.

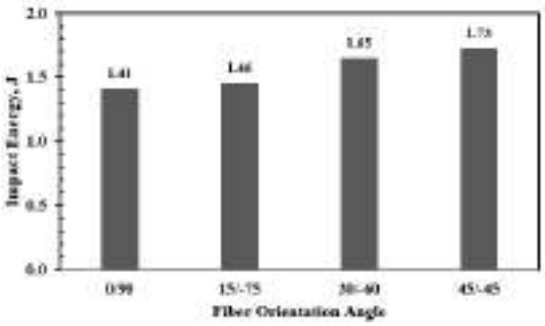

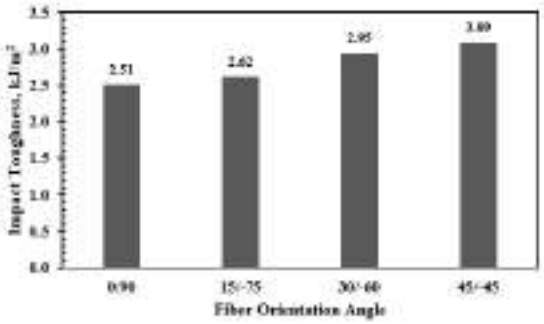

Fig. 4. Absorbed energy and impact toughness of the unnotched samples subjected to flatwise impact loading

The samples subjected to edgewise loading gave the improvement trend with increase in orientation angle like flatwise ones(45°/-45°) orientation angle gave the 2.03 times better results both energy and toughness values of the (0°/90°) arrangement. Maximum absorbed energy and impact toughness values was found as 3.07 J and 34.82 kJ/m^2.

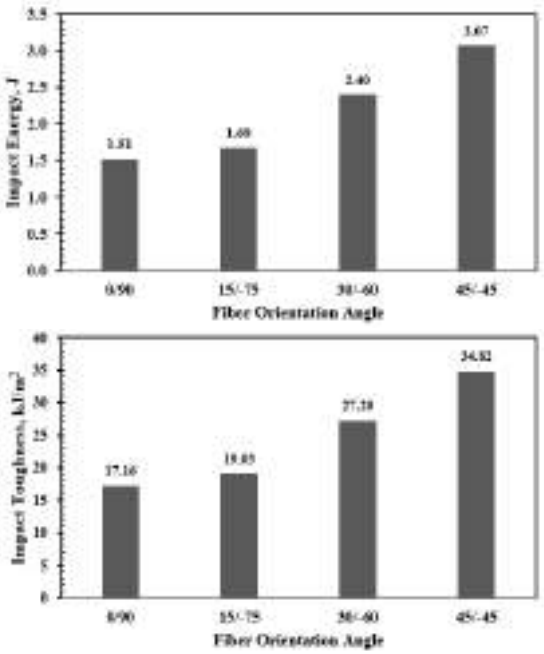

Fig. 5. Absorbed energy and impact toughness of the notched samples subjected to edgewise impact loading

The failure modes and damage types of the notched and unnotched samples after low velocity impact experiments were given in Figure 6(a) and Figure 6(b), respectively. It was very obvious that the higher orientations showed the less damage. Also, notched samples had the more destruction due to the edgewise replacement. Failure of the samples of (0°/90°) begun with the matrix fragmentation and flowed by delamination, fiber breakage and fiber pull out. Also, notched ones had the laminate fracture.

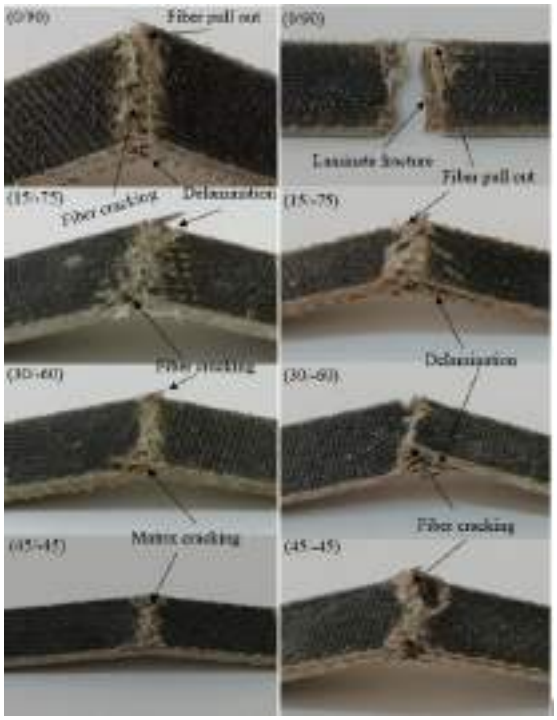

(a) (b)

Fig. 6. Damage types for; (a) unnotched samples subjected to flatwise impact, (b) notched samples subjected to edgewise impact

4. CONCLUSIONS

In this work, the effect of fiber orientation angle on the impact behaviors of the basalt fiber reinforced composite laminates were experimentally investigated. Charpy impact tests as low velocity impact were conducted to observe energy absorption and impact strength characteristics of the samples with four different orientation. The unnotched and notched samples subjected to flatwise and edgewise impact loadings, respectively, were prepared at four different orientation angles (0°/90°, 15°/-75°, 30°/-60° and 45°/-45°). Higher fiber orientation resulted with the increase in energy absorption and impact strength for all samples. Maximum increases in impact energy and impact toughness were obtained from (45°/-45°) orientation as 22.7% and 23.1% for notched samples. Also, unnotched samples with (45°/-45°) were 2.03 times of energy absorption and toughness values of the (0°/90°) samples. The damage were started with matrix cracking and followed by delamination, fiber breakage and fiber pull out as the orientation angle decreased.

As seen in the results, the effect of fiber orientation on energy absorption characteristics was very significant. It can be a reference guide for in the usage of related applications.

REFERENCES

Bozkurt, Ö. Y., Bulut, M., & Özbek, Ö. (2016, March). Effect of fibre orientations on damping and vibration characteristics of basalt epoxy composite laminates. *In Proceedings of the World Congress on Civil, Structural, and Environmental Engineering (CSEE'16)*, Prague (pp. 30-31).

Bozkurt, Ö. Y., Erkliğ, A., & Bulut, M. (2018). "Hybridization effects on charpy impact behavior of basalt/aramid fiber reinforced hybrid composite laminates." *Polymer Composites*, 39(2), 467-475.

Czigány, T., Vad, J., & Pölöskei, K. (2005). "Basalt fiber as a reinforcement of polymer composites." *Periodica Polytechnica Mechanical Engineering*, 49(1), 3-14.

Demirci, M. T., Tarakçıoğlu, N., Avcı, A., & Erkendirci, Ö. F. (2014). "Fracture toughness of filament wound BFR and GFR arc shaped specimens with Charpy impact test method." *Composites Part B: Engineering*, 66, 7-14.

Fiore, V. I. N. C. E. N. Z. O., Di Bella, G., & Valenza, A. (2011). "Glass–basalt/epoxy hybrid composites for marine applications." *Materials & Design*, 32(4), 2091-2099.

Flášar, O. (2018). "Experimental Investigation of CFRP Impact Toughness and Failure Modes." *Advances in Military Technology*, 13(1).

Jamshaid H. (2017). "Basalt fiber and its applications." *J Textile Eng Fashion Technol.* 1(6):254-255.

Sim, J., & Park, C. (2005). "Characteristics of basalt fiber as a strengthening material for concrete structures." *Composites Part B: Engineering*, 36(6-7), 504-512.

Subagia, I. A., Kim, Y., Tijing, L. D., Kim, C. S., & Shon, H. K. (2014). "Effect of stacking sequence on the flexural properties of hybrid composites reinforced with carbon and basalt fibers." *Composites Part B: Engineering*, 58, 251-258.

Wittek, T., & Tanimoto, T. (2008). "Mechanical properties and fire retardancy of bidirectional reinforced composite based on biodegradable starch resin and basalt fibres." *Express Polym Lett*, 2, 810-822.

Zhang, Y., Yu, C., Chu, P. K., Lv, F., Zhang, C., Ji, J., ... & Wang, H. (2012). "Mechanical and thermal properties of basalt fiber reinforced poly (butylene succinate) composites." *Materials Chemistry and Physics*, 133(2-3), 845-849.

Zhong, Y., & Joshi, S. C. (2015). "Impact behavior and damage characteristics of hygrothermally conditioned carbon epoxy composite laminates." *Materials & Design* (1980-2015), 65, 254-264.

CISET - 2nd Cilicia International Symposium on Engineering and Technology
10-12 October, 2019, Mersin / TURKEY

THE IMPLEMENTATION OF REAL TIME WINDOW FUNCTIONS ON FIELD PROGRAMMABLE GATE ARRAY

Turgay KAYA*[1], Seda ARSLAN TUNCER [2]

[1] Firat University, Faculty of Engineering, Department of Electrical-Electronics Engineering, Elazig, TURKEY, tkaya@firat.edu.tr

[2] Firat University, Faculty of Engineering, Department of Software Engineering, Elazig, TURKEY, satuncer@firat.edu.tr

ABSTRACT
In this paper, the real-time design of FIR filter using window function, which is preferred in digital signal processing, is presented for the Altera EP4CE115C7 FPGA (Field Programmable Gate Array). In this study, cosh and exponential functions, which are widely used in literature and which have superior advantages to other window functions, were used. Both window functions were designed in real-time using a floating point number system on the FPGA. The window functions obtained were compared according to different spectral parameters with other window functions in published literature. According to the comparison results, the window function implemented in real-time had a better ripple ratio and larger sidelobe roll-off ratio. Along with the window functions implemented in real-time on the FPGA, a structure has been created that is easy to apply and can be used in many areas such as signal and image processing and digital filter design.

Keywords: *Window function, cosh window, exponential window, FPGA.*

* Turgay KAYA tkaya@firat.edu.tr

1. INTRODUCTION

Window functions (or windows in short) are time domain functions used to eliminate Gibbs' oscillations formed by the interruption of Fourier series that are used in the design of nonrecursive digital filters (FIR Finite Impulse Response). Window functions are preferred in many areas such as digital filter design, classification of cosmic data [1,2], development of the reliability of weather forecasting models [3] the detection of diseases in biomedical areas [4] and speech processing [5].

The windows used in different areas are classified into two groups with fixed and adjustable parameters [6]. The fixed windows have window length N, which is the only variable and they control the main lobe width, one of the window spectral parameters. Adjustable window functions provide a more useful window amplitude spectrum with the help of two or more independent variables. Dolph-Chebyshev [7], Kaiser [8,9] and Saramaki [10] windows can be shown as adjustable two-parameter windows functions. An ultraspherical window function with three parameters is another commonly used function in published literature [11-13]. The ultraspherical window has spectral parameters such as the main lobe width, the ripple ratio, the null-to-null width, and a user-defined sidelobe model. In addition, other window functions developed with the Kaiser window equation in literature are presented in [14,15]. These new window functions show more useful spectral characteristics than the two- and three-parameter window functions commonly used in literature.

Recently, FPGAs have been commonly used in real-time application studies. FPGAs are preferred in many different areas such as chaotic system applications [16], random number generators [17] and emotional robotic control applications [18]. Also, FPGAs are used in digital filter design and other applications [19,20]. Window function designs on FPGAs are available in the literature. In [21], the use of the Kaiser window function for FIR filter design was implemented on FPGA. In the study, it was emphasized that the design results are better than the results obtained by traditional methods. Also, the design of the Hamming and Kaiser window on FPGA was shown in [22]. Kaiser and Hamming windows were used for FIR filter design at work and simulation and implementation results were compared. The window function design using the CORDIC algorithm was given in [23]. In the study, the authors performed different window function design with similar performance using fewer pipeline stages. In [24], VLSI architecture for blackman window function design was proposed. The work has parallel and pipeline architecture. In addition, CORDIC-based VLSI architecture of popular window functions were given in [25]. The design was implemented in fixed point number system.

This paper generates cosh and exponential window functions based on the Kaiser window designed in real-time on FPGA. The cosh window was more easily designed because there is no power series expansion in its time domain function. The window functions obtained as a result of the designs were compared with other window functions found in published literature by comparing their different spectral parameters and showing the more successful results that were obtained.

In the system design, a floating point number system was used instead of a fixed point number system. Thus, the window function generated according to the coefficients obtained at the FPGA output ensured that the spectral parameters achieved more successful results.

The designs were presented to the user as a basic hardware module for the design of digital filters that are used to reduce noise in areas such as signal and image processing.

2. WINDOW FUNCTIONS

2.1. Window Function Spectrum

The windows are usually classified according to their spectral characteristics and compared with other windows according to these characteristics. The frequency spectrum of a window can be defined as follows.

$$W(e^{j\omega T}) = |A(\omega)|e^{j\theta(\omega)} = e^{-j\omega(N-1)T/2}W_0(e^{j\omega T}), \quad = \omega(0) + 2\sum_{n=1}^{(N-1)/2}\omega(nT)\cos\omega nT \tag{1}$$

where, $\boldsymbol{W_0(e^{jwT})}$ is the amplitude function of the window, N is the window length and T is called the sampling period. $A(w) = |W_0e^{jwT}|$ and $\boldsymbol{\theta(w) = -w(N-1)T/2}$ are the amplitude and phase spectrum of the window from equation (1), respectively. The normalized amplitude spectrum of a window can be obtained by the following equation [14].

$$|\boldsymbol{W_N(e^{jwT})}| = \boldsymbol{20log_{10}(|A(w)|/|A(w)|_{max})} \tag{2}$$

The spectral parameters determining the performance of the windows are the main lobe width (ω_M), the null-to-null width (ω_N), the ripple ratio (R) and the sidelobe roll-off ratio (S).

These values can be found from the window spectrum response as follows [14].

ω_M = two times half main lobe width = $2\omega_R$

R = maximum sidelobe amplitude in dB – main lobe amplitude in dB = S1

S = maximum sidelobe amplitude in dB – minimum sidelobe amplitude in dB = S1 – SL

The desired properties of the window amplitude spectrum are.

Narrow main lobe width

Small ripple ratio

Large sidelobe roll-off ratio.

The main lobe width determines the width of the transition band between the pass band and stop band of the window, the ripple ratio determines the ripples at the pass band and stop band, and the sidelobe roll-off ratio determines the distribution of the stop band energy.

2.2. Kaiser Window

In discrete time, the equations for the Kaiser window can be defined as follows.

$$w[n] = \begin{cases} \dfrac{I_0(\alpha_k\sqrt{1-\left(\dfrac{2n}{N-1}\right)^2})}{I_0(\alpha_k)} & |n| \le \dfrac{N-1}{2} \\ 0 & otherwise \end{cases} \tag{3}$$

where, α_k is an adjustable parameter, N is the window length and $I_0(x)$ is the modified Bessel function In the Kaiser window, the increase in the α_k value causes a wider main lobe width and smaller ripple ratio.

2.3. Cosh Window

The cosh window function is obtained by writing the cosh function instead of the modified Bessel function of the first kind of order zero ($I_0(x)$) in the Kaiser window function [14].

$$\omega_c(n) = \begin{cases} \dfrac{\cosh\left(\alpha_c\sqrt{1-\left(\frac{2n}{N-1}\right)^2}\right)}{\cosh(\alpha_c)} & |n| \le \dfrac{N-1}{2} \\ 0 & otherwise \end{cases} \quad (5)$$

2.4. Exponential Window

The exponential window, another developed two parameter window function, was obtained by writing the exponential function, showing similar characteristics, instead of the $I_0(x)$ function, in a similar way to the cosh window function [15].

$$\omega_c(n) = \begin{cases} \dfrac{exp\left(\alpha_e\sqrt{1-\left(\frac{2n}{N-1}\right)^2}\right)}{exp(\alpha_e)} & |n| \le \dfrac{N-1}{2} \\ 0 & otherwise \end{cases} \quad (6)$$

3. IMPLEMENTATION OF WINDOW FUNCTIONS ON THE FPGA

In this section, the designs of cosh and exponential windows, window functions commonly used in literature with good spectral parameters, on the FPGA are presented step by step. For the cosh window, the expression $\alpha_c\sqrt{1-\left(\frac{2n}{N-1}\right)^2}$ in equation 5 and then $w_c(n)$ value were calculated using values of N=51 α_c=1.76 and N=31 α_c=5.86. Figure 1 shows the circuit designed to calculate $\alpha_c\sqrt{1-\left(\frac{2n}{N-1}\right)^2}$ using Quartus software.

The values for const 2 and alpha are as follows.

const2=0.04 (3d23d70a HEX) and alpha= 1.76 (3fe147ae HEX) for N=51

const2=0.066 (3d872b02 HEX) and alpha= 5.86 (40bb851f HEX) for N=31

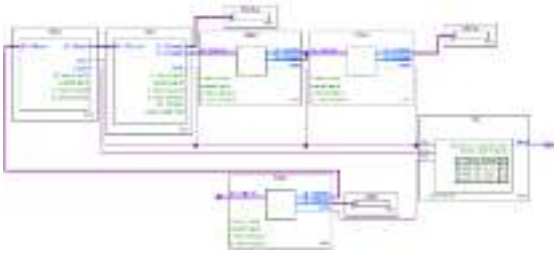

Fig. 1. Implementation of the expression $\alpha_c\sqrt{1-\left(\frac{2n}{N-1}\right)^2}$

IP cores (Intellectual Property core) using floating point number systems were used in the implementation of the circuit [26]. Three multiplications, a subtraction and a square root IP core were used in the circuit. To calculate the result of applying the values to the input of each multiplication, subtraction and square root IP cores, cycles of 5, 10 and 28 are required, respectively. A PLL (Phase Locked Loop) circuit was also used to calculate the $w_c(n)$ value in a synchronous manner. The PLL IP core has the ability to divide or multiply the clock signal applied to its input. With this feature, the clock signal was converted to c0, c1 and c2 clock signals in order for the system to operate synchronously. While the clock signal used in the system is 400 MHz, the c0, c1 and c2 values are 400, 20 and 7.548 MHz, respectively. The values obtained from the circuit in Figure 1 are given as input to the exponential modules in Figure 2 for the calculation of $w_c(n)$. It is understood that the cosh function can be written as in Equation 7.

$$cosh(x) = \frac{e^x + e^{-x}}{2} \quad (7)$$

The circuit design giving the result of Equation 5 by using Equation 7 can be implemented as shown in Figure 2. Exponential, addition and division IP cores were used in this circuit. These IP cores give results in 17, 10 and 6 clock cycles, respectively. As a result, $w_c(n)$ values for n=0,1,2,… (N-1)/2 are calculated at 228.7 kHz.

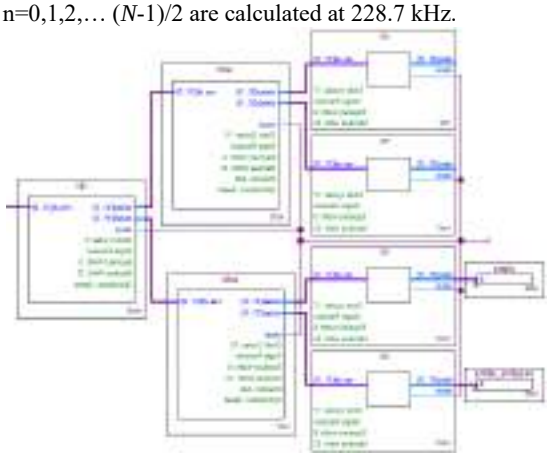

Fig. 2. Implementation of Equation 7 in the FPGA environment

Each result was stored at 228.7 kHz to a memory circuit to show the consistency of the obtained results when compared with mathematical results. Figure 3 shows the memory hardware required to store each value into memory. A 5-bit counter was used to save the results to the desired addresses in the memory. The counter frequency is the same as the memory clock frequency.

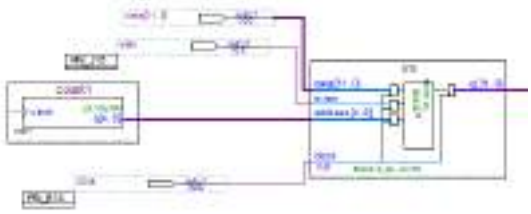

Fig. 3. Design used to save the results in memory

In this application, results were obtained using values of N=51 and α_c=1.76. The hexadecimal numbers obtained from output q in Figure 3 are presented in Figure 4 and these numbers were obtained at a frequency of 228.7 kHz.

Fig. 4. The calculated real time results the values for N=51 and αc=1.76.

Altera Quartus software allows data to be written to memory units in a text file in a mif or hex format. The results obtained in real-time can be easily read from these files.

The IEEE 754 floating point format is 32 bit which is the most common form to represent real numbers. In this format, floating point numbers are shown with 3 sections. These sections are expressed as a sign, an exponent and a mantissa. The sign bit is the first bit of the 32-bit number, followed by the 8-bit number exponent and remaining bits are the mantissa. The sign (S) bit takes the value 0 for positive numbers and 1 for negative numbers. The exponent (E) bits can represent both negative and positive exponents. To obtain the exponent of the floating number, the bias value is added to the 8-bit exponent. M indicates the bits that represent the floating number.

$$\text{Number Value} = (-1)^S * 2^{E-127} * (1.M) \quad (8)$$

According to the hexadecimal system, the floating point equivalent to the 23rd value (3F7CF3B8)H generated by the system for N=51 α_c=1.76 values will be 0011 1111 0111 1100 1111 0011 1011 1000 =0.98809.

For the exponential function, the results were obtained using the values N=51, α_e=1.76 and N=31 α_e=5.86. The term $\alpha\sqrt{1-\left(\frac{2n}{N-1}\right)^2}$ is common to them, as given in equations 5 and 6. The circuit, the design of which is presented in Figure 1, can be used for the exponential function. The circuit output is given as an input to equation 6 using the values obtained from Figure 1 for N=51, α_e=1.76 and N=31 α_e=5.86. The circuit designed on the FPGA for Equation 6 is given in Figure 5. Two exponential and one division IP core were used for this circuit design. These IP cores are need 17 and 6 clock cycles respectively to generate results. Each value is obtained at a frequency of 328.17 kHz using Equation 6. The results obtained were written in the memory hardware, the design of which is given in Figure 3.

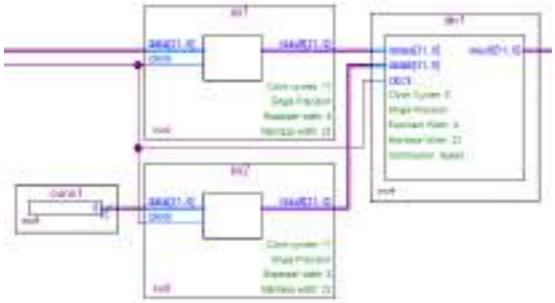

Fig.5. Implementation of the exponential function on the FPGA

The problem in designing for both cosh and exponential windows is that mathematical operations take too much time in the floating number system. However, the use of this number system is more advantageous than the fixed number system because more suitable spectral parameters can be obtained from the amplitude responses of the window functions. Quartus software developed by Altera includes IP cores for performing mathematical operations such as multiplication, division and exponentiation, and it allows such mathematical expressions to be easily performed. The number of LEs (Logic Elements) and the number of IP cores used in the cosh and exponential window function design are given in Table 1, and the numbers of clock cycles required for the calculation of the values given to the input of the IP cores in the floating point numbering system are given in Table 2.

Table 1: Numbers of LEs (Logic Elements) and hardware modules

	LE	Add	Mult	Exp
Cosh	10883	3	3	4
Exp	6351	1	3	2
	Div	Sqrt	RAM	Counter
Cosh	1	1	1	1
Exp	1	1	1	1

Table 2: Numbers of clock cycles required for the hardware modules used

	Add	Mult	Exp	Div	Sqrt
Clock number	10	5	17	6	28

4. DESIGN RESULTS

Cosh and exponential window functions designed on the FPGA were compared using different features. Spectrum behaviors of cosh and exponential window functions for the same window length and same alpha parameter are shown in Figure 6. The numerical values for the amplitude response obtained are given in Table 3.

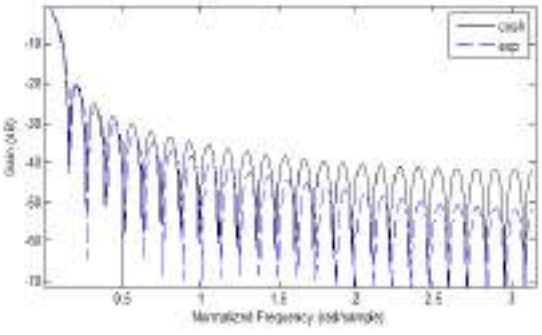

Fig. 6. Cosh and exponential window spectrum for N=51 and α=1.76

Table 3: The obtained data for cosh and exponential windows

Parameter	Window type	
	Cosh	Exponential
N	51	51
α	1.76	1.76
w_R	0.1411	0.150
S (dB)	21.56	31.18
R (dB)	-20.26	-20.63

The spectrum of cosh and exponential windows for fixed bandwidth and fixed window length are illustrated in Figure 7 and the numerical data is given in Table 4.

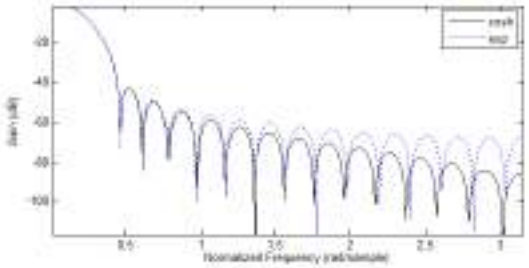

Fig. 7. Cosh and exponential window spectrum for N=31 and α=5.86

Table 4: The obtained data for cosh and exponential windows

Parameter	Window type	
	Cosh	Exponential
N	31	31
α	5.86	5.86
w_R	0.451	0.451
S (dB)	43.13	24.88
R (dB)	-43.01	-42.92

Figures 6 and 7 show the amplitude spectrums drawn in MATLAB software for the coefficients obtained from the window functions designed on the FPGA. Figure 8 shows the design experiment for both exponential and cosh windows. The 23rd value (3F7CF3B8) obtained for the cosh window is shown in Figure 9. The first two bits of the sign are the last two bits of the 24th value and the last two bits are the first two bits of the 22nd value. The intervening 32 bits represent the 23rd value.

Fig. 8. A view of the experimental systems

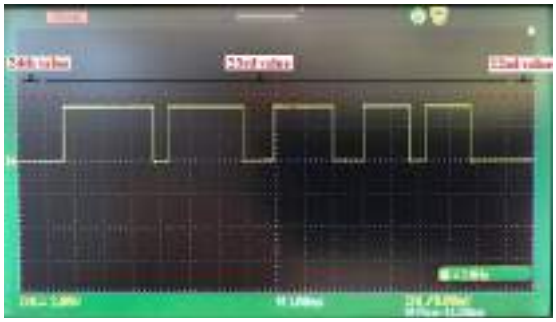

Fig. 9. Oscilloscope view of 23rd value (3F7CF3B8)

5. CONCLUSION

In this paper, cosh and exponential window functions were designed in real-time for a FPGA. The amplitude response was drawn using the coefficient values of the designed functions, and the commonly used spectral parameter values were obtained and presented in tables. These window functions are the functions obtained from the Kaiser window that is commonly used in published literature. The floating point number system was used in the designs which is a disadvantage in terms of running time. Hardware that can operate with the fixed point number system could be used in order to eliminate this disadvantage; however, the coefficient values of the window functions would be obtained as approximate values, thus the desired spectral parameter amplitude responses could not be achieved. Thus, window functions can be used as a module for numerical filter design, which is used to eliminate noises in areas such as signal processing and image processing.

REFERENCES

1- E. Torbet, M. J. Devlin,W. B. Dorwart, et al., "A measurement of the angular power spectrum of the microwave background made from the high Chilean Andes," The Astrophysical Journal, vol. 521, pp. L79–L82, 1999.

2- B. Picard, E. Anterrieu, G. Caudal, and P. Waldteufel, "Improved windowing functions for Y-shaped synthetic aperture imaging radiometers," in Proc. IEEE International Geoscience and Remote Sensing Symposium (IGARSS '02), vol. 5, pp. 2756–2758, Toronto, Ont, Canada, June 2002.

3- P. Lynch, "The Dolph-Chebyshev window: a simple optimal filter," Monthly Weather Review, vol. 125, pp. 655–660, 1997.

4- M. Dessouky, H. Sharshar, Y. Albagory, "A novel tapered beamforming window for uniform concentric circular arrays", Journal of Electromagn. Waves and Appl, 20/4: 2077-2089, 2006.

5- A. Antoniou, "Digital signal processing: signal, systems, and filters", New York: McGraw-Hill; 2005.

6- D. Ashutosh, J. Alok, CS. Pramod, "Design and performance analysis of adjustable window functions based cosine modulated filter banks", Digital Signal Processing, 23/1: 412-417, 2013.

7- C.L. Dolph, "A current distribution for broadside arrays which optimizes the relationship between beamwidth and side-lobe level", *Proc. IRE*, June, 34, 335-348, 1946.

8- J.F. Kaiser, "Nonrecursive digital filter design using I_0-sinh window function", *Proc. IEEE Int. Symp. Circuits*

and Systems, San Francisco, Calif., USA, 20-23 April, p. 20-23, 1974.

9- J.F. Kaiser, R.W. Schafer, "On the use of the I_0-sinh window for spectrum analysis", *IEEE Trans. Acoustics, Speech, and Signal Processing*, 28/1, 105- 107, 1980.

10- T. Saramaki, "Finite impulse response filter design", *in Handbook for Digital Signal Processing*, S.K. Mitra and J.F. Kaiser, Eds. Wiley & Sons, New York, NY, US, 1993.

11- S.W.A. Bergen, A. Antoniou, "Generation of Ultraspherical window functions", in XI European Signal Processing Conference, Toulouse, France, September, 2, 607-610, 2002.

12- S.W.A. Bergen, A. Antoniou, "Design of Ultraspherical Window Functions with Prescribed Spectral Characteristics", EURASIP Journal on Applied Signal Processing, 13 2053-2065, 2004.

13- S.W.A. Bergen, A. Antoniou, "Design of Nonrecursive Digital Filters Using the Ultraspherical Window Function", EURASIP Journal on Applied Signal Processing, 12, 1910-1922, 2005.

14- K. Avci, A. Nacaroğlu, "Cosh window family and its application to FIR filter design", International Journal of Electronics and Communications-AEU, 63 906-917, 2009.

15- K. Avci, A. Nacaroğlu, "A new window based on exponential function", IEEE Ph.D. Research in Microelectronics and Electronics (PRIME 2008), June Istanbul, Turkey, 69-72, 2008.

16- E. Avaroğlu., T. Tuncer, A.B. Özer, B. Ergen, M. Türk, "A novel chaos-based post-processing for TRNG", Nonlinear Dyn., 1–11, 2015.

17- E. Avaroğlu., T. Tuncer, A.B. Özer, M. Türk, "A new method for hybrid pseudo random number generator". J. Microelectron. Electron. Compon, 4(4), 303–311, 2014.

18- C. Dominguez, H. Hassan, A. Crespo, "Emotional robot control architecture implementation using FPGAs", Journal of Systems Architecture, 72, 29–41, 2017.

19- M.G. Egila, M.A. El-Moursy, A. E.El-Hennawy, H.A. El-Simary, A. Zaki, "FPGA-based electrocardiography (ECG) signal analysis systemusing least-square linear phase finite impulse response (FIR) filter", Journal of Electrical Systems and Information Technology, 3, 513–526, 2016.

20- R. Lehto, T. Taurén, O.Vainio, "Recursive FIR filter structures on FPGA", Microprocessors and Microsystems, 35, 595–602, 2011.

21- G. Jinding, H. Yubao and S. Long, "Design and FPGA Implementation of Linear FIR Low-pass Filter Based on Kaiser Window Function", Fourth International Conference on Intelligent Computation Technology and Automation, 496-498, 2011.

22- A. Kulkarni, R. Sindal "Implementation and Performance Analysis of Kaiser and Hamming Window Techniques on FPGA", Int. Journal of Engineering Research and Applications, 11, 113-116, 2016.

23- S. Aggarwal, K. Khare, "Efficient Window-Architecture Design using Completely Scaling-Free CORDIC Pipeline", 26th International Conference on VLSI Design and the 12th International Conference on Embedded Systems, 60-65, 2013.

24- K. C. Ray and A. S. Dhar, "High throughput VLSI architecture for Blackman windowing in real time spectral analysis", Journal of Computers, 3,5, 54-59, 2008.

25- V. Kumar, K.C. Ray, Preetam Kumar, "A VLSI architecture of CORDIC-based popular windows and its FPGA prototype", International Journal of High Performance Systems Architecture, 7,2, 57-69, 2017.

26- K. Khare, R.P. Singh, N. Kahere, "Comparison of pipelined IEEE-754 standard floating point adder with unpipelined adder", Journal of Scientific and Industrial Research, 65, 900-904, 2006.

CISET - 2nd Cilicia International Symposium on Engineering and Technology
10-12 October, 2019, Mersin / TURKEY

AMBIENT PARTICLE MATTER POLLUTION NEAR UNIVERSITY REGION OF KONYA CITY

Sukru Dursun [*1], Hysen Mankolli [2], Lyudmyla Symochko [3] and Zeynep Cansu Ayturan[4]

[1] Environmental Engineering Department, Konya Technical University, Konya, Turkey, sdursun@ktun.edu.tr

[2] Expert in Ecology, Plainfield, Illinois, USA, hysenmankolli@yahoo.com

[3] Faculty of Biology, Uzhhorod National University, Voloshyna Str. 32, Uzhhorod, Ukraine, lyudmilassem@gmail.com

[4] Environmental Engineering Department, Konya Technical University, Konya, Turkey, zcayturan@ktun.edu.tr

ABSTRACT
In the developing world, environmental pollution is a problem caused by human intentionally or unexpected situation. People are directly or indirectly affected by the resulting environmental pollution. There is no energy source in the world to continue continuously forever. Although air appears to be an inexhaustible source of energy, the danger of this source as a result of pollution increases the importance of measures that human beings will take care of air quality. Air pollution is really an important problem today due to its negative effects on human health, visibility, materials, plants and animal health. One of the major environmental pollution problems in recent years is air pollution in the world. Air pollution is caused by housing activity, traffic and industry. In addition, meteorological factors and topographic structure prevent the pollution from spreading in the atmosphere. Air pollution indicators need to be predicted and air pollution warning systems should be developed in order to minimize human exposure to air pollution. In this investigation, different diameter particulate matters levels near the University urban side were investigated during winter period 2018-2019 and comparison were made for levels of different PM size. Investigation of was concentrated to guess source of pollutant by comparing particulate size.

***Keywords**: Environment, pollution, air, traffic, particle matter, modelling map, $PM_{2.5}$, PM_{10}*

[*] Corresponding Author: e-mail: sdursun@ktun.edu.tr ; tel: +905365954591

1. INTRODUCTION

The effects of air pollution, increasing population, growth of cities and the development of industry continue to increase and varying content. While air pollutants emitted from a local source have local effects, energy consumption in urban centres, fossil fuel combustion and increased motor vehicles cause deterioration of air quality. Pollutants from traffic, transport, industry and heating are the main causes of air pollution. Air pollutants emission expressed as the sum of the emissions obtained by multiplying the activity data and emission factors annually for certain pollutants. It includes national emissions of major air pollutants by years and source sectors. Particulate Matter (PM10) and other particles smaller than 10 micrometres in diameter size that may be reached the lung, causing inflammation or heart and lung diseases, which may adversely affect humans' health. The concentration of pollutants in the outdoor air is a basic indicator of air pollution in the ambient conditions. With this rationale "Turkey's National Air Quality Monitoring Network" in 81 provinces are collected data by air quality monitoring stations in installation, also from the web address "www.havaizleme.gov.tr" continuous and online internet presented for the public monitoring (URL-1). Figure 1 shows the number of air treatment stations since 2005.

In order to improve air quality, "Turkey Air Action Plans" scope; efforts are being made to control the type of fuel used for heating purposes, improve combustion systems, facade coating in buildings, training of heating burners and increase the effectiveness of measures to reduce the amount of pollution caused by motor vehicles. Both local administrations and Provincial Directorates of the Ministry of Environment and Urbanization are carrying out continues studies to control air pollution. Limit values of Average PM10 concentrations over the last five years (2013-2017) has given in Figure 2. During last twenty-seven years (1990-2016) sums of PM10, SO_2, NH_3, CO NOx, and NMVOC for the emission has given in Figure 3.

Airborne particulate matter (PM) is considered to be an important in air pollutant for urban areas (Zamora et al, 2012; Khan et al., 2010; Liu et al., 2013). There are a total of 4 sub-versions of particulate matter as total suspended particles in the air, inhalable particles, harmless particles and very harmless particles. Their abbreviated names are TMS, PM10, PM2.5 and PM1.0 respectively. The aerodynamic diameters of these particulate matter are 100, 10, 2.5 and 1.0 µm, respectively (Liu et al., 2013; Wang et al., 2008). Air containing high concentrations of particulate matter (PM) is dangerous for human health and the environment. High concentrations of PM in the air threaten the human respiratory system and thus the cardiovascular system. There is a significant link between the increase in PM values and increases in mortality or increases in disease rates (Liu et al., 2013; Wang et al., 2008; Panyacosit & Amann, 2000).

Particulates may be very small solid or liquid-like particles that emit in the atmosphere, apart from large particles which can rapidly precipitate due to their density in the atmosphere. In terms of mass and composition; coarse particles with an aerodynamic diameter greater than 2.5 µm and fine particles with an aerodynamic diameter less than 2.5 µm. Fine particles; aerosols, particles formed as a result of combustion, condensed organic and metal vapours. Large particles; in general, crustal materials include dust delivered to the atmosphere from roads and industries. Suspended particulate matter is a term used for solids and liquids that are introduced into the environment from various natural and artificial sources. Particulate matter can be composed of many natural sources such as combustion of fuels, diesel engines, construction and industrial activities, the reaction of ammonia, sulphur and nitrogen oxides in the air and plant pollen and ground dust. Particulate matter, in terms of quality and quantity; it varies widely depending on particle size, density, chemical composition and health potential (Özdemir, 2008). National "Air Quality Index", the EPA Air Quality Index for Turkey was created by adapting legislation and limit values. PM10 air quality index for air quality is given in Table 1.

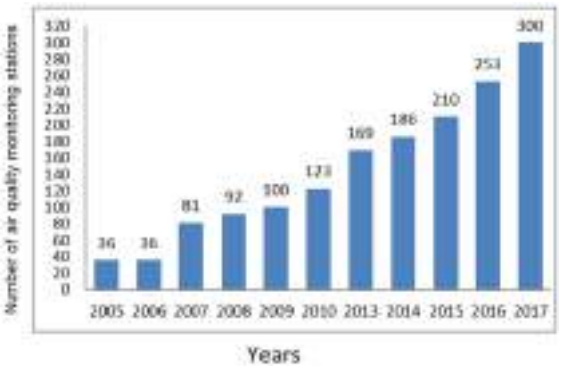

Figure 1. Number of air quality monitoring stations by years in Turkey (Source: URL-2 Turkish Ministry of Environment and Urbanization, environmental impact assessment (EIA), General Directorate of Permit and Inspection, Laboratory, Measurement and Monitoring Department)

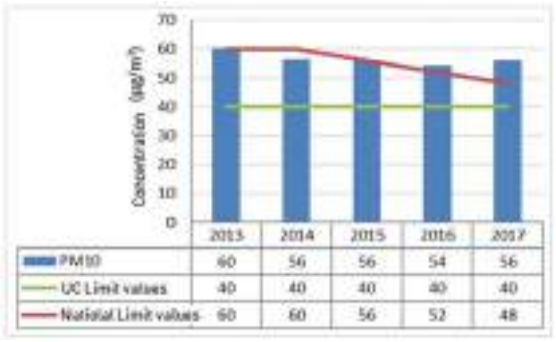

Figure 2. Limit values of Average PM10 concentrations over the last five years (2013-2017) (URL-2)

Particulates may be very small solid or liquid-like particles that emit in the atmosphere, apart from large particles which can rapidly precipitate due to their density in the atmosphere. In terms of mass and composition; coarse particles with an aerodynamic diameter greater than 2.5 µm and fine particles with an aerodynamic diameter less than 2.5 µm. Fine particles; aerosols, particles formed as a result of combustion, condensed organic and metal vapours. Large particles; in general, crustal materials include dust delivered to the atmosphere from roads and industries. Suspended particulate matter is a term used for solids and liquids

that are introduced into the environment from various natural and artificial sources. Particulate matter can be composed of many natural sources such as combustion of fuels, diesel engines, construction and industrial activities, the reaction of ammonia, sulphur and nitrogen oxides in the air and plant pollen and ground dust. Particulate matter, in terms of quality and quantity; it varies widely depending on particle size, density, chemical composition and health potential (Özdemir, 2008). National "Air Quality Index", the EPA Air Quality Index for Turkey was created by adapting legislation and limit values. PM10 air quality index for air quality is given in Table 1.

Today, nearly 200 air pollutants have been identified. These five basic contaminants from the National Air Quality Index is calculated in Turkey. However, many measuring stations measure only two main pollutants, sulphur dioxide (SO_2) and particulate matter (PM10). The remaining main pollutants, fine particulate matter (PM2.5), carbon monoxide (CO), nitrogen dioxide (NO_2) Lead (Pb) and ozone (O_3) are not widely measured nationwide. The destruction of airborne particulate matter pollutants in human health is briefly in following sections.

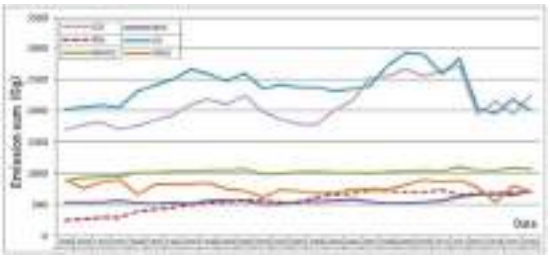

Figure 3. Sums of PM10, SO_2, NH_3, CO NO_X, and NMVOC for the emission (1990-2016) (Tosun, 2017)

Table 1. PM10 air quality index for air quality of Turkey (URL-4)

Air Quality Index	Health Level	Colours	PM10
AQI level	Air quality	Air Quality is indicated by the following colours	24 hours mean
1	Very good	Light Green	0 - 25
2	best	Green	26-69
3	Enough	Dark Green	70-109
4	medium	Yellow	110-139
5	Poor	Orange	140-599
6	Too bad	Red	> 600

Short-term limit value -STL- 24 hours 95%/year. For the protection of human health	140µg/m³	
Winter Season Average (October 1 - March 31). For the protection of human health	112µg/m³	The limit value is reduced annually by an equal amount every 12 months, starting from 01.01.2008 to 90 µg/m3 (45% of the limit value) by 01.01.2014.
LTL-yearly. For the protection of human health	78 µg/m³	The limit value is reduced annually by an equal amount every 12 months, starting from 01.01.2008 to 60 .20g / m3 (40% of the limit value) by 01.01.2014

Particulate Matter (PM10, PM2.5 flying powders) in the air is one of the most important pollutants affecting human health. The negative effect on particle size and health is linearly linked. More than 10 microns of PM are kept in the nose. Smaller than 10 microns accumulate by reaching the lungs and bronchi through the respiratory tract; In addition to the physical properties of particulate matter, its chemical composition is also very important for health. Particulate substances may contain heavy metals such as mercury, lead, cadmium, and carcinogenic chemicals and may pose a significant threat to health. These toxic and cancerous chemicals combine with moisture and turn into acid. Since soot, fly ash, gasoline and diesel vehicle exhaust particles contain carcinogenic substances such as coal tar component, inhalation of them for long periods causes cancer.

Particulates are mainly caused by explosions, thermal power plants, industrial sectors requiring high temperatures, material and stone quarries, cement sector, fires and waste to be burned in Biomass power plants, volatile waste generated by incineration of waste and gases released by geothermal power plants. Particles consisting of solid and liquid small particles adversely affect our lives and form the basis of various health problems. The way to prevent this is clean energy and production by taking measures in accordance with the rules and regulations (WHO, 2006).

European Union policies which The EU's long-term goal is to achieve air quality that will not create unacceptable impacts and risks on human health and the environment. The EU operates at several levels to reduce exposure to air pollution: Laws; cooperation and research with international, national and regional authorities and informal organizations, as well as sectors responsible for air pollution. EU policies aim to reduce exposure to air pollution by setting limits and target values for air quality and reducing emissions. In late 2013, the European Commission adopted a proposal for a “Clean Air Quality Package”, which included new measures to reduce air pollution (ATS, 2000).

In general, all concentrations decreased in both seasons with increasing wind speed depending the topography. This is probably the result of higher rates increasing the dilution effect. On the other hand, high velocities increase the rate of PM remixing from soil to atmosphere and the effect of transporting over long distances (Chaloulakou et al., 2003; Harrison et al., 2001). The decrease in the concentrations during the summer with the increasing wind speed can be explained as the dilution effect is greater than the effect of PM transport from the soil.

Precipitation, which is another meteorological factor, affects PM concentrations significantly. This effect is the removal of the particles from the atmosphere by washing, as well as decreasing the re-mixing of the particles into the air with the effect of wind and decreasing the concentration values in the air (Chaloulakou et al., 2003). In Konya, precipitation is observed in the months of November -April, which are usually the could period of winter and spring months. During precipitation, most of pollutant materials were removed by dissolving in rainwater but only limited organic compounds in low concentration and aromatic compounds are not be removed.

In this case of Konya study, the changes in airborne particulate matter concentrations in the residential areas around the University campus were investigated. The results showed that the local and temporal variations of PM10-PM0.5 concentrations were significant relation high population area with decreasing winter temperature. It was determined that wind direction, speed and precipitation had significant effects on concentrations. Especially in winter months when the weather is humid, despite the increase in fossil fuel combustion for heating purposes, decreases in concentrations and high values in east/north winds are observed. However, it is necessary to know not only the concentrations of particulate matter in the air but also their elemental content in order to determine the source of particulate matter precisely. Based on the elemental content and diffraction of PM, it

is possible to obtain information about sources and their contribution to concentrations using various statistical methods and models. In the subsequent findings of the study, it aims to achieve these goals.

2. MATERIALS AND METHODS

2.1. Sampling area

In this present study, 22 sampling points were selected in the Bosna-Hersek district of Konya city center in Turkey. In these sampling points, particulate matter measurement was done during different time periods of day which are shown in Figure 4-5. Particulates were measured during the four days of a week (Tuesday, Friday, Saturday, Sunday) at designated sampling points with certain time periods (determined time periods are 08.00, 11.00, 13.00, 16.00, 20.00).

Figure 4. The location of the sampling area on map

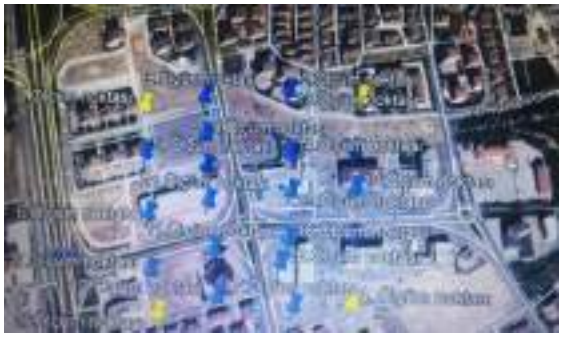

Figure 5. Marked measurement points on the map

Particle Mater measurements were performed using the equipment shown in Figure 6.

Figure 6. Particle matter measurement equipment (Particle Counter PCE-PCO 1)

2.2. Modelling Program

Surfer-16 software is a type of programme that is a Golden Software used to preparation of the contour diagram. The coordinates are located in the lower left corner of the icon description. Horizontal and vertical icons can be found in the opening part of the program so user can easily perform the series without using the upper bar part. In order to prepare contour diagrams, the x, y coordinates we received from the land in the columns A, B that we have prepared in Microsoft Excel are transferred and the Surfer program is opened. Then the data menus are followed, the database file prepared in Excel is selected and in the drop-down menu, the columns in the database file in Excel will be selected which coordinates will be included in the program.

3. RESULTS

3.1. Modelling of measurement

3.1.1. Modelling of time distribution (PM2,5 / PM10) by hourly

According to Figure 7, the PM2.5 values at the 1st measurement point and at the 15th measurement point was found higher than the other points for the measurements made in Tuesday and Friday. When these values were evaluated according to EPA and WHO standards, (limit value of 35 $\mu g/m^3$ for 24 hours set by EPA and limit value 25 $\mu g/m^3$ for 24 hours set by WHO), these values were above the limit values. In Figure 8, the PM2.5 values around the measurement points 4,13, 14, 19 was found higher than the other points for Saturday and Sunday and above limit values set by EPA and WHO. The results related to PM2.5 are rational when the households and work centres around this area considered. For work days (Tuesday and Friday) the concentration may be affected from traffic and stack of the houses while for weekends (Saturday and Sunday) the concentrations may be affected from only stacks and found lower than work days.

Figure 7. Model distribution map prepared by the results of time 08.00 am for PM2.5 (Tuesday, Friday)

Figure 8. Model distribution map prepared by the results of time 08.00 am for PM2.5 (Saturday, Sunday)

When the Figure 9 was evaluated, the PM10 concentrations were found lower than PM2.5 concentrations with respect to average of all measurement days. Maximum PM 10 concentration reached in a week was measured as 95 μg/m^3 which is lower than the value given in air quality of Turkey (Table 1).

Figure 9. Model distribution map prepared by 08.00 am for PM10 (Tuesday, Friday, Saturday, Sunday)

In the models shown, the measurement results at the measurement points from 1 to 22 for PM2.5 and PM10 was evaluated and the model is shown as the week without any time discrimination. In the model created below, at the measurement points of 15, 16, 19 and 22, PM values were found higher on the days determined. When these values were evaluated according to EPA and WHO, it was observed that these values were found above the limits (Figure 10). Also, this model shows that in the morning hours of all measurement days PM concentrations were measured higher than the other time periods.

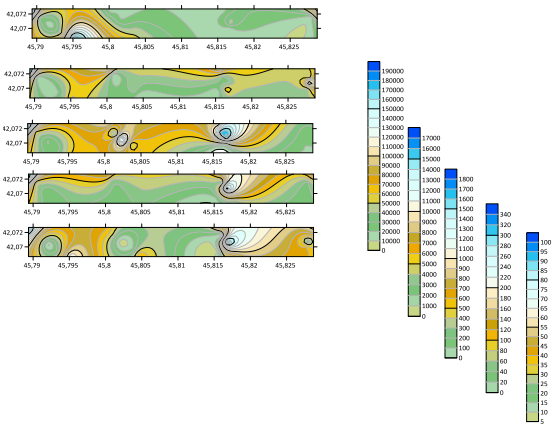

Figure 10. Model distribution map prepared with the results of PM measurement made during all week of different time periods of 08.00, 11.00, 13.00, 16.00, 20.00

4. DISCUSSION

Model maps were formed based on the measurement results made at 22 different points during the week and at weekends. According to the WHO and EPA limit values, it was observed that the PM2.5 and PM10 limit values were exceeded at some measurement points. It has been observed that wind direction, speed and precipitation have significant effects on concentrations. However, in order to determine the sources of particulate matter, it is necessary to know not only the concentrations of airborne particulate matter but also their elemental contents. Based on the elemental content of PM, it is possible to obtain information about sources and their contribution to concentrations using various methods and models.

Turkish Air Quality Assessment and Management Regulation (HKDYY) has been implementing a stricter limit value for air quality parameters every year with a gradual reduction (URL-3). Decreasing the limit values specified each year and increasing the number of stations measured continuously play a role in increasing the total number of exceedances. In 2017, the daily limit value was determined as 70 μg/m^3 for the PM10 parameter and 175 μg/m^3 for the SO_2 parameter. In 2017, the total number of exceedances is 13827 for PM10 and 256 for SO_2. In the period between 2015-2017, according to the number of exceeding the limits calculated on the basis of all stations; although both limit values were reduced by 12.5% in 2017 compared to 2016, there was a 36% increase in the number of exceedances for PM10 parameter and a 20% decrease in the number of exceedances for SO_2 parameter (URL-2).

5. RECOMMENDATIONS

The most important source of particulate matter in the study environment is traffic. Therefore, in the area where the measurement is carried out, public transportation is very important in terms of decreasing the particulate matter level. Particulate matter concentrations are very low in areas with low traffic density. In addition, the use of particulate filters in diesel vehicles should be considered. Regular maintenance and cleaning of the filter must be carried out on vehicles using a particle filter. The filters in the air conditioning and ventilation systems of the vehicles should be replaced at regular intervals. Care should be taken to ensure that the filters and air conditioners used are in compliance with the standards. When such changes are made in ventilation systems, particulate matter concentrations will decrease. If the streets and streets where the study is carried out with water at regular intervals, a decrease in particle concentrations will occur. Our duty as a society to reduce air pollution: A significant part of air pollution is caused by automobiles. Using less fuel by preferring public transportation, Maintenance of vehicles on time, Preference of walking or biking transportation to places within walking distance, not to start the vehicle during pauses and waiting, save energy by turning off lights and electrical appliances when not in use, Clean energy (wind, geothermal, solar energy), renewable energy sources should be encouraged, the importance of environmental protection and training should be prepared to inform the public.

REFERENCES

American Thoracic Society (ATS) (2000). "What constitutes an adverse health effect of air pollution?" American Journal of Respiratory and Critical Care Medicine, 161, 665–673.

Chaloulakou A., Kassomenos P., Spyrellis N., Demokritouc P., Koutrakis P. (2003) "Measurements

of PM10 and PM2,5 Particle Concentrations in Athens, Greece", Atmospheric Environment, 37, pp. 649-660.

Harrison R.M., Yin J., Mark D., Stedman J., Appleby R.S., Booker J., Moorcroft S. (2001) "Studies of the Coarse Particle (2,5-10 μm) Component in UK Urban Atmospheres", Atmospheric Environ, 35, pp. 3667-3679.

Khan MF, Hirano K, Masunaga S. (2010) "Quantifying the sources of hazardous elements of suspended particulate matter aerosol collected in Yokohama", Japan. Atmos Environ, 44, pp. 2646-57. doi:10.1016/j.atmosenv.2010.03.040.

Liu YJ, Zhang TT, Liu QY, Zhang RJ, Sun ZQ, Zhang MG. Liu et al., (2013) "Seasonal variation of physical and chemical properties in TSP, PM10 and PM2.5 at a roadside site in Beijing and their influence on atmospheric visibility". Aerosol Air Qual Res 2014, 14, pp. 954–69. doi:10.4209/aaqr. Liu et al., 2013.01.0023.

Özdemir F. (2008) Türkiye geneli ̇nde ̇kükürt dioksi ̇t ve parti ̇küler madde ki ̇rli ̇li k dağilimlarinin analizi. Yıldız Teknik University, Istanbul.

Panyacosit L, Amann M. (2000) Interim Report A Review of Particulate Matter and Health : Focus on Developing Countries Approved by Project Leader.

Tosun E, (2017) The Evaluatıon Of Turkey's Aır Quality Data Between 2009 AND 2016. MSc. Thesis, Hacettepe University, Ankara, Turkey.

URL-1, www.havaizleme.gov.tr [Accessed 12/03/2019].

URL-2, Turkish Ministry of Environment and Urbanization, environmental impact assessment (EIA), General Directorate of Permit and Inspection, Laboratory, Measurement and Monitoring Department) https://ced.csb.gov.tr/birimler/laboratuvar-olcum-ve-izleme-dairesi-baskanligi/184 [Accessed 15/03/2019].

URL-3, Çevre ve Sehircilik Bakanlıgı, Hava Kalitesinin Degerlendirme ve Yönetimi Yönetmeligi, Ankara, (2008).
http://www.mevzuat.gov.tr/Metin.Aspx?MevzuatKod=7.5.12188&MevzuatIliski=0&sourceXmlSearch=hava%20kalitesi [Accessed 18/03/2019].

URL-4, https://www.csb.gov.tr/dokumanlar/ [Accessed 12/05/2019].

World Health Organization (WHO), Air Quality Guidelines: Global Update (2006). Particulate matter, ozone, nitrogen dioxide and sulphur dioxide, World Health Organization, Regional Office for Europe, Copenhagen.

Wang S, Zhao Y, Chen G, Wang F, Aunan K, Hao J. (2008) "Assessment of population exposure to particulate matter pollution in Chongqing, China". Environ Pollut;153:247–56. doi:10.1016/j.envpol.2007.07.030.

Zamora E, Scholar M, Major CS. (2012) *Using Image Processing Techniques to Estimate the Air Quality. UNLV,* Univ. Nevada, Las Vegas, Las Vegas:, p. 101.

PHYSICAL, CHEMICAL AND MICROBIOLOGICAL QUALITIES OF POTABLE WATER USED IN DIFFERENT POULTRY FARMS A REVIEW

Mostafa MAAROOF1, Sukru DURSUN1, Maan T. MAAROOF2
1Environmental Engineering Department, Engineering & Natural Science Faculty, Konya Technical University, Konya, TURKEY, mmaaroof@selcuk.edu.tr, sdursun@selcuk.edu.tr
2Department of Veterinary Public Health, College of Veterinary Medicine, University of Mosul, Mosul, IRAQ,maantahir@uomosul.edu.iq

ABSTRACT
In the poultry works, the utilization of water with sufficient physical, compound and microbiological quality is of crucial significance. Since numerous fowls approach a similar water source, quality issues will influence an incredible number of creatures. The drinking water assumes a significant job in the transmission of some bacterial, viral and protozoan infections that are among the most well-known poultry ailments. Significant components to anticipate waterborne sicknesses in oven generation are the assurance of supply sources, water purification and the quality control of microbiological, substance and physical attributes. Water is a basic supplement for feathered creatures and subsequently quality safeguarding is major for good crowd execution. The rancher may avoid numerous maladies in winged animal runs by controlling the nature of the ingested water, will unquestionably bring about diminished expenses and expanded benefit, two fundamental points of creature generation these days.

Drinking water for poultry isn't liable to specific microbiological, compound and physical necessities, along these lines speaking to a potential transmission course for pathogenic microorganisms and contaminants and additionally getting to be unacceptable for water-controlled drugs**.**

Keywords: *DRINKING WATER, ANIMALS HEALTH, POULTRY FARMS, SURFACE WATER*

1. INTRODUCTION

The nature of drinking water for domesticated animals is a subject of most extreme significance, as it can straightforwardly and by implication influence creature wellbeing and profitability (Umar et al., 2014). Albeit general proposals just as explicit rules for poultry water quality are accessible (Carter and Sneed, 1996; Amaral, 2004), ranchers are frequently unconscious of the significance of water quality (Umar et al., 2014). In the European Union (EU), this subject has gotten little consideration as far as EU enactment, as drinking water for poultry isn't liable to specific microbiological, concoction and physical prerequisites. Guideline (EC) 852/2004 on the cleanliness of groceries sets up least necessities for domesticated animals drinking water, however no subjective parameters are recorded Gathering Directive 98/58/EC on cultivated creature welfare expresses that 'all creatures must approach an appropriate water supply or have the option to fulfill their liquid admission needs by different methods', albeit no reasonableness edges are shown, (Carter and Sneed, 1996).

As of late, the European Food Safety Authority (EFSA, 2011) demonstrated ranch water as one of the wellsprings of direct sullying with Campylobacter for animals and people. Campylobacter is more helpless than E. coli to water chlorination and it was accounted for a 3.5-overlap danger of disease for grill runs provided with unchlorinated versus chlorinated water in addition, C. jejuni has been separated from the biofilm of areola drinking frameworks for poultry when the flying creatures were likewise colonized (Zimmer et al., 2003), in spite of the fact that there is constrained proof for such drinking frameworks to be the wellspring of Campylobacter colonization. This might be because of inability to recognize Campylobacter in water because of deficient water volumes prepared or of microorganisms in a reasonable, yet not culturally, state (Sparks, 2009).

All the Information on the microbiological, substance and physical nature of drinking water for domesticated animals in Italy are rare. Additionally, in the poultry part, groundwater is much of the time utilized, with no obligatory periodical water quality controls being mentioned for this wellspring of water supply. At last, turkeys are frequently treated with meds, including antimicrobials, managed with drinking water, and some concoction and physical water properties like pH, hardness and iron levels may meddle with medication disintegration and steadiness in water Consequently, the present investigation expected to evaluate the microbiological, substance and physical nature of savoring water business turkey ranches provided with either tap or well water. Various factors putatively connected with water quality (e.g., ecological conditions, cultivation rehearses, season, water distribution framework, and so forth.) were likewise examined, and water quality at various testing destinations along the ranch water pipeline was evaluated (Scandurra, 2013).

2. Water as a vehicle of infection for poultry

Water is the most inexhaustible and broadly appropriated synthetic compound on the planet. In the characteristic state, water is probably the most flawless compound known; by and by, it is right now hard to discover a freshwater source that has not been changed by man. This reality is identified with qualities of nations being developed, for example, Brazil, where wastewaters from farming and urban territories, which may contain elevated amounts of pathogenic microorganisms, are discarded in the dirt or into the sea-going condition. The buildups are then conveyed to the shallow and underground waters by the downpour. The utilization of utilization water with high physical, substance and microbiological characteristics is of major significance in creature generation in light of the fact that numerous creatures approach a similar water source and an issue in the water quality would influence an extraordinary number of creatures. (European Commission, 2004).

This is especially important in poultry generation, where one single water source serves a huge number of creatures. Thusly, control estimates must be considered as a need, so as to counteract the event of illnesses that are spread through water, and would surely bring about incredible financial misfortunes. Despite the fact that water does not give perfect conditions to the pathogenic microorganism to duplicate, they will by and large make due for sufficient opportunity to permit waterborne transmission. Water is, in this way, a superb transmission course of specialists in charge of human and creature ailments, predominantly those in which fecal-oral transmission happens since pollution of water supplies is still progressively expanding because of urban and country exercises. Preventive measures and furthermore answers for issues that as of now exist must be the point of each individual. (Lund, 1996),

3. Sources of water for poultry

Water sources utilized by the Australian poultry industry are changed and furthermore vary among states and regions and among provincial and urban regions. Essential water hotspots for supply to poultry include (Ogata, N & Shibata, T. 2008).

3.1. Mains or town water

Mains water is commonly treated and sterilized preceding circulation and is, consequently, the liked and most bio secure water for poultry. Sanitation of mains water at the homestead site is exceptional, albeit a few makers may utilize a sanitizer to control biofilm and another non-explicit microbial develop in drinking or cooling frameworks. Now and again, mains water has been found to have abnormal amounts of coliforms requiring treatment, (for example, treating the mains supply with chlorination). With decreased water accessibility in numerous regions of Australia, limitations have been put on some serious animals and mechanical offices to diminish mains water use. This has required the utilization of choices, for example, bore or surface water. Some water specialists likewise command that poultry ranches can just access recommended stream rates (liters every second) from the mains supply. This expects makers to utilize ranch water stockpiling with site dissemination through siphons, so as to give extra water in the midst of higher interest. (Kapperud et al., 1993).

3.2. Bore or underground water

The utilization of underground water is basic in Australia, especially where the quality (particularly the saltiness) is reasonable for use in poultry. The appropriateness of bore water shifts essentially between regions, with certain

territories, for example, south-east Queensland by and large being positive, while others, for example, North and North-focal Victoria are variable. The state divisions of the essential business can give data on water quality to certain territories. Underground water is generally considered to have an okay of containing avian pathogens, so on-ranch sanitation is remarkable for this water source. Shallow bores or spring water, be that as it may, might be influenced by surface run-off and can, especially after overwhelming downpours, contain levels of coliforms including E. coli. The nearness of E. coli demonstrates fecal issue, for example, from brushing creatures, has tainted the drag through surface run-off (Rice, EW et al ,2007).

3.3. Surface water (dams, reservoirs, channel, rivers and streams)

Surface water gives the most astounding danger to potential defilement with avian pathogens, especially those related with sea-going water winged animals, for example, AI and EDS infections and microorganisms related with water run-off, for example, E. coli, Campylobacter spp. what's more, Salmonella spp. Successful sanitation of surface water is required to lessen the danger of an EAD in poultry. Surface water that gives a changeless or transient living space for waterfowl, especially the Anseriformes (ducks, geese, swans) or Charadriiformes (shorebirds), is at most noteworthy danger of defilement with AI infection. The techniques required to adequately sterilize surface water and take out avian pathogens are commonly more in fact complex than idea by water clients. Variables affecting the viability of surface water sanitation include (Selleck, PW. Et al 2003).

• The avian pathogen included
• The nature of the water and its natural burden, pH, and solutes
• The sanitizer utilized
• The contact time between the sanitizer and the water
• The turbidity of the water.

Indeed, even after these angles are considered and tended to there are mechanical, support and observing variables that can likewise impact the adequacy of water sanitation.

3.4. Downpour water (rain water, carted water, recycled water)

The origin of alternative water sources should be identified in order to evaluate their biosecurity risk. For instance, water carted from a secure mains supply is associated with much lower risk than water from a lake or dam. With this knowledge, the necessary actions should be taken to ensure that the water is a secure and biologically safe supply for poultry. Other horizontal contacts such as vehicular and personnel movements should also be assessed for their biosecurity risk. (Senne, DA 2003).

4. POULTRY DISEASES POTENTIALLY TRANSMITTED BY WATER

4*.1. Bacterial Diseases*

A. Chronic Respiratory Disease (CRD)

Etiologic Agent: Mycoplasma gallisepticum. The disease might be complicated by the presence of Escherichia coli.

- Main clinical signs: respiratory distress, weight loss, respiratory rales, decreased egg production, poor flock uniformity and feed conversion, increased carcass condemnation.

The etiological agent may contaminate water by the expectorations of the birds and Escherichia coli may be present by fecal contamination of the drinking water. (Brown TM et al 1995).

B. Colibacillosis

- Etiological Agent: Escherichia coli.
- Main signs: exacerbation of respiratory symptoms, which are complicated by septicemia, occurring after stressing situations. The pathogen may be present due to fecal pollution of the water. (Amaral LA do, 2004).

C. Avian Cholera

- Etiological agent: Pasteurella multocida.
- Main signs: appetite loss, prostration, decreased egg production, cyanotic combs, high mortality, and respiratory signs.

The pathogen may be present as a result from fecal pollution of the water.

D. Fowl Typhoid

- Etiological agent: Salmonella Gallinarum.
- Main signs: prostration, green diarrhea, mortality, and decreased production.

The agent may be present in the water as a result of fecal contamination.

4*.2. Diseases caused by virus Newcastle Disease*

A. Newcastle Disease

- Etiological agent: Paramyxovirus.
- Main signs: respiratory, neural or digestive signs, decreased egg production, high mortality.

The etiological agent may be present in the water due to pollution by feces and discharges from the respiratory tract of infected birds. (Amaral LA do 2004)

B. Infectious bronchitis

- Etiological agent: Coronavirus.
- Main signs: respiratory impairment, decreased egg production.

The etiological agent may contaminate water by fecal pollution or by discharges from the respiratory tract of infected birds. (Amaral LA do 2004)

C. Marek's disease

- Etiological agent: Herpesvirus.
- Main signs: weight loss, paralysis, and mortality.

The etiological agent may be present in the water due to epithelial desquamation of infected birds.

D. Avian encephalomyelitis

- Etiological agent: Picornavirus.
- Main signs: ataxia, tremor of head, neck, and limbs.

The agent may be present in water due to fecal contamination.

E. Gumboro disease

- Etiological agent: Birnavirus.
- Main signs: paleness, prostration, and low resistance.

The etiological agent may be present in water due to fecal contamination.

4**.3. Protozoan Diseases**

A. Histomoniasis

Etiological agent: Histomonas meleagradis.

Main signs: prostration, ruffled feathers, and yellowish diarrhea.

The etiological agent may be present in the water by fecal pollution.

B. Coccidiosis

- Etiological agent: Eimeria sp.
- Main signs: dark feces with blood, drooping wings, ruffled feathers, loss of pigmentation in the shanks and combs, and flock yield lower than expected.

The etiological agent may be present in the water by fecal pollution. (Amaral LA do 2004).

5. **Conclusion**

The distinctive water sources could securely be utilized as drinking water for poultry; as long as it is available inside the adequate scope of drinking water quality for poultry. Recommending the advantages of treatment of water sources on improving poultry farms wellbeing and welfare. Attract thoughtfulness regarding the significance of keeping up the sterile nature of put away water.

6. Reference

Amaral L. (2004). "Drinking water as a risk factor to poultry health". Rev. Bras. Cienc. Avic . 6:191–199.

Amaral LA do, (2004) "Drinking Water as a Risk Factor to Poultry Health" *Brazilian Journal of Poultry Science.* ISSN 1516-635X Oct - Dez 2004 / v.6 / n.4 / 191 – 199.

Brown TM, Beck MM, Schulte DD, Jones DD, Douglas JH, Scheideler SE. (1995) "Nipple waterers for chick batteries: design, efficiency and cost analysis" *Poultry Science* 74:457-462.

Carter T. A., Sneed R. E. (1996) "Drinking water quality for poultry" North Carolina Cooperative Extension Service 2:88:5.

European Commission. (2004). "Council Regulation (EC) No 852/2004 of the European Parliament and of the Council of 29 April 2004 on the hygiene of foodstuffs". *Off. J. Eur. Union* L139:1–54.

European Food Safety Authority. (2011). "The European Union Summary Report on Trends and Sources of Zoonoses, Zoonotic Agents and Food-borne Outbreaks in 2009". *EFSA Journal*. 9:2090.

Kapperud G., Skjerve E., Vik L., Hauge K., Lysaker A., Aalmen I., Ostroff S., Potter M.. (1993) "Epidemiological investigation of risk factors for Campylobacter colonization in Norwegian broiler flocks" *Epidemiol. Infect*. 111:245–256.

Lund V. (1996). "Evaluation of E. coli as an indicator for the presence of Campylobacter jejuni and Yersinia enterocolitica in chlorinated and untreated oligotrophic lake water". *Water Res*. 30:1528–1534.

Ogata, N & Shibata, T (2008), "Protective effect of low concentration chlorine dioxide gas against influenza A virus infection" *Journal of General Virology*, vol. 89, pp. 60–67.

Rice, EW, Adcock, NJ, Sivaganesan, M, Brown, JD, Stallknecht, DE & Swayne, DE (2007) "Chlorine inactivation of highly pathogenic avian influenza virus (H5N1)", *Emerging Infectious Diseases, vol*. 13, pp. 1568–1570.

scandurra S. (2013). 'Veterinary drugs in drinking water used for pharmaceutical treatments in breeding farms". PhD Thesis, University of Bologna, Bologna (Italy).

Selleck, PW, Arzey, G, Kirkland, PD, Reece, RL, Gould, AR, Daniels PW & Westbury, HA (2003), "An outbreak of highly pathogenic avian influenza in Australia in 1997 caused by an H7N4 virus*", Avian Diseases, vol. 47,* pp. 806–811.

Senne, DA 2003, 'Avian influenza in the western hemisphere including the Pacific Islands and Australia', Avian Diseases, vol. 47, pp. 806–811

Sparks N. (2009). "The role of the water supply system in the infection and control of Campylobacter in chicken". *Worlds Poult. Sci. J*. 65:459–474.

Umar S., Munir M. T., Azeem T T., Ali S., Umar W., Rehman A., Shah M. A.. (2014) "Effects of water quality on productivity and performance of livestock: A mini review" . *Veterinaria* 2: 11–15.

Zimmer M., Barnhart H., Idris U., Lee M. (2003). "Detection of Campylobacter jejuni Strains in the Water Lines of a Commercial Broiler House and Their Relationship to the Strains That Colonized the Chickens". *Avian Dis*. 47:101–107.

OPTIMIZATION OF PRODUCTION TIMES OF POWER TRANSFORMERS USING DEVELOPED ARTIFICIAL BEE/ANT HYBRID HEURISTIC ALGORITHM

Mehmet Zile*[1]

[1]Mersin University, Erdemli UTIYO, Department of Information Technologies and Information Systems, Mersin, Turkey, mehmetzile@mersin.edu.tr

ABSTRACT
In today's market and competition conditions, it is vital for companies to quickly and accurately return to the demands. In order to determine the correct price for the product and to use the limited resources in the most efficient way during the bid phase, it is important for all companies to estimate the time with low deviation to the new demands. In this study, artificial bee / ant hybrid heuristic algorithm is developed which predicts the production time of power transformers. Based on this developed algorithm, an interface was created to estimate the production time of transformers in Visual Studio programming. It was understood that the values obtained from this computer program were close to the actual values measured and recorded previously. With this program, it is possible to estimate the production time of power transformers.

Keywords: *Power Transformers, Transformers Production Time, Hybrid Heuristic Optimization*

* Mehmet Zile

1. INTRODUCTION

An enterprise that produces power transformers must know the production times significantly in order to carry out its activities effectively. It is not possible to be consistent and useful for all activities carried out in the enterprise such as preparation of power transformer production plans, short and long term estimations, preliminary cost calculation and pricing without knowing the standard times. Knowing production times will significantly reduce production costs. Power transformer sector is a sector where production is made according to order and competition. Accurate determination of delivery time and cost of incoming orders provides a great competitive advantage over other companies in the sector. In this study, the optimization of transformer production times has been realized with artificial bee/ant hybrid algorithm developed. Using the Visual Studio program, the optimization interface of transformer production times has been created. Using the created computer program, transformer production times have been estimated at optimum values.

2. THE PRODUCTION OF POWER TRANSFORMERS

Transformers are one of the most important elements during the transmission of electrical energy to remote areas. Transformers; conducts electricity transmission, distribution and consumption stages. Transformers are the devices that can change the voltage and current values of electrical energy according to the needs. Transformer production consists of winding, stringing, mechanical production, assembly operation and finishing operations operation. The winding operation is carried out by winding the bobbins with aluminum or copper conductor after the necessary insulation material preparation, carpentry and machine preparation operations are completed. Different winding techniques are used depending on the strength, voltage level and customer requirements. Sequence operation is the process of stacking thin siliceous hairs on top of each other. In production, high-conductivity, low losses, quality cold-rolled silicon steel sheet is used. In modern machines with microprocessor control, the sliced sheets are then cut in accordance with the core structure and the sheeting process of the cut sheets is performed on the looms. At the end of the winding and sequencing operations, the section called active part is completed by passing the produced coil to the core and performing interconnection operations. The active part is placed in the transformer boiler which is completed in mechanical production after being fired for drying process. In the scope of the final operations, the oil of the transformer, the necessary final controls, the corrective or preventive works, if any, and the testing of the transformer are included. Power transformer production scheme is given in Figure 1. According to the cooling situation, the transformers are divided into dry type and oil type. The difference of oil type transformers from dry type transformers is the cooling process with oil. In dry type transformers, cooling is provided by fan. In oil type transformers, coils are formed by winding copper or aluminum conductors. The coils and the active part go through the firing process.

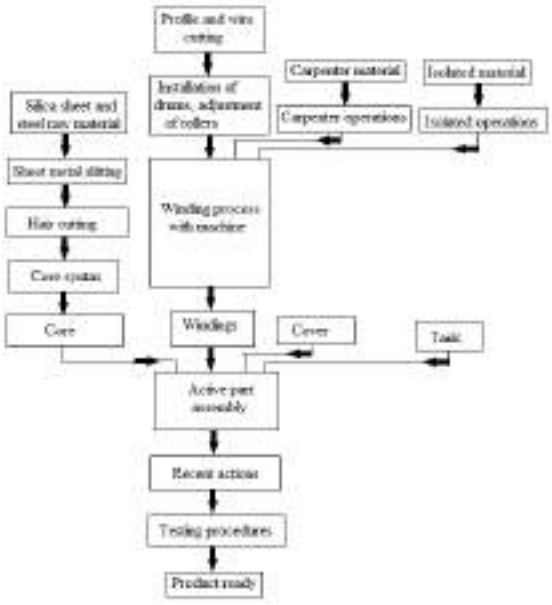

Fig. 1. Power transformer production scheme.

In dry type transformers, the coils are coated with resin after winding. It is important that the total duration of the work can be estimated in a realistic way in order to calculate the production cost of the orders of the power transformers in the bid phase correctly. Although transformers are produced with many different designs, the processing and transport times of each different designs are random variables with different probability distributions. The waiting times of the power transformers depending on the workload in the existing workshop, raw material status in stocks, machine failure and waste rates are also random variables. For all these reasons, the system has a stochastic and dynamic structure. Processing times, cycle time average, variances, workload, idle waiting, number of jobs waiting in queue, waiting times in average queue, etc. characteristics related to work or workshop. Historical data should be used for previously manufactured products. It is a big problem for the company to determine the production time of an order that is not produced by the company before. The different combinations and interactions of the material type, production technique and similar product characteristics to be used for the production of the product that the customer wants to order are quite different from each other in terms of the processing times of the works and therefore the completion times. In this study, hybrid heuristic algorithm production times which are developed by using technical characteristics of transformer effecting time and production times obtained from production are estimated. They modeled the production system under certain assumptions taking into account the arrival, waiting, and average processing times of the orders, then using these models to make time estimates for the characteristics of the workshop or work.

3. DEVELOPED ARTIFICIAL BEE/ANT HYBRID HEURISTIC ALGORITHM

Herd intelligence, a new branch of nature-inspired algorithms, has focused on modeling insect behavior in

order to develop effective meta-heuristic methods that use insectic problem-solving skills of insects. One of the most important parts of collective intelligence, which is the result of the interaction between insects, is the sharing of information between individual insects. Honey bees give information about the quality of the source they find by oscillation dance. Through this dance, the bees find a quality source and share their knowledge of direction, distance and amount of nectar with other bees. Thanks to this successful mechanism, the colony is directed to regions with high quality resources **(**Banharnsakun, 2011; Gao, 2012; Teodorovic, 2015). Natural behavior of bees is given in Figure 2.

Fig. 2. Natural behavior of bees.

Bee resource search behavior, learning, remembering and sharing information are one of the most interesting research areas of herd intelligence. The algorithm has been developed based on the behavioral characteristics of honey bees. The pheromones, which the ants actually use to find the shortest path, are a kind of chemical secretion that some animals use to influence other animals of their own species. As the ants move, they leave their pheromones that they have stored in the paths they have crossed (Dorigo, 2004). They prefer the path where pheromone is more likely to be the least. Its instinctive behavior explains how they find the shortest path to food, even if a pre-existing path is unavailable (Laptik, 2012). Considering that each ant leaves the same amount of pheromone at the same speed. It may take a little longer than the normal process if the ant recognizes the barrier and chooses the shortest path. Each ant takes a step-by-step decision-making policy starting from the source node and creates a solution to the problem. On each node, the local information is stored in the node itself or the arcs that exit from this node are read by the ant. The next step is to decide which node to use when going randomly (Laptik, 2017). Natural behavior of ants is given in Figure 3.

Fig. 3. Natural behavior of ants.

An ant hits the node from the node until it reaches the destination node, completes its forward movement and goes back to the motion mode. The optimization potentials through the behavior of ants colony and during the analysis has been realized that the ants are able to find the shortest path to reach the food from the nest that can be used in solving complex problems.

4. OPTIMIZATION OF PRODUCTION TIMES OF POWER TRANSFORMERS

Developed artificial bee/ant hybrid heuristic algorithm is given Figure 4.

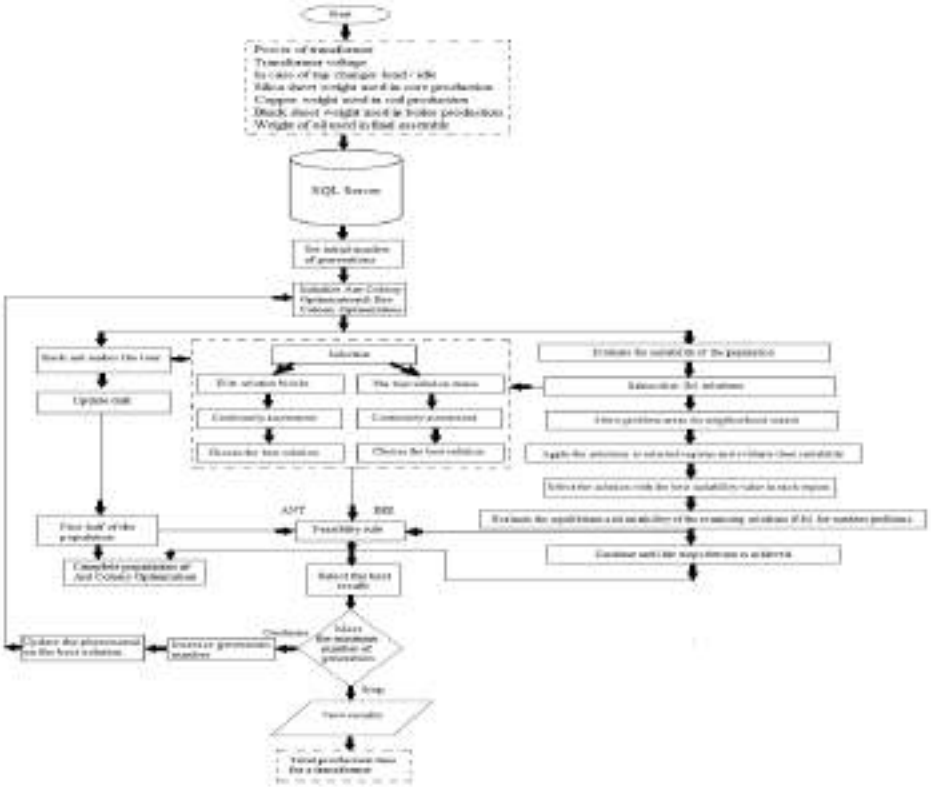

Fig. 4. Developed artificial bee/ant hybrid heuristic algorithm

The interface created in the Visual Studio program based on the developed ant bee algorithm is given in Figure 5.

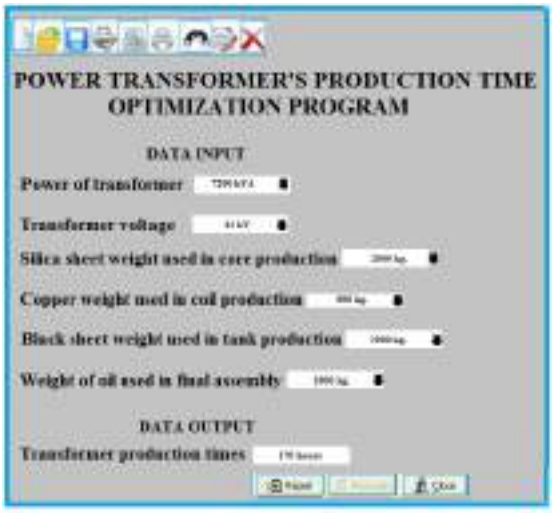

Fig. 5. The interface created in the Visual Studio program based on the developed ant bee algorithm.

A total of 4 samples, 7 inputs, 1 output, were taken in the optimization interface of transformer production times with Visual Studio program. As shown in Table 1, the production time of the power transformers of different power and voltage is estimated by the algorithm and computer program.

Table 1, the production time of the power transformers of different power and voltage.

Power (kVA)	160000	60000	10000	7200
Voltage (kV)	315	120	25	23
Silica sheet weight (kg.)	40000	13000	3000	2000
Copper weight (kg.)	6500	3000	1500	600
Black sheet weight (kg.)	17000	5000	1250	1000
Oil weight (kg.)	35000	1100	3000	2000
Time (hour)	1600	650	190	170

When the results obtained were compared with the data recorded in the production record of the manufacturing companies, it was found that there was no significant difference. In this study, it was understood that the algorithm and computer program created reflect the real values.

5. CONCLUSION

Using the study, it will be possible to respond more accurately and in a shorter time for the labor times of the orders requested by the proposal department. By contributing positively to the competitiveness of the company, the engineering time spent will be reduced and the market share of the company will increase due to faster and more accurate costs. Production Time studies, which are long and hard work in the company, will be fast and cheap and advantage will be gained in international competition.

REFERENCES

Banharnsakun A., Achalakul T., Sirinaovakul B., (2011). "The Best-So-Far Selection in Artificial Bee Colony Algorithm", *Appl. Math. Comput.* vol. 11, pp. 2888-2901.

Dorigo, M., Stutzle, T. (2004). "Ant Colony Optimization'', The MIT Press, pp 33-41.

Gao, W., Liu S., Huang L., (2012). "A Global Best Artificial Bee Colony Algorithm for Global Optimization", *J. Comput. Appl. Math.* 236 pp. 2741-2753.

Gao, W., Liu S., (2012). "A Modified Artificial Bee Colony Algorithm", *Comput. Oper. Res.* 39, pp. 687-697.

Laptik, R. (2012). "Ant System with Distributed Values of Pheromone Evaporation", *Elektronika Ir Elektrotechnika*, Vol. 18, No.8, pp. 69-72.

Laptik R., Navakauskas D. (2017). "Application of Ant Colony Optimization for Image Segmentation'', *Elektronika Ir Elektrotechnika*, Vol. 80, No.8, pp. 13-18.

Teodorovic D., Selmic M., Davidovic T., (2015). "Bee Colony Optimization Part II: The Application Survey", *Yugoslav Journal of Operations Research*, vol.25, no.2, pp.185-219.

CISET - 2nd Cilicia International Symposium on Engineering and Technology
10-12 October, 2019, Mersin / TURKEY

RISK ASSESSMENT ANALYSIS IN POWER TRANSFORMER CENTER IN ERDEMLI DISTRICT OF MERSIN

Mehmet Zile*[1]

[1]Mersin University, Erdemli UTIYO, Department of Information Technologies and Information Systems, Mersin, Turkey, mehmetzile@mersin.edu.tr

ABSTRACT
Investigations have been carried out in building type transformer substations in Erdemli District of Mersin Province and potential hazards, risks caused by them and the effects that these risks may have on personnel, operation, environment and living things have been emphasized. The risks that may arise from the potential hazards encountered in the substation have been determined and the measures to be taken have been determined. Risk Assessment Analysis has been conducted and assessments have been made on how much the risk value would fall if measures have been taken in substations.

Keywords: *Power Transformer Center, Risk Assessment Analysis, Occupational Health and Safety*

* Mehmet Zile

1. INTRODUCTION

Today, major developments in technological developments have affected every area of life. The costs incurred by enterprises as a result of occupational accidents are much higher than the costs required for applications to prevent accidents. Firms that avoid applications in line with financial interests are subject to much heavier financial liabilities. Today, the population and the number of settlements are increasing rapidly. As a result of this increase, there are fatal and seriously injured work accidents if the necessary precautions are not taken due to the physical structures and working environments of the electricity distribution centers. The units in the electricity distribution substations have many dangerous risks in terms of occupational health and safety in terms of operations and working conditions. Unfortunately, deaths and injuries due to substations are increasing rapidly (Zile 2017; Zile 2019).

In this study, measures to be taken in order to minimize the risks that may occur in transformer distribution centers in Erdemli District of Mersin Province have been emphasized in terms of occupational health and safety.

2. OCCUPATIONAL HEALTH AND SAFETY

Occupational health and safety according to the World Health Organization and the International Labor Organization; to protect, improve and maintain the physical, mental and social conditions of all employees regardless of their sector or duty. The main duty of the state is to protect human health and to ensure safety. The state has an obligation to protect private and public sector employees. In the private sector, this responsibility rests with the employer. The law imposes sanctions on employers who violate occupational health gains. Occupational health and safety practices increase productivity prevent costs incurred in the face of unfavorable situations and increase profitability. Occupational health and safety is effective in the psychological, sociological and economic development of society (Zile 2018; Zile 2018).

3. TRANSFORMER SUBSTATIONS

The voltage generated in the power plants is increased and delivered to the district, town or city where the electricity is to be delivered. When the electrical energy reaches the desired region, it is reduced from high voltage to medium voltage and transmitted to each district. Finally, medium voltage is reduced to low voltage by distribution transformers and transmitted to each neighborhood. High voltage, medium voltage and low voltage transformers are needed for these voltage reductions. Energy transmission lines and transformer centers are given in Figure 1.

Transformer substations can be lowering or amplifying according to their function. Amplifier transformer substations are located at the power plant outlet to increase the voltage, while lowering transformer substations are located at the city entrances and distribution centers to reduce the high voltage.

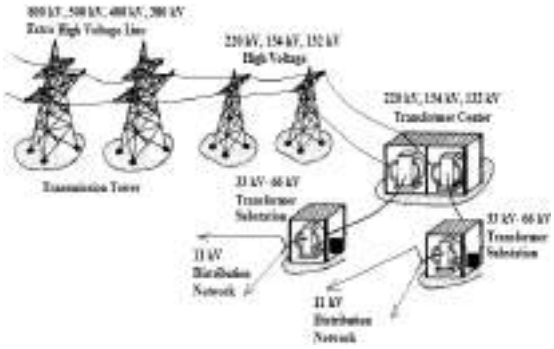

Fig.1. Energy transmission lines and transformer centers

The transformer substations are of three types: building type, pole type and open floor type. Building type transformers are used to convert medium voltage electricity from the switchyard to low voltage. Building type transformers are suitable for electricity larger than 380 kilowatts. Installation locations are solid floors and are generally located in areas that do not impair visuality in order to avoid environmental pollution. Direct type transformers are suitable for powers below 380 kVA. The pole type transformers placed on the poles transmit the electricity coming from the building type transformer to the user. Open switchyard areas are areas where high voltage electricity from the plant is converted to medium voltage electricity. They are usually located outside the city center. Electrical voltages above 36 kV are reduced in the open switchyard. The construction of short distance power lines is classified as “very dangerous”. Therefore, the units located in the electricity distribution centers contain many risks regarding occupational health and safety in terms of the operations and working conditions.

4. RISK FACTORS AND MEASURES TO BE TAKEN AT TRANSFORMER STATIONS IN ERDEMLI DISTRICT

Risk factors that may cause occupational accidents and occupational diseases in the substations are related to the general structure of the transformer building, the interior design, the features of the tools in the building, the usage period, the maintenance and the presence of the necessary stimulants and protectors. Personal errors are errors caused by factors such as lack of information, carelessness, incompetence, neglect, physical and psychological problems. Technical errors are errors related to technical equipment, equipment, type of materials, durability and order. Unexpected situations are caused by natural disasters such as earthquake, lightning, flood and storm. The measures to be taken by the employees in high voltage transmission facilities have a direct effect on the protection of their lives. These reasons should be meticulous in the measures to be taken. When performing maintenance and repair operations, the voltage must first be cut off. It is necessary to prevent another person who is unaware of this measure from re-energizing. For this purpose,

locking devices should be used indicating that the devices are working on the line by placing small signs on the devices and that the breakers should not be closed. In addition to removing the voltage, a voltage check is required. The re-supply of the voltage must be carried out when it is decided that it will not pose a danger after the end of the necessary operations. In high-voltage plants with disconnected voltage, a short-circuited device must be earthed prior to operation. Operators should control and prevent all circuit closures during the work. There may be situations where the voltage cannot be cut off in the whole area during operation. No persons other than officials should be allowed into the facility. If necessary, materials such as insulated gloves, insulated shoes, insulate carpets should be used. The phases of the circuit breakers and disconnectors must be checked using the necessary equipment. In medium voltage installations, there must be a locking system between the cell doors and bus bar disconnectors. The opening of the cell door must be prevented before the bus bar disconnectors are opened. All earthling switch blades must be closed. Static capacitors must be discharged before each operation. All leads must be earthed. There should be signs indicating where the breakers and separators in the area belong and should be designed to be readable remotely. Helmets, columns and bands should be used without removal. The helmets should be checked frequently and tested to ensure that they do not lose their protective properties as a result of wear. Body and abdomen protectors should be worn against puncture, cutting, molten metal splashes and chemicals. Hand and arm protectors should be used against flame, heat, impact, cut, acid dust splashes, electrical and radiation burns. The basic determinant of the choice of personal protective equipment is the need. Appropriate equipment should be preferred. However, the right hardware choice alone is not enough. It is of great importance to have training on the effective use of the equipment and to have the equipment inspected.

5. RISK ASSESSMENT ANALYSIS IN POWER TRANSFORMER CENTER IN ERDEMLI DISTRICT

Risk Assessment and Analysis is defined as the work to be carried out in order to determine the existing or potential hazards in the workplace, the grading of risks arising from the hazards, the determination, implementation and monitoring of control measures. Employees should be discussed at the substations and their hazards should be listed, reports of accidents occurring should be examined, information on the tools and equipment used should be examined, all hazards that may arise due to various reasons should be determined and risks that may arise from these hazards should be determined. Matrix Analysis, Fine-Kinney Method, Energy Analysis, Hazard and Operability Method (HAZOP), Error Tree Analysis, Error Type and Effects Analysis (FMEA), Event Tree Analysis, Cause-Effect Diagrams, Deviation Analysis, Initial Hazard Analysis, Checklists, If-So Analyzes etc. There are many methods available; the most commonly used is the matrix method, which is a method of analyzing risk severity and probability into components. In this method; the risk of a danger is analyzed on the basis of how often the probability of occurrence can be seen and how serious the negative outcome of the threat may be (Zile 2018; Zile 2019). The likelihood of danger is given in Table 1.

Table 1: Probability table of danger

Possible Value	Probability
Very small (1)	Hardly ever
Small (2)	Very few (once a year), only in abnormal cases
Medium (3)	Less (once every three months)
High (4)	Frequently (once a week)
Very high (5)	Very often (every day), under normal operating conditions

Id = 5 daily emergence of danger
Id = 4 occurrences weekly
Id = 3 occurrences monthly
Id = 2 three-month hazards
Id = 1 yearly occurrence of danger
Id = 0 no danger

are expressed. Table 2 sets the severity rating.

Table 2: Severity rating table

Violence	Ratings
Very light (1)	No loss of work hours, can be remedied immediately, requiring first aid
Light (2)	Mild injury, inpatient / injury
Medium (3)	Mild injury, inpatient / injury
Serious (4)	Serious injury, long-term treatment, occupational disease
Very serious (5)	Death, continuous incapacity

'Death, continuous incapacity' (Severity = 5)
'Serious injury, long-term treatment, occupational disease '(Severity = 4)
'Mild injury, inpatient / injury' (Severity = 3)
'No loss of working day, outpatient treatment without permanent effect '(Severity = 2)
'No loss of working hours, can be remedied immediately, requiring first aid' (Severity = 1)
'The danger never occurs '(Severity = 0)

are expressed. As shown in Table 3, the score matrix is determined by the comparative linguistic variable membership function of the two hazard factors and sub-criteria.

Table 3: Score matrix

Violence / Probability	Very low (1)	Low (2)	Medium (3)	High (4)	Very high (5)
Very low (1)	1 Negligible	2 Negligible	3 Low	4 Low	5 Low
Low (2)	2 Negligible	4 Low	6 Low	8 Medium	10 Medium
Medium (3)	3 Low	6 Low	9 Medium	12 Medium	15 High
High (4)	4 Low	8 Medium	12 Medium	16 High	20 High
Very high (5)	5 Low	10 Medium	15 High	20 High	25 Intolerable

The score table is given in Table 4.

Table 4: Score table

NON-TOLERABLE FOLDABLE RISKS (25)	The work should not be started until the identified risk is reduced to an acceptable level, and if there is ongoing activity, it must be stopped immediately. If it is still not possible to reduce the risk despite the measures taken, the activity should be canceled.
IMPORTANT RISKS (15,16,20)	The work should not be started until the identified risk is reduced, if there is ongoing activity, it must be stopped immediately. If the risk is related to the continuation of the work, urgent measures should be taken and the result of these measures should be decided to continue the activity.
INTERMEDIATE RISKS (8,9,10,12)	Activities should be initiated to reduce identified risks.
FOLDABLE RISKS (2,3,4,5,6)	Additional control processes may not be needed to eliminate identified risks. However, existing controls must be maintained
INSIGNIFICANT RISKS (1)	It may not be necessary to plan control processes and keep records of the activities to be carried out to eliminate identified risks.

The risk assessment and analysis for transformer substations is shown in Table 5. The existing risks of the transformer substations have been examined. 18 risks have been identified. 3 of these risks are intolerable risk. 4 of these risks are significant risk. 5 of these risks are intermediate risk. 6 of these risks are foldable risk. In Erdemli Transformer Station investigated, it is understood that the risks posing high risk are 'Lack of door-lock system in cells inside transformer building', 'Cutter cover open' and 'Lack of insulating mats or insufficient '.

Table 5: The risk assessment and analysis for transformer substations.

HAZARD	RISK	PROBABILITY	VIOLENCE	DEGREE OF RISK
Lack of health and safety signs and safety instructions in the transformer building	Work accident, injury/death as a result of failure to follow instructions	1	5	5
Incomplete or illegible warning signs	Work accidents, injuries/deaths due to lack of information	2	5	10
No labeling on the LV panel and panel doors not closing	Injury due to accidental touch or incorrect maneuver and death	1	5	5
Lack of door-lock system in cells inside transformer building	Injury/death from energized cell	5	5	25
Openings around the circuit breakers in the cell doors	Injury/death from contact with energy field	4	5	20
Exposed cable ducts	Injury due to tripping/falling	4	2	8
Cutter cover open	Injury/death from contact with energy field	5	5	25
LV panel doors do not close	Injury or death from accidental touching or incorrect maneuvering	4	5	20
Lack of soil separator	Injury/death due to incorrect maneuver	3	5	15
No switch lever on LV distribution / control panel	Accidental contact injury/death	1	5	5
Possibility of scrap-inert material in the building	Injury due to closed escape routes in emergencies	3	2	6
Inadequate building interior lighting	Work accident due to lack of lighting	3	2	6
Old cables used	Injury/death due to electrical leakage	1	5	5
No fire extinguisher	Injury and death as a result of fire	2	5	10
Lack of insulating mats or insufficient	Crash and death due to maneuvering	5	5	25
Defective breaker	Injury/death from contact with the energized area due to non-operative separation	2	5	10
Remote control systems of circuit breakers do not work	Injury and death as a result of breaker burst	2	5	10
Forgetting cutter cover open	Injury/death from contact with energy field	4	5	20

6. CONCLUSION

In the study, occupational health and safety risks have been determined in Erdemli Transformer Substation and suggestions for solving problems have been presented. A field study has been carried out to measure the devices in the substations and make risk assessments at the substations. The risk assessment was then carried out using the Matrix Method, and as a result it became clear that the substations were very dangerous working areas. The risks identified during the risk assessment and their solutions are discussed.

According to the risk numbers shown in Table 5 as a result of the risk assessment, it is seen that 39% of the 18 identified risks are high risk. As a result of this study, it is seen that the substations are very risky places and it is highly probable that the work accidents occurring here will result in death. It is obvious that even if precautions are taken, the risks persist and therefore the employees should be very careful.

In addition to the concrete measures to be taken to reduce the accidents at the substation, the employees should be motivated, work-related training should be increased and their knowledge and skills should be increased in order to reduce the dangers caused by employee errors.

REFERENCES

Zile M., (2017). **"**Patlayıcı ortamlarda gerçekleşen ölümlü is kazalarının analizi, bu kazalardaki kusurların ve kusur oranlarının belirlenmesi**",** *Uluslararası Hakemli İs Güvenligi ve Çalışan Sağlığı Dergisi*, Vol. 1, No. 2, pp. 76-90.

Zile M., (2019). **"**Investigation of the failures in transformer centers in erdemli district and precautions to take**",** *2. International Mersin Symposium*, Vol.1, pp. 75-85.

Zile M., (2018). **"**Analysis of the legal aspects of work accidents**",** *International Scientific An Vocational Studies Journal*, Vol. 2, No. 1, pp. 1-7.

Zile M., (2018). "Measures to be determined and received in universities of occupational health and safetely risks", *Turkish Journal of Enginering*, Vol. 2, No. 1, pp. 35-37.

Zile M., (2018). **"**Actions to be taken to prevent negative consequences in the workplace during emergencies**",** *International Advanced Researches and Engineering Journal*, Vol. 2, No. 2, pp. 177-184.

Zile M., (2018). **"**Determining statistical survey of occupational ınjurıes in mines risk analysis modelling, software developed on the basıs of fuzzy logic to prevent job accidents**",** *International Journal OnTechnical And Physical Problems Of Engineering*, Vol. 10, No. 36, pp. 30-38.

CISET - 2nd Cilicia International Symposium on Engineering and Technology
10-12 October, 2019, Mersin / TURKEY

WASTE MANAGEMENT AND COST ANALYSIS OF CONSTRUCTION SITES: A COMPARATIVE STUDY ON ANKARA (BILKENT) AND MERSIN CITY HOSPITALS IN TURKEY

Aysun Kırbıyık[1] and Aydeniz Demir Delil[1*]

[1]Mersin University, Faculty of Engineering

Department of Environmental Engineering

Mersin, Turkey, aydenizdemir@mersin.edu.tr

ABSTRACT

Unfortunately, recycling and reuse of waste materials in construction sector is very less than the developed countries like other sectors. Currently, many construction projects have begun to perform in the context of urban transformation. One of them is constructing city hospitals which have started in Turkey. In our country, during the construction process of health complex, the amount of construction wastes is excessive.

In this study, with considering Mersin and Bilkent Integrated Health Campus Project, which were built to improve health sector, waste compositions are defined, waste management systems have been reviewed, waste information has been compared and the results have been evaluated. Whole waste amounts and costs are summarized on the basis of monthly and cumulative totals, and waste recovery, recycling and disposal facilities are reviewed on the basis of cities. As a result, although both campuses have same methodology for the construction, Bilkent Integrated Health Campus has more different kinds of hazardous waste if they compared with regarding types of produced wastes. It has been considered that the reason behind this is the fact that waste companies have been working in a more systematic way and they are more experienced at determining waste composition in Ankara.

Keywords: *Construction Waste, Cost Analysis, Hazardous Waste, Disposal, Recycling*

1. INTRODUCTION

Building waste of the construction sector takes an important place in the waste production which is one of the significant environmental problems of our age. As a result of the construction activities, the building materials/components can be reused and recycled as raw materials for the production of other products. Recycled construction materials contribute to sustainability by providing ecological value as well as economic benefit to the structure in which they are used.

According to the estimations of the US Environmental Protection Agency (US EPA), waste of building materials as the output of building renovation and demolition account for 25%-30% of the waste generated each year in the United States (Guy and Shell, 2002). It has been known that the amount of structural waste in Europe is about 180 million tons per year and the percentage of reuse or recycling ranges between 5% and 98% of the member countries. The studies which aim at increasing these percentages have been continued (Dorsthorst and Kowalczyk, 2002). According to the European Commission DG ENV, Final Report Task 2-Management of, Construction and Demolition (C&D) Waste, the most successful countries in this category are the Netherlands (98%) and Denmark (94%). Since these countries have developed their own rules and regulations, they highly utilize reusable or recycled structural waste that they disposed (European Commission, 2011).

The most common valid method of recycling is "scrapping in the field" in Turkey. The costs of transporting and storing construction wastes are more expensive than recycling cost. In Turkey 125 million tons of excavation wastes are disposed per year. There has been a substantial increase in this amount of waste due to the urban transformation. Approximately, 0.6 m^3 material from each 1 m^3 can be recycled (Kılıç, 2015).

Most of these materials can be reused and/or recycled. With these materials, environmental impacts of construction sector can be decreased. Therefore, the most practical approach to minimizing the effect of waste on the environment is to prevent generating waste (Ekanayake and Ofori, 2004; Yuan and Shen, 2011; Wang and Tam, 2014). Thus, leaving wastes of construction sector in nature in an uncontrolled way and pollution of soil/water resources can be prevented.

The components of building materials such as concrete, metal, steel, wood, ceramics, plastic, glass which are generated as a result of production of construction, renovation, repair and demolition activities of buildings have high recycling potential.

Construction wastes present an enormous amount of building materials which have valuable natural resources. Furthermore, they consume a massive landfill space, which additionally decreases scarce land resources. Moreover, they contain harmful substances that jeopardize human well being and the surrounding natural environment (Umar et al., 2017).

Construction waste management (CWM) strategies need to be carried out by means of effective policies in order to prevent the rapid depletion of resources and to "transform" generated wastes which are hazardous for environmental and human health into economic input. This approach, as it is applied in the whole world, is the basis of sustainable environment and development which has been increasingly accepted as a primary target in our country. It is completely accepted that the CWM results are influenced by the environmental sustainability (Chen et al., 2000; Cole, 2000; Tam et al., 2006) and economic sustainability factors (Duran et al., 2006).

Establishing a management plan for wastes before they are generated is one of the most significant issues. Waste Management System (WMS) consists of waste generation, collection, processing recovery and final disposal steps. The efficiency and sustainability of the WMS depends on its integration with the system of city or country.

Recently, various projects have started to be carried out for urban transformation. Urban transformation includes activities for the purpose of renewal, remediation and sanitation in areas where the use of the settlement area has lost its intended use or in areas where any natural affairs city may be damaged in the slum areas (Çakır, 2014).

One of the urban transformation studies that have been initiated for the purpose of healthcare in our country is the construction of city hospitals which are being constructed in many cities. The city hospitals which are under construction in 16 provinces have been completed in 2016. By the end of 2018, this number is to be doubled and 34 city hospitals in total will be ready to provide service. It has been presumed that many kinds of waste will come out during the construction of city hospitals. This study is expected to raise awareness of waste management for new construction projects to begin.

In recent years, the construction industry has begun to have awareness of the reuse of waste and recyclable materials. For the first step, it is necessary to analyze the generated wastes in order to recycle construction waste and to establish a CWM plan.

In this study, Mersin Integrated Health Campus (MIHC) and Bilkent-Ankara Integrated Health Campus (BIHC) which are construction sites have been analyzed in terms of the wastes generated.

The methods of reuse, recovery, recycling and disposal of wastes for waste management on two campuses have been examined. The cost of waste management has been calculated by determining whether there is a difference between the amounts of waste generated by two construction sites.

2. MATERIAL AND METHOD

It has been planned that the city hospitals which have been constructed by public and private sectors profoundly contribute to the health sector in Turkey. However, while building city hospitals, substantial waste will be generated. Therefore, WMS must be planned before the establishment of constructions. Before starting the excavation step, WMS has been set up according to the wastes that could arise during the construction of the health campus. Photographs of the two city hospitals have been shown in Fig. 1(a) and 1(b).

Fig. 1(a) Bilkent-Ankara Integrated Health Campus

Fig. 1(b) Mersin Integrated Health Campus

During planning the WMS; at first, the construction methods of these projects have been examined and characterizations of waste have been evaluated based on whether similar projects were previously carried out or not. The waste codes that can be formed according to the 'Regulation on Waste Management' have been determined (WMR, 2015). Then, according to the waste management hierarchy, environmental engineers and waste companies have negotiated and decided on where they store the waste and how to utilize the generated wastes. Waste hierarchy refers to the 3Rs of reduce, reuse and recycle, classifying waste management options in terms of the waste minimization goal (Umar et al., 2017; Unnikrishnan and Singh, 2010). Two of the 3Rs (2R=Reduce and Reuse) are considered high-priority for development (Sakai et al., 2017). However, it has been more focused on reuse and recycle options in this study.

2.1. Waste Management System of Mersin Integrated Health Campus

As it has been shown in Fig. 2., during the construction of the MIHC, excavation activities are primarily carried out. Some part of the excavation soil that generated during the excavation operations have been disposed in the site in which permitted by the municipality and some part of them has been accumulated in the construction site for filling.

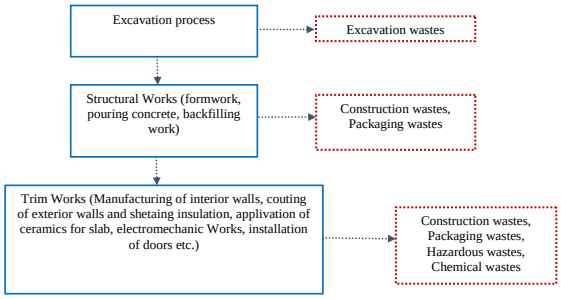

Fig. 2. Mersin Integrated Health Campus Flow Scheme

In the second step, rough construction has been carried out and construction waste and packaging waste have been generated. The resulting construction waste has been dumped into this area since it will be used as filling material in the construction project. Packaging wastes have been sent off to recycling company which is licensed by the Ministry of Environment and Urbanization. Construction, packaging, hazardous and chemical wastes have generated throughout the craftsmanship process in the construction process. The hazardous wastes have generated due to the isolation, maintenance activities of machinery and equipment, chemical materials, printers in the offices, infirmary and cafeteria in Mersin Integrated Health Campus. Hazardous wastes have been stored in temporary storage areas determined within the site such as in waste vegetable oil bins in the cafeteria; in boxes for cartridges in the offices, and in special boxes for medical waste in infirmary. Afterwards, waste materials have been collected by the mobile crane or scooping machines which are controlled by waste management staff of Consultant Company for MIHC and they have transported to the hazardous waste area in the construction site.

The wastes have been separated according to their codes in storage area and they have been weighed by the weighing instrument in the storage area and recorded. Waste storage area is composed of three main parts covered with 30mx10mx3m, covered with impermeable concrete, surrounded by sheet metal.

Hazardous wastes have been allocated in the first section, packaging wastes, non-hazardous wastes in the second section and scrap metal has been restored in the third section. The hazardous wastes accumulated in the first section have been stored separately in the containers with regarding their types and degree of hazard-which may leak-temporarily stored in the pool covered by the special leak-proof membrane system. Table 1 has shown the WMS implemented at the Mersin Integrated Health Campus.

Table 1. Waste Management System Table for Mersin Integrated Health Campus

Waste Management System Table				
Waste Code	**Recycling off site**	**Out-of-site recovery**	**Storage**	**Other Disposal Methods**
Iron and Steel **(17 04 05)**	X	-	-	-
17 09 01, 17 09 02 ve 17 09 03 mixed construction and demolition wastes outside **(17 09 04)**	-	-	X	-
Paper and Cardboard Packaging (**15 01 01) (20 01 01)**	X	-	-	-
Plastic (**15 01 02**) **(20 01 39)**		-	-	-
Metallic Packaging (**15 01 04**) **(20 01 40)**		-	-	-
Glass Packaging (**15 01 07) (20 01 02)**		-	-	-
Domestic Waste	-	-	X	-
Glass Fiber Wastes **(10 11 03)**	-	X	-	-
Hazardous material contaminated packaging containing residues **(15 01 10)**	-	X	-	-
Dirty absorbents with dangerous substances, filter materials, swabs, protective clothings **(15 02 02)**	-	-	-	X
Contaminated metal waste with hazardous substances **(17 04 09)**	-	-	-	X
Oil Filter **(16 01 07)**	-	-	-	X
20 01 25 liquid and solid oils outside (**20 01 26**)	-	X	-	-
Isolation Wastes **(17 06 03)**	-	X	-	-

In the second part, packaging wastes and non-hazardous wastes have been stored in a controlled manner without being mixed with each other. Domestic wastes have been stored in containers in the areas that have been determined within the borders of the site and they have been taken on a daily basis by Domestic Waste Truck of Toroslar Municipality. Packaging wastes have been managed by the recycling company which is in charge in the region where.

2. 2. Waste Management System of Bilkent-Ankara Integrated Health Campus

Fig. 3 lists the wastes generated during the construction of the BIHC. Some part of the generated excavated soil during excavation activities has been transported by licensed trucks and they have been disposed in the dump site which has been determined by the municipality. The other part has been stored in the construction site for filling activities.

Fig. 3. Bilkent-Ankara Integrated Health Campus Flow Process Chart

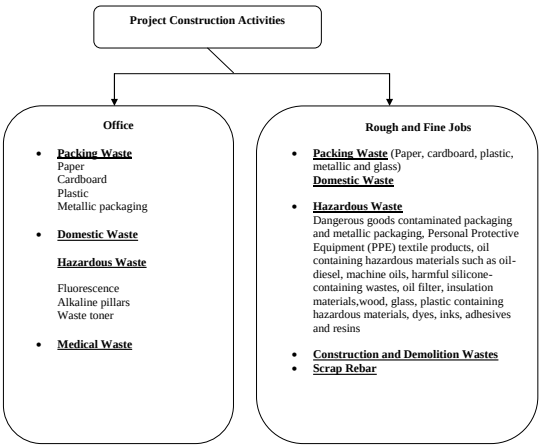

In the rough construction phase, construction and packaging wastes have been generated. The management of packaging wastes is the same as in Mersin. Hazardous wastes have been stored in temporary storage areas determined within the site. The process and waste management performed for all waste types in Bilkent is the same as in Mersin. Table 2 has shown the WMS with regarding type of waste implemented at the Bilkent Integrated Health Campus.

Table 2. Waste Management System Table for Bilkent Integrated Health Campus

Waste Code	**Recycling off site**	**Out-of-site recovery**	**Storage**	**Other Disposal Methods**
Iron and Steel **(17 04 05)**	X	-	-	-
17 09 01, 17 09 02 and 17 09 03 mixed construction and demolition wastes outside **(17 09 04)**	-	-	X	-
Glass Fiber Wastes **(10 11 03)**	-	X	-	-
Waste Printing Toners Containing Hazardous Materials **(08 03 17)**	-	-	-	X
Other Pillars and Accumulators **(16 06 05)**	-	-	-	X
Containers containing hazardous substances or contaminated with dangerous substances **(15 01 10)**	-	-	-	X
Dangerous materials contaminated absorbents, filter materials, cleaning cloths, protective clothing **(15 02 02)**	-	-	-	X
Contaminated metal waste with hazardous substances **(17 04 09)**	-	-	-	X
Oil Filters **(16 01 07)**	-	-	-	X
20 01 25 liquid and solid oils outside (**20 01 26**)	-	X	-	-
17 06 01 ve 17 06 03 insulation materials outside **(17 06 04)**	-	-	-	X
To prevent infection, collect wastes and dispose of wastes subject to special treatment **(18 01 03)**	-	-	-	X
Fluorescent lamps and other mercury-containing wastes **(20 01 21)**	-	-	-	X

Waste materials have been collected by the mobile crane or scooping machines which are controlled by waste management staff and they have transported to the hazardous waste area in the construction site. Wastes are separated according to the codes in storage area. At certain intervals, wastes have been sent to recycling, recovery or disposal plant with regarding the current situation of storage area. Domestic wastes of BIHC have been stored in containers in the areas that have been determined within the borders of the site and they have been taken on a daily basis by domestic waste truck of Çankaya Municipality.

3. RESULTS AND DISCUSSION

3.1. Comparison of Mersin and Bilkent Integrated Health Campus

Two campuses have been compared in terms of site, construction period, the maximum number of workers working during construction, and the number of personnel and beds after the hospital was opened.

Table 3. has shown comparative information on two health campuses. When it is evaluated in terms of construction site and number of beds, it is seen that BIHC is about three times larger than MIHC in terms of number of beds and the size of site.

Table 3. Comparison of Mersin and Bilkent Integrated Health Campus

Properties	Mersin	Bilkent
Construction Area	369.592,00 m^2	1.285.798,00 m^2
Number of Workers During Construction	4.000 worker	8.000 worker
Number of Worker-Day During Construction	1.200.000 worker/day	4.500.000 worker/day
Number of Beds	1.294 piece	3.804 piece
Daily Number of Total Patients	10.000 worker	35.000 worker

Every project has diverse amount of waste from the same source of materials; consequently, an enermous amount of waste exists in the construction operations, and lots of it is not known or is undetectable (Spies, 2009). When the Fig. 4(a) and Fig. 4(b) showing relations work progress and construction wastes of Mersin and Bilkent Integrated Health Campus are examined it is seen that the amount of construction waste increases with the progress of work in both projects.

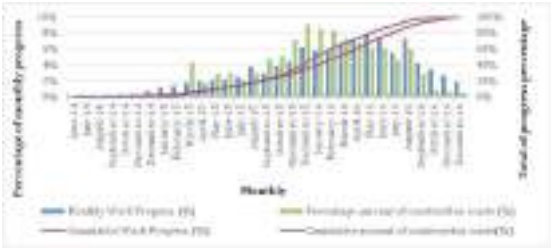

Fig. 4a) Relation between work progress and construction waste of Mersin Integrated Health Campus

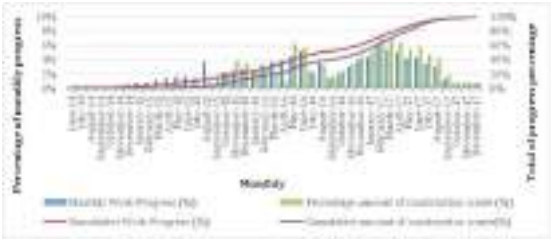

Fig. 4b) Relation between work progress and construction waste of BIHC

However, due to administrative and managerial problems between June 2016 and December 2016, the progress of work slowed down and the amount of construction waste decreased in the Bilkent Integrated Health Campus. As these problems have been resolved by December 2016, it has continued amount of waste has increased in parallel with this progress.

3.2. Comparison of Construction Wastes of Mersin and Bilkent Integrated Health Campus

Fig. 5(a) and 5(b) have shown that construction waste amount of MIHC and BIHC has increased on monthly basis. When they are examined, it is seen that the amount of construction waste increases on the basis of months as the work progresses on both campuses. A total of 33.389,26 tons of construction waste have been generated in the MIHC until the construction completed. The generated construction waste has been accumulated in the site and then it has been poured into the area which is close to the construction site by the staff of consulting company. The area was permitted by Toroslar Municipality. The municipality then uses these wastes as filling material for the construction work to be carried out in this area. Likewise, a large part of the excavation wastes generated during excavations at MIHC side have been utilized as filling material in the project site. For construction wastes, waste fee per ton is paid to waste consulting firm. Aftermath of abolishing use of weighbridge, paying fee per time has been decided together with the consulting company and payments have been started to make per time. After the weighbridge was removed, the fee per trip was

determined together with the waste consultant firm and the consultant company started to pay the fee per trip.

1 Ton Waste Cost = $3.1

Aftermath of abolishing use of weighbridge, payment per time = $40

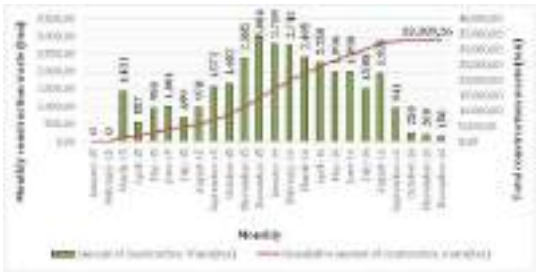

Fig.5a) Amount of construction waste of MIHC

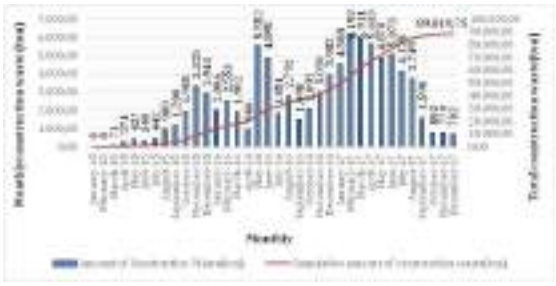

Fig.5b) Amount of construction waste of BIHC

When the amount of construction waste amount of BIHC is examined, it is seen that 89.019,75 tons of construction have been generated until the construction completed. The generated waste has been accumulated in the site and then it has been poured into the area which is 10 km away from BIHC, determined as storage area by Çankaya Municipality for the construction waste. The construction waste has been poured into this area by the trucks driven by the staff of Çankaya Municipality. The municipality then reuses the wastes accumulated here as a filling material in construction and road construction. Çankaya Municipality has been paid a fee of USD 77 per truck. Figures 6(a) and 6(b) have shown the graphs on the number of driving cycles of trucks on monthly basis of MIHC and BIHC.

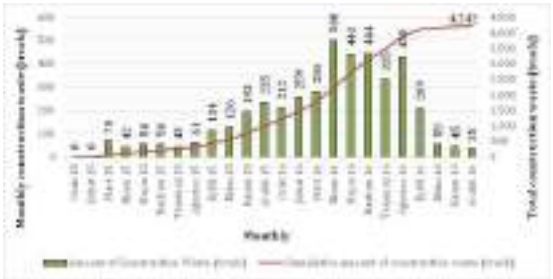

Fig.6a) Number of driving cycle of trucks for construction waste of MIHC

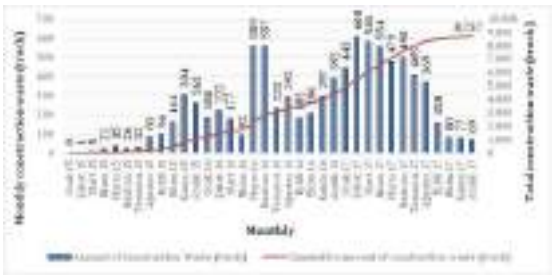

Fig. 6b) Number of driving cycle of trucks for waste of Bilkent Integrated Health Campus

When the graphs are examined, it is seen that the driving cycles of trucks in Bilkent twice more than in Mersin. When it is assessed in terms of the amount of construction waste, the amount of waste generated in Bilkent is three times higher, depending on the size of the project. Due to width of the site of the project in Bilkent, the waste storage areas are also wider, and the amount of waste is higher, and the trucks have been fully filled. However, in Mersin, trucks have been sent without being filled full because it has less waste storage area and payment has been made per ton.

Figures 7(a) and 7(b) have shown the amount of scrap rebar generated from Mersin and Bilkent Integrated Health Campus.

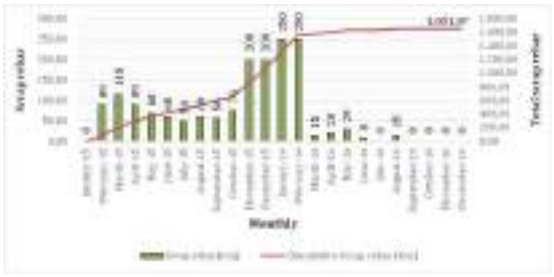

Fig. 7a) Amount of scrap rebar of Mersin Integrated Health Campus

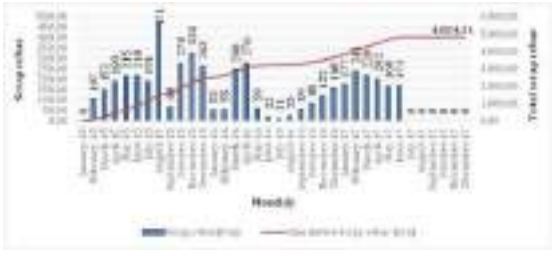

Fig. 7b) Amount of scrap rebar of Bilkent Integrated Health Campus

Construction wastes present a large amount of building materials, which are a waste of valuable metals like scrap rebar (Umar et al., 2017). When construction wastes are examined, it has been observed that a total of 1.651,07 tons of waste rebar generated in Mersin and 4.834,31 tons of waste rebar in Bilkent. In Mersin, USD 245.543,58 has been gained from the sale of scrap rebar. The average price of rebar is USD 149 in both Mersin and Ankara. In Bilkent, USD 718.948,46 income has been gained from its sales. Scrap rebar is mentioned as 17 04 05 code in Regulation on Waste Management and rebar which is generated in the site of the project has been recycled out of the site.

Construction waste consists of hazardous materials, such as waste printing toners, harmful silicones, alkaline batteries and fluorescent lamps and other mercury-containing wastes. Construction materials are the most common asbestos-containing products as hazardous materials (Li et al., 2014). Butera et al. reported that PCBs and PAHs were detected in all 33 construction waste samples (Butera et al., 2014).. Therefore, the amount of hazardous waste generated during construction activities is also evaluated within the waste management system.

Figures 8(a) and 8(b) have shown the amount of generated hazardous waste in Mersin and Bilkent Integrated Health Campuses. When the graphs have been examined, it can be seen that similar construction materials have been used in both projects and hazardous waste has been generated in proportion to the size of the construction. However, the types of hazardous wastes have differed since one of the construction sites is located in a rainy region in Mersin, while the other construction site is in a cold region, in Ankara.

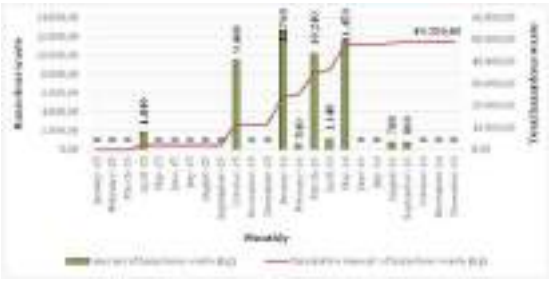

Fig. 8a) Amount of hazardous waste of Mersin Integrated Health Campus

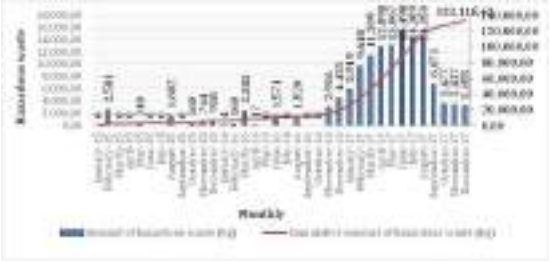

Fig. 8b) Amount of hazardous waste of BIHC

In Bilkent, more heat insulation membrane, i.e. 17 06 04 code (rock wool) has been seen, while in Mersin more water insulation membrane, i.e. 10 11 03 code (fiber glass) has emerged. If fiber glass wastes are categorized as non-hazardous waste according to Regulation on Waste Management Annex-1, they have been recycled by recycling company. If rock wool wastes are categorized as probable hazardous waste, they are analyzed in order to determine whether hazardous or not. Then, if they are hazardous, they send to disposal plant; if they are non-hazardous they are recovered. However, since analyzing is not cost effective and there is no facility to recover rock wool waste in the region, rock wool waste has been sent to disposal plant from Bilkent.

While USD 3.633,84 has been spent for the recovery of fiber glass waste, USD 16.108,20 has been spent for rock wool waste. The cost of the recovery of fiber glass is USD 0.12 per kg in Mersin, while the cost of rock wool waste is USD 0.15 per kilogram in Bilkent. Although recovering fiber glass is not cost-effective rather than recovering rock wool, it is profitable since it can be recovered and contribute to the economy.

08 03 17 has been given as waste code for toners of printers in the offices which are containing hazardous waste and total amount of waste is 60.00 kg in Mersin and 252.40 kg in Bilkent. The unit price for the disposal of the toner in Mersin is USD 1.34 and it is USD 2 in Bilkent. In order to prevent the disposal cost of toner waste, using refillable toners in printers is an appropriate method.

The packages which consist of contaminated of hazardous substances coded with 15 01 10 have stemmed from inside of the site. While 15 01 10 coded packages waste has been generated 3.220 kg in Mersin, it has been emerged 8.587,20 kg in Bilkent. The unit price of the waste is USD 0.38 in Mersin and it is USD 0.75 in Bilkent. The recycling for this waste type has been spent USD 340.51 in Mersin while USD 2.201,79 has been spent for disposal in Bilkent.

Absorbents, filter materials, cleaning cloths, protective clothing have been contaminated with 15 02 02 coded hazardous wastes due to the contaminated belongings of the staff with hazardous substances. It has been observed that 15 02 02 coded waste has been generated 300 kg in Mersin and 1.408 kg in Bilkent. The amount of 15 02 02 coded waste in Bilkent is five times larger than in Mersin. It can be deduced that the reason behind this is related to the number of personnel and personnel circulation. The unit cost of disposal in Mersin is USD 1.15 and it is USD 0.78 in Bilkent. The cost is lower in Bilkent than Mersin because there are too many licensed plants that provide disposal of the waste coded with 15 02 02. There is no plant that provides waste disposal in this code in Mersin.

Hazardous substances coded with 17 05 03 which consists of soil and stones have been generated within the site of the project. It has been generated 1.580 kg in Mersin and 3.254 kg in Bilkent. The unit cost of

waste disposal in Mersin is USD 0.32 and it is USD 0.16 in Bilkent.

Although the same method of construction has been applied in two projects, the reason why more types of wastes have been generated in Bilkent is that waste companies are more diverse and more experienced in determining the waste composition of Ankara and its surroundings and that the health campus is under continuous control of the Ministry of Environment and Urbanization. The transporting cost of the hazardous waste is USD 3.290 in Mersin, USD 9.169 in Bilkent. The cost of transporting of the wastes is higher in Bilkent since the wastes have been more frequently transported.

In addition to the large volume of waste generated in construction projects, there are also numerous types of small quantities of wastes, like packaging wastes. Packaging wastes comprise only a small part of the total construction waste by weigh (Li et al., 2013). Characterization studies show that packaging wastes constitute 20% of the amount of solid waste generated from construction projects. According to the packaging waste regulation, which is organized in accordance with the European Union (EU) directives, packaging waste has a target of 60% recycle by 2020 (USEPA, 2013). The total amount of packaging waste generated in Bilkent is 84.526,44 kg and 26.410,00 kg in Mersin. The amount of packaging waste of the two campuses is parallel to the size of projects.

Another waste type consisted of in construction project is domestic solid wastes resulting from the use of employees. Total amount of domestic waste is 12.550 tons in Bilkent while the amount of domestic waste is 4.580 tons in Mersin. The difference between the amount of occurred domestic waste is due to the number of personnel.

Waste vegetable oil (WVO) coded with 20 01 26 has been consisted of cooking activities in the refectory within the site of the project. The total amount of waste vegetable oil in Bilkent and Mersin are 3.626 kg and 685 kg respectively. The amount of generated WVO has been related to the nutritional requirement of the staff. Although the number of staff in Bilkent is twice times bigger than in Mersin, the amount of generated WVO is five times higher than the amount of generated WVO in Mersin. The reason for this is that despite the fact that there are cafeterias in both campuses; the catering company in Mersin has outsourced food in a certain amount.

The total amount of medical waste is 599 kg in Bilkent and it is 570 kg in Mersin. Although the number of personnel in Bilkent is twice times bigger than Mersin, the amount of medical waste is approximately the same. Since the absence of a public hospital nearby neighborhood of MIHC to carry out health control for the recruitments, all the tests and health controls have been conducted in infirmary inside the MIHC. Therefore, the amount of medical waste has been found out higher. However, there is a public education and research hospital in Bilkent and this causes a decrease in the amount of generated medical waste.

3. 3. Cost Analysis

Expenditures for construction waste of Mersin and Bilkent city hospital (debris+ hazardous waste), expenditures for WMS and monthly income distribution from sale of scrap have been indicated in Fig.9a) and Figure 9b). The income from the sale of scrap rebar is USD 245.543,58 in Mersin. The revenue generated from the sale of scrap rebar is close to expenditure for waste management. The income from the sale of scrap rebar is USD 718.948,46 for Bilkent. This case can be a good example for establishing waste management system by contractor companies in the next construction projects.

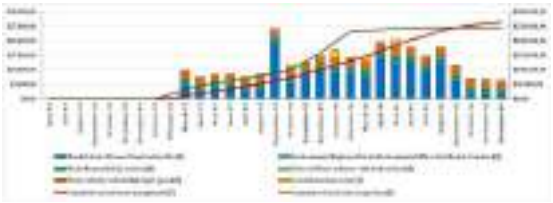

Fig.9a) Expenditures for Construction Waste of Mersin City Hospital (Debris+ Hazardous Waste), WMS and Monthly Income Distribution from Sale of Scrap

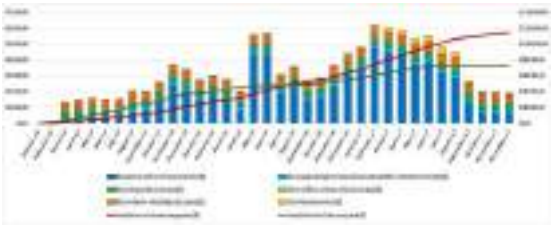

Fig. 9b) Expenditures for Construction Waste of Bilkent City Hospital (Debris+ Hazardous Waste), WMS and Monthly Income Distribution from Sale of Scrap

While the total cost of construction is USD 188.964.879 and the total cost of waste management is USD 266.339 in Mersin, the total cost of construction is USD 632.361.799 and the total cost of waste management is USD 1.146.332 in Bilkent. When the ratio of construction costs and waste management costs is compared, it is determined that waste management costs constitute 0.14% of total construction cost in Mersin and 0.18% of total construction cost in Bilkent.

Table 4. has shown the waste and cost analysis for both integrated health campuses. As it can be seen in the table, more hazardous waste types have been generated in the Bilkent-Ankara. It has been considered that the more systematic working approach has been carried out by the waste companies in

determining the waste composition of Ankara and these companies are more experienced and under the control with continuous supervision by the Ministry of Environment and Urbanization.

Table 4. Total Cost of Waste Disposal Table

Total Cost of Waste Disposal Table						
Project	Waste Type	Waste Code	Descriptions	Amount of Waste (kg)	Shipping Price ($)	Total Amount ($)
MERSİN	Hazardous Waste	08 03 17	Waste print cartridges that containing hazardous materials	60,00	3,81	80,73
		10 11 03	Non-hazardous glass fiber waste	20.660,00	1.062,11	3.634,03
		15 01 10	Contaminated packaging with hazardous wastes	3.220,00	340,61	1.218,68
		15 02 02	Textile product that contains dangerous substance in the project site	300,00	161,65	347,60
		17 05 03	Soil containing dangerous substances	1.580,00	194,45	518,56
		17 06 03	Waste insulation materials	22.050,00	1.283,53	4.227,93
		17 06 04	Non-hazardous insulation material	1.380,00	243,84	577,21
	TOTAL			**50.505,00**	**3.290,00**	**10.604,73**
BİLKENT	Hazardous Waste	06 08 02	Silicon packings	898,40	66,91	558,41
		08 03 17	Waste print cartridges that containing hazardous materials	252,40	25,34	480,90
		13 02 05	Waste vehicle oil	1.885,20	272,87	2.174,67
		15 01 10	Contaminated packaging with hazardous wastes	8.587,20	1.154,17	5.552,85
		15 01 11	Pressurized metal packaging with hazardous substances	674,40	55,88	832,76
		15 02 02	Textile product that contains dangerous substance in the project site	1.408,00	99,31	1.021,50
		16 01 07	Oil filters removed from vehicles	181,80	13,21	229,66
		16 06 04	Waste batteries produced in offices	97,00	7,20	146,06
		17 02 04	Silicon package with hazardous waste content	5.076,00	461,89	4.267,09
		17 04 09	Metals containing hazardous waste residues	376,00	32,80	1.151,27
		17 05 03	Soil containing dangerous substances	3.254,40	161,71	406,54
		17 06 03	Waste insulation of materials	2.700,00	168,83	1.865,37
		17 06 04	Earthwool waste with rubber panel particules	106.491,43	6.551,28	11.236,74
		20 01 21	Waste fluorescent lamps	28,00	3,65	449,65
		20 01 27	Adhesives with dangerous substance content	1.208,40	94,45	1.166,78
	TOTAL			**137.345,23**	**9.169,51**	**31.540,25**

Although the amount of construction waste in Bilkent is about three times larger than Mersin and also its hospital size is three times larger than hospital size of Mersin, the cost of construction waste is approximately four times higher than the cost of construction waste in Mersin. The reasons behind this can be stated as construction waste storage area is 10 km away from the health campus in Bilkent while it is 1.5 km away from the Mersin Integrated Health Campus; while the fee for storage area has been paid to municipalities per ton in Ankara, payment has been made for construction waste per ton in Mersin while it has been made for construction waste per driving cycle of truck in Bilkent.

4. CONCLUSIONS

All waste amounts and costs on monthly basis have been calculated and the conditions of recovery, recycling and disposal facilities have been examined in this study. As a result, although the construction method of the two projects is the same, it has been found that there are more hazardous waste types have been generated in Bilkent. On the other hand, since there is no facility to recover some of the wastes that are generated in Mersin and Bilkent, the wastes have been disposed and they cannot be recovered. Thus, not only economic loss has been emerged but also the cost has increased since disposal is not a cost-effective method.

In order to decrease the cost of hazardous waste, the Ministry of Environment and Urbanization should not only give licenses to waste companies but also determine the cost of recovering, recycling, disposal or storage of waste. In this way the cost of waste will be under the control of state and waste companies will not frighten the producer with high costs.

The Ministry of Environment and Urbanization should increase the number of waste management companies under the control of the municipalities and in all provinces the ministry should ensure the establishment of the recovering, recycling, disposal or storage facilities of the wastes that can be generated which are listed on Regulation on Waste Management Annex-1. Thus, transportation cost will be minimized, and profit will be made. It is also considered that 3R and waste related directives to be performed by The Ministry of Environment and Urbanization will play an important role in WMS. 3R and waste management policies, including waste prevention, will play a crucial role.

In order to encourage the producers, storage areas for construction waste should be located near the areas where such large projects have been carried out. It is also necessary to establish technology in the municipalities that can recycle construction waste. Technology which recycles concrete waste and appropriate technologies which provide reuse of aggregate that obtained as a result of recycling concrete waste of the construction sites should be used in the projects. Thus, construction waste will be utilized not only as a filling material but also they will become economically valuable.

REFERENCES

Butera, S., Christensen, T.H., Astrup, T.F. (2014). “Composition and leaching of construction and demolition waste: inorganic elements and organic compounds.” Journal of Hazardous Materials, Vol. 276, pp. 302–31.

Chen, Z., Li, H. and Wong, C.T. (2000). “Environmental management of urban construction projects in China.” *Journal of Construction Engineering Management*, Vol. 126, pp. 320–324.

Cole, R.J. (2000). “Building environmental assessment methods: assessing construction practices.” *Construction Management and Economics*, Vol. 18, pp. 949–957.

Çakır, A.R. (2014). Recycling Construction Waste Debris During Urban Transformation Process. PhD Thesis, Yıldız Technical University, Istanbul, Turkey.

Dorsthorst, B.J.H. and Kowalczyk, T. (2002). “Design for Recycling”, *Digital Proceedins of the CIB Task Group 39-Deconstruction Meeting*, CIB Publication 272: 70-79.

Duran, X., Lenihan, H. and O'Regan, B. (2006). "A model for assessing the economic viability of construction and demolition waste recycling-the case of Ireland." *Resources Conservation and Recycling*, Vol. 46, pp. 302–320.

Ekanayake, L.L. and Ofori, G. (2004). "Building waste assessment score: design-based tool". *Build Environment*, Vol. 39, pp. 851-861.

European Commission DG ENV, Final Report Task 2-Management of C&D Waste. (2011).http://ec.europa.eu/environment/waste/pdf/2011_ CDW_Report.pdf, accessed 24 January 2015).

Guy, B. and Shell, S. (2002). "Design for Deconstruction and Materials Reuse", *Digital Proceedings of the CIB Task Group 39-Deconstruction Meeting*, CIB Publication 272, 189-209.

Kılıç, N. (2015). "Recycling in Urban Transformation" http://www.izto.org.tr/portals/0/argebulten/6kentseldonusumatagi.pdf. accessed 24 January 2015).

Li, J., Ding, Z., Mi, X., Wang, J. (2013). "A model for estimating construction waste generation index for building project in China." *Resources Conservation Recycling*, Vol.74, pp. 20–26.

Li, J., Dong, Q., Yu, K., Liu, L. (2014). "Asbestos and asbestos waste management in the Asian-Pacifc region: trends, challenges and solutions." *Journal of Cleaner Production*, Vol. 81, pp. 218–226.

Sakai, S., Yano, J., Hirai, Y., Asari, M., Yanagawa, R., Matsuda, T., Yoshida, H., Yamada, T., Kajiwara, N., Suzuki, G., Kunisue, T., Takahash, S., Tomoda, K., Wuttke, J., Mahlitz, P., Rotter, V.S., Grosso, M., Astrup, T.F., Cleary, J., Oh, G., Liu, L., Li, J., Ma, H., Chi, N.K. and Moore, S. (2017). "Waste prevention for sustainable resource and waste management." *Journal of Material Cycles and Waste Management*, Vol. 19: pp. 1295–1313.

Spies, S. (2009). "3R in construction and demolition waste (CDW)-potentials and constraints." GTZ–German Technical Cooperation, Germany.

Tam, V.W., Tam, C-M., Yiu, K.T. and Cheung, S.O. (2006). "Critical factors for environmental performance assessment (EPA) in the Hong Kong construction industry." *Construction Management and Economics*, Vol. 24, pp. 1113–1123.

Umar, U.A., Shafiq, N., Malakahmad, A., Nuruddin, M.F. and Khamidi, M.F. (2017). "A review on adoption of novel techniques in construction waste management and policy." *Journal of Material Cycles and Waste Management*, Vol. 19, pp. 1361–1373.

Unnikrishnan, S., Singh, A. (2010). "Energy recovery in solid waste management through CDM in India and other countries." *Resources Conservation and Recycling*, Vol. 54, pp. 630–640.

USEPA (2013). *Packaging Waste Management Regulation.*

Wang, J., Li, Z., Tam, V.W., (2014). "Critical factors in effective construction waste minimization at the design stage: A Shenzhen case study, China," *Resource Conservation and Recycling*, Vol.82, pp.1–7.

Waste Management Regulation (WMR), T.C. Official Gazette Number 29314, 02.04.2015.

Yuan, H. and Shen, L. (2011). "Trend of the research on construction and demolition waste management." *Waste Management*, Vol. 31, pp. 670–679.

CISET - 2nd Cilicia International Symposium on Engineering and Technology
10-12 October, 2019, Mersin / TURKEY

The production of novel Magnesium Alloys and Investigation of their mechanical properties

Azim GÖKÇE[a], Güven YARKADAŞ[b], Hüseyin ŞEVİK[b],

[a] Sakarya Uygulamalı Bilimler Üniversitesi, Teknoloji Fakültesi, Sakarya, Türkiye, e-mail: azimg@subu.edu.tr
[b] Mersin Üniversitesi, Metalurji ve Malzeme Mühendisliği, Mersin, Türkiye, e-mail: sevik@mersin.edu.tr

ABSTRACT

In this study, Mg-Sn-Al based alloy was produced as the main alloy and Al-5Ti-1B master alloy which has grain refining properties is added to this alloy. And then, microstructure studies of the produced alloys were carried out. Then the tensile test was performed to determine its mechanical properties. The obtained experimental results exhibited that the grain size of the main alloy was decreased with addition of grain refining. It is concluded that the mechanical properties of the main alloy were improved significantly with the addition of Al-5Ti-1B master alloy.

Keywords: *Mg alloys, Ti-B, mechanical properties.*

1. INTRODUCTION

Researchers' interest in aluminum-based, magnesium-based alloys and carbon fiber composites for automotive components is based on a combination of high strength properties and low density. In the past decade, aluminum and polymers have successfully replaced steel due to their specific good strength properties[1-5]. Today, the average weight of a car varies between 1100 and 1400 kg. Reducing vehicle weight is inevitable in order to reduce travel costs and CO_2 emissions causing adverse environmental impacts. Also it should be noted that the new generation of electric vehicles need to be lighter because heavier vehicles require larger lithium-ion batteries and this causes a significant increase in vehicle costs[3,6-9]. Magnesium (Mg) alloys with low density and the good strength-to-weight ratio is considered to be one of the lightest metallic materials. However, when compared to pure magnesium alloys with aluminum alloys, their properties such as tensile strength, creep resistance, abrasion and corrosion are not sufficient to achieve the required strength as an automobile component. Therefore, magnesium is often alloyed using different elements. In recent years, many researchers have been developing new magnesium alloys and studying their mechanical properties. One of these designed alloys is Mg-Sn-Al ternary alloy. Although this alloy considered as promising, it is noticed that the improvements are not enough and so, this alloy system is not commercialized yet[7-11].

This study is focusing on the properties of the Mg-5Sn-3Al alloy and the effects of Al-5Ti-1B alloy addition to the base system in terms of grain refining and mechanical properties. Microstructural studies of the produced alloys were also carried out.

2. EXPERIMENTAL DETAILS

Pure Mg, Sn, and Al were used to produce Mg-5Sn-3Al alloy. For the addition of Ti-B, Al-5Ti-1B master alloy was used in the production of the second alloy. Melting process was carried out in SiC crucible in 15kW capacity induction furnace. Alloys were then produced on a 100 Ton cold chamber die casting machine. During the production, the liquid alloy must be protected from the atmosphere to prevent oxidation during melting. In this study, 98% CO2 and 2% SF6 (sulfurhexafluoride) mixed gas were used as protective atmosphere.

Conventional metallographic processes were carried out to examine the microstructures of the produced alloys. First, the samples were passed through 400,600,1000 and 1500 mesh abrasives and then polished using a 0.05 micron Al_2O_3 solution. The most commonly used acetic glycol chemical solution for magnesium alloys (20 ml acetic acid, 1 ml nitric acid, 60 ml ethylene glycol, 19 ml water) was used for etching. Vickers hardness measurement method was used for microhardness tests and 10g load was used. Tensile tests were performed on the Raagen tensile tester. Four tensile tests were performed from each alloy and the mean was accepted as experimental result.

3. RESULTS AND DISCUSSION

3.1. Microstructures

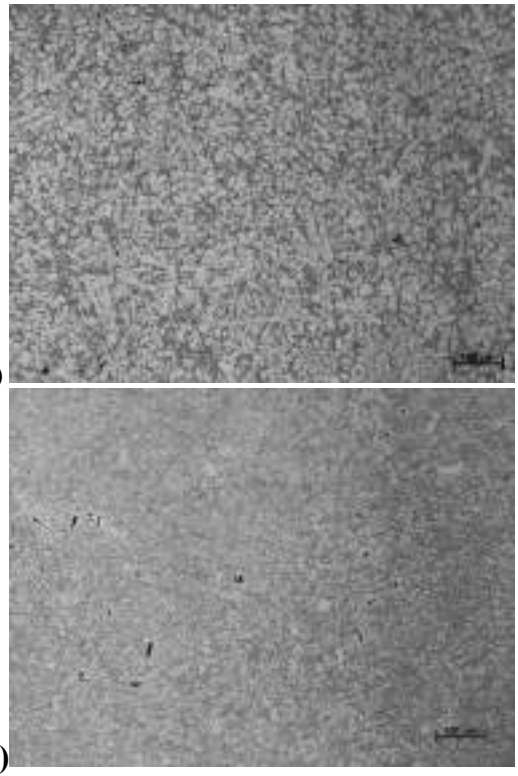

Fig. 1. Optic micrographs of a) Mg-5Sn-3Al and b) Mg-5Sn-3Al-TiB alloy.

Fig. 1 displays the optic micrographs of the Mg-5Sn-3Al and Mg-5Sn-3Al-TiB alloy, respectively. As is shown clearly in these micrographs, the grain size of the Mg-5Sn-3Al alloy was decreased with addition of TiB. According to literature[3,6,10], Sn solubility is found to be ~14.85% at 561°C while it diminishes to nearly zero at room temperature leading to a secondary phase formation during solidification. Thus, the intermetallic Mg_2Sn which has a relatively high melting temperature (770°C) could be formed. In this study, the microstructure of Mg-5Sn-3Al alloy mainly consists of primary α-Mg dendrite grains with Mg_2Sn intermetallic phase surrounding their boundaries.

3.2. Mechanical Properties

The yield strength, tensile strength, elongation to failure and microhardness are shown in Fig.2. It can be seen clearly from Fig.2 that the tensile properties of the Mg-5Sn-3Al alloy were remarkably affected by addition of grain refining-TiB. The microhardness, yield tensile strength and elongation values of the Mg-5Sn-3Al alloy were found as 53,1 Vickers, 120 MPa, 186 MPa, and 12,4%, respectively. The alloy containing grain refining presents the highest microhardness values with 61.2 Vickers, and 14 percent higher than those of the Mg-5Sn-3Al alloy, respectively. Compared to the Mg-5Sn-3Al alloy, the Mg-5Sn-3Al-TiB alloy exhibits noticeable enhancement in the yield, tensile strength, and elongation

with 145 MPa, 207 MPa, 15,5%, respectively. Increase in mechanical properties can be mainly ascribed to grain refinement.

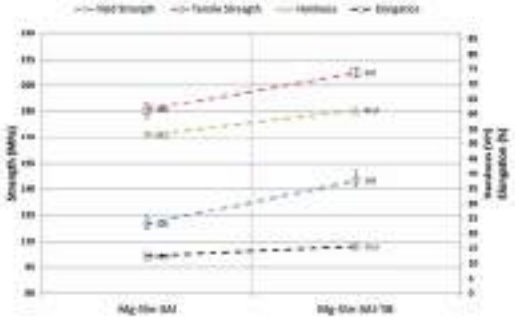

Fig. 2. Mechanical properties of alloys.

4. CONCLUSION

The effect of grain refining on the mechanical properties of Mg-5Sn-3Al alloy was investigated. The results can be summarized as following:

1. The Mg-5Sn-3Al alloy consists of α-Mg and Mg_2Sn intermetallic phases. With the addition of TiB, the grain size of Mg-5Sn-3Al alloy was decreased.
2. The mechanical properties of the Mg-5Sn-3Al alloy were improved with the addition of TiB.

REFERENCES

1. Blawert, C., Hort, N., Kainer, K. U. (2004). "Automotive applications of magnesium and its alloys." Trans. Indian Inst. Met., Vol. 57, No. 4, p.p 397-408.

2. Poddar P., Das A. and Sahoo K. (2014) "Dry sliding wear characteristics of rheocast Mg-Sn based alloys.",Materials and Design, vol. 54, p.p. 820-830.

3. Mayyas A., Qattawi A., Omar M. and Shan D., (2012) "Design for sustainability in automotive industry: A comprehensive review, Renewable and Sustainable Energy Reviews." Vol. 16, pp. 1845-1862

4. Friedrich, H., Mordike, B. (2006). Magnesium Technology, Germany.

5. Park, S., Jung, J., Yoon, J. and You, B. (2015) "Influence of Sn addition on the microstructure and mechanical properties of extruded Mg–8Al–2Zn alloy" Mat. Sci. and Eng. A vol. 626, p.p. 128–135.

6. Germen G., Şevik H. and Kurnaz C. (2013) "Influence of strontium addition on the mechanical properties of gravity cast Mg-3Al-3Sn alloy" 3rd Inter. Advanced in Applied Phy. and Mater. Sci. Cong. AIP Publishing, Antalya, p.p. 199-202.

7. Kim, J., Kang, N., Yim C. and Kim B. (2009) "Effect of calcium content on the microstructural evolution and mechanical properties of wrought Mg–3Al–1Zn alloy." Mater. Sci. and Eng. A, vol. 525, p.p. 18-29.

8. Zhao, P., Wang, Q., Zhai, C. and Zhu, Y. (2007) "Effects of strontium and titanium on the microstructure, tensile properties and creep behavior of AM50 alloys." Mater. Sci. Eng. A vol. 444, p.p. 318–326.

9. Lee, Y., Dahle, A. and Stjohn, D. H. (2000) "The role of solute in grain refinement of magnesium" Metal. and Mater. Trans. A, vol. 31, pp. 2895-2906.

10. Nayyeri, G. and Mahmudi, R.(2010) "Effects of Sb additions on the microstructure and impression creep behaviour of a cast Mg-5Sn alloy." J. Mater. Sci. and Eng. A. vol. 527, pp. 669-678.

11. Pan, H., Qin, G., Xu, M., Fu, H., Ren, Y., Pan, F., Z. Gao, C. Zhao, Q. Yang, J. She, B. Song. (2005) "Enhancing mechanical properties of Mg-Sn alloys by combining addition of Ca and Zn." Mat. and Desg. Vol. 83, p.p. 736-745.

CISET - 2nd Cilicia International Symposium on Engineering and Technology
10-12 October, 2019, Mersin / TURKEY

XAFS, A Powerful Technique for Electronic and Crystal Structure Analysis

Osman Murat OZKENDIR*[1]

[1]Tarsus University, Faculty of Technology, Energy Systems Engineering Department, Tarsus, Mersin, Turkey, ozkendir@gmail.com

ABSTRACT

In this study, a powerful x-ray technique XAFS (x-ray absorption fine structure) spectroscopy is recognized, which can give best solutions to many problems confronted during scientific studies on materials. XAFS provides fruitful data for the investigation of the electronic and crystal structure properties at the same time. Besides, ionic substitutions in a host ionic coordination is really a big challenge where all things should be processed succesfully to yield best results in a study. To identify the electronic, chemical and crystal properties of the substituted or doped ions in the host materials need a powerful technique to collect data which can yield exact information about the new situation of the substituted/doped element and its environment; XAFS. XAFS is a synchrotron based technique and assumed as one of the most powerful research technique. XAFS is used to probe the electronic and bonding properties of elements and attracts a huge attention of the scientists due to its fruitful properties.

Keywords: *Absorption, Spectroscopy, Synchrotron radiation, XAFS*

* Corresponding Author ozkendir@gmail.com

1. INTRODUCTION

Technology is based on the knowledge on materials and their different aspects in science. To improve the properties of the materials, techniques should be picked up elaborately and serve for the desired analysis. Spectroscopy is one of the major branch of the scientific methods to probe on the materials characterization. Spectroscopy uses light and its interactions with atoms or molecules. Most popular spectroscopy techniques are related on photon absorption and electron emission processes. The absorption spectra deals with the how photons absorbed by the electrons, while emission spectroscopy is related mainly where an electron is emitted as a result of its interaction with an incoming photon (Ozkendir, 2006).

When a photon impinge on an electron with a minimum energy of its bond energy to the atom, an excitation process occurs. The energy and a very small value of work function, that helps the electron to move from the core level to the valence levels, cause an instability in the atomic levels. With this energy, the hole left behind should be occupied quickly by the most convenient electrons that obeys quantum selection rules. Relocate to a new state closer to core level is a relaxation for the electrons to emit their excess energy and become a host with lower energy. Thus, during the relocation process, emitted energy can get away from the atom and called as the Fluorescence Yield. If the released energy (photon) interact with an electron on its way, the electron may reject from its level and become and Auger electron. Mainly processes are similar, but the name given to these techniques are related with your obtained outputs. If its photon, it is absorption. But, if the output is an electron, so this technique is called as a photoelectron spectroscopy.

Here, we are interested in absorption process for this study. In an absorption process, the wavelength of the light is important. The wavelength should be smaller than the atoms distance. So, energy can penetrate through the material, interact and get out with the traces of the electronic or atomic interactions which carries important informations about the properties of the materials.

X-rays delivered at Synchrotron Radiation (SR) facilities have a wide range of application in scientific studies, such as; Particle physics and nuclear physics research, Materials science and applications, Accelerator release systems (HSS) and nuclear waste conversion, Nuclear technology, Defense and security industry, Space industry, Life sciences and medical applications, Accelerated radiation sources, Food industry, Mining industry, Information and Communication technologies, Photonic research and applications, Biotechnology, Nanotechnology, Archaeology, Jewelery, Environmental Applications etc.

X-ray Absorption Spectroscopy (XAS) is one of the most popular x-ray technique and yields data on the electronic structure, chemical bonding and crystal structure properties of the selected atom in its environment in the material. Conventional x-ray sources may support XAS for the energy range of the 3d metals. However, conventional can not provide an x-ray range above the 3d levels. Thus, a more powerful and high resolution x-ray source is needed for hard x-rays, i.e., synchrotron. High flux, high resolution and very wide energy range makes the synchrotron facilities a unique center for powerful techniques that can be used in science. X-ray Absorption Fine Structure (XAFS) spectroscopy is a synchrotron based technique which needs a wide energy range (~app. 1 keV) for a measurement. XAFS is a very powerful technique and has advantages like;

- İts Element Specific
- Its sensitive to the local structure
- It can measure mixtures
- Applicable to solids, liquids, gasses
- Applicable to low and high temperatures
- Applicable to high pressure
- It has high sensitivity to electronic properties
- It has easy measurement and analysis
- Its non-destructive

XAFS is used for the investigations on; Semiconductor and superconductor films, Magnetic structure for alloys and films, Dynamics of catalysis, Active point of fuel cell, Nano-scaled and mesoscopic materials, In-situ measurement of real samples etc..

2. METHOD AND DISCUSSIONS

The technique is an extended type of absorption spectroscopy and the data collection process also deals with a long range (tail) energy which is a result of the scattering mechanisms processed by the photoelectrons which are excited with an excess photon energy.

The XAFS spectra can be processed in two main regions, as given in figure 1. The low photon energy part of the spectra is called as the XANES (X-ray Absorption Near-Edge Spectroscopy) region. The XANES part of the XAFS spectra includes fruitful information on the electronic and bonding properties of the atoms which are excited with the incoming photons.

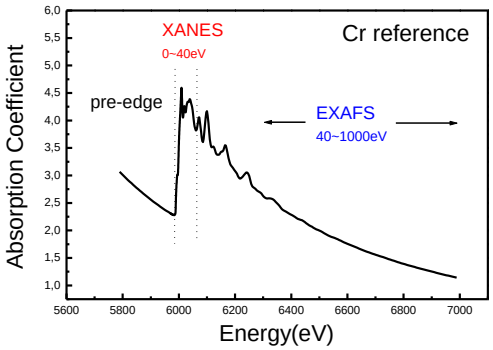

Figure 1. Raw XAFS Spectra of a 3d metal (Cr) K-edge.

The region 40-50 eV above the XANES part is called as the EXAFS (Extended-XAFS) region and it's a tail part along with a range of 400-1000 eV photon

energy. The EXAFS spectra is a result of the emitted photoelectrons from the source atom with kinetic energy. Photoelectrons can travel through the neighboring atoms and their outer shell electrons' force them via coulombic repulsion on the photoelectron. At the interaction point, incoming wavefunction of the photoelectrons' interfere with its outgoing wavefunctions, and cause fluctuations on the spectra; positive when interference is in phase, negative when interference is out of phase. The interaction points also provide data about the scattering mechanism (fig. 2) and atomic distances on a one dimensional axis when aFourier Transformation is applied (fig. 3).

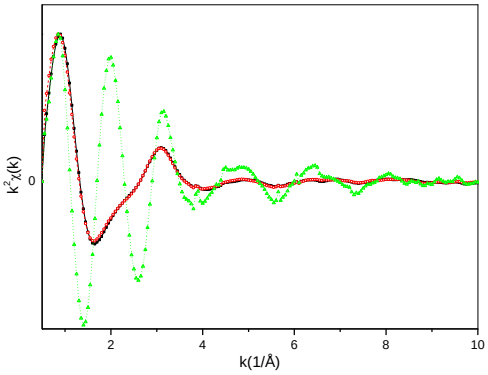

Fig. 2. XAFS scattering intensities.

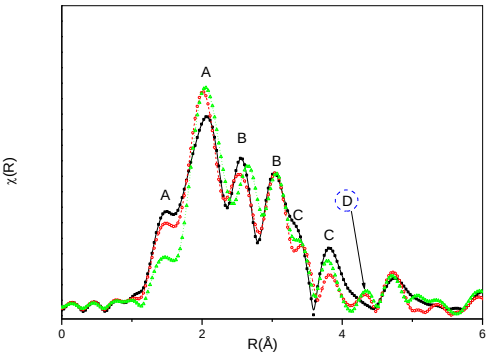

Fig. 3. Fourier Transformed scattering intensity data.

The EXAFS technique provides so valuable information about the crystal structure properties of materials and it can support crystal structure analysis in coordination with the collected data from other techniques.

There are several superiorities of EXAFS then other techniques. One of them is the advantage to determine the positions of light elements which are doped or substituted in low amounts. The data collected in XAFS measurements are element specific. So, this characteristic is used to define to atomic locations. In this manner, an example is given in fig. 4.

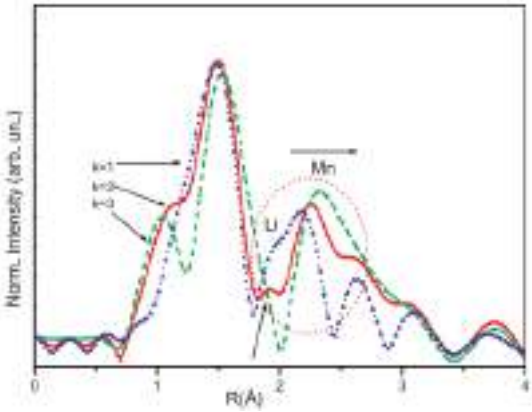

Fig. 4. The normalized FT of the "k-weighted" EXAFS signal comparison.

In the figure, the light atoms positions are determined by the procedure of the "k-weight" in EXAFS analysis (Ozkendir et al, 2019).

.

3. CONCLUSIONS

The technique XAFS (x-ray absorption fine structure) spectroscopy can give best solutions to many problems confronted during scientific studies on materials. One of the main problem in investigations are the determination of the electronic and crystal structure properties at the same time. Besides, ionic substitutions in a host ionic coordination is really a big challenge where all things should be processed succesfully to yield best results in a study. To identify the electronic, chemical and crystal properties of the substituted or doped ions in the host materials needs a powerful technique to collect data which can yield exact information about the new situation of the substituted/doped element and its environment; that is the XAFS. XAFS is a synchrotron based technique and assumed as one of the most powerful research technique. XAFS is used to probe the electronic and bonding properties of elements and attracts a huge attention of the scientists due to its fruitful properties.

REFERENCES

Ozkendir, O.M. (2006). MnS, ZnO Ve SnO2 Ince Filmlerin Elektronik Yapisinin X-Isini Sogurma Spektroskopisi ile Incelenmesi, Cukurova University, Adana, Turkey

Ozkendir O. M., Harfouche M., Ulfat I, Kaya C., Celik G., Ates S., Aktas S., Bavegar H., Colak T. (2019) "Boron activity in the inactive Li2MnO3 cathode material", *Journal of Electron Spectroscopy and Related Phenomena*, Vol. 235, pp.23–28

CISET - 2nd Cilicia International Symposium on Engineering and Technology
10-12 October, 2019, Mersin / TURKEY

Living and Working with Radiation

Osman Murat OZKENDIR*[1]

[1]Tarsus University, Faculty of Technology, Energy Systems Engineering Department, Tarsus, Mersin, Turkey, ozkendir@gmail.com

ABSTRACT

Synchrotron radiation facilities are important centers that provide high quality, wide range and high resolution x-rays for spectroscopic studies and boost scientific studies. During the creation for the x-ray processes, workers should be aware of the understanding the mechanism and conditions of radiation emission and should be informed on the radiation safety procedures. Radiation emitted by synchrotron centers, which are so necessary in the field of science, is extremely dangerous, but it is a part in scientific studies. People whose working place is synchrotrons are stated in the literature as radiation workers. In this study, results of a survey with multiple choice answers are discussed. For this study, a worldwide survey was conducted to determine the awareness levels of employees and users of the synchrotron centers; i.e., radiation workers. The questionnaire was applied to 125 participants from 11 different countries (Italy, Sweden, USA, Germany, Romania, Turkey, Jordan, Pakistan, Iran, Thailand and Japan).

Keywords: *Particle accelerators, Synchrotron radiation, Radiation, Radiation Workers*

* Corresponding Author ozkendir@gmail.com

1. INTRODUCTION

Obtaining electromagnetic radiation from free electrons is a classical phenomenon. It is known that the irradiation (synchrotron radiation, braking radiation or free electron laser and neutrons produced by the direct use of charged particle etc.) bundles obtained from particle accelerators and using these bundles as primary bundles are used in hundreds of fields today. Synchrotron radiation has high luminance values (about 10^5 times as strong as conventional x-ray tubes) and it is emitted over a wide energy range from infrared to hard x-ray region (Ozkendir, 2006).

X-rays delivered at Synchrotron Radiation (SR) facilities have a wide range of application in scientific studies, as;Particle physics and nuclear physics research,Materials science and applications, Accelerator release systems (HSS) and nuclear waste conversion, Nuclear technology, Defense and security industry, Space industry, Life sciences and medical applications, Accelerated radiation sources, Food industry, Mining industry, Information and Communication technologies, Photonic research and applications, Biotechnology, Nanotechnology, Archaeology, Jewelery, Environmental Applications etc.

Radiation is the emission or transmission of energy in the form of electromagnetic waves or particles. The study field of the radiation is "Radiation of radioactive substances emitting rays such as alpha, beta, gamma" or "All of the elements that make up any electromagnetic radiation emitted in space". X-rays, ultraviolet rays, visible rays, infrared rays, microwaves, radio waves and magnetic fields are parts of the electromagnetic spectrum. Electromagnetic particles are defined by frequency and wavelengths. Since alpha, beta, gamma, x-rays and cosmic rays and neutrons are at very high frequencies, electromagnetic particles contain energy that can break chemical bonds (Yavaş., 2009).

The harmful effects of radiation vary with the dose and duration of exposure. The occurrence of damages in which the dose increase is effective is called a deterministic effect (dose dependent) and these are examples of burns in the skin, cataracts, changes in blood, and decrease in sperm production. Generally, this type of effect is not found in diagnostic radiology, and may be involved in external radiotherapy and radionuclide treatments. Cancer-induced and genetic effects can be shown for damages that can occur even at low doses, which are called stochastic effects (dose independent) and do not depend on the dose taken.

The uses of synchrotron radiation and centers are extremely important as described in the previous sections. Due to the working mechanisms in the synchrotron centers, radiation formation jeopardizes the health of personnel and others. There are many informative data regarding synchrotron radiation in the literature. However, researches have not been conducted about the radiation produced by synchrotron radiation and what can be done as occupational health and safety to protect against radiation sufficiently yet. In this respect, our study maintains its originality. In this study, the general condition of the synchrotron centers and the prepared questionnaires conducted in the laboratories of mixed countries were analyzed in order to determine the existing radiation problems in the synchrotron centers.

2. MATERIALS AND METHOD

A questionnaire including 33 question is applied to the radiation workers (scientist, engineers, users and workers) who work at synchrotron facilities to determine the awareness on radiation safety. The questionnaire was applied via the internet by addressing a link on google forms. When the number of attendee reached to 125, the systems is closed for responses. The analysis were conducted by the data collected from the responses to the questions of the questionnaire. Here, some parts of the questionnaire is subject to this study.

3. RESULTS AND DISCUSSIONS

The participants of the study were; 68.8% male and 31.22% women. The ages of the participants are determined as, 40.8% is 41-50 years, 13.6% is 61 years and above, and 40% is 31-40 years. With this question, it is seen that the participants are mainly from the middle age group. According to the given responses to the question “You have graduated from…”; 91.2% of the users were post graduated (MSc / PhD) and only 8.8% have BSc graduates.

In another question, participants were asked about their work experience. According to the responses, 70.4% of the radiation workers has 5 years and more working experience at radiation facilities. %79.2 of the participants were determined to work at beamline hutches and rest are working at machine group or at the accelerator ring.

Another question was about the self confidence of the radiation workers about their knowledge on the radiation safety (as given in figure 1).

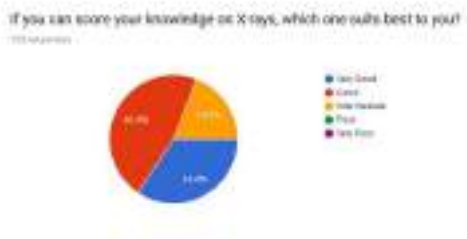

Figure 1. If you can score your information on the X-ray, which one is best for you?

According to the responses, only 46.6% of the participants have a high confidence on their knowledge on radiation.

One of the most important challenge of the workers of large workplaces or laboratories equipped with a wide range of different techniques and devices is that employees do not have sufficient information of the area in which they work. For this purpose, radiation workers were asked the question "what is synchrotron"? 96.3% of the participants responded as “ An extremely powerful x-ray source”. The response shows the participants are aware of their work field. Rest of the participants replied as “A powerful Radiation Generator” and this can also be accepted correct.

In another question, the radiation workers were asked as, "Did you take any course on radiation safety

and health before you started working at Synchrotron?". Its compulsary for workers to be examined for the health check before work and every six months. So workers should know their rights and should be informed about safety regulations. 71% of the participants replied this question as “Yes”. However, 29% of the participants replied as “No”. Actually, this is not acceptable for permanent workers, but it is acceptable for “Users”, who are not working at beamline hutches permanently.

The participants are also asked if they have any experience as a radiation worker before a synchrotron facility. Only 26.4% of the participants replied “Yes”. To keep on the research of the radiation experience of the participants, they are asked for the annual frequency of the performed courses or seminars on “Radiation safety and Health” topics performed by their institution, as given in figure 2.

Fig. 2. What is the number of performed courses and seminars on Radiation Safety?

According to the results; 61.6% says 1-2, 14.4%says 3-5 and %24 says none. A synchrotron facility should perform at least 1 course seminar on radiation safet in a year. The answer “none” may come from the users who works at different organizations and just visit synchrotrons to collect data for short times.

There are different types of radiation, but mainly radiation is classified in two part; ionizing and non-ionizing radiation. Ionizing radiation is the main topic for Radiation safety procedures for workers. In another question, participants are asked if they heard about the “Ionizing Radiation” or “not”.

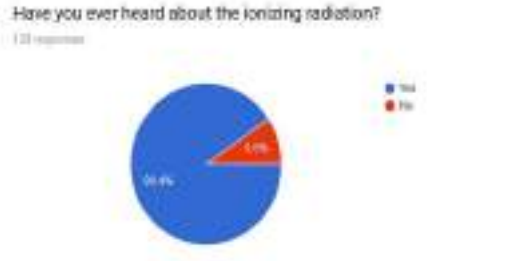

Fig. 3.Participants are asked if they heard about the ionizing radiation or not.

90.4% of the participants responded to this question as “Yes”, but 9.6% responded as “No”. Answer “No” is a problem for a facility, because all of the workers of a facility who works there should be aware of the “Ionizing Radiation”. These responses may come from the users who are new in synchrotron, then this answer become meaningful.

For the next question, in figure 4, the participants are directed a question to measure their awareness on the radiation protection at their facilities or at the beamline hutches for “Users”.

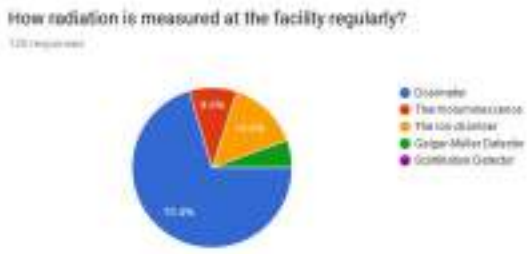

Fig. 4.How radiation is measured at the facility regularly?

The participants answered to this question mainly as “Dosimeter”, which is a personel wear and mostly used for safety precaution.

For the final question, the participants are asked if the know the maximum annual dose a human should expose to?

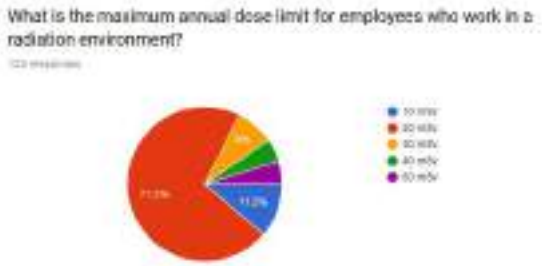

Fig. 5.Participants are asked about the annual dose limit for employees.

The participant are mainly responded as "20 mSv/year", which is correct. However 28.8% of the rest respondend different answers. The confusion may come from the weak information participants may have. Because 1mSv/y for the general public, 20mSv/y for a registered radiation worker is known, where 5o mSv/y is the maximum dose of being healthy.

4. CONCLUSIONS

In this study, awareness of the radiation workers about the radiation safety and health regulations at their working places. The participants, who are machine scientist, beamline scientists and users, are directed a 33 question including questionnaire. The questions were

prepared to measure the basic information and approach of the radiation workers against radiation at synchrotron radiation facilities which are one of the biggest radiation emitting centers. The responses collected from the participants have shown that, the radiation workers mainly have a high conciousness about the radiation protection and they are aware of the potential danger at their work places. However, still there are much work to do to update and upgrade the knowledge on the radiation safety regulations for the workers. Besides, cautions on the regulations should be taught by an on-site learning procedures.

REFERENCES

Ozkendir, O.M. (2006). MnS, ZnO Ve SnO_2 Ince Filmlerin Elektronik Yapisinin X-Isini Sogurma Spektroskopisi ile Incelenmesi, Cukurova University, Adana, Turkey

Yavaş Ö., Yiğit Ş., 2009. SASE X-SEL: Fiziği, Projeler ve Uygulama Alanları, http://thm.ankara.edu.tr.

CISET - 2nd Cilicia International Symposium on Engineering and Technology
10-12 October, 2019, Mersin / TURKEY

THE PRODUCTION OF NI-AL INTERMETALLIC-REINFORCED NICKEL-MATRIX COMPOSITES FROM NI-AL POWDERS

Öyküm Başgöz [*1], Ömer Güler [2], Seval Hale Güler [3] and İskender Özkul [4]

[1] Mersin University, Engineering Faculty, Metalurgical and Material Eng. Dept., Mersin, Turkey, oykumbasgoz@mersin.edu.tr

[2] Mersin University, Engineering Faculty, Metalurgical and Material Eng. Dept., Mersin, Turkey, oguler@mersin.edu.tr

[3] Mersin University, Engineering Faculty, Metalurgical and Material Eng. Dept., Mersin, Turkey, shguler@mersin.edu.tr

[4] Mersin University, Engineering Faculty, Mechanical Eng. Dept., Mersin, Turkey oykumbasgoz@mersin.edu.tr

ABSTRACT
Intermetallic have been found in a lot applications because of their various properties and have been the subject of many scientific studies. Especially Ni_3Al is one of the most important intermetallic and is widely used in high temperature applications. Especially, reinforcing commercially available Ni_3Al with various metal matrices is one of the most studied subjects. In this study, Ni-Al powders were added to nickel matrix and heat treated at 700 °C. Hence, the formation of Ni_3Al in the matrix was provided while the heat generated during the formation. The exposure heat also helped to sinter the Ni matrix. Thus, in-situ Ni_3Al reinforced Nickel matrix composite was produced. In addition to Ni_3Al, other intermetallic such as NiAl were also formed in the structure. The increased reinforcement ratio caused the composite to increase its hardness.
Keywords: *Ni_3Al, intermetallic, composite, in-situ*

[*] Corresponding Author

1. INTRODUCTION

Intermetallic compounds are crystalline compounds or solid solutions formed by two or more pure metals. Intermetallic are between metals and ceramics, which are chemically dissimilar to one another, in narrow composition ranges and within simple ratios (Özdemir, *et. al*., 2004). Nickel and aluminum Al_3Ni, Al_3Ni_2, Al_3Ni_5, NiAl, Ni_3Al make compounds between metals. Nickel-rich NiAl and Ni_3Al in intermetallic compounds, are candidates for high temperature applications and coating processes and are the two most important aluminites in the Ni-Al system (Westbrook, *et. al*., 2000, Morsi, et. Al., 2001). These are the most stable structures in the Al-Ni system. In addition, they have the highest melting point, very low density, good strength properties and corrosion and oxidation resistance at high temperatures (Morsi, et. Al., 2001). The Ni_3Al intermetallic compound has the L12 crystal structure, a derivative of the surface-centered cubic structure (fcc), and the NiAl structure B2, a derivative of the volume-centered cubic structure (bcc).
Ni_3Al has a L12 (cP4) crystal structure below the peritectic temperature of 1395 °C. There are 4 atoms in the unit cell. There are a total of one Al atom at the corners of this lattice and a total of 3 Ni atoms at the surface centers of the lattice. Ni_3Al is an interesting material due to its excellent strength and oxidation resistance at high temperatures (Özdemir, *et. al*., 2004, Westbrook, *et. al*., 2000, Anton, *et. al*., 1989). Ni_3Al is the most important reinforcing component in nickel based superalloys. The single crystals of Ni_3Al are ductile at high temperatures, but polycrystalline materials show brittle grain breakage with little plasticity (Dey, 2003). This effect persists in high purity materials. It can be said that the brittleness originates from the material itself when it is seen brittle even in the absence of impurities at the grain boundaries.
In this study, the Ni-Al powder mixture was added to the Ni matrix in various ratios and intermetallicities such as NiAl and Ni3Al were formed in the matrix by using SHS method.

2. EXPERİMENTAL METHOD

In the experiments, 5%, 10% and 20% of Ni-Al powder mixture was added to Ni matrix. For this purpose, 86.4% Ni (Merck) powder and 17.6% Al (Roth) powder were first mixed in a mechanical stirrer for 30 minutes. Subsequently, this powder mixture was added to the Ni matrix separately in 5%, 10%, 20% by weight and the new powder mixture was mixed in the mechanical mixer for a further 15 minutes. The resulting powders were then made into pellets having a diameter of 12 mm and a height of 6 mm under a stretch of 500 MPa. The resulting pellets were heat-treated at 700 °C. Then the internal structure of the obtained samples were examined under optical microscope and the microhardness of the samples were taken and the mechanical properties of the composites were determined.

2.1.1. The third level headings

These headings should be in 10pt, italic, and sentence case. Insert one blank line before and after the headings. The further lower level headings should be avoided.

3. RESULT AND DISCUSSION

Figure 1 shows the Al-Ni phase diagram. The Ni_3Al intermetallic is formed in a very narrow composition. Therefore, the initial Ni-Al powder mixture was made according to this range. However, it should be noted that the matrix is Ni and inevitably there are variations in phase ratios in some regions. That means that Ni_3Al may form in some regions, while NiAl intermetallic may occur in some regions.

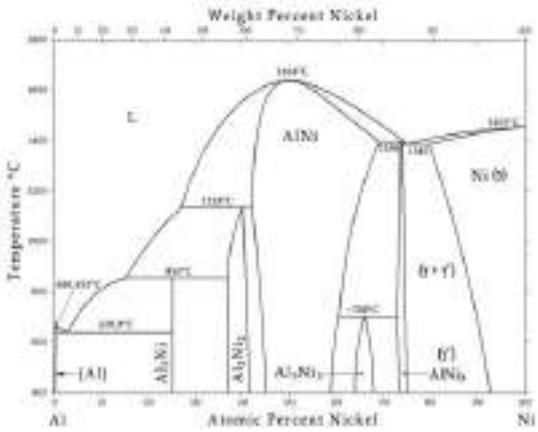

Fig.1. Al-Ni phase diagram (Dey, 2003)..

The microstructure images of the composites produced in Figure 2 are given. The microstructure shown in Figure 2a belongs to a 5% reinforced sample and two structures similar to the eye are seen in the middle of the picture. The black part is a void, and the white structure around the void is Ni-Al intermetallic. All of the other white parts in the structure, in other words, are Ni matrix. Black small structures are the voids that have been produced by powder metallurgy. Similar structures apply to the 10% sample given in Figure 2b. In Figure 2c., the distribution within the 20% sample is given. As it is seen, the intermetallic formed in the heat treatment question are distributed homogeneously in the structure.

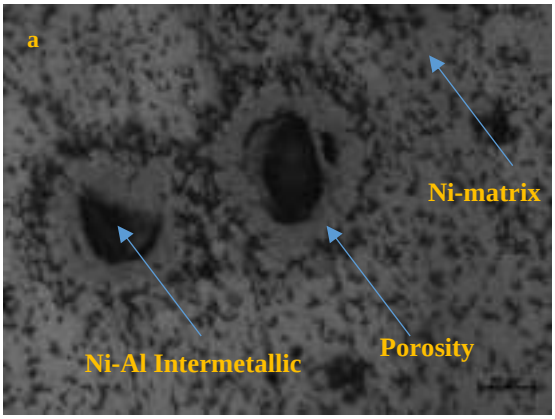

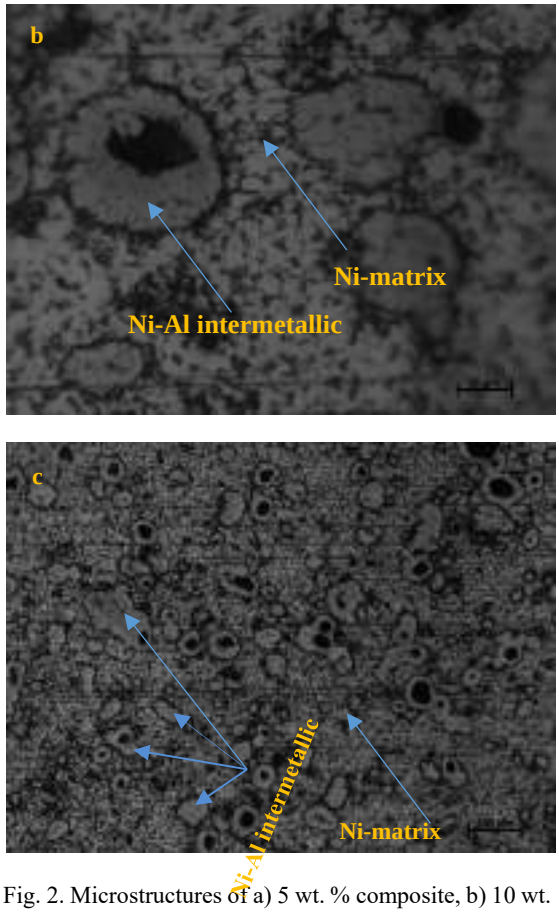

Fig. 2. Microstructures of a) 5 wt. % composite, b) 10 wt. % composite, c) 20 wt.% composite

The Ni-Al mixture was pelleted without addition to the Ni matrix and heat-treated at 700 °C. The microstructure view of the obtained structure is given in Figure 3a-c. As can be seen from the figure, three different phases were found in the structure. The most important and the dominant phase of the structure is Ni_3Al. The other phase is the NiAl intermetallic found in white clumps. The last structure seen in the structure is an eutectic structure. This eutectic structure is thought to be the eutectic of Al-Al_3Ni in the phase diagram given in Figure 1. Because the eutectic point in the equilibrium diagram only points to this structure. The XRD analysis from the intermetallic produced in Figure 3d is given. As seen, Ni_3Al is dominant in the structure. In addition, it can be said that NiAl intermetallic are formed. XRD analysis shows that Ni-Al intermetallic synthesis is synthesized when the Ni-Al powder mixture is heat treated at 700 °C. Similar cases exist in the literature (Guler, *et. al.,* 2015, Guo, *et. al.,* 2011).

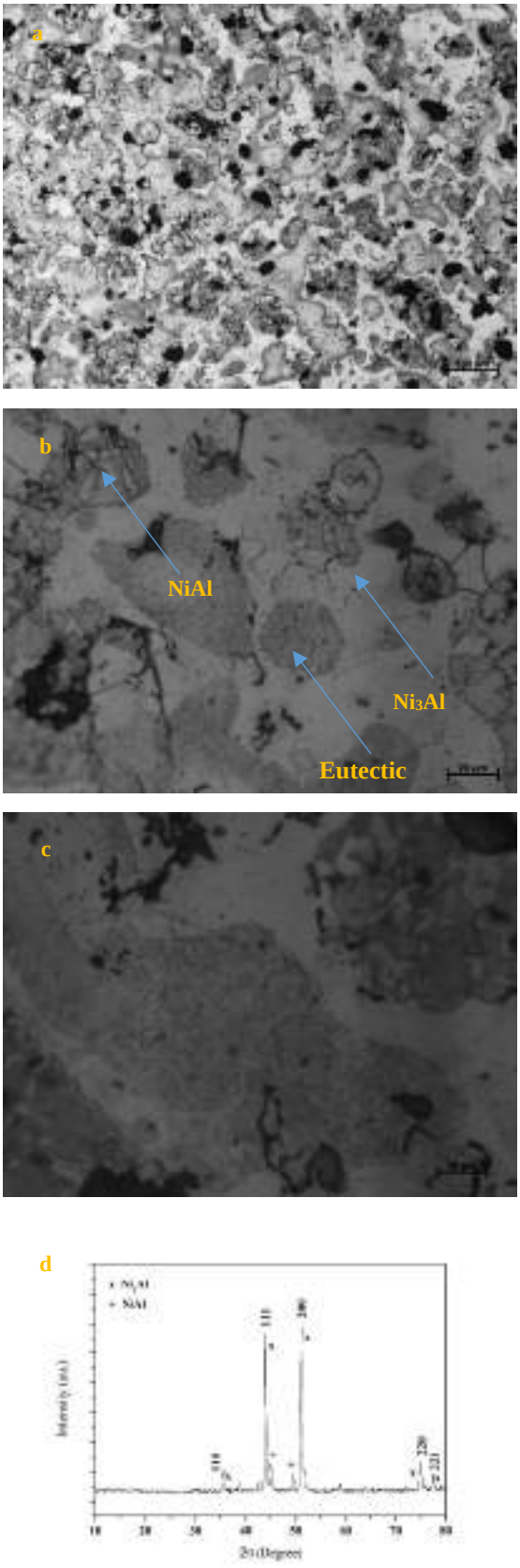

Fig. 3. a),b),c) Microstructures, d) XRD spectra of Ni_3Al intermetallic synthesized from Ni-Al powder mixture

It is seen in Figure 3 that Ni matrix Ni_3Al reinforced composite can be produced by adding Ni-Al powder

mixture in different proportions to Ni matrix and heat treatment at 700 °C. In addition, the micro-hardness of the composites shows that hard phases are formed in the structure and the matrix is soft.

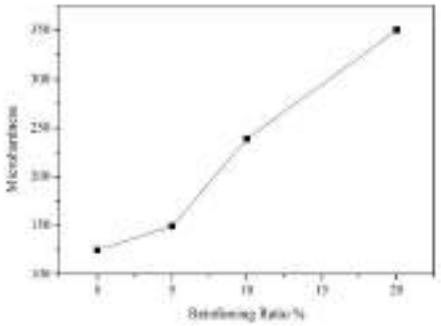

Fig. 4. Microhardness changing for different reinforcing ratio

The effect of the 5% reinforcement rate on the hardness increase of the nickel matrix was relatively limited. However, when the reinforcement ratio increased to 10%, the hardness increased to 240 HV. If the reinforcement ratio increases to 20%, the hardness value is increased to 350 HV.

4. CONCLUSION

Nickel aluminite reinforced composites with nickel matrix were successfully produced by adding Ni-Al powder mixture to Ni matrix and heat treatment at 700 °C. It was seen that Ni_3Al was formed by heat treatment of Ni-Al powder mixture at 700 °C. It has been observed that the strength ratio raised with the increase of reinforcement ratio in the composites obtained.

REFERENCES

Özdemir Ö., (2004). " Basınç Destekli Yanma Sentezi İle Üretilen Ni-Al İntermetalik Malzemelere Kobalt İlavesinin Etkisinin İncelenmesi.", Doktora Tezi, pp 4, Sakarya.

J. H. Westbrook, R. L Fleischer (2000). "Structural Applıcatıons Of Intermetallıc Compounds." *John Wıley & Sons, Ltd.*

K. Morsi (2001). "Review: reaction synthesis processing of Ni–Al intermetallic materials." *Materials Science and Engineering A*, Vol. 299, pp. 1-15.

Anton D.L., Shah D.M., Duhl D.N., Giamei A.F. (1989), "Sellecting High Temperature Structural İntermetallic Compound.", *The Engineering Aproach, JOM*, pp 12-17

DEY G.K. (2003). "Physical Metallurgy of Nickel Aluminide.", *Sadhana*, Vol 28, pp 247-262.

Ö. GÜLER, E. Evin, O. Yilmaz, S.H. GÜLER (2015). "The effect of SiC decomposition on microstructure of Ni_3Al." *Journal Of Optoelectronıcs And Advanced Materials*, Vol. 17, pp. 1099-1105.

J.T. Guo, L.Y. Sheng, Y. Xie, Z.X. Zhang, V.E. Ovcharenko, H.Q. Ye, (2011). "Microstructure and mechanical properties of Ni_3Al and Ni_3Al–1B alloys fabricated by SHS/HE." *Intermetallics*, Vol. 19, pp. 137-142.

GRAPHENE PRODUCED WITH USING SURFACTANT FROM EXPANDED GRAPHITE

Ali Sönmez [1], Ömer Güler [2], Öyküm Başgöz *[3] and Seval Hale Güler [4]

[1] Mersin University, Engineering Faculty, Metalurgical and Material Eng. Dept., Mersin, Turkey, alisnmezz@gmail.com

[2] Mersin University, Engineering Faculty, Metalurgical and Material Eng. Dept., Mersin, Turkey, oguler@mersin.edu

[3] Mersin University, Engineering Faculty, Metalurgical and Material Eng. Dept., Mersin, Turkey, oykumbasgoz@hotmail.com

[4] Mersin University, Engineering Faculty, Metalurgical and Material Eng. Dept., Mersin, Turkey, shguler@mersin.edu.tr

ABSTRACT
Graphene is a single layer of graphite with hexagonal structure which have stacked layers. Graphene has recently been recognized by its researchers due to it have sp^2 bonds in hexagonal lattice, the two-dimensional structure of a single atomic thickness, and its superior electrical, electrochemical, optical, thermal, mechanical properties and lightness. Liquid phase exfoliation (LPE) is the most promising method of graphene research to produce high quality graphene in the production of single or low layer graphene layers. In addition, LPE is an easy and inexpensive method as well as enables the production of higher capacity graphene. LPE method in the production of graphene is the use of surfactant mainly to make water suitable as a means of exfoliation. Furthermore, graphene adsorbable surfactants provide an effective charge by electrostatic repulsion to prevent the re-aggregation of graphene sheets, thus providing stabilization against the recombination of suspended graphene layers. Because 1,2-Dichlorobenzene or ortho-dichlorobenzene (O-DCB) is both effective as solvent for graphene synthesis, it is one of the best production of graphene by the liquid phase exfoliation method. In this study, graphite powders were mixed in an acid solution of H_2SO_4 and HNO_3 for 12h. The resulting powder was washed with distilled water until a neutral pH was obtained and then subjected to thermal treatment to obtain expanded graphite. The resulting powder was then mixed in an ultrasonic homogenizer in a mixture of O-DCB for 2h using 50 % strength and then it was examined by Transmission electron microscope (TEM) and X-ray photoelectron spectroscopy (XPS).

Keywords: *Graphene, ortho-dichlorobenzene, Expanded Graphite, LPE.*

Corresponding Author

1. INTRODUCTION

Graphene is known as a surprising material in recent years due to its new features related to its two-dimensional structure (Monajjemi, 2017). Its intriguing properties such as high strength, an optical transmittance of 97,7 %, carriermobility as high as 200,000 $cm^2 V^{-1} s^{-1}$ at room temperature and a Young's modulus of 0.5–1 TPa, perfect electrical conductivity and high thermal conductivity make it promising for various applications (Arao *et. al.*, 2017). Due to these features of graphene, flexible devices, high-frequency transistors, energy storage and transducers, sensors, biomedical applications and the production of new generation composites have been demonstrated that graphene can be made easily (Wei, *et. al*, 2015). Today, the most widely used methods in the production of graphene; mechanical exfoliation, chemical method (reduction of graphene oxide), chemical vapor deposition (CVD), epitaxial growth in silicon carbide, liquid phase exfoliation method (LPE), electrochemical exfoliation, the solvothermal method, arc discharge (Lee, *et. al*., 2019)

Commercialization of graphene-oriented applications is inevitable, but cost-effective and high-quality serial production is needed (Xu, *et. al*., 2014). Since the first day it was found and applied, the liquid phase exfoliation method has been proposed as the most promising method of graphene research to produce high quality single or low layer graphene sheets in solvent dispersion forms. The main advantage of this process is a simple and sizable process in which pure graphite or expanded graphite is applied directly to a solvent process to weaken the Van Der Waals tensile forces between graphene interlayers (Durge, *et. al.,* 2014). Many successes have been achieved in the production of graphene by liquid phase exfoliation method by using numerous solvent systems and suitable surfactants (Huo , *et. al*.2015). Although the Liquid Phase Exfoliation Method is a relatively easy and inexpensive method, the quality of the products produced is higher than the products produced by other methods (Zhu, *et. al*., 2013).

In this study, graphite powders were mixed in an acid solution of H_2SO_4 and HNO_3 for 12h. The resulting powder was washed with distilled water until a neutral pH was obtained and then subjected to thermal treatment to obtain expanded graphite. The resulting powder was then mixed in an ultrasonic homogenizer in a mixture of O-DCB for 2h using 50 % strength. The main purpose of this study is to investigate the effects of O-DCB which is used as solvent in graphene synthesis by liquid phase exfoliation method in graphene production.

2. EXPERIMENTAL PROCEDURE

Hexagonal graphite powders was waited at 90 ºC for 2 h to remove the humidity. The dried HG was mixed with saturated acid consisting of concentrated H_2SO_4 and HNO_3 for 12 h to form the graphite intercalated compound (GIC). It was carefully washed with distilled water. Then, GIC was heated at 1000 ºC to form expanded graphite (EG).

The graphene-sheets were still bonded with weak van der Waals forces at some points in EG. Therefore, EG was incurred to a final exfoliation to obtain graphene-sheet by ultra-sonication in O-DCB. The suspension of 0.07 mg/ml concentration of EG with O-DCB was prepared. The solution of EG was kept at multi-frequency ultra-sonication homogenizer for 1h. Then, the mixture was centrifuged at 5000 rpm for 8 hours to remove O-DCB. The low density material suspended at the top layer of centrifuged solution was collected for further characterization.

Transmission electron microscope (HRTEM) (JEOL Jem 1100) was used to investigate the microstructure of graphene samples. The samples were chractersized via X-ray photoelectron spectroscopy (XPS) (Specs-Flex) and Raman Spectroscopy (WITech alpha 300-R 512 nm wavelenght).

3. RESULTS AND DISCUSSION

Graphite consists of a stack of flat graphene-layer. Bonding between layers is via weak van der Waals bonds, which allows layers of graphite to be easily separated, or to slide past each other. The aim of this study is exfoliation of graphite layers in order to product the graphene. A solvent is necessary to separate the layers. The distance of layers should be sufficient in order to enter the solvent atoms between layers. So, hexagonal graphite powders were expanded by acid and thermal treatments. After those processes, the gap between hexagonal sheets extends and the weak bonds between the sheets easily break off via entering-solvent-atoms. Following this process increases the distance between the hexagonal layers and solvent atoms easily fill these gaps, provide the rupture of the weak bonds between the layers.

In previous our studies, different solvents (Such as DMF, NMP eg.) were used for graphene synthesis via Liquid Phase Exfoliation (LPE). It was shown in literature that O-DCB also is suitable a solvent because of its surface properties.

TEM images of samples were given after LPE process by using O-DCB as solvent. As the figure shows that, exfoliation was succeed and layers were separated from each other's. The width of the layers was 200 nm above. There is a dark-colored contamination in figure 1.a. It is believed that the contamination was sediments of solvent while using the production of amorphous carbon or graphene.

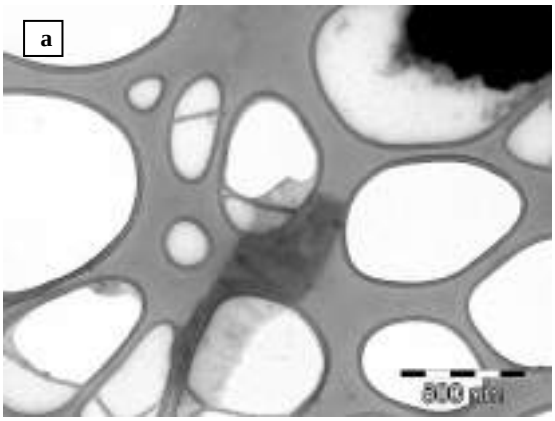

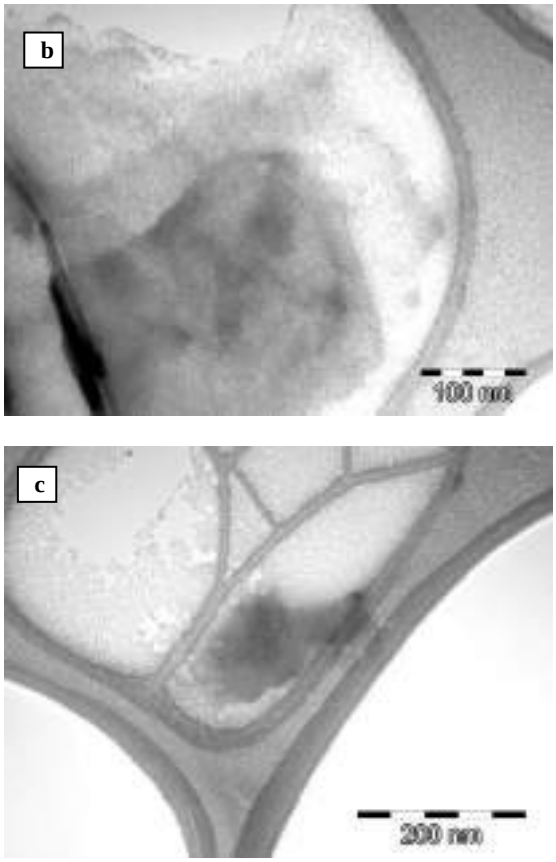

Fig. 1. (a),(b),(c) TEM micrographs of high magnification of synthesized graphene layers

In figure 2, XPS spectra analysis of samples were given. Figure 2a. shows general XPS spectra, Figure 2b. shows fitting of XPS peaks. As the figure shows that, synthesized graphenes contain C-C bonds over 80 %. In addition, C-O bonds exist in samples. We think that C-O bonds formed when EG was produced. Because, graphite powders were treated with acids and powders were heated to high temperature.

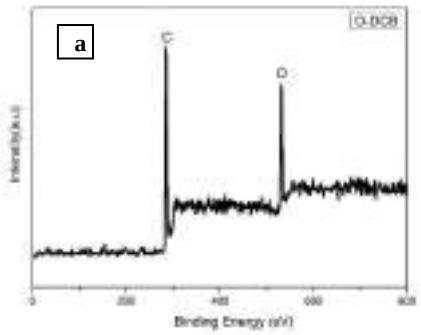

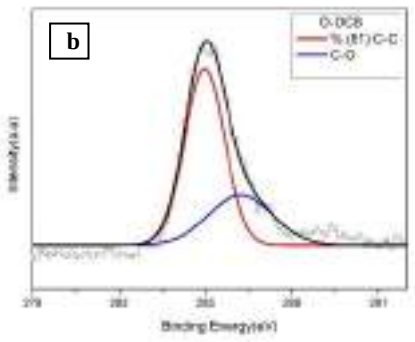

Fig. 2. (a) general XPS spectra, (b) XPS spectra fitting of synthesized Graphene layers

Figure 3 shows the Raman spectra of synthesized graphenes. In Raman spectra of graphenes, 3 characteristic peaks were shown. D peak (at 1350 cm^{-1}) relate to defects in graphenes (in sheets basal plane or sheet edges). G peak (at 1582 cm^{-1}) relates to C atoms vibrations having sp^2 hibritazition in hexagonal lattice. 2D peak (at 2700 cm^{-1}) indicates graphenes existence in powders. In Raman spectra of our samples, these peaks exist. The intensity of 2D peak is weak. This show that not only graphene exist in samples but also graphene nanosheets. The intensity of D peak is comparatively high. This show that defects exist in synthesized powders. We think that these defect formed during ultrasonic process.

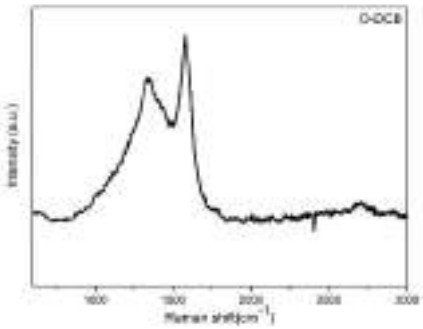

Fig. 3. Raman Spectra of synthesized graphene layers

In this study, the analyzes show that production of graphene nanosheets were achieved with Liquid-Phase Exfoliation method by using O-DCB as solvent.

4. CONCLUSION

In this study, O-DCB was used as solvent in graphene synthesis via LPE method. In first step, EG was produced. Subsequently, EG was sonicated in O-DCB in order to synthesis graphene. It shown that graphene was synthesized by using O-DCB. But, graphene nanosheets also form together with graphene in samples.

Acknowledgments

We would like to acknowledge the financial support from Mersin University Department of Scientific Research Projects (Project No: 2018-3-TP2-3085).

REFERENCES

Monajjemi, M. (2017). "Liquid-phase exfoliation (LPE) of graphite towards graphene: An ab initio study." *Journal of Molecular Liquids*, Vol. 230, pp. 461-472.

[Arao, Y., Mori, F., & Kubouchi, M. (2017). "Efficient solvent systems for improving production of few-layer graphene in liquid phase exfoliation." *Carbon*, Vol. 118, pp. 18-24.

[Wei, Y., & Sun, Z. (2015). "Liquid-phase exfoliation of graphite for mass production of pristine few-layer graphene." *Current opinion in colloid & interface science*, Vol. 20, pp. 311-321.

Lee, X. J., Hiew, B. Y. Z., Lai, K. C., Lee, L. Y., Gan, S., Thangalazhy-Gopakumar, S., & Rigby, S. (2019). "Review on graphene and its derivatives: Synthesis methods and potential industrial implementation."*Journal of the Taiwan Institute of Chemical Engineers*, Vol. 98, pp. 163-180.

Xu, J., Dang, D. K., Liu, X., Chung, J. S., Hur, S. H., Choi, W. M., ... & Kohl, P. A. (2014). "Liquid-phase exfoliation of graphene in organic solvents with addition of naphthalene." *Journal of colloid and interface science*, Vol. 418, 37-42.

Durge, R., Kshirsagar, R. V., & Tambe, P. (2014). "Effect of sonication energy on the yield of graphene nanosheets by liquid-phase exfoliation of graphite."*Procedia Engineering*, Vol. 97, pp. 1457-1465.

Huo, C., Yan, Z., Song, X., & Zeng, H. (2015). "2D materials via liquid exfoliation: a review on fabrication and applications." *Science Bulletin*, Vol. 60, pp. 1994-2008.

Zhu, L., Zhao, X., Li, Y., Yu, X., Li, C., & Zhang, Q. (2013). "High-quality production of graphene by liquid-phase exfoliation of expanded graphite." *Materials Chemistry and Physics*, Vol. 137, pp. 984-990.

Hydraulic jump energy dissipation evaluation in rough bed channels via kernel based approach

Seyed Mahdi Saghebian[1*] Daniel Dragomir-Stanciu[2]
[1]Department of Civil Engineering, Ahar Branch, Islamic Azad University – Ahar-Iran
Email: smsaghebian@iau-ahar.ac.ir; smsaghebian@gmail.com
[2]UMFST, Faculty of Engineering, Department of Electrical Engineering,Târgu Mureș, Romania,
Email: daniel.dragomir-stanciu@umfst.ro

ABSTRACT

Hydraulic jump is a useful means of dissipating the excess energy of supercritical flow so that objectionable scour in the downstream is minimized. The estimation of hydraulic jump energy dissipation plays an important role in designing of hydraulic structures. In this study, the hydraulic jump energy dissipation was assessed in channels with rough beds using kernel based Support Vector Machine approach. Experimental datasets were applied to develop the models. The results showed that the SVM model is successful in estimating the relative energy dissipation. I it was observed the developed models for trapezoidal channel are more accurate than rectangular channel. It was observed that rough element geometry is affective in estimation of the energy dissipation. The sensitivity analysis results revealed that Froude number had the more dominant role on the modeling.

Key words: *Trapezoidal channel, Energy dissipation, Rough element, SVM.*

1. Introduction

For transition of a supercritical flow into a subcritical flow in an open channel, a hydraulic jump phenomenon is used. Hydraulic jumps can occur downstream of hydraulic structures, such as normal weirs, gates and ogee spillways. It is considered as rapidly varying flow, and this type of flow regime transformation is associated with severe turbulence and flow energy dissipation (Hager, 1992). Based on energy dissipating action of hydraulic jumps, stilling basin is one of the possible solutions which may be adopted. In order to design an optimal hydraulic structure, different devices such as sills, baffle blocks, end sills, roughness elements, and roller buckets are used in hydraulic structures. However modeling hydraulic jump characteristics owns great importance since it plays an important role in designing hydraulic structures. So far, hydraulic jumps have been extensively studied in order to explain the complex phenomenon of the hydraulic jump and to estimate its characteristics. Hager and Bremen (1989) investigated the internal flow features of hydraulic jumps in trapezoidal channels. Finnemore et al. (2002) stated that Froude number has significant impact on characteristics of hydraulic jump. Ayanlar (2004) investigated the hydraulic jump properties in channels with corrugated beds. Bilgin (2005) collected some experiments in a channel with smooth bed in order to investigate the distribution of shear stress for turbulent flow. However, due to the complexity and uncertainty of the hydraulic jump phenomenon, the classical models often don't show desired accuracy and the application of many formulas are limited to special cases of their development. Therefore, it is essential to use other methods which are more accurate in predicting the hydraulic jump parameters such as energy dissipation.

The Meta model approaches such as Artificial Neural Networks (ANNs), Neuro-Fuzzy models (NF), Genetic Programming (GP), and Support Vector Machine (SVM), have been applied in investigating the hydraulic and hydrologic complex phenomena in recent decades. Prediction of total bedload (Chang et al., 2012), prediction of daily river flow (Delafrouz et al. 2018), modeling flow resistance in open channels with dune bedform (Roushangar et al., 2018), water level prediction (Ghorbani et al. 2017), and predicting of sediment transport in circular channels (Roushangar and Ghasempour, 2017) are some examples of the Meta model approaches applications. In the present study, the relative energy dissipation is assessed in rectangular and trapezoidal channels with rough beds using the SVM as a kernel based approach. Different models were developed to determine the most effective combination for predicting the relative energy dissipation. Then, the sensitivity analysis was performed in order to determine the most important variables in modeling.

2. Materials and Methods

2.1. Used Data Sets

The experimental data presented by Carollo et al. (2007) and Evcimen (2012) were used for prediction relative energy dissipation. Carollo et al. (2007) studded hydraulic jump in smooth and rough rectangular channels. 372 tests were performed under different hydraulic condition. The experiments of Evcimen (2012) were intended for hydraulic jump in trapezoidal channels and the impact of prismatic roughness on hydraulic jump was assessed. The ranges of experimental data used in experiments are given in Table 1. In this table Fr_1 is downstream flow Froude number, S is space between rough elements, Y is sequence depth ratio and H is height of rough elements.

Table 1. The range of experimental data used in this study.

Researcher	Channel type	Parameters				No. of data
		Fr_1	S (cm)	Y	H (cm)	
Carollo et al. (2007)	Rectangular	0.1-10	-	2.8-10	0.46-3.2	300
Evcimen (2012)	Trapezoidal	3.92-13.2	2-10	4.15-14.9	1-3	107

2.2. Support Vector Machine

Support vector machines (SVM) approach which developed by Vapnik in 1995, is known as structural risk minimization (SRM), which minimizes an upper bound on the expected risk, as opposed to the traditional empirical risk (ERM) which minimizes the error on the training data. The SVM method is based on the concept of optimal hyper plane that separates samples of two classes by considering the widest gap between two classes. Support Vector Regression (SVR) is an extension of SVM regression. The aim of SVR is to characterize a kind of function that has at most ε deviation from the actually obtained objectives for all training data yi and at the same time it would be as flat as possible. SVR formulation is as follows:

$$f(x) = w\varphi(x) + b \tag{1}$$

Where φ(x) denotes a nonlinear function in feature of input x, b is called the bias and the vector w, is known as the weight. The coefficients of equation (1) are predicted by minimizing regularized risk function as expressed below:

$$R_{\min} = C\frac{1}{N}\sum_{i=1}^{n} L_{\varepsilon}(t_i, y_i) + \frac{1}{2}\|w\|^2 \tag{2}$$

Where

$$L_{\varepsilon}(t_i, y_i) = \begin{cases} 0 & |t_i, y_i| \le \varepsilon \\ |t_i, y_i| - \varepsilon & \text{Otherwise} \end{cases} \tag{3}$$

The constant C is the cost factor and represents the trade-off between the weight factor and approximation error. ε is the radius of the tube within which the regression function must lie. The $\boldsymbol{L_{\varepsilon}(t_i, y_i)}$ represents the loss function in which yi is forecasted value and ti is desired value in period i. Since some data may not lie inside the ε-tube, the slack variables (ξ, ξ*) must be introduced. These variables represent the distance from actual values to the corresponding boundary values of ε–tube. Therefore, it is possible to transform equation (2) into:

$$R_{\min} = C\sum_{i=1}^{n}\left(\xi_i,\ \xi_i^*\right) + \frac{1}{2}\|w\|^2 \tag{4}$$

Using Lagrangian multipliers in equation (4) thus yields the dual Lagrangian form:

$$Maxl(\alpha_i, \alpha_i^*) = -\varepsilon\sum_{i=1}^{n}\left(\alpha_i + \alpha_i^*\right) + t_i\sum_{i=1}^{n}\left(\alpha_i - \alpha_i^*\right) - \frac{1}{2}\times\sum_{i=1}^{n}\times\sum_{j=1}^{n}\left(\alpha_i - \alpha_i^*\right) - \left(\alpha_j - \alpha_j^*\right) - K(x_i, x_j) \tag{5}$$

Where αi and αi* are Lagrange multipliers and l(αi, αi*) represents the Lagrange function. K(xi, xj) is a kernel function to yield the inner products in the feature space φ(xi) and φ(xj). In general, there are several types of kernel function, namely linear, polynomial, radial basis function (RBF) and sigmoid functions.

Performance criteria

In the current study, the model's performance was evaluated using three statistical parameters: Correlation Coefficient (R), Determination Coefficient (DC), and Root Mean Square Errors (RSME), as depicted in equation (6).

$$DC = 1 - \frac{\sum_{i=1}^{N}\left(l_o - l_p\right)^2}{\sum_{i=1}^{N}\left(l_o - \overline{l_p}\right)^2},$$

$$\mathrm{R} = \frac{\sum_{i=1}^{N}\left(l_o - \overline{l_o}\right)\times\left(l_p - \overline{l_p}\right)}{\sqrt{\sum_{i=1}^{N}\left(l_o - \overline{l_o}\right)^2 \times \left(l_p - \overline{l_p}\right)^2}}, \tag{6}$$

$$\mathrm{RMSE} = \sqrt{\sum_{i=1}^{N}\frac{\left(l_o - l_p\right)^2}{N}}$$

where l_o, l_p, $\overline{l_o}$, $\overline{l_p}$, N respectively are: the measured values, predicted values, mean measured values, mean predicted values and number of data samples.

Using non-normalized data in estimation of the intended parameter may lead to undesirable accuracy; therefore, all datasets were normalized before modeling. This will increase the capability of the SVM model. The equation (7) was used to normalize the data utilized in this study:

$$x_n = 0.1 + 0.9\times\left(\frac{x - x_{\min}}{x_{\max} - x_{\min}}\right) \tag{7}$$

Where x_n, x, x_{max}, x_{min} respectively are: the normalized value of variable x, the original value, the maximum and minimum of variable x.

3. Simulation and models development

3.1. Input variables

Appropriate selection of input parameters is an important step in modeling process using an intelligent technique. Based on the experimental studies by [Hager (1989), Carllo et al. (2007)] the important variables which affect the energy dissipation can be a function of *(y_1, y_2, V, L, E_j, μ μ, g, ρ, H, S)*. In which y_1 and y_2 are sequent depth of upstream and downstream, *V* is upstream flow velocity, *μ* is water dynamic viscosity, *g* is gravity acceleration, *L* is length of jump, *ρ* is density of water, *Ej (= E_1 - E_2)* in which E_1 and E_2 are energy per unit weight before and after the jump, *H* is rough element height, and S is space between rough elements. Using dimensional analysis and considering y_1, *g* and *μ* as repeating variables the effective parameters can be expressed as following:

$$\boldsymbol{f\left(\frac{h_2}{h_1}, \frac{E_L}{E_1}, \frac{L_J}{h_1}, Fr_1, R_n, B, \frac{s}{h_1}\right) = 0}$$

$$f\left(\frac{y_2}{y_1}, \frac{E_j}{E_1}, \frac{L}{y_1}, Fr_1, Re, \frac{H}{y_1}, \frac{S}{y_1}\right) = 0 \quad (8)$$

in which Fr_1 is flow Froude number and *Re* is flow Reynolds number According to the experimental studies by Elevatorski (2008) and Ranga Raju et al. (1980) hydraulic jump characteristics only depend on Froude number and Reynolds number has not effective role in predicting process. Therefore, in this study, the models of Table 2 were considered for modeling the energy dissipation in channels with different shapes and bed conditions.

Table 2. Developed Models for predicting E_L/E_1.

Rough channels	
Model	Input variable(s)
R (I)	Fr_1
R (II)	Fr_1, y_2/y_1
R (III)	Fr_1, $(y_2-y_1)/y_1$
R (IV)	Fr_1, H/y_1
R (V)	Fr_1, S/H

4. Results and Discussion

4.1. Selecting the kernel type

For determining the best performance of SVM and selecting the best kernel function, model *R(III)* of rectangular channel was predicted via SVM using various kernels. Figure 1 shows the results of statistical parameters of different kernels. According to the results, using kernel function of RBF led to better prediction accuracy in comparison to the other kernels. Therefore, RBF kernel was used as core tool of SVM which was applied for the rest of models.

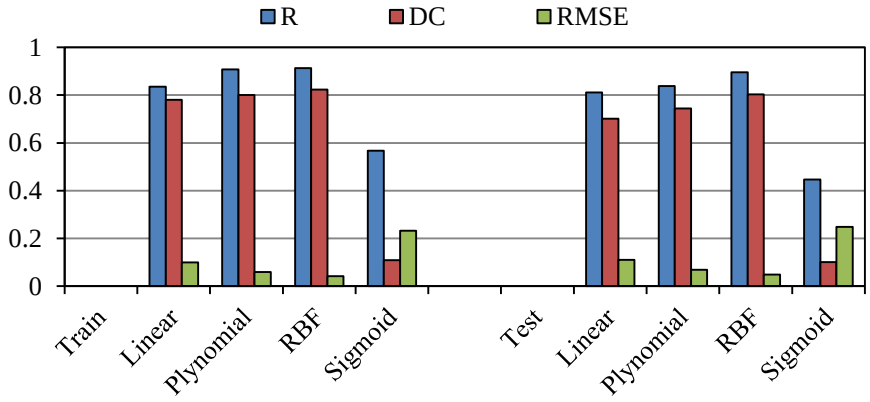

Fig. 1. Statistical parameters of the SVM models for smooth channels.

4.2. Developed models for rough channels

For evaluating the relative energy dissipation in rough channels with different shape, several models were development based on flow and channels geometry and tested with SVM. The obtained results from SVM models for predicting the hydraulic jump relative energy dissipation in rectangular and trapezoidal channels with rough beds are indicated in Table 3 and Fig. 2. The superior performance for rectangular channel was obtained for the model *R(III)* with input parameters of Fr_1, $(y_2-y_1)/y_1$. According to the obtained results, it could be inferred that adding y_2/y_1 and $(y_2-y_1)/y_1$ and H/y_1 as an input parameters caused an increment in models efficiency. However, for this state the variable $(y_2-y_1)/y_1$ was more effective than variables y_2/y_1 and H/y_1 in improving the model efficiency. For trapezoidal channel, the superior performance was obtained for the model *R(V)* with input parameters of Fr_1, *S/H*. variable *S/H* shows the impact of the rough elements geometry on predicting the relative energy dissipation. It could be stated that the applied method in the case of trapezoidal channel can successfully predict the relative energy dissipation using only the upstream flow characteristic (Fr_1) as input data.

Table 3. Statistical parameters of the SVM models for rough channels.

Channel type	Models	Performance criteria					
		Train			Test		
		R	DC	RMSE	R	DC	RMSE
Rectangular	R (I)	0.858	0.683	0.066	0.814	0.661	0.073
	R (II)	0.903	0.815	0.048	0.892	0.768	0.055
	R (III)	0.913	0.824	0.042	0.896	0.804	0.049
	R (IV)	0.887	0.785	0.064	0.886	0.745	0.067
Trapezoidal	R (I)	0.905	0.822	0.049	0.904	0.804	0.052
	R (II)	0.910	0.825	0.043	0.906	0.809	0.050
	R (III)	0.912	0.831	0.041	0.909	0.811	0.045
	R (IV)	0.938	0.879	0.038	0.927	0.857	0.040
	R(V)	0.942	0.885	0.036	0.935	0.858	0.039

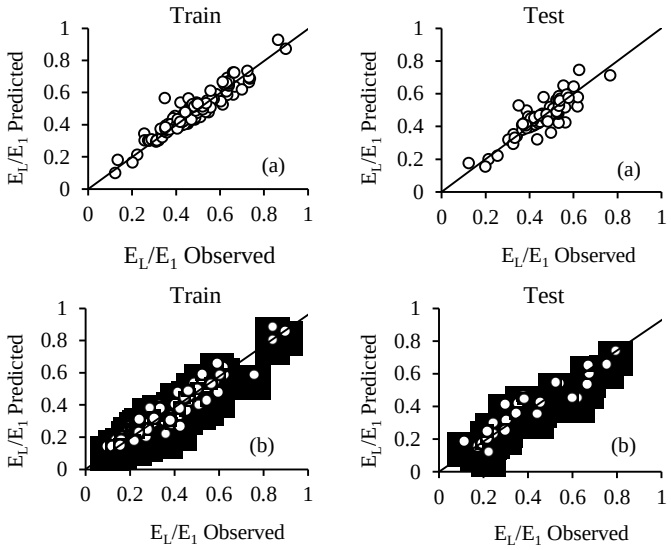

Fig. 2. Comparison of observed and predicted relative energy dissipation for superior mode in rough channels; (a) rectangular channel, (b) trapezoidal channel.

4.3. Sensitivity analysis

To investigate the impacts of different employed parameters from the best proposed models on hydraulic jump energy dissipation prediction via SVMs, sensitivity analysis was performed. In order to evaluate the effect of each parameter, the model was run with all input parameters and then, one of the input parameters was eliminated and the SVM model was re-run. Table 4 shows the sensitivity analysis results. From Table 4, it could be induced that variable Fr_1 is the most important variable in the hydraulic jump relative energy dissipation prediction in rough channels.

Table 4. Relative significance of each of input parameters of the best models for each channel.

Channel type	Eliminated variable	Performance criteria for test series		
		R	DC	RMSE
Rectangular	Fr_1, $(y_2-y_1)/y_1$	0.896	0.804	0.049
	Fr_1	0.547	0.511	0.115
	$(y_2-y_1)y_1$	0.814	0.661	0.073
Trapezoidal	Fr_1, S/H	0.935	0.858	0.039
	Fr_1	0.635	0.551	0.099
	S/H	0.904	0.804	0.052

5. Conclusion

In the present study, a kernel based approach was applied to estimate the hydraulic jump energy dissipation in rectangular and trapezoidal rough channels. Different models were developed based on flow and rough elements characteristics. It was observed that the superior performance in rectangular channel was the model *R(III)* with parameters of Fr_1, $(y_2-y_1)/y_1$. It was found that H/y_1 as an input parameter improved the model efficiency. For the case of trapezoidal channel, the model *R(V)* with parameters of Fr_1, *S/H* was superior. It was found that the rough elements geometry has impact on predicting the relative energy dissipation.

It showed that the applied method in the case of trapezoidal channel can successfully predict the relative energy dissipation using only the upstream flow characteristic as input data. The sensitivity analysis showed that Fr_1 had the most effective role in estimation of the relative energy dissipation.

REFERENCES

Ayanlar K. (2004). 'Hydraulic Jump on Corrugated Beds". M. Sc. Thesis. Middle East Technical University, Department of Civil Engineering, Ankara, Turkey.

Bilgin A. (2005). "Correlation and Distribution of Shear Stress for Turbulent Flow in a Smooth Rectangular Open Channel". *Journal of Hydraulic Research*, 43(2), 165–173.

Carollo F. G., Ferro V. and Pampalone V. (2007). "Hydraulic jump on rough beds". *Journal of Hydraulic Engineering*, 133, 989–999.

Chang C. K., Azamathulla H. M., Zakaria N. A. & Ghani A. A. (2012). "Appraisal of soft computing techniques in prediction of total bed material load in tropical rivers". *Journal of earth system science*, 121(1), 125-133.

Delafrouz H., Ghaheri A. and Ghorbani M. A. (2018). "A novel hybrid neural network based on phase space reconstruction technique for daily river flow prediction". *Soft Computing*, 22(7), 2205-2215.

Elevatorski E. A. (2008). "*Hydraulic Energy Dissipators*". McGraw-Hill, New York.

Evcimen T. U. (2012). "Effect of prismatic roughness on hydraulic jump in trapezoidal channels (Doctoral dissertation)". Middle East Technical University, Department of Civil Engineering, Ankara, Turkey.

Finnemore J. E. & Franzini B. J. (2002). "*Fluid mechanics with engineering applications*". McGraw-Hill, New York, NY, 790.

Ghorbani M. A., Deo R. C., Karimi V., Yaseen Z. M. and Terzi O. (2017). "Implementation of a hybrid MLP-FFA model for water level prediction of Lake Egirdir, Turkey". *Stochastic Environmental Research and Risk Assessment*, pp.1-15.

Hager W. H. & Bremen R. (1989). "Classical Hydraulic Jump: Sequent Depths". *Journal of Hydraulic Research*, 27(5), 565-85.

Hager W. H. (1992). "*Energy Dissipators & Hydraulic Jumps*". Kluwer Academic Publication, Dordrecht, The Netherlands, pp. 151-173.

Ranga Raju K. G., Mittal M. K., Verma M. S. & Ganeshan V. R. (1980). "Analysis of Flow over Baffle Blocks and End Sills". *Journal of Hydraulic Research*, 18(3), 227–241.

Roushangar K. & Ghasempour R. (2017). "Prediction of non-cohesive sediment transport in circular channels in deposition and limit of deposition states using SVME". *Water Science & Technology: Water Supply*, 17(2), 537-551.

Vapnik V. (1995). "*The Nature of Statistical Learning Theory*". Springer-Verlag, New York, 1-47.

CISET - 2nd Cilicia International Symposium on Engineering and Technology
10-12 October, 2019, Mersin / TURKEY

WASTE ALMOND SHELL REINFORCED POLYDIMETHYLSILOXANE RUBBER COMPOSITES

Ahmet GÜNGÖR [1] and İsmail Kutlugün AKBAY [*2]

[1] Mersin University, Engineering Faculty, Chemical Engineering Department, Mersin, TURKEY, ahmet.gungor@mersin.edu.tr

[2] Mersin University, Engineering Faculty, Chemical Engineering Department, Mersin, TURKEY, akbay@mersin.edu.tr

ABSTRACT
Elastomeric materials are widely utilized with various filler materials to enhances the mechanical, thermal and rheological properties. Conventional fillers such as carbon black, silica used in the industry improve the desirable properties of elastomeric materials, there is a need for the development of new fillers in that they are non-biodegradable, harmful to both of worker and environmental health. In this context, the usage as filler material of agricultural wastes within the rubber matrix have been investigated. In this study, almond shells (AS) as agricultural wastes were used and the investigation of bio-based filler material in polydimethylsiloxane (PDMS) matrix were performed. PDMS with different AS content were prepared and mechanical, rheological and swelling properties of produced composite was investigated. Analysis results showed that the addition of waste almond shell was significantly enhanced the mechanical and vulcanization properties of composites. Besides, gel content analysis result implied that the AS is in well corporate with the PDMS matrix. The characterization results revealed that the usage of almond shell as a bio-based filler material is a valuable alternative in terms of economic and environmental issues.

Keywords: *Almond Shell, Bio-based Filler, PDMS, Rubber, Waste Management*

[*] Corresponding Author

1. INTRODUCTION

Polydimethylsiloxane (PDMS), also known as dimethylpolysiloxane or dimethicone, belongs to a group of polymeric organosilicon compounds that are commonly referred to as silicones. PDMS is the most widely used silicon-based organic polymer, and is particularly known for its unusual rheological (or flow) properties(Leite *et al.*, 1994). PDMS is optically clear, and, in general, inert, non-toxic, and non-flammable. It is one of several types of silicone oil (polymerized siloxane). Its applications range from contact lenses and medical devices to elastomers; it is also present in shampoos, food (antifoaming agent), caulking, lubricants and heat-resistant tiles (Kuo, 2009).

In rubber composite production, the rubber blending prepares a new composite with a wide range of uses, creating an edge over the interesting properties of the mixture component while avoiding economic and technical uncertainties related to the synthesis of new composite materials. Blending two or more kinds of elastomers or addition of the different filler is effective ways in the production of materials that has non-blending nature in the rubber (Martinez *et al.*, 2011). Natural rubber, ethylene propylene diene terpolymer (EPDM) materials are frequently used in rubber applications owing to its excellent tensile properties (Da Maia *et al.*, 2013). Nevertheless, ozone and chemical resistance is quietly low because of the highly unsaturated polymeric backbone of elastomers. Thus, the use of elastomeric materials with high mechanical, thermal and rheological properties that suitable for the field of use has gained importance in recent years (Nabil *et al.*, 2013).

Elastomeric materials are frequently utilized with various filler materials to enhances its properties in parallel with the field of usage. In the choice of filling material, it is important to use materials which will generally improve the mechanical and rheological properties of the elastomer. Although conventional fillers such as carbon black, silica used in the industry improve the desirable properties of elastomeric materials, there is a need for the development of new fillers in that they are non-biodegradable, harmful to worker and environmental health. (Rausch *et al.*, 2004). In order to handle with the above-mentioned problems, natural materials such as pistachio, walnut shell, and fish scales could be used as bio-based and bio-degradable filler in rubber industry (Karaağaç, 2014) (Akbay *et al.*,2018; Güngör *et al.*, 2019).

Almonds are a type of biomass nut shell and are frequently cultivated in many areas of the world including India, America, Iran, and Turkey (Ebringerová *et al.*, 2007). According to the 2017 data, global output of almonds was four million tons annually. Almond shells account for around 40–78% of the total fruit weight, so around 11–23 million tons of shells were residuals (Li *et al.*, 2018). This enormous amount of shells has great economic and practical potential, and research into the best solution to use the shell is attracting increasing attention. In addition, bio-based filler obtained from agricultural waste such as sugarcane bagasse (Santos *et al.*, 2015), rice husk (Sae-Oui *et al.*, 2002), coconut husk (Sareena *et al.*, 2012) and walnut shell (Güngör *et al.*, 2019) stalk are also used to reinforce rubbers because of their abundance and as an economical solution for waste management .

Although the use of different agricultural products as filler material in rubber exists in the literature, with our best knowledge, the almond shell (AS) is not used. In this study, almond shell with different amount as a bio-based filler material was added into PDMS matrix. The mechanical, rheological and swelling properties of the composite material were investigated.

2. MATERIAL & METHODS

The silicone rubber used was polydimethyl siloxane (PDMS) supplied by Wacker Chemie. 2,5-bis-(tert-butylperoxo)-2,5dimethylhexane (C6) was utilized as the crosslinking agent and it was also bought from Wacker Chemie. Almond shell (AS) was taken from a local market around in Mersin, Turkey. The almond shell was cleaned by tap and de-ionized water three times. After that, the cleaned almond shell was dried at 55 ^{o}C in a laboratory scale oven. Dried almond shell was ground with laboratory type grinder and the ground particles were sieved with laboratory type sieve machine. During the study, only particles below 250 microns of the ground almond shell were used.

The PDMS with different AS content were prepared by using the components that was tabulated in Table 1.

Table 1. The recipe of PDMS/AS Composite

Materials	Function	phr
PDMS	Rubber	100
C6	Crosslinking Agent	3
Almond Shell	Bio-Based Filler	0, 5, 10, 15

PDMS compound with Almond Shell (AS) and crosslinking agent was compounded with a Baihong mark ML-132 model Kneader type closed mixer. After the rubber mixture were reached up to 80 ^{o}C, the mixture process was stopped and produced composite were pressed in a Baihong mark HL-66 model laboratory scale two-roll mill in order to prepare a 2 mm sheet-shaped material. the obtained sheet-shaped composite was transferred into a 2 mm mound and curing process was done in a thermal hydraulic press under 20 MPa pressure at different for moving die rheometer (MDR) specified minutes (Akbay, *et al.*, 2017).

The mechanical properties of PDMS/Almond Shell (AS) composites were calculated according to the ASTM D412 standard. The mechanical test was carried out using Shimadzu AGS-X universal testing machine with a 20 kN gauge and the crosshead speed was done at a 100 mm/min. In addition, the hardness values of produced composites were calculated via laboratory type Shore A testing machine (Özdemir *et al.*, 2018).

The crosslinking density (gel content) of the PDMS/AS materials was determined by using traditional Soxhlet extraction method and was calculated using Eq. (1);

$$Gel\ Content\ (\%) = {}^{w_f}/_{w_i} * 100 \quad (1)$$

where w_f and w_i are related to the final and initial weight of sample, respectively. The solvent used in the experiment was tetrahydrofuran (THF) and the experiments were carried out at 70^{o}C.

The swelling ratio of the PDMS/AS materials was

calculated by using petri cup and the swelling medium was selected as toluene all the experiments. The swelling ratio of the obtained composites was calculated using Eq. (2);

$$Swelling\ Ratio\ (\%) = {}^{w_f - w_i}/_{w_i} * 100 \quad (2)$$

where w_i and w_f are also associated with the initial and final weight of sample, respectively (Akbay *et al.*, 2018).

Vulcanization process of PDMS/AS composite were simulated with Moving Die Rheometer at 170 °C. Besides, cure rate index (CRI) was calculated by using MDR data with Eq. (3), where t_{90} is the optimum cure time and t_{s2} is the scorch time (Güngör *et al.*, 2018).

$$CRI = {}^{100}/_{(t_{90} - t_{s2})} * 100 \quad (3)$$

3. RESULTS & DISCUSSIONS

3.1. Rheological Properties

In order to determine the vulcanization parameters and rheological properties of PDMS/AS materials, MDR test was performed and the obtained torque curves were given in Fig. 1. The maximum torque values (M_H) is related to the tensile properties of the composites and the high torque values implies that the composites has high mechanical properties (Güngör *et al.*, 2019). As can be concluded in Fig. 1, M_H values of composites increased with the addition of AS within the rubber matrix.

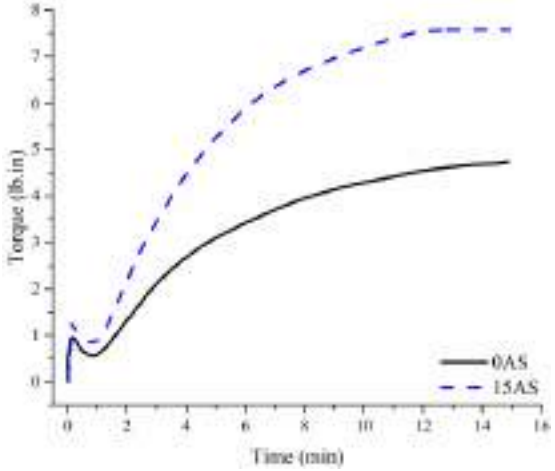

Fig. 1. MDR curves of EPDM/BCS composites

Vulcanization parameters of PDMS/AS materials was tabulated in Table 1. Optimum vulcanization time (t_{90}) and scorch time (t_{s2}) are important variables in order to estimate the vulcanization process (Güngör *et al.*, 2018). The low t_{90} and high t_{s2} the value implies that whether the obtained materials are sufficient in terms of rheological properties. As can be concluded from the Table 1, the t_{90} values of sample decreased while t_{s2} value increased with the addition of AS within the silicone matrix. Also, the cure rate index value was increased. Consequently, the AS addition into the rubber matrix has improved the rheological properties of produced composite materials.

Table 1. Vulcanization parameters of PDMS/AS composites

Composite	t_{s2} (min)	t_{90} (min)	CRI
0AS	1.09	14.11	7.68
15AS	1.19	12.27	9.03

3.2. Swelling Properties

The determined gel content and swelling ratio of PDMS/AS composites are shown in Figure 3. Gel content and swelling ratio are related to the crosslink density of rubber material (Akbay *et al.*,2018; Güngör *et al.*, 2019). Concisely, gel content and swelling ratio are associated with the mechanical and rheological properties of the rubber material. Besides, it is well-known that the gel content and swelling ratio are adversely proportional to each other. As can be seen from Fig. 2, the crosslinking density of PDMS based composites considerably increased with the addition of AS within the PDMS matrix. The gel content of produced composite achieved at 85.2% for 15AS sample while swelling ratio of PDMS based composite materials determined as around at 124.3% for 10 BCS sample. Consequently, the optimum AS content confirmed as 15 phr according to the swelling properties. Also, the obtained outcomes are concordance with the rheological analysis results.

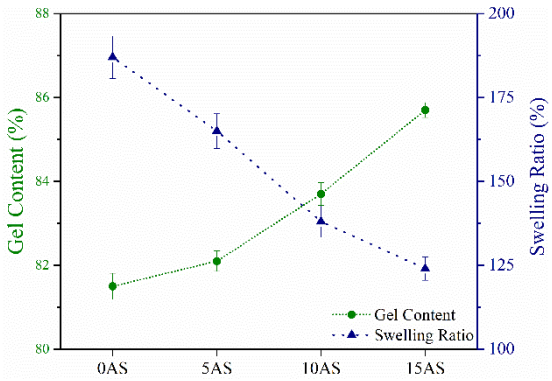

Fig. 2. Swelling properties of PDMS/AS composites

3.3. Mechanical Properties

The mechanical properties of PDMS/AS composite are shown in Fig. 2. As can be concluded from the Fig.2, the AS addition within the PDMS matrix has considerably effected the tensile properties of produced materials. AS addition increased tensile strength and elongation at break values. Moreover, the addition of AS above 15 phr was also studied, but the results of the analyzes were not given in this work because it had a negative effect on the rheological properties of the material. In addition, the hardness value of samples increased with the increase of AS content in PDMS matrix. Moreover, the mechanical analysis results and rheological properties of samples are compatible with each other.

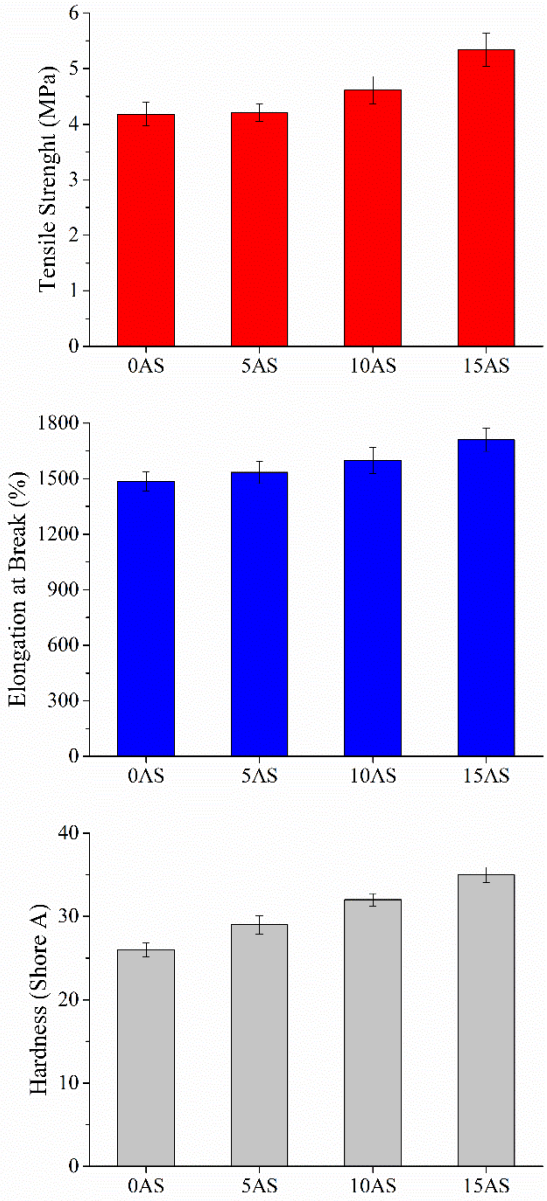

Fig. 2. Tensile test results of PDMS/AS composites

4. CONCLUSION

In this study, the waste almond shell (AS) as a bio-based filler was investigated whether AS will be a filler material for PDMS rubber. In this context, PDMS rubber with different AS content were produced. Tensile, rheological and swelling properties of prepared composites were characterized. Rheological properties and vulcanization parameters of prepared samples showed that the addition of AS within the PDMS rubber as a bio-based filler material considerably enhanced the vulcanization process. Besides, tensile properties of composites revealed that the tensile strength, hardness and elongation at break values of produced composites has considerably improved with the addition of AS into the rubber matrix. Also, AS addition has also increased the crosslinking density samples according to the swelling and gel content analysis results of composites, which this result is compatible with the other characterization studies. Consequently, the obtained results imply that the usage of almond shell as a bio-based filler material is a significant alternative in terms of economic and environmental issues.

REFERENCES

Akbay, İ. K., Güngör, A. and Özdemir, T. (2017) 'Optimization of the vulcanization parameters for ethylene–propylene–diene termonomer (EPDM)/ground waste tyre composite using response surface methodology', *Polymer Bulletin*, Vol. 74, No.12, pp.5095-5109.

Akbay, İ. K., Güngör, A. and Özdemir, T. (2018) 'Using fish scales (Sardina pilchardus) within ethylene-propylene-diene ter monomer rubber as bio-based filler', *Journal of Applied Polymer Science*, Vol. 135, No. 39, pp. 1–8.

Ebringerová, A. *et al.* (2007) 'Chemical valorization of agricultural by-products: Isolation and characterization of xylan-based antioxidants from almond shell biomass', *Bioresources*, Vol. 3 No. 1, pp. 60–70.

Güngör, A. *et al.* (2018) 'Flexible X/Gamma ray shielding composite material of EPDM rubber with bismuth trioxide: Mechanical, thermal investigations and attenuation tests', *Progress in Nuclear Energy*, Vol. 106, pp. 262–269.

Güngör, A., Akbay, I. K. and Özdemir, T. (2019) 'Waste walnut shell as an alternative bio-based filler for the EPDM: mechanical, thermal, and kinetic studies', *Journal of Material Cycles and Waste Management*. Springer Japan, Vol. 21, No. 1, pp. 145–155.

Karaağaç, B. (2014) 'Use of Ground Pistachio Shell as Alternative Filler in Natural Rubber/Styrene–Butadiene Rubber-Based Rubber Compounds', *Polymer Composites*, Vol. 35, No. 2, pp. 245–252.

Kuo, A. C. M. (2009) 'Polymer Data Handbook, 2nd ed. Polymer Data Handbook, 2nd ed . Edited by James E. Mark (University of Cincinnati, OH). Oxford University Press: New York. 2009 . xii + 1250 pp. $195.00. ISBN 978-0-19-518101-2 .', *Journal of the American Chemical Society*, Vol. 131, No. 44, pp. 16330–16330.

Leite, C. A. P. *et al.* (1994) 'Surface dynamics of polydimethylsiloxane rubber', *Polymer*. Elsevier, Vol. 35, No. 15, pp. 3173–3177.

Li, X. *et al.* (2018) 'Study of almond shell characteristics', *Materials*, Vol. 11, No. 9, pp. 1782-1794.

Da Maia, J. V. *et al.* (2013) 'Influence of gas and treatment time on the surface modification of EPDM rubber treated at afterglow microwave plasmas', *Applied Surface Science*. Elsevier B.V., Vol. 285(PARTB), pp. 918–926.

Nabil, H., Ismail, H. and Azura, A. R. (2013) 'Compounding, mechanical and morphological properties of carbon-black-filled natural rubber/recycled ethylene-propylene-diene-monomer (NR/R-EPDM) blends', *Polymer Testing*. Elsevier Ltd, Vol. 32, No. 2,

pp. 385–393.

Özdemir, T. *et al.* (2018) 'Nano lead oxide and epdm composite for development of polymer based radiation shielding material: Gamma irradiation and attenuation tests', *Radiation Physics and Chemistry*, Vol. 144, pp. 248-255.

Rausch, L. J., Bisinger, E. C. and Sharma, A. (2004) 'Carbon black should not be classified as a human carcinogen based on rodent bioassay data', *Regulatory Toxicology and Pharmacology*, Vol. 40, No. 1, pp. 28–41.

Sae-Oui, P., Rakdee, C. and Thanmathorn, P. (2002) 'Use of rice husk ash as filler in natural rubber vulcanizates: In comparison with other commercial fillers', *Journal of Applied Polymer Science*, Vol. 83, No. 11, pp. 2485–2493.

Santos, R. J. dos *et al.* (2015) 'Sugarcane bagasse ash: new filler to natural rubber composite', *Polímeros*, Vol. 24, No. 6, pp. 646–653.

Sareena, C., Ramesan, M. T. and Purushothaman, E. (2012) 'Utilization of peanut shell powder as a novel filler in natural rubber', *Journal of Applied Polymer Science*, Vol. 125, No. 3, pp. 2322–2334.

CISET - 2nd Cilicia International Symposium on Engineering and Technology
10-12 October, 2019, Mersin / TURKEY

WASTE HAZELNUT SHELL AS A BIO-BASED FILLER IN POLYDIMETHYLSILOXANE RUBBER

İsmail Kutlugün AKBAY [1] and Ahmet GÜNGÖR*[2]

[1] Mersin University, Engineering Faculty, Chemical Engineering Department, Mersin, TURKEY, ahmet.gungor@mersin.edu.tr

[2] Mersin University, Engineering Faculty, Chemical Engineering Department, Mersin, TURKEY, akbay@mersin.edu.tr

ABSTRACT
Hazelnut is one of the most produces nuts in the Turkey with a very high amounts of its shell that could be used as an engineering material as bio-based filler material. Waste management is one of the most rising topics in the World. To exceed this situation, we aimed to partly replace PDMS with waste hazelnut shell without decrease a great deal of properties. Waste hazel nut shells are obtained from local shops and milled to enhance the interaction with the rubber matrix. The vulcanization tests showed that the addition of waste hazelnut shell particles improve the initiation period of vulcanization processes. The mechanical test results showed that the addition of waste hazelnut shell particles improve the toughness of the composites and it increase the possible waste management circumstances. The gel content and swelling ratio tests suggests that the filler is in well conformity with the PDMS matrix. The results indicated that, waste hazelnut shell could be used as a valuable and handy filler material for both PDMS and other types of rubber.

Keywords: *Hazelnut, Nut Shell, PDMS, Rubber, Waste Management*

* Corresponding Author

1. INTRODUCTION

The usage of biological based polymeric material is very important for economic and environment development. Such a bio-based polymeric material is hazelnut shell.

One of the polymers untested in blending with hazelnut shell particles is polydimethylsiloxane (PDMS). Polysiloxanes are one of the most investigated and useful polymers in the modern world, as this category of polymers shows a diversity of properties combinations not common to other macromolecules: flexible backbone, stability in atmospheric conditions, permeability for different gaseous molecules, hydrophobicity and antiadhesivity, chemical and physiological inertness. One of the main disadvantages of polysiloxane is poor mechanical properties and high cost (Chassé *et al.*, 2012) (Choi *et al.*, 2011).

Rubber materials are often used with different filler materials in order to improve their properties in accordance with the field of use. Among these fillers, silica is the most preferred because it significantly increases the mechanical and rheological properties. With the use of waste hazelnut shell particles, this cost of silica can be saved (Sareena *et al.*, 2012).

Hazelnut or nut is one of the most cultivated and marketed nuts in the world. Turkey is the largest hazelnut producing area in the world, over Italy. Throughout the kernel collecting and industrial processing, a large number of by-products, containing green leafy cover, shell and skin, is acquired. Their discarding represents both an economic drawback for the producers and a serious environmental drawback due to the burning of the crop remainders (Esposito *et al.*, 2017).

There are numerous studies that have been investigated for the probable use of bio-based fillers in rubber studies. Menon et al. studied the natural rubber (NR) modified with cashew nut shell liquid with different amounts and the tear strengths and tensile properties are enriched (Menon *et al.*, 1998). Botros et al studied a natural rubber based lignin containing composite material and it increased the all properties of the composite after the addition (Botros *et al.*, 2005). Shivamurthy et al. studied jatropha seed cake leftover within epoxy and the usage of the jatropha seed cake waste improved the mechanical and wear properties of the composites (Shivamurthy *et al.*, 2014). Karaağaç has experimented procedure of pistachio shells as reinforcement filler in NR/SBR rubber composites (Karaağaç, 2014).

Although the use of different bio-based products as filler material in rubber exists in the literature, with our best knowledge, the hazelnut shell is not used within PDMS rubber. In this study, ground waste hazelnut shell particles with different amount as a filler material was added within PDMS. The mechanical and vulcanization and swelling properties of the composite material were examined.

2. MATERIAL & METHODS

Waste hazelnut shells *(Corylus colurna)* (NS) was bought from local bazaars around Mersin. The waste hazelnut shells was washed by tap water five times and the washed material was dried at 35 °C in a laboratory scale oven. After that, washed and cleaned waste hazelnut shells was ground with laboratory type grinder machine. Then, the ground particles were sorted by size with a laboratory type shaking sieve machine. During the study, only particles below 250 microns of the ground waste hazelnut shells were used.

The PDMS with different NS content were produced with using the chemicals that was summarized in Table 1.

Table 1. The recipe of PDMS/NS Composite

Materials	Function	phr
Silicone (VMQ type)	Rubber	100
CC6	Curing Agent	3
Waste Hazelnut Shell	Bio-Based Filler	0-2-5-10

Rubber compound with waste hazelnut shell (NS) was mixed with a Baihong mark ML-132 model Kneader type closed mixer. After the rubber mixture were reached up to 60 °C, the blending was stopped and prepared material were flattened in a Baihong mark HL-66 model laboratory scale two-roll mill to prepare a 2 mm-shaped compound. After that, the prepared material was taken into a 2 mm mold and vulcanized in a thermal hydraulic press under 20 MPa pressure for moving die rheometer (MDR) specified minutes (Akbay, *et al.*, 2017).

The tensile properties of PDMS/NS composites were concluded in accordance with the ASTM D412 Type C standard. The mechanical test was completed by Shimadzu AGS-X universal testing machine with a 20 kN gauge. The crosshead speed was done at a 50 mm/min rate according to the ASTM D412 Type C standard. In addition, the hardness values of prepared samples were obtained by using laboratory type Shore A testing apparatus (Özdemir *et al.*, 2017).

The gel content of the PDMS/NS composite was performed via Soxhlet extraction method and was calculated using Eq. (1);

$$Gel\ Content\ (\%) = {}^{w_f}/_{w_i} * 100 \quad (1)$$

where w_i and w_f are represents to the initial and final weight of sample, respectively. The solvent utilized in the experiment was tetrahydrofuran and the experiments were carried out at 70°C.

The swelling ratio of the PDMS/NS composite was done by using petri cup and toluene was used as the swelling medium all the experiments. The swelling ratio of the samples was calculated using Eq. (2);

$$Swelling\ Ratio\ (\%) = {}^{w_f - w_i}/_{w_i} * 100 \quad (2)$$

where w_i and w_f are represents to the initial and final weight of sample, respectively (Akbay *et al.*, 2018).

Vulcanization process of PDMS/NS composites were done by using Moving Die Rheometer at 170 °C. Cure rate index (CRI) was computed from MDR data with Eq. (3), where t_{90} is the optimum cure time and t_{s2} is the scorch time (Güngör *et al.*, 2018).

$$CRI = {}^{100}/_{(t_{90} - t_{s2})} * 100 \quad (3)$$

3. RESULTS & DISCUSSIONS

3.1. Tensile Properties

The tensile properties of PDMS/NS sample are given in Fig. 1. The mechanical test results showed that the adding of waste hazelnut shell (NS) into the composite matrix enhanced the tensile properties. NS addition increased both tensile strength and elongation at break values up to 10 percent. Higher NS amounts were also studied; however, higher NS content decrease the mechanical properties drastically. Because of the disproportionate amount of filler used, decrement of free spaces has been occurred between the rubber chains, resulting in decreased mechanical properties. In addition, the hardness value of samples decreased with the increase of NS content in silicone matrix.

3.2. Vulcanization Properties

To estimate the vulcanization procedure and vulcanization properties of PDMS/NS composites, MDR test was done and torque curves were given in Fig. 2. The maximum torque (M_H) provides information about the mechanical properties of the material and the high torque values indicates that the prepared composite has high tensile properties (Güngör *et al.*, 2019). The results showed that the prepared PDMS/NS composites has increased the vulcanization properties of the samples. Moreover, imitation period of the prepared samples was increased with the increasing NS content.

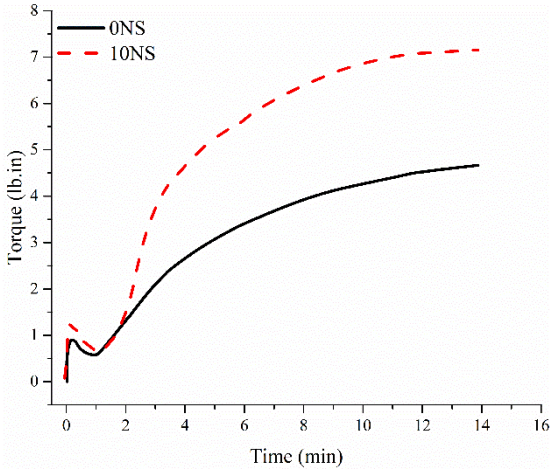

Fig. 2. MDR curves of PDMS/NS composites

Vulcanization parameters of PDMS/NS composite was given in Table 1. Optimum vulcanization time (t_{90}) and scorch time (t_{s2}) are noteworthy parameters to assess the vulcanization process (Güngör *et al.*, 2018). The high t_{s2} value and the low t_{90} value indicate that the material is adequate in terms of vulcanization properties. As can be understood from the Table 1, mechanical tests are in line with the data when the vulcanization parameters are considered. Moreover, the higher cure rate index value was obtained in 10NS sample compared to control sample.

Table 1. Vulcanization parameters of PDMS/NS composites

Sample	t_{s2} (min)	t_{90} (min)	CRI
0NS	1.11	13.32	8.19
10NS	1.69	11.51	10.18

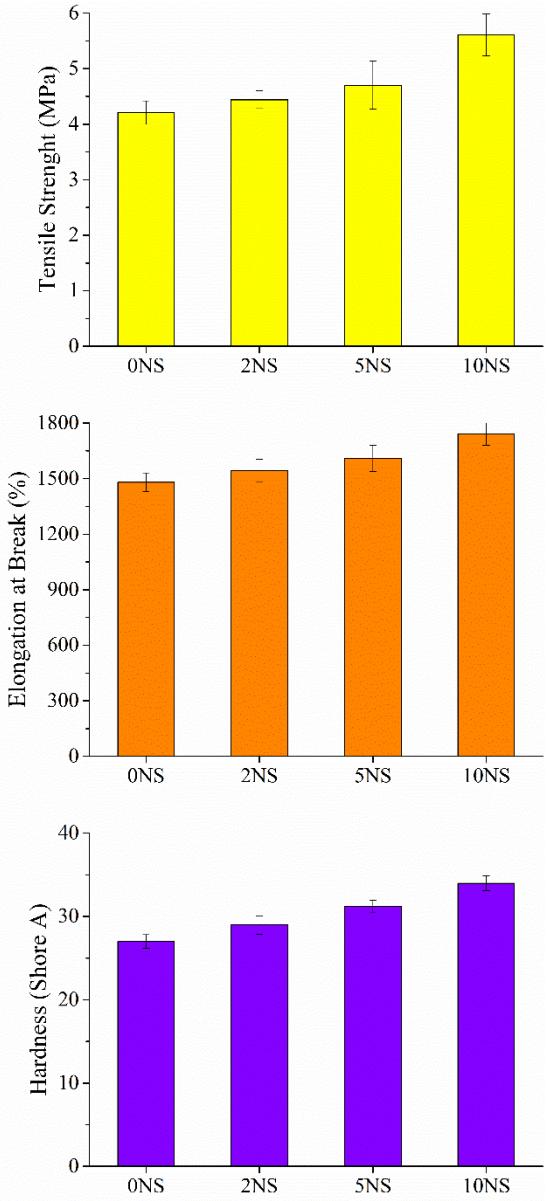

Fig. 1. Mechanical test results of PDMS/NS composites

3.3. Swelling Properties

The gel content and swelling ratio of PDMS/NS composite are shown in Figure 3. Gel content and swelling ratio are related with the crosslink density of rubber composite (Akbay *et al.*,2018; Güngör *et al.*, 2019). Therefore, it gives information about the mechanical properties of the material. Besides, it is recognized that the gel content and swelling ratio are inversely proportional to each other. As can be concluded from Fig. 3, the addition of NS into the silicone matrix

has noticeably advanced the crosslink density of prepared samples. The gel content of prepared samples reached at around 88% for 10 NS sample while swelling ratio of samples determined as around 120% for 10 NS sample. Thus, the best resulting NS content concluded as 10 phr according to the swelling properties. Also, the achieved results are compatible with the tensile and vulcanization results.

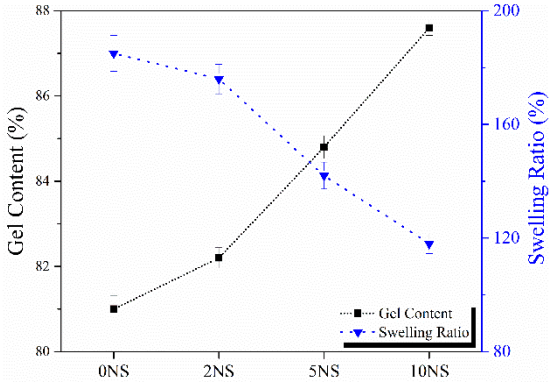

Fig. 3. Gel content and swelling ratio of PDMS/NS composites

4. CONCLUSION

In this study, we aimed to use waste hazelnut shells as a bio-based filler within the Silicone rubber. Without using any chemicals or used any useful resources, we manage to improve the properties of a highly used engineering rubber, which is PDMS. The MDR test results showed that the addition of NS particles increased the t_{s2} values up to 1.69 minutes which is very good for rubber moulding processes. Mechanical properties of samples have increased with the addition of the NS particles. Additionally, increasing together for values of elongation break and tensile strength values indicates the toughness of the samples has increased which could amplify the usage circumstances of the prepared composite. Swelling analysis were done in order to understand the gel content variation for different NS containing PDMS composite. The gel content and swelling ratio results revealed that the accumulation of NS particles is adequate to improve its swelling properties. The study, according to the analysis, indicated that the best accomplishing sample is 10NS. The results are trustworthy enough to practise waste hazelnut shell particles within PDMS and other polymeric and rubber materials as a bio-based filler material for both economical and waste management purposes.

REFERENCES

Akbay, İ. K., Güngör, A. and Özdemir, T. (2017) 'Optimization of the vulcanization parameters for ethylene–propylene–diene termonomer (EPDM)/ground waste tyre composite using response surface methodology', *Polymer Bulletin*, Vol. 74 No. 12, pp. 5095–5109.

Akbay, İ. K., Güngör, A. and Özdemir, T. (2018) 'Using fish scales (Sardina pilchardus) within ethylene-propylene-diene ter monomer rubber as bio-based filler', *Journal of Applied Polymer Science*. John Wiley and Sons Inc., Vol. 135 No. 39.

Botros, S., Eid, M. and Nageeb, Z. (2005) 'Thermal Stability and Dielectric Relaxation of NR/Soda Lignin and NR/thiolignin Composites', *Egypt. J. Solids*, Vol. 28 No. 1, pp. 67–83.

Chassé, W. *et al.* (2012) 'Cross-Link Density Estimation of PDMS Networks with Precise Consideration of Networks Defects', *Macromolecules*. Vol. 45 No. 2, pp. 899–912.

Choi, S.-J. *et al.* (2011) 'A Polydimethylsiloxane (PDMS) Sponge for the Selective Absorption of Oil from Water', *ACS Applied Materials & Interfaces*. American Chemical Society, Vol. 3 No. 12, pp. 4552–4556.

Esposito, T. *et al.* (2017) 'Hazelnut (Corylus avellana L.) Shells Extract: Phenolic Composition, Antioxidant Effect and Cytotoxic Activity on Human Cancer Cell Lines.', *International journal of molecular sciences*. Vol. 18 No. 2.

Güngör, A. *et al.* (2018) 'Flexible X/Gamma ray shielding composite material of EPDM rubber with bismuth trioxide: Mechanical, thermal investigations and attenuation tests', *Progress in Nuclear Energy*, Vol. 106, pp. 262-269.

Güngör, A., Akbay, I. K. and Özdemir, T. (2019) 'Waste walnut shell as an alternative bio-based filler for the EPDM: mechanical, thermal, and kinetic studies', *Journal of Material Cycles and Waste Management*. Vol. 21 No. 1, pp. 145–155.

Karaağaç, B. (2014) 'Use of Ground Pistachio Shell as Alternative Filler in Natural Rubber/Styrene–Butadiene Rubber-Based Rubber Compounds', *Polymer Composites*, Vol. 35 No. 2, pp. 245–252.

Menon, a R. R., Pillai, C. K. S. and Nando, G. B. (1998) 'Physicomechanical properties of filled natural rubber vulcanizates modified with phosphorylated cashew nut shell liquid', *Journal of Applied Polymer Science*, Vol. 68 No. 8, pp. 1303–1311.

Özdemir, T. *et al.* (2017) 'Nano lead oxide and epdm composite for development of polymer based radiation shielding material: Gamma irradiation and attenuation tests', *Radiation Physics and Chemistry*, Vol. 144, pp. 248–255.

Sareena, C., Ramesan, M. T. and Purushothaman, E. (2012) 'Utilization of peanut shell powder as a novel filler in natural rubber', *Journal of Applied Polymer Science*. Wiley Subscription Services, Inc. Vol. 125 No. 3, pp. 2322–2334.

Shivamurthy, B. *et al.* (2014) 'Mechanical properties and sliding wear behavior of jatropha seed cake waste/epoxy composites', *Journal of Material Cycles and Waste Management*, Vol. 17 No. 1, pp. 144–156.

MICROWAVE-ASSISTED BIODIESEL PRODUCTION FROM OLEIC ACID

Servet Boluk [*1], Ozgur Sonmez [2]

[1] Mersin University, Faculty of Science and Letters, Chemistry, Mersin, Turkey, servetboluk@gmail.com

[2] Mersin University, Faculty of Science and Letters, Chemistry, Mersin, Turkey, ossonmez@mersin.edu.tr

ABSTRACT

In this work, microwave-assisted esterification of oleic acid was carried out in the presence of methanol and 1-butyl-3 methylimidazolium hydrogen sulphate ([BMIM]HSO_4) which is an ionic liquid. Parametric studies have been carried out to investigate optimum conditions (amount of catalyst, reaction time, amount of ionic liquid and temperature). Also, the effects of different catalysts and heating systems have been investigated at the same conditions. A maximal yield of 90.87% was obtained while mole ratio of methanol to oil, ionic liquid dosage, reaction temperature and reaction time were 9:1, 20%, 120 and 90 min, respectively. Oleic acid esterification was carried out using the microwave, ultrasonic and mechanical methods and thus the effect of different methods has been examined. Microwave method has been found to be more effective than the other two methods. In addition, the effect of different catalysts on the esterification of oleic acid was investigated using 1 methylimidazolium hydrogen sulphate ([HMIM] HSO_4), 1-butyl-3 methylimidazolium hydrogen sulphate ([BMIM]HSO_4) and H_2SO_4. It was found that ([BMIM]HSO_4) has the high catalytic activity due to its reusability and high yield, although approximately 2% higher yield was obtained when H_2SO_4 was used.

Keywords: *Biodiesel, Ionic liquid, Renewable energy, Microwave, Esterification*

[*] Corresponding Author

1. INTRODUCTION

There are various methods for producing biodiesel, different conditions and various raw materials. Biodiesel is an alternative, efficient, 100% natural and clean energy source to oil diesel (Sani et al., 2012). Biodiesel can be produced by transesterification of triglycerides or esterification of free fatty acids using short chain alcohols such as methanol or ethanol. In both methods, different types of catalysts are used (Mostafaei et al., 2015). Traditionally, acidic and basic homogeneous catalysts such as sodium hydroxide, potassium hydroxide, sulfuric acid, phosphoric acid have been used in both transesterification and esterification reactions (Ding et al., 2018; Felizardo et al., 2006). However, despite the high efficiency achieved with the use of these catalysts, they have disadvantages such as by-product formation, corrosion of equipment, large quantities of waste water and difficult to recover (Ding et al., 2018; Park et al., 2010). Experts work on alternative catalysts to prevent these problems. Nowadays, as an alternative green catalyst, ionic liquids are used in biodiesel production. Ionic liquids that are a kind of salt, have important properties such as their thermal stability, ease of recovery, and low vapor pressure, which makes them an alternative to hazardous and volatile chemicals (Mohammad et al., 2012; Mohammad et al., 2014; Ullah et al., 2017). Ionic liquids are formed by "loosely" coordinating a large organic cation with an anion. The properties of anion and cation can be changed with combinations changes (Keskin et al., 2007). These properties of ionic liquids cause them to be used in a wide variety of chemical applications. The acidic and basic behavior of ionic liquids can be adjusted by changing the cation-bound anion (Mohammad et al., 2013). In addition, ionic liquids can easily be separated from the reaction mixture, and therefore, ionic liquids cause less environmental pollution due to their reusability compared to conventional catalysts (Xu et al., 2015).

In the conventional biodiesel production, a transesterification or esterification reaction is performed by thermal heating in the presence of a catalyst, and the energy consumption is high as the reaction takes a long time. Therefore, there is a need to develop new biodiesel production methods. Recently, as a green method, microwave-assisted biodiesel production method has been developed for biodiesel production. In contrast to conventional heating, microwave assisted heating provides homogeneous heating, the reaction takes place in a shorter time, and it is easier to separate the glycerin from the biodiesel. Microwave heating reduces costs, is energy efficient and allows for more pure products (Bokhari et al., 2015; Buasri et al., 2016; Handayani et al., 2012). In addition, microwave-assisted heating allows chemical reactions to be carried out in a cleaner, more convenient and safe manner (Hsiao et al., 2011).

In this study, it is aimed to develop alternative green methods in biodiesel production. For this purpose, esterification of oleic acid was carried out by microwave assisted heating under two different ionic liquid catalysts. The effect of catalyst type, amount, temperature, reaction time and molar ratio of methanol/oleic acid was investigated and discussed. In addition, esterification of oleic acid was carried out with homogeneous acidic catalyst and conventional heating method under the specified conditions and thus the comparison of the classical method with the green method was made.

2. MATERIAL AND METHODS

Firstly 0.05 mol (15.8 mL) of oleic acid and methanol and catalyst in the specified proportions were added to a 100 mL volume of teflon reactor. The parameters tested were temperature (60-120 °C), reaction time (5-90 min), amount of ionic liquid (1-20% w / w) and methanol-oleic acid molar ratio (3:1-15:1).

After reaching the time set for the reaction, the reaction vessel was allowed to cool to room temperature by continuing stirring in the microwave. The reaction mixture, which then came to room temperature, was transferred to a separatory funnel to allow the products to separate from the by-products and allowed to stand for 24 hours to form two different phases. After two different phases were formed, the upper phase was washed three times with ultra-pure water to remove unreacted methanol and impurities. The upper phase consisting essentially of methyl oleate was removed after separate washing and heated at 105 °C for 24 hours to remove unreacted methanol and water. The experiments were repeated three times.

2.1. Determination of Acidity Value

The acid value of the obtained product was determined using standard acid / base titration method to measure. A solution of 0.1 M KOH was prepared by dissolving 5.6 g of KOH in 1 L of ethanol. 25 ml of ethanol was added to a flask and neutralized by titrating KOH to the turning point under phenolphthalein indicator. 1 gram of the methyl oleate mixture synthesized in neutralizing ethanol was added and titrated with 0.1 M KOH solution to the turning point under phenolphthalein indicator. The acid value of the product was calculated by the following formula:

$$A = \frac{V \times C_{KOH} \times M_{W(KOH)}}{m_{MO}} \quad (1)$$

V : Volume of KOH standard solution spent for methyl oleate titration
C_{KOH} : Concentration of potassium hydroxide standard solution
$M_{W(KOH)}$: Molecular weight of KOH
m_{MO} : Weight of methyl oleate
A : The acid value of the product

2.2. Calculation of Methyl Oleate Conversion Based on Acidity Number

Methyl oleate conversion was calculated using the following equation using acidity values:

$$Conversion = \frac{A_f - A_l}{A_f} \times 100 \quad (2)$$

A_f : The acidity of oleic acid (First)
A_l : The acidity of the product (Last)

2.3. *Calculation of Methyl Oleate Yield*

Methyl oleate content was calculated using the following equation:

$$Yield = \%A_{MO} \times \frac{m_1}{m_2} \times 100 \quad (3)$$

$\%A_{MO}$: Methyloleate ratio (from GC-FID)
M_1 : Mass of product
M_2 : Mass of oleic acid

3. RESULTS AND DISCUSSION

3.1. Effect of Temperature

Temperature is one of the most important factors that may affect the methyl oleate yield. Experiments were conducted between 60-120 °C to investigate the effect of temperature on methyl oleate yield and conversion and the results were discussed. The reaction time, methanol / oleic acid ratio and [BMIM]HSO_4 were kept constant for 30 min, 9:1 molar ratio and 10% (w/w%), respectively. In Figure 1, it is seen that both conversion and methyl oleate yield increases with temperature increase. As we all know, increasing the reaction temperature facilitates molecular collision and miscibility of the reactants. As a result, the reaction rate and the conversion of oleic acid increase with increasing temperature. However, at higher temperatures (above 100 °C) the effect of temperature remains weaker. Because at these temperatures, methanol passes into vapor phase and its interaction with oleic acid decreases (Zhang et al., 2012).

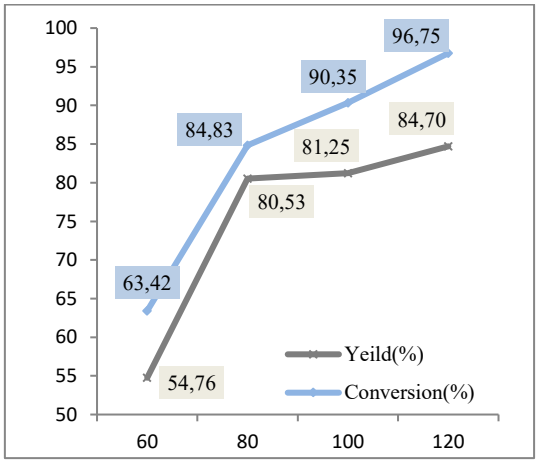

Fig. 1. Effect of reaction temperature on methyl oleate yield (Reaction parameters: 30 min, 9:1 Methanol/Oleic Acid molar ratio, 10% [BMIM] Ionic liquid)

3.2. *Effect of Reaction Time*

Reaction time is another important factor affecting methyl oleate yield. The effect of the reaction time was investigated by performing experiments between 5 and 90 minutes. When examined figure 2, it is seen that the reaction equilibrium shifts to the products with increasing reaction time and thus the yield of methyl oleate increases. Further increase in time (45 min., 60 min., 75 min. and 90 min.) did not lead to a significant increase in methyl oleate yield, indicating that the reaction was near equilibrium.

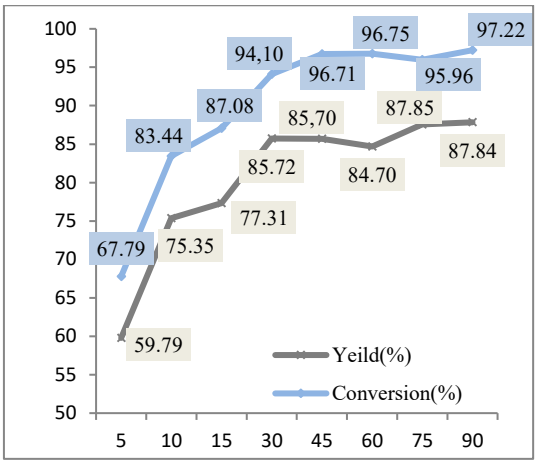

Fig. 2. Effect of reaction time on methyl oleate yield (Reaction parameters: 120°C, 9:1 Methanol/Oleic Acid molar ratio, 10% [BMIM] Ionic liquid)

3.3. *Effect Molar Ratio of Methanol/Oleic Acid*

Another important parameter that has an effect on biodiesel yield is the molar ratio of methanol/oleic acid. To obtain the best conditions for biodiesel production, the experiments were carried out at 120 °C with a reaction time of 30 min., 10% [BMIM]HSO_4 and 3:1, 6:1, 9:1, 12:1, 15:1 methanol/oleic acid molar ratios. In figure 3, when the molar ratio is increased from 3:1 to 9:1, the yield and conversion increased from 76.93% and 82.72% to 85.72% and 94.10%, respectively. When the molar ratio of methanol to oleic acid is greater than a certain value, the amount of methanol has little effect on the reaction rate (Li et al., 2014). When the molar ratio increases, the oleic acid and the ionic liquid used as the catalyst become diluted. As a result, yield decreases (Zheng et al., 2017).

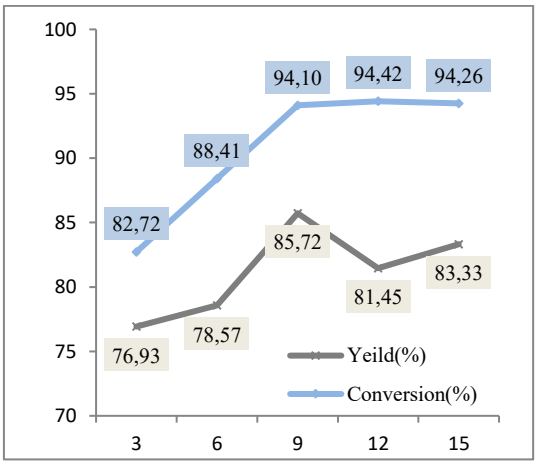

Fig. 3. Effect of molar ratio of methanol/oleic acid on methyl oleate yield (Reaction parameters: 30 min, 120°C, 10% [BMIM] Ionic liquid)

3.4. *Amount of Catalyst*

The amount of catalyst also plays an important role in the esterification reaction. Changing amount of catalyst [BMIM]HSO_4 (1%; 3%; 5%; 10%; 15%; 20%). Experimental results are shown in figure 4 increases in both yield and conversion were observed by increasing the amount of ionic liquid used as the catalyst. When the amount of [BMIM]HSO_4 is small, the low number of active sites in the catalyst to accelerate the reaction between methanol and oleic acid leads to low yield (Zheng et al., 2017). The increase in the amount of ionic fluid causes an increase in the viscosity of the reaction medium, which affects mass transfer and reaction speed (Li et al., 2014).

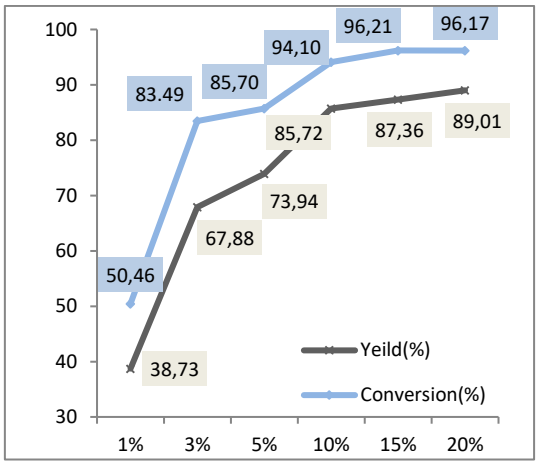

Fig. 4. Effect of catalyst [BMIM] on methyl oleate yield (Reaction parameters: 30 min, 120°C, 9:1 Methanol/Oleic acid molar ratio)

Experiments were performed under the conditions determined using the recovered ionic liquid and the results are shown in Figure 5. When Figure 5 is examined, there is a decrease in both conversion and yield towards 4. usage. The maximum reduction was about 10% after 4. usage.

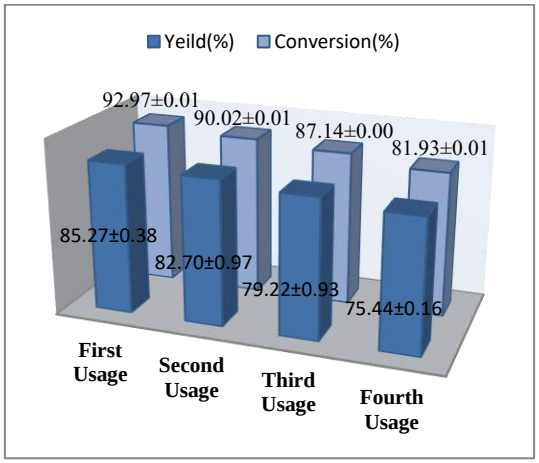

Fig. 5. Effect of re-use of ionic liquid on methyl oleate yield in microwave assisted process (Reaction parameters: 30 min, 120°C, 9:1 Methanol/Oleic acid molar ratio, 10% [BMIM] Ionic liquid)

3.5. Effect of Different Catalysts

In the production of biodiesel, the amounts of catalyst as well as the effects that they may have depending on the type are important. For this purpose, the effect of catalyst type on yield and conversion was investigated by using three different catalysts, [BMIM]HSO_4, [HMIM]HSO_4 and H_2SO_4. The results are shown in Figure 6. The highest methyl oleate yield and conversion were observed under H_2SO_4 catalysis under similar reaction conditions. The yield obtained when H_2SO_4 is used is 87.74%. The yields when [BMIM]HSO_4 and [HMIM]HSO_4 were used were 85.72% and 81.97%, respectively. It is thought that the number of ions provided by the chemicals used as catalysts is the most important factor. Therefore, it is thought that the efficiency of H_2SO_4 is high and it provides cationic superiority compared to other chemicals with two H^+ cations. The difference in yield between ionic liquids can be explained by its solubility during the reaction due to the difference between polar structures. Therefore, the use of ionic liquids compared to H_2SO_4 is primarily environmentalist, their reaction-related enhanceability and low corrosive effects.

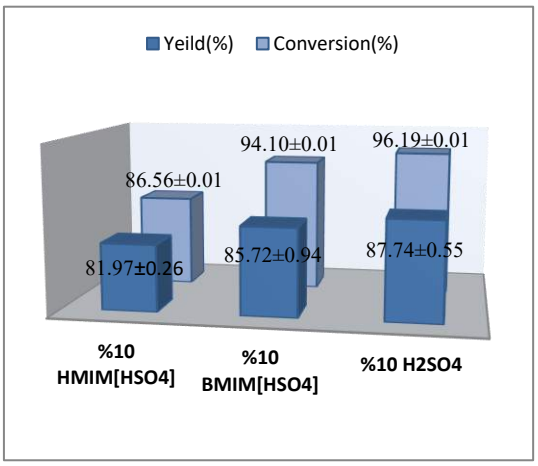

Fig. 6. Effect of different catalyst usage on methyl oleate yield (Reaction parameters: 30 min, 120°C, 9:1 Methanol/Oleic acid molar ratio, 10% [BMIM] Ionic liquid)

3.6. Effect of Different Heating Types

The effects of different types of heating in biodiesel production are effective in transformation. Microwave-assisted, ultrasonic-assisted and conventional (convection) heating types were applied under reaction conditions. The results are shown in Figure 7. The highest methyl oleate yield was 80.53% microwave-assisted under similar reaction conditions. The lowest yield was obtained using the classical method. This may be due to increased efficiency of activation by localized heating in the microwave. Therefore, it is believed that methanol provides better mixing and the catalyst can be involved in the more efficient reaction.

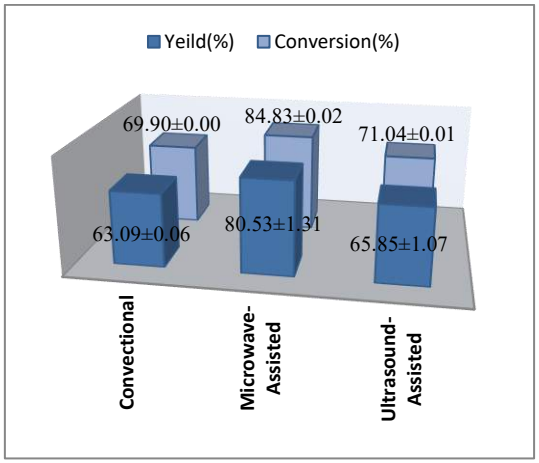

Fig. 7. Effect of different heating types on methyl oleate yield (Reaction parameters: 60 min, 80°C, 9:1 Methanol/Oleic Acid molar ratio, 10% [BMIM])

4. CONCLUSION

In order to investigate the effect of different catalyst types, three different catalysts were used in microwave assisted esterification of oleic acid. Among these catalysts, the highest yield and conversion were achieved when H_2SO_4 was used. However, H_2SO_4 has some disadvantages such as being corrosive, unrecoverable and causing environmental pollution. These disadvantages can be overcome by using ionic liquids as catalysts. It was also observed that [BMIM]HSO_4 was more effective than [HMIM]HSO_4 usage.

In the experiments carried out with different biodiesel production methods, classical method, microwave assisted and ultrasonic assisted methods were compared. At this stage the methyl oleate yield of the methods were observed. The highest yield was observed in microwave assisted method with 80.53%.

Re-usability of the catalyst in microwave-assisted biodiesel production was observed with reductions in yields 4 repetitions. Methyl oleate yields due to reuse were 85.27%, 82.70%, 79.22% and 75.44% respectively. According to this, methyl oleate yield was found to have lost about 10% in the fourth usage.

It was observed that microwave assisted esterification reactions were advantageous with these experiments. Likewise, the reusability of [BMIM] HSO_4 ionic liquid as a catalyst compared to other catalysts was found to be of great advantage with the methyl oleate yield in the reactions and the environmental properties mentioned in the thesis.

In this study, in order to find the most suitable conditions for the esterification reaction, the main reaction parameters affecting biodiesel conversion were studied and satisfactory results were obtained. However, further work is needed to improve reaction conditions. Further investigation of the effect of reaction time on biodiesel yield can give more satisfactory results. The biphasic formation was observed before the ionic liquid removed by washing was separated and reused. This is an important factor affecting efficiency and reuse. Therefore, it is important to wait at least 1 week to achieve separation.

Additional studies can be carried out by producing acidic catalysts which have more than one cationic structure and their polarity is stable with appropriate solubility to the reaction medium. These data are thought to be effective in the results.

ACKNOWLEDGEMENTS

The authors thank the Research Fund of Mersin University in Turkey with Project Number: 2018-1-TP2-2910

REFERENCES

- Bokhari, A., Chuah, L. F., Yusup, S., Ahmad, J., Shamsuddin, M. R., Teng, M.K. (2015). "Microwave-assisted methyl esters synthesis of kapok (ceiba pentandra) seed oil: Parametric and optimization study." *Biofuel Research Journal*, Vol. 2, No. 3, pp. 281–287.
- Buasri, A., Lukkanasiri, M., Nernrimnong, R., Tonseeya, S., Rochanakit, K., Wongvitvichot, W., Loryuenyong, V. (2016). "Rapid transesterification of jatropha curcas oil to biodiesel using novel catalyst with a microwave heating system." *Korean Journal of Chemical Engineering*, Vol. 33, No. 12, pp. 3388–3400.
- Bundhoo, Z. M. (2018). "Microwave-assisted conversion of biomass and waste materials to biofuels." *Renewable and Sustainable Energy Reviews*, Vol. 82, No. 5, pp. 1149–1177.
- Demirbas, A. (2008). "Biofuels sources, biofuel policy, biofuel economy and global biofuel projections." *Energy Conversion and Management*, Vol. 49, No. 8, pp. 2106–2116.
- Ding, H., Ye, W., Wang, Y., Wang, X., Li, L., Liu, D.,Gui, J., Song, C., Ji, N. (2018). "Process intensification of transesterification for biodiesel production from palm oil: microwave irradiation on transesterification reaction catalyzed by acidic imidazolium ionic liquids." *Energy*, Vol. 144, pp. 957–967.
- Felizardo, P., Correia, M.J.N., Raposo, I., Mendes, J. F., Berkemeier, R., Bordado, J. M. (2006). "Production of biodiesel from waste frying oils." *Waste Management*, Vol. 26, No. 5, pp. 487–494.
- Hsiao, M. C., Lin, C. C., Chang, Y. H., (2011). "Microwave irradiation-assisted transesterification of soybean oil to biodiesel catalyzed by nano powder calcium oxide." *Fuel*, Vol. 90, No. 5, pp. 1963-1967.
- Keskin, S., Kayrak D., Talay, U. A., Öner, H. (2007). "A review of ionic liquids towards supercritical fluid applications." *The Journal of Supercritical Fluids*, Vol. 43, No. 1, pp. 150–180.
- Li, Y., Hu, S., Cheng, J., Lou, W. (2014). "Acidic ionic liquid-catalyzed esterification of oleic acid for biodiesel synthesis." *Chinese Journal of Catalysis*, Vol. 35, No. 3, pp. 396-406.
- McKendry, P. (2002). "Energy production from biomass (part 2): conversion technologies." *Biosource Technology*, Vol. 83, No. 1, pp. 47–54.
- Mohammad, F. A. H., Nor, A. S. A. (2012). "An overview of ionic liquids as solvents in biodiesel synthesis." *Renewable and Sustainable Energy Reviews*, Vol. 16, No. 8, pp. 5770–5786.
- Mohammad, F. A. H., Nor, A. S. A. (2013).

"Optimization of oleic acid esterification catalyzed by ionic liquid for green biodiesel synthesis." *Energy Conversion and Management,* Vol. 76, pp. 818–827.

- Mohammad, F. A. H., Nor, A. S. A., Ramli, M. (2014). "Esterification of oleic acid to biodiesel using magnetic ionic liquid: multi-objective optimization and kinetic study." *Applied Energy*, Vol. 114, pp. 809–818.
- Mostafaei, M., Ghobadian, B., Barzegar, M., Banakar, A. (2015). "Optimization of ultrasonic assisted continuous production of biodiesel using response surface methodology." *Ultrasonics Sonochemistry,* Vol. 27, pp. 54–61.
- Oumer, A.N., Hasan, M.M., Aklilu, T.B., R., Mamat, A.A. (2018). "Bio-based liquid fuels as a source of renewable energy: a review." *Renewable and Sustainable Energy Reviews*, Vol. 88, pp. 82–98.
- Handayani, P., Abdullah, A., Hadiyanto, H. (2017). "Biodiesel production from nyamplung (calophyllum inophyllum) oil using ionic liquid as a catalyst and microwave heating system." *Bulletin of Chemical Reaction Engineering & Catalysis*, Vol. 12, No. 2, pp. 293-298.
- Park, J. Y., Kim, D.K. (2010). "Esterification of free fatty acids using water-tolerable amberlyst as a heterogeneous catalyst." *Bioresource Technology*, Vol. 101, No. 1, pp. 62–65.
- Sani, Y. M., Daud, W. M. A. W., & Abdul Raman, A. A. (2013). "Biodesel feedstock and production technologies: successes, challenges and prospects (Vol. 4, pp. 77-101). Intech. Croatia.
- Ullah, Z., Bustam, M. A., Man, Z., Khan A. S., Muhammad, N., Sarwono, A. (2017). "Preparation and kinetics study of biodiesel production from waste cooking oil using new functionalized ionic liquids as catalysts." *Renewable Energy*, Vol. 114, Part B, pp. 755–765.
- Xu, W., Ge, X. D., Yan, X. H., Shao, R. (2015). "Optimization of methyl ricinoleate synthesis with ionic liquids as catalysts using the response surface methodology." *Chemical Engineering Journal*, Vol. 275, pp. 63–70.
- Zhang, L., Cui, Y., Zhang, C., Wang, L., Wan, H., Guan, G. (2012). "Biodiesel production by esterification of oleic acid over brønsted acidic ionic liquid supported onto Fe-incorporated SBA-15." *Industrial & Engineering Chemistry Research*, Vol. 51, No. 51, pp. 16590-16596.
- Zheng, Y., Zheng, Y., Yang, S., Guo, Z., Zhang, T., Song, H., Shao, Q. (2017). "Esterification synthesis of ethyl oleate catalyzed by Brønsted acid–surfactant-combined ionic liquid" *Green Chemistry Letters and Reviews*, Vol. 10, No. 4, pp. 202-209.

CISET - 2nd Cilicia International Symposium on Engineering and Technology
10-12 October, 2019, Mersin / TURKEY

ELECTRICAL CONDUCTIVITY PROPERTIES OF Cu-FeCr/FeB COMPOSITES

Husain Rajab Husain Hraam*[1], Osama Ali Ehbil Kriewah[1], Mehmet Akkaş[2] and Serkan Islak[2]

[1] Kastamonu University, Institute of Science, Kastamonu, Turkey, hraam.hrh@gmail.com, osamakrewa00@gmail.com

[2] Kastamonu University, Engineering and Architecture Faculty, Mechanical Engineering, Kastamonu, Turkey, mehmetakkas@kastamonu.edu.tr, serkan@kastamonu.edu.tr

ABSTRACT
Although copper and its alloys have very good electrical conductivity, they have weak mechanical properties. This is a point that should be focused on scientists working on materials technologies. In this study, we added FeCr and FeB into copper and tried to improve the mechanical properties without decreasing the electrical conductivity. Cu-FeCr/FeB composites were produced via powder metallurgy method. Optical microscope was used to determine the distribution of the supplements. Hardness was measured for mechanical properties. The electrical conductivity properties of the coatings were evaluated with eddy current instruments. Although the electrical conductivities of the composites are very small compared to the Cu material, it has been determined that the composites exhibit a very good hardness values in comparison to the Cu material.

Keywords: *Electrical conductivity, Hardness, Copper, FeCr, FeB*

* Corresponding Author

1. INTRODUCTION

Copper and copper alloys are one of the most important groups of commercial metals. They are widely used because of their excellent electrical and thermal conductivity, corrosion resistance and ease of production (ASM Handbook, 1996; Deshpande and Lin, 2006). Pure copper parts produced by powder metallurgy are used in electrical and electronic applications due to their high electrical conductivity. However, low hardness, strength and poor wear resistance limit the use of pure copper. The mechanical properties and wear resistance of copper can generally be improved either by the aging hardening mechanism or by the addition of the harder second phases (Tjong and Lau, 2000; Dong et al., 2001). In aging hardening, the addition of a small amount of chromium and zirconium to copper causes the precipitation of secondary hard phases insoluble in copper at low temperatures. Alloys hardened by this aging lose their strength at temperatures above 500 °C due to structural instability due to grain coarseness of precipitated hard phases (Correia et al., 1997). In the second method, copper matrix composite materials are produced by adding carbide, oxide and borides to copper. The properties of copper can be improved by producing particulate reinforced copper matrix composite materials. Ductile copper generally exhibits poor wear resistance. The material is removed from the copper surface during the abrasion process of the copper on the hard-counter material. Composite materials are produced to reduce the amount of wear products (Alpas et al., 1993).

Ceramic reinforced metal matrix composite materials are used for structural applications in the wear industry due to their super toughness and wear resistance. Especially alumina and silicon carbide based composite materials do not lose their hardness and abrasion resistance in high temperature applications (Chang and Lin, 1996; Upadhyaya and Upadhyaya, 1995; Ritasalo et al., 2011). Copper matrix composite materials are alternative materials where high electrical / thermal conductivity and good abrasion resistance are desired. When carbide reinforced copper composite materials are taken into consideration, studies conducted with SiC in the literature are remarkable. Efe et al., Cu-SiC composites made by cold pressing technique, followed by sintering at different temperatures by reinforcing SiC into copper in different proportions. Increased SiC added to the composites produced by cold pressing showed a high amount of porosity and consequently a decrease in electrical conductivity values (Celebi Efe et al., 2011). In another study, Efe et al., the effect of grain size of SiC on electrical conductivity was investigated. Increased grain conductivity of Cu-SiC composites has been found as less electron will be distributed as grain size increases (Celebi Efe et al., 2012). Zhan and Zhang plated the SiC particles by electroplating with nickel to obtain a stronger bond at the Cu and SiC interface in Cu-SiC composites. While the relative densities of the coated composites were higher than those of the uncoated composites, the electrical conductivity did not change much. However, the mechanical properties of the coated composites were better due to the strong interface bonding (Zhan and Zhang, 2003). Andic et al. studied the effect of alumina on sinterability by adding different proportions of Al_2O_3 to pure copper. They found that the porosity volume decreased with increasing sintering temperature and increased with increasing alumina. Grain growth in Al_2O_3 adversely affected the electrical and mechanical properties of the composite (Adric et al., 2004).

2. EXPERIMENTAL STUDIES

In this study, Cu powder (10 µm particle size, 99.9% purity) as matrix powder and FeB (about 90 µm particle size, ≥ 97.5% purity) and FeCr (about 40 µm particle size, ≥ 97.5% purity) as reinforcements powders were used. Reinforcements were added to Cu as 5% FeB, 5% FeCr and 2.5% FeB + 2.5% FeCr. For mixing, the powders were subjected to agitation at 45 rpm for 20 minutes in turbula. For this process, 10 pieces of 100Cr6 steel balls were used and each ball had a diameter of 10 mm. In the pressing process, the powder was placed in a cylindrical mold having a diameter of 20 mm. The powders were pressed at 500 MPa. The samples were sintered in a tube oven in the protective argon gas atmosphere. Sintering temperature was 900ºC, sintering time was 120 minutes, heating and cooling rate was 10 ºC/min. The microstructure of the obtained samples was examined by optical microscope (OM). The hardness was measured under a load of 1 kg with a microhardness device and at a waiting time of 15 seconds by using SHIMADZU HMV-G21 model microhardness machine. Hardness values were obtained from the upper and lower layers of the samples to determine the hardness; therefore, five hardness values were obtained from each sample. The samples were baked and sanded by passing through coarse and fine sanding steps, respectively, and subsequently polished using 3- and 1-micron diamond solutions, respectively. The electrical conductivities of samples were measured according to ASTM E1004-02 standard with eddy current principle.

3. RESULTS AND DISCUSSION

Optical microscope (OM) photographs of Cu-FeB/FeCr composites produced by powder metallurgy (PM) are shown in Figures 1-4. When the microstructure is examined, there are three different structures. Of these, dark gray and sharp cornered grains show FeB and FeCr, light gray Cu matrix and finally black regions show pores. FeB and FeCr particles are uniformly distributed in the Cu matrix. Lee et al. reported that if the reinforcing particles were not homogeneously distributed, the mechanical and electrical properties of the composite would be negatively affected (Lee et al., 2001).

Fig. 1. OM photograph of un-reinforced copper material

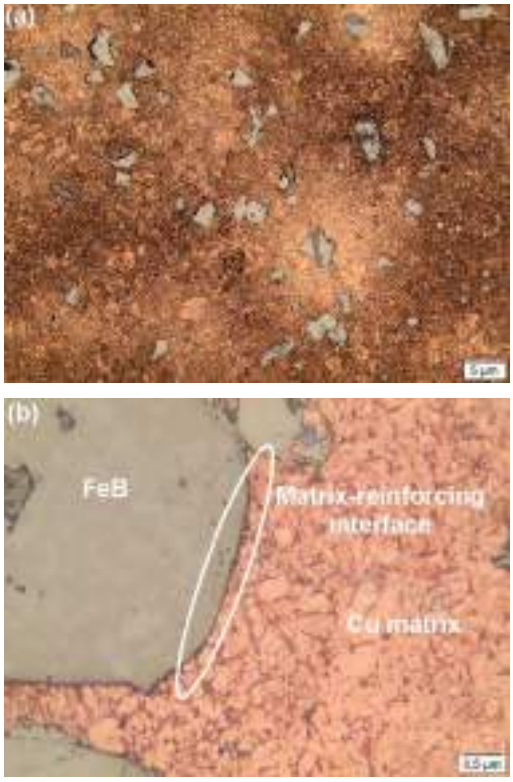

Fig. 2. OM photograph of Cu-5FeB composite: (a) General view and (b) matrix-reinforcing interface

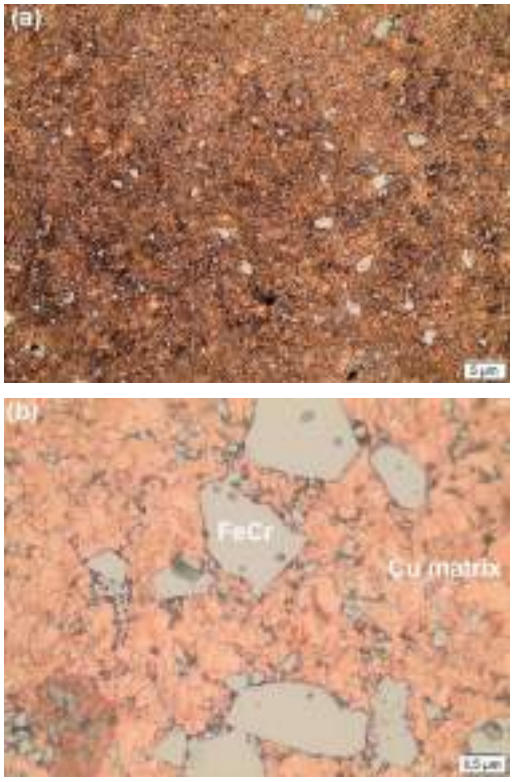

Fig. 3. OM photograph of Cu-5FeCr composite: (a) General view and (b) matrix-reinforcing interface

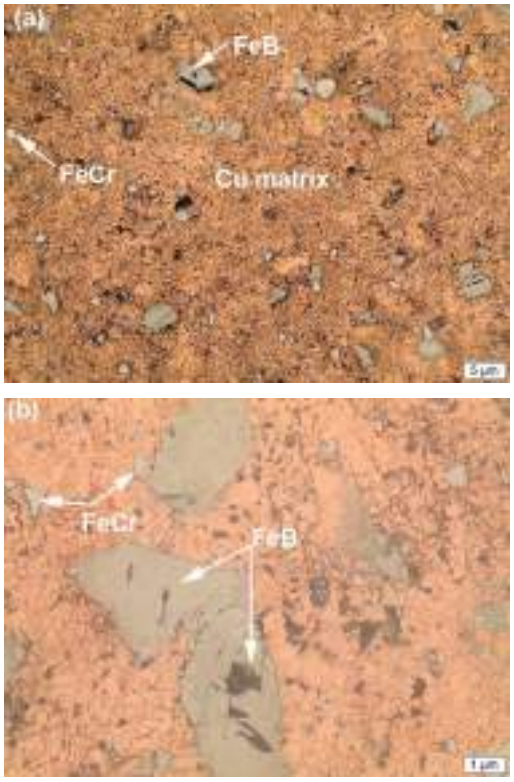

Fig. 4. OM photograph of Cu-2.5FeB-2.5FeCr composite: (a) General view and (b) matrix-reinforcing interface

Figure 5 shows the hardness and electrical conductivity values of Cu-FeB/FeCr composites produced with PM. There was a significant increase in the hardness of Cu-FeB/FeCr composites produced by the addition of reinforcement. The hardness of the pure copper produced was 40.1 HV_1, while the hardness of Cu-5FeB, Cu-5FeCr and Cu-2.5FeB-2.5FeCr composites were measured as 51.6 HV_1, 55.4 HV_1 and 55 HV_1, respectively. This hardness increase was caused by the distribution strengthening effect of FeB/FeCr. In addition, reinforcements caused an increase in the density of dislocation and as a result of this it is thought that the hardness of the composites increased (Sabatello et al., 2000).

Electrical conductivity test results of Cu-FeB/FeCr composites are given in Figure 5. As the reinforcement was added to the Cu matrix, the electrical conductivity of the composites decreased. The electrical conductivity of Cu without addition was measured as 85.5% IACS, Cu-5FeB, Cu-5FeCr and Cu-2.5FeB-2.5FeCr composites as electrical conductivity 68.5% IACS, 66.7% IACS, and 62.3% IACS, respectively. Porosity can be considered as the reason of the low conductivity of pure copper. As is known, if an electrical field is applied to a full dense solid, free electron accelerate and collide with lattice atoms to reduce or lose their kinetic energy. The resulting current is proportional to the average electron velocity determined by the intensity of the applied electric field and the frequency of the collision. In an ideal crystal, electrons move without encountering resistance. But in real crystals, electrons collide with phonons, dislocations, voids, foreign additive atoms, and any lattice defects.

They limit the movement of electrons (Ulutaş and Turhan, 2017). In addition, it has been stated in the studies that both the oxides formed on the powder particle surfaces before sintering and the oxides that may be formed due to the sinter atmosphere during sintering reduce the electrical conductivity of the powder metal samples (Deshpande and Lin, 2006; Akhtar et al., 2009).

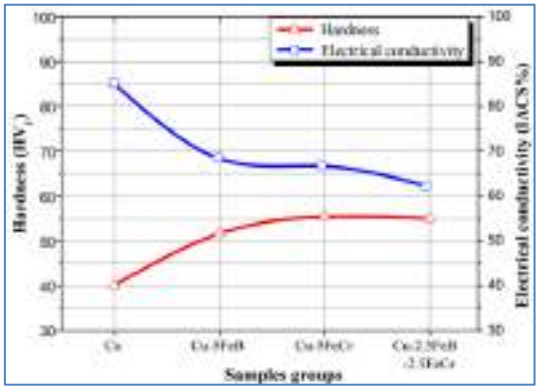

Fig. 5. Graphic of hardness and electrical conductivity of samples

4. CONCLUSION

Cu-FeB / FeCr composite materials were successfully produced by powder metallurgy. Optical microscope images showed that the reinforcing elements were homogeneously distributed in the matrix. Due to the addition of reinforcement, the hardness of the composites increased significantly while the electrical conductivity decreased.

REFERENCES

Adric, Z. Tasic, M. Korac, M. Jordavic, B. and Maricic, A. (2004). "Influence of alumina content on the sinterability of the Cu-Al_2O_3 pseudo alloy (composite)", *MTAEC9* 38, pp. 245-248.

Akhtar, F., Askari, S.J., Shah, K.A., Du, X. and Guo, S. (2009). "Microstructure, mechanical properties, electrical conductivity and wear behavior of high-volume TiC reinforced Cu-matrix composites". *Materials Characterization* 60, pp. 327-336.

Alpas, A.T., Hu, H. and Zhang, J. (1993). "Plastic deformation and damage accumulation below the worn surfaces". *Wear* 162–164, pp. 188-195.

ASM Handbook (1990). *Properties and Selection: Nonferrous Alloys and Special-Purpose Materials*, Vol.2, 10th ed.

Celebi Efe G., Yener, T. Altinsoy, I. Ipek, M. Zeytin, S. and Bindal, C. (2011). "The effect of sintering temperature on some properties of Cu–SiC composite". *Journal of Alloys and Compounds* 509, pp. 6036-6042.

Celebi Efe, G. Zeytin, S. and Bindal, C. (2012). "The effect of SiC particle size on the properties of Cu–SiC composites". *Materials & Design* 36, pp. 633-639.

Chang, S. and Lin, S. (1996). "Fabrication of SiCw reinforced copper matrix composite by electroless copper plating". Scripta Materialia 35, pp. 225-231.

Correia, J.B. Davies, H.A. and Sellars, C.M. (1997). "Strengthening in rapidly solidified age hardened Cu-Cr and Cu-Cr-Zr alloys". *Acta Materialia* 45, pp. 177-190.

Deshpande, P.K. and Lin, R.Y. (2006). "Wear resistance of WC particle reinforced copper matrix composites and the effect of porosity". *Materials Science and Engineering: A* 418, pp. 137-145.

Dong, S.R., Tu, J.P. and Zhang, X.B. (2001). "An investigation of the sliding wear behavior of Cu-matrix composite reinforced by carbon nanotubes". *Materials Science and Engineering*: A 313, pp. 83-87

Lee, D.W., Ha, G.H. and Kim, B.K. (2001). "Synthesis of Cu-Al2O3 nano composite powder". *Scripta Materialia*, Volume 44, Issues 8–9, 18 May, pp. 2137-2140

Ritasalo, R. Liua, X.W. Söderberg, O. Keski-Honkola, A. Pitkänen, V. and Hannula, S-P. (2011). "The Microstructural Effects on the Mechanical and Thermal Properties of Pulsed Electric Current Sintered Cu-Al_2O_3 Composites". *Procedia Engineering* 10, pp. 124-129.

Sabatello, S. Frage, N. and Dariel, M.P. (2000). "Graded TiC-based cermets". *Materials Science and Engineering:* A 288, pp. 12-18.

Tjong, S.C. and Lau, K.C. (2000). "Tribological behaviour of SiC particle-reinforced copper matrix composites". *Materials Letters* 43, pp. 274-280.

Ulutaş, A. ve Turhan, H., (2017). "Toz Metalurjisi İle Üretilen Cu-FeB Kompozit Malzemelerin Mikroyapı ve Elektriksel Özelliklerinin İncelenmesi". *Technological Applied Sciences (NWSATAS)*, 12(2), pp. 43-52.

Upadhyaya, A. and Upadhyaya, G.S. (1995). "Sintering of copper-alumina composites through blending and mechanical alloying powder metallurgy routes". *Materials & Design* 16, pp. 41-45.

Zhan, Y. and Zhang, G. (2003). "The effect of interfacial modifying on the mechanical and wear properties of SiC_p/Cu composites". *Materials Letters* 57, pp. 4583-4591.

CISET - 2nd Cilicia International Symposium on Engineering and Technology
10-12 October, 2019, Mersin / TURKEY

UPPER CRETACEOUS RUDIST-BEARING LIMESTONES OF THE ANAMAS-AKSEKİ CARBONATE PLATFORM (WESTERN OF THE CENTRAL TAURIDES, TURKEY)

Cemile SOLAK [*1], Kemal TASLI [1] , Hayati KOÇ[1]

[1] Mersin University, Faculty of Engineering, Department of Geological Engineering, Mersin, Turkey,
e-mail:cemilesolak@mersin.edu.tr; ktasli@mersin.edu.tr

ABSTRACT
The Anamas-Akseki Carbonate Platform which is located at the western part of the Central Taurides covers Triassic-Eocene aged successions. The rudist-bearing limestones which is characterized the Upper Cretaceous are common in the platform and they were called different names such as Seyran Dağ Limestone and Saytepe Formation. The aim of this study is to determine the stratigraphic distributions of them (at the stage level) by using benthic foraminifera in the Upper Cretaceous of the Anamas-Akseki Carbonate Platform. The Upper Cretaceous is represented by the Cenomanian and the upper Campanian-Maastrichtian limestones in the study area. While the Cenomanian is composed of thick-bedded limestones and dolomitized limestones, the upper Campanian-Maastrichtian is comprised of thick-bedded to massive limestones intercalated with rudist-bearing limestones. The rudists in the upper Campanian-Maastrichtian are represented by mostly fragmented rudist shells. Complete rudist specimens are rare and and did not preserve in growth position. In the upper Campanian rudist shell fragments are mostly mm-scale and not identifiable. In the Maastrichtian, laterally discontinuous and patchy distributed rudist shell fragments are common. Complete rudist specimens are mostly in the upper Maastrichtian and partially identifiable. Therefore, the chronostratigraphic interpretations of the rudist-bearing limestones are based on the presence of benthic foraminifera in this study.
Murciella gr. *cuvillieri* for the upper Campanian and larger hyaline-walled benthic foraminifers (*Orbitoides* sp., *Siderolites* sp., *Omphalocyclus* sp.) and *Rhapydionina liburnica* for the Maastrichtian have been used as an index species in this study.

Keywords: *Upper Cretaceous, Rudist, Limestone, Carbonate platform, Central Taurides*

[*] Corresponding Author

1. INTRODUCTION

Rudists are quite common in the Cretaceous carbonate successions of the peri-Mediterranean carbonate platforms (e.g., Taurides; Poisson, 1977, Monod, 1977; Sarı and Özer, 2001, 2002; Sarı *et al*., 2004; Solak, 2019; Solak *et al*., 2017, 2019; Apennines: Carannante *et al*., 1998, 2003; Ruberti and Toscano, 2002; Simone *et al*., 2003; Adriatic; Korbar *et al*., 2001; Steuber *et al*., 2005). The Upper Cretaceous rudist-bearing limestones are frequently used as guide levels in stratigraphic level determination. It was determined that the thick outer layer of the rudists found in the Upper Cretaceous shallow water carbonate sequences is the most suitable material for SIS (Steuber, 2001, 2003). Therefore, Sr-isotope analysis has been frequently used in the Upper Cretaceous shallow-water rudist-bearing limestones for last 20 years.

Rudist-bearing limestones are frequently found in the different stages of the Upper Cretaceous successions in the Taurides. Complete rudist specimens are more well-preserved in the limestones of the Bey Dağları Carbonate Platforms (Western Taurides) (e.g., Sarı and Özer, 2001, 2002; Solak *et al*., 2018) than Anamas-Akseki Carbonate Platform (Central Taurides) (e.g., Solak *et al*., 2017, 2019). In the Anamas-Akseki Carbonate Platform rudist specimens are mostly fragmented, and in growth position are rare. Because the rudist determinations are not possible from the shell fragments, the ages of the rudist-bearing limestones determine by using benthic foraminifera.

This study aims to explain the stratigraphic distributions throughout the Upper Cretaceous of the rudist-bearing limestones in the Anamas-Akseki Carbonate Platform.

2. GEOLOGICAL SETTING

Anamas-Akseki Carbonate Platform is exposed at the western part of the Central Taurides which is located between the Western Taurides and Eastern Taurides. It is bounded by the Antalya Nappes (Poisson *et al*., 1984) and Antalya Basin to the west and by the Beyşehir-Hoyran-Hadım Nappes (Monod, 1977; Poisson *et al*., 1984) to the east and covers the Mesozoic platform carbonates and Paleocene-Eocene units (Monod, 1977; Şenel, 1996).

The Mesozoic succession which unconformably overlies the Paleozoic units starts with the Upper Triassic clastic units and limestones (Dumont and Kerey, 1975; Şenel, 1996). The Jurassic and Cretaceous are composed of very thick platform carbonate succession. The Cretaceous platform carbonate succession is unconformably overlain by Paleocene-Eocene units in the study area.

The focus of this study is the Upper Cretaceous rudist-bearing limestones in the studied sections of the Anamas-Akseki Carbonate Platform.

3. MATERIAL AND METHODS

The study area is located at the central part of the Anamas-Akseki Carbonate Platform. This study is based on the three measured stratigraphic sections in the study area. Stratigraphic sections were measured and sampled from the eastern, approximately middle and western parts of the platform.

Rudist-bearing limestones were observed macroscopically and existing changes were carefully recorded. Because the rudists are embedded in the matrix, to collect rudist specimens was not possible. The limestone samples were collected for the benthic foraminiferal biostratigraphy and thin-section method was used in this study. Sampling frequency is approximately 2 meters interval.

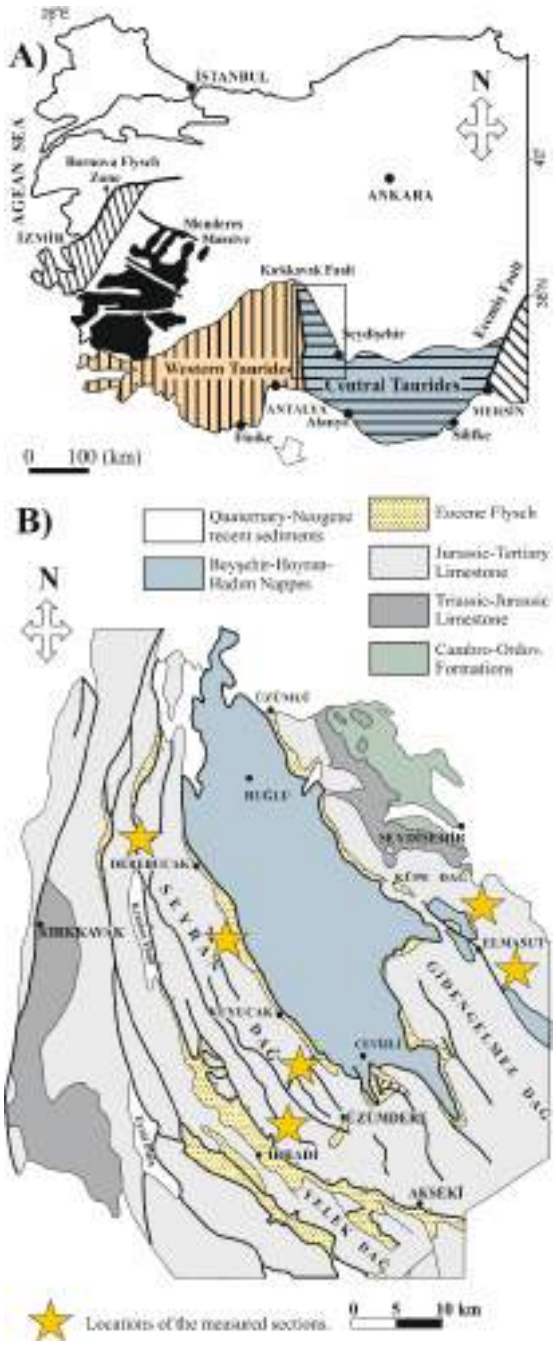

Fig. 1. A. Geographical subdivision of the Taurides (simplified after Özgül, 1984). B. Schematic geological map of the Akseki-Seydişehir region (modified after Monod, 1977) showing the distribution of the measured stratigraphic sections in the Anamas-Akseki Carbonate Platform.

4. RESULTS

The Upper Cretaceous succession in the Anamas-Akseki Carbonate Platform which unconformably overlie the Lower Cretaceous is composed of Cenomanian and Upper Campanian-Maastrichtian limestones. In the Anamas-Akseki Carbonate Platform the Upper Cretaceous successions contain regional-scale a major unconformity which leads the lack of the Turonian-lower Campanian (Solak, 2019; Solak *et al*., 2017, 2019). The Cenomanian limestones do not include rudist or rudist shell fragments in the study area. The unconformably overlying the upper Campanian-Maastrichtian succession is composed of mostly rudist-bearing limestones (Fig. 2 and 3). The lower parts of the upper Campanian do not include rudist/rudist fragments and in the upper parts, these fragments are mm-scale and more sparse according to Maastrichtian.

The rudists in the Maastrichtian are mostly laterally discontinuous and presents patchy distributional pattern (Fig. 2B and 3D). Complete rudist specimens are mostly toppled (Fig. 3B and C).

The Cenomanian is characterized by *Spiroloculina cretacea*, *Chrysalidina gradata*, *Biconcava bentori*, *Pastrikella biplana* and *Pseudorhapydionina dubia* species. The upper Campanian is assigned to the presence of *Murciella* gr. *cuvillieri*. The Maastrichtian is characterized by the occurrence of larger hyaline foraminifera *Orbitoides* sp., *Lepidorbitoides* sp., *Omphalocyclus* sp. and *Siderolites* sp.

Fig. 2. A, B. The Maastrcihtian rudist-bearing limestones in the Anamas-Akseki Carbonate Platform.

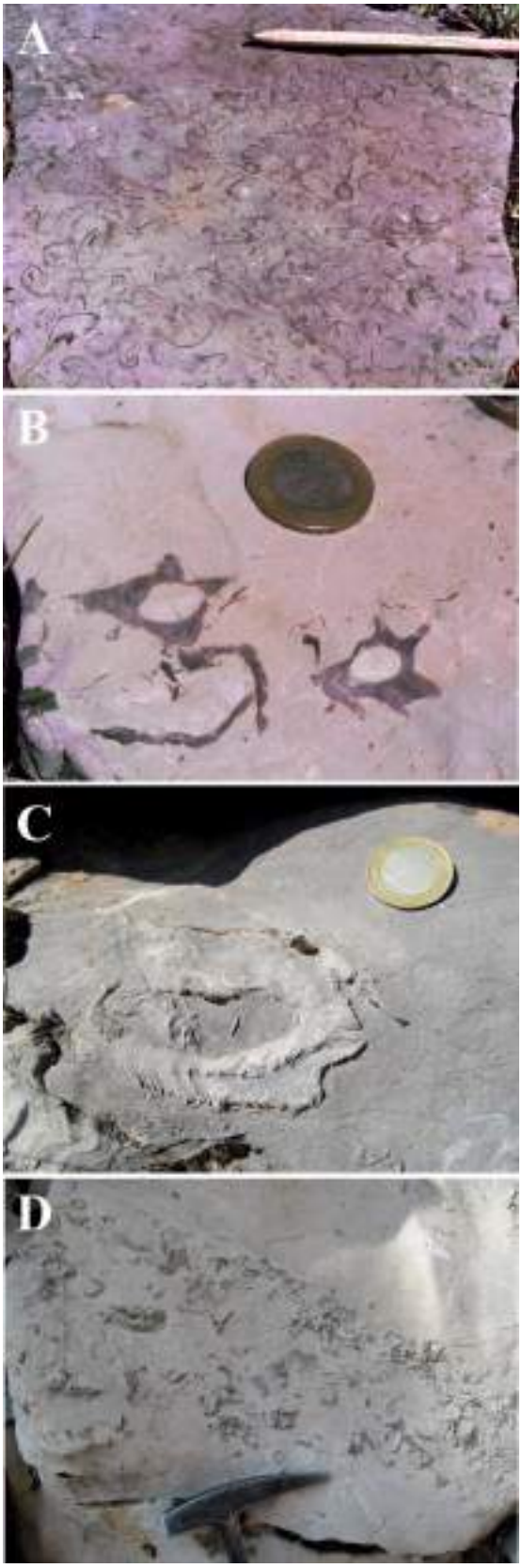

Fig. 3. The upper Maastrichtian rudist-bearing limestones in the Anamas-Akseki Carbonate Platform.

In the upper Maastrichtian which includes *Rhapydionina liburnica* the identifiable rudist fauna

consists of mainly radiolitids including *Bournonia triangulata*, *B. adriatica* and *B.* cf. *quadripinnea* which suggest a late Maastrichtian age (Solak *et al*., 2019).

5. CONCLUSION

In the Anamas-Akseki Carbonate Platform the Cenomanian limestones do not contain mostly rudist/rudist shell fragments. Rudist-bearing limestones are found in the upper Campanian-Maastrichtian successions.

Complete rudist specimens in growth position are rare and most of rudists were fragmented. Thus, the identifiable rudist fauna is limited. Rudist-bearing limestones in the study area deposited in peritidal-subtidal environments of restricted platform.

ACKNOWLEDGEMENTS

This study was supported by the Scientific and Technological Research Council of Turkey (TUBITAK) with Project Number 115Y130.

REFERENCES

Carannante, G., Ruberti, D. and Sirna, G. (1998). "Senonian rudist limestones in the Sorrento Peninsula sequences (Southern Italy)." *Geobios Mémoire Spécial*, Vol. 22, pp. 47–68.

Carannante, G., Ruberti, D. and Simone, L. (2003). Sedimentological and Taphonomic Characterization of Low-Energy Rudist-Dominated Senonian Carbonate Shelves (Southern Apennines, Italy). *Proceedings of the North African Cretaceous rudist and coral formations and their contributions to carbonate platform development.* NATO ASI Series, Kluwer.

Dumont, J., F. and Kerey, E. (1975). "Eğridir Gölü güneyinin temel jeolojik etüdü." *Türkiye Jeoloji Kurultayı Bülteni*, Vol. 18/2, pp. 169-174.

Korbar, T., Fuček, L., Husinec, A., Vlahović, I., Oštrić, N., Matičec, D. and Jelaska, V. (2001). "Cenomanian Carbonate Facies and Rudists along shallow intraplatform basin margin-the Island of Cres (Adriatic Sea, Croatia)." *Facies*, Vol. 45, pp. 39–58.

Monod, O., 1977. Recherches géologiques dans le Taurus occidental au sud de Beyşehir (Turquie) Ph.D. Thesis. Université de Paris-Sud Orsay (unpubl.).

Özgül, N. (1984). "Stratigraphy and tectonic evolution of the Central Taurides." *Proceedings of the International Symposium on the Geology of the Taurus Belt*. Mineral Research and Exploration Institute-Geological Society of Turkey, Ankara, pp. 77–90.

Poisson, A. (1977). Recherches géologiques dans les Taurides occidentales. Ph.D. Thesis, Université de Paris–Sud, Orsay, p. 795.

Poisson, A., Akay, E., Dumont, J.F. and Uysal, S. (1984). "The Isparta angle: a Mesozoic paleorift in the Western Taurides". *Proceedings of the International Symposium on the Geology of the Taurus Belt*, 1983, Mineral Research and Exploration Institute-Geological Society of Turkey, Ankara, pp. 11–26.

Ruberti, D. and Toscano, F. (2002). "Microstratigraphy and taphonomy of rudist shell concentrations in Upper Cretaceous limestones, Cilento area (central-southern Italy)." *Geobios*, Mémoire special, 24, 228–240.

Sarı, B. and Özer, S. (2001). "Facies characteristics of the Cenomanian−Maastrichtian sequence of the Beydağları carbonate platform in the Korkuteli area (western Taurides)." *International Geology Review*, Vol. 43, pp. 830−839.

Sarı, B. and Özer, S. (2002). "Upper Cretaceous stratigraphy of the Beydağları carbonate platform, Korkuteli area (Western Taurides, Turkey)." *Turkish Journal of Earth Sciences*, Vol. 11, pp. 39–59.

Sarı, B., Steuber, T. and Özer, S. (2004). "First record of Upper Turonian rudists (Mollusca, Hippuritoidea) in the Bey Dağları carbonate platform, Western Taurides (Turkey): taxonomy and strontium isotope stratigraphy of *Vaccinites praegiganteus* (Toucas, 1904)." *Cretaceous Research*, Vol. 25, pp. 235–248.

Simone, L., Carannante, G., Ruberti, D., Sirna, M., Sirna, G., Laviano, A. and Tropeano, M. (2003). Development of rudist lithosomes in the Coniacian-Lower Campanian carbonate shelves of central-southern Italy: high-energy vs low-energy settings. *Palaeogeography, Palaeoclimatology, Palaeoecology*, Vol. 200, pp. 5-29.

Solak, C. (2019). Anamas–Akseki ve Bey Dağları Karbonat Platformlari ile Bornova Fliş Zonu'nun Güneybati Kesimindeki Üst Kretase İstiflerinin Stratigrafisi, Paleo–Ortamsal Analizi ve Bentik Foraminifer Mikropaleontolojisi. Ph.D. Thesis, Mersin University, 305 p (in Turkish).

Solak, C., Taslı, K. and Koç, H. (2017). "Biostratigraphy and facies analysis of the Upper Cretaceous–Danian? platform carbonate succession in the Kuyucak area, western Central Taurides, S Turkey." *Cretaceous Research*, Vol. 79, pp. 43–63.

Solak, C., Taslı, K. and Koç, H. (2018). "Alacadağ (Finike, Antalya) Kuzeyindeki Üst Kretase Kireçtaşlarının Foraminiferleri ve Çökelme Ortamları." 2. Kapadokya Yerbilimleri Sempozyumu, pp. 158-159.

Solak, C., Taslı, K., Özer, S. and Koç, H. (2019). "The Madenli (Central Taurides) Upper Cretaceous platform carbonate succession: Benthic foraminiferal biostratigraphy and platform evolution." *Geobios*, Vol. 52, pp. 67–83.

Steuber, T. (2001). "Strontium isotope stratigraphy of Turonian-Campanian Gosau-type rudist formations in the Northern Calcareous and Central Alps (Austria and Germany)." *Cretaceous Research*, 22, 429-441.

Steuber, T. (2003). "Strontium isotope stratigraphy of Cretaceous hippuritid rudist bivalves: rates of morphological change and heterochronic evolution." *Palaeogeography, Palaeoclimatology, Palaeoecology*, Vol. 200, 221-243.

Steuber, T., Korbar, T., Jelaska, V. and Gušić, I. (2005). "Strontium-isotope stratigraphy of Upper Cretaceous platform carbonates of the island of Brać (Adriatic Sea, Croatia): implications for global correlation of platform evolution and biostratigraphy." *Cretaceous Research*, Vol. 26, pp. 741-756.

Şenel, M. (1996). "Anamas-Akseki Otoktonu güney kenarını temsil eden Pirnos Bloğu'nun stratigrafik özellikleri ve paleocoğrafik yorumu; Orta Toroslar, Türkiye (Stratigraphic features and paleogeographical interpretation of the Pirnos Block representing the southern side of the Anamas-Akseki Autochton)." *Bulletin Geological Society of Turkey*, Vol. 39, pp. 19-29 (in Turkish).

CISET - 2nd Cilicia International Symposium on Engineering and Technology
10-12 October, 2019, Mersin / TURKEY

GEODETIC STUDIES ON PRODUCING BASEMAPS

Güler YALÇIN [1], Cafer İlker ÜSTÜNER [*2], Ali ÖZKAN [3], Selim Serhan YILDIZ [4], Burak UŞAK [5]

[1] Osmaniye Korkut Ata University, Engineering Faculty, Department of Geomatics Engineering, Osmaniye, Turkey, guleryalcin@osmaniye.edu.tr

[2] Osmaniye Korkut Ata University, Engineering Faculty, Department of Geomatics Engineering, Osmaniye, Turkey, ilkerustuner@osmaniye.edu.tr

[3] Osmaniye Korkut Ata University, Vocational School of Osmaniye, Map and Cadastre Program, Osmaniye, Turkey, aliozkan@osmaniye.edu.tr

[4] Osmaniye Korkut Ata University, Engineering Faculty, Department of Geomatics Engineering, Osmaniye, Turkey, serhan@osmaniye.edu.tr

[5] Osmaniye Korkut Ata University, Engineering Faculty, Department of Geomatics Engineering, Osmaniye, Turkey, burakusak@osmaniye.edu.tr

ABSTRACT
Basemaps that show the current status of specific area or borders, such as a province, gives valuable information on land. Basemaps constitute a base for many study or engineering projects, such as a cadastral system, a construction project, preparation and implementation of infrastructure plans and superstructure projects. In this context, the position accuracy of basemap information is very important. This position information can be only obtained by constructing precise and accurate geodetic network. CORS (Continuously Operating Reference Stations / TUSAGA-Active-TR) method can be used for accurate and efficient studies in basemap production. In this study, it is aimed to introduce geodetic techniques, data, products and importance of these, showing steps for producing basemaps, and showing steps for collecting detail points by using CORS method in a case study.

Keywords: *Basemap, Geodesy, GNSS, CORS-TR*

[*] Corresponding Author

1. INTRODUCTION

Maps form the basis of many projects on earth. Therefore, basemaps showing the current situation of the land are needed for technical projects to be carried out by local governments, investor public institutions or private sector. They are used as the basis for the preparation and implementation of infrastructure plans and superstructure projects such as sewage, electricity, drinking water, wastewater treatment, natural gas for urbanization efficiently. In addition, according to the purpose of the project, they are considered as tools in geographical information systems. These maps which can be produced in large scales such as 1/1000, 1/2000 and 1/5000 constitute the basis of urbanization activities and maintain their importance in fields such as military, medicine, architecture, archeology, agriculture and forestry, and these current maps are expected to be up to date and high accuracy is requested (Gezmis, 2017). In the basemaps, forest, stream, hill, river building, highway, railroad, power transmission line, channel, slope, well, pole, wall, wire mesh as natural and artificial features are shown as everything, they also contain cadastral data. (Gezmiş, 2017; Tekin, 2017).

Basemaps fall under the category of large-scale maps. Therefore, production standards throughout the country should comply with the Large-Scale Map and Map Information Production Regulation (BÖHHBÜY). The regulation covers the technical principles for producing, compiling, analyzing, storing, visualizing, applying and changing terrain on large scale maps and map information" (BÖHHÜY, 2018: Article 2). However, large-scale maps and map information is to be obtained by TUSAGA-Active (Turkey National Fixed GNSS Network) System, or terrestrial and photogrammetric techniques. (BÖHHÜY, 2018: Article 2).

Natural and artificial details in the current maps produced using terrestrial (classical) methods are measured GNSS (Global Navigation Satellite System) receivers and total stations based on the measurements and calculations of polygon, triangulation, photogrammetric triangulation and leveling points. The basemaps produced by using photogrammetric methods are the maps produced by obtaining data from aerial photographs of the land, although they include terrestrial field studies. With TUSAGA-Active method, position information can be obtained in cm accuracy and with post-processing operations in mm accuracy. Information obtained from TUSAGA-Active stations is utilized in many areas (Yıldırım et.al., 2007), and TUSAGA-Active method is used for the accuracy analysis of the existing maps produced by different methods. (Tekin, 2017).

In this article, geodetic studies carried out in the production of maps by using terrestrial methods are discussed and the importance of geodetic studies is emphasized.

2. GEODESY

Geodesy is a discipline that deals with time-dependent measurement and representation of the earth in three-dimensional space, including the field of gravity. (Krakiwsky and Well, 1971). As Robert Helmert pointed out in 1880, today, in its current, basic and brief definition, geodesy is the measurement and mapping of the earth" (Torge, 2001). Earth measurements can be divided into national measurements or geodetic measurements and plane measurements. National measurements are to obtain the surface of a country with the help of enough fixed-point coordinates. Plane measurements, which can also be referred to as detail measurements, are obtained as the detailed shape of the earth for a local region, usually by omitting the curvature of the earth and the gravity field. (Torge, 2001).

With technological advances in the last 20-30 years, geodetic calculations have become possible to be performed directly by computers instead of classical methods, and angle and length measurements can be performed by electromagnetic measurements and the need for a more current definition has been developed in terms of geodetic applications and results. In this context, geodesy is a science that deals with measuring and transferring the earth and other celestial bodies to the map in three dimensional and time variable space, together with the gravitational field. This definition necessitates the evaluation of geodesy by moving from 3 dimensions to 4 dimensions in position determination. In this context, modern geodesy continues its activities on three main issues: Location determination (determination of the geometric shape of the earth as land, sea and glacier surface), determination of the earth's gravity area and hence the geoid (Üstün and Demirel, 2013).

3. GEODETIC STUDIES IN BASEMAP PRODUCTION BY TERRESTRIAL METHODS

The greatest requirement for the acquisition of spatial data is the establishment of horizontal and vertical control networks. To be used in the determination of location and gravity area; there are geodetic networks established by the General Directorate of Mapping that provide consistent, accurate, up-to-date and easily accessible latitude, longitude, altitude, gravity and their time-dependent changes: Turkey's National Horizontal Control Network, Turkish National Fundamental GPS (Global Positioning System) Network (TUTGA), Turkish National Vertical Control Network (TUDKA), Turkish National Fixed GPS Network (TUSAGA), Turkey National Fixed GNSS Stations Network – Active (TUSAGA-Active), Turkish National Sea Level Monitoring System (TUDES), Turkish National Gravity Network, Turkish National Magnetic Network (HGM, 2019).

Nowadays, the increasing need for precise location determination and real-time acquisition of location is very important for geodetic and engineering studies. Within the scope of classical mapping applications, with the developments in satellite positioning systems, measurements have been started to be used instead of classical measurement methods of triangulation network. One of the important works is the TUTGA facility based on satellite techniques. 296 in 1997, 207 in 1998 and 91 in 1999 TUTGA points were established. TUTGA; consists of approximately 700 points that is continuously updated and with the accuracy of 1-3 cm (HGM, 2019).

With the advancing technology, the use of GPS to produce economic, fast and efficient data in location-based planning and management has become widespread. The most modern example of this situation is the GPS

CORS (Continuously Operating Reference Stations / TUSAGA-Active-TR). With this method, it is possible to achieve real-time economic, fast and efficient data targeted to be reached. The basic operating principle of the system is that the corrections at the reference stations which are continuously monitored are transmitted in real time to the mobile receiver by means of a communication (GPRS-General Packet Radio Service, Internet etc.) (Kahveci, 2009). Due to the earthquakes, GNSS has been introduced to the use of point displacements up to 2-3 m depending on the magnitude of the earthquake, continuous monitoring of the displacements in the coordinates of the triangulation points and obtaining precise location information. For these purposes, fixed GNSS stations (Figure 1) and TUSAGA-Active points (Figure 2), which obtain data 24/7, were presented to users (HGK, 2016).

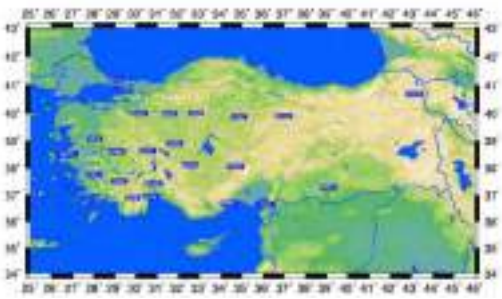

Fig. 1. Distribution of Turkish National Fixed GNSS Network (TUTGA) points

Fig. 2. Distribution of Turkish National Fixed Network GNSS-Active stations

In the production of large-scale maps and the establishment of a reliable geodetic network, the Large-Scale Map and Map Information Production Regulation (BÖHHBÜY) is taken into consideration. It is clearly stated that should be complied with in large scale map production in article 5 of this regulation. (BÖHHBÜY, 2018). In the geodetic network to be established, three-dimensional networks and points formed by space and satellite techniques, to be used or to be established, are classified according to the Regulation as A, B, C degree networks and points, I., II., III. and IV. degree leveling network and points (BÖHHBÜY, 2018: Article 8). Site selection and installation of C1, C2 and C3 grade points, measurement by GNSS technique, principles of forming C3 grade GNSS network, requirements of polygon measurements, leveling measurements, height measurements are stated in article 10 to 44 of the regulation. Articles 44 to 50 of the regulation cover the principles and criteria of detail measurements, which are the basic measurements in the basemap production. Therefore, an important part of the 107-article Regulation is devoted to geodetic studies and detail measurements, which constitute a significant part of the basemap production by using terrestrial methods.

"Geodesy Studies and Detail Measurements" is an important and needed step for basemap production process with terrestrial methods after "Planning" that is the first step before "Office Studies" that is the last step.

4. CASE STUDY: OSMANIYE KORKUT ATA UNIVERSITY CAMPUS

To prepare the basemap of Osmaniye Korkut Ata University (OKU) Karacaoğlan Campus, the locations of the planned geodetic network points were established. It was decided to use the GPS static measurement technique to determine the point locations of the geodetic network and a measurement session plan was prepared. The measurements were made in order to obtain the measurement accuracy of class C2 specified in BÖHHBÜY. In other words, geodetic GNSS receivers that can record from at least six satellites at the same time were used, recording interval was kept less than 15 seconds, recording time was taken 60 minutes for a single session on bases. An example of the measurement schedule for the measurements is shown in Figure 3. In the measurements, 2 Geomax Zenith25, 1 Geomax Zenith35 Pro and 1 Topcon GR5 + model GNSS receivers belonging to the Geomatics Engineering Surveying Laboratory were used (Figure 4). Observation files obtained after the measurements were converted to RINEX (Receiver Independent Exchange Format) format by using "teqc" program obtained from UNAVCO website (UNAVCO, 2019). The obtained RINEX observation file is shown in Figure 5.

Fig. 3. GPS Measurement Chart

Fig. 4. Laboratory GNSS equipment

Fig. 5. RINEX observation file

The obtained data, IGS precision trajectory and clock information was used to compensate. Data adjustment was carried out by GAMIT, an academic GNSS data processing software developed by MIT (Massachusetts Institute of Technology), and the exact coordinates were obtained in IGS14 datum and reference epoch 2018.5. Further information on the precise trajectory and time information for IGS products can be found at IGS's http://www.igs.org/products website. The RINEX file format of an example IGS-Final Orbit file is shown in Figure 6. The corresponding file was downloaded from SOPAC (Scripps Orbit and Permanent Array Center) servers (SOPAC, 2019). Coordinate values of the fixed points of the campus network on the UTM projection were calculated.

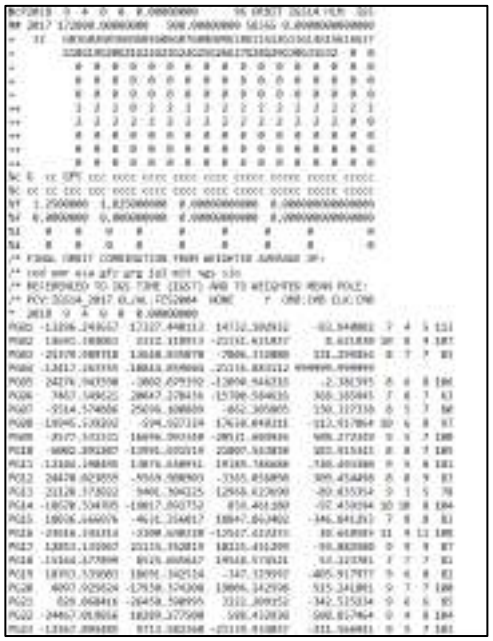

Fig. 6. IGS .sp3 precise orbit file

After the establishment of the OKU campus network, the new points considering the BÖHHBÜY regulations in order to produce the campus basemap were added to this network. The densification points are C4 degrees. The precise coordinates of the relevant points were determined by terrestrial methods based on the coordinates of the OKU campus network. The measurement of the detail points in the basemap production is determined by terrestrial methods and GNSS RTK (Real Time Kinematic) method over the campus network points (Figure 7).

Fig. 7. OKÜ Karacaoğlan Campus

5. CONCLUSION

In this study, it is aimed to show importance of geodetic data, products and techniques in the term of

producing basemaps. The necessity of accurate position information requires accurate measurements and reliable geodetic network. This study shows the importance of producing basemaps with accurate position information in a case study that is realized collaborative works.

CORS networks make significant contributions to geodetic projects requiring high accuracy. As it is possible to obtain cm-level results in CORS networks, its use in projects requiring high accuracy has become even more important. CORS networks have been continuously used in recent years by all persons and institutions dealing with geomatics and surveying. The measurement results using these networks provide three-dimensional coordinate accuracy. The measurement results using these networks provide three-dimensional coordinate accuracy. As a result, the use of CORS measurement method in digital basemap production works is beneficial in terms of completion of the works in a shorter time. In addition, the measurements made with CORS-TR system have a positive effect on cost.

REFERENCES

BÖHHBÜY (2018). http://www.mevzuat.gov.tr/MevzuatMetin/3.5.20181196 2.pdf (Son Erişim: 18.07.2019)

Gezmiş, Ö. (2017). Sayısal Halihazır Haritaların Cors Yöntemleri Kullanılarak Doğruluk Analizi: İller Bankası Uzmanlık Tezi. https://www.ilbank.gov.tr/dosyalar/uzmanliktezleri/1469 7.pdf (Son Erişim: 16.05.2019)

HGK (2016). Türkiye Ulusal Jeodezi Komisyonu Türkiye Ulusal Jeodezi Programı. Harita Genel Komutanlığı, Ankara.

HGM (2019). Harita Genel Müdürlüğü. Jeodezi Dairesi Başkanlığı Faaliyetleri. https://www.harita.gov.tr/images/jeodezifaaliyetler/d5a4 eb6752402a7.pdf (Son Erişim: 26.04.2019)

Kahveci, M. (2009). Gerçek Zamanlı Ulusal Sabit GNSS (CORS) Ağları ve Düşündürdükleri. Jeodezi, Jeoinformasyon ve Arazi Yönetimi Dergisi. (2009/1, Sayı: 100)

Krakiwsky, E. J. and Wells, D. E. (1971). Coordinate Systems in Geodesy. Canada: University of Brunswick.

Yıldırım Ö., Bakıcı S, Cingöz A., Erkan Y., Gülal E., Dindar A. A. (2007). TUSAGA-AKTİF (CORS TR) Projesi ve Ülkemize Katkıları. TMMOB Harita ve Kadastro Mühendisleri Odası Ulusal Coğrafi Bilgi Sistemleri Kongresi 30 Ekim –02 Kasım 2007, KTÜ, Trabzon. https://web.itu.edu.tr/tahsin/cbs2007/bildiri/S_139.pdf , (Son Erişim Tarihi: 18.07.2019)

SOPAC Web Site. http://sopac-old.ucsd.edu/dataBrowser.shtml (Son Erişim Tarihi: 15.07.2019)

Tekin, Ö. F. (2017). Sayısal Halihazır Haritaların Cors Yöntemleri Kullanılarak Doğruluk Analizi: İller Bankası Uzmanlık Tezi. https://www.ilbank.gov.tr/dosyalar/uzmanliktezleri/1464 9.pdf (Son Erişim: 16.05.2019)

Torge, W. (2001). Geodesy. Berlin: Walter de Gruyder.

UNAVCO İnternet Sitesi. https://www.unavco.org/software/data-processing/teqc/teqc.html#publications (Son Erişim Tarihi: 15.07.2019)

Üstün, A and Demirel, H. (2013). Matematiksel Jeodezi.

CISET - 2nd Cilicia International Symposium on Engineering and Technology
10-12 October, 2019, Mersin / TURKEY

USING THE GEOGRAPHIC INFORMATION SYSTEM MERSIN UNIVERSITY'S FIBER OPTIC NETWORK CONSTRUCTION OF INFRASTRUCTURE

Fırat SÖNMEZ, Erdinç AVAROĞLU

Mersin University, Turkey, frt.sonmez@gmail.com

Mersin University, Turkey, eavaroglu@mersin.edu.tr

ABSTRACT
Keeping the infrastructure information in Geographic Information Systems (GIS) environment ensures reliable, systematic and up-to-date data, as well as accurate decision making and results in planning and operation phases. Thanks to these systems, access to infrastructure information that is difficult and costly is ensured in a healthy way. For this purpose, Mersin University fiber optic network infrastructure information system has been established. Thanks to the system, it is ensured that fiber optic network infrastructure networks are kept with a standard and systematic structure and the data is kept up-to-date with the necessary queries and analyzes with the web application.

Keywords: *Geographic Information System, Infrastructure Information System, Mersin University*

1. INTRODUCTION

Geographic Information Systems (GIS) are the informations systems that deal with collecting, storing, displaying up-to-date data belonging to the surface or the subsurface of Earth, also doing, examining, analysing relational modelling between related data with a correct planning method. Geographic Information Systems are also used by Infrastructure Information Systems (IIS). A lot of information about Internet, natural gas, electric networks and water pipelines are reachable by using GIS and this provides examining, analysing and doing relational modelling quickly. By this way, expenses can be reduced and it helps to establish infrastructure systems in a short while and in a convenient manner (Murat,2010)

In Turkey, the infrastructure networks has been managed by classical methods in recent years, however it is impossible to manage those networks by classical approaches since the population has increased day by day and the needs of the people has also escalated proportionally regarding the population. Therefore, the solution to those issues is based on establishing Infrastructure Information System in order to solve infrastructure-related problems rapidly and decide what to do in a secure fashion (Yılmaz).

A lot of institutions has already started establishing their own infrastructure information systems i.e Campus Information System of Middle East Technical University (Erk,2011) is one of them in which GIS was used. Moreover, İGDAŞ and İSKİ Infrastructure Information Systems of Istanbul Metropolitan Municipality (Erk,2011) could be counted as some other examples of GIS projects. Besides, Infrastructure Information Systems has become widespread all over Turkey.

When the technology, which is improving really fast, is taken into consideration, the communication of the universities with the world is quite important. Currently, the medium that provides fast communication with the parties is the Internet and fiber networks are the fastest Internet providers of the world. That is why fiber networks are really important. It is really hard to manage Mersin University's fiber optic infrastructure with those classical methods when the importance of the university in Turkey and in the world is considered. For that reason, the fiber optic network infrastructure information system has been established in this study. Thanks to this system, the fiber optic network system was kept in a standardized and systematic format. Moreover, the web application provided an opportunity to query and analyze the data in an up-to-date structure.

In the 2nd part of this study, it is mentioned about the fiber optic infrastructure information system of Mersin University and there are some explanations about the method. Apart from that the findings were discussed in the 3rd chapter and the results are shown in the last chapter.

2. MERSIN UNIVERSITY FIBER OPTIC NETWORK INFRASTRUCTURE INFORMATION SYSTEM (MÜFOAABS)

Mersin University Fiber Optic Network Infrastructure Information System is established through transferring numerical and verbal data to electronic platforms and associating those data with each other.

The infrastructure data of the fiber optic network infrastructure of Mersin University are currently stored by the staff, who are appointed by the institution, using classical methods. By using MÜFOAABS, the spatial status of the Internet providing fiber optic networks in the Campus like soil type, how many meters below the soil should the wires be buried etc. and attribute information of the fiber optic cables like cable type, calibre, date of manufacture etc. can be stored in the system by the help of GIS map tool. By this way, the main purpose is to use the fiber optic network infrastructure information system of Mersin University optimally.

3. THE OPERATIONS AND THE BENEFITS OF MERSIN UNIVERSITY FIBER OPTIC NETWORK INFRASTRUCTURE INFORMATION SYSTEM

3.1. Digitization

Before the information systems were established, the plans and the drawings that belonged to fiber optic networks were kept on paper. Those can be transferred to digital environment by the help of GIS technology. Using GIS softwares, the scanned drawings can be coordinated by using desired projection and coordinate system. By üthis way, the drawings are put into a coordinate system that is acknowledged by the universal authorities. After coordinating phase, the elements on the network plans are transferred into point and line formats. The total sum of all those phases are called as digitization.

After finishing all the digitization process and combining all those, the fiber optic network that belongs to all the Campus would be put and displayed on a computer screen. This gives an opportunity to save tons of paper and carry all the stuff in a small USB device (Yılmaz)

Figure 1. MÜFOAABS System

3.2. Database Creation

Currently, solutions are created by keeping numeric and non-numeric data of the fiber optic network of Mersin University on paper. In case of MÜFOAABS, a database containing all fiber optic network information is created. With the creation of this database, inserting new data or updating existing data of the fiber optic network can be done in a regular, fast and secure way. This type of high cost and important network data needs to be stored in a systematic manner.

3.3. Associating Graphical Data with Verbal Data

With the help of GIS software graphical data in computers and databases containing network data can be associated. This association can be from graphical data to database or vice versa. This means, an element from graphical data can be viewed in database, as well as an entry in the database can be viewed as graphical data. The process of associating graphical data with verbal data provides a fast way to access data. If there is a problem in any area of the network or in case a maintenance-repair etc. operation is needed, accessing data of network element like calibre, flow, length etc. in a secure and fast way could help to make a healthy and correct decision for solving the problem.

Figure 2. MÜFOAABS Information Entry

4. CONCLUSION

Infrastructure information systems created with GIS are time-saving and make efficient and systematic use of financial resources. Since those systems are in a data structure with analysis and querying capabilities, they allow accurate decision-making and planning. Those systems make it possible to do healthy and functional interventions in infrastructure operations. Integrating those systems to some systems in cities allow them to be comfortable, clean and systematic.

ACKNOWLEDGEMENTS (OPTIONAL)

Acknowledgements of support for Mersin University Scientific Research Projects Unit with Project Number 2019-2-TP2-3615 are welcome.

REFERENCES

EKİN Erk, (2011), Hizmet yönetiminde bulut CBS uygulamaları: Eskişehir alt yapı hizmetleri örneklemi.

GÜNERİ Murat, (2010), Ulaşım ağları temel veri altyapısının oluşturulması.

KAYNARCA Mustafa, Antalya Altyapı Bilgi Sistemi, TMMOB COĞRAFİ BİLGİ SİSTEMLERİ KONGRESİ 2011 31 Ekim – 04 Kasım 2011, Antalya.

KAYNARCA Mustafa , ASAT Genel Müdürlüğü Altyapı Bilgi Sistemi Uygulamaları, TMMOB COĞRAFİ BİLGİ SİSTEMLERİ KONGRESİ 2013 11–13 Kasım 2013, Ankara

KAYNARCA Mustafa , ASAT Genel Müdürlüğü Altyapı Bilgi Sistemi Uygulamaları, TMMOB COĞRAFİ BİLGİ SİSTEMLERİ KONGRESİ 2013 11–13 Kasım 2013, Ankara

YILMAZ A.Gökhan, M. Erol KESKİN, ALTYAPI BİLGİ SİSTEMİ, Süleyman Demirel Üniversitesi,İnşaat Mühendisliği Bölümü, Isparta

CISET - 2nd Cilicia International Symposium on Engineering and Technology
10-12 October, 2019, Mersin / TURKEY

INVESTIGATION OF THE SENSITIVITY TOLERANCE PARAMATER TO NOISE-RELATED EFFECT USING SAMPLE ENTROPHY

Veysel Alcan *[1] and Murat Uçar [2]

[1] Tarsus University, Technology Faculty, Department of The Software Engineering, Mersin, Turkey, alcanveysel@tarsus.edu.tr

[2] İskenderun Technical University, Faculty of Business and Management Sciences, Department of Management Information Systems, Hatay, Turkey, murat.ucar@iste.edu.tr

ABSTRACT
Electromyography (EMG) signals are random, chaotic and nonlinear signals. Because the human body has a flexible dynamic system that exhibits rich behavior and can adapt to unpredictable and constantly changing environments. It is a challenge to distinguish between a wide variety of potential behaviors of the muscular and nervous system and their variability, randomness, and complexity. Thus, to handle such time series, nonlinear dynamic analysis methods in state- space (phase-space) rather than time-space may be more effective in measuring complexity or irregularity. Among many different nonlinear dynamic methods, Entropy has received wide attention due to its ability to measure complexity within biological signals. However, due to the intrinsic sensitivity of the algorithms, the selection of parameters has gained importance. The parameters must be selected carefully. The aim of this study was to investigate the sensitivity of r parameter values to raw (noised) and filtered (de-noised) EMG signals recorded from 11 normal and 11 abnormal groups. It was also an analysis to determine the appropriate r parameters for Sample Entropy in order to obtain better discriminatory results for normal and abnormal groups. We found that the spikes and outliers within signals caused by the noise can effect Entropy value. Therefore, it must be considered the filtering process of the signals before calculating Entropy for better distinguishing chaotic data.

Keywords: *Sample Entropy, Complexity, Electromyography, Signal Processing*

*Corresponding Author

1. INTRODUCTION

The physiological signals obtained from the human muscle and nervous system, such as EMG, are very important time series to define biomechanical and muscle-nerve models, as well as pathological features such as aging, disease diagnosis, disease progression. In EMG studies, measurements in both the time and frequency plane are widely used by practitioners and researchers. However, EMG signals are random, chaotic and nonlinear signals. Because the human body has a flexible dynamic system that exhibits rich behavior and can adapt to unpredictable and constantly changing environments. It is a challenge to distinguish between a wide variety of potential behaviors of the muscular and nervous system and their variability, randomness, and complexity. In addition, certain patterns can be discovered in a stochastic process to obtain more information about the physiology or disease behind signal fluctuations (Pincus, 2001). That is, approaching such time series by nonlinear dynamic analysis methods in state-space (phase-space) rather than time-space may be more effective in measuring complexity or irregularity (Lipsitz, 1992). Among many different nonlinear dynamic methods, Entropy has received wide attention due to its ability to measure complexity within biological signals (Pincus, 1991; Pincus et al,1992; Porta et al., 1998; Richman&Moorman, 2000; Bandt et al., 2002). Entropy is defined as the loss of information within time series or signals. First, Pincus developed Aproximate Entropy (ApEn) as a measure of regularity, which is relatively stable and demonstrates reasonable robustness to noise to measure levels of complexity in medium- length time series (Pincus, 1991; Pincus et al 1992). Later, Richman and Moorman introduced Sample Entropy (SampEn) as an algorithm to address ApEn's shortcomings, such as strong sensitivity to input parameters, poor performance in short-length data, and self-matching (Richman&Moorman, 2000). SampEn is defined as the conditional probability of similarity vector at dimensions m and (m+1) to maintain similarity.

> Entropy metrics of SampEn algorithms generally measure the similarity of patterns as an indication of the unpredictability or irregularity of a time series. These are called vectors in the state space representation.

However, due to the intrinsic sensitivity of the algorithms, the selection of parameters has gained importance. The parameters must be selected carefully. The results obtained during the experimental process with different parameters can be very different. Obviously, this is a troublesome situation to be addressed. It has been reported that the effect of parameter N on entropy result, especially in the calculation of SampEn, has no major effect (Richman&Moorman, 2000). The choice of parameters m and r attracted more attention due to the natural sensitivity of SampEn compared to parameter (Castiglioni& Di Rienzo, 2008). The choice of m may depend on the length of the time series. Selection of r seems to be more difficult (Richman&Moorman, 2000; Pincus, 1991). A larger Standard Deviation (SD) will increase the value of r considering a vector match or vice versa. To avoid a significant noise contribution in the SampEn calculation, a larger r must be selected (Mayer et al., 2014). The amount of variance in time series may affect the calculation of entropy.

The aim of this study was to investigate the sensitivity of r parameter values to raw data (noisy) and filtered data. It was also an analysis to determine the appropriate r parameters for SampEn in order to obtain better discriminatory results for normal and abnormal groups.

1. METHOD AND MATERIALS

1.1 Data

All data used were from the on-line databases whose source was from Batallón de sanidad (BASAN) Universidad Militar Nueva Granada and TecnoParque SENA nodo Manizales. This database contains samples from 11 subjects with knee abnormality previously diagnosed by a professional and 11 normally. These data were collected with electromyography and goniometry equipment MWX8 Datalog Biometrics Database was used as the non-pathological (normal group) and non- pathological (abnormal group) data.

In this study, we used only one data group which subjects undergo the movement to analyze the behavior associated with the knee muscle, from a sitting position. The surface EMG signals with 4 electrodes were recorded from vastus medialis (VM), semitendinosus (ST), biceps femoris (BF) and rectus femoris (RF) muscles.

2.2 Sample Entophy

To calculate SampEn, the number of m patterns replacing the data points and the pattern number of m + 1 are calculated. A threshold (r) defines what is counted as similar patterns because the patterns are generally not exactly the same (the threshold is usually set to 0.1 to 0.2 times the standard deviation of the signal). In SampEn, the percentage of Xm (j) vectors within the tolerance range r of Xm (i), excluding self-matching, is calculated by the Eq. (1):

$$A_i^{(m)}(r) = \frac{N_i^{(m)}(r)}{N - m\tau - 1}, \qquad (1)$$

Where, m denotes the embedded size (length of patterns to be compared), r, similarity criterion, τ = time delay variable and N denotes the length of the data. Ni (m) (r) denotes the number of js in the range di, $j \le r$, and $1 \le j \le N - m\tau$ is $j \neq i$.

Then the percentage average Ai (m) (r) above $1 \le i \le N - m\tau$ is determined by the Eq. (2):

$$\Psi^m(r) = \frac{1}{N - m\tau} \sum_{i=1}^{N-m\tau} A_i^{(m)}(r) \qquad (2)$$

Similarly, Ψ (m + 1) (r) is defined after increasing the dimension to m + 1. The SampEn value of the u time series is then defined as the negative natural logarithm of the probability of similar patterns of length m to the probability of similar patterns of length m + 1, and SampEn is calculated with the Eq. (3):

$$\boldsymbol{SampEn\ (m,\tau,r\ ) = -ln\frac{\psi^{(m+1)(r)}}{\psi^{(m)(r)}}} \qquad (3)$$

Each individual time series was subjected to calculation of SampEn (m,r,N) under combinations of r = 0.10, 0.15, 0.20, and 0.25. The parameter r represented the variance tolerance in the time series. In order to allow comparison of the results of our study with the findings of the previously studies in the literature, we selected the m parameter as 2.

3. RESULTS AND DISCUSSION

We aimed to investigate sensitivity of r parameter to noise-related signal fluctuations as well as to determine the appropriate r tolerance parameter providing the best discrimination between normal and abnormal groups by analyzing both raw and filtered EMG signals using SampEn. Firstly, raw and filtered EMG signals were compared by choosing tolerance parameter r = 0.10, r = 0.15, r = 0.20, and r = 0.25 as shown Fig. 1, Fig. 2, Fig. 3, and Fig. 4, respectively.

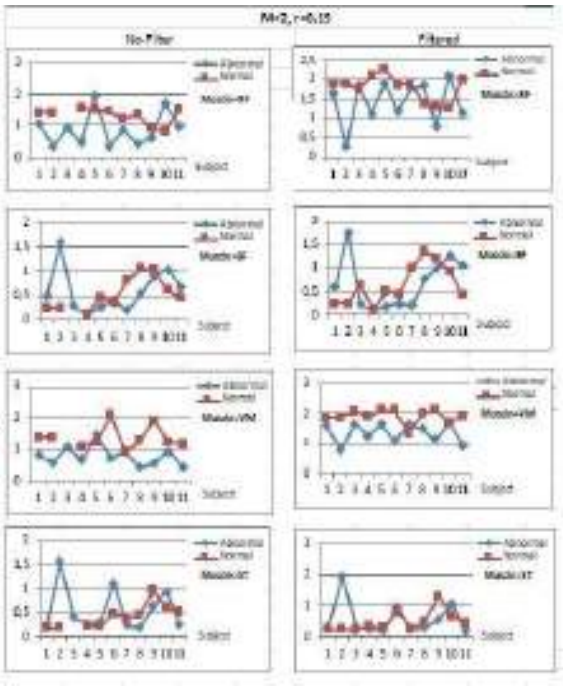

Fig. 1. Comparison of SampEn values for raw and filtered EMG signals recorded from different muscle when tolerance parameter was chosen as 0.10.

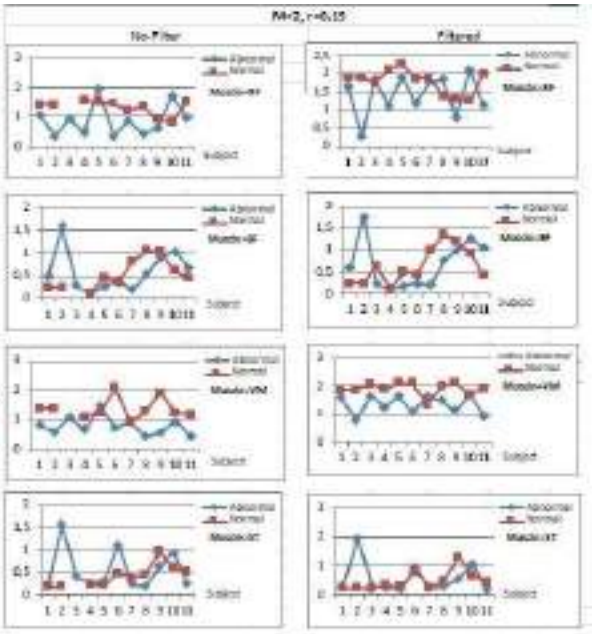

Fig. 2. Comparison of SampEn values for raw and filtered EMG signals recorded from different muscle when tolerance parameter was chosen as 0.15.

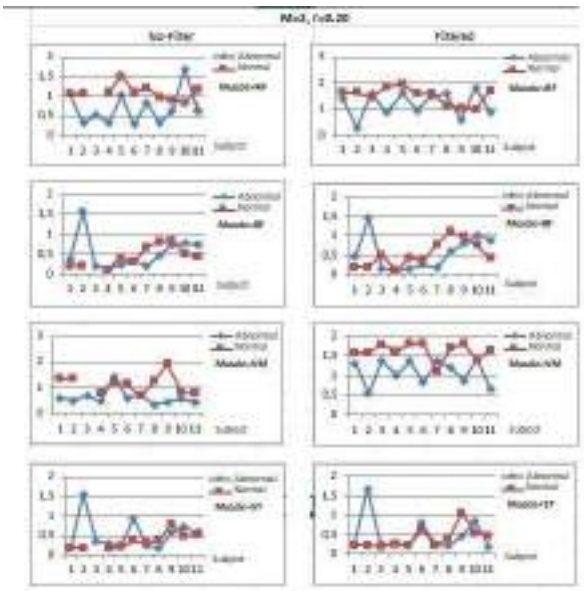

Fig. 3. Comparison of SampEn values for raw and filtered EMG signals recorded from different muscle when tolerance parameter was chosen as 0.20.

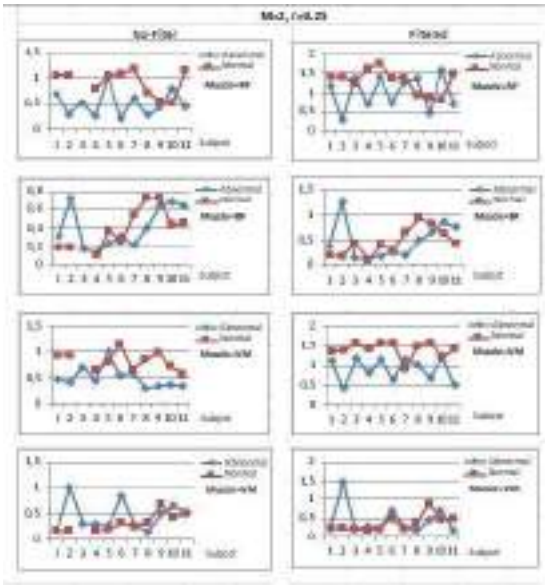

Fig. 4. Comparison of SampEn values for raw and filtered EMG signals recorded from different muscle when tolerance parameter was chosen as 0.20.

Overall the results demonstrate that SampEn are sensitive to r parameter in raw (noised) or filtered (denoised) EMG signals. In Fig1, especially for VM muscles, we found that noise factor effects on entropy value when compared the other muscles. We also founded that SampEn of the EMG signals with the both raw and filtered were also able to discriminate between normal and abnormal groups. The SampEn algorithm would achieve high entropy values in normal and low entropy values in abnormal groups apart from subject 2 (abnormal group). Perhaps, abnormality of Subject 2 may be affected by many pathophysiologic mechanism as well as anatomic factors. Yet, for filtered EMG, entropy showed a better distinction between groups.

Within the tolerance range r, the SampEn value will be low if the probability of observing similar patterns of length m and m + 1 is equal. Conversely, if similar patterns of length m are likely to obtain more than similar patterns of length m + 1, the signal is more complex and the SampEn value is higher. In raw EMG signals, they have sharp spikes and outliers caused by noise. These spikes and outliers can also be visually observed in the signal as shown in the Fig. 5.

Fig. 5. The representation of tolerance r for signals.

These spikes and outliers caused by the noise may effect matching vector. Over value of tolerance r is considered 0 by SampEn algorithm because of conditional probability. The larger standard deviation increases the tolerance r to evaluate a match or vice versa. Therefore, it seems difficult to determine r properly. Two methods are commonly used in the selection of r. In the first method, r is selected between 0.1 and 0.25 times the standard deviation of the entire time series within a tolerance level, ± r * standard deviation(SD). The other method is to use a fixed tolerance value (between 0.1 and 0.25). That is, the r value does not depend on the standard deviation of each vector during comparison. In this study, we compared different r values and found that it provides a consistent value between different r values in order to investigate the problems of relative consistency for SampEn calculations in EMG datasets.

4. CONCLUSION

The sensitivity of the r parameter to change due to pathological conditions of the disease may be due to the low sensitivity of the signal to the noise factor. Otherwise, we cannot assume that entropy can distinguish chaotic data. Therefore, it is important that the signals are free of noise before calculating Entropy and Filtering of raw data sets should be importantly considered when choosing Entropy parameters for EMG studies because of noises factors.

REFERENCES

Bandt, C., and Pompe, B. (2002) “Permutation entropy: a natural complexity measure for time series.” *Phys Rev Lett.*, Vol.88, No.17, pp.174102.

Castiglioni, P. and Di Rienzo, M. (2008) “How the threshold “r” influences approximate entropy analysis of heart-rate variability.” *Comput. Cardiol.,* Vol. 35, pp.561–564

Lipsitz, L.A. and Goldberger, A.L., (1992) “Loss of complexity and aging.” *JAMA*. Vol.267, No.13, pp.1806–1809

Mayer, C.C., Bachler, M., Hörtenhuber, M., Stocker, C., Holzinger, A., Wassertheurer, S. (2014) “Selection of entropy-measure parameters for knowledge discovery in heart rate variability data.” *BMC Bioinform.*, Vol.5, No.6, S2.

Pincus, S.M. (1991) “Approximate entropy as a measure of system complexity.” *Proc Natl Acad Sci*., Vol.88, No.6, pp.2297–3016.

Pincus, S.M. and Huang, W-M. (1992) “Approximate entropy: statistical properties andapplications.” *Commun Stat Theory Methods*., Vol.21, No.11, pp.3061–3077.

Pincus, S.M. (2001) “Assessing serial irregularity and its implications for health.” *Annals of the New York Academy of Sciences*, Vol.954, No.1, pp.245-267.

Porta, A., Baselli, G., Liberati, D., Montano, N., Cogliati, C., Gnecchi-Ruscone, T., Malliani, A., Cerutti, S. (1998) “Measuring regularity by means of a corrected conditional entropy in sympathetic outfow.” *Biol Cybern.,* Vol.78, No.1, pp.71–78.

Richman, J.S. and Moorman, J.R. (2000) “Physiological time-series analysis using approximate entropy and sample entropy.” *Am J Physiol Heart Circ Physiol*., Vol.278, No.6, pp.2039–2049.

CISET - 2nd Cilicia International Symposium on Engineering and Technology
10-12 October, 2019, Mersin / TURKEY

EXPERIMENTAL ANALYSIS OF DIRECT SHEAR TEST FOR DRY SAND

Eyyüb Karakan [*1], Zelal Ebren [2]

[1] Kilis 7 Aralik University, Faculty of Engineering and Architecture, Department of Civil Engineering, Kilis, Turkey, eyyubkarakan@kilis.edu.tr

[2] Hasan Kalyoncu University, Faculty of Engineering, Department of Civil Engineering, Gaziantep, Turkey, zelalebren@hotmail.com

ABSTRACT
Soils can be found not only in saturated form but also partially saturated or dry in nature. This makes a difference in measuring the shear strength parameters of soils. For this purpose, the changes of strength parameters of completely dry sand soils for different relative densities and normal stresses were investigated. An experimental investigations of the direct shear test have been performed under five different normal stress and constant sample volume. During the determination of the soil shear strength in the laboratory, the soil can be loaded differently by different test methods. This fact has an influence on stress-strain distribution in the sample. In this study, direct shear test, which is one of the most used in the literature, was preferred.

Keywords: *Dry sand, Direct shear test, Stress strain distribution, Relative density*

[*] Corresponding Author

1. INTRODUCTION

The basic engineering property of the soil that controls the stability of the soil mass under structural loads is defined as shear strength. Soil shear strength parameters (angle of internal friction and cohesion) identifying accurately is of paramount importance in the design of buildings. The internal friction angle and cohesion of the soil can be determined by both laboratory and field tests. One of the most common tests to determine internal friction angle and cohesion values in the laboratory is direct shear tests.

Muawia (2013) investigated the reliability of using the direct shear test for different clay contents and different moisture contents using an adequate shearing strain. His result shows that the cohesion of the mixture was found to increase consistently with the increase of clay content.

In fact, as reported in the literature, the grain size distribution of the soil has a significant impact on the mechanical behaviors of geotechnical materials (Kokusho et al. 2004; Wichtmann and Triantafyllidis 2009; Yan and Dong 2011; Wang et al. 2013; Wichtmann and Triantafyllidis 2013; Liu et al. 2014; Norsyahariati et al. 2016; Wang et al. 2017, 2018b, c).

Kokusho et al., (2004) were performed on granular soils consisting of sand and gravel with different particle gradations and different relative densities reconstituted in laboratory. They found that only a small difference was observed in undrained cyclic shear strength or liquefaction strength defined as the cyclic stress causing 5% double amplitude axial strain for specimens having the same relative density.

Yan and Dong (2011) were studied through a series of numerical triaxial tests using the three-dimensional (3D) discrete-element method. They found that an assemblage with a wider particle grading gives more contractive response and behaves toward strain hardening upon shearing.

Wang et al., (2018b) investigated, the effect of volumetric content of coarse grains fv (volumetric ratio of coarse grains to the whole sample; grain size > 2 mm) on the mechanical behavior of the lower part interlayer soil was investigated by carrying out monotonic triaxial tests. They showed that increasing the volumetric content of coarse grains fv led to more significant dilatancy.

Vallejo et al. (2000) measured the shear strength and the porosity of the kaolinite clay–sand mixtures with various clay content. The shear strength of the mixtures was governed by sand at clay content lower than 25%, while governed by clay at clay content higher than 60%.

Dafalla (2013) investigated the effects of clay content and moisture content on shear strength of clay–sand mixtures. As the water content increased, the cohesion and internal friction angle of clay–sand mixtures decreased.

Soils can be found not only in saturated form but also partially saturated or dry in nature. This makes a difference in measuring the shear strength parameters of soils. For this purpose, the changes of strength parameters of completely dry sand soils for different relative densities and normal stresses were investigated. An experimental investigations of the direct shear test have been performed under five different normal stress (50, 75 100,125 and 150 kPa) and constant sample volume. In this study, direct shear test, which is one of the most used in the literature, was preferred.

2. LABORATORY EXPERIMENTS

Full dry sand was used to perform the experiments for determining the shear strength parameters. The average density of particles (ρ_s) value of sand is 2.63 Mg/m³. The properties of the sand used are listed in Table 1. The grain size distribution is presented in Figure 1; the sand was classified SW according to USCS.

The normal stresses 50, 75, 100, 125, 150 kPa have been applied. The soil is sheared under the constant horizontal displacement velocity of 0.1 mm/min until the horizontal deformation reaches the limit of 12 mm. The shear test is performed when constant sample volume is applied. The shear tests have been performed from very loose to dense (Dr=30%-80%). The peak soil shearing strength has been determined according to the maximum ratio of tangential and normal stresses.

The conventional direct shear test procedures followed ASTM D3080 (2004). The direct shear tests were performed for dry soil conditions. A single specimen was used for each test, and the shear stress vs. shear displacement response was continuously monitored during the test.

Table 1. Properties of dry sand

Property	Value
Specific Gravity (G_s)	2.63
Maximum void ratio (e_{max})	0.6
Minimum void ratio (e_{min})	0.3
Effective size, D_{10} (mm)	0.26
Median diameter, D_{50} (mm)	0.69
Uniformity coefficient (C_u)	6.54
Coefficient of gradation (C_c)	1.08
Soil Classification (USCS)	SW

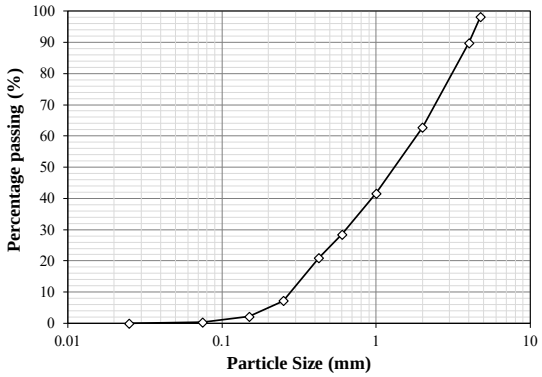

Fig. 1. Grain size distribution of dry sand

3. RESULTS AND DISCUSSION

In the sequel, the shear strength obtained from direct shear tests is presented in order to analyses the influence of the key parameters on the mechanical behavior of the dry sand under different normal stress. In this study, the shear strengths of dry sand were measured using the direct shear test. The shear strength with different relative

densities and normal stresses were measured, and results obtained from the tests were compared with respect to shear stress. In addition, the effect of normal stress on the shear strength was discussed based on theoretically derived chart and graphical comparisons.

3.1. Effect of Normal Stress

Firstly, the influence of the normal stress on the mechanical behaviour of the dry sand is studied. Figure 2a to 2e shows the test results obtained from direct shear tests with the applied under constant normal stresses for different relative densities. The experiments shown in Figure 2 were performed under 50, 75, 100, 125 and 150 kPa. As was expected, the shear strength of the dry sand increased with normal stress, while it increases with relative densities.

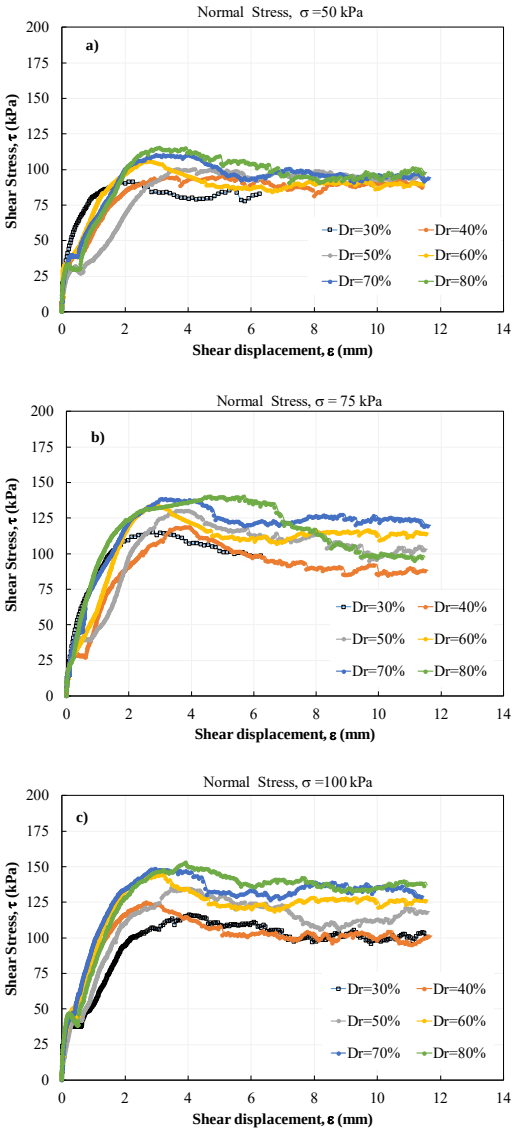

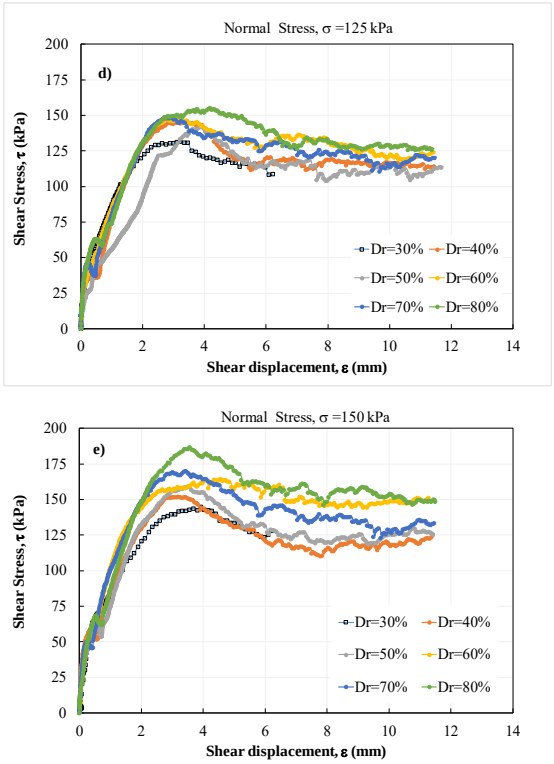

Fig. 2. Shear stress - displacement relationship for different normal stresses (50, 75, 100, 125, 150 kPa)

The results of the experiments carried out under 50 kPa normal stress and 6 different relative densities are shown in Figure 2a. As shown in Figure 2a, the minimum shear stress value was obtained for Dr = 30%, while the highest shear stress value under the same stress was obtained for Dr = 80%. The minimum shear stress value shown in Figure 2a is 91.5 kPa for Dr = 30%, and the maximum shear stress is 115.8 kPa for Dr = 80%. As expected from the experimental results, the maximum shear stresses increased as the relative densities increased. However, when the test results obtained under normal stress of 50 kPa were examined, it was observed that as the relative density increase from loose (Dr = 30%) to dense (Dr = 80%), the maximum shear stress increased in a very narrow band. In addition, it has been found that as the normal stress increases from 75 to 150 kPa, the resulting maximum shear stress increases relatively (Figure 2b-2e). Similar results were obtained in experiments under normal stress of 75, 100 and 125 kPa.

The tests were performed at a maximum normal stress of 150 kPa (Figure 2e). Figure 2e shows the results of the experiments performed under 6 different relative densities under normal stress of 150 kPa. The highest shear stress in the experiments was obtained for a relative stress of Dr = 80% and a normal stress of 150 kPa. The lowest shear stress was 143.65 kPa and the highest shear stress was 186.4 kPa for 150 kPa normal stress.

In all experiments, the maximum shear stress was obtained when the horizontal displacement was between 2 and 4 mm and independent of the relative densities (Figure 2).

3.2. Relative Density-Shear Stress Relationship

To study this effect, dry sand with six relative densities were taken. For this series of tests, the relative density was increased from 30% to 80% and the normal stress for each interface was varied from 50 kPa to 200 kPa. Using the test results, the shear stress - shear displacement of dry sand was created for different relative densities as shown in Figure 3a-3f. A series of simple shear tests were conducted to investigate the stress-strain relationship and dilation behavior of the dry sand with different relative densities. As seen clearly in Figure 3a, the lowest shear stress is obtained for the most loose (Dr = 30%) relative density.

From figures 3a-f, it can be seen that the shear strength of the dry sand, increases significantly with the progress of horizontal displacement, due to the good adhesion between the grains of dry sand. The values of the shear stress at the peak are 91.5, 115.24, 116, 131,64 and 144.74 kPa for normal stresses of 50, 75, 100, 125 and 150 kPa, respectively for lowest relative density (Dr=30%). After each peak, there is a decrease of shear stress until a residual value. The residual shear stress at the residual are 83.06, 98.7, 100.48, 108.69 and 127.74 kPa for normal stresses of 50, 75, 100, 125 and 150 kPa, respectively for lowest relative density (Dr=30%).

For denser samples, Figure 3f shows that the shear stress increases continuously with the progress of the test up to peak stress after that there is a decrease of shear stress until a residual value. The peak values obtained in the test are 115.84, 140.89, 153.76, 156 and 187.61 kPa for a normal stress of 50, 75, 100, 125 and 150 kPa, respectively. The residual values obtained at the end of the test are 42.7, 73.4, 136.3 and 205.4 kPa for a normal stress of 50, 75, 100, 125 and 150 kPa, respectively.

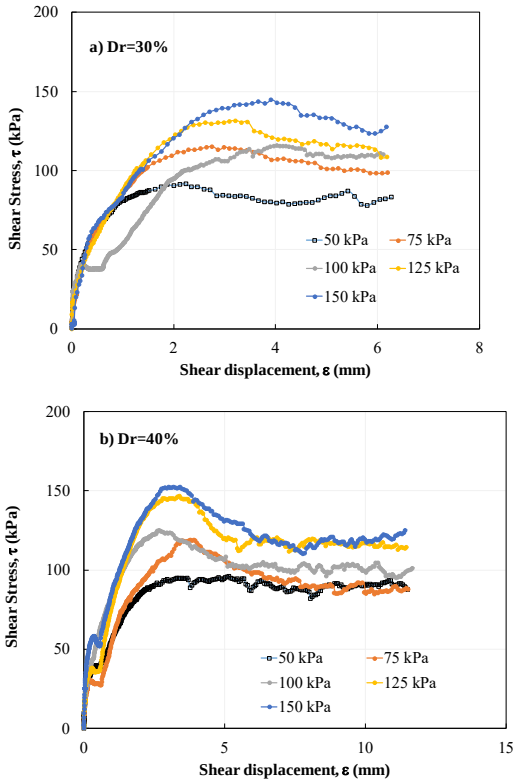

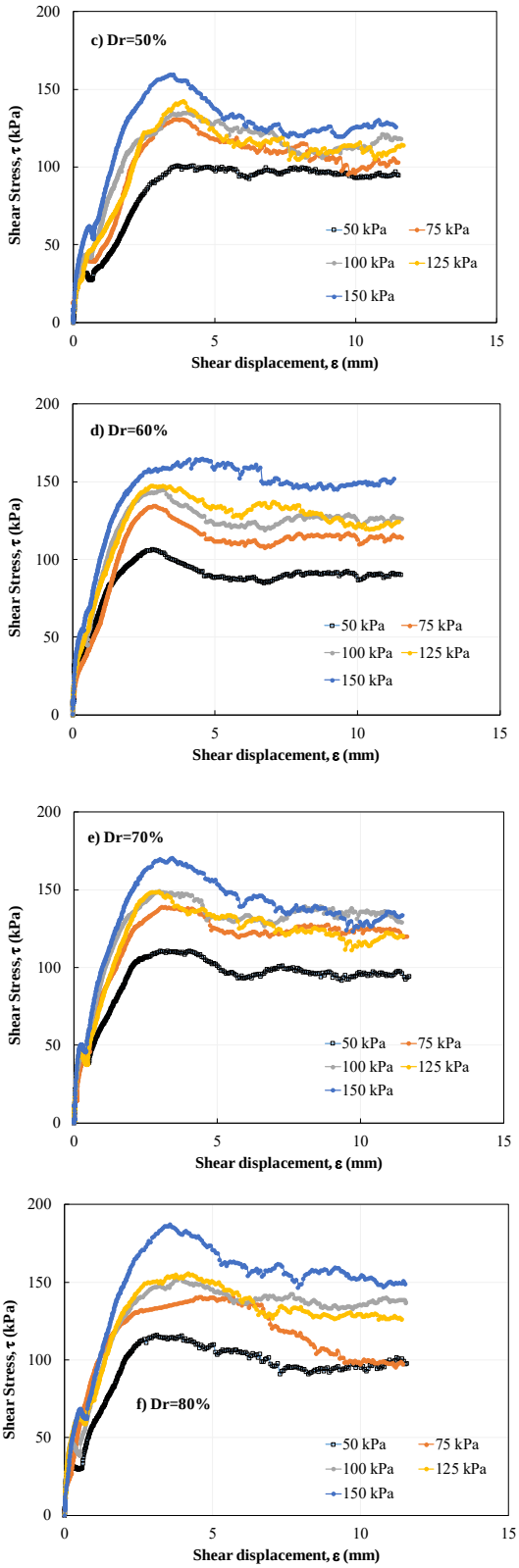

Fig. 3. Shear Stress – displacement relationship for different densities.

3.3. Relative Density-Internal Friction Angle of Relationship

Using the test results, the internal friction angles of dry sand was created for different relative densities as shown in Figure 4. The cohesion of the sand was assumed to be zero because comparison was made based on the internal friction angle only and because the apparent cohesion was sufficiently so small.

In this study, the experimental results showed that the greatest effect was relative density. The results showed that for both peak and residual internal friction angle increased with an increase in relative density.

The peak internal friction angles obtained in the test are 28°, 29.5°, 30.5°, 31°, 31.1°, and 35.7° for a relative density of 30, 40, 50, 60,70 and 80%, respectively. The residual internal friction angles obtained at the end of the test are 20°, 20.65°, 20.94°, 21.58°, 21.66°,27.16° for a relative density of 30, 40, 50, 60,70 and 80%, respectively (Figure 4).

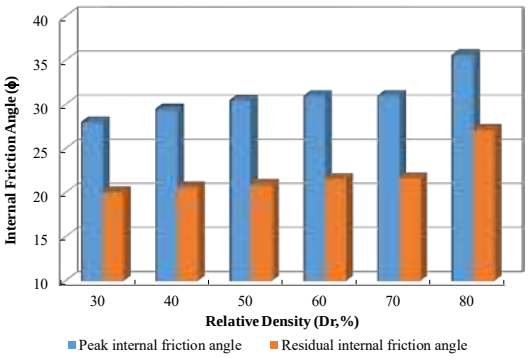

Fig. 4. Internal friction angle - relative density relation

4. CONCLUSION

A set of experimental tests were conducted on well graded sand samples to understand the effect of relative density on the physical and mechanical properties of the samples. Moreover, this study investigated the effect of the relative density of a dry sand on the shearing behaviors using a direct shear apparatus.

The variations of the friction angle for the soil and the maximum vertical displacement with the relative density were analyzed. The result of the direct shear test indicated that, when the normal stress increased, also the internal friction angle increased.

At the densities which the samples were tested, it is noted an increment in the maximum and residual shear stress with the increment in normal stress, which involves increment of the physical characteristics such as the internal friction angle.

REFERENCES

References should be listed in alphabetical order in the reference section.

ASTM (2017) Standard practice for classification of soils for engineering purposes (Unified Soil Classification System). American Society for Testing and Materials, West Conshohocken

Dafalla MA (2013) Effects of clay and moisture content on direct shear tests for clay–sand mixtures. *Adv Mater. Sci Eng* 2013:562726.

Kokusho, T., T. Hara, and R. Hiraoka. 2004. "Undrained shear strength of granular soils with different particle gradations." *J. Geotech. Geoenviron. Eng.* 130 (6): 621–629. https://doi.org/10.1061/(ASCE)1090 - 0241(2004)130:6(621).

Muawia, A.D., (2013). "Effects of Clay and Moisture Content on Direct Shear Tests for Clay-Sand Mixtures." *Journal of Advances in Materials Science and Engineering*, pp. 1-8, December, 21.

Vallejo LE, Mawby R (2000) Porosity influence on the shear strength of granular material–clay mixtures. *Eng Geol.* 58(2):125–136

Yan, W. M., and J. Dong. 2011. "Effect of particle grading on the response of an idealized granular assemblage." Int. J. Geomech. 11 (4): 276–285. https: // doi.org/10.1061/(ASCE)GM.1943-5622.0000085.

Wang, H. L., R. P. Chen, S. Qi,W. Cheng, and Y. J. Cui. 2018a. "Long-term performance of pile-supported ballastless track-bed at various water levels." *J. Geotech. Geo environ. Eng.* 144 (6): 04018035. https://doi.org/ 10. 1061 / (ASCE)GT.1943-5606.0001890.

Wang, H. L., Y. J. Cui, F. Lamas-Lopez, N. Calon, G. Saussine, J. C. Dupla, J. Canou, P. Aimedieu, and R. P. Chen. 2018b. "Investigation on the mechanical behavior of track-bed materials at various contents of coarse grains." *Constr. Build. Mater.* 164 (Mar): 228–237. https://doi.org/10 .1016/j.conbuildmat.2017.12.209.

Wang, H. L., Y. J. Cui, F. Lamas-Lopez, J. C. Dupla, J. Canou, N. Calon, G. Saussine, P. Aimedieu, and R. P. Chen. 2017. "Effects of inclusion contents on resilient modulus and damping ratio of unsaturated track-bed materials." *Can. Geotech. J.* 54 (12): 1672–1681. https://doi.org/10.1139/cgj-2016-0673.

Wang, H. L., Y. J. Cui, F. Lamas-Lopez, J. C. Dupla, J. Canou, N. Calon, G. Saussine, P. Aimedieu, and R. P. Chen. 2018c. "Permanent deformation of track-bed materials at various inclusion contents under large number of loading cycles." *J. Geotech. Geoenviron. Eng.* 144 (8): 04018044. https: // doi. org / 10. 1061 / (ASCE) GT. 1943-5606.0001911.

Wang, J. J., H. P. Zhang, S. C. Tang, and Y. Liang. 2013. "Effects of particle size distribution on shear strength of accumulation soil." *J. Geotech. Geoenviron.* Eng. 139 (11): 1994–1997. https: // doi. org / 10. 1061 / (ASCE) GT.1943-5606.0000931.

Wichtmann, T., and T. Triantafyllidis. 2009. "Influence of the grain-size distribution curve of quartz sand on the small strain shear modulus Gmax." *J. Geotech. Geoenviron. Eng.* 135 (10): 1404 – 1418. https: // doi. org /10.1061/(ASCE)GT.1943-5606.0000096.

Wichtmann, T., and T. Triantafyllidis. 2013. "Effect of uniformity coefficient on G/Gmax and damping ratio of uniform to well-graded quartz sands." *J. Geotech. Geoenviron. Eng.* 139 (1): 59–72. https: // doi. org / 10. 1061 /(ASCE)GT.1943-5606.0000735.

CISET - 2nd Cilicia International Symposium on Engineering and Technology
10-12 October, 2019, Mersin / TURKEY

EFFECT OF GRAIN SIZE DISTRIBUTION OF DRY SAND

Eyyüb Karakan [*1], Zelal Ebren [2]

[1] Kilis 7 Aralik University, Faculty of Engineering and Architecture, Department of Civil Engineering, Kilis, Turkey, eyyubkarakan@kilis.edu.tr

[2] Hasan Kalyoncu University, Faculty of Engineering, Department of Civil Engineering, Gaziantep, Turkey, zelalebren@hotmail.com

ABSTRACT
This paper focuses on the effects of the grain size distribution on shear strength of dry sands. A series of direct shear tests were performed to characterize the shear strength of the dry sands. Two different type of sands were used in this study. The basic properties of the sands, such as the median particle diameter (D_{50}), coefficient of uniformity (Cu), and coefficient of curvature (Cc), were used to analyze the effects. Results from the direct shear tests indicate that the range of the angle of shearing resistance of the well graded sand is higher than the poor graded sand. The internal friction angle is generally increasing with increasing the median particle diameter and the relative density (Dr), and decreasing with increasing the coefficient of uniformity.

Keywords: *Shear Strength, Direct Shear Test, Dry Sand, Median Particle Diameter.*

[*] Corresponding Author

1. INTRODUCTION

Basically triaxial compression test, direct shear test and unconfined compression tests are laboratory methods that determine the shear strength of soils. The direct shear test was used more widely to investigate the shear strength of the granular soils by Fannin et. al. (2005), Asadzadeh and Soroush (2009), and Nam et al. (2011). The literature review indicated that many fundamental parameters of the granular soil may affect the shear strength of the soil (Simoni and Houlsby, 2006).

The main parameters are listed the water content, density, specimen size (Cerato and Lutenegger, 2006), particle size (Ueda et al., 2011), particle shape (Azéma1et al., 2012), relative density and so on. In this study, the effects of the grain size distribution on the shear strength of the dry soil were investigated. Some of the parameters, which are the median particle diameter, coefficient of uniformity, and relative density, were used for the purpose of analysis.

2. TESTED SOIL AND TESTING METHOD

In this study two different dry sand was used. The soils were sieved and particle size distributions are shown in Figure 1. The detailed results of all basic properties are tabulated in Table 1. For the direct shear test, the inner size of the rectangular shear box is 60 mm × 60 mm in plan, and 20 mm in height. The specimen, which water content is zero, was poured by using dry deposition method.

Thirty direct shear tests for two soils curves were carried out. After applying vertical pressure equal to 50 kPa, 75 kPa, 100 kPa, 125 kPa, and 150 kPa on the specimen in the shear box, horizontal thrust was acted on the upper box until the soil failure. The testing table for direct shear test which was made in this study as shown in Table 2. In the tests, the rate of horizontal loading is controlled at 1 mm/min The rate of displacement was selected with reference to ASTM D3080-90 (ASTM, 1990).

Table 1. Index properties of two different sand samples

USCS classification	SW	SP
D_{10}	0.26	0.14
D_{30}	0.69	0.245
Median Particle Diameter, D_{50}	1.4	0.34
D_{60}	1.7	0.41
Coefficient of uniformity, Cu	6.5	2.93
Coefficient of curvature, Cc	1.08	1.04
Specific gravity, Gs	2.63	2.69

Table 2. Testing table for direct shear test

Soil Type	Dr (%)	Normal Stress (kPa)
SW	30	50
	50	75
	70	100
SP	30	125
	50	150
	70	

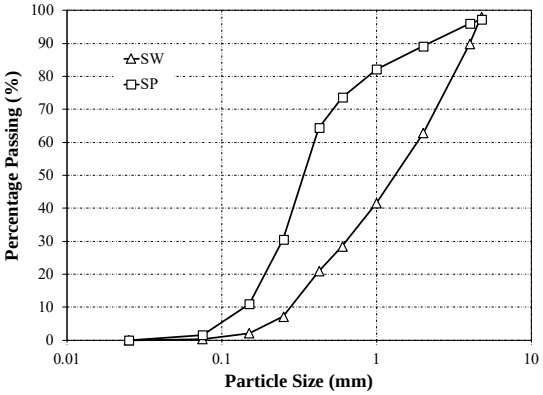

Fig. 1. Particle size distribution of sands

3. TEST RESULTS

For the direct shear tests, the peak internal friction angle (ϕ) is defined by a linear fit through the origin in the plot of peak o shear stress against normal stress (Fig. 2). It has been observed that shear stress is highest in the sample with a relative density of 70% for SW. In addition, it has been observed that shear stress is lowest in the sample with a relative density of 30% for SP. As the relative density in SW increases, the internal friction angle of the soil increase. This is due to the gradation of the soil samples and the shape of soil particles (Christopher A. B. et al., 2008). The maximum shear stress was obtained 170 kPa for SW under the 150 kPa normal stress. The minimum shear stress was obtained 49 kPa for SP under the 50 kPa normal stress.

According to Figure 3, the peak internal friction angles a range between 28° and 31° for SW, a range between 36° and 38° for SP. In addition, the residual internal friction angles a range between 20° and 24.66° for SW, a range between 35.57° and 37.85° for SP. This results are similar with studied by Asadzadeh and Soroush (2009), and Nam et al. (2011).

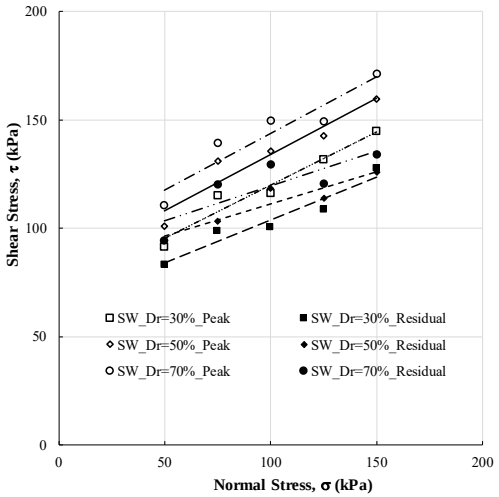

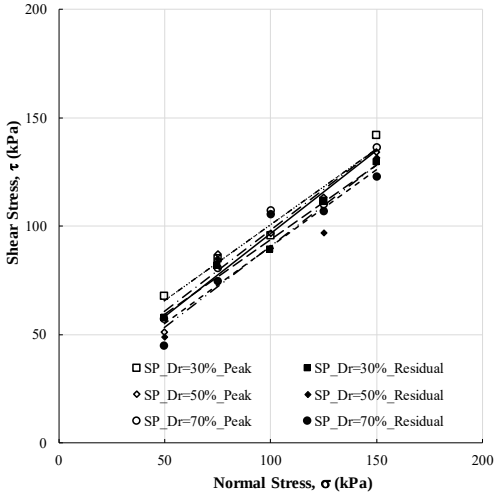

Fig. 2. Shear stress against normal stress at peak and residual from direct shear tests

Data from present study (Figs. 2a and 2b) are reproduced in Fig. 3 for the purpose of analyzing the effects of grain size distribution. It is observed from the plots that the internal friction angle is generally increasing with increasing the median particle diameter, and a linear relation of the median particle diameter may express the effects.

It is clear from the plots that the angle of shearing resistance is generally decreasing with the increment of the coefficient of uniformity. It is observed from the figure that the residual angle of shearing resistance is increasing with increasing the relative density.

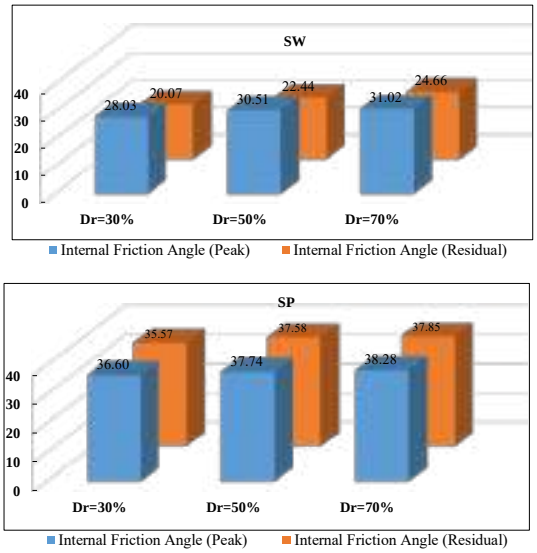

Fig. 3. Relative density (D_r) internal friction angle (ϕ) relationship

4. CONCLUSION

The purpose of this study is to find out the effect of grain size distribution of dry sand. A series of experiment has been carried out and analyzed. The following conclusions can be obtained from the results of the experimental work.

The basic properties of soil affect the mechanical behavior of soil. The gradation of the soils affects the packing of the soils, causing them to exhibit different strengths.

The morphological and mineralogical properties of soil particles affect the mechanical behavior of soil. Shape of the soil particle can influence the packing of the soil, hence altering the mechanical behavior of the soil. The particle size gradation in the soil may also contribute to the strength of the soil.

Direct shear box test results show that the friction angle of soil increases then decreases as the relative density.

REFERENCES

ASTM (1990). Standard test method for direct shear test of soils under consolidated drained conditions, ASTM D3080-90. Philadelphia, PA: American Society for Testing and Materials.

A.B. Christopher, B.E. Tuncer, H.B. Craig and M.M. David, Geological and physical factors affecting the friction angle of compacted sands, Journal of Geotechnical and Geoenvironmental Engineering, 134(10), 1476 – 1489, (2008).

Asadzadeh, M. and Soroush, A. (2009). Direct shear testing on a rockfill material. The Arabian Journal for Science and Engineering, 34(2): 378-396.

Azéma1 E., Estrada N., and Radjaï, F. (2012). Nonlinear effects of particle shape angularity in sheared granular media. Physical Review E 86: 041301.

Cerato, A. B. and Lutenegger, A. J. (2006). Specimen Size and Scale Effects of Direct Shear Box Tests of Sands. Geotechnical Testing Journal 29: 507–516.

Fannin, R.J., Eliadorani, A. and Wilkinson, J.M.T. (2005). Shear strength of cohesionless soils at low stress. Géotechnique, 55(6): 467-478.

Nam S, Gutierrez M., Diplas, P. and Petrie, J. (2011). Determination of the shear strength of unsaturated soils using the multistage direct shear test. Engineering Geology, 122(3-4): 272-280.

Simoni, A. and Houlsby, G.T. (2006). The direct shear strength and dilatancy of sand-gravel mixtures. Geotechnical and Geological Engineering, 24: 523-549.

Ueda, T., Matsushima, T. and Yamada, Y. (2011). Effect of particle size ratio and volume fraction on shear strength of binary granular mixture. Granular Matter 13: 731-742.

CISET - 2nd Cilicia International Symposium on Engineering and Technology
10-12 October, 2019, Mersin / TURKEY

EVALUATION OF THE ZONING PEACE ARRANGEMENT IN TERMS OF CONTENT

Güler YALÇIN,[1] Burak UŞAK*[2]

[1] Osmaniye Korkut Ata University, Engineering Faculty, Department of Geomatics Engineering, Osmaniye, Turkey, guleryalcin@osmaniye.edu.tr

[2] Osmaniye Korkut Ata University, Engineering Faculty, Department of Geomatics Engineering, Osmaniye, Turkey, burakusak@osmaniye.edu.tr

ABSTRACT
Turkey has faced with great difficulties in urbanization in the past until today. The administrations have not been able to bring radical solutions to these problems and have brought various amnesties with their short-term transition policies. "Zoning Peace Arrangement" that is entered into force on 18.05.2018 with the provisional article is the latest version of the amnesty. As it can be understood from the article of the law, these existing problems have introduced temporary arrangements. In this paper the content, possible benefits and problems, violation to existing laws and regulations of this regulation are examined.

Keywords: *Construct, Registration, Zoning law, Zoning peace*

1. INTRODUCTION

3194 numbered Zoning Law and Planned Areas Type Zoning Regulation (PATZR) are the first guiding arrangements on planned urbanization, progress and control of urban development in Turkey.

Zoning Law ensures that the plan, science, health and environmental conditions of the settlements and the constructions in these places are appropriate (Zoning Law, Article 1). Planned Areas Type Zoning Regulation sets out the principles and procedures for the design and supervision of buildings and structures in accordance with the plan, science, health and sustainable environmental conditions (Planned Areas Type Zoning Regulation, Article 1).

Legal bases are the cornerstones of the legal structure. The legal basis of construction in the Zoning Law, which was prepared as a legal basis for the construction of cities, is “Building License”. Building License is an inspection regulation with the aim to protect and develop the zoning scheme which is established with the zoning legislation and zoning plans. It has been brought in order to keep the rights and powers of individuals and communities on the land they own within the boundaries of zoning and to make changes and additions to existing structures under supervision and supervision and to take necessary measures (Gerem, 2014). The Zoning Law states that the structure can be constructed in accordance with the zoning plan, regulations, licenses and annexes, and that all buildings within the scope of the law, with some exceptions, are required to obtain building licenses from municipalities and governorships.

Turkey has so far always lived and still live in hardship on unplanned urbanization, illegal construction and slum. This problem was sometimes overlooked by the administrations and sometimes remained in the background due to the different country agendas. Amnesties were introduced at different times by adding temporary articles to the Zoning Law or by different laws (Tercan, 2018). Despite the contradiction to law and order and control in law, amnesty was introduced at different times by adding temporary articles to the Zoning Law.

Despite the importance given to the plans adopted in the legal arrangements and the importance given to the development of cities, unplanned urbanization, illegal construction and shanty housing problems continued in our country. Subsequently, temporary articles and amnesties added to this law were brought and temporary solutions to the problems were presented. However, despite these solutions, more than 50% (ie, about 13 million in numbers) have been said to have an anti-zoning structure corresponding to Independent Sections according to the figures announced today. This situation has caused many legal conflicts between the citizen and the state (Environment and Urban Ministry, 2019).

With a similar application to the previous zoning amnesties, Article 16 of 7143 numbered law that came into effect on 18.05.2018 was added to 3194 numbered Zoning Law. After this, the so-called “Zoning Peace Arrangement” has been introduced.

2. ZONING PEACE ARRANGEMENT

The practice called the zoning peace regulation is like the amnesties previously issued and is an arrangement brought to the immovable property. Unlike previous amnesties, the article of the law gives the person the right to use the existing buildings and buildings that are against zoning, until a new building or urban transformation activities are carried out. In this case, the person cannot obtain the right of ownership of the structure but gains the possession of the structure.

It is declared that Building Registration Certificate (BRC) to be given after the necessary actions to the structures contrary to the zoning legislation or license is the solution of the zoning problems. Zoning peace is the process for which Building Registration Certificates ("Certificate" or "Certificates") will be issued for buildings which were built without licenses and which lack proprietorship certificates. The Certificate will be issued for buildings built before December 31, 2017. At first applications are made up until October 31, 2018 and the registration fee must be paid by December 31,2018. It is at the discretion of the Council of Ministers to extend the application and registration fee deadline by up to one year. (Now the registration fee deadline is extended by 31.012.2019) (CNN Türk, 2019). Applications for the Certificate can be made electronically through e-Devlet (the "e- Government Gateway" which provides access to various public services electronically from a single point). Relevant forms are submitted through e-Devlet to Ministry of Environment and Urbanization to be examined by the authorized person in the Ministry. Only one Certificate will be issued for each building. The registration fee is calculated based on the land's property tax value and the approximate building costs (Gürkaynak Esq et.al., 2018). This includes all unlicensed or contradictory structures in rural and urban areas built before 31 December 2017. The purpose of this regulation is to resolve the dispute between the citizen and the state and to record the structures which are against zoning, unlicensed or contrary to the license annexes (Environment and Urban Ministry, 2019). It is understood that the most important and most important objective of the zoning peace arrangement is to provide

Problems stemming from non-zoning and non-permissive structures have made the citizen and the state victim in many areas. Lawsuits were filed in this process for both the state and the citizen. This process, which was brought to court by the opening of the lawsuits, increased the density of the files in the state institutions rapidly and therefore the process became unable to proceed. Because there are long-lasting courts, it has become challenging for the citizen. economic resources for future urban transformation practices.

It is also obvious that it is difficult for municipalities to implement demolition decisions on such structures.

The state also suffers from great losses in taxes and revenues that it cannot collect due to unlicensed and unregistered structures in economic terms.

The citizen is also suffering from the dispute due to the unregistered structure. Infrastructure facilities such as electricity, water, natural gas, etc. cannot be installed on the structure which is not allowed to use the building. In addition to this, the citizen cannot perform any sales transaction and any transaction based on this subject and the structure cannot be accepted as an economic value. In any bank transaction, collateral or mortgage cannot be shown for illegal structures and it loses its right to use credit.

Building registration document that gives formality to buildings within the scope of zoning peace regulation are

provided after applying to the Ministry of Environment and Urbanization or the institutions to be authorized by the Ministry of Environment and Urbanization.

For structures building registration certificate provides:

(i) to temporarily subscribe to water, electricity and natural gas services,

(ii) to revoke demolishment decisions and outstanding administrative fines,

(iii) to complete deficient work of the certificated sections of buildings under constructions as the Certificate can also be issued for the completed sections of buildings under construction,

(iv) to conduct basic repair and alteration works (Notification, 2018; Gürkaynak Esq et.al., 2018).

There are exceptions where building registration certificate cannot be issued:

(i) areas indicated under the Bosporus Law No. 2960 as within the Bosporus coast line and preview area,

(ii) areas indicated in the same law as within the Istanbul Historical Peninsula,

(iii) the historical area defined under the Law No. 6546 on Establishment of Directorate of Canakkale Wars Gelibolu Historical Area,

(iv) premises subject to the private property of third parties, and

(v) public premises which are designated for social purposes and allocated to relevant institutions accordingly. (Gürkaynak Esq et.al., 2018).

The usage period of the given building registration documents is not unlimited; it is until the reconstruction of the structure and the implementation of urban transformation.

2.1. Examination of Zoning Peace Regulation in Terms of Content

It is seen that the regulation aims to register the informal real estate market for earthquake risk which is one of the biggest problems faced by the country in urbanization. In addition, it is stated that the structures constructed before 31 December 2017 are included in this regulation and the structures carrying disaster risk will be evaluated according to the declaration of the individuals. There are problems in the background of these two issues that conflict with this regulation, whose real purpose is to record and take measures against disaster risk. Firstly, it is not possible to fully check whether the structures built up to the specified date continue to be built after the specified date. The construction might be started after the regulation enters into force and these are the structures whose construction has been completed with the aim of making the regulation illegal and illegal in compliance with the opportunity by knowing this opportunity. This situation makes the planned urbanization policy, which is tried to be kept under control, even more difficult; on the other hand, it increases the number of structures that may carry disaster risk.

The existing construction structure, property status and other aspects of the structures that carry or are not at risk of disaster will be declared and recorded by the individual. It can be understood that the administrations prepared an environment for the idea of keeping the zoning order under control and creating a planned urbanization order that is resistant to disaster risk by the "Building Registration Certificate" given in line with these records. However, the implementation of the existing structures carrying the risk of disaster is under the responsibility of the related units. In fact, while an easier and more accessible control mechanism is wanted to be established, the system is left to the savings of building owners. In this case, the control mechanism of the structures at risk of disaster has turned into a more complex and uncertain structure.

"Building Registration Certificate" is given for the purpose of "using the building". With this certificate, formal use was brought to existing informal infrastructure to control the use of electricity, water and natural gas and economic losses arising from informal use were prevented. However, this decision, which can be considered as positive for the citizen, has eliminated the concept of "Building Using Permission" in the Zoning Law. This permit is a document showing that the use of the building is allowed in exchange for the approval of the building's compliance with all plan projects specified in the license. In case there is no permission to use the building, that is, if the building does not comply with the projects stated in the license and its annex, no infrastructure service can be provided to the building. It may also be decided to demolish and suspend construction of buildings that are contrary to the license. In this regulation, the right of forgiveness of the demolition decision and fines approved by the building registration document to the building owner conflicts with the concept of "license" which is essential for the usage permission granted to the buildings and invalidates the related articles of the Zoning Law.

Another issue in the zoning peace regulation is related to the structures built on the immovables belonging to the Treasury and Municipalities. In case the structures obtained from the Building Registration Certificate are built on the immovable properties of the Treasury, these immovables are allocated to the Ministry. Upon the request of Building Registration Certificate holders and their legal or contractual successors, the immovables shall be sold directly by the Ministry at fair value. In this case, the revenues are recorded as income in the general budget. If the buildings with the Building Registration Certificate are built on the immovable properties belonging to the municipalities, the immovables shall be sold directly by the municipalities at the fair value on the request of the owners of the Building Registration Certificate and their legal or contractual successors. The structures in the immovable property owned by third parties and the structures located on the land allocated for the social equipment of the Treasury shall not be benefited from the provisions of this article. These issues are uncertain. Except for the exceptions that will not be issued the building registration document mentioned above, there is no situation specified and it is possible for the real estate belonging to the treasury and the municipality to obtain property based on the fair value by issuing the building registration certificate. The state-owned public goods are defined in the Turkish Civil Code as unattended places and public-owned goods are under the rule and disposition of the State. In other words, unattended places, public-owned goods and public service goods are under the control of the state. According to the Turkish Civil Code, the transfer of unattended property owned by the state is not possible in any way; in the transfer of public-owned and service goods, it is required to remove allotments first. In the case of allocation, a public interest

situation is also required.

As stated in the Cadastre Law, areas such as pasture, plateau, barracks and threshing are under the control of the state and cannot be acquired by means of reconstruction and revival. However, after this regulation was introduced, the construction of these buildings started except for the areas that are exempted under the zoning peace regulation, and the way to grant property rights with the building registration certificate is opened. When the Pasture Law and Cadastre Law are examined, it is clear that this ownership cannot be formed. It is also uncertain whether the buildings built on such areas can be given ownership within the scope of ownership. In addition, when the statement that the building registration document is valid until the possible urban transformation project, it is seen that the above-mentioned areas may be subject to zoning application in the future.

3. BENEFITS OF ZONING PEACE REGULATION

The benefits of this regulation can be examined in two areas: citizen and state. Benefits for the citizen can be listed as follows:

- The demolition decision or the cancellation of the fines imposed on the buildings on which the building registration certificate is received,
- Temporary connection of electricity, water and natural gas,
- Citizens can carry out transactions that are subject to sale for their official structures,
- Immovables with building registration certificates can be shown as mortgages or guarantees,
- In buildings where building registration certificate is obtained, it is possible to switch to floor ownership with the exemption of all the owners and change the breed,
- The zoning peace and the conflict with the state ends and the risks of the files in the municipalities are eliminated.

The benefits of the zoning peace regulation for the state are:

- First, the income obtained within the scope of reconstruction peace is provided with economic resources for future urban transformation practices,
- As the real estate tax, which can be collected from the unregistered condition and only because of the property of a land, will begin to be collected from the building property with the transition to floor ownership, the tax losses are eliminated and the tax revenues increase,
- With the disappearance of disputes between citizens and the state, densities in institutions and courts are reduced,
- The unregistered immovable market is registered with the building registration document and control is provided in the immovable market,
- As the owners who obtain a building registration certificate will have mortgage rights on these structures, the cash inflow to the markets will increase with the bank credits to be used.

4. UNCERTAINTIES IN ARRANGEMENT OF ZONING PEACE AND POSSIBLE PROBLEMS

The biggest problem that emerges within the scope of reconstruction peace is that the earthquake resistance of the building is undisputed to the responsibility of the owners. Leaving the earthquake resistance of the building under the responsibility of the owner in the reconciliation peace will cause the process to be delayed or not needed in an uncontrollable urban transformation. It will continue to pose a significant risk in the most risk groups, multi-story but less developed buildings (Özelmacıklı and Baz, 2018). The authority of the administrations in taking measures, inspections and necessary controls on earthquake constitutes a serious part of public order. Therefore, it is not acceptable for the administration to leave this authority to private individuals or building owners. In this way, the administration renders its undisputed responsibility unclear and does not have a clear framework to whom the responsibility and defect shall be attributed to the problems arising from the earthquake. In legal terms, Özlüer (2018) concluded that this is intended to warn building owners and that "responsibility" is not used as a legal concept within the scope of liability law. This provision, which will have no effect other than warning and encouraging the owner to take precautions on the durability of the building, is a warning to prevent the owner from misrepresenting the building as the Building Registration Certificate is issued based on the declaration of the building owner. It is clear that the building has not become lawful "with the Building Registration Certificate and that the Building Registration Certificate will not be a scientific and legal basis for the durability of the building during the urban transformation studies to be carried out on these buildings.

It is not clear how to evaluate the buildings to be carried out by the appraisal firms in the buildings that obtain a building registration certificate.

It is unclear what procedures will be applied to the structures that are planned to be formalized after the zoning peace regulation is put into practice.

Prior to this arrangement, the contradiction of zoning and the situation in which the opposing structures became official because of disrupting the environmental order, the problems of zoning that are clearly seen in the present are ignored in a sense.

5. CONCLUSION

The zoning peace regulation is aimed at eliminating the disputed situation between the state and the citizen. With this regulation, it is aimed to create financial resources for urban transformation studies and to easily register the areas at risk of disaster with declarations.

With this regulation, the structures constructed by the citizen unlawfully have been legalized within the scope of the law and the temporary subscriptions to these immovables, being able to take part in the transactions that are subject to economic sale and taking ownership of the building registration certificate are seen as positive results for the citizen.

Regarding the state, registering the informal real estate market and creating financial resources for urban transformation, it can be seen that the regulation has positive results.

It is an undeniable fact that the arrangement of zoning peace gives rise to many uncertainties in terms of its negative consequences and content, apart from these positive consequences for the citizen and the state. It is

observed that the control and supervision of the building is given by the declaration of the building registration document, while the control and inspections are in the responsibility of the administration, leaving the earthquake resistance of the building to the declaration of the persons makes the responsibility of the administration in this matter controversial. Furthermore, except for certain exceptions, the article concerning the allocation of immovable properties belonging to the Treasury and the municipality conflicts with the laws such as the Cadastre Law and the Pasture Law in force.

While the zoning peace regulation aims to generate financial resources for urban transformation, on the one hand, it may delay the urban transformation process with the uncertainty and open-ended items it contains. It is thought that these problems will cause losses from the income obtained and new problems may arise in the background while trying to solve the troubled process.

REFERENCES

Cadastre Law numbered 3402. RG. No: 19512 Publication date: 21.06.1987. https://www.mevzuat.gov.tr/MevzuatMetin/1.5.3402.pdf [Accessed 20.04.2019].

CNN Turk Web Site https://www.cnnturk.com/turkiye/imar-barisi-basvurulari-icin-sure-uzatildi [Accessed 22.04.2019].

Environment and Urban Ministry Web Site Zoning Peace https://webdosya.csb.gov.tr/db/imarbarisi/icerikler/brosur-20180603111057.pdf [Accessed 23.04.2019].

Gerem, M. (2014). Licensing in Reconstruction Law. https://www.turkhukuksitesi.com/makale_1767.htm [Accessed 23.08.2019].

Gürkaynak Esq, G., Yılmaz, İ., Yeşilaltay, B. and Utkan, N. (2018). Turkey: Recent Developments on Zoning Peace. http://www.mondaq.com/turkey/x/737712/real+estate/Recent+Developments+on+Zoning+Peace. [Accessed 22.08.2019].

Law on Restructuring Taxes and Other Receivables and Amendments to Some Laws numbered 7143 RG No: 30425 Publication date: 18.05.2018 http://www.resmigazete.gov.tr/eskiler/2018/05/20180518-3.htm [Accessed 23.04.2019].

Notification (2018). Notification on Procedures and Principles Regarding Building Registration Certificate. RG No: 31443 Publication date: 06.06.2018 http://www.resmigazete.gov.tr/eskiler/2018/06/20180606-8.htm [Accessed 19.04.2019].

Özelmacıklı, M., H. and Baz, İ. (2018). İmar Barışı'nın Getirdikleri ve Yaşanabilecek Aksaklıklar, Istanbul Commerce University Journal of Technology and Applied Sciences, Volume 1, No 1, pp. 65-72.

Özkaya Özlüer, I. (2018). A Juristic Approach to Regulating Zoning Peace, İnonu University Journal of Law, S.2, pp. 313-340.

Pasture Law numbered 4342. RG No:23272 Publication date: 28.02.1998. http://www.mevzuat.gov.tr/MevzuatMetin/1.5.4342.pdf [Accessed 20.04.2019].

Planned Areas Type Zoning Regulation. RG No: 30113 Publication date: 03.07.2017 http://www.mevzuat.gov.tr/Metin.Aspx?MevzuatKod=7.5.23722&MevzuatIliski=0&sourceXmlSearch [Access 25.04.2019].

Tercan, B. (2018). Reconstruction Amnesty Since 1948. Architecture, 403, 20-26, Chamber of Architects, Ankara.

Zoning Law numbered 3194. RG No: 18749 Publication date: 09.05.1985 https://www.mevzuat.gov.tr/MevzuatMetin/1.5.3194.pdf [Accessed 20.04.2019].

CISET - 2nd Cilicia International Symposium on Engineering and Technology
10-12 October, 2019, Mersin / TURKEY

SEISMIC SITE EFFECTS OF SOIL AMPLIFICATIONS IN KAHRAMANMARAS GAYBERLİ NEIGHBORHOOD

Eyyüb Karakan[1*], Kübra Ceren[2]

[1]Kilis 7 Aralık University, Faculty of Engineering and Architecture, Civil Engineering Department, Kilis, Turkey, eyyubkarakan@kilis.edu.tr

[2] Kilis 7 Aralık University, Graduate School of Natural and Applied Sciences, Civil Engineering, Kilis, Turkey, kubraceren1994@gmail.com

ABSTRACT

Active and engaged in a host of major faults in tectonic Kahramanmaras, Turkey has an important position. Active faults and high groundwater level of Kahramanmaras cause some geotechnical problems in Kahramanmaras. Kahramanmaras has a vertical sloping terrain. When the historical tectonic activity is examined, it has experienced great earthquakes and caused great material and moral losses. For this reason, geotechnical and tectonic surveys are required in Kahramanmaras province**.** Within the scope of this study, linear, equivalent linear and nonlinear analyzes of the soil were shown by using DEEPSOİL program in Gayberli-Hacı Bayram Veli Neighborhood, which is declared as a risky region in Kahramanmaras Province Center, and the dynamic behavior of the soil was calculated by using the appropriate correlations in the literature. The results of the analysis obtained with the help of the Deepsoil program and amplification factor values were compared with each other and information was obtained about how the dynamic behavior of the soil changes. As stated in the study, in order to determine the possible disaster hazard risks and engineering parameters of the soil, and to guide the necessary precaution projects and some basic and soil survey reports in the study area, the number and quality of the drilling works, geophysical studies, paleoseismological studies and samples taken from the drilling studies. As a result of laboratory tests, all studies and measurements, geotechnical and finally settlement suitability of the area was evaluated.

Keywords: *Deepsoil, Microzonation, Dynamic Analysis, Soil behaviour*

1. INTRODUCTION

Minimizing the damage caused by earthquakes that cause serious loss of life and property in our country is one of the fundamental tasks of engineering science. One of the most important factors causing loss of life and property in earthquakes is the characteristics of the floors on which the structures are built (Akın M., 2015). Behavior of engineering structures during earthquakes and possible damages depend on the structural properties as well as the properties of the foundation system and the ground layers of the structure. Anticipating soil behavior during an earthquake is very important in minimizing the loss of life and property in a possible earthquake (Kayacı S., 2015). Determination of engineering properties of soils is of great importance in minimizing soil behavior and/or damages under dynamic loads (Akın M., 2015). One of the studies aimed at minimizing earthquake damage is microzonation studies. (Kepçeoğlu Ö., 2008). Microzonation studies include the division of the region into meaningful small regions depending on the general soil conditions of the region, the determination of the dynamic behavior of the soil layers, the transfer of the findings obtained in the region to the maps and their evaluation. For this reason, the only solution to minimize the loss of life and property that may occur as a result of earthquakes is to conduct dynamic behavior analysis of soils, to interpret the results of the analysis correctly, to create zoning plans according to this dynamic behavior analysis and to make static calculations according to this dynamic behavior analysis. Local soil conditions, which are one of the most important factors causing damage to structures under earthquake loads, cause the geotechnical properties of soils to vary within the region and the resulting damage varies, so investigating local soil conditions in areas with high earthquake risk, more realistic and minimizes any damage that may occur (Karasu M., 2009).

The 1-D equivalent linear site response analysis, first presented by Schnabel et al. (1972, 1973), is a well known and widely used method. It is used to predict the transformation of earthquake movements as it moves upwards along the ground profile. It assumes a vertical propagation of shear waves through a homogeneous half-space between the horizontal layers of a ground profile modeled as a visco-elastic material with a constant damping ratio across all frequencies. (Idriss and Sun, 1992). These calculations are performed in the frequency domain, greatly increasing the speed and numerical stability of the calculations. However, in order to model the nonlinear response of the ground in the frequency domain, an iterative procedure is required.

In the microzonation study based on the soil augments of Erzincan province, the data of drilling wells drilled by the General Directorate of State Hydraulic Works were used (Özyazıcıoğlu M., 2019). Equivalent-linear magnification analysis was performed with the help of the program called Edushake/Proshake. Analysis was performed using 8 different bedrock data and acceleration-time history and mean apparent spectral acceleration (PSA) graphs of the average motion on the ground surface were obtained.

In order to form a basis for microzonation study, dynamic behavioral characteristics of Van Yüzüncü Yıl University campus soils were determined (Akın M., 2015). As stated in the study, especially the loss of life and property caused by earthquakes in Turkey in 1999 and beyond, once again revealed the social and economic dimension of the earthquake and its effects. Dynamic soil properties should be examined in accordance with microzonation principles considering the effects of natural disasters such as earthquakes. For this purpose, the findings obtained from the drilling works and geophysical methods and dynamic soil properties were determined in the campus area of Van Yüzüncü Yıl University and as a result, a settlement evaluation was made to guide the future plans for the campus area.

Within the scope of this study, microzonation study of 29.9 hectare area and its surroundings, declared as a risky region in Kahramanmaras province, was carried out in 2013 by Kahramanmaras Municipality, Analiz company has obtained detailed geotechnical data about this region and it has been declared as a risky region by the decision of Council of Ministers numbered 2013/4252.

The data used in this study were analyzed by Analiz company. In order to evaluate the 29,9 hectare area and its surroundings declared as risky zone in Kahramanmaras city center within the scope of the Law numbered 6306, it has been obtained from the preparation of microzonation studies and preparation of reports based on 1/5000 and 1/1000 scaled zoning plan of 215,80 hectare area. The area where the microzonation study is conducted is the Gayberli-Hacı Bayram Veli Neighborhood of Kahramanmaras Province. In the selected area, Analiz company conducted a microzonation study and within the scope of this microzonation study, a total of 63 drilling wells with a total depth of 1278 meters and a depth of 15-30 meters were drilled in the region. During the boreholes, Standard Penetration Test (SPT) was performed every 1.5 meters and a total of 170 presiometer tests were performed. Vertical electric drilling (DES) surveys at 14 points, official surveys at 60 points, microtremor measurement at 60 points, resistivity tomography at 54 points, seismic reflection measurements at 42 profiles were performed. In paleoseismological studies, 7 pits with a depth of 3 meters and an observation pit with a width of 30 meters were opened and the amplification factor of the soil was calculated. Detailed information has been obtained about the dynamic behavior of this area which is declared as a risky zone.

2. STUDY AREA

Kahramanmaras province Located between the 37-38 northern parallels and the 36-37 eastern meridians, the northern part of which is highly mountainous, the province of Kahramanmaras generally includes the mountains which are extensions of the Eastern and Southeastern Taurus Mountains and the depression areas between them. As stated in the microzonation study, our study area is 215.80 hectares including 29.9 hectares in the city center and its environs. The study area includes Oruç Reis, Malik Ejder, Barbaros, Hacı Bayram Veli and Gayberli Neighborhoods from west to east.

When the geology of the study area is examined; as indicated in the microzonation study in the study area, as a result of the geological studies conducted in the study area, four different environments such as filling, alluvium, slope debris and rotational formation were encountered. The fill in the study area is 0-10 meters thick and consists

of clay, sand and gravel. It cannot be used as a foundation material due to its heterogeneous structure. In the study area 6-20 meters thick alluvial and silty sandy clay layer was observed. Slope debris fragments were also observed at different locations in the study area and varying in depth from 0 to 20 meters thick. This heterogeneous soil structure in the study area adversely affects the superstructure as it is not an engineeringly reliable soil layer.

3. MATERIALS AND METHODS

Soils show different behavior characteristics under dynamic loads. Soil surveys are performed to learn the index properties and bearing strength of soils, but soil studies do not give detailed information about the dynamic behavior of soils. There is a lot of computer software that can analyze dynamic behavior of soils. Within the scope of this study, with the help of Deepsoil program, linear, equivalent and nonlinear analyzes in frequency domain and nonlinear analysis in time domain were made according to acceleration records of 17 August 1999 Kocaeli Earthquake and the amplification factor of the soil was calculated by using literature relations. As a result of the analysis, acceleration, response spectrum and amplification factor graphs were obtained and detailed information about the dynamic behavior of the soil was obtained according to the results of this analysis. The data obtained from the microzonation study were used in the analyzes. There are SPT-N numbers in 10 of the drillings. V_{s30} shear wave velocity is required for data entry into deepsoil program.

In this article, shear wave velocity is calculated by Iyisan (1996) correlation as shown in Equation 1 in the layers that are subjected to Standard Penetration Test (SPT). In this study Midorikawa (1987) correlation coefficient was calculated with the help of the correlation and obtained growth factors are shown in Table 1. Midorikawa with the classification;

0.0 - 2.0 amplification value C (low hazard)

2.0 - 4.0 amplification value B (medium hazard)

4.0 - 6.5 amplification value is classified as A (high hazard).

10 wells with SPT-N value were used in the analysis. The shear wave velocity values obtained from the wells of SK10, SK16, SK19, SK22, SK23, SK28, SK31, SK36, SK38, SK40 with the SPT-N value by means of İyisan (1996) formula were used in the analyzes. Since there is no detailed information about bedrock depth in the study area, since the shear wave velocity reaches 760 m/sec according to UBC97, our bedrock depth is considered as the bedrock where the shear wave velocity reaches this value and the bedrock depth is considered as It was found for drilling well. It was calculated as 87 meters for SK10 drilling well, 110 meters for SK16 drilling well, 110 meters for SK19 drilling well, 95 meters for SK22 drilling well, 160 meters for SK23 drilling well, 100 meters for SK 28 drilling well, 95 meters for SK 31 drilling well, 130 meters for SK36 drilling well, 86 meters for SK38 drilling well and 170 meters for SK40 drilling well. As a result of the geophysical measurements, V_{s30} was obtained from the shear wave field measurements. Interpolation was carried out depending on the depth until the bedrock value, ie 760 m/sec, was found for each borehole using the shear wave velocity at 30 meters. When the boreholes and geophysical measurements in the study area are compared with each other, high SPT-N strokes and reflux values are seen in the wells. Since the reflection value is used in cases where SPT-N number of strokes is greater than 50, drilling wells indicate that the ground is very hard. However, when the geophysical measurements are examined, the V_{s30} shear wave values in the study area are very low. V_{s30} shear wave values are 129-392 m/sec in fill, 230-325 m/sec in alluvium, 282-433 m / sec in slope debris, 260-615 m/sec in cyclic formation. When the shear wave velocity values are examined, most of the boreholes yielded reflux but the shear wave velocity values indicate that the bedrock is not this depth since the ground does not reach 760 m/sec at 30 meters.

Table 1. Amplification Factor Calculated by Midorikawa (1987) Correlation

Drilling Number	$V_{S,30}$ (m/sec)	Amplification Factor
SK10	241.83	2.52
SK16	293.87	2.25
SK19	359.21	1.99
SK22	338.83	2.06
SK23	357.02	1.99
SK28	368.06	1.96
SK31	312.64	2.16
SK36	315.12	2.15
SK38	387.93	1.90
SK40	401.55	1.86

3.1. IYISAN (1996) Relation and Midorikawa (1987) Amplification Factor

There are empirical relations developed by many researchers to obtain shear wave velocity with SPT-N pulse numbers. The Iysian (1996) correlation also provides V_S shear wave velocity based on SPT-N strokes in all soil types.

Midorikawa (1987) Borcherdt et al. (1991), by observing and analyzing the shear wave velocity during ground motion, the average value of the resulting velocity has a significant effect on the amplification levels occurring in soils at a certain depth on the surface. (Belice A., 2006).

$$Vs = 51.5 * N^{0.516} \quad (1)$$

$$A=68*V_{s,30}^{-0.6} \quad (V_s<1100\ m/sec) \quad (2)$$

$$A=1 \quad (V_s>1100\ m/sec) \quad (3)$$

$$V_{s,30} = \frac{30}{\sum_{i=1}^{N} \frac{H_i}{V_{s,i}}} \quad (4)$$

A: relative amplification factor for maximum ground speed

AHSA: Average horizontal spectral amplification over a period of 0.4-2.0 sec

$V_{s,30}$=Average shear wave velocity at a depth of 30 meters

V_1= Average S-wave velocity corresponding to a depth of a quarter-wave length for one second wave

4. RESULT AND DISCUSSION

This study was carried out on the preparation of microzonation studies based on 1/5000 and 1/1000 scaled zoning plan of a total area of 215.80 hectares in order to evaluate the 29.9 hectare area and its surroundings declared as risky zone in the center of Kahramanmaras in the scope of the law numbered 6306 and the preparation of microzonation studies. and Deepsoil program were used in the frequency domain of Gayberli-Hacı Bayram Veli Neighborhood, linear equivalent in frequency domain and nonlinear analysis in clock domain were made according to 17 August 1999 Kocaeli (M_w=7.4) acceleration record and Midorikawa (1987) correlation was calculated with the help of soil growth factor. SPT-N number of hits was recorded in most of the 63 drillings carried out in the Gayberli-Hacı Bayram Veli Neighborhood. As a result of the analyzes performed with Deepsoil program, acceleration-time (Fig. 1a), response spectrum-T (period) (Fig. 1b) and amplification factor-T (period) (Fig. 1c) graphs were obtained.

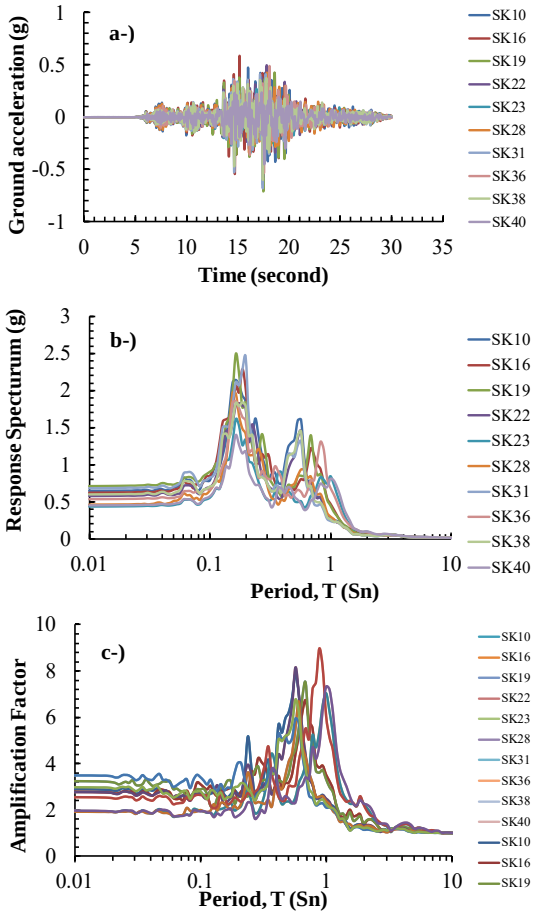

Fig 1. Acceleration-time (Fig. 1a), response spectrum -T (period) (Fig. 1b) and amplification factor-T (period) (Fig. 1c) graphs for lineer analysis

When the results of linear analysis in the frequency domain are examined; In the acceleration-time graph data, there are no large changes in the acceleration value of the 10 selected drillings. Only drilling in SK19 has a greater acceleration value than the others (Fig. 1a). The acceleration values of the selected 10 drillings ranged from 0.42 g to 0.69 g. When the response spectra-T (period) graphs of the layer closest to the surface are examined, sounding SK19 has the highest response spectrum value and no significant differences are observed between the response spectra values of the other drillings. Response spectrum values ranged from 1.39 to 2.49. When the response spectrum-T (period) graphs of the bedrock layer are examined, there is a slight difference between the response spectra.

When the amplification factor graph is examined, the amplification values vary from 5.96 g to 8.29 g.

When the results of equivalent linear analysis in frequency domain are examined; acceleration-time values were lower in the frequency domain than linear analysis results and the acceleration values varied between 0.22 g and 0.51 g. The response spectrum values of the surface layer were also lower in the linear analysis results in the frequency domain and the results ranged from 0.75 g to 1.64 g. The response spectrum values of the bedrock are again in agreement with each other and do not show large differences (Fig. 2)

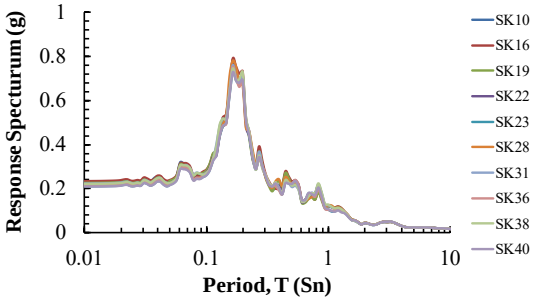

Fig 2. Response specturum period relationship for bedrock of equivalent linear analysis

When non-linear analysis results are analyzed in the field of clock; In the frequency domain linear and equivalent linear analysis results were found to have lower values. The acceleration values range from 0.17 g to 0.31 g. The response spectrum values of the surface layer ranged from 0.58 g to 1.46 g. These results are in agreement with the response spectra of the bedrock and no major changes were observed. The amplification factor ranged from 3.70 g to 4.80 g (Fig. 3).

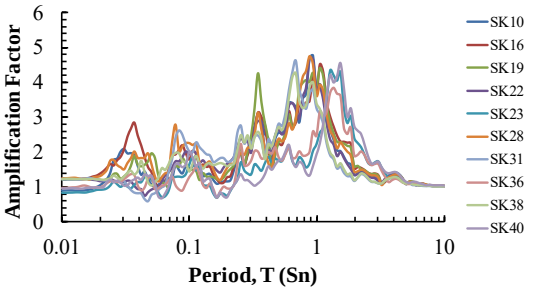

Fig 3. Amplification factor period graphs for non-linear analysis

When the results of the three analyzes were compared with each other, the highest acceleration, response spectrum and amplification values were obtained as a result of linear analysis in the frequency domain. In this case, it is considered that one type of analysis cannot provide clear information about the dynamic behavior of

the soil. In addition, although the selected 10 drillings were located in the same neighborhood, they showed different behavior characteristics due to different acceleration, response spectrum and amplification factor values in different analysis types. As a result of this study, it determined the characteristics of dynamic behavior depending on local soil conditions and showed how important the soil dynamic behavior is.

Midorikawa (1987) as a result of the calculations made with the correlation of the lowest soil amplification was 3.08 and the highest soil amplification was obtained as 4.53. Midorikawa (1987) results are obtained according to the classification of the hazard class is done according to the hazard area is seen to have medium and more high danger. This was demonstrated by the results of the analysis performed by Deepsoil program.

5. CONCLUSIONS

The reflection of the borehole shows that the borehole has a very hard ground layer, but when the geophysical measurements made in addition to the drilled boreholes are examined, the shear wave velocity is very low at the depths of the SPT-N strokes, moreover, most of the boreholes at a depth of 30 meters produced reflux however, shear wave velocity of the bedrock with a depth of 30 meters was not measured in any of the geophysical measurements. This indicates that geophysical measurements should be taken, as the boreholes drilled when the soil surveys, microzonation studies or any studies related to the soil are performed may give misleading results.

The amplification values obtained in this study vary between 1.86 and 2.52. According to Midorikawa (1987), B and C class is low and medium dangerous. Since the working area has high amplification factors under dynamic loads, this area presents a great danger in the event of an earthquake and dynamic behavior analysis of the soil in this region must be performed.

ACKNOWLEDGEMENTS

This study is supported by Kilis 7 Aralık University Scientific Research Project No. 12271.

REFERENCES

Ansal A. ‘Sahaya Özel Tasarım Depremi’, 8. Ulusal Deprem Mühendisliği Konferansı, 2015.

Akın M.K., Akın M., Akkaya İ., Özvan A., Üner S., Selçuk L., Tapan M. , (2015). ‘’Mikrobölgeleme Çalışmasına Altlık Oluşturmak Üzere Van Yüzüncü Yıl Üniversitesi Kampüs Zemininin Dinamik Özelliklerinin Belirlenmesi.’’ Jeoloji Mühendisliği Dergisi.

Hashash YMA (2009) DEEPSOIL V 3.7, *Tutorial and User Manual. 2002-2009*, University of Illinois at Urbana-Champaign, Urbana, Illinois

İyisan R. (1996). ‘Zeminlerde Kayma Dalgası Hızı ile Penetrasyon Deney Sonuçları Arasındaki Bağıntılar.’’ TMMOB İnşaat Mühendisleri Odası Teknik Dergi, Cilt:7, Sayı:1.

Idriss IM, Sun JI (1992) *User’s manual for SHAKE91: a computer program for conducting equivalent linear seismic response analyses of horizontally layered soil deposits*. Center for Geotechnical Modeling, Department of Civil and Environmental Engineering, University of California

Karasu M. (2009). Bakırköy İlçesi’nin Mikrobölgelemesi, Yüksek Lisans Tezi, Yıldız Teknik Üniversitesi, İstanbul, Türkiye.

Kayacı S. (2018). ‘‘Çok Kanallı Yüzey Dalgası Analiz Yöntemi (MASW) İle Zemin Özellikleri ve Sıvılaşma Potansiyelinin Belirlenmesi: Arifiye-Sakarya Örneği.’’ Sakarya Üniversitesi Fen Bilimleri Enstitüsü Dergisi.

Belice A. (2006). Eskişehir Yerleşim Yeri Zeminin Büyütme Etkisinin Makaslama Dalga Hızına (Vs) Bağlı Olarak Belirlenmesi, Yüksek Lisans Tezi, Balıkesir Üniversitesi, Balıkesir, Türkiye.

Kepçeoğlu Ö. (2008). Bursa İli Güzelyalı Beldesi İçin Mikrotremor Ölçümlerine Dayanan Bir Mikrobölgeleme Uygulaması, Yüksek Lisans Tezi, İstanbul Teknik Üniversitesi, İstanbul, Türkiye.

Mert M. (2018). Zeminlerin Sıvılaşma Potansiyelinin Doğrusal ve Doğrusal Olmayan Analizlerle Değerlendirilmesi, Yüksek Lisans Tezi, Eskişehir Osmangazi Üniversitesi, Eskişehir, Türkiye.

Schnabel P, Seed HB, Lysmer J., (1972) *Modification of Seismograph Records for Effects of Local Soil Conditions.* Bulletin of the Seismological Society of America; 62 (6): 1649-1664.

Schnabel P, Seed HB, Lysmer J., (1973), *Erratum: Modification of Seismograph Records for Effects of Local Soil Conditions.* Bulletin of the Seismological Society of America; 63 (2): 750.

UBC97

Özyazıcıoğlu M., Dönmezçelik K., Orhan S., Özkan M., (2019). ‘‘Erzincan İli Zemin Büyütmelerine Dayalı Mikrobölgeleme Çalışması.’’, Artvin Çoruh Üniversitesi, Doğal Afetler ve Çevre Dergisi

Yağcı B. (2005). Mikrobölgeleme Metodolojileri Ve Balıkesir İçin Bir Uygulama, Doktora Tezi, Balıkesir Üniversitesi, Balıkesir, Türkiye.

2013/4252 sayılı bakanlar kurulu kararı

http://kyhdata.deprem.gov.tr/2K/genAcc.php?dst=TU9EVUxFX05BTUU9ZXZ0RmlsZSZNT0RVTEVfVEFTSz1zaG93Jk1PRFVMRV9TVUJUQVNLPUFMTCZNT0RVTEVfVEFSR0VUPW9sZCZUQVJHRVQ9MTk5OTA4MTcwMDAxMzlfODEwMSZUQVJHRVRfU0VSSUFMPTEwNjQ%3D.

CISET - 2nd Cilicia International Symposium on Engineering and Technology
10-12 October, 2019, Mersin / TURKEY

INFLUENCE OF DOPING ON THE ELECTRICAL CONDUCTIVITY OF THE ELECTROLYTIC GELS

Veysel Alcan*[1] and Osman Murat Özkendir[2]

[1]Tarsus University, TechnologyFaculty, Department of The Software Engineering, Mersin, Turkey, alcanveysel@tarsus.edu.tr

[2] Tarsus University, Technology Faculty, Department of The Energy Systems Engineering, Mersin, Turkey, ozkendir@tarsus.edu.tr

ABSTRACT
The surface electromyogram (sEMG) electrodes are commonly used with electrolytic gel layer. The quality measurement of the sEMG signal is generally defined by the ratio between the measured EMG signal and the unwanted noise contributed from different sources called Signal to Noise Rate (SNR). One of the potentially large sources of noise is that caused by the electrode-skin interface. Thus, the skin contact layer should achieve good electrode-skin contact, low electrode-skin impedance respect to impedance and chemical reactions at the interface of the skin. The gel layer significantly can improve signal electrode-skin impedance quality by effectively reducing the impedance present at the electrode-skin interface. The aim of the present study is to compared five different gels, and to investigate conductivity properties of gels to obtain high conductive composition. In order to increase the conductivity of the electrode-skin surface, we prepared new four different gels (TypeII= Routine + B_2O_3, TypeIII=Routine +FeS, TypeIV=Routine +Mn, and TypeV= Routine +$Nd_{0,4}Fe_{0,6}BO3$) by doped routine best-selling industrial gel (type1=Routine). In order to compare electrical conductivity of gels, surface electromyography signals with different gels were recorded by evoked same stimulus. sEMG measurements were compared with nerve conduction studies (NCSs) including sensory median nerve test. We found that TypeII with light boron atoms added gel had the only gel form that increased its conductivity. The reason of such a result were related with the low potential values of boron in the gel form, that may cause to rearrangement in the bond structures of the atoms in its vicinity.

Keywords: Electrolytic Gel, Electrode-Skin Impedance, Surface Electromyography, Nerve Conduction Studies

* Corresponding Author

1. INTRODUCTION

The surface electromyogram (sEMG) is the more common non-invasive method to measure muscle activity that can be recorded by applying conductive electrodes to the skin surface. Accurate measurement of the sEMG signal depends on a variety of factors such as the characteristics and the positioning of the electrodes, crosstalk, the interactions of the electrodes, the amplifiers, the conversion and storage of signals, noise and other electrical activities. Noise factor is one of the most important factors affecting the accuracy and quality of signal recording. The quality measurement of the sEMG signal is generally defined by the ratio between the measured EMG signal and the unwanted noise contributed from different sources called Signal to Noise Rate (SNR). In order to reduce noise during SEMG recording, it is very important to kept a minimum of the possible sources of noise. One of the potentially large sources of noise is that caused by the electrode-skin interface (Hermens et al., 1999).Noise from electrode-skin interaction is caused by the fluctuations in the impedance between the electrode and the skin, which generally converts the ionic currents produced in the muscles into electrical current, that is, differences in impedance between the skin and the electrode. The electrical conductivity of the skin depends on many factors such as the epidermal stratum corneum layer consisting of dead skin, sweat, cleaning, anatomy and electrodermal activity etc. (Martinsen et al., 1999). In order to decrease electrode-skin impedance effects, one effective method is to develop several types of electrodes used in electrophysiological measurements. The electrode structure for electrical measurements heavily influences the signals that are measured. So it is important to find the best-suited electrode according to application (Rahal et al., 2009). Due to many advantages, the Silver/Silver Chloride (Ag/AgCl) electrodes consisted of a layer of silver chloride, often in the form of a gel surrounding a metallic part are most commonly used as wet (hydrogel) electrodes in electrophysiological measurements.

Another effective method is to develop the material forming the skin contact layer should achieve good electrode-skin contact, low electrode-skin impedance respect to impedance and chemical reactions at the interface of the skin. The surface EMG electrodes are commonly applied on the skin with conductive gel as a chemical interface between the skin and the metallic part of the electrode. Therefore, these electrodes are called wet electrodes or gelled electrodes because of using an electrolytic gel layer. The gel layer changes skin to a highly ion-conductive layer by applying to moisturize the skin outer layer. On the other word, the metallic part of the electrode allows free conduction of the current in the muscle through the connection between the electrolyte and the electrode. Oxidative and reductive chemical reactions occur in the contact area of the metallic part and in the gel layer (Gerdle et al., 1999**)**. The Gel layer significantly improves signal quality by effectively reducing the impedance present at the electrode-skin interface. However, there are also some disadvantages in the use of electrodes with gel, such as skin irritations, bacterial growth, especially for long-term recordings, signal disruption with sweat, and dehydrated gel producing high impedance and increased motion artifact (Searle et al., 2000; Jung et al., 2012).

In order to keep the SNR or conductivity of electrode-skin layer high, chemical and various electrical properties of conductive gels commonly used in biomedical field have been investigated and it has been reported that the electrode gels could introduce large changes in the electrical conductivity, corresponding with the different composite in the gel (Tronstad et al., 2010; Guiseppi-Elie, 2010; Kara et al., 2017)

The advances in the material science, particularly, biologic signal transmission for therapeutic or diagnostic purposes in biomedical field emphasis the need to evaluate the products used in these procedures and the electrical conductivity of the biological tissues. The aim of the present study is to prepared novel four different gels by doping to a common-used commercial gel and investigate conductivity properties of gelsto obtain high conductive composition

2. METHOD AND MATERIALS

2.1.Preparation of The Gels

In order to increase the conductivity of the electrode-skin surface, we prepared new four different gels by doped routine best-selling industrial gel (Konix@ultrasound Gel,USA) which is widely used in medical applications such as EMG, ECG, EEG, Ultrason and TENS. This routine gel contained Deionized Water, Carbomer, Trietanol amin, Mono Propylene Glycol, Benzyl Alcohol, Methylchloroisothiazolinone, and Methylisothiazolinone substances and compounds.

Metals are the main group of elements that carry free electrons in case of a forced attract them in one direction, i.e., electrical conductivity. In metals, the outer Shell electrons are just located above the valence levels and bonded weakly to the atoms. So, in case of a weak interaction, these electrons can make them free electrons and move among the atoms freely. In case of the stack of atoms in a volume, i.e. bulk, the electrons tend to move on the surface to free themselves from the high potential among the atoms which are located in the depth of the surface. When a powerful electrical field applied on these electrons cause a force that make them move on the surface (where less potential presents), which is called as the conductivity of the material. It is known that, the most effective conductors are metals with a single valence electron. Silver, copper and gold are known as the best conductors with single electrons in the valence bands

Free electrons are the sources of the current in a material. Among the elements, half metals and metals in solutions have a high influence on the free electrons motions, due to the change at the barriers created by the atomic potentials. Free electrons travel among the atoms in a varying interstitial potential. So, if one would like to increase the conductivity in the material, it should be focused on the interstitial potential to change the media positively for free electrons. The dopants given in Table 1 are half metals or metal/metal compounds and proposed to change the potential values either positively or negatively. Metals (Fe, Mn or Nd) were proposed to the study to govern the processes in the solution. The main problem was suggested as their being heavy than all

elements in the routine gel. Despite the electron supporting role of the heavier elements in the gel, the postula was suggested that the higher potential of the metals may increase the interstitial potential for the free electrons during their travel among the atoms. The increase in the potential may result a sudden decay in electrons' kinetic energy that decreases the conductivity. Only half metallic boron was out of this criteria, because it is light than most of the elements in the gel.

The properties of five gel types with different composition are listed in Table 1.

Table 1. Gel types with different doped sunstance and compositions

Gel Type	Ingredient	Proportion(gr)	
		Routine	Additive
TypeI	Routine	1,59	-
TypeII	Routine+ B_2O_3	1,59	0,03
TypeIII	Routine +FeS	1,19	0,03
TypeIV	Routine +Mn	1,83	0,17
TypeV	Routine+ $Nd_{0,4}Fe_{0,6}BO_3$	2,54	0,04

2.2. Experimental Protocol

All gels in this study were used with similar Silver/Silver-Chloride (Ag/AgCl) electrode type. Before each gel test, the skin was cleaned with alcohol. Skin temperature was maintained at 320 C; room temperature between 22^0 C and 25^0 C. During the measurement, sweat activity was controlled and cleaned before tests. In order to compare electrical conductivity of gels, surface EMG signals with different gels were recorded by evoked same stimulus. EMG measurements were compared with nerve conduction studies (NCSs) including sensory median nerve test. NCS test was conducted with a Viasys Medelec Synergy EMG device. Filter settings for sensory NCS was 20 Hz. Sweep speed was 1 ms/division and sensitivity was 20 µV/div and increased if needed. All electrodes were 10 mm in diameter. Distance between the recording electrodes was 3-5 cm. Distance between stimulator electrodes was 3 cm. Stimulation intensity was 10-30 mA, duration 0.1-0.2 ms for sensory NCS.

2.3. Signal Processing

For median sensory NCS, digit II (finger)-wrist median sensory nerve conduction velocity and palm-wrist median sensory nerve conduction velocity were orthodromically recorded by surface stimulation from digit II and mid palm. Latencies of the sensory nerve action potentials(SNAP) were measured to the negative peak. Amplitude was measured from baseline to peak point of SNAP. The analysis software of the EMG device was used for calculation of the latency and amplitude.

3. DISCUSSION AND RESULTS

The parameters from SNAP recorded simultaneously on the same test subject were compared between different electrode gel types, represented in table 2. The electrical conductivity measurements of the gels revealed a higher amplitude of the TypeII than the others.On the other hand, TypeII had lower latency than the others. Types III and V had lower and roughly equal amplitude as well as equal latency, but with a slightly lower amplitude for Type V.

Table 2. GB Electrode-Disc Ag/AgCl electrode

Electrode Type	Latency (ms)	Peak Amplitude (µV)	Peak-Peak Amplitude (µV)
TypeI	3,10	41,1	45,0
TypeII	3,00	44,4	48,6
TypeIII	3,25	29,3	37,7
TypeIV	3,15	39,6	39,0
TypeV	3,15	27,3	35,3

Fig.2 also clearly shows that the differences between the latency and amplitude measurements from different gels.

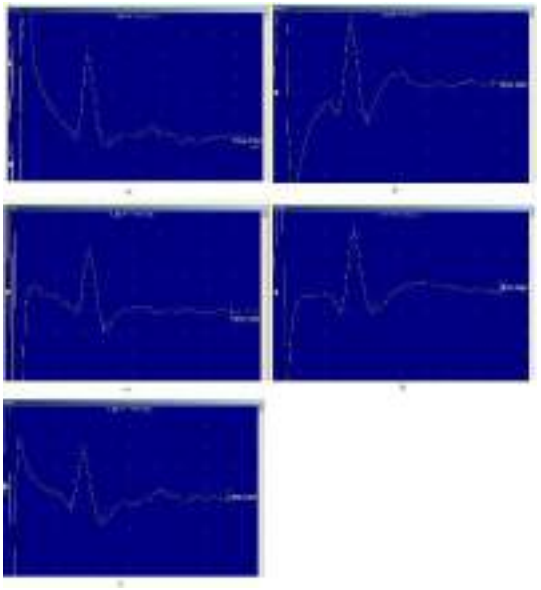

Fig. 1. Comparison of gels for median sensory measurement a) Routine b) Routine +B_2O_3c) Routine +FeS d) Routine +Mn e) Routine +$Nd_{0,4}Fe_{0,6}BO_3$

In this study, we aimed to modify the properties of best-selling commercial gel by doping different substance and compounds to improve the electricalconductivity and transport properties. We prepared five different gel types. TypeII gel provided an increased amplitude to NCS test in partially filled Boron composite. This confirms the postulate stated as above that, light boron atoms decrease the average value of the interstitial potential and support the current in the gel. So, free electrons moved longer in the boron doped routine gel. In case of dopants in such a media, the dopants may behave like a point defect which is known to be bless by altering the band gap positions of their neighboring atoms. Besides, lowering the interstitial potential in the gel form, may cause to rearrangement in the bond structures of the atoms in its vicinity. The values collected for the boron doped samples confirms the best results with its small volume, that it has an influence on the electronic properties of atoms around to arrange themselves, not to ruin like other metals. Conductivity

values indicate the rate at which the conductive gel conducts the electrical current. In other words, it shows the value of resistivity. For sEMG recordings, the electrode-skin impedance can be electrically modelled. Fig.2 shows the electrode-skin interface and electrical model where E_{he} represents the electrode potential, C_d and R_d the represents the double layer capacitance and impedances of the electrode–electrolyte interface, respectively. R_s represent resistance of the electrolyte and the leads, $R_e$represents the resistance of the Epidermis, C_e represents the capacitance induced by the nonconductive stratum corneum layer, R_u represent the overall resistance of the tissue underneath the epidermis layer.

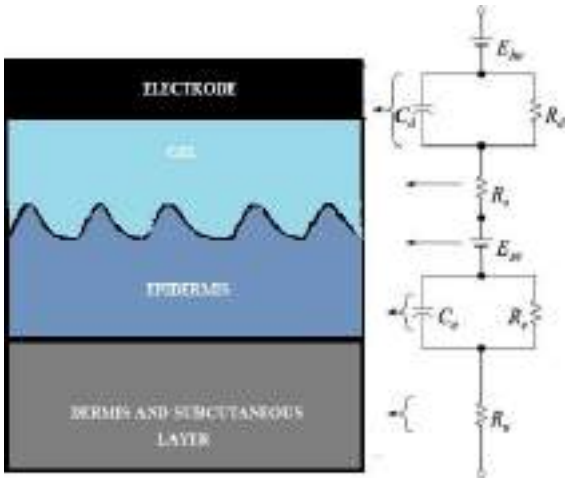

Fig. 2. The electrode-skin interface and its electrical model.

C_d capacitance and R_d resistance vary with the properties of the electrode used as well as electrolyte used in gel. The conductivity of a gel depends on the proportion of dissolved solids in it or how the doped substance makes a compound by changing its resistivity. As a result of these changes, low resistivity causes high conductivity or vice versa. The value of the ionic current passing through the skin surface causes to pass to the electrode's metallic part at a higher value due to its high conductivity. This could lead to increased signal amplitude.

4. CONCLUSION

For many biomedical imaging and signal processing application, low electrode-skin impedance or high signal to noise ratio is very important in terms of signal quality, the lowest signal loss and imaging performance. In this study, most known metals (iron and manganese) and half metallic boron were added to routine gel and their conductivity changes are tested. Interestingly, light boron atoms added gel has the only gel form that increased its conductivity. Metal added gel conductivity goes worse and increased its resistivity. From this point, it is concluded that, presence of light element boron in the gel decreased the average interstitial potential where free electrons move. Besides, boron has also added some positive results like having low mass and financially more economic than other dopants.

This study will need further investigate for different properties of gels used, for example sorption characteristics, electrical characteristics, skin conductance measurement, measurement under sweat and pressure conditions, etc.

REFERENCES

Gerdle, B., Karlsson, S., Day, S., Djupsjöbacka, M, (1999). "*Acquisition, Processing and Analysis of the Surface Electromyogram." Modern Techniques in Neuroscience,*Windhorst U and Johansson H. Ed., Vol.26, Springer Verlag, Berlin, pp.705-755.

Guiseppi-Elie, A. (2010) "Electroconductive hydrogels: Synthesis, characterization and biomedical applications."*Biomaterials*,Vol.31, No.10, pp.2701–2716.

Hermens, H.J., Freriks B., Disselhorst-Klug, C. and Rau, G. (2000). "Development of recommendations for SEMG sensors and sensor placement procedures."*J Electromyogr Kinesiol,*Vol.10, No.5, pp.361-374.

Jung, H.C., Moon, J.H., Baek, D.H., Lee, J.H., Choi, Y.Y., Hong, J.S. and Lee. S.H. (2012). "CNT/PDMS composite flexible dry electrodes for long-term ECG monitoring."*IEEE Trans. Biomed. Eng.*, Vol.59, No.5, pp.1472–1479.

Kara, S., Konal, M., Ertaş, M. and Uzunoğlu, C.P. (2017). "The electrical characteristics of electroconductive gels used in biomedical applications." *Proc., Medical Technologies National Congress, TIPTEKNO*, pp.1-4.

Martinsen,O.G., Grimnes, S. and Haug, E.(1999)."Measuring depth depends on frequency in electrical skin impedance measurements."*Skin Res. Technol,*Vol.5, No.3, pp.179–81.

Rahal, M., Khor, J.M., Demosthenous, A., Tizzard A. and Bayford, R. (2009). "A comparison of electrodes for neonate electrocal impedance tomography." Physiol. Meas.,Vol.30, No.6, pp.73–84.

Searle, A. and Kirkup, L. (2000). "A direct comparison of wet, dry and insulating bioelectric recording electrodes." *Physiol. Meas.*, Vol.21, No.2, pp.271–283.

Tronstad, C., Johnsen, G.K., Grimnes, S. and Martinsen, O.G. (2010). "A study on electrode gels for skin conductance measurements."*Physiol. Meas.*, Vol.31, No.10, pp.1395–1410 .

CISET - 2nd Cilicia International Symposium on Engineering and Technology
10-12 October, 2019, Mersin / TURKEY

MARBLE POTENTIAL OF THE MERSIN REGION

Hayati KOÇ *[1]

[1] Mersin University, Faculty of Engineering, Department of Geological Engineering, Mersin, Turkey.
e-mail:hakoc@mersin.edu.tr

ABSTRACT

Natural building stones have been used for different purposes in human life throughout history. The most well-known type of natural building stones is marble. Marble which is a metamorphic rock is formed by crystallization of carbonate rocks by metamorphosis under heat and pressure. In commercial terms, any kind of rock that looks good when polished is considered as marble. But, each marble found in nature has different physic-mechanical properties. Therefore, the usage areas of marbles vary according to these properties.

Mersin and around are represented by clastic rocks containing limestone-dolomite intercalations in the Paleozoic. In the Mesozoic period, it generally dominated by platform carbonate rocks which also contains clastic rocks at the base and ophiolitic and ophiolitic mélange units at the top levels. The Cenozoic in Mersin and around is represented by units which are composed of dominant clastic rocks intercalated by limestone. Of these, especially Mesozoic and Cenozoic carbonate rocks are operated as marble.

Keywords: *Marble, Limestone, Mersin.*

* Corresponding Author

1. INTRODUCTION

It is a known fact that marble is an important material in human life from past to present. In the past, it was used extensively in the construction of buildings, monuments, beams etc. Today, it is widely used for restoration of historical monuments, flooring and covering of buildings, interior and exterior of buildings, landscaping, pedestrian paths and sidewalks (Vardar, 1990; Demir *et al*., 2006).

Marble formed by crystallization of carbonate rocks such as dolomite, limestone and dolomitic limestone by metamorphosis under heat and pressure is a metamorphic rock. The main mineralogical component is calcite. The colors of marble are usually black, gray, beige and white, depending on the secondary minerals can be in different colors. In the commercial sense, marble is considered to be any kind of durable rock (limestone, travertine, granite, syenite, serpentine, diabase, etc.) that can be cut and processed, which looks good when polished.

The following parameters are especially important for the operation of marbles. These are geological parameters; discontinuity planes such as foliation, fracture, bedding, color and pattern homogeneity, block quality and cut-polishing, geomechanical and physical properties; resistance to atmospheric and chemical effects (Şentürk *et al*., 1995). In Turkey for newly introduced marbles, parameters such as color, polishing and hardness are often emphasized however, physic-mechanical properties are often neglected or a trial-and-error method is preferred. All of this affects the economy negatively and the loss of material value caused by not having control of our marble is inevitable (Teymen, 2017).

According to 2018 data MTA, Turkey's potential reserves of natural stone are 5,161 million cubic meters. According to the 2016 data of Istanbul Marble and Granite Processors Chamber of Tradesmen, Turkey took sixth place in the world natural stone production, after China, India, Italy, Spain and Iran. According to 2018 "Natural Stones Sector Report in of the Ministry of Trade, Turkey in 2016; after China and Italy, it ranked third in the world natural stone exports (https:/www.imib.org.tr). There are total 2241 quarry which have a processing permit in Turkey and 70 of them are located in Mersin (https://stoneworldtr.com). The aim of this study is to explain stratigraphic levels of quarries which are operated as marble in the Mersin area.

2. GEOLOGICAL SETTING

Mersin and around are located in the central part of the Taurus Mountains in the Alpine-Himalayan belt. In this area non-metamorphic rocks generally outcrop (Fig. 1). These rocks were evaluated into 3 eras. First era is the Paleozoic. In this period units generally consist of alternation of clastic (conglomerate, sandstone, claystone, mudstone, shale) and carbonate rocks (limestone, dolomite, dolomitic limestone) (Gökten, 1976; Demirtaşlı 1984; Demirtaşlı *et al*., 1984; Koç, 2003; Özgül, 1984; Alan *et al*., 2007; Taslı *et al*., 2007; Koç and Taslı, 2010) (Fig. 2a). Although carbonated levels of these units contain marble potential, they are not generally operated as marble because they are medium-thick bedded and have abundant fracture, and also their physico-mechanical properties are not suitable.

Second era is the Mesozoic. Mesozoic base generally consists of clastic and carbonated rocks (Fig. 2b). Jurassic-Cretaceous periods in the Mesozoic are represented by carbonated rocks which are the products of Tethys ocean (Gökten, 1976; Demirtaşlı 1984; Demirtaşlı *et al*., 1984; Koç, 2003; Özgül, 1984; Alan *et al*., 2007; Taslı *et al*., 2007; Koç and Taslı, 2010). These carbonated units are gray-cream-beige colored, medium-thick bedded, occasionally massive, locally with abundant fossil shells. It can be operated as a high degree marble in terms of these properties and physico-mechanical structure. The most common marble production in Mersin and around is made from these units. Another common rock group in the region is ophiolitic and ophiolitic mélange units which is the Late Cretaceous aged (Özgül, 1984; Alan *et al*., 2007; Taslı *et al*., 2007; Koç and Taslı, 2010) (Figs. 1 and 2). Triassic-Jurassic-Cretaceous carbonated rock blocks within the ophiolitic mélange unit are seen as other common marble fields operated in the region.

Third era is the Cenozoic. In the Cenozoic, Paleogene is represented by clastic rocks which is locally dominated by carbonate rocks (Gökten, 1976; Demirtaşlı *et al*., 1984; Özgül, 1984; Alan *et al*., 2007; Kunt and Koç, 2019) (Fig. 2c). In this period, limestones which are thick, horizontal bedded, massive, generally with macro fossiliferous and fossil shells and pinkish colored can be operated as marble. Neogene starts with clastics, continues with carbonated units and ends with clastic units intercalated carbonate. Limestones which are light beige-cream colored, thick-bedded, massive, horizontal-bedded, with macro-fossiliferous and fossil shells, has the characteristics of being operated as marble although their physico-mechanical properties are weak.

3. RESULTS AND CONCLUSION

When the rock groups outcropping in the Mersin region and the marble fields operated in the region are evaluated together, the following results are obtained.

- In the areas where the Paleozoic units are exposed, only the Permian limestones are rarely operated as marble.

-The Upper Jurassic dolomites operated sparsely, the Cenomanian-Senonian limestones which are thick-bedded and contain rudist and fossil shells and also fossil-free are the most widely operated marble fields. Other widely operated marble fields are the Mesozoic limestone-dolomite blocks which are exposed in the Late Cretaceous aged ophiolitic mélange units.

-In the region, the Eocene limestones which are pink colored and fossiliferous are also operated as marble. Other marble fields in the region are the Miocene reef limestones with abundant fossil which are yellowish-beige colored.

- Other areas exposed by stratigraphic units observed in the fields operated in Mersin region can be also evaluated in terms of marble potential.

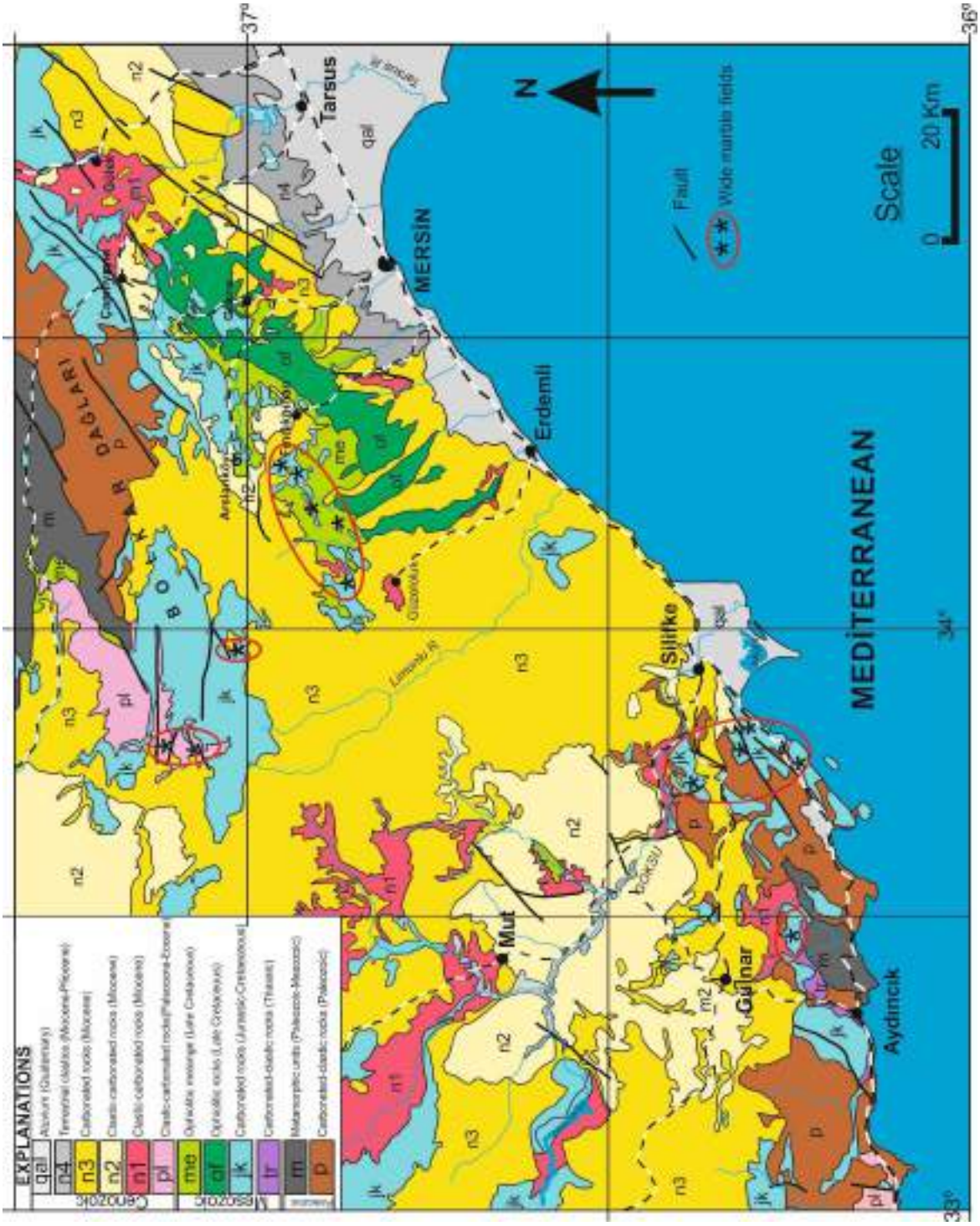

Fig. 1. Simplified geological map of the Mersin and around (modified after MTA, 2009)

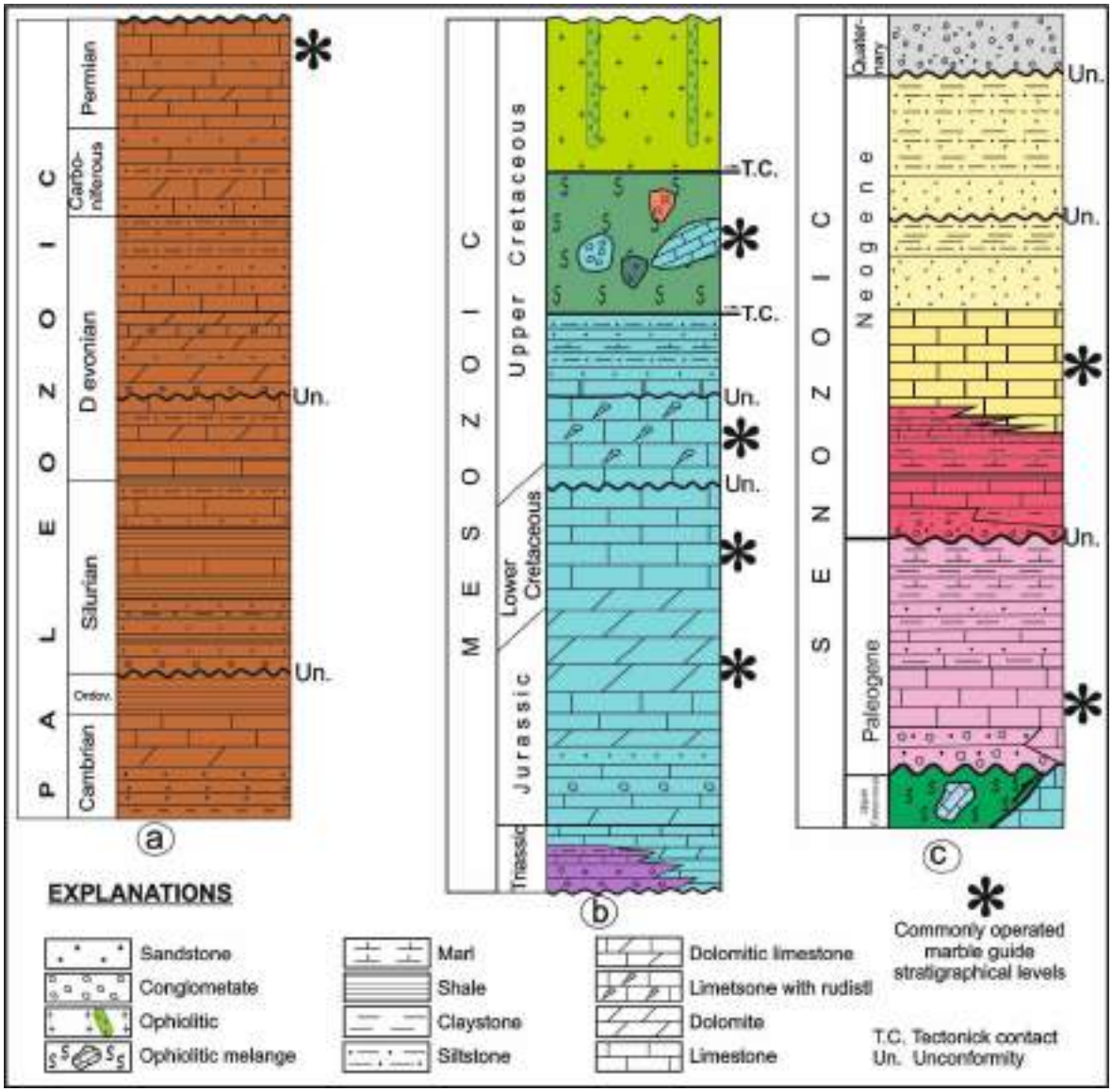

Fig 2. Generalized stratigraphic sections of the outcrops in and around Mersin. a) Paleozoic period, b) Mesozoic period, c) Cenozoic period.

REFERENCES

Alan, İ., Şahin, Ş., Keskin, H., Altun, İ., Bakırhan, B., Balcı, V., Saçlı, L., Pehlivan, Ş., Kop, A., Hanilçi. and Çelik, Ö.F. (2007). Orta Toroslar'ın Jeodinamik Evrimi, Ereğli (Konya)–Ulukışla (Niğde)–Karsantı (Adana)–Namrun (Mersin) Yöresi. MTA Raporu, No:11006, 245 pp.

Demir, İ., Başpınar, M. S. and Görhan, G. (2006). Afyonkarahisar-Ayazini Tüflerinin Mekanik Özellikleri ve Yapı Taşı Olarak Kullanılabilirliği. Türkiye 5. Mermer ve Doğaltaş Sempozyumu Bildiriler Kitabı, pp. 31-38.

Demirtaşlı, E. (1984). "Stratigraphy and Tectonics of the area between Silifke and Anamur, Central Taurus Mountains". Proceedings of the International Symposium on the Geology of the Taurus Belt, Ankara, Turkey, pp.101-1118.

Demirtaşlı, E., Turhan, N., Bilgin, A.Z. and Selim, M. (1984). "Geology of the Bolkar Mountains". Proceedings of the International Symposium on the Geology of the Taurus Belt, pp.125-141.

Gökten, E. (1976). "Silifke yöresinin temel kaya birimleri ve Miyosen stratigrafisi." *Türkiye Jeoloji Kurultayı Bülteni,* Vol. 2, No. 19, pp. 117-126.

Koç, H. (2003). Tectono-stratigraphy and geological evolution of Aydıncık (Mersin) Area, PhD Thesis, University of Çukurova, Adana, Turkey.

Koç, H. and Taslı, K. (2010). Litho-biostratigraphy and event analysis of the Cenomanian-Maastrichtian sediments in the Central Taurides (S Turkey). Tübitak Project no. 109Y161, Report, 94 p. (in Turkish, unpublished).

Kunt, S.K. and Koç, H. (2019). Stratigraphic and Micropaleontological Investigation of Late Paleocene-Eocene Units in the North of Yüğlük Mountain (Bolkar Mountains, Central Taurides). *Çukurova University Journal of the Faculty of Engineering and Architecture*, 34 (1), pp. 169-182.

Özgül, N. (1984). "Stratigraphy and Tectonic Evolution of the Central Taurides". Proceedings of the International Symposium on the Geology of the Taurus Belt, pp.79-99.

Şentürk, A., Gündüz, L. and Sarıışık, A. (1995). Yapı taşı olarak kullanılan endüstriyel kayaçlara teknik bir bakış. Endüstriyel Hammaddeler Sempozyumu, pp. 333-334.

Taslı, K., Altıner, D., Eren, M., Özkan-Altıner, S. and Koç, H. (2007). Bolkar Dağları (Orta Toroslar) Jura-Kretase Karbonat İstifinin Foraminifer Biyostratigrafisi. TUBİTAK Projesi, Proje no: ÇAYDAG-103Y192, 124 sayfa.

Teymen, A. (2017). Osmaniye/Kadirli Kireçtaşlarının Doğaltaş Özelliklerinin İncelenmesi. Türkiye 9. Uluslararası Mermer ve Doğaltaş Kongresi ve Sergisi Bildiriler Kitabı, pp. 271-282.

Vardar, M. (1990). Mermerlerin Uygarlık Tarihindeki Yeri. *Mermer Dergisi*, İstanbul. pp.12.

Web Map Tile Service, https://stoneworldtr.com [Accessed 20 August 2019].

Web Map Tile Service, https:/www.imib.org.tr [Accessed 20 August 2019].

Web Map Tile Sevice, http://www.mta.gov.tr doc/ADANA.pdf [Accessed 10 Jule 2019].

CISET - 2nd Cilicia International Symposium on Engineering and Technology
10-12 October, 2019, Mersin / TURKEY

ENVIRONMENTAL DAMAGES CAUSED BY OPEN CAST MINES EXPLOITATION IN THE TOURISTIC AREA OF KRUJA, ALBANIA.

Marpol KOÇO[1], Edmond HOXHA[1]

[1]Polytehcnic University, Faculty of Geology and Mining,
Department of Mining Resource Engineering, Rruga e Elbasanit, Tirana – Albania
marjo_peko87@hotmail.com; ehoxha63@gmail.com

ABSTRACT
Kruja is a medieval city, in Albania, that was first mentioned in the IX century, in a church document of the year 879. The city of Kruja is one of the most visited tourist areas in Albania. According to statistics released by the Tourist Service Directory in the Municipality of Kruja, this city has visited around 300,000 local and foreign tourists every year. Since about 30 years in the Kruja touristic area, mining activity has begun for the use of construction materials through the open cast mining exploitation. This kind of exploitation has been done without respecting the basic environmental protection standards, creating a major environmental problem and negatively affecting the development of tourism. Entities that engage in mining activities in the area designated as a protected natural landscape have not rigorously applied the technical design of mining facilities opening and exploitation, creating technical security problems and environmental protection. This article identifies environmental damages caused by open cast mining exploitation, presents mapping of damages and provides recommendations for environmental rehabilitation and mining activity in the future. Damage mapping on the environment is done using GIS technology and air photography.

Keywords: *Tourist Areas; environment; open cast mines, rehabilitation, GIS, area photos.*

INTRODUCTION, KRUJA REGION

Kruja is a medieval city, in Albania, that was first mentioned in the IX century, in a church document of the year 879. *Kruja* is located between Mount Krujë and the Ishëm River, the city is only 20 km north from the capital of Albania, Tirana. It was inhabited by the ancient Illyrian tribe of the Albani. In 1190 Kruja became the capital of the first autonomous Albanian state in the middle ages, the Principality of Arbër. Later it was the capital of the Kingdom of Albania. The city of Kruja is one of the most visited tourist areas in Albania. The museums of Krujë include the Skanderbeg Museum, located in the environs of the Krujë Castle, and the national ethnographic museum. According to statistics released by the Tourist Service Directory in the Municipality of Kruja, this city has visited around 300,000 local and foreign tourists every year.

2. MINING ACTIVITY IN KRUJA AREA

The mining activity in Kruja started mainly for construction materials exploitations. The activity is by opencast mining method. Actually in this region are operating around 40 mining licensed operators[i] (Fig.1).

Fig.1 General Map of Mining Operators in Kruja Region. [Source: https://akbn.maps.arcgis.com/apps/webappviewer/index.html?id=1783114e15074dd3b2a2f0b5d36048a6**]**

As it is shown in Fig.1 this activity is developing just in front of the touristic zone of Kruja city making a very ugly impression of this area. The open cast mine is developed in a surface around 100 km^2. From all of the Mining Licenses a very considerable number of these have been inside the protected area (Fig.2).

Fig.2 Map of Mining Operators inside the Protected Area border. [Source: https://akbn.maps.arcgis.com/apps/webappviewer/index.html?id=1783114e15074dd3b2a2f0b5d36048a6]

3. DAMAGES ON KRUJA REGION CAUSED BY MINING ACTIVITY

The main damages are as follows:

Air Quality: Due to mass explosions, heavy machinery works in areas where mining works are built up large dust that is deposited in the surrounding forests, agricultural lands meanwhile hurt the health of people, also this impact is present on the turistic city of Kruja, creating a bad environment for the people living there and for the tourist visiting the city. The procesess which impacted the environment are: Excavation process; Drilling process; Charnging and disccarging of inertes; etc. (Fig.4)

Fig.4 View of mining works in Kruja region.

Water quality: Due to the exploitation of opencast mines near them are deposited stockyards that slid into the water springs of the area causing their pollution, damaging the quality of water used for livestock but also for agriculture. In the time of raining the polluted water impact the waters of small water streams. From the other side the argila wastes impacts on the enovironment because there have been not implemented the collecting chanels and damps.

3.1. Landscape

Landscape damage is very serious, I can call it as catasrophe. Throughout the area are created pits, abysses and new stocks that have changed the natural profile of the mountain. Figure 5 shows two images of the damaged area in 2007 and 2019, where it is clearly the major damage caused.

Fig.5 Damaged zones, year 2007 and 2019
[Source: Imagery Google Earth]

3.2. Forest Damage

Comparison between the two images of 2007 and 2019 shows a damage to a very large area of forests mainly with shrubs and small trees. Figure 5 shows the comparison of two images of damaged areas. It is clear that damage has doubled over 12 years and the lack of rehabilitation measures. Total damaged surface is around 145 ha, respectiveley: Zona 1, 34,9 ha; Zona 2, 56.8 ha; Zona 3, 46,8 ha; Zona 4, 1.9 ha; Zona 5, 4.17 ha.

3.3. Damage to pastures and vegetation

Due to massive outbreaks and mountain erosion, the pastures have also been severely damaged. The vegetation is very small. Dust is the main cause of vegetation breakdown in this area, as well as dumping unnecessary soils.

3.4. Tourism Damage

Before developing these works the landscape was very interesting. Now there are only abysses, pits, and dusts deposited without criteria. The most negative impact is because this mining are just before entring the historic city of Kruja, one of the best turistic destination of Albania. The first impression of the tourists are openpit mining, pollution, big truck, dust, noise atc.

3.5. Damage to Flora and Fauna

A large number of plants have been destroyed by excavation and deposit of deposited soil. While due to noise, massive outbreaks, water and air pollution, many animals have left the area, bringing the impoverishment of the fauna and flora of the area.

3.6. Acoustic pollution

From a quiet and relaxed area, Kruja has turned into a noisy pitch where the noise level is out of any standard, thus causing the disturbance of tranquility and natural equilibrium. Major explosions in winter time can also be the cause for the creation of avalanches and slides. Well-being and health of the inhabitants: All this destruction of the environment certainly has a negative impact on the residents of the area, who have lost their former tranquility. The area is a protected area and in oposite there have been allowed mining activities without any criteria.

3.7. Waste deposits, stocks, etc.

As it is known open cast mining exploitation is accompanied with a lot of massive waste deposits, which are big problem for the environment.

3.8. Damages on health

All these massive works very close to the Kruja city where are living around. The total population of Krujë is 59,814 (2011 census), in a total area of 339.02 km^2 and the mining works have also impact on the helath of people because of impact on the air and water pollution.

3.9. Damages on economy

The mining works in touristic and protected area also bring damages in economy because there will be many measures to make the rehabilitation of the area. According of the law the rehabilitation must be the mining companies, but actually in most cases no rehabilitations actions are taken. In the future government will be forced to make rehabilitation measures which will bring extra cost in economy.

3.10. *Human life risk*

Because of the mining activity and abandoned mining activity there are created many danger zones for peoples and animals also. Actually there is no measure to protected the danger zones creating so the high risk for the community and animals living in this area.

3.11. Risk of landslides

Open cast mining, because of non-criteria mining has created many slender slopes

4. IDENTIFICATION OF DAMAGED ZONES AND MAP CONSTRUCTION USING GIS TECHNOLOGY

Given the experience of using GIS in similar cases, the ArcGIS 10.3 program was used to build Digital Maps.

Some of the steps followed by problem identification to the final map of the damaged areas are as follows: (1) Collection of existing materials; (2) Determining the location of open cast mines; (3) Contact with state institutions; (4) Field visits and measurements (point coordinates were taken with GPS Garmin Oregon 600t; (5) Layout of field data in ArcGIS 10.3 and BaseCamp; (6) Building GIS maps for damaged areas, Protected Areas, Mining Licenses, etc.

The final map of damaged zones is presented in Fig.6 together with a comparison of 2007 and 2019 year.

Fig.6 Damages zones 2019 and a comparision 2007 – 2019. [Source: GIS Map the authors; Imagery, Google Earth]

5. REHABILITAION OF DAMAGED ENVIRONMENT

Due to the severe environmental situation in the Kruja zone, urgent rehabilitation measures are needed.

Rehabilitation measures should include: (1) Soil transport; (2) Soil and stockpiling; (3) Covering stocks with and as well as shrub and grass planting; (4) Scale opening; (5) Digging and filling; (6) In order to preserve the flora and fauna, there should be ambushes and walls to prevent eventual leakage of the soil as a result of precipitation and consequently the discharge of sterols into the waters (streams, watersheds, lakes); (7) Planting of seedlings is recommended for slope adjustment.

5. CONCLUSIONS & RECOMENDATIONS

Conclusions:

(1) The scale of environmental damage due to mining in Albania is extremely high and extends across the country. These damaged areas require the taking of urgent technical and administrative measures to eliminate irreparable consequences in the future;

(2) The existing legal framework for environmental protection from mining is not correctly applied and therefore does not provide for effective protection of the environment;

(3) The mining exploitation methods do not sufficiently consider the protection of the environment from mining;

(4) Mining risk to human life and the environment due to mining is evident, high risk and neglected by everyone.

(5) Damage to the environment, water, infrastructure, forests, agricultural lands, flora and fauna in the National Park of Dajti Mountain is very high, affects a considerable area and requires emergency interventions;

Recommendations:

(1) It is recommended to immediately stop the mining activity in the Kruja zone in the Protected Area;

(2) It is recommended to conduct a full scientific study to determine the exact level of damages caused, and to take environmental rehabilitation measures, reforestation, animal breeding and conservation, reservoirs, cleaning of water.

(3) It is necessary to set up a Task Force to monitor the implementation of the existing Law on Mines, Environment and Protected Areas, with the objective of preserving the environment in accordance with European Union norms;

(4) It is recommended to draft and approve new mining quarrying methods and regulations.

REFERENCES

Hoxha E "*Rehabilitation of the environment damaged by mining activity*"

Hoxha E "*Sistemet e Informacionit Gjeografik* (GIS)" 2004;

https://en.wikipedia.org/wiki/Kruj%C3%AB"
https://www.infrastruktura.gov.al/revokohen%204%20lejeve%20minerare%20ne%20zonen%20e%20krujes/

http://www.akbn.gov.al/

Google earth

[i] https://*akbn.maps.arcgis.com/apps/webappviewer/index.html?id=1783114e15074dd3b2a2f0b5d36048a6*

CISET - 2nd Cilicia International Symposium on Engineering and Technology
10-12 October, 2019, Mersin / TURKEY

EFFECT OF ORIENTAL SWEET GUM OIL (STYRAX) ON CHARACTERISTICS OF CHITOSAN CRYOGEL SCAFFOLDS

Didem Demir and Nimet Bölgen Karagülle*

Mersin University, Engineering Faculty, Chemical Engineering Department, Mersin, Turkey

ABSTRACT

In the last few years, there has been a growing interest in the use of medicinal plant compounds for the treatment of tissue damages with the approach of tissue engineering. The resin obtained from Oriental sweetgum tree (Liquidambar orientalis Miller) is one of these plant compounds and has been widely used for many years as a household remedy in the folk medicine of Turkey in the treatment of skin problems, coughs and ulcers. This resin is called as storax or styrax and has good antiseptic properties due to its major components such as ester, alcohol, phenolic and volatile compounds. The aim of this study was to develop styrax incorporated cryogel scaffolds for tissue engineering applications as a wound dressing material, particularly for ulcer wounds. With this aim, novel cryogel scaffolds were produced by combining a traditional medicinal balsam (styrax) with a biocompatible and biodegradable polymer (chitosan). The cryogel scaffolds were fabricated by crosslinking of chitosan with glutaraldehyde in the presence of different amounts of styrax in cryogenic conditions. Three dimensional cryogels fabricated by cryogelation are soft, porous, stable in form and can be easily cut in any desired shape. The cryogels were characterized by gel fraction, porosity and swelling ratio analyzes. The characterization results of this study concluded that the newly developed styrax loaded chitosan composite cryogels with highly porous morphology, high swelling ability and mechanical stability can be promising candidates for using as novel scaffolds/wound dressing materials for ulcer wounds or any other tissue engineering applications.

Keywords: *Oriental sweet gum, Styrax, Chitosan, Cryogel, Wound dressing, Tissue engineering*

* Corresponding Author: nimetbolgen@yahoo.com, nimet@mersin.edu.tr

1. INTRODUCTION

Plants with healing properties have been used extensively for the treatment of various diseases since ancient times. At that time, everything was based on experience, as there was not enough information about the causes and treatment methods of the diseases. Over time, the use of certain medicinal plants for the treatment of diseases was discovered (Petrovska, 2012). Thus, many plant species began to be used for pharmaceutical purposes due to their numerous pharmacological activities.

Oriental sweet gum tree (Liquidambar orientalis Miller) is one of the herbaceous plant commonly known as Sığla/Günlük tree in Turkey. A balsam called "styrax" or "storax" obtained by injuring this tree has been used and traded for thousands of years and is an important source for cosmetics, pharmaceuticals and chemical industries (Arslan *et al.*, 2016). Styrax is a semi-solid and sticky material that can be characterized by a styrene-like odor (Fernandez *et al.*, 2004). The main components of the styrax are acid, ester, alcohol, phenolic and volatile compounds. Styrax has good antiseptic properties and it has been widely used as a topical parasiticide and expectorant for the treatment of skin disorders.

On the other hand, in the last decade, there has been great interest in polymeric-based materials containing medicinal plant compounds for the treatment of wound, burn and tissue related diseases. Polymers of both natural and synthetic origin have been used to prepare various types of composite materials including hydrogels, cryogels, electrospun membranes, etc. Among them, cryogels are unique features due to their highly interconnected pore structure. The macroporous structure of cryogels allows the diffusion of solvents, provides a suitable environment for cell proliferation and exhibits good mechanical stability due to the high water retention capacity (Bakhshpour *et al.*, 2019). This property makes them attractive materials for cell culturing, drug delivery and wound healing (Wartenberg *et al.*, 2017).

In this study, we aimed to combine the healing and antimicrobial properties of styrax with the unique structural properties of cryogels in order to produce a wound dressing material that has the potential to be used in tissue engineering applications. The cryogels were fabricated by crosslinking of chitosan with glutaraldehyde in the presence of styrax. The combination of polymers with other compounds can influence the cryogel properties and therefore extend their application potential. Therefore, we determined the effect of styrax amount on the basic characteristics of cryogels before the biological studies. The physical morphology, gel fraction, porosity and swelling ratio of cryogels were investigated.

2. MATERIAL AND METHODS

2.1. Materials

Medium molecular weight chitosan was purchased from Sigma Aldrich, USA. Glutaraldehyde (25%, v/v, aqueous) and acetic acid (100%, glacial) were obtained from Merck, Germany. Styrax was supplied from a local market in Muğla Province, Turkey. Distilled water was used in experimental steps.

2.2. Method

The cryogels were prepared at 2% (w/v) constant chitosan concentration. The calculated amount of chitosan was weighed and 6% (v/v) acetic acid solution was added. The polymer solution was mixed by using a magnetic stirrer at room temperature until a homogeneous mixture was obtained. Styrax was added to the 2.5 mL of chitosan solutions at different amounts (1:3, 1:5, 1:7 and 1:10, w:w) and the solutions were stirred continuously at room temperature until the balsam is completely dissolved. Then, 1 mL of glutaraldehyde (3%, v/v) was added to each styrax-polymer mixture. The mixtures were immediately transferred into plastic syringes and incubated into a refrigerated bath circulator (Daihan, WCL-P12, Korea) for crosslinking reaction at -16°C. After 2 hours incubation, the syringes were placed in the freezer at -16°C for 24 hours. After cryotropic gelation was completed, the scaffolds were thawed at room temperature and the monoliths were immersed in distilled water to remove the unreacted residues. Before carrying out characterizations, all samples were freeze-dried by using a lyophilizer (Labconco, FreeZone Benchtop Freeze DrySystem-7670531, USA).

The fabrication steps of styrax loaded chitosan cryogels are summarized in Figure 1.

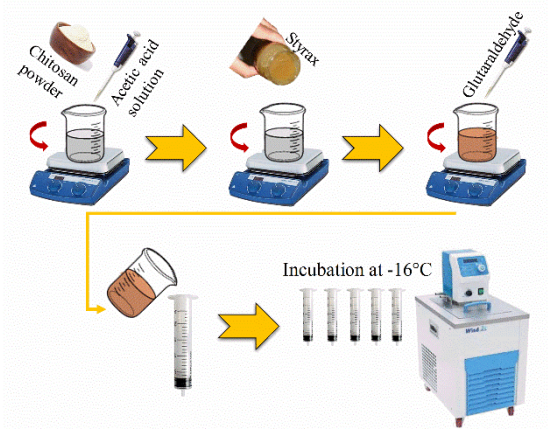

Fig. 1. Fabrication steps of styrax loaded chitosan monolithic cryogels

2.3. Characterization Studies

The gel fraction (W_g) after crosslinking at cryogenic conditions was calculated by the extraction of samples in distilled water. For this purpose, the samples removed from the syringes were washed in a large volume of distilled water for 72 h by changing the water medium every day to remove the residues such as unreacted polymer, styrax and crosslinking agent. The cryogels after extraction were freeze-dried. The W_g of the samples defined as the amount of crosslinked gel network was calculated as follow:

$$W_g = M_d/M_i \times 100 \quad (1)$$

where M_d and M_i are the weights of cryogels just after preparation and freeze drying, respectively.

Porosity which designates the presence of overall pores in the cryogels network was determined by ethanol

penetration method. A disc-shaped scaffold sample was immersed in a falcon tube containing absolute ethanol. Firstly, the known volume of cryogel (V) was immersed in ethanol for 5 min and then pressed to force air from the cryogel and allow the ethanol to penetrate and fill the pores completely. Then, the cryogel was kept again in ethanol ($\rho_{ethanol}$= 0.987 g/mL) for 2 h and weighed after the excess ethanol on the surface was blotted. The porosity (PR) was calculated from the following equation:

$$PR= (M_2-M_1)/\rho_{ethanol}.V \quad (2)$$

where M_1 and M_2 are the mass of the cryogel before and after immersion in ethanol.

For the swelling kinetics measurements, the dry cryogels produced in the form of the monolith and 2 cm in diameter were cut into cylindrical specimens with a length of about 15 mm. The samples were immersed in distilled water at 37°C. The mass of the cryogels was measured (n = 3, after blotting on filter paper) until equilibrium was reached at the specified time intervals (15, 30, 60, 90 and 120 min). The percent swelling ratio (SR%) of cryogels was determined using the following equation.

$$SR\%= M_t/M_0\times100 \quad (3)$$

where Mt is the mass of the swollen sample at any time and M_0 is the initial mass of the dry sample.

3. RESULTS AND DISCUSSION

3.1. Physical morphology

Cryogels were prepared with plain chitosan solution and different amounts of styrax added chitosan solution to determine the possible effect of balsam oil on the physical properties of synthesized cryogels. The macroporous cryogels were fabricated successfully by crosslinking of chitosan with glutaraldehyde in the presence of styrax. The produced cryogels were in monolith shape as seen in Figure 2. The chitosan cryogels showed a yellowish color as a result of the double bonds after glutaraldehyde crosslinking (Demir *et al.*, 2016). S0, S3 and S5 cryogels which were prepared with low amounts of styrax did not show a significant deformation after applying force. However, the S7 and S10 cryogels were deformed when the applied force was increased. Therefore; S0, S3 and S5 samples were used in the following parts of the study.

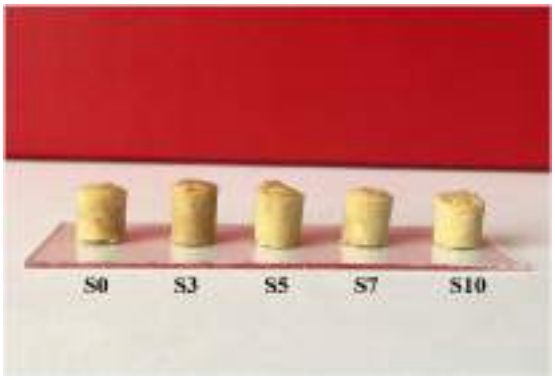

Fig. 2. Physical shape of cryogels in dry form

3.2. Gel Fraction

After the crosslinking reaction of chitosan and glutaraldehyde in the presence of styrax at -16°C were completed, ice crystals were removed from the cryogels and then the cryogels were freeze-dried. The gel fractions of the cryogels were determined gravimetrically. The gel fraction yields (Wg) of the fabricated samples were tabulated as can be seen from Table 1. The addition of styrax did not significantly impact the gel fraction yields which are approximately 85% for all prepared gels. For all cryogels reported here, the gel fractions indicate that about 85% of the ingredients in the feed was incorporated into the gel network (Okay 2015).

Table 1. Gel fraction of chitosan and styrax incorporated chitosan cryogels

Samples	Wg, %	Std. dev.
S0	87.56	2.09
S3	84.59	1.95
S5	81.94	1.38

3.3. Porosity

Table 2 shows the percent porosity of the chitosan and styrax loaded chitosan cryogel scaffolds based on the ethanol displacement method. Porosity plays an important role in the design of a scaffold for tissue engineering applications as a wound dressing material, drug delivery system or cell culturing. Scaffolds should have high porosity for cell growth, flow transport of nutrients and metabolic waste (Hosseinkhani *et al.*, 2014). In this study, the plain chitosan cryogel sample hasan effective porosity of around 80%. However, with the addition of styrax, the porosity of cryogels decreased. This may be due to the hydrophobic feature of the balsam oil.

Table 2. Porosity of chitosan and styrax incorporated chitosan cryogels

Samples	PR, %	Std. dev.
S0	80.78	1.86
S3	61.19	2.67
S5	58.25	2.31

3.4. Swelling Ratio

The swelling ratios of cryogels are presented in Figure 3. All samples exhibited a swelling behavior and have the ability to retain more water than their dry weight. It is observed that when the amount of styrax increased, the swelling ratio of cryogels decreased significantly. A less porous and more rigid structure was formed as styrax amount increased, therefore the swelling ratio was decreased.

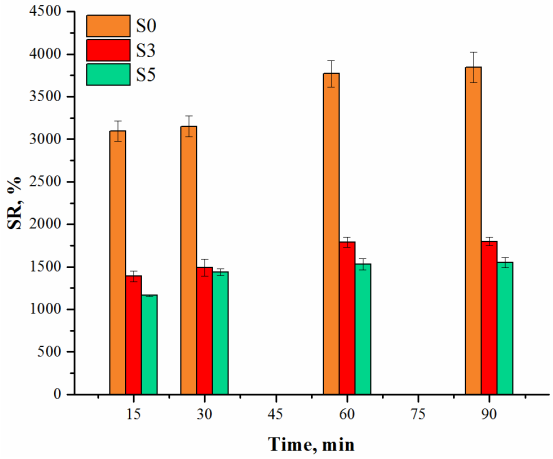

Fig. 3. Swelling ratio values of chitosan and styrax incorporated chitosan cryogels

4. CONCLUSION

Human have been using medicinal plant compounds since ancient times for treatment of several diseases. Using the medical potential of traditional herbal products especially for tissue engineering has attracted great attention in recent years. Styrax is one of them and offer a wide range of medical application. The natural wound healing potential of styrax can be well transfered into a polymeric material using for tissue engineering applications as a wound dressing material. In our study, different amounts of styrax loaded chitosan scaffolds were fabricated by using cryogelation method. This method has many proven advantages like interconnected porous structure, elasticity, controlled mechanical stability and high swelling ability. The effects of different amounts of styrax on the cryogel properties were investigated. The physical morphology and mechanical stability of cryogels change with increasing styrax ratio in the initial polymer solution. Furthermore, the porosity decreases as the amount of styrax is increased.

The use of natural compounds of medicinal plants with polymeric scaffolds for tissue engineering applications area is new. Not many publications are available in this field. Natural, biocompatible and biodegradable plant extracts loaded polymeric materials such as styrax incorporated chitosan cryogels produced and characterized in our study can be utilized in the field of tissue engineering as new wound dressing materials.

REFERENCES

Arslan, M. B. and Şahin, H. T. (2016). "Unutulan Bir Orman Ürünü Kaynağı: Anadolu Sığla Ağacı (Liquidambar orientalis Miller)." *Journal of Bartın Faculty of Forestry*, Vol. 18, No. 1, pp. 103-117

Bakhshpour, M., Idil, N., Perçin, I. and Denizli, A. (2019). "Biomedical Applications of Polymeric Cryogels." *Applied Sciences*, Vol. 9, No. 553, pp. 1-22.

Demir, D., Öfkeli, F., Ceylan, S. and Bölgen Karagülle, N. (2016). "Extraction and characterization of chitin and chitosan from blue crab and synthesis of chitosan cryogel scaffolds." *Journal of the Turkish Chemical Society, Section A: Chemistry*, Vol. 3, No. 3, pp.131-144

Fernandez, X., Lizzani-Cuvelier, L., Loiseau, A-M., Perichet, C., Delbecque, C. and Arnaudo, J-F. (2004). "Chemical composition of the essential oils from Turkish and Honduras Styrax." *Flavour and Fragrance Journal*, Vol. 20, pp. 70-73

Hosseinkhani, M., Mehrabani, D., Karimfar, M. H, Bakhtiyari, S., Manafi, A. and Shirazi, R. (2014). "Tissue engineered scaffolds in regenerative medicine." *World Journal of Plastic Surgery*, Vol. 3, No. 1, pp. 3-7

Okay, O. (2004). *Polymeric cryogels: macroporous gels with remarkable properties, elementary structural analysis*, Springer International Publishing, Switzerland.

Petrovska, B. B. (2012). "Historical review of medicinal plants' usage." *Pharmacognosy Reviews*, Vol. 6, pp. 1-5

Wartenberg, A., Weisser, J., Thein, S., Suso, H-P., Schmidt, R. and Schnabelrauch, M. (2017). "Cryogels as potential scaffolds for wound healing applications." *Proc., 4th Euro BioMAT*, pp. 26-29

DESIGN OF MACROPOROUS CHITOSAN CRYOGELS LOADED WITH GREEN SYNTHESIZED AgNPs

Didem Demir[1], Seda Ceylan[2] and Nimet Bölgen Karagülle[1*]

[1]Mersin University, Engineering Faculty, Chemical Engineering Department, Mersin, Turkey

[2]Adana Alparslan Türkeş Science and Technology University, Engineering Faculty, Biongineering Department, Adana, Turkey

ABSTRACT

The application of scaffolds loaded with metallic nanoparticles has become a newly emerging research field in tissue engineering and regenerative medicine. Silver nanoparticles (AgNPs) are one of them due to their physicochemical and antimicrobial properties. AgNPs can be green synthesized by using plant extracts due to many advantages such as less biohazard, environmentally friendly and very short reaction time. *Myrtus communis* (Myrtle), locally known as "Mersin tree" in the Mediterranean region of Turkey, has been used in many pharmacological studies owing to its antibacterial properties for wound healing. Hence, our study aims to investigate the production of silver nanoparticles with a green synthesis approach by using Myrtle leaf extract and to examine the effect of AgNPs on the properties of chitosan-gelatin composite cryogels. The biosynthesized AgNPs were characterized by Ultraviolet-visible (UV-Vis) spectrophotometer and Dynamic Light Scattering (DLS) method of Zeta Sizer. The chitosan-gelatin and AgNPs incorporated chitosan-gelation cryogels were chemically characterized by Fourier Infrared Spectroscopy (FTIR). The morphology of AgNPs on cryogel networks was determined by Scanning electron microscopy (SEM). The swelling ratio and degradation behavior of cryogels were investigated gravimetrically. The results demonstrated that the green synthesized silver nanoparticles could be used as an antimicrobial scaffold for the future applications of tissue engineering after determining the antimicrobial properties of cryogels.

Keywords: *Myrtus communis, Silver nanoparticles, Green synthesis, Chitosan, Gelatin, Cryogel*

* Corresponding Author: nimetbolgen@yahoo.com, nimet@mersin.edu.tr

1. INTRODUCTION

Polymeric composite biomaterials and their application as scaffolds in regenerative medicine have increased for different therapeutic needs (Samal *et al.*, 2015, Natarajan *et al.*, 2019). In particular, scaffolds for tissue engineering coupled to metal nanoparticles (Ag, Au, Pt, Pd, etc.) due to their unique optical, electrical, mechanical, magnetic, chemical and antibacterial properties (Shameli *et al.*, 2012). The fabrication of advanced scaffolds, for tissue engineering with controlled antibacterial properties, is very essential for patients because an ideal implant should have the ability to regenerate tissue and treat the infection by releasing an antibacterial agent in a controlled manner (El-Kady *et al.*, 2012). Nowadays, green process for the synthesis of AgNPs has attracted wide interest because of its rapidity, simplicity, being ecofriendly and cheap (Zulkifli *et al.*, 2017, Raja *et al.*, 2017). One of the green methods of AgNPs synthesis is the utilization of different plants and their parts (Raja *et al.*, 2017) . The reaction time is very short compared to other synthesis methods and this process does not involve specific media and culture conditions. Various plants have been used to synthesize silver nanoparticles, such as *Delonix elata*, *Azadirachta indica*, *Tephrosia purpurea*, *Melia dubia*, *Tribulus terrestris*, *Artemisia nilagirica*, *Boerhaavia diffusa*, *Ficus religiosa*, *Melia azedarach* and *Piper pedicellatum* (Yadav *et al.*, 2016) .

Myrtle is found throughout the Mediterranean, and it is a small tree with star-like flowers. In this study, AgNPs were synthesized using Myrtle leaf extract as a reducing agent and the biosynthesized AgNPs incorporated with chitosan-gelatin cryogel scaffolds. Green synthesized AgNPs were characterized by UV-Vis and DLS analyzes. In addition to this, the effect of AgNPs on the characteristics of gelatin-chitosan scaffolds was analyzed. Chemical groups and morphology of AgNPs on cryogel structures were demonstrated by FTIR and SEM. Swelling ratio and degradation profile of the scaffolds were also determined.

2. MATERIAL AND METHODS

2.1. Materials

Myrtle leaves were collected from plants growing wild in Mersin, Turkey. Chitosan (medium molecular weight) was purchased from Sigma Aldrich, USA. Glutaraldehyde (25%, v/v), acetic acid (100%, glacial) and $AgNO_3$ were obtained from Merck, Germany. Aqueous solutions and dilutions in experiments were prepared with distilled water.

2.2. Method

2.2.1. Green synthesis of AgNPs

The freshly collected leaves of Myrtle were washed with water to remove the dust present on the surface and then rinsed at least two times with distilled water. The washed leaves were kept overnight at 65°C in an oven. The dried leaf pieces were powdered with a ceramic mortar. For the preparation of leaf extract, the powdered leaves were taken in a beaker containing distilled water. The extract was filtered by using a cheesecloth. The aqueous extract was stored at 4 °C until utilization for the green synthesis of AgNPs.

For the green synthesis of AgNPs at room temperature, the extract was added in aqueous $AgNO_3$ solution. The volumetric ratio of $AgNO_3$ solution and leaf extract was 10:90, v/v. The mixtures were incubated at room temperature (28 ± 2°C) at dark conditions for 48 hours to avoid the photo activation of $AgNO_3$. The samples were centrifuged at 4500 rpm for 5 min. The obtained AgNPs were separated from the solutions and then washed for with distilled water.

2.2.2. Production of AgNPs loaded chitosan-gelatin cryogels

Chitosan and gelatin were weighed (50:50, wt:wt) and dissolved in 5 ml of 6% acetic acid solution. Different ratios of concentrated solution of AgNPs (1:0.5, 1:1, 1:2 and 1:3, wt:wt, polymer:AgNPs) were added to the homogeneous polymer solution. 1.25 mL of 1% (v/v) glutaraldehyde solution was added to the obtained mixture and the solution was rapidly poured into the plastic syringes and incubated -12°C for 3 h. At the end of the incubation time, all samples were stored for 24 h in the freezer at -16°C. The prepared samples were thawed at room temperature and washed repeatedly with distilled water to remove the unreacted ingredients. The samples were then freeze-dried. The dried samples were stored in the refrigerator in sealed containers at +4°C for further analysis.

The AgNPs free chitosan-gelatin cryogels (1:0) were produced using the experimental steps described above, respectively.

2.3. Characterization Studies

2.3.1. Characterization of green synthesized AgNPs

The UV-Vis spectrophotometer was used (Chebios Optimum-One UV-Vis, Italy) to confirm the formation of AgNPs. The absorption spectrum was analyzed within the wavelength range of 350-600 nm. The particle size distribution of the synthesized AgNPs was characterized by DLS (Zetasizer Nano ZS90, Malvern, England).

2.3.2. Characterization of AgNPs loaded cryogels

Characterization studies of scaffolds consist of collecting information which might elucidate how the material will perform under specific conditions. In this matter, techniques such as FTIR, SEM, swelling ratio and degradation degree were used to investigate the properties of scaffolds for possible tissue engineering applications.

Chemical compositions of the obtained cryogel scaffolds were performed by FTIR (PerkinElmer, FT-IR/FIR/NIR Spectrometer Frontier-ATR, USA). FTIR spectra of the samples were obtained in the wavelength range of 550–4000 cm^{-1}.

Morphology of AgNPs on the structure of chitosan-gelatin scaffolds was investigated by SEM analysis (SEM, Supra 55, Zeiss, Germany) after coating with platinum.

The swelling ratio of cryogels was determined in distilled water at 37°C. At pre-determined swelling times, the scaffolds were weighted after removing the excess water from their surface. The filter paper was used to remove the excess water. The swelling ratio (SR, %) of the cryogels was calculated using the following equation:

$$SR, \% = \frac{Ww - Wd}{Wd} \times 100 \quad (1)$$

where Ww represents the weight of the wet cryogels absorbing water and Wd is the weight of the dry cryogels before swelling.

In order to determine the average weight loss, three scaffolds were prepared and dry weight of scaffolds was recorded. After that, scaffolds were transferred to 15 mL falcon tubes filled with distilled water. Tubes were placed in a water bath and the temperature of the water bath was adjusted to 37°C (Daihan Scientific Co. Ltd., WiseBath WB-22, Korea). At regular time points, scaffolds were withdrawn, dried, and weighed. Finally, weight loss of the scaffolds was calculated by Equation 2:

$$DR, \% = \frac{Wi - Wf}{Wi} \times 100 \quad (2)$$

where Wi is the initial dry weight of scaffold, Wf is the final dry weight of scaffold and DR% is the percentage degree of degradation or degradation rate.

3. RESULTS AND DISCUSSION

3.1. Characterization of AgNPs

The yellowish color of extract turned to light brown (after 2 hours) and then dark brown (after 48 hours) after addition of $AgNO_3$ solution (Figure 1A). The color change of solution was attributed to the excitation of surface plasmon resonance of AgNPs.

The synthesis of the AgNPs in aqueous solution of $AgNO_3$ was demonstrated by measuring the UV-Vis spectra of the solution at a wavelength range from 350 to 600 nm, after diluting the sample with distilled water Figure 1B). In the UV-Vis spectrum, a broad peak observed at nearby 435 nm indicated the formation of AgNPs.

DLS studies of the colloidal AgNPs were carried out to investigate the average size of the synthesized particles. The particle size distribution curve of synthesized AgNPs was shown in Figure 1C. The average size of AgNPs was 22.22 nm while the standard deviation was 9.19.

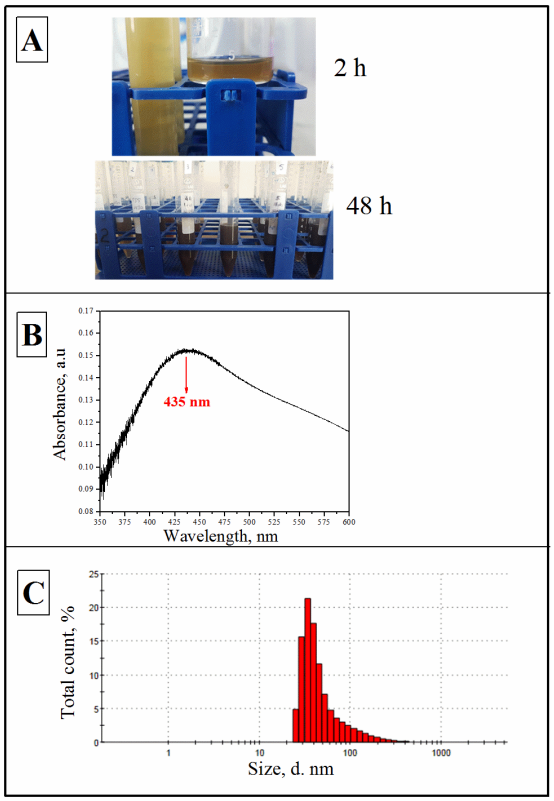

Fig. 1. The color change of the leaf extract after addition to $AgNO_3$ solution (A), UV-Vis spectrum (B) and DLS analysis of green synthesized AgNPs

3.2. Physical morphology of cryogels

The digital camera photography of the cryogels under daylight is demonstrated in Figure 2. It is shown that the synthesized cryogels are in monolith shape. After the addition of AgNPs into the structure, the color of cryogels changed from light yellow to dark brown. In other words, with the increase in the amount of AgNPs, the color of the cryogels became darker brown. It was apparent that the AgNPs was successfully added to the structure of cryogels.

Fig. 2. Digital photography of synthesized cryogels in wet form

3.3. Internal morphology of cryogels

The shape and morphology of AgNPs on cryogel network were characterized using SEM as demonstrated in Figure 3. The surface of pore walls of plain chitosan

cryogel displays a smooth morphology (Figure 3A). However, as adding the AgNPs into the network, AgNPs started to be observed on the pore walls of the microspheres (Figure 3B and 3C).

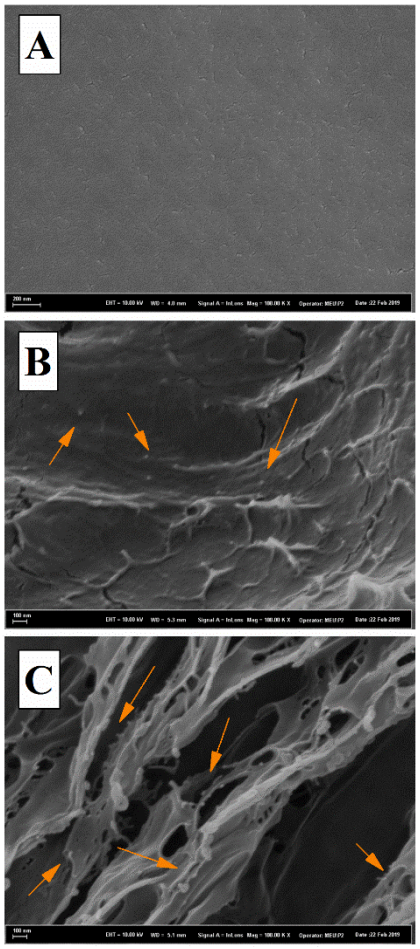

Fig 3. Internal morphology of cryogels. A) 1:0, B) 1:3 and C) 1:5 samples. Arrows are showing the particles on the polymer walls of cryogels.

3.4. Chemical structure of cryogels

The chemical composition of cryogels was determined by FTIR spectrophotometer in the wavelength range of 550-4000 cm^{-1}. The FTIR spectra of the synthesized cryogels are shown in Figure 4. The addition of AgNPs on the chitosan-gelatin cryogel network had no influence on the characteristic peaks of chitosan and gelatin polymers, which reveals that the synthesis procedure did not affect the chemical structure of the cryogels.

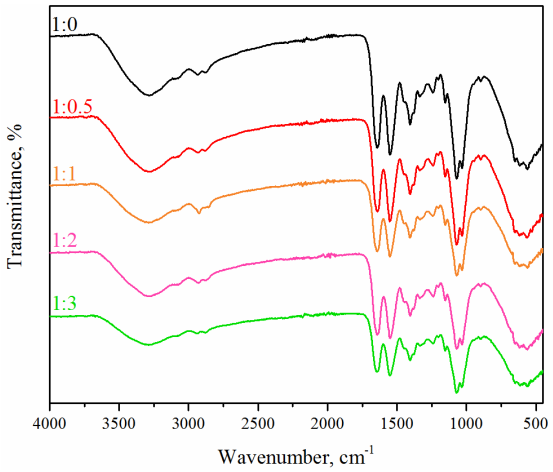

Fig. 4. FTIR spectra of cryogels

3.5. Swelling ratio of cryogels

High swelling rate is an important property of cryogels due to their highly interconnected macroporous structure. The swelling rates in different periods (10, 20, 30, 60, 90 and 120 min) are presented in Figure 5. The results have shown that the swelling rate of the cryogels decreases with increasing the ratio of AgNPs.

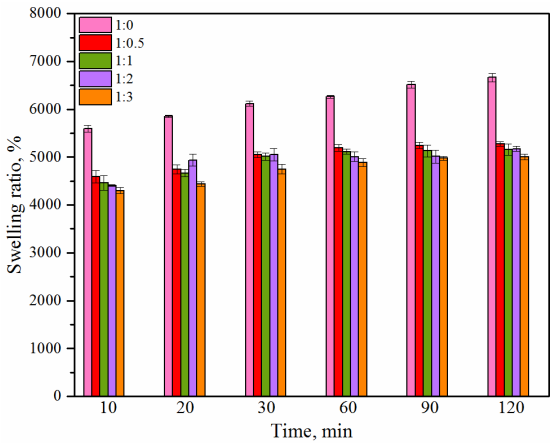

Fig. 5. Swelling ratio of cryogels

3.6. Degradation behavior of cryogels

Percentage degradation of chitosan-gelatin and different amounts of AgNPs loaded chitosan-gelatin cryogels was monitored for two weeks at 37°C as shown in Figure 6. The degradation of plain chitosan-gelatin cryogels was found up to around 7% within 14 days of incubation. The cryogels incorporated with high amounts of AgNPs degraded quickly in two weeks when compared with the low degradation rate of plain cryogels, which might be due to the release of loaded AgNPs on the surface of cryogels into the external environment.

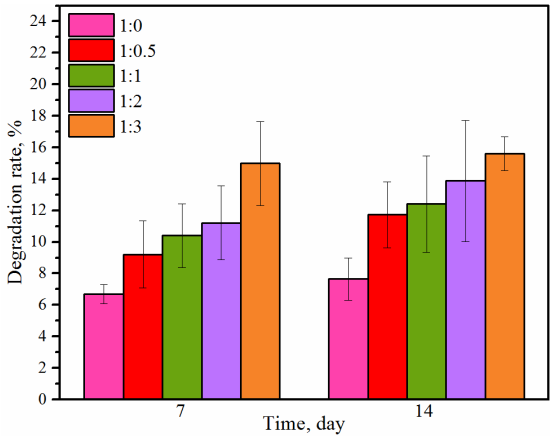

Fig. 6. Degradation behavior of cryogels

5. CONCLUSION

A one step green synthesis of AgNPs was achieved by mixing $AgNO_3$ solution with Myrtle leaf extract. The extract acted as a reducing agent. The green synthesis of AgNPs using plant extracts is an eco-friendly method when compared to other chemical and physical fabrication methods. The UV-Vis spectroscopy profile showed a well defined optical absorption peak due to the SPR phenomenon of AgNPs. The green synthesized AgNPs were added at different ratios to the structure of chitosan-gelatin cryogels. Resulting cryogels exhibit macroporous structure with high swelling capacities. The nanoparticles incorporated cryogels can be candidate materials for various applications including bactericidal, wound healing, tissue engineering and other medical fields.

REFERENCES

Samal, S. K., Dash, M., Shelyakova, T., Declercq, H. A., Uhlarz, M., Bañobre-López, M., Dubruel, P., Cornelissen, M., Herrmannsdörfer, T., Rivas, J., Padeletti, G., Smedt, S. D., Braeckmans, K., Kaplan, D. L. and Dediu, V. A. (2015). "Biomimetic magnetic silk scaffolds." *ACS Applied Materials and Interfaces*, Vol. 7, No. 11, pp. 6282–6292.

Natarajan, D. and Kiran, M. S. (2019). "Fabrication of juglone functionalized silver nanoparticle stabilized collagen scaffolds for pro-wound healing activities." *International Journal of Biological Macromolecules*, Vol. 124, pp. 1002-1015.

Shameli, K., Bin Ahmad, M., Jaffar Al-Mulla, E. A., Ibrahim, N. A., Shabanzadeh, P., Rustaiyan, A., Abdollahi, Y., Bagheri, S., Abdolmohammadi, S., Usman, M. S., Zidan, M. and Usman, M. S. (2012). "Green biosynthesis of silver nanoparticles using Callicarpa maingayi stem bark extraction." *Molecules*, Vol. 17, No. 7, pp. 8506-8517.

El-Kady, A. M., Rizk, R. A., El-Hady, B. M. A., Shafaa, M. W., and Ahmed, M. M. (2012). "Characterization, and antibacterial properties of novel silver releasing nanocomposite scaffolds fabricated by the gas foaming/salt-leaching technique." *Journal of Genetic Engineering and Biotechnology*, Vol. 10, No.2, 229-238.

Zulkifli, F. H., Hussain, F. S. J., Zeyohannes, S. S., Rasad, M. S. B. A. and Yusuff, M. M. (2017). "A facile synthesis method of hydroxyethyl cellulose-silver nanoparticle scaffolds for skin tissue engineering applications." *Materials Science and Engineering C*, Vol. 79, pp. 151-160.

Raja, S., Ramesh, V. and Thivaharan, V. (2017). "Green biosynthesis of silver nanoparticles using Calliandra haematocephala leaf extract, their antibacterial activity and hydrogen peroxide sensing capability." *Arabian Journal of Chemistry*, Vol. 10, No. 2, pp. 253-261.

Yadav, J. P., Kumar, S., Budhwar, L., Yadav, A. and Yadav, M. (2016). "Characterization and antibacterial activity of synthesized silver and iron nanoparticles using Aloe vera." *Journal of Nanomedicine & Nanotechnology* Vol. 7, No. 3, pp. 1-7

CISET - 2nd Cilicia International Symposium on Engineering and Technology
10-12 October, 2019, Mersin / TURKEY

THE PRODUCTION OF ASH-FREE COAL BY SOLVENT EXTRACTION METHOD

Dicle Tek [*1], Ozgur Sonmez [2]

[1] Mersin University, Faculty of Science and Letters, Chemistry, Mersin, Turkey, dicle4733@hotmail.com

[2] Mersin University, Faculty of Science and Letters, Chemistry, Mersin, Turkey, ossonmez@mersin.edu.tr

ABSTRACT

In this study, solvent extraction of Zonguldak coal was carried out by using three different organic solvents under mild conditions and then ash-free coal (AFC) was prepared. The organic solvents used were N-methyl-2-pyrrolidone (NMP), dimethylformamide (DMF) and 1-methylnaphthalene (1-MN). It was found that solvent properties and extraction temperature were important parameters affecting the extraction yield. The highest extraction yield in solvent extraction of Zonguldak coal was obtained using NMP, while the lowest yield was obtained using DMF. The ash content of the ashless coal obtained using 1-MN was determined to be less than the ash content of the ashless coals obtained using NMP and DMF which are polar solvents. Ash content of ashless coals obtained varies between 0.03-0.11%.. On the other hand, the amount of ash remaining of the solid residues after the extractions increased compared to the original coal.

Keywords: *Coal, solvent extraction, ashless coal, NMP, DMF, 1-MN*

[*] Corresponding Author

1. INTRODUCTION

Today, coal is one of the most important sources of energy and accounts for ~25% of worldwide energy consumption (Priscilla et.al, 2017). It can be expected to be used in the coming years due to its abundant reserves as well as being economically viable. Today, climate change is one of the most important environmental problems and greenhouse gases are one of the factors that cause climate change. Increased population and developing economies cause greenhouse gases to increase. One of the factors that cause the increase in greenhouse gases is the use of fossil fuels, especially coal. Although there is a shift towards renewable resources to minimize the environmental impact of fossil fuels, it is expected that fossil fuels will continue to play a dominant role in the energy sector. Therefore, it must be developed alternative processing technologies for efficient and environmentally friendly utilization of poor quality coals. One of the methods of the efficient uses of lignite is to produce AFC. AFC has beneficial uses such as being a binder for coke production (Chang et al., 2014), fuel for low-temperature catalytic gasification (Sharma et al.2008; Lee et.al.,2015) and direct carbon for fuel cells (Vu and Lee, 2016).

Thermal extraction of coal with various organic solvents is a useful method both for investigating the structure of coal and for obtaining high value-added products from coal. During the extraction of the coal with organic solvents, the solvent enters the coal matrix and breaks the interactions between the coal molecules, allowing the coal to dissolve. There are two types of intermolecular interaction in coals. These are covalent and non-covalent interactions. It has been reported in many studies that the solubility of coals in organic solvents stems from non-covalent interactions. These non-covalent interactions are hydrogen bonds, pi-pi interactions, charge transfer interactions, and ionic interactions (Sonmez and Giray, 2011). Consequently, the solvent dissolves a great organic part of the coal. While the soluble part of the coal is dissolved into the solvent, most of the mineral grains and a portion of carbon remain insoluble (Wijaya and Zang, 2011). The residual coals (after solvent extraction) can be used effectively for power generation or steam generation (Rahman et al.,2013). Some industrial solvents such as 1-MN, NMP, quinoline, tetralin, and corbol oil can be used as extraction solvents to extract coal and produce AFC.

2. MATERIAL AND METHODS

In this study, a bituminous Zonguldak coal of Turkey origin was used. The coal sample was firstly pulverized to below 60 mesh and dried at 80 °C for 12 h in vacuum before the experiments. Table 1 and 2 list the proximate and ultimate analyses of sample. All solvents used were commercial pure chemical reagents without further purification. The same experiment was performed three times to ensure repeatability.

Table 1. Proximate analyses

Ash	Volatile matter (%)	Fixed carbon (%)
6.2	28.9	64.9

Table 2. Ultimate analysis of Zonguldak coal (dry ash free basis).

C (%)	H (%)	N (%)	S (%)	O*(%)
91.8	3.9	1.3	0.7	2.3

*by diff

2.1. Solvent Extraction of Coal

The coal sample (2.0 g) and 40 mL solvent were placed in a 250-mL round-bottomed flask fitted with a reflux condenser. Then the mixture was refluxed for 2 h and filtered.

After the extraction, the solid residue and the liquid phase were separated by filtration. The residue was washed with deionized water, methanol, then with acetone, and then dried in vacuum at 80 °C for 12 h. The extraction yield is defined as follows:

$$\text{Yield (wt\%,daf)} = [(1-Mr/Mc)/(1-Ac/100)]\times 100 \quad (1)$$

where, Mc (g), Mr. (g), and Ac (wt%, db) are the initial mass of the coal, the mass of the residue, and the ash content of the initial coal, respectively.

2.2. AFC Production

When NMP and DMF were used as extraction solvents, the anti-solvent was water. When 1-MN was used as an extraction solvent, after the liquid extract was concentrated, excess n-hexane was added to the extract to obtain AFC. Calculation of the AFC yield was as follows:

$$\%AFC = [AFC\ (g)\ /coal\ (g) x(1-ashx0{,}01)]\ x100 \quad (2)$$

3. RESULTS AND DISCUSSION

3.1. Extraction Yield

Solvent extraction of coal is one of the methods used to obtain clean, environmentally sensitive products with high added value from coal. In this study, Zonguldak coal was extracted by using three different solvents to obtain AFC and the results are shown in Figure 1.

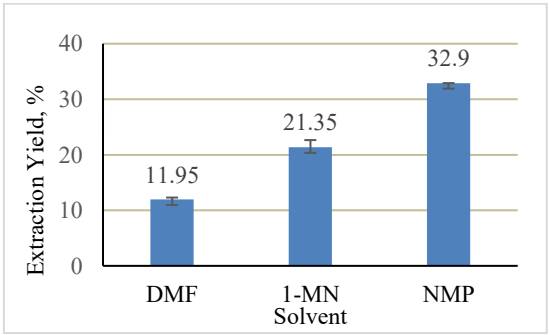

Fig.1. Extraction yields of Zonguldak coal obtained by using three different solvents

Since the experiments are carried out under open air pressure, the extraction temperature is the boiling point of the solvent used. One of the reasons for achieving low extraction efficiency in experiments with DMF can be considered as the low extraction temperature (153 °C). The temperature causes loosening in the structure of the

coal and facilitates the dissolution of the coal in the organic solvent. On the other hand, polar solvents are more effective in the solvent extraction of coal than a polar or low polarity solvents. Polar solvents interact with polar groups in the coal, in particular with oxygenated polar groups, breaking non-covalent bonds such as hydrogen bonds and ionic interactions between coal molecules, causing relaxation in the macromolecular structure of the coal. In Figure 1, although the DMF is a highly polar compound, the extraction efficiency obtained is the lowest, but the extraction efficiency is considerably higher than DMF, although it is a 1-MN a polar solvent. The Zonguldak coal used in this study is a bituminous coal and bituminous coals are mostly composed of aromatic groups and therefore the pi-pi and charge transfer interactions are dominant (Pan et.al. 2013). As shown in Figure 1, the yield obtained using NMP is higher than the other two solvents. In addition to being an aprotic polar solvent for coal, NMP is a good H-bond acceptor and has an affinity for aromatic groups. NMP contains a pyrrolidone ring that interacts strongly with aromatic rings and breaks charge transfer and pi-pi interactions between aromatic groups (Chen et.al., 1998; Shui et al.,2006). On the other hand, pi-pi interactions between 1-MN and coal cause the coal to dissolve in 1-MN (Pan et al., 2013).

3.2. Ash Contents of AFC

Table 3 shows the yields and ash amounts of AFCs prepared. While the ash content of the original Zonguldak coal was 6.2%, it was found that the ash contents of the AFCs obtained from the experiments varied between 0.03% and 0.11%. As shown in Table 3, the ash content of AFC obtained using 1-MN as the solvent is less than the ash content of AFCs obtained with polar solvents NMP and DMF. This result shows that some ash materials can also be extracted during solvent extraction, especially when polar solvents are used. Minerals such as aluminum silicates and silicon minerals are covalently bonded to oxygenated functional groups in coals. In addition to these minarets, some calcium and iron atoms may be extracted during solvent extraction (Yoshida et.al., 2004; Sakanishi et al.,2002).

Table 3. Ash contents of AFC with extraction yields and AFC yields

Solvent	Yield, %	AFC Yield,%	Ash in AFC,%	Ash in Residue, %
DMF	11.95	9.6	0.11	7.4
1-MN	21.35	21.2	0.03	8.6
NMP	32.9	31.3	0.09	10.0

When polar solvents were used, the ash content of AFC obtained by NMP is lower than that obtained by DMF. It is thought that the amount of ash-free coal obtained by NMP is high, which causes the amount of ash to be relatively low.

On the other hand, the ash content of the solid residue remaining after extraction was higher than the original coal. During extraction, the ash-forming mineral substances will remain in the solid residue as they are not dissolved in the organic solvent. Since the organic part of the coal also passes into the solvent phase, the mineral content in the solid residue will increase relatively. Therefore, increases in ash amounts of solid residues have been observed. As the extraction yield increased, the ash content of the solid residue increased.

AFCs yields were also calculated in this study and the results are given in Table 3. As can be seen, AFC yields and extraction yields differ. Dissolution of some coal molecules in antisolvents (water or hexane) added to the extracts during AFC preparation is considered to be a factor that causes AFC yields to be lower than extraction yields.

4. CONCLUSION

In this study, solvent extraction of Zonguldak coal was carried out using different organic solvents under mild conditions and ashless coals were prepared. NMP, DMF and 1-MN were used as extraction solvents. We obtained the following conclusions:

The best yield in solvent extraction of Zonguldak coal was obtained using NMP, while the lowest yield was obtained using DMF. Solvent properties and extraction temperature are considered to be important parameters affecting the extraction yield. For example, although the polarity of DMF (3.82 D) is close to the polarity of NMP (4.1 D), the extraction efficiency is low. This shows that not only the polarity is effective, but it also the temperature affects the extraction efficiency.

It was found that the ash amounts of AFCs obtained ranged between 0.03% and 0.11%. It was observed that ash content of ashless coal obtained with 1-MN, which is a polar solvent, had the lowest ash content, and whereas ash content of ashless coal obtained with polar solvents NMP and DMF was observed to be higher. This shows that polar solvents also extract some minerals.

ACKNOWLEDGEMENTS

The authors thank the Research Fund of Mersin University in Turkey with Project Number: 2017-2-TP2-2534

REFERENCES

- Priscilla, L., Kong, Y., Yoo, J., Choi, H., Rhim, Y., Lim, J.,Rhee, Y. (2017). “Steam Gasification of Thermally Extracted Ash-Free Coals: Reactivity Effects Due to Parent Raw Coals and Extraction Solvents.”.*Energy and Fuels*, 31(10), pp. 10505–10514.
- Chang, C., T. Whang, D. Huang, D. Wang, S. Tsai, M. Hung. (2014). “Thermoplasticity and strength improvement of coking coal by addition of coal extracts.” *Fuel*, 117, pp.364-371.
- Chen, C., J. Gao, Y. Yan. (1998). “Role of noncovalent bonding in swelling of coal.” *Energy and Fuels*, 12(6), pp. 1328-1334
- Lee, G.G., W.K. Kim, D.L. Vu. (2015). “Gasification of ash-free coal prepared with microwave method.” *Korean Journal of Chemical Engineering, 32*, pp.1784-1788.
- Pan, C.X., X.Y. Wei, H.F. Shui, Z.C. Wang, J. Gao, C. Wei, X.Z. Cao, Z.M. Zong. (2013). “Investigation on the macromolecular network structure of Xianfeng lignite by a new two-step depolymerization.” *Fuel,*

109, pp. 49-53.

- Rahman, M., A. Samanta, R. Gupta. (2013). "Production and characterization of ash-free coal from low-rank Canadian coal by solvent extraction." *Fuel Processing Technology,* 115, pp. 88-98.
- Sakanishi K., Saito I., Ishom T., Watanabe I., Mochida I., Okuyama N., Deguchi T., Shimasaki K. (2002). "Characterization and elution behaviors of organically associated minerals in coals during acid treatment and solvent extraction." *Fuel*, 81, pp.1471-1475.
- Sharma, A., I. Saito, and T. Takanohashi. (2008). "Catalytic steam gasification reactivity of hypercoals produced from different rank of coals at 600-775 °C." *Energy and Fuels,* 22, pp.3561-3565.
- Shui, H., Z. Wang, G. Wang. (2006). "Effect of hydrothermal treatment on the extraction of coal in the CS2/NMP mixed solvent." *Fuel,* 85(12-13),1798-1802.
- Sönmez, Ö. and E.S. Giray. (2011). "Producing ashless coal extracts by microwave irradiation." *Fuel* 90(6), pp. 2125-31.
- Vu, D.L. and C.G. Lee. (2016)." Oxidation of ash-free coal sub-bituminous and bituminous coals in a direct carbon fuel cell." *Korean Journal of Chemical Engineering,* 33(2), pp. 507-513.
- Yoshida, T., Li, C., Takanohashi, T., Mtsumura, A., Sato, S., Saito, I., Fujita, M. (2004). "Effect of extraction conditions on "hypercoal" production (2)-effect of polar solvents under hot filtration." *Fuel Processing Technology*, 86, pp. 61-72.
- Wijaya, N. and L. Zang. (2011). "A critical review of coal demineralization and its implication on understanding the speciation of organically bound metals and submicrometer mineral grains in coal." *Energy Fuels,* 25, pp. 1-6.

AN ANALYSIS OF THE EFFECTS OF FEATURE SELECTION METHODS IN CLASSIFYING TURKISH HATEFUL MESSAGES

Habibe Karayiğit [*1], Çiğdem Acı [2] and Ali Akdağlı [3]

[1] Mersin University, Engineering Faculty, Electric-Electronic Engineering, Mersin, Turkey, d2014242@mersin.edu.tr

[2] Mersin University, Engineering Faculty, Computer Engineering, Mersin, Turkey, caci@mersin.edu.tr

[3] Mersin University, Engineering Faculty, Electric-Electronic Engineering, Mersin, Turkey, akdagli@mersin.edu.tr

ABSTRACT
With the increasing popularity of social networks in recent years, there has been a huge increase in abusive and hateful messages. For the detection and analysis of such messages, various NLP (Natural Language Processing) studies are conducted in many languages. In Turkish, such studies are generally about cyber violence. In our study, BoW (Bag of Words), bi-gram, tri-gram feature selection methods are applied on a message dataset obtained from Instagram that contains abusive and hateful messages in Turkish. SVM (Support Vector Machine) classifier is used to analyze the dataset. As a result of the classification accuracy scores, BoW method was the most successful feature selection with 95.71% in the train set and 93.74% in the test set.

Keywords: *feature selection, hateful message, instagram, abusive message.*

* Habibe Karayiğit

1. INTRODUCTION

Social networks are online platforms which let people talk to each other, share ideas and activities, or make new friends. Internet usage in the world and particularly in the use of social media Turkey has been ranking the first place. According to statistics, there are 52 million active users of social media in Turkey in 2019. Social media is so popular that there is an increase in abusive and hateful messages.

The majority of the people knows the abusive, obscene and vulgar words in Turkish. When spoken verbally or in writing for insults, it can lead to resentment, controversy, quarrels, even murders among people, or to bring legal problems to those who say them (Güneş *et al.*, 2009). Abusive expressions that can cause such serious events can be easily written on social media among people.

To their credit, social networks platforms are also taking steps to mitigate damage, e.g., providing users with tools to flag abusive behavior (Kayes *et al*., 2015). Early detection and validation of aggressive and abusive messages can also prevent cyber-attacks (eg spam, hacking, malware) (Erkal *et al.,* 2015).

Different feature selection methods are used to determine the frequencies of words in NLP (Natural Language Processing). The classification achievement score can be increased by using different feature selections. For this reason, in our study, we use different feature selection methods and analyze abusively and hate speech. We use SVM (Support Vector Machine) as the classifier.

The rest of this study is organized as follows: Section 2 summarizes the relevant studies in this area. Section 3 provides information on the materials and methods used. Section 4 presents the numerical results of feature selection and classification. Finally, Section 5 provides information on future studies.

2. PREVIOUS STUDIES

Recently, studies on abusive and hateful speech in different languages are increasing. For example; In a study on hate speech (Waseem and Hovy, 2016), a dataset was obtained from Twitter and demographic features were tagged in this dataset. In order to perceive racist and sexist messages, character n-grams and hate speech were tried to be determined.

The focus of another work (Davidson *et al.*, 2017) was mainly to distinguish between hateful and offensive language. According to the authors, offensive the language contains offensive terms, which aren't necessarily inappropriate, while hate speech intends to be derogatory, humiliating or insulting.

(Golbeck *et al.,* 2017) focused on online trolling and harassment on Twitter. They first used various online sources, e.g., blocklists, to produce a list of keywords used for collecting harassing tweets with high probability.

(Ribeiro *et al.,* 2017) in their study, they tried to identify hateful users. Therefore, detecting inappropriate user behavior is a different, but closely related task.

(Chatzakou *et al.,* 2017) detected cyberbullying and created a dataset from Twitter. The final dataset contains 9.484 tweets, labeled as one of four categories: 1) bullying, 2) aggressive, 3) spam, or 4) normal.

There is no Turkish study on abusive or hate speech analysis but there are Turkish studies on cyberbullying. A dataset (Özel *et al.,* 2017) was created with Turkish cyber violence messages from Twitter and Instagram. They have classified with multiple machine learning techniques. As a result, they achieved the best value with MNB classifier at a rate of 84%.

In another Turkish study (Bozyiğit *et al.,* 2017), an example of the misuse of social media, a Turkish dataset containing 3000 messages such as threats, insults, coercion, and cyberbullying was created. They observed that the DVM classifier gave the best classification result.

3. MATERIAL AND METHODS

The Turkish language is an agglutinative language in terms of its structure. The Turkish language belongs to the Oghuz phrase of the Ural-Altaic language family, the branch of Turkish languages (Ergin, 1998). The stems of the words remain constant in the Turkish language. Additions to the stems of words change the meaning of the words. A situation that can be explained with a sentence in other languages can be explained in one word thanks to the suffixes in Turkish. For example, a sentence written in English as "I cannot stop" is sufficient to express it as "duramıyorum" in Turkish.

3.1. DATASET AND BALANCING

When an unbalanced dataset is subjected to classification, the algorithms cannot accurately predict the characteristics of the data distribution. The accuracy values obtained the result in a certain margin of error among the class values of the feature being sought in the dataset. (Haibo *et al.,* 2009).

Oversampling method; the goal is to bring the number of class labels that are less in number to the number of class labels that are more in number (Baesens *et al*., 2015).

Undersampling method; the target attribute is the approximation of the number of class labels (majority class) to the number class label (minority class) (Baesens *et al*., 2015).

3.2. PRE-PROCESSING AND FEATURE SELECTION

The main purpose of the pre-processing step is to reveal important attributes that can distinguish sample categories from textual data and convert them into the appropriate format (Srividhya *et al.*, 2010). Correcting spelling errors in the dataset, deleting symbols and symbols, removing stop words and separating sentences into word groups, converting words into lower case letters are in the pre-processing step.

Feature selection is the selection of properties that determine the frequency values of groups of words in the dataset. At this step, irrelevant and unnecessary data in the dataset is extracted and the dataset is passed to the classification stage in a reduced size.

BoW (Bag of Word) divides the words in the sentence into individual groups. While bi-gram separates the words in the sentence into groups of two, tri-gram separates the words in the sentence into groups of three.

Table 1. Feature selection step (BoW, bi-gram, tri-gram)

Message	"Kendi mutluluğundan başka hedefi olmayan insan en kötü insandır"
BoW	'kendi', 'mutluluğundan', 'başka', 'hedefi', 'olmayan', 'insan', 'en', 'kötü', 'insandır'
bi-gram (n=2)	'kendi mutluluğundan', 'mutluluğundan başka', 'başka hedefi', 'hedefi olmayan'…….
tri-gram (n=3)	'kendi mutluluğundan başka', 'mutluluğundan başka hedefi', 'başka hedefi olmayan'

TF-IDF (Inverse Document Frequency) is used for feature extraction. TF-IDF is the multiplication of the frequency of a term in messages and the logarithmic ratios of the number of messages to the number of messages containing the relevant term. The weight of a term in the dataset is obtained as a result of this process.

3.3. CLASSIFICATION

When classification algorithms work, textual data is converted to numeric data. The success of classification algorithms depends on the number of samples in the train set, the size of the feature vector, and the effective pre-processing step. The classifier used in our study is SVM.

SVM is mainly concerned with solving two classes of problems and in classification problems; there are two different types of SVM, linear and non-linear (Burges, 1998). The main purpose of the SVM method is to obtain an extreme plane or linear classification function, which can distinguish two classes from each other and at a maximum distance to both classes (Çoban *et al.,* 2018).

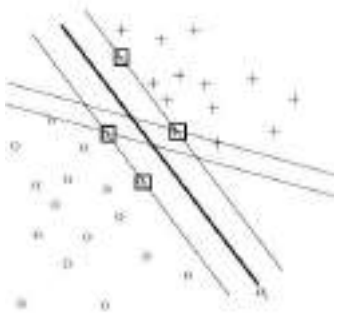

Fig. 1. SVM Classifier

In this method, an unlimited number of planes are created to group the data, and the most suitable of these plane is selected (Hearst et al., 1998). The advantages of this method are that it gives good results for most problems and is strong against excessive compliance (Bozyiğit *et al.,* 2017).

3.4. MODEL SUCCESS CRITERIA

The basic concepts used in classification are accuracy, precision, recall, and F-score. The success of the model is related to the number of samples assigned to the correct class and the number of samples assigned to the wrong class (Coşkun and Baykal, 2011).

The results of the classification can be expressed with the confusion matrix of performance information. In the confusion matrix, the rows represent the actual numbers of the samples in the test set and the columns represent the prediction of the model.

Table 2. Proposed class representation

		Proposed Class	
		Class=1	Class=0
True Class	Class=1	TP (True Positive)	FN(False Negative)
	Class=0	FP (False Positive)	TN (True Negative)

The most popular and simple method used to measure model performance is the accuracy of the model. Accuracy value is the ratio of the number of correctly classified samples (TP + TN) to the total number of samples (TP + TN + FP + FN) (Coşkun and Baykal, 2011).

$$Accuracy = \frac{TP+TN}{TP+FP+FN+TN} \quad \text{(Eq 1.)}$$

4. NUMERICAL RESULTS

The dataset we created consists of hate messages tagged as 1 and 0 taken from Instagram social media platform. Instagram and many other social media platforms allow sharing and comments on accounts that are accessible. Instagram can be accessed from Facebook API (Application Programming Interface) or Instagram API feature can be used. By getting an Instagram account, an access token is obtained. Using the obtained access token code, the comments in the open account can be obtained with the program written in Python.

Table 3. Created Turkish hateful phrases dataset

Social Media	Account	Hateful Messages	Neutral Messages
INSTAGRAM	Magazine account Football teams and some football player accounts	10528	19826

In order to balance the Turkish dataset, oversampling was performed. The hate message number is randomly increased to equalize the number of neutral messages.

A number of preprocessing steps were performed on the oversampling Turkish dataset. Numeric characters, unnecessary link addresses, and punctuation are cleared. All letters are translated to lower case. The words in the Turkish stop words list were ejected from the dataset. The correction was made according to Turkish language and spelling rules in the dataset. Words with dots or asterisks are corrected. A hate expression intended to be made with emoji has been translated into words.

The labeling process is labeled as 1 if there is hateful or abusive, or 0 as otherwise. Osmaniye YSSMTA High School IT students helped us about labeling and correcting spelling errors.

In the feature selection process, the dataset was selected according to three feature selection methods (BoW, bi-gram, tri-gram), and feature extraction was made with TF-IDF and classification process was concluded with SVM. The SVM algorithm is chosen as

the classifier because it has good generalization ability in sentiment analysis.

Figure 2 shows the success rate in the train set and Figure 3 shows the rate in the test set based on BoW, bi-gram and tri-gram feature selection methods.

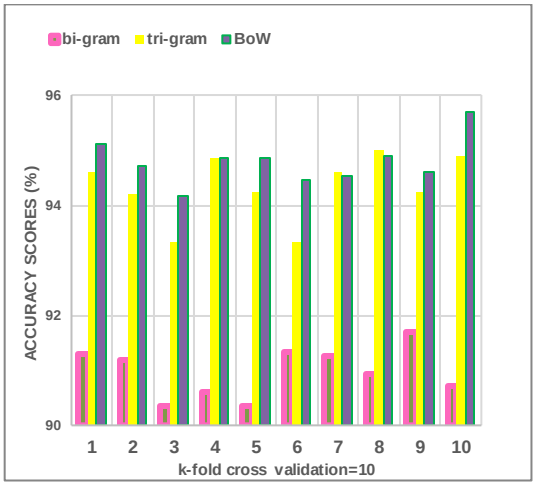

Figure 2. Train set SVM classification accuracy scores according to feature selections

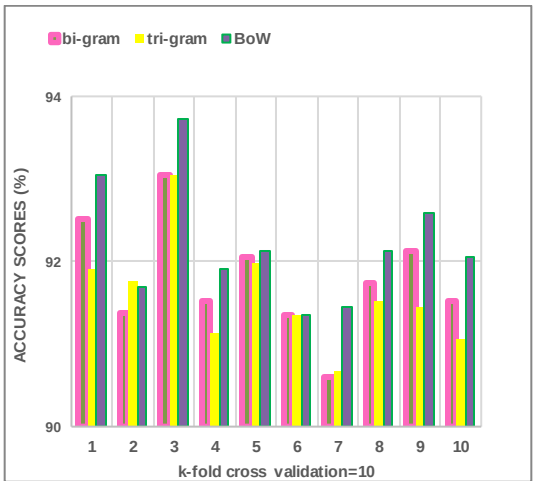

Figure 3. Test set SVM classification accuracy scores according to feature selections

Accuracy results between 90% and 100% of SVM classifier are presented using the data in the dataset. According to feature selections (Bow, bi-gram, tri-gram) of SVM classifier, the highest accuracy values in the education set were 95.71%, 95.14%, 94.99%, respectively. The highest values in the test set in order of feature selection (BoW, bi-gram, tri-gram); 93.74%, 93.05%, 93.05%.

Since the dataset is an increased sample set, the classification accuracy value is assumed to be more successful.

If we evaluate the accuracy success of BoW, bi-gram and tri-gram feature selections, it is seen that BoW feature selection is slightly more successful in both education and test set compared to other feature selections. Accuracy values of BoW feature selection in the dataset constitute the highest train and test values in the dataset. These accuracy values are 95.63% for the train set and 93.74% for the test set.

5. RESULTS AND DISCUSSIONS

With the spread of social media, annoying abusive and hateful messages are increasing day by day. While there are frequent studies analyzing hate and abusive messages on social media in different languages than Turkish, no such study has been found in the Turkish language.

In our study, a comprehensive dataset containing Turkish social media messages obtained from Instagram was prepared.

There are 30354 Turkish messages in the dataset, one-third of which contains abusive and hateful phrases the other part contains ineffective messages. Hate and ineffective messages are synchronized by oversampling the dataset. The most successful accuracy result of the classification is 95.71% in train set of BoW+TF-IDF+SVM and 93.74% in test set of the BoW+TF-IDF+SVM. The BoW feature selection is the most appropriate for our dataset. BoW feature selection, operation in the dataset regardless of term position and word order has been an important factor that increases success.

In the following studies, it is planned to increase the messages in the dataset and to classify with different methods. In the following studies, it is planned to increase the messages in the dataset and to classify with different methods. It is also considered to update the dataset.

REFERENCES

15 Maddede Türkiye'nin Dijital Tablosu: We Are Social 2019 Türkiye Raporu!, https://medium.com/@gamzenurluoglu/15-maddede-türkiyenin-dijital tablosu-we-are-social-2019-türkiye-raporu ebc034d01ef3 [Accessed: August 12, 2019].

Baesens, B., Van Vlasselaer, V., Verbeke, Wouter. (2015). *Fraud analytics using descriptive, predictive, and social network techniques: a guide to data science for fraud detection*, Wiley, North Carolina, U.S.A.

Burges, C.J.C. (1998) "A Tutorial on Support Vector Machines for Pattern Recognition." *Journal Data Mining and Knowledge Discovery archive*, Vol.2 No.2, pp. 121-167.

Bozyigit, A., Utku, S., Nasiboğlu, E. (2018). "Sanal Zorbalık İçeren Sosyal Medya Mesajlarının Tespiti." *10.1109/UBMK.2018.8566529*.

Chatzakou, D., Kourtellis, N., Blackburn, J., De Cristofaro, E., Stringhini, G. and Vakali, A. (2017). "Mean birds: Detecting aggression and bullying on Twitter." *In 9th ACM WebScience*, Troy, New York, USA, pp. 13-22.

Coşkun, C., Baykal, A. (2011). "Veri Madenciliğinde Sınıflandırma Algoritmalarının Bir Örnek Üzerinde Karşılaştırılması." *Akademik Bilişim'11,* Malatya, Turkey, pp.51-58.

Çoban, Ö., Tümüklü-Özyer, G., Bölümü, B.M. (2018). "The impact of term weighting method on Twitter sentiment analysis." *Pamukkale University Journal of Engineering Sciences,* Vol. 24, No.2, pp. 283–291.

Davidson, T., Warmsley, D., Macy, M. and Weber, I. (2017). "Automated hate speech detection and the problem of offensive language." *ICWSM*, Montreal, CANADA, pp. 512-515.

Ergin, M. (1998). *Üniversiteler İçin Türk Dili*, Bayrak, Istanbul, Turkey.

Erkal, Y., Sezgin, M., ve Gündüz, S. (2015). "A new cybersecurity alert system for Twitter." *IEEE 14th International Conference on Machine Learning and Applications (ICMLA)*, Miami, FL, A.B.D., pp. 766-770.

Golbeck, J., Ashktorab, Z., Banjo, R. O., Berlinger, A., Bhagwan, S., Buntain, C., Cheakalos, P., Geller, A.A., Gergory, Q., Gnanasekaran, R. K., Gunasekaran, R.R., Hoffman, K.M., Hottle, J., Jienjitlert, V., Khare, S., Lau, R., Martindale, M.J., Naik, S., Nixon, H. L., Ramachandran, P., Rogers, K. M., Rogers, L., Sarin, M. S., Shahane, G., Thanki, J., Vengataraman, P., Wan, Z., and Wu, D. M. (2017). "A large labeled corpus for online harassment research." *In 9th ACM Web Science*, pp.229–233.

Güneş, A. (2009). "Mizah Dergilerinde ve İnternette Küfürlü Sözleri Yazımları." *Çevrimiçi Tematik Türkoloji Dergisi*, Vol.1, No.2, pp. 61-67.

Haibo, H., Garcia, E.A. (2009). "Learning from Imbalanced Data." *IEEE Transactions on Knowledge and Data Engineering*, Vol. 21, No. 9, pp.1263–1284.

Hearst, M.A., Dumais, S.T., Osuna, E., Platt, J., Scholkopf, B. (1998). "Support vector machines." *IEEE Intelligent Systems and their Applications*, Vol.13, No.4, pp. 18–28.

Kayes, I., Kourtellis, N., Quercia, D., Iamnitchi, A. and Bonchi, F. (2015). "The Social World of Content Abusers in Community Question Answering." *WWW '15 Proceedings of the 24th International Conference on World Wide Web,* Florence, Italy, pp. 570-580.

Özel, S. A., Saraç, E., Akdemir S. and Aksu, H. (2017). "Detection of cyberbullying on social media messages in Turkish." *in 2017 International Conference on Computer Science and Engineering (UBMK)*, Antalya, Turkey, pp. 366–370.

Practical Guide to deal with Imbalanced Classification Problems in R, https:// www.analyticsvidhya. com/ blog / 2016/03/practical-guide-deal-imbalanced-classification-problems/ [Accessed: May 06, 2019].

Ribeiro, M. H., Calais, P. H., Santos, Y. A., Almeida, V. A., and Meira Jr, W. (2017). ""Like Sheep Among Wolves": Characterizing Hateful Users on Twitter." *WSDM'18,* Los Angeles, California, USA.

Srividhya, V., Anitha, R. (2010). "Evaluating Preprocessing Techniques in Text Categorization." *International Journal of Computer Science and Application Issue,* Vol. 47, No. 11, pp. 49-51.

SVM (Support Vector Machine, Destekçi Vektör Makinesi), http://bilgisayarkavramlari. Sadievren seker .com/2008/12/01/svm-support-vector-machine-destekci-vektor-makinesi/ [Accessed: July 20, 2019].

Waseem, Z. and Hovy, D. (2016). "Hateful Symbols or Hateful People? Predictive Features for Hate Speech Detection on Twitter." *Association for Computational Linguistics,* San Diego, California, pp. 88-93.

CISET - 2nd Cilicia International Symposium on Engineering and Technology
10-12 October, 2019, Mersin / TURKEY

FUEL PROPERTIES OF DIESEL BLENDED WITH ALTERNATIVE FUELS

Ibrahim Aslan RESITOGLU

Mersin University, Vocational School of Technical Sciences, Automotive Technology, Mersin, Turkey,
aslanresitoglu@gmail.com

ABSTRACT
Nowadays, many researches are focused on alternative fuels in internal combustion engines because fossil-based fuels have many negation not only environmental aspects but also economical aspects. Especially, Diesel engines need alternative fuels because of their widespread use and harmful emissions mainly Nitrogen Oxides and Particulate Matter. Alcohols and biodiesel are the main alternative fuels to diesel fuel. They can be used in diesel engines as additive without any modification of engine. In this study, the effect of blending alcohols (ethanol, methanol, 2-propanol, 2-butanol) and biodiesel with diesel fuel on the diesel fuel properties was investigated experimentally. The alcohols were blended as 15% and biodiesel as 20%, 40% and 60% with diesel fuel. The results showed that the use of alcohols with diesel fuel as alternative fuels leads to a decrease in density, viscosity, calorific value, flash point and cetane number values. On the other hand, biodiesel led to an increase in density, viscosity and flash point values, and a decrease in Calorific value and Cetane Number.

Keywords: *Diesel, Alternative Fuels, Alcohols, Biodiesel, Fuel Specifications*

1. INTRODUCTION

Nowadays, most of the energy needs are met by fossil fuels. In the transport sector, particularly diesel and gasoline vehicles, fossil fuels are commonly used energy sources (Barreto, 2018). However, instability in the prices of these fuels, increases in energy consumptions, environmental factors and the limited availability of these resources have led to the search for alternative energy sources (Ugurlu and Oztuna, 2015). Biodiesel and alcohols, which are biomass energy sources, are among the alternative energy sources for diesel fuel (Erdiwansyah *et al.*, 2019).

Biodiesel is the name given to esters formed by the reaction of oils in the presence of any alcohol and catalyst. Many types of edible or non-edible oil can be used in biodiesel production. Soybean, canola, sunflower are the most common vegetable oils used in biodiesel production (Hosseinzadeh-Bandbafha *et al.*, 2018). Apart from these vegetable oils, animal fats and waste oils is widely used in the production of biodiesel. In particular, the use of waste oils results in significant reductions in biodiesel production costs (Hajjari *et al.*, 2017). Many scientific studies on the production of biodiesel and the use of biodiesel in compression ignition (CI) engines are being carried out by researchers (Abed *et al.*, 2019; Goga *et al.*, 2019; Asokan *et al.*, 2019; Manigandan *et al.*, 2019). In these studies, It seemed that the biodiesel has a positive effect for diesel engines. Compared to diesel fuel, oxygen content in its structure, high flash point, improvement effect of engine emission characteristics and production with domestic resources are generated the main advantages of biodiesel (Singh *et al.*, 2019).

Alcohols are the most common sources of energy used as alternative fuels in diesel engines after biodiesel (Yusri et al., 2017). Alcohols obtained from vegetable wastes and renewable biological sources can be used as alternative fuels in CI engines by blending with diesel fuel in certain ratios. Thanks to the oxygen content, it improves the combustion efficiency and creates a catalyst effect on the engine characteristics (Tutak et al., 2015). Compared to biodiesel, alcohols have lower density and viscosity values, which make it advantageous to use alcohols with biodiesel (Emiroğlu and Şen, 2018).

The properties of fuels provide preliminary information on fuel efficiency and quality. Considering the various standards developed on fuel properties, it is possible to make comments on the similarity of alternative fuel types to diesel fuel and their usability in diesel engines. In this study, the effect of blending biodiesel and 4 different alcohol types with diesel fuel on the diesel fuel properties was investigated experimentally. After the alternative fuels were blended with diesel fuel in certain ratios, the basic fuel properties as density, viscosity, calorific value, flash point and Cetane number of each mixture were determined. The obtained values were compared with the fuel standard values.

2. MATERIAL AND METHODS

This section clearly describes the process of preparing fuels and determining the properties of fuels.

2.1. Preparation of Fuels

The biodiesel used in the study was obtained from a commercial company. Ethanol, Methanol, 2-Butanol and 2-Propanol were got commercially from Merck.

In this study, 7 different fuel mixtures were prepared by blending biodiesel and alcohols with diesel fuel in different ratios. Biodiesel was blended as 20%, 40% and 60% and 4 different types of alcohol (ethanol, methanol, 2-propanol, 2-butanol) as 15% with diesel fuel. High rates of blending of alcohols with diesel fuel have a negative effect on diesel fuel properties and combustion efficiency. Therefore, the ratio of alcohols in diesel was determined as 15%. Mixture fuels are named as indicated in the table below, taking into account the fuel content in them (Table 1).

Table 1. The blends

Fuel Code	Fuel rates
D	%100 Diesel
BI20	%20 Biodiesel + %80 Diesel
BI40	%40 Biodiesel + %60 Diesel
BI60	%60 Biodiesel + %40 Diesel
ET15	%15 Ethanol + %85 Diesel
ME15	%15 Methanol + %85 Diesel
PR15	%15 2-Propanol + %85 Diesel
BU15	%15 2-Butanol + %85 Diesel

2.1. Determination of Fuel Properties

In determining the properties of fuels, 5 different property values (density, viscosity, calorific value, Cetane number and Flash Point) were measured.

In the measurement of density, Kyoto Electronic DA-130 Density Meter was used. The measuring range is 0-2 g/cm^3 and 0-40 ^{o}C. The device is measured according to TS 6311 and ASTM D 4052-96 standards.

In determining viscosity values, Saybolt Universal Viscometer was used. It consist mainly a heater, fuel cup and fuel spill part. In the measurements carried out at 40 ^{o}C, the flow times of the samples were determined and these values were used in the conversion table and the viscosity values of each mixture were determined. Measurements were made in accordance with TS EN 14214 standard.

IKA-Werke C2000 calorimeter was used for the measurement of calorific values of fuels. Measurements can be made in TS1740, ASTM 240D, ISO1928, DIN51900, BSI standards.

TANAKA Flash Point Detection Device was used to determine the flash point of fuels, while ZX-440 Analyzer was used to determine Cetane numbers.

3. RESULT AND DISCUSSION

In this section, the comparison of the density, viscosity, calorific value, flash point and cetane number values of the mixtures and diesel with each other and also with the EN 590 and EN 14214 standards are discussed in detail.

EN 590 and EN 14214 are the standards published

by the European Committee for Standardization that describes the physical properties of diesel fuel and biodiesel respectively (Table 2).

Table 2. EN 590 (Diesel) and EN 14214 (Biodiesel) Standards

	EN 590	EN14214
Density at 15 ºC (kg/m³)	820-845	860-900
Viscosity kinematic at 40ºC (mm²/s)	2.0-4.5	3,5-5
Calorific value (MJ/kg)	-	-
Flash Point (ºC)	Min 55	Min 101
Cetane number	Min 51	Min 51

3.1. Density

Density is defined as the weight of the unit volume. Fig. 1 shows the density values for the mixtures. Density values increased with the use of biodiesel and decreased with alcohol use. The lowest density value was obtained with PR15 fuel using 15% propanol with 832.84 kg/m³. The highest density value was obtained with BI60 fuel. Considering the EN 590 standard, it was found that all alcohol mixtures were in compliance with the standard. Due to the high-density values of biodiesel, density values of biodiesel mixtures were obtained higher than EN590 standard.

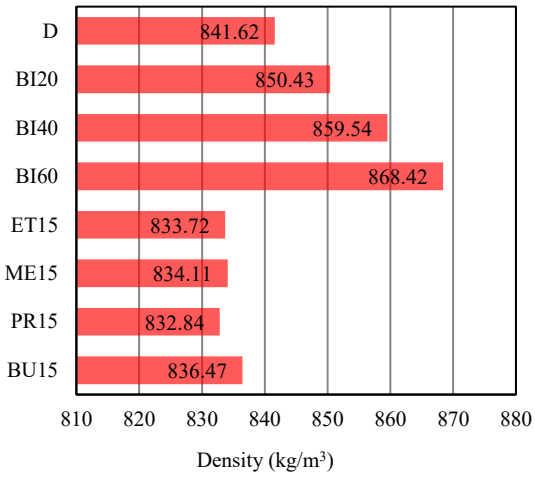

Fig. 1. Density value of blends

3.2. Viscosity

Viscosity is the strength of fluids to flow and is an important factor for diesel engines, especially fuel supply and injection systems. Temperature and pressure significantly affect viscosity. The viscosity of diesel fuel directly affects the injector spray characteristics and consequently the combustion in the cylinder.

The viscosity values of the mixtures are shown in Fig. 2. Similar to density values, viscosity values decreased with the use of alcohols and increased with the use of biodiesel. The lowest viscosity value was obtained with ME15 fuel as 2,348 mm²/s, while the highest viscosity value was measured as 3,732 mm²/s with BI60 fuel. All the viscosity values of the mixtures comply with EN590 standard.

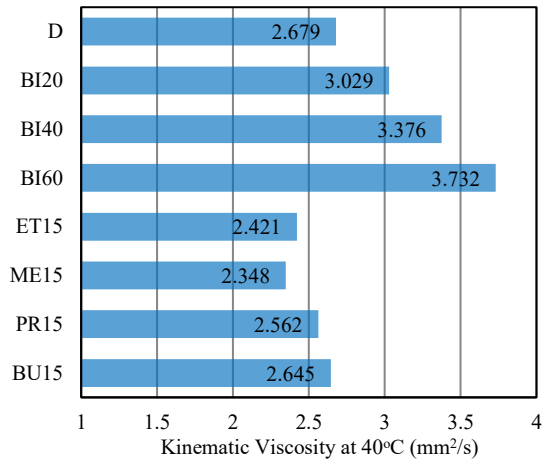

Fig. 2. Viscosity value of blends

3.3. Calorific Value

The calorific value is equal to the thermal energy given to the environment when the fuel is fully burned in a continuous flow open system and the end-products are converted into combustion products. In other words, the calorific value of a fuel is equal to the absolute value of the combustion enthalpy of the fuel. The calorific values of fuels are usually given by the energy of the unit mass (kj/kg or kcal/kg).

The calorific value depends on the phase of H_2O in the end-products. Thus, it is called as the higher calorific value (HHV) in the liquid phase of the H_2O at the end-combustion products and the lower calorific value (LHV) in the vapor phase of the H_2O at the end-combustion products.

The calorific value or combustion enthalpy of a fuel can be calculated from the enthalpy of formation of compounds involved in the combustion process. The higher calorific value of a fuel is equal to the lower calorific value and the latent heat of evaporation of the water vapor in the post-combustion products. Since the water is always present as steam at the end of combustion temperatures in the engines, the calorific value should be given as the lower calorific value. The calorific value is desired to be large because it indicates the amount of fuel energy.

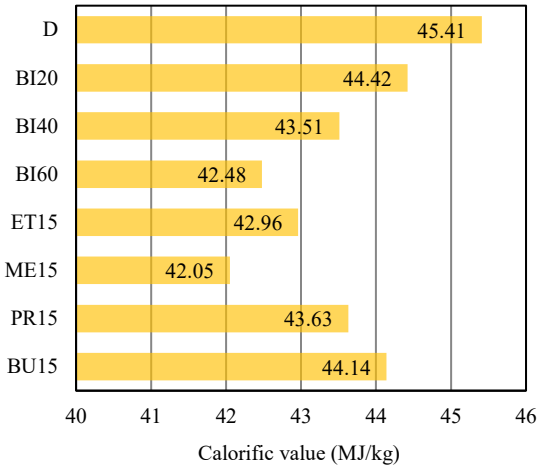

Fig. 3. Calorific value of blends

The calorific value of each mixture is shown in Fig.3. The calorific values of all of the mixtures were measured at a lower value than that of fossil based diesel fuel produced from crude oil. Calorific value is the most important indicator of fuel performance. However, although the use of biodiesel and alcohol causes a decrease in calorific value, it improves combustion performance. The main reason for this is that biodiesel and alcohols contain oxygen in the content and this has a catalytic effect on combustion.

3.4. Flash Point

In order for a liquid fuel to burn, the vapor of fuel must be mixed with the air in certain proportions. The easier a fuel can become vapor, the easier it is to form a flammable mixture with air. This easily combustible property of the fuel is determined by the flash point. The flash point of a flammable object is the lowest temperature at which it emits a vapor, which forms a flammable mixture with air. The flash point is not a fuel feature directly related to engine performance. Rather, it is measured to determine the safe handling and storage of fuels.

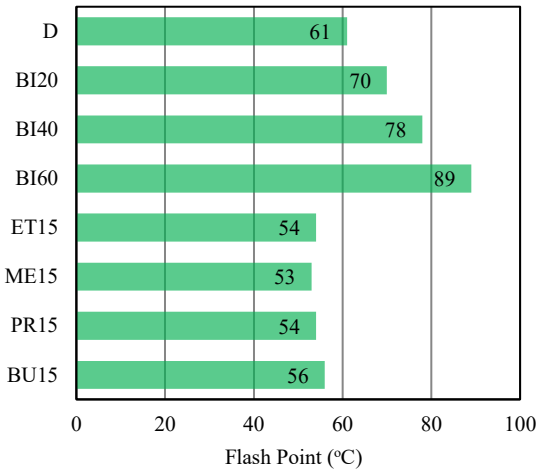

Fig. 4. Flash Point value of blends

Fig. 4 shows flash point values for mixtures and diesel. Significant increases in flash point values have been achieved with the use of biodiesel fuel. This is very useful for safer storage and transfer of diesel fuel. The flash point values of alcohol-containing mixtures were lower than those of diesel. The lowest flash point value was measured with a methanol-containing fuel mixture. Compared to EN 590 standard, ME15 has a flash point of 2 °C, ET15 and PR15 of a flash point of 1 °C lower. This has a limiting effect on the further use of alcohol-containing fuels by 15%.

3.5. Cetane Number

In diesel engines, the measure showing the fuel's self-ignition capability is called the Cetane number. It is one of the most important features of diesel fuel. The increase in the number of Cetane reduces the ignition delay time, which forms the most important part of the combustion process in the diesel engine, and therefore reduces the amount of fuel accumulated in the combustion chamber before sudden combustion. This leads to a decrease in the pressure increase rate during the sudden combustion phase.

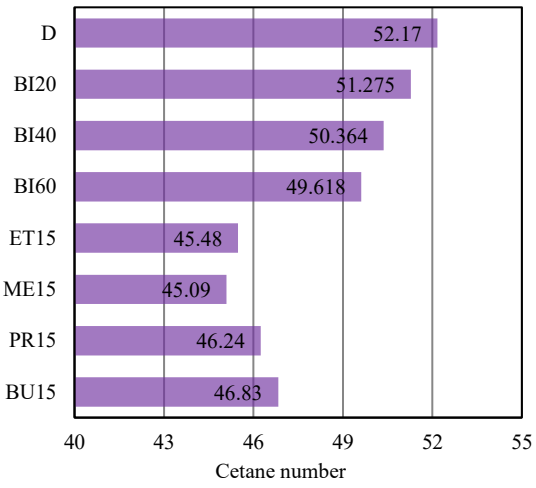

Fig. 5. Cetane Number of blends

Fig. 5 shows the values of the Cetane number of fuels. The use of biodiesel and alcohols with diesel fuel caused a decrease in the Cetane number values. The lowest Cetane number was measured as 45.09 with ME15 fuel.

4. CONCLUSION

As a result of the diesel blending of biodiesel and alcohol fuels which are alternative to diesel fuel, significant changes have been made on the fuel properties. Density and viscosity values increased with the use of biodiesel fuel compared with diesel fuel, but decreased with the use of alcohol fuels. The use of biodiesel and alcohols has led to some reductions in calorific value. However, oxygen content of biodiesel and alcohols completely prevents the decrease in combustion performance due to the decrease in calorific value. The flash point values of biodiesel-containing mixtures are higher than those of diesel fuels. This situation makes biodiesel storage and transfer processes safer. Some decrease in Cetane numbers was observed with the use of biodiesel and alcohols.

ACKNOWLEDGEMENTS

This study was supported by Mersin University Scientific Research Projects Unit. (Project Code: 2018-2-AP3-2964)

REFERENCES

Abed, K. A., Gad, M. S., El Morsi, A. K., Sayed, M. M. Abu Elyazeed, S. (2019). “Effect of biodiesel fuels on diesel engine emissions.” *Egyptian journal of petroleum*, Vol. 28, No. 2, pp.183-188.

Asokan, M. A., Prabu, S. S., Bade, P. K. K., Nekkanti, V. M., Gutta, S. S. G. (2019). “Performance, combustion and emission characteristics of juliflora biodiesel fuelled di diesel engine.” *Energy*, Vol. 173, pp. 883-892.

Barreto, R. A. (2018). "Fossil fuels, alternative energy and economic growth." *Economic Modelling,* Vol. 75, pp. 196-220.

Emiroğlu, A. O. and Şen, M. (2018). "Combustion, performance and exhaust emission characterizations of a diesel engine operating with a ternary blend (alcohol-biodiesel-diesel fuel)." *Applied Thermal Engineering,* Vol. 133, pp. 371-380.

Erdiwansyah, Mamat, R., Sani, M. S. M., Sudhakar, K., Kadorahman, A., Sardjono, R.E. (2019). "An overview of Higher alcohol and biodiesel as alternative fuels in engines." *Energy Reports,* Vol. 5, pp. 467-479.

Goga, G., Chauhan, B. S., Mahla, S. K., Cho, H. M., (2019). "Performance and emission characteristics of diesel engine fueled with rice bran biodiesel and n-butanol." *Energy Reports*, Vol. 5, pp. 78-83.

Hajjari, M., Tabatabaei, M., Aghbashlo, M., Ghanavati, H. (2017). "A review on the prospects of sustainable biodiesel production: A global scenario with an emphasis on waste-oil biodiesel utilization." *Renewable and Sustainable Energy Reviews*, Vol. 72, pp. 445-464.

Hosseinzadeh-Bandbafha, H., Tabatabaei, M., Aghbashlo, M., Khanali M., Demirbas, A. (2018). "A comprehensive review on the environmental impacts of diesel/biodiesel additives." *Energy Conversion and Management,* Vol. 174, pp. 579–614.

Manigandan, S., Gunasekar, P., Devipriya, J., Nithya, S. (2019). "Emission and injection characteristics of corn biodiesel blends in diesel engine." *Fuel*, Vol. 235, pp. 723-735.

Singh, D., Sharma, D., Soni, S. L., Sharma, S., Kumari, D. (2019). "Chemical compositions, properties, and standards for different generation biodiesels: A review." *Fuel*, Vol. 253, pp. 60-71.

Ugurlu, A. and Oztuna, S. (2015). "A comparative analysis study of alternative energy sources for automobiles." *International Journal of Hydrogen Energy*, Vol. 40, pp. 11178-11188.

Yusri, I. M., Mamat, R., Najafi, G., Razman, A., Awad, O. I., Azmi, W.H., Ishak, W. F. W., Shaiful, A. I. M. (2017). "Alcohol based automotive fuels from first four alcohol family incompression and spark ignition engine: A review on engine performance and exhaust emissions." *Renewable and Sustainable Energy Reviews*, Vol. 77, pp. 169–181.

Tutak, W., Lukacs, K., Szwaja, S., Bereczky, A. (2015). "Alcohol-diesel fuel combustion in the compression ignition engine." *Fuel*, Vol. 154, pp. 196-206.

CISET - 2nd Cilicia International Symposium on Engineering and Technology
10-12 October, 2019, Mersin / TURKEY

PHYTOREMEDIATION POTENTIAL OF LEAD BY ROSEMARY (*ROSMARINUS OFFICINALIS*) ASSISTED WITH CITRIC ACID AND HUMIC ACID IN CONTAMINATED SOIL

Zeynep Görkem DOĞAROĞLU[*1] and Abdullah EREN[2]

[1] Mersin University, Engineering Faculty, Environmental Engineering Department, Mersin, TURKEY, gorkemgulmez@gmail.com

[2] Mardin Artuklu University, Vocational College of Kızıltepe, Mardin, TURKEY, abdullaheren@artuklu.edu.tr

ABSTRACT

Phytoextraction technologies are known as remediation technologies that worldwide for decontamination of heavy metal contaminated soil. However, these technologies are very slow to remediate for some heavy metals (such as Pb) contaminated soil. For this reason, the different chelating agents can be used to accelerate the process. In this study, the phytoremediation potential of lead by rosemary in the presence of citric acid and humic acid was investigated. Organic acids were added to increase phyto-extraction capacity. In the experiments; the soil sample treated with the combination of 0, 5, 10, 20 and 40 mg/kg Pb, and organic acids (0.005 mM citric acid and 2% humic acid) and then they were incubated for four weeks. Plants were grown for 45 days in these soil samples. At the end of the experiment, dry weight of plant, N, P, K, Fe, Mn, Zn, and Cu uptake and also the Pb-phytoextraction capacity of rosemary were determined. Results showed that these micronutrients uptake by rosemary increased with the organic acid treatment at the increasing Pb concentrations. However, it has been determined that there were antagonistic or synergistic effects between metallic or non-metallic micronutrients and Pb concentrations in contaminated soils. By the way, these results proved that the presence of organic acids in Pb-contaminated soils can be enhanced the Pb-phytoextraction with rosemary.

Keywords: *Citric acid; Humic acid; Lead; Organic chelators; Rosemary*

[*] Corresponding Author

1. INTRODUCTION

Since people perceived the universe as human-oriented until recently, nature ranked second in their lives and research. But in recent years, the investigations about the environment pollution have been great attention by researchers. The rough definition of pollution is the materials that come out with human activities, in ecosystems and have a negative impact on the nature component. With the onset of industrialization in the world, anthropogenic impurities have been started to exist in the environment. The most known of these anthropogenic impurities are heavy metals. Lead (Pb), among heavy metals is one of the most polluting substances that can be attributed to industrial use (Alves *et al.,* 2016). Pb is a potentially toxic heavy metal in soil even at low concentration because of its persistence in the environment (Freitas *et al.,* 2013, Attinti *et al.,* 2017).

Until recently, physical and chemical remediation techniques have been used for decontamination of heavy metal polluted soils. These techniques are effective in removal heavy metals but they are costly and require may toxic chemicals for washing soil with some solvents (Abbaslou *et al.,* 2018). On the other hand, phytoremediation, is a green and ecofriendly technique, is not required any chemicals or external energy. Phytoextraction, is a type of phytoremediation, uses for decontamination of heavy metal polluted soils via green plants. In a successful metal phytoextraction, first of all the metal should be solubilized in soil fraction to uptake by plants root, and transport and accumulate in plants green parts (Fine *et al.,* 2014, Attinti *et al.,* 2017). Phytoremediation of heavy metal contaminated sites has been widely applicate in the worldwide. However, in order to find the optimum phytoremediation technique, it is necessary to find the technique which should be the cheapest, maximum accumulation and the least damage to the environment. Nowadays, the phytoremediation technique that only green plant application is out of date, instead of this, the phytoremediation with chelator assist is prominence (Fine *et al.,* 2014). For this reason, it is important to find most suitable chelators, which should be cheapest, most effective -but ecofriendly- and get the maximum efficiency, to determine the optimum chelator. These chelating agents help to metal solubilization (Sudova *et al.,* 2007; Bhargava *et al.,* 2012 Barbafierri *et al.,* 2017). However, after the treatment of chelators, heavy metals such as Pb have some risks as infiltrate to groundwater or as persist in the soil matrix. Due to the risks like these, nowadays researchers canalized to investigate safer chelators for the environment. Ethylenediamine tetra acetic acid (EDTA) is most used chelator in phytoextraction process (Lin *et al.,* 2009; Bhargava *et al.,* 2012; Fine *et al.,* 2014; Barbafierri *et al*., 2017). Besides that, Ethylenediamine disuccinic acid (EDDS), nitrilotriacetic acid (NTA), and diethylenetriamine-pentaacetic acid (DTPA) have also been using widely. By the way, citric acid (CA), as a natural chelating agent, has been one of the most used in metal phytoextraction processes. However, there are many conflicting data about the efficiency of citric acid in phytoremediation. For example, Freitas *et al.,* (2013) reported that the citric acid enhanced the Pb solubilization and thus uptake and translocation of Pb increased by maize and vetiver plants in contaminated soil with battery recycling activities. Also, Han *et al.,* (2018) reported the citric acid application in phytoextraction process promoted the accumulation of Pb in underground parts of Iris halophile. On the other hand, Chen *et al.,* (2003) reported the application of citric acid in soil with Pb contaminated, decreased the uptake of Pb in radish.

Although there have been many studies about chelating agent assisted in phytoremediation of Pb, there is lack of knowledge about the natural organic acids assisted, especially humic acid (HA). However, this is important to assess the technical and environmental applicability of the phytoremediation with natural organic acid assisted process. The goal of this study was to find an effective method in phytoextraction of Pb with rosemary (Rosmarinus officinalis) and to assess the effectiveness of citric acid and humic acid in phytoextraction. In this study, nitrogen (N), phosphate (P), potassium (K), iron (Fe), zinc (Zn), coper (Cu), and manganese (Mn) elements interaction with Pb, and the effects of these organic acids on these elements was also assessed.

2. MATERIALS AND METHOD

2.1. Experimental materials

The soil sample used in pot experiments was collected from 0-30 cm depth of Artuklu-Mardin region in South-Eastern Turkey, were air dried and sieved with 4 mm mesh. The pots were filled with 2 kg of sieved Pb-contaminated soil samples.

The citric acid monohydrate (Merck 100244 - 99.5% purity) was used in the experiments as 0.005 mM citric acid source, and leonardite, which contains humic and fulvic acid, were used as the source of 2 % humic acid. The pH range of leonardite has changed between 3.5 and 5.5.

2.2. Pot Experiments

In the pots experiments, the 0.005 mM citric acid and 2% humic acid were added to every pot which include at different concentrations (0, 5, 10, 20, and 40 mg Pb/kg) of Pb-contaminated soils. All the soil samples in pots were incubated for 4 weeks under controlled conditions. To determine the effectiveness of organic acids in Pb phytoextraction, control groups of organic acids has not been included any citric acid or humic acid. The experiments were designed at a complete randomized block and haave been conducted in triplicate.

Rosmarinus officinalis plants, obtained from greenhouse of Mardin metropolitan municipality via cutting method. Rosemary plants were grown during 3 months in non-contaminated soil after sowing in pots. Plants were transferred to the other pots filled with Pb-contaminated soil after first growth period (3 months) and grown for 45 days to determine the phytoextraction capacity of rosemary and effectiveness of organic acids. There was one plant in every pot and they were watered every day. The experiments were conducted at room temperature. All experiments were done in three replicates. After the second growth period (45 days), plants were harvested 1 cm above the ground and then washed with deionized water to remove of the possible contaminants. For the determination of dry weight (DW)

of plants, they were dried in an oven until to achieve constant weight at (65°C for 24 h). The dried plants were digested with 5 mL, 12 M HNO_3 using a microwave oven (MarsXpress CEM). All the plant samples' solutions were diluted to 10 mL with deionized water, and Pb content and P, K, Fe, Zn, Cu, and Mn concentration of plants were determined by using inductively coupled plasma-mass spectrometry (ICP-MS) (Agilent 7500ce Model ICP-MS) in three replications. Also, nitrogen concentration was determined by using Kjeldahl method (ISO 11261-2003).

2.3. Statistical Analysis

Duncan test was applied according to Bek (1986), and all data were evaluated according to the factorial trial design by using SPSS 22.0 statistical program. The data were subjected to the analysis at the 1% level of significance shown as $p<0.01$.

3. RESULTS AND DISCUSSION

3.1. Chemical and physical properties of the soil

The soil sample used in the experiments contained 2.02% organic matter, 40% clay, 38.2% silt, and 21.8% sand, thus it can be classified as clay based on hydrometer methods mentioned by Bouyoucos (1951). Besides, the pH value of soil sample was 7.52 as slightly alkaline. Soil texture is one of the most important parameter because availability and mobility of organic and inorganic materials, water retention, and also pore space are affected by soil texture (Khadka *et al.*, 2017). Thus, physical and chemical properties of the soil sample are shown in Table 1.

Table 1. physical and chemical properties of the soil sample

Parameters	Results	References
Texture	Clay	Bouyoucos, 1951
Salt	0.18%	Soil Survey Staff, 1951
$CaCO_3$	8.20%	Loeppert *et al.*, 1996
Organic Matter	2.02%	Kacar, 1995
Field Capacity	29.4%	Alpaslan *et al*., 1998
N	1.08%	Bremner and Mulvaney, 1982
P	12.6 P_2O_5	Olsen, 1954
K	80.1 K_2O	Richards, 1954
Fe	20.7 mg/kg	Lindsay and Norvell, 1978
Cu	4.24 mg/kg	
Mn	58.7 mg/kg	
Zn	6.15 mg/kg	

3.2. Nutrient concentration in plants

It is not surprising that the interaction between a toxic metal and other toxic metal or essential metals can be dramatically change the toxicity of toxic metal in the soil and plant systems (Lopez Alonso *et al.,* 2004). In this section, if the citric acid and humic acid addition was effective to uptake of minerals in Pb-contaminated soil, or not, were determined. Citric acid and humic acid contain some different functional groups, such as phenolic, carboxylic, sulfhydryl and hydroxyl groups. These functional groups allow to humic acid or citric acid many capabilities that plants growth and nutrition improvements, formation of heavy metal complexes and antiviral activity (Gomes de Melo *et al.*, 2016). The nutrition elements as N, P, and K was determined in Pb-contaminated soil sample with and without organic acids, also initial concentrations of these nutrients were given in Table 1. Nitrogen and P uptake by rosemary in contaminated soil decreased with increasing Pb concentrations. Besides that, the presence of organic acids in contaminated soil caused lower decreasing than without organic acid addition for N and the decreasing rate was as 42.5% at without organic acids, 30.27% at citric acid treatment, and 27.35% at humic acid treatment ($p\leq0.01$). By the way, it was 40.91% at without organic acids, 20.19% at citric acid treatment, and 43.5% at humic acid treatment, for P ($p\leq0.01$). This antagonistic interaction between Pb and P may occur due to the occurrence insoluble P complexes with Pb in soil and/or plants tissue (Kabata-Pendias and Pendias, 2001), thus the plants growth and development was negatively affected. For the K uptake by rosemary, the minimum decreasing was at citric acid treatment as 1.43% and also 41.8% decreasing was observed at without organic acid treatment, while 35.03% increasing was determined at humic acid treatment.

Iron, Zn, Mn, and Cu are micronutrients (also they are heavy metals) that are essential for biological and physiological activities in very small quantities (Shahid *et al.*, 2015; Yadav *et al.*, 2018). For this, it was evaluated that how the presence of Pb, Pb and citric acid, and also Pb and humic acid affects the uptake of these micronutrients by rosemary. The Fe concentrations in plants have changed with different application when there was no organic acid treatment and organic acids treatments. Results showed that the Fe uptake by rosemary significantly affected from addition of organic acids. The absence of Pb and presence of citric acid or humic acid has been increased the uptake of Fe by rosemary. The uptake of Fe increased with increasing Pb concentration in soil at the treatment of only-Pb, and Pb and citric acid ($p\leq0.01$). The increasing uptake results can be related to the functional groups of organic acids. On the other hand, the absence of organic acids, the increasing uptake results can about the Pb and Fe competition in soil fraction. However, it was decreased with increasing Pb concentration in soil after the 100 mg/kg Pb at treatment of humic acid ($p\leq0.01$). It is known that the previous studies proved that the humic substance, especially humic acid, is the natural iron binding chelator (Laglera and van der Berg, 2009; Catrouillet *et al.*, 2014; Yang *et al.*, 2017). Also, according to our knowledge the iron bind capacity is an important factor to formation of Fe-humic acid complexes (Laglera and van der Berg, 2009). By the way, there is a competition between iron and the other metals, such as Pb, Zn and Cu, to bind to organic acids and/or to intake to plants. Thus this result demonstrated that there was no sufficient ligand concentration at the concentration of 200 mg/kg Pb (Fig. 1a).

The interaction between Zn and Pb, and also the effects of organic acids on the uptake of Zn by rosemary was shown in Fig. 1b ($p \leq 0.01$). According to Kabata-Pendias and Pendias (2001), there is an antagonistic effect on translocation of Zn and Pb in plants. However, it was determined that the uptake of Zn by rosemary increased with increasing Pb concentration in soil. This result can be related to presence of Fe/Mn oxides in soil fraction, due to their impact on Pb/Zn mobility and bioavailability (Mouni *et al.*, 2017). The application of organic acids to non-Pb-contaminated soil caused a decreasing in the uptake of Zn by rosemary, compared to absence of both organic acids and Pb in soil. Nevertheless, Zn uptake increased in the presence of organic acids, the maximum uptake was observed at the concentration of 25 mg/kg Pb in humic acid and Pb treatment. After this concentration, the uptake of Zn decreased with increasing Pb concentration in humic acid treatment. The contrary results determined in only-Pb application and in citric acid-Pb application. The antagonistic or synergistic effects between heavy metals in multi-metal-containing soil may affect the toxicity in plants (Chibuike and Obiora, 2014). Some researchers investigated the effects between Pb and Cu (Nicholls and Mal, 2003), and six different heavy metals which are Cr, Cd, Co, Mn, Hg and Pb (Ghani, 2010). Researchers noted that these antagonistic or synergistic effects between heavy metals are related to metal concentrations. In this study, it was determined also the Mn and Cu concentration in plants, besides Zn and Fe, and the organic acids effects on these metals uptake by rosemary at increasing Pb concentrations (Fig. 1c and 1d). The maximum Mn concentrations in rosemary were observed in the treatment of humic acid and increasing Pb concentrations. Results showed that humic acid was more effective on Mn solubility than citric acid ($p \leq 0.01$). However, the presence of Pb in the soil samples caused the antagonistic effect on the uptake of Mn in rosemary (Fig.1c), like the investigation of Sharma and Dubey (2005). The authors explained this as two mechanisms that can be in the decrease of micro and macronutrient uptake under Pb stress. One of these mechanisms is the size of the ion radius and the other one is the disorder of cell membrane and enzyme systems depending on metal-induce (Sharma and Dubey, 2005). This result changed in Cu uptake. The uptake of Cu by rosemary enhanced with the increasing Pb concentrations in all the treatments. However, the treatment of citric acid and humic acid has been accelerated the uptake of Cu ($p \leq 0.01$) (Fig. 1d).

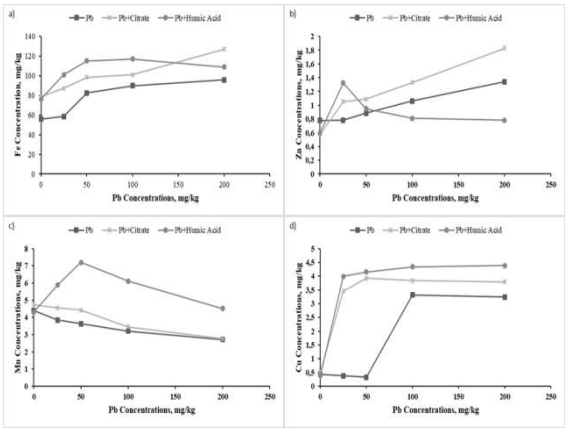

Fig.1. The effects of organic acids on micronutrient concentrations (a) Fe, b)Zn, c)Mn, and d)Cu) in rosemary

3.2. Phytoextraction capacity of Rosemary

The dry weight and Pb content have been determined to evaluate the Pb-phytoextraction capacity of rosemary. The biomass of selected plants is important to evaluate the successful phytoremediation process. Results showed that the dry weight of rosemary was significantly decreased with increasing Pb concentration ($p<0.01$). The maximum decreasing was observed at Pb-only treatment. The addition of organic acids in Pb-contaminated soil decelerated the decreasing of the dry weight of rosemary (Fig. 2a). The maximum dry weight was determined at the treatment of citric acid which absence of Pb contamination (0 mg Pb/ kg) as 2.13 g/plant. However, it decreased with the presence of increasing Pb concentrations and citrate. By the way, the minimum decreasing trend was determined in the treatment of humic acid, and the maximum decreasing trend was determined in Pb-only treatment. Freitas *et al.*, (2013) showed that after the citric acid treatment in Pb-contaminated soil, the dry weight of maize and vetiver plants decreased, as in our results. By the way, the authors noted that the Pb content in plants was increased by the application of citric acid as 14 times and 7.2 times, respectively. In this study, it was determined that the Pb content in rosemary plants increased with the treatment of organic acids. It was also determined that humic acid treatments were more effective in Pb uptake than citric acid treatment (Fig.2b).

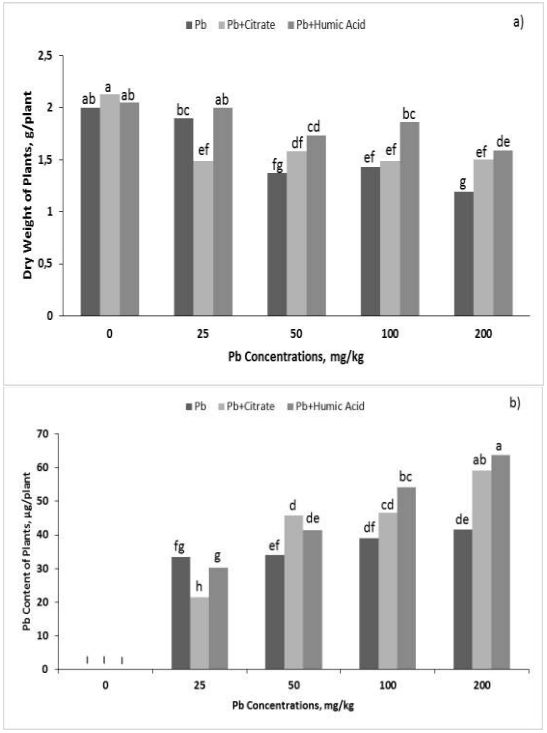

Fig. 2. a) The dry weight of rosemary at different types of Pb treatment and b) The Pb content in dry weight of rosemary at different Pb concentration. Different letters represent statistical significance at $p < 0.01$.

4. CITATION AND REFERENCE LIST

Kjellsen, K. O., Detwiller, R. J. and Gjorv, O. E. (1990). "Backscattered electron imaging of cement pastes hydrated at different temperatures." ACI Materials Journals, Vol. 20, No. 2, pp. 308-311.

Abbaslou, H., Bakhtiari, S., Hashemi, S. S. (2018). "Rehabilitation of iron ore mine soil contaminated with heavy metals using rosemary phytoremediation-assisted mycorrhizal arbuscular fungi bioaugmentation and fibrous clay mineral immobilization." Iran J Sci Technol Trans Sci, Vol. 42, pp. 431–441.

Alpaslan, M., Günes, A., Inal, A. (1998). "Test Technique." Ankara University Faculty of Agriculture, Publication No. 1502, pp. 455.

Alves, J. C., Souza, A. P., Pôrto, M. L. A., Fontes, R. L. F., Arruda, J., Marques, L. F. (2016). "Potential of sunflower, castor bean, common buckwheat and vetiver as lead phytoaccumulators." Revista Brasileira de Engenharia Agrícola e Ambiental, Vol.20, No.3, pp.243–249.

Attinti, R., Barrett, K. R., Datta, R., Sarkar, D. (2017). "Ethylenediaminedisuccinic acid (EDDS) enhances phytoextraction of lead by vetiver grass from contaminated residential soils in a panel study in the field." Environmental Pollution, Vol. 225, pp. 524-533.

Barbafieri, M., Pedron, F., Petruzzelli, G., Rosellini, I., Franchi, E., Bagatin, R., Vocciante, M. (2017). "Assisted phytoremediation of a multi-contaminated soil: Investigation on arsenic and lead combined mobilization and removal." Journal of Environmental Management, Vol. 203, pp. 316-329.

Bek, Y. (1986). "Research and trial methods." Cukurova University Faculty of Agriculture. Lecture notes. Publication No: 92, Adana.

Bhargava, A., Carmona, F. F., Bhargava, M., Srivastava, S. (2012). "Approaches for enhanced phytoextraction of heavy metals." Journal of Environmental Management, Vol. 105, pp.103-120.

Bouyoucos, G. J. (1951). "A recalibration of hydrometer for making mechanical analysis of soils." Agronomy Journal, Vol. 43, pp.434-438.

Bremner, J. M., Mulvaney, C. S. (1982). "Nitrogen-total." Methods of Soil Analysis, Part 2, Chemical and Microbiological Properties, A.L. Page, R.H. Miller, D.R. Keeney Ed. Vol.2, Madison, WI: American Society of Agronomy, pp. 595-624.

Catrouillet, C., Davranche, M., Dia, Al., Bouhnik-Le Coz, M., Marsac, R., et al., .. (2014). "Geochemical modeling of Fe(II) binding to humic and fulvic acids." Chemical Geology, Vol. 372, pp.109-118.

Chen, Y.X., Lin, Q., Luo, Y.M., He, Y.F., Zhen, S.J., Yu, Y.L., Tian, G.M., Wong, M.H. (2003). "The role of citric acid on the phytoremediation of heavy metal contaminated soil." Chemosphere, Vol. 50, pp. 807–811.

Chibuike, G. U., Obiora, S. C. (2014). "Heavy metal polluted soils: effect on plants and bioremediation methods." Applied and Environmental Soil Science, Vol. 2014, 12 pages.

Gomes de Melo, B. A., Lopes Motta, F., Santana, M. H. A. (2016). "Humic acids: Structural properties and multiple functionalities for novel technological developments." Materials Science and Engineering C, Vol. 62, pp. 967–974.

Fine, P., Paresh, R., Beriozkin, A., Hass, A. (2014). "Chelant-enhanced heavy metal uptake by Eucalyptus trees under controlled deficit irrigation." Science of the Total Environment, Vol. 493, pp. 995–1005.

Freitas, E. V., Nascimento, C. W., Souza, A., Silva, F. B. (2013). "Citric acid-assisted phytoextraction of lead:A field experiment." Chemosphere, Vol. 92, pp. 213–217.

Ghani, A. (2010). "Toxic effects of heavy metals on plant growth and metal accumulation in maize (Zea mays L.)." Iranian Journal of Toxicology, Vol. 3, No. 3, pp. 325-334.

Han, Y., Zhang, L., Gu, J., Zhao, J., Fu, J. (2018). "Citric acid and EDTA on the growth, photosynthetic properties and heavy metal accumulation of Iris halophila Pall. cultivated in Pb mine tailings." International Biodeterioration & Biodegradation, Vol. 128, pp.15-21.

ISO 11261 (2003). *ISO 11261: Soil quality – Determination of total nitrogen – modified Kjeldahl method.* English Version. https://www.ecn.nl/docs/society/horizontal/STD6161_Kj-N.pdf

Kabata-Pendias, A., Pendias, H. (2001). "Lead." Trace elements in soil and plants. 3rd Edition, CRC Press LLC, Florida.

Kacar, B. (1995). "Chemical analysis of plant and soil." Soil Analysis. Ankara University Faculty of Agriculture, Education, Research and Development Foundation Publications, No: 3, Ankara.

Khadka, D., Lamichhane, S., Shrestha, S. R., Pant, B. (2017). "Evaluation of soil fertility status of regional agricultural research station, Tarahara, Sunsari, Nepal." Eurasian J Soil Sci., Vol.6, No.4, pp. 295 -306.

Laglera, L. M., van den Berg, C. M. G. (2009). "Evidence for geochemical control of iron by humic substances in seawater." Limnol. Oceanogr., Vol.54, No.2, pp.610–619.

Lin, C., Liu, J., Liu, L., Zhu, T., Sheng, L., Wang, D. (2009). "Soil amendment application frequency contributes to phytoextraction of lead by sunflower at different nutrient levels." Environmental and Experimental Botany, Vol. 65, pp. 410–416.

Lindsay, W. L., Norvell, W. A. (1978). "Development of a DTPA soil test for zinc, iron, manganese, and copper." Soil Science Society of America Journal, Vol.42, pp.421-428.

Loeppert, R. H., Suarez, D. L. (1996). "Carbonate and gypsum." Methods of soil analysis. Part 3. Chemical Methods, D.L. Spark Eds, Madison, Wisconsin, USA, pp.437-474.

Lopez Alonso, M., Montaña, F. P., Miranda, M., Castillo, C., Hernandez, J., Benedito, J. L. (2004). "Interactions between toxic (As, Cd, Hg and Pb) and nutritional essential (Ca, Co, Cr, Cu, Fe, Mn, Mo, Ni, Se, Zn) elements in the tissues of cattle from NW Spain." BioMetals, Vol. 17, pp.389–397.

Mouni, L., Belkhiri, L., Bouzaza, A., Bollinger, J.-C. (2017). "Interactions between Cd, Cu, Pb, and Zn and four different mine soils." Arab J Geosci, Vol.10, No. 77, pp.1-9.

Nicholls, A. M., Mal, T. K. (2003). "Effects of Lead and Copper Exposure on Growth of an Invasive Weed, Lythrum Salicaria L. (Purple Loosestrife)." Ohio Journal of Science (Ohio Academy of Science), Vol.103, No.5, pp. 129-133.

Olsen, S. R., Cole, C. V., Watanabe, F. S., Dean, L. A. (1954). "Estimation of available phosphorus in soils by extraction with sodium bicarbonate." USDA Circular, No. 939, U. S. Department of Agriculture, Washington DC.

Richards, L. A. (1954). "Diagnosis and improvement of saline and alkali soils." United States Department of Agriculture Handbook. Vol.60, No.94.

Shahid, M., Pinelli, E., Dumat, C. (2015). "Review of Pb availability and toxicity to plants in relation with metal speciation; role of synthetic and natural organic ligands." Journal of Hazardous Materials, Vol. 219– 220, pp. 1– 12.

Sharma, P., Dubey, R. S. (2005). "Lead toxicity in plants." Braz. J. Plant Physiol., Vol. 1, No.1, pp. 35-52.

Soil Survey Staff (1951). "Soil survey manual." U.S. department of agriculture, Handbook No, 18. U.S Government Print Office. Washington.

Sudova, R., Pavlıkova, D., Macek, T., Vosatka, M. (2007). "The effect of EDDS chelate and inoculation with the arbuscular mycorrhizal fungus Glomus intraradices on the efficacy of lead phytoextraction by two tobacco clones." Applied Soil Ecology, Vol. 35, pp. 163–173.

Yadav, K. K., Gupta, N., Kumar, A., Reece, L. M., Singh, N., Rezania S., Khan, S. A. (2018). "Mechanistic understanding and holistic approach of phytoremediation: A review on application and future prospects." Ecological Engineering, Vol.120, pp. 274–298.

Yang, R., Su, H., Qu, S., Wang, X. (2017). "Capacity of humic substances to complex with iron at different salinities in the Yangtze River estuary and East China Sea." Scientific Reports, Vol. 7, No.1381, pp.1-9.

5. CONCLUSION

Although heavy metal pollution is a major problem in the environment, the real problem is heavy metal pollution in the soil, as it affects human health closely. Therefore, heavy metal removal from soils is very important for environmental and social health. One of the effective, natural and cheap removal process is phytoremediation, is known as the plant based removal method. However, the phytoremediation process may not effective without any chelating agent, because of the low solubility of some metals, such as Pb, in the natural environmental media. In this study, the assistance of citric acid and humic acid was effective in the Pb-phytoextraction by rosemary. By the way, humic acid can be more preferred then citric acid for the removal of Pb from the soil. This may be caused by active functional groups on humic acid.

CISET - 2nd Cilicia International Symposium on Engineering and Technology
10-12 October, 2019, Mersin / TURKEY

TENSILE AND FLEXURAL CHARACTERISTICS OF GLASS/POLYESTER FIBER REINFORCED COMPOSITE PIPES SUBJECTED TO DIFFERENT LOADING RATE

Özkan Özbek [*1], Ömer Yavuz Bozkurt[1] and Mehmet Sami Kanat[2]

[1] Gaziantep University, Faculty of Engineering, Mechanical Engineering Department, Gaziantep, Turkey
[2] Akbor Boru Sanayi ve Ticaret Limited Şirketi, Aksaray, Turkey

ABSTRACT

The current paper described an experimental investigation about the effect of loading rate on the tensile and flexural characteristics of glass/polyester fiber reinforced composite pipes. The samples subjected to uniaxial tensile and three point bending experiments with four different loading rate as 2 mm/min, 5mm/min, 10mm/min and 15 mm/min were fabricated by continuous filament winding technique. Also, detailed investigations on fracture mechanisms were performed to understand failure modes. The results showed that the loading rate were found to have significant influences on tensile and flexural responses of composite pipes. The increase in loading rate resulted with increase in tensile strength, tensile modulus and flexural strength. In the view of failure modes, higher loading rate gave the more catastrophic breakages caused from load carrying capacity rising. In general, failure modes can be given as matrix cracking, delamination and fiber breakage, respectively.

Keywords: *Glass Fiber, Tensile, Flexural, Loading Rate*

[*] Corresponding Author: ozkanozbek@gantep.edu.tr

1. INTRODUCTION

In recent years, the use of polymer based composite pipes in engineering applications such as transportation of a highly abrasive fluid, water/waste water transmission lines has been a potential way to provide the opportunity for resolving of the corrosion trouble of the classical metallic-based engineering materials. Furthermore, they exhibits the higher specific strength, specific stiffness and longer fatigue life according the use in a system. Several methods such as hand layup, vacuum assisted resin transfer molding, prepreg winding, filament winding are present to obtain them in the literature. Amongst them, filament winding is the most efficient technique by possessing ease to production, tailorability, flexibility in process, automatized, less amount of waste material, one-piece fiber usage.

So far, a few number of studies devoted to examine the effect of loading rate have been found in the literature (Miyano *et al.*, 1994; Hsiao *et al.*, 1998). An experimental study (Gilat *et al.*,2002) was conducted to investigate the effect of fiber orientation angle and loading rate on the tensile characteristics of the carbon/epoxy composites. Shokrieh *et al.* (2009) examined the effect of loading rate on the quasi-static and dynamic behaviors of glass/epoxy fiber reinforced composites. Increasing in loading rate resulted with the increase in tensile modulus and tensile strength. Jacob *et al.* (2004) presented a review study about the strain rate effects on the mechanical characteristics of the polymer-based composite materials.

In this study, the effects of loading rate on the tensile and flexural responses of glass/polyester fiber reinforced composite pipes have been investigated. The samples having 600 mm diameter have been fabricated by continuous filament winding technique. In order to examine the effects of the loading rate in detail, the loading rates of 2, 5, 10 and 15 mm / min were used.

2. MATERIALS & METHOD

2.1. Fabrication of Samples

The glass roving fiber with 2400 tex and 17 μm monofilament diameter, provided from Cam Elyaf A. Ş., Turkey, was used as reinforcement material. The mixture of the polyester resin (BOYTEK PW05) and hardener with the stoichiometric ratio of 98:2 in weight were utilized to form matrix of the samples.

A continuous filament winding machine shown in Figure 1, was used to fabricate all considered samples. All production stages were carried out in Akbor San. ve Tic. Ltd. Şti., Aksaray, Turkey. Firstly, release wax application was performed to mandrel and glass wool was wrapped to obtain smooth surface inside of the sample. Then resin mixture was deposit and the wrapping process of the reinforcements with 100 number of glass fibers together was conducted.

Fig. 1. Continuous filament winding technique

The silica sand was used for strengthening in the middle part of the pipe. Finally, glass fibers was again wrapped and finally glass wool was applied on the outer surface as seen in Figure 2. The all samples were cut on the longitudinal axis of the pipe as shown in Figure 3. The thickness of the samples were measured as 9.5 ± 0.15 mm.

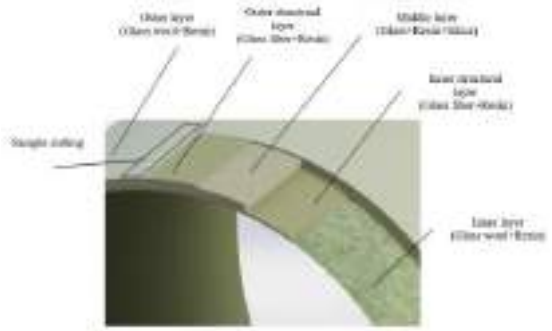

Fig. 2. The pipe structure

Fig. 3. Tensile and flexural samples

2.2. Mechanical Tests

The uniaxial tensile and three point bending experiments were conducted on the 300 kN capacity Shimadzu AG-X Series universal testing machine as shown in Figure 4 and Figure 5. The tensile and flexural samples prepared by according to ASTM D3039 (2000) and ASTM D790 standards (2008), respectively were exposed to different loading rates of 2 mm/min, 5 mm/min, 10 mm/min and 15 mm/min.

Fig. 4. Tensile test

Fig. 5. Three point bending test

The sample dimensions for tensile experiments had 300 mm x 25 mm in length and width, respectively. For the flexural loading, span to depth ratio was used as 16:1 and dimensions of the samples were 200 mm x 12.7 mm in length and width, respectively. At least five number of samples were used for each test to ensure experimental reliability. Load-displacement data was recorded by data acquisition system and tensile strength (σ_t), tensile modulus (E_t), flexural strength (σ_f) and flexural modulus (E_f) were calculated from following equations:

$$\sigma_t = P/A \quad (1)$$

$$E_t = \sigma_t/\varepsilon \quad (2)$$

$$\sigma_f = 3PL/(2bd^2) \quad (3)$$

$$E_f = mL^3/(4bd^3) \quad (4)$$

where P, A, ε, L, m, b and d represent the maximum load, cross-sectional area, tensile strain, span length, the slope of initial tangent line, width and thickness of the samples, respectively.

3. RESULTS & DISCUSSIONS

3.1. Tensile Response

The tensile strength and the tensile modulus obtained from the uniaxial tensile experiments were given in Figure 6. Maximum increase in tensile strength was achieved as 7.96% with 37.28 MPa value of the sample subjected to 10 mm/min loading rate. Although slightly decrease below 1% were happened on 15 mm/min, it can be said that strength tendency effected with loading rate change in positive manner. Also, increasing trend on modulus of the samples rate was observed that caused from the loading rate increments. Maximum improvement on tensile modulus was 10.9%. This increase in tensile strength with loading rate was attributed to the increased strength of the glass fibers with loading rate as reported in Okoli's & Smith's study (1999).

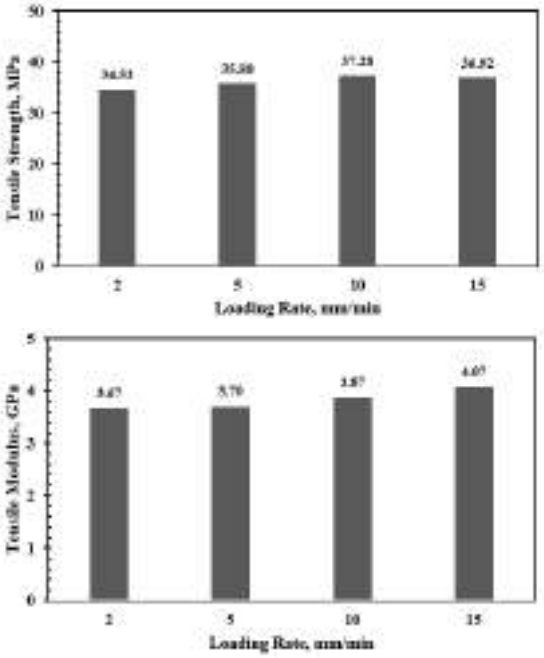

Fig. 6. Tensile strength and tensile modulus

The stress-strain response for considered samples were presented in Figure 7. Increasing in loading rate resulted with the increasing in strain at failure and higher stiffness of the samples except 15 mm/min.

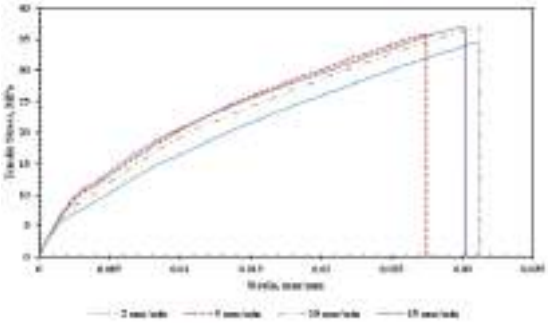

Fig. 7. Stress-strain diagrams

Failure modes of the samples were given in Figure 8. Generally, samples showed the matrix fragmentation, delamination of the layers, fiber breakage failure modes (Fotouhi *et al.*, 2016). The main damage mechanisms were found as delamination triggered by matrix cracking.

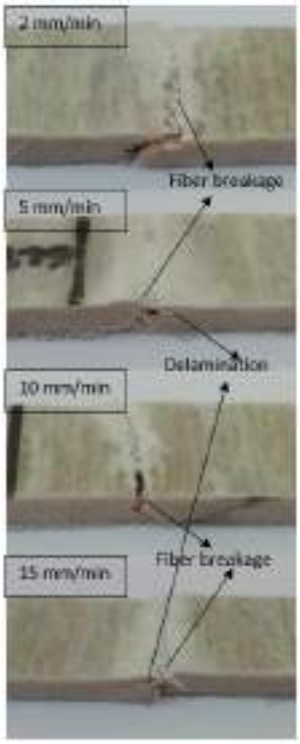

Fig. 8. Damage shapes of tensile samples

3.2. Flexural Response

The flexural strength and flexural modulus, given in Figure 9, were obtained from three point bending experiments. With the increment of loading rate, increasing tendency were found on flexural strength, but irregular trend was seen on flexural modulus results. The samples loaded with 15 mm/min rate showed the maximum strength as 118.10 MPa that was 46.9% higher than the sample with 2 mm/min loading rate.

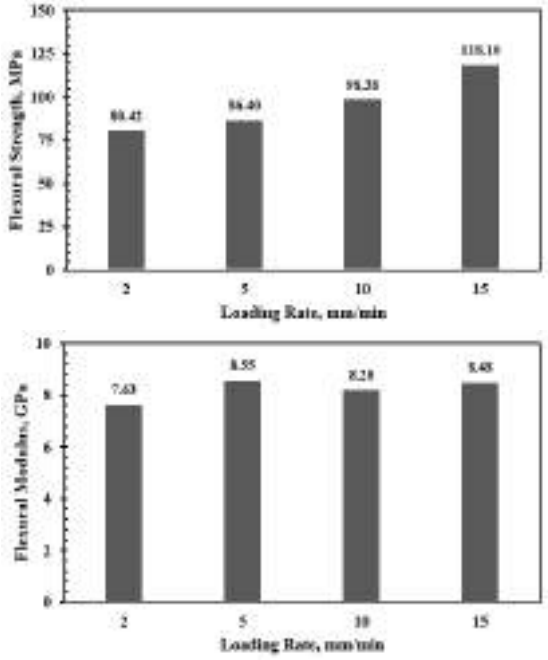

Fig. 9. Flexural strength and flexural modulus

The load-displacement response of each configuration, shown in Figure 10, showed that the higher loading rate resulted with the higher elongation at break. Figure 11 presents the damage shapes of the samples under flexural loading. When loading rate was increased, more catastrophic failures were observed because of higher load carrying capacity. The first crack occurred in middle part (silica sand region) and propagated to outer layers.

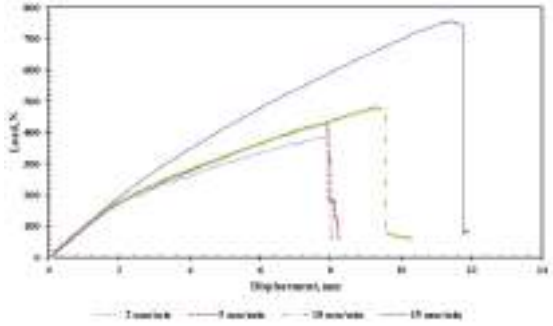

Fig. 10. Load-displacement curves

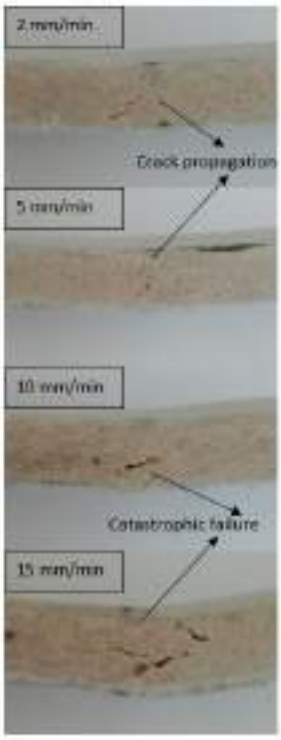

Fig. 11. Damage shapes of tensile samples

4. CONCLUSIONS

In this study, the effect of loading rate on the tensile and flexural characteristics of composite pipes fabricated by continuous filament winding technique samples were investigated. Glass fiber reinforcement and polyester resin were used as components of the samples. The results showed that the loading rate had a very significant influences on examined mechanical behaviors. Higher loading rate resulted with the higher strength, modulus not only in tensile response but also in flexural

characteristics. Matrix fragmentation, delamination of layers and fiber breakage were observed as failure modes. With higher load carrying capacity led to more catastrophic failures especially in flexural samples. In conclusion, loading rate proved the magnificent effect on the tensile and flexural characteristics of the filament wound structures.

REFERENCES

ASTM D3039 (2008). "Standard test method for tensile properties of polymer matrix composite materials".

ASTM D790 (2000). "Test Methods for Flexural Properties of Un-reinforced and Reinforced Plastics and Electrical Insulating Materials".

Fotouhi, M., Suwarta, P., Jalalvand, M., Czel, G., & Wisnom, M. R. (2016). "Detection of fibre fracture and ply fragmentation in thin-ply UD carbon/glass hybrid laminates using acoustic emission." *Composites Part A: Applied Science and Manufacturing*, 86, 66-76.

Hsiao, H. M., & Daniel, I. M. (1998). "Strain rate behavior of composite materials." *Composites Part B: Engineering*, 29(5), 521-533.

Jacob, G. C., Starbuck, J. M., Fellers, J. F., Simunovic, S., & Boeman, R. G. (2004). "Strain rate effects on the mechanical properties of polymer composite materials." *Journal of Applied Polymer Science*, 94(1), 296-301.

Miyano, Y., McMurray, M. K., Enyama, J., & Nakada, M. (1994). "Loading rate and temperature dependence on flexural fatigue behavior of a satin woven CFRP laminate." *Journal of Composite Materials*, 28(13), 1250-1260.

Gilat, A., Goldberg, R. K., & Roberts, G. D. (2002). "Experimental study of strain-rate-dependent behavior of carbon/epoxy composite." *Composites Science and Technology*, 62(10-11), 1469-1476.

Okoli, O. I., & Smith, G. F. (1999). "Aspects of the tensile response of random continuous glass/epoxy composites." *Journal of reinforced plastics and composites*, 18(7), 606-613.

Shokrieh, M. M., & Omidi, M. J. (2009). "Tension behavior of unidirectional glass/epoxy composites under different strain rates." *Composite Structures*, 88(4), 595-601.

CISET - 2nd Cilicia International Symposium on Engineering and Technology
10-12 October, 2019, Mersin / TURKEY

ANALYSIS OF FOLDS IN LOWER DEVONIAN SIĞIRCIK FORMATION IN AYDINCIK (MERSİN) AREA

Birsen Feray BİÇGEL [1], Erol ÖZER* [1]

[1] Mersin University, Faculty of Engineering, Department of Geological Engineering, Mersin, Turkey,
e-mail:erolozer@mersin.edu.tr

ABSTRACT

Folded structure are seen in Precambrian aged Sipahili formation and the Early Devonian aged Sığırcık formation in Aydıncık (Mersin) region. In this study, we performed tectonic analysis of these folds. As a result of the analysis, it is aimed to obtain information about folding mechanism from tectonic structures in the region. Descriptive analysis was performed on small-scale folds, dynamic analysis was performed on small-scale ptygmatic folds in the region. Descriptive analysis results of folds in the region; according to aspect ratio broad, according to tightness of folding parameter close, according to bluntness of folds parameters subangular, according to Fleuty's classification semi-tight, according to geometric asymetric and localy recumbent fold, according to morphology similar and according to isogonal classification 1B parallel fold classification.

In all of the studies, it was calculated that, the first layer length of the ptygmatic folds and the resistance of the competent layer were directly proportional in the same lithologies. First length and the final length of fold ratio was found approximately 4. As a result of this finding, the contribution of the matrix resistance to folding is more effective than resistance of the competent layer. It is thought that the shortening of the fold lengths might be independent of internal force.

Keywords: *Folds, Descriptive Analysis, Dynamic Analysis, Paleozoic, Aydıncık.*

1. INTRODUCTION

In the Aydıncık (Mersin) region, the Pre-Cambrian Sipahili formation and the Lower Devonian aged Sığırcık formation appear to be folded within the Geyik Mountain Tectonic Union called Özgül (1976). In this study, tectonic analysis of these folded structures was made and it was aimed to obtain information about the fold formation mechanism from tectonic structures in the region. Descriptive analysis was performed on small scale folded structures in the region, and dynamic analysis was performed on small scale ptygmatic folds.

Geological characteristics of the region are taken from Demirtaşlı (1984), Koç (2003) and Koç at al. (2005).

Fig. 1. Location map of the study area.

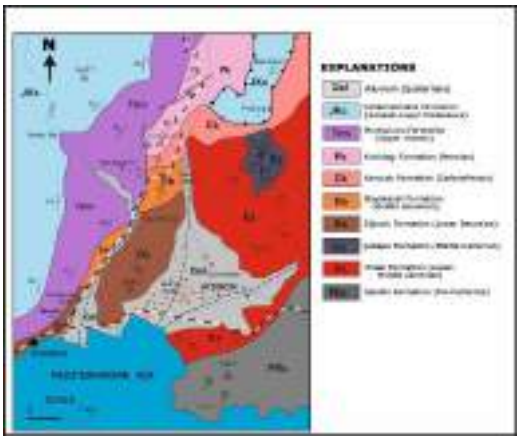

Fig. 2. The geological map of the Aydıncık (Mersin) region (modified after Koç, 2003).

2. STRUCTURAL ANALYSIS

In this study, measurements of ptygmatic folds in the Sığırcık formation, which were intensely folded under shear forces, were carried out and analysis studies were performed. Measurements were taken from all ptygmatic folds in the study area by metric measurement method and each fold was evaluated separately. The findings and evaluations obtained within the scope of the study are given below.

2.1. Descriptive Analysis

The folded structures observed in the study area were evaluated according to Fleuty (1964), Moores and Twiss (1992), Ramsay (1967) and different classification systems. Moores and Twiss (1992) have defined the geometry of a curved surface in their work using 3 parameters. These parameters are the aspect ratio (P), the tightness of the folding and the bluntness of the folds. These parameters were measured in a study on an example fold shown in Fig. 3. The aspect ratio (P) is the ratio of the amplitude (A) of a fold and the distance (M). According to the measurements made on the fold, the aspect ratio (P) was calculated as 0.54. This data shows that this fold is classified as a broad fold according to the aspect ratio.

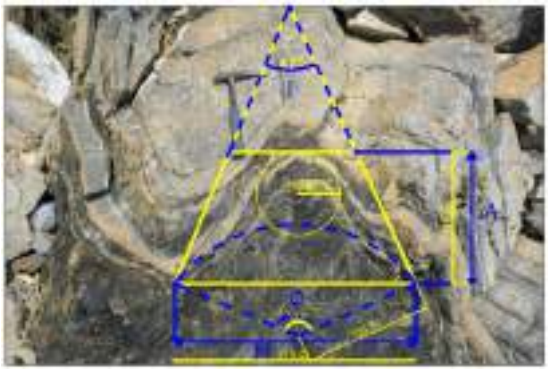

Fig. 3. Numerical data of descriptive analysis of fold.

According to the tightness of the folding parameter, folding angle (Ø) was 133 degrees and the interlimb angle (I) was measured 47 degrees. These data show that the fold is in a closed fold class.

Moores and Twiss (1992) define the bluntness of folds by the formula b = rc / ro. According to this formula, b value on the sample fold was calculated as 0.31. This value shows that the fold takes place in the subangular class.

According to Fleuty (1964) classification, interlimb angle of the folds in the study area is between 31-70 and is partly in the tightness of folding class.

When the folds in the region are classified morphologically, it is determined that the layer thickness is located in the similar fold class due to the fact that the layer thickness is thicker than the limbs (Fig. 4a). The isoclinal-recumbent fold observed in the study area is presented in Fig. 4b.

Fig. 4. Morphologically similar fold (a) and geometrically isoclinal-recumbent fold (b).

Ptygmatic folds developed by folding of very hard elastic quartzites veins within siltstones.

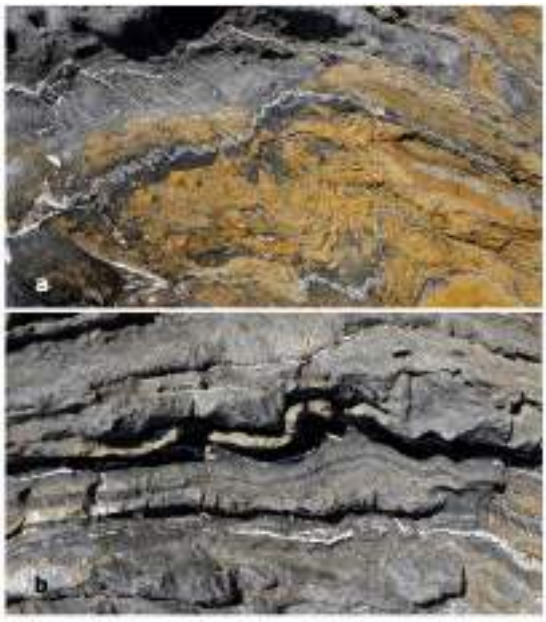

Fig. 5. Ptygmatic folds according to formation mechanics (a) and geometrically asymmetric folds (b).

Extension cracks due to shear stresses are seen in the folded layers (Fig. 6). The positions of the extension cracks developed parallel to the maximum pressure stress. Considering its relationship to the curved structure, it is seen that the extension cracks are perpendicular to the fold axis.

Fig. 6. Field view of extension cracks formed by shear.

2.2. Dynamic Analysis

Ramsay and Huber (1987) describing the resistance bucling in a single competent layer in a matrix of less competent rock are examined under the assumptions of lineer Newtonian viscosity of the materials. One of the general characteristics of these single layer folds is that they generally show a constant relationship between layer thicknesses. There are resistant forces for developing of a fold. The resistant force (the competent layer resistant) F_{int} is internal forces and external forces F_{ext} (matrix resistant) act together against the development of a fold with first wave length: W_1 .

Internal forces (resistance of the competent layer)

$$F_{int}=\frac{2\pi^2\mu_1 d^3 e'_x}{3W1^2 e_x} \quad (1)$$

External forces (matrix resistance)

$$F_{ext}=\frac{\mu_2 w1 e'_x}{\pi e_x} \quad (2)$$

In these formulas;
e_x : shortening strain
e'_x: shortening rate
μ_1 : viscosity of competent layer
μ_2 : viscosity of matrix
d : thickness of competent layer

Measurements were made for five small-scale ptygmatic folds in the study area. The matrix of ptygmatic folds was siltstone and the competent layer was quartzite. Acceptances for the formulas (https://www., Falalaev, 2010);

e'_x : $10^{-14}s^{-1}$ (Twiss and Moores, 1973)

μ_{ef} : shear stress / $3|e'_x|$

μ_1 (viscosity of layer) = 10^{19} PaS

μ_2 (viscosity of matrix) = 10^{18} PaS

Measurements of ptygmatic fold 1 (Fig. 7.):

d = 0.4 cm
w = 0.75 cm
l_0 = 101 cm
l_1 =25 cm
$ex = \frac{l1-l0}{l0}$=-0,75 (%75 shortening rate)

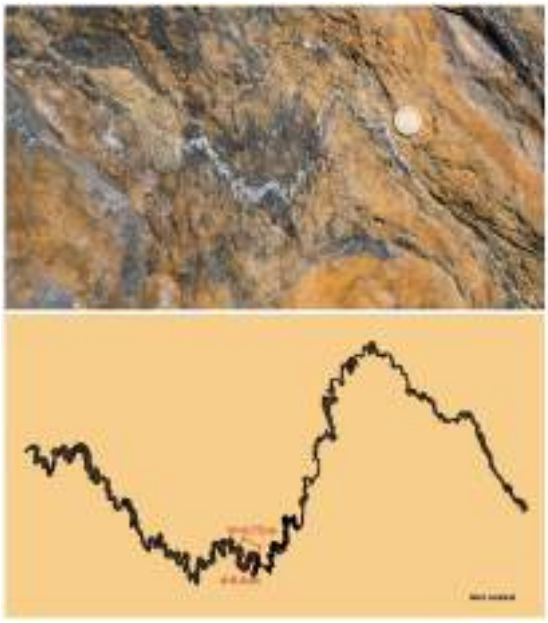

Fig. 7. Image of drawing ptygmatic fold 1.

Competent layer resistance from the first formula;

$F_{int}=\frac{2\pi^2\mu_1 d^3 e'_x}{3W1^2 e_x}$ = 997,15 N/m (1)

Matrix layer resistance from the second formula;

$F_{ext}=\frac{\mu_2 w1 e'_x}{\pi e_x}$ = 91,85 N/m (2)

In all of the dynamic analysis of ptygmatic folds results were given in tables (Table 1).

Table 1. Dynamic analysis results of ptygmatic folds.

Fold number	Competent layer resistance (F_{int}-N/m)	Matrix resistance (F_{ext}-N/m)	First length (cm)	Final length (cm)
1	997,15	91,85	101	25
2	2368,67	98,73	340	90
3	524,47	33,88	171	37
4	243,34	38,66	50	17
5	165,85	27,60	128	32

Total resistance forces and first and last aspect ratios were compared. As seen in Table 2, the first-to-last aspect ratios vary between 2.94-4.62, while the total resistance force varies between 193.55 and 2467.40 (Fig. 8, Fig. 9).

Table 2. Total residence forces and length rates.

Fold number	Ftot=Fint/Fext (N/m)	l0/l1
1	1089,00	4,04
2	2467,40	3,78
3	558,33	4,62
4	281,74	2,94
5	193,55	4,00

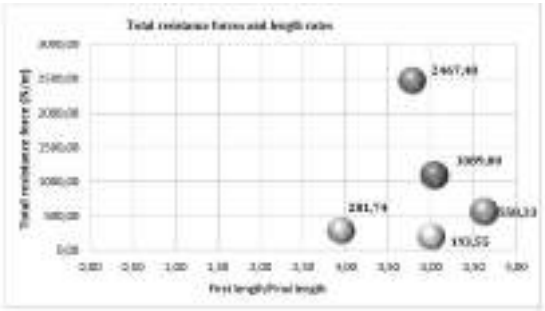

Fig. 8. The graphic of the total resistance forces and length rates of folds.

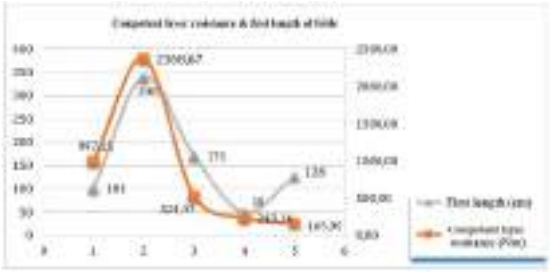

Fig. 9. The graphic of the compotent layer resistance and first length of folds.

3. RESULTS AND CONCLUSIONS

Descriptive analysis was performed on small-scale folds, dynamic analysis was performed on small-scale ptygmatic folds in the region. Descriptive analysis results of folds in the region; according to aspect ratio broad, according to tightness of folding parameter close, according to bluntness of folds parameters subangular, according to Fleuty's classification semi-tight, according to geometric asymetric and localy recumbent fold, according to morphology similar and according to isogonal classification 1B parallel fold classification.

In all of the studies, it was calculated that, the first layer length of the ptygmatic folds and the resistance of the competent layer were directly proportional in the same lithologies. First length and the final length of fold ratio was found approximately 4. As a result of this finding, the contribution of the matrix resistance to folding is more effective than resistance of the competent layer. It is thought that the shortening of the fold lengths might be independent of internal force.

When all the results were evaluated together, according to the results of the dynamic analysis, there was no significant change in the first-to-last aspect ratios of the ptygmatic folds formed in the region, but changes in

the total resistance force from 193,55 to 2367.40 N / m were observed.

It has been determined that the first layer lengths of the folds and the effective layer resistance force applied will vary in direct proportion to each other for the same lithologies.

Similar values were found in the last 3 bends in the matrix resistance force, while the first values yielded higher results.

Despite the differences in the effective forces applied to the folds, a 4-fold difference was found between the first and last aspect ratios. For this reason, it is thought that the contribution of matrix resistance force to folding from the resistance forces forming the ptygmatic fold is more than the effective force and the shortening of the fold lengths may be independent of the effective force

REFERENCES

Carreras, J., Druguet, E., Griera, A., (2004). Shear zone-related folds. *Journal of Structural Geology,* Vol. 27 (2005), pp. 1229-1251.

Demirtaşlı, E., (1984). Stratigraphy and tectonics of the area between Silifke and Anamur, Central Taurus Mountains. *Geology of the Taurus Belt International Symposium*, pp. 101-108, Ankara.

Falalaev, G. N., (2010). Rock creep degree assessment. *Journal of Mining Science,* Vol. 46, No.1.

Fleuty, M. J., (1964). The description of folds. *Proc. Geol. Assoc.* Vol. 75, pp. 461-492.

Huddleston, P.J., (1973). Fold morphology and some geometrical implications of theories of fold development. *Tectonophysics*, Vol. 16, pp. 1-46.

Koç, H. (2003). Aydıncık (İçel) yöresinin tektono-stratigrafisi ve jeolojik evrimi. Doktora thesis, Çukurova University, Adana.

Koç, H., Ünlügenç, U.C. Özer, E. (2005). Tectono-Stratigraphical Investigation of an Area Between Aydıncık-Bozyazı (Mersin), Central Taurus, Turkey, *Türkiye Jeoloji Bülteni*, Vol. 48, No. 1, pp. 1-26.

Özgül, N., (1976). Toroslar'ın Temel Jeolojik Özellikleri. *Türkiye Jeoloji Kurultayı Bülteni*, Vol.19, pp. 65-68, Ankara.

Ramsay, J.G., (1967). *Folding and fracturing of rocks*. New York: McGraw-HillBook.

Ramsay, G.R., Huber, M., (1987). *The tecniques of modern structural geology Vol. 2: fold and fractures.* London: Academic Press Inc.

Some useful numbers on the engineering properties of materials (geologic and otherwise)., https://www.jsg.utexas.edu/tyzhu/files/Some-Useful-Numbers.pdf [Accessed 21 May 2019].

Twiss, R.J., Moores, E.M., (1973). *Structural geology*. New York: W. H. Freemanand Company.

CISET - 2nd Cilicia International Symposium on Engineering and Technology 10-12 October, 2019, Mersin / TURKEY

ALUMINUM BRAKE CAR PEDAL DESIGN, PRODUCTION AND TESTING

Necdet Yusuf TOKSÖZ *[1], Ahmet Erdem ÖNER*[2]

[1]Toyotetsu Otomotiv Parçaları San. ve Tic. A.Ş., Kocaeli, Turkey
(toksozy@toyotetsu.com.tr)
[2]Toyotetsu Otomotiv Parçaları San. ve Tic. A.Ş., Kocaeli, Turkey
(onera@toyotetsu.com.tr)

ABSTRACT
The carbon emission reduction in the automotive sector and the demand for vehicles consuming less fuel and 100% electric vehicles accelerated the vehicle lightening works in the automotive sector. The automotive industry has started researching and using materials that will pass the lighter but also required strength tests successfully. In this context, aluminum is one of the most used materials. Aluminum, which is approximately 1/3 of light weight more than steel (Al: 2.73 g / cm³, Steel: 7.85 g / cm³), comes to steel level as a result of the material studies. For this reason, the automotive industry manufacturers have started to studies in the field of automotive parts made of aluminum material. Normally, the brake pedals thickness 8 mm solid sheet materials are used in production.When the pedal is designed according to its position in the vehicle, the pedal used in the study is 774 gr. In this study, the application techniques of aluminum materials which are increasing in automotive sector in the pedal part have been examined and aluminum pedal has been redesigned .The aim was to reduce the weight of the aluminum pedal to 35-50% compared to the steel pedal and the design was analyzed in the Ansys program and the optimum value was achieved and the ideal design was produced. In order to apply fatigue tests to the produced aluminum pedal, the Pedal Tester which in our R & D Center was used and the produced pedal was tested for 1,000,000 cycles. As a result of the project, a lighter aluminum brake pedal has been designed, prototype product has been produced which fulfills the expected function, meets the relevant standards, and a quality product has been produced by performing the required quality tests.

Keywords: *Aluminum Pedal, Pedal Tester, Pedal Fatigue Test, Car, Pedal MIG Welding, Pedal ANSYS Analyze*

1. INTRODUCTION

The search for alternative materials within the vehicle lightening is an area that the automotive sector needs to advance with the developing technology in recent years. In this direction, the mechanical tests of the brake pedal to be made of aluminum material which can replace the brake pedal which is produced from steel material considering the safety risk in the current situation of the vehicles have been the subject of this project.

With this study, it was desired to experience the pedal of aluminum material production. The aim of the project is to the pedal part produced so far from steel; to re-design according to the desired strength values, to make engineering and mechanical analysis, material selection using a new generation of aluminum series to meet the desired mechanical and test standards to make the prototype of the pedal part, to perform tests.

2. METHOD

2.1. Aluminum Brake Pedal CAD Design

Design criteria has been determined according to producing pedal by Toyotetsu-Turkey. The design of the aluminum brake pedal is based on the steel brake pedal design as shown in Figure 1.

Figure-1 Designed Brake Pedal

The steel pedal used in the mass production shown in gray and the newly designed aluminum pedal shown in yellow as seen at the figure-1

2.2. Aluminum Brake Pedal Ansys Fatigue Test

Fatigue analysis of the aluminum brake pedal, which was completed in the design phase, was performed in Ansys program as shown in Figure 2.

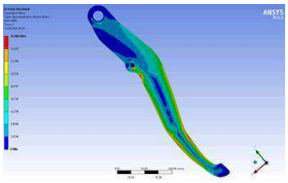

Figure 2: Analyze Works

The load value used in the analysis using Ansys program was determined as 500N which is exposed to in real environment and 5083 series Aluminum material was selected as the material. As a result of the analysis, it was found that 10 mm thick aluminum pedal was suitable for fatigue analysis under 500N load. The total deformation analysis of the pedal part in Ansys program is shown in Figure 3. As a result of this analysis, the deformation values that the pedal part can show under load remained within safe limits.

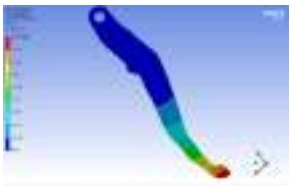

Figure 3: Total Deformation Analysis of the Pedal Parts in Ansys Analysis

2.3. Aluminum Brake Pedal Ansys Lifetime Test

The design, which gave positive results in fatigue analysis, was performed to life test again as shown in Figure 4 in Ansys program.

Şekil 4: Lifetime Test Results on Designed Pedal

Following these tests, has passed the life test in accordance with the relevant standards and regulations is produced with domestic raw materials, it is tested with the test apparatus designed in the Toyotetsu laboratory and the life test results with 1000.000 cycle presses are also verified in real environment. According to the appropriate design in the analysis environment, pedal parts are manufactured in Aluminum. The aluminum pedal arm part was produced at 5083 series 10mm thickness aluminum plate. The other bracket of the pedal, called the "seat", is also determined 5754 series Aluminum materials and welded with MIG welding. In this way, Aluminum pedal prototype was produced.

2.4. Aluminum Pedal MIG Welding

In aluminum pedal production, body and bracket are combined with MIG welding method. CMT welding technique is used in the jointing process. AlMg5 1.0 Aluminum wire was used for 5083 series and 5454 series Aluminum welding joining.100% He gas was chosen as the shielding gas. The welded aluminum pedal is shown in figure-5

Figure-5

2.5. Pedal Test Assembly Design and Production for Life Test

After the aluminum pedal was produced, the analyzes performed at Ansys. The analyzes were also performed in

the laboratory and the results of the analysis were verified. A pedal test equipment for pedal fatigue tester is shown in Figure 5.

Figure 5: Pedal Fatigue Tester

In the pedal tester shown in Figure 5, 250.000, 500.000,750.000 and 1.000.000 cycle tests were performed for aluminum pedal under the 500N load. The results of the simulation program were confirmed by laboratory tests and after 1.000.000 cycle test was acceptable. Surface cracks that may occur on the surface of the material were examined by applying liquid penetrant test to the pedal part produced during these periods and no problems were encountered. The penetration test results are shown in Figure 6.

Figure 6: Penetration Test Undestructive Test Pedal

3. RESULTS

In the first phase of the project, the subject of aluminum pedals, which are not found in the literature, was researched in line with the literature studies, design studies were made for aluminum material and prototype pedals were produced. The life cycle tests of the new aluminum pedal were performed and acceptable results were obtained. Table 1 shows the weight gain obtained by the aluminum pedal.

Table 1 Comparison of the weight gain of pedal part

Pedal	**Weight (g)**		Material	Total Weight (g)
	Arm	**Pad**		
Al.	388 g	11 g	Arm;5083 Pad; 5454 Aluminum	399 g
Steel	741 g	33 g	SPH440-OD Steel	774 g

4. CONCLUSION

The use of aluminum pedals in automotive is a unique issue that not encountered in literature studies. With this study, pedal weight gain approximately %50 decreased, lighter result in a reduction in fuel economy and a relatively reduced CO2 gas emission. This result is an indication that there will be a very important economic development with our aim in the article.

5. REFERENCE LIST

HIRSCH, J., (2014). 'Recent development in aluminium for automotive applications'. Hydro Aluminium Rolled Products GmbH, R&D Bonn, Germany.

https://www.assanaluminyum.com/~/media/files/arge/yayinlar/p3.ashx?la=tr-tr(Accessed:29.08.2019)
DÜNDAR, M., GÜNGÖR, G. 'Otomotiv Sektöründe Alüminyum Uygulamaları Ve Sürekli Döküm Tekniği İle Üretilmiş Alüminyum Levha Alaşımları'.

www.Standardandpoors.Com/Ratıngsdirect (Accessed: 29.08.2019) Global Auto Industry 2018: At A Crossroad, October, 2017.

ALBAK, E., İ., (2019). 'Optimum Design of Brake Pedal Using Topology Optimization Method Intended for Weight Reduction On the Formula SAE Car', Bursa Uludağ Üniversitesi, Mühendislik Fakültesi, Otomotiv Mühendisliği Bölümü, Bursa.

FIBER PRODUCTION FROM PLA/PU BLENDS BY ELECTROSPINNING AND CHARACTERIZATION OF FIBERS

Sema Samatya Yılmaz*[1] and Ayşe Aytaç [1,2]

[1] Kocaeli University, Institute of Science, Polymer Science and Technology Department, Kocaeli, Turkey, sema.samatya@gmail.com

[2] Kocaeli University, Engineering Faculty, Chemical Engineering Department, Kocaeli, Turkey, aaytac@gmail.com

ABSTRACT

One of the most widely used biodegradable polymers among renewable materials is poly (lactic acid) (PLA). PLA has high strength and high modulus values. But, its low toughness limits some industrial application area. Polyurethanes (PU) are known as highly elastic, blood and tissue compatible polymers and are among the leading synthetic polymers used in the medical field. PLA/PU polymer blend is prepared to balance stiffness and toughness between these two polymers. Thus, a single structure with the desired properties will be obtained. The most effective technique for nanofiber production is "Electrospinning". In the previous studies, PU/PLA blends were prepared by different methods (such as extrusion, solution casting), but there is no study in the literature to obtain the fiber of PU/PLA blend by electrospinning. It is thought that thanks to PU/PLA nanofiber, thinner and more flexible biodegradable surfaces with good physical and mechanical properties can be obtained and these surfaces can be used in the medical field. In this study, 80%, 60%, 50% solutions of polyurethane/poly(lactic acid) blend were prepared in suitable solvent medium and fiber was obtained by electrospinning method. The obtained fibers were characterized by polarized optical microscope (POM), Fourier-Transform Infrared Spectroscopy (FTIR), Thermogravimetric analysis (TGA), and contact angle tests. It was observed that the smooth uniform and homogeneous fiber distribution for 5PLA5PU sample in POM images. Besides, the hydrophobic surface structure was observed generally for all prepared fibers.

Keywords: *Poly(lactic acid)/Polyurethane blends, Nanofiber, Electrospinning, PLA/PU fiber*

* Sema Samatya Yılmaz

1. INTRODUCTION

Nanotechnology has begun to show interest in renewable materials as raw materials for the production of value-added products due to the increasing global energy demand in environmental and energy research. The fiber diameter of nanofibers at the nanometer level increases the surface/volume ratio of the material and the mechanical properties of the fibers (*Kiper, 2018*). The most efficient method for the production of polymer-based nanofibers is electrospinning. The electrospinning is a multidisciplinary method that includes fluid dynamics, polymer chemistry, basic physics, electrical physics, mechanical and textile engineering disciplines.

Among the most widely used renewable materials, Poly (lactic acid) (PLA) is considered to be the strongest potential candidate for the replacement of petroleum-based polymers due to its environmentally friendly properties such as biodegradability, biocompatibility and renewability. The fact that they can be obtained in medical purity, having adjustable physical and mechanical properties and easily adapting to a biological environment increased the use of polyurethanes for biomedical purposes. PLA/TPU polymer blend is made to balance stiffness and toughness.

It is seen that polyester/polyether or polyol based thermoplastic polyurethanes are preferred in studies to toughen PLA. The most important reason for this; PLA is partially compatible with the polyester or polyether group forming the PU soft segment (*Feng et al 2011; Hong et al., 2011; Li et al., 2007; Nijenhuis et al., 1996; Anderson et al., 2003, Piorkowska et al., 2006*). To balance the stiffness and toughness, there are few studies on the production of PLA/PU polymer blends and few studies on the various uses of the products obtained. Yuan and Ruckenstein aimed to toughen PLA with 5% by weight poly(epsilon-caprolactone) (PCL) diol and triol terminated PU. The crosslink density was thought to be related to the diol/triol ratio in the PU structure. Maximum PLA strength was obtained with PU blend with diol/triol=1/9 (*Yuan et al., 1998*). Li and Shimuzi studied that the toughness of PLA/Poly(ether)urethane blends. They found that increases in % elongation and impact strength by increasing the TPU composition in the blend for the TPU elastomer toughening PLA blend (*Li et al., 2007*). Hong et al. examined miscibility with PLA/TPU blends in varying ratios. In the study, it was shown that the components were partially compatible as a result of dislocation the glass transition temperature of the blend (*Hong et al., 2011*). In the Han and Huang study, izod impact test and tensile tests of PLA/TPU blends prepared by melt blending method showed that toughness properties of PLA based blend improved by adding TPU to the mixture (*Han et al., 2011*). Feng et al. reported that the addition of TPU based on the length formed during the deformation in the tensile test, the PLA based mixture shifted from brittle to the ductile structure. Micromechanical analysis to evaluate the toughness of mixtures showed that crack initiation resistance and crack propagation resistance were increased in toughened mixtures (*Feng et al., 2011*). The polymer blend nanocomposites based on thermoplastic polyurethane (PU), polylactide (PLA) and surface-modified carbon nanotubes were prepared by melt mixing and investigated these structures for their mechanical, dynamic mechanical and electroactive shape memory properties. (*Raja et al., 2013*). Sethi et al. aimed to prepared and characterized a cellulose nanocrystalline reinforced semi-interpenetrated network (SIPN) derived from polylactic acid (PLA) and polyurethane (PU) polymers. SIPN films were prepared using solvent casting from 1,4-dioxane solution. The increase in thermomechanical properties indicates that the reinforced PU network in the PLA matrix can increase the thermal behavior of the material (*Sethi et al., 2017*).

In this study, it was aimed to obtain nonwoven surface fiber tissue by electrospinning method which is one of the production methods provided by nanotechnology. In the previous studies, the PU/PLA blend was prepared by the traditional production methods in surface production, but there is no study in the literature to obtain the fiber of PU/PLA blend by electrospinning.

2. MATERIAL AND METHOD

2.1. Materials

The studies started with the selection of the appropriate solvent which should be used for the dissolution of both polymers separately. In the literature, the solvent of PU is Dimethylformamide (DMF) or tetrahydrofuran (THF), and the solvent of PLA is chloroform or THF. Although THF is considered to be a common solvent, it is not suitable for use in biomedical and healthcare. Therefore, since DMF and chloroform solvents are compatible with biomedical applications, it was decided to start studies on these solvents. It was not found in the literature that the PLA solution was prepared with 100% DMF. Dimethylformamide was obtained from Merck.

Since it is known that DMF is a solvent for PU in accordance with the information in the literature, firstly, literature researches have been made to determine the type of PLA that can be solved in DMF and compatible with biomedical studies. Then, it was decided to use the poly (lactic) acid type which can be used in electrospinning method which is compatible with literature. PLA was found to be soluble with 100% DMF. Poly (lactic) acid commercially available as 4043D, was obtained from NatureWorks.

After decided on the type of PLA, a literature search was conducted to determine the type of PU. When choosing the polyurethane to be used in the study, attention was paid to be biocompatible, harmless to human body and FDA approved. In this way, Polyurethane type has been selected to meet the expectations. Estane® GP52DTNAT055 was selected as aromatic polyether-based thermoplastic polyurethane. It was obtained from Lubrizol (Velox).

The PLA and PU polymers were separately dissolved in 100% DMF. However, the fiber could not be obtained by electrospinning with this solution. It was decided to use chloroform. Chloroform/DMF mixed solvent was used in the study. Chloroform was also obtained from Merck.

No information has been found in the literature regarding the dissolution of polyurethane polymer in Chloroform. Therefore, experimental studies were carried out to determine the proportions of solvents (Chloroform/DMF) in solution. For PLA and PU, the most homogeneous dissolution rate and the solvent ratio

that provides fiber formation were determined separately. Thus, a suitable solvent ratio for the PLA/PU blend was also found.

In the studies, 8mL Chloroform/2mL DMF solvent ratio was used for raw PU, raw PLA and PU/PLA blends. Then solutions with a concentration of 10% were prepared.

2.2. Method

Electrospinning method was selected for preparation nanofiber production. A simple electrospinning device is shown in Fig 1. Electrospinning system; It is a visibly open system consisting of a feed pump, syringe, needle tip (nozzle head) and power supply:

1. High voltage (power supply),
2. Feeding unit (syringe, polymer solution, spinneret),
3. Collector (conductor plate, rotary cylinder etc.).

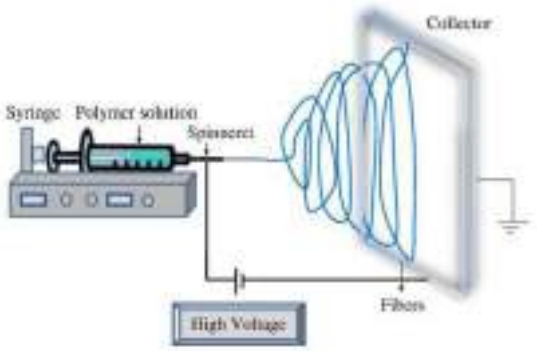

Fig. 1. Electrospinning method

The operating principle of this technique is explained easily as follows. The polymer is dissolved in a suitable solvent or heat melted, placed in a glass pipette or syringe with a small hole in the end. A voltage of up to 50 kV is then applied between the polymer solution or polymer melting and a collector plate opposite the open end of the pipette. Meanwhile, the taylor cone is formed by the effect of the force applied while the polymer is in the form of a droplet at the needle tip. The polymer at the needle tip becomes thinner and becomes conical. Then, when the applied voltage overcomes the surface tension of the polymer, whipping instability occurs, the fibers begin to accumulate in the collector.

To obtain fiber by this method, it is necessary to provide the appropriate conditions. Solution parameters process variables and environmental conditions are effective parameters in electrospinning. These parameters were examined one by one in our electrospinning studies to create fiber.

2.2.1. Solution preparation

PU, PLA and PU / PLA blends were prepared in 5 different solutions for studies. PLA and PU granules were dried in an oven at 80°C for 12 hours and then were used for solution preparation.

1 g of PLA and 1 gr PU was dissolved separately in 8 mL of Chloroform / 2 mL of DMF solution with the mouth of the beaker covered with aluminium foil covering parafilm and stirring at room temperature for 4 hours. The prepared 10% concentration of PLA solution was completely homogeneously dissolved and then it was used at the electrospinning.

The PU swelled considerably in the solvent and became almost non-solvent. Afterwards, a few experiments were carried out to determine that the suitable temperature for the dissolution was 120 °C. After stirring at room temperature for 4 hours, the PU solution was stirred at 120 ° C for 30 minutes with the mouth closed again. Thus, a completely homogeneous dissolution process was obtained. The prepared 10% PU solution was completely homogeneously dissolved and then used in electrospinning.

For the preparation of PU/PLA blends, 80%, 60%, 50% ratios were determined. After two treatments, it was decided how to make the mixtures. The first process was dissolved in raw PU and raw PLA then mixed. In the second process, PU and PLA were simultaneously dissolved in a single beaker at determined rates. Electrospinning was performed after both treatments. To evaluate fiber formation, surface images of the obtained fibers after both processes were examined. It was observed that the fibers were bead-free on the surface having the same diameters on average. In the last step, it was observed that the increased temperature had no negative effect on the fiber formation of PLA polymer. In this way, it was decided to continue the studies by dissolving PU and PLA polymers together at one time.

PU/PLA studies were mixed at room temperature by first covering the mouth of the beaker over aluminium foil until the PLA was dissolved. It took 3 hours on average. The solution was then stirred at room temperature for a further 1 hour to swell the PU polymer in the mixture thoroughly. The PU polymer was then dissolved at 120 °C for 30 minutes. Thus, a homogeneous mixture which is completely dissolved in PU/PLA blend solutions was obtained. The prepared solutions and their codes are shown in Table 1. The prepared 10% PU/PLA solutions were completely homogeneously dissolved and then used for the electrospinning.

Table 1. Codes of studied samples

Sample Code	PU (gr)	PLA (gr)	Blend Ratios (%)
Raw PU	1	-	-
Raw PLA	-	1	-
8PU2PLA	0.8	0.2	80
6PU4PLA	0.6	0.4	60
5PU5PLA	0.5	0.5	50

The conductivity of the solvents was measured with a liquid conductivity meter at room temperature (24°C). It was determined as 0.4 µS / cm for DMF and 0.0 µS / cm for Chloroform.

2.2.2. Electrospinning Treatment

The prepared solutions were used in electrospinning without waiting. Electrospinning was performed primarily for raw PLA and raw PU. Process conditions were determined as 0.5 mL/h feed rate, 20 cm distance and 15 kV applied voltage. Each of the PU/PLA blended solutions showed electrospinning ability under the same process conditions. Process conditions were determined

as 0.5 mL / h feed rate, 20 cm distance and 18 kV applied voltage. The codes of the fibers were worked in the same way as those of the solutions.

In the electrospinning process, a blunt needle tip with a diameter of 0.91mm (20G gauge/inch) was used which was suitable for 10% solution concentration. When environmental conditions were evaluated, the studies were carried out at room temperature and relative humidity of 65%.

The electrospinning device used in the studies is shown in Fig 2. Also, Fig 3 shows the image of the fiber obtained by the electrospinning device. Furthermore, in Fig 4, the fiber obtained from raw PU was removed from aluminium foil and taken into hand and its flexibility was observed.

Fig. 2. Elektrospinning device used in studies

Fig. 3. Formed fiber surface image

Fig. 4. Fiber flexibility of raw thermoplastic polyurethane polymer (TPU)

3. DISCUSSION

Characterization tests were performed to evaluate the structure of the obtained fibers.

3.1. Surface Appearance of Obtained Fibers by Polarized Optical Microscope (POM)

In this study, the surface images of the fibers obtained were visualized with Nikon Eclipse LV100 POL brand POM device. It is the most important analyzer that can be easily used to have an idea of fiber formation. Surface images of the studied fibers are given in Fig 5.

It has been observed that raw PLA and raw PU are solved in suitable solvent medium and bead-free fiber extraction is achieved with appropriate electrospinning conditions. Fiber fineness is thought to be close to each other. After this analysis, it was decided to make PU/PLA blends. Because, the fiber formation process, which forms the basis of our studies, has been completed and it has been seen that fiber can be formed.

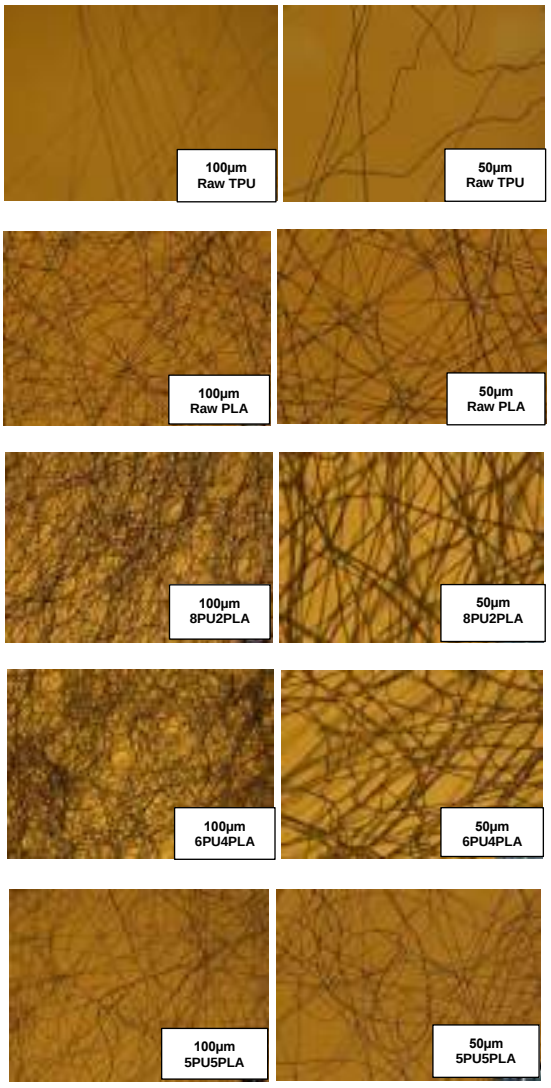

Fig. 5. POM surface images of raw PLA, raw PU and different ratios of PU/PLA fibers

When the fibers obtained from PLA/PU different ratio blend solutions were compared, it was observed that all fibers were bead-free. However, considering the fiber fineness fiber smoothness fiber distribution homogeneity, the finest smooth fibers appear to be coded 5PU5PLA. There is an equal amount of PLA and PU in the solution of this fiber.

3.2. Fourier Transform Infrared Spectroscopy (FTIR)

Chemical structure of raw PLA, raw PU and PLA/PU blend nanofibers was determined by the FTIR-ATR spectrometric measurements. The FTIR-ATR spectrum of the nanofibers was given in Fig 6. FTIR analyses of the samples were performed to determine the possible interactions between the components of the bonds and mixtures in the structure of the polymers. IR spectra in the range of 500-4000 cm-1 were taken during the analysis. Perkin Elmer Spectrum 100 FTIR device with ATR unit was used in the study.

Characteristic peaks of PLA; 2957 cm^{-1} ($–CH_2$ tensile vibration), 1748 cm^{-1} (C = 0 tensile vibration), 1445 cm^{-1} (OH bending vibration), 1220-1185 cm^{-1} and 1086 cm^{-1} (-O strain vibration) were determined (*Wu et al., 2005; Gu et al., 2008*).

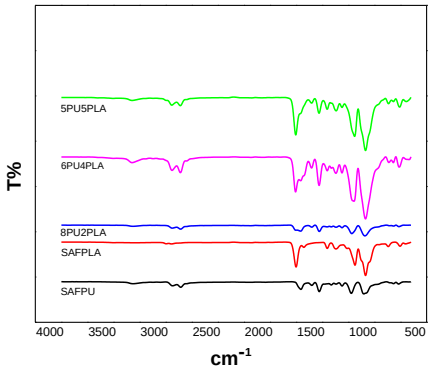

Fig. 6. FTIR Spectrum of raw PLA, raw PU and PU/PLA blends

The characteristic peak of PU is 1600 cm^{-1} and belongs to aromatic C = C group vibrations. In raw PU and PLA/PU blends, the peak of 1600 cm^{-1} is clearly seen. In raw PLA, this peak is not observed. It showed that belongs to vibrations (N-H)+(C-N) at 1530 cm^{-1} peak; to CH_2 at 1452 cm^{-1} peak ; to CH_2 at 1366 cm^{-1} peak; and to vibrations (N-H)+(C-N)+(C-H) at 1311 cm^{-1} peak; to the carbonyl group C-O-C group vibrations at 1260 cm^{-1} peak and to C-O-C vibrations at 1088 cm^{-1} peak. The peaks seen in the PU nanofiber and blends of PU/PLA belong to N-H group vibrations at 3318 cm^{-1} peak; to CH tensile vibration at 2932 cm^{-1} peak and to C = O stress vibrations at 1704-1753 cm^{-1} peaks (*Pradhan., 2012*).

The decrease in the peak of 3330 cm^{-1} was seen in all nanofiber FTIR spectrum can be interpreted as decreasing the number of hydrogen bonds formed between the hard and soft parts of the urethane phase mixture. The 869 cm^{-1} peak of DMF solvent belongs to C-N symmetrical stress (*Saafan., 2006*) and 754-761 cm^{-1} peaks of Chloroform solvent belong CCl_3 d-tensile peak *(URL_1)*.

According to the results, it is seen that DMF and chloroform solvents are removed as much as possible from the structure of the fibers by electrospinning. This shows that our studies are progressing in a positive direction. Because, no matter how far the solvents go away from the structure, it can be foreseen that the successful results can be achieved with the fibers that we will use as raw materials afterwards.

3.3. Thermogravimetric Analysis (TGA)

Thermogravimetric analysis of the fibers was carried out with Metler Toledo TGA 1, in the range of 25°C to 600°C, with a heating rate of 10°C/min. During the measurements, high purity nitrogen gas was fed to the system at a flow rate of 50 ml/min. TGA decomposition curves of raw PLA, raw PU and PLA/PU blended fibers are shown in Fig. 7. To make a complete comparison, initially examine the decomposition curves of Raw PU and Raw PLA which we can take as reference.

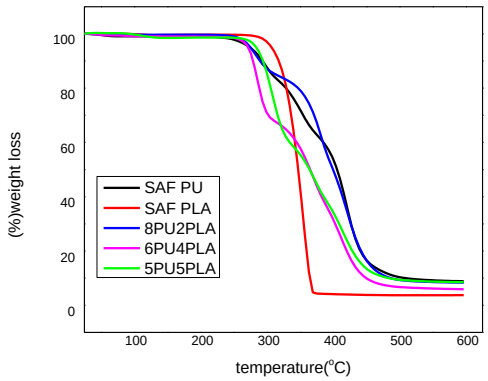

Fig. 7. TGA decomposition curves of Raw PLA, Raw PU, PU/PLA Fibers

Raw PU maintained 95% by weight of up to 274°C and 90% by weight of up to 293°C. The temperature at which thermal decomposition began was found to be about 361°C. T_{endset} value was determined as 446°C, the decomposition continued to 599.83°C and 8.82% residue was observed to finish the process at this temperature.

The temperature at which raw PLA retains 95% by weight is 307°C and at 317°C at 90% by weight. According to the analysis, the temperature at which PLA began to decompose was 327°C. Decomposition lasted for 560.83°C and ended with 3.71% residue. T_{endset} value was observed as 366°C. TGA decomposition values of all fibers are given in table 2.

When the PLA/PU blends are examined, it is seen that the 8PU2PLA coded nanofiber is closest to the raw PU decomposition curve. With the addition of PU to the structure of other nanofibers, it is observed that the initial weight conservation temperatures begin to drop and that the decomposition temperatures follow a temperature below the decomposition temperature of PLA compared to that of raw PLA.

It was observed that the sample coded 5PLA5PU, which had a smooth uniform and homogeneous fiber distribution in POM and showed a curve at the average values of both raw PLA and raw PU temperatures in TGA.

Table 2. TGA decomposition values of Raw PLA, Raw PU, PU/PLA fibers

Sample Codes	Tonset (ºC)	Tendset (ºC)	Tmax (ºC)	Residue 600ºC (%wt)
Raw PLA	327.12	366.30	354.65	8.82
Raw PU	361.07	466.74	420.08	3.71
8PU2PLA	343.10	451.86	381.49	8.31
6PU4PLA	272.44	351.94	285.87	5.88
5PU5PLA	288.08	376.50	308.10	8.51

3.4 Surface characterization of obtained fibers by contact angle method

Surface water affinity properties of pure PU, Pure PLA and PLA / PU blend fibers were determined by water contact angle measurements.

Wettability properties of prepared PLA/PU fibers were determined by using the Hanging Droplet method with the Attension Theta Lite device at room temperature (20˚C ± 2˚C). Water droplets in the amount of 10µl were dropped onto the surface and measurements were taken at 5 different points for each fiber surface and the average values were reported.

The Attension Theta Lite Device and the Stable Droplet Method Image were shown in Fig. 8 and the contact angles on the surfaces were given in Fig. 9.

Fig. 8. Attension theta lite device and static droplet method image

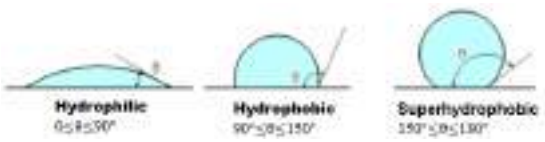

Fig. 9. Contact angle on surfaces (*Bağçeci, 2010*)

Fig. 10 shows the state of water retention for 9 seconds. When we examined the water retention ability of raw PLA, raw PU and PLA/PU fibers for 9 seconds, it was seen to have a stable path. Averages of ± 3 angle value changes of 9sec time were taken from 5 different points of each fiber. According to the comparative graph of raw PU, raw PLA and PLA/PU fibers, it is hydrophobic when it is between 90°≤θ≤150° angle. Raw PLA, raw PU and 8PU2PLA have a hydrophobic surface structure with an average angle of 120°. It was observed that the 5PLA5PU sample at 90º angle and the 6PU4PLA sample at 100º angle exhibited hydrophobic properties.

When the other PLA/PU blend was examined, it was observed that the contact angle of the blends was lower than the contact angle values of raw PLA and raw PU fibers. In the study, the formation of hydrophobic fibers is expected and desirable. In the continuation of the study, usability will be investigated in different fields other than medical applications.

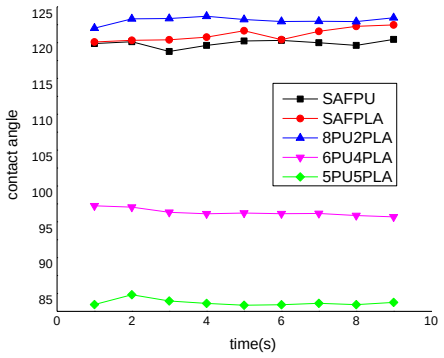

Fig. 10. Comparison of water retention capability of fibers for 9s

4. CONCLUSION

The fibers from PU/PLA blends were prepared by electrospinning in this study. Solutions were prepared to take into account the dissolution properties of both polymers. The 8mL Chloroform/2mL DMF solvent ratio was the most important part of my work. Because the process of fiber formation became clear with the proportions of these solvents. PLA was homogeneously dissolved when the temperature was increased with 100%DMF. This solution may not form fibers by electrospinning, but in other applications (such as film, coating) it is believed that the PLA solution dissolved in 100% DMF can yield efficient results.

Another result of the studies is chloroform which increases the fiber formation properties for PLA and PU. Because DMF solvent has a low conductivity value. However, the chloroform solvent has no conductivity value. In this way, it is easier to overcome the surface tension with the applied tension for a polymer solution with low surface tension in the electrospinning method, thus providing regular fiber formation.

It was observed that the smooth uniform and homogeneous fiber distribution for sample coded 5PLA5PU in POM. A curve at the average values of both raw PLA and raw PU temperatures in TGA was obtained for this sample. According to contact angle measurements, the hydrophobic surface structure was observed for all prepared fibers.

It is thought that PLA surfaces used in biomedical application fields, tissue engineering and academic studies in the world will find a wide range of usage of fiber surface obtained with PLA/PU blend by electrospinning production technique.

REFERENCES

Anderson K. S., Lim S. H., Hillmyer M. A., (2003). Toughening of polylactide by melt blending with linear low-density polyethylene, *J. Appl. Polym. Sci*., 89, 3757–3768.

Bağçeci B. İ., (2010). "Nano Particle Surface Coating", Gazi University, Institute of Science and Technology, *Master Thesis*, Ankara, 269938.

Feng F., Ye L., (2011). Morphologies and mechanical properties of polylactide/thermoplastic polyurethane elastomer blends, *J. Appl. Polym. Sci.,* 119, 2778–2783.

Gu S. Y., Yang M., Yu T., Ren T. B., Ren J., (2008). Synthesis and characterization of biodegradable lactic acid-based polymers by chain extension, *Polym. Int.,* 57, 982–986.

Han J. J., Huang H. X., (2011). Preparation and Characterization of biodegradable polylactide/thermoplastic polyurethane elastomer blends, *J. Appl. Polym. Sci*., 120, 3217–3223.

Hong H., Wei J., Yuan Y., Chen F.-P., Wang J., Qu X., Liu C. S., (2011). A novel composite coupled hardness with flexibleness polylactic acid toughen with thermoplastic polyurethane, *J. Appl. Polym. Sci*.,121, 855–861.

Kiper, A.G., (2018). "Obtaining Nanofiber from Natural Cellulose by Electrospinning Method", Istanbul Technical University, Institute of Science and Technology, *Master's Thesis*, Istanbul.

Li Y., Shimizu H., (2007). Toughening of polylactide by melt blending with a biodegradable poly(ether)urethane elastomer, *Macromol. Biosci*., 7, 921–928.

Mohan Raja 1, Sung Hun Ryu, A.M. Shanmugharaj, (2013). Thermal, mechanical and electroactive shape memory properties of polyurethane (PU)/poly (lactic acid) (PLA)/CNT nanocomposites, *European Polymer Journal*, 49,3492–3500

Nijenhuis A., Colstee J. E., Grijpma D. W., Pennings A. J., (1996). High molecular weight poly(L-lactide) and poly(ethylene oxide) blends: thermal characterization and physical properties, *Polymer*, 37, 5849.

Piorkorwska E., Kulinski Z., Galeski A., Masirek-R., (2006). Plasticization of semicrystalline poly(L-lactide) with poly(propylene glycol), *Polymer*, 47, 7178-7188.

Pradhan, K.C., Nayak, P.L., (2012). Synthesis and Characterization of Polyurethane Nanocomposite from Castor Oil- Hexamethylene Diisocyanate (HMDI), Pelagia Research Library, 3(5), 3045-3052.

Sethi J., lllikainen M., Sain M., Oksman K., (2017). Polylactic acid/polyurethane blend reinforced with cellulose nanocrystals with semi-interpenetrating polymer network (S-IPN) structure, *European Polymer Journal Volume,* 86, Pages 188-199

Saafan SA, El-Nimr MK, El-Ghazzawy EH, (2006). Study of Dielectric Properties of Polypyrrole Prepared using Two Different Oxidizing Agents, *Journal of Applied Polymer Science*, 99:3370-3379.

URL_1,*http://vpl.astro.washington.edu/spectra/chcl3.htm*, 28.08.2019

Wu C. S., Liao H. T., (2005). A new biodegradable blends prepared from polylactide and hyaluronic acid, *Polymer*, 46, 10017–10026.

Yuan Y., Ruckenstein E., (1998). Polyurethane toughened polylactide, *Polym. Bull*., 40, 485–490.

CISET - 2nd Cilicia International Symposium on Engineering and Technology
10-12 October, 2019, Mersin / TURKEY

SYNTHESIS AND CHARACTERIZATION OF (BIMETALLIC IRON-ZINC NANOPARTICLES)/CARBON COMPOSITE MATERIAL FOR NAPTHOL BLUE BLACK DECOLORISATION BY HETEROGENEOUS FENTON-LIKE REACTION

Ege Karadeniz [1], Deniz Uzunoğlu [*2] and Ayla Özer [3]

[1] Mersin University, Engineering Faculty, Department of Chemical Engineering, Mersin, Turkey, egekaradeniz@teknopanel.com.tr

[2] Mersin University, Engineering Faculty, Department of Chemical Engineering, Mersin, Turkey, denizuzunoglu4@gmail.com

[3] Mersin University, Engineering Faculty, Department of Chemical Engineering, Mersin, Turkey, ayozer@mersin.edu.tr

ABSTRACT
In this work, the synthesis and characterization of [(Fe-Zn NPs)/C] were carried out and then it was evaluated as a heterogeneous catalyst in the Fenton-like reaction of NBB. The characterization studies showed that the synthesized composite material had amorphous structure and it contained C, O, Fe, and Zn elements. Also, it was observed by SEM analysis that iron-zinc nanoparticles (Fe-Zn NPs) formed between the carbon microspheres indicating the hydrochar structure. The Fenton-like decolorisation ability of [(Fe-Zn NPs)/C] was also evaluated and the results demonstrated that [(Fe-Zn NPs)/C] could be a promising Fenton-like catalyst for the decolorisation of NBB dyestuff from aqueous solutions. The optimum experimental conditions of this Fenton-like reaction were determined to be 3.0 of initial pH, 50 mM of H_2O_2 concentration, 40 ºC of temperature, 700 mg/L of initial dyestuff concentration, and 0.25 g/L of catalyst concentration.

Keywords: *Composite material, Decolorisation, Fenton-like reaction, Heterogeneous catalyst, Hydrochar, Napthol Blue Black*

[*] denizuzunoglu4@gmail.com

1. INTRODUCTION

The rapid urbanization and industrialization have recently caused a serious environmental concern due to the huge amount of wastewater generation. The paper, textiles, dyeing of cloth, printing, pharmaceutical, and cooking industries generate the large quantities of colored wastewater due to the using dyestuffs (Kumar et. al., 2019). The unrestrained discharge of these colored wastewaters into the receiving waters negatively affects the aquatic life and also human life via nutrient cycle because the dyestuffs are mostly toxic, carcinogenic, mutagenic or allergenic (Tarkwa et al., 2018). Therefore, these types of wastewaters must be treated according to the regulations before the discharging of them. There are many chemical, physical, and biological methods for the removal of dyestuffs from wastewaters. The advanced oxidation processes (AOP) based on the production of free radicals, such as Fenton, photo-Fenton, sono-Fenton processes, ozonation, electrochemical oxidation, photolysis with H_2O_2, and O_3 electro-Fenton, have great importance for the treatment of the wastewaters containing the dyestuffs, which are difficult to remove by conventional methods. In the Fenton processes, high oxidizing agent •OH radicals are used to oxidize the dyestuffs. It provides the degradation of complex structured dyestuffs to smaller organic molecules or the completely oxidization of it to CO_2 and H_2O (Khan et al., 2019). Homogeneous Fenton process, in which soluble iron is the catalyst, has been extensively studied and widely applied commercially for the dyestuff treatment (Gu et al., 2019). However, the difficulty of the homogenous catalyst recovery and tight pH range for reaction are reported as disadvantages (Vu et al., 2019). In order to overcome these disadvantages of the homogeneous Fenton process, some attempts have been made to develop heterogeneous catalysts, especially iron based nanoparticles. The metallic and bimetallic iron nanoparticles can be synthesized by various methods such as chemical precipitation, microemulsion, hydrothermal synthesis, thermal degradation, sonochemical synthesis, and electrochemical deposition (Yavari et al., 2016). In order to improve the catalyst properties of the nanoparticles synthesized by these methods, the nanoparticles can be combined with various carbonaceous materials such as cellulose, glucose, agricultural waste, animal manure, food waste, and so on (Wang et al., 2018). In this respect, (bimetallic iron-zinc nanoparticles)/carbon composite material [(Fe-Zn NPs)/C] was synthesized by combined co-precipitation/hydrothermal carbonization method and then, [(Fe-ZnNPs)/C] was evaluated as a heterogeneous catalyst in the Fenton-like reaction of Napthol Blue Black (NBB) dyestuff.

2. EXPERIMENTAL SECTION

2.1. Synthesis and Characterization of (Bimetallic Iron-Zinc Nanoparticles)/Carbon Composite Material

In the synthesis of (bimetallic iron-zinc nanoparticles)/carbon composite material [(Fe-Zn NPs)/C]; $Fe(NO_3)_3$, $Zn(NO_3)_2$, and D-glucose were dissolved in 60 mL of distilled water and then, the solution pH was adjusted to 11 with NaOH solution and it was magnetically stirred for 1.0 h. After that, the obtained black colored suspension containing bimetallic Fe-Zn NPs was autoclaved at 130 °C for 10 h into a Teflon-lined stainless steel autoclave. After autoclave process, [(Fe-ZnNPs)/C] was obtained and then, it was washed several times with distilled water and dried at 110 ºC for 6 h. [(Fe-ZnNPs)/C] was stored in the refrigerator at +4 °C for further experiments (Liang et al., 2017). The characterization of [(Fe-ZnNPs)/C] was performed using Scanning Electron Microscope (SEM-Zeiss/ Supra 55, Germany), Energy Dispersive X-ray Spectroscopy (EDX- Zeiss/Supra 55, Germany), and X-ray Diffractometer (XRD-Philips XPert, Netherlands).

2.2. Decolorisation of Napthol Blue Black via Fenton-like Reaction

In the Fenton-like experiments, the desired amount of [(Fe-Zn NPs)/C] was added to 100 mL of NBB dyestuff solutions at desired initial pH and initial dye concentrations. The flasks containing the solutions were agitated in the water bath for 30 minutes to make certain desorption-adsorption equilibrium of NBB dyestuff aqueous solution with the catalyst. Then, 5 ml of H_2O_2 solutions were added to the aqueous dyestuff solutions including the catalyst. After that, the samples were taken at pre-determined time intervals and the catalyst were removed by centrifuge. The concentration of NBB dyestuff was observed by using the UV-vis spectrophotometer at the wavelength of 628 nm. The decolourisation percentage for NBB dyestuff was expressed in terms of the decrease in UV-vis absorbance.

3. RESULTS AND DISCUSSIONS

3.1. Characterization of [(Fe-Zn NPs)/C]

The structure and phase purity of [(Fe-Zn NPs)/C] were investigated by XRD analysis. The obtained XRD pattern of [(Fe-Zn NPs)/C] was given in Fig. 1. Accordingly, narrow and sharp peaks showing a certain crystal structure could not be obtained; however, only a wide peak was obtained at 20 º, which is related to the amorphous and non-graphite carbon structure (Liang et al., 2017). As a result, the composite material synthesized in this study does not have a specific crystal structure; it is an amorphous material.

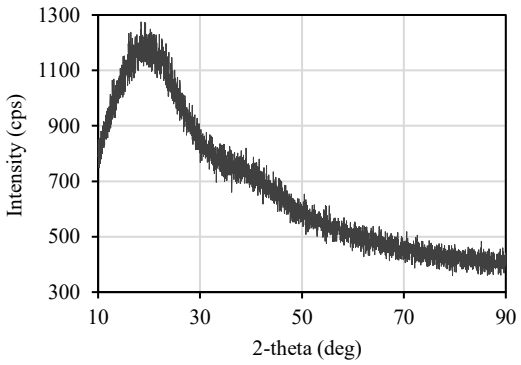

Fig. 1. XRD pattern of [(Fe-Zn NPs)/C]

The elemental content of [(Fe-Zn NPs)/C] was determined by EDX analysis. The corresponding SEM image of [(Fe-Zn NPs)/C] and EDX mapping images were shown in Figs. 2. (a)-(f). Accordingly, the microspheres had the element of carbon indicating the hydrochar structure while the iron-zinc nanoparticles (Fe-Zn NPs) formed between the microspheres had the elements of iron, zinc, and oxygen. Besides, [(Fe-Zn NPs)/C] contained 58 %, 12 %, 19 %, and 10% by mass of carbon, oxygen, iron, and zinc elements, respectively.

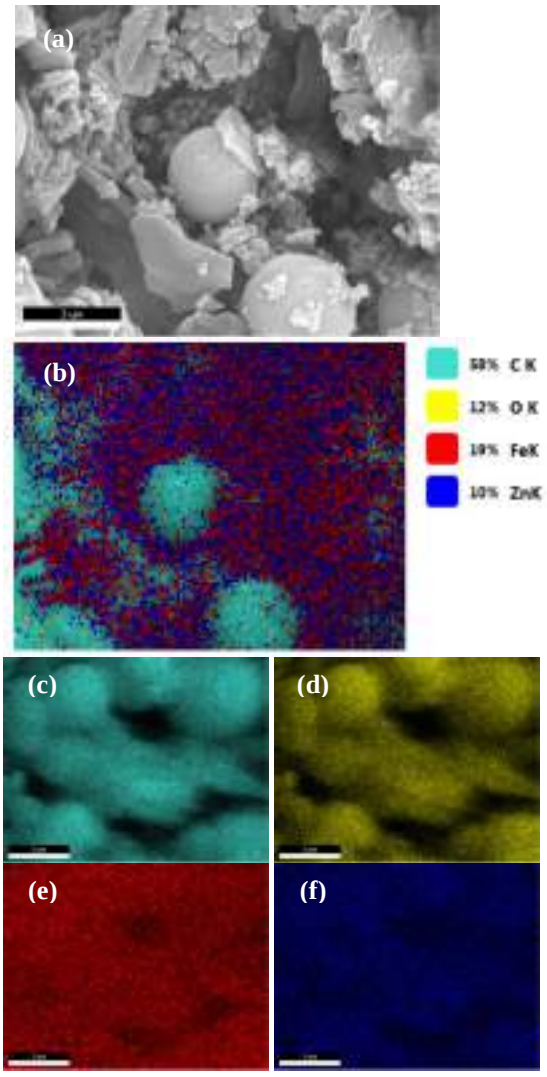

Fig. 2. (a) The corresponding SEM image of [(Fe-Zn NPs)/C], (b) EDX mapping image of [(Fe-Zn NPs)/C], (c) Carbon mapping, (d) Oxygen mapping, (e) Iron mapping, (f) Zinc mapping

The morphology of [(Fe-Zn NPs)/C] was investigated before and after Fenton-like reaction by SEM analysis given in Figs. 3. (a)-(c). According to Fig. 3. (a); it was observed that the Fe-Zn NPs formed between the carbon microspheres indicating the hydrochar structure as observed in EDX analysis. The blown-up image of the nanoparticles between the microspheres was presented in Fig. 3. (b). The mean particle size of these nanoparticles before the Fenton-like reaction was calculated as 37.43 nm by Image-J program whilst this value was calculated as 68.84 nm after the decolorisation of NBB dyestuff via Fenton-like reaction (Fig. 3. (c)). As a result, mostly regular spherical nanoparticles were observed before the Fenton-like reaction while after the Fenton-like reaction, both the particle size increased due to the agglomeration of the nanoparticles, and the regular spherical forms of the nanoparticles destroyed.

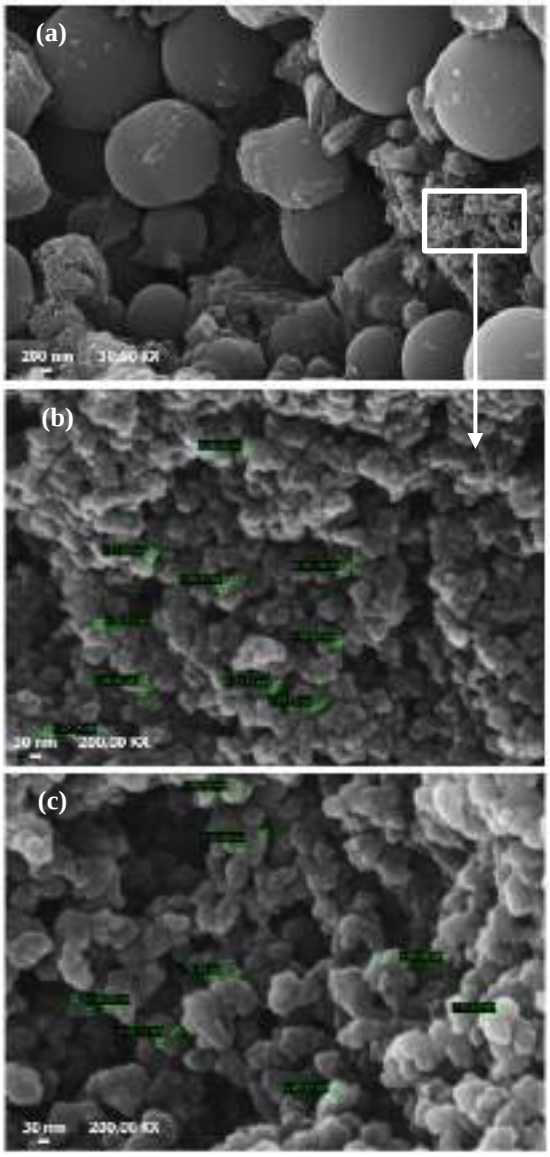

Fig. 3. SEM images of (a) [(Fe-Zn NPs)/C] at 30.00 KX before the Fenton-like reaction, (b) [(Fe-Zn NPs)/C] at 200.0 KX before the Fenton-like reaction, (c) [(Fe-Zn NPs)/C] at 200.0 KX after the Fenton-like reaction

3.2. Decolorisation of NBB Dyestuff with Heterogeneous Fenton-like Reaction

3.2.1. Determination of Heterogeneous Fenton-like Catalyst Properties of [(Fe-Zn NPs)/C] and Its Compounds

The heterogeneous Fenton-like catalyst properties of (Fe-Zn NPs)/C and its compounds such as Fe-Zn NPs,

Fe NPs/C, and Zn NPs/C were determined by calculating decolorisation efficiencies of them for the selected model pollutant of NBB dyestuff decolorisation. Accordingly, the color removal capacities of [(Fe-Zn NPs)/C], Fe-NPs/C, Fe-Zn NPs, and Zn NPs/C were 96.61, 68.08, 48.43, and 26.01 mg/g, respectively (experimental conditions: initial pH 3.0, 100 mg/L initial dyestuff concentration, 50 mM H_2O_2 concentration, 1.0 g/L catalyst concentration, 25°C temperature). As a result, the Fenton-like decolorisation studies for NBB dyestuff were performed with [(Fe-Zn NPs)/C] because it had the maximum color removal capacity among the other catalysts.

3.2.2. Effect of Environmental Conditions of Fenton-like Decolorisation of NBB Dyestuff with [(Fe-Zn NPs)/C]

The initial pH of solution is a substantial parameter to design a treatment process. For this reason, the effect of initial pH on the decolorisation of NBB dyestuff with [(Fe-Zn NPs)/C] was investigated at the experimental conditions of 100 mg/L initial dyestuff concentration, 50 mM H_2O_2 concentration, 1.0 g/L catalyst concentration, 25°C temperature for the initial pH range of 3.0-5.0. The color removal capacities at the equilibrium time of 90 min in the initial pH range of 3.0-5.0 were shown in Fig. 4. Accordingly, the color removal capacities decreased slightly with the increase in the initial pH. Therefore, it could be said that this process enables to study at the wide initial pH range, which is an advantage for the industrial applications. The increasing of initial pH causes the decomposition of H_2O_2 to O_2 and H_2O; and so, the fewer OH• radical forms during the reaction; as a result, the decolorisation percentages reduce with the increase in the initial pH. Another reason may be the decrease in oxidation potentials of the produced OH• radicals at the higher initial pHs; and so, the decolorisation percentages may reduce with the increase in the initial pH (Khataeet al., 2017). For these reasons, the studying at mild acidic conditions can be suggested for the decolorisation of NBB dyestuff with [(Fe-Zn NPs)/C].

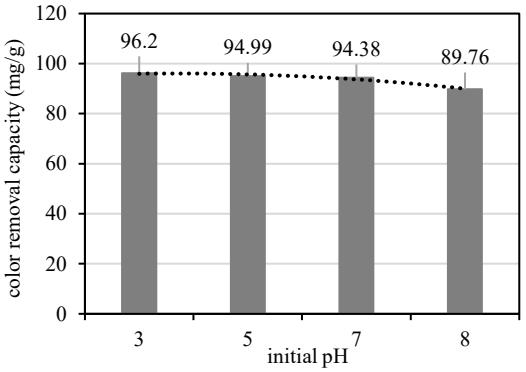

Fig. 4. Effect of initial pH (experimental conditions: 100 mg/L initial dyestuff concentration, 50 mM H_2O_2 concentration, 1.0 g/L catalyst concentration, 25°C temperature)

The effect of H_2O_2 concentration on the decolorisation of NBB dyestuff was investigated by varying H_2O_2 concentration from 1.0 mM to 50 mM at the fixed other conditions (initial pH of 3.0, initial dyestuff concentration of 100 mg/L, catalyst concentration of 1.0 g/L, temperature of 25°C). The color removal capacities at the equilibrium time of 90 min in the H_2O_2 concentration range of 1.0-50 mM were shown in Fig. 5. As can be seen in Fig. 5, the color removal capacities increased prominently with increase in H_2O_2 concentration from 1.0 mM to 15 mM, and the increase rate declined thereafter. The reason for this slowdown in the increase rate at the higher H_2O_2 concentrations may be explained with the scavenging effect of OH• radical. At higher H_2O_2 concentrations, the formed OH• radicals reacted with H_2O_2 in the medium and the less oxidative radicals of HO_2• formed at the end of the reaction ($H_2O_2 + OH\cdot \rightarrow HO_2\cdot + H_2O$), and so; the color removal amounts decreased at the higher H_2O_2 concentrations because there were fewer strong radicals of OH• in the medium (Khataeet al., 2017). Consequently, due to the fact that the maximum color removal capacity was obtained at 50 mM H_2O_2 concentration, the other experiments were carried out by using 50 mM H_2O_2.

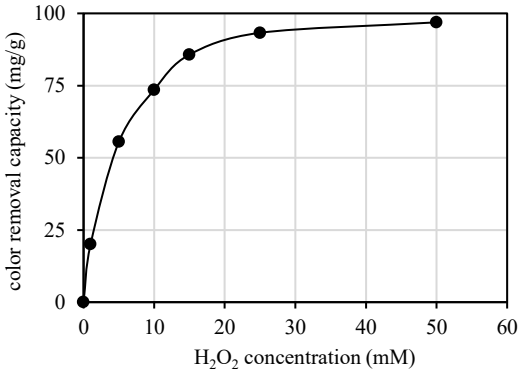

Fig. 5. Effect of H_2O_2 concentration (experimental conditions: initial pH 3.0, 100 mg/L initial dyestuff concentration, 1.0 g/L catalyst concentration, 25°C temperature)

The effect of temperature on the decolorisation of NBB dyestuff with [(Fe-Zn NPs)/C] was investigated at the experimental conditions of initial pH of 3.0, 100 mg/L initial dyestuff concentration, 50 mM H_2O_2 concentration, 1.0 g/L catalyst concentration for the temperature range of 25-55.

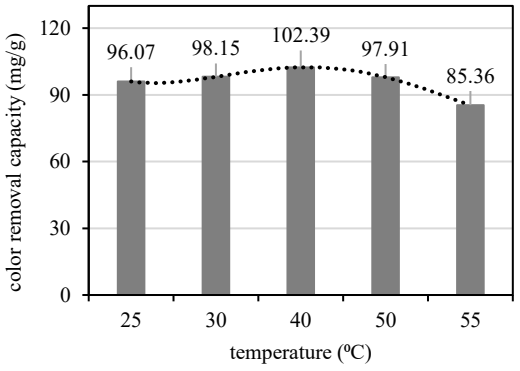

Fig. 6. Effect of temperature (experimental conditions: initial pH 3.0, 100 mg/L initial dyestuff concentration, 50 mM H_2O_2 concentration, 1.0 g/L catalyst concentration)

The color removal capacities in the temperature range of 25-55 were presented in Fig. 6. As shown in Fig. 6, the color removal capacity increased up to 40 ºC, and it decreased slightly thereafter. Accordingly, this process enables to study at the wide temperature range, which is an advantage for the industrial applications. On the other hand, the optimum temperature could be selected as 40 ºC due to the obtained maximum color removal capacity at this temperature.

The effect of initial dyestuff concentration on the decolorisation of NBB dyestuff was investigated by varying initial dyestuff concentration from 100 mg/L to 1200 mg/L at the fixed other conditions (initial pH of 3.0, H_2O_2 concentration of 50 mM, catalyst concentration of 1.0 g/L, temperature of 40°C). The color removal capacities at the equilibrium time of 90 min in the initial dyestuff concentration range of 100-1200 mg/L were shown in Fig. 7. As can be seen in Fig. 7, the color removal capacity increased up to 700 mg/L, and it remained nearly constant thereafter. This could be explained as follows (Hassani et al., 2018):

(a) The increase in the initial dyestuff concentration causes the adsorption of dyestuff molecules on the surface of catalyst, and so; the dyestuff molecules adsorbed on the surface of catalyst may block the active sites of catalyst. As a result of it, the fewer •OH radicals form and thus, the color removal capacities may decline.
(b) When there are more dyestuff molecules in the reaction medium, they compete against the intermediates produced during the Fenton-like reaction and thus, the color removal capacities may decline.

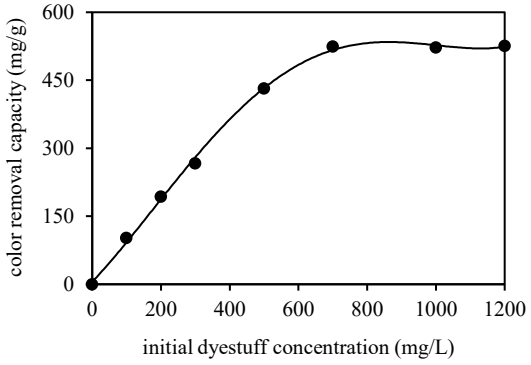

Fig. 7. Effect of initial dyestuff concentration (experimental conditions: initial pH 3.0, 50 mM H_2O_2 concentration, 1.0 g/L catalyst concentration, 40°C temperature)

The effect of catalyst concentration on the decolorisation of NBB dyestuff with [(Fe-Zn NPs)/C] was investigated at the experimental conditions of initial pH of 3.0, 100 mg/L initial dyestuff concentration, 50 mM H_2O_2 concentration, 40°C temperature for the catalyst concentration range of 0.25-3.0. The color removal capacities at the equilibrium time of 90 min in the catalyst concentration range of 0.25-3.0 were shown in Fig. 8. As seen in Fig. 8, the color removal capacities decreased with increasing catalyst concentration. In general, the color removal capacity is expected to increase with the increase in the catalyst concentration because the more catalysts in the reaction medium, the more H_2O_2 is expected to decompose to OH• radicals. However, it has been reported in the literature that the excessive catalyst loading causes a decrease in the color removal due to the scavenging effect of OH• radicals. Accordingly, the formed OH• radicals react with the excess iron ions in the reaction medium, arising from the iron based catalyst, (Fe^{2+} + OH• → Fe^{3+} + OH^-) (Wang et al., 2016). For the same reason, the catalyst concentrations higher than 0.25 g/L caused the reduction of the color removal capacities in this study, and so; the optimum catalyst concentration was determined as 0.25 g/L.

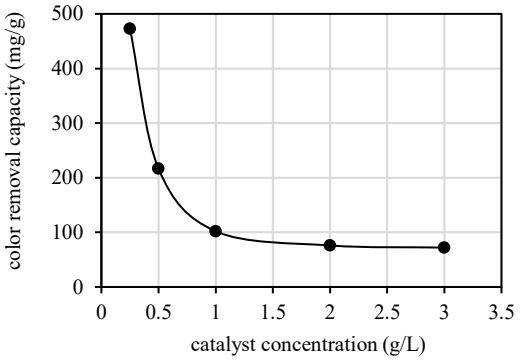

Fig. 8. Effect of catalyst concentration (experimental conditions: initial pH 3.0, 100 mg/L initial dyestuff concentration, 50 mM H_2O_2 concentration, 40°C temperature)

5. CONCLUSION

In this study, iron-zinc nanoparticles (Fe-Zn NPs) were firstly synthesized in the presence of glucose by co-precipitation method using NaOH and then, the iron-zinc nanoparticles/carbon composite [(Fe-Zn NPs)/C] was synthesized by the hydrothermal carbonization of the glucose in the solution containing Fe-Zn NPs. Next, the usability of [(Fe-ZnNPs)/C] as a heterogeneous catalyst in the decolorisation of NBB dyestuff via Fenton-like reaction was investigated. The decolorisation could be achieved when both oxidant (H_2O_2) and catalyst [(Fe-Zn NPs)/C] were present together in the reaction medium, thus proving that the dyestuff was decolorized by Fenton-like reaction. The studies showed that the optimum initial pH, H_2O_2 concentration, temperature, initial dye concentration, and catalyst concentration for Fenton-like decolorisation of NBB dyestuff with [(Fe-ZnNPs)/C] were determined to be 3.0, 50 mM, 700 mg/L, and 0.25 g/L, respectively. Moreover, this process enables to study at the wide initial pH and temperature range, which is an important advantage for the industrial applications. Consequently, the present study has revealed significant outputs to the synthesis of an effective Fenton-like heterogeneous catalyst, which could be important for the contribution to the related literature as well as the water treatment applications.

REFERENCES

Gu, T., Dong, H., Lu, T., Han, L., and Zhan, Y. (2019). "Fluoride ion accelerating degradation of organic pollutants by Cu (II)-catalyzed Fenton-like reaction at wide pH range." *Journal of hazardous materials*.,Vol. 377, pp. 365–370.

Hassani A., Çelikdağ G., Eghbali P., Sevim M., Karaca S., and Metin Ö. (2018) "Heterogeneous sono-Fenton-like process using magnetic cobalt ferrite-reduced graphene oxide ($CoFe_2O_4$-rGO) nanocomposite for the removal of organic dyes from aqueous solution." *Ultrasonics Sonochemistry*, Vol. 40, pp. 841-852.

Khan, J., Tariq, M., Muhammad, M., Mehmood, M. H., Ullah, I., Raziq, A., and Niaz, A. (2019). "Kinetic and thermodynamic study of oxidative degradation of acid yellow 17 dye by Fenton-like process: Effect of HCO_3^-, CO_3^{2-}, Cl^- and SO_4^{2-} on dye degradation." *Bulletin of the Chemical Society of Ethiopia*, Vol. 33, No. 2, pp. 243-254.

Khataee A., Gholami P., and Vahid B. (2017) "Catalytic performance of hematite nanostructures prepared by N_2 glow discharge plasma in heterogeneous Fenton-like process for acid red 17 degradation." *Journal of Industrial and Engineering Chemistry*, Vol. 50, pp. 86-95.

Liang C., Liu Y., Li K., Wen J., Xing S., Ma Z., and Wu Y. (2017) ""Heterogeneous photo-Fenton decolorisation of organic pollutants with amorphous Fe-Zn-oxide/hydrochar under visible light irradiation." Separation and Purification Technology, Vol. 188, pp. 105-111.

Tarkwa, J. B., Oturan, N., Acayanka, E., Laminsi, S., and Oturan, M. A. (2019). "Photo-fenton oxidation of Orange G azo dye: Process optimization and mineralization mechanism." *Environmental Chemistry Letters*, Vol. 17, No. 1, pp. 473-479.

Vu, A. T., Xuan, T. N., and Lee, C. H. (2019). "Preparation of mesoporous $Fe_2O_3 \cdot SiO_2$ composite from rice husk as an efficient heterogeneous Fenton-like catalyst for degradation of organic dyes." *Journal of Water Process Engineering*, Vol. 28, pp. 169-180.

Wang N., Zheng T., Zhang G., and Wang P. (2016) "A review on Fenton-like processes for organic wastewater treatment." *Journal of Environmental Chemical Engineering*, Vol. 4(1), pp. 762-787.

Wang T., Zhai Y., Zhu Y., Li C., and Zeng G. (2018) "A review of the hydrothermal carbonization of biomass waste for hydrochar formation: Process conditions, fundamentals, and physicochemical properties." *Renewable and Sustainable Energy Reviews*, Vol. 90, pp. 223-247.

Yavari S., Mahmodi N. M., Teymouri P., Shahmoradi B., and Maleki A. (2016) "Cobalt ferrite nanoparticles: preparation, characterization and anionic dye removal capability." *Journal of the Taiwan Institute of Chemical Engineers*, Vol. 59, pp. 320-329.

AVOIDING INFINITE-PRECISION ARITHMETIC FOR BEE COLONY OPTIMIZATION ALGORITHMS: COST-BASED ABC

Zeki Yetgin [*1] and Nasır Can Kırık [2]

[1] Mersin University, Faculty of Engineering, Department of Computer Engineering, Mersin, Turkey, zyetgin@mersin.edu.tr
[2] Mersin University, Institute of Science, Department of Computer Engineering, Mersin, Turkey, can@mersin.edu.tr

ABSTRACT
Optimization algorithms generally evaluate the solutions using cost (objective) functions where smaller cost indicates better solution. Artificial Bee Colony Optimization (ABC) uses fitness function to evaluate the solution goodness where higher fitness is for better solution. The fitness function is implemented by inverting cost to fitness in zero-one scale. However, this type of conversion may require infinite-precision arithmetic when the cost value approaches to zero. In this case, floating-point implementation of the fitness function, commonly used in literature, only provides an approximation for the actual fitness. This implementation issue has prevented the ABC Algorithms from being fully explored. To do best of our knowledge, this article is the first that studied the implementation issue of the fitness function and propose to use floating-point variant of ABC, namely Cost-based ABC. Two ABC Algorithms and their cost-based variants are analysed. The result show that Cost-based ABCs better explores the solution space.

Keywords: *cost-based ABC, bee colony algorithm, fitness function, infinite precision*

[*] *Corresponding Author*

1. INTRODUCTION

Artificial Bee Colony (Karaboga 2005) is inspired by the intelligent behavior of honey bees. ABC is a population based heuristic algorithm that explores for a population of food sources (solutions) and exploits (improves) them until the sources have no longer potentials. Once exploiting a particular source reaches to a trial limit, the source is replaced by a new one. Exploration implies finding new candidate solutions whereas exploitation means searching for better solutions around the current ones. Scout bees discover new sources while worker and onlooker bees exploits the available sources. Worker bees only exploit its assigned food source whereas onlookers selectively exploit the good sources according to their fitnesses, e.g. nectar amount. Scout, worker and onlooker phases are sequentially iterated in a loop. One of prominent feature of the algorithm is its efficiency against its simplicity. Algorithm has few parameters to control the colony, such as colony size and maximum iterations.

ABC algorithm has an increasing popularity in scientific community. It has been applied in solving many problems. Some examples are signal-image-video processing problems such as image enhancement (Chen, Li & Yu 2017), compression (Ismail & Baskaran 2014), edge detection (Deng & Duan 2014), motion estimation (Cuevas et al. 2013), network problems such as frequency assignment(Chaves-González et al. 2010), node placement (Hashim, Ayinde & Abido 2018), network attacks (Lozano et al. 2017), intrusion detection (Aldwairi, Khamayseh & Al-Masri 2015), machine learning problems such as training neural networks (Karaboga, Akay & Ozturk n.d.), feature selection (Keles & Kilic 2018), clustering (Karaboga & Ozturk 2011), and among many others(Akay & Karaboga 2015; Liu, Ma & Yang 2017; Apalak, Karaboga & Akay 2014; Abro & Mohamad-Saleh 2014; Kang, Li & Ma 2013). In literature, ABC algorithm is initially proposed for optimization of numeric functions (Karaboga 2005). Since then many ABC variants (Karaboga et al. 2014; Jia, Duan & Khan 2015; Huang, Wang & Yang 2016) have been proposed for various type of optimizations such as constrained, multiobjective, continuous and combinatorial design problems. Karaboga and his friends provided a comprehensive survey (Karaboga et al. 2014) that analyses these problems with the focus on ABC drawbacks. According to the survey studies, the great potential of ABC seems very clear with its good exploration capability but also a strong need to alleviate the weakness in exploitation capability (local search) and, thus, the greedy behaviors around near optimal solutions. Similar to other swarm optimizations, the ABC algorithm also suffers from early maturity.

Majority of the works in literature seems to improve the local search (exploitation) ability of the bees, which help avoiding early maturity either by escaping from local solutions or shifting towards the global solution. The original bees search around the current solution for a random neighbor towards to one of the existing solutions during local search. Some articles (Gao & Liu 2012)(Zhu & Kwong 2010) allow bees to search around the best solution of the current population. Although such approaches enable bees to converge the optimal solution very soon, they increases possibility of local stuck around the near optimal solution. Thus, (Gao & Liu 2012) also improves exploration ability of the scout bees by using chaotic and opposition based initialization. (Sun, Chen & Zhang 2018) allows bees to search around a random existing solution for random neighbour towards to current solution, which is quite opposite of the original approach. Authors claim that this approach can expand the search range of new solution and further improve the exploration ability of ABC algorithm. In order to improve the exploitation ability of the algorithm, some ABC algorithms use exploitation operators such as mutation and/or crossover operators as in Gauss mutation(Cheng & Jiang 2012), Cauchy mutation (He et al. 2015), differential evolution mutation (He et al. 2015), simulated annealing operator (Chen, Sarosh & Dong 2012), Rosenbrock operator (Kang, Li & Ma 2011).

All the forementioned ABC algorithms use floating-point implementations, as defacto standart, while demonstrating their studies and thus suffer from infinite-precision requirement of the fitness function. In original ABC, the fitness value is scaled to zero-one interval for positive cost values and this may cause high precision requirement when the cost value approximates to zero expectedly. The fitness values of two neighbours around a food source are expected to be close to each other and thus possibly incorrectly compared due to the floating-point approximation during exploitation phase. In this article, current floating-point implementation of ABC algorithms is demonstrated as an issue, an ABC variant that removes the infinite-precision requirement using floating-point arithmetic is proposed.

The article is organized as follows. Next section provides the original ABC. Third section provides the proposed ABC variant with the issue of floating-point arithmetic. The fourth section provides the experimental results and the last section gives concluding remarks and future directions.

2. ABC ALGORITHM

Typical optimization problem is defined as min $\{ f(x) \mid f(x)$ is the cost function and $x \in R^D$ is a solution on D-dimensional domain $\}$. According to ABC Algorithm, food sources are considered as potential solutions and bees searches for the position of the best food source. The basic ABC algorithm requires few parameters, such as the number of food sources denoted as *NS*, maximum iterations denoted as *MaxIter*, and the trial limit denoted as *limit*. As given in Algorithm 1, the ABC algorithm has three phases. In first phase, scout bees randomly explore the food space to find initial food sources, which are the initial solutions denoted as $X=(x_1, x_2,\ldots,x_{NS})$ and formulated in Eq. (1).

$$\boldsymbol{x_i(j) = x_{\min(j)} + rand(0,1).\left(x_{\min(j)} + x_{\max(j)}\right)} \quad (1)$$

where j is the updating dimension $\in \{1, 2,\ldots,D\}$, x_{min} and x_{max} are upper and lower bound solutions respectively. Any scout discovering the food source $x_i \in R^D$ becomes a worker bee with its associated food source in its memory. The bees measure the quality of the source x_i using the fitness function, formulated on basis of the cost function $f(x)$ in Eq. (2).

$$\boldsymbol{fitx_i = fit(x_i) = \begin{cases} 1/(1+f(x_i)), & f(x_i) > 0 \\ 1 + abs(f(x_i)), & f(x_i) \le 0 \end{cases}} \quad (2)$$

In second phase, each worker *i* exploits its food source x_i by randomly searching its neighbourhood for a better solution. This phase is equivalent to local searching around the source, which forms a candidate $v_i \in R^D$ by updating a randomly selected dimension *j* of the solution x_i towards one of the existing solution $x_k \neq x_i$ formulated in Eq. (3). The workers replace the source x_i with the candidate v_i if later is better, formulated in Eq. (4).

$$\boldsymbol{v_i(j) = x_i(j) + rand(-1,1).\left(x_i(j) - x_k(j)\right)} \quad (3)$$

$$\boldsymbol{x_i = \begin{cases} v_i, & fitv_i > fitx_i \\ x_i, & fitv_i \leq fitx_i \end{cases}} \quad (4)$$

where $k \in \{1, 2, \ldots, NS\}$ is the randomly chosen indice and $k \neq i$, $j \in \{1, 2, \ldots, D\}$ indicates a random dimension selected to be updated.

Algorithm 1. Basic ABC Algorithm (*MaxIter, NS, limit*): return $\boldsymbol{x_{best}}$ variables: $\boldsymbol{x_{best}}$= null, $c_i = 0$ for all *i=1..N*

% Scout Bees Phase : initialization of food sources
(1) Generate *NS* sources $X = (\boldsymbol{x_1}, \boldsymbol{x_2}, \ldots, \boldsymbol{x_{NS}})$
with $FitX = (\text{fit}\boldsymbol{x_1}, \boldsymbol{fitx_2}, \ldots, \boldsymbol{fitx_{NS}})$,
using Eq.(1)
(2) for *iter=1* to *MaxIter* do
% Worker Bees Phase
(3) for *i=1* to *NS* do
(4) v_i= LocalSearch(x_i), according to Eq.(3)
(5) if fitv_i > *fit*x_i then
(6) $x_i = v_i$
(7) $c_i = 0$
(8) else $c_i = c_i + 1$
% Onlooker Bees Phase
(9) *P* = SelectionProbalities(Fit*X*), according to Eq.(5)
(10) for *j=1* to *NS* do
(11) *i*= RouletteWheelSelection(*P*)
(12) v_i = LocalSearch(x_i), according to Eq(3)
(13) if fitv_i > *fit*x_i then
(14) $x_i = v_i$
(15) $c_i = 0$
(16) else$c_i = c_i + 1$
% Scout Bees Phase
(17) for *i= 1* to *NS* do
(18) if c_i > *limit* then
(19) x_i = GenerateRandomSolution( )
according to Eq(1)
(20) $c_i = 0$
(21) $\boldsymbol{x_{best}}$= BestSolution({$\boldsymbol{x_{best}}$,*X*})

In third phase, workers announce the information about the food sources such as nectar amount and position by dancing in the hive. Onlookers bees watch the dances of these bees and select a random food source among the sources in such a way that better sources have more chance to be selected. The selection probabilities, $P = (p_1, p_2, \ldots, p_{NS})$, are formulated in Eq. (5) where p_i is the selection probability of the source x_i.

$$\boldsymbol{p_i = \frac{fitx_i}{\sum_{k=1}^{NS} fitx_k}} \quad (5)$$

Then, they exploit (local search with source update) their food sources in the same fashion as workers do. Thus, onlookers mostly gather around globally better solutions to make global improvements. All bees keep track of the best food sources during searching for the sources. Any bee that cannot exploit its food source (improve its solution) within some trial limit becomes scout again and finds a random food source throughout the space. The algorithm repeats worker-onlooker-scout phases until the maximum cycles are completed. When algorithm terminates one bee in current population is expected to have the best food source in its memory.

3. COST-BASED ABC

When ABC Algorithm is considered for minimization problems, fitness function is formulated by inverting the cost function, as shown in Equation (2). This scales the positive cost values to the fitness values in zero-one range and may cause floating-point numbers in high precision. The floating-point number is represented as *significand x base*^{exponent} where significand, base and exponent are implemented as integers and the precision is the number of digits in the significand. For example, 0.01 (1 x 10^{-2}) and 0.00000001 (1 x 10^{-8}) both requires 1 digit precision (see Table 1).

Considering 8-digit precision hardware, the number of digits in significand (precision) and exponent part of cost and fitness values are given in Table 1 for demonstration purpose. When the cost value becomes less than 1.0e-8 value (e.g., 0.9e-8 and 0.1e-8), the corresponding fitness values are approximated to 1.0 due to exceeding the precision limit. Considering Table 1, one can easily notice that exceeding the exponent value 8 may require more than 8-digit precision. In practice, modern computer systems usually uses single (e.g "float"type in C) or double (e.g "double" type in C) precision. In single precision, 24 bits (precision) + 8 bits (exponent) = 32 bits are used whereas in double precision, 53 bits (precision) + 11 bits (exponent) = 64 bits are used. It means single precision requires about 8 digits, double precision requires about 16 digits precision.

Table 1. Cost and fitness values on 8-digit precision hardware

cost			*fitness = 1/(1+cost)*		
v	*p*	*e*	*v*	*p*	*e*
1.0e-1	*1*	*1*	*0.90909091*	*8*	*0*
1.0e-2	*1*	*1*	*0.99009901*	*8*	*0*
1.0e-8	*1*	*1*	*0.99999999*	*8*	*0*
0.9e-8	*1*	*1*	*1.0*	*1*	*0*
0.1e-8	*1*	*1*	*1.0*	*1*	*0*

v: value, p: precision digits, e: exponent digits

Considering double precision, when the cost values approximate to zero by exceeding the $1.0e^{-16}$ the corresponding fitness values will be approximated due to higher precision requirement. The approximation caused by the floating-point arithmetic particularly affect the exploit phase of ABC algorithm where two fitness values in the same neighbourhood are compared, as formulated in Eq. (4). Since they are in the same neighbourhood, their fitness values are expected to be close to each other and any aproximation due to floating-point arithmetic may easily result in wrong computation. In order to remove the infinite-precision requirement of the fitness formulation, we propose to use cost values rather than fitness in exploit phase, formulated in Eq. (6).

$$\boldsymbol{x_i} = \begin{matrix}\{\boldsymbol{v_i}, \boldsymbol{costv_i} < \boldsymbol{costx_i}\} \\ \{\boldsymbol{x_i}, \boldsymbol{costv_i} \geq \boldsymbol{costx_i}\}\end{matrix} \quad (6)$$

Also we propose an update on formulation of selection probabilities, which uses fitness values, as shown in Eq. (5). First, we suggest a normalization on cost value in Eq. (7) to shift all cost values to positive domain in case that cost values may be negative. If we know in advance that the cost values are positive, we can skip Eq. (7) just to reduce the time complexity. Then, we suggest scaling the cost value to (0 1] range as usual formulated in Eq. (8), and compute the selection probability p_i as formulated in Eq. (9).

$$\boldsymbol{costx_i} = \boldsymbol{costx_i} - \mathbf{min}_{\boldsymbol{i=1..NS}}\, \boldsymbol{costx_i} \quad (7)$$

$$\boldsymbol{scalex_i} = \mathbf{1}/(\mathbf{1} + \boldsymbol{costx_i}) \quad (8)$$

Note that the "fitness" term is removed from equations just in order for readers not to make any wrong inference. The proposed ABC doesn't use the fitness, instead uses cost values. Also note that the Cost-based ABC still interfere infinite-precision requirement in Eq. (8-9). However, since there is no comparision of floating-point numbers, it doesn't affect the result. Furthermore, this also helps escaping from local minima in that onlookers can emphasize all near-optimal solutions equally because they possibly compute equal selection probability due to floating-point approximation.

$$\boldsymbol{p_i} = \frac{\boldsymbol{scalex_i}}{\sum_{\boldsymbol{k=1}}^{\boldsymbol{NS}} \boldsymbol{scalex_k}} \quad (9)$$

4. EXPERIMENTAL RESULTS

Four ABC variants, i-ABC, ii-global best (gbest) guided ABC, named as GABC(Zhu & Kwong 2010), and their cost-based versions, iii-Cost-based ABC and iv-Cost-based GABC, are compared based on 9 benchmark functions given in Table 2. GABC only propose an update on local search procedure as follows;

$$\boldsymbol{v_i(j)} = \boldsymbol{x_i(j)} + \boldsymbol{rand}(\mathbf{-1}, \mathbf{1}).\big(\boldsymbol{x_i(j)} - \boldsymbol{x_k(j)}\big) + \boldsymbol{rand}(\mathbf{0}, \boldsymbol{C}).\big(\boldsymbol{x_{best}(j)} - \boldsymbol{x_i(j)}\big) \quad (10)$$

where x_{best} is the best solution so far, C is an positive constant, here $C = 1.5$ is used as recommended in (Zhu & Kwong 2010). The benchmark functions have different characteristics such as multimodal and non-convex (*Ackley*, *Qing*, *Egg Crate, Xin-She Yan, Rosenbrock*), multimodal and convex (*Rastrigin*), unimodal and non-convex (*Griewank*), unimodal and convex (*Brown, Sphere*). The benchmark functions are tested for the maximum number of iterations *MaxIter* = 5000, the number of food sources *NS* = 60, the problem dimension *D = 50*, and the parameter *limit = NS × D*.

Table 2a. Typical benchmark function definitions

Name	Function Definition
Ackley	$\boldsymbol{f_1} = -\mathbf{20}.\boldsymbol{exp}(-\mathbf{0.2}\sqrt{\frac{\mathbf{1}}{\boldsymbol{n}}\sum_{\boldsymbol{i=1}}^{\boldsymbol{n}} \boldsymbol{x_i^2}}) - \boldsymbol{exp}(\frac{\mathbf{1}}{\boldsymbol{n}}\sum_{\boldsymbol{i=1}}^{\boldsymbol{n}} \boldsymbol{cos}(\mathbf{2\pi x_i})) + \mathbf{20} + \boldsymbol{e}$
Brown	$\boldsymbol{f_2} = \sum_{\boldsymbol{i=1}}^{\boldsymbol{n-1}} (\boldsymbol{x_i^2})^{(\boldsymbol{x_{i+1}^2}+\mathbf{1})} + (\boldsymbol{x_{i+1}^2})^{(\boldsymbol{x_i^2}+\mathbf{1})}$
Griewank	$\boldsymbol{f_3} = \mathbf{1} + \sum_{\boldsymbol{i=1}}^{\boldsymbol{n}} \frac{\boldsymbol{x_i^2}}{\mathbf{4000}} - \prod_{\boldsymbol{i=1}}^{\boldsymbol{n}} \mathbf{cos}\left(\frac{\boldsymbol{x_i}}{\sqrt{\boldsymbol{i}}}\right)$
Qing	$\boldsymbol{f_4} = \sum_{\boldsymbol{i=1}}^{\boldsymbol{n}} (\boldsymbol{x^2} - \boldsymbol{i})^2$
Rastrigin*	$\boldsymbol{f_5} = \mathbf{10n} + \sum_{\boldsymbol{i=1}}^{\boldsymbol{n}} (\boldsymbol{x_i^2} - \mathbf{10}\boldsymbol{cos}(\mathbf{2\pi x_i}))$
Sphere	$\boldsymbol{f_6} = \sum_{\boldsymbol{i=1}}^{\boldsymbol{n}} \boldsymbol{x_i^2}$
Egg Crate	$\boldsymbol{f_7} = \boldsymbol{x^2} + \boldsymbol{y^2} + \mathbf{25}(\boldsymbol{sin^2(x)} + \boldsymbol{sin^2(y)})$
Xin-SheYan	$\boldsymbol{f_8} = \left(\sum_{\boldsymbol{i=1}}^{\boldsymbol{n}} \boldsymbol{sin^2(x_i)} - \boldsymbol{e}^{-\sum_{\boldsymbol{i=1}}^{\boldsymbol{n}} \boldsymbol{x_i^2}}\right) \boldsymbol{e}^{-\sum_{\boldsymbol{i=1}}^{\boldsymbol{n}} \boldsymbol{sin^2}\sqrt{\boldsymbol{|x_i|}}}$
Rosenbrock	$\boldsymbol{f_9} = \sum_{\boldsymbol{i=1}}^{\boldsymbol{n}} [\mathbf{100}(\boldsymbol{x_{i+1}} - \boldsymbol{x_i^2})^2 + (\mathbf{1} - \boldsymbol{x_i})^2]$

Table 2b. Typical benchmark function ranges

Name	Range	Min
Ackley	(−32.768,32.768)	0
Brown	(−4, 4)	0
Griewank	(−600,600)	0
Qing	(−10,10)	0
Rastrigin*	(-5.12, 5.12)	0
Sphere	(−100,100)	0
Egg Crate	(−500,500)	0
Xin-SheYan	(−10,10)	-1
Rosenbrock	(−50, 50)	0

However with this limit setting, the Rastrigin function is reached to global min zero for all ABC variants, thus the *limit = 0.1 x NS x D* is considered only for Rastrigin function. The colony has equal number of worker bees and onlooker bees, considered equal to *NS*. 16 digits precision (double type) is considered for fitness values. Each experiment for the same parameter settings repeated *20* times and the average values are used to compute the performance metrics, such as min, max and mean of cost function values.

The experimental results are provided in Table 3-4 and Figure 1-4 where tables demonstrate the comparison of the objective performances with achieved min, max and mean cost values and figures show the evolution curves of the four ABC variants. The Table 3 clearly shows that Cost-based ABC is superior to original ABC, particularly for those functions where the original ABC achieves a cost value having the absolute exponent value around 16 or above. The reason is the fact that the original ABC suffer from infinite-precision requirement occurring during the exploit phase. Bees are possibly unable to discriminate which solutions have better fitness values due to approximating the fitness values forcing 16 digits precision or more. For *Ackley* and *Rosenbrock* although Cost-based ABC performs slightly better than the ABC, both should be considered to achieve similar performance due to fluctuations caused by random nature of the problem. The further lower level headings should be avoided.

Table 3a. Performance of ABC

Function	Best	Mean	Worst
Ackley	5.06e-14	6.32e-14	6.84e-14
Brown	7.48e-16	9.59e-16	1.21e-15
Griewank	0	9.44e-17	1.11e-16
Qing	9.59e-16	2.68e-15	1.29e-14
Rastrigin*	0	2.27e-14	1.14e-13
Sphere	7.67e-16	9.45e-16	1.14e-15
EggCrate	6.53e-16	7.95e-16	9.86e-16
Xin-SheYang	7.66e-17	9.73e-17	1.11e-16
Rosenbrock	0.52e-02	0.17	0.82

Table 3b. Performance of Cost-based ABC

Function	Best	Mean	Worst
Ackley	4.35e-14	6.29e-14	6.84e-14
Brown	8.27e-48	3.02e-46	8.82e-46
Griewank	0	0	0
Qing	2.33e-17	7.06e-16	7.16e-15
Rastrigin*	0	1.99e-14	5.68e-14
Sphere	3.68e-43	3.59e-42	1.78e-41
EggCrate	1.42e-33	1.21e-32	5.91e-32
Xin-SheYang	6.45e-35	5.06e-34	5.39e-33
Rosenbrock	0.14e-02	0.04	0.19

Similarly, Cost-based GABC is superior to original GABC due to the same reason. While GABC seems to perform slightly better than the ABC, its superiority depends on the characteristic of the cost functions. For multi-modal and non-convex problems, GABC may falsely converge to one of near optimal solution at one local minima. For example, for Rosenbrock, GABC versions are not better than the original ABC. For unimodal and convex problems, such as Sphere and Brown functions, GABC and Cost-based variants seems to performs best.

The evolution curves of mean cost values across the iteretations are given in Figure 1-8. Excluding Ackley and Rosenbrock, the figures clearly show that the legacy ABC versions (ABC, GABC) converge to a mean cost value around 1.0e-16 and hardly penetrate this limit due to the limitation of floating-point implementation. Ackley and Rosenbrock reaches to maximum convergence dept around the cost value 1.0e-14 and 1.0e-2 respectively. However, the cost-based ABC versions (Cost-based ABC, Cost-based GABC) can approach to global minimum better than the legacy ones, overcoming the floating-point limitation for all the functions.

Table 4a. Performance of GABC

Function	Best	Mean	Worst
Ackley	4.35e-14	5.63e-14	6.48e-14
Brown	7.29e-16	8.54e-16	9.98e-16
Griewank	0	7.77e-17	1.11e-16
Qing	5.30e-16	8.08e-16	1.39e-15
Rastrigin*	0	0	0
Sphere	5.33e-16	7.26e-16	9.32e-16
EggCrate	5.34e-16	7.63e-16	9.96e-16
Xin-SheYang	6.63e-17	9.41e-17	1.11e-16
Rosenbrock	0.73e-02	7.68	86.74

Table 4b. Performance of Cost-based GABC

Function	Best	Mean	Worst
Ackley	4.35e-14	5.41e-14	6.48e-14
Brown	2.63e-72	2.63e-71	1.01e-70
Griewank	0	0	0
Qing	1.70e-24	1.49e-21	6.55e-21
Rastrigin*	0	0	0
Sphere	2.79e-69	1.07e-68	3.39e-68
EggCrate	5.38e-64	3.87e-63	1.95e-62
Xin-SheYang	3.88e-37	5.86e-32	4.08e-31
Rosenbrock	0.14e-02	9.03	68.50

Since the experiment is done on 16-digit floating-point precision, one can observe that floating-point implementations particularly affect the legacy ABC versions for the cost values less than around $1.0e^{-16}$. That is the cost values less than around $1.0e^{-16}$ will be approximated for legacy versions. However, it doesn't mean that the global minimum zero is unreachable for legacy versions. The legacy versions could reach to global minimum without reaching the limit $1.0e^{-16}$. For example, in Figure 5, GABC suddenly drops to global minimum zero after around the cost value $1.0e^{-15}$ at iteration around 4700. Global minimum is reached in Figure 3 for cost-based versions and Figure 5 for GABC based versions (GABC, Cost-based GABC).

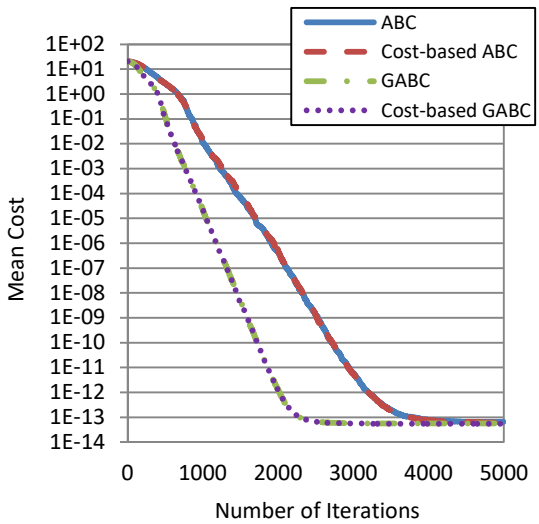

Figure 1. Evolution curves for Ackley

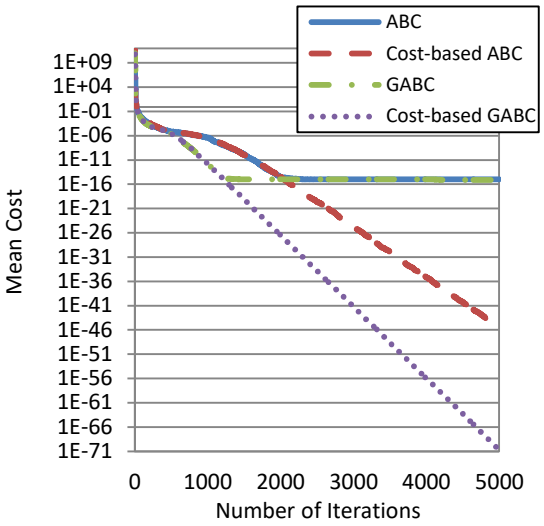

Figure 2. Evolution curves for Brown

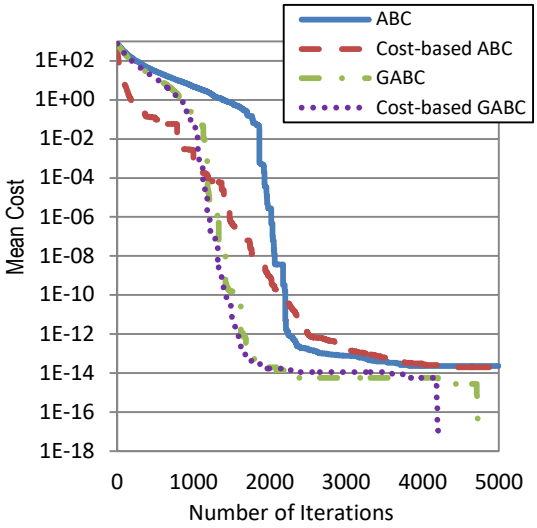

Figure 5. Evolution curves for Rastrigin

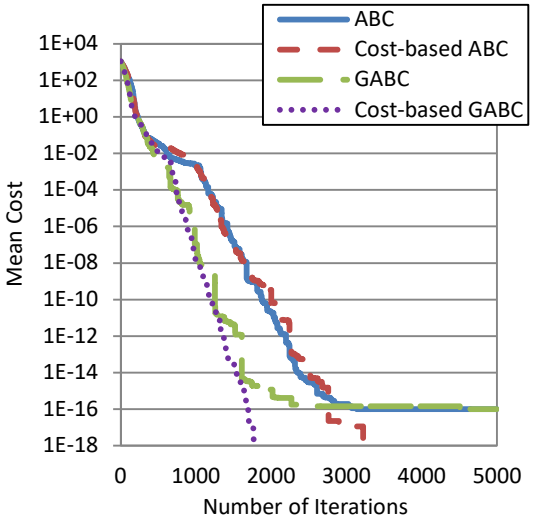

Figure 3. Evolution curves for Griewank

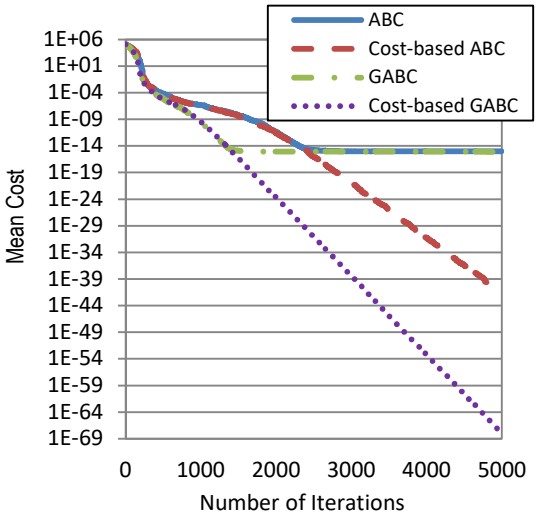

Figure 6. Evolution curves for Sphere

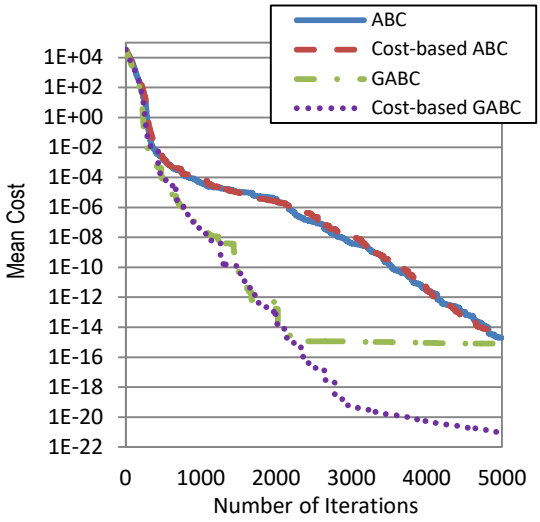

Figure 4. Evolution curves for Qing

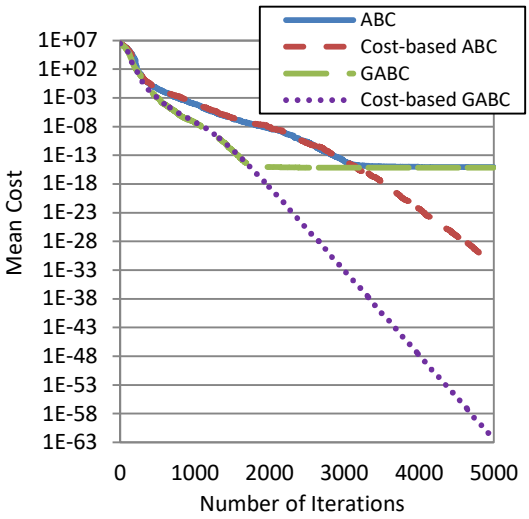

Figure 7. Evolution curves for Egg Crate

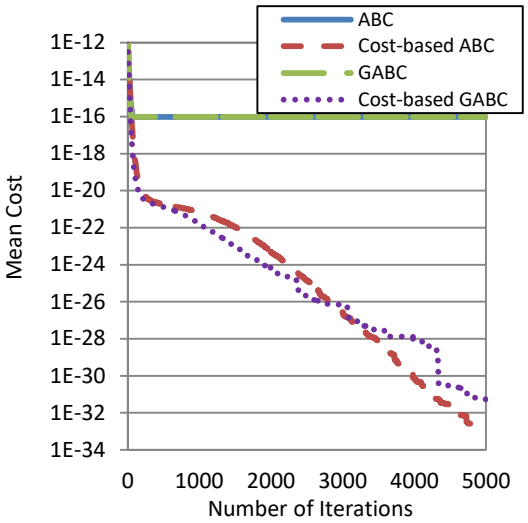

Figure 8. Evolution curves for Xin-SheYang

5. CONCLUSION

In this article, current implementations of Bee Colony Algorithm for minimization problems are demonstrated as an issue that requires infinite-precision arithmetic and a simple approach, namely Cost-based ABC, is proposed to avoid it. The proposed approach stands using cost values rather than fitness since the fitness definition in ABC not only converts the cost to the fitness but also converts the exponent requirement of the cost to the precision requirement of the fitness. Since the exponent value(e.g. 512) can scale much more than the precision(e.g. 16), current ABC variants could not be scalable in floating-point precision. This article provides awareness about the infinite-precision requirement of current ABC implementations and also comparisons of ABC variants relying on floating-point implementation as defacto standard. This implementation issue has prevented the ABC Algorithms from being fully explored. The experimental results of this article demonstrated that Cost-based ABC variants can better converge to the global minimum at higher precision.

6. REFERENCES

Abro, AG & Mohamad-Saleh, J 2014, 'Enhanced probability-selection artificial bee colony algorithm for economic load dispatch: A comprehensive analysis', *Engineering Optimization*, vol. 46, no. 10, pp. 1315–1330, retrieved July 19, 2019, from <http://www.tandfonline.com/doi/abs/10.1080/0305215X.2013.836639>.

Akay, B & Karaboga, D 2015, 'A survey on the applications of artificial bee colony in signal, image, and video processing', , vol. 9, pp. 967–990, retrieved July 12, 2019, from <https://link.springer.com/content/pdf/10.1007%2Fs11760-015-0758-4.pdf>.

Aldwairi, M, Khamayseh, Y & Al-Masri, M 2015, 'Application of artificial bee colony for intrusion detection systems', *Security and Communication Networks*, vol. 8, no. 16, pp. 2730–2740, retrieved July 12, 2019, from <http://doi.wiley.com/10.1002/sec.588>.

Apalak, MK, Karaboga, D & Akay, B 2014, 'The Artificial Bee Colony algorithm in layer optimization for the maximum fundamental frequency of symmetrical laminated composite plates', *Engineering Optimization*, vol. 46, no. 3, pp. 420–437, retrieved July 19, 2019, from <http://www.tandfonline.com/doi/abs/10.1080/0305215X.2013.776551>.

Chaves-González, JM, Vega-Rodríguez, MA, Gómez-Pulido, JA & Sánchez-Pérez, JM 2010, 'Swarm Intelligence, Scatter Search and Genetic Algorithm to Tackle a Realistic Frequency Assignment Problem', in Springer, Berlin, Heidelberg, pp. 441–448, retrieved July 12, 2019, from <http://link.springer.com/10.1007/978-3-642-14883-5_57>.

Chen, J, Li, C & Yu, W 2017, 'Adaptive Image Enhancement Based on Artificial Bee Colony Algorithm', in *Proceedings of the International Conference on Communication and Electronic Information Engineering (CEIE 2016)*, Atlantis Press, Paris, France, retrieved July 12, 2019, from <http://www.atlantis-press.com/php/paper-details.php?id=25872629>.

Chen, S-M, Sarosh, A & Dong, Y-F 2012, 'Simulated annealing based artificial bee colony algorithm for global numerical optimization', *Applied Mathematics and Computation*, vol. 219, no. 8, pp. 3575–3589, retrieved July 19, 2019, from <https://www.sciencedirect.com/science/article/pii/S0096300312009514>.

Cheng, X & Jiang, M 2012, 'An Improved Artificial Bee Colony Algorithm Based on Gaussian Mutation and Chaos Disturbance', in Springer, Berlin, Heidelberg, pp. 326–333, retrieved July 19, 2019, from <http://link.springer.com/10.1007/978-3-642-30976-2_39>.

Cuevas, E, Zaldívar, D, Pérez-Cisneros, M, Sossa, H & Osuna, V 2013, 'Block matching algorithm for motion estimation based on Artificial Bee Colony (ABC)', *Applied Soft Computing*, vol. 13, no. 6, pp. 3047–3059, retrieved July 12, 2019, from <https://www.sciencedirect.com/science/article/pii/S1568494612004401>.

Deng, Y & Duan, H 2014, 'Biological edge detection for UCAV via improved artificial bee colony and visual attention', *Aircraft Engineering and Aerospace Technology*, vol. 86, no. 2, pp. 138–146, retrieved July 12, 2019, from <http://www.emeraldinsight.com/doi/10.1108/AEAT-10-2012-0164>.

Gao, W & Liu, S 2012, 'A modified artificial bee colony algorithm', *Computers & Operations Research*, vol. 39, no. 3, pp. 687–697, retrieved July 19, 2019, from <https://www.sciencedirect.com/science/article/pii/S0305054811001699>.

Hashim, HA, Ayinde, BO & Abido, MA 2018, 'Optimal Placement of Relay Nodes in Wireless Sensor Network

Using Artificial Bee Colony Algorithm', retrieved July 12, 2019, from <http://arxiv.org/abs/1803.02441>.

He, X, Wang, W, Jiang, J & Xu, L 2015, 'An Improved Artificial Bee Colony Algorithm and Its Application to Multi-Objective Optimal Power Flow', *Energies*, vol. 8, no. 4, pp. 2412–2437, retrieved July 19, 2019, from <http://www.mdpi.com/1996-1073/8/4/2412>.

Huang, F, Wang, L & Yang, C 2016, 'A new improved artificial bee colony algorithm for ship hull form optimization', *Engineering Optimization*, vol. 48, no. 4, pp. 672–686, retrieved July 19, 2019, from <http://www.tandfonline.com/doi/full/10.1080/0305215X.2015.1031660>.

Ismail, MM & Baskaran, K 2014, *Hybrid Lifting Based Image Compression Scheme Using Particle Swarm Optimization Algorithm and Artifical Bee Colony Algorithm*, retrieved July 19, 2019, from <www.ijarcce.com>.

Jia, D, Duan, X & Khan, MK 2015, 'Modified artificial bee colony optimization with block perturbation strategy', *Engineering Optimization*, vol. 47, no. 5, pp. 642–655, retrieved July 19, 2019, from <http://www.tandfonline.com/doi/abs/10.1080/0305215X.2014.914189>.

Kang, F, Li, J & Ma, Z 2011, 'Rosenbrock artificial bee colony algorithm for accurate global optimization of numerical functions', *Information Sciences*, vol. 181, no. 16, pp. 3508–3531, retrieved July 19, 2019, from <https://www.sciencedirect.com/science/article/pii/S0020025511001988>.

Kang, F, Li, J & Ma, Z 2013, 'An artificial bee colony algorithm for locating the critical slip surface in slope stability analysis', *Engineering Optimization*, vol. 45, no. 2, pp. 207–223, retrieved July 19, 2019, from <http://www.tandfonline.com/doi/abs/10.1080/0305215X.2012.665451>.

Karaboga, D 2005, 'An idea based on Honey Bee Swarm for Numerical Optimization', *Technical Report TR06, Erciyes University*, no. TR06, p. 10, retrieved July 12, 2019, from <http://mf.erciyes.edu.tr/abc/pub/tr06_2005.pdf>.

Karaboga, D, Akay, B & Ozturk, C 'Artificial Bee Colony (ABC) Optimization Algorithm for Training Feed-Forward Neural Networks', in *Modeling Decisions for Artificial Intelligence*, Springer Berlin Heidelberg, Berlin, Heidelberg, pp. 318–329, retrieved July 12, 2019, from <http://link.springer.com/10.1007/978-3-540-73729-2_30>.

Karaboga, D, Gorkemli, B, Ozturk, C & Karaboga, N 2014, 'A comprehensive survey: artificial bee colony (ABC) algorithm and applications', *Artificial Intelligence Review*, vol. 42, no. 1, pp. 21–57, retrieved July 12, 2019, from <http://link.springer.com/10.1007/s10462-012-9328-0>.

Karaboga, D & Ozturk, C 2011, 'A novel clustering approach: Artificial Bee Colony (ABC) algorithm', *Applied Soft Computing*, vol. 11, no. 1, pp. 652–657, retrieved July 12, 2019, from <https://www.sciencedirect.com/science/article/pii/S1568494609002798>.

Keles, MK & Kilic, U 2018, 'Artificial Bee Colony Algorithm for Feature Selection on SCADI Dataset', in *2018 3rd International Conference on Computer Science and Engineering (UBMK)*, IEEE, pp. 463–466, retrieved July 12, 2019, from <https://ieeexplore.ieee.org/document/8566287/>.

Liu, Y, Ma, L & Yang, G 2017, 'A Survey of Artificial Bee Colony Algorithm', in *2017 IEEE 7th Annual International Conference on CYBER Technology in Automation, Control, and Intelligent Systems (CYBER)*, IEEE, pp. 1510–1515, retrieved July 12, 2019, from <https://ieeexplore.ieee.org/document/8446301/>.

Lozano, M, García-Martínez, C, Rodríguez, FJ & Trujillo, HM 2017, 'Optimizing network attacks by artificial bee colony', *Information Sciences*, vol. 377, pp. 30–50, retrieved July 12, 2019, from <https://www.sciencedirect.com/science/article/pii/S0020025516312075>.

Sun, L, Chen, T & Zhang, Q 2018, 'An Artificial Bee Colony Algorithm with Random Location Updating', *Scientific Programming*, vol. 2018, pp. 1–9, retrieved July 19, 2019, from <https://www.hindawi.com/journals/sp/2018/2767546/>.

Zhu, G & Kwong, S 2010, 'Gbest-guided artificial bee colony algorithm for numerical function optimization', *Applied Mathematics and Computation*, vol. 217, no. 7, pp. 3166–3173, retrieved July 19, 2019, from <https://www.sciencedirect.com/science/article/pii/S0096300310009136>.

CISET - 2nd Cilicia International Symposium on Engineering and Technology
10-12 October, 2019, Mersin / TURKEY

HONEY FORMATION OPTIMIZATION: HFO

Zeki Yetgin [*1] and Mustafa Şamdan [2]

[1] Mersin University, Faculty of Engineering, Department of Computer Engineering, Mersin, Turkey,
zyetgin@mersin.edu.tr

[2] Mersin University, Faculty of Engineering, Information Technologies Research and Application Center, Mersin, Turkey,
msamdan@mersin.edu.tr

ABSTRACT
In this paper, a new optimization algorithm, namely Honey Formation Optimization (HFO), is proposed. In contrary to the Artificial Bee Colony Optimization (ABC) variants in literature, the HFO considers food sources consisting of many components and model the honey formation inside bees as a process of mixing the components with their special enzymes during chewing up the food source. We believe that bees analyse the amounts of components inside the food source and attempt more to collect weaker (less amount) components to improve the honey formation process. Thus, each time a worker exploits a food source it selects a component in such a way that weaker components are more frequently selected. The approach decomposes the solution into components where each component is evaluted by a component fitness function. The honey formula maps the component fitnesses to honey amount and considered as the equivalance of the fitness function. The worker bee uses the fitness of the selected component to evaluate the food source and does local search only around the selected component. The HFO and ABC Algorithms are compared on the basis of 9 benchmark functions. The result shows that HFO performs better than the ABC.

Keywords: *ABC, bee colony algorithm, honey formation, function decomposition*

[*] Corresponding Author

1. INTRODUCTION

Artificial Bee Colony (Karaboga 2005) is inspired by the intelligent behaviour of honey bees. Scout, worker and onlooker bees form a colony and cooperatively search for food source positions. In ABC algorithm, scouts find initial positions of the food sources and then they are converted to workers. Workers exploit these sources and announce the information about them to onlooker bees in hive. Onlooker bees pay more visits to the better food sources and exploit them in the same way as workers do. Exploiting a food source means local search around the source and keeping track of the better food source. ABC algorithm has an increasing popularity in scientific community. It has been applied in solving many problems, such as image enhancement (Chen, Li & Yu 2017), compression(Ismail & Baskaran 2014), motion estimation (Cuevas et al. 2013), network attacks(Lozano et al. 2017), intrusion detection (Aldwairi, Khamayseh & Al-Masri 2015), training neural networks (Karaboga, Akay & Ozturk n.d.), feature selection (Keles & Kilic 2018), clustering(Karaboga & Ozturk 2011), and among many others(Akay & Karaboga 2015; Liu, Ma & Yang 2017; Apalak, Karaboga & Akay 2014; Abro & Mohamad-Saleh 2014; Kang, Li & Ma 2013). In literature, ABC algorithm is initially proposed for optimization of numeric functions (Karaboga 2005). Since then many ABC variants(Karaboga et al. 2014; Jia, Duan & Khan 2015; Huang, Wang & Yang 2016) have been proposed for various type of optimizations such as constrained, multiobjective, continuous and combinatorial design problems. Karaboga and his friends provided a comprehensive survey (Karaboga et al. 2014) that analyses these problems with the focus on ABC drawbacks. According to the survey studies, the great potential of ABC seems very clear with its good exploration capability but also a strong need to alleviate the weakness in exploitation capability (local search).

Majority of the ABC versions in literature focus on the exploit phase (Gao & Liu 2012; Wang, Guo & Liu 2019; Han, Gong & Sun 2015; Shah et al. 2014; Cheng & Jiang 2012; He et al. 2015; Chen, Sarosh & Dong 2012; Kang, Li & Ma 2011),which improve the local search capability of bees (workers or onlookers). The original bees search around the current solution for a random neighbour towards to one of the existing solutions. Some articles(Gao & Liu 2012)(Shah et al. 2014) allow bees to search around the best solution of the current population. Although such approaches enable bees to converge the optimal solution very soon, they increases possibility of local stuck around the near optimal solution. Thus, (Gao & Liu 2012) also improves exploration ability of the scout bees by using chaotic and opposition based initialization(Sun, Chen & Zhang 2018) allows bees to search around a random existing solution for random neighbour towards to current solution, which is quite opposite of the original approach. Authors claim that this approach can expand the search range of new solution and further improve the exploration ability of ABC algorithm.

All the forementioned ABC algorithms assume single component inside a food source and no honey formation inside bees. We considered that the honey formation starts when the bees chew up the food source, e.g. nectar, with their special enzymes and meanwhile they can analyse which components are needed to improve the quality of honey. The HFO Algorithm is actually a framework that can be applied to any ABC algorithms. It requires four major changes from existing ABC versions: i) solution decomposition into components where the component fitness function is composed from the cost function ii) honey formula mapping the component fitnesses to the solution fitness iii) a selection strategy for worker bees to select the weaker component randomly iv) applying local update only to the selected component. No change in onlooker phase is required. However optionaly, instead of using fitness function, honey formula could still be used in onlooker phase. Also when the number of component is one, HFO becomes equal to original ABC algorithm.

The article is organized as follows. Next section provides the original ABC. Third section provides the proposed HFO algorithm. The fourth section provides the experimental results and the last section gives concluding remarks and future directions.

2. ABC ALGORITHM

The basic ABC algorithm requires few parameters, such as the number of food sources denoted as NS, maximum iterations denoted as MaxIter, and the trial limit denoted as limit. As given in Algorithm 1, the ABC algorithm has three phases. In first phase, scout bees randomly explore the food space to find initial food sources, which are the initial solutions denoted as X=(x_1, x_2,…,x_{NS}) and formulated in Eq. (1).

$$x_i(j) = x_{\min(j)} + rand(0,1).\left(x_{\min(j)} + x_{\max(j)}\right) \quad (1)$$

where j is the updating dimension ∈ {1, 2,…,D}, x_{min} and x_{max} are upper and lower bound solutions respectively. Any scout discovering the food source $x_i \in R^D$ becomes a worker bee with its associated food source in its memory. The bees measure the quality of the source x_i using the fitness function, formulated on basis of the cost function *f(x)* in Eq. (2).

$$fitx_i = fitness(x_i) = \begin{cases} 1/(1+f(x_i)), & f(x_i) > 0 \\ 1 + abs(f(x_i)), & f(x_i) \le 0 \end{cases} \quad (2)$$

In second phase, each worker *i* locally updates its food source x_i as a result of randomly searching its neighbourhood for a better solution. This phase is equivalent to local update procedure defined in Eq. (3-4), which forms a candidate $v_i \in R^D$ by updating a randomly selected dimension j of the solution x_i towards one of the existing solution $x_k \neq x_i$ formulated in Eq. (3). The workers replace the source x_i with the candidate v_i if later is better, formulated in Eq. (4). Local update procedure also updates a trial counter. If worker i cannot (update) improve its current solution x_i, the trial counter c_i will be incremented, otherwise the counter is reset to zero.

$$v_i(j) = x_i(j) + rand(-1,1).\left(x_i(j) - x_k(j)\right) \quad (3)$$

$$\begin{cases} x_i = v_i, & c_i = 0, \quad fitv_i > fitx_i \\ c_i = c_i + 1, & fitv_i \leq fitx_i \end{cases} \quad (4)$$

where k ∈ {1, 2, . . . , NS} is the randomly chosen indice and k ≠ i ,j ∈ {1, 2, . . . , D} indicates a random dimension selected to be updated. In third phase, workers announce the information about the food sources such as nectar amount and position by dancing in the hive. Onlooker bees watch the dances of these bees and select a random food source among the sources in such a way that better sources have more chance to be selected.

Algorithm 1. Basic ABC Algorithm (MaxIter, NS, limit): return Best

(1) Generate random NS solutions (Eq. 1)
(2) for iter =1 to MaxIter do
(3) for each worker:
(4) - apply local update procedure to the associated solution of the worker (Eq. 3-4)
(5) P←selection probabilities of solutions proportional to their fitness values(Eq.2, 5)
(6) for each onlookers:
(7) - select a random solution according to selection probability P
(8) - apply local update procedure to it (Eq. 3-4)
(9) for each scouts:
(10) - replace the associated solution with a random solution if the solution is not I updated for limit iteration (Eq. 1)
(11) keep track of Best solution so far

The selection probabilities, P = (p_1, p_2,…,p_{NS}), are formulated in Eq. (5) where p_i is the selection probability of the source x_i.

$$p_i = \frac{fitx_i}{\sum_{k=1}^{NS} fitx_k} \quad (5)$$

Then, they exploit their food sources in the same fashion as workers do (local update procedure). Thus, onlookers mostly gather around globally better solutions to make global improvements. All bees keep track of the best food sources during searching for the sources. Any bee that cannot exploit its food source (improve its solution) within some trial limit becomes scout again and finds a random food source throughout the space. The algorithm repeats worker-onlooker-scout phases until the maximum cycles are completed. When algorithm terminates one of the bees in current population is expected to have the best food source in its memory.

3. HFO ALGORITHM

The proposed HFO algorithm is given in Algorithm 2 below. HFO generalizes the ABC algorithm where single component assumption equalizes the both. The main difference is that the HFO assumes food sources each consisting of K components and worker bees attempting more to search for components that are needed according to current honey form inside bees. Every food source x_i has its own honey form produced from it. Thus, the food source and its honey form are associated.

Algorithm 2. HFO Algorithm (MaxIter, NS, limit, K): return Best

(1) Generate random NS solutions (Eq.1)
(2) for iter =1 to MaxIter do
(3) for each worker:
(4) - P ← selection probabilities of components in current solution, inversely proportional to their component fitnesses (Eq. 8)
(5) - select a random component according to selection probability P
(6) - apply local update procedure to the selected component (Eq. 9-10)
(7) P← selection probabilities of solutions, proportional to their fitnesses (Eq. 5, 12)
(8) for each onlookers:
(9) - select a random solution according to selection probability P
(10) - apply local update procedure (Eq. 3, 11)
(11) for each scouts:
(12) - replace the associated solution with a random solution if the solution is not updated for limit iteration (Eq.1)
(13) keep track of Best solution so far

The honey form or equivalently the food source is considered as a solution and the components of the food source are sub solutions. The HFO finally finds the source that produce the best honey form. HFO uses cost-based approach : instead of using fitness, cost values are used whenever two solutions or components are compared. This is due to floating-point precision issue in implementations. The HFO requires to desing two concept: i) solution decomposition: component design where *c.* component of solution x_i is denoted as ${x_i}^c$ ii) fitness function decomposition on components: component fitness design where the fitness of the component ${x_i}^c$ is denoted as ${fitx_i}^c$ while its cost is denoted as $f({x_i}^c)$

One major form of solution decomposition is given in Eq. (6) where a solution $x_i \in R^D$ is partitioned into K non-overlapping sub solutions, causing a shift from the space R^D to $R^{D/K}$, with D/K as the dimension of components. Components are seperated by pipe symbols in Eq. (6) just for visualization.

$$x_i = \left[\underline{x_{i1}}^1, \underline{x_{i2}}^1, \ldots \underline{x_{i(D/K)}}^1 \,\middle|\, \underline{x_{i(D/K+1)}}^2, \underline{x_{i(D/K+2)}}^2 \ldots \underline{x_{i(2D/K)}}^2 \,\middle|\, \ldots . \right]$$
$$= \left[{x_i}^1 \,\middle|\, {x_i}^2 \,\middle|\, \ldots \right] \quad (6)$$

Among many forms of solution decomposition, following shows an overlapping form of components where half of each component is overlapped with the neighbour components.

$$x_i = [\ \underline{\quad x_i^1 \quad}\ \ \underline{\quad x_i^2 \quad}\ \ \underline{\quad x_i^3 \quad}, \ldots] \quad (7)$$

The solution should be decomposed into components in such a way that the honey formula can bind the component fitnesses to the original fitness function. Honey formula should be designed in such a

way that better component should produce better honey (solution) for any component.

According to HFO, the worker *i* evaluates the components of x_i and more probably modify (local update) the weaker component due to the fact that the component in less amount are more vital and more needed to improve the current honey form. Let ${x_i}^c \subseteq x_i$ be the *c*. component of x_i.The selection probability of component *c* for the worker *i*, denoted as P_i^c, is inversely proportional to its fitness, formulated in Eq. (8) where the component cost $f({x_i}^c) = cost{x_i}^c$ naturally measures the inverse fitness of the component *c* of x_i.

$$P_i^c = \begin{Bmatrix} \frac{f({x_i}^c)+1}{\sum_{j=1}^{K}(f({x_i}^j)+1)} \; if\; f(x)\; is\; in\; positive\; domain \\ \\ \frac{f({x_i}^c)-min_{k=1..K}\;(f({x_i}^k))+1}{\sum_{j=1}^{K}(f({x_i}^j)-min_{k=1..K}\;(f({x_i}^k))+1)} \quad otherwise \end{Bmatrix} \quad (8)$$

The local update procedure for worker bees is applied on component basis, which is formulated in Eq. (9-10) where *c* is the selected component and *j* is the updating dimension of the component *c* during local search around x_i. Note that the proposed local update procedure can be applied to any ABC variant not limited to Eq. (9-10). The idea here is the workers modifies the selected component according to their local search strategies.

$${v_i}^c(j) = {x_i}^c(j) + rand(-1,1).\left({x_i}^c(j) - {x_k}^c(j)\right) \quad (9)$$

$$\begin{Bmatrix} x_i = v_i, c_i = 0, & f(v_i{}^c) < f(x_i{}^c) \\ c_i = c_i + 1, & otherwise \end{Bmatrix} \quad (10)$$

When comparing two solutions x_i and v_i in onlooker phase, we also prefer to use cost function rather than fitness function since the fitness definition in original ABC may cause implementation issue related to infinite precision requirement at the term 1/(1+cost). Thus, the local update procedure for onlooker is modified using Eq. (11) as follows

$$\begin{Bmatrix} x_i = v_i, c_i = 0, & F(v_i) < F(x_i) \\ c_i = c_i + 1, & otherwise \end{Bmatrix} \quad (11)$$

where the $F(x)$ is the cost form of honey formula, formulated in Eq.(12). Honey formula F(x) is an approximation to the original cost function f(x) or must have equivalence relation with the f(x). Honey formula benefits from the cost function decomposition in that the cost function could be expressed in terms of component costs.

$$F(x_i) = \sum_{c=1}^{K} f({x_i}^c) \cong f(x_i) \quad (12)$$

One other advantage of using F(x) is that the solution cost is computed using the component cost values $f({x_i}^c)$ that are already computed during local update procedure. This reduces the complexity of HFO. The cost function approximation using the summation of component cost values are one form of honey formula, among many others.

The fitness form of honey formula $F_{fit}(x_i)$ is given in Eq.(13) that is only used in Eq.(14) to compute the selection probabilities p_i of solutions for onlookers. $F_{fit}(x_i)$ is also an approximation to the $fitx_i$.

$$F_{fit}(x_i) = \begin{Bmatrix} \frac{1}{F(x_i)+1} & if\; f(x)\; in\; positive\; domain \\ \frac{1}{F(x_i)-\min_{k=1..NS} F(x_k)+1} & otherwise \end{Bmatrix} \quad (13)$$

$$p_i = \frac{F_{fit}(x_i)}{\sum_{k=1}^{NS} F_{fit}(x_k)} \quad (14)$$

HFO does not require any change in onlooker bees except using cost function f(x) when comparing two solutions. However, the approximated version of cost function F(x) could optionally be used to benefit from cost function decomposition. Cost functions could not be easily decomposed into component cost functions. Some cost functions are seperable and easily expressed in terms of component costs. Thus, one can consider cost function approximation if it allows cost function decomposition on components.

3.1. Component Design

The component cost functions $f({x_i}^c)$ and component itself ${x_i}^c$ must be considered together in design. Component design is problem specific and must be done for each benchmark functions. Here we propose some design strategies for component and its cost functions. Let the cost function f(x) expressed as f(x) = g(x) + h(x) and $\boldsymbol{g(x)} = \sum_i term1(x_i)$ and $\boldsymbol{h(x)} = \sum_i term2(x_i)$ then

1.form: if g(x)≥0, h(x)≥0, g(x)>>h(x) then ${x_i}^c$ is non-overlapped and partition on g(x) as follows:
$f({x_i}^c) = g({x_i}^c) + h(x)/K$

2.form: if g(x)≥0, h(x)≥0, g(x) and h(x) comparable (approximately in the same range) then ${x_i}^c$ is non-overlapped and partition on f(x) as follows :
$f({x_i}^c) = g({x_i}^c) + h({x_i}^c)$

3.form: if *term1* or *term2* is a function of both x_i and x_{i+1} then ${x_i}^c$ is overlapped one element with the neighbour component (last element repeats only in the last component to equalize the number of elements in all components) and partition on f(x).

4.form: if f(x) changes sign depending on x or seems hard to partition then ${x_i}^c$ is non-overlapped and try partitioning on f(x).

Note: partitioning on f(x) means applying the original cost function f directly to the sub-solution ${x_i}^c$, thus no need to express the f(x) as g(x) + h(x).

4. EXPERIMENTAL RESULTS

ABC and HFO algorithms are compared based on 9 benchmark functions given in Table 1. The benchmark functions have different characteristics such as multimodal and non-convex (Ackley, Qing, Egg-Crate, Xin-She Yan, Rosenbrock), multimodal and convex(Rastrigin), unimodal and non-convex(Griewank), unimodal and convex(Brown, Sphere). The functions are tested for the maximum number of iterations *MaxIter = 5000*, the number of food sources *NS=60*, the problem dimension *D=50*, and the parameter *limit=NS×D* and

the number of components *K=10* for HFO.

Table 2. Typical benchmark functions

Name	Function	Range	Min
Ackley	$f_1 = -20exp(-0.2\sqrt{\frac{1}{n}\sum_{i=1}^{n} x_i^2}) - exp(\frac{1}{n}\sum_{i=1}^{n} cos(2\pi x_i)) + 20 + e$	(−32.768, 32.768)	0
Brown	$f_2 = \sum_{i=1}^{n-1} (x_i^2)^{(x_{i+1}^2+1)} + (x_{i+1}^2)^{(x_i^2+1)}$	(−4, 4)	0
Griewank	$f_3 = 1 + \sum_{i=1}^{n} \frac{x_i^2}{4000} - \prod_{i=1}^{n} cos(\frac{x_i}{\sqrt{i}})$	(−600, 600)	0
Qing	$f_4 = \sum_{i=1}^{n} (x_i^2 - i)^2$	(−10,10)	0
Rastrigin*	$f_5 = 10n + \sum_{i=1}^{n} (x_i^2 - 10cos(2\pi x_i))$	(-5.12, 5.12)	0
Sphere	$f_6 = \sum_{i=1}^{n} x_i^2$	(−100, 100)	0
Egg Crate	$f_7 = \sum_{i=1}^{n} x_i^2 + 25 \sum_{i=1}^{n} sin^2(x_i)$	(−500, 500)	0
Xin-SheYan	$f_8 = \left(\sum_{i=1}^{n} sin^2(x_i) - e^{-\sum_{i=1}^{n} x_i^2}\right) e^{-\sum_{i=1}^{n} sin^2\sqrt{\lvert x_i \rvert}}$	(−10,10)	-1
Rosenbrock	$f_9 = \sum_{i=1}^{n-1} [100(x_{i+1} - x_i^2)^2 + (1 - x_i)^2]$	(−50, 50)	0

However with this limit setting, the Rastrigin function is reached to global min zero for both ABC and HFO, thus the *limit = 0.1xNS x D* is considered only for Rastrigin function. The colony has equal number of worker bees and onlooker bees, considered equal to NS. Each experiment for the same parameter settings repeated 20 times and the average values are used to compute the performance metrics, such as min, max and mean of cost function values. The component desing for each benchmark functions are provided in Table 3 where the details of component desing is given in previous section.

The experimental results are provided in Table 4 and Figs. 1-9 where tables demonstrate the comparison of the objective performances with achieved min, max and mean cost values and figures show the evolution curves of ABC and HFO. The Table 4 clearly shows that HFO is superior to original ABC for all functions. Particularly, for unimodal and convex problems the HFO performs best. However, for many difficult functions such as Rosenbrock, Egg-Crate,and Xin-She Yan that are multimodal and non-convex the HFO also performs good. The evolution curves of mean cost values across the iterations are given in Figs. 1-9.

Table 3. Component desing for bencmark functions

Objective Functions	Component Overlapped	Component Cost Function Form#	Partition on g(x) or f(x)
Ackley	No	2	f(x)
Brown	Yes(1 element)	3	f(x)
Griewank	No	1	g(x)= $\sum_{i=1}^{n} \frac{x_i^2}{4000}$
Qing	No	2	f(x)
Rastrigin*	No	2	f(x)
Sphere	No	2	f(x)
EggCrate	No	1	g(x)= $\sum_{i=1}^{n} x_i^2$
Xin-SheYang	No	4	f(x)
Rosenbrock	Yes(1 element)	3	f(x)

Table 4.Performance comparison : ABC versus HFO

Objective Functions	ABC			HFO		
	Best	Mean	Worst	Best	Mean	Worst
Ackley	5.06e-14	6.32e-14	6.84e-14	7.99e-15	**7.99e-15**	7.99e-15
Brown	7.48e-16	9.59e-16	1.21e-15	9.42e-48	**3.22e-47**	1.10e-46
Griewank	0	9.44e-17	1.11e-16	0	**0**	0
Qing	9.59e-16	2.68e-15	1.29e-14	2.33e-17	**7.06e-16**	7.16e-15
Rastrigin*	0	2.27e-14	1.14e-13	0	**0**	0
Sphere	7.67e-16	9.45e-16	1.14e-15	2.81e-44	**1.67e-43**	4.10e-43
EggCrate	6.53e-16	7.95e-16	9.86e-16	1.13e-34	**5.80e-34**	2.74e-34
Xin-SheYang	7.66e-17	9.73e-17	1.11e-16	3.50e-37	**5.64e-33**	3.14e-32
Rosenbrock	0.52e-02	0.17	0.82	2.17e-06	**1.16e-05**	4.38e-05

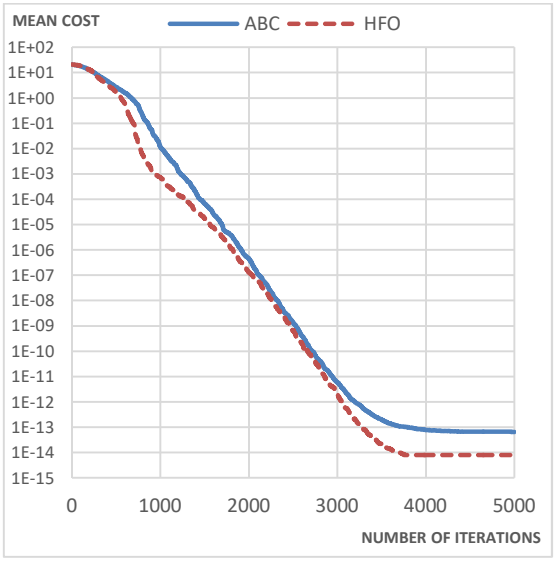

Fig. 1. Evolution curves for Ackley

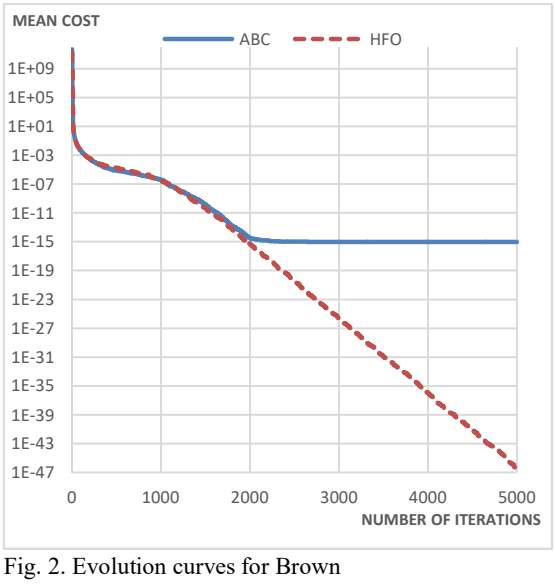

Fig. 2. Evolution curves for Brown

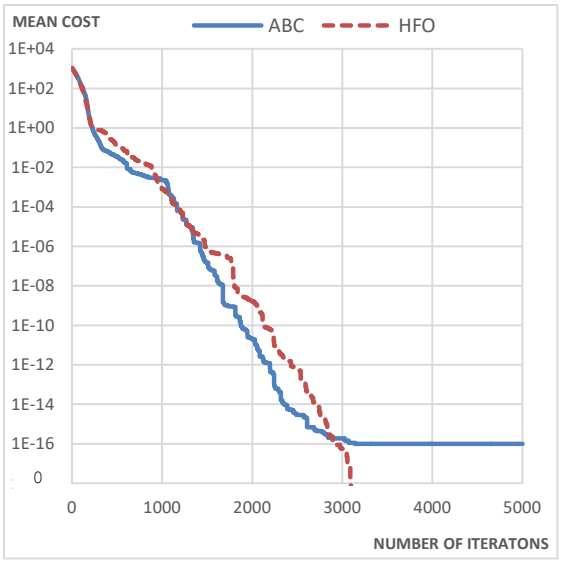

Fig. 3. Evolution curves for Griewank

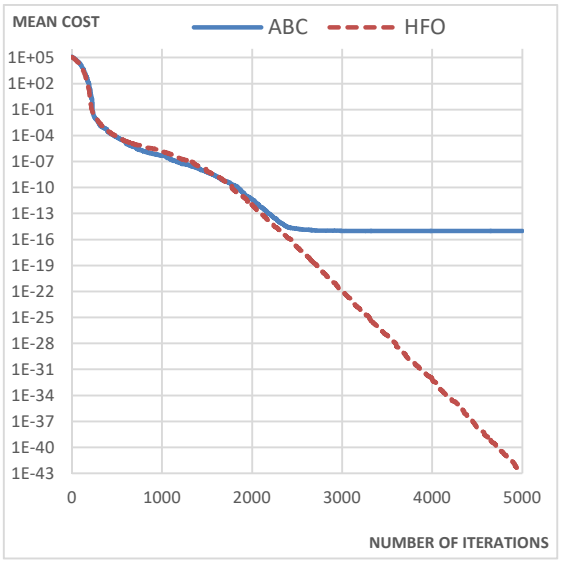

Fig. 6. Evolution curves for Sphere

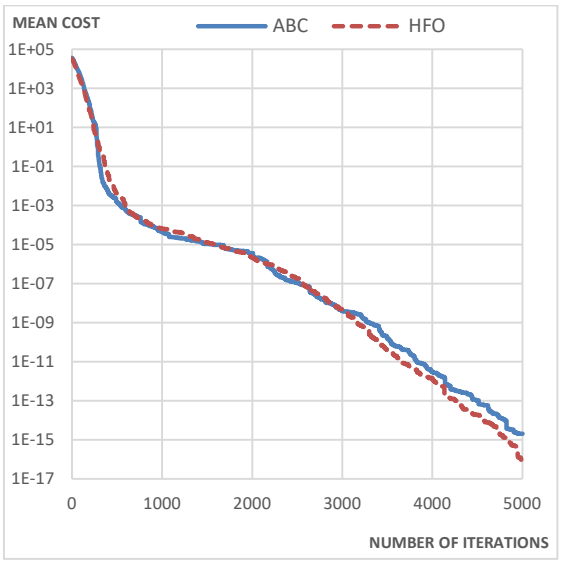

Fig. 4. Evolution curves for Qing

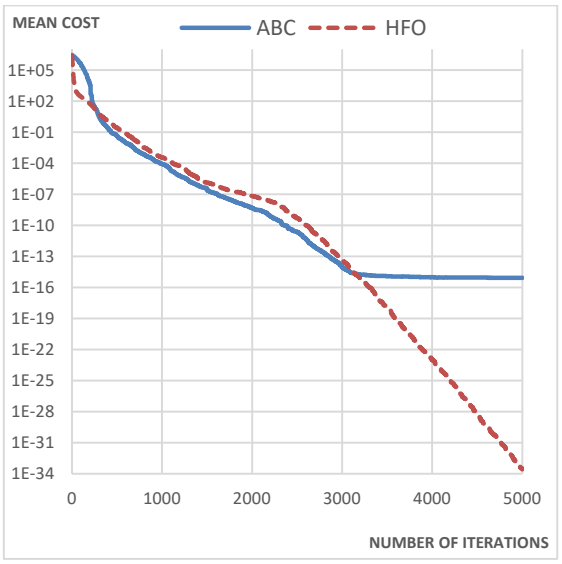

Fig. 7. Evolution curves for Egg Crate

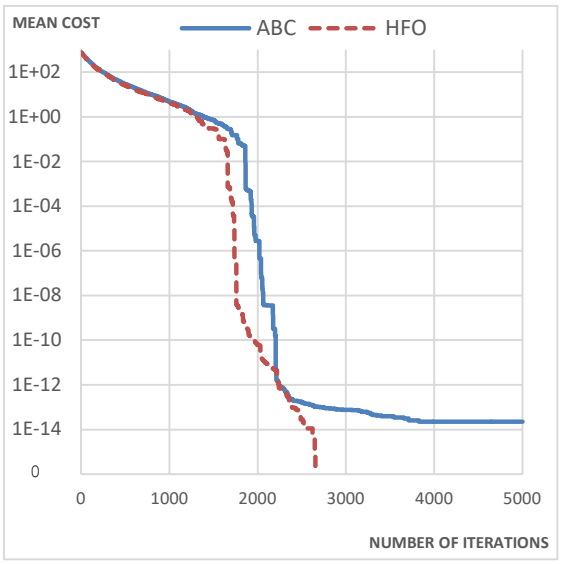

Fig. 5. Evolution curves for Rastrigin

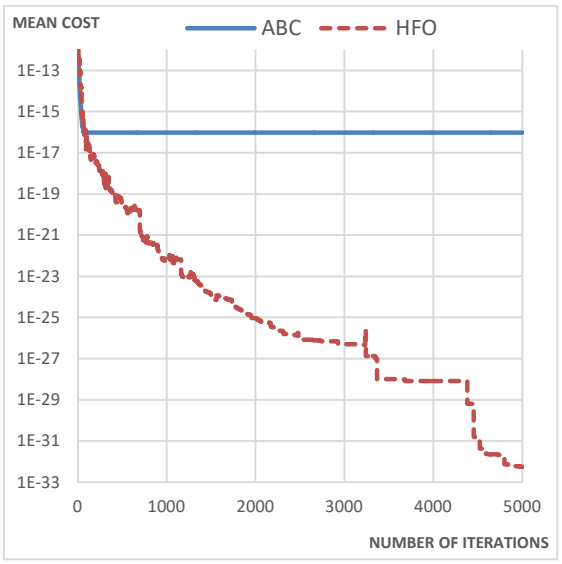

Fig. 8. Evolution curves for Xin-SheYang

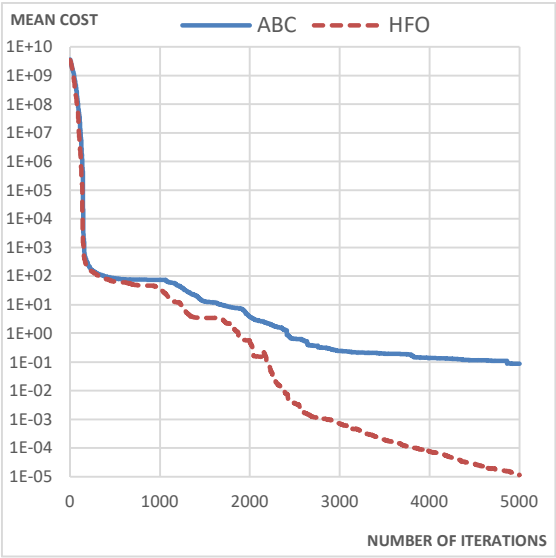

Fig. 9. Evolution curves for Rosenbrock

The figures clearly show that the HFO converge speed is also better than ABC. The ABC sometimes converge to a mean cost value around 1.0e-16 due to the limitation of floating-point implementation. However, the HFO can converge to global minimum at much wider precision.

5. CONCLUSION

In this article, a new optimization algorithm namely Honey Formation Optimization (HFO) is introduced. HFO extends the Artificial Bee Colony Algorithm by considering multiple components in food sources and worker bees searching more frequently for the components in less amount due to fact that the component in less amount more limits the honey formation process and thus more vital for worker bees. For single component assumption, HFO and ABC become equal. The proposed optimization is a framework that could be applied to any ABC variant. It doesn't propose to change the behaviours of onlooker bees but only propose to apply the local update procedure (local search phase) of existing ABC variants onto the selected component. The components are considered as sub solutions and honey formation process mix up the components towards better honey fitness. Although the theoretical framework ABC has no problem, it suffers from infinite-precision requirement of fitness function. Thus, the local update procedure of HFO uses cost functions rather than the fitness in implementation. The experimental results demonstrates that HFO can performs better and converge earlier than the ABC. However, HFO uses honey formula that requires design for both solution decomposition and cost function decomposition together. Thus, some functions are difficult or even impossible to decompose perfectly. In such cases new approaches are required to partition functions on the basis of component design.

6. REFERENCES

Abro, AG & Mohamad-Saleh, J (2014), "Enhanced probability-selection artificial bee colony algorithm for economic load dispatch: A comprehensive analysis", *Engineering Optimization*, Vol. 46, No. 10, pp. 1315–1330.

Akay, B & Karaboga, D (2015), "A survey on the applications of artificial bee colony in signal, image, and video processing", *Signal, Image and Video Processing*, vol. 9, pp. 967–990.

Aldwairi, M, Khamayseh, Y & Al-Masri, M (2015), "Application of artificial bee colony for intrusion detection systems", *Security and Communication Networks*, Vol. 8, No. 16, pp. 2730–2740.

Apalak, MK, Karaboga, D & Akay, B (2014), "The Artificial Bee Colony algorithm in layer optimization for the maximum fundamental frequency of symmetrical laminated composite plates", *Engineering Optimization*, Vol. 46, No. 3, pp. 420–437.

Chen, J, Li, C & Yu, W (2017), "Adaptive Image Enhancement Based on Artificial Bee Colony Algorithm", *in Proceedings of the International Conference on Communication and Electronic Information Engineering (CEIE 2016)*, Atlantis Press, Paris, France.

Chen, S-M, Sarosh, A & Dong, Y-F (2012), "Simulated annealing based artificial bee colony algorithm for global numerical optimization", *Applied Mathematics and Computation*, Vol. 219, No. 8, pp. 3575–3589.

Cheng, X & Jiang, M (2012), "An Improved Artificial Bee Colony Algorithm Based on Gaussian Mutation and Chaos Disturbance", *in Springer*, Berlin, Heidelberg, pp. 326–333.

Cuevas, E, Zaldívar, D, Pérez-Cisneros, M, Sossa, H & Osuna, V (2013), "Block matching algorithm for motion estimation based on Artificial Bee Colony (ABC) ", *Applied Soft Computing*, Vol. 13, No. 6, pp. 3047–3059.
Gao, W & Liu, S (2012), "A modified artificial bee colony algorithm", *Computers & Operations Research*, Vol. 39, No. 3, pp. 687–697.

Han, YY, Gong, D & Sun, X (2015), "A discrete artificial bee colony algorithm incorporating differential evolution for the flow-shop scheduling problem with blocking", *Engineering Optimization*, Vol. 47, No. 7, pp. 927–946.

He, X, Wang, W, Jiang, J & Xu, L (2015), "An Improved Artificial Bee Colony Algorithm and Its Application to Multi-Objective Optimal Power Flow", *Energies*, Vol. 8, No. 4, pp. 2412–2437.

Huang, F, Wang, L & Yang, C (2016), "A new improved artificial bee colony algorithm for ship hull form optimization", *Engineering Optimization*, Vol. 48, No. 4, pp. 672–686.

Ismail, MM & Baskaran, K (2014), "Hybrid Lifting Based Image Compression Scheme Using Particle Swarm Optimization Algorithm and Artifical Bee Colony Algorithm",.

Jia, D, Duan, X & Khan, MK (2015), "Modified artificial bee colony optimization with block perturbation strategy", *Engineering Optimization*, Vol. 47, No. 5, pp. 642–655.

Kang, F, Li, J & Ma, Z (2011), "Rosenbrock artificial bee colony algorithm for accurate global optimization of numerical functions", *Information Sciences*, Vol. 181, No. 16, pp. 3508–3531.

Kang, F, Li, J & Ma, Z (2013), "An artificial bee colony algorithm for locating the critical slip surface in slope stability analysis", *Engineering Optimization*, Vol. 45, No. 2, pp. 207–223.

Karaboga, D (2005), "An idea based on Honey Bee Swarm for Numerical Optimization", technical report-tr06, Erciyes university, engineering faculty, computer engineering department, vol. 200, pp. 1-10.

Karaboga, D, Akay, B & Ozturk, C "Artificial Bee Colony (ABC) Optimization Algorithm for Training Feed-Forward Neural Networks", *in Modeling Decisions for Artificial Intelligence*, Springer Berlin Heidelberg, Berlin, Heidelberg, pp. 318–329.

Karaboga, D, Gorkemli, B, Ozturk, C & Karaboga, N 2014, "A comprehensive survey: Artificial bee colony (ABC) algorithm and applications", *Artificial Intelligence Review*, Vol. 42, No. 1, pp. 21–57.

Karaboga, D & Ozturk, C (2011), "A novel clustering approach: Artificial Bee Colony (ABC) algorithm", *Applied Soft Computing*, Vol. 11, No. 1, pp. 652–657.

Keles, MK & Kilic, U (2018), "Artificial Bee Colony Algorithm for Feature Selection on SCADI Dataset", *in 2018 3rd International Conference on Computer Science and Engineering (UBMK)*, IEEE, pp. 463–466.

Liu, Y, Ma, L & Yang, G (2017), "A Survey of Artificial Bee Colony Algorithm", *in 2017 IEEE 7th Annual International Conference on CYBER Technology in Automation, Control, and Intelligent Systems (CYBER)*, IEEE, pp. 1510–1515.

Lozano, M, García-Martínez, C, Rodríguez, FJ & Trujillo, HM 2017, "Optimizing network attacks by artificial bee colony", *Information Sciences*, Vol. 377, pp. 30–50.

Shah, H, Herawan, T, Naseem, R & Ghazali, R (2014), "Hybrid guided artificial bee colony algorithm for numerical function optimization", *Lecture Notes in Computer Science (including subseries Lecture Notes in Artificial Intelligence and Lecture Notes in Bioinformatics)*, Vol. 8794, No. 7, pp. 197–206.

Sun, L, Chen, T & Zhang, Q (2018), "An Artificial Bee Colony Algorithm with Random Location Updating", Scientific Programming, Vol. 2018, pp. 1–9.

Wang, S, Guo, X & Liu, J (2019), "An efficient hybrid artificial bee colony algorithm for disassembly line balancing problem with sequence-dependent part removal times", *Engineering Optimization*, pp. 1–18.

CISET - 2nd Cilicia International Symposium on Engineering and Technology
10-12 October, 2019, Mersin / TURKEY

MODELING OF HISTORICAL FOUNTAINS BY USING CLOSE-RANGE PHOTOGRAMMETRIC TECHNIQUES

Ali Ulvi [*1], Abdurahman Yasin Yiğit [2] and Murat Yakar [3]

[1] Selcuk University, Hadim Locational High School, Architecture And City Planning, Konya, Turkey, aliulvi@selcuk.edu.tr
[2] Geomatic Engineering, Turkey, abdurahmanyasinyigit@gmail.com
[3] Mersin University, Faculty of Engineering, Geomatic Engineering, Mersin, Turkey, myakar@mersin.edu.tr

ABSTRACT
It is inevitable to see historical monuments in every geography where man exists. Most of the architectural monuments that have witnessed history have been completely or partially destroyed for different reasons. Especially natural disasters such as earthquakes, floods, and fires, as well as wars, misuse and unconscious use cause these damages. Architectural monuments bearing the traces of history are one of the most important means of transferring history to future generations. The preservation and transfer of this cultural heritage to new generations are one of the common tasks of all peoples in the world. In this context, with the developing technology, efforts to document the cultural heritage in the digital platform in 3D have accelerated. There are many 3D modeling methods in the literature. Photogrammetry technique, which is one of the 3D modeling methods, enables us to create photo-realistic models. The photogrammetry technique gives more meaningful results in terms of speed and accuracy compared to traditional methods. This study involves the production and documentation of a 3D model of historical fountains by using close-range photogrammetry.

Keywords: *Historical artifacts, Photogrammetry, Close-Range photogrammetry, Documentation, 3D Model*

[*] Corresponding Author

1. INTRODUCTION

Historical artifacts are a cultural heritage that includes all experiences from past to present. Cultural heritage is a historical monument with certain criteria (witnessing a different tradition, the product of creative human genius, representing one or more, etc.), that are protected and transmitted for the benefit of future generations (URL1). Cultural heritages represent the bond between people from the past to the present and to the future. Cultural heritage reflects the history and essence of humanity and ensures the continuity of traditions and diversity. Cultural heritage can contain many concepts. A cultural heritage that reflects the dusty pages of history can be grouped under 3 main headings: concrete, abstract and natural cultural heritage.

Tangible Cultural Assets: It is divided into two groups as movable and immovable heritage. Monuments, sculptures, paintings, archaeological works, inscriptions, books, landscapes and so on.

Intangible Cultural Assets: Folklore, traditions, language, oral history, etc.

Natural Heritage: Culturally important landscapes and biodiversity (URL2.

2. THE IMPORTANCE OF DOCUMENTATION OF HISTORICAL ARTEFACTS

Ever since humanity began to play a role in the history scene, artifacts that trace of history in every geography has emerged. There are any more historical monuments, especially in areas where access to minimum living requirements and opportunities (food, housing, education, etc.) is easy. Therefore, as the cradle of civilizations, there are many cultural and historical heritages on Anatolian lands. Documentation and preservation of cultural assets that have hundreds of years of knowledge of many peoples and which must be hand down the next generations are indispensable (Uslu et al, 2016). Throughout history, due to the, and natural richness it has housed, different communities have existed in Anatolia. In Today's in the Republic of Turkey (Anatolia Region) at the end of the year 2018, by The Ministry of Culture and Tourism 108813 units, the immovable asset was registered as a cultural asset.

Table 1. 2018 year-end distribution of immovable cultural assets located in Turkey (URL3)

The registered immovable cultural property in Turkey	Real estate count
Example of Civil Architecture	69.104
Religious Structures	10.147
Cultural Structures	12.53
Administrative Structures	2.985
Military Structures	1.252
Industrial and Commercial Structures	4.171
Cemeteries	5.169
Martyrdoms	307
Monuments And Landmarks	375
Ruins	2.702
Streets Protected	71

Destruction of cultural heritage due to natural disasters or human factors, making recompenses as a result of damage, knowing where they belong to the missed works, preserving their original features and keeping them back in their original places is very important (Demirkesen et al, 2005). It is possible to transfer historical works including all phases of history and giving us any clues about history to future generations through healthy documentation. Documentation of historical or cultural structure covers the entire steps which are necessary for determining the current state of the structure (shape and position) in three-dimensional space that are surveys, process, storage and presentation (Georgopoulos and Ioannidis, 2004).

3. DOCUMENTATION METHODS

Documentation can be defined as the determination of the current status of cultural assets in different scales and qualities (drawings, plans or other graphic narration, photographs, digitized documents, etc.). Information about the state of the structure or area at the time of study and the documentation stage at which the document is produced form the basis of the whole process. Today, different techniques are used in the documentation of cultural heritage and this issue is developing rapidly in parallel with technological developments. In addition to producing information on various physical, social, economic, cultural and historical aspects of cultural assets in different qualities and scales, processing and converting the produced data into usable information is an indispensable requirement for protection. General documentation techniques are shown in figure 1 (Pakben, 2013).

Fig. 1. General documentation techniques

3.1. Documentation Method with Photography

Photography is a means of communication. The rules for detecting messages also apply to the detection of a photo. It is natural for people living in different cultures to perceive the same message differently. Especially the indicators with symbolic meanings have different meanings according to cultural characteristics (Bodur, 2006).

As a visual text, the product photo should be able to identify the product correctly and effectively. The effective use of photography forms the basis of visual communication (Grill and Scanlon, 2003). The purpose of documentation with the photograph is completed by taking a large number of photographs from general photographs of buildings (facades, building environment, etc.) to detailed photographs (interior and exterior photographs).

3.2. Documentation Method by Using Video

It is possible to document structures with video shooting. The surroundings, facades, and interiors of the building are visited and recorded. During this recording, shooting should be performed with an as little shake and heavy motion as possible. Thus, the details of the structure can be seen clearly in the video.

3.3. Classical Documentation Methods

The idea of protecting cultural heritage has emerged for the measures taken for the protection, renovation, and restoration of historical monuments. With the development of technology, the techniques used to document historical artifacts for many years started to be known under the name of classical techniques.

•Linear Documentation
•Written Documentation
•Graphic Documentation
•Information Sheet

Classical documentation techniques are can be collected under the above headings.

3.4. Modern Documentation Methods

Modern documentation techniques are frequently preferred by different disciplines when traditional methods are inadequate in the documentation of historical monuments. Particularly facade silhouettes, building decorations, 3D documentation on digital platform and so on. It would be more accurate to use modern methods for their work.

Modern documentation methods are divided into photogrammetry and laser scanning. In our study, the close-range photogrammetry method, which is one of the photogrammetric methods, was preferred.

3.4.1. Documentation with close-range photogrammetry method

Photogrammetry is a successful documentation method that especially has accuracy, flexibility, and practicality. As an indispensable part of restoration projects, drawings related to the current situation (detection drawings) can be obtained by the photogrammetric method accurately and reliably in a short time. Also, with this method, analytical documentation (materials, distortions, authenticity, etc.) can also be used for studies.

The close-range photogrammetry technique has been used for archaeological surveys and documentation of historical monuments for many years. With the development of digital techniques, photogrammetry has become a more efficient and economical method for the documentation and preservation of architectural works. In recent years, as a result of developments in digital photogrammetry and computer technology, the creation of a 3D model of buildings has been among the current research topics. 3D building models are becoming increasingly compulsory for urban planning and tourism. (Suveg and Vosselman, 2000).

The 3D photo modeling used in this study is very effective in understanding terrestrial objects that are actually inaccessible. The use of photo models from existing objects facilitates the understanding of complex terrestrial structures (Dorffner and Forkert, 1998).

4. MATERIALS AND METHODS

Nikon D3100 camera (fig. 3), Cygnus Topcon KS-102 non-reflector total-station (fig. 2), and PhotoModeler UAS software, which enables 3D drawing and point cloud production from photographs, are used as the hardware.

Fig. 2. Cygnus topcon ks-102 total-station

Fig. 3. Nikon D3100 photograph cameras (URL4)

Table 2. Nikon D3100 Technicial Specifications

Sensor size	23,1 x 15,4 mm
Total megapixels	14.80
Max. image resolution	4608 x 3072
Weight	505 g
Dimensions	124 x 96 x 75 mm
Pixel density	3,99 MP / cm²

Planned geodetic measurement and photographing should be performed in order to make 3D modeling with the digital photogrammetric method. For geodetic measurement of the control points on ancient artifacts to be used in the photogrammetric evaluation, a geodetic network that covers the object completely in all aspects should be established primarily in such terrestrial photogrammetric and modeling studies.

In this context, a geodetic network has been established in the local coordinate system to cover the historical structure completely from all directions. In selecting the control points where the measuring device will be installed, the locations that will see the structure fully are preferred. Considering the physical properties of the surface of the structure, attention was paid to the selection of sharp lines and clear control points (Uysal et al, 2015).

The stage of taking photographs of the historical fountain was made from different angles according to the convergent shooting principles, taking into account

that at least four photographs were included for each detail point. The photographs were taken from different angles on the days and times when the structure and weather were suitable. With the double-image photogrammetry method, each photograph is overlapped with other photographs with common target points and is referenced to each other. There were no situations in front of the building that would prevent the building or any part of the building.

5. STUDY AREA

Fig. 4. Study area and Sultan Water Fountain

Taşkent is a small town situated on the Göksu valley canyons on the Taşeli Plateau in the Middle Taurus Mountains. 135 km of Konya province about 100 km south of the Mediterranean coast away, located in the Mediterranean region. Sultan Water Fountain N 36 ° 55'17.5 "E 32 ° 29'25.7" is located in the coordinates (URL5).

Information on Sultan Suyu Fountain from the 110th page of the journal "Mecmuatül Tevarî-Ül Mevleviye", which was published in 1203 in the form of the official newspaper of the time, found in the Directorate of Konya Antiquities Museum (URL 6) is available. Also information from local residents is available. According to this information, the first state of the fountain was made during the Anatolian Seljuk Sultan Alaeddin Keykubad (1192-1237). Later, in 1982, it was learned that the single-arched section in the middle of the fountain was built and in 1998 the present state was made.

6. APPLICATION OF PHOTOGRAMMETRY IN ARCHITECTURAL STUDIES

Data processing in the photogrametry consists of coordinate calculations and generating a 3D model. Coordinates of points are calculated in a local system with surveying and leveling. Basically, all detail points of the structure measured with Total Station equipment are transferred to the computer. In Netcad software, the 3D coordinates of the point are calculated. In the fieldwork some surveys are made for controlling the detail points as the same detail point is observed from different polygon points. At the end of all calculations and controls, the coordinates of points are saved in .txt format. Camera calibration parameters of the Canon D3100 camera are calculated in PhotoModeler software and saved as a .cam format. For absolute orientation, the .txt and .cam files are used (Uysal et al., 2013).

Checkpoints that appear in two or more images are marked because the PhotoModeler software performs mutual and absolute orientation at the same time (Yastıklı, 2013). After marking the control points, a photograph was selected as a reference and matching of each control point was shown in the other marked photos.

After that, the orientation process was done according to the bundle method in PhotoModeler software. The orientation results using 45 photographs are shown in figure 5.

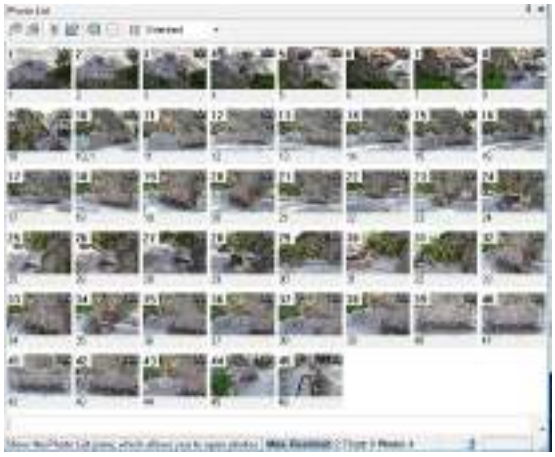

Fig. 5. The result of the orientation

After the orientation process, 3D model production was started.First, the details of the pairs of the same detail were drawn (fig.6-7) and the skeleton of the fountain was completed (fig.8).

Fig. 6. Detail drawing

Fig. 7. Detail drawing

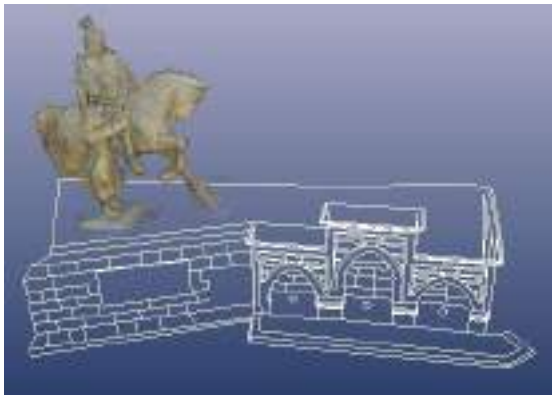

Fig. 8. The basic skeleton of the Sultan Water Fountain

Afterward, texture coating was performed on the basic skeleton (fig.9).

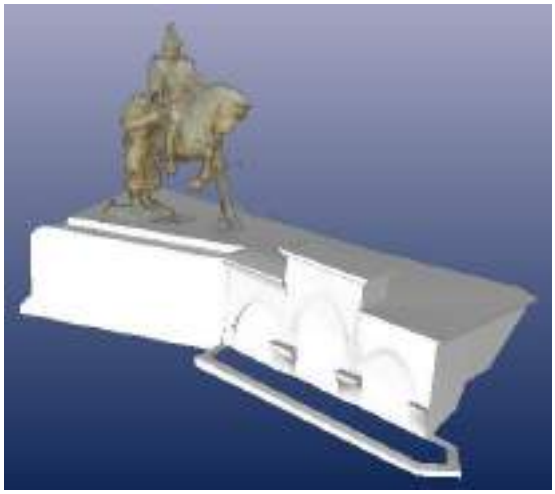

Fig. 9. The 3D shaded model

As a result of all processes, a 3D model of the historical Sultan fountain was produced on the digital platform and the documentation work was completed (fig.10).

Fig. 10. 3D model of the Sultan Water Fountain

7. CONCLUSİONS

The use of advanced technologies in the documentation of historical and cultural heritage is necessary to achieve accurate and high precision and fast and effective results. The vector study is not always sufficient to document the details of the historical monument and to collect all the details of the structure. Advanced documentation techniques allow for precise accuracy of the survey of sections of complex geometry (dome, arch, etc.) encountered in historical buildings.

It is advantageous to use photogrammetric methods instead of traditional methods that require long and laborious measurements especially in the documentation and evaluation of stone surfaces and high structure. In the photogrammetric documentation of historical buildings, all the details on the building can be handled together and as a whole. This makes it especially easy to produce the necessary bases for the hand down and documentation of historical buildings to the next generations. In addition to three-dimensional vector data by photogrammetric methods, texture data is also provided. This data is very important in terms of giving the real appearance to the objects to be re-formed in three dimensions and increasing the comprehension of the user. This texture data reflects the geometric properties of three-dimensional objects, ie the metric properties are overlapped with vector data. Since these textures are taken from the photos of the building, they create more realistic models.

It is seen that three-dimensional models produced using photogrammetric techniques can be used as a source in restoration projects and this model can also export VRML format to be used in different applications (Carry and Bell, 1997).

REFERENCES

Bodur, F. (2006). “Fotoğraf ve renk: fotoğraftaki renklerin iletilerin algılanmasındaki rolleri.” Ç.Ü. Sosyal Bilimler Enstitüsü Dergisi, Vol 15, No. 1, pp. 77-86)

Carey, R. and Bell, G. (1997). “The Annotated VRML 2.0 Reference Manuel”, Addison Wesley Developers Press

Demirkesen, A.C., Özlüdemir, M.T. and Demir, H.M. (2005). “Kapadokya örneğinde tarihi ve kültürel mirasın korunması ve bu işlemlerde harita mühendislerinin yetki ve sorumlulukları.” TMMOB Harita ve Kadastro Mühendisleri Odası 10. Türkiye Harita Bilimsel ve Teknik Kurultayı, Ankara

Dorffner, L. and Forkert, G. (1998). “Generation And Visualization Of 3D Photo-Models Using Hybrid Block Adjustment With Assumptions On The Object Shape” ISPRS Journal Photogrammetry and Remote Sensing, Vol.53, pp.369-378

Georgopoulos A. and Ioannidis G. (2004). “Photogrammetric and urveying methods for the geometric recording of archaeological monuments.” Archaeological Surveys, FIG Working Week 2004 Athens, Greece, May 22– 27

Grill T. and Scanlon M. (2003). Fotoğrafta Kompozisyon. (N. Sipahi, Translate to Turkish.), İstanbul: Homer Kitabevi.

Pakben, U. (2013). Tarihi yapıların rölöve ve analizlerinde kullanılan ileri belgeleme teknikleri, Dokuz Eylül University, İzmir, Turkey.

Suveg, I. And Vosselman, G. (2000). 3D Reconstruction of Building Models ", IAPRS, Vol. XXXIII, Amsterdam, 2000.

Uysal, M., Toprak, A.S., and Polat N. (2013). "Photo realıstıc 3d modelıng wıth uav: gedik ahmet pasha mosque ın afyonkarahisar". International Archives of the Photogrammetry, Remote Sensing and Spatial Information Sciences, Volume XL-5/W2, 2013 XXIV International CIPA Symposium, 2 – 6 September 2013, Strasbourg, France

Uslu, A., Polat, N., Toprak A.S. and Uysal, M. (2016). "Kültürel Mirasın Fotogrametrik Yöntemle 3B Modellenmesi Örneği." Harita Teknolojileri Elektronik Dergisi, Vol 8, No. 2, pp. (165-176)

Uysal, M., Uslu, A., Toprak, A.S. and Polat, N. (2015). "Arkeolojik Eserlerin Fotogrametrik Yöntemle 3 Boyutlu Modellenmesinde Menagas Mezarı Steli Örneği." TUFUAB VIII. Teknik Sempozyumu, pp: 252-254, Konya.

Yastıklı, N. (2014). "Yersel Fotogrametrinin Tersine Mühendislik Uygulamalarında Kullanımı." UZAL-CBS Sempozyumu, İstanbul.

URL1
Web Map Tile Service, https://www.cekulvakfi.org.tr/proje/cekulun-kulturel-miras-anlayisi [Accessed 11 July 2019]

URL2
Web Map Tile Service, https://yoldanciktim.com/kulturel-miras-nedir/ [Accessed 11 July 2019]

URL3
Web Map Tile Service, http://www.kulturvarliklari.gov.tr/TR-44798/turkiye-geneli-korunmasi-gerekli-tasinmaz-kultur-varlig-.html [Accessed 11 July 2019]

URL4
Web Map Tile Service, https://www.digicamdb.com/specs/nikon_d3100/ [Accessed 11 July 2019]

URL5
Web Map Tile Service, http://konya.com.tr/portfolio-item/taskent/ [Accessed 11 July 2019]

URL6
Web Map Tile Service, http://kazancihaber.com/haber_detay.asp?haberID=2642 [Accessed 11 July 2019]

CISET - 2nd Cilicia International Symposium on Engineering and Technology
10-12 October, 2019, Mersin / TURKEY

ANODIC OXIDATION OF PHTHALIC ACID IN EXTREMELY ACIDIC MEDIUM IN THE PRESENCE CrVI

Yusuf Aktaş [1], and Belgin Gözmen Sönmez[*1]

[1] Mersin University, Science and Arts Faculty, Chemistry Department, Mersin, Turkey, yaktas@sisecam.com

ABSTRACT
In this study, mineralization of phthalic acid added to chromium medium by electrochemical anodic oxidation method to represent organic residue in chromium medium were investigated. In anodic oxidation with BDD anode of phthalic acid (initial form potassium hydrogen phthalate, KHP) BDD anode in chromium and acidic media, the effects of cathode type, current density and electrolysis time were investigated. As a result of electrolysis experiments, stainless steel cathode was preferred in terms of persulfate production, cost and ease of use. After electrode selection, the effect of current density, amount of CrVI in solution and electrolysis time on KHP mineralization was realized by using response surface method and central composite design. The optimum parameters were determined as 70 mA/cm^2 current density, CrVI ratio 12.5%, and time 377 min, where 89.79% mineralization efficiency could be achieved with a desirability value of 1.00.

Keywords: *Phthalic acid, Anodic Oxidation, Mineralization, Chromium, Optimization*

[*] B. Gozmen (bgozmen@mersin.edu.tr)

1. INTRODUCTION

The most important chemical species of chromium are trivalent and hexavalent chromium, which hexavalent chromium is more toxic due to its high solubility in aqueous media, resulting in a high mobility inside the environment. In contrast, trivalent chromium is much less toxic due its low solubility in water and lower mobility, besides this species has important functions in the metabolism of glucose (Almazán-Sáncheza *et al.*, 2011). There are various chemical and physical means for separation and disposal of chromium (Lugo-Lugo *et al.*, 2010; Olmez, 2009).

When a concentrated and refinable chromium stream is achieved, it is possible to reuse these pretreated wastes as new products. In some cases, the existence of organic pollutants obstructs the reuse of the regenerated chromium materials. In this study the chromium species polluted with a representative refractory organic species (phthalic acid) is investigated by means of electro-oxidation with BDD anode.

The main advantage of electro oxidation technology is that no chemicals are used. In fact, only electrical energy is consumed for the mineralization of organic pollutants on high oxidation power anodes. The activity of the electro-generated hydroxyl radicals is strongly related to their interaction with the anode surface. As a general rule, the weaker the interaction, the lower is the electrochemical activity towards oxygen evolution (high O_2 over-voltage anodes) and the higher is the chemical reactivity toward organics oxidation. BDD provides highest O_2 over potential and is an excellent anode for any kind of organic compounds (Comninellis, 2008; Vatistas, 2012).

Electro-oxidation with BDD anode is an effective way to decompose persistent organic species through mineralization to carbon dioxide and water (Panizza *et al.*, 2008; Matzek and Carter, 2016). The •OH radicals are produced on BDD anode surface and sulfate radicals are formed directly or through interaction with •OH radicals as illustrated in Fig 1 and Eq. (1-5) (Lee *et al.*, 2018; Davis *et al.*, 2014):

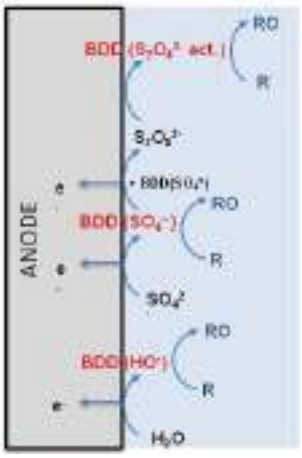

Fig. 1. Hydroxyl and sulfate radicals formation on BDD anode (Electron 4 water, 2019)

$$RH + SO_4^{\bullet -} \rightarrow R\bullet + SO_4^{2-} \quad (1)$$

$$S_2O_8^{2-} + R\bullet \rightarrow SO_4^{\bullet -} + SO_4^{2-} + R^+ \quad (2)$$

$$HSO_4^- + \bullet OH \rightarrow SO_4^{\bullet -} + H_2O \quad (3)$$

$$H_2SO_4 + \bullet OH \rightarrow SO_4^{\bullet -} + H_3O^+ \quad (4)$$

$$SO_4^{\bullet -} + SO_4^{\bullet -} \rightarrow S_2O_8^{2-} \quad (5)$$

BDD electrodes have extreme stability under anodic polarization and high overpotential for water dissociation (Chaplin, 2014; Perez et al., 2012). BDD anode can be used in conjunction with BDD cathode, however it has limitations due to cathode deposition and regeneration. Therefore, in this study BDD, 316-L steel and Titanium grade-2 cathodes are compared in terms of their persulfate production capacity and reusability. 316-L steel and Titanium grade-2 are easily available materials. 316-L is selected due to its low cost and high current efficiency, while Titanium grade-2 has modest cost and high resistivity at acidic media.

The objectives of this study is to determine a suitable cathode for mineralization of phthalic acid in solutions containing sulfate at and use surface response method to investigate the effect of factors namely current density, percentage of CrVI/Total chromium and time during mineralization of phthalic acid at chromium and sulfate rich acidic solutions.

2. MATERIALS AND METHODS

2.1. Anodic Oxidation Experiments

In the experiments, approximately 10 μm boron doped diamond coated niobium electrode (BDD, Condias GmbH) was used as an anode. Different types of electrodes were used as cathodes (stainless steel 316L, titanium grade 2, BDD). The combined electrode set (CONDIACELL® Stack Modell EAOP® Testkit) with 3 anodes and 2 cathodes provides an impact surface of approximately 200 cm^2. The system where electro oxidation experiments were performed was given in the Fig 2.

Synthetic solutions containing total chromium around 4% in terms of Cr_2O_3, app. 10% Na_2SO_4, 20 g potassium hydrogen phthalate (KHP) per 1232 g solution, various $Na_2Cr_2O_7$ and initial pH adjusted to 1.8-2.0 were studied. Solutions described above weighs approximately 1230 g and 1L of this solution was transferred to conduct electro oxidation experiment and remaining was stored as initial sample. Total chromium levels were selected so that the conductivity was around 50 mS/cm, which can be a level useful for industrial applications. Total chromium and sulfate input was provided by addition of $Cr(OH)SO_4$. The pH was adjusted by adding 1:1 H_2SO_4 (app.15-20 g).

The apparatus used at electrolysis experiments is given in Fig 2.

Fig. 2. Electro-oxidation test apparatus

The direct current source has 20V and 50A limits. The borosilicate glass reaction vessel was specially designed to provide full accommodation of the electrodes and supply efficient mixing with magnetic stirrer. The peristaltic pump equipped with a sintered glass opening onto the surface of the solution provided the ceasing of the bubbles encountered especially at the initial steps of the experiments.

2.2. Methods of Analysis

Total Organic Carbon (TOC) analyzes were performed with a TOC analyzer (Shimadzu) containing Solid Incineration Module (SSM), since the samples were not prone to liquid injection.

Cr (III) and Cr (VI) content were determined by potentiometric titration. If both Cr species were present at the same time and in high amounts, the amount of Cr (VI) was found by direct titration with $FeSO_4$; after oxidation and removal of the oxidant, total Cr content was determined by titration with $FeSO_4$ and Cr (III) amount was calculated from the difference. In case Cr (VI) was found in trace levels, UV-VIS photometric method was used which works with diphenyl carbazide staining principle.

In the persulfate (PS) analysis, calibration was prepared at 352 nm with PS standards in the 0.5 - 20 mg/L concentration range using 0.02 M sodium PS ($Na_2S_2O_8$ corresponding to 4760 mg/L) stock solution to prepare calibration standards. In the method, 5 g of KI and 0.3 g of $NaHCO_3$ were dissolved in 50 ml volumetric flask for calibration standards and sample, the standard or sample was added, followed by stirring to 50 mL, waiting for 15 minutes and measured on the spectrophotometer.

2.3. Experimental Design and Optimization

The effects of three independent variables (current density, CrVI%, and time) on electro-oxidation of KHP solution were studied by central composite design (CCD) at five levels ($-\alpha$, -1, 0, +1, $+\alpha$) using Design Expert 11.

The process was optimized and the effect of current density (60–80 mA/cm^2), CrVI% (5–20), and time (120–360 min) was investigated (labeled as X_1, X_2, and X_3, respectively).

3. RESULTS AND DISCUSSION

It was aimed to use persulfate oxidant produced from sulfate ions in mineralization of phthalic acid solution in acidic medium containing chromium species by anodic oxidation method. For this reason, firstly, the electrolytic persulfate (PS) formation performance of cathode species was evaluated.

3.1. Persulfate Production of Different Cathodes at Constant Current Density

Persulfate measurement experiments covered a period of 480 minutes and the solution to be electrolyzed contained 100 g/L Na_2SO_4 solution adjusted to pH 1.8 by adding 40 mL H_2SO_4. Analysis results with BDD, Ti Gr-2 and 316 SS cathodes at 50 mA / cm^2 current density are given in Fig. 3.

Fig. 3 showed that the highest persulfate formation is obtained in BDD/SS electrode pair. During electrolysis, the pH and temperature of the medium were also monitored and the temperature increased to ~50 °C after 120 minutes at all electrodes and increased to 59 °C, 56°C and 51 °C for BDD, Ti-Gr 2 and SS, respectively, as the electrolysis time increased.

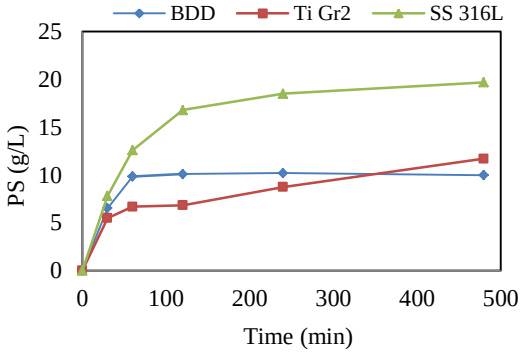

Fig. 3. Persulfate formation when 2 cathodes were used against 3 BDD anodes, j = 50 mA / cm^2

3.2. Optimization of Mineralization

The TOC Removal of KHP was carried out by the electro-oxidation experiments at acidic condition, and the results were given in Table 1. The model fitted was observed to be quadratic model. The quality of the model fitted was evaluated by analysis of variance (ANOVA).

When the results of ANOVA of the models were examined (Table 2), it was observed that the F values of the model was higher than the tabulated F value [$_{F0.05,df(n-(df+1))}$] with a very low p values (< 0.0001). A small p value (Prob > F) indicated that the terms have improved the model.

Table 1. Central composite experimental design and results of electro-oxidation of KHP

Run	Parameters			Response
	J (mA/cm^2)	CrVI (%)	Time (min)	TOC Removal (%)
1	80	20	360	92,0
2	70	12,5	240	61,2
3	60	5	360	78,2
4	86,8	12,5	240	75,5
5	70	25,1	240	61,7
6	70	12,5	240	62,6
7	70	12,5	240	61,7
8	80	5	120	30,5
9	53,2	12,5	240	46,3
10	70	12,5	240	61,5
11	60	20	360	81,1
12	70	12,5	441,8	94,4
13	60	20	120	30,2
14	80	20	120	39,1
15	70	12,5	240	67,4
16	70	0	240	41,9
17	70	12,5	38,2	8,9
18	70	12,5	240	68,7
19	60	5	120	20,4
20	80	5	360	91,9

Table 2. Analysis of variance results for the validation of the quadratic model proposed

Source	Sum of Squares	df	Mean Square	F-value	p-value
Model	11060	9	1229	64.64	0.0001
X_1:J	632	1	632	33.24	0.0002
X_2:CrVI%	222	1	222	11.68	0.0066
X_3:time	9851	1	9851	518.12	0.0001
X_1X_2	2.07	1	2,07	0.1090	0.7481
X_1X_3	3.90	1	3,90	0.2054	0.6601
X2X3	29.59	1	29.59	1.56	0.2406
X_1^2	0.9491	1	0.9491	0.0499	0.8277
X_2^2	174	1	174	9.13	0.0129
X_3^2	179	1	179	9.40	0.0119
Residual	190	10	19.01		
Lack of Fit	136	5	27.23	2.52	0.1663
Pure Error	53.95	5	10.79		
Cor Total	11251	19			

The experimental data provided the input for the polynomial second degree model (Eq. (6)).

$$TOC\ Removal\ \% = +63.72 + 6.80\,X_1 + 4.04X_2 + 26.86X_3 - 0.5089X_1X_2 + 0.6986X_1X_3 - 1.92X_2X_3 - 0.2566X_1^2 - 3.5X_2^2 - 3.52X_3^2 \quad (6)$$

In this study the following parameters were the most influential (in order of decreasing significance): time > current density >CrVI%. The quality of the fit of the model was expressed by the correlation coefficient (R^2) of 0.9831 which is used to check the correlation between the experimental data and predicted responses (Fig. 4).

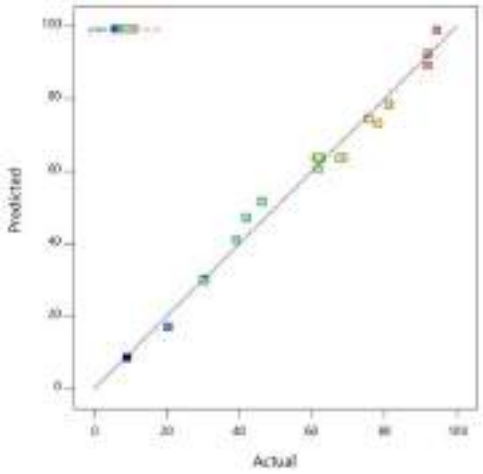

Fig. 4. Predicted vs experimental plot

The combined effect of time and initial CrVI % on mineralization of KHP, while holding other variable constant, is shown in Fig. 5.

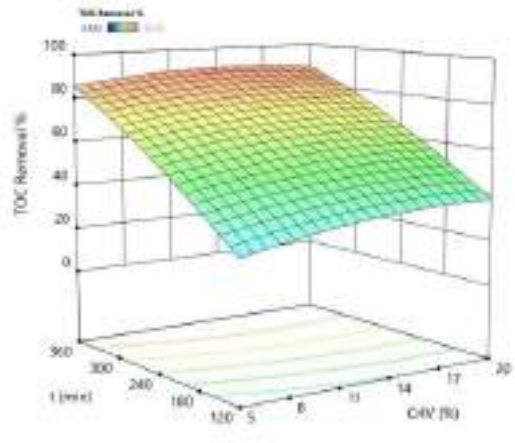

Fig. 5. Three-dimensional response surface plots showing the effects of significant interactions between time and CrVI% (J=75 mA/cm^2)

The electrolysis time is an important parameter and in order to obtain 90% mineralization, a 360 min (6 hours) electrolysis time is required. However, since the initial TOC of the solution is too high (9400 mg/L), this time is considered reasonable. When we look at the effect of the amount of CrVI in the medium, it can be said that the presence of 12.5% CrVI catalyzes the mineralization.

Fig. 6 presents the effect of time and current density on the mineralization efficiency of KHP at constant CrVI % value. High current density is required for effective mineralization, but is not applicable as the medium is exposed to overheating when 80 mA/cm^2 is applied.

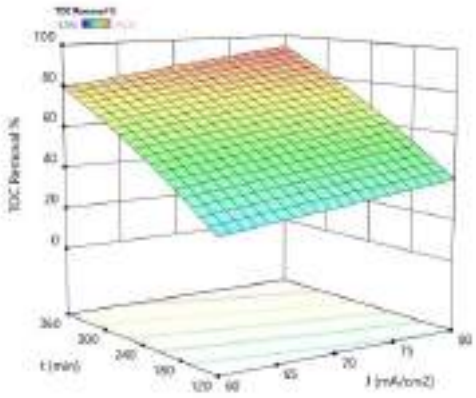

Fig.6. Three-dimensional response surface plots showing the effects of significant interactions between time and current density (CrVI%=12.5)

Within the experimental range for each variable and by setting 90% as the minimum acceptable TOC removal %, the optimum parameters were determined as 70 mA/cm^2 current density, CrVI 12.5%, and time 377 min, where 89.79% mineralization efficiency could be achieved with a desirability value of 1.00.

4. CONCLUSION

In this study, TOC removal of an synthetic KHP solution with high TOC content was investigated by using anodic oxidation which is one of the electro oxidation methods. The production of persulfate from the sulfate ions present in the solution prepared under highly acidic conditions was targeted. It was determined that KHP was effectively mineralized by sulfate radicals obtained from the activation of persulfate (electrolysis or metal catalyzed). Optimum working conditions; 70 mA/cm^2 current density, 377 min electrolysis time and 12.5% CrVI were found.

ACKNOWLEDGEMENTS

We would like to thank the Mersin University Scientific Research Projects Unit for the financial support (BAP 2018-2-TP3-2941).

REFERENCES

Almazán-Sáncheza, P.T., Lugo-Lugoa, V., Linares-Hernándezb, I., Martínez-Mirandab, V., Velázquez-Peñaa, S. and Roa-Moralesc, G. (2011). "Reduction of Cr(VI) from the electroplating industry using an iron-BDD electrochemical system." *ECS Transactions*, Vol 36, No. 1, pp. 331-339.

Chaplin, B.P. (2014) "Critical review of electrochemical advanced oxidation processes for water treatment applications." *Environ. Sci. Processes Impacts*, Vol 16, No. 6, pp. 1182-1203.

Comninellis, C., Kapalka, A., Malato, S.,2 Parsons, S. A., Poulios I. and Mantzavinos, D. (2008) "Perspective advanced oxidation processes for water treatment: advances and trends for R&D." *Journal of Chemical Technology and Biotechnology*, Vol. 83, No. 769–776.

Davis J., James C. B., Farrell J. (2014) "Understanding persulfate production at boron doped diamond film anodes.", *Electrochimica Acta*, Vol. 150, pp. 68–74.

Electron 4 water, http://electron4water.com/archivos/projects/noemo (Accessed 18 June 2019).

Lee C., Kim H. and Park N. (2018) "Chemistry of persulfates for the oxidation of organic contaminants in water,." *Membrane Water Treatment*, Vol. 9, No. 6, pp. 405-419.

Lugo-Lugo, V., Barrera-Díaz, C., Bilyeu, B., Balderas, P., Ureña, F. and Sánchez, V. (2010). "Cr(VI) reduction in wastewater using a bimetallic galvanic reactor." *Journal of Hazardous Materials*, Vol. 176, No. 1-3, pp. 418-425.

Matzek, L. W. and Carter, K.E. (2016) "Activated persulfate for organic chemical degradation: A review" *Chemosphere*, Vol. 151, pp. 178-188.

Olmez-Hanci T. (2009). "The optimization of Cr(VI) reduction and removal by electrocoagulation using response surface methodology." *Journal of Hazardous Materials*, Vol. 162, No. 2-3, pp. 1371-1378.

Panizza, M., Brillas, E. and Comninellis, C. (2008) "Application of boron-doped diamond electrodes for wastewater treatment." *J. Environ. Eng. Manage.*, Vol. 18, No. 3, pp. 139-153.

Perez, G., Ibanez, R., Urtiaga, A.M. and Ortiz, I. (2012) "Kinetic study of the simultaneous electrochemical removal of aqueous nitrogen compounds using BDD electrodes." *Chem. Eng. J.*, Vol. 197, pp. 475-482.

Vatistas, N. (2012) "Electrocatalytic properties of BDD anodes: its loosely adsorbed hydroxyl radicals." International *Journal of Electrochemistry*, Vol. 2012, pp. 1-7.

CISET - 2nd Cilicia International Symposium on Engineering and Technology
10-12 October, 2019, Mersin / TURKEY

PERFORMANCE COMPARISON OF REINFORCEMENT LEARNING ALGORITHMS ON CART-POLE CONTROL PROBLEM

Huseyin Emre OZGUR [*1], Mehmet Ilteris SARIGECILI [2]

[1] Adana Alparslan Turkes Science and Technology University, Engineering Faculty, Mechanical Engineering Department, Adana, Turkey, huseyinemre@yandex.com

[2] Cukurova University, Engineering Faculty, Mechanical Engineering Department, Adana, Turkey, msarigecili@cu.edu.tr

ABSTRACT
Machine learning-based control is an emerging and promising area in control applications. Reinforcement Learning is an attractive part of machine learning. In this study, five different Reinforcement Learning algorithms (i.e. Deep-Q Networks, Trusted Region Policy Optimization, Proximal Policy Optimization, Asynchronous Advantage Actor-Critic and Actor-Critic using Kronecker-Factored Trust Region) and their performances at three different levels of time step (i.e. 10^5, 10^6 and 10^7) are presented on the inverted pendulum on cart since it is a basic problem studied widely in control.

Keywords: *reinforcement learning, machine learning-based control, cart-pole*

[*] Corresponding Author

1. INTRODUCTION

Balancing of a body is a very important objective that has many applications. Cart pole is a basic and important control problem used for modeling balancing. Cart pole is actually an inverted pendulum mounted on cart which is able to move horizontally. Cart pole has been modeled by Sutton et. al. (Barto, Sutton, & Anderson, 1983). OpenAI Gym Environment uses Sutton's cart pole model (OpenAI, 2019). The cart pole representation in OpenAI has been shown in Figure 1.

Fig. 1. OpenAI Gym CartPole Environement

Machine learning-based control (MLC) is an emerging alternative for conventional controllers. Any nonlinear or complex dynamic system can be controlled by utilizing MLC. As a controller, model parameters can be optimized by data-driven approaches. Reinforcement Learning (RL) approach is one of the predominant learning methods. RL is simply based on rewarding desired system behavior and punishing undesired system behavior. The general flow of RL algorithms has been shown in Figure 2. The agent interacts with the environment (action a_i) based on state s_i. Then new state s_{i+1} and reward r_{i+1} can be obtained from interaction.

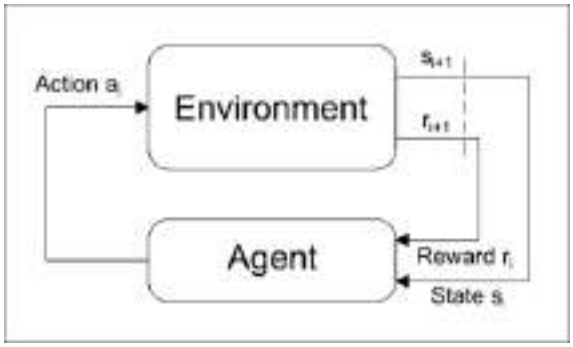

Fig. 2. General reinforcement learning flow

There are various algorithms in literature for implementing RL. Q-learning is a well-known algorithm by its model-free approach. In Q-learning method, Q-tables are created for storing Q-values for corresponding actions in Markov Decision Process. In Q-learning approach, agent learns by using stored data (as offline learning). The states, actions, and rewards have to be stored (in general after an episode) before being used for learning. This method is sample efficient. In this method, first a Q-value approximator network should be built then optimal policy can be determined from approximate values. But in complex situations, it may not be possible to produce a stable network and approximation. Watkins and Dayan (Watkins & Dayan, 1992) presented technical details about Q-learning.

Even though Q-learning is very useful, it falls short when there is a huge number of action-value pairs needed in storing for every state. Hence, to overcome the difficulty of recording a huge amount of data, a neural network model is utilized as Q-value approximator and called as Deep-Q Networks (DQN). DQN has been used for RL approach on Atari games by Mnih et. al. (Mnih et al., 2013).

Disadvantages of Q-learning approaches in complex systems have been tried to be overcome by direct policy optimization method as presented by Sutton et. al. (Sutton, McAllester, Singh, & Mansour, 2000). In policy optimization methods, the agent learns from its online interactions with the environment and hence probabilities of actions can be obtained directly.

Unfortunately, in policy optimization processes, obtaining stable gradient update might be a problem. Therefore, more stable gradient update algorithm, Trusted Region Policy Optimization (TRPO) algorithm has been presented by Schulman et. al. (Schulman, Levine, Moritz, Jordan, & Abbeel, 2015). In TRPO, updated policy cannot be very different from previous policy. Similarly, Schulman et. al. (Schulman, Wolski, Dhariwal, Radford, & Klimov, 2017) presented Proximal Policy Optimization (PPO) which has a similar goal to TRPO but it is easier to implement. There are also studies on combining both value prediction and policy prediction approaches. In Asynchronous Advantage Actor-Critic (A3C) algorithm (Mnih et al., 2016), two separate networks are used: one for actor and one for critic. In the learning process, actor approximates/applies policy by using critic's Q-value approximations. Asynchronous Advantage Actor-Critic (A2C) is deterministic, synchronous version of A3C algorithm. Wu et. al. (Wu, Mansimov, Liao, Grosse, & Ba, 2017) improved actor-critic approach by implementing trust region with Kronecker-factored approximate curvature and named as Actor-Critic using Kronecker-Factored Trust Region (ACKTR). The ACKTR improved the usability of Actor-Critic approaches for both discrete and continuous domains.

2. MATERIAL AND METHOD

In this study, OpenAI Gym (Brockman et al., 2016) CartPole-v1 environment has been used as a testbed. The cart pole environment has 4 observation parameters and 2 action parameters. Observation parameters can be named as cart position, cart velocity, pole angle, and pole end velocity. In a similar fashion, action parameters can be named as push the cart to left and right. The maximum time step has been determined as 500. When center of cart leaves screen or angle of the pole (zenith, θ) exceeds range of ±12°, episode of training resets. The environment, and the angle θ have been presented on Figure 3.

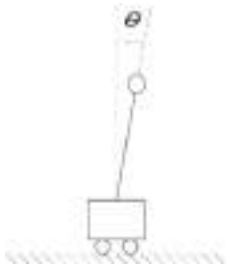

Fig. 3. Representation of Cart-Pole

In order to find the optimal algorithm usage, both value optimization and policy optimization algorithms have been utilized. Value optimization (DQN) and 4 Policy optimization algorithms (PPO, TRPO, A2C, and ACKTR) have been examined in three different levels of time steps (10^5,10^6,10^7) to observe the performance of each algorithm on balancing problem of cart-pole. Hyper-parameters have been kept same as assumed by Open AI Gym Baseline samplings. Hyper-parameters haven't been changed to utilize Baselines selected and published (predefined) values for eliminating biased results. For comparison purposes, average reward of each episode has been selected as the evaluation parameter. Open AI's environments and algorithms (Dhariwal et al., 2017) have been used to simulate and train inverted pendulum. Each time step passing without termination increases reward output of trial as 1. Hence the longest balanced session will have the highest reward output.

3. RESULTS

The five different algorithms (DQN, TRPO, PPO, A2C, and ACKTR) have been used to train the system for balancing problem on cart-pole. The performance graphs of different algorithms in 10^5 time-step limit has been shown in Figure 4. 10^5 time-steps has been selected to inspect sample efficiency of related algorithms. DQN has shown adequate performance in 10^5 steps. The average reward of 200 achieved in $6x10^4$ time-steps by DQN. Both PPO and ACKTR showed low performance for first 10^5 steps. A2C algorithm implementation started to show adequate performance through 1e5 steps. The TRPO algorithm showed superior performance with consistent reward increases from early start. In general, the basic algorithms have shown better performance. PPO algorithm is based on TRPO algorithm. Similarly, ACKTR algorithm is based on A2C. The advancements on basic algorithms cannot be seen on the first simulation results (10^5 time-steps). This might be caused by inadequate hyper-parameter or tuning parameter selection and implementations of algorithms. But in general, first 10^5 steps give important indicators for algorithm performances on cart-pole, or simple control problems.

In order to achieve deeper understating about algorithm performances, results of several levels of time-steps have been inspected. The performance results of the tested algorithms for different time step levels (10^5, 10^6, 10^7) have been shown in Table 1. The selection of different time-step levels might show the performance characteristics of the inspected algorithms. From the results, it can be seen that DQN showed adequate performance for all three time-step levels. Even though PPO algorithm has shown increased performance but improvements can be seen at 10^6 steps. Similarly, A2C algorithm has shown adequate performance for first 10^5 time-steps then has improved its performance significantly for 10^6 and 10^7 time steps. ACKTR algorithm has shown similar performance characteristics at 10^5. Later on performance of ACKTR has improved drastically for 10^6 and 10^7 time-steps. ACKTR has the second-best performance characteristics. The best results (in terms of performance) have been obtained by TRPO algorithm. The TRPO showed excellent performance characteristics for all of the time-step levels.

4. DISCUSSION AND FUTURE STUDIES

MLC is an emerging area. MLC is advantageous for controlling complex systems or systems with limited

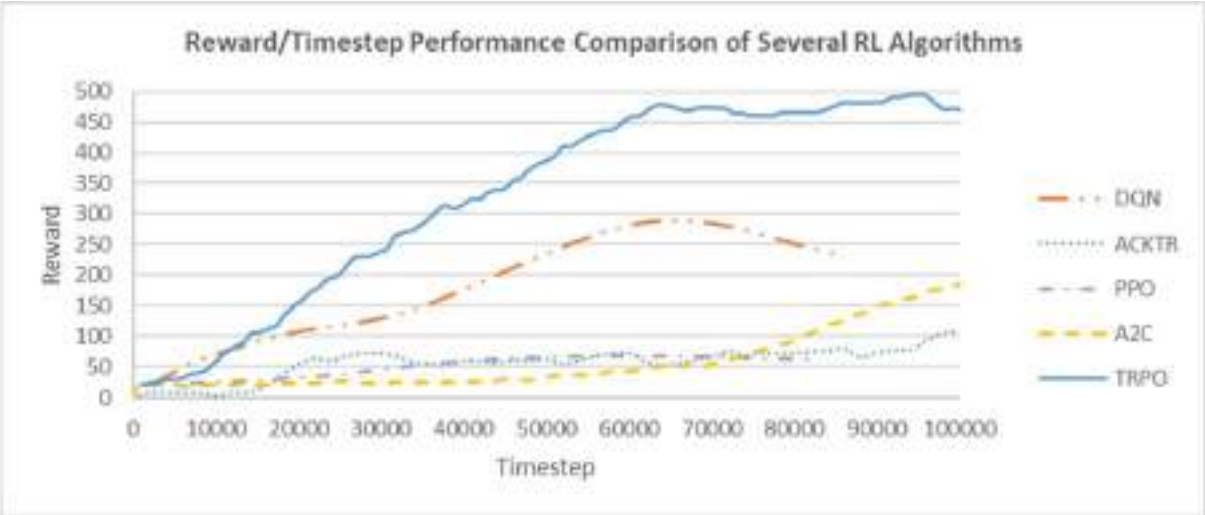

Fig. 4. The graph of time-step performances

Table 1. The tested algorithm's reward outputs by using 3 time-step levels

Items	10^5	10^6	10^7
DQN	233	263	136
PPO	65.5	310	235
TRPO	471	500	500
A2C	185	309	324
ACKTR	107	465	481

dynamic characteristic information. MLC utilizes data-driven approaches to solve optimization problems. In this study, as our first step to MLC, several RL algorithms (DQN, TRPO, PPO, A2C, and ACKTR) have been inspected in terms of average reward performance by considering 3 time-step levels on cart-pole control problem. The study gave first insights about different RL algorithms on the control problem. After trial processes, TRPO and ACKTR algorithms showed superior performances compared to DQN, PPO, and A2C on the cart-pole problem. In future studies, hyper-parameter tuning of TRPO and ACKTR algorithms can be pursued for achieving further performance improvements for cart-pole and more complex problems.

4. REFERENCES

Barto, A. G., Sutton, R. S., & Anderson, C. W. C. W. (1983). Neuronlike Adaptive Elements That Can Solve Difficult Learning Control Problems. IEEE Transactions on Systems, Man and Cybernetics, SMC13(No:5 September/October), 834–846. https://doi.org/10.1109/TSMC.1983.6313077

Brockman, G., Cheung, V., Pettersson, L., Schneider, J., Schulman, J., Tang, J., & Zaremba, W. (2016). OpenAI Gym, 1–4. https://doi.org/10.1021/am3026129

Dhariwal, P., Hesse, C., Klimov, O., Nichol, A., Plappert, M., Radford, A., … Zhokhov, P. (2017). OpenAI Baselines. GitHub Repository. GitHub.

Mnih, V., Badia, A. P., Mirza, M., Graves, A., Lillicrap, T. P., Harley, T., … Kavukcuoglu, K. (2016). Asynchronous Methods for Deep Reinforcement Learning, 48. Retrieved from http://arxiv.org/abs/1602.01783

Mnih, V., Kavukcuoglu, K., Silver, D., Graves, A., Antonoglou, I., Wierstra, D., & Riedmiller, M. (2013). Playing Atari with Deep Reinforcement Learning, 1–9. Retrieved from http://arxiv.org/abs/1312.5602

OpenAI. (2019). Openai Gym CartPole-v1 Environment. Retrieved August 26, 2019, from https://gym.openai.com/envs/CartPole-v1/

Schulman, J., Levine, S., Moritz, P., Jordan, M. I., & Abbeel, P. (2015). Trust Region Policy Optimization. Retrieved from http://arxiv.org/abs/1502.05477

Schulman, J., Wolski, F., Dhariwal, P., Radford, A., & Klimov, O. (2017). Proximal Policy Optimization Algorithms, 1–12. Retrieved from http://arxiv.org/abs/1707.06347

Sutton, R. S., McAllester, D. A., Singh, S. P., & Mansour, Y. (2000). Policy gradient methods for reinforcement learning with function approximation. In Advances in neural information processing systems (pp. 1057–1063).

Watkins, C. J. C. H., & Dayan, P. (1992). Technical Note: Q-Learning. Machine Learning, 8(3), 279–292. https://doi.org/10.1023/A:1022676722315

Wu, Y., Mansimov, E., Liao, S., Grosse, R., & Ba, J. (2017). Scalable trust-region method for deep reinforcement learning using Kronecker-factored approximation, 1–14. Retrieved from http://arxiv.org/abs/1708.05144

EFFECT OF FLIGHT HEIGHT ON DEM AND ORTHOPHOTO

Mehmet Özgür Çelik [*1], Aydın Alptekin[2], Fatma Bünyan Ünel [3], Lütfiye Kuşak [4] and Murat Yakar [5]

[1] Mersin University, Engineering Faculty, Geomatic Engineering Department, Mersin, Turkey, mozgurcelik@mersin.edu.tr

[2] Mersin University, Engineering Faculty, Geomatic Engineering Department, Mersin, Turkey, aydinalptekin@mersin.edu.tr

[3] Mersin University, Engineering Faculty, Geomatic Engineering Department, Mersin, Turkey, fatmabunel@mersin.edu.tr

[4] Mersin University, Engineering Faculty, Geomatic Engineering Department, Mersin, Turkey, lutfiyekusak@mersin.edu.tr

[5] Mersin University, Engineering Faculty, Geomatic Engineering Department, Mersin, Turkey, myakar@mersin.edu.tr

ABSTRACT
Digital elevation map (DEM) and orthophoto of an area will be created in a short time with the help of Unmanned aerial vehicle (UAV). UAV and Global Positioning system (GPS) has been used to create actual, reliable and high resolution maps since last decade. In this study, the effect of flight height on DEM and orthophoto was investigated. Two flight plans which are at 30 and 50 meters elevation were prepared. Pictures taken with UAV were used to produce DEMs and orthophotos. Resolution of maps were compared when maps were produced. More detailed and high resolution maps were created with 30 meters when compared with 50 meters elevation flight height. As a result of the study, it was understood that flight height should be determined depending on the structure of the land, accuracy and precision expected from the work.
Keywords: *Unmanned aerial vehicle (UAV), Digital Elevation Map (DEM), Orthophoto, Resolution, Ground Sampling Distance (GSD).*

[*] Corresponding Author

1. INTRODUCTION

Aydınlar Pond located in Avgadı Neighborhood of Erdemli District of Mersin Province was determined as the study area. In this study, the unmanned aerial vehicle (UAV) was used in the selected study region and flights were made at different heights within the same time frame. Digital elevation model (DEM) and orthophoto image were produced from photos taken with UAV by photogrammetric methods. Differences between DEMs and orthophotos with different height and ground sampling distance (GSD) were investigated. To examine the effect of height on a resolution, Aydınlar Pond in Erdemli district which is a wetland area was preferred. In the study area, firstly, flights were made to be 0.82cm/pixel GSD at a height of 30 m and then 1.37cm/pixel GSD at a height of 50 m. DEMs and orthophotos were produced. The effect of changes in GSD values on the DEM and orthophoto was investigated.

2. STUDY AREA

Aydınlar Pond, which is the working area, is located 35.5 km from Erdemli district and 90.3 km from Mersin city centre. The size of the area is 15224.94 m^2.

Fig. 1. Aydınlar Pond

3. PHOTOGRAMMETRY

The photogrammetry is the science that allows the determination of the position, shape and size of objects on the earth through overlapping pictures. Photogrammetry with developing technology gives faster and more accurate results than conventional terrestrial measurements. Nowadays, air photogrammetry, which is the sub-branch of frequently preferred photogrammetry, can determine the shape, position and size of the objects in space through UAV. In this study, data such as DEM and orthophoto image of the study area were obtained by using UAV. Photogrammetric approach was used to generate this data (Yakar and Dogan, 2017). This approach is also referred to as Structure-from-Motion (SfM) (Dellaert et al., 2000; Furukawa and Hernández, 2013). SFM; is an algorithm that aims to create the 3D structure of the object with camera parameters from image sets taken from different viewpoints of an object or a piece of land (Dellaert et al., 2000; Furukawa and Hernández, 2013). In other words, 3D modelling is a classical photogrammetry approach that uses stereo image technique to produce the model by detecting the common points of the desired object in the captured images (Yakar and Dogan, 2017). With the development of technology, the use of the SfM photogrammetric approach in 3D modelling has started to increase (Kolzenburg et al., 2016). In this study, DEM and orthophoto images were produced by *using Agisoft Metashape Professional.1.5.0* program which uses the SfM algorithm.

4. UNMANNED AERIAL VEHICLE (UAV)

UAV is a concept that emerged in the 70s (Newhall, 1969; Whittlesley, 1970). With advancing technology, helicopters, aircraft, rotary / fixed-wing UAVs were produced (Ozemir and Uzar, 2016). UAV has contributed significantly to the process of making various maps for analysis, inquiry, 3D modelling and digital imaging (Ozemir and Uzar, 2016; Nex and Remondino, 2013). UAVs are unmanned vehicles that can be used in many areas such as cartography, military activities, agricultural studies and engineering projects that perform flights according to remote control or a flight plan. In other words, it is a measuring device that can be controlled automatically, semi-automatically or manually depending on or without a flight plan (Eisenbeiss, 2009; Ceylan et al, 2014). UAV consists of a digital camera and GPS integration (Eisenbeiss, 2003; Yılmaz et al., 2018). Especially with the development of the software industry and technology in recent years, the use of UAV has become widespread. It has influenced many occupations and fields of study and has given a new dimension to cartography. It has become an important source of data on inspection, surveillance, production of various maps and 3D modelling (Nex and Remondino, 2013). Compared to other aircraft, the main difference is that there is no physical pilot (Eisenbeiss, 2004; Rawat and Lawrence, 2014). UAVs have high performance at low cost and integrated with various imaging devices with sensors such as thermal, infrared, hyperspectral, radar, chemical and biological. There are many advantages such as providing natural disasters to ground stations, coordinating the data instantly thanks to being integrated with GPS (Yılmaz et al., 2018) and greatly facilitating the problem of time encountered in classical measurement methods. In this study, Parrot Anafi UAV was used in order to produce precision, reliable and rapid production of the field's DEM and orthophoto (Fig. 2).

Fig.2. PARROT Anafi

The following table shows the technical specifications of the Parrot Anafi UAV.

Table 1. Technical properties of Anafi Parrot (Parrot, 2018)

Property	Value
Drone weight	320 g
Controller weight	386 g
Battery weight	126 g
Max. flight time	25 min
Max. horizontal speed	15.2 m /s
Max. vertical speed	4 m/s
Max. wind resistance	13.9 m/s
Max. transmission range	4000 m
Max. altitude	150 m
Operating temperature range	-10-40 C°
Camera	21 MP
Resolution	4608x3456
Focal length	4 mm
Pixel size	1.34 x 1.34 µm

5. GLOBAL NAVIGATION SATELLITE SYSTEM (GNSS)

GNSS is a system for determining the position of any object in the world with radio signals. In the study, it was used to determine the coordinates of the ground control points established before the flight with UAV. The coordinated photographs are coordinated with the photographs obtained from the flights performed at different heights (30 m and 50 m).

6. MATERIALS AND METHODS

Flight plans were prepared in Pix4Dcapture application in the study area. For a flight at a height of 30 m, GSD is 0.85cm/pixel (Fig.3) and for a 50 m height, GSD is 1.37cm/pixel (Fig.4). The transverse and longitudinal overlap is set at 80% in flight plans. Photos were taken with the camera axis in a vertical position.

Fig.3. Flight plan for a height of 30 m

Fig.4. Flight plan for a height of 50 m

5 gcp was installed to cover the area (Fig. 5). The coordinates of the gcps were connected to TUSAGA Active CORS-TR system with *Satlab SL800* GNSS receiver in UTM projection, ITRF-96 datum (EPSG: 5255), GRS80 ellipsoid, 2005.0 epoch, 3 degree 33. measured in the slice (Fig. 6)

Fig. 5. Gcp marking

Fig. 6. Gcp measurement

The coordinate values of the measured gcps are shown in table 2 below.

Table 2. Gcp coordinate value

In this study, it is planned to determine the effect of altitude on the produced DEM and orthophoto from the flights performed at different heights. 450 photographs were taken at a height of 30 m and 259 photographs were taken at a distance of 50 m (Fig. 7, Fig. 8).

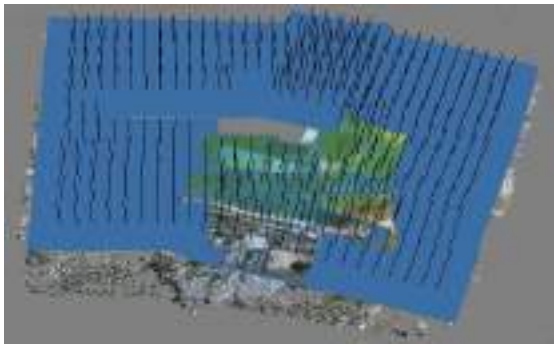

Fig. 7. Photos taken at a height of 30 m

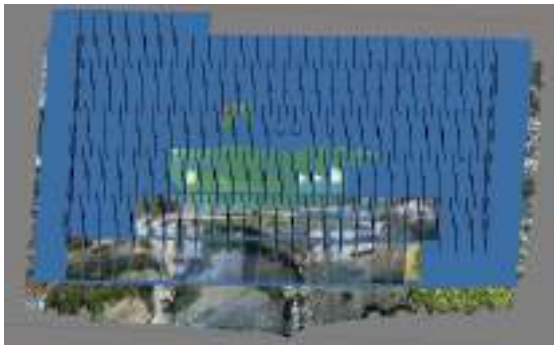

Fig. 8. Photos taken at a height of 50 m

With the photographs taken, Agisoft. Metashape Professional.1.5.0 program was used. The photographs were directed in the program. The estimated shape of the 3D model is generated by a sparse point cloud. All photos containing the images are matched. Internal matching elements, camera calibration information and distortion errors were calculated by this matching process.

Table 3. Calibration coefficients and correlation matrix for 50 m

	Value	Error	F	Cx	Cy	B1	B2	K1	K2	K3	P1	P2
F	3057.15	1.1	1.00	-0.19	0.03	0.06	-0.02	-0.13	0.36	-0.49	0.69	0.11
Cx	32.6817	0.047		1.00	0.15	0.03	0.12	0.12	-0.27	0.38	-0.51	0.05
Cy	3.27868	0.026			1.00	0.11	0.01	0.01	-0.03	0.03	0.04	0.00
B1	-7.05016	0.019				1.00	-0.93	-0.91	-0.81	0.91	0.01	-0.07
B2	-6.0193734	0.021					1.00	0.00	-0.86	0.81	0.02	0.07
K1	-0.0837674	2.6e-005						1.00	-0.87	0.78	-0.09	-0.02
K2	0.0128361	7e-005							1.00	-0.97	0.22	0.05
K3	-0.0086692	6e-005								1.00	-0.31	0.06
P1	0.00374189	2.7e-006									1.00	0.08
P2	0.00025403	2e-006										1.00

Table 4. Calibration coefficients and correlation matrix for 50 m

	Value	Error	F	Cx	Cy	B1	B2	K1	K2	K3	P1	P2
F	3031.44	1.2	1.00	0.05	-0.04	0.06	0.04	-0.16	0.42	-0.66	0.76	0.06
Cx	33.1364	0.040		1.00	0.73	0.05	0.15	0.14	-0.35	0.48	-0.64	0.00
Cy	3.09888	0.040			1.00	-0.00	0.05	0.13	-0.36	0.46	-0.58	0.09
B1	-4.0701	0.049				1.00	-0.90	0.88	-0.01	0.01	0.03	0.01
B2	0.228655	0.040					1.00	0.81	0.01	-0.01	0.03	-0.00
K1	-0.0848744	3.1e-005						1.00	-0.79	0.71	-0.12	-0.05
K2	0.0142818	3.4e-005							1.00	-0.90	0.24	0.01
K3	-0.0020434	4.7e-005								1.00	-0.32	0.01
P1	0.00266191	2.1e-006									1.00	0.00
P2	0.00031087	1.4e-006										1.00

Then, a dense point cloud was formed. DEMs were generated from dense point clouds (Fig. 9, Fig. 10) and orthophoto (Fig. 11, Fig. 12) were generated from DEM.

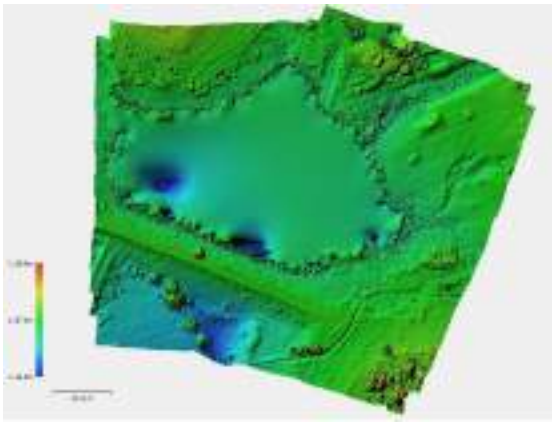

Fig. 9. DEM for 30 meters.

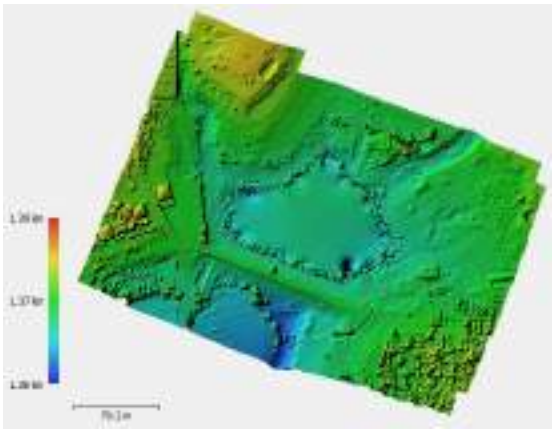

Fig. 10. DEM for 50 meters

.

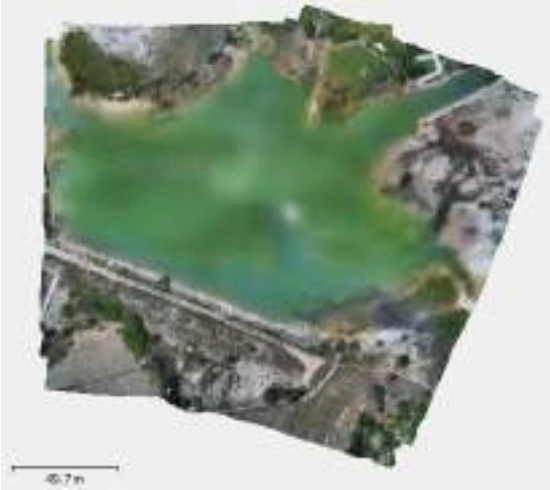

Fig. 11. Ortophoto for 30 meters

Fig. 12. Ortophoto for 50 meters

The process steps performed during the study are shown in the following figure.

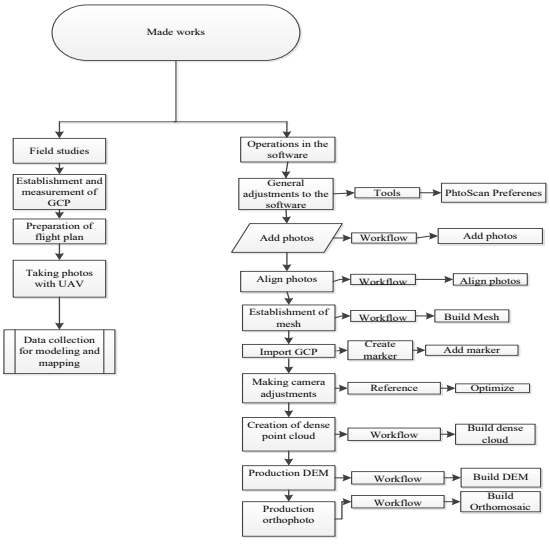

Fig. 13. Work flow chart

7. FINDINGS

In the study conducted in a flight from a height of 30 m DEM_{GSD}: 4.24cm/pixel, $orthophoto_{GSD}$: 1.09cm/pixel. In the 50 m flight, DEM_{GSD} is 6.78cm/pixel and $orthophoto_{GSD}$ is 1.74cm/pixel. Based on these data, it was determined that flight height directly affected the resolution of digital products (such as DEM, orthophoto) depending on the terrain structure, desired accuracy and sensitivity (Fig. 14, Fig. 15). To obtain more detailed and reliable information about the terrain, it has been determined that low altitude flights should be performed. Although UAVs have many advantages, they have been determined as a result of the wind which is effective during the field study, including the shortness of time in the air and the inability to work optimally in windy weather.

Fig. 14. An image from a 30 meters flight

Fig. 15. An image from a 50 meters flight

5. CONCLUSION

The output products obtained as a result of the study DEM and orthophoto images; Horizontal position error for flight at 30m height: ± 1.30cm, vertical position error: ± 0.32cm, total error: ± 1.34cm was determined. For the flight at 50 m height, horizontal position error: ± 3.80cm, vertical position error: ± 0.56cm, total error: ± 3.84cm.

It has been determined that flight height directly affects the resolution of the output products to be obtained. Geomorphological structure of the study area, land use, the accuracy of the expected work and the height of flight required to change depending on the determined.

REFERENCES

Ceylan, M., Doner, F. and Ozdemir, S. (2014). "Use of unmanned aerial vehicle systems in data collection and mapping studies." *5. Remote Sensing-GIS semposium*, Istanbul, Turkey.

Dellaert, F. Seitz, S. M., Thorpe, C. E. and Thrun, S. (2000). "Structure from motion without correspondence. Proceedings*." IEEE Conference on Computer Vision and Pattern Recognition*, CVPR 2000 (Cat. No.PR00662), Hilton Head Island, SC, pp. 557-564 Vol. 2, doi: 10.1109/CVPR.2000.854916.

Eisenbeiss, H. (2003). Positions und orientierungsbestimmung eines autonomen helikopters-vergleich zwischen direkter georeferenzierung und aerotriangulation mit videobilddaten, Diploma Thesis, Institute for Photogrammetry and remote sensing, University of Technology, Dresden, Germany.

Eisenbeiss, H. (2004) "A mini unmanned aerial vehicle (UAV): system overview and image acquisition." *International Archives of Photogrammetry, Remote Sensing and Spatial Information Sciences*, vol. 36, part 5/W1, on CD-ROM.

Eisenbeiss, H. (2009). UAV Photogrammetry, ETH Zurich for the degree of Doctor of Science, ISNN 0252-9335, ISBN: 978-3-906467-86-3, Zurich, Switzerland.

Furukawa, Y., Hernández, C. (2013). "Multi-View Stereo: A Tutorial." *Foundations and Trends® in Computer Graphics and Vision*, Vol. 9, No. 1-2, pp. 1-148.

Kolzenburg, S., Favalli, M., Fornaciai, A., Isola, I., Harris, A. J. L., Nannipieri, L. And Giordano, D. (2016). "Rapid updating and improvement of airborne lidar DEMs through ground-based sfm 3-d modelling of volcanic features." *IEEE Transactions on Geoscience and Remote Sensing*, Vol. 54, No. 11, pp. 6687-6699.

Newhall, B. (1969). "Airborne camera: The world from the air and outer space." *Hasting House Trowbridge&London,* pp. 144.

Nex, F. and Remondino, F. (2014). "UAV for 3D mapping applications: a review." *Applied Geomatics*, Vol. 6, Issue 1, pp.1-15.

Ozemir, I. and Uzar, M. (2016). "The generation of photogrammetric data with unmanned aerial vehicle." *6. Remote Sensing-GIS DEMposium*, Adana, Turkey, pp. 245-254.

Parrot (2018) "Anafi User Manual v2.2." pp.1-73.

Rawat K. S. and Lawrence E. E. (2014). "A mini-UAV VTOL Platform for Surveying Applications." *International Journal of Robotics and Automation (IJRA)* Vol. 3, No. 4, pp. 259-267.

Whittlesley, J. H. (1970). "Tethered Balloon for Archaeloogical Photos, In Photogrammetric Engineering." 36 2, pp. 181-186.

Yılmaz, H. M., Mutluoglu, O., Ulvi, A., Yaman, A. and Bilgilioglu, S. S. (2018). "Created Tree Dimensional Model of Aksaray University Campus With Unmanned Aerial Vehicle." *Journal of Geomatics*, No. 2018;3(2), pp. 129-136.

Yakar, M. and Dogan, Y. (2017). "3D Modelling of Silifke Asagi Dunya Sinkhole by Using UAV." *Afyon Kocatepe University Journal of Science and Engineering*, Special Issue, pp. 94-101.

CISET - 2nd Cilicia International Symposium on Engineering and Technology
10-12 October, 2019, Mersin / TURKEY

AVAILABILITY OF ANAFI PARROT IN DISASTER SITE MODELLING

Aydın Alptekin [*1], Mehmet Özgür Çelik [2], Lütfiye Kuşak [3], Fatma Bünyan Ünel [4] and Murat Yakar [5]

[1] Mersin University, Engineering Faculty, Geomatic Engineering Department, Mersin, Turkey, aydinalptekin@mersin.edu.tr

[2] Mersin University, Engineering Faculty, Geomatic Engineering Department, Mersin, Turkey, mozgurcelik@mersin.edu.tr

[3] Mersin University, Engineering Faculty, Geomatic Engineering Department, Mersin, Turkey, lutfiyekusak@mersin.edu.tr

[4] Mersin University, Engineering Faculty, Geomatic Engineering Department, Mersin, Turkey, fatmabunel@mersin.edu.tr

[5] Mersin University, Engineering Faculty, Geomatic Engineering Department, Mersin, Turkey, myakar@mersin.edu.tr

ABSTRACT
Photogrammetric methods have become popular for modelling the engineering projects in the last decade. Unmanned aerial vehicle (UAV) has been widely used in natural disaster management studies in last years. Disaster site modelling has become easier due to the technological advances. Many kinds of UAV exists. In this study, advantages and disadvantages of ANAFI Parrot in 3D modelling of a disaster site have been discussed. It is cheap and has a low weight. Flight time is enough to take pictures of the disaster area, like landslide, rockfall, flood and earthquake. The batteries run out fast. In modelling disaster areas ANAFI can be easily used.

Keywords: *Unmanned aerial vehicle, Anafi parrot, Natural disaster, Advantages and disadvantages*

[*] Corresponding Author

1. INTRODUCTION

The population of our country increases continually. As a result of this situation, new houses are needed. Most of them have built without considering the disaster potential of the site. Natural disasters cause loss of life and property. Modelling them is very important to suggest solutions for preventing from their negative effects. Technological advances in photogrammetry and remote sensing methods have made modelling process easier.

Landslide and rockfall, which are common natural disaster types, occur as a result of change in forces on soil and rock masses. Slope gradient determines the direction of mass motion. Therefore, actual digital elevation model (DEM) of the terrain is very crucial in natural disaster site modelling and monitoring studies. Until recently, data taken from Google Earth or topographical maps were used to generate DEM. They will give approximate values not sensitive results. Nowadays, unmanned aerial vehicle (UAV) has being used for preparing actual DEM. UAV can give us information about steep and dangerous topography where we cannot reach easily. In this study, we investigate the advantages and disadvantages of ANAFI Parrot (Fig. 1) in natural disaster site modelling studies by using Samsung Galaxy S7 and iPhone 5S smartphones. A smartphone is needed to fly Anafi. Technical properties of Anafi Parrot is shown in Table 1.

Fig.1. ANAFI Parrot

Table 1. Technical properties of Anafi Parrot (Parrot, 2018)

Property	Value
Drone weight	320 g
Controller weight	386 g
Battery weight	126 g
Max. flight time	25 min
Max. horizontal speed	15.2 m /s
Max. vertical speed	4 m/s
Max. wind resistance	13.9 m/s
Max. transmission range	4000 m
Operating temperature range	-10-40 C°

UAV has a wide study area including agriculture, forests, military purposes and engineering projects. UAV technology has been used to prepare 3D models of terrain and buildings since last decade. There are many types of UAV. Nassi et al., 2019 have described properties of commercial UAV types. Anafi, which is a cheap UAV, has started to be used in engineering projects. Costantino et al. 2019 have used Anafi to create 3D model of a church. Palestini and Basso 2019 have used Anafi to get 3D information in a river basin. We used ANAFI, which was launched in 2018, in a landslide site and now we will give our experience with it.

2. SMARTPHONE APPLICATIONS

To use ANAFI, 3 free applications available in AppStore needed to be installed in your smartphone. Anafi requires FreeFlight 6, Ctrl+Parrot 2 and Pix4Dcapture apps to fly. All of them is compatible with Anafi Sky controller 3.

With FreeFlight 6 (Fig. 2), we can fly ANAFI freely. Current version is 6.5.3. We can take pictures, record video and decide the maximum distance and speed of ANAFI from remote controller.

Fig. 2. FreeFlight 6 application

With Ctrl+Parrot 2 (Fig.3), we introduce the ANAFI to Android smartphone, then click OPEN PIX4DCAPTURE. With Pix4Dcapture, we can organize the flight plan by deciding flight height, flight speed, overlap amount and angle of camera. In IOS (Fig. 4) and Android (Fig.5), the settings have little differences. We can see the flight time according to our arrangements.

Fig. 3. Ctrl+Parrot 2 application

Fig 4. Flight settings in IOS

Fig. 5. Flight settings in Android

3. FLIGHT

In order to fly ANAFI Parrot, we need to download and install 3 free applications on our IOS and Android smartphones. ANAFI has maximum wind resistance of 50 km/h (13.9 m/s). Therefore, we need to check the weather conditions before attempting to fly ANAFI. We used UAV Forecast application to control fly availability. It has 16GB microSD card installed in ANAFI. The minimum height of flight is 20 meters. Ground sampling distance (GSD) value decreases with increasing flight height.

We use USB Cable to connect our smartphone with Parrot Skycontroller 3.

There are 2 types of flight mode in ANAFI, Freeflight and flight plan. With Freeflight application, we can make free flights. In order to prepare point cloud and Digital elevation map (DEM), we need flight plan. We can decide the flight area, height, speed and overlay amount with using Pix4Dcapture (Fig. 6) application.

In Pix4Dcapture application, we can choose 4 types of flight plan (Fig. 7). They are polygon, grid, double grid and circular.

We need to check the battery amount before planning the flight area. If the planned mission has not completed with the mounted battery, we can call the drone to the home point. In that case with Android we cannot send the drone to the place where it left to resume and complete the mission. However, we can send the drone with IOS smartphone to resume the mission.

In Android, we can decide overlay amount. In IOS phone we can decide front and side overlays separately.

Fig. 6. Flight plan in Pix4Dcapture application

Fig. 7. Plan mission in Pix4Dcapture

In Android you need Ctrl+parrot 2 and Pix4Dcapture, however in IOS you only need Pix4Dcapture application to prepare flight plan.

There are 4 batteries in the Anafi carrying bag. When battery is fully charged, we first make flight plan and start to fly. Then when 10% battery, we need to take the drone to the home point. Therefore, with each battery we can take pictures for 18 minutes. Then we need to change the battery and prepare a new flight plan.

4. PROBLEMS ENCOUNTERED

In Android smartphone, we first need to open Ctrl+Parrot Application and then click pix4Dcapture. In IOS smartphone you do not need Ctrl+Parrot application.

In Android smartphone, we can only decide overlap percentage. However, in IOS we can decide front and side overlaps.

When we prepare a flight plan far away from us, the drone starts to fly. When it reaches to a distance longer than 4000 metres, it hovers. At that time, we call the drone back to the home point. It did not warn us when starting flight.

We need to see ANAFI always in the air, as it may drop when it touches something.

We need to use ground control points (GCP) to georeference the site to which system we want.

The battery of remote controller decreases faster. You need a power bank to charge it in field.

We can easily transfer pictures to computer.

We need to prepare flight plan for 18 minutes to complete the mission safely.

In circular plan, we were unable to choose the camera angle in both Android and IOS.

Base map of the study area is seen in IOS phone in a short time, while in Android phone it is seen in 2 or 3 minutes.

Sometimes the remote controller was unable to send the flight plan to Anafi. We closed everything and then power on. So, the problem was solved.

In IOS phone, we took less than the number of photos than we took. When we import the photos in Agisoft software, we failed to align the photos. We were unable to solve that problem in IOS smartphone. However, in Android phone we took the number of photos we took.

5. CONCLUSION

ANAFI Parrot has too many advantages and disadvantages. It is cheap and easy to carry. It has less flight time. The battery amount decreases faster. As the problem of taking less photo than taken in IOS, we prefer

to use Android. It can be used safely in natural hazard sites.

REFERENCES

Costantino, D., Carrieri, M., Garofalo, A.R., Angelini, M.G., Baiocchi, V. and Bogdan, A.M. (2019). "Integrated survy for tensional analysis of the vault of the church of San Nicola in Montdoro" 2nd International conference of geomatics and restoration, Milan, Italy, pp. 455-460.

Nassi, B., Shabtai, A., Masuoka, R. and Elovici, Y. (2019), "SoK - Security and Privacy in the Age of Drones: Threats, Challenges, Solution Mechanisms, and Scientific Gaps" https://arxiv.org/pdf/1903.05155.pdf, pp. 1-17.

Palestini, C. and Basso, A. (2019). "3D detection and reconstruction experiments in river basins." 8th International workshop 3D-Arch, Bergamo, Italy, pp. 543-550.

Parrot (2018) "Anafi User Manual v2.2" pp.1-73.

CISET - 2nd Cilicia International Symposium on Engineering and Technology
10-12 October, 2019, Mersin / TURKEY

ABSORPTION PERFORMANCE OF NANOPATTERNED AZO

Erdem Aslan *[1] and Ekin Aslan [2]

[1] Department of Electrical and Electronics Engineering, Hatay Mustafa Kemal University, Hatay, TURKEY, erdem.aslan@mku.edu.tr

[2] Department of Electrical and Electronics Engineering, Hatay Mustafa Kemal University, Hatay, TURKEY, ekin.aslan@mku.edu.tr

3

ABSTRACT
Using aluminum-doped zinc oxide (AZO) which is an alternative plasmonic material can provide a tunable low-loss solution for absorber metamaterial in also point of decreasing cost in optical applications. In this context, the parameters of AZO with an improved carrier concentration by a thermal process are utilized to numerically analyze a mirror layer absorption and metamaterial absorber performances. In order to show mirror-layer- performance of AZO, the transmittance and reflectance spectra of AZO layers of different thicknesses in near-infrared and visible range are examined via finite difference time domain (FDTD) method, whether if it can be used as a mirror layer. A new mirror layer with a metal/AZO layer is analyzed numerically in order to reduce the amount of metal in the design, the cost of metal, the low reflectance. It is understood Al layer can be used as a sole back-reflector layer due to the absorption of AZO film. Finally, in order to see the absorber performance of AZO nanoparticles, we analyze the absorber design with honeycomb-shaped AZO nanoantennas.

Keywords: *Alternative plasmonics, AZO, Metamaterial absorber*

* Corresponding Author

1. INTRODUCTION

Noble metals with plasma frequencies limited in the near-infrared are lossy materials in optical regime (Riley *et al.*, 2016). To reduce the loss of a plasmonic system, alternative materials such as highly doped semiconductors have been attracting attention in plasmonics and metamaterial applications because of their tunable free carrier concentrations in optical frequency region (Lin *et al.*, 2016; Zheng *et al.*, 2018). Aluminum-doped zinc oxide (AZO) is a heavily doped semiconductor with broad band-gap (Zheng *et al.*, 2018). This capability of supporting high dopant concentrations and tunable material properties, occupy an important place in plasmonic designs (Riley *et al.*, 2016). Therefore, many studies have focused on the properties of AZO in the visible and near-infrared region (Li *et al.*, 2008; Ehrmann and Reineke-Koch, 2010) and some have been concentrated on absorption characteristic of plasmonic devices using AZO (Sun *et al.*, 2018; George *et al.*, 2017).

A novel metamaterial absorber design using periodic patterned AZO resonators is presented in this study. Numerical results showing spectral absorption response in the infrared compared to one with a planar thin-film design are discussed. The field enhancement caused by AZO nanopattern arrays is numerically investigated to explain plasmonic effects.

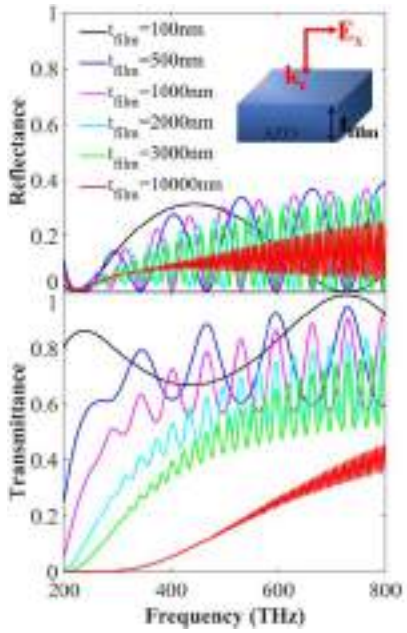

Fig. 1. Reflectance and transmittance spectra of an AZO film as a mirror layer. The schematic view of the film is given inset.

2. MATERIAL AND METHODS

Proposed structures are analyzed by using finite-difference-time-domain (FDTD) method. During the simulations, unless otherwise indicated, the analyses are performed under *x*-polarization, periodic boundary conditions are chosen as *x*- and *y*-axes, perfectly matched layers are used along the *z*-axis. The Plasma (Drude) model is used for AZO as a material model in FDTD simulations; the plasma frequency $\omega_p = 2.5828 \times 10^{15}$ rad/s, the permittivity $\varepsilon = 4.5$ and the plasma collusion $\nu_C = 1.4585 \times 10^{14}$ rad/s are taken as given in a study for thermally processed (TP) atomic layer deposition (ALD) AZO (Riley *et al.*, 2016). Riley et al. (2016) provided a blueshift in the crossover wavelength and increase in the carrier concentration. In this study, a metal-free design or design with minimal-metal usage is aimed by utilizing these improved properties.

3. RESULTS AND DISCUSSION

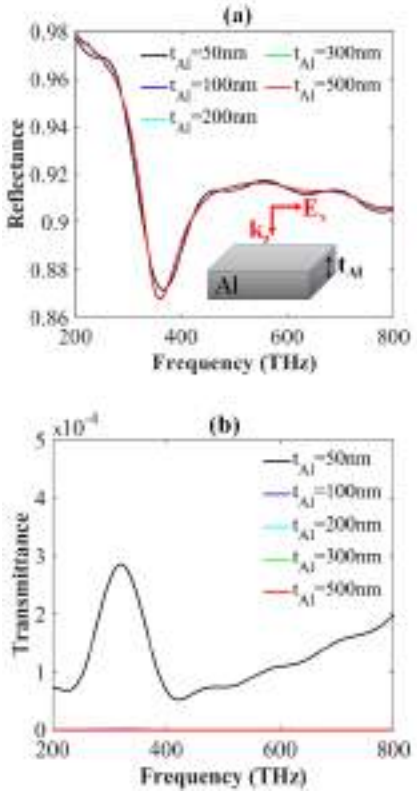

Fig. 2. Reflectance and transmittance spectra of an Al film with various thickness. The schematic view of the film is given inset.

The first stage of our design is to determine the mirror-layer performance of TP-AZO (Riley *et al.*, 2016) by making a film thickness sweep. Fig. 1 shows the reflectance and transmittance spectra of a TP-AZO film as a mirror layer. The schematic view of the film is given inset. It is expected for an absorber metamaterial (Aslan *et al.*, 2017a; Aslan *et al.*, 2017b; Aslan *et al.*, 2019) to improve reflection characteristic and minimize transmission characteristic of the film while increasing the film thickness t_{film}. As seen from this figure, AZO film from 100 nm to 10 μm still exhibits transmission in visible ranges and and also absorption in the near infrared. Thus, it can be understood from the figure, a TP-AZO film cannot be used as a stand-alone mirror layer.

Aluminum (Al) can be used as a back-reflector layer in the absorber design with regard to its good adhesion, lower cost, and less sensitivity to oxidation (Sun *et al.*, 2018). To view back-reflector performance of an Al film, the reflectance and transmittance spectra at near-infrared and visible frequencies are given in Fig. 2 for different-thick Al film. The dielectric constants of Al used for

simulations are taken from Palik (1985). According to the figure, optimally 100 nm-thick Al film is a good reflector even if it is not a perfect reflector in given frequency ranges. It exhibits undesired lower reflectance values at around 360 THz. In this context, a new mirror layer with a metal/AZO layer is analyzed numerically in order to reduce the amount of metal in the design, the cost of metal, and undesired lower reflectance. Fig. 3 shows the reflectance and transmittance spectra of an Al film coated an AZO film as a back-reflector layer with various thicknesses. Larger thicknesses of the AZO film and 50 nm-thick Al layer considerably reduce the transmittance of the mirror layer (Figure 3 - upper panel). 50 nm-thick Al layer can be chosen as metal sheet. The thickness of AZO layer must be taken smaller due to its absorption character. However, this absorption character of AZO cannot provide maximum reflection (Fig. 3 - lower panel). Thus, as can be understood from Figs. 2 and 3, 100 nm-thick Al layer must be used as a good back-reflector layer to ensure near-0-transmittance and near-1-reflectance.

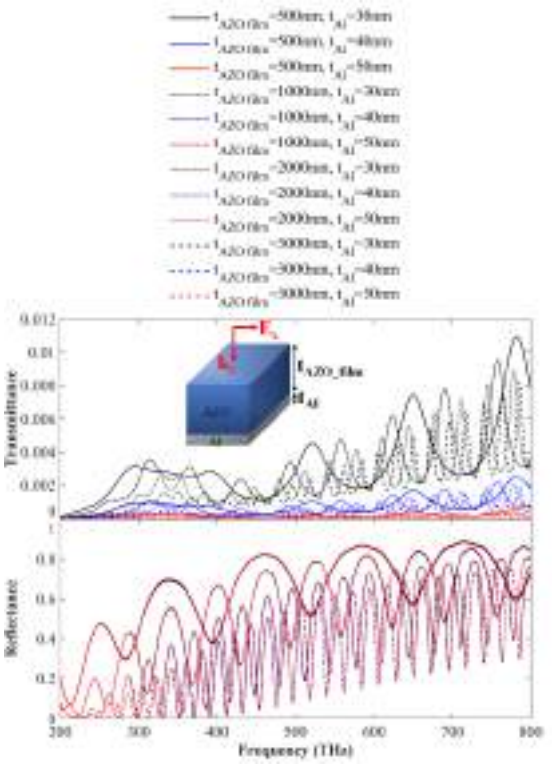

Fig. 3. Reflectance and transmittance spectra of an Al film coated an AZO film with various thicknesses. The schematic view of the film-set is given as inset.

In order to see the absorber performance of AZO nanoparticles, we analyze the absorber design with honeycomb-shaped AZO nanoantennas. The schematic view for the unit cell of honeycomb-shaped metamaterial-plasmonic absorber is given in Figure 4a. In this schematic representation, *L* is the width of each honeycomb shaped nanoantenna, *G* is the distance between the nanoantennas. The functional layers of the unit-cell are an Al ground plane, magnesium fluoride (MgF_2) layer as a dielectric spacer and the upper AZO nanoantennas. In the analyses, the structure is illuminated under x-polarization case and propagation direction is z-axis. Absorption responses (Figure 4b-c) are calculated as $A = 1 - R - T$ from the obtained reflectance and transmittance data (Aslan *et al.*, 2017a; Aslan *et al.*, 2017b; Aslan *et al.*, 2019). These spectra show that the honeycomb-shaped AZO nanopatterns are not able to provide perfect plasmonic absorption.

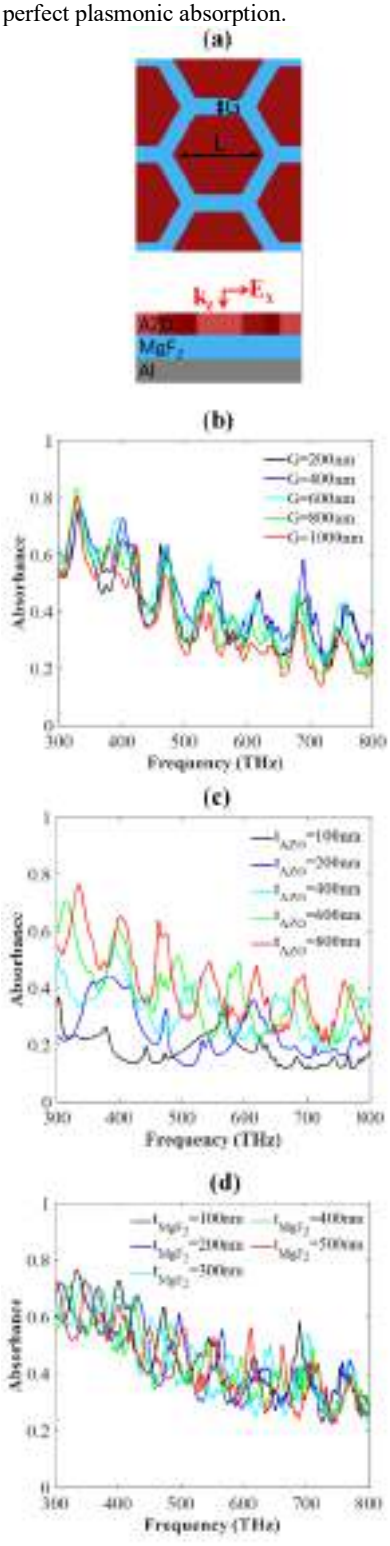

Fig. 4. (a) The schematic view of the absorber design with honeycomb-shaped AZO nanoantennas. The absorbance spectra of the design for various **(b)** *G*, **(c)** t_{AZO}, and **(d)** t_{MgF2} values.

4. CONCLUSION

In conclusion, we have analyzed the absorption performance of an AZO film, an Al/AZO layer, the absorber design atop honeycomb-shaped AZO nanopatterns in order to provide a tunable, low-loss, and low-cost solution to absorber metamaterial with alternative plasmonics.

ACKNOWLEDGEMENTS

The work described in this paper is supported by Scientific Research Projects Coordination Center of Hatay Mustafa Kemal University (Project No: 19.M.016).

REFERENCES

Aslan, E., Aslan, E., Turkmen, M., and Saracoglu, O. G. (2017). "Experimental and numerical characterization of a mid-infrared plasmonic perfect absorber for dual-band enhanced vibrational spectroscopy." *Optical Materials*, Vol. 73, pp. 213-222.

Aslan, E., Aslan, E., Turkmen, M., and Saracoglu, O. G. (2017). "Metamaterial plasmonic absorber for reducing the spectral shift between near-and far-field responses in surface-enhanced spectroscopy applications." *Sensors and Actuators A: Physical*, Vol. 267, pp. 60-69.

Aslan, E., Aslan, E., Saracoglu, O. G, and Turkmen, M. (2019). "An effective triple-band enhanced-infrared-absorption detection by honeycomb-shaped metamaterial-plasmonic absorber." *Sensors and Actuators A: Physical*, Vol. 288, pp. 149-155.

Ehrmann, N. and Reineke-Koch, R. (2010). "Ellipsometric studies on ZnO:Al thin films: refinement of dispersion theories. " *Thin Solid Films*, Vol. 519, No. 4, pp.1475–1485.

George, D., Adewole, M., Hassan, S., Lowell, D., Cui, J., Zhang, H., Philipose, U., and Lin, Y. (2017). "Coupling of surface plasmon polariton in Al-doped ZnO with Fabry-Pérot resonance for total light absorption." *Photonics*, Vol. 4, No. 2, pp. 35.

Li, Q. H., Zhu, D., Liu, W., Liu, Y., and Ma, X. C. (2008). "Optical properties of Al-doped ZnO thin films by ellipsometry." *Appl. Surf. Sci.*, Vol. 254, No. 10, pp. 2922–2926.

Lin, J. Y., Zhong, K. D., and Lee, P. T. (2016). "Plasmonic behaviors of metallic AZO thin film and AZO nanodisk array." *Opt. Express*, Vol. 24, No. 5, pp. 5125–5135.

Palik, E. D. (1985). *Handbook of Optical Constants of Solids*, Academic Press, Orlando, US.

Riley, C. T., Smalley, J. S. T., Post, K. W., Basov, D. N., Fainman, Y., Wang, D., Liu, Z., and Sirbuly, D. J. (2016). "High-quality, ultraconformal aluminum-doped zinc oxide nanoplasmonic and hyperbolic metamaterials." *Small*, Vol. 12, No. 7, pp. 892–901.

Sun, K., Riedel, C. A., Wang, Y., Urbani, A., Simeoni, M., , Mengali, S., Zalkovskij, Bilenberg, M., B., de Groot, C. H., and Muskens, O. L. (2018). "Metasurface optical solar reflectors using AZO transparent conducting oxides for radiative cooling of spacecraft." *ACS Photonics*, Vol. 5, pp. 495−501.

Zheng, H., Zhang, R.-J., Li, D.-H., Chen, X., Wang, S.-Y., Zheng, Y.-X., Li, M.-J., Hu, Z.-G., Dai, N. and Chen, L.-Y. (2018). "Optical properties of al-doped ZnO films in the infrared region and their absorption applications." *Nanoscale Research Letters*, Vol. 13, pp.149.

AZO METAMATERIAL FOR DUAL-BAND PERFECT ABSORPTION

Erdem Aslan *[1] and Ekin Aslan [2]

[1] Department of Electrical and Electronics Engineering, Hatay Mustafa Kemal University, Hatay, TURKEY, erdem.aslan@mku.edu.tr

[2] Department of Electrical and Electronics Engineering, Hatay Mustafa Kemal University, Hatay, TURKEY, ekin.aslan@mku.edu.tr

[3]

ABSTRACT

An alternative plasmonic material, aluminum-doped zinc oxide (AZO) can provide a tunable low-loss and low-cost contribution to absorber metamaterial concept in optical applications. With this viewpoint, a metamaterial absorber with circular patterned AZO nanoantenna arrays is numerically analyzed, whether if it can ensure a perfect absorbance. The parameters of AZO with an improved carrier concentration by a thermal process are utilized in finite difference time domain (FDTD) simulations. A dual-band perfect absorption can be provided with optimized geometrical parameters.

Keywords: *Alternative plasmonics, Nanopatterned AZO, Metamaterial absorber*

* Corresponding Author

1. INTRODUCTION

Alternative plasmonic materials can be substitute for noble metals with limited plasma frequencies in the near-infrared and lossy behavior at optical frequencies (Riley *et al.*, 2016). To reduce metal losses, highly doped semiconductors as alternative materials have been involved into plasmonics. Their tunable free carrier concentrations in optical frequency region have rendered possible their metamaterial applications (Lin *et al.*, 2016; Zheng *et al.*, 2018).

One of the alternative plasmonic material Aluminum-doped zinc oxide (AZO) is a heavily doped semiconductor with broad band gap (Zheng *et al.*, 2018). This support of high dopant concentrations and tunable material composes an important role in plasmonic metamaterial designs (Riley *et al.*, 2016). Hence, literature has possessed many studies focused on the optical properties of AZO in the visible and near-infrared region (Li *et al.*, 2008; Ehrmann and Reineke-Koch, 2010). Some have been concentrated on absorption character of plasmonic structures using AZO (Sun *et al.*, 2018; George *et al.*, 2017).

A novel metamaterial absorber with circular patterned AZO nanoantenna arrays is numerically analyzed and presented in this study, whether if it can provide a perfect absorption. Numerical results indicate dual-band perfect absorption in mid-infrared regime for optimized geometrical parameters.

2. MATERIAL AND METHODS

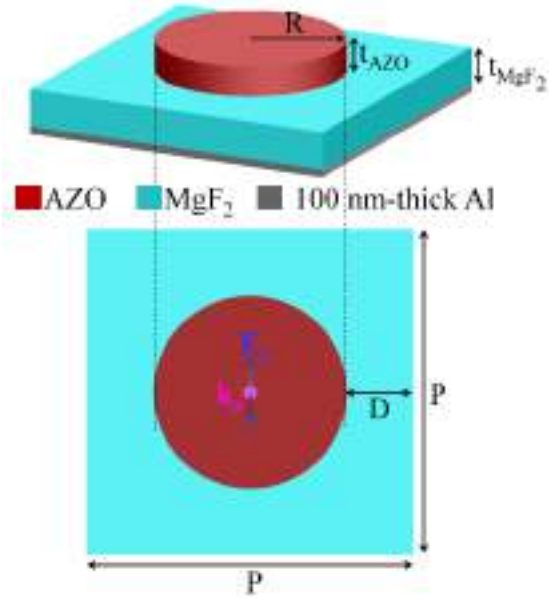

Fig. 1. The schematic view of the designed unit cell.

Proposed structure is analyzed by using finite-difference-time-domain (FDTD) method. Unless otherwise indicated, during the simulations; periodic boundary conditions are chosen as *x*- and *y*-axes, perfectly matched layers are used along the *z*-axis. Unit cell is illuminated under *y*-polarization, along the *z*-axis (Fig. 1). As seen from Fig. 1, unit cell is constructed from bottom to top as a back-reflector 100 nm-thick aluminum (Al) film, a magnesium fluoride (MgF_2) spacer layer, and AZO nanoantenna. The plasma (Drude) model is used for AZO as a material model in FDTD simulations; the plasma frequency $\omega_p = 2.5828 \times 10^{15}$ rad/s, the permittivity $\varepsilon = 4.5$ and the plasma collusion $\nu_C = 1.4585 \times 10^{14}$ rad/s are taken as given in a study for thermally processed (TP) atomic layer deposition (ALD) of AZO (Riley *et al.*, 2016). Riley et. al. (2016) provided a blueshift in the crossover wavelength and increase in the carrier concentration. The dielectric constant of Al used for simulations and refractive index of MgF_2 are taken from Palik (1985) and Dodge (1984), respectively. Geometrical parameters expressing the unit cell are the radius of circular AZO nanoantenna *R*, semi-distance between nanoantennas *D*, and the periodicity of unit cell *P* (Fig. 1). Here, t_{MgF_2} and t_{AZO} are the thicknesses of spacer layer and AZO nanoantennas, respectively.

3. RESULTS AND DISCUSSION

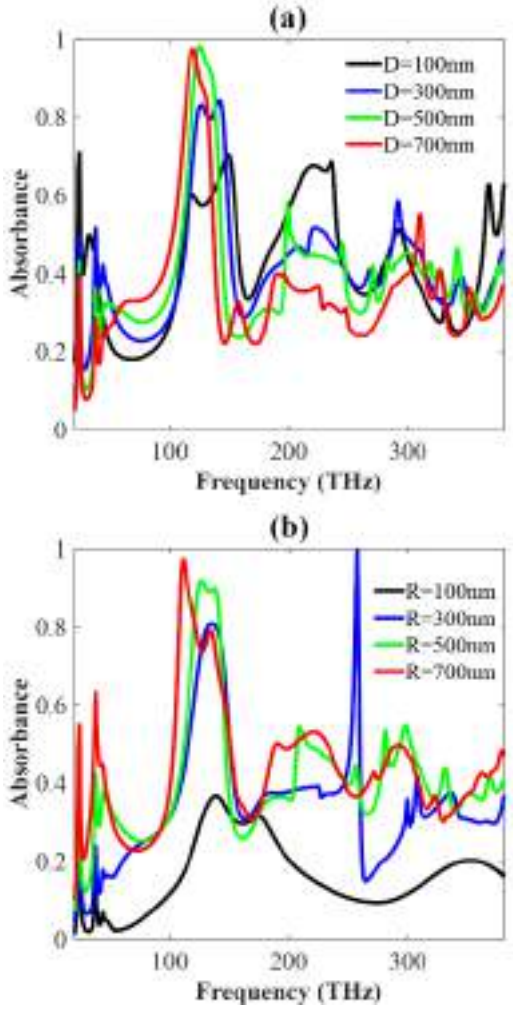

Fig. 2. The absorption spectra of the designed structure corresponding to **(a)** *D* (*R* = 500 nm) and **(b)** *R* (*D* = 400 nm) sweeps (t_{MgF_2} = 500 nm, t_{AZO} = 400 nm).

The first process of our design is to determine the absorption performance of AZO nanoantenna arrays by making a geometrical parameter sweep in mid- and -near infrared regime. Fig. 2 shows the absorbance spectra of a

designed absorber structure. Absorption responses are calculated as $A = 1 - R - T$ from the obtained reflectance and transmittance data (Aslan *et al.*, 2017a; Aslan *et al.*, 2017b; Aslan *et al.*, 2019). Here, a good absorption in mid-infrared regime is observed and the increases of R and D induce higher absorption.

Secondly, the effect of material thicknesses of the proposed structure is numerically analyzed. Fig. 3 shows absorption spectra of the designed structure corresponding to t_{MgF_2} and t_{AZO} variations. While small values of t_{MgF_2} yield more specific multi resonant response, bigger values of t_{AZO} cause to bigger absorption at only one resonance.

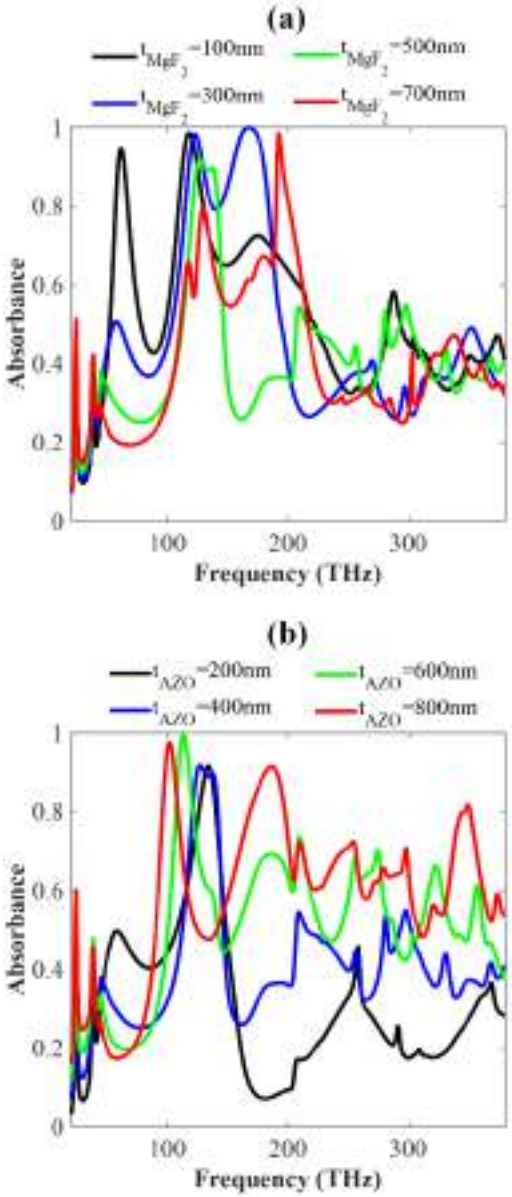

Fig. 3. The absorption spectra of the designed structure corresponding to **(a)** t_{MgF_2} (t_{AZO}= 400 nm) and **(b)** t_{AZO} (t_{MgF_2}= 500 nm) sweeps (R = 500 nm, D = 400 nm).

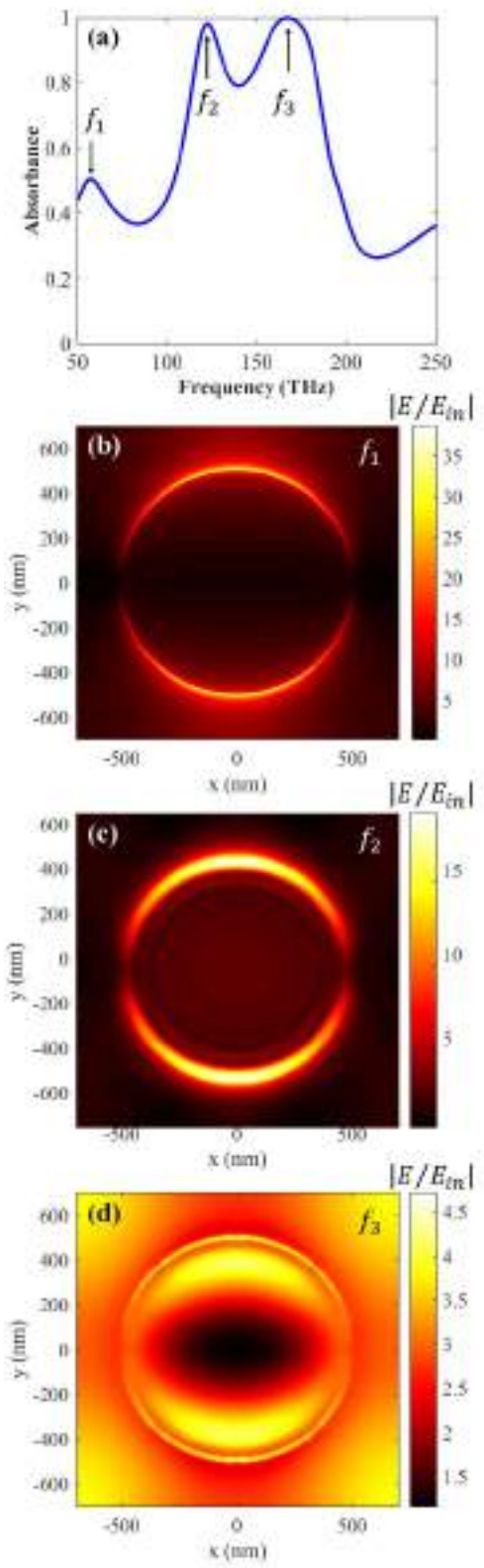

Fig. 4. (a) Absorption spectra for chosen geometrical parameters. Spatial $|E/E_{in}|$distributions at **(b)** f_1 = 58 THz, **(c)** f_2 = 122 THz, and **(d)** f_3 = 167 THz. (R = 500 nm, D = 400 nm, t_{MgF_2}= 300 nm, and t_{AZO}= 400 nm).

Following, the chosen parameters are $R = 500$ nm, $D = 400$ nm, $t_{MgF_2} = 300$ nm, and $t_{AZO} = 400$ nm. Fig. 4a shows the first resonant band at f_1 with semi-absorption and a dual-band perfect absorption at f_2 and f_3. For these parameters, field distributions are investigated by simulations. Fig.4b-d shows spatial *E*-field enhancements ($|E/E_{in}|$) atop the surface between the spacer layer and nanoantenna arrays for three resonant modes in mid-infrared. Resonant frequencies are f_1 = 58 THz, f_2 = 122 THz, and f_3 = 167 THz. Furthermore, spatial *H*-field enhancements ($|H/H_{in}|$) is given in Fig. 5 for same location. At f_1, the design exhibits quite high *E*-field and *H*-field enhancements.

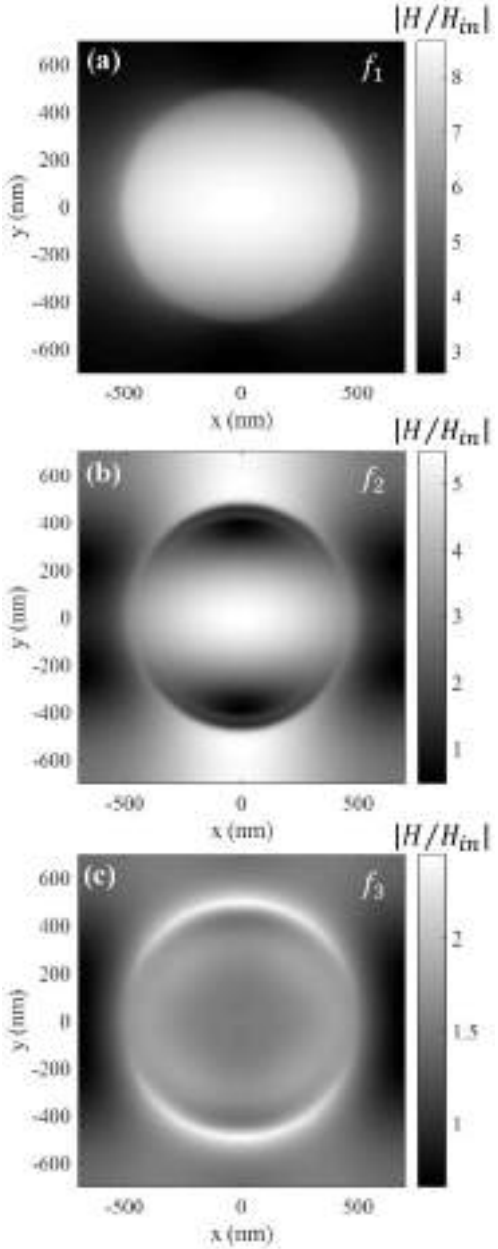

Fig. 5. Spatial $|H/H_{in}|$distributions at **(a)** $f_1 = 58$ THz, **(b)** $f_2 = 122$ THz, and **(c)** $f_3 = 167$ THz. ($R = 500$ nm, $D = 400$ nm, $t_{MgF_2} = 300$ nm, and $t_{AZO} = 400$ nm).

4. CONCLUSION

In conclusion, a metamaterial absorber with circular patterned AZO nanoantenna arrays is numerically analyzed by using FDTD method. Geometrical parameter sweeps yield a dual band perfect absorber design constructed with an alternative plasmonic material for an optimized parameter set. This design can be a good candidate as a dual-band perfect absorber constructed with alternative plasmonic phenomena. Although the first resonance at f_1 cannot be used for perfect absorption, the high magnetic field enhancement can be used in other applications.

ACKNOWLEDGEMENTS

The work described in this paper is supported by Scientific Research Projects Coordination Center of Hatay Mustafa Kemal University (Project No: 19.M.016).

REFERENCES

Aslan, E., Aslan, E., Turkmen, M., and Saracoglu, O. G. (2017). "Experimental and numerical characterization of a mid-infrared plasmonic perfect absorber for dual-band enhanced vibrational spectroscopy." *Optical Materials*, Vol. 73, pp. 213-222.

Aslan, E., Aslan, E., Turkmen, M., and Saracoglu, O. G. (2017). "Metamaterial plasmonic absorber for reducing the spectral shift between near-and far-field responses in surface-enhanced spectroscopy applications." *Sensors and Actuators A: Physical*, Vol. 267, pp. 60-69.

Aslan, E., Aslan, E., Saracoglu, O. G, and Turkmen, M. (2019). "An effective triple-band enhanced-infrared-absorption detection by honeycomb-shaped metamaterial-plasmonic absorber." *Sensors and Actuators A: Physical*, Vol. 288, pp. 149-155.

Dodge, M. J. (1984). "Refractive properties of magnesium fluoride." *Applied Optics*, Vol. 23, pp. 1980-1985.

Ehrmann, N. and Reineke-Koch, R. (2010). "Ellipsometric studies on ZnO:Al thin films: refinement of dispersion theories. " *Thin Solid Films*, Vol. 519, No. 4, pp.1475–1485.

George, D., Adewole, M., Hassan, S., Lowell, D., Cui, J., Zhang, H., Philipose, U., and Lin, Y. (2017). "Coupling of surface plasmon polariton in Al-doped ZnO with Fabry-Pérot resonance for total light absorption." *Photonics*, Vol. 4, No. 2, pp. 35.

Li, Q. H., Zhu, D., Liu, W., Liu, Y., and Ma, X. C. (2008). "Optical properties of Al-doped ZnO thin films by ellipsometry." *Appl. Surf. Sci.*, Vol. 254, No. 10, pp. 2922–2926.

Lin, J. Y., Zhong, K. D., and Lee, P. T. (2016). "Plasmonic behaviors of metallic AZO thin film and AZO nanodisk array." *Opt. Express*, Vol. 24, No. 5, pp. 5125–5135.

Palik, E. D. (1985). *Handbook of Optical Constants of Solids*, Academic Press, Orlando, US.

Riley, C. T., Smalley, J. S. T., Post, K. W., Basov, D. N., Fainman, Y., Wang, D., Liu, Z., and Sirbuly, D. J. (2016). "High-quality, ultraconformal aluminum-doped zinc oxide nanoplasmonic and hyperbolic metamaterials." *Small*, Vol. 12, No. 7, pp. 892–901.

Sun, K., Riedel, C. A., Wang, Y., Urbani, A., Simeoni, M., , Mengali, S., Zalkovskij, Bilenberg, M., B., de Groot, C. H., and Muskens, O. L. (2018). "Metasurface optical solar reflectors using AZO transparent conducting oxides for radiative cooling of spacecraft." *ACS Photonics*, Vol. 5, pp. 495−501.

Zheng, H., Zhang, R.-J., Li, D.-H., Chen, X., Wang, S.-Y., Zheng, Y.-X., Li, M.-J., Hu, Z.-G., Dai, N. and Chen, L.-Y. (2018). "Optical properties of al-doped ZnO films in the infrared region and their absorption applications." *Nanoscale Research Letters*, Vol. 13, pp.149.

CISET - 2nd Cilicia International Symposium on Engineering and Technology
10-12 October, 2019, Mersin / TURKEY

ABSORPTION CHARACTERISTICS OF 3D-PATTERNED AZO NANOANTENNAS

Erdem Aslan [*1] and Ekin Aslan [2]

[1] Department of Electrical and Electronics Engineering, Hatay Mustafa Kemal University, Hatay, TURKEY, erdem.aslan@mku.edu.tr

[2] Department of Electrical and Electronics Engineering, Hatay Mustafa Kemal University, Hatay, TURKEY, ekin.aslan@mku.edu.tr

3

ABSTRACT

A 3D-nanopatterned aluminum-doped zinc oxide (AZO) layer can provide low-loss and low-cost contribution to perfect absorber metamaterial concept in optical applications. In this context, a perfect absorber with AZO nanoantenna designed as a 3D nanopatterned structure with a circular section built on a square-shaped base is numerically investigated, whether if it can ensure a perfect absorbance. Plasma (Drude) parameters of AZO with an improved carrier concentration by a thermal process are used in finite difference time domain (FDTD) simulations. A parameter sweep set is concluded with a dual-band perfect absorption.

Keywords: *AZO, 3D-nanopatterned antenna, Perfect absorber*

[*] Corresponding Author

1. INTRODUCTION

Whereas nobel metals possess limited plasma frequencies in the near-infrared and lossy behavior at optical frequencies, alternative plasmonic materials can be a good substitution for noble metals (Riley *et al.*, 2016). In order to decrease metal losses and cost, highly doped semiconductors as alternative materials can be involved into plasmonics. An attractive role in metamaterial applications can be rendered by their tunable free carrier concentrations in optical frequency region Lin *et al.*, 2016; Zheng *et al.*, 2018).

Aluminum-doped zinc oxide (AZO) is a heavily doped semiconductor with broad band gap as an alternative plasmonic material (Zheng *et al.*, 2018). This high dopant concentration and tunable character constitute an important opportunity in plasmonics (Riley *et al.*, 2016). Thus, many studies focused on the optical properties of AZO in the visible and near-infrared region have come up in the literature (Li *et al.*, 2008; Ehrmann and Reineke-Koch, 2010). Some of these have been concentrated on absorber behavior of plasmonic structures containing AZO (Sun *et al.*, 2018; George *et al.*, 2017).

A novel metamaterial absorber with AZO nanoatenna designed as a 3D nanopatterned structure with a circular section built on a square-shaped table is numerically analyzed for perfect absorption and presented in this study. Via numerical results, dual-band perfect absorption is observed in mid-infrared regime for an optimized geometrical parameter set.

2. MATERIAL AND METHODS

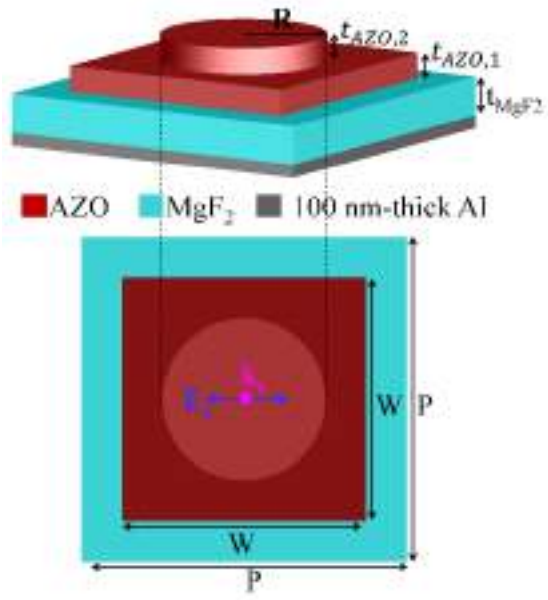

Fig. 1. The schematic view of the designed unit cell.

Proposed structure is analyzed by using finite-difference-time-domain (FDTD) method. Unless otherwise indicated, during the simulations; periodic boundary conditions are chosen as *x*- and *y*-axes, perfectly matched layers are used along the *z*-axis. The unit cell of the designed structure is illuminated under *x*-polarization, along the *z*-axis (Fig. 1). The unit cell construction is formed from bottom to top as a back-reflector 100 nm-thick aluminum (Al) film, a magnesium fluoride (MgF_2) spacer layer, and AZO nanoantenna as seen from Fig. 1. The plasma (Drude) model is used for AZO as a material model in FDTD simulations; the plasma frequency $\omega_p = 2.5828 \times 10^{15}$ rad/s, the permittivity $\varepsilon = 4.5$ and the plasma collusion $\nu_C = 1.4585 \times 10^{14}$ rad/s are taken as given in a study for thermally processed (TP) atomic layer deposition (ALD) of AZO (Riley *et al.*, 2016). The dielectric constant of Al used for simulations and refractive index of MgF_2 are taken from Palik (1985) and Dodge (1984), respectively. AZO nanoatenna is designed as a 3D nanopatterned structure as a circular section built on a square-shaped table. The geometrical parameters of the 3D nanopatterned antenna are the radius of circular AZO section *R*, the width of AZO square table *W*, the thickness of circular AZO section $t_{AZO,2}$, and the thickness of square-shaped AZO table $t_{AZO,1}$ (Fig. 1). Other parameters are the periodicity of unit cell *P* and the thicknesses of spacer layer t_{MgF_2} (Fig. 1).

3. RESULTS AND DISCUSSION

In order to determine the absorption performance of 3D AZO nanoantenna arrays, a geometrical parameter sweep set is performed in mid- and -near infrared regime. Absorbance spectra of the designed metamaterial absorber are given in Fig. 2. Spectral absorption behaviors are calculated as $A = 1 - R - T$ from the obtained reflectance and transmittance data (Aslan *et al.*, 2017a; Aslan *et al.*, 2017b; Aslan *et al.*, 2019). Here, a dual-perfect absorption in mid-infrared regime is observed, and the increasing *R* and optimally small values *W* and *P* induce higher absorption.

Following, we numerically analyze the effect of material thicknesses of the proposed structure. The absorption spectra of the designed structure corresponding to $t_{AZO,1}$, $t_{AZO,2}$, and t_{MgF_2} variations are shown Fig. 3. While increasing values of $t_{AZO,1}$ yield mostly affect hybridization of modes (Zhang *et al*. 2017), $t_{AZO,2}$ variation adjusts absorption of dual-modes (Fig. 3a,b). Further, Fig. 3c shows that an optimum t_{MgF_2} value can redound hybridization and can ensure perfect absorption of dual resonances.

Finally, the chosen parameters are R = 400 nm, W = 1100 nm, P = 1400 nm, t_{MgF_2} = 300 nm, $t_{AZO,1}$ = 300 nm, and $t_{AZO,2}$ = 300 nm for a perfect absorption at dual resonances. Fig. 4a indicates a dual-band perfect absorption at f_1 and f_2. Resonant frequencies are f_1 = 116 THz and f_2 = 181 THz. For chosen parameters, field distributions are investigated by simulations via the field monitors M_1 and M_2 (Fig.4a inset yields the location of the monitors in the design). Fig.4b-e shows spatial *E*-field enhancements ($|E/E_{in}|$) for dual resonant modes in mid-infrared. At f_1, the design exhibits quite high *E*-field enhancements.

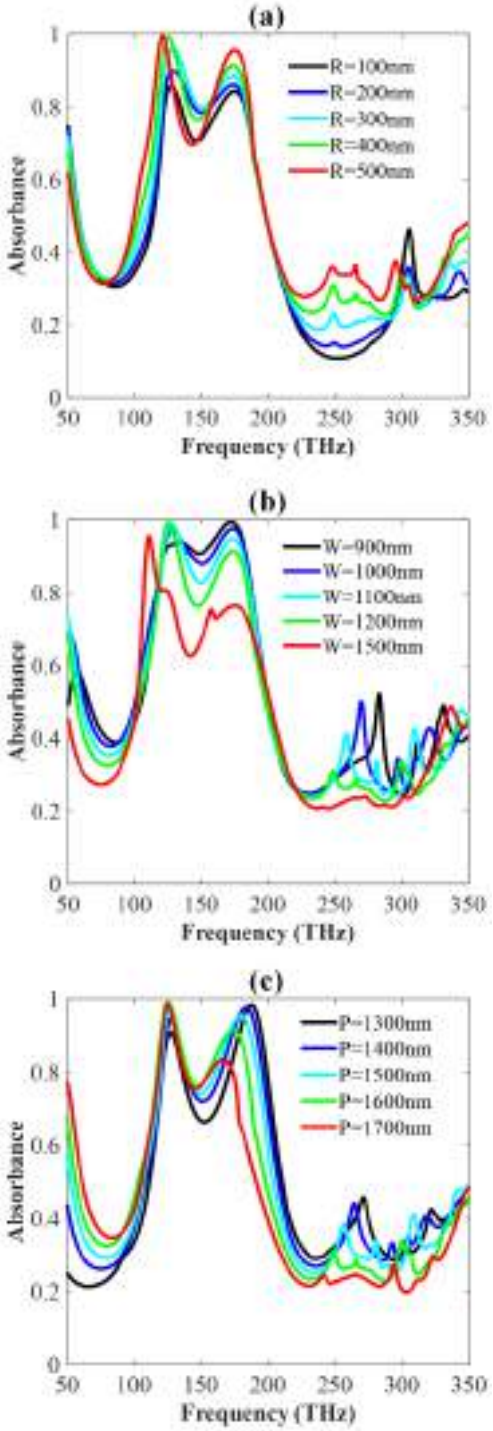

Fig. 2. The absorption spectra of the designed structure corresponding to **(a)** R (W = 1200 nm, P = 1400 nm), **(b)** W (R = 400 nm, P = 1400 nm), and **(c)** P (R = 400 nm, W = 1200 nm) sweeps (t_{MgF_2}= 300 nm, $t_{AZO,1}$= 200 nm, $t_{AZO,2}$= 200 nm).

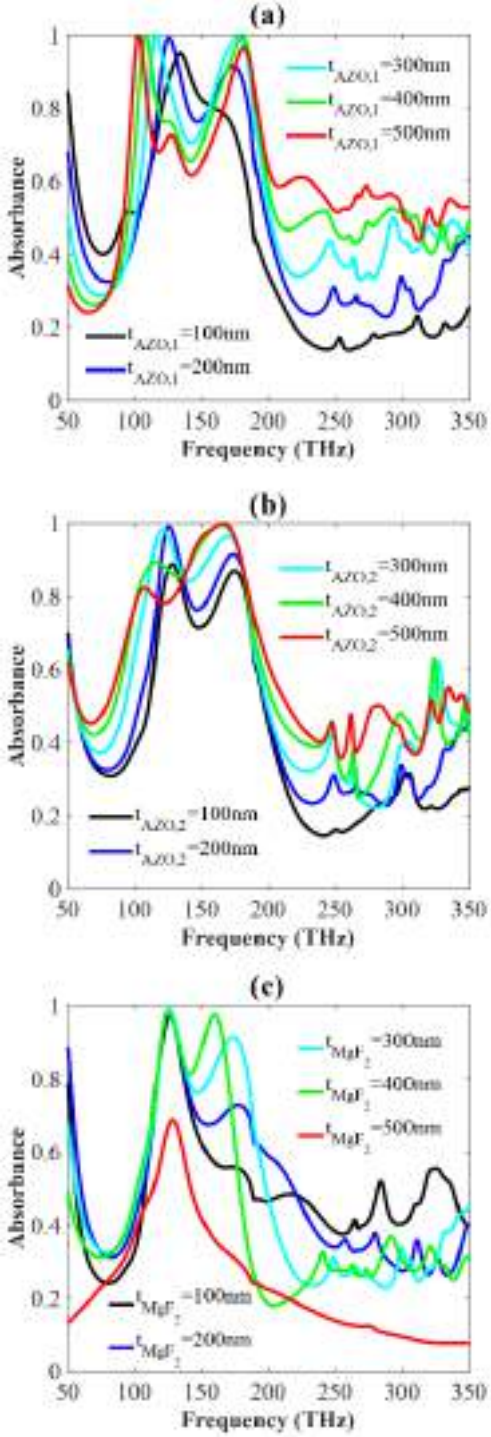

Fig. 3. The absorption spectra of the designed structure corresponding to **(a)** $t_{AZO,1}$ ($t_{AZO,2}$= 200 nm, t_{MgF_2}= 300 nm), **(b)** $t_{AZO,2}$ ($t_{AZO,1}$= 200 nm, t_{MgF_2}= 300 nm), and **(c)** t_{MgF_2} ($t_{AZO,1}$= 200 nm, $t_{AZO,2}$= 200 nm) sweeps (R = 400 nm, W = 1200 nm, P = 1400 nm).

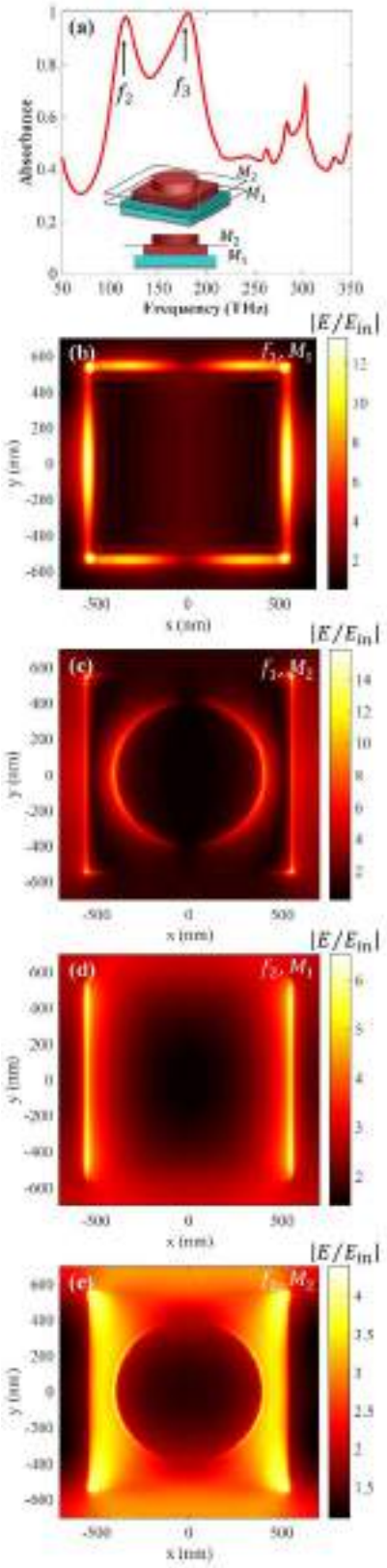

Fig. 4. (a) Absorption spectra for chosen geometrical parameters. Spatial $|E/E_{in}|$distributions **(b)** on M_1 at f_1, **(c)** on M_1 at f_1, **(d)** on M_1 at f_2, and **(e)** on M_2 at f_2 (The schematic view of the field monitors is given as inset of panel **a**).

4. CONCLUSION

Consequently, a metamaterial absorber with 3D nanopatterned structure as a circular AZO section built on a square-shaped AZO table is numerically investigated by using FDTD method. Geometrical parameter sweeps are performed to see the absorption character of the proposed design. A dual band perfect absorber design constructed with an alternative plasmonic material for an optimized parameter set is presented.

ACKNOWLEDGEMENTS

The work described in this paper is supported by Scientific Research Projects Coordination Center of Hatay Mustafa Kemal University (Project No: 19.M.016).

REFERENCES

Aslan, E., Aslan, E., Turkmen, M., and Saracoglu, O. G. (2017). "Experimental and numerical characterization of a mid-infrared plasmonic perfect absorber for dual-band enhanced vibrational spectroscopy." *Optical Materials*, Vol. 73, pp. 213-222.

Aslan, E., Aslan, E., Turkmen, M., and Saracoglu, O. G. (2017). "Metamaterial plasmonic absorber for reducing the spectral shift between near-and far-field responses in surface-enhanced spectroscopy applications." *Sensors and Actuators A: Physical*, Vol. 267, pp. 60-69.

Aslan, E., Aslan, E., Saracoglu, O. G, and Turkmen, M. (2019). "An effective triple-band enhanced-infrared-absorption detection by honeycomb-shaped metamaterial-plasmonic absorber." *Sensors and Actuators A: Physical*, Vol. 288, pp. 149-155.

Dodge, M. J. (1984). "Refractive properties of magnesium fluoride." *Applied Optics*, Vol. 23, pp. 1980-1985.

Ehrmann, N. and Reineke-Koch, R. (2010). "Ellipsometric studies on ZnO:Al thin films: refinement of dispersion theories. " *Thin Solid Films*, Vol. 519, No. 4, pp.1475–1485.

George, D., Adewole, M., Hassan, S., Lowell, D., Cui, J., Zhang, H., Philipose, U., and Lin, Y. (2017). "Coupling of surface plasmon polariton in Al-doped ZnO with Fabry-Pérot resonance for total light absorption." *Photonics*, Vol. 4, No. 2, pp. 35.

Li, Q. H., Zhu, D., Liu, W., Liu, Y., and Ma, X. C. (2008). "Optical properties of Al-doped ZnO thin films by ellipsometry." *Appl. Surf. Sci.*, Vol. 254, No. 10, pp. 2922–2926.

Lin, J. Y., Zhong, K. D., and Lee, P. T. (2016). "Plasmonic behaviors of metallic AZO thin film and AZO nanodisk array." *Opt. Express*, Vol. 24, No. 5, pp. 5125–5135.

Palik, E. D. (1985). *Handbook of Optical Constants of Solids*, Academic Press, Orlando, US.

Riley, C. T., Smalley, J. S. T., Post, K. W., Basov, D. N., Fainman, Y., Wang, D., Liu, Z., and Sirbuly, D. J. (2016). "High-quality, ultraconformal aluminum-doped zinc oxide nanoplasmonic and hyperbolic metamaterials." *Small*, Vol. 12, No. 7, pp. 892–901.

Sun, K., Riedel, C. A., Wang, Y., Urbani, A., Simeoni, M., , Mengali, S., Zalkovskij, Bilenberg, M., B., de Groot, C. H., and Muskens, O. L. (2018). "Metasurface optical solar reflectors using AZO transparent conducting oxides for radiative cooling of spacecraft." *ACS Photonics*, Vol. 5, pp. 495−501.

Zhang, J., Liao, Z., Luo, Y., Shen, X., Maier, S. A., Cui, T. J. (2017). "Spoof plasmon hybridization." *Laser & Photonics Review*, Vol. 11, No. 1, pp.1600191.

Zheng, H., Zhang, R.-J., Li, D.-H., Chen, X., Wang, S.-Y., Zheng, Y.-X., Li, M.-J., Hu, Z.-G., Dai, N. and Chen, L.-Y. (2018). "Optical properties of al-doped ZnO films in the infrared region and their absorption applications." *Nanoscale Research Letters*, Vol. 13, pp.149.

CISET - 2nd Cilicia International Symposium on Engineering and Technology
10-12 October, 2019, Mersin / TURKEY

AN INVESTIGATION OF FLOTATION BEHAVIOUR OF SILICA SANDS WITH HIGH IRON CONTENT

Ilgin Kursun [1], Mert Terzi [2], Mustafa Cinar [3] and Orhan Ozdemir [*4]

[1] Istanbul University-Cerrahpasa, Eng. Faculty, Mining Eng. Dept., Istanbul, Turkey, ilginkur@istanbul.edu.tr

[2] Istanbul University-Cerrahpasa, Eng. Faculty, Mining Eng. Dept., Istanbul, Turkey, mert.terzi@istanbul.edu.tr

[3] Canakkale Onsekiz Mart University, Eng. Faculty, Mining Eng. Dept., Canakkale, Turkey, mcinar@comu.edu.tr

[4] Istanbul University-Cerrahpasa, Eng. Faculty, Mining Eng. Dept., Istanbul, Turkey, orhanozdemir@istanbul.edu.tr

ABSTRACT

In this study, the removal of quartz from the magnetite concentrate, which was produced by gravity and magnetic separation of a silica sand with high iron content obtained from Canakkale region, using flotation method was investigated. In the flotation experiments, cationic flotation under acidic and alkaline conditions, and anionic flotation in alkaline conditions were performed. Ethylenediamine and sodium oleate were used as collectors for cationic and anionic flotation experiments, respectively, and the best results were obtained by cationic flotation in the acidic conditions.

Moreover, the zeta potential measurements were performed with pure quartz and magnetite samples. The effects of different ethylenediamine concentrations (50-150 g/t) on the zeta potential of quartz and magnetite sample were investigated. Finally, the results obtained from this study have been evaluated in terms of both technical and economical applicability of the flotation method for the removal of quartz from magnetite concentrate.

Keywords: *Flotation, Quartz, Magnetite, Zeta Potential*

[*] Corresponding Author

1. INTRODUCTION

Iron is the fourth most abundant metal in the Earth's crust. The main minerals of iron ore are hematite, magnetite, titano-magnetite, goethite, and siderite. Today, in many countries, most of the rich iron ore reserves are depleted, and the sustainable production of low grade iron ores has become a critical debate in mining industry. For example, magnetite and ilmenite deposits are common in coastal sands. Many such deposits have been studied as potential sources of iron ore (Christie and Brathwaite, 1997; Liu et al., 2014).

The application of various methods such as flotation, gravity and magnetic separation for the recovery of iron from low grade iron ores has been investigated by many researchers (Li et al., 2010; Seifelnassr et al., 2013; Flippov et al., 2014). In particular, reverse flotation is an indispensable process for producing hematite concentrates in the low grade iron ore industry. The same method can be applied to reduce the SiO_2 content in magnetite concentrates after processing by low intensity magnetic separation. In this process, quartz, the main gangue mineral, is floated with cationic or anionic collectors. Many researches have been conducted on the collectors and flotation mechanisms which are the key factors in the reverse flotation process. Anionic collectors are mainly consist of fatty acid, alkyl sulfonic acid, alkyl sulfuric acid, alkyl hydroxamic acid, and sodium or potassium salts (Cao et al., 2013).

Despite the recent success of reverse anionic flotation of iron ores, reverse cationic flotation remains the most popular flotation scheme used in the iron ore industry. Various amines are used as cationic collectors during reverse flotation of iron ores. Initially, quaternary ammonium salts were used as collectors, but later studies showed that the most effective cationic collectors that can be used for this purpose are hydrolyzed reagents that offer both ionic and molecular species in the aqueous phase (Flippov et al., 2014). Yuhua and Jianwei (2005) have shown that quaternary ammonium salts exhibit better selectivity and collectability than dodecylamine salts in the case of quartz from magnetite. Zero point of charge (ZPC is a very important feature used to characterize the electrical double layer and the mineral surfaces in flotation. ZPC can be used to estimate that if a mineral surface is whether positive or negatively charged at a given pH range. ZPC values of different minerals in an ore are important in terms of determining the flotation conditions and enabling the effective separation of one mineral from others (Yiğit and Özkan 2007; Jordens et al. 2013).

In literature, the ZPC values of quartz range from 1.7 to 2.6. These differences may arise from the difference in production, store, and surface properties of the quartz powder. ZPC of quartz can be established only by extrapolation since it occurs in low pH range, and the acid side of the curve is not accessible to electrokinetic measurement (El-Salmawy et al., 1993; Bu et al, 2017). On the other hand the ZPC of magnetite values range from 3 to 7 (Kosmulski, 2009). Milonjić et al. (1983) stated that the ZPC of magnetite decreased to 3.8 after the treatment with HCl due to possible structure changes on the magnetite surface.

In this study, the removal of quartz from the magnetite concentrate, which was produced by gravity and magnetic separation of a silica sand with high iron content obtained from Canakkale region, using flotation method was investigated. Moreover, the effects of different ethylenediamine (Flotigam EDA) concentrations (50-150 g/t) on the zeta potential of quartz and magnetite sample were investigated. Finally, the results obtained from this study have been evaluated in terms of both technical and economical applicability of the flotation method for the removal of quartz from magnetite concentrate.

2. MATERIAL AND METHOD

2.1. Material

High iron content decomposed silica ore used in the study was obtained from Çanakkale region, Turkey. In the characterization studies; physical, chemical, and mineralogical properties of the samples were determined by particle size distribution analysis, chemical analyzes by XRF method, and optical microscope investigations on representative samples. Particle size distribution and optical microscopy were performed on the ROM samples. On the other hand, the samples were reduced to suitable particle size distributions using an agate grinder for the instrumental analyzes such as XRF and XRD.

Particle size distribution analyzes for the samples were performed in accordance with TS 3530 EN 933-1 standard by using Retsch AS200 Basic sieve shaker and Impact brand ISO3310-1: 2000 test sieve series. The d80 and d50 sizes of the sample were determined as 0.867 mm and 0.364 mm, respectively. Chemical analyzes were performed by XRF method in order to determine the chemical content of the sample. The results of chemical analysis performed with Skyray EDX 3000D XRF are presented in Table 1.

Table 1. Results of chemical analysis

Oxide	Assay Value (%)	Oxide	Assay Value (%)
Al_2O_3	2.48	Na_2O	0.92
Fe_2O_3	7.59	P_2O_5	0.043
K_2O	0.16	SiO_2	61.93
CaO	0.32	TiO_2	0.45
MgO	0.61	LOI	5.71

In order to describe the minerals in the samples, mineralogical examinations were carried out on the particle size fractions. A trinocular microscope (SOIF BK-POL) was used for the optical examination and imaging studies. It was determined that the dominant mineral in the sample was quartz which was mostly colorless but also observed in different colors. Iron content was mainly attributed to magnetite mineral which was partly free and partly locked with quartz particles. On the other hand, calcite, mica, and albite minerals which lost their euhedral forms as a result of decomposition were secondary minerals in the sample. Trace amounts of rutile and apatite minerals were also observed. It was determined that the minerals in the sample did not accumulated in a certain fraction, and showed a relatively homogeneous distribution. However, it was found that the degree of liberalization, especially in terms of quartz and magnetite, increased after the particle size of 0.125 mm.

In order to obtain the pre-enriched concentrates to be used in the flotation experiments, the samples were processed by using the procedure including scrubbing,

gravity, and magnetic separation steps, which the details were given elsewhere (Ozdemir et al., 2019).

Since the magnetite concentrate produced as a result of pre-enrichment does not have sufficient purity to be used in surface chemistry studies, the sample was subjected to magnetic separation process before the zeta potential measurements using a hand magnet until the non-magnetic minerals in the sample were completely removed (Figure 1). Additionally, XRD graph of the purified sample was shown in Figure 2.

Non-magnetics | Purified sample

Fig. 1. Purification of magnetite pre-concentrate

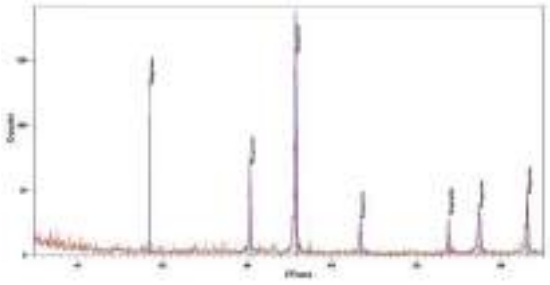

Fig. 2. XRD graph of the purified magnetite sample

Table 2. Conditions of flotation experiments

	Variable Conditions		Constant Conditions	
	Anionic Flotation	Cationic Flotation	S/L Ratio (%)	10
pH	11	3	Mixing Speed (rpm)	1000
Collector (g/t)	500	200	Air Flow Rate (L/min)	10
Frother (g/t)	500	100	C/D/A Conditioning (min)	5
Depressant (g/t)	500	-	F Conditioning (min)	1
Activator (g/t)	500	-	Flotation Time (min)	5

Digital image processing (DIP) method, which was successfully applied in the evaluation of processing results of ores that mainly contain minerals with obvious color differences such as feldspar in previous studies (Özdemir et al., 2016; Kurşun et al., 2018), was used in the determination of mineral contents of the products obtained from flotation experiments, and indirect calculation of recovery rates. In the DIP analyses, the samples were photographed using an optical microscope under appropriate lighting conditions, and the ratio of dark and light colored minerals in the microscope images were determined by using open source Image J software. ImageJ is an open source Java image processing program. 8-bit, 16-bit, and 32-bit images can be analyzed and processed in the program (Rasband, 2019). The analysis procedure performed on the microscope images with 3264x1836 resolution is as follows:

1. As a first step, the microscope images were converted to 8-bit grayscale (Image> Type> 8-bit) in order to perform the thresholding,
2. The resulting 8-bit images were converted to a 2-color (black and white) by specifying a threshold value (Image > Adjust > Threshold). Threshold value was determined automatically by software in the images of concentrates where dark minerals are predominant, and manually in the images of concentrates where light minerals are predominant to an optimum value where the processed image represents the original image in terms of black and white minerals.
3. The ratio of black pixels to white pixels in the 2-color image was calculated using Analyze> Measure. The principle of the measurements is based on the calculation of the ratio of black pixels to white pixels in any given image.

The percentage area value obtained after this process represents the cross-sectional area (CSA) of the dark minerals in the sample relative to the white minerals. The image processing steps with ImageJ are given in Figure 3,

2.1. Method

In the context of flotation experiments, the conventional flotation experiments were performed in order to obtain a final concentrate from the magnetite pre-concentrate. The conventional flotation experiments were conducted using a set-up consisting of a lab scale Denver D-12 flotation device and an Orion A211 tabletop pH meter. In the experiments, reverse flotation method (floating of silicate minerals from iron concentrate) were applied, and the applicability of both anionic and cationic flotation schemes were examined.

Flotigam EDA and NaOl were used as the collector in cationic and anionic flotation experiments, respectively. Additionally, MIBC was used as a frother. CaCl2 was used as a quartz activator in anionic flotation, HCl and NaOH as pH adjusters, and corn starch (25% amylose/75% amylopectin) as an iron depressant in anionic flotation. The conditions of the anionic and cationic flotation experiments are presented in Table 2.

The zeta potential measurements were made by electrophoretic method on purified magnetite concentrate by using Brookhaven Zetaplus instrument. The measurements were carried out at 1% solids ratio. For this purpose, 1 g sample was mixed with 100 mL ultrapure water using a magnetic stirrer at 500 rpm for 30 min. After the mixing, the suspensions were stabilized for 20 min for the settling of coarse particles in order to obtain a stable suspension. The desired pH values were adjusted by using 0.1 M HCl and 0.1 M NaOH for the acidic and alkaline conditions, respectively. Finally, the system was brought to equilibrium in terms of pH after further mixing for 5 min. Each zeta potential value was obtained with the average of at least 20 measurements, and the standard error of the measurements was calculated as approximately ±3 mV.

and the examples of the original and processed images are given in Figure 4.

(a) **(b)** **(c)**

Fig. 3. Cross sectional area calculation with ImageJ: 8-bit conversion (a), thresholding (b), %Area calculation (c)

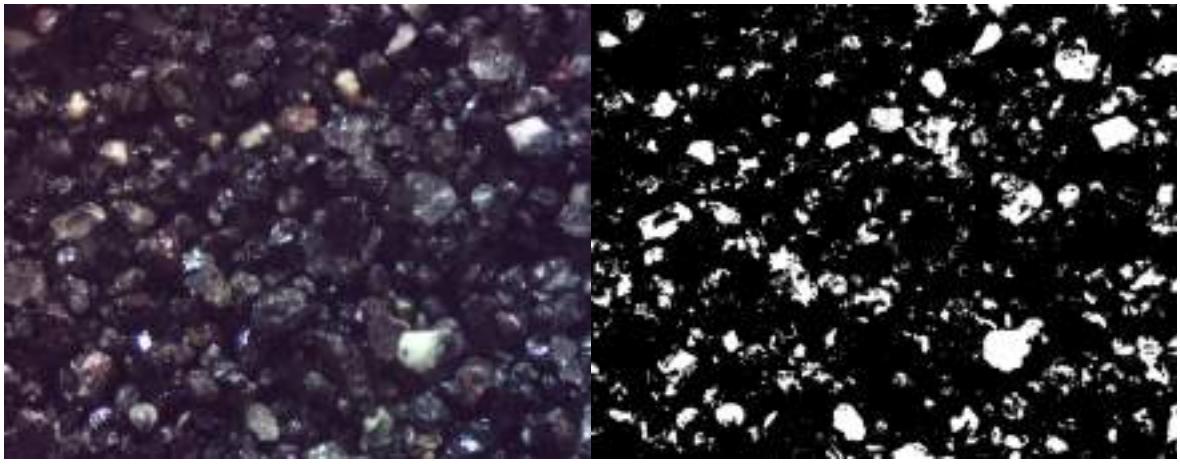

(a) **(b)**

Fig. 4. Examples of original (a) and processed (b) images

3. RESULTS

3.1. Anionic Flotation Experiments

CSA values obtained from the anionic reverse flotation experiments using NaOl as the collector and the recovery rates calculated based on these values are presented in Table 3, and the microscope images of the products are shown in Figure 5.

Table 3. Results of anionic flotation experiments

Product	Wgt. (%)	CSA (%)	100-CSA (%)	Mag. Rec. (%)	Qtz. Rec. (%)
Tail.	1.80	78.01	21.99	1.66	2.58
Conc.	98.20	84.76	15.24	98.34	97.42
Feed	100.00	84.64	15.36	100.00	100.00

As a result of the anionic reverse flotation experiments using NaOl, a slight increase, 84.64% to 84.76%, in CSA value of the concentrate (sinking) was obtained. On the other hand, 1.66% of the magnetite content was lost in the tailing fraction.

When the results were analyzed in terms of quartz removal, it was determined that only 2.58% of the quartz content in the feed sample could be removed with the anionic reverse flotation using NaOl.

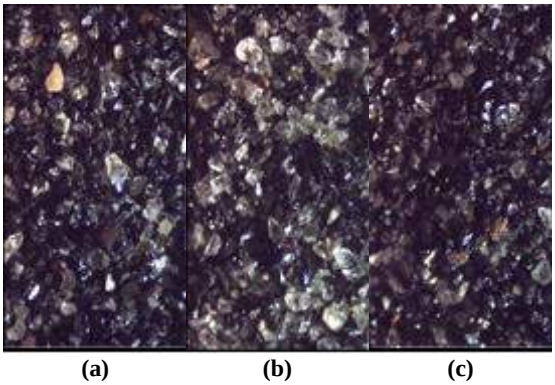

(a) **(b)** **(c)**

Fig. 5. Microscope images of products obtained from anionic reverse flotation experiments; feed (a), tailing (b), concentrate (c)

3.2. Cationic Flotation Experiments

CSA values obtained from the anionic reverse flotation experiments using Flotigam EDA as the collector, and the recovery rates calculated based on these values are presented in Table 4, and the microscope images of the products are seen in Figure 6.

Table 4. Results of cationic flotation experiments

Product	Wgt. (%)	CSA (%)	100-CSA (%)	Mag. Rec. (%)	Qtz. Rec. (%)
Tail.	4.30	73.07	26.93	3.71	7.54
Conc.	95.70	85.16	13.94	96.29	92.46
Feed	100.00	84.64	15.36	100.00	100.00

As a result of cationic reverse flotation experiments using Flotigam EDA, a slight increase, 84.64% to 85.16%, in CSA value of concentrate (sinking) was obtained. However, 3.71% of the magnetite content was lost in the tailing fraction.

When the results were analyzed in terms of quartz removal, the anionic reverse flotation experiments using Flotigam EDA, it was found that 7.54% of the quartz content in the feed sample could be removed. However, the results obtained with Flotigam EDA were relatively higher than the results obtained with NaOl in terms of both increase in CSA value of the concentrate and quartz removal.

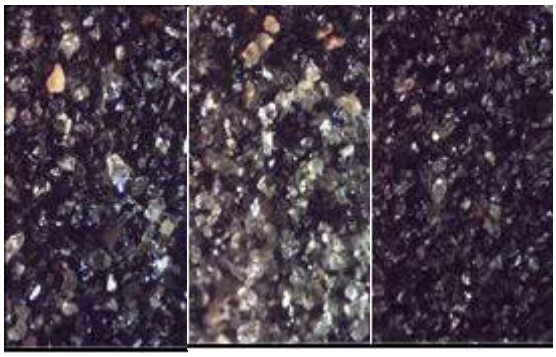

(a) (b) (c)

Fig. 6. Microscope images of products obtained from cationic reverse flotation experiments; feed (a), tailing (b), concentrate (c)

3.3. Zeta Potential Measurements

Zeta potential results of pure quartz and pure magnetite samples are shown in Figure 7. The ZPC value of the magnetite was determined as approximately 3.8. It was thought that the difference between the obtained ZPC value of the magnetite and the values presented in the previous studies might be attributed to possible alteration of the magnetite samples due to weathering conditions in the ore reserve.

On the other hand, the quartz sample showed a negative surface charge in the examined pH range. However, under high alkaline conditions, the quartz surface charge decreased up to -60 mV due to the increase in OH- concentration. In case of extrapolation of the obtained zeta potential profile, it can be seen that the ZPC of the quartz will be about pH = 1.8. This result reveals that the obtained zeta potential curve is similar to the typical zeta potential curves of the quartz in literature, and is consistent with previous studies.

The surface charges of quartz and magnetite minerals in the range of pH 2 to 4 indicated different marking supported by measurements, and it was determined that the difference between the surface charge of these two minerals reached a maximum level at pH 3. Therefore, adsorption characteristics of Flotigam EDA to the surface of these minerals at pH 3 was also examined by further the zeta potential experiments.

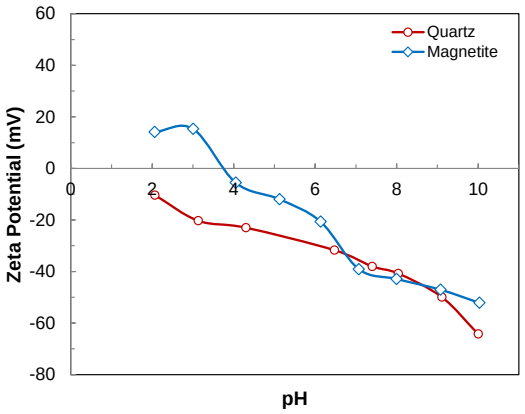

Fig. 7. Zeta potential profiles of magnetite and quartz samples as a function of pH

3.4. Quartz/Magnetite-EDA Interactions

As seen in Figure 8, Flotigam EDA adsorbed onto the surface of quartz at pH 3 at all dosages examined, but not adsorbed onto the surface of magnetite. The zeta potential of quartz mineral tended to increase positively due to increase in the EDA dosage. The natural zeta potential value of quartz mineral, which was -23 mV at pH 3, increased to approximately -6 mV in the presence of 150 g/t Flotigam EDA. This result clearly demonstrated that Flotigam EDA successfully adsorbed on the quartz surface at pH 3. However, there was no significant change in the surface charge of the magnetite in all EDA dosages used. This indicated that Flotigam EDA did not adsorb on the magnetite surface at pH 3.

This result is an important finding that quartz and magnetite can be separated successfully by cationic reverse flotation method especially at 100 g/t, and higher Flotigam EDA dosages.

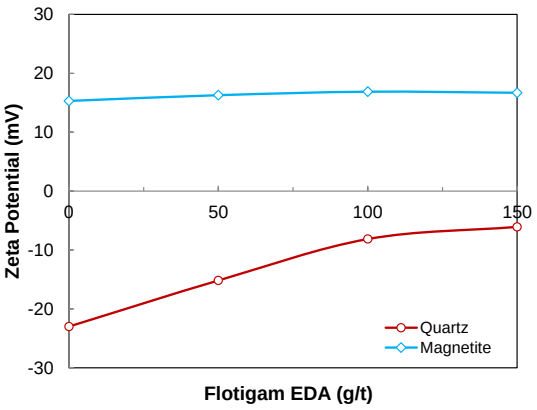

Fig. 8. Variation in quartz and magnetite zeta potential according to Flotigam EDA dosage

4. DISCUSSUION AND CONCLUSION

In this study, the removal of quartz from the magnetite concentrate, which was produced by gravity and magnetic separation of a silica sand with high iron content obtained from Canakkale region, using flotation method was investigated. In this context, the usability of both anionic and cationic flotation schemes was examined.

CSA value of concentrate increased to 84.76% and 85.16% as a result of the anionic flotation experiments using NaOl and the cationic flotation experiments using Flotigam EDA as the collector, respectively. The increase in CSA values of concentrates were slight in both cases, as a result of the low amount of quartz floating due to difficulties encountered in froth formation and stability. However, the results obtained with Flotigam EDA were higher than of NaOl in terms of both increase in CSA value of the concentrate and quartz removal. Moreover, the zeta potential measurements were performed with pure quartz and magnetite samples. The negative zeta potential of quartz increased to positive values with the increasing EDA concentration. This indicated that Flotigam EDA successfully adsorbed onto the quartz surface. However, no significant changes were observed in the surface charge of the magnetite in all EDA dosages examined. This clearly showed that EDA did not adsorb on magnetite at pH 3.

As a result of this study, the separation mechanism of quartz and magnetite minerals found in high iron content weathered silica ore by cationic flotation was explained, and it was revealed that it is possible to produce a mild graded iron concentrate from the ore. However, further investigations of the causes and possible solutions to the difficulties encountered in froth formation and stability, as well as the possibility of removing impurities in the iron concentrate by chemical methods, is recommended for further studies.

REFERENCES

Bu, X., Evans, G., Xie, G., Peng, Y., Zhang, Z., Ni, C. and Ge, L. (2017). "Removal of fine quartz from coal-series kaolin by flotation." *Applied Clay Science*, Vol. 143, pp. 437-444.

Cao, Z., Zhang, Y. and Cao, Y. (2013). "Reverse flotation of quartz from magnetite ore with modified sodium oleate." *Mineral Processing and Extractive Metallurgy Review*, Vol. 34, No. 5, pp. 320-330.

Christie, T. and Brathwaite, B. (1997). "Mineral commodity report 15—Iron." *NZ Min*, Vol. 22, pp. 22-37.

El-Salmawy, M. S., Nakahiro, Y. and Wakamatsu, T. (1993). "The role of alkaline earth cations in flotation separation of quartz from feldspar." *Minerals Engineering*, Vol. 6, No. 12, pp. 1231-1243.

Filippov, L. O., Severov, V. V. and Filippova, I. V. (2014). "An overview of the beneficiation of iron ores via reverse cationic flotation." *International Journal of Mineral Processing*, Vol. 127, pp. 62-69.

Jordens, A., Cheng, Y.P. and Waters, K.E. (2013). "A Review of the Beneficiation of Rare Earth Element Bearing Minerals." *Minerals Engineering*, Vol. 41, pp. 97-114.

Kosmulski, M. (2009). *Surface charging and points of zero charge*, CRC Press, Florida, USA.

Kurşun İ., Terzi M. and Özdemir O. (2018). "Evaluation of digital image processing (DIP) in analysis of magnetic separation fractions from Na-feldspar ore", *Arabian Journal of Geosciences*, Vol. 11, pp. 462.

Li, C., Sun, H., Bai, J. and Li, L. (2010). "Innovative methodology for comprehensive utilization of iron ore tailings: Part 1. The recovery of iron from iron ore tailings using magnetic separation after magnetizing roasting." *Journal of Hazardous Materials*, Vol. 174, No. 1-3, pp. 71-77.

Liu, S., Zhao, Y., Wang, W. and Wen, S. (2014). "Beneficiation of a low-grade, hematite-magnetite ore in China." *Minerals & Metallurgical Processing*, Vol. 31, No. 2, pp. 136-142.

Milonjić, S. K., Kopečni, M. M. and Ilić, Z. E. (1983). "The point of zero charge and adsorption properties of natural magnetite." *Journal of Radioanalytical Chemistry*, Vol. 78, No. 1, pp. 15-24.

Özdemir O., Kurşun İ., Terzi M. and Yilmaz K. (2016). "An Investigation of Digital Image Processing (DIP) Method for Analysis of Grade of Feldspar Ore Based on Color Differences." *Proc., 6th International Conference on Computer Applications in the Minerals Industries*, AGRO ARGE, Istanbul Turkey, Paper No.55, pp.1-4.

Rasband, W.S., http://rsb.info.nih.gov/ij/ [Accessed 28 Aug 2019].

Seifelnassr, A. A., Moslim, E. M. and Abouzeid, A. Z. M. (2013). "Concentration of a Sudanese low-grade iron ore." *International Journal of Mineral Processing*, Vol. 122, pp. 59-62.

Yiğit, E. and Özkan Ş.G. (2007). *Flotasyon Yöntemi ve Uygulamaları*, İstanbul Üniversitesi Mühendislik Fakültesi Yayınları, Istanbul, Turkey.

Yuhua, W. and Jianwei, R. (2005). "The flotation of quartz from iron minerals with a combined quaternary ammonium salt." *International Journal of Mineral Processing*, Vol. 77, No. 2, pp. 116-122.

CISET - 2nd Cilicia International Symposium on Engineering and Technology
10-12 October, 2019, Mersin / TURKEY

EFFECTS OF ZIRCON AND CORUNDUM BASED ADDITIVES ON TECHNOLOGICAL PROPERTIES OF WALL TILE ENGOBES

Resul Ihsan Cakici [1], Ilgin Kursun [2], Mert Terzi [3] and Orhan Ozdemir [*4]

[1] Istanbul University-Cerrahpasa, Eng. Faculty, Mining Eng. Dept., Istanbul, Turkey, rcakici@yurtbay.com.tr

[2] Istanbul University-Cerrahpasa, Eng. Faculty, Mining Eng. Dept., Istanbul, Turkey, ilginkur@istanbul.edu.tr

[3] Istanbul University-Cerrahpasa, Eng. Faculty, Mining Eng. Dept., Istanbul, Turkey, mert.terzi@istanbul.edu.tr

[4] Istanbul University-Cerrahpasa, Eng. Faculty, Mining Eng. Dept., Istanbul, Turkey, orhanozdemir@istanbul.edu.tr

ABSTRACT

In this study, the effects of zircon and corundum based whitening agent additives on the engobe properties in the production of wall tiles, which is an important end product for ceramic industry, were investigated. Firstly, physical, chemical, and mineralogical properties of 14 different whitening agent additives were determined. According to the results of the characterization tests, the whitening agent additives were classified into 3 different groups, namely corundum, zircon, and corundum + zircon. These additives were used in different ratios in the standard engobe recipe, and then engobes and tablets of the each recipes were prepared.

The whiteness/color (*L*, *a*, *b*, *ΔE*), water absorption, and thermal expansion properties of these engobes and tablets, which were prepared by using different additives, were determined. According to the results, it was determined that especially corundum based materials were conforming the engobe standards in terms of whiteness/color, water absorption, and thermal expansion properties. The results of this study have clearly showed that fine sized (d_{50}: 2.496 μm, d_{80}: 9.153 μm) and corundum-based whitening agent additives can be preferred in the wall tile engobes.

Keywords: *Ceramics, Whitening Agents, Zircon, Corundum, Wall Tile, Engobe*

[*] Corresponding Author

1. INTRODUCTION

Ceramic is an inorganic compound formed by the coupling and sintering of one or more metals with non-metallic elements. Ceramics are usually produced by high temperature baking of clay, kaolin, and similar substances formed by the weathering of rocks under external conditions. They can be defined as the semi-glassy materials obtained by mixing & grinding of metallic and non-metallic minerals into powder, and firing this mixture after giving a certain form (TCPC, 2003).

Materials used in the construction industry such as floor and wall tiles, sinks, toilets, reservoirs, bricks, and tiles used in bathrooms and kitchens are produced by the ceramics industry. The production of ceramics in Anatolia, which dates back to many millennia ago, has been moved to industrialization in the second half of the 20th century. As a result of these developments, Turkey has become one of the world's leading countries in the ceramic tile production in a short period of 40 years (Bevilacqua, 2013; Kara, 2013).

In the ceramics industry of Turkey, which has an important place in industrial production and the economy of the country, there is an urgent need to lower the costs to competitive rates in order to secure its position in the World ceramics market. The main cost inputs in the ceramic production are energy, labor, and raw materials. Energy consumption is due to usage of natural gas in ceramic production, especially at the firing of ceramics. Natural gas is an energy source imported by the country, and hence, currently there is no cheaper alternative for the production. In Turkey, which is already placed below the European average in labor costs, it is not possible to achieve a further decrease. Therefore, the only remaining cost input to optimize is raw materials. In this respect, the selection of raw materials used in ceramic production is of great importance in order to reduce total costs (Şahin, 1997; Çakıcı, 2014).

Zircon and baddeleyite minerals, which has chemical formulas of $ZrSiO_4$ and ZrO_2, respectively, are among the natural and economic minerals of the zirconium element. Significant amounts of zircon are concentrated in the several beach sand reserves of Turkey. However, no zircon production is being made in the country, and all the required input has been realized from imports (İpekoğlu, 1999; SPOT, 2001). Zircon is used in the ceramic industry for the production of tiles, sanitary ware, and table ceramics, as well as in the production of glaze, frit, and paints used in ceramic production (Zucca, 2013). Zircon prices, on the other hand, rise to very high levels from time to time due to the supply and demand balance as well as the policies implemented by the zircon producers (Karaveli et al., 2008). These speculative fluctuations in zircon prices lead users to search for alternatives. Titanium dioxide and tin oxide can be used instead of zirconium oxide as opacifier in ceramic glazing and enamels (İpekoğlu, 1999; Pekkan and Karasu, 2009).

In this study, the effects of zircon and corundum based whitening agent additives on the engobe properties in the production of wall tiles, which is an important end product for ceramic industry, were investigated. Firstly, physical, chemical, and mineralogical properties of 14 different whitening agent additives were determined. These additives were used in different ratios in the standard engobe recipe, and then engobes and tablets of the each recipes were prepared. Finally, whiteness/color (L, a, b, ΔE), water absorption, and thermal expansion properties of these engobes and tablets, which were prepared by using different additives, were determined, and economical applicability of the investigated materials were discussed.

2. MATERIAL AND METHOD

2.1. Material

In the first stage of the experimental studies, chemical analyzes of the agents were performed by XRF method in order to determine the chemical composition of the whitening agent additives to be examined as zircon substitutes. Rigaku ZSX Primus XRF device was used in the analyses. Additionally, phase characteristics of the whitening agent additives were determined by XRD analyses. Rigaku Rint 2000 was used for XRD analyses, which were performed at 40 kV/30 mA Cu Kα radiation at 2°/min. scanning speed conditions.

Whitening agents were classified into 3 main groups by their chemical contents and phase properties. The first group consists of corundum based samples. The samples containing high amounts of zircon, and no corundum were included in the second group. The third and last group were differentiated by both corundum and zircon containing samples. Al_2O_3 and ZrO_2 grades of whitening agents used in experimental studies are presented in Table 1.

Table 1. Al_2O_3 and ZrO_2 grades and classification of whitening agents used in experimental studies

Group	Sample Code	Al_2O_3 (%)	ZrO_2 (%)	Dominant Phase
1	K1	98.80	-	Corundum
	K2	98.60	-	
	K3	97.70	-	
	K4	97.30	-	
	K5	93.10	0.65	
	K6	90.90	-	
	K7	89.90	-	
2	Z1	1.57	61.20	Zircon
	Z2	0.67	48.60	
3	KZ1	85.50	6.17	Corundum Zircon
	KZ2	78.70	8.69	
	KZ3	59.50	22.70	
	KZ4	50.90	30.20	
	ZK1	23.10	43.10	

Particle size distribution is a very important material property in ceramic production, especially in the glaze and engobe preparation stages. The materials that have particle size higher than the desired values prolongs and complicates the preparation process of glaze and engobe, and they have negative effects on the homogenity. The maximum particle size of the zircon used in glaze and engobe preparation should be 9 μm (d_{50} = 1,2-2 μm) (Snyders et al., 2008).

In this context, the particle size distribution analysis of whitening agents used in the experimental studies were performed. The particle size distribution analysis of the agents was performed using laser diffraction method using the Malvern Mastersizer 2000 V5.60 instrument. The d_{50} and d_{90} sizes of whitening agents are shown in Figure 1.

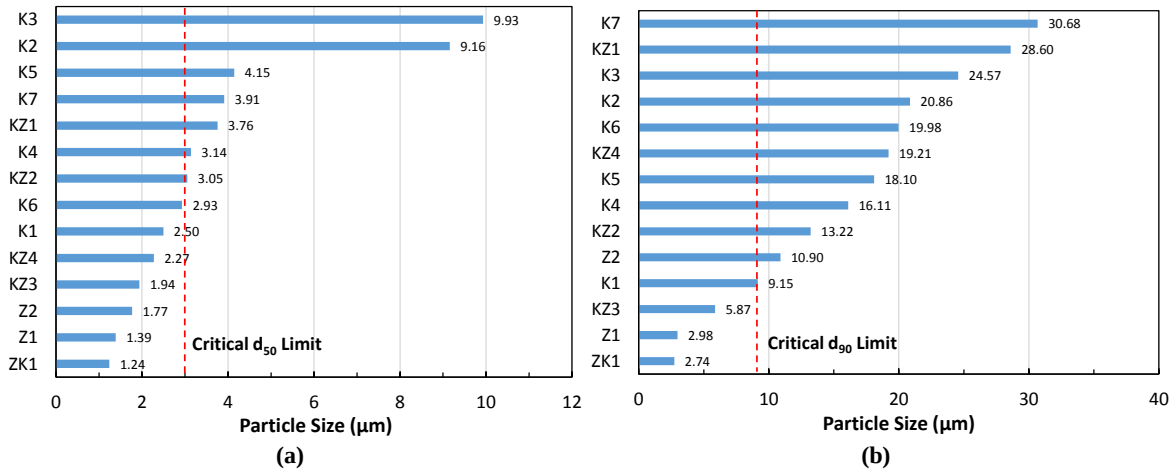

Fig. 1. d_{50} (a) and d_{90} (b) sizes of whitening agents

As seen from Fig. 1 that d_{50} sizes of the samples ranged between 1.2 and 10 µm. For the ceramic production, it is acceptable that the zircon to have a d_{50} size in the range of 2-3 µm. However, d_{50} size above this limit are generally not preferred.

Moreover, the d_{90} value of the zircon to be used in the process should be under 9 µm. In this context, it was seen that only 4 materials have the desired particle size distribution as the d_{90} value of the other samples is higher than 10 µm. It is important that the particle size distribution is within the desired range to ensure that the material has more homogeneous distribution in the recipe, and the grinding times are not excessive.

2.1. Method

Engobe is a layer applied on the tile before glazing and acts as a primer between tile and glaze. It closes the open pores, and the glaze is applied more firmly on the tile owing to the application of engobe.

In the wall tile production experiments, monoprosis (single firing) was applied and the standard engobe recipe used is presented in Table 2. In addition to zircon, the whitening agents and two different opaque frits; drained clay, kaolin, quartz, and alumina (Al_2O_3) samples, which were obtained from Istanbul Sile region, Portugal, Aydin Cine region and a processing plant operating in Konya Seydisehir region, respectively, included in the recipe.

Table 2. Standard engobe recipe used in the experiments

Material	Ratio (%)
Zircon/Whitening Agent	8
Opaque Frit I	28
Opaque Frit II	11
Quartz	25
Drained Clay	10
Kaolin	13
Al_2O_3	5
Total	100

Different egobe recipes were prepared by using 50% zircon + 50% whitening agent and 25% zircon + 75% whitening agent ratios, and these engobes were applied to the tile using a pulling apparatus at a density of 1800 g/L. *L*, *a*, and *b* values of the tiles were determined by Minolta CR-300 series chromo-meter color measurement device. Subsequently, tablets of the whitening agents that were in compliance to the standard values in tile tests, were prepared. The tablets containing a total of 25 g constituents were pressed under 25 bar pressure and fired at 1125°C for 36 min. In addition to the *L*, *a*, and *b* values of the pressed and fired tablets, the water absorption values of the agents were also determined.

Finally, the thermal expansion coefficients of the samples that the technological properties were found to be complying the standards in terms of water absorption and whiteness values, were measured by Netzsch DIL 402 PC dilatometer. Thermal expansion coefficient measurements were conducted at 900°C.

3. RESULTS

3.1. Whiteness/Color Measurements

The results of whiteness/color measurements and standard values of samples are presented in Table 3.

Table 3. Results of whiteness/color measurements

Code	Zircon/Whitening Agent Ratio (%)					
	50/50			25/75		
	L	*a*	*b*	*L*	*a*	*b*
KZ1	90.68	+0.64	+6.10	90.20	+0.58	+5.81
K7	90.70	+0.48	+5.79	90.31	+0.58	+6.15
KZ4	90.52	+0.60	+5.30	90.67	+0.44	+6.09
Z2	90.50	+0.53	+5.55	90.80	+0.48	+6.05
K3	91.11	+0.47	+5.70	91.22	+0.45	+6.32
KZ2	90.75	+0.48	+5.79	90.35	+0.44	+6.12
Z1	91.01	+0.43	+5.43	90.50	+0.34	+5.81
K1	90.74	+0.51	+5.85	90.48	+0.50	+6.48
K2	90.96	+0.59	+5.82	90.46	+0.64	+6.14
K6	90.34	+0.47	+6.60	89.96	+0.18	+7.04
KZ3	89.54	+0.47	+6.10	89.18	+0.54	+5.55
ZK1	90.25	+0.48	+6.32	89.99	+0.44	+6.38
K5	90.12	+0.53	+6.54	89.24	+0.49	+6.42
K4	91.20	+0.48	+6.53	90.12	+0.57	+6.15
STD	91.30	+0.56	+5.70	89.84	+0.79	+6.59

In the experiments that the zircon/whitening agent ratio were 50/50, it was observed that all samples had *L* values close to the standard. The difference between *L* value of the sample and the standard should not be exceeded the value of 1. In this respect, it can be said that

the all samples can be used as an alternative to sole zircon usage in the applied recipe. Moreover, the *L* values of all the tablets prepared in the prescription were also met the standard in case of the zircon/whitening agent ratio was 25/75. Therefore, it was concluded that all whitening agents could be added to recipe at a rate of 75% as a substitution to zircon.

3.2. Water Absorption Measurements

The results of water absorption measurements and standard values of samples are presented in Table 4.

When the results of the recipe where the zircon/whitening agent ratio was 50/50 taken into the consideration, it was seen that the water absorption values of all samples are within the acceptable limits. Therefore, it can be said that the test results are favorable, and these alternative whitening agents can be used as a substitute material at a rate of 50% instead of zircon in this recipe. However, in the recipe where zircon/whitening agent was 25/75, it was observed that the water absorption values of KZ1, K7, K3, Z1, and K2 samples are much higher than the standard values. Therefore, it can be concluded that these whitening agents could not be used at a 75% substitution ratio.

On the other hand, the water absorption values of ZK1, K5, and KZ3 samples were found to be very low compared to the standard. It was determined that these whitening agents also could not be used at a 75% substitution ratio.

Table 4. Results of water absorption measurements

Sample Code	Water Absorption (%)	
	50/50	25/75
KZ1	5.63	10.60
K7	5.80	10.60
KZ4	4.47	6.86
Z2	4.59	5.50
K3	6.75	8.32
KZ2	4.82	6.77
Z1	4.55	7.11
K1	4.30	5.83
K2	6.16	10.90
K6	4.70	6.21
KZ3	3.86	1.14
ZK1	4.65	3.96
K5	4.29	3.37
K4	5.12	5.14
STD	5.09	5.54

3.3. Thermal Expansion Measurements

The results of the thermal expansion coefficient measurements performed on K1, Z2, and KZ4 samples, which were found to be complying the standards in terms of water absorption and whiteness values, are presented in Table 5.

Table 5. Results of the thermal expansion coefficient measurements

Zircon/Whitening Agent Ratio (%)	Sample Code	Thermal Expansion Coefficient ($\times 10^{-7}$)		
		400ºC	500ºC	600ºC
50/50	K1	77.01	81.18	90.87
	Z2	74.76	78.77	87.93
	KZ4	76.88	81.06	90.43
25/75	K1	78.89	83.07	92.07
	Z2	76.32	80.59	90.13
	KZ4	77.70	81.74	91.10
-	**STD**	**76.67**	**80.94**	**90.78**

According to the results of the thermal expansion coefficient shown in Table 5, it was determined that all three samples gave positive results in terms of compliance with the thermal expansion coefficient standards. However, considering that the main purpose of the study is cost reduction, it can be said that the optimum result is obtained with K1 sample, which has the lowest cost among the 3 samples, at the 25/75 zircon/whitening agent ratio.

4. DISCUSSUION AND CONCLUSION

In this study, the effects of zircon and corundum based whitening agent additives on the engobe properties in the production of wall tiles, which is an important end product for ceramic industry, were investigated.

According to the findings obtained from the whiteness/color (*L*, *a*, b, and *ΔE*), water absorption, and thermal expansion measurements of engobes, which were prepared by using whitening agents to a substitute to zircon at the rates of 50% and 75%, engobes that has acceptable technological properties in terms of complying the standards can be produced using especially corundum based materials.

Moreover, considering the cost reduction target in the study, apart from the suitability of its technological properties, it was concluded that the optimum result could be obtained with corundum based K1 sample. The particle size distribution of this sample (d_{50}: 2.496 μm, d_{80}: 9.153 μm) is also very similar to the zircon used in the standards.

As a result, it has been clearly demonstrated from this study that the ground corundum with a particle size distribution within the required limits can be successfully used in wall tile engobe recipes in substitution to zircon.

REFERENCES

Bevilacqua, P. (2013). "Ceramic Industry World Market", *Raw Materials Requirement*, University of Trieste, Italy.

Çakıcı, R.İ. (2014). Investigation of Alternative Raw Materials Used in Ceramic Production and Cost Reduction Studies, Master Thesis, Istanbul University, Istanbul, Turkey.

İpekoğlu, B. (1999). "Zircon" *Industrial Mineral Inventory of Turkey*, G. Önal, A.E. Yüce, I. Özpeker, A. Güney, Eds., Istanbul Mineral Exporters' Association, Istanbul, Turkey, pp. 228-233.

Kara, A. (2013). *Combined Use of Alkaline and Earth Alkaline Oxides Containing Raw Materials in Ceramic Tile and Sanitaryware Formulations*, Anadolu University, Eskişehir, Türkiye.

Karaveli, K., Karasu, B. and Onal, H.S. (2008). "Production of Zircon-Freeopaque Wall Tile Frits and Their Use in Ceramic Industry", *Proc., Xth World Congress on Ceramic Tile Quality (Qualicer 2008)*, Castallón, Spain, pp. 43-49.

Pekkan, K. and Karasu. B. (2009). "Research on the Usage of R_2O-RO-(ZrO_2)-B_2O_3-Al_2O_3-SiO_2 Glass-Ceramic Systems In The Single Fast-Fired Wall Tile Opaque Glazes", *Afyon Kocatepe University Journal of Science*, Vol. 9, pp. 37-44.

Snyders, E., Potgieter, J.H. and Nel J.T. (2008). "The Upgrading of an Inferior Grade Zircon to Superior Opacifier for Sanitary Ware and Glazes", *Journal of the South African Institute of Mining and Metallurgy*, Vol. 105, pp. 459-464.

SPOT (2001). *Madencilik Özel İhtisas Komisyonu Refrakter Killer ve Şiferton-Manyezit-Dolomit-Olivin-Zirkon-Disten, Sillimanit, Andaluzit Çalışma Grubu Raporu*, State Planning Organization of Turkey, Ankara, Turkey.

Şahin, A.İ., (1997). "The Properties of Engop Clays Produced by Kalemaden", *Proc., 8th National Clay Symposium*, Dumlupinar University, Kutahya, Turkey, pp. 271-276.

TCPC (2003). *Ceramics in Turkey, the History of Earth and Fire*, Turkish Ceramic Promotion Committee, Central Anatolian Exporter Union, Ankara, Turkey.

Zucca, A. (2013). *Industrial Ceramic Technology: Characteristics of Raw Materials and Ceramic Properties*, University of Cagliari, Italy.

CISET - 2nd Cilicia International Symposium on Engineering and Technology
10-12 October, 2019, Mersin / TURKEY

A REVIEW ON SURFACE CHEMISTRY PROPERTIES OF ZEOLITES

Ilgin Kursun [1], Mehmet Faruk Eskibalci [2], Mert Terzi [3] and Orhan Ozdemir [*4]

[1] Istanbul University-Cerrahpasa, Eng. Faculty, Mining Eng. Dept., Istanbul, Turkey, ilginkur@istanbul.edu.tr

[2] Istanbul University-Cerrahpasa, Eng. Faculty, Mining Eng. Dept., Istanbul, Turkey, eskibal@istanbul.edu.tr

[3] Istanbul University-Cerrahpasa, Eng. Faculty, Mining Eng. Dept., Istanbul, Turkey, mert.terzi@istanbul.edu.tr

[4] Istanbul University-Cerrahpasa, Eng. Faculty, Mining Eng. Dept., Istanbul, Turkey, orhanozdemir@istanbul.edu.tr

ABSTRACT

In this study, the surface properties of zeolite samples were reviewed in detail. In this context, the pH profile, zeta potential, contact angle measurements along with flotation experiments for several zeolite samples were summarized in order to determine the surface properties of the zeolite.

In the case of the pH profiles of the zeolite samples, it was determined that the pH of the zeolite was approached to a certain buffer pH (~8) value at acidic, alkaline, and natural pH values. The results of zeta potential measurements showed that zeolite had negative surface charge at all pH values. In the presence of cationic surfactants, the zeta potential of zeolite sample became positive. Moreover, zeolite surface was found to be hydrophilic according to the results of the contact angle measurements, and showed a hydrophobicity with the increasing cationic surfactant concentration. The results of the zeta potential and contact angle measurements along with micro-flotation experiments using surfactants with different carbon chain lengths (HTAB, TTAB, and DTAB) showed that these surfactants were successfully adsorbed on the surface of zeolite samples, which significantly affected the surface properties of zeolite.

As a result of this study, it was revealed that there is a significant correlation between the findings which are presented in literature on the surface properties of zeolite samples.

Keywords: *Zeolite, Surface Chemistry, Zeta Potential, pH, Contact Angle*

1. INTRODUCTION

Zeolites can generally be defined as alkali and earth alkali elements containing aqueous aluminum silicates that has micro-pores in their crystal structure (Breck, 1974). There are 50 natural zeolites and 200 synthetic zeolite minerals known which are classified into two main groups namely; natural and synthetic zeolites (Gottardi and Galli, 1985). They have several important properties such as high ion exchange capacity, microporous structure, ability to function as a molecular sieve, regular crystal structure, the ability to absorb water in their structure, and removal of the cations in the surface structure of the absorbed water after drying (Öter, 2002).

* Corresponding Author

Moreover, their ability to absorb wide range of different ions had enabled them to find application as adsorbants in environmental analytical chemistry (Ulusoy and Albayrak, 2009).

The crystal size of the zeolites can range from a few centimeters to 15-20 cm. Geometry of their crystal structure, such as pore size (6.6-11.8 Å) and channel structure (2.2-8 Å) are among their important physical properties (Şener, 2013). Moreover, ion exchange capacities of zeolites, which is approximately 700 meq/100 g., can reach up to 900 m^2/g. in their surfaces.

Depending on the exchangeable ions within their structure, different colors may be involved for each zeolite. Therefore, they can be colorless, white and sometimes, yellow brown or red depending on the level of iron hydroxide contamination. On the other hand, many cobalt zeolites are blue while dry and lilac-red when heated (Tsitsishvili et al., 1992).

The density of zeolites are generally varies between 1.9-2.3 g/cm^3 according to the cations in their structures. The surface selectivity of the zeolites used as adsorbents is based on the Si/Al ratio. Aluminum-based zeolites can preferentially absorb the strong polar molecules. The increase in silicon content in the structure causes their hydrophobic character to become more pronounced. The transition from hydrophilic behavior to hydrophobic behavior is based on Si/Al ratio, and it occurs when this ratio is approximately 20 (Dikmen, 2008).

Clay is another natural adsorbent which has an important place in waste water treatment by adsorption method. Similar to zeolites, clay is among the important inorganic compounds that found naturally in Earth's crust. Their absorption properties are resulted from large surface areas and ion exchange capacities. Clay minerals affect metal ions owing to the negative charge in their structure. Zeolite is also a natural adsorbent, just like clay and chitosan. The natural adsorbents are easy to obtain and manufacture, less costly, and they do not require pre-treatment, therefore they are more preferred.

Moreover, the natural adsorbents are less harmful to the environment as they do not generate waste in high quantities. However, as a disadvantage, they cannot be applied to all materials. In addition, high temperature provides a more efficient retention of metal ions in zeolites coordination areas (Virta, 2002). Therefore, low-cost zeolites creates a possibility to remove waste waters contaminated with heavy metals for many industries around the world (Grant, 1987).

Just as the zeolites can easily adsorb water, the adsorbed water can also be removed without deterioration in their crystal structure and moisture absorption properties (desorption). Because of these properties, activated natural zeolites are widely used as desiccants. The fact that zeolites do not lose their moisture absorption properties even at low relative humidity which is an important feature (Bilgin, 2009).

The weakly interchangeable cations due to the four-sided structure of the zeolite can be replaced by ions in the solution by washing the zeolite with another ion-containing solution. The introduction of trivalent aluminum instead of Si^{4+} into the four-sided silica of the zeolite structure leads to the deterioration of electrical neutrality and the formation of negative charge. To restore neutrality, positively charged cations enter the structure. Since these mobile cations are weakly attached to the structure by Van der Waals force, they can easily be replaced by cations in solution. This displacement occurs both on the surface and inside the particle. The cation exchange capacity of the zeolite is the number of displaceable cations per unit volume or unit weight. The cation exchange capacity also depends on the nature of the cation (size, valence), temperature, cation concentration in the solution, and the structure of the zeolite (Çulfaz and Baş, 1989).

In this study, the surface properties of zeolites used have been tried to be revealed in detailed in terms of their pH profiles, zeta potential, contact angle, and flotation properties.

2. SURFACE PROPERTIES OF ZEOLITES

2.1. pH Profile of Zeolites

The pH profile of zeolites is an important parameter in terms of both the surface dissolution and environmental/industrial applications. Therefore, it is necessary to determine the chemical behavior of zeolite suspensions in natural, acidic, and basic environments in order to learn the structure of the zeolite. The pH change in acidic, natural, and basic conditions depending on the conditioning period of the zeolite is shown in Figure 1. As seen from Figure 1, after adding the zeolite into the water, the pH of the pure water rapidly changed to the buffer pH of the zeolite, which was approximately 9, and it showed no further change for 3 h. In literature, this situation is explained by the reaction of H^+ ions in the suspension with the oxygen atoms in the broken bonds to decrease the positive charge deficiency in the broken Si-O-Si bonds on the zeolite surface according to the reaction given in Eq. 1 where SiO_2 is expressed in the form of $Si(OH)_4$ (Baes and Mesmer, 1976; Ersoy and Celik, 2002).

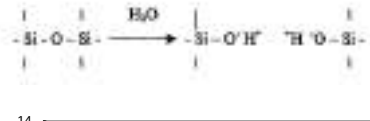

(1)

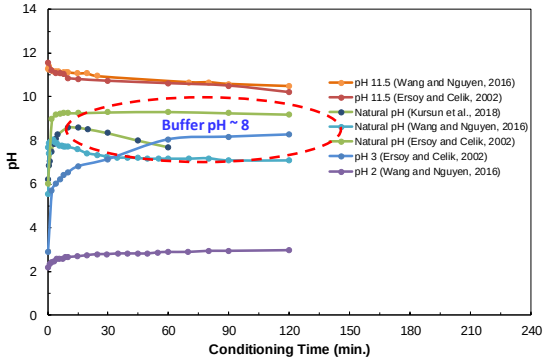

Fig. 1. pH profile of zeolites according to the conditioning period

At acidic pH, the pH of suspension rapidly increased after the addition of zeolite and reached to a buffer at pH 8 within 90 min. Similar to natural pH, the increase observed at acidic pH can also be explained by the combination of Si-O-Si bonds with the H^+ ions in the suspension, as well as the displacement of H_3O^+ ions in the solution with aluminum in the structure as a result of

the de-alumination reaction, and hence the decrease of the concentration of H^+ ions in the environment.

In alkaline pH, pH of the suspension pH reached a buffer around pH 10 after 4 h. This can be attributed to a phenomenon which resulted by a transfer of a portion of the Si atoms in the structure to the solution and formation of structures such as $Si(OH)^{3-}$, $Si(OH)_4$ with the OH-ions (Breck, 1974) and the reduction of hydroxyl ions in the medium by reaction between Mg^{2+} and Fe^{3+}, which are also transferred to the solution from zeolite structure, and with OH-ions.

When all these results are taken into the consideration, it can be said that the behavior of zeolite at different pH values to have a buffer around pH 9. Previous studies in literature on this subject have also confirmed this situation (Wang and Nguyen, 2016).

2.2 Zeta Potential of Zeolites

2.2.1. Natural zeolites

As seen in Figure 2, as a result of the zeta potential measurements with different zeolite samples, zeolites showed negative surface charge at all pH regions, and no zero point of charge (SYN) could be obtained. This can be explained by the fact that the zeolite balances the excess positive charge in the environment due to the introduction of Al^{3+} ions instead of Si^{4+} in the crystal structure.

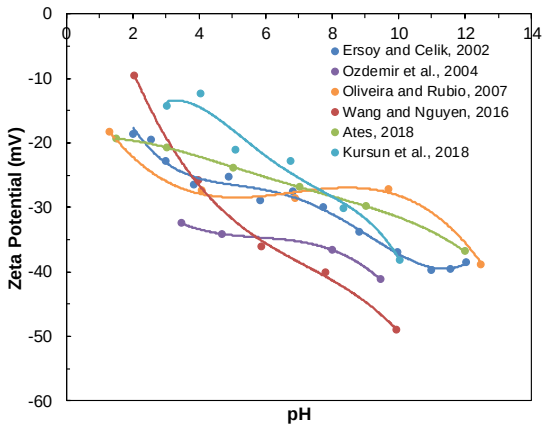

Fig. 2. Zeta potential-pH profile of different zeolite samples

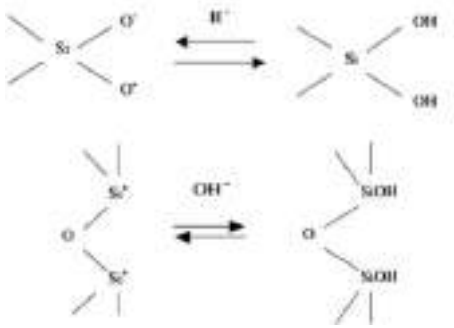

Fig. 3. Charging on zeolite surface by the dissolution of Si(Al) sites

However, ions such as Na^+, K^+, Ca^{2+}, and Mg^{2+} enter the zeolite channels to compensate for the lack of positive charge in the lattice of the zeolite. Therefore, zeolites have little or no interest in anionic ions (Haggerty and Bowman, 1994). In addition, the bonds broken as a result of Si-O-Si (siloxane group) grinding on the zeolite surface may also cause the zeolite to gain negative surface charge (Wang and Nguyen, 2016).

2.2.2. Modified zeolites

The modification of zeolite can be described as altering the properties of the zeolite surface in various ways. Surface modification can be classified into three groups as thermal (heat treatment), hydrothermal, and chemical. Changes in the chemical structure of the adsorbent surface are called chemical modifications.

Zeta potential results of natural zeolite and hexadecyl trimethyl ammonium bromide (HTAB) modified zeolite samples are shown in Figure 4. As seen in Figure 4, surface charge of natural zeolite, which had negative surface charge at all pH values, became positive after the modification due to the electrostatic adsorption of positively charged amine molecules to the zeolite surface.

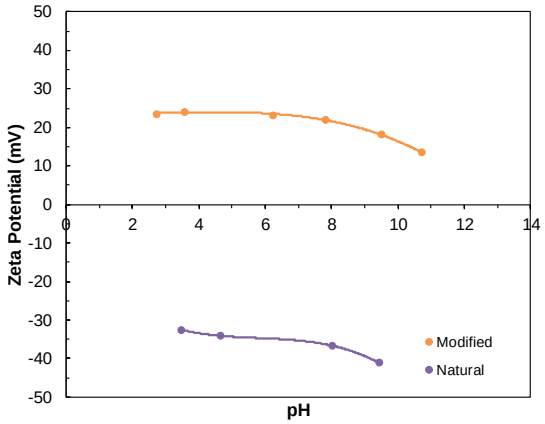

Fig. 4. Zeta potential of natural and modified zeolite samples (Ozdemir et al., 2004)

Zeta potentials of the zeolite samples modified by cationic surfactants (HTAB, TTAB, DTAB, and GTAP) with different chain lengths are also shown in Figure 5.

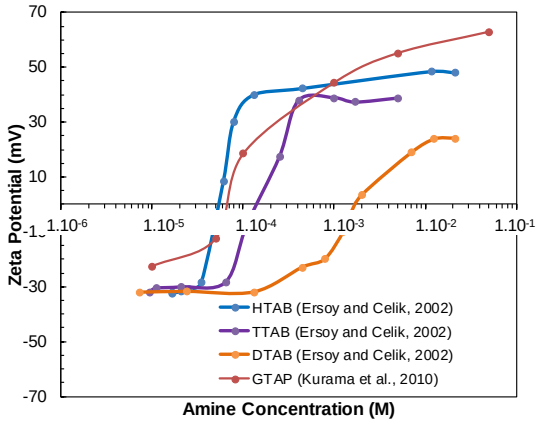

Fig. 5. Zeta potential profile of the zeolite samples modified by cationic surfactants with different chain

lengths

No significant change was observed in negative surface charge of zeolite due to ion exchange between Ca^{2+}, Na^{+}, K^{+}, and Mg^{2+} ions and amine ions on the surface of zeolite at low concentrations. The negative surface charge of the zeolite gradually decreased, and then became positive as amine molecules being adsorbed onto the zeolite surfaces by means of electrostatic interaction with the increasing amine concentration. Hence, the surface of the zeolite has been successfully modified with different surfactants. It is possible to use zeolites especially for the treatment of textile wastewater owing to this modification. It is also seen that the carbon length of the surfactant is important in the modification of the zeolite. Additionally, it was seen that the adsorption density was higher with GTAP (18C) compared to HTAB, TTAB, and DTAB, which have carbon lengths of 18, 14, and 12C, respectively.

Positive charge on the zeolite surface allows the adsorption of anions such as chromate and nitrate. Moreover, the modified zeolite can also adsorb both inorganic anions and cations and non-polar organic impurities from wastewater. Therefore, modified zeolites are absorbents that highly sought after owing to their low cost and ability to adsorb various pollutants. Cleaning of ground water and using as a layer under waste storage areas for cleaning the leaks that may occur from waste depots are important examples of their applications.

2.3. Micro-flotation of Zeolites

The results of flotation of zeolite, with cationic collectors of different chain lengths are shown in Figure 6. As seen from Figure 6, the zeolite can be floated with all of the investigated collectors. Previous work on the subject showed that the highest flotation efficiency can be achieved with lower concentrations and increasing chain length (Fuerstenau et al, 1964; Leja, 1982; Ersoy and Celik, 2002, Kurama et al, 2010). Therefore, it can be concluded that amines with high chain lengths makes the zeolite more hydrophobic.

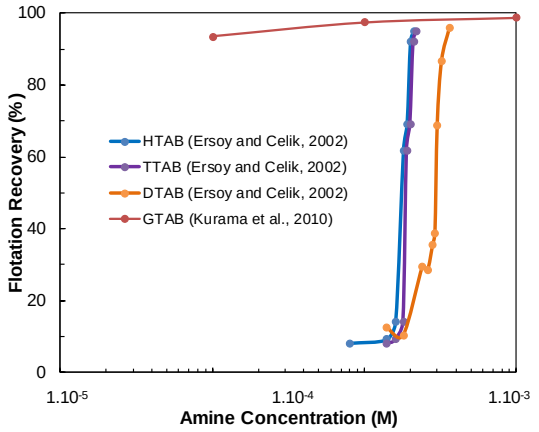

Fig. 6. Flotation recovery of zeolite with cationic surfactants with different chain lengths (Micro-flotation with HTAB, TTAB, DTAB; DAF flotation with GTAP)

2.4. Contact Angle of Zeolites

The zeolite was found to be hydrophilic as the contact angle of the zeolite in pure water could not be determined using sessile drop method (0º). However, when the contact angle of powder sample was measured using thin layer wicking (TLW) method, much higher contact angle was obtained as seen in Figure 7. Additionally, the contact angle of zeolite conditioned with HTAB increased (48º). This finding clearly showed that HTAB was successfully adsorbed onto the zeolite surface, and increased the contact angle, and hence, zeolite surface became hydrophobic.

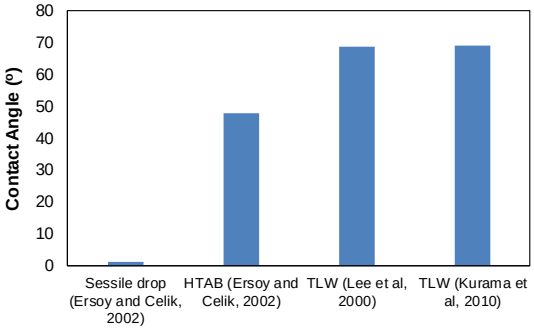

Fig. 7. Contact angle of zeolite (a) in the absence (b) in the presence of chemicals depending on methods

3. DISCUSSUION AND CONCLUSION

In this study, the surface properties of zeolite samples in literature were reviewed in detailed. In this context, the pH profile, zeta potential, and contact angle measurements, and flotation experiments with several zeolite samples were summarized, to determine the surface properties of the zeolite.

According to pH profiles of zeolite that were obtained as a results of the experiments conducted at different pH levels, it was revealed that the pH of zeolite attracted itself to a buffer pH for all instances at acidic, basic and natural pH values.

As a result of the zeta potential measurements, it was determined that zeolite had negative surface charge at all pH values. The zeta potential measurements of zeolite carried out with surfactants having different carbon chain lengths (GTAP, HTAB, TTAB, and DTAB) showed that they were successfully adsorbed to negatively charged zeolite surfaces and made them positive. This results also confirms that the modified zeolite can be used as adsorbent in adsorption of ions in waste water.

Additionally, the result of micro-flotation experiments with same surfactants showed that zeolite can be successfully floated with amines. It was also determined that the surfactants with higher chain length provides better flotation recovery rates.

Finally, the zeolite was found to be hydrophilic as the contact angle of the zeolite in pure water could not be obtained (0º). On the other hand, the contact angle measurements conducted in the presence of HTAB showed that the contact angle of the zeolite increased. The zeolite surface became hydrophobic by the adsorption of the HTAB molecules. This result confirms both zeta potential and flotation behavior of zeolite.

These studies also indicate that there is a significant correlation between the results obtained in different measurements. Some further studies to be conducted in

order to reveal surface properties of the zeolite in detail will provide a better understanding of the underlying mechanism of the relationship between zeolite and surfactants in the application of zeolite with physicochemical and chemical methods. This will surely enhance the development of the widespread use of zeolites, especially for the modified ones, in the industry.

REFERENCES

Ates, A. (2018). "Effect of alkali-treatment on the characteristics of natural zeolites with different compositions", *Journal of Colloid and Interface Science*, Vol. 523, pp. 266-281.

Baes, C.F. and Mesmer, R.E. (1976). *The hydrolysis of cations*, Wiley, New York, USA.

Bilgin, Ö. (2009). Investigation of the raw material properties of Gördes zeolite ores and searching their useability in different sectors, PhD Thesis, Dokuz Eylul University, Izmir, Turkey.

Breck, D.W. (1974). *Zeolite Molecular Sieves*, John Wiley, New York, USA.

Çulfaz, M. and Baş, B. (1989). "Na-Mg Double Ion Exchange Equilibrium in Zeolite X", *Proc., 6th Chemistry and Chemical Engineering Symposium*, Ege University, Izmir, Turkey.

Dikmen, S. (2008). Preparation of HDTMA Modified Zeolite and Adsorption of Nitrate from Aqueous Solutions, PhD Thesis, Anadolu University, Eskisehir, Turkey.

Ersoy, B. (2000). Investigating of the Adsorption Mechanisms of Various Cationic Surface Active Agents onto Clinoptilolite (Natural Zeolite) and Capture of the Non-Ionic Organic Contaminants in Liquids by Modified Clinoptilolite, PhD Thesis, Istanbul Technical University, Istanbul, Turkey.

Ersoy, B. and Çelik, M.S. (2002). "Electrokinetic properties of clinoptilolite with mono and multivalent electrolytes", Microporous *Mesoporous Mater.*, Vol. 55, pp. 305-312.

Fuerstenau, D.W., Healy, T.W. and Somasundaran, P. (1964). "The role of the hydrocarbon chain of alkyl collectors in flotation", *Transactions, AIME*, Vol. 229, pp. 321-325.

Gottardi, G. and Galli, E. (1985). *Natural Zeolites*, Springer-Verlag, Berlin, Germany.

Grant, D.C., Skribi, M.C. and Saha, A.K. (1987). Removal of Radioactive Contaminants from Westvalley Waste Streams Using Natural Zeolites, *Environ. Prog.*, Vol. 6, pp. 104-109.

Haggerty, G. M., and Bowman, R. S. (1994). "Sorption of chromate and other inorganic anions by organo-zeolite." *Environmental Science & Technology*, Vol. 28, No. 3, pp. 452-458.

Kurama, H., Karagüzel, C., Mergan, T. and Çelik, M.S. (2010). "Ammonium removal from aqueous solutions by dissolved air flotation in the presence of zeolite carrier", *Desalination*, Vol. 253, pp. 147–152.

Kurşun Ünver, İ., Terzi, M., Batjargal, K., Özdemir, O. (2018). "Electrokinetic Evaluation of the Effects of Acid Modification Processes on Natural Zeolites", *Proc., 16th International Mineral Processing Symposium*, METU, Antalya, Turkey, pp. 309-313.

Lee, J.Y., Lee, S.H. and Kim S.W. (2000). Surface tension of silane treated natural zeolite", *Materials Chemistry and Physics*, Vol. 63, pp. 251-255.

Leja, J. (1982). *Surface Chemistry of Froth Flotation*, Plenum Press, New York, USA.

Oliveira, C.R. and Rubio, J. (2007). "Adsorption of Ions onto Treated Natural Zeolite", *Materials Research*, Vol. 10, No. 4, pp. 407-412.

Ozdemir, O., Armagan, B., Turan, M. and Celik, M.S., (2004). "Comparison of the adsorption characteristics of azo-reactive dyes on mezoporous minerals", *Dyes and Pigments*, Vol. 62, No. 1, pp. 49-60.

Öter, Ö. (2002). Acid-Base Modification of Zeolite and Environmental Protection Applications of Modified Zeolite, Master Thesis, Dokuz Eylul University, Izmir, Turkey.

Şener, A.G. (2013). Coagulation of Zeolite Suspension with Inorganic Salts Having Cations of Different Valance, Master Thesis, Selcuk University, Konya, Turkey.

Tsitsishvili, G. V., Andronikashvili, T. G., Kirov, G. N., amd Filizova, L. D. (1992). *Natural Zeolites*, Ellis Horwood Ltd, Chichester, West Sussex, UK.

Ulusoy, G., Albayrak, M. (2009). "Mineralogical and technological properties of the zeolites from Foça (İzmir), Bigadiç (Balıkesir) and Gördes (Manisa)", *Mineral Res. Exp. Bull.*, Vol. 139, pp. 61-74.

Virta, R. (2002). *USGS Minerals Information*, US Geological Survey Mineral Commodity Summary.

Wang, X. and Nguyen, A.V. (2016). "Characterisation of Electrokinetic Properties of Clinoptilolite Before and After Activation by Sulphuric Acid for Treating CSG Water", *Microporous and Mesoporous Materials*, Vol. 220, pp. 175-182.

CISET - 2nd Cilicia International Symposium on Engineering and Technology
10-12 October, 2019, Mersin / TURKEY

A MULTISCALE ENTROPY BASED APPROACH FOR ANALYSIS OF SURFACE EMG SIGNALS

Hilal Kaya [1], Emine Uçar [2] and Veysel Alcan [*3]

[1] Ankara Yıldırım Beyazıt University, Faculty of Engineering and Natural Science, Department of Computer Engineering, Ankara, Turkey, hilalkaya@ybu.edu.tr

[2] İskenderun Technical University, Faculty of Business and Management Sciences, Department of Management Information Systems, Hatay, Turkey, emine.ucar@iste.edu.tr

[3] Tarsus University, Technology Faculty, Department of Software Engineering, Mersin, Turkey, alcanveysel@tarsus.edu.tr

ABSTRACT

Electromyography (EMG) is a technique whereby electrical activity is measured from muscles at rest state and during some activities in multiple time scales. The analysis of EMG signals are very important to diagnose neuromuscular diseases and disorders of motor controls. Since EMG signals are non-stable random time series, distinguishing these signals from one another is hard. In this paper, we proposed a multiscale entropy (MSE) based approach for extracting the optimal features for the classification process. MSE was developed for evaluating the complexity of time series over different time scales. Under MSE method, sample entropy (S_E) of the EMG signals were calculated after successive coarse-graining to extract dynamics at MSE scale factors of 5 to 29.

The 8-channel EMG dataset used in this study was loaded from the UCI (University of California, Irvine) database. Volunteer participants consist of healthy adults (3 males and 1 female) aged between 25 and 30 years. The recording time of the EMG signals is 10 seconds. The physical action classes in the dataset are bowing, clapping, handshaking, hugging, jumping, running, standing, seating, walking, and waving. Results of our study showed that after MSE scale of 5, curves of MSE results are behaving together so the features are becoming non-discriminatory for the larger scale factors so a reduced set of MSE values would be sufficient to classify the groups effectively.

Keywords: *Time series, EMG signals, Multiscale entropy, Scale factor*

[*] Corresponding Author

1. INTRODUCTION

Electromyography (EMG) is an electro-physiological test which is used to investigate the electrical potential of nerves and muscles and to diagnose diseases. The Electromyogram signals are utilized as a diagnostic tool to identify neuromuscular diseases and disorders of motor control. The analysis of EMG signals are also important in order to detect prosthetic hands, arms or legs control.

Generally, in the performed applications, the first way is to make feature extraction by preprocessing EMG signals, and then to evaluate the results with different classification methods based on these features. Since EMG signals are non-stable random time series, distinguishing these signals from one another is hard.

In the literature, comprehensive researches have been made in the field of classification of EMG signals and various approaches have been presented. Abdullah et al., used surface EMG signals to record electrical activity of muscle cells and for identifying actions. In this study they used Wavelet Packet Decomposition (WPD) for feature extraction and different ensemble tree classifiers like Random Forest, Rotation Forest and MultiBoost for classification. The findings showed that Random Forest algorithm achieved the best performance with a total classification accuracy of 92.1% (Abdullah et al., 2017). In previous studies authors used EMG signals for detecting disease. Biagetti et al., used surface electromyography signal to obtain the power spectrum of the motor unit action potential. They used these extracted parameters to estimate cadence and muscle fatigue (Biagetti et al., 2016).

Jung et al., proposed a method for EMG signals' pattern classification with using Yule-Walker algorithm and the LVQ (Jung et. al., 2007). In another study Sezgin analyzed surface EMG signals by using bispectrum and determined the quadratic phase coupling of each EMG episode. Then he used this features of the analyzed EMG signals for classifying the aggressive and normal actions (Sezgin, 2012). Zhang et al., proposed a wavelet based neuro-fuzzy approach to classify EMG signals for movement recognition in their study. They analyzed EMG signals by using wavelet transform and constructed feature vectors by using singular value decomposition(SVD) transform from wavelet coefficients for further movement recognition (Zhang et al., 2002). Acar and Özerdem used AR Burg Method for estimating the power spectral density (PSD) of EMG signals. By applying statistical methods to each signal's PSD maps, they acquired the texture feature vectors of EMG signals. Then they used the PSD based feature vectors as inputs for kNN classifier (Acar & Özerdem 2014). In another study Aydın and Akyüz used six different entropy methods for analyzing the surface EMG signals and used nonlinear support vector machines for classifying normal and aggressive actions. Their findings showed that Shannon Entropy and Permutation Entropy are the highest performers in the classification of physical activities through EMG (Aydın & Akyüz 2016).

In this paper, we proposed a multiscale entropy based approach for extracting the optimal features for the classification process. Multiscale entropy (MSE) has been created to assess the complexity of time series over different time scales. In 2002, Costa et al., have introduced a method to calculate multiscale entropy (MSE) for complex time series. Their results showed that MSE rigorously distinguishes healthy and pathologic groups (Costa et al., 2002). In another study Gao et. al, utilized multiscale entropy method for the aim of separating normal healthy EEG from epileptic seizure EEG (Gao et al., 2015). Istenic et al. suggested a multi-scale entropy-based approach to automatically classify data with neuromuscular disorders from data without neuromuscular disorders. Their results showed that it is appropriate for fast and non-invasive discrimination of healthy and neuromuscular patient groups, but it does not specify the type of pathology (Istenic et. al., 2010).

The manuscript is arranged as follows. Second section contains a brief description about used data and multiscale entropy, third section consists of the results and discussion of the method and fourth section of the manuscript contains the conclusion.

2. METHOD AND MATERIALS

2.1. Data

The 8-channel EMG dataset analyzed in this study was loaded from the UCI (University of California, Irvine) database (Lichman, 2013). Volunteer participants consist of healthy adults (3 males and 1 female) aged between 25 and 30 years. The recording time of the EMG signals is 10 seconds. The physical action classes in the dataset are bowing, clapping, handshaking, hugging, jumping, running, standing, seating, walking, and waving.

2.2. Multiscale Entropy

Entropy qualifies creation of information in a dynamical system. Traditional approaches on measuring the complexity of biological signals fail to account for the multiple time scales i.e. real-world datasets obtained in biomedical time series (Costa et al., 2005). MSE extends sample entropy (S_E) to multiple time scales or signal resolutions to provide an additional aspect when the time scale of interest is unknown. Like any entropy measures, MSE aims to make an assessment of the complexity of time series as in the state when you do not have any idea on what the signal represents, you will not know what time scale would be most enlightening for understanding the signal. The main purpose to select MSE in this study is that our dataset includes different complexities for 10 different physical action states as they have multiple unknown time scales.

MSE consists of two main procedures, first is coarse-graining and second is the calculation of S_E algorithm for each coarse-grained (simplified) time series that represent the system dynamics on different scales. Multiple coarse-grained time series are constructed by averaging the data points within non-overlapping time series parts of increasing length, τ (i.e., the scale factor) as seen in (1):

$$y_j^\tau = {}^1\!/_\tau \ \sum_{i=(j-1)\tau+1}^{j\tau} x_i \,, 1 \le y_j \le {}^N\!/_\tau \quad (1)$$

where τ is the timescale of relevance, y_j is a data point in the newly set time series (by averaging), x_i is a data point in the original time series and N is the length of the original time series. MSE uses the S_E algorithm to calculate an entropy value at each time scale. A major issue when applying the MSE algorithm is to provide

enough data points at the largest time scale because too few values at a time scale perform inconsistent S_E results.

The value of τ is usually chosen as a percentage of the standard deviation of the interested signal. In the original algorithm proposed by Costa et al., the value of τ is constant for all scale factors (Costa et al., 2002). As mentioned in Equation (1), the process can be evaluated as a low-pass filtering followed by a down sampling. As a result, when the scale factor increases, the standard deviation of the resulting filtered and reconstructed time series may become lower and therefore, the patterns may become closer. In this study, after several experiments, the most informative scale factor value τ is evaluated as 5. After 5 constructed MSE values, features are no longer distinctive and the classification of the groups are not feasible as will be emphasized in Results section.

3. RESULTS AND DISCUSSION

In this study, MSE algorithm is experimented on an 8-channel EMG dataset including time series of 10 seconds during 10 different action states (bowing, clapping, handshaking, hugging, jumping, running, standing, seating, walking, and waving) of 4 healthy adults. Firstly, for each of these 8 channels, 29 entropy values are calculated for different MSE scales as seen in Fig. 1. Groups of the classes in the dataset are aggressive and normal and represented by blue and red colors on the graph, respectively.

After these experiments, it's seen that after the scale value of 5, curves of MSE values are behaving together so the values are becoming non-discriminatory for the larger scale values. When these signals were examined, it was determined that the first 5 MSE values were sufficiently descriptive to discriminate the different groups.

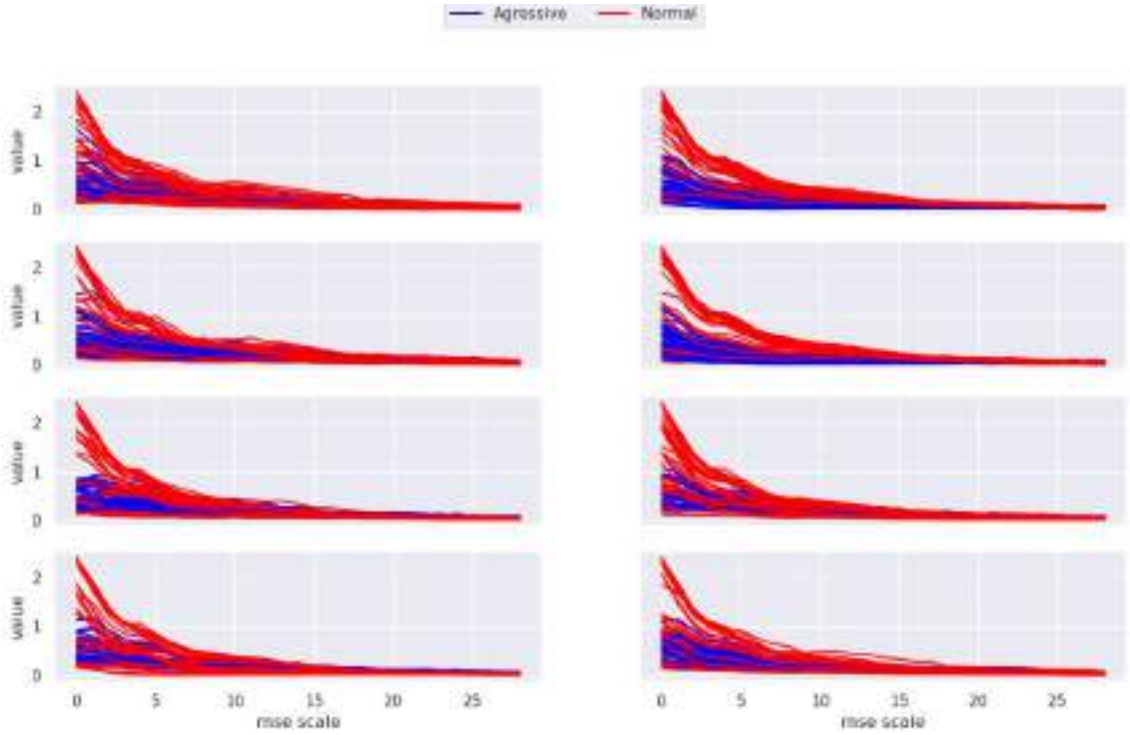

Figure 1. Calculated MSE values for each of 8-channels using various MSE scales

The first 5 of the calculated MSE values were grouped on the graph to see whether these values would be sufficient in the classification process. In order to display the first five MSE values on a two-dimensional graph, these 5 properties were reduced to 2 by applying principal component analysis (PCA). PCA is a feature reduction method that is used where lots of data, all very confusing, too many variables to consider exists, some of them are probably insignificant. This method was introduced firstly in 1901 by Karl Pearson and became a well-known statistical technique used in many signal processing applications (Han, 2004). Groups on graph formed by using a part of entropy values after reducing first 5 MSE values to 2 by PCA method, are represented in Fig. 2.

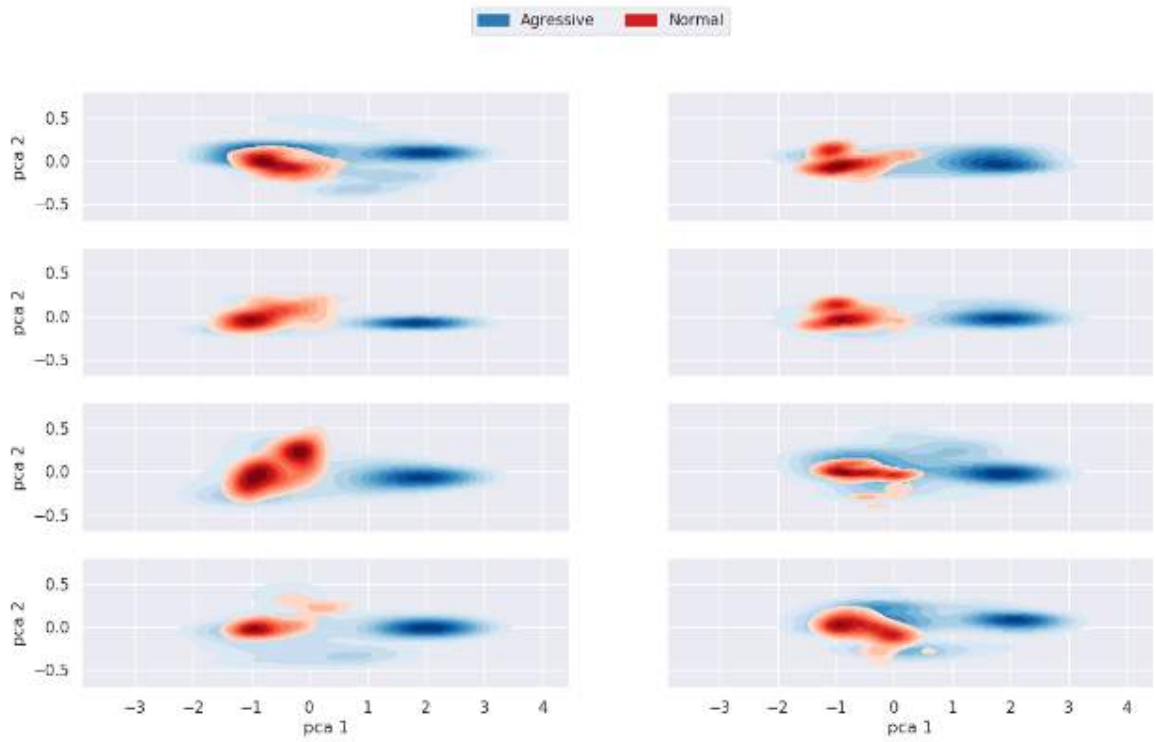

Figure 2. Representation of groups on graph formed by using a part of entropy values

On Fig. 2, "pca1" on the x-axis is the first principal component of the first 5 MSE values determined by PCA method and "pca2" on the y-axis is the second principal component of the first 5 MSE values determined by PCA method.

The characteristics of the graph in Fig. 2 shows that the first 5 MSE values that were reduced to 2 by PCA method has been enough for the classification process on the dataset of this study. Two classes including aggressive and normal groups were clearly grouped as seen in the figure.

4. CONCLUSION

EMG signals are generally used as a tool to diagnose neuromuscular diseases and disorders of motor controls. In these kinds of applications, the first step is to make feature extraction by preprocessing EMG signals, and then to evaluate the results with different classification methods based on these features. Since EMG signals are non-stable random time series, distinguishing these signals from one another is hard.

In this study, to overcome these distinguishing problems, we proposed a MSE based approach for extracting the optimal features for classification. MSE was used for evaluating the complexity of time series over different unknown and complex time scales. First 5 MSE values of this study behaved more distinctive and sufficient for deciding the results. Results of our study showed that a part of calculated MSE values would be enough to classify the groups effectively. As a result, when the scale factor increases, the standard deviation of the resulting time series may become lower and therefore, the patterns may become closer as represented in Fig. 1.

For the expansion of this study as a future work, we plan to find the best scale factor value using statistical methods or optimization methods. Also we will compare the results of different classification methods on the MSE features for various time-scales.

REFERENCES

Abdullah, A.A., Subasi, A., & Qaisar, S.M. (2017). Surface EMG Signal Classification by Using WPD and

Ensemble Tree Classifiers. *in CMBEBIH 2017*, Springer, pp. 475–481.

Biagetti, G., Crippa, P., Orcioni, S., & Turchetti, C. (2016). Surface EMG Fatigue Analysis by Means of Homomorphic Deconvolution. *in Mobile Networks for Biometric Data Analysis*, Springer, pp. 173–188.

Jung, K. K., Kim, J. W., Lee, H. K., Chung, S. B. and Eom, K. H. (2007). "EMG pattern classification using spectral estimation and neural network," *in SICE*, 2007 Annual Conference, pp. 1108–1111.

Sezgin, N. (2012). "Analysis of EMG Signals in Aggressive and Normal Activities by Using Higher Order Spectra", *The Scientific World Journal*, Volume 2012.

Zhang, X., Yang, Y., Xu, X., Zhang, M., (2002). "Wavelet based neuro-fuzzy classification for EMG control", *Communications, Circuits and Systems and West Sino Expositions, IEEE 2002 International Conference on*, vol.2, pp.1087,1089.

Acar, E. Özerdem, M. S. (2014). "Saldırgan hareketlerine ilişkin EMG işaretlerinin AR tabanlı k-NN ile sınıflandırılması". *22nd Signal Processing and Communications Applications Conference*, Trabzon.

Aydın S., Akyüz S., (2016). "Normal ve Agresif Kas Hareketlerinin Elektrofizyolojik Entropiler Cinsinden Sınıflandırılmasında Destek Vektör Makineleri," *in ELECO 2016, Elektrik - Elektronik ve Biyomedikal Mühendisliği Konferansı*.

Costa, M., Goldberger, A.L., & Peng, C.K. (2002). Multiscale entropy analysis of complex physiologic time series. *Physical review letters, 89 6*, 068102.
Gao, J., Hu, J., Liu, F., & Cao, Y. (2015). Multiscale entropy analysis of biological signals: a fundamental bi-scaling law. *Front. Comput. Neurosci.*. 9:64.

Istenic, R., Kaplanis, P. A., Pattichis, C. S., and Zazula, D. (2010). "Multiscale entropy-based approach to automated surface EMG classification of neuromuscular disorders," *Med Biol Eng Comput*., vol. 48, no. 8, pp. 773–781.

Lichman, M. (2013). "Irvine, CA: University of California, School of Information and Computer Science," [Online]. Available: http://archive.ics.uci.edu/ml.

Costa, M. & Goldberger, A.L. & Peng, C.K. (2005). Multiscale entropy of biological signals. *Physical review. E, Statistical, nonlinear, and soft matter physics.* 71. 021906. 10.1103/PhysRevE.71.021906.

Han, D., Rao, Y.N., Principe, J.C. and Gugel, K., (2004). "Real-time PCA (principal component analysis) implementation on DSP," *2004 IEEE International Joint Conference on Neural Networks (IEEE Cat. No.04CH37541)*, Budapest, 2004, pp. 2159-2162 vol.3. doi: 10.1109/IJCNN.2004.1380953

CISET - 2nd Cilicia International Symposium on Engineering and Technology
10-12 October, 2019, Mersin / TURKEY

DESIGN OF A UNIFORM ICE CUTTING DEVICE

Mehmet Ilteris SARIGECILI [*1] and Ibrahim Deniz AKCALI [2]

[1] Çukurova University, Enginering Faculty, Mechanical Engineering Department, Adana, Turkey, msarigecili@cu.edu.tr

[2] Çukurova University, Enginering Faculty, Mechanical Engineering Department, Adana, Turkey, idakcali@gmail.com

ABSTRACT
The large amounts of shredded ice required in hot regions can be obtained instantaneously by cutting small and uniform ice particles from a big block of ice. There are three important objectives in the design of such a machine that can perform this process. The first one is controlling the cutting tool speed in such a way that each cutting process is to be performed at an average same speed while cutting time and feeding time are simultaneously kept at the same level within each cycle of cutting. The second one is to provide a constant force for the feeder during the cutting phase. The final one is to feed the ice block towards cutting tool at a desired displacement until the next cutting process starts. In this study, a procedure to design a compact machine that can successfully realize these three objectives is demonstrated.

Keywords: *Ice-Cutting, Slider-Crank, Force Control, Speed Control, Feeder Design*

[*] Corresponding Author

1. INTRODUCTION

In hot climate regions, the instantaneous shredded ice production is especially important for food industry such as for fish storage at counters or for use in cold drinks. Shredded ice particles prepared in production site cannot be transported to other destination points either because they melt under hot environment or because they are rejoined together to form a block under cold conditions. Hence, design of a compact machine that instantaneously cuts ice blocks into ice particles of desired uniform size is needed.

There are machines, both in the market and in the literature, which convert block materials into pieces. Out of the commercially available ones, ice cutting machines that can produce big cubic ice particles by first cutting ice blocks longitudinally at equal intervals and then cutting these ice strips transversely can be cited (Erdil, 1998). Other than these, it is also possible to observe the use of jaw, rotary cone, hammer and roller crushers, as utilized in mining, which are readily available on the market, (Norman, 1985). However, these designs not only occupy more space due to their large sizes but also consume large amounts of energy. More importantly, the dimensions of the particles thus obtained are non-uniform. On the other hand, home-use ice-cutting machines with a cutting knife on a compact, rotating disc are also commercially available. Unfortunately, their capacity is small and is not sufficient.

Upon review of the already existing machinery in this respect, a new design based on a new approach has been put forward in this work. Fundamental methods together with their implementation are demonstrated here.

2. METHOD

The approach to the problem of designing the compact ice-cutting machine consists of the following steps.

Firstly, the requirements of the needed ice cutting machine are listed as:

- The minimum contact between cutter and ice to prevent corrosion
- Controlled feeding
- Capability to control the size of ice particles
- Operation of ice cutter in hygienic conditions
- A compact design

Secondly, based on these requirements, ice cutting machine is designed as a combination of two different mechanisms, namely ice cutter mechanism and ice feeder mechanism. Designs of these mechanisms are explained below.

2.1. Synthesis of Ice Cutter Mechanism

A slider-crank mechanism is preferred for the ice cutting process. An ice block, which is fed perpendicular to the motion plane of slider-crank mechanism, will be cut at a defined thickness with a cutter placed on piston during both forward and backward strokes of the piston for a full rotation of the crank. Since the dynamic effects are very small under these conditions, the design of the slider-crank mechanism performing cutting process can be considered as a kinematic problem. Therefore, identifying the corresponding piston positions for ice cutting as well as keeping the average piston speed constant at these positions for obtaining uniform ice particles should be attained.

In Figure 1, the ice cutting mechanism is shown schematically and crank is made of a circular disk. The crank length, connecting rod length and the eccentricity between the crank center and the piston sliding axis are represented by X_1, X_2 and X_3, respectively. The ice cutter attached to the piston is planned to cut the ice block fed perpendicular to its line of action. While the crank rotates in the counter clockwise direction, the piston arrives at the bottom dead point (B.D.P.) represented by D and at the top dead point (T.D.P.) represented by F. Ice cutting is performed between points B and C. On the other hand, ice cutting does not occur when piston goes from point C to D and returns back from point D to C; the same is true when piston goes from point B to F and returns back from F to B. However, the ice block moves forward due to the force acting from the feeder in this non-ice-cutting period. As soon as the cutter and the ice block come into contact, the motion of the ice stops because the reaction force of the cutter is compensated by the thrust from the feeder. Therefore, in order for the uniform ice cutting process to be realized, it is necessary that in the non-ice-cutting motion phases, time intervals be equal and that ice block be fed forward uniformly.

In the kinematic synthesis of the slider-crank mechanism of Figure 1, the following definitions are made: When the crank is at point A2, the crank angle measured with respect to horizontal axis is θ_0 and the piston is at point C. When the crank rotates in the counter clockwise direction by an amount of $\Delta\theta$ and reaches the point A4, the piston gets to the point B. The cutting process occurs at a displacement of ΔS. The starting position of the cutting process is represented by S_0. Based on these quantities, the relation between crank angle θ and piston displacement S can be given as follows (Akçalı and Arıoğlu, 2011):

$$S^2 + z_3 \sin\theta - z_1 \cos\theta + z_2 = 0 \quad (1)$$

where

$$z_1 = 2X_1 \quad (2)$$

$$z_2 = X_1^2 + X_3^2 - X_2^2 \quad (3)$$

$$z_3 = 2X_1X_3 \quad (4)$$

An ice block has the dimensions of 850 *mm* x 90 *mm* x 110 *mm*. By considering that the ice block is cut along 90 *mm* width; the length of the block is 850 *mm*; and each cutting operation is performed for 2 *mm* thickness; then 2x2 *mm* = 4 *mm* ice is cut from the block in each full cycle of crank rotation. Therefore, full cutting of the ice block requires 850/4 = 212 cycles. If the ice block is required to be cut around 2 min approximately (1.78 *min*) the crank speed is calculated as 212/1.78 = 119 *rpm*.

From these definitions, the dimensions of the ice cutting mechanism is determined by Subdomain Method and listed in Table 1 (Erdil, 1998). The design dimensions listed in Table 1 as well as crank speed of 119 *rpm* can be used to analyze the piston position vs. piston velocity. From this analysis, the positions of points B and C as well as the time intervals for each period can be nicely identified.

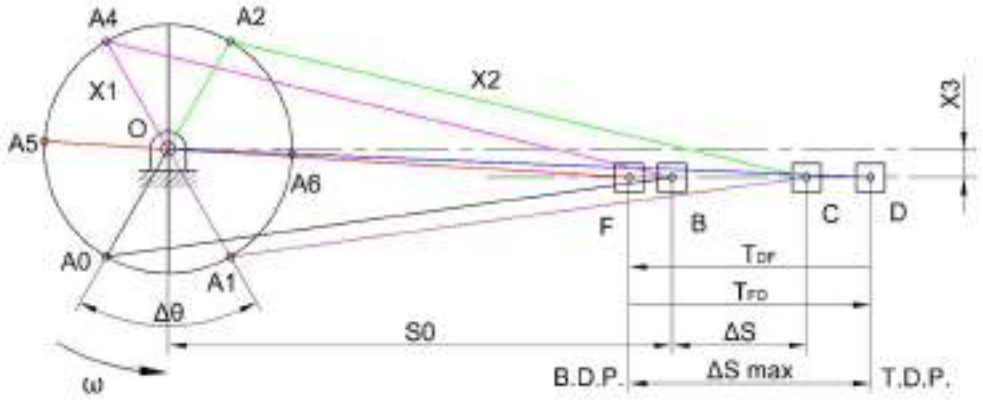

Fig. 1. Ice cutter slider-crank feeder mechanism

Table 1. The dimensions of the ice cutter slider-crank mechanism

X_1 (*mm*)	X_2 (*mm*)	X_3 (*mm*)	S_0 (*mm*)	$\Delta\theta$ (°)	θ_0 (°)
-150	690	31	-639	-60	106.5

2.2. Design of Feeder for Ice Cutter

There are two distinct phases in feeding the ice block to the ice cutter mechanism: (1) the ice block and the ice cutter is in contact hence there is no motion in the ice block (i.e. during the cutter motions from points B to C and from C to B in Figure 1 and (2) the ice block and the ice cutter are not in contact hence the ice block is free to move (i.e. during the cutter motion from points C to D and back from D to C as well as from points B to F and back from F to B in Figure 1). The main requirement for the first stage is that pushing the ice block with a sufficient force to balance the reaction force coming from the ice cutter to the ice block and for the second stage is to let the ice block move to yield a uniform cutting thickness.

A slider-crank mechanism has been chosen as the concept design to realize the above two requirements. The schematic representation of the feeder slider-crank mechanism is shown in Figure 2. The dimensions of the mechanism of interest are crank and connecting rod lengths (L_1 and L_2, respectively) and eccentricity between the crank center and piston line of action (L_3). The centers of gravity of crank and connecting rod are away from points O and B by r_{G1} and r_{G2}, respectively. The masses of crank, connecting rod and piston are represented by m_1, m_2, and m_C. The mass moment of inertia for crank and connecting rod are shown by I_{G1} and I_{G2}, respectively. The variables are crank angle θ and connecting rod angle β, with corresponding sign conventions. F_B and m_B stand for external load applied and external mass added to bare bucket mass, respectively. In Figure 2, ground, crank, connecting rod and piston of the slider-crank mechanism are identified by numerals 1, 2, 3 and 4, respectively.

In the first stage of the feeding process where the cutting process takes place, a constant pushing force is desired at each crank angle of Figure 2 by considering static conditions because of no motion at the feeder mechanism. At this point, the problem is transformed into the selection of appropriate operating parameters so that any existing slider-crank mechanism can be used as a feeder in the ice cutting process. Hence, a piston pushing force can be created by applying an external force at point B as shown in Figure 2. However, since the crank angle changes for each cutting cycle piston pushing force has a non-linear relationship with respect to the change in crank angle. Thus, in order to ensure a constant external pushing force, a suitable helical spring is attached to the crank.

The output-input force relationships to control piston force by means of a suitable rotational spring attached to

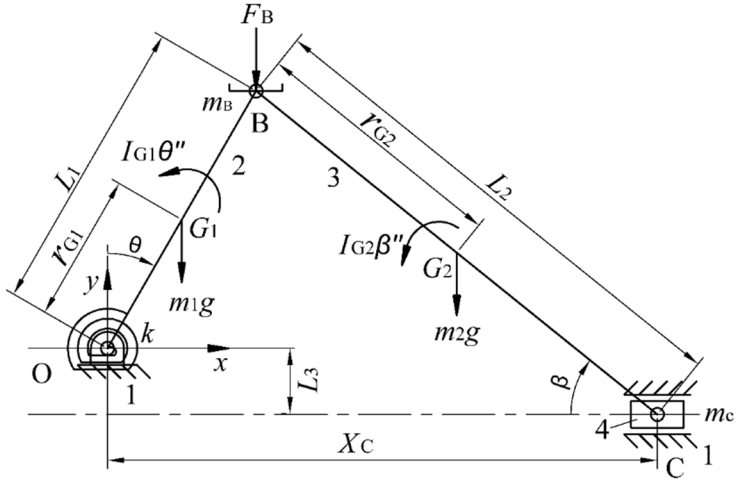

Fig. 2. Feeder slider-crank mechanism

the crank in a slider-crank mechanism has been shown in a recent publication (Sarigecili and Akcali, 2019a). To explain the work, it is sufficient to point to the net pushing force on the piston, which is given below:

$$Q_{net} = \frac{1}{(\tan(90-\theta)+\tan\beta)} * \left(F_B - \frac{k(\theta-\theta_0^*)}{L_1\cos(90-\theta)} \right) \quad (5)$$

where θ, β, θ_0^*, k and Q_{net} represent crank angle, connecting rod angle, spring neutral position, spring constant and net pushing force on the piston, respectively. By writing the necessary force requirement at three different crank positions, k, θ_0^* and Q_{net} are eventually evaluated (Sarigecili and Akcali, 2019a).

In the second stage of the feeding process, after the contact between the cutter and ice block is terminated, the pushing force coming from the feeder is utilized to provide free movement of the ice block, by overcoming resisting forces including inertial and friction effects. The main goal here is to calculate displacement of the ice block, under the effect of piston pushing force as a function of the crank angle of the feeder, elapsed during the time interval, until the cutter comes in contact with the ice again.

A dynamic model of the feeder slider-crank mechanism has been developed for this purpose, given in the publication (Sarigecili and Akcali, 2019b). The model is briefly explained by the resulting second order differential equation given below:

$$A_0(\theta) + A_1(\theta)\dot{\theta}^2 + A_2(\theta)\ddot{\theta} = 0 \quad (6)$$

where A_0, A_1 and A_2 are suitably expressed by the dimensionless numbers ($\lambda_1 - \lambda_{11}$) in Eqs. (7) – (9).

$$A_0 = \begin{bmatrix} \lambda_9(\theta-\theta_0^*)[1-\mu\tan\beta] + \mu\cos\theta(\lambda_4\lambda_7 + \lambda_6\lambda_7\lambda_3) + \\ \sin\theta(-\lambda_7 - \lambda_8 - \lambda_6\lambda_7 + \lambda_6\lambda_7\lambda_3 - \lambda_5\lambda_7\lambda_2) + \\ \mu\sin\theta\sin\beta\sec\beta(\lambda_7 + \lambda_8 + \lambda_4\lambda_7 + \lambda_6\lambda_7 + \lambda_5\lambda_7\lambda_2) \end{bmatrix} \quad (7)$$

$$A_1 = \begin{Bmatrix} \cos\theta\sin\theta(-\lambda_4 - 2\lambda_3\lambda_6 + \lambda_3^2\lambda_6) + \\ \cos\theta\sin^2\theta\sec\beta(-\lambda_1\lambda_3\lambda_6 - \lambda_1\lambda_4) + \\ \cos^2\theta\tan\beta(\lambda_3\lambda_6 + \lambda_4) + \\ \cos\theta\sin^2\theta\tan^2\beta\sec\beta(-\lambda_1\lambda_3\lambda_6 - \lambda_1\lambda_4) + \\ \mu\cos\theta\sin^2\theta\tan\beta\sec\beta(\lambda_1\lambda_3\lambda_6 - \lambda_1\lambda_3^2\lambda_6) + \\ \mu\cos^2\theta\tan^2\beta(-\lambda_3\lambda_6 + \lambda_3^2\lambda_6) + \\ \mu\cos\theta\sin^2\theta\tan^3\beta\sec\beta(\lambda_1\lambda_3\lambda_6 - \lambda_1\lambda_3^2\lambda_6) + \\ \mu\cos^2\theta(-\lambda_3\lambda_6 + \lambda_3^2\lambda_6) - \mu\cos^2\theta\sec^2\beta(\lambda_{11}) + \\ \mu\cos\theta\sin^2\theta\tan\beta\sec^3\beta(\lambda_1\lambda_{11}) + \\ \sin^2\theta\tan\beta(-\lambda_4 - \lambda_3\lambda_6) + \\ \sin^3\theta\tan\beta\sec\beta(-\lambda_1\lambda_4 - \lambda_1\lambda_3^2\lambda_6) + \\ \cos\theta\sin\theta\tan^2\beta(\lambda_4 + \lambda_3^2\lambda_6) + \\ \sin^3\theta\tan^3\beta\sec\beta(-\lambda_1\lambda_4 - \lambda_1\lambda_3^2\lambda_6) - \\ \cos\theta\sin\theta\sec^2\beta(\lambda_{11}) + \sin^3\theta\tan\beta\sec^3\beta(\lambda_1\lambda_{11}) \end{Bmatrix} \quad (8)$$

$$A_2 = \begin{Bmatrix} (1+\lambda_{10}) + \mu\tan\beta(-1-\lambda_{10}) + \cos^2\theta(\lambda_6 + \lambda_4 + \lambda_2^2\lambda_5) + \\ \mu\cos^2\theta\tan\beta(-\lambda_6 + \lambda_3\lambda_6 - \lambda_2^2\lambda_5) + \\ \cos\theta\sin\theta\tan\beta(2\lambda_3\lambda_6 + 2\lambda_4) + \\ \mu\cos\theta\sin\theta\tan^2\beta(-\lambda_3\lambda_6 - \lambda_3^2\lambda_6) + \\ \mu\cos\theta\sin\theta(-\lambda_3\lambda_6 - \lambda_3^2\lambda_6) - \mu\cos\theta\sin\theta\sec^2\beta(\lambda_{11}) + \\ \sin^2\theta(\lambda_6 - 2\lambda_3\lambda_6 + \lambda_3^2\lambda_6) + \\ \mu\sin^2\theta\tan\beta(-\lambda_6 + \lambda_3\lambda_6 - \lambda_2^2\lambda_5) + \\ \sin^2\theta\tan^2\beta(\lambda_4 + \lambda_3^2\lambda_6) - \sin^2\theta\sec^2\beta(\lambda_{11}) + \\ \sin^2\theta(\lambda_2^2\lambda_5) \end{Bmatrix} \quad (9)$$

$$\lambda_1 = \frac{L_1}{L_2};\ \lambda_2 = \frac{r_{G1}}{L_1};\ \lambda_3 = \frac{r_{G2}}{L_2};\ \lambda_4 = \frac{m_C}{m_B};\ \lambda_5 = \frac{m_1}{m_B};$$
$$\lambda_6 = \frac{m_2}{m_B};\ \lambda_7 = \frac{g}{L_1};\ \lambda_8 = \frac{F_B}{m_B L_1};\ \lambda_9 = \frac{k}{m_B L_1^2};$$
$$\lambda_{10} = \frac{I_{G1}}{m_B L_1^2};\ \lambda_{11} = \frac{I_{G2}}{m_B L_2^2} \quad (10)$$

A numerical method called 4th order Runge-Kutta method (Chapra and Canale, 2010) has been applied in the solution of Eq. (6) accompanied by appropriate initial conditions as in the form of:

$$\theta(t_0) = \theta_0 \quad (11)$$
$$\omega(t_0) = \omega_0 \quad (12)$$

2. IMPLEMENTATION

Solid model of the ice cutting and ice feeding mechanisms are presented in Figure 3. The dimensions of the slider-crank mechanism which will perform ice cutting process has been synthesized in Section 1.1 and listed in Table 1. The crank speed has also been identified as 119 rpm. The change in piston position and velocity with respect to time are determined under this constant crank speed. Their graphs are shown in Figure 4.

In Figure 4, piston position is represented by "continuous line" and piston speed is represented by "dash point". In this slider-crank mechanism, B.D.P. is 539 *mm* and T.D.P. is 839 *mm*. The cutting process starts at piston position of 639 *mm* (S_0) and continues up to 729 *mm*. For a full cycle of crank rotation in Figure 4, the piston performs cutting for a period of 0.05 *s* during the displacements in between B – C and C – B whereas the piston moves freely for a period of 0.20 *s* during the displacements through C – D – C and B – F –B. In this second time period, the ice block pushed by the feeder system starts free motion. Therefore, the feeder system should provide an equal amount of ice displacement for the corresponding period of 0.20 *s* in each cycle. A minimum of 850 *mm* stroke is mandatory in the required feeder slider-crank mechanism for achieving the cutting process discussed in the previous paragraph. Hence, a slider-crank mechanism with physical dimensions as listed in Table 2 has been selected.

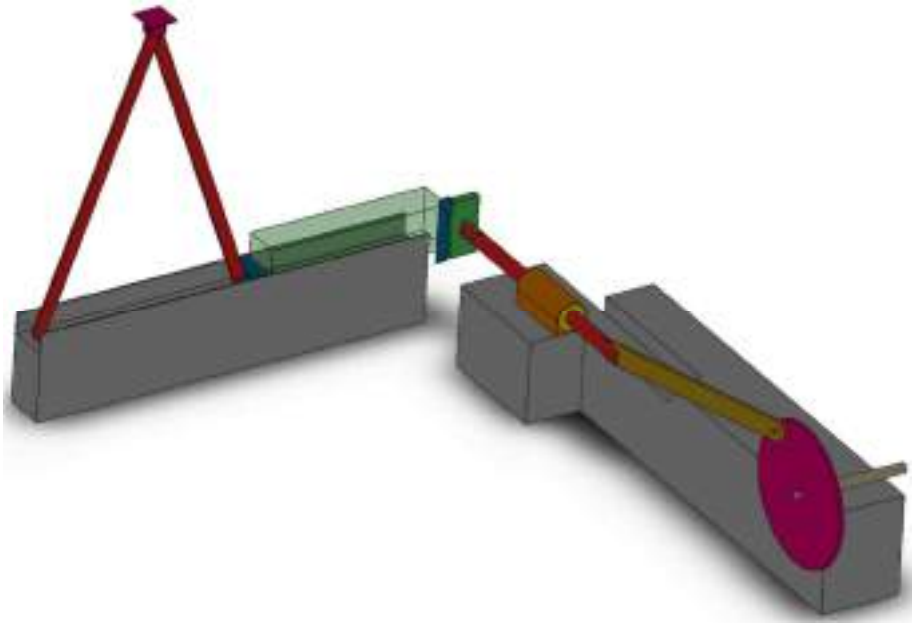

Figure 3. The solid model of the ice-cutting machine

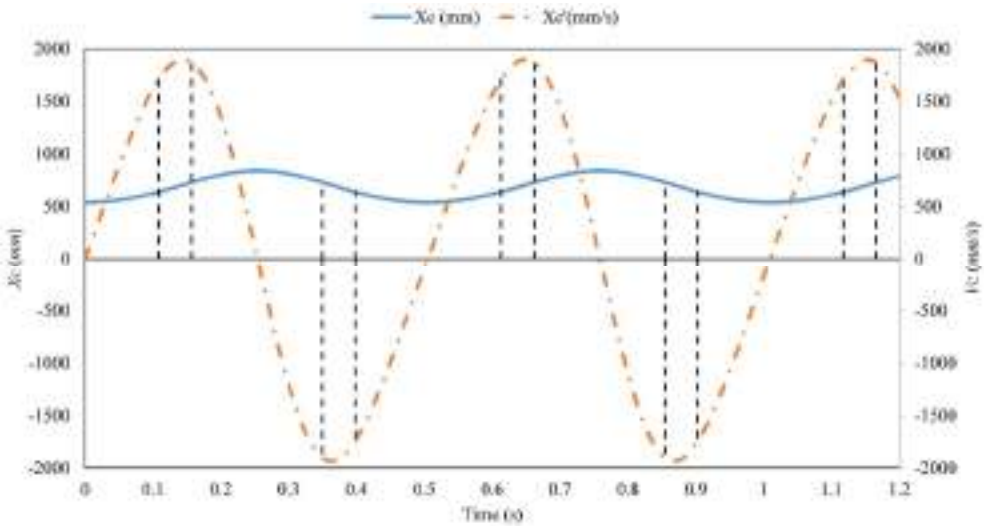

Figure 4. The piston position and velocity vs. time in slider-crank mechanism

Table 2. The physical parameters of the feeder slider-crank mechanism

L_1 (m*m*)	750	m_1 (*kg*)	1.814
L_2 (*mm*)	750	m_2 (*kg*)	1.814
L_3 (*mm*)	0	m_C (*kg*)	0.760
r_{G1} (*mm*)	375	I_{G1} ($kg.m^2$)	0.090
r_{G2} (*mm*)	375	I_{G2} ($kg.m^2$)	0.090

When the 850 *mm* ice block is loaded to the feeder system, the initial crank angle and piston positions of the feeder mechanism would be 20° and 513 *mm*. At the end of the ice cutting process where the ice block is shredded fully, the crank angle and piston positions of the feeder system would be 65.3° and 1363 *mm*. Considering these data together with a net piston pushing force of 25 *N* in the feeder, the operation parameters can be obtained as discussed in Section 1.2 and listed in Table 3. From these calculations, it is found out that a static load of 3.7 *kg* at point B as well as a spring at the crank center with a spring coefficient of 53.9 *Nm* and a spring neutral position of 47.3° should be applied.

Analysis of Figure 4 reveals that cutting process takes place in 0.05 *s* (B – C and C – B) where the piston of feeder does not move. However, as soon as the cutting process ends an external constant force F_B should be applied since external mass m_B cannot start the motion of ice block by the feeder. As a matter of fact, this external force behaves as a manual control button which must be applied externally when it is desired to cut the ice. Hence, a constant 20 *N* external force is assumed to be applied right after each cutting process. The motion of the feeder piston is calculated from the solution of crank angle in Eq. (6). In order to depict the feeder piston motion and the net pushing force on the piston in more detail under the given conditions, they are drawn separately in Figure 5 and Figure 6, respectively. In Figure 5, horizontal sections depict where cutting process occurs and parabolic sections represent the free motion of the feeder piston. It should also be noted in Figure 6 that during the cutting

process, 25 *N* net pushing force can be clearly observed since there is no motion. However, during the free motion of the feeder piston, the 25 *N* net pushing force is used to overcome inertia and frictional forces and a net force between 0.10 *N* and 0.40 *N* is calculated from the mass and acceleration of the feeder piston.

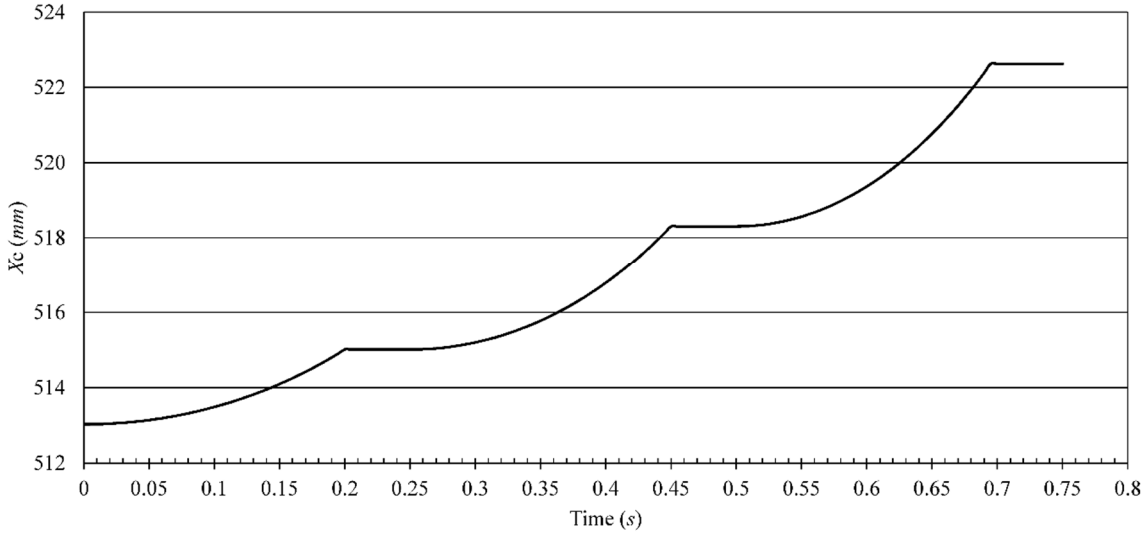

Fig. 5. Piston position vs. time at feeder slider-crank mechanism during ice cutting

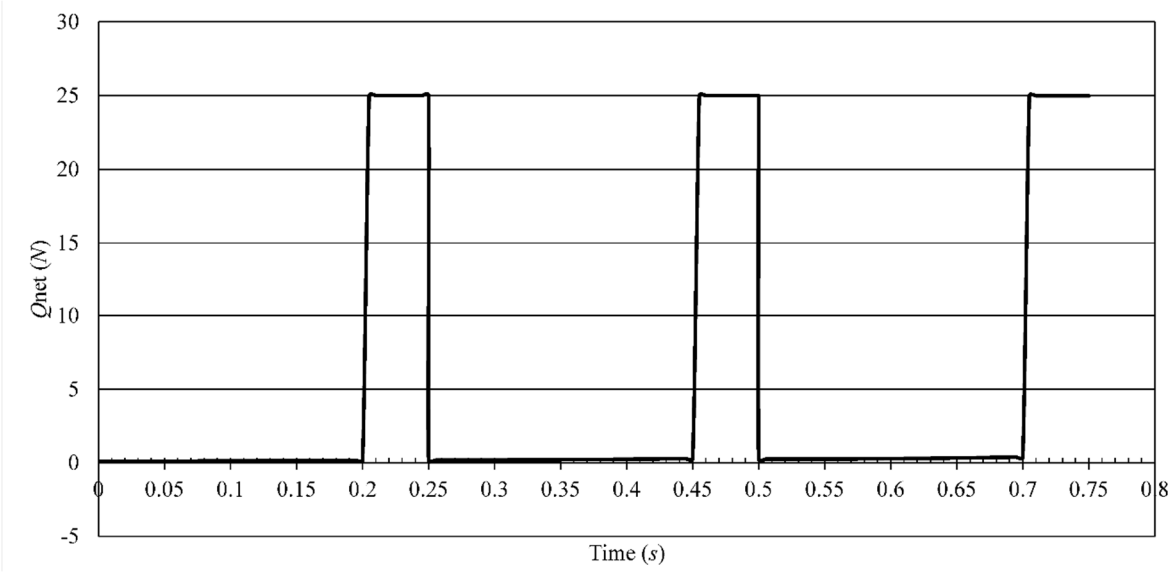

Fig. 6. Piston force vs. time at feeder slider-crank mechanism during ice cutting

Table 3. Operation parameters of the feeder slider-crank mechanism

θ_0 (°)	20	θ_0^* (°)	47.3	μ	0.3
θ_1 (°)	47.3	k (Nm)	53.9	ω_0 (r/s)	0
θ_2 (°)	65.3	m_B (kg)	3.7		

3. CONCLUSION

In this study, a design of a uniform ice cutting device has been shown to meet the following criteria:

- Provide uniform ice feeding displacements within desirable ice feeding times,
- Provide uniform ice pushing force during the cutting phase,
- Ensure uniform ice feeding for the next cutting phase.

Conclusively, the results have demonstrated that during cutting operation static pushing force from feeder slider-crank mechanism can be kept at a constant value by choosing suitable operating conditions (i.e. a static vertical force applied at crank pin center as well as a spring applied on the crank with the corresponding spring constant k and spring neutral positon θ_0^*). However, this force is not sufficient to move the ice block during the feeding phase hence an extra input force should be applied at point B to feed the ice block to the ice cutter. This force value can also be instantly adjusted by visual inspection over the relationships between the force applied and the displacement obtained in the slider of the feeder mechanism.to yield a desirable ice particle size. In this way, this extra input force can be considered as the manual means not only to control whether the machine should instantly start ice-cutting or not but also to control ice particle size. As a result, the design of a machine which cuts uniform ice particles from an ice block has been successfully implemented.

REFERENCES

Erdil, A. H. (1998). Ice grating machine, MSc Thesis, Çukurova University, Institute of Natural and Applied Sciences, Adana, Turkey.

Norman, L. W. (1985). *SME Mineral Processing Handbook*, American Institute of Mining, Metallurgical and Petroleum Engineers, Inc. New York, USA.

Akçalı İ. D. and Arıoğlu M. A. (2011). "Geometric design of slider–crank mechanisms for desirable slider positions and velocities." *Forschung im Ingenieurwesen*, Vol.75, pp.61–71. DOI: 10.1007/s10010–011–0134–7.

Sarigecili, M. I. and Akcali, I. D. (2019a). "Development of constant output-input force ratio in slider-crank mechanisms." *Inverse Problems in Science and Engineering*, Vol.27, No.5, pp. 565-588. DOI: 10.1080/17415977.2018.1470625

Sarigecili, M. I. and Akcali, I. D. (2019b). "Estimation of operation parameters for required piston positions and speeds in a slider-crank mechanism." Submitted to *The Proceedings of the Institution of Mechanical Engineers, Part K: Journal of Multi-body Dynamics.*

Chapra, S. C. and Canale, R. P. (2010). *Numerical Methods for Engineers*, Sixth ed. McGraw-Hill, New York, USA.

CISET - 2nd Cilicia International Symposium on Engineering and Technology
10-12 October, 2019, Mersin / TURKEY

EFFECTS OF WEATHERING ON PETROGRAPHIC PROPERTIES OF THE BASALTS EMPLOYED IN DİYARBAKIR CITY WALLS

Felat DURSUN [*1], Tamer TOPAL[2]

[1] Dicle University, Engineering Faculty, Department of Mining Engineering, Diyarbakır, Turkey, felatdursun@gmail.com

[2] Middle East Technical University, Engineering Faculty, Department of Geological Engineering, Ankara, Turkey, topal@metu.edu.tr

ABSTRACT

The Diyarbakir City Walls (DCW) are among the largest and most impressive monuments from ancient times. City Walls of Diyarbakır are appreciated as a masterpiece structural design of human history. Hence, the UNESCO World Heritage Committee added this remarkable structure into the World Heritage List. Basalts with two different types of textures were used in the construction of the DCW. Although basalt is known as a long-lasting construction material it starts to deteriorate once it is quarried and subjected to the environmental and structural stresses. Like many other historical structures around the world, the DCW are suffering from stone deterioration. This deterioration of the City Walls damages their integrity, aesthetic value and structural stability. This study aims to understand the impact of weathering on the mineralogical, petrographic and microfracture properties of the basalts used in the construction of the DCW. For this purpose, fresh and relatively weathered samples collected from the study area and their mentioned properties were investigated through optical microscopy and electron microprobe. The results reveal that although primary minerals are conserved in most of the weathered samples, olivine phenocrysts are partly replaced by iddingsite which is the main alteration product observed in the weathered basalt samples. Microfracture studies confirmed that olivine and pyroxene are the most vulnerable minerals. Moreover, it is found that most of the microfractures originate from the edges of the vesicles.

Keywords: *Basalt, City Walls, Petrography, Microfracture, Diyarbakır*

[*] Corresponding Author

1. INTRODUCTION

Stone monuments are the most visible and essential structures of our cultural heritage; however, many of the historical structures around the world are now suffering from the stone deterioration (Pope *et al*., 2002; Fitzner, 2004). From a geological point of view, the nature of stone deterioration is associated with intrinsic factors (mineralogical, chemical or structural characteristic) and extrinsic ones (environmental conditions, weathering agents or interventions). Moreover, rates of deterioration can change in response to changes in environmental conditions or interventions. For instance, extensive exposure of the stone to weathering episodes (e.g., freezing and thawing; wetting and drying) or inappropriate repair techniques can accelerate the process of stone deterioration (Warke *et al*., 2006). Although numerous studies and projects have been conducted to preserve cultural heritage the long-term activity of stone material and its deterioration mechanisms are not yet well understood (Winkler, 1997; Bell, 2007). In order to preserve our cultural heritages, it is essential to investigate the damaging deterioration mechanisms of stone and to propose remedies that can protect stone structures.

Diyarbakır is a city located in the southeastern part of Turkey. The city occupies a remarkable position at the midpoint of geo-strategically important locations. During its long history, Diyarbakır was seized many times and ruled by more than thirty tribes, states, and Imperials (Parla, 2004). Therefore, civilization in Diyarbakır has never been interrupted. The remains and artifacts of the ruled civilizations can be found all around the city. Considering their scale, structural elements, construction techniques and material applications, the Diyarbakır City Walls (DCW) are symbolizing the traces of the cultures, ruled in the region (Fig. 1). The DCW, as an architectural character, are therefore, the masterpiece of the skills of the people of the ancient and modern era. As a result, The DCW have officially acknowledged the status of World Heritage Site by UNESCO in 2015 (UNESCO, 2015).

Fig. 1. Aerial view of the study area (captured from Google Earth)

Basalt is the main construction material of the City Walls. It has been employed in almost all of their architectural elements. Like many other historical structures, the DCW are also suffering from stone deterioration. A large variety of types of deterioration, including cracks, detachments, material losses, discolorations and biological colonization can be observed in different sections of the City Walls. This deterioration of the City Walls damages their integrity, aesthetic value and structural stability.

Mineralogical composition, texture and structure are the main factors controlling the physico-mechanical properties of rock materials. Therefore, it is essential to define the mineralogical and petrographic characteristics of rock materials to evaluate their engineering properties accurately (Zalesskii, 1967; Bell 1992).

Petrographic investigations not only provide knowledge on the mineralogical state and provenance of rock materials, they also can be used as a strong tool for evaluating its weathering potential and durability. They help also to understand why the behavior of macroscopically similar rock materials differ with respect to environmental conditions and their weathering potential (Dreesen and Dusar, 2004).

The present study aims to understand the effect weathering on the basalt used in the DCW by investigation their mineralogical, petrographic and microfracture properties. To accomplish these, several field studies and laboratory research were carried out. The field studies consist of site observation and sampling. Site observation was done in different periods and for different motivations. During the site observation, the general state of conservation of the site was examined. Special emphasis was given to the forms of stone weathering on the walls. For sampling, fresh and weathered basalt samples were collected from the different sections of the DCW. Fresh basalt blocks were taken from the outcrops along the City Walls and quarries in the vicinity of the site. Oriented samples were extracted from the surface, using jackhammers. In addition to the fresh samples, during the field survey special emphasis was given to collecting weathered samples. Due to the emergency conditions in the region, it is difficult to investigate and to sample all the sections of the DCW. However, it was possible to collect weathered basalt samples from some relatively secure sections of the DCW.

A total of 35 weathered samples were collected from different sections of the DCW. The second stage was laboratory studies. The laboratory stage included mineralogical, petrographic and microfracture studies. For this purpose, a total of 32 (20 from the outcrops and 12 from different sections of the DCW) thin sections were prepared from the fresh and weathered basalt samples. Thin sections were examined under a petrographic optical microscope equipped with a camera system to determine and quantify their mineral composition, texture and structure. The petrographic examinations of the samples were performed using Nikon microscopes and cameras located in the Department of Geological Engineering at METU. During the investigation, particular attention was paid to the identification of the rock-forming minerals and the presence of secondary minerals. Grain sizes, grain boundaries, bonding structure, micro-fractures and type of matrix were also described. Much attention was devoted to the thin sections made from the weathered samples. The microfracture properties, on the other hand, were investigated using optical microscopy and back-scattered views obtained from The Electron Probe Microanalyser (EPMA). The investigations were performed using the JEOL-JXA-8230 electron microprobe device located in the Central Laboratory at METU. For the microfracture investigation, a total of nine basalt samples (one fresh massive, one fresh vesicular,

and finally, one weathered basalt sample) collected from the DCW were used. During the investigations microfracture type, amount, orientation and density of the samples were examined.

2. RESULTS

2.1. Source of the Material

The locally available basalt material originated from the lava eruptions of Karacadağ volcano ca. 40 kilometers southwest of the DCW. Ercan *et al*. (1991) have divided the volcanic activity of the Karacadağ into the three main phases. The basalts employed in the construction of the DCW belong to the second phase of the activity and are classified as Karacadağ Volcanics. Basalts with different types of textures were commonly used in the construction of the DCW. These are classified as massive and vesicular basalts. Some basalts locally display amygdaloidal texture were also employed in the DCW.

2.2. Mineralogical and Petrographic Properties of the Fresh Basalts

In hand specimen, fresh basalts are brown, dark grey and black. Some of them contain secondary minerals. The basalts are subdivided by texture into massive and vesicular groups. Thin section views show that the mineral assemblages of the massive and vesicular basalts are similar and characterized by the presence of plagioclase, pyroxene and olivine minerals, which are commonly euhedral to subhedral in shape. The groundmass is composed largely of plagioclase. The plagioclase microlites are more likely to be lath-shaped, and less pyroxene is found in their groundmass (Fig. 2a and b). The presence of the secondary minerals can also be seen in the thin sections, and especially easily in some vesicular samples with calcite precipitations (Fig. 2c and d).

2.3. Mineralogical and Petrographic Properties of the Weathered Basalts

To the unaided eye, the weathered basalts have a pale brown to yellowish color tending towards red. Their surfaces reveal different forms of weathering, mostly in the form of flaking. Thin section examinations indicate that, like the fresh samples, the weathered samples also contain plagioclase, pyroxene and olivine minerals. Although primary minerals are preserved in most of the weathered samples, olivine phenocrysts were partly replaced by iddingsite (Fig. 3a, b and c). As the major weathering product, iddingsite is observed frequently in olivine phenocrysts, even in some of the fresh basalt samples. However, visually compared to the fresh samples, the degree of iddingisitization was distinctly increased in the weathered basalt sections. Iddingsitization most frequently developed on the edges and cracks of the olivine minerals. The thin section analyses, moreover, reveal different degrees of oxidation. The olivine and pyroxene crystals were discolored due to iron-oxide mobilization. Iron oxide stained inwards by penetrating the crack faces along the microfractures (Fig. 3d). The crystal boundaries (particularly of olivine and pyroxene) are the weakest zones for microfracture formations. Most of the cracks in the weathered samples originate and propagate through these weak zones.

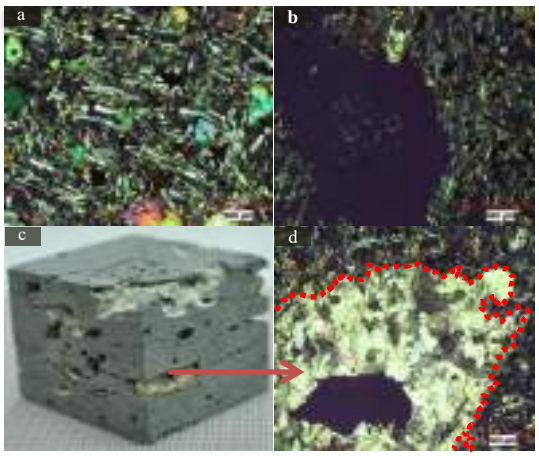

Fig. 2. Photomicrographs illustrating overall mineralogical and textural features of the fresh (a) massive and (b) vesicular basalt samples; (c,d) hand specimen and photomicrograph view of a vesicular sample displaying calcite replacement (calcite filling is roughly indicated by the dotted lines)

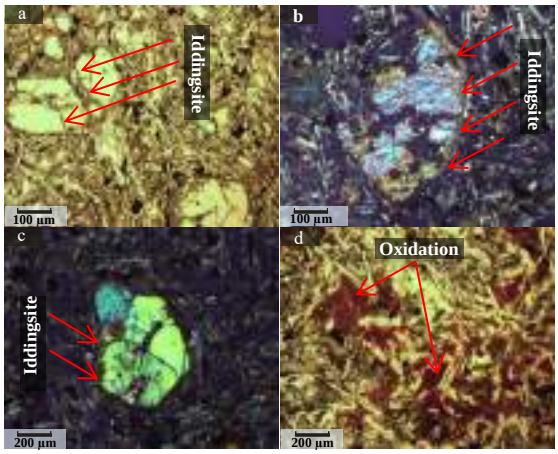

Fig. 3 Photomicrographs of the weathered basalt samples (a,b,c) iddingsite formation at the rim of olivine crystals; (d) precipitation of hydroxides (ppl view)

2.4. Microfracture Properties of the Basalts

The fresh massive basalt sample has some structural microfractures. These microfractures are commonly tight and frequently intragranular (i.e., occurring within the grains of the mineral). However, the microfractures in the vesicular sample are both intragranular and transgranular (i.e., crossing the grains and grain boundaries). The intragranular microfractures in the massive and vesicular samples developed within mineral crystals of olivine and pyroxene. The microfractures in the massive sample do not have a specific direction; however, many of them are along the grain boundaries (Fig. 4a). The microfractures in the vesicular sample have relatively simple branched and dendritic patterns. The investigations found that most of the microfractures initiate at the edges of the vesicles (Fig. 4b).

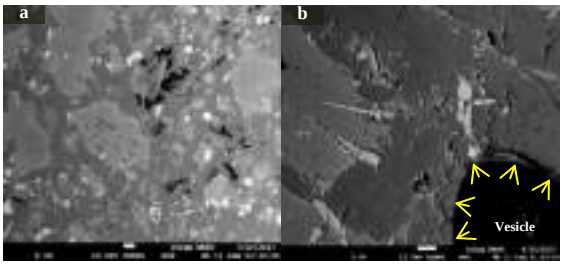

Fig. 4. Back-scattered images displaying the microfracture morphology of the (a) fresh massive and (b) fresh vesicular basalt samples

In order to assess the effect of weathering on the microfractures, a sample with scaling and flaking deterioration patterns was collected from the DCW and examined. The groundmass and phenocrysts of this section are highly microfractured. The increase in the numbers of vesicles seems to increase the number of microcracks drastically (Fig. 5). Unlike the other samples, some of the microfractures resulted in micro-detachments in the fabric of the weathered sample.

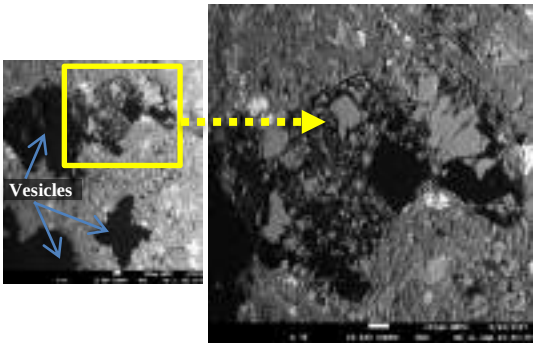

Fig. 5. Back-scattered images showing vesicle-associated crack propagation in a weathered basalt sample

3. CONCLUSIONS

As a combination and reflection of influences of the various civilizations that have settled in the region, the DCW are among the most gigantic surviving structures from ancient times. Basalts with two different types of textures were employed in the construction of the DCW. Although basalt is known as a long-lasting construction material it starts to deteriorate once it quarried and subjected to the environmental and structural stresses. Like numerous historical structures around the world, the DCW are also suffering from stone deterioration. A large variety of weathering patterns can be observed on the basalts used in the DCW. Thus, it is vital to investigate the causes of basalt deterioration and suggest proper materials and construction techniques to assist conservation studies. This study aims to understand the effects of basalt weathering by investigating their mineralogical, petrographic and microfracture properties. Mineralogical and petrographic investigations of the basalt samples reveal that both fresh and weathered samples consist predominantly of plagioclase, pyroxene, and olivine. The minerals are set in the groundmass consisted of the same minerals. Although primary minerals are preserved in most of the weathered samples, olivine phenocrysts are partially replaced by iddingsite, which is the main alteration product, observed in the weathered basalt samples. Therefore, crystal rims (particularly of olivine and pyroxene) represent the weak zones for crack development, and hence, for the secondary mineral precipitation.

The microfracture studies indicate that the microcrack morphology of the massive basalt samples differed significantly from that of vesicular samples. The crystal boundaries of olivine and pyroxene are the weakest zones for the microcrack formations. The fresh samples have different forms of intragranular and transgranular structural microfractures. The orientation of the microfractures is commonly along the grain boundaries. The olivine and pyroxene crystals, even those in the groundmass, are more susceptible to weathering than the plagioclases. Thus, most of the microfractures are developed along the grains of these susceptible crystals. Most of the microfractures in the examined weathered sample originate from the edges of the vesicles. As the distance of the crystal from the vesicles increases, the microfracture density falls rapidly and the reverse is also observed. Thus, it can be easily stated that the pore pressure in the vesicles, especially after the freezing-thawing cycles and salt crystallization, triggers microfracture development.

REFERENCES

Bell, F. G. (2007). *Basic Environmental and engineering geology*. Whittles Publishing

Bell, F. G. (1992). *Engineering properties of soils and rocks*, 3rd edn. Butterworth-Heinemann, London

Dreesen, R., Dusar, M. (2004). "Historical building stones in the province of Limburg (NE Belgium): role of petrography in provenance and durability assessment." *Materials Characterization* 53:273–287

Ercan, T., Şaroğlu, F., Turhan, N., Matsuda, J.I., Ui, T., Fujitani, T., Notsu, K., Bağırsakçı, S., Aktimur, S., Can, B., Emre, Ö., Akçay, A.E., Manav, E., and Gürler, H. (1991). "The geology and petrology of Karcadağ Volcanites." *Bull Geol Congr Turkey* 6:118–133

Fitzner, B. (2004). "Documentation and evaluation of stone damage on monuments." *Proc., 10th International Congress on Deterioration and Conservation of Stone*. Stockholm, Sweden, pp 677–690

Parla, C. (2004). "Osmanlı Öncesinde Diyarbakır: Kente Hakim Olanlar ve Bıraktıkları Fiziksel İzler." *Proc., I. Uluslararası Oğuzlardan Osmanlıya Diyarbakır Sempozyumu. Diyarbakır, Diyarbakır, Turkey.* pp 247–283

Pope, G.A., Meierding, T.C., Paradise, T. (2002). "Geomorphology's role in the study of weathering of cultural stone." *Geomorphology* 47:211– 225

UNESCO. (2015). "Report of the decisions adopted by the World Heritage Committee." 39th Session of WHC-15/39.COM/19, Bonn, Germany

Warke, P.A., McKinley, J., Smith, B.J. (2006). "Weathering of building stone: Approaches to assessment." *Fracture and Failure of Natural Building Stones Applications in the Restoration of Ancient Monuments.* Springer, pp 313–327

Winkler, E.M. (1997). *Stone in architecture: Properties, durability*. Springer-Verlag Berlin Heidelberg, New York

Zalesskii, B. V. (1967). *Physical and Mechanical Properties of Rocks*. Academy of Sciences of the USSR. Moscow, Russia

CISET - 2nd Cilicia International Symposium on Engineering and Technology
10-12 October, 2019, Mersin / TURKEY

DESIGN ANALYSIS OF A COMPOUND FRESNEL SOLAR CONCENTRATOR (CFC) USING RAY TRACING METHOD

Kaan Yaman *[1] and Bahadır Sayıncı[2]

[1] Mersin University, Engineering Faculty, Department of Mechanical Engineering, Mersin, Turkey, yamankaan@mersin.edu.tr

[2] Mersin University, Engineering Faculty, Department of Mechanical Engineering, Mersin, Turkey, bsayinci@mersin.edu.tr

ABSTRACT
In most cases, it is imperative that systems with solar concentrators tracking the sun precisely. In this paper, a compound Fresnel solar concentrator (CFC) system was designed using an arched Fresnel lens, a compound parabolic reflector as a secondary reflector and an evacuated-tube as an absorber. In the study, the optical model of CFC, based on the MCRT analysis, the impact of tracking errors on the optical performance of CFC developed. In cases where solar tracking was precise, the optical efficiency of CFC with secondary reflector was 92.2%. Besides, it had an optical efficiency of 79.8% when the tracking error was about 2°. When the longitudinal incidence angle is 20°, it was seen that the majority of the rays of CFC with secondary reflectors were received by the absorber, where the optical efficiency was 80.4%. It has been found that the designed CFC can be used in solar applications required high concentration within the tracking sensitivity.

Keywords: *Solar Concentrator, Arched Fresnel Lens, Compound Parabolic Reflector, MCRT, Ray-Tracing.*

* Corresponding Author

1. BACKGROUND

Solar energy is a strong competitor in renewable energy sources. In many solar energy applications, it is desirable to obtain energy at higher temperatures whenever possible. For this, solar radiation often is concentrated by placing an optical device between the sun and the absorber surface. When it comes to concentrate solar energy, a solar concentrator usually needs to follow the sun as the position of the sun in the sky changes all the time. Moreover, there may be a lag even when tracking the sun. This is the main factor affecting the performance of systems with high solar concentrators (Yaman and Arslan 2018; Zheng et al. 2014). In this paper, a compound Fresnel solar concentrator (CFC) system was designed using an arched Fresnel lens, a compound parabolic reflector as a secondary reflector and an evacuated-tube as an absorber. In the study, the optical model of CFC, based on the MCRT analysis, the impact of tracking errors on the optical performance of CFC developed.

2. DESCRIPTION OF THE CFC

2.1. Design of the Arched Fresnel Lens

The design of arched Fresnel lenses is based on geometric optical principles . When the Fresnel lenses are arched or domed, the prisms are arranged semi-circular orbit around the focal point. Fig. 1 shows the optical principle of an arched Fresnel lens.

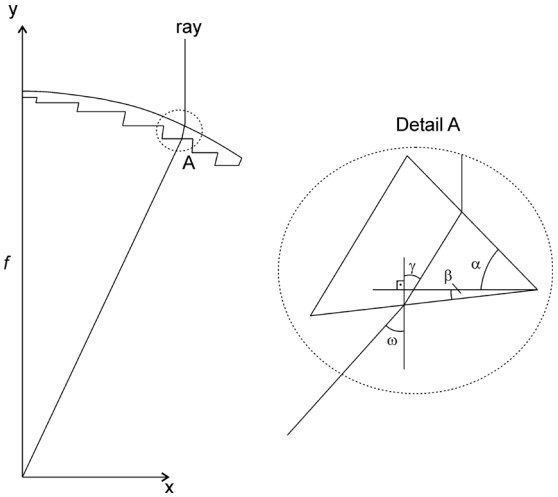

Fig. 1. Reflection and refraction angles for arched Fresnel lens.

In Fig. 1, the following two equations can be obtained from the geometric relationship:

$$\boldsymbol{\sin \alpha = n \sin(\alpha - \gamma)} \quad (1)$$

$$\boldsymbol{n \sin(\beta + \gamma) = \sin(\beta + \omega)} \quad (2)$$

where n the refractive index of the PMMA used in the manufacture of the Fresnel lens is defined as α prism angle, ω refraction angle, and β prism inclination angle. In Eq. (1), γ is obtained for $\alpha = \omega$ as follows:

$$\sin \omega = n \sin(\omega - \gamma) \quad (3)$$

$$\gamma = \omega - \arcsin\left(\frac{\sin \omega}{n}\right) \quad (4)$$

Eq. (2) can be rewritten as follows:

$$n = \frac{\sin(\beta+\omega)}{\sin(\beta+\gamma)} \quad (5)$$

and

$$\frac{n+1}{n-1} = \tan\left(\beta + \frac{\omega+\gamma}{2}\right) \cot\left(\frac{\omega-\gamma}{2}\right) \quad (6)$$

Thus, it was simplified the expression and found β like this:

$$\beta = \arctan\left(\frac{n+1}{n-1} \tan\left(\frac{\omega-\gamma}{2}\right)\right) - \frac{\omega+\gamma}{2} \quad (7)$$

2.2. Design of the Compound Parabolic Reflectors

In Cartesian coordinates, the involute section of the reflector is formulated as follows, depending on the half acceptance angle (Q_a) and the receiver radius (r):

$$\begin{cases} x = r(\sin\phi - \phi\cos\phi) \\ y = -r(\cos\phi + \phi\sin\phi) \end{cases} \quad (8)$$

where the half-acceptance angle and the cavity receiver diameter is taken as 45° and 14.27 mm, respectively. ϕ is angle to the axis of the parabola in the $-(\pi/2 + Q_a) \subseteq \phi \subseteq 0$. And parabolic section is obtained as follows:

$$\begin{cases} x = \frac{r}{\cos\phi - 1}\left[\cos Q_a - \cos(\phi - Q_a) + \cdots \right. \\ \left. (2\pi - \phi + 2Q_a)\sin(\phi - Q_a)\right] \\ y = \frac{-r}{\cos\phi - 1}\left[\sin Q_a + \sin(\phi - Q_a) - \cdots \right. \\ \left. (2\pi - \phi + 2Q_a)\cos(\phi - Q_a)\right] \end{cases} \quad (9)$$

where $2Q_a \subseteq \phi \subseteq \pi$.

2.3. Optical Characterization of CFC

The optical performance of the CFC is determined by the optical efficiency (η_o) and the geometric concentration ratio (C) using Eqs. (10) and (11), respectively.

$$\eta_o = I_r / I_a \quad (10)$$

$$C = A_a / A_r \quad (11)$$

where I_r is solar flux received by the cavity receivers and I_a is solar flux received by the reflectors. A_a and A_r represent the Fresnel lens aperture and the absorber areas, respectively. Finally, the optical concentration ratio can be written as:

$$\eta_c = \frac{I_r/A_r}{I_a/A_a} = \eta_o C \quad (12)$$

The considered CFC includes the aperture width $W = 410$ mm, focal length $f = 550$, pitch of the prism chain 3 mm, concentrator length $L = 1000$, and geometric concentration ratio $C = 9.15$. It is assumed that the reflectivity of the parabolas is 1.0 (no scatter) and the absorptivity of the cavity receiver is 1.0 (no

reflectance or transmittance), and that the optical properties are independent of temperature.

2.4. MCRT Analysis

In solar energy applications, it is possible to design system components using Monte Carlo ray tracing (MCRT) analysis [e.g., Refs. (Ustaoglu et al. 2016; Wang, Wang, and Tang 2016)]. The MCRT is based on the laws of reflection to specify the direction and point of intersection of an incident and reflected rays. Thus, the incidence and reflection of the sun's rays could simulate and the solar energy collected by the receivers could determine. A ray tracing simulation was implemented for geometrical optical performance of the CFC using Tonatiuh (v2.2), an open-source MCRT tool. In MCRT analysis, reflections are formulated as follows:

$$r = l - 2(n \cdot l)n \tag{13}$$

where r and l are the reflected and incident vectors, respectively. n is the normal surface and is formulated as follows:

$$n = \frac{\Delta f}{\|\Delta f\|} \tag{14}$$

where $\Delta f = \left[\frac{\partial f}{\partial x}, \frac{\partial f}{\partial y}, \frac{\partial f}{\partial z}\right]^T$ is the gradient of $f(x, y, z)$.

3. RESULTS AND DISCUSSIONS

Based on the mathematical relationship mentioned above, the compound Fresnel concentrator was designed and a CAD model was created (Fig. 2). Then, the prepared CAD model was import to the optical simulation tool for MCRT analysis. The CFC was positioned horizontally with the longitudinal direction north-south. The MCRT analysis has a number of tracing rays of about 10^6 to ensure that the final results are independent of the number of rays (Xu and Qu 2014). The intensity of solar radiation was 1000 W/m^2 and the spatial profile was uniform. Besides, the heat losses were neglected, the only concentrated solar heat flux was focused in the analyzes.

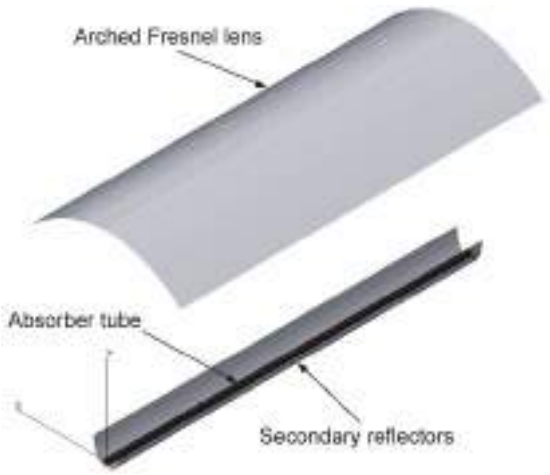

Fig. 2. Proposed compound Fresnel solar concentrator.

Fig. 3 shows the ray tracing diagrams for possible tracking errors of the CFC. In order to further explore the CFC's characteristic of concentrated solar radiation, ray tracing was detailed on compound parabolic reflectors. In cases where solar tracking is precise, it is seen that the majority of concentrated solar energy was absorbed by CFC without and with secondary reflectors. The rays that are refracted and reflected with the increase of the solar tracking error tend to deviate from the absorber. Furthermore, it is clear that tracking accuracy became increasingly important in the absence of secondary reflectors.

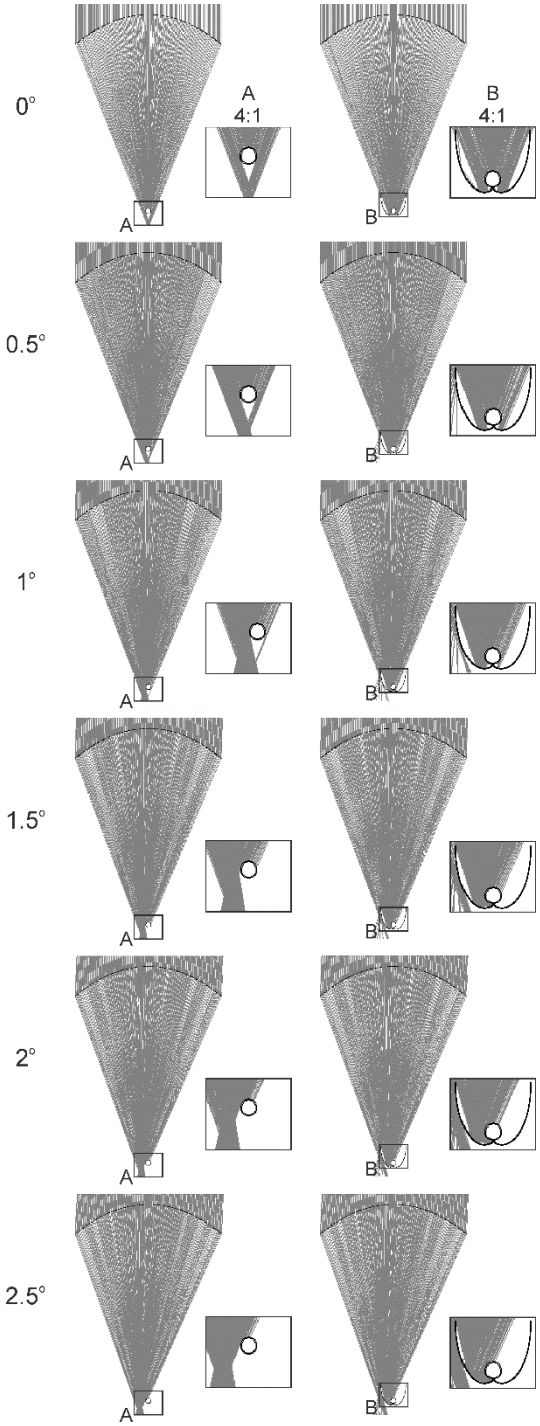

Fig. 3. The ray tracing diagram of CFC without and with secondary reflectors. for possible tracking errors.

Fig. 4 shows the variation in optical efficiency of the CFC with and without secondary reflectors for different tracking errors. In cases where solar tracking was precise, the solar collection efficiency, i.e. optical efficiency, of CFC with and without secondary reflector was 92.2% and 79.9%, respectively. When the solar tracking error is within 1.5°, the CFC without secondary reflector concentrated the solar radiation up to 78.2%. when the tracking error angle is bigger than 1°, the optical efficiency of the CFC without secondary reflector significantly decreased. When the secondary reflector is used in the CFC, the collection efficiency was less sensitivity to solar tracking error. Thus, it had an optical efficiency of 79.8% when the tracking error was about 2°. This value was a relatively good result, as Li et al. (2013) stated the allowable solar tracking error 1.4° for the Fresnel lens.

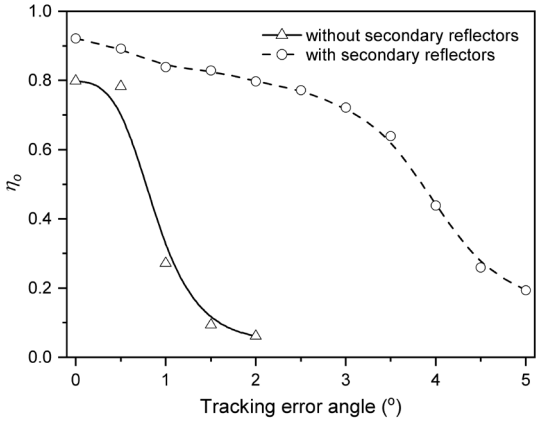

Fig. 4. Optical efficiency *vs*. tracking error angle for CFC with/without secondary reflectors.

In linear concentrator systems, the variation in the longitudinal incidence angle in addition to the solar tracking error will affect the collection efficiency. Fig. 5 shows the variation in optical efficiency of the CFC with and without secondary reflectors for longitudinal incidence angle. When the longitudinal incidence angle is 10°, it was seen that the majority of the rays of CFC with and without secondary reflectors were received by the absorber. As this value increased, there was a significant downward trend in CFC without secondary reflectors. When the secondary reflector is used in CFC, this value is 20°, where the optical efficiency was 80.4%. A similar tendency was observed in the cylindrical compound Fresnel concentrator designed by Zheng et al. (2014), when the longitudinal incidence angle was 20°, most of the incidence rays reached the absorber.

4. CONCLUSIONS

A solar concentrator usually has to follow the sun in the sky to concentrate on solar energy. Moreover, there may be a lag even when tracking the sun. This is the main factor affecting the performance of systems with high solar concentrators. In this paper, a compound Fresnel solar concentrator (CFC) system was designed using an arched Fresnel lens, a compound parabolic reflector as a secondary reflector and an evacuated-tube as an absorber.

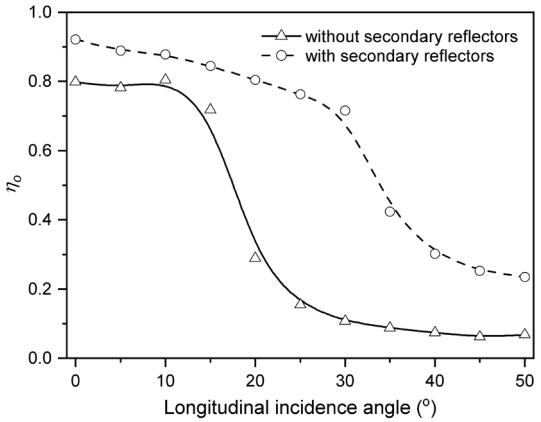

Fig. 5. Optical efficiency *vs*. longitudinal incidence angle for CFC with/without secondary reflectors.

In the study, the optical model of CFC, based on the MCRT analysis, the impact of tracking errors on the optical performance of CFC developed. In cases where solar tracking was precise, the optical efficiency of CFC with and without secondary reflector was 92.2% and 79.9%, respectively. Besides, it had an optical efficiency of 79.8% when the tracking error was about 2°. When the longitudinal incidence angle is 20°, it was seen that the majority of the rays of CFC with secondary reflectors were received by the absorber, where the optical efficiency was 80.4%. Designed CFC can be used in solar energy applications where high concentration is required within the tracking sensitivity referred to above.

REFERENCES

Li, P. W., Peter, K., and Matthew, M. (2013). "Modeling of solar tracking for giant Fresnel lens solar stoves." *Sol Energy*, Vol. 96, pp. 263–73.

Ustaoglu, A., Alptekin, M., Okajima, J., and Maruyama, S. (2016). "Evaluation of uniformity of solar illumination on the receiver of compound parabolic concentrator (CPC)." *Sol Energy* Vol. 132: pp. 150–64.

Wang, Q., Wang, J., and Tang, R. (2016). "Design and optical performance of compound parabolic solar concentrators with evacuated tube as receivers." *Energies,* Vol. 9, No.10, pp.795.

Xu, D. and Qu, M. (2014). "Compound parabolic concentrators in solar thermal applications: a review." *In Proceedings of the ASME 2013 7th International Conference on Energy Sustainability*, Minneapolis, MN, USA, 1–10.

Yaman, K. and Arslan, G. (2018). "Modeling, simulation, and optimization of a solar water heating system in different climate regions." *Renew Sustain Energy*, Vol. 10, No. 2, 023703.

Zheng, H., Feng, C., Su, Y., Dai, J., and Ma, X. (2014). "Design and experimental analysis of a cylindrical compound fresnel solar concentrator." *Sol Energy*, Vol. 107, pp. 26–37.

CISET - 2nd Cilicia International Symposium on Engineering and Technology
10-12 October, 2019, Mersin / TURKEY

COMPARISON OF DC-DC CONVERTERS FOR MAXIMUM POWER POINT TRACKING IN PHOTOVOLTAIC SYSTEMS

Shahabullah AMİN [1], Ali AKDAĞLI [2] and Volkan YAMAÇLI [*3]

[1] Mersin University, Engineering Fac., Electrical-Electronics Eng. Dept., Mersin, TURKEY, shahabullaha@gmail.com

[2] Mersin University, Engineering Fac., Electrical-Electronics Eng. Dept., Mersin, TURKEY, akdagli@mersin.edu.tr

[3] Mersin University, Engineering Fac., Electrical-Electronics Eng. Dept., Mersin, TURKEY, vyamacli@mersin.edu.tr

ABSTRACT
Electrical energy has a vital role in human life and day-by-day the demand for electrical energy has been increased. Energy demand is need to be fulfilled by environmentally friendly energy sources in order to preserve nature and continuous energy production. Photovoltaic (PV) systems are widely used to overcome electrical energy needs in the world whose conversion of available sources to electrical energy reduces environmental impacts. In order to produce electrical energy efficiently by using solar energy systems; the system must operate in a way that they the output power should be maximized. For this purpose DC-DC converter topologies are used to obtain the best result in DC energy-producing system, so for getting the best result in PV system one of the most effective way and widely used MPP (Maximum Power Point) method to get the maximum power is using different DC-DC converter topologies which are been explained in this paper.

Keywords: *Photovoltaic System, DC-DC Converter Topologies, DC Energy-Producing System, MPP*

[*] Corresponding Author

1. INTRODUCTION

Producing clean and efficient electricity energy is a big concern for humanity and it is important to find alternatives for producing electricity instead of using fossil fuels to generate required energy, which affects global climate in bad way (Guilbert, Collura, and Scipioni 2017). Producing electricity from renewable energy sources, which is neater, is clean and does not that bad effect on climate. Photovoltaic energy is one of those environmentally friendly energy-generating systems, which are neat, clean and very efficient.

In PV systems photovoltaic cells are used for generating electrical energy from solar energy which has rapid growth over the last few years. Photovoltaic material is the key component in this system when sunlight hits the cell it causes some electron movement in the semiconductor used in the cell which results in the electron moves to the negative electrode and holes moves to positive electrodes and an electrical current is been generated to supply to the external load (Reshma Gopi and Sreejith 2018).

PV panels are designed to output 12V and 24V as standard but it can be changed by bringing changes in PV cell connection inside the panel, connecting cells in parallel will result in a higher current while connecting it in series will give a higher output voltage in the result. In a PV panel, the cell connection is a combination of parallel and series connection of PV cells. Solar share reached 36% of all newly added power capacity in 2018 with 102GW of newly added power generation, renewable energy resources contribute 33% of installed power generation capacities in total while all solar power plants produce only 2,2% of the world output capacity in 2018 (Xiao, Ozog, and Dunford 2007). The total installed capacity of PV power at the end of 2018 was more than 500GW (Power 2019). According to forecast worldwide new installation will add between 270GW and 310GW electricity in 2019 and 2020 thus solar power will be producing 4% of the world's electrical energy by the end of 2020 (Jäger-Waldau 2019).

PV power generation has many advantages such as simplicity in allocation, high mobility, need less time for installation, noiseless, doesn't emit pollution, longer life time, portability of parts, and capability of output power to match the load requirement. Hence it gained high significance as a renewable energy source (Mehdipour and Farhangi 2011). PV power varies with isolation, temperature, and load characteristics and it is directly proportional to irradiance and inversely proportional temperature (Reshma Gopi and Sreejith 2018; Hossain, Rahim, and Selvaraj 2018).for efficiency purpose and for matching peak load requirement the PV system should work very efficiently or it must produce the maximum power at available condition, to obtain this result of some MPPT (Maximum PowerPoint Tracking) methods are used to produce as much energy as the PV the system can produce (Mehdipour and Farhangi 2011).

In this paper, different DC-DC converter topologies are used and explained how it affects the output of the PV system. DC-DC converters are generally used to produce a regulated voltage from a source that may or may not be well controlled to a load that may or may not be constant, it operates at more than 90% efficiency and comes in isolated and non-isolated verities (Durán et al. 2007).

Buck, Boost, and Buck-Boost converter topologies are been used in this paper. A buck converter steps a voltage down producing a voltage lower than input voltage while the output current is higher than the input current (Chomsuwan et al., n.d.). Boost converters are used to step the voltage up in which the output current is lower than the input current. In addition, the Buck-Boost converters step a voltage up and down, It produces voltage equal to, higher or lower than the input voltage (Durán et al. 2007).

The DC-DC converter topologies provide low cost, lightweight, compact, efficient and reliable system to design for electrified automotive application. It can be used to interface the electrical power train by chopping or boosting the voltage levels (Hulugappa and Kusagur 2017).

Transferring DC voltage of one verity to another verity is usually done by a DC-DC converter, due to variation in voltages required by different devices the converters become a necessity for providing the exact needed voltage from the available voltage (Durán et al. 2007). DC-DC converters provide precise and smooth power regulation and are been used for extraction of maximum PV power under any condition too (Garrigós et al. 2014).

2. DC-DC CONVERTER TOPOLOGIES

Converters are circuits made to convert the direct current voltage from one level to another level, which is been controlled to give the desired output voltage (Rajakumari, Student, and Professor 2018).

DC-DC converters are used for better efficiency in utilization of PV cells. MOSFET and IGBT are used as switching devices in converters (Xiao, Ozog, and Dunford 2007; Reshma Gopi and Sreejith 2018).

The efficiency of converters $\eta_{converter}$ is calculated as below:

$$\eta_{converter} = \frac{V_{out}*I_{Out}}{V_{in}*I_{in}} = \frac{V_{in}*I_{in}}{\text{-----------}} \quad \text{----------} (1)$$

Where V_{out} , I_{out} are output voltage and current, V_{in} , I_{in} are the input voltage and current and P_{loss} is the power loss of converter.

The three different converter topologies used in this paper are explained below

2.1. Boost converter topology

This type of converter topology has an output voltage higher than the input voltage, is one of the converter topologies used to extract the maximum power from PV cells. Figure 1 shows the circuit diagram of the boost converter. The two modes of the operation, and design equations of the boost converter are explained below:-

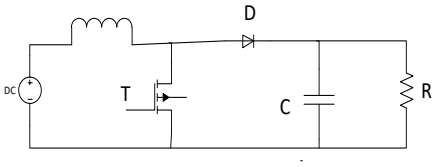

Fig 1. Circuit diagram of Boost converter

Boost converter operates in two modes, Figure 2 and 3 show the two states of operation of boost converter. Figure 2 shows the state 1 of operation of boost converter in which the switch (S1) is turn on ($t=t_{on}$), at this on time the current through inductor 'IL' rises linearly and is greater than zero, the output current is been supplied by output capacitor which has large enough capacity to supply to the load during t_{on} time of (S1).

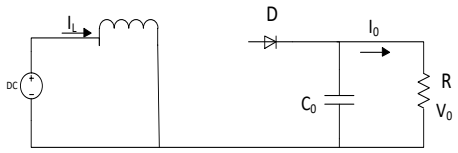

Fig.2. State 1 operation of boost converter

State two starts when the switch (S1) is turned off ($t=t_{off}$), in this state the current flows through the inductor, capacitor, and load. During this t_{off} state, the stored energy in inductor is been delivered to load and the capacitor stores energy for the next cycle, this mode of the boost converter is been figured in Figure 3.

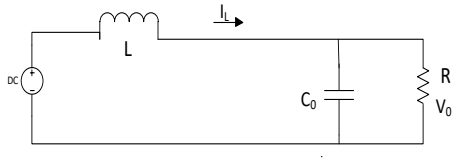

Fig 3. State 2 operation of boost converter

Eq. (2) shows the output voltage (V_o) of the boost converter:

$$\frac{V_s}{\quad} \text{ - - - - - - - - - - - - - - - - - - } (2)$$

Where V_o is output voltage, D is the duty cycle for boost converter and Vs is the source voltage.

Boost inductance is selected on the base of maximum allowable ripple current. The peak inductor current ripple is given is calculated through the Eq. (3).

$$\text{——- } (3)$$

L is inductor and F_s is switching frequency of boost converter and the switching time is given by Eq. (4).

$$\frac{V_s}{V_o \;\; V_s} \text{ - } (4)$$

Boost converter topology works in two continuous and discontinuous modes, in continuous mode of boost converter the inductor current (I_L) is always greater than zero while in discontinuous mode of it the amplitude of the current is too high, the inductor maybe completely discharged before the end of the whole commutation cycle, this commonly occurs in light loads.

2.2. Buck converter topology

Buck converter topology of DC-DC converters steps up the current while it steps down the voltage at the output, the efficiency of a buck converter is above 90%, Figure 4 shows the circuit topology of it.

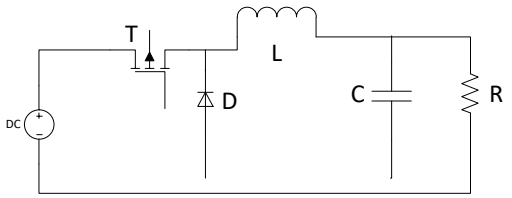

Fig 4. Circuit diagram of Buck converter

The two switches of buck converter (usually a diode and a transistor) control the current through the inductor. During turn-on state of the switch (S1), the current starts increasing while the inductor starts to produce an opposing voltage across its terminals, which cause a decrease in the voltage at output, turn-on state of the buck converter topology is figured in Figure 5.

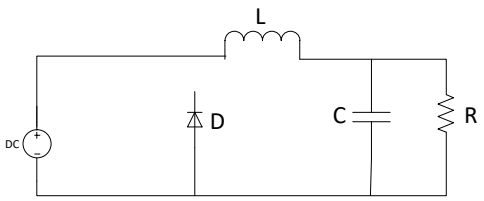

Fig 5. Turn on state of Buck converter

In this turn-on state of buck converter the transistor switch is closed (on) and the diode at this state is reverse biased which means that diode switch is off so the path of diode acts as an open circuit.

Turn off state of buck converter the transistor switch is turned off which will act like an open circuit and the diode path start passing current, during this state the load is been supplied by energy stored in the capacitor and inductor, Figure 6 is the circuit diagram of this turn off state of the buck converter.

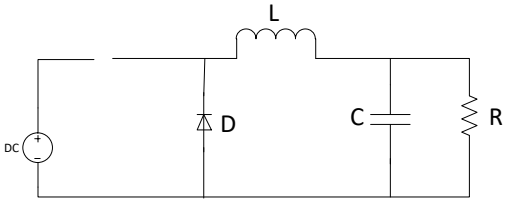

Fig 6. Turn off state of Buck converter

Buck converter operates in two continuous and discontinuous modes like boost converter, in continuous mode of it the current through inductor is always greater than zero while in discontinuous mode the inductor current may fall to zero during part of the period.

Eq. (5) calculates the output voltage of the buck converter and the voltage through the inductor is been calculated by Eq. (6).

$$V \quad V \quad V \text{ - - - - - - - - - - - - - - - - - - } (5)$$

$$V \quad \frac{dI_L}{} \text{ ---------- (6)}$$

$$D \quad \frac{V_o}{V_s} \text{ ---------- (7)}$$

$$\frac{V_s - V_o}{V_o} \text{ ---------- (8)}$$

Eq. (7) is used to find the duty cycle of buck converter, in the discontinuous mode of boost converter Eq. (8) is used to find the switching time.

The capacitor value is taken large enough in buck converter for maintaining a constant voltage across the load terminal during commutation cycle and thus the output current is constant which is equal to inductor current.

2.3. Buck-Boost converter topology

Buck-boost topology of converter is a type of DC-DC converters, which work as both buck and boost converter. The output voltage is either greater than or less than the input voltage. It is equivalent to flyback converter using a single inductor instead of transformer. The polarity of output voltage is opposite than the input voltage in this converter topology. The output voltage of the buck-boost converter is adjustable and based on the duty cycle of the switching transistor. Fig (7) shows the circuit diagram of this topology. The two switches used in this topology are usually a Transistor and a Diode.

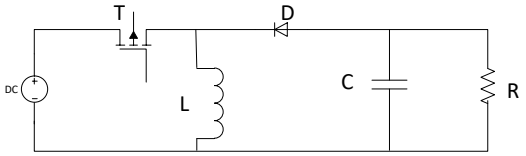

Fig 7. Circuit of Buck-Boost converter

If the duty cycle is more than 50% The buck-boost converter operates as a boost converter and when the duty cycle is less than 50% if the duty the converter operates to step down the voltage like buck converter. During turn-on state of the converter, the source is directly connected to inductor and it causes storing energy in it and at this turn on state, capacitor supplies energy to the load. When the converter is in its turn off state the inductor supplies energy to both capacitor and load, in result the capacitor is been energized for the next period. The output voltage ranges are Vs to zero and Vs to infinite respectively in the buck-boost converter. Turn-on state is shown in Figure 8.

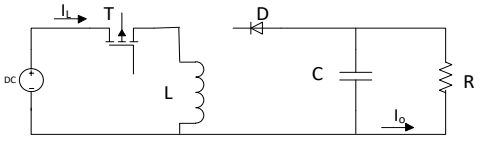

Fig 8. Turn on state of Buck-Boost converter

Turn off state of buck-boost converter is shown in Figure 9.

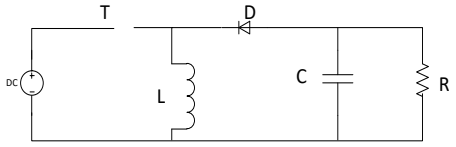

Fig 9. Turn off state of Buck-Boost converter

Mathematical equations of Buck-Boost converter are described below:

$$D \quad \frac{V_o}{V_o - V_s} \text{ ---------- (9)}$$

$$\frac{V_s}{} \text{ ---------- (10)}$$

$$V \quad \text{—} V \text{ ---------- (11)}$$

$$I \quad \frac{V_s}{} \text{ -------- (12)}$$

Eq. (9) is of duty cycle, Eq. (10) is for switching time Eq. (11) and Eq. (12) are the output voltage and the current limit at the output of the buck-boost converter. T is the commutation period during which the switch is turned on.

For remaining the polarity of source and output voltage, same a switch is used instead of diode this converter is non-inverting Buck-Boost converter.

3. RESLTS AND DISCUSSION

Boost, buck and buck-boost converter topologies are studied and input-output charts for these systems are given below. Figure 10 shows that the output signal has higher amplitude compared to input signal while it is the opposite for buck converter topology given in Figure 11. Buck-boost converter topology can also increase or decrease output voltage with reference to input signal according to applied duty cycle to the converter; Figure 12 shows that duty cycle is lower than 50% since output voltage is lower and negative than input signal.

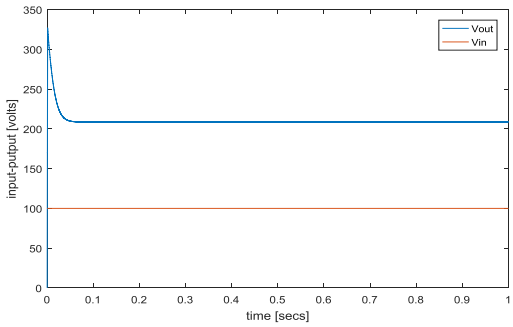

Fig 10. Boost converter input and output signals

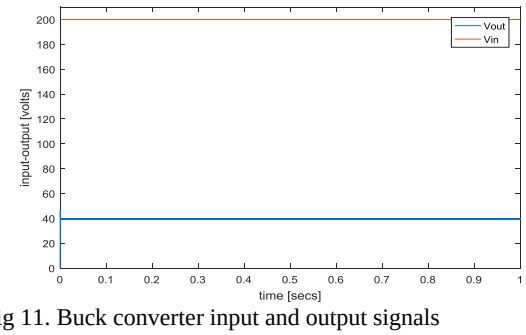

Fig 11. Buck converter input and output signals

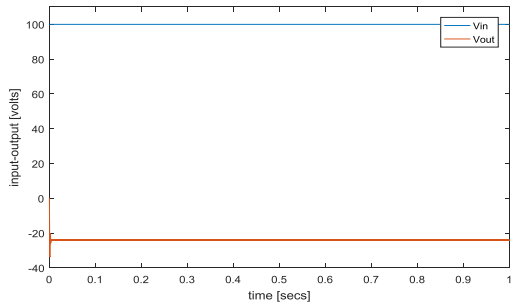

Fig 12. Buck-Boost converter input and output signals

4. CONCLUSION

In this work, boost, buck and buck-boost converter topologies are investigated in order to show their suitability for photovoltaic panels and energy systems. As boost converter amplifies the input voltage depending on inductance and capacitance values; buck converter decreases the voltage. Buck-boost converter also inverts the voltage characteristic which is suitable in some DC study areas in literature and practice. Since boot converter output voltage fluctuates at first, it would be better to use a low-pass in order to get desires results in early milliseconds. In results it can be easily seen that boost, buck and buck-boost converter topologies can be used in photovoltaic energy systems in order to adjust system voltage just before DC-AC inverters or with purpose of solely using DC voltage.

REFERENCES

Chomsuwan, Komkrit, Prapart Prisuwanna, Veerapol Monyakul, and Technology Development Agency. n.d. “Photovoltaic Grid-Connected Inverter Using Two-Switch Buck-Boost Converter,” 1527–30.

Durán, E, J Galán, J M Andújar, Dpto De Ing Electrónica, De Sist Infor, and Universidad De Huelva. 2007. “A N Ew A Pplication of the B Uck -B Oost -D Erived C Onverters to O Btain the I-V C Urve of P Hotovoltaic M Odules.” 2018 International Conference on Advancement in Electrical and Electronic Engineering (ICAEEE) 7 (4): 413–17.

Garrigós, A., J. L. Lizán, J. M. Blanes, and R. Gutiérrez. 2014. “Combined Maximum Power Point Tracking and Output Current Control for a Photovoltaic-Electrolyser DC/DC Converter.” International Journal of Hydrogen Energy 39 (36): 20907–19. https://doi.org/10.1016/j.ijhydene.2014.10.041.

Guilbert, Damien, Stefania Maria Collura, and Angel Scipioni. 2017. “DC/DC Converter Topologies for Electrolyzers: State-of-the-Art and Remaining Key Issues.” International Journal of Hydrogen Energy 42 (38): 23966–85. https://doi.org/10.1016/j.ijhydene.2017.07.174.

Hossain, M. Z., N. A. Rahim, and Jeyraj a/l Selvaraj. 2018. “Recent Progress and Development on Power DC-DC Converter Topology, Control, Design and Applications: A Review.” Renewable and Sustainable Energy Reviews 81 (July 2017): 205–30. https://doi.org/10.1016/j.rser.2017.07.017.

Hulugappa, Veeresh, and Ashok Kusagur. 2017. “Comparative Analysis of DC-DC Converter Topologies with Soft-Switching Techniques.” 2016 International Conference on Electrical, Electronics, Communication, Computer and Optimization Techniques, ICEECCOT 2016, 106–10. https://doi.org/10.1109/ICEECCOT.2016.7955195.

Jäger-Waldau, Arnulf. 2019. “Snapshot of Photovoltaics—February 2019.” Energies 12 (5). https://doi.org/10.3390/en12050769.

Mehdipour, Abbas, and Shahrokh Farhangi. 2011. “Comparison of Three Isolated Bi-Directional DC/DC Converter Topologies for a Backup Photovoltaic Application.” 2011 2nd International Conference on Electric Power and Energy Conversion Systems, EPECS 2011, 1–5. https://doi.org/10.1109/EPECS.2011.6126822.

Power, For Solar. 2019. “Rapport Sur Les Nouvelles Capacités de Génération d’électricité de Sources Renouvelables Installées En 2018.”

Rajakumari, RFelshiya, PG Student, and Associate Professor. 2018. “Analysis and Assessment of DC-DC Converter Topologies for PV Applications.” International Journal of Pure and Applied Mathematics 118 (24): 1–18.

Reshma Gopi, R., and S. Sreejith. 2018. “Converter Topologies in Photovoltaic Applications – A Review.” Renewable and Sustainable Energy Reviews 94 (May): 1–14. https://doi.org/10.1016/j.rser.2018.05.047.

Xiao, Weidong, Nathan Ozog, and William G. Dunford. 2007. “Topology Study of Photovoltaic Interface for Maximum Power Point Tracking.” IEEE Transactions on Industrial Electronics 54 (3): 1696–1704. https://doi.org/10.1109/TIE.2007.894732.

CISET - 2nd Cilicia International Symposium on Engineering and Technology
10-12 October, 2019, Mersin / TURKEY

ARTIFICIAL NEURAL NETWORK IMPLEMENTATION FOR DC-DC CONVERTERS IN SOLAR POWER SYSTEMS

Shahabullah AMİN [1], Volkan YAMAÇLI [*2] and Ali AKDAĞLI [3]

[1] Mersin University, Engineering Fac., Electrical-Electronics Eng. Dept., Mersin, TURKEY, shahabullaha@gmail.com

[2] Mersin University, Engineering Fac., Electrical-Electronics Eng. Dept., Mersin, TURKEY, vyamacli@mersin.edu.tr

[3] Mersin University, Engineering Fac., Electrical-Electronics Eng. Dept., Mersin, TURKEY, akdagli@mersin.edu.tr

ABSTRACT
Renewable energy plays a vital role recently, in power generation especially Photovoltaic (PV) systems which generates electrical energy by using solar power. Electrical PV systems are on the top of the renewable energy list due ease of accessibility in any place with solar radiation. PV systems depend on temperature, moisture and solar irradiance. The power generation by using PV panels is directly proportional to irradiance and indirectly proportional to the temperature and moisture. The efficiency of PV systems depends on producing maximum electrical energy in any available condition of solar irradiance and temperature; MPP (Maximum Power Point) techniques are used to do so. Different MPP techniques and algorithms are used to extract maximum power from the solar PV panel. In this work, artificial neural network (ANN) and different DC-DC converter topologies are used in order to simulate and track the maximum power point for a designed PV system which would help feature extraction of PV system depending on irradiance other variables which affect the efficiency.

Keywords: *PV (Photovoltaic), MPP (Maximum Power Point), ANN (Artificial Neural Network), DC-DC Converter Topologies.*

[*] Corresponding Author

1. INTRODUCTION

Photovoltaic (PV) energy is one of those renewable energies which help to produce electrical energy without using fossil fueled power plants. Most of the electrical energy generated is from combustible fuel such as oil, coal, gas and nuclear power that are unfriendly energy sources to the environment, generating electrical energy from these kinds of sources spread heavily polluted gas and hazard (Sunny, Ahmed, and Hasan 2017). Renewable energy sources, which are quite friendly to the environment, are the best alternative to be utilized for generating electrical energy. Electrical energy demand is increasing day by day; to overcome this need of electricity it is needed to utilize the sources whose conversion methods to electrical energy is environmentally friendly and efficient. PV electrical energy generation is among the environmentally friendly renewable energy generation and is one of the best alternative to replace the pollution and hazard emitting energy generating systems and to face the need of electricity (Dkhichi et al. 2017).

Contribution renewable energy is 33% of all installed power generation capacities in total while 2.2% of its production is contributed by solar power in 2018 (Xiao, Ozog, and Dunford 2007). The solar photovoltaic add 36% of all newly added power capacity in 2018. the total installed capacity of the solar energy at the end of 2018 was more than 500GW. New installation of solar energy around the world will add 270-310GW electricity in 2019 and 2020 thus solar power will produce 4% of the world energy at the end of 2020 (Jäger-Waldau 2019).

Photovoltaic energy systems have advantages such as scalability, dispatch ability, low cost, low maintenance, and low operational pollution hence has emerged as one of the most promising amongst all the renewable energy resources (Agha, Koreshi, and Khan 2018).

Solar energy can be extracted by two main forms, solar thermal is the first form in which the energy is used for heating water and then uses it for various purposes and the second one is by using a PV panel which produce electrical energy from solar energy. In this type of energy conversion The output power is indirectly proportional to temperature of weather and directly proportional to irradiance, increasing in irradiance causes an increase in output power while the increase in temperature, causes a decrease in output power (Lq et al., n.d.).

Tracking maximum power point is a necessity of the solar system to have the best efficiency; there are three widely used techniques to do so sun tracking, MPPT and to utilize both of them simultaneously.

DC-DC converters are used to extract maximum power point of PV arrays, The DC-DC converter topologies has advantages such as lightweight, compact, low cost, efficient and reliable system to design. It can be used to interface the electrical power train by stepping up or stepping down the voltage levels (Hulugappa and Kusagur 2017).

For extracting maximum output power from PV systems fractional open-circuit voltage (FOL), fuzzy logic based MPPT, Hill climbing (HC) method, incremental conductance (IC), artificial neural network (ANN) based MPPT and etc… are the used most popular MPPT algorithms (Jyothy and Sindhu 2018).

DC-DC converter topologies and ANN-based MPP method are used to extract the maximum power from the solar PV system. Buck, Boost and Buck-Boost converter topologies are been used in this paper to do so.

Buck converter steps the current up and the voltage down to the required voltage, Boost converter steps up the voltage and steps down the current and the buck-boost converter works as both boost and buck converter. If the duty cycle of Buck-Boost converter is greater than 50% it will work as Boost converter, else it will work as buck converter (Paper et al. 2007).

Artificial neural network (ANN) algorithm is mathematical designed models which mimic the human biological neural network behavior. It is widely used to model complex relationship between inputs and outputs in nonlinear systems, The ANN consists of inputs, and at least 1 hidden layer and one output layer (Khanam and Foo 2018).

In this paper, artificial neural network-based MPP method is implemented in order to extract the maximum power feature of designed PV system. MPP methods and DC converter topologies are widely used to extract the maximum power from a PV system at any available irradiance.

2. PHOTOVOLTAIC ARRAY MODELLING

PV arrays consist of PV panels, which comprise PV cells. The PV connection depends upon the required output, for high voltage output the cells should be series connected while for high output current the cells should be parallel connected (Naveen and Dahiya 2018). The output voltage of a typical silicon solar PV cell is between 0.5-0.6 V while the current output is 28-35 ml Amps per square centimeter. The one diode PV cell satisfies the requirement of modeling and is simple amongst the different modeling approaches.

Fig (1) shows the one diode model of a PV cell.

PV cell has parasitic series and shunt parallel resistance and is a current source device.

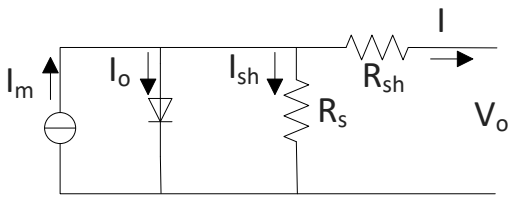

Fig 1. One diode model of PV cell

Current of module is represented by I_m, the current leakage of diode is represented by I_o, I_{sh} is the current through shunt resistance, I represents the output current and the output voltage is been represented by V_o .

The equations below represents the current and voltage relationship of a PV cell:

$I = I$ - - - - - - - - - - - - - - (1)

$\frac{}{\qquad}$ - - - (2)

N_p and N_s is the number of parallel and series connected modules in an array, ideality factor is a, photovoltaic current is I_{pv} given by Eq (3), reverse

current leakage is represented by I_o given by Eq (4) and thermal voltage is V_t shown in Eq (5).

---------- (3)

I_{SCN}, I_{PVN} represents current of short circuit and photovoltaic, V_{OGN} is voltage of open circuit at nominal conditions (1^{kw} irradiance and 25 C temperature), difference of nominal and operating temperature in kelvins is represented by ΔT, temperature coefficient of current is K_I, G is operating and G_N is nominal irradiance respectively.

---------- (4)

---------- (5)

Number of series-connected cells in a module is N_{CS} , Boltzmann constant is K, charge on an electron is q and T is the PN junction temperature in kelvins.

3. Artificial Neural Network (ANN):

ANN method can be classified as indirect method or a method of artificial intelligence. The ANN method is based on a central nervous system, this technique is based on set of electrical neurons, which are modeled by complex and nonlinear function whose weights (w_i) are determined by studying the inputs and outputs of PV system for period of time, hence it need adaptation period to update the weights until the network reaches the steady state equilibrium, Because of this it can be considered as a system capable of machine learning. In this method the weight W_{ij} corresponds to the I input with respect to the neuron j.

Figure 2 shows the three layers of ANN method.

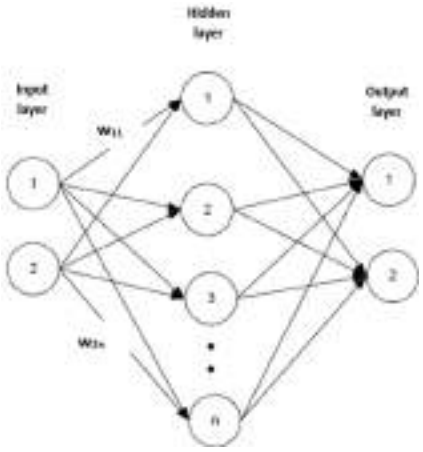

Fig 2. Three layers of ANN method

ANN method can provide a very accurate MPPT without knowing exactly the PV system parameters**.**

4. DC-DC converter topologies

Converters are electrical circuits which steps up or steps down DC voltage , these circuits are controlled to get the desired output voltage(Rajakumari, Student, and Professor 2018).

DC-DC converters are used for effective utilization of PV cells. IGBT and MOSFET are used as switching devices in converters (Laamami, Benhamed, and Sbita 2017; Reshma Gopi and Sreejith 2018).

The efficiency of converters η is calculated as below:

$$\text{converter} \quad \frac{V_{out}*I_{Out}}{V_{in}*I_{in}} \quad \frac{V_{in}*I_{in}-P_{loss}}{V_{in}*I_{in}} \quad \text{---------- (6)}$$

V_{out}, I_{out} are the voltage and current at output, V_{in}, I_{in} are the voltage and current at input and the power loss of converter is P_{loss}.

The three different converter topologies used in this paper are explained below -

4.1. Boost converter topology

This topology has an output current less than input current and the voltage at output greater than the input voltage, this converter topology is one most used converter topologies for extracting maximum power from PV panel. Figure 3 is circuit diagram of the boost converter. The two operation modes and equations of design for boost converter are explained below:-

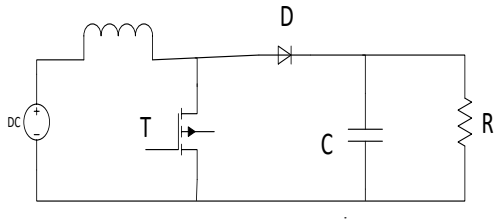

Fig 3. Circuit diagram of Boost converter

Figure 4 and 5 show the two states of operation of boost converter. Figure 4 is state 1 of operation in which the switch (S1) is turn on ($t=t_{on}$), at this on time the current through inductor *IL* rises linearly and is greater than zero, output capacitor which has large enough capacity supplies the to the load during this t_{on} time of (S1).

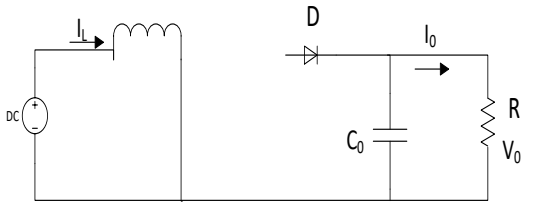

Fig 4. State 1 operation of boost converter

As the switch (S1) is turned off ($t=t_{off}$) State two starts, during this state the current flows through the inductor, capacitor, and load in this state. The inductor delivers its stored energy to load and the capacitor stores energy for the next cycle, this mode is figured in fig (5).

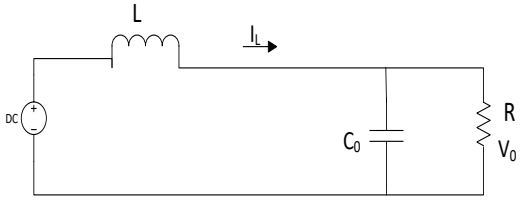

Fig 5. State 2 operation of boost converter

Eq (7) shows the output voltage (V_o) of the boost converter:

$$\frac{V_s}{\quad} \text{ - - - - - - - - - - - - - - - - - - } (7)$$

In equation above V_s is the source voltage, D is the duty cycle and output voltage is V_o.

The selection of boost inductance is done on the base of maximum allowable ripple current. The peak inductor current ripple is given is calculated through the equation (8).

$$\frac{V_s *}{F_s} \text{ - - - - - - - - - - - - - - - - - } (8)$$

Where L is inductor and F_s is switching frequency of boost converter and the switching time is given by equation (9).

$$\frac{V_s *}{V_o - V_s} \text{ - - - - - - - - - - - - - - - - - - } (9)$$

Boost converter topology works in two continuous and discontinuous modes, in continuous mode of boost converter the current through inductor current (I_L) is always greater than zero while in discontinuous mode the amplitude of the current is too high, the inductor current maybe fall to zero before the end of the whole commutation cycle, in light loads it commonly occurs.

4.2. Buck converter topology

This type of DC-DC converters steps up the current while it steps down the voltage at the output, the efficiency of a buck converter is above 90%, the circuit topology of Buck topology is figured in Figure 6.

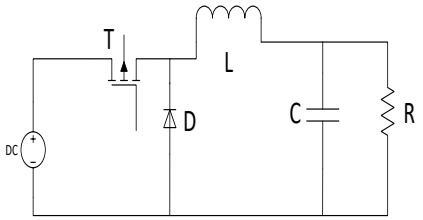

Fig 6. Circuit of Buck converter

Two switches of buck converter (usually a diode and a transistor) control the current through the inductor. During turn-on state of the switch (S1), the current starts increasing through the inductor and the inductor starts to produce an opposing voltage across its terminals, which cause a decrease in the voltage at output, turn-on state of the buck converter is figured in Figure 7.

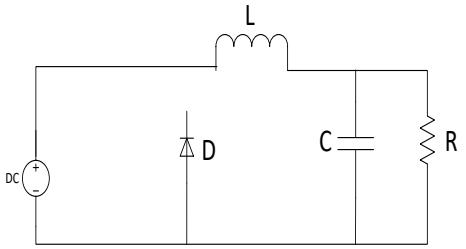

Fig 7. Turn on state of Buck converter

During turn-on state of buck converter the transistor switch is closed (on) and the diode is reverse biased so the path of diode acts as an open circuit.

The transistor switch will act like open circuit while the converter is in its Turn off state and the diode path start passing current, the energy stored in the inductor and capacitor is been supplied to the load during this state, Figure 8 is the circuit of this turn off state of the buck converter.

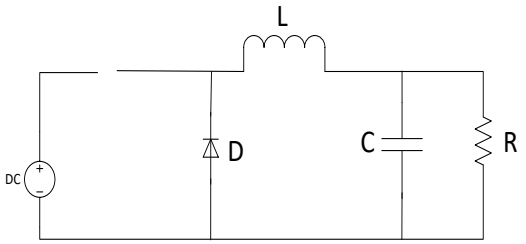

Fig 8. Turn off state of Buck converter

Buck converter operates in two continuous and discontinuous modes like boost converter, during continuous mode of it the inductor current is always greater than zero while in discontinuous mode the inductor current may fall to zero during part of the period.

Eq (10) calculates the voltage at the output buck converter and the voltage across the inductor is been calculated by Eq (11).

$$V \quad V \quad V_L \text{ - - - - - - - - - - - - - - - - - - } (10)$$

$$V \quad \frac{dI_L}{\quad} \text{ - } (11)$$

$$D \quad \frac{V_o}{V_s} \text{ - } (12)$$

$$\frac{V_s - V_o}{V_o} \text{ - } (13)$$

Eq (12) is used to find the duty cycle of buck converter, in the discontinuous mode of boost converter equation (13) is used to find the switching time.

The capacitor value of the buck converter is taken large enough for maintaining a constant voltage across the load terminal during commutation cycle and thus the output current is constant which is equal to inductor current.

4.3. Buck-Boost converter topology

Buck-boost converter topology work as both buck and boost DC-DC converter. The voltage at output is either greater than or less than the voltage at input. It is

equivalent to flyback converter using a single inductor instead of transformer. The polarity of output voltage is opposite than the input voltage in this topology. The output voltage is adjustable which is based on the duty cycle. Figure 9 shows the circuit topology of this converter. The two switches used in this topology are usually a Transistor and a Diode.

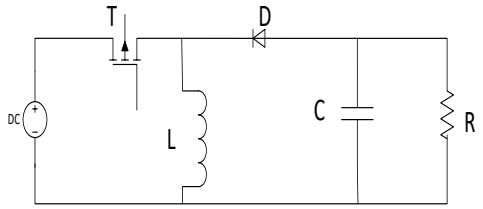

Fig 9. Circuit diagram of Buck-Boost converter

Buck-boost converter works as a Boost converter when the duty cycle is more than 50% else the converter work as a Buck converter. During turn-on state of the converter, the source is connected directly to the inductor, which results in storing energy in the inductor and the capacitor supplies energy to the load. When the converter is in its turn off state the inductor supplies energy to both capacitor and load, in result the capacitor is been energized for the next period. The output voltage ranges are V_s to zero and V_s to infinite respectively in the buck-boost converter. Turn-on state is shown in Figure 10.

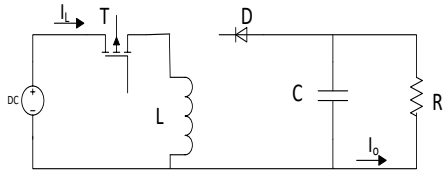

Fig 10. Turn on state of Buck-Boost converter

Turn off state of buck-boost converter is figured in fig (11).

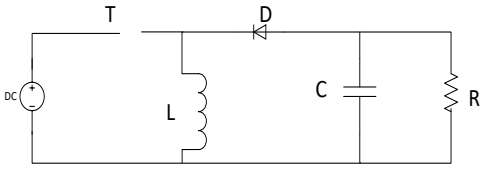

Fig 11. Turn off state of Buck-Boost converter

Mathematical equations of Buck-Boost converter are described below:

$$D \quad \frac{V_o}{V_o - V_s} \text{ - - - - - - - - - - - - - - - - - - } (14)$$

$$\frac{V_s}{} \text{ - - - - - - - - - - - - - - - - - - } (15)$$

$$V \quad \text{——} V_s \text{ - - - - - - - - - - - - - - - - } (16)$$

$$I \quad \frac{V_s T}{} \text{ - - - - - - - - } (17$$

Equation (14) is of duty cycle, equation (15) is for switching time equation (16) and (17) are the output voltage and the current limit at the output of the buck-boost converter. T is the commutation period during which the switch is turned on.

For remaining the polarity of source and output voltage, same a switch is used instead of diode this converter is non-inverting Buck-Boost converter.

5. RESULTS

Boost, buck and buck-boost converter topologies are studied and input-output charts for these systems are given below. Figure 12 shows the PV panel implementation of converters and Table 1 shows the initial and optimized values by using artificial neural network method.

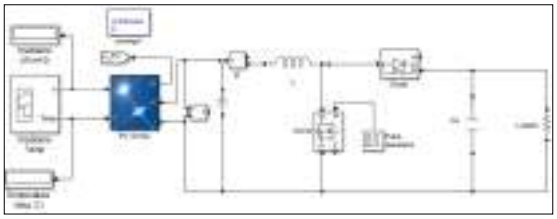

Fig 12. PV panel implementation with converter topologies

Table 1. Initial and optimized results for system

Variables	Initial	5 Neurons	10 Neurons
Amplitude (volts)	220.00	219.45	220.04
Frequency (Khz)	20	23.87	24.55
Pulse Width (%)	65	69.12	70.08
Delay (secs)	0	0	0
Err (%)	0	2.5e-3	1.8e-4

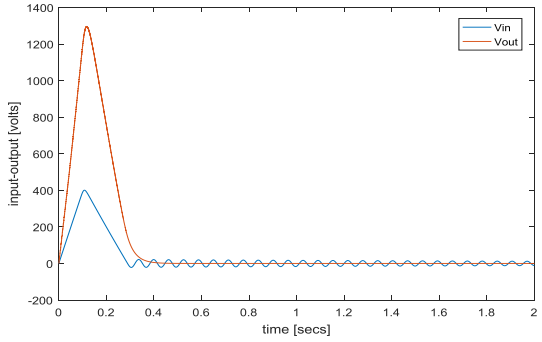

Fig 13. Input-Output signals for initial values

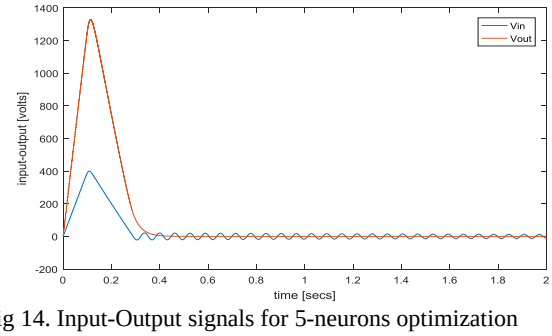

Fig 14. Input-Output signals for 5-neurons optimization

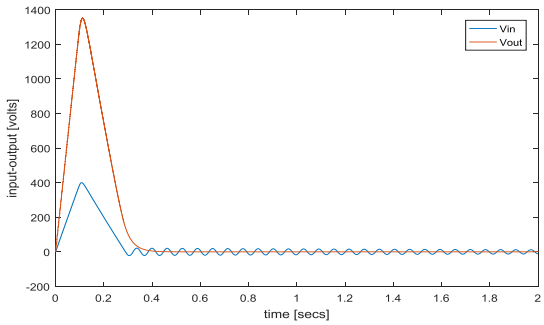

Fig 15. Input-Output signals for 10-neurons optimization

6. CONCLUSION

In this work, boost, buck and buck-boost converter topologies are studied and parameters are estimated by using artificial neural networks. The output voltage overshoots in first 0.4 seconds and continues as desired later. In results it can be easily seen that boost, buck and buck-boost converter topologies can be used in photovoltaic energy systems in order to adjust system voltage for photovoltaic energy systems. Designed PV system has been sampled in order to train the 5- and 10-neurons ANN topologies in order to achieve system features and voltage output by only using ANNs without running actual simulation. This study shows that the artificial neural networks can be used in electric based problems to lower simulation time and to use resources efficiently.

REFERENCES

Agha, Haider Saif, Zafar Ullah Koreshi, and Mohammad Bilal Khan. 2018. "Artificial Neural Network Based Maximum Power Point Tracking for Solar Photovoltaics." 2017 International Conference on Information and Communication Technologies, ICICT 2017 2017-December: 150–55.

https://doi.org/10.1109/ICICT.2017.8320180.

Dkhichi, Fayrouz, Benyounes Oukarfi, David Ouoba, Abderrahim Fakkar, and Amina Achalhi. 2017. "Behavior of Neural Network MPPT Technique on a PV System Operating under Variable Load and Irradiation." Proceedings of 2016 International Conference on Electrical Sciences and Technologies in Maghreb, CISTEM 2016, no. Figure 2: 1–4.

https://doi.org/10.1109/CISTEM.2016.8066822.

Hulugappa, Veeresh, and Ashok Kusagur. 2017. "Comparative Analysis of DC-DC Converter Topologies with Soft-Switching Techniques." 2016 International Conference on Electrical, Electronics, Communication, Computer and Optimization Techniques, ICEECCOT 2016, 106–10.

https://doi.org/10.1109/ICEECCOT.2016.7955195.

Jäger-Waldau, Arnulf. 2019. "Snapshot of Photovoltaics—February 2019." Energies 12 (5).

https://doi.org/10.3390/en12050769.

Jyothy, Lakshmi P.N., and M. R. Sindhu. 2018. "An Artificial Neural Network Based MPPT Algorithm for Solar PV System." Proceedings of the 4th International Conference on Electrical Energy Systems, ICEES 2018, 375–80. https://doi.org/10.1109/ICEES.2018.8443277.

Khanam, Jobeda, and Simon Y. Foo. 2018. "Neural Networks Technique for Maximum Power Point Tracking of Photovoltaic Array." Conference Proceedings - IEEE SOUTHEASTCON 2018-April: 1–4. https://doi.org/10.1109/SECON.2018.8479054.

Laamami, Samah, Mouna Benhamed, and Lassaad Sbita. 2017. "Artificial Neural Network-Based Fault Detection and Classification for Photovoltaic System." International Conference on Green Energy and Conversion Systems, GECS 2017, no. 1.

https://doi.org/10.1109/GECS.2017.8066211.

Lq, Hyhorsphqwv, Rqwuro Xwrpdwlrq Qjlqhhulqj, Xpdu Xvvdlq E L G D D, Qvwlwxwh Ri, Vxpdqnur Jpdlo, F R P Vkrhekxvvdlq, Jpdlo Frp, and Delg Qlwvul. n.d. "8Qlyhuvlw \ Ri . Dvkplu 6Ulqdjdu , Qgld" 3: 1–5.

Naveen, and Anil Kumar Dahiya. 2018. "Implementation and Comparison of Perturb Observe, ANN and ANFIS Based MPPT Techniques." Proceedings of the International Conference on Inventive Research in Computing Applications, ICIRCA 2018, 1–5.

https://doi.org/10.1109/ICIRCA.2018.8597271.

E. Duran, J. A. Galan, J. Manuel, and Andujar Marquez. 2007. "A New Application of the Buck-Boost-Derived Converters to Obtain the I-V Curve of Photovoltaic Modules A New Publication of the B Uck -B Oost -D Erived C Onverters to O Btain the I-V C Urve of P Hotovoltaic M Odules," no. September 2015.

https://doi.org/10.1109/PESC.2007.4342022.

Rajakumari, RFelshiya, PG Student, and Associate Professor. 2018. "Analysis and Assessment of DC-DC Converter Topologies for PV Applications." International Journal of Pure and Applied Mathematics 118 (24): 1–18.

Reshma Gopi, R., and S. Sreejith. 2018. "Converter Topologies in Photovoltaic Applications – A Review." Renewable and Sustainable Energy Reviews 94 (May): 1–14. https://doi.org/10.1016/j.rser.2018.05.047.

Sunny, Md Samiul Haque, Abu Naim Rakib Ahmed, and Md Kamrul Hasan. 2017. "Design and Simulation of Maximum Power Point Tracking of Photovoltaic System Using ANN." 2016 3rd International Conference on Electrical Engineering and Information and Communication Technology, ICEEiCT 2016, 1–5. https://doi.org/10.1109/CEEICT.2016.7873105.

Xiao, Weidong, Nathan Ozog, and William G. Dunford. 2007. “Topology Study of Photovoltaic Interface for Maximum Power Point Tracking.” IEEE Transactions on Industrial Electronics 54 (3): 1696–1704. https://doi.org/10.1109/TIE.2007.894732.

CISET - 2nd Cilicia International Symposium on Engineering and Technology
10-12 October, 2019, Mersin / TURKEY

THE GUI APPLICATION FOR CALCULATING THE DRAG TORQUE IN A DISENGAGED MULTI-DISC WET CLUTCH USING MULTIPLE MODELS

Ali Magdi Sayed Soliman [1], Suleyman Cinar Cagan [*2], and Berat Baris Buldum [3]

[1] Mersin University, Engineering Faculty, Mechanical Engineering Department, Mersin, Turkey, ali.magdi.sarhan@gmail.com

[2] Mersin University, Engineering Faculty, Mechanical Engineering Department, Mersin, Turkey, cinarcagan@mersin.edu.tr

[3] Mersin University, Engineering Faculty, Mechanical Engineering Department, Mersin, Turkey, barisbuldum@mersin.edu.tr

ABSTRACT
In the automatic transmission system of automobiles, clutches effectively contribute to fuel consumption. The internal resistance of transmission fluid between the clutch discs and plates causes a loss in power. In this work, efforts have been made to shed light on using programming skills to create a computer program that facilitates the calculation of this power loss, referred to drag torque. This paper is limited to reviewing different modeling techniques to calculate the drag torque in disengaged multi-disc wet clutches by using a computer program written in Python 3. For developing the graphical user interface of the program, Tkinter and Matplotlib libraries have been used. This computer program provides a fast way to enter and modify the numerical values of the necessary operating and geometrical parameters. After that, the processing using wet clutch mathematical models inside the black box is done by calculating the drag torque and revealing four required graphs.

Keywords: *Computer Program, Drag Torque, Transmission Fluid, Wet Clutch, Python 3*

[*] Corresponding Author

1. INTRODUCTION

Transmission systems are used to ensure the mobility of automobiles by transmitting the drive torque from the automobile engine, via the driveshaft, to the wheels and also allow the variation in the speed/torque ratio. Different types of transmission systems exist, but currently, dual-clutch and automatic transmission systems are the most popular due to their superior technology. In this paper, we only focus on the automatic transmission. As known, in an automatic car, there is no clutch pedal as the gear ratios are changed automatically without any input from the driver.

Automatic transmission systems are comprised mainly of a few parts such as torque converter, planetary gear sets, friction clutches and brakes, oil pump, valve bodies, and hydraulic system (Venu, 2013). Friction clutch, inside the automatic transmission system, is used to combine the engine with the output unit. The friction clutch has two states: engagement and disengagement. When the clutch is engaged, the friction discs and the separator plates approach and squish together to become as one part, and thus the torque, coming from the engine, is transmitted.

On the other hand, when the clutch is disengaged, there will be a little gab with fluid flowing radially through the clutch pack, between the friction disc and the separator plate. As a result of that, the friction discs, in this case, should rotate loosely without transmitting any torque. Since the rotating friction discs operate in oil bath, these friction clutches are also referred to as wet clutches and have the advantage of dissipating the heat of friction discs (Neupert *et al.*, 2018). However, wet clutches due to the viscosity of the transmission fluid exhibit a problem of drag torque (Peng *et al.*, 2019) and consequently, the torque transmitted during disengagement is considered a power loss (Iqbal *et al.*, 2013).

2. DRAG TORQUE

Studying drag torque is so necessary for transmission engineers to improve the energy efficiency of transmission systems. Drag torque leads to loss of power, and hence high fuel consumption. In wet clutches, drag torque occurs during disengagement since the gaps between the spinning discs and the stationary plates are filled with transmission fluid. Thus, a shear force due to the viscosity of the transmission fluid, as shown in Fig. 1, is generated, attempting to counter the rotational motion of the spinning disc (Madhavan *et al.*, 2012). This shear force is referred to as drag torque, as well.

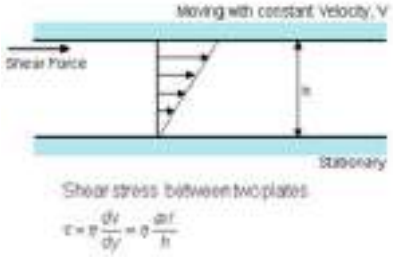

Fig. 1. Pictorial representation of the viscous shearing of fluid flowing between two parallel plates

The typical curve of the drag torque in a wet clutch against the relative speed between the clutch disc and plate is shown in Fig. 2 (Madhavan *et al.*, 2012). As shown, in the region I, drag torque is linearly proportional to the relative speed. In this case, the clutch discs will be fully filled with the transmission fluid on their surfaces since the surface tension forces keep the oil film full, complete. In region II, starting from the critical relative speed point, the drag torque decreases when the relative speed increases because the centrifugal forces become dominant, existing some air pockets. Eventually, in region III, the increase in the relative speed leads to an increase in the drag torque. That is because the transmission fluid creates a mist over the clutch discs (Venu, 2013).

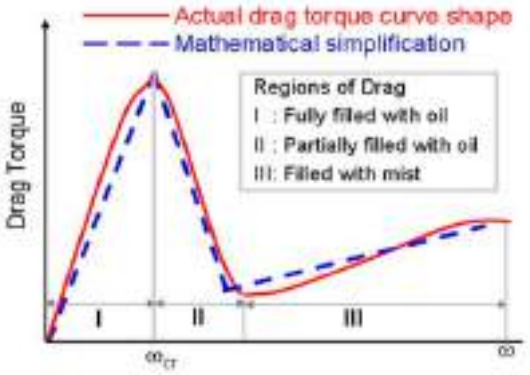

Fig. 2. Typical drag torque curve

The drag torque increases when the following occur (Naunheimer *et al.*, 2010):

- Grooves are not considered.
- The area of clutch discs increases
- The temperature of transmission fluid decreases.
- The flow rate increases.
- The clearance between the clutch discs and plates decreases.
- The number of clutch discs increases.

3. Mathematical models

A mathematical model is a simplified representation and abstraction of reality for the sake of well understanding a problem and demonstrating it analytically. Many efforts have been made by various authors to put a mathematical model that reaches the required engineering-level accuracy and calculate the drag torque in wet clutches.

3.1. Theoretical Model (Kitabayashi *et al.*, 2003)

In this model, Kitabayashi et al. presented the drag torque in wet clutch during disengagement for the following conditions:

- The transmission fluid is in steady-state.
- The transmission fluid is an incompressible oil.
- The friction discs in the disengaged clutch are non-grooved.
- The clutch plates operate in the laminar regime.

Due to the viscous shearing force, the drag torque is obtained using the law of viscosity as shown in Eq. (1):

$$T = N\, r_m\, F_{shearing} \tag{1}$$

where shearing force $F_{shearing}$ is calculated as in Eq. (2):

$$F_{shearing} = \frac{\mu\, A\, v}{h} = \frac{\mu\, \pi\, (r_2{}^2 - r_1{}^2)\, v}{h} \tag{2}$$

Therefore, the drag torque can be obtained from Eq. (3):

$$T = \frac{N\, r_m\, \mu\, \pi\, (r_2{}^2 - r_1{}^2)\, \omega\, r_m}{h} \tag{3}$$

where N is the number of discs, r_1 is the inner radius, r_2 is the outer radius, r_m is the mean radius, μ is the dynamic viscosity of the transmission fluid, ω is the relative speed of the clutch discs and plates, and h is the clearance between the discs and plates.

The disadvantage of this mathematical model is that it only describes the first region of the typical drag torque curve where the drag torque is linearly proportional to the relative speed. Furthermore, the effects of capillary and surface tension forces on the transmission fluid have not been taken into consideration (Yuan *et al.*, 2007).

3.2. Surface Tension Model (Yuan *et al.*, 2007)

Yuan et al. introduced the surface tension model taking into account the surface tension forces and the rupture of the transmission fluid film at the high-speed region. They estimated the drag torque for the following conditions:

- The transmission fluid is in steady-state.
- The transmission fluid is an incompressible oil.
- The friction discs in the disengaged clutch are non-grooved.
- The clutch plates operate in turbulent regime subject to the centrifugal effect.

The equivalent out radius of the film r_o can be obtained from Eq. (4):

$$\frac{\rho\, \omega^2}{2}\left(f + \frac{1}{4}\right) r_o{}^2 - \frac{\mu\, Q}{2\, \pi\, r_m\, h^3\, G_r} r_o + \frac{\mu\, Q}{2\, \pi\, r_m\, h^3\, G_r}\, r_1 - \frac{2\, \sigma \cos(\theta)}{h} - \frac{\rho\, \omega^2}{2}\left(f + \frac{1}{4}\right) r_1{}^2 = 0 \tag{4}$$

Therefore, the drag torque is expressed as in Eq. (5):

$$T = 2\, \pi\, N \int_{r_1}^{r_o} \frac{\mu\, \omega\, r^3}{h}\, (1 + 0.0012\, Re^{0.94})\, dr = 2\, \pi\, N\, \frac{\mu\omega}{h}\, (1 + 0.0012\, Re^{0.94})\left(\frac{r_o{}^4}{4} - \frac{r_1{}^4}{4}\right) \tag{5}$$

where r_o is the equivalent out radius of the transmission fluid as shown in Fig. 3 and Re is the characteristic Reynolds number. The drawback of this mathematical model is that it cannot describe the drag torque accurately at high speeds.

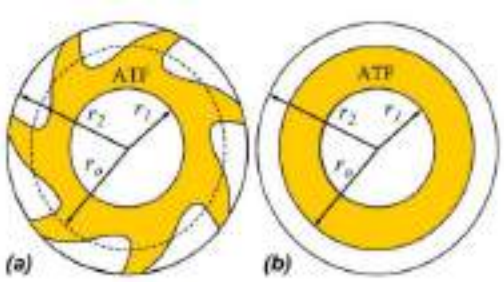

Fig. 3. Pictorial representation of the equivalent out radius of the transmission fluid

3.3. Shrinking Oil Film Model (Li *et al.*, 2013)

Unlike the surface tension model, this model describes the drag torque at high speeds accurately with the following conditions:

- The transmission fluid is in steady-state.
- The transmission fluid is an incompressible oil.
- The friction discs in the disengaged clutch are non-grooved.
- The clutch plates operate in the laminar regime.
- The gravity is neglected.

The flow rate Q needed to maintain a complete oil film between the clutch discs and plates is given in Eq. (6):

$$Q = \frac{\frac{6\, \mu}{\pi\, h^3} \ln\left(\frac{R_1}{R_2}\right)}{\frac{27\, \rho}{70\, \pi^2\, h^2}\left(R_2{}^{-2} - R_1{}^{-2}\right)} + \frac{\sqrt{\left(\frac{6\, \mu}{\pi\, h^3} \ln\left(\frac{R_1}{R_2}\right)\right)^2 - \frac{81\, \rho^2 \omega^2\, \left(R_2{}^{-2} - R_1{}^{-2}\right)\left(R_1{}^2 - R_2{}^2\right) - 540\, \rho\left(R_2{}^{-2} - R_1{}^{-2}\right) \Delta P}{700\, \pi^2\, h^2}}}{\frac{27\, \rho}{70\, \pi^2\, h^2}\left(R_2{}^{-2} - R_1{}^{-2}\right)} \tag{6}$$

If the actual flow rate is greater than or equal to the feed flow Q, the equivalent radius of oil film R_s, shown in Fig. 4, will be equal to the outer radius of the clutch disc or plate. Otherwise, the equivalent flow rate will be obtained as in Eq. (7).

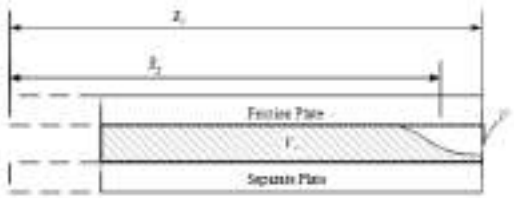

Fig. 4. Pictorial representation of the equivalent radius of oil film

$$R_s = \sqrt{\frac{Q_{actual}}{Q}\, R_2{}^2 + R_1{}^2 \left(1 - \frac{Q_{actual}}{Q}\right)} \tag{7}$$

Finally, the drag torque can be obtained from Eq. (8):

$$T = N \frac{\pi\, \mu\, \omega}{2\, h}\, (R_s{}^4 - R_1{}^4) \tag{8}$$

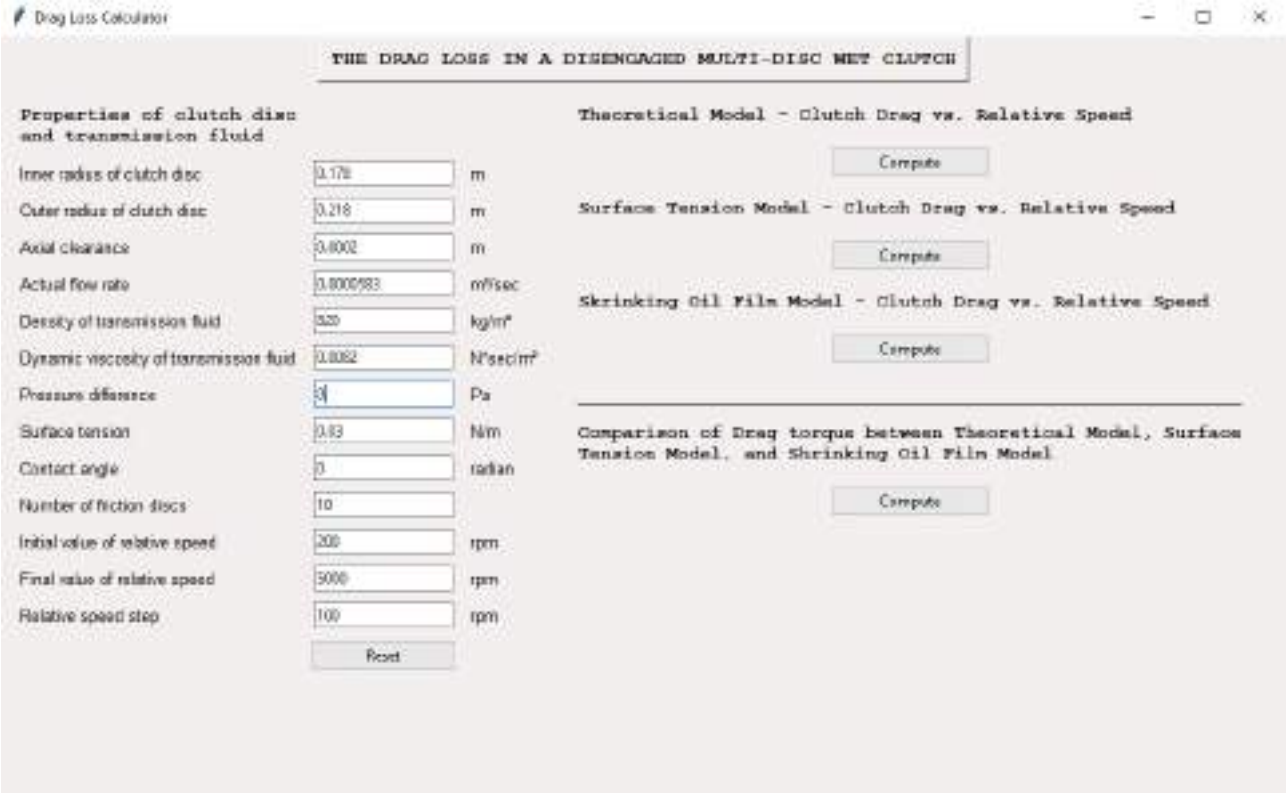

Fig. 5. Main window of the GUI application

4. GUI APPLICATION

To make the drag torque calculation process extremely easy, we decided to create a GUI application. The GUI application was developed in the python programming language (python 3) since it has many libraries that make developing GUI applications so easy. From among these libraries, the Tkinter library, as well as Matplotlib library, were used. Tkinter library serves to readily design the GUI application using ready functions or widgets such as label, entry, frame, and button, and Matplotlib library serves to plot graphs. Using such a GUI application will free the users from knowing the complete details about the drag torque modeling techniques in the black box. Furthermore, the users will interactively calculate the drag torque and get the required graphs without wasting much time.

In Fig. 5, the developed application is shown. As exhibited on the left side of the main window, there are labels of clutch disc and transmission fluid properties as well as entry boxes in which the user will enter numerical values. To delete and reset all the entered numerical values at once, the user can use the reset button existed below. The flowchart in Fig. 6 shows the calculation procedure occurring inside the program. When the user enters the numerical values of all the properties and then presses on the "compute" buttons on the right side of the program, computations are done inside the black box to eventually provide four graphs (Figs. 7 to 10) to the user.

Fig. 6. Calculation procedure of the GUI application

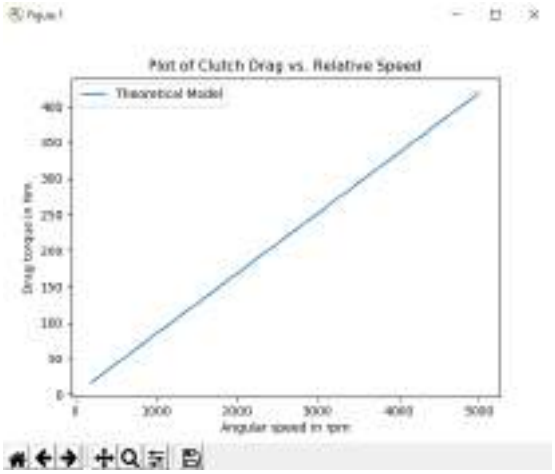

Fig. 7. Plot of drag torque versus relative speed using the theoretical model

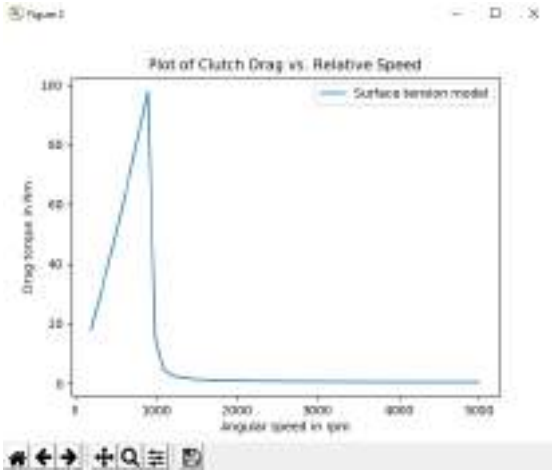

Fig. 8. Plot of drag torque versus relative speed using the surface tension model

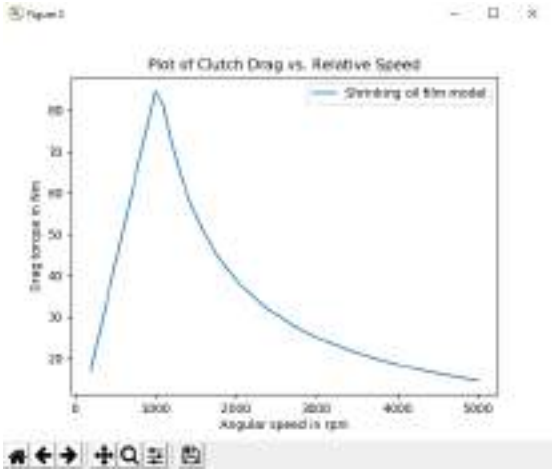

Fig. 9. Plot of drag torque versus relative speed using the shrinking oil film model

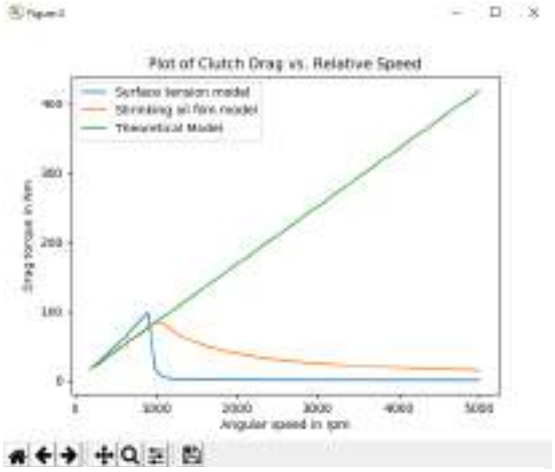

Fig. 10. Plot of the comparison between the three models

Fig. 7 shows a plot of drag torque against relative speed using the theoretical model. In this graph, the drag torque is linearly proportional to the relative speed. Accordingly, this graph describes only region I of the typical drag torque curve; therefore, at high speeds, this model fails. Using the surface tension model, Fig. 8 shows a more reasonable curve. In the beginning, the drag torque linearly increases as long as the relative speed increases. Next, starting from the critical relative speed, the curve goes down and nearly approaches zero since the centrifugal forces begin to dominate over the surface tension forces. Hence, this model is not realistic or resembling the typical drag torque curve.

The shrinking oil film model in Fig. 9 seems to be close to the typical drag torque curve. In this model, the decrease of drag torque in region II does not approach zero. Amongst the three models mentioned above, the shrinking oil film model predicts the drag torque more accurately. Finally, Fig. 10 shows a comparison between the three models. The interactive navigation toolbar existed on the figures below serves to configure the appearance of the graph, pan, zoom, and navigate through the data set.

5. CONCLUSION

This paper suggests the idea of using programming skills to facilitate the calculations in mechanical engineering issues. Hence, an actual example in the automotive sector has been introduced to validate this idea. We created a Windows GUI application in the python programming language to readily calculate the drag torque in disengaged multi-disc wet clutches by using three different modeling techniques. In future studies, we aim to add all the modeling techniques in the literature to this developed program.

REFERENCES

Iqbal, S. *et al.* (2013) “Mathematical model and experimental evaluation of drag torque in disengaged wet clutches”, *ISRN Tribology.*

Kitabayashi, H., Li, C. Y. and Hiraki, H. (2003) “Analysis of the various factors affecting drag torque in

multiple-plate wet clutches", *SAE Technical Papers*.

Li, H., Jing, Q. and Ma, B. (2013) "Modeling and parametric study on drag torque of wet clutch", *Lecture Notes in Electrical Engineering*, 193 LNEE, Vol. 5, pp. 21-30.

Madhavan, J. *et al.* (2012) "Application of simulation based methods in development of wet clutch system", *SAE Technical Papers*.

Naunheimer, H., Bertsche, B., Ryborz, J., and Novak, W. (2010). *Automotive Transmissions*, Springer Science & Business Media, Berlin, Germany.

Neupert, T. *et al.* (2018) "Parameter study on the influence of a radial groove design on the drag torque of wet clutch discs in comparison with analytical models"**,** *Tribology International,* Vol. 119, pp. 809-821.

Peng, Z. and Yuan, S. (2019) "Mathematical model of drag torque with surface tension in singe-plate wet clutch", *Chinese Journal of Mechanical Engineering*, Vol. 32.

Venu, M. K. K., (2013). Wet clutch modeling techniques and design optimization of clutches in an automatic transmission, Master's Thesis, Chalmers University of Technology, Goteborg, Sweden.

Yuan, Y. *et al.* (2007) "An improved hydrodynamic model for open wet transmission clutches", *Journal of Fluids Engineering, Transactions of the ASME*, 129(3), pp. 333-337.

CISET - 2nd Cilicia International Symposium on Engineering and Technology
10-12 October, 2019, Mersin / TURKEY

PARALLELIZATION OF DRAGONFLY OPTIMIZATION ALGORITHM ON DISTRIBUTED AND SHARED MEMORY ARCHITECTURES

Ramazan POLAT*[1], Ali AKDAĞLI [2] and Çiğdem ACI[3]

[1] Mersin University, Department of Electrics and Electronics Engineering, Mersin, Turkey, ramazanpolat@mersin.edu.tr

[2] Mersin University, Department of Electrics and Electronics Engineering, Mersin, Turkey, akdagli@mersin.edu.tr

[3] Mersin University, Department of Computer Engineering, Mersin, Turkey, caci@mersin.edu.tr

ABSTRACT

Nowadays, the analysis of nature-inspired meta-heuristic optimization algorithms with parallel computing and programming techniques has been frequently studied by researchers. In these studies, significant improvements have been made in the running time of the algorithm using shared and distributed memory architectures. The design of Dragonfly Algorithm (DA), which is one of the optimization algorithms used in recent years, takes the visceral behavior as an example, is designed with Shared and Distributed Memory (SDM). This algorithm, which deals with the instinctive behaviors of animals in nature, was examined behavior in which the optimal value was calculated of each dragonfly over a certain function in order to reach the most appropriate result. The performance of the DA formulation was investigated using single or multi-modal comparison functions of different sizes. Later, CUDA infrastructure which is developed by NVIDIA, is used to code parallel functions. The performance of the parallelized state of DA was analyzed on the test functions and compared with the performance of the series. The size of the problem is considered as 10 test functions. The performance analysis of 500 dragonflies was performed at 500 iterations. Compared with 500 dragonflies on the CPU, it has spent 65% less time, and the system is even faster. It took 91942 seconds for serial operations with 500 dragonflies on the GPU, and 5240 seconds for parallel operations. When we rate the system, 95% less time is spent.

Keywords: *Dragonfly Algorithm, Optimization, Multi-tier Distributed and Shared Memory, Parallelization, CUDA Programming*

* Ramazan POLAT

1. INTRODUCTION

Recently, with the increasing amount of data used in meta-heuristic algorithms, it has become unable to meet the requirements of applications running by algorithms that process large-scale data in existing systems in terms of speed and cost. Therefore, with the rapid development of technology, the importance of algorithms in terms of time and cost has increased. Accordingly, researchers have turned to general-purpose Graphics Processing Unit (GPU) programming techniques in parallel programming, a new approach that offers low cost and high performance. Parallel programming is a form of programming that aims to distribute and dissolve tasks that require a large amount of processing and time. In other words, if a large amount of calculations are required, these calculations are shared and calculated by using multiple algorithms and techniques. On a computer using traditional methods, commands are processed sequentially and only one command can be processed per unit time; A software designed with parallel programming logic can process multiple commands on different processors simultaneously, providing a great benefit in both time and resource usage. Nature-inspired optimization algorithms can have high iterations and population numbers with long-lasting calculations due to their nature. In order to solve these problems, many studies have been carried out in the literature about parallelizing these algorithms. In these studies, significant improvements have been made in the running time of the algorithm using shared and / or distributed memory architectures.

Recommended by Mirjalili in 2015, DA is a nature-inspired optimization algorithm that studies the static and dynamic behavior of dragonfly swarms in nature and mathematically modeling them. This algorithm was developed by examining the two main instinctive behaviors of dragonfly insects, which are identified as food search and enemy avoidance. When the dragonflies are in swarm, they exhibit specific signaling movements and communicate intelligently. These behaviors are examined and shared in detail in Mirjalili's article, in which mathematical modeling is clearly demonstrated. However, as with other nature-inspired algorithms, the DA consumes a lot of processor time in high iterations and population numbers.

In the study conducted by Ç. Acı and H. Gülcan, the application of the improved DA with the Brownian motion to the weld beam design problem was addressed and achieved success with a 20% lower calculation. In the study conducted by M. M. Mafarja, Binary Dragonfly Algorithm(BDA) was proposed. 18 UCI datasets were used to evaluate the performance of the proposed approach and the results of the method were compared with the results of Particle Swarm Optimization (PSO), Genetic Algorithms (GA) in terms of classification accuracy and number of qualifications selected. The results showed the successful ability of BDA. In the study performed by Arun Vikram K, he made a sample DA application for optimal performance analysis of process parameters in milling operation. In milling operation, while performing tangential and right-angle operations on A-axis, optimum solution is focused on producing process parameters such as surface roughness and surface hardness. In his study, F. Katircioglu has performed the edge detection and segmentation thesis by using the threshold method in color images using DA. The results of the mathematical applications were compared with the Gravity Search Algorithm (GSA) and Harmonic Search Algorithm (HSA) in the literature. As a result of the study performed with DA algorithm, the proposed algorithm was found to be powerful in numerical image segmentation and edge detection. In the study conducted by M.Kıran and A. Çınar in relation to CUDA, parallel application of tree seed algorithm on GPU with CUDA infrastructure was discussed. As a result of experimental studies, it has been observed that parallel version of algorithm provides performance increase up to 184.65 times for some problems compared to serial version. In 2008, Garland. Conducted a medical evaluation with CUDA for image processing in the medical field and performed performance evaluations on CPU and GPU.

2. DRAGONFLY ALGORITHM

The dragonfly fly with its large united eyes and strong transparent wings is known for its glamorous colors and long bodies. The world also has many different dragonfly species. The life cycle consists of two important stages: larvae and adults. Hunting features unique and rarely seen intelligent behavior. In the static flock, dragonfly flies in small groups and move back and forth to hunt. Local movements and sudden changes in the flight path are the main characteristics of the static flock. In dynamic flocks, however, a large number of dragonflies travel in large groups for migration. According to Reynold, herd behavior is based on three basic principles. Separation; It means preventing collision with other people in the neighborhood. Alignment; It shows the speed harmony with other individuals in the neighborhood. Harmony; It refers to the tendency of individuals towards the center of the neighborhood mass. The main purpose of any herd is to survive, and therefore individuals should head towards food resources. Besides this main action, the flock can be disturbed by enemies from the outside. If these two behaviors are added, the location update process uses five main factors. This behavior of the herd is formulated and used in the solution of optimization problems. Figure 1 shows the five main factors among individuals in the herd.

a Separation, b Alignment, c Harmony, d Food, e Enemy

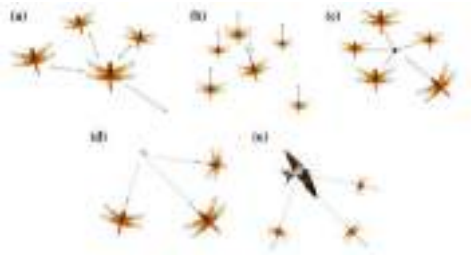

Fig. 1. Five basic factors among individuals in the herd

Each of these behaviors is modeled mathematically as follows:

$$S_i = -\sum_{j=1}^{N} X - X_j \quad (1)$$

In equation (1);

X indicates the position of the current individual. Xj is j. shows the position of the neighboring individual. N gives the number of neighboring individuals.

$$A_i = \frac{\sum_{j=1}^{N} V_j}{N} \quad (2)$$

In equation (2);

Vj indicates j. shows the speed of the neighboring individual.

$$C_i = \frac{\sum_{j=1}^{N} X_j}{N} - X \quad (3)$$

The attraction towards the food source is calculated as in Equation (3).

$$F_i = X^+ - X \quad (4)$$

In equation (4);

X+ indicates the position of the food source. Behavior against an enemy danger is calculated as follows.

$$E_i = X^- + X \quad (5)$$

In equation (5);

X indicates the position of the threatening enemy.

$$\Delta X_{t+1} = (sS_i + aA_i + cC_i + fF_i + eE_i) + w\Delta X_t \quad (6)$$

In equation (6);

The parameter s is the separation, a parameter is the alignment, the c parameter is the fit, the f parameter is the nutrient, the e parameter is the weight of enemy factors. Also, w value t. indicates the inertia weight in the loop.

$$X_{t+1} = X_t + \Delta X_{t+1} \quad (7)$$

After calculating the step vector, the position vector given in Equation (7) below is calculated.

$$X_{t+1} = X_t + Levy(d) \times X_t \quad (8)$$

Random walking (Le'vy flight) was used to improve randomness, stochastic behavior and the discovery characteristics of dragonflies. In this case, the positions of the dragonflies were updated using the following equation

Parameter t in equation (8) represents the current cycle and parameter d represents the size of the position vector.

$$Levy(x) = 0.01 \times \frac{r_1 \times \sigma}{|r_2|^{1/\beta}} \quad (9)$$

$$\sigma = \left(\frac{\tau(1+\beta) \times \sin\left(\frac{\pi\beta}{2}\right)}{\tau\left(\frac{1+\beta}{2}\right) \times \beta \times 2^{\left(\frac{\beta-1}{2}\right)}} \right)^{1/\beta} \quad (10)$$

Equation (9) Le'vy flight is given.

$$\tau(x) = (x-1)! \quad (11)$$

$$T(x) = \left| \frac{\Delta x}{\sqrt{\Delta x^2} + 1} \right| \quad (12)$$

$$X_{t+1} = \begin{cases} -X_t, & r < T(\Delta X_{t+1}) \\ X_t, & r \geq T(\Delta X_{t+1}) \end{cases} \quad (13)$$

Equation (9 - 13) shows Le'vy flight parameters.

2.1. PARALLELIZATION

DA has been implemented in two main stages within the framework of data parallelism and task parallelism. In order to ensure data parallelism, random numbers are generated and sent to GPU memory in batch. The threads that had to make a call to generate random numbers at each iteration were recovered from this workload to gain speed. The placement of the objective function values of the dragonfly in memory and the placement of the best dragonfly parameters in memory are the same in both serial and parallel applications. Within the framework of task parallelism, the comparison functions, the positions of the dragonflies, the source of the food and the creation of the enemy's positions were re-encoded in parallel and the processes processed step by step were adjusted to be processed simultaneously. In this study, the parallel loop structure of MATLAB is used in the context of task sharing. The parallel for loop performs the work of a normal for loop in a parallel structure. Comparative functions are written in MATLAB environment in series and the same MATLAB function file is used for dragonflies in the algorithm. In parallel application, separate function files have been converted to MEX extensions with the help of GPU-Coder plugin in MATLAB environment for dragons. MEX files are also used in our MATLAB application.

3. RESULTS AND DISCUSSIONS

For comparison for parallelization with 500 dragonflies, the algorithm applied in 500 cycles is tested 10 times in parallel in all functions between F1 and F10 and the results are shown.

As shown in Table 1, it took 91942 seconds for all functions with 500 dragonflies. It takes 10083 seconds for CPU-based parallel operations. When we rate the results, 90% less time is spent. It takes 5240 seconds for GPU-based parallel processing with CUDA architecture. When we compared the results, it was seen that it spent 95% less time.

Table 1. 10 times Parallel DA Test with 500 Dragonflies in 500 cycles

F	Series(sec)	CPU(sec)	GPU(sec)
F1	7.029,87	448,17	443,76
F2	6.630,64	606,43	543,16
F3	6.590,95	1.158,75	480,85
F4	6.611,81	1.125,10	444,49
F5	8.472,80	1.283,07	624,75
F6	11.073,81	1.183,65	497,91
F7	10.322,51	1.193,41	504,54
F8	12.834,67	1.524,12	672,24
F9	11.470,01	1.126,92	530,11
F10	10.904,96	434,30	498,63
Sum	91.942,03	10.083,93	5.240,44
	%100	%10,9	%5,7

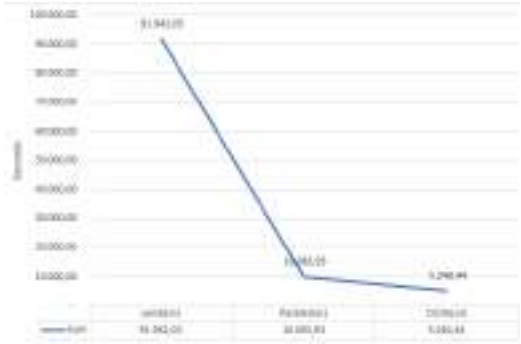

Fig. 2. 10 times Parallel DA Test with 500 Dragonflies in 500 cycles

4. CONCLUSION

In this study, parallelization of DA optimization algorithm on PDB architectures is examined. DA, which is one of the most successful and newest of nature-inspired metaphorical optimization algorithms, is coded on Serial and Parallel level and the results and time are focused on CPU and GPU. Algorithms were run 10 times at each level and the results were compared with the average of the efficiency, and the sum of the time and speed were compared. Serial encoded DA is encoded in parallel. Parallel version was tested with 500 dragonflies. It was operated with 500 dragonflies for 65% less time. It was then re-coded in parallel to make it work on the GPU. GPU-encoded DA spent 95% less time. The efficiency of parallel programming has been demonstrated on both CPU and CUDA based GPUs. The CUDA architecture has made significant gains.

5. REFERENCES

C. W. Reynolds, C. W., Reynolds, C. W., and R. Craig W. (1987). “Flocks, herds and schools: A distributed behavioral model,” in Proceedings of the 14th annual conference on Computer graphics and interactive techniques - SIGGRAPH ’87, vol. 21, no. 4, pp. 25–34.

Ç. İ. Acı and H. Gülcan (2019). “A Modified Dragonfly Optimization Algorithm for Single- and Multiobjective Problems Using Brownian Motion,” Comput. Intell. Neurosci., vol. 2019, pp. 1–17.

F. Katircioğlu (2017). “Renkli Görüntüler İçin Yusufçuk Algoritması Kullanılarak Benzerlik Görüntüsüne Dayalı Eşikleme.” Düzce Üniversitesi Bilim ve Teknoloji Dergisi, 5 (2017) 506-523

K. Arun Vikram, C. Ratnam, V. Lakshmi, A. Sunny Kumar, and R. Ramakanth (2018). “Application of dragonfly algorithm for optimal performance analysis of process parameters in turn-mill operations- A case study,” IOP Conf. Ser. Mater. Sci. Eng., vol. 310, no. 1, p. 012154.

M. Garland. (2008). “Parallel Computing Experiences with CUDA,” IEEE Micro, vol. 28, no. 4, pp. 13–27.

M. S. Kıran and A. C. Çınar (2018). “Ağaç-tohum algoritmasının CUDA destekli grafik işlem birimi üzerinde paralel uygulaması,” Gazi Üniversitesi Mühendislik-Mimarlık Fakültesi Derg., vol. 2018, no. 2018, pp. 1397–1409

M. M. Mafarja, D. Eleyan, I. Jaber, A. Hammouri, and S. Mirjalili (2017). “Binary Dragonfly Algorithm for Feature Selection,” Proc. - 2017 Int. Conf. New Trends Comput. Sci. ICTCS 2017, vol. 2018-Janua, pp. 12–17.

S. Mirjalili (2016). “Dragonfly algorithm: a new meta-heuristic optimization technique for solving single-objective, discrete, and multi-objective problems,” Neural Comput. Appl., vol. 27, no. 4, pp. 1053–1073.

The MathWorks, “Parallel Computing ToolboxTM User’s Guide R2019a,” https://www.mathworks.com/help/parallel-computing [Accessed 15 Sep 2019].

CISET - 2nd Cilicia International Symposium on Engineering and Technology
10-12 October, 2019, Mersin / TURKEY

INVESTIGATION OF MECHANICAL PROPERTIES OF GEOFOAM MATERIALS UNDER DYNAMIC LOADS CAUSED BY ROCK FALL

Özgür Lütfi Ertuğrul[*1], Semih Aşıcı[2]

[1] Assoc, Prof.Dr. , Mersin University, Faculty of Eng., Dept. of Civil Engineering, Mersin, Turkey, ertugrul@mersin.edu.tr

[2] Grad. Student, Mersin University, Faculty of Eng., Dept. of Civil Engineering, Mersin, Turkey, asici.semih@gmail.com

ABSTRACT

The aim of this study is to investigate the potential application of geofoam materials as impact absorbers under the sudden loads such as impact induced by falling rocks. In mountains regions, rock fall hazards may cause significant losses to civil engineering structures. Geofoam absorbers may serve to diminish the effect of rock fall impact. Within this study, dynamic analysis of rocks with different collision velocities and weights were carried out using ANSYS software based on finite element method. In the numerical model, behavior of the geofoam was taken into account by implementing a bi-linear stress-strain model. Analysis results include displacement, stress and strain values of the geofoam material. In the light of these data, the response attributes of the geofoam material to a rock fall impact were investigated. It was observed that increased geofoam density reduces stress and displacement values of the protected structure while it causes increase in induced stress levels. As a result of the study, it is seen that geofoam type damping materials may be installed on civil engineering structures to minimize effect of rock fall hazard on these structures to a certain extend.

Keywords: *Geofoam, Dynamic Analysis, Rock Fall Hazard, Impact Absorber*

[*] Corresponding Author

1. INTRODUCTION

Rock falls typically occurring in mountainous regions cause a major threat for surrounding lifelines, and civil engineering structures. Depending of the size and falling trajectory of the rocks, significant amounts of energy are released when rocks hit structures. This energy must be effectively damped in order to reduce the damage to the engineering structures. Materials with high damping capacity can be installed on a concrete structure in order to reduce the transfer of impact energy to the structural elements.

The damping material acts as a shock absorber to dissipate some of the impact energy, dissipate contact stresses, reduce the maximum load on the affected structure and increase the duration of action.

In this study, explicit dynamic method was used to simulate rock fall impact on the geofoam block. In order to understand the dynamic response of the material, a rectangular prism shaped geofoam was considered as an absorber resting on an infinitely rigid structure. The finite element analysis of the model was performed by using ANSYS package program.

2. LITERATURE REVIEW

The damping material on the protection structure must be capable of absorbing energy due to plastic compression. Impact absorbers should distribute the force at the impact point to a larger area on the protection structure. These type of materials must have low densities to minimize dead load while withstanding impact forces without damage under their long service life.

The dynamic force applied due to a mass falling on the damping layer is expressed by Eq (1).

$$P_{max} = 1.765 * r^{0.2} * M_E^{0.4} * (\frac{m*v^2}{2})^{0.6} \quad (1)$$

The impact force depends on the elastic modulus (M_E) of the damping layer, sphere radius (r), rock mass (m) and impact velocity (v). Due to their low density and good energy absorbing properties, styrofoam is generally used to protect structures exposed to heavy rock fall impact loads (Volkewein *et al*., 2011). A comparison of the relative transmitted impact forces on concrete roofing for sand, rubber and styrofoam materials is shown in Figure 1.

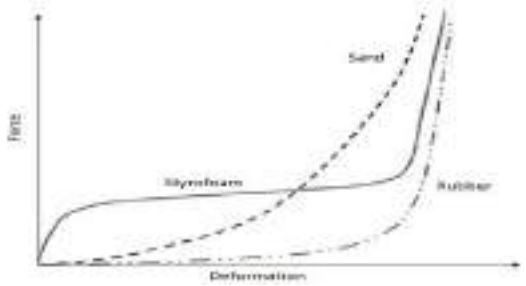

Figure 1. Transmitted impact forces for sand, rubber and styrofoam (Volkewein *et al*., 2011)

These results show that the styrofoam, which starts to absorb energy as soon as the effect occurs, is more effective in absorbing and dispersing impact force than sand. However, tests have also shown that unreinforced styrofoam may break under high impact loads and must be reinforced with polypropylene strips that distribute impact force over a larger area.

The mechanism of impact energy absorption on rock shed galleries is related to two types of forces caused by the rock fall effect: weight impact force and transmitted impact force. Figure 2 shows the transmitted impact force caused by the weight impact force on the protection structure (Yoshida *et al*.,1987).

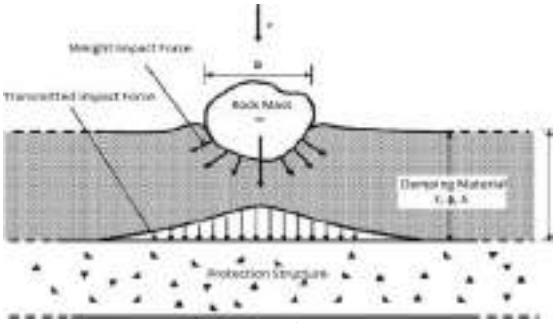

Figure 2. Transmitted impact force caused by the weight impact (Wyllie, 2017).

While the damping material absorbs impact energy, the protection structure can increase the force due to the dynamic forces being transmitted on the roof beams. The full-scale testing of the protection structure shows that the transmitted impact force for rigid structures such as concrete structures can be between 1.5 and 2 times the weight impact force. However, there is no simple relationship between these two forces due to the complex dynamic behavior of the damping layer and the underlying beams (Wyllie, 2017).

2.1. Geofoam

According to ASTM, geofom is defined as a block or planar rigid cellular foam polymeric material used in geotechnical engineering applications (ASTM-1,2005).

The multi-purpose use of Geofom in geotechnical engineering projects increases the cost-effectiveness of the material. Commonly used geofom types are expanded polystyrene (EPS) or extruded polystyrene foam (XPS).

EPS is considered a suitable material due to its low density, good thermal insulation, superior vibration absorption properties and lateral deformation properties. Figure 3 shows an example of vibration damping with EPS on the infrastructure instead of a conventional compressed earth fill.

Figure 3. Vibration damping with EPS on the infrastructure instead of a conventional compressed earth fill.

2.2. Basic Properties and Test Methods of Geofoam

The basic characteristics of the geofoam can be classified into four categories as physical, mechanical, thermal and durability (Koerner, 2005).

Physical properties include dimensions, density, moisture absorption and oxygen index. The physical properties at different densities for EPS and XPS are shown in Table 1 and Table 2.

Table 1. Physical property requirements for EPS geofoam (ASTM D6817)

Type	EPS 15	EPS 19	EPS 22	EPS 29	EPS 39
Density (kg/m^3)	14.4	18.4	21.6	28.8	38.4
Compressive Strength, min. kPa %1	25	40	50	75	103
Compressive Strength, min. kPa %5	55	90	115	170	241
Compressive Strength, min. kPa %10	70	110	135	200	276
Flexural Strength, kPa	172	207	276	345	414
Oxygen index, (%)	24	24	24	24	24

Table 2. Physical property requirements for XPS geofoam (ASTM D6817)

Type	XPS 20	XPS 21	XPS 26	XPS 29	XPS 36
Density kg/m^3	19.2	20.8	25.6	28.8	35.2
Compressive Strength, min. kPa %1	20	35	75	105	160
Compressive Strength, min. kPa %5	85	110	185	235	335
Compressive Strength, min. kPa %10	104	104	173	276	414
Flexural Strength,kPa	276	276	345	414	517
Oxygen index, min volume %	24	24	24	24	24

2.3 Physical Properties of Geofoam

Geofoam density is measured according to the directions of ASTM-C578. Typical geofoam density ranges from 11 kg/m^3 to 48 kg/m^3 . Geofoam also plays an important role in applications such as moisture absorption and thermal insulation. According to ASTM C578, the maximum absorption value of the geofoam is 0.3%.

2.4 Mechanical Properties of Geofoam

Research shows that geofoam materials should be considered as elasto-viscoelastic material (Yoshida *et al.*,1987), (Koerner, 2005), (Wyllie, 2017). The typical stress-strain behavior graph of the EPS geofoam under compression is shown in Figure 4.

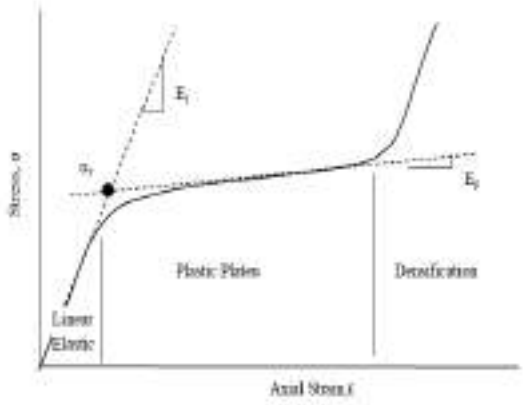

Figure 4. Typical stress-strain behavior graph of EPS geofoam under pressure (Ertuğrul, 2011)

Geofoam is a linear elastic material characterized by 1% axial tension by Hooke's law. According to Koerner (2005) the mechanical properties of geofoam can be classified as compression behavior, tensile and bending resistance, shear strength and compression creep behavior.

3. METHODOLOGY

In this study, rectangular prism shaped geofoam block model was produced in ANSYS. Geofoam block was assumed to rest on an infinitely rigid structure and boundary conditions were defined accordingly. A circular block was considered as an object falling from certain elevations. A simple sketch of the model was depicted in Figure 5**Hata! Başvuru kaynağı bulunamadı.**. In order to generate impact force, collision analyzes were performed using explicit finite element method scheme of ANSYS.

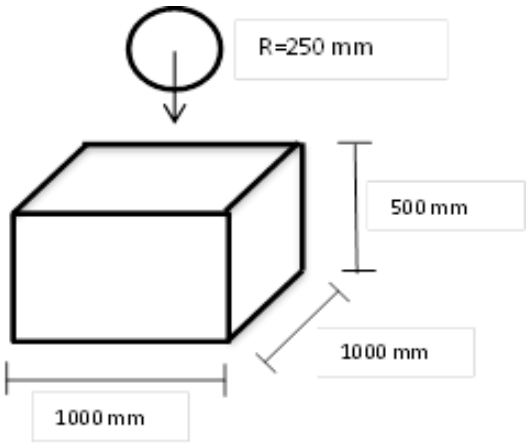

Figure 5. Dimensions of the Numerical Model

3.1. Model Parameters

The model consists of two parts: rock and geofoam. Falling rock is modeled as a solid body, so the deformations during the movement of the solid body are minimized. The use of rigid body representation for rock saves significant time without affecting the overall result. The geofoam layer is modeled as a deformable body and the bilinear properties of the material are defined. Bilinear data of the geofoam materials were obtained from the graphs given in Figure 6.

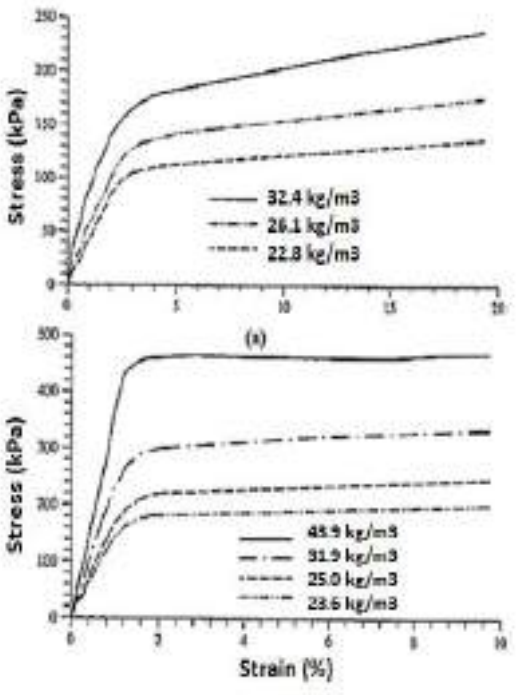

Figure 6. Typical EPS and XPS stress-strain behavior (Koerner, 2005**)**

3.1.1. EPS model parameters

Two different types of EPS were used for energy damping. Table 3 shows the properties of EPS materials.

Table 3 Properties of EPS

Damping Material	Properties	Value	Unit
EPS-1	Density	22,8	kg/m^3
	Modulus of Elasticity	3,797	MPa
	Yield Strength	101	kPa
	Tangent Modulus	182	kPa
EPS-2	Density	32,4	kg/m^3
	Modulus of Elasticity	9,368	MPa
	Yield Strength	167	kPa
	Tangent Modulus	393	kPa

3.1.2. XPS model parameters

Two different types of XPS were used for energy damping. Table 4 shows the properties of XPS materials.

Table 4 Properties of XPS

Damping Material	Properties	Value	Unit
XPS-1	Density	23,6	kg/m^3
	Modulus of Elasticity	13,7	MPa
	Yield Strength	171	kPa
	Tangent Modulus	236	kPa
XPS-2	Density	43,9	kg/m^3
	Modulus of Elasticity	35,1	MPa
	Yield Strength	445	kPa
	Tangent Modulus	75	kPa

4. RESULT AND DISCUSSION

Finite element modeling procedures of rock fall on the geofoam are explained in this section. Finite element modeling is performed by using ANSYS Workbench v15.0 package program. Throughout the modeling process, appropriate material properties and contact types are assigned for each of the materials used. The mesh quality of the model is checked by applying mesh convergence analysis. Then, the necessary limit conditions are taken into consideration and the dynamic loads are applied to the system. In order to create inertia loading, gravity has been taken into consideration and standard gravity is taken as 9.8060 m/s^2. In the designed model, the non-linear analysis module was used since the control surface had a large deflection potential. The impact of falling rock on the geofoam is simulated with a faster and more accurate solution by using explicit dynamic analysis module for impact analysis.

4.1. Finite Element Method

The finite element model of the dynamic analysis used for the mechanical behavior of the damping material is shown in Figure 7. Rock and geofoam materials are defined as shell elements. The friction type interaction was selected for the contacts between the structures in the model. In reality, these contacts should be more complex, however theoretically simplified interaction state is selected in order to decrease computing time.

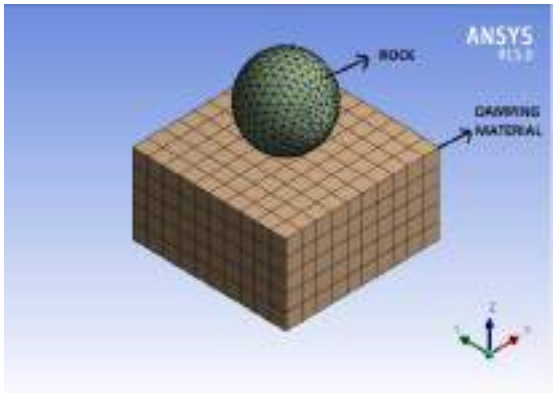

Figure 7. Mesh structure of the finite element model

4.2. Stress Analysis of Model

Stress is the internal resistance of a material to the distorting effects of an external force or load. In the analyses, only the stress values of the geofoam in the downward direction (-z direction) were examined.

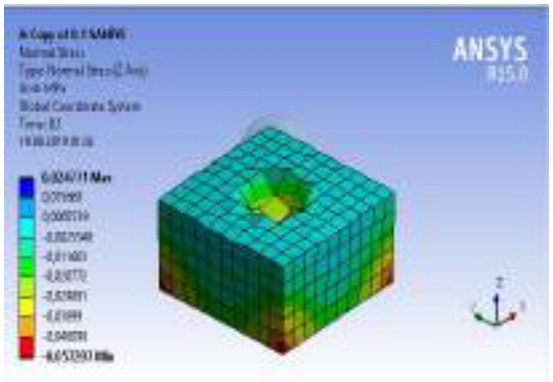

Figure 8. Stress contour of the impact

Figure 8 shows the stress contours of the geofoam due to the impact analysis of the rock weighing 300 kg at a speed of 4 m/s.

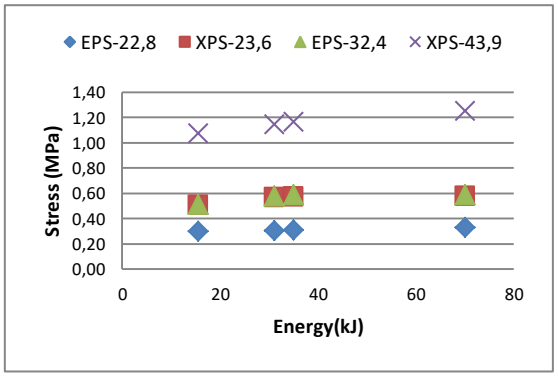

Figure 9. Stress - Energy diagram

The maximum normal stress values on the surface of the geofoam material due to rock fall are shown in Figure 9. It is seen that the geofoam reaches the maximum stress value at the impact point and large stresses also occur at the base of the material.

4.3. Strain Analysis of Model

Strain refers to the extent to which a material under load changes its shape compared to the state before the load is applied. In the analyses, the strain values of the geofoam in the horizontal direction (x- direction) were examined.

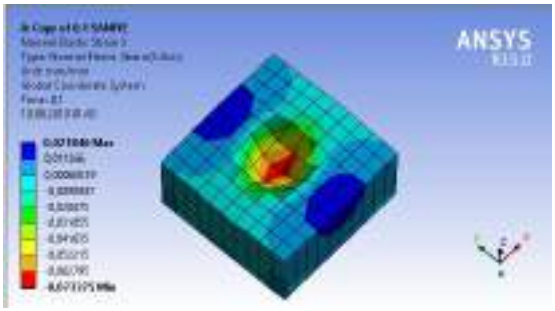

Figure 10. Strain contour of the impact

Figure 10 shows the strain contour of the geofoam's surface caused by impact of the rock.

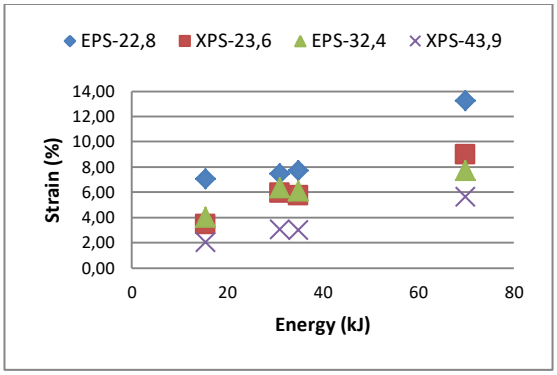

Figure 11. Strain-Energy Diagram

The maximum normal strain value on the geofoam surface due to the collision analysis of the rock is shown in Figure 11. It was observed that increasing density of the geofoam material is causing a decrease in the compressional strain values.

4.4. Deflection Analysis of Model

Deflection of the geofoam occurs due to the externally applied loads and the force of gravity. For these analyses, only the deflection of the geofoam in the downward direction were examined.

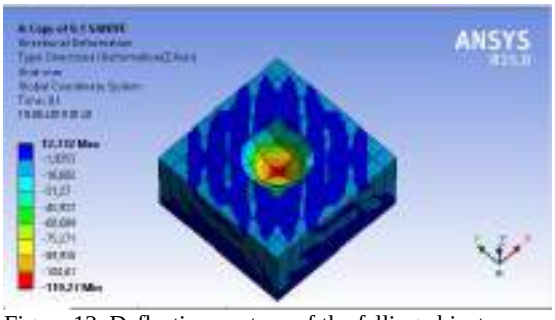

Figure 12. Deflection contour of the falling object impact

Figure 12 shows the deflection contour of the geofoam caused by impact of the rock.

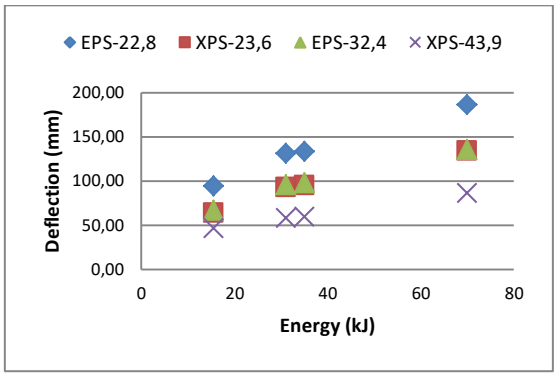

Figure 13. Deflection-Energy Diagram

Figure 13 shows the displacement values of the collision energies on the geofoam in detail. As the collision energies in the system increase, the displacement values in the beam increase as expected.

5. CONCLUSION

Rock fall impacts cause a serious damage to civil engineering structures. This destructive effect should be attenuated in an acceptable way and major catastrophes should be prevented. Therefore, the loads that will occur in the structure due to collision must be estimated and structural design of protective shelters should be made in this direction. Geofoam materials have a significant application potential for being used as damping materials considering their mechanical properties. Since these materials significantly reduce the high energies generated by the rock fall, it is necessary to know some properties of the material to be used.

In this study, potential applications of geofoam to reduce effect of impact type forces induced by rockfalls were investigated. It was observed that the mechanical behavior created by the rock falling on the geofoam changes depending on the density and stiffness of the material used. Increased material density decreases stress and displacement values while it causes increase in stress values. Results indicated that approximately two times increase in the density of expanded polystyrene geofoam may lead to three to four times decrease in the impact induced displacements in the geofoam body. Similar behavior was observed in strain levels however low density absorbers are more successful in reducing the compressional forces transferred to the structure. It can be concluded that an optimum selection of deformation and load reduction characteristics are required for the successful design of a geofoam impact absorber.

REFERENCES

ASTM, Standard guide for use of expanded polystyrene (EPS) geofoam in geotechnical projects, American Society of Testing Materials, Pennsylvania, 2005,

Ertuğrul, Ö. L. (2011). Influence of Deformable Geofoam Buffers on the Static and Dynamic Behaviors of Cantiliver Retaining Walls. PhD Thesis. Middle East Technical University, Ankara Turkey

Koerner, R. M. (2005). Designing with Geosynthetics, Prentice Hall, New Jersey, The USA.

Masuya, H., Maegawa, K. and Mizuki, A., Yoshida, H. (1987) "Impulsive loads by rock falls on steel rocksheds (in Japanese). " *Journal of Structural Engineering.* Vol. 36-A, pp. 41-49.

Volkwein, A. (2011) "*Rockfall characterisation and structural protection – a review.* " *Natural Hazards and Earth System Sciences*, pp. 2617–2651.

Wyllie, D. C. (2017) *Rock Fall Engineering*. s.l. : CRC Press, Florida , The USA.

CISET - 2nd Cilicia International Symposium on Engineering and Technology
10-12 October, 2019, Mersin / TURKEY

NUMERICAL MODELING OF THE ROCKFALL INDUCED IMPACT ON SIMPLY SUPPORTED RC BEAMS

Özgür Lütfi Ertuğrul *[1], Semih Aşıcı[2]

[1] Assoc, Prof.Dr. , Mersin University, Faculty of Eng., Dept. of Civil Eng., Mersin, Turkey, ertugrul@mersin.edu.tr

[2] Grad. Student, Mersin University, Faculty of Eng., Dept. of Civil Eng., Mersin, Turkey, asici.semih@gmail.com

ABSTRACT

Within this study, dynamic response of a structural beam element to impact type forces are investigated through numerical analyses performed by ANSYS Explicit Dynamics Software. In the analyses, reinforced concrete structure is modeled with the RHT concrete model, a macro-scale material model that includes the necessary properties for defining the correct dynamic strength at the respective stress ratios and pressures to ensure minimum limits. As the output parameters, displacement, stress and strain values of the reinforced concrete beam element were monitored during and after the impact. In the light of the registered data, the effects of impact type forces on the structural beam elements were investigated. Results indicate that increasing energy of the impact action also causes increase in the displacement, stress and strain values within the reinforced concrete beam as expected, and even exceed the permissible values thus leading to structural collapse. Special energy absorption layers could be used to reduce the effect of impact for reinforced concrete structures which are prone to impact type collisions such as rockfall and landslides.

Keywords: *RHT Concrete Model, Impact, Beam element, Energy absorption*

1. INTRODUCTION

Rock fall type disasters are defined as the sudden and rapid movement of rocks breaking down the hillside or slopes in mountainous areas by the gravity. Rock falls can prevent transportation, damage buildings or highways and cause long-term economic damage. Therefore, the hazards of rock falls must be considered in the planning and design of lifelines, highways and residential areas.

During a rockfall activity, depending on the size and velocity of falling rock fragments, impact forces at different kinetic energy levels can affect to civil engineering structures. These collisions may cause structural damage. Therefore, protection shields or barriers are required to protect main structure. Protection structures should be designed to absorb the high impact energy of falling rocks. Direct impact of rock fragments to reinforced concrete structures can lead to very large displacements leading to serious damage to the structures.

In this study, analyses were performed using ANSYS explicit dynamics software based on finite difference method. To understand the effect of a rock hitting a structure with high energy levels, a simple supported reinforced concrete beam model was modeled.

2. LITERATURE REVIEW

When a falling rock collides directly with a protection structure, the maximum impact force generated at that time is much greater than the weight of the rock and therefore causes great damage (Lo *et al*., 2016).

According to Newton's second law of motion, the impact force of a falling object on a surface can be determined as a momentum change over a given time interval. However, it is difficult to measure the speed of an object before and after a collision within a certain time interval. Alternatively, the conversion of energy from gravitational potential energy to kinetic energy should be considered.

Masuya (2008) has described the history of rock fall research in Japan, also presented combined experimental and analytical dynamic effects of rock fall protection structure.

Schellenberg *et al*., (2005) carried out a series of rock fall impact tests on six reinforced concrete slabs with a cushion layer consisting of compacted gravel. Concrete cubes of 800 kg and 4000 kg, respectively, were dropped with different falling heights. The authors concluded that obtaining experimental data in rock fall galleries can be used to develop design methods for protection structures.

Yılmaz *et al.* (2016) investigated the impact response of reinforced concrete beams having the same transverse and longitudinal reinforcement ratio using different impact energies.

3. METHODOLOGY

In this study, a simple support beam is modeled which consists of a fixed end constrained support and a movable support on the other end, which do not transfer moment at both ends. Figure 1 shows the dimensions of the structural model.

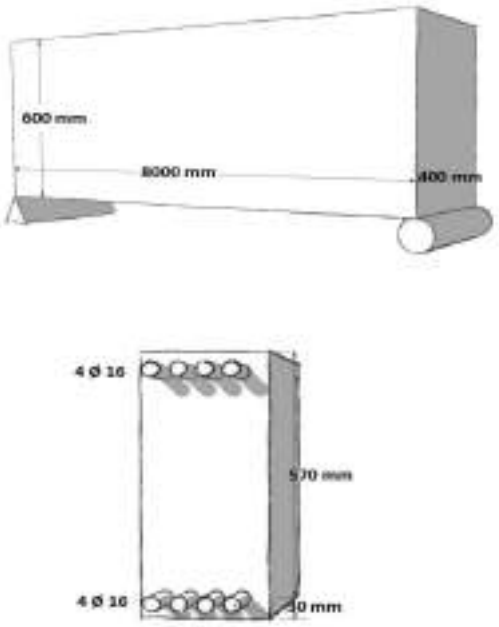

Figure 1. Cross-sectional view of R/C beam

3.1. Model Parameters

The dynamic model consists of two parts: a spherical body with velocity and simply supported beam structure. The falling sphere is modeled as a solid body, so the deformations during the impact are negligible. The use of rigid body representation for falling rock fragment saves significant computing time without significantly affecting the overall result. Reinforced concrete structure is modeled with the RHT concrete model, a macro-scale material model that includes the necessary properties for defining the correct dynamic strength at the respective stress ratios and pressures to ensure minimum limits.

3.1.1. Structural model parameters

RHT concrete model is used in the reinforced concrete beam used for protection structure. Table 1, shows the values used for the concrete model. This model contains the necessary features for the definition of the correct dynamic force at the stress ratios and pressures acting on the concrete**.** (Borrvall, T. *et al*,.2011)

Table 1. RHT concrete model values

Properties	Value	Unit
Density	2314	kg/m^3
Compressive Strength	$3,5\times10^7$	Pa
Bulk Modulus	$3,527\times10^{10}$	Pa
Shear Modulus	$1,67\times10^{10}$	Pa
Solid Density	2750	kg/m^3
Porous Soundspeed	2920	m/s
Initial Compaction Pressure	$2,33\times10^7$	Pa
Solid Compaction Pressure	6×10^9	Pa

4. RESULT AND DISCUSSION

Finite element modeling was performed using ANSYS Workbench v15.0 program. In the modeling process, suitable material properties and connection types are assigned for each of the materials used. The mesh quality of the model was checked by applying mesh convergence analysis. After that, the necessary limit conditions were taken into consideration and the dynamic loads were applied to the system. In order to create inertia loading, gravity has been taken into consideration and standard gravity is taken as 9.8060 m/s^2. The nonlinear analysis scheme was preferred since the designed control surface has a large deflection attribute.

4.1. Finite Element Method

Before starting numerical analyses, the structures and modeling types for the structures were determined. The beam is modeled as a shell body, and the reinforcement elements in the beam are modeled as a line body. The relevant model to be used for the CAD model and the finite element model is shown in Figure 2.

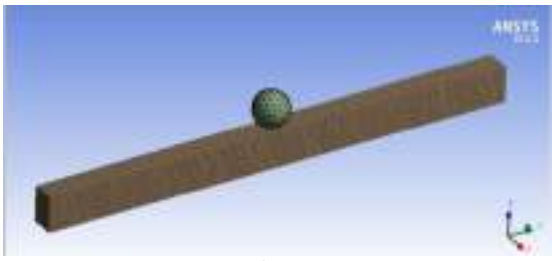

Figure 2. Mesh structure of the model

Some structural interactions were applied to the model. In reality, different structural interactions may be possible, but in theoretical analysis, simplified contact situations have been assumed for the sake of computing time. These assumptions and idealizations are:

- Friction interaction between all components.
- Reinforced interaction between the beam and the reinforcements in it.

4.2 Beam Deflection Analysis

Only the displacement values of the beam's midpoint in the downward direction (-z direction) were examined.

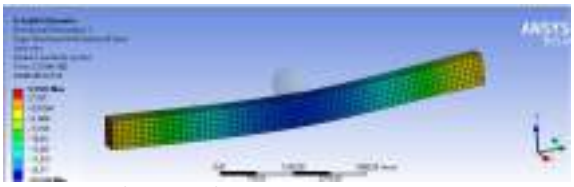

Figure 3 Deflection of the beam during impact

Figure 3 shows the maximum displacement contours of the beam as a result of the impact analysis of the rock weighing 500 kg at a speed of 7 m/s.

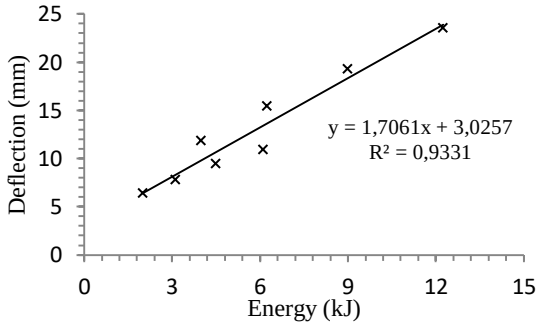

Figure 4. Deflection - Energy Graph

Figure 4 shows the displacement values of the collision energies on the beam in detail. As the collision energies in the system increase, the displacement values in the beam increase as expected.

4.3. Beam Stress Analysis

Stress values in normal direction (-z direction) in the upper part of the beam were examined. Figure 5 shows the maximum contact stress at the beam surface as a result of the collision analysis of the rock weighing 500 kg colliding at a speed of 7 m/s. It is seen that the beam reaches the maximum stress value at the impact point.

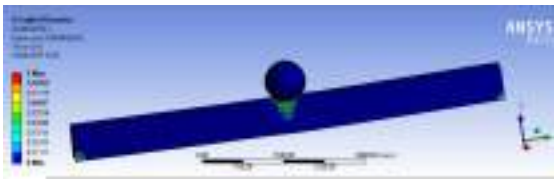

Figure 5 Damaged finite elements of the beam

Figure 6 shows the damaged finite element cells of the section taken from the collision point. When the section is examined, it is observed that the concrete structure is damaged where the impact occurred.

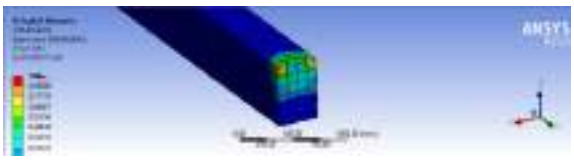

Figure 6 Cross section of the beam at the contact surface

Figure 7. shows the stress values at different impact energy levels. As it can be observed from the graph, the increase of the collision energy caused an increase in the contact stress values. It can be observed that there is some scatter in the data. Since the element size were the maximum obtained from the mesh convergence criteria to decrease run time of the model, numerical errors may slightly affect the results. To get more realistic results, mesh size should be selected much finer levels.

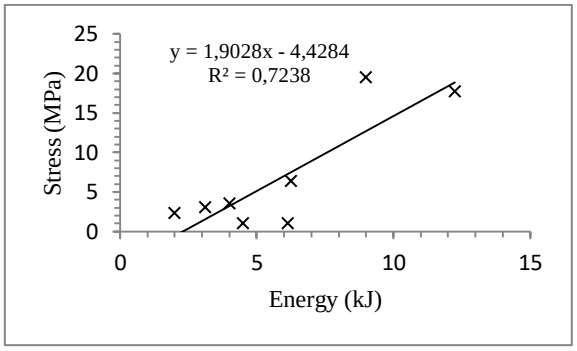

Figure 7 Stress – Energy Graph

4.4. Beam Strain Analysis

The strain values that occur in the upper part of the beam and in the direction of the beam clearance (y - direction) are examined. When the unit deformation value of the reinforced concrete beam is 0.35%, it is assumed that the beam reaches the final bending limit value.

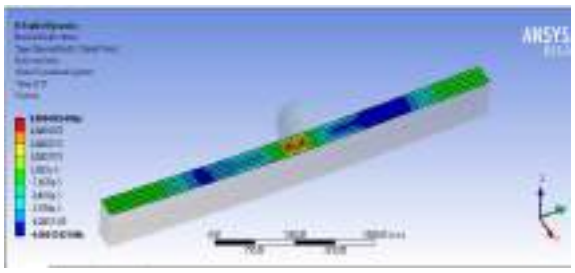

Figure 8 Strain contour of beam

When the values in Figure **9** are examined, it is observed that as the impact energy increases, the unit deformation increases and even exceeds the allowed limit value.

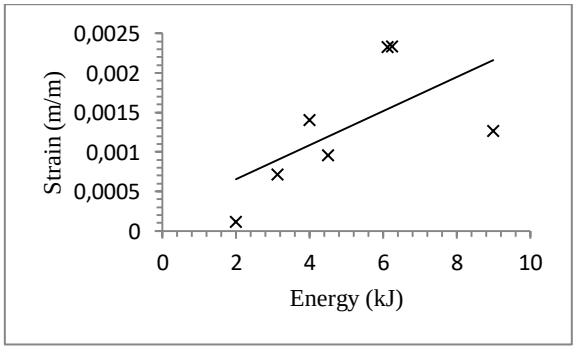

Figure 9 Strain – Energy graph

5. CONCLUSION

Within this study, dynamic response of a structural beam element to impact type forces are investigated through numerical analyses performed by ANSYS Explicit Dynamics Software. In the light of the registered data, the effects of impact type forces on the structural beam elements were investigated. Results indicate that increasing energy of the impact action also causes increase in the displacement, stress and strain values within the reinforced concrete beam as expected, and even exceed the permissible values thus leading to structural collapse.

Reinforced concrete structures lose their bearing capacity and break during collisions with high energy levels. The impact of high-energy collision conditions on the reinforced concrete structures, which are also used as protection structures, is well known and it is necessary to design the reinforced concrete structures safely. In this study the displacement, stress and strain performances of the beam under different impact energies are investigated. Special energy absorption layers could be used to reduce the effect of impact for reinforced concrete structures which are prone to impact type collisions such as rockfall and landslides.

REFERENCES

Borrvall, T., Riedel, W. (2011) "The RHT CONCRETE model in LS-DYNA" 8th European LS-DYNA Users Conference, Strasbourg, France

Lo, C-M., Lee, C-F., Lin, M-L. (2016) Consideration of the Maximum Impact Force Design for the Rock-Shed Slab, Journal of Geography & Natural Disasters,

Masuya, H. (2008). "History And Highlıghts Of Rock Fall Research In Japan." Interdisciplinary Workshop on Rockfall Protection, Morschach, Swiss, pp. 67-74

Schellenberg, K., Volkwein, A., Roth, A., Vogel, T. (2005), "Large-Scale Impact Tests On Rock Fall Gallerıes" IABSE Symposium, Lisbon, Portugal, pp. 497-504

Yılmaz, C. And Dok, G. (2016). " Farklı Çapma Etkilerine Maruz Kalmış Betonarme Kirişlerin Davranışının Belirlenmesi." 4th International Symposium on Innovative Technologies in Engineering and Science, Antalya, Turkey, pp. 1413-1419

CISET - 2nd Cilicia International Symposium on Engineering and Technology
10-12 October, 2019, Mersin / TURKEY

INFLUENCE OF COAGULANT TYPE IN REMOVAL OF TELON RED A2FR TEXTILE DYE BY CHEMICAL COAGULATION

Bahadır K. KÖRBAHTİ [*1], Fırat AKCAN [2], Eray AYTEKİN [3], Diren SAPAN [4], Asena NAL [5], Burcu KESEN [6], Ahmet ALTINTOP [7], Nejla Eylül KELEŞ [8] and Meltem GÖKTAŞ [9]

[1] Mersin University, Faculty of Engineering, Chemical Engineering Department, Mersin, Turkey, e-mail: korbahti@mersin.edu.tr

[2] Mersin University, Faculty of Engineering, Chemical Engineering Department, Mersin, Turkey, e-mail: frtakcn_34@outlook.com

[3] Mersin University, Faculty of Engineering, Chemical Engineering Department, Mersin, Turkey, e-mail: erayaytekin33@gmail.com

[4] Mersin University, Faculty of Engineering, Chemical Engineering Department, Mersin, Turkey, e-mail: sapan_can34@hotmail.com

[5] Mersin University, Faculty of Engineering, Chemical Engineering Department, Mersin, Turkey, e-mail: asenal96@outlook.com

[6] Mersin University, Faculty of Engineering, Chemical Engineering Department, Mersin, Turkey, e-mail: burcukesen0133@gmail.com

[7] Mersin University, Faculty of Engineering, Chemical Engineering Department, Mersin, Turkey, e-mail: ahmetfna26@gmail.com

[8] Mersin University, Faculty of Engineering, Chemical Engineering Department, Mersin, Turkey, e-mail: eylulkeles19@gmail.com

[9] Mersin University, Faculty of Engineering, Chemical Engineering Department, Mersin, Turkey, e-mail: meltemgoktas969@gmail.com

ABSTRACT
In this study, the removal of Telon Red A2FR (TR A2FR) textile dye was investigated by chemical coagulation using aluminum sulfate ($Al_2(SO_4)_3$) and iron (II) sulfate ($FeSO_4$) inorganic coagulants in a batch system. The influence of coagulant type was studied in the range of 100-500 mg/L Telon Red A2FR textile dye concentration and 1-5 g/L coagulant dosage for acidic, natural, and basic pH conditions. Dye removal efficiency using aluminum sulfate and iron (II) sulfate was obtained between 13.1-99.6% and 4.8-94.2%, respectively. The removal capacity using aluminum sulfate and iron (II) sulfate was achieved between 2.41-610.65 mg dye/g coagulant and 2.57-116.22 mg dye/g coagulant, respectively. Dye removal efficiency and removal capacity were obtained as basic pH > natural pH > acidic pH. The performance of aluminum sulfate was found better than iron (II) sulfate.

Keywords: *Coagulation, Aluminum sulfate, Iron (II) sulfate, Telon Red A2FR, Textile dye, Wastewater treatment.*

[*] Corresponding Author

1. INTRODUCTION

Inorganic and organic chemical compounds including textile dyes are using in large amounts in textile industries (Körbahti, 2007, 2011; Körbahti and Turan, 2016a, 2016b). Textile dyes are organic chemical substances that are used in coloring of textile materials by dyeing and printing of fibers, yarns and woven/knit apparel (Körbahti, 2007, 2011; Körbahti and Turan, 2016a, 2016b). The application of color to the textile material with some degree of colorfastness by continuous and batch processes is known as textile dyeing process. The primary source of wastewater in dyeing operations is the spent dye bath and rinsing processes that contains residual dye, salt, organic and inorganic chemicals (Körbahti, 2007, 2011; Körbahti and Turan, 2016a, 2016b). The presence of these compounds and dyes in textile industry effluents results in undesirable environmental impacts (Körbahti, 2007, 2011; Körbahti and Turan, 2016a, 2016b).

Coagulation is a chemical method applied in water and wastewater treatment prior to sedimentation and filtration in order to enhance the ability of a treatment process to remove particles (Tchobanoglous *et al*., 2004; MRWA, 2009). Coagulation is relatively simple and cost-effective, provided that chemicals are available and dosage is adapted to the water composition (Tchobanoglous *et al*., 2004; MRWA, 2009). Coagulation is a process used to neutralize charges and form a mass large enough to settle or be trapped in the filter (Tchobanoglous *et al*., 2004; MRWA, 2009). Once the charge is neutralized, the small-suspended particles are capable of sticking together. The slightly larger particles formed through this process are called microflocs (Tchobanoglous *et al*., 2004; MRWA, 2009). Rapid-mix to properly disperse the coagulant and promote particle collisions is needed to achieve good coagulation and formation of the microflocs (Tchobanoglous *et al*., 2004; MRWA, 2009).

Inorganic coagulants such as aluminum and iron salts are the most commonly used as coagulants. The choice of coagulant depends upon the type of suspended solid to be removed, raw water conditions, facility design, and cost of the chemical (Tchobanoglous *et al*., 2004; MRWA, 2009). When these substances added to water, highly charged ions neutralize the suspended particles. The inorganic hydroxides that are formed produce short polymer chains which enhance the microfloc formation. In this study, the removal of Telon Red A2FR textile dye was investigated by chemical coagulation using aluminum sulfate ($Al_2(SO_4)_3$) and iron (II) sulfate ($FeSO_4$) inorganic coagulants in a batch system.

2. MATERIAL AND METHODS

The batch experimental system was composed of three mixers. The reaction medium was continuously stirred at 400 rpm for the homogenization. The reaction temperature was monitored with a glass thermometer immersed. Aluminum sulfate ($Al_2(SO_4)_3.14H_2O$) and iron (II) sulfate ($FeSO_4.7H_2O$) inorganic coagulants were used in the treatment. The pH of the reaction medium was adjusted using 1 M HCl and 1 M NaOH solutions. In the runs of natural pH, HCl and NaOH solutions were not added. 5 mL samples were taken at appropriate time intervals for analysis and measurements. The color of the aqueous medium was analyzed using UNICO 4802 UV/Vis double beam spectrophotometer. pH was measured using WTW inoLab BNC720 pH meter.

D-optimal response surface design with three factors at three levels was applied to the experimental data using Design-Expert® 10. The independent variables were pH condition, acidic (A), natural (N), basic (B); initial dye concentration, 100-500 mg/L; and coagulant dosage, 1-5 g/L. The performance of the process was evaluated by analyzing the response of color removal.

3. RESULTS AND DISCUSSION

Two important factors in coagulation are pH and coagulant dosage. Therefore, the influence of coagulant type in removal of Telon Red A2FR textile dye was investigated in the range of 100-500 mg/L Telon Red A2FR textile dye concentration and 1-5 g/L coagulant dosage for acidic, natural, and basic pH conditions. In this study, aluminum sulfate ($Al_2(SO_4)_3$) and iron (II) sulfate ($FeSO_4$) coagulants were used as coagulants due to their extensive usage in water and wastewater treatment facilities. Table 1 shows the influence of coagulant type in removal of Telon Red A2FR textile dye by chemical coagulation.

Table 1. Influence of coagulant type in removal of Telon Red A2FR textile dye by chemical coagulation

Coagulant	Dye Removal Efficiency (%)	Removal Capacity (mg dye/g coagulant)
$Al_2(SO_4)_3$	13.1 - 99.6	2.41 - 610.65
$FeSO_4$	4.8 - 94.2	2.57 - 116.22

3.1. Coagulation Using Aluminum Sulfate

The optimal pH range for aluminum sulfate is approximately 5.5 to 6.5, with adequate coagulation possible between pH 5 to pH 8 under some conditions. Reaction 1 occurs when aluminum sulfate is added to the water containing alkalinity. Reaction 1 shifts the carbonate equilibrium and decrease the pH. However, CO_2 gas evolves with sufficient alkalinity and the pH is not drastically reduced (Tchobanoglous *et al*., 2004). When sufficient alkalinity is not present to neutralize the sulfuric acid production, the pH may be reduced in reaction 2 (Tchobanoglous *et al*., 2004):

$$Al_2(SO_4)_3.14H_2O + 6HCO_3^- \rightleftharpoons 2Al(OH)_3 + 6CO_2 + 14H_2O + 3SO_4^{-2} \quad (1)$$

$$Al_2(SO_4)_3.14H_2O \rightleftharpoons 2Al(OH)_3 + 8H_2O + 3H_2SO_4 \quad (2)$$

In the study, dye removal efficiency and removal capacity using aluminum sulfate was obtained between 13.1-99.6% and 2.41-610.65 mg dye/g coagulant, respectively, as outlined in Table 1. Dye removal increased with increasing dye concentration and decreasing $Al_2(SO_4)_3$ dosage. In Figures 1 and 2, dye removal efficiency and removal capacity were obtained as basic pH > natural pH > acidic pH. The highest dye removal efficiency and removal capacity were achieved with 500 mg/L Telon Red A2FR and 1 g/L $Al_2(SO_4)_3$ at basic pH conditions.

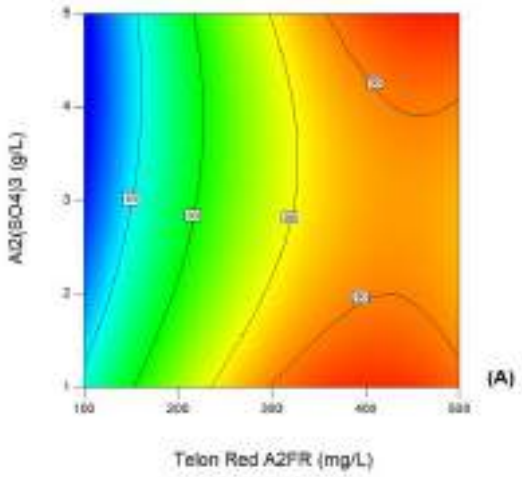

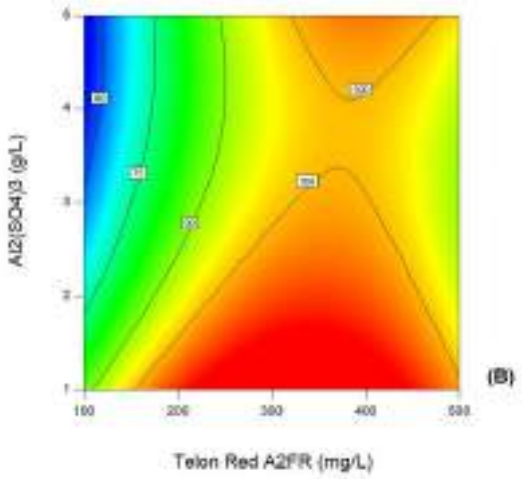

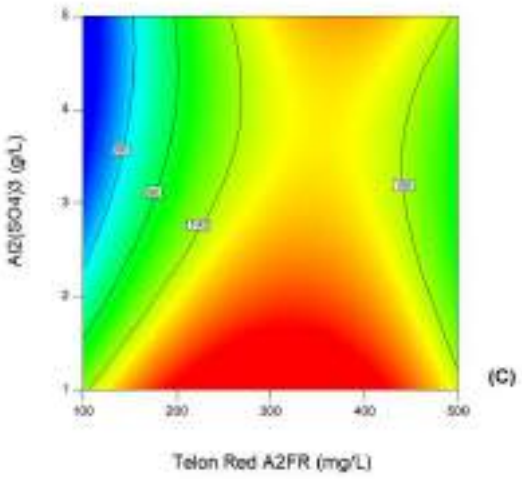

Figure 1. Effect of process parameters in dye removal efficiency of Telon Red A2FR textile dye using $Al_2(SO_4)_3$ coagulant. (A) acidic pH condition, (B) natural pH condition, (C) basic pH condition.

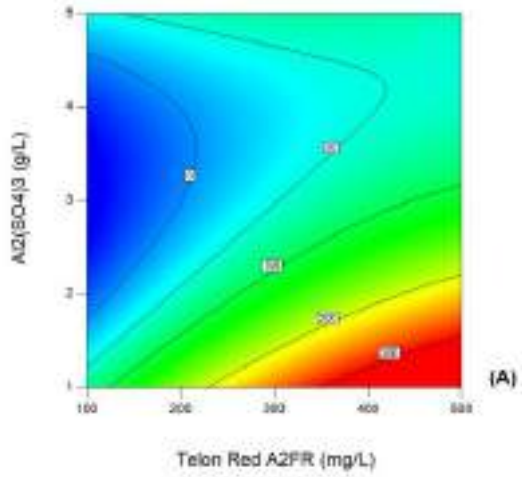

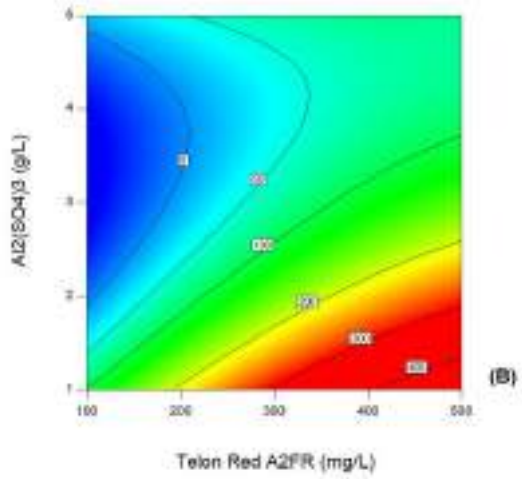

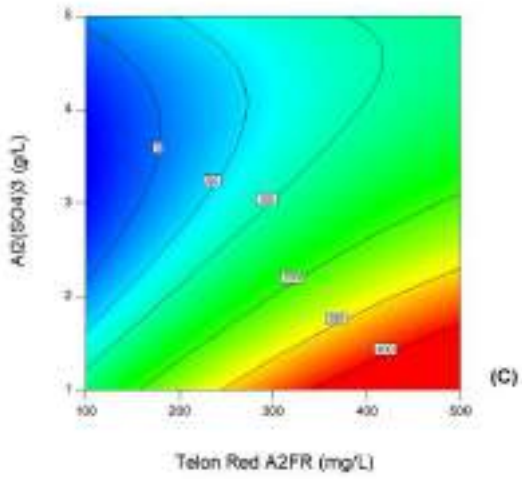

Figure 2. Effect of process parameters in removal capacity of Telon Red A2FR textile dye using $Al_2(SO_4)_3$ coagulant. (A) acidic pH condition, (B) natural pH condition, (C) basic pH condition.

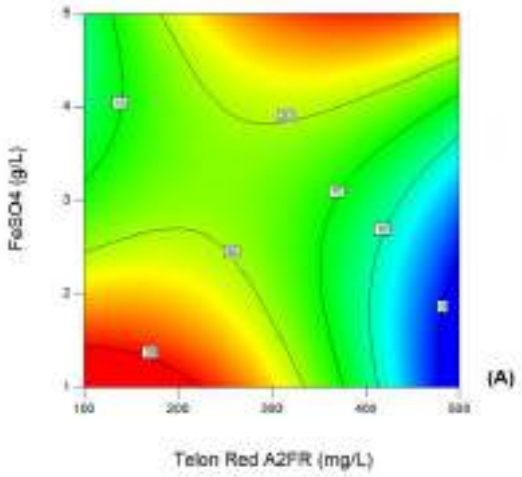

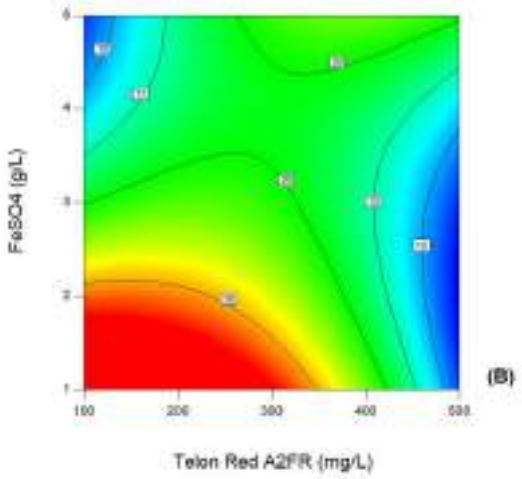

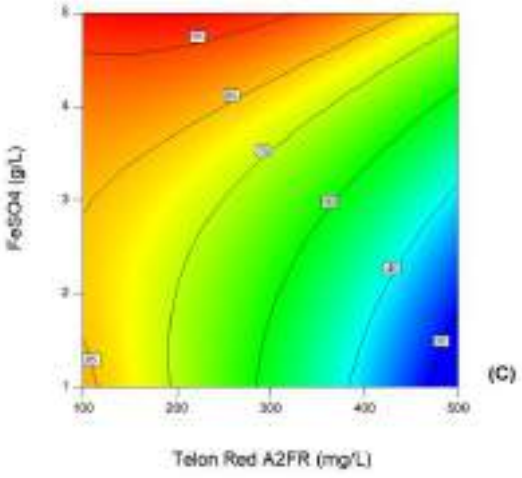

Figure 3. Effect of process parameters in dye removal efficiency of Telon Red A2FR textile dye using $FeSO_4$ coagulant. (A) acidic pH condition, (B) natural pH condition, (C) basic pH condition.

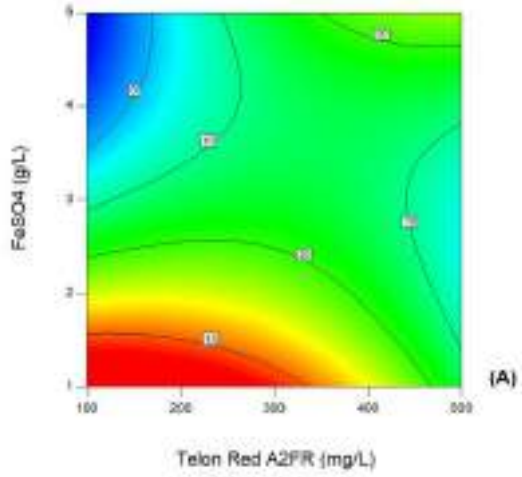

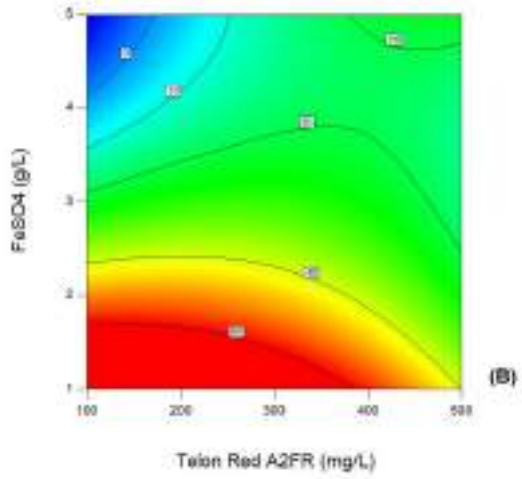

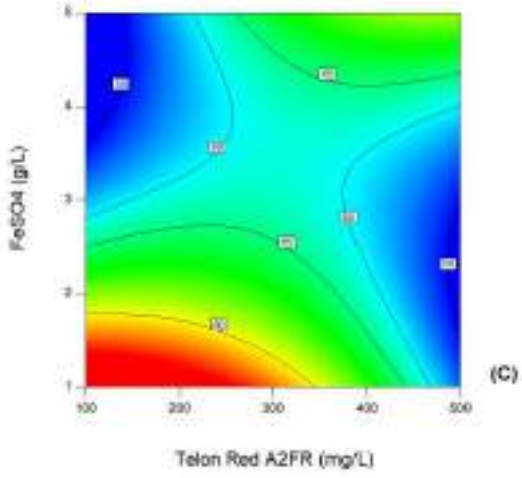

Figure 4. Effect of process parameters in removal capacity of Telon Red A2FR textile dye using $FeSO_4$ coagulant. (A) acidic pH condition, (B) natural pH condition, (C) basic pH condition.

3.2. Coagulation Using Iron (II) Sulfate

Iron salts generally have wider pH range for effective coagulation than aluminum that change from 4 to 9. Reaction 3 occurs when iron (II) sulfate is added to the water in the presence of alkalinity (Tchobanoglous *et al*., 2004). When sufficient alkalinity is not present to neutralize the sulfuric acid production, the pH may be reduced in reaction 4 (Tchobanoglous *et al*., 2004):

$$FeSO_4.7H_2O + 2HCO_3^- \rightleftharpoons Fe(OH)_2 + 2CO_2 + \\ +7H_2O + SO_4^{-2} \quad (3)$$

$$FeSO_4.7H_2O \rightleftharpoons Fe(OH)_2 + 5H_2O + H_2SO_4 \quad (4)$$

In the study, dye removal efficiency and removal capacity using iron (II) sulfate was obtained between 4.8-94.2% and 2.57-116.22 mg dye/g coagulant, respectively, as outlined in Table 1. Dye removal increased with decreasing dye concentration and increasing $FeSO_4$ dosage. In Figures 3 and 4, dye removal efficiency and removal capacity were obtained as basic pH > natural pH > acidic pH. The highest dye removal efficiency was achieved with 100 mg/L Telon Red A2FR and 5 g/L $FeSO_4$, and the highest removal capacity was achieved with 300 mg/L Telon Red A2FR and 1 g/L $FeSO_4$ at basic pH conditions.

4. CONCLUSION

The influence of coagulant type was investigated in the removal of Telon Red A2FR textile dye by chemical coagulation in a batch system. Aluminum sulfate ($Al_2(SO_4)_3$) and iron (II) sulfate ($FeSO_4$) coagulants were used as inorganic coagulants due to their extensive usage in water and wastewater treatment facilities. Dye removal efficiency using aluminum sulfate and iron (II) sulfate was obtained between 13.1-99.6% and 4.8-94.2%, respectively. Removal capacity using aluminum sulfate and iron (II) sulfate was achieved between 2.41-610.65 mg dye/g coagulant and 2.57-116.22 mg dye/g coagulant, respectively. Dye removal efficiency and removal capacity were found as basic pH > natural pH > acidic pH. The highest efficiencies were achieved at basic pH conditions. Dye removal increased with increasing dye concentration and decreasing $Al_2(SO_4)_3$ dosage when $Al_2(SO_4)_3$ coagulant was used. However, dye removal increased with decreasing dye concentration and increasing $FeSO_4$ dosage when $FeSO_4$ coagulant was used. The performance of aluminum sulfate was found better than iron (II) sulfate.

REFERENCES

Körbahti, B.K. (2007). “Response surface optimization of electrochemical treatment of textile dye wastewater”, *Journal of Hazardous Materials*, Vol. 145, No. 1-2, pp. 277-286.

Körbahti, B.K. (2011). “Optimization of Electrochemical Oxidation of Textile Dye Wastewater using Response Surface Methodology (RSM)”, Gökçekuş H., Türker U., LaMoreaux J.W. (Eds.), *Survival and Sustainability: Environmental Concerns in the 21st Century*, Springer-Verlag, Berlin, Germany, Part 7, pp. 1181-1191.

Körbahti, B.K. and Turan, K.M. (2016a). “Electrochemical Decolorization of Reactive Violet 5 Textile Dye using Pt/Ir Electrodes”, *Journal of the Turkish Chemical Society, Section A: Chemistry*, Vol. 3, No. 3, pp. 229-246.

Körbahti, B.K. and Turan, K.M. (2016b), “Evaluation of Energy Consumption in Electrochemical Oxidation of Acid Violet 7 Textile Dye using Pt/Ir Electrodes”, *Journal of the Turkish Chemical Society, Section A: Chemistry*, Vol. 3, No. 3, pp. 75-92.

Minnesota Rural Water Association (MRWA). (2009). “Coagulation”, *Minnesota Water Works Operations Manual*, USA.

Tchobanoglous G, Burton F, Stensel H. (2004). *Wastewater Engineering, Treatment and Reuse*. McGraw-Hill, USA.

AKKALE CISTERN IN MERSIN-ERDEMLI: STATIC ANALYSIS AND RISK ASSESSMENT

Pierluigi Abiuso[1], Donato Abruzzese[*1], Piera Cammarano[1], Srey Mom Vuth[1], Paola Paterna[1], Nida Nayci[2]

[1] Univ.of Rome "Tor Vergata", Faculty of Engineering, Dept.Civil Eng.&Computer Sciences, Rome, Italy, abruzzese@uniroma2.it

[2] University of Mersin, Faculty of Architecture, Graduate Program in Conservation of Cultural Assets, Mersin, Turkey, nidanayci@mersin.edu.tr

ABSTRACT

The paper deals with the structural analysis of the ancient cistern located in archaeological site of Akkale in Erdemli (Mersin) in Turkey. The cistern, even though discovered many years ago, has been for longtime abandoned. Recent policy is oriented in reuse of the structure, as archaeological/monumental site, as well as to rehabilitate the architecture in order to preserve it. A team from University of Rome "Tor Vergata" and from University of Mersin, organized a surveying campaign for structural analysis and evaluations on existing conditions of the building, its material and structural risk assessments, since the site will be opened to visitors. Surveying activity of the geometry of the monument and limited analysis of samples collected on site provided basic and ineludible information to use in the subsequent numerical/geometric analysis. The Cistern is one of the biggest closed reservoirs of ancient Olbian region of Eastern Rough Cilicia from late Antiquity Period, realized partially buried in the soil, with a large roof supported by a double order of masonry arches. The analysis has been carried out performing standard simplified approach, but also comparing the results with more sophisticated Finite Element models. The results of the analysis are encouraging, and it seems that only limited works should be done in order to allow visiting people inside the structure. Further and periodical chemical analysis are suggested, in order to monitor the state of the material and the possible decay.

Keywords: *Akkale, Cistern, Masonry Structure, Structural Analysis, Risk Assessment*

*Corresponding Author

1. INTRODUCTION AND HISTORICAL FRAMEWORK

Erdemli-Silifke coastal region (Mersin), which was called as the *Olba Territorium* in Eastern Rough Cilicia during ancient times, possess one of the richest water works and rainwater cistern systems of classical times. Need for fresh water is one of the crucial factors in development of cities throughout history. The hot and drought climate of the region caused scarce surface and ground water as similar today. For this reason; important settlements of the Olba region were supported by fresh water collected from springs of higher sections of the Lamas Valley and transmitted via underground galleries, surface water channels and aquaducts travelling approximately 30 km. distance. During the Roman and Late Antiquity periods, there were three remarkable water works in the region: Olba, Diocaesarea, Elauissa Sebaste-Korykos water systems (Bildirici, 2009). These historic water systems are named after the cities that they used to serve. Among them; Eluissa Sebaste-Korykos water system was developed to transport water from the Lamas Valley to the important coastal settlements of Elauissa-Sebaste and Korykos. The fresh spring collected at 100 m of the Lamas Valley and 17 km away from Kızkalesi was transmitted through galeries (1.5 x 1.5 m) carved into the western façade of the valley towards the Kayacı location by coastal plain; and then transferred along the coast passing hills via surface water channels and valleys via aquaducts until the port settlements of Elauissa/Sebaste and Korykos located in the west (Bildirici, 2009). This water system has seven aquaducts in total; which makes it remarkable when compared to other two systems of the region.

Akkale, located in Tırtar of Erdemli town today, was one of the important ancient port towns of Olba Territorium during classical times. Archaelogical surveys conducted by Mersin University Research Centre of Cilician Archaeology (KAAM) and Mersin Museum since 2017 proved that ancient settlement of Akkale used to be small but important settlement functioned as a port facility housing significant monuments such as harbour bath, accommodation

facility (inn), public cistern, monumental tomb and remains of religious buildings (Aydınoğlu, 2017). There is one of the largest public cisterns of Olbian region located in the centre of this facility, which is called as Akkale cistern. Archaeological surveys also showed that remains of water channels that led from Elauissa-Sebaste Korykos water work towards Akkale. Moreover, there were other water structures excavated nearby Akkale cistern indicating that there was an integrated water distribution network through the settlement. Akkale cistern could have functioned as the main reservoir of this harbor facility, where the water taken from Elauissa- Sebaste Korykos water work, was stored before its distribution to important buildings of the settlement such as bath building, fountain (located on the paved street of the city), and even ships awaiting in the harbor.

Fig.1- Large cistern structure in Akkale site.

1.1 Description of Akkale Cistern

Akkale cistern testifies with a potential volume of 7000 m^3 (7 million liter) for activities of local population in managing the harbor traffic and other public representative function. The cistern has rectangular plan with 21.53 x 36.40 m. It was constructed with stone masonry technique which was embedded into rock-cut terrain. North wall of the cistern is supported by terrain while south wall is constructed with stone masonry wall of 1.50 to 1.80 m. thickness. The interior height of cistern is 9.80 m with a vaulted superstructure supported by two rows of arcades. Each arcade has seven arches supported by eight pillars. The cistern has flat roof cladded with cut stone pavements, remains of which can be seen today.

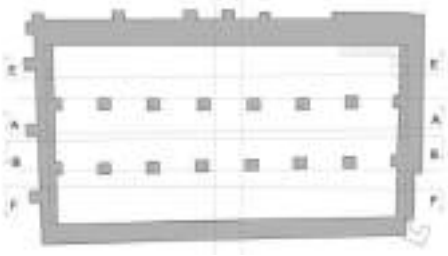

Fig. 2 – Plan of the Cistern

There is secondary masonry wall attached to west facade of the building which was used as walking platform to enter into the cistern. There are three window openings in this facade, where the third one located in the south opens to stone stairs leading into the cistern. It must have been used for control and cleaning of the reservoir as typically seen in ancient public cisterns of the region. The top level of east facade is slightly demolished; but remains of window sills show that there must have been three windows on this facade as well.

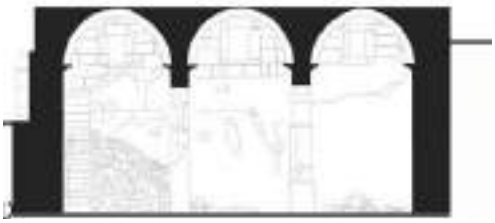

Fig.3 – Transversal cross section of Cistern

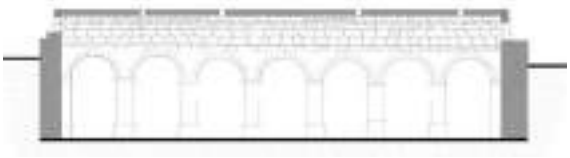

Fig.4 - Longitudinal cross section of Cistern

2. AIM OF THE PAPER

Showing a valuable example of ancient hydraulic engineering of the Olba region; Mersin University, Mersin Museum (Ministry of Culture and Tourism) and Çukurova Regional Development Agency joined their institutional capacities in order to conduct historical survey of Akkale ancient settlement, to start architectural conservation process for the ancient cistern and visitor management program for the whole site. The research program named as “Feasibility Research for Survey, Conservation and Presentation of Akkale (Erdemli) Archaeological Sites” has been conducted by a multidisciplinary team composed from archaeologists, conservation architects, geological engineers, structural engineers and city planner; and supported by Çukurova Regional Development Agency and Mersin University during 2017-2018.

Within the framework of this wider research program; this paper focuses on structural surveys that have been prepared in order to contribute to the study of the Akkale cistern. The focus analysis has several targets:

a) to assess historical safety of the structure (cistern) now-as-the-past, trying to understand the behavior of the original structure, as per original construction. It means consider the cistern full of the water, as it could be at the peak of its activity.
b) to assess static conditions of the existing structure (cistern without water), related mostly to the surrounding conditions offered by the terrain and soil characteristics.
c) to develop proposals in order to guarantee structural safety of the building during architectural conservation studies, possible reinforcing/

strengthening activity in local critical parts

d) to guarantee safety during possible cleaning activity inside the construction as well as during possible local excavation activity outside the construction.
e) finally, but not less important, provide some information and suggestions for possible future re-use of the Cistern for visitor purpose.

3. GENERAL INFORMATION ON THE STRUCTURE AND DATA COLLECTION

The existing information available for the structures has been provided after the archaeological and architectural survey of the building. The provided documents include;

- Surveying maps, plans, cross sections, side views, internal and external, provided by a surveying by Total Station equipment. Generally it considers a number of point to be connected afterword in order to reconstruct the imagine of the structure.
- Maps, plans, cross sections, side views, internal and external, carried out by a meticulous, even been still preliminary, reconstruction work, trying to provided most of the information useful to understand functions, structure, construction technique, architectural details of the cistern.
- Preliminary geological and geotechnical investigation on the soil.
- Material information provided by Conservation Laboratory of Ministry of Culture in İstanbul.

The documentation obtained preliminarily has been very useful to perform a satisfactory first level of structural analysis of the construction, as well as to assess risk conditions for several and different situations such as during further surveying, archaeological excavation, local maintenance or reinforcing works, public access to the structure.

The information obtained for the soil mechanic characteristics and the strength/elastic modulus/weight of the construction material needs to be included in the second phase of the research to clarify following questions:

- How much the lateral walls could be considered as part of the construction instead of part of the soil, in the sense that the possible cladding on the wall should be considered not structural
- The same than the previous question, related to the floor (apparently only natural excavated rock surface).
- Is there is any crack in the floor rock or in the wall, which will also testify some settlement (apparently not existing) of the structure?
- Elastic modulus, specific weight, cohesion, hardness, ultimate resistance stress of the different rocks/material available on the site (1-barrel vault, 2-longitudinal arches, 3-columns, 4-lateral wall, 5-filling material, 6-foundation/surrounding local rock).

The visual geomorphology of the site let us presume that the soil surrounding the cistern has some characteristics of limestone rock, with limited fractures.

Several NDT (Non Destructive Test) help much in collecting information on hidden or buried parts, what could be very useful to have the comprehensive picture of the structure and its behavior. Some of those tests, already provided by the geologist team, are listed below:

a) Electric MASW analysis, in order to obtain a deeper information on the subsoil condition.
b) Georadar (also called GPR - Ground Penetrating Radar, Ground Probing Radar), using different kind of antenna, producing different wave length in order to penetrate more into the soil, or, even, if rolled on the wall, in order to know more about the cross section of the lateral structures (plaster thickness, cladding thickness, hardness of different layered material).
c) Structural Endoscopy, where the amount and the size of the cavities will suggest this kind of investigation.

The tests a) and b) where has been carried out, and some additional information has been collected, even though not so useful for the structural analysis, as it could be expected before the tests. In fact the quite large in homogeneity of the subsoil does not help in recognizing difference in hardness of the rocks.

4. GENERAL COMMENT ON THE STATIC OF THE STRUCTURE.

The first, visual, assessment of the structure gives the impression of a solid and robust structure. The quality of the barrel vault and the connected arches, made by quite well cut stones, with very limited thickness of mortar in the joints, let us be confident that this part of the structure is in quite good conditions.

The other structural elements, it means the lateral walls and columns, are in different conditions. The structure of the columns is not completely visual accessible, since covered by plaster or heavy leakage of water, which produces some calcareous deposit on it. Almost the same comment for the lateral walls, covered by plaster and/or calcareous incrustation.

The vertical loads have been obtained assuming the specific weight of the stone, mortar, rocks, according to the experience of the investigation team and the available literature on the subject.

The horizontal loads have been carried out according to the geometry of the structure (thrust of barrel vault and longitudinal arches), from the water pressure (during the "historical" analysis of the past of the cistern), from the ground pressure and also from earthquake.

What we assume valid and reliable is the process to evaluate the static condition of the structure, by analyzing with simplified and traditional method the structure and comparing those results with some global analysis carried out with structural analysis code by computer.

The single specific weight of the materials have been considered in order to perform numerical analysis, as for barrel vault stone, arch stone, masonry wall, filling, columns.

5. GEOLOGICAL GEOTECHNICAL PROPERTIES OF ROCKS USED IN AKKALE RUINS

Extensive geological and geotechnical studies carried out in the field and laboratory shown that most of the construction material for the cistern was limestone

blocks. A full report by Güler and Tağa (2018) is available, from where most of the following information are taken.

In the respect of the monument, no sample has been taken from the construction, but several photos and *de visu* inspection. Then most of the collected results come from the analysis of surrounding local material, assumed belonging to the same kind of rocks.

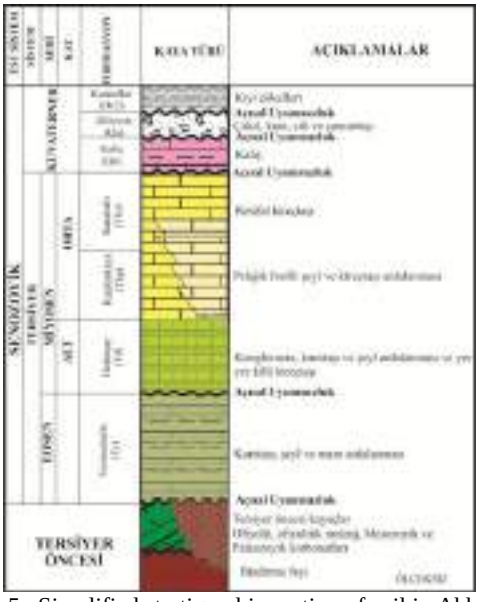

Fig. 5. Simplified stratigraphic section of soil in Akkale (extract from Güler&Taga, 2018)

Mechanical properties of the limestone blocks and bedrock one used in the cistern structure were determined by experiments carried out in the field and in the laboratory. The mechanical properties of rock blocks used in the cistern structure were determined by sonic velocity and Schmitd hammer tests which are non-destructive test techniques (NDT), in respect of the monumental condition of the site. The mechanical properties of the limestone in the bedrock were determined by direct method on the samples taken from the limestone block in the laboratory

In addition, the mechanical properties were determined by bringing the limestone block, which was determined on site, to the laboratory in order to interpret the laboratory experiments with the experiments carried out on the spot (Table 1).

The physical and mechanical properties has been taken from block stones-cylindrical core samples drilled in the rocks, similar at that one existing in the Cistern, in the surrounding. The results are given in Table 2.

Accordingly, average uniaxial compressive strength values of rocks were determined.

The axial deformations occurring at each load stage of the uniaxial compressive strength test of the limestone unit in Akkale site were recorded and the modulus of elasticity was determined. The unit volume weight (γ, kN/m3), uniaxial compressive strength (σc, MPa) and elasticity modulus (E, GPa) of the rock to be used in the restoration of the large cistern in Akkale site were determined in the laboratory (Table 2). Poisson ratio (υ) was determined in the field by ultrasonic test, also non-destructive test techniques.

Table 1. Mechanical parameters of rock blocks in cistern structure determined by nondestructive testing methods (extract from Güler&Taga, 2018)

	Schmidt Hammer		Ultrasonic Speed	
	Ultimate	Elastic	Poisson	Dynamic
	47,51	15,35	0,22	29,59
	51,31	16,57	0,21	19,32
	51,31	16,57	0,21	20,59
	57	18,34	0,21	22,52
	37,97	16,24	0,21	23,68
	78,12	24,42	0,21	31,48
	53,52	17,27	0,21	32,3
	46,2	14,92	0,21	23,76
Max	78,12	24,42	0,22	33,42
Min	37,97	12,14	0,21	12,28
average	54,23	17,22	0,21	21,85
St dev	9,46	2,82	0,00	5,42

Of course such a results, even being correlated according to Son-Reb method, coupling Schmidt hammer and Ultrasonic device, are relatively reliable. But in some way it gives us reasonable values to use as basic information on the construction material.

Tab 2. Mechanical properties of limestone in Akkale site (extract from Güler&Taga, 2018)

Sample name	σc MPa	E GPa
A1	63,27	12,67
A2	39,45	9,00
A3	35,12	9,33
A4	41,15	10,00
B1	42,63	13,33
B2	47,21	12,86
B3	74,62	11,76
B4	69,17	16,55
B6	33,68	16,67
B7	39,48	9,67
n	12	12
Max	74,62	16,67
Min	33,68	9,00
STDEV	13,44	2,52
Average	49,93	12,49

The Elastic modulus of the material is quite high, in fact comparable with that one of a typical concrete for construction. This means that not particular deformation due to concentrated loads could be expected (see the key stone of the arches in the vault, or "tip-toe" of some damaged column) to be measured. It means negligible deformations.

The resistance stress, the limit stress measured of course is a little bit scattered, due to different condition of the tested cores, but the final consideration could be that the value of compressive resistance is quite high, comparable with a soft marble (soft granite), and the medium value appear to be comparable, if not higher, with that one of a good concrete for construction. It means that the material could stand the stress, even concentrated, due to the dead load or other possible (reasonable) live load.

Considering that for the Neapolitan yellow tuff, volcanic soft rock, the value of the porosity range from

20 to 40 % (Aurisicchio et al. 1982), and the value of 15-25 for a compact limestone, the final consideration could be that the construction material of the Akkale Cistern can be assumed to be a good strong and resistant material with a moderate (probably negligible under certain circumstances) porosity. Just for reference, we can recall the compressive resistance value for a good tuff, measured not bigger than 10 MPa, and the value for a compact limestone (soft, hard) ranging from 20 to 100 MPa.

6. SIMPLE ANALYSIS OF THE BARREL VAULTS AND ARCHES

In order to assess the historical stability, in the following has been considered the effect of the water pressure (now not existing anymore) on the external wall. The calculation has been carried out with hydraulic pressure("illo tempore") and horizontal thrust of the arch. As usual, in these simplified schemes, we analyze a slice of the masonry wall, assuming that all the cistern will have a similar behavior of that one analyzed.

Fig. 6 – Inner view of the Cistern

Considering the potential overturning of the lateral wall, due to the soil external pressure and to the water pressure (when the cistern was filled by water) and the opposite resistance given by the weight of the wall and the all the other structure, like vault and filling, the result of the calculation gives:

$$\eta := \frac{M_s}{M_r} = 1.136$$

where η represents the safety from geometrical point of view of the barrel vault and wall under potential water pressure and thrust of arch, by rotation equilibrium at point A (see sketch).

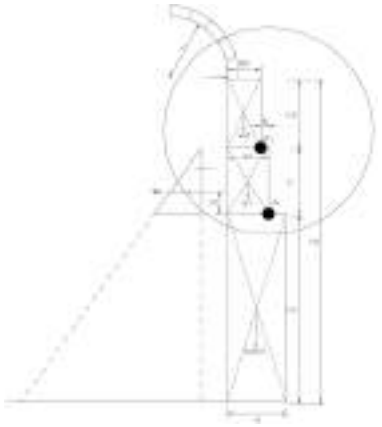

Fig.7- Water pressure diagram and vault thrust on the Cistern wall

Calculation of the stability of the wall has been also performed, with the effect of the horizontal thrust of the arch but without Hydraulic Pressure:

$V_{arc} := V_1 = 31.008\,kN$

$$\mathbf{F_{Arc\ hor} := \frac{q \cdot L^2}{8 \cdot f} = 15.504\,m \cdot \frac{kN}{m}}$$

$\mathbf{Th_{arch} = 0.6\,m}$ (thickness of the arch)

$Th_{real} = 0.4\,m$

Rotation around " A" without water pressure

Stabilizing moment: $\mathbf{M_S := 126.588\,kN \cdot m}$

Overturning moment: $\mathbf{M_0 := = 82.171 \cdot kN \cdot m}$

$$\eta := \frac{M_S}{M_r} = 1.541$$

where η represents the safety coefficient from geometrical point of view for the system barrel_vault-wall in the existing condition with thrust of arch, without water pressure. Rotation assumed at point A (see sketch)

7. THE VERTICAL SUPPORTING STRUCTURES: THE CENTRAL STONE PILLARS

Resistance of the column related to the effect of the vault can calculate by assuming the area above the columns affecting the load on the column itself. The load on the single column can be evaluated:

$W_{total} := W_{A.influence} \cdot 1.10 + W_{column} = 415.049\,kN$

The compressive stress induced in the material of the columns:

$$\mathbf{\sigma := \frac{W_{total}}{A_1} = 0.288 \cdot MPa}$$

And if Fcd, the reference ultimate stress of the material, can be assumed equal to:

$$F_{cd} := 1.5\,MPa$$

then the safety coefficient for compressive stress in the columns can be assessed as:

$$\eta_2 := \frac{F_{cd}}{\sigma} = 5.204$$

We can state that the structural safety coefficient for the columns is quite satisfactory.

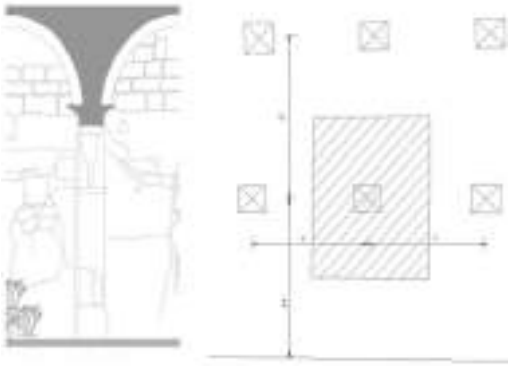

Fig,8 – The analysis of a typical central column

8. THE VERTICAL SUPPORTING STRUCTURES: THE LATERAL WALLS

The structural perimetral walls, without further and deeper investigations, are still cryptic.

In fact the structure of the walls of the cistern could be made in different way:

Digged in the local rocky, almost compact material, at the end covered with plaster, to make even the surface. The upper part, emerging on the soil surface, is clearly made by well cut stones, likely local limestone, even brought there for nearby sites;

- Digged in the local rocky, maybe fractured rocky material, at the end covered by an other layer of stones, for structure or isolation purpose. The upper part made by cut stones.

After that the further structural analysis for the static stability of the cistern will be definitely more reliable.

Anyway, as already state at the beginning of this report, the apparent, visible, wall structure, buried as well as emerging, suggests a high level of stability.

9. THE FOUNDATION

As said for the walls, also the foundation suggests several doubts about the geometry and structure morphology.

We cannot assess if the foundation is composed only by the enlarged base of the pillars, even being itself quite sufficient for the dead load (only barrel vault roof and columns resting on each foundation base) or if the base of the columns are embedded in a sort of reverse plate made by material added to the existing soil, to prevent the water leakage, or to add structural behavior.

The visual, limited, inspection suggests the first case, considering the added material as a sort of "water proof" plaster on the pavement.

Despite the fact that a deep investigation has been carried out with georadar and geoelectric investigations have been performed, it is not yet possible give the final answers to these questions.

10. THE GLOBAL ANALYSIS. LINEAR AND NON-LINEAR BEHAVIOR

The structural model prepared in order to simulate the existing structure has been arranged according to the hypothesis described in the previous text. The walls have been considered embedded in the rock, and, where buried, connected to the surrounding soil with suitable mechanical links.

Fig.9-Longitudinal view of the arches in the Cistern

The following figures show the tridimensional FEM models of the considered structure. In the first image we have the drawing of external walls masonry modeled with bi-dimensional finite elements of shell type. In the same image we can see the modeling of the supporting system of the soil, in the detail we have that the structure is partial underground therefore the translations in three directions have been considered as restrained**.**

Fig.10-FEM structural model for the only wall of the Cistern

The same restraint is shown in the second figure, where the modeling of barrel vaults and arcs is also shown. In the detail we have realized the FEM model using bi-dimensional shell elements for walls, arcs and barrel vaults while the columns have been modeled with mono-dimensional finite elements, type frame.

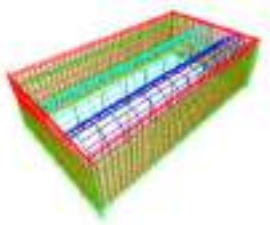

Fig.11-FEM structural model with all the structural elements

The next figure shows the zoom on the barrel vault and arch modeling. We need to explain that the filling load was applied considering a solid element representative of the granular material present on the barrel vaults. That choice is correct because the non-structural material is characterized by a unit volume weight but not by resistance parameter, therefore modeling of this element allows to consider in the

analysis only the mass of filling material and to neglect the contribution of stiffness made to the structure.

Fig.12. Representation of the filling element representative of the load applied at the structure

The seismic behavior was assess by carrying out a dynamic linear analysis of the structure, and evaluating periods and vibration modes in order to calculate the horizontal actions in the modal-spectral condition.

Regarding the modal structure behavior we have a first natural vibration period of 0,146s with a frequency of 6,77 Hz corresponding to the translation vibration mode in y direction, or rather in the more flexible direction .

In the following fig.13 we show modal response and vibration mode of structural elements in the modal condition case.

Fig.13. Modal response and vibration mode of structural elements

The analysis of structure behavior was conducted considering different load conditions. In the specific case we show the barrel vault response in seismic load condition, and the fig.14 shows the compressive stress S22 contour.

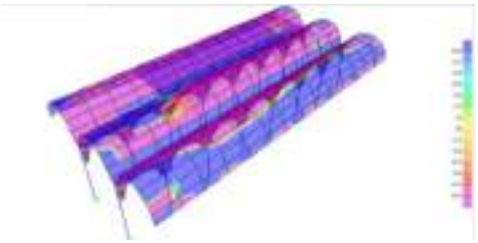

Fig.14-FEM structural model results for the Cistern's vault. Compressive stress S22

The contour represents the stress response of barrel vaults and arcs when we have the seismic load in the x direction, or else, in the axis of barrel vault direction and we can see that the stress of masonry element change in a range of +50MPa and -50MPa.

In this case, we propose images of the most burdensome load condition by way of example.

In the follow we will show the section cut in two different position of barrel vault, or in other words, in the two most important sections of barrel vault in terms of static structural behavior, then in the key section and in the impost section of considered element. The section cut allows us to evaluate the resultant forces in there section, integrating the stress.

The tables summarize the results for each section and for each barrel vaults in terms of horizontal, vertical forces and stress characteristic.

Table 3. Stress in the vault according to FEM Model

Position	Horizontal force [kN]	Vertical force [kN]	Resultant [kN]	σ [Mpa]
Key Block of vault	27,33	22,89	35,65	0,033
Impost Block of vault	20,00	50,00	53,85	0,2

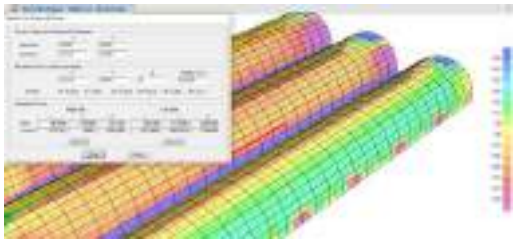

Fig.15 - Stress in the vault according to FEM Model

In this section we show the base reaction at the supporting restraint for each load conditions of columns that are mono-dimensional finite elements.

In the detail in the following tables we can see the values of axial force (P), shear force (V2,V3), bending moment (M2,M3), torsion (T) and the stress values (S11).

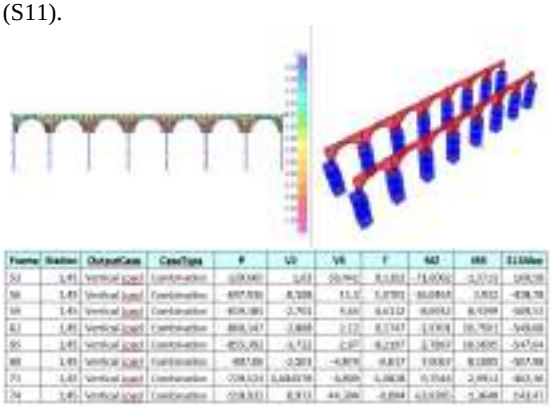

Fig.16 – Vertical Stress in the columns according to FEM Model

11. RESULTS AND COMMENTS

The structural stability of the historical cistern in Akkale has been analyzed in the following way:

- A simple numerical analysis, in the frame of the masonry analysis for arch, vault and cupola, in this case having the barrel vault and the arch as main important structural elements supporting the roof
- A more sophisticated Finite Element Analysis has been carried out in order to identify some specific behavior of the coupled barrel vaults and arches;
- One specific numerical analysis has been done on

some columns;
- An assess of the foundations has been performed.

The results of these analysis are quite encouraging, meaning that no specific critic section or structural element has been found during the numerical evaluation.

The investigation on site and in laboratory on similar material to that one existing in the Cistern gave some very positive results in term of resistance, confirming the comment done after the numerical analysis. No damage has been suffered by the monument during these investigations, since the only contact with the Cistern material has been done adopting Non Destructive Test, respecting the monument.

The safety factor which can be mentioned at the end of all the tests and analysis, if nothing special will happen to the structure in the near future, is quite high, we can state around "5".

12. RISK ANALYSIS AND SUGGESTION TO IMPROVE THE SAFETY OF THE STRUCTURE, SHORT AND LONG TERM

Not many suggestions could be given in order to improve the structure without suitable and further investigation on structural elements, material, soil. As previous stated, the structure appear quite solid, and light archaeological activities or investigation could be performed without particular precaution, in addition to typical reasonable precaution adopted in construction site.

In advanced step, when the cistern will be considered to be open to visitors, probably a deeper risk analysis should be performed.

From the report describing the analysis carried out on site as well as in the laboratory, it is clear that the material constituting the structure of the Akkale Cisterne can be considered a "good" construction material, with mechanic characteristic comparable with that of a good modern concrete.

At this point the only question arises about the amount of "local" damage of the structural elements, due to the intentional human vandalism, to the aging use of the structure or the atmospheric attack. This kind of damage in most of the case is visible, measurable but limited. In some rare point the damage is hidden (like in the bottom of some columns) since the visible part do not guarantee about internal, hidden, condition. Probably one deeper analysis could be a careful endoscopy investigation of some part of the bottom of the columns and other suspect masonry element.

Of course, now that we have more information about the existing material, after a deeper study and pondering on the possible local intervention on the stones, a reasonable static, and not only cosmetic, conservation solution could be found.

ACKNOWLEDGEMENTS

The authors are gratitude to colleagues in our project team, Assoc.Prof.Dr. Umit Aydınoğlu, Dr. Ahmet Mörel for their archaeological surveys; Assist.Prof.Dr. Hidayet Tağa and Prof.Dr.Cuneyt Özdemir for their geological surveys, who altogether provided multidisciplinary outcomes of the whole research. We also give special thanks to architect Gökçe Turkoğlu, archaeologist Okan Özdemir and restoration specialist Vejda Arslan for their great supports during architectural surveys and drawings of the project. Lastly, we thank to Betül Kiminsu -the principal architect from Adana Regional Survey and Monuments Directorate, Ministry of Culture and Tourism- for her coordination supports during project.

REFERENCES

Abruzzese, D., G.Lanni. (1998). "On the strength of historical reinforced masonry buildings with crossed vaulted floors" *Proc. XI ECEE*, Paris

Abruzzese, D., G.E. Cinque, G. Lo Gatto. (2004). "Analysis of a Roman masonry flat-slab in Hadrian's Villa, Tivoli" *Proc. "Structural Analysis of Historical Constructions"*, University of Padova

Aurisicchio, S.; Evangelista A.; Masi P. (1982). "Il tufo giallo napoletano: permeabilità ed impregnabilità con monomeri acrilici." *Rivista Italiana di Geotecnica,* Roma

Aydınoğlu, U., (2017). "Archaeological Report, Feasibility Research for Survey" *Conservation and Presentation of Akkale (Erdemli) Archaeological Sites.*

Akgül, Z. (1980). "The Basilica Cistern, (Istanbul)" *Aytur Turistik Yayincilik*, Istanbul

Bildirici, M., (2009). "Tarihi Su yapıları -Konya Karaman Niğde Aksaray Yalvaç Side Mut Silifke", *T.C. Çevre ve Orman Bakanlığı Devlet Su İşleri Genel* Müdürlüğü, Ankara, 486-487.

Borel, L., C. March, S. Desoutter. (2007). "El Nabih Cistern" *Centre d'Etudes Alexandrines, in Alexandrie, Mètaphore de la francophonie*

Como, M. (2016). "Statics of Historic Masonry Constructions" *Springer Series in Solid and Structural Mechanics, Springer*

Gueguen, Philippe. (2013). "Seismic Vulnerability of Structures" *John Wiley & Sons, Inc.* ,London

GÜLER, C., H. TAĞA,(2018). "Akkale (Erdemli-Mersin) Ören yeri Büyük Sarnıç Yapısı ve Civarında Gerçekleştirilen Jeolojik-Jeofizik Çalışmalar" *Scientific Report*, Mersin, 27 February 2018

Haselberger, L., R. Holod, R. Ousterhout, (2016). "Against Gravity" University of Pennsylvania

Koyuncu, I.; Altinbas, M.; Aydin, A.F.; Guclu, S.; Turken, T.; Ecis, R.; Yildiz, A.; Tutuncu, H.. (2012). "Nomad Cisterns in Antalya, Turkey" *Proceedings of the 3rd IWA Specialized Conference on Water and Wastewater Technologies in Ancient Civilization*, Istanbul, Turkey, 22–24 March

Mays, L., G. P. Antoniou, A. N. Angelakis. (2013). "History of Water Cisterns: Legacies and Lessons" *Water, Vol.5, Issue 4, Nov. 2013*

CISET - 2nd Cilicia International Symposium on Engineering and Technology
10-12 October, 2019, Mersin / TURKEY

Application of Supercritical Drying for Food Products

Eda ADAL [*1]
[1] Gaziantep University, Engineering Faculty, Food Engineering, Gaziantep, Turkey, adal@gantep.edu.tr

ABSTRACT

Drying is used to lower the moisture content and to prolong the shelf life of food so as to reduce water activity and prevent spoilage. When the food products are dried, they go through some changes that decrease their quality compared to fresh material. The aim of development drying technologies is to reduce these changes while increasing process efficiency. There are several drying methods that are used in the food industry. Conventional air-drying is the most commonly used drying process in the food. It produces products that are characterized by low porosity and high density. The conventional air-drying is commonly occurred under high temperature (65-85°C) which causes damage to the microstructure and may also have a negative effect on the color, texture, taste, aroma and nutritional value of the product e.g. oxidation vitamins. There is a need for new drying technique that could be used in food industry. When compared supercritical CO_2 with a conventional air-drying technique, it has good outcomes. Supercritical fluid environment has been seen to retain product shape much better than air-dried. Supercritical CO_2 techniques have been previously attracted interest in other industries e.g. for drying gel components of silica and create other inorganic porous structures. In food industry, supercritical fluid processing method is becoming a popular focus of research. In this study, working principle, application, advantageous and limitation of supercritical drying and effect of it on food materials will be presented by giving examples.

Keywords: *Supercritical drying, food, vegetables, fruits*

[*] Corresponding Author

1. INTRODUCTION

The principle of drying (or dehydration) is to remove water from foods. The main purpose of drying is to lower the moisture content and to extend the shelf life of food in order to reduce water activity and prevent spoilage. Water activity is a very important factor to control the shelf life, because most bacteria are unable to grow below a value of 0,91 and moulds growth decreases below 0,80 (Brown et al., 2008). Water activity also inhibits the activity of enzymes. When the food products are dried, they go through some changes that reduce their quality compared to fresh material. The aim is to improve drying technologies to minimize these changes while maximizing process efficiency (Fellows, 2000). Changes in nutritional value and color play a significant role in some foods but the main changes in dried foods are related to the texture (microstructure) and loss of aroma. Food structure influences nutritional availability, chemical and microbiological stability as well as texture physical properties. Additionally, moisture removal reduces the weight and the bulk of food products and facilitates transport and storage. It also decreases costs of both transport and storage (Brown et al., 2008; Fellows, 2000).

There are several drying methods that are used in the food industry. The most commonly used drying process in the food industry is conventional air-drying. It produces products that are characterized by low porosity and high density. The conventional air-drying is commonly occurred under high temperature (65-85°C) which causes damage to the microstructure and may also have a negative influence on the color, texture, taste, aroma and nutritional value of the product e.g. oxidation vitamins (Brown et al., 2008; Fellows, 2000).

Other alternatives for air-drying are for example freeze-, microwave-, vacuum- and osmosis drying. In freeze drying, the desired preservative effect is achieved by reduction of water activity without heating the food. Freeze-drying works by freezing the material below the eutectic point of the mixture and then reducing the surrounding pressure and adding enough heat to allow the frozen water in the material to sublime directly from the solid phase to gas. Freeze-dried products which have good nutritional qualities and sensory characteristics are better retained than in air-drying. Also the porosity of the products is higher than e.g. in air-drying and microwave drying (Brown et al., 2008; Fellows, 2000). However, the operation is slower than conventional drying and the technique is generally considered to be expensive and energy consuming (Brown et al., 2008; Fellows, 2000). Microwave has a low thermal conductivity which has positive effect to heat transfer. This prevents damage to surface, improves moisture transfer during the later stages of drying and eliminates case hardening (Fellows, 2000). Microwave drying promotes quick drying, but it is difficult to control the rapid mass transport which may cause damage in the form of "puffing". In addition, this technique is associated with high start-up costs and ongoing costs (Brown et al., 2007). In vacuum drying the partial vacuum is drawn in the chamber and steam or hot water is passed through the hollow shelves to dry the food. Rapid drying and limited heat damage to the foods make it suitable for heating-sensitive food. However the rapid drying and high temperatures causes greater changes to the texture of foods than moderate rates of drying and lower temperatures. As in a freeze-drying, reverse osmosis dry the food without heat and produce good retention of sensory and nutritional qualities. In reverse osmosis the high pressure is used to separate water from low-molecular-weight solutes (monosaccharide). These all methods have relatively high capital costs and low production rates (Fellows, 2000).

There is a need for new drying technique that could be used in food industry. The possibility of drying with supercritical CO_2has been examined and it has good outcomes compared with a conventional air-drying technique. Supercritical fluid environment has been seen to retain product shape much better than air-dried. Supercritical CO_2 techniques have been previously attracted interest in other industries e.g. for drying gel components of silica and create other inorganic porous structures (Brown et al., 2008). In food industry, supercritical fluid processing method is becoming a popular focus of research. Supercritical CO_2 drying method is described in the following section.

2. SUPERCRITICAL FLUID

A supercritical fluid (Figure 1) is a substance which has temperature and pressure above its critical point. It can diffuse through solids like gas, and dissolve materials like liquid. When substance reaches close to the critical point, small changes in pressure or temperature result in large changes in density, allowing many properties to be used. Supercritical fluids, in particular CO_2, are used in the industry generally as a substitute for an organic solvent like hexane and dichloromethane in extraction process. Supercritical fluid extraction is the process separating one component from another using supercritical fluid as the extracting solvent.

Advantages of using supercritical fluid compared to using of organic solvent are that there will always be some residual solvent using of organic material like hexane in an extraction process. These residual remains could be harmful of environment and consumers. CO_2 is easy to remove simply by reducing the pressure and disappear almost leaving no trace. That is why it is very environmental friendly to use. A particular advantage of supercritical fluid as a drying method is that vapour-liquid interfaces and capillary-induced tensile stress can be avoided. The product preserves its structure after process, supercritical fluids causing no tension on the surface of the product. CO_2 has a low critical temperature 31°C and pressure 73.8 bar. That is an advantage to compare as conventional drying. CO_2 is a non-polar solvent, therefore the solubility of water is quite modest. Increasing the solubility of polar substrates is possible via adding small quantities of co-solvent, for example ethanol. Adding co-solvent in the extraction process its become more selectivity and it gives further dimension to the range of solvent. The mechanism of using co-solvent is thought to involve specific chemical and physical interactions between co-solvent and solute, including hydrogen bonding and dipole-dipole attractions (Ekart et al., 1993).

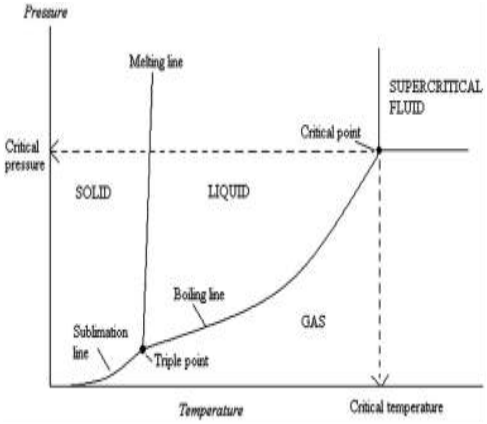

Figure 1. Phase diagram of a pure substance. The supercritical state is achieved above a critical point, which is the highest temperature and pressure at which vapour/liquid equilibrium can exist (Brown et al., 2008)

3. SUPERCRITICAL CO_2 DRYING METHOD

3.1 Background

There has been only little study in the field of food processing. However, supercritical drying methods are already used in pharmaceutical and chemical industries. In pharmaceutical industries there is a large interest in preparing pure powders and aerosols (Tedeschi et al., 2009). Usually the problem has been the tendency of small particles to agglomerate during powder preparation. In chemical indistry, in fabrication of nanostructures (gels) made up of silicon there has been a problem because gels collapse easily. This is due to the surface tension in the rinse solution. Also the impact of capillary forces in collapse has been noticed (Namatsu et al. 1999). Supercritical drying methods have shown potential to solve these problems during manufacturing of gels and powders (or aerosols).

3.2 Formation of capillary forces during drying

Agglomeration due to adhesion caused by capillary forces during the drying process can be reduced, if not completely nullified, if the liquid phase contact with the particles can be removed while avoiding formation of a gas-liquid interface between two or more particle surfaces. Formation of gas-liquid interface usually leads to formation of capillary forces. In Figure 2 there is a depiction of capillary forces in different drying methods. Evaporation (A) crosses the gas–liquid phase boundary leading to capillary forces. During freeze drying (B), low temperature and low pressure are used and the liquid is first frozen then removed by sublimation. If the pressure is not sufficiently low, condensation is possible and leads to formation of capillary forces. Supercritical drying (C) takes path to high temperature and high pressure completely avoiding the formation of capillary forces through the entire process.

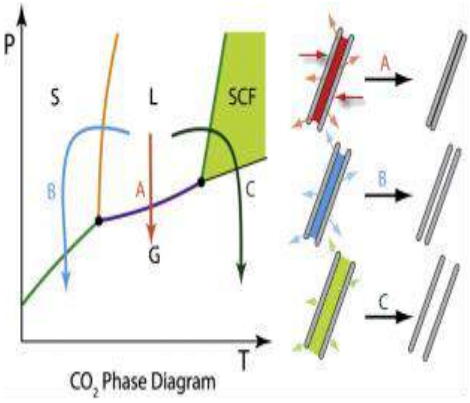

Figure 2. A depiction of capillary forces in different drying methods (Tedeschi et al., 2009)

3.3 Preparation of an aerosol

Particle matrix is first mixed with a pre-solvent to form a slurry. Pre-solvent (such as isopropanol) can be removed from particle matrix by liquid CO_2. Because of liquid CO_2's surface tension properties it will preferentially wet the particle surface thus replacing the pre-solvent. After that the liquid CO_2 is taken past the critical point by applying heat and thus the formation of a liquid-gas interface is avoided completely. The supercritical fluid can then be vented from the containing vessel, leaving a dry, dispersible product (Tedeschi et al., 2009).

3.4 Fabrication of nanostructure gels

Namatsu et al. (1999) noticed in their study that silicon patterns free from any collapse were obtained by using supercritical drying in fabrication. This is due to surface tension of the rinse solution (supercritical CO_2 in this case). Supercritical CO_2 has a surface tension of zero and that's why it didn't cause the gel to collapse.

4. EQUIPMENT FOR SUPERCRITICAL DRYING

Because supercritical drying has only few applications in food processing, there are no commercial equipment available. However, this method is used in other industries, such as medical and chemical industries and equipment for these are commercially available. In Figure 3 there is a schematic representation of an apparatus that was used in a study (Brown et al., 2008). In this study they investigated if supercritical drying method is suitable for drying carrots. The Figure and more information about the study are shown below.

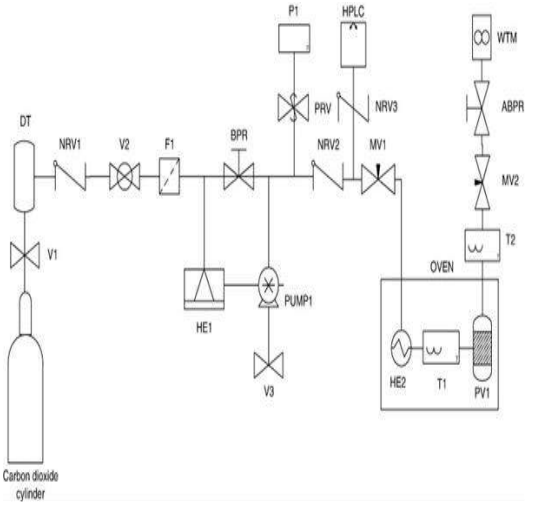

Figure 3. Schematic representation of the experimental apparatus (Brown et al., 2008)

5. APPLICATION: DRYING OF CARROTS WITH SUPERCRITICAL CO_2

Brown et al (2008) dried carrots with supercritical CO_2, modified supercritical CO_2 (includes ethanol) and air. Using supercritical CO_2 in drying process of foods the products were more porous and had lower density and also softer texture than those products which were dried using air. Samples were dried until <10 % w/w moisture content was reached. The fastest drying method was drying with air; it took only 50 minutes to reach the wanted moisture content (10 % w/w). Drying with supercritical CO_2 took 150 minutes and drying with modified supercritical CO_2 took 110 minutes to reach the 10 % w/w moisture content. The moisture removal increased with increasing temperature.

5.1 Drying kinetics in supercritical drying

In Figure 4 there are drying profiles for raw carrot pieces. As can be seen from the Figure, the driest products were obtained with modified supercritical CO_2. According to Brown et al. (2008), the differences in moisture content between carrots dried in pure or modified CO_2 became statistically significant at end of 90 min. Drying to any particular moisture content was seen to take longer for supercritical drying than for air-drying, although comparisons of this nature must be treated with caution due to the different flow regimes. The shape of the drying profiles in this Figure can be seen to differ between air and pure supercritical CO_2. This indicates that the drying kinetics between air-drying and supercritical drying is different. They suggested that air-drying kinetics follow first order relationship. In contrast supercritical CO_2 drying seemed to follow zero order relationship. This finding suggests that supercritical drying with CO_2 proceeds via a different mechanism to that occuring in air-drying (Brown et al., 2008). More information about heat and mass transfer mechanisms during supercritical drying should be gained in the future.

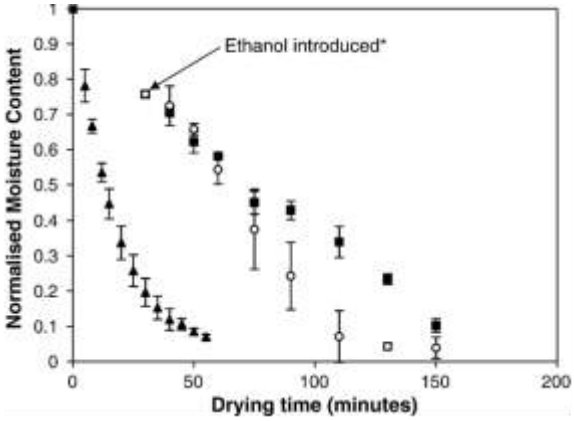

Figure 4. Drying profiles for raw carrot pieces dried in air (▲), pure $scCO_2$ (■) and scCO2 modified with 6 mol% ethanol (○). All experiments were carried out at 20 MPa and 50 °C (Brown et al., 2008).

5.2 Method's effect on material

5.2.1 Texture

In Figure 5 there are carrots which have been dried with different methods in the study (Brown et al., 2008). All carrot pieces were circular in cross-sectional shape before drying. As it can be noticed from the Figure 3, the samples dried with supercritical CO_2 maintained the original structure better compared to drying with air. Using modified supercritical CO_2 the original structure was maintained best (d), the sample had low density and porous structure with increased intercellular space. A temperature change from 50 ºC to 60 ºC (b and c) produced a sample which had structure closer to the original structure.

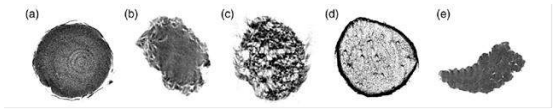

Figure 5. Cross-sectional X-ray images of (a) raw carrot pieces dried in (b) pure $scCO_2$ at 50 ºC, (c) pure $scCO_2$ at 60 ºC, (d) modified $scCO_2$ at 50 ºC, (e) air at 50 ºC (Brown et al., 2008)

5.2.2 Color

Supercritical CO_2 -method also affects the color of the products. Raw carrot (a) is darker than the other samples due to higher moisture content. The results indicated that the color was paler in those products (b, c and d in the picture above) which were dried using either pure or modified supercritical CO_2 compared to raw products (a in the picture above). Supercritical drying can lead to a decrease in the transparency of the products cell walls, but it is reversible when rehydrated. In air-drying the products were darker than the raw products, because the cellular structure is collapsed during air-drying which leads to products shrinkage and therefore also to the increase in carotene concentration (e in the picture above). The carrot which was dried with pure supercritical CO_2 at temperature of 50 ºC had almost the same density as the carrot dried with air (e) but there is happening less

shrinkage (Brown et al., 2008).

6. EXPERIMENTAL PILOT STUDIES

When a new food processing method is under development, many experiments are needed to determine, which materials are suitable for this process. Development may arise from a lack of suitable application for processing certain materials. Supercritical fluid is regarded as a potential, gentle drying method of natural extracts which typically contain some sensitive substances. Some experimental pilot studies have already been done: Meterc et al. (2008) studied drying of aqueous green tea extracts using a supercritical fluid spray process.

Green tea leaves contain polyphenols, which are composed of seven kinds of catechins and their derivates. One of them, epigallocatechin gallate (EGCG), is at least 100 times more effective than vitamin C and 25 times more effective than vitamin E. EGCG is the major component of the polyphenolic fraction of green tea; it makes about 10 - 50 % of the total green tea catechins. (Meterc et al. 2008).

Green tea's active ingredients are usually isolated by extraction with different organic solvents or water. The solvent is then removed by different processes, e.g. by spray drying or by freeze drying. As an alternative to these processes a high-pressure technique called "particles from gas saturated solutions" (PGSS) can be used. The maximum operating pressure of the plant (Figure 6.) is 200 bar and the maximum temperature is 250 ºC. The flow of the heated green tea solution (i.e. green tea leaves extracted with water) can be adjusted to a maximum of 5 kg/h. CO_2 is stored at vapor pressure in a high-pressure tank. It is taken as liquid from the tank with a certain pump and the flow is adjusted to 10-60 kg/h. Subsequently the gas is heated in a heat exchanger. CO_2 is led through a valve into the static mixer where it contacts with a solution to be dried. During the mixing supercritical CO_2 is partly dissolved in the green tea solution and the mixture is sprayed via a single path nozzle into a spray tower. As the gas is expanded, fine droplets are formed. The green tea extract is “inside” the droplets. The heated gas evaporates the solvent (water), which is exhausted together with CO_2 by a blower. The obtained powder is collected at the bottom of the spray tower. Because of the sensitive particles of green tea the temperature on the spray tower is limited to 70 ºC. Powders with different water and polyphenol content can be produced by changing process parameters (Meterc et al. 2008).

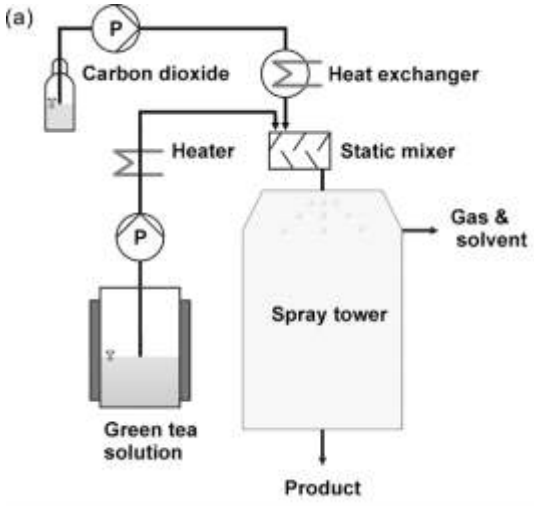

Figure 6. Flow scheme of the PGSS (particles from gas saturated solution) drying pilot plant (Meterc et al., 2008).

There are two options to remove the solvent completely. The temperature in spray tower can be increased and less CO_2 is used. The other possibility is to work at lower temperature with increasing the mass flow of CO_2. Very high temperatures in the process result in degradation of polyphenols (Meterc et al. 2008).

In this experiment the residual water content of the product varies from 5.95 to 13.05 %. The particles obtained were spherical with an approximate size smaller than 10 µm. Like the most supercritical fluid processes the drying is carried out at low temperature (30-60 ºC) and in an inert, oxygen-free atmosphere. This makes the process very promising for sensitive substances, like the polyphenols of the green tea. Dry and free flowing powders were obtained by the spray process without degradation of the active ingredients (Meterc et al. 2008).

7. CONCLUSION

Food products go through some changes during drying process. These changes reduce the quality of food products when compared to fresh products, especially their texture, nutritional value and color are affected and there can also occur some aroma losses. Because of effects mentioned above, it is desired that there will be improvements in drying technologies. It is profitable to try to minimize undesired changes in the material and at the same time to maximize the efficiency of the process.

At the moment, there isn’t any method to fill the wanted goals, so there is still a need for new drying technique that could be used in food industry. One possible technique could be drying with supercritical fluid because it retains products shape much better than air-drying, it has low processing temperature (31.1 °C) and also lower capital costs than e.g. freeze drying.

Drying with supercritical CO_2 has been examined and it has good outcomes compared with a conventional air-drying technique. Supercritical drying methods are already used in pharmaceutical and chemical industries and they have shown potential to solve some problems e.g. in manufacturing gels and powders. In food industry, a

lot of research on supercritical fluid processing method has proven that it has potential also in food industry.

REFERENCES

Brown ZK, Fryer PJ, Norton IT, Bakalis S, Bridson RH. 2008. Drying of foods using supercritical carbon dioxide - Investigation with carrot. Innovative Food Science and Emerging Technologies. 9;280-9.

Ekart M, Bennet K, Ekart K, Guardial G, Liotta C, Eckert C. Cosolvent interactions in supercritical fluid solutions. 1993.AICHe Journal 39:235-248

Fellows PJ. 2000. Food Processing Technology: Principles and Practice. Cambridge: Woodhead Publishing Ltd.

Meterc D, Petermann M, Weidner E. 2008. Drying of aqueous green tea extracts using a supercritical fluid spray process. J of Supercritical Fluids 45; 253-9.

Namatsu H, Yamatzaki K and Kurihara K. 1999. Supercritical drying for nanostructure fabrication without pattern collapse. Microelectronic engineering 46;129-32.

Tedeschi S, Stevens N, Cepeda D, Lee Y-Y, Powers K, Ranade M, El-Shall H. 2009. Novel supercritical fluid processing techniques for the production of an aerosol. Powder technology 191;188-93.

CISET - 2nd Cilicia International Symposium on Engineering and Technology
10-12 October, 2019, Mersin / TURKEY

BIOCLIMATIC EVALUATIONS IN THE MOUNTAINOUS ECOSYSTEM OF DAJT: CASE STUDY TIRANA, ALBANIA

Prof. Dr. Hysen Mankolli*[1], Prof. Assoc. Dr. Lyudmyla Symochko[2], Prof. Assoc. Dr. Flora Merko[3] and Prof. Dr. Sukru Dursun[4]

[1] University of Maryland College Park, Illinois, USA, hysenmankolli@yahoo.com

[2] Uzhhorod National University, Faculty of Biology, Uzhhorod, Ukraine, lyudmilassem@gmail.com

[3] Durres University, Department of Economics, Durres, Albania, floramerko@yahoo.it

[4] Konya Technical University, Engineering and Natural Science Faculty, Konya, Turkey, sdursun@ktun.edu.tr

ABSTRACT
Albania is located on the western part of the Balkan Peninsula, between 39 38' and 42 39' latitude and between 19 16' and 21 4' longitude. It is bordered by Greece in the East and South east, by Macedonia in the East-Northeast and by Kosovo in the northeast, North and Northwest: Adriatic and Joni sea from the west and southwest borders of the country. The country covers a surface of about 28.748 km². The coastal area is 7000 km2 or 25% of the national territory; the Mediterranean watershed includes 28748 km2. Country's Protected area is app.162 529 ha which means 5.8% of the territory. The climatic elements that determined an eco-climate zone are combinations. Their comprehensiveness and coactions give stable contours of eco-climatic indexes. The determination of an eco-climatic zone takes in consideration indexes that are repetitive and sustainable on time and space. These indexes have abiotic and biotic nature. In every case factor that condition eco-climatic of a macrozone or microzone are geophysics as: latitude, altitude above sea level, atmospheric and biotic phenomena's and presence of natural or cultivated vegetation. The bioclimatic concept is wide and from ecologic viewpoint shows the combination of content elements that determine plant and animal life. The climatic data for a many year's period where minimal and maximal temperature, relative humidity air and precipitation on micro zone in territorial areas Tirana, Albania, take on study, we have values from coefficients of Q on limit boundary (up and down). The indexes Q from applied of the Emberger method is on limits from 142.2- to 205.7. Eco zone of Tirana classification on bioclimatic model, humid with value (Q) over 90. In table no.5 we have coefficient Q for more micro zones Dajt of Tirana, Albania. Based on obtained results from the data processing according to Emberger and Rivas S. Martinez's Method, and the discussions about the study "Bioclimatic evaluations in the mountainous ecosystem of Dajt-Tirana" is concluded: 1. The index Q is oscillated from 142, to 205,7. For Tirana eco zone (the humid variant of bioclimatic) Q values are over 90. 2. The index Ic. The continental index is oscillated from 26,4 to 29,3. The ecosystem of Dajt-Tirana based on index Ic or continental index is evaluated on sub Continental - Continental – Mediterranean macroclimate. The changes among the studied micro zones results with a little climate change and are part of a bioclimatic type. 3. The index It. The termotipos index is oscillated from 381 to 456. Dajt eco-zone based on index It is considerate with termotemplado micro-bio- climate, in which take parts: Fushë-Dajt, Rrëzë-Dajt and infratemplado ones in which take parts Linëza. 4. The index Io. The ombrotipos index is oscillated from 2,2 to 3,7. Tirana eco-zone based on index Io is considerate with a dry Semiarido micro-bio- climate 2.0-3.6, in which take parts: Fushë-Dajt, Rrëzë-Dajt, Linëz. 5. Evaluation of micro-zones ecoclimatic indexes the minimal average temperature on Rrëzë-Dajt results – 2,6 °C. The minimal average annual temperature on Rrëzë-Dajt results 10,2 °C. The minimal average monthly precipitation on Rrëzë- Dajt results 1558 mm.

Keywords: *Ecosystem, Environment, Bioclimatic Factor, Evaluation, Mountain Dajt, Albania*

* hysenmankolli@yahoo.com

1. INTRODUCTION

Albania is located on the western part of the Balkan Peninsula, between 39 38' and 42 39' latitude and between 19 16' and 21 4' longitude. It is bordered by Greece in the East and South east, by Macedonia in the East-Northeast and by Kosovo in the northeast, North and Northwest: Adriatic and Joni and Seas from the west and southwest borders of the country. The country covers a surface of about 28.748 km². The coastal area is 7000 km2 or 25% of the national territory; the Mediterranean watershed includes 28748 km2. Country's protected area is app.162 529 ha which means 5.8% of the territory.

The climatic elements that determined an eco-climate zone are connected with each-other. Their comprehensiveness and coactions give stable contours of eco-climatic indexes. The determination of an eco-climatic zone takes in consideration indexes that are repetitive and sustainable on time and space. These indexes have a biotic and biotic nature. In every case factor that condition eco-climatic of a macro zone or micro zone are geophysics as: latitude, altitude above sea level, atmospheric and biotic phenomena's and presence of natural or cultivated vegetation. The bioclimatic concept is wide and from ecologic viewpoint shows the combination of content elements that determine plant and animal life.

The bio-climate zone is considered as a combination among the vegetation area and climatic elements with indexes: temperature, precipitations, wind, air humidity etc. This combination creates a complete, continued and stable view of an area or some ecologic areas in relation to indexes of bio-climate content elements. On eco zones environment resources are in correlation with biotic resources. They present a special importance from the point of study, evaluation, usage, preservation and improvement of natural resources. In every ecologic zone biotic and a biotic component are combined their interaction has an impact on evolution and balance ecosystem progress. Beside the factors that indicate on improvement or no on an ecosystem, anthropogenic factor has a great importance for ecosystem. The eco-climatic resources are considered decisive on plant cultivation, because they implicate growth plant, as a consequence, his production. These sources have a relation with eco-climatic cultivated zone. The climate components of an eco-zone react in an unseparation way and induce to each other revealing compensate effects.

The more important eco-climatic indicators for study aspects are: sun-light, precipitations, temperatures, relative air humidity, wind and other atmospheric phenomenon. Case by case, the eco-climatic factors study on time and space give sufficient information for agro-ecosystem cultivation.

2. MATERIAL AND METHODS

The climatic data are a result of temperature and precipitation indexes obtained from observations on Dajt-Tirana eco-zone. Among these indexes is a significant relation. This data are gathered on Hydrometeorology Institute's stations in Dajt-Tirana. This data period is over than three decades from 1970 to 2010.
The methodology used is been based on Emberger's and Rivas Martinez theory and comparative method [2, 16].
As a supplied method is been used the statistic, table, graphic, map-maker and investigated one.
Classification Rivas Martines based on climatic index Ic, It, Io (Martinez Rivas. S.1996.

Ic, that is an annual thermal interval index calculated as

Ic = Tmax-Tmin
It, that is a thermatic index (or termotipo) calculates as (1)
It = (T+ m+ M)*10
Io, that is an ombrothermic index (or ombrotibo) calculated as
Io = 10x Pp /Tp

where: Tmax = average temperature of the hottest month of the year; Tmin = the average temperature of the coldest month of the year; Pp = sum of the monthly mean rainfall data (mm) of the months in which the average temperature is >0°C; Tp = sum of the mean temperature values for months with T>0°C; T = mean annual temperature; m = mean of the minimum temperature of the coldest month in the year; M = mean of the maximum temperature of the hottest month in the year.

Classification Emberger based on pluviometric index, Q is results (EMBERGER 1969).

$$Q = \frac{2000\,P}{(M-m)(M+m)} \qquad (2)$$

where: Q = coefficient index; P = annual precipitation; M = Mean of the maximum temperature of the coldest month in the year in °K (Calvin); m = mean of the minimum temperature of the coldest month in the year in °K (Calvin);

2.1. The Climatic Data

Table 1 shows temperature and precipitation for Dajt – Tirana ecosystem between 1970 and 2000.

Table 1. Temperature and precipitation for Dajt - Tirana

Climatic data	Average precipitation (mm)			Average air temperature in °C			Maximal air temperature in °C			Minimal air temperature in °C		
Months	Fushë -Dajt	Rrëzë-Dajt	Linëz -Dajt	Fushë -Dajt	Rrëzë -Dajt	Linëz -Dajt	Fushë -Dajt	Rrëzë -Dajt	Linëz -Dajt	Fushë -Dajt	Rrëzë -Dajt	Linëz -Dajt
I	124.5	91	86	5.5	3.8	7.5	8.7	8.1	11.3	2.3	-1	3.7
II	165.8	191	152.3	2.7	1.5	5.2	6.4	5.5	9.6	-0.7	-2.6	0.8
III	101.7	81	60.1	8.6	6.1	10.7	12.6	10.4	17.8	4.7	1.7	3.7
IV	126.9	130.5	84.7	14	10.5	13.8	16.2	15.2	19.,2	7.7	5.8	8.5
V	159.9	67.5	147.5	15.9	14.2	17.9	20.2	19.4	22.7	11.8	9.3	13.2
VI	142.3	192	251.7	16.2	15.7	19.6	20.8	19.6	23.8	11.8	11.2	15.4
VII	111.9	94	45.3	26.3	21.2	24.4	27.1	25.6	30.1	15.0	16.1	18.6
VIII	56.5	49.2	33.7	20	19.2	22.3	24.9	24.7	23.6	15.3	14.8	15.4
IX	123.8	147.1	112.4	17.4	16.8	20.2	22.7	21.9	26.9	12.5	11.6	13.6
X	159.6	126.9	119.7	13.5	12.9	16.8	18.5	17.4	22.0	8.8	8.4	11.6
XI	123.1	168	125.1	9.3	10.6	11.2	13	12.5	13.1	5.8	3.7	5.9
XII	162.9	123.2	109.2	7	8.6	9.3	9.7	8.7	13.0	3.8	1.6	5.6
Years total	1559	1461.4	1203									

4. RESULTS

Albania is a small country; there are important climatic differences, (1, 6]. which are result of the very broken country's relief. Four climatic zones: Lowland-Mediterranean Zone, Hilly-Mediterranean Zone, Pre-mountain-Mediterranean Zone and Mountain-Mediterranean Zone; and 13 sub zones are identified inside the country. Typical Mediterranean climate characterizes the lowlands and the plains. The mountainous area has in principle typical continental climate with a slight Mediterranean influence. But there is a significant difference between the North and the South. In the South the summers are drier and the differences between summer and winter temperatures are not as big as in the North.

In the interior part of Albania there is no balanced impact of the Mediterranean Sea climate anymore. Therefore the daily differences between maximum and minimum temperatures are considerably higher than at the coast. Also the annual precipitation is in the mountainous areas higher than in the lowlands at the coast The Dajt ecosystem is located on North-East of Tirana zone in Albania. The relief is mainly mountain relief (the highest height 1613 m) with the mountainsides very sloping and divided by the hydro graphic network mainly with temporal flow. In the mountainous ecosystem of Dajt-Tirana, there are 4 main kinds of land: brown forest umber-gray, and pasture mountainous land. In the mountainous ecosystem of Dajt-Tirana has Mediterranean Climate, north counter mountain sub zones, with 1600 mm rain-fall per year, concentrated mainly in the second part of the year and very intensive[17, 18]. Snow-falls long nearly 10 days.

The data climatic for same year's period where minimal and maximal temperature and precipitation on micro zone in territorial areas Dajt-Tirana, Albania, take on study, we have value from coefficients of Q with small limits boundary.

The indexes Q from applied method Emberger is on limits 142.2-205.7.

Eco zone in the mountainous ecosystem of Dajt-Tirana classification on bioclimatic model, humid with value (Q) over 90. In table no.2 we have coefficient Q for more micro zones of Tirana, Albania**.**

Table 2. Coefficient Q, Analyzing data from Emberger Method

No	Microzones	M max	m min	Pm/year	Q
1	Dajt-Fushe	27.1	-0.7	1558	205.7
2	Dajt-Reze	25.6	-2.6	1461	182.1
3	Dajt-Linez	30.1	0.8	1202	142.2

The data climatic for same years period where minimal and maximal temperature and precipitation on micro zone in territorial areas Dajt-Tirana, Albania, take on study, we have value from coefficients Ic, It, Io with moderation limits boundary.

The indexes Ic from applied method Rivas Martine's is on limits 26.4-29.3.

The indexes It from applied method Rivas Martine's is on limits 332-456.

The indexes Io from applied method Rivas Martines is on limits 2.2-3.7.

Eco zone in the mountainous ecosystem of Dajt-Tirana, have more classification on bioclimatic models. In table no.3 we have coefficient Ic, It, Io.

Table 3. Coefficient Ic, It, Io, Analyzing data from Rivas Martine's Method

Micro zones	T	m	M	Tp	Pp	Ic	It	Io
Dajt-Fushe	10.3	-0.7	27.1	375	139	26.4	38.1	3.7
Dajt-Reze	10.2	-2.6	25.6	372	117	28.3	33.2	3.2
Dajt-Linez	14.7	0.8	30.1	536	120	29.3	45.6	2.2

where: Tmax = average temperature of the hottest month of the year;

Tmin = the average temperature of the coldest month of the year;

Pp =.sum of the monthly mean rainfall data (mm) of the months in which the average temperature is 0°C;

Tp =.sum of the mean temperature values for months with T>0°C;

T =.mean annual temperature; m =.mean of the

minimum temperature of the coldest month in the year;
M = mean of the maximum temperature of the hottest month in the year.

5. CONCLUSION

Based on obtained results from the data processing according to Emberger and Rivas S. Martinez's the conclusions are: Dajt-Tirana ecozone ass bioclimatic Humid (with humidity) and the values of index Q are higher than 90.

The ecosystem of Dajti based on the indicator Ic or continental index is evaluated in Subcontinental-Continental Macroclimate: Mediterranean. The changes between taken in the study result in small climatic changes and are classified in a type of bioclimate. The ecozone of Tirana based on index It is considered in Microbioclimate Termotemplado where belong Dajt fushe, Dajt Rezë and infratemplado where Lineza belongs. The ecozone of Tirana based on the index Io is considered in Microbioclimate Semiarid, microbioclimate Seco 2.0-3.6, (dry) Dajt Fushë, Dajt Rezë, Linëz. Climatic indicators minimal average monthly temperature results in Dajt Rëzë with minus – 2.6 C°,the minimal average annual temperature results in Dajt Rezë with 10.2 C°, maximal annual rain result in Dajt Fushë with 1558 mm.

REFERENCES

Anderson, E.A. (1976), A Point Energy and Mass Balance Model of a Snow Cover, NOAA Technical Report NWS 19, 150 pp., U.S. Dept. of Commerce, Silver Spring, Maryland;

Brasnett, B., 1999: A global analysis of snow depth for numerical weather prediction. J. Appl. Meteor., 38, 726-740;

Brosnahan, Tom et al (1999):Mediterranean Europe,4th Edition, Lonely Planet Publications Pty Ltd, Victoria, Australia;

Cezar Kongoli12, 2015. Optımal Interpolatıon Of In-Sıtu And Satellıte Passıve Mıcrowave Data For Global Snow Depth Estımatıon, International Journal Of Ecosystems And Ecology Science (Ijees): Vol. 5 (4): 637- 642 (2015);

Cezar Kongoli12, 2016. Large - Scale Snow Depth – Elevatıon Relatıonshıps Of World's Major Mountaın Regıons, International Journal Of Ecosystems And Ecology Science (Ijees): Vol. 6 (4): 653-658 (2016);

Cezar Kongoli12, Robert J. Kuligowski2, Sean Helfrich2, Peter Romanov32, 2014. Monıtorıng Precıpıtatıon And Snow Cover Usıng Multı-Sensor Satellıte And In-Sıtu Data, International Journal Of Ecosystems And Ecology Science (Ijees); Vol. 4 (2): 293-300 (2014);

Cezar Kongoli12, Sean Helfrich2, Robert J. Kuligowski2, 2015. Satellıte-Based Estımatıon Of Hydrologıc Components – Applıcatıon To Snow And Precıpıtatıon, International Journal Of Ecosystems And Ecology Science (Ijees): Vol. 5 (2): 261- 268 (2015);

Cezar Kongoli12, Yu Zhang3, Zhengtao Cui42, Robert J. Kuligowski2, 2017. Estımatıon Of Snow And Raınfall For Hydrologıcal Analysıs Of A Mıd-Wınter Floodıng Event In Western Unıted States, International Journal Of Ecosystems And Ecology Science (Ijees): Vol. 7 (4): 651-656 (2017);

EMBERGER (1969): "Climatique la Tunisia",Tunis, Tunisi;

Giordano A, (1998): Soil and soil conservation with focus on Remote sensing, IAO, 116 monografic, IAO, Florence Italy;

Gjiknuri L., Haxhia I., Mullai A., Bega F.(1993): Stock taking of rare species of plants and animals of important ecological systems and ecological landscape elements;

Hall, D.K. and G.A. Riggs, 2007. Accuracy assessment of the MODIS snow-cover products, Hydrological Processes, 21(12):1534-1547, DOI: 10.1002/hyp.6715;

Hall, D.K., G.A. Riggs, V.V. Salomonson, N.E. DiGirolamo and K.A. Bayr, 2002. MODIS snow-cover products, Remote Sensing of Environment, 83:181-194;

Hodo, P.&Dinga, L. (2000). Vegetation of Albania In Guide to albanian Natural Treasures, p. 167;
Hydrology of Albania (1984): Alb. Ac.Scien. p.220. Tirana;

Hysen Mankolli12, Andi Mankolli3*, 2017. Snow And Raın Precıpıtatıon In Some Regıons Of Albanıa, International Journal Of Ecosystems And Ecology Science (Ijees): Vol. 7 (3): 645-650 (2017);

Kongoli, C. and S. Helfrich, 2015. A multi-source interactive analysis approach for Northern hemispheric snow depth estimation, Proceedings of the Geoscience and Remote Sensing Symposium (IGARSS), IEEE International, Milan, Italy, DOI: 10.1109/IGARSS.2015.7325878;

Kongoli, C. E. and Bland, W. L.(2000) : Long-term snow depth simulations using a modified atmosphere-land exchange model, Agr. Forest Meteorol., 104, 273–287;
Land Evaluation of Lebna Catchments, Tunisia ,(2002): same authors IAO, Florence, Italy;

Liu, Y., C. D. Peters-Lidard, S. V. Kumar, K. R. Arsenault, and D. M. Mocko (2015), Blending satellite-based snow depth products with in situ observations for streamflow predictions in the Upper Colorado River Basin, Water Resour. Res., 51,1182–1202, doi:10.1002/2014WR016606;

Mankolli H, Peçuli V, (2005): Workshop: The theory and practice evaluations over eco-climate on ecosystems, Tirana, Albania;

Mankolli H,(2001): Bioclimate evaluation with IDRISI programs, Agricultural Sciences Newsletter, NR.1, p.23-28, Albania;

Mankolli H,(2002): The bioclimatic of Korça on focus of classification Rivas S. Martinez, Agricultural Sciences Newsletter, NR. 3, p.36-38, Albania;

Mankolli H,(2006): II International Symposiium of Ecologists ,"The bioclimatic classifications of some microareas on Albania", Mankolli H, of Montenegro,p.99-100, 24.09;

Mankolli H,(2007): I Symposium for protection of natural lakes "Towards a set of bio-indicators and eco-areas management at the Prespa watershed in Albania", in Republic of Macedonia, Ohrid,p.59-60,31.05 - 03.06;

Maracchi G, (1983): "Elementi di agrometeorologia "CNR-IATA, Florence, p.124-131;

Martinez Rivas. S.(1996):"Global Biocliomatique clasificasion" Madrid, Espania, p.27-38;

CISET - 2nd Cilicia International Symposium on Engineering and Technology
10-12 October, 2019, Mersin / TURKEY

SYNTHESIS OF Co_3O_4/Fe_3O_4 BIMETALLIC NANOPARTICLES FOR EFFECTIVE ADSORPTION OF TETRACYCLINE

Muhammed MUSA[1], Hatice HASAN [1], Hülya MALKOÇ[1], Memduha ERGÜT [*1], Deniz UZUNOĞLU[1], and Ayla ÖZER [1]

[1]Mersin University, Engineering Faculty, Department of Chemical Engineering, Mersin, Turkey,

E-mails: memduha.ergut@gmail.com, denizuzunoglu4@gmail.com, ayozer4@gmail.com

ABSTRACT

In the present study, cobalt oxide/iron oxide bimetallic nanoparticles (Co_3O_4/Fe_3O_4 NPs) were synthesized by chemical co-precipitation method. The synthesized Co_3O_4/Fe_3O_4 NPs were characterized by SEM, and XRD analysis and then they were utilized for an adsorbent for removal of a kind of antibiotic as Tetracycline (TC) from aqueous solutions. According to characterization results, small plate-like structures and agglomerated irregular spherical nanosized particles (101.85 ± 15.04 nm) were formed. The XRD data confirmed the structure of synthesized adsorbent was Co_3O_4/Fe_3O_4 due to obtained peaks. The optimum tetracycline adsorption conditions were determined as an initial pH of solution 9.0, temperature 55°C, and adsorbent concentration 3.0 g/L. A linear increase was observed in equilibrium uptakes of TC with the increasing the initial dye concentrations. The experimental equilibrium data was the best agreement to Langmuir isotherm model. The maximum monolayer coverage capacity of Co_3O_4/Fe_3O_4 NPs for TC adsorption found to be 149.26 mg/g at 55°C optimum temperature. The experimental kinetic adsorption data were defined as the best agreement with the pseudo-second-order kinetic model. Weber Morris model results showed that both the film (boundary layer) and intra-particle diffusion were effective the adsorption process. The thermodynamic studies suggested that the adsorption process was endothermic, spontaneous and the positive ΔS value indicated increased disorder at the solid-solution interface during the adsorption. Moreover, the synthesized adsorbent showed high adsorption efficiencies at the end of seven sequence usages.

Keywords: *Cobalt oxide, Iron oxide, Bimetallic nanoparticles, Tetracycline removal, Adsorption*

[*] Corresponding Author

1. INTRODUCTION

Antibiotics a kind of significant pharmaceutical ingredients, have been used for many decades as both human and veterinary medicines (Cao *et al.,* 2018).

Tetracycline (TC, $C_{22}H_{24}N_2O_8$) is the second most widely used antibiotics family in the world. TCs are often used in human therapy and livestock industry due to their broad-spectrum antimicrobial activity against a variety of pathogens (Erşan *et al.,* 2013; Bao *et al.,* 2013).

However, nowadays, the presence of antibiotics in the environment and their potential threat to human health and aquatic ecology has lead to great concerns. Because antibiotics taken by humans and animals are not completely absorbed in the body. It has been suggested that about 90% of an administrated dose of antibiotic may be excreted through urine and feces (Turku *et al.,* 2007). In addition, the removal of these drug residues reaching sewage treatment plants can not be fully achieved due to their resistance to biological degradation. Therefore, antibiotic residues can easily mix with surface and ground waters. They also pose a risk for ecological and aquatic environments due to their toxic effects and long half-life (Zhao *et al.,* 2011; Güler and Türkay., 2016).

It has been reported that the antibiotics concentrations in untreated domestic wastewater range between 100 ng/L and 6 μg/L, while the concentrations in pharmaceutical and hospital wastewater can reach up to 100–500 mg/L (Cao *et al.,* 2018).

Therefore, the treatment of wastewater containing antibiotic residues with high organic load is one of the important environmental problems. So, it is necessary to develop inexpensive and efficient treatment methods for this purpose.

The oxidation methods, membrane filtration, reverse osmosis, ultrafiltration, Fenton process, and adsorption are applied as alternative treatment methods for the removal of antibiotics from wastewaters. Adsorption is commonly believed the easiest and cheapest one among these techniques.

Graphene oxide (Gao *et al.,* 2012), carbon nanotubes (Ji *et al.,* 2010), silica (Turku *et al.,* 2007), kaolinite (Li *et al.,* 2010), goethite (Zhao *et al.,* 2011), clay mineral illite (Chang *et al.,* 2012), montmorillonite (Parolo *et al.,* 2008); biosorbents such as maize stalks (Balarak *et al.,* 2016), *Pachydictyon coriaceum* and *Sargassumhemiphyllum* (Li *et al.,* 2015); activated carbon (Martins *et al.,* 2015), chitosan (Kang *et al.,* 2010); composite materials such as Fe_3O_4@SiO_2-Chitosan/graphene oxide nanocomposite (Huang *et al.,* 2017), Heteropolyacid–chitosan/TiO_2 composites (Yu *et al.,* 2014); nanomaterials such as Co-doped UiO-66 nanoparticle (Cao *et al.,* 2018) and Fe/Ni bimetallic nanoparticles (Dong *et al.,* 2018), and cobalt ferrite nanoparticles (Zhao *et al.,* 2014) were used as adsorbents for the removal of TC.

The aim of this work synthesis and characterization of bimetallic Co_3O_4/Fe_3O_4 NPs and investigate the adsorption of TC on Co_3O_4/Fe_3O_4 NPs. In this study, the experimental parameters that affect the adsorption of TC on Co_3O_4/Fe_3O_4 NPs such as initial pH of the solution, adsorbent concentration, initial TC concentration, and temperature were optimized to obtain maximum TC removal yield and also, the reusability of adsorbent was tested. The thermodynamic, equilibrium, kinetic, and mass transfer modeling studies were also carried out to evaluate the adsorption process.

2. MATERIALS and METHODS

2.1. Materials

All of the chemicals were of analytical grade and they were used without further purification. For the synthesis of Co_3O_4/Fe_3O_4 bimetallic nanoparticles, $Fe(NO_3)_2.9H_2O$ and $Co(NO_3)_2.6H_2O$ were supplied from Across. Tetracycline hydrochloride ($C_{22}H_{24}N_2O_8.HCl$) was purchased from Sigma Aldrich. The chemical structure of TC antibiotic was presented in Fig. 1.

A stock solution of 250 mg/L of Tetracycline (TC) was first prepared and then the desired antibiotic concentrations were prepared by appropriate dilutions from the stock solution. The initial pHs of the solutions was adjusted with 0.1 N hydrochloric acid and/or 0.1 N sodium hydroxide.

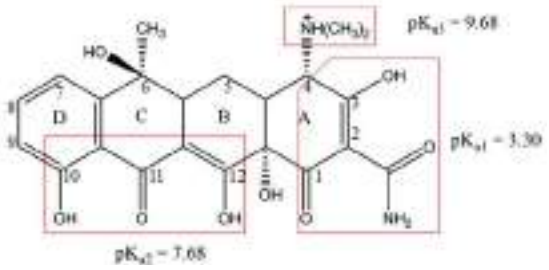

Fig.1. The structure of tetracycline, the framed regions represent the structural moieties associated with the three acidic dissociation constants (pKa).

2.2. Synthesis and Characterization of Co_3O_4/Fe_3O_4 NPs

The synthesis of Co_3O_4/Fe_3O_4 bimetallic nanoparticles (Co_3O_4/Fe_3O_4 NPs) was carried out by chemical co-precipitation method. In the experiments, 25 mL of 0.1 M $Fe(NO_3)_2.9H_2O$ and 25 mL of 0.2 M $Co(NO_3)_2.6H_2O$ solution were mixed at room temperature for 15 min. Then 1.0 M sodium hydroxide solution was slowly added to the prepared solution. This mixture constantly stirred until the pH of 11.0 was reached. The changing of the color of the salt solution to intense black indicated the formation of Co_3O_4/Fe_3O_4 NPs. The obtained final mixture was kept under vigorous stirring for 3 h at 90°C. The formed nanoparticles were separated by centrifugation and then collected nanoparticles were washed several times with deionized water and dried in an oven at 105°C overnight.

The morphology of the Co_3O_4/Fe_3O_4 NPs was analyzed by Scanning Electron Microscope (SEM) analysis with Zeiss/Supra 55 SEM and the crystal structure was determined by X-ray Powder Diffraction (XRD) analysis, using nickel-filtered Cu Kα radiation in a Philips XPert MPD apparatus operated at 40 kV and 30 mA, in the 2θ range of 10°–90°.

2.3. Adsorption Studies

The batch adsorption experiments were carried out in 250 mL Erlenmeyer flasks containing 100 mL of TC antibiotic solution. 0.1 g of adsorbent, except for adsorbent concentration experiments, was contacted with 100 mL of TC solution at known initial antibiotic concentration and initial pH of solutions. Then the flasks were agitated at a constant temperature and shaking rate. Samples were taken before mixing the Co_3O_4/Fe_3O_4 NPs and TC solution and at pre-determined time intervals for the unadsorbed antibiotic concentration in the solution. Samples were centrifuged and the supernatant liquid was analyzed by UV-vis spectrophotometer at the wavelength of 360 nm.

The adsorbed amount of TC [q_e; (mg/g)] and the percentage of adsorption [Adsorption (%)] at equilibrium were calculated with Eqs. (1) and (2) as presented follows:

$$q_e\ (mg/g) = \frac{}{} V \quad (1)$$

$$\text{Adsorption (\%)} = \left[\frac{}{}\right] \cdot 100 \quad (2)$$

Where C_o (mg/L) and C_e (mg/L) are the initial and equilibrium concentrations of TC solution, respectively; and m(g) is the mass of adsorbent, and V(L) is the volume of the liquid phase.

3. RESULTS and DISCUSSIONS

3.1. The Characterization of Co_3O_4/Fe_3O_4 NPs

The morphology of Co_3O_4/Fe_3O_4 NPs before and after adsorption was determined by SEM analysis and SEM images obtained at different magnifications were presented in Fig. 2.

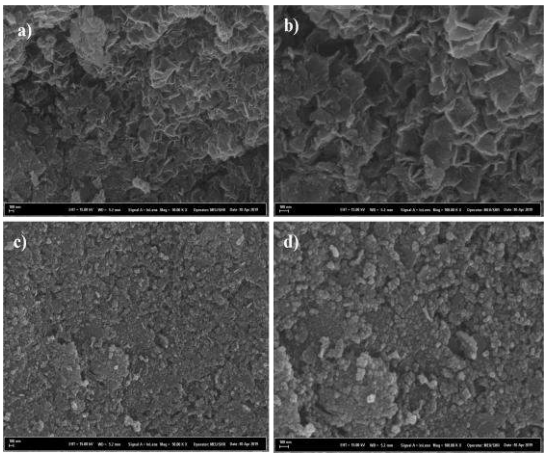

Fig.2. SEM images obtained at different magnifications before a) 100 KX, b)50 KX; after c) 100 KX, d) 50 KX.

SEM images of the synthesized Co_3O_4/Fe_3O_4 NPs showed that small plate-like structures and agglomerated irregular spherical particles were formed. The SEM images obtained after the adsorption process showed that the morphological structure changed significantly; plate-like structures were disappeared and the nanosized, spherical, and agglomerated particles appeared. The mean particle size of the spherical particles was determined as 101.85 ± 15.04 nm by Image J program.

The XRD pattern of synthesized Co_3O_4/Fe_3O_4 NPs was presented in Fig. 3.

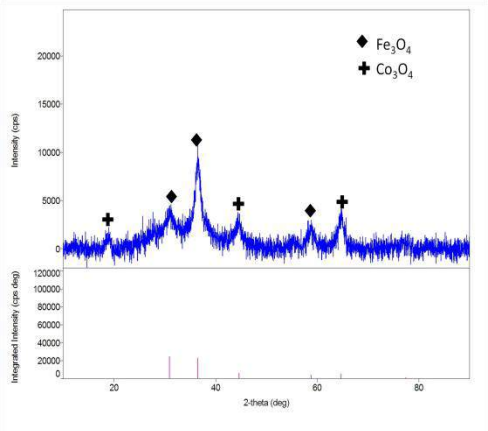

Fig.3. XRD diagram of synthesized Co_3O_4/Fe_3O_4 NPs

The peaks at 2θ = 30.91°, 36.46°, 64.46°, and 58.83° correspond to Fe_3O_4 and the peaks at 2θ = 19.02°, and 44.59° showed the Co_3O_4 phase (Manigandan *et al.*, 2013).

3.2. Effects of Environmental Conditions on the Adsorption

3.2.1. Effect of initial pH

The initial pH is one of the most important parameter affecting the adsorption of TC on the active adsorbent surface. The interaction between the TC molecules and the adsorbent is mainly dependent on the TC species and variation of the surface loading of the adsorbent.

The isoelectric point (pH_{IEP}) of Co_3O_4/Fe_3O_4 NPs was determined by solid addition method at different pH (3.0 - 12) values (Uzunoğlu *et al.*, 2016). The variation of the isoelectric point with pH was presented in Fig. 4.

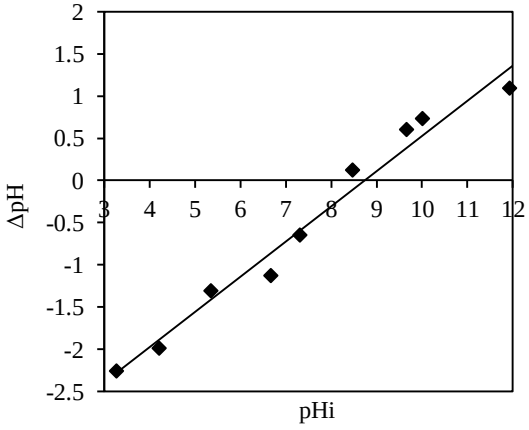

Fig.4. The isoelectric point of Co_3O_4/Fe_3O_4 NPs

TC molecules are very sensitive to the initial pH of the solution due to their protonation status. As shown in Figure 8, the isoelectric point at which the surface electrical charge of Co_3O_4/Fe_3O_4 NPs changes from negative to positive value was found to be pH 8.47.

Accordingly, the surface of Co_3O_4/Fe_3O_4 NPs was charged negatively below pH 8.47 and positively charged above this pH value. However; the structure of TC contains many polar and ionizable groups, including amino, carboxyl, phenol, alcohol, and ketone. The TC molecules can be present in three forms, cationic (pH<3.3), zwitterionic (3.3<pH<7.7) and anionic (pH>7.7) in aqueous solutions at different pH values (Roca Jalil *et al.,* 2018). In this case, there is an electrostatic interaction depending on the initial pH values in the adsorption of TC on Co_3O_4/Fe_3O_4 NPs surface. The effect of initial pH on the adsorption of TC to Co_3O_4/Fe_3O_4 NPs was given in Fig. 5.

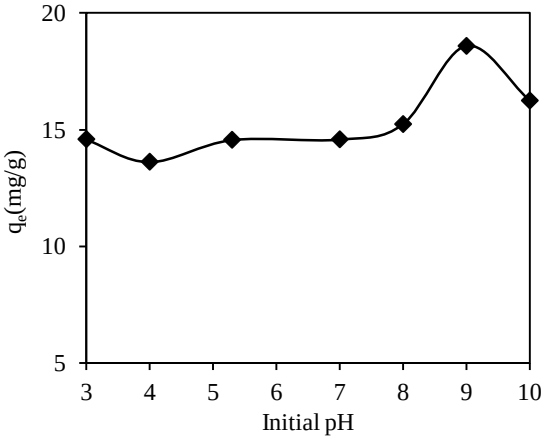

Fig.5. Effect of initial pH on the adsorption of TC (Co=50 mg/L; Xo=1.0 g/L; T=25 °C; t=180 min)

As shown in Figure 5, the highest adsorption capacity was obtained at the initial pH: 9.0. At pH: 9.0, the TC molecules are in anionic form, while the adsorbent surface is positively charged. Therefore, the amount of TC adsorbed is the highest due to the increased electrostatic attraction between the TC molecules and the adsorbent surface at pH: 9.0.

3.2.2. Effect of initial TC concentration

The effect of initial antibiotic concentration on adsorption was depicted in Fig. 6. As can be seen from Fig. 6, the adsorption capacities increased linearly (q_e=0.3047*C_o, R^2=0.999) in the studied TC concentrations as a result of the increase in the driving force (ΔC) to get over mass transfer resistances of the pollutant between the aqueous and solid phases.

3.2.3. Effect of adsorbent concentration

The adsorbent concentration effect on the equilibrium uptake was presented in Fig.7. According to Fig. 7, a decrease was observed in adsorption capacity by increasing the adsorbent concentration from 0.5 g/L to 3.0 g/L. However, the adsorption percentages increased by increasing the adsorbent concentration values. Therefore, although the highest adsorption capacity for tetracycline antibiotic was obtained at 0.5 g/L of adsorbent concentration, the optimum adsorbent concentration was determined as 3.0 g/L, since the highest removal yield was obtained at this adsorbent concentration value.

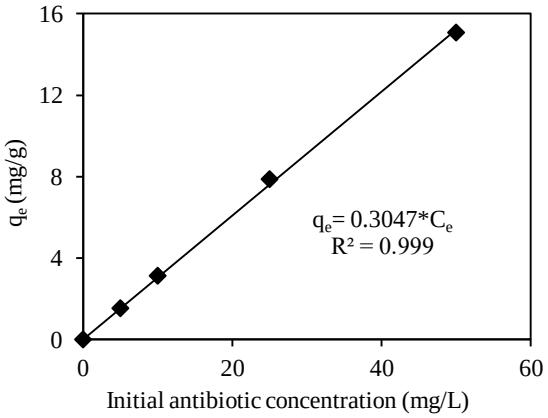

Fig.6. Effect of initial antibiotic concentration on the adsorption of TC (pH=9.0; Xo=3.0 g/L; T=25 °C; t=420 min)

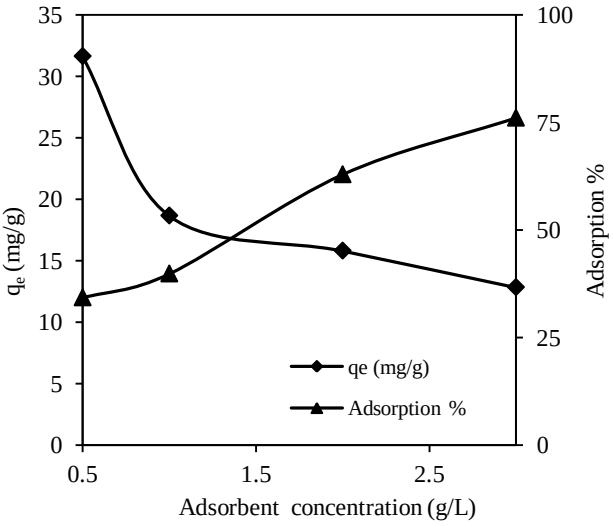

Fig.7. Effect of adsorbent concentration on the adsorption of TC (Co=50 mg/L, pH=9.0; T=25 °C; t=420 min)

3.2.4. Effect of temperature

The effect of temperature was presented in Fig. 8. According to Fig. 8, the high adsorption capacity was obtained with increase in temperature from 25°C to 55°C. Therefore, the optimum temperature value for TC adsorption was determined as 55°C. This operation temperature indicated that the studied adsorption process was endothermic nature.

3.3. Thermodynamic Parameters

The temperature effect was also confirmed with thermodynamic studies by calculating the entropy change (ΔS), enthalpy change (ΔH), and Gibbs energy change (ΔG). ΔH and ΔS were calculated from the slope and intercept of the linear plot of ln K_c versus 1/T according to Van't Hoff equation (Eq. 3), while ΔG was calculated according to Eq. 4.

$$\ln K_c = (—)- (—) \cdot - \quad (3)$$

$$\Delta G = - RT \ln Kc = \Delta H - T\Delta S \quad (4)$$

In this study, the linear form of Van't Hoff equation for the adsorption of TC onto Co_3O_4/Fe_3O_4 NPs was found as ln K_c = - 7918.4 x – + 26.67 with the regression coefficient 0.999 (data not shown) and the thermodynamic parameters were calculated and presented in Table 1. According to Table 1, the calculated ΔG values had negative indicating that adsorption was spontaneous. The positive value of ΔS suggested that randomness of the adsorbed dye species at the solid-solution interface during adsorption and the studied adsorption systems were endothermic (ΔH>0).

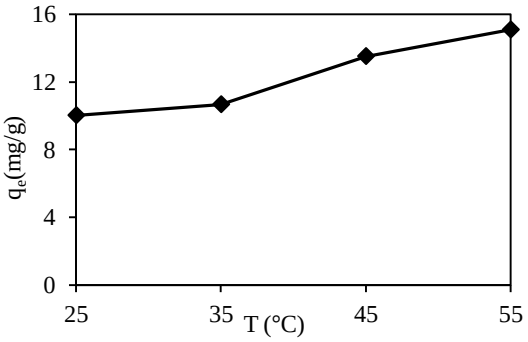

Fig. 8. Effect of temperature on the adsorption of TC (Co= 50 mg/L, pH=9.0; Xo=3.0 g/L; t=420 min)

Table 1. Thermodynamic parameters of adsorption

Thermodynamic parameters				
T (K)	*Kc*	*ΔH (kJ/mol)*	*ΔS (kJ/mol.K)*	*ΔG (kJ/mol)*
298	1.1132	65.83	0. 221	-0.265
318	5.6439			-4.575
328	12.824			-6.957

3.4. The reusability of adsorbent

The operation cost is one of the important issues that need to be carefully considered. Therefore, operation cost can be significantly be reduced owing to adsorbent reusability in practical applications. The reusability of the adsorbent was evaluated through seven recycled tests. The results regarding the TC adsorption efficiency for seven cycles of the adsorbent were given in Fig. 9. Between each cycle of use, the adsorbent was separated from the solution with Whatman #1 filter paper, washed several times with deionized water and then applied for the next experiment without any modifications. After each recycling test, the adsorption percentage of TC was determined. As seen in Fig. 9, the adsorption %, of TC declined slightly from 99.43% in the first cycle to 88.42% after seven cycles of adsorption for 15 mg/L of TC solution. This result showed that the adsorbent can be recycled and reused for at least seven successive cycles without any significant loss of its efficiency.

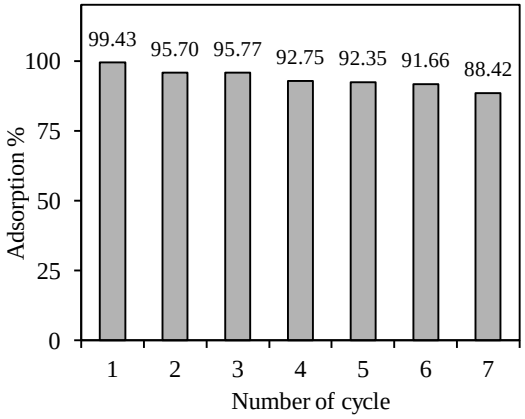

Fig.9. Reusability of adsorbent within experimental runs for seven successive cycles (Co=10 mg/L, pH=9.0; Xo=3.0 g/L; t=420 min)

3.5. Equilibrium, Kinetic, and Mass Transfer Modelling

3.5.1. Equilibrium modeling

The well-known linearized forms of the Langmuir and Freundlich isotherm models were used to describe the adsorption equilibrium. The linearized forms of Langmuir and Freundlich isotherm models were given in Eqs. (5) and (6):

$$\text{Langmuir:} \quad — = \frac{}{Q^{\circ} b} \; — \; \frac{}{Q^{\circ}} \quad (5)$$

$$\text{Freundlich:} \quad \ln q_e = \ln K_F + (-) \ln C_e \quad (6)$$

Langmuir isotherm model based on the assumption of maximum adsorption corresponds to a saturated monolayer of adsorbed molecules on the adsorbent surface with constant energy. Freundlich isotherm model suggests non-ideal sorption that involves heterogeneous surface energy systems (Malik, 2004).

The isotherm constants with regression coefficients (R^2) were presented in Table 2. According to Table 2, Langmuir isotherm model was better fitted to experimental equilibrium data. This result showed that the adsorption occurred at specific homogeneous sites within the adsorbent forming monolayer coverage of TC at the surface of Co_3O_4/Fe_3O_4 NPs. The maximum monolayer coverage capacity of Co_3O_4/Fe_3O_4 NPs was determined as 149.26 mg/g at 55°C which is the optimum temperature. Moreover, as seen in Table 2, the

maximum monolayer coverage capacity values of adsorbent for TC increased by increasing temperature may be due to the endothermic nature of the studied adsorption process. The comparison of Q^o values of various types of adsorbents for TC adsorption was presented in Table 3.

Accordingly, it was seen that the adsorption capacity of Co_3O_4/Fe_3O_4 NPs was comparable with other adsorbents reported in earlier studies.

Table 2. The constants of the adsorption isotherm models with regression coefficients (pH=9.0; Xo=3.0 g/L; t=420 min)

T (^{o}C)	Langmuir isotherm model			Freundlich isotherm model		
	Q^o (mg/g)	b (L/mg)	R^2	K_F (mg/g)/(L/mg)1/n)	1/n	R^2
25	21.053	0.03536	0.999	1.0114	0.6988	0.995
35	55.249	0.01745	0.998	1.0443	0.8627	0.991
45	135.135	0.01380	0.997	1.9397	0.8699	0.979
55	149.254	0.01020	0.999	1.4745	1.0089	0.994

Table 3. The maximum monolayer adsorption capacity values (Q^o) of various types of adsorbents in the literature

Adsorbent	Q^o (mg/g)	Reference
Fe_3O_4@SiO_2-Chitosan/GO	151.4	(Huang *et al.*, 2017)
NH_2-MIL 101(Cr)	14	(Tian *et al.*, 2016)
Zn-AC	51.65	(Takdaştan *et al.*, 2016)
Cu_2O-TiO_2-Pal	113.6	(Shi *et al.*, 2016)
$GBCM_{350}$ activated carbon	58.2	(Álvarez-Torrellas *et al.*, 2016)
Co_3O_4/Fe_3O_4 NPs	149.25	This study

3.5.2. Kinetic modeling

The adsorption kinetics was elucidated by correlating the adsorption kinetic data using the linear forms of the Lagergen's pseudo-first-order and the pseudo-second-order kinetic models. The linearized forms of pseudo-first-order and the pseudo-second-order kinetic models were given in Eqs. (7) and (8), respectively (Mall *et al.*, 2007) :

Pseudo first order: $\log (q_e - q_t) = \log (q_e) - \frac{}{}$ (7)

Pseudo second order : $\frac{}{} = (\frac{}{_2}) + \frac{}{}$ (8)

Table 4. Kinetic and intra-particle mass transfer model parameters (pH=9.0, Xo=3g/L, t=420 min)

For the adsorption of TC onto Co_3O_4/Fe_3O_4 NPs, the parameters of the pseudo-first-order and pseudo-second-order kinetic models with regression coefficients were presented in Table 4. From Table 4, higher values of R^2 and the consistency between experimental and calculated uptake values showed better agreement of the pseudo-second-order kinetics.

3.5.3. Effect of mass transfer

Weber-Morris model was used to determine the boundary layer and intra-particle diffusion mechanism between TC and adsorbent. Weber-Morris intraparticle diffusion model is expressed by the following Eq.(9) ;

$$q_t = K_i . t^{0.5} + I \quad (9)$$

In Weber-Morris equation; I is the intercept related to the boundary layer effect and K_i is the intraparticle diffusion rate constant which can be evaluated from the slope of the linear plots of qt versus $t^{0.5}$. According to this model, if the only intraparticle diffusion is the rate-controlling step in the adsorption process, the plot of uptake (q_e) versus the $t^{0.5}$ should be linear and these lines pass through the origin. On the other side, the Weber-Morris plot can be linear and also has intercept value if the adsorption system follows both intraparticle and film diffusion (Wu *et al.*, 2009). The model parameters and regression coefficients were summarized at Table 4. Based on the results, it was observed a multilinear plot (figure not shown) indicated that both intraparticle and film diffusion were effective on the adsorption.

Co (mg/L)	qe, exp (mg/g)	Pseudo-first-order			Pseudo-second-order			Weber-Morris Model		
		$k_1(min^{-1})$	qe,cal_1 (mg/g)	R^2	k_2 (g/mg.min)	qe,cal_2 (mg/g)	R^2	Ki ($mg/g.min^{0.5}$)	I	R^2
5	2.503	0.003685	2.3637	0.936	0.002233	2.749	0.970	0.0332	0.8925	0.995
10	3.163	0.004376	2.2014	0.960	0.004520	3.300	0.995	0.1009	0.9907	0.982
25	7.879	0.008521	7.3198	0.954	0.002852	8.453	0.991	0.3489	1.1454	0.990
50	15.086	0.005758	13.3967	0.919	0.00071	17.065	0.972	0.563	1.9738	0.998

Moreover, according to Table 4; it was seen that the internal (Ki) and external diffusion constants (I) gradually increased with increasing initial dye concentration.

4. CONCLUSION

In this study, Co_3O_4/Fe_3O_4 NPs was synthesized by co-precipitation method for the removal of TC which is a kind of antibiotic from the aqueous solutions. The characterization studies of Co_3O_4/Fe_3O_4 NPs were carried out by SEM and XRD analysis. According to XRD results the peaks were obtained correspond to Fe_3O_4 and Co_3O_4.

The adsorption was highly dependent on initial pH, adsorbent concentration, initial TC concentration, and temperature. The kinetics of TC adsorption on Co_3O_4/Fe_3O_4 NPs follows the pseudo-second-order model. The equilibrium data fitted well in the Langmuir model of adsorption, showing monolayer coverage of TC molecules at the outer surface Co_3O_4/Fe_3O_4 NPs. The maximum monolayer coverage capacity of Co_3O_4/Fe_3O_4 NPs for TC adsorption determined to be 149.26 mg/g. Both intraparticle and film diffusion effects were determined on the adsorption process. Moreover, the adsorbent showed reusability at least seven sequence usages without loss of adsorbent property. The TC adsorption onto Co_3O_4/Fe_3O_4 NPs was found to be feasible and spontaneous from thermodynamic studies.

Consequently, these results provided the synthesis of an efficient adsorbent for effective removal of antibiotic contaminants like TC in wastewater.

NOMENCLATURE

b : A constant related to the affinity of the binding sites (L/mg)
C_e : Unadsorbed Cr(VI) metal ion concentration at equilibrium (mg/L)
C_o : Initial Cr(VI) metal ion concentration (mg/L)
K_F : Freundlich constant indicating adsorption capacity ((mg/g)/(L/mg)$^{1/n}$)
K_i : Intraparticle diffusion rate constant (mg/g.min$^{0.5}$)
k_1 : Pseudo first order kinetic rate constant (1/min)
k_2 :Pseudo second order kinetic rate constant (g/mg.min)
q_e :Adsorbed amount per unit mass of adsorbent (mg/g)
q_{e,cal_1} :Calculated adsorbed amount per unit mass of adsorbent from pseudo first order kinetic model (mg/g)
q_{e,cal_2} :Calculated adsorbed amount per unit mass of adsorbent from pseudo second order kinetic model (mg/g)
$q_{e,exp}$:Experimental adsorbed amount per unit mass of adsorbent (mg/g)
q_t :Adsorbed amount per unit mass of adsorbent at any time (mg/g)
Q_o :Maximum monolayer coverage capacity of adsorbent (mg/g)
1/n : Freundlich constant indicating adsorption intensity

REFERENCES

Álvarez-Torrellas, S., Ribeiro, R. S., Gomes, H. T., Ovejero, G., & García, J. (2016). "Removal of antibiotic compounds by adsorption using glycerol-based carbon materials". *Chemical Engineering Journal*, Vol. 296, pp. 277-288.

Balarak, D., Mostafapour, F. K., & Azarpira, H. (2016). "Adsorption isotherm studies of tetracycline antibiotics from aqueous solutions by maize stalks as a cheap biosorbent." *International Journal of Pharmacy and Technology*, Vol. 8, No. 3, pp. 16664-16675.

Bao, X., Qiang, Z., Ling, W., & Chang, J. H. (2013). "Sonohydrothermal synthesis of MFe_2O_4 magnetic nanoparticles for adsorptive removal of tetracyclines from water." *Separation and Purification Technology*, Vol.117, pp.104-110.

Cao, J., Yang, Z. H., Xiong, W. P., Zhou, Y. Y., Peng, Y. R., Li, X., ... & Zhang, Y. R. (2018). "One-step synthesis of Co-doped UiO-66 nanoparticle with enhanced removal efficiency of tetracycline: Simultaneous adsorption and photocatalysis." *Chemical Engineering Journal*, Vol. 353, pp.126-137.

Chang, P. H., Li, Z., Jean, J. S., Jiang, W. T., Wang, C. J., & Lin, K. H. (2012). "Adsorption of tetracycline on 2: 1 layered non-swelling clay mineral illite." *Applied Clay Science*, Vol. 67, pp. 158-163.

Dong, H., Jiang, Z., Zhang, C., Deng, J., Hou, K., Cheng, Y., ... & Zeng, G. (2018). "Removal of tetracycline by Fe/Ni bimetallic nanoparticles in aqueous solution." *Journal of colloid and interface science*, Vol. 513, pp. 117-125.

Erşan, M., Bağda, E., & Bağda, E. (2013). "Investigation of kinetic and thermodynamic characteristics of removal of tetracycline with sponge like, tannin based cryogels." *Colloids and surfaces B: Biointerfaces*, Vol. 104, pp. 75-82.

Gao, Y., Li, Y., Zhang, L., Huang, H., Hu, J., Shah, S. M., & Su, X. (2012). "Adsorption and removal of tetracycline antibiotics from aqueous solution by graphene oxide." *Journal of colloid and interface science*, Vol. 368, No.1, pp.540-546.

Güler, Ü. A. (2016). "Aljinat-TiO_2-Alg Kompozitinin Sentezi ve Sulu Çözeltilerden Tetrasiklin Gideriminde Kullanılabilirliği ve Karakterizasyonu." *Karaelmas Science and Engineering Journal*, Vol. *6*, No.1, pp. 130-135.

Huang, B., Liu, Y., Li, B., Liu, S., Zeng, G., Zeng, Z., ... & Yang, C. (2017). "Effect of Cu (II) ions on the enhancement of tetracycline adsorption by Fe_3O_4@SiO_2-Chitosan/graphene oxide nanocomposite." *Carbohydrate polymers*, Vol. 157, pp. 576-585.

Ji, L., Chen, W., Bi, J., Zheng, S., Xu, Z., Zhu, D., & Alvarez, P. J. (2010). "Adsorption of tetracycline on single-walled and multi-walled carbon nanotubes as affected by aqueous solution chemistry." *Environmental toxicology and chemistry*, Vol. 29, No. 12, pp. 2713-2719.

Kang, J., Liu, H., Zheng, Y. M., Qu, J., & Chen, J. P. (2010). "Systematic study of synergistic and antagonistic effects on adsorption of tetracycline and copper onto a chitosan." *Journal of Colloid and Interface Science*, Vol. 344, No.1, pp.117-125.

Li, W. C., & Wong, M. H. (2015). "A comparative study on tetracycline sorption by Pachydictyon coriaceum and Sargassumhemiphyllum." *International journal of environmental science and technology*, Vol. 12, No. 8, pp. 2731-2740.

Li, Z., Schulz, L., Ackley, C., & Fenske, N. (2010). "Adsorption of tetracycline on kaolinite with pH-dependent surface charges." *Journal of colloid and interface science*, Vol. *351*, No.1, pp. 254-260.

Malik, P. K. (2004). "Dye removal from wastewater using activated carbon developed from sawdust: adsorption equilibrium and kinetics." *Journal of Hazardous Materials*, Vol. 113, No.1-3, pp. 81-88.

Mall, I. D., Srivastava, V. C., & Agarwal, N. K. (2007). "Adsorptive removal of Auramine-O: Kinetic and equilibrium study." *Journal of Hazardous materials*, Vol. 143, No.(1-2), pp. 386-395.

Manigandan, R., Giribabu, K., Suresh, R., Vijayalakshmi, L., Stephen, A., & Narayanan, V. (2013). "Cobalt oxide nanoparticles: characterization and its electrocatalytic activity towards nitrobenzene." *Chemical Science Transactions*, Vol. 2, No.1, pp. 47-S50.

Martins, A. C., Pezoti, O., Cazetta, A. L., Bedin, K. C., Yamazaki, D. A., Bandoch, G. F., ... & Almeida, V. C. (2015). "Removal of tetracycline by NaOH-activated carbon produced from macadamia nut shells: kinetic and equilibrium studies." *Chemical Engineering Journal*, Vol. 260, pp. 291-299.

Parolo, M. E., Savini, M. C., Valles, J. M., Baschini, M. T., & Avena, M. J. (2008). "Tetracycline adsorption on montmorillonite: pH and ionic strength effects." *Applied Clay Science*, Vol. *40*, No. 1-4, pp.179-186.

Roca Jalil, M., Toschi, F., Baschini, M., & Sapag, K. (2018). "Silica Pillared Montmorillonites as Possible Adsorbents of Antibiotics from Water Media." *Applied Sciences*, Vol. 8, No. 8, pp.1403.

Shi, Y., Yang, Z., Wang, B., An, H., Chen, Z., & Cui, H. (2016). "Adsorption and photocatalytic degradation of tetracycline hydrochloride using a palygorskite-supported Cu_2O–TiO_2 composite." *Applied Clay Science*, Vol. 119, pp. 311-320.

Takdastan, A., Mahvi, A. H., Lima, E. C., Shirmardi, M., Babaei, A. A., Goudarzi, G., ... & Vosoughi, M. (2016). "Preparation, characterization, and application of activated carbon from low-cost material for the adsorption of tetracycline antibiotic from aqueous solutions." *Water Science and Technology*, Vol. *74*, No.10, pp. 2349-2363.

Tian, N., Jia, Q., Su, H., Zhi, Y., Ma, A., Wu, J., & Shan, S. (2016). "The synthesis of mesostructured NH 2-MIL-101 (Cr) and kinetic and thermodynamic study in tetracycline aqueous solutions." *Journal of Porous Materials*, Vol. *23*, No. 5, pp. 1269-1278.

Turku, I., Sainio, T., & Paatero, E. (2007). "Thermodynamics of tetracycline adsorption on silica." *Environmental Chemistry Letters*, Vol. *5*, No. 4, pp. 225-228.

Uzunoğlu, D., & Özer, A. (2016). "Adsorption of Acid Blue 121 dye on fish (Dicentrarchus labrax) scales, the extracted from fish scales and commercial hydroxyapatite: equilibrium, kinetic, thermodynamic, and characterization studies." *Desalination and Water Treatment*, Vol. 57, No. 30, pp.14109-14131.

Wu, F. C., Tseng, R. L., & Juang, R. S. (2009). "Initial behavior of intraparticle diffusion model used in the description of adsorption kinetics." *Chemical Engineering Journal*, Vol. 153, No. (1-3), pp.1-8.

Yu, X., Lu, Z., Wu, D., Yu, P., He, M., Chen, T., ... & Feng, Y. (2014). "Heteropolyacid–chitosan/TiO_2 composites for the degradation of tetracycline hydrochloride solution." *Reaction Kinetics, Mechanisms and Catalysis*, Vol.111, No. 1, pp. 347-360.

Zhao, X., Wang, W., Zhang, Y., Wu, S., Li, F., & Liu, J. P. (2014). "Synthesis and characterization of gadolinium doped cobalt ferrite nanoparticles with enhanced adsorption capability for Congo Red." *Chemical Engineering Journal*, Vol. 250, pp.164-174.

Zhao, Y., Geng, J., Wang, X., Gu, X., & Gao, S. (2011). "Adsorption of tetracycline onto goethite in the presence of metal cations and humic substances." *Journal of colloid and interface science*, Vol. 361 No. 1, pp. 247-251.

CISET - 2nd Cilicia International Symposium on Engineering and Technology
10-12 October, 2019, Mersin / TURKEY

ROBUST CONTROL OF BOOST CONVERTER USING INTERVAL TYPE-2 TSK FUZZY LOGIC CONTROLLER

Ö. Fatih Keçecioğlu [1], Ahmet Gani *[2] and Erdal Kılıç[3]

1 Kahramanmaraş Sütçü İmam University, Faculty of Engineering and Architecture, Department of Electrical and Electronics Engineering, Turkey, Kahramanmaraş, fkececioglu@ksu.edu.tr

2 Kahramanmaraş Sütçü İmam University, Faculty of Engineering and Architecture, Department of Electrical and Electronics Engineering, Turkey, Kahramanmaraş, agani@ksu.edu.tr

3 Kahramanmaraş Sütçü İmam University, Faculty of Engineering and Architecture, Department of Electrical and Electronics Engineering, Turkey, Kahramanmaraş, ekilic@ksu.edu.tr

ABSTRACT

DC-DC converters are electronics elements which change voltage level based on switching. Unlike linear circuit topologies, modeling and controlling of DC-DC converter circuits are very difficult because of their switched structure. Conventional controllers such as PI, PD and PID are insufficient to control non-linear systems. These controllers cannot give good performance under transient and steady state conditions. Intelligent controllers based on fuzzy logic are required in order to improve the performance of non-linear systems. Fuzzy logic control methods are used to solve many engineering problems. Interval Type-2 Takagi-Sugeno-Kang Fuzzy Logic controller (IT2TSKFLC) is more robust to overcome uncertainties and nonlinearities compared to Type-1 Fuzzy Logic controller (T1FLC). In the present study, an IT2TSKFLC is proposed for the robust control of boost converter. The dynamic performance of proposed controller was analyzed under disturbances such as input voltage change and output load change using MATLAB/Simulink.

Keywords: *Robust Control, Boost Converter.*

*Ahmet GANİ

1. INTRODUCTION

DC-DC converters are circuits which change the voltage level to another one depending on the state of the switching element. While some converters are used to decrease or increase voltage, some types are used to both increase and decrease voltage such as buck, boost, buck-boost type. Boost DC-DC converters are circuits which convert input voltage level to an output voltage level upper than the input voltage level [Kececioglu et al., 2018]. Boost DC-DC converters are particularly used renewable energy applications. Many studies are available in the literature to control boost type DC-DC converters. The dynamic characteristic of boost DC – DC converters are non-linear due to parasitic resistances, stray capacitances and leakage inductances of the components [Ozarslan et al., 2014]. PI controller has many disadvantages such as slow transient response and more overshoot. To overcome these problems, there are various intelligent control methods such as fuzzy logic control (FLC), artificial neural network control (ANNC) and neuro-fuzzy control (NFC) in the literature. Among the various control techniques, the most commonly used technique in control systems is fuzzy logic. Fuzzy logic can be used to describe the behavior of complex systems which are difficult to modeling mathematically. Fuzzy logic control is the mathematical expression of linguistic variables by means of experience. For that reason, fuzzy logic is frequently used in various academic fields such as decision-making, pattern recognition, nonlinear approach and data analysis [Acikgoz, 2018]. There are uncertainties in many of the systems in the real world. Various fuzzy control methods have been implemented in many nonlinear systems. Type-1 fuzzy logic control (T1FLC) has some limitations for the expression of uncertainties. However, the main feature of Interval Type-2 Takagi-Sugeno-Kang Fuzzy Logic controller (IT2TSKFLC) is the footprint of uncertainty (FOU) that describes the uncertainties. Moreover, IT2TSKFLC is more robust to overcome uncertainties compared to T1FLC [Acikgoz et al., 2017]. The present study is organized as follows: Boost DC-DC converter is analyzed in Section 2. The design of IT2TSKFLC structure is explained in Section 3. Simulation results are presented in Section 4. The conclusions of the present study are given in Section 5.

2. ANALYSİS OF BOOST CONVERTER

Boost DC-DC converter circuit model is composed of a switch S, a diode D, an inductor L, a capacitor C and a resistance R that is used as a load. The circuit model of a boost DC-DC converter is shown in Fig. 1.

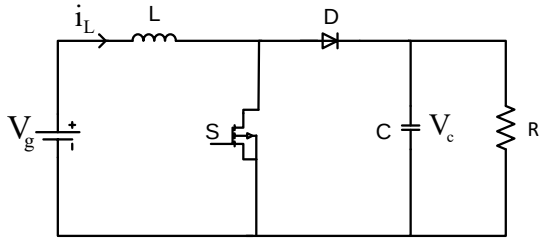

Fig. 1. Boost DC-DC Converter Circuit

At a steady state mode, boost converter has two operating modes. In the first operating mode, switch S is turned on, and the diode is reverse biased. The equivalent circuit of the first operating mode is shown in Fig.2.

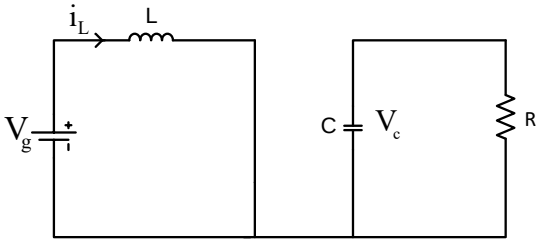

Fig. 2. Equivalent Circuit of First Operating Mode

$$L\frac{di_L}{dt}=V_g \tag{1}$$

$$C\frac{dV_C}{dt}=\frac{-V_C}{R} \tag{2}$$

In the second operating mode, switch S is turned off, and the diode is forward biased. The equivalent circuit of second operating mode is shown in Fig.3.

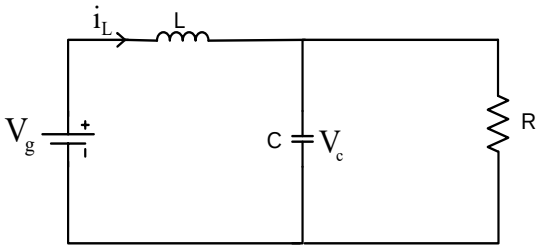

Fig. 3. Equivalent Circuit of Second Operating Model

The equations defining the dynamic behavior of the circuit are given in Eqs.3 and 4 using Kirchoff's current and Kirchoff's voltage laws for the second operating mode.

$$V_g-L\frac{di_L}{dt}-V_C=0 \tag{3}$$

$$C\frac{dV_C}{dt}=\left(i_L-\frac{V_C}{R}\right) \tag{4}$$

The relationship between the output and input voltage at steady state mode for boost DC-DC converter is defined in Eq. 5.

$$V_0=\frac{1}{1-D}V_g \tag{5}$$

The duty cycle rate for a boost DC-DC converter is given in Eq. 6.

$$D = \frac{T_{on}}{T} = \frac{T_{on}}{T_{on} + T_{off}} \quad (6)$$

T_{on} denotes logic 1 duration of PWM, T_{off} is the logic 0 duration of PWM, T represents the period of PWM, and D defines the duty cycle [Kececioglu et al., 2019].

3. THE DESIGN OF INTERVAL TYPE-2 TSK FUZZY LOGIC CONTROLLER

The expert is required to solve the problem of defining the rules and parameters of the membership function in the design of T1FLC. The expert's linguistic definitions may result in various uncertainties. In addition, defining the crisp values required for the membership function may also be problematic (Karanjkar, 2014). Such problems may lead to some instabilities such as measurement errors and changes in operating conditions of the controller. Moreover, in IT2TSKFLCs, these instability conditions can be listed as membership function uncertainties, which can eliminate adverse effects arising out of instability conditions. The four main parts of IT2TSKFLC are fuzzifier, a rule base, fuzzy inference, and type reducer. IT2TSKFLC and T1FLC significantly differs from each other in terms of type reduction. Type reducer converts Type-2 information to Type-1 information, and the output of type-reduction block is called type-reduced set. Then, this type reduced set is used in the defuzzification process (Kumbasar *et al*., 2012).The internal structure of IT2TSKFLC is shown in Fig. 4.

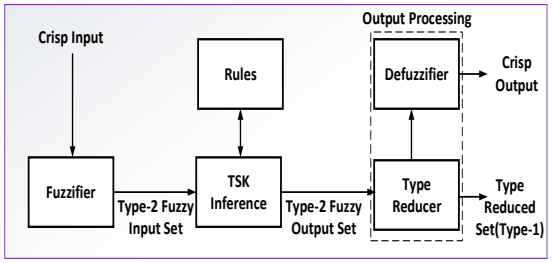

Fig. 4. The internal structure of IT2TSKFLC

Takagi-Sugeno-Kang (TSK) is a fuzzy modelling method proposed by Takagi, Sugeno and Kang. It can comprise high-dimensions, nonlinearity and complexity (Takagi et al., 1985). The structure of an interval type-2 TSK model offers two inputs and a single output using rules in Eq. 7 (Mendel, 2001):

$$R_i : IF\ x_1 \text{ is } \tilde{A}_{1i} \text{ AND} \ldots x_n \text{ is } \tilde{A}_{ni} \text{ THEN } LF_i = c_{0i} + c_{1i}x_1 + \ldots + c_{ni}x_n \quad (7)$$

Here i = 1…r represents the IF-THEN rules of the fuzzy system; $x_1, \ldots, x_n$ are input variables and $\tilde{A}_{ni}$ is membership function (MF) of IT2TSKFLC for the variable n and rule r ; LF_i is the rule output; and $c_0 + c_1 + \ldots + c_n$ are the consequent parameters. As shown in Fig.5, Gaussian type MF is used in the present study. The mathematical equations for Gaussian type MF are given in Eqs 8-9:

$$\bar{\mu}_{ij} = \exp\left\{-\frac{1}{2}\left(\frac{x_i - c_{ij}}{\bar{\sigma}_{ij}}\right)^2\right\} \quad (8)$$

$$\underline{\mu}_{ij} = \exp\left\{-\frac{1}{2}\left(\frac{x_i - c_{ij}}{\underline{\sigma}_{ij}}\right)^2\right\} \quad (9)$$

where c_{ij} is the mean value, σ_{ij} is the standard deviation, and x_i is the input variable.

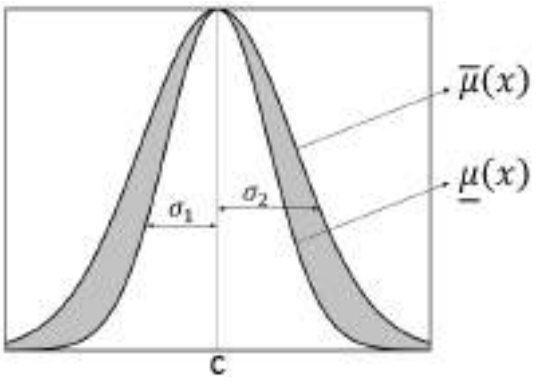

Fig. 5. Gaussian type-2 fuzzy set

The t-norm operation is defined in Eq. 10:

$$f_i = \prod_{j=1}^{n} \mu(x_j) \quad (10)$$

A normalized firing strength is expressed in Eq. 11:

$$\bar{f}_i = \frac{f_i}{\sum_{k=1}^{r} f_k} \quad (11)$$

$\bar{f}_i$ represents normalized firing strength. IT2TSKFLC contains lower and upper membership functions in case of uncertainties (Chang et al., 2011). The firing strengths of a fuzzy rule are given as lower and upper in Eqs.12-13 using the t-norm operator, respectively.

$$\underline{f}_i = \prod_{j=1}^{n} \underline{\mu}(x_j) \quad (12)$$

$$\bar{f}_i = \prod_{j=1}^{n} \bar{\mu}(x_j) \quad (13)$$

One of the closed-form type reduction and defuzzification methods, Biglarbegian-Melek-Mendel (BMM) is preferred in IT2TSKFLC (Biglarbegian *et al.*, 2010). Closed mathematical form type reduction and the defuzzification process of the proposed IT2TSKFLC can be calculated using Eq. 14.

$$Y_{BMM} = q\frac{\sum_{i=1}^{r} f_i\, LF_i}{\sum_{i=1}^{r} f_i} + (1-q)\frac{\sum_{i=1}^{r} \bar{f}_i\, LF_i}{\sum_{i=1}^{r} \bar{f}_i} \qquad (14)$$

4. SIMULATION STUDIES

In the proposed IT2TSKFLC, inputs are the error (e) and change of error (de) between reference output voltage and measured output voltage of boost converter. A Gaussian membership function was selected for each input as shown in Fig. 6.

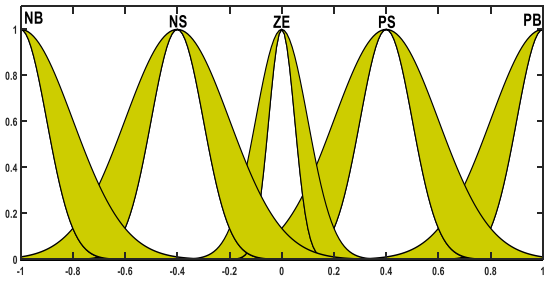

Fig. 6. Gaussian membership functions selected for e and de

The value range was selected as [-1, 1] for Gaussian membership functions. The linguistic expressions used for e and de in the model designed in Matlab/Simulink are Negative Big (NB), Positive Big (PB), ZE (S), Negative Small (NS), and Positive Small (PS). The rule base consisting of these linguistic expressions are given in Table 1.

Table 1. 5x5 rule base

$x_1(e)$ \ $x_2(de)$	NB	NS	ZE	PS	PB
NB	LF_1	LF_2	LF_1	LF_1	LF_5
NS	LF_6	LF_7	LF_8	LF_9	LF_{10}
ZE	LF_{11}	LF_{12}	LF_{13}	LF_{14}	LF_{15}
PS	LF_{16}	LF_{17}	LF_{18}	LF_{19}	LF_{20}
PB	LF_{21}	LF_{22}	LF_{23}	LF_{24}	LF_{25}

In general, some assumptions are made in the circuit design process. Circuit parameters of the designed DC-DC boost converter circuit are given in Table 2.

Table. 2 Circuit parameters of the designed DC-DC boost converter

Parameters	**Symbol**	**Value**
Input Voltage	V_g	30.7 V
İnductor	L	0.1 mH
Capacitor	C	81.6 µF
Load resistance	R	15 Ω
Output (Load) Voltage	V_c=V_o	60 V
Switching frequency	f_s	40 Khz
Duty Cycle	D	0.49
Inductor current change	Δi_L (%20 ripple)	1.628 A
Output (Load) Voltage Change	ΔV_c (%1 ripple)	0.6V
Output Power	P_0	250W

Output voltage level was set to 60V DC, and an output power of 250W was aimed. All circuit elements were assumed to be ideal, and power losses were ignored. When so, output power was assumed to be equal to input power. The input current of the circuit is calculated using Eq. 15:

$$I_g = \frac{P_i}{V_g} \qquad (15)$$

When the ripple in the inductor current is assumed to be 20%, the inductor current change can be calculated as follows:

$$\Delta I_L = \%c.I_g \qquad (16)$$

The necessary inductance value can be calculated using Eq. 17:

$$L = \frac{V_0 D(1-D)}{f\,\Delta I_L} \qquad (17)$$

Similarly, the output capacitor value bears importance in ensuring a sufficient output voltage ripple. The capacitor value for an output voltage ripple of 1% is calculated using Eq. 18:

$$C = \frac{I_0 D}{f\,\Delta I_C} \qquad (18)$$

Two different controlling scenarios were applied in order to test the dynamic performance of IT2TSKFLC. In the first scenario, the input voltage was changed. In the second scenario, the output load was changed.

The structure of IT2TSKFLC boost converter controller is shown in Fig.7.

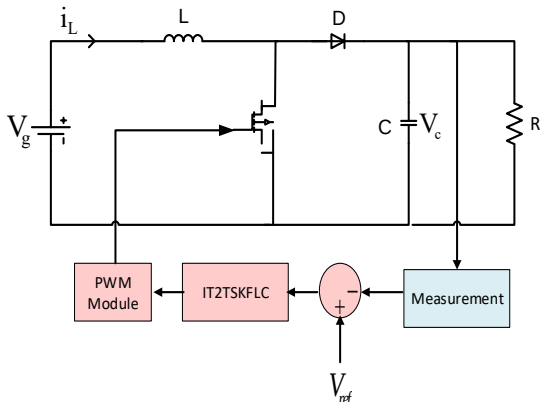

Fig. 7. The structure of the proposed IT2TSKFLC boost converter controller

In the first scenario, the input voltage was increased from 30.7V to 32V at 0.1 secs. The response of the proposed controller for the input voltage changes is shown in Fig.8.

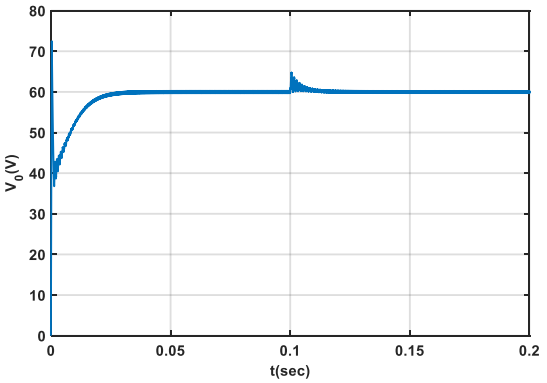

Fig.8. The response of the proposed controller for the input voltage change

As shown in Fig.8, a The proposed controller tracked again reference voltage at a duration as short as 0.01 secs after the input voltage was increased to 32V at 0.1 secs. In the second scenario, the load resistance was decreased from 15 Ω to 7.5 Ω at 0.1 secs. The response of the proposed controller for the load change is shown in Fig.9.

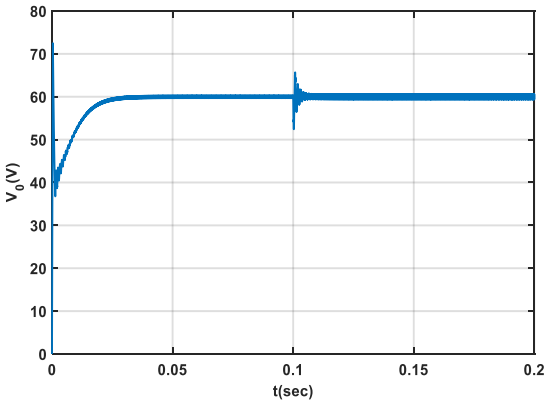

Fig.9 The response of the proposed controller for the load change

As shown in Fig.9, the ripple value increased from 0.6 V to 1.3V when the output load resistance was decreased. The proposed controller tracked again reference voltage at a duration as short as 0.004 secs, and thus showed a successful tracking performance.

5. CONCLUSION

In the present study, the dynamic performance of IT2TSKFLC was analyzed for controlling a boost converter. A simulation model was created using MATLAB/Simulink in order to evaluate the dynamic performance of the proposed controller. Two different simulation scenarios (input voltage change and output load change) were applied in order to test the stability and robustness of the proposed controller. The findings of the simulation studies demonstrated that the proposed controller showed an effective dynamic performance.

REFERENCES

Acikgoz, H. (2018). "Speed Control of DC Motor Using Interval Type-2 Fuzzy Logic Controller." *International Journal of Intelligent Systems and Applications in Engineering*, Vol. 6, No. 3, pp. 197-202.

Biglarbegian, M. Melek, W. W., and. Mendel, J. M.(2010). "On the stability of interval type-2 TSK fuzzy logic control systems," Systems, Man, and Cybernetics, Part B: Cybernetics, IEEE Transactions on, Vol. 40, No. 3, pp. 798–818.

Chang, C.C. Lin, C.J. (2011). "LIBSVM: A library for support vector machines," ACM Trans. Intel. Sys. and Tech., Vol. 2, No.3, pp. 1–27.

Karanjkar, D.S. Chatterj, S. Kumar, A. Shimi, S .L. (2014)."Fuzzy Adaptive Proportional-Integral-Derivative Controller with Dynamic Set-Point Adjustment for Maximum Power Point Tracking in Solar Photovoltaic System", Systems Science & Control Engineering, Vol. 2, No.1, pp.562-582.

Kumbasar, T. Eskin, I. Guzelkaya, M. Yesil, E., (2012). "Type-2 Fuzzy Model Based Controller Design for Neutralization Processes", ISA Transactions, Vol. 51, No. 2, pp. 277-287.

Mendel, J.M. (2001). "Uncertain Rule-Based Fuzzy Logic Systems" Introduction and New Directions. Prentice Hall.

Takagi, T. Sugeno, M. (1985) "Fuzzy Identification of Systems and Its Applications to Modeling and Control," IEEE Transactions on Systems, Man, and Cybernetics, Vol. SMC-15, No. 1, pp. 116–132.

CISET - 2nd Cilicia International Symposium on Engineering and Technology
10-12 October, 2019, Mersin / TURKEY

PRODUCTION of CoNiMnFe HIGH ENTROPY ALLOYS with MECHANICAL ALLOYING

Iskender ÖZKUL [*1], Ömer GÜLER[2] and Canan Aksu CANBAY[3] , Tuncay ŞİMŞEK[4]

[1] Mersin University, Engineering Faculty, Mechanical Eng., Mersin, Turkey
[2] Mersin University, Engineering Faculty, Metallurgical and Material Eng., Mersin, Turkey
[3]Firat University, Science Faculty, Physics Dep., Elazig, Turkey
[4]Mersin University, Architecture Faculty, Department of Industrial Design, Mersin, Turkey

ABSTRACT
High entropy alloys have been promising alloys since 2004 due to their high mechanical and physical properties. In this study, especially on the high magnetic properties of CoNiMnFe alloy we have researched. Alloying was carried out by mechanical alloying method using high purity elemental metals. The sample was then sintered in an argon medium in an induction furnace with high speed heating. The samples were analyzed by SEM, EDS and XRD.

Keywords: *High entropy alloys, XRD, EDS, SEM, CoNiMnFe*

[*] İskender ÖZKUL

1. INTRODUCTION

Alloy on earth has played a major role in the advancement of human history. The area of metallurgy has been developing rapidly since arsenic and copper alloys, which were formed accidentally in 3000 BC (Murty *et al.* 2019). It has started to show itself in the last hundred years in innovative materials as well as in general materials. High entropy alloys in one of the type of novel materials are a rapidly developing alloy type (Diao *et al.* 2017). High temperature resistance, oxidation resistance and high strength properties are encountered in many applications in the manufacturing industry. These alloy types are generally formed by alloying metallic elements equal to 4 or more atoms atomically (Yeh *et al.* 2004; Gali *et al.* 2013). Two of these elements generally occupy more space in chemical composition. These alloys are prepared according to Hume-Rothery rules (Hume-Rothery 1926; Murty, Yeh, Ranganathan and Bhattacharjee 2019). The concentration of the elements in the alloy is between at.% 5 and 35. Mixing the elements in a crucible creates higher entropy. If this entropy value is less than 1, it is called as low entropy alloy, if it is between 1 and 1.5, it is called middle entropy alloy and if it is above 1.5, it is called high entropy alloy series (Gali and George 2013). Serious lattice distortions, sluggish diffusion, high entropy are observed in the structure of alloys. At the same time, the lattice structures are in the form of face-centered cubic (FCC), body-centered cubic (BCC) and hexagonal closed packed (HCP).

In this study, four elements Fe, Co, Ni and Mn which have magnetic properties were produced by mechanical alloying and micro structures were investigated.

2. EXPERIMENTAL

High purity (99.9%) elemental metals were prepared as Fe, Co, Ni and Mn equal molar ratio.

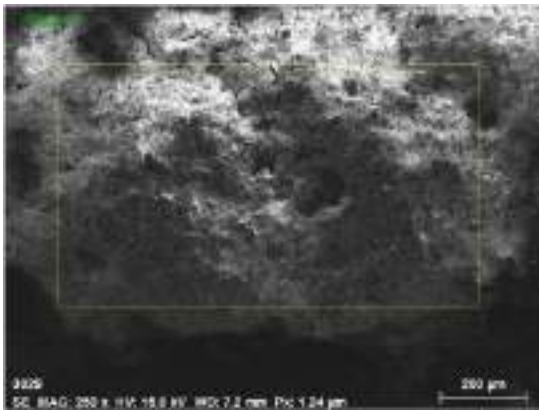

El	AN	Series	Net unn. C [wt.%]	norm. C [wt.%]	Atom. C [at.%]	Error (1 Sigma) [wt.%]
Co	27	K-series	973	59.34	51.04	50.66	2.94
Ni	28	K-series	348	18.87	21.33	21.07	1.71
Mn	25	K-series	711	22.63	19.47	20.48	1.19
Fe	26	K-series	222	9.42	8.18	8.38	0.77
Total:			114.26	100.00	100.00		

Fig. 1. Chemical composition of the 1hour mechanical alloying.

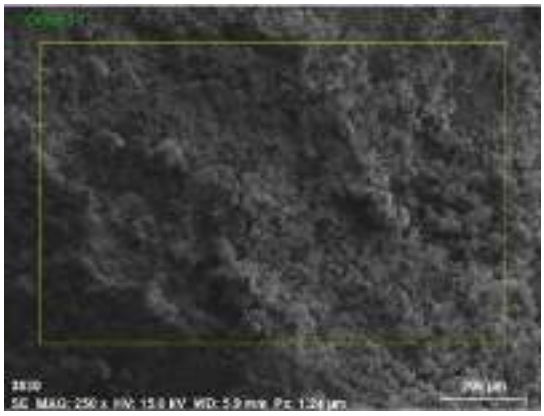

El	AN	Series	Net unn. C [wt.%]	norm. C [wt.%]	Atom. C [at.%]	Error (1 Sigma) [wt.%]
Mn	25	K-series	776	35.84	28.25	29.23	1.79
Fe	26	K-series	696	35.16	28.03	28.52	1.96
Co	27	K-series	348	28.60	22.80	21.99	1.94
Ni	28	K-series	269	28.24	20.92	20.25	1.98
Total:			125.43	100.00	100.00		

Fig. 2. Chemical composition of the 100hour mechanical alloying.

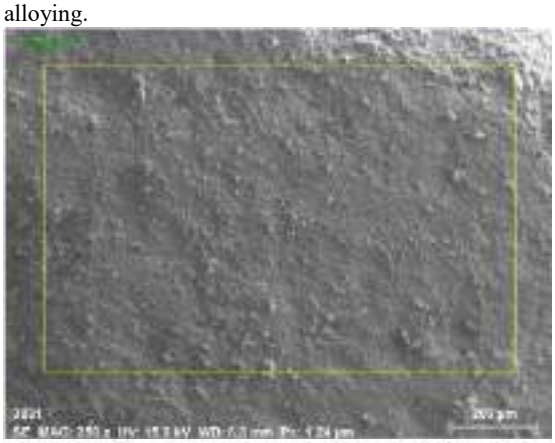

El	AN	Series	Net unn. C [wt.%]	norm. C [wt.%]	Atom. C [at.%]	Error (1 Sigma) [wt.%]
Fe	26	K-series	562	38.92	29.65	30.17	2.10
Mn	25	K-series	691	36.24	27.61	28.56	1.91
Co	27	K-series	341	32.71	24.92	24.02	2.23
Ni	28	K-series	205	23.40	17.83	17.26	1.97
Total:			131.36	100.00	100.00		

Fig. 3. Chemical composition of the sintered 100hours mechanical alloying.

In argon medium, the mixture was placed into the bulk container with a ball-to-powder (BPP) ratio of 20: 1. The powder mixture was milled using a Retsch PM 100 brand apparatus. The mill was operated for 100 hours for mechanical alloying at 250 RPM. The samples were taken in the first hour of the study. Some of the sample obtained after 100 hours was sintered at high temperature in the induction furnace with high heating speed. The obtained results were determined by EDS device. These results are shown in Figure 1-3.

3. RESULTS AND DISCUSSIONS

The obtained three samples were analyzed for phase transformation with Differential thermal analysis (DTA). The obtained results are presented in Figure 4.

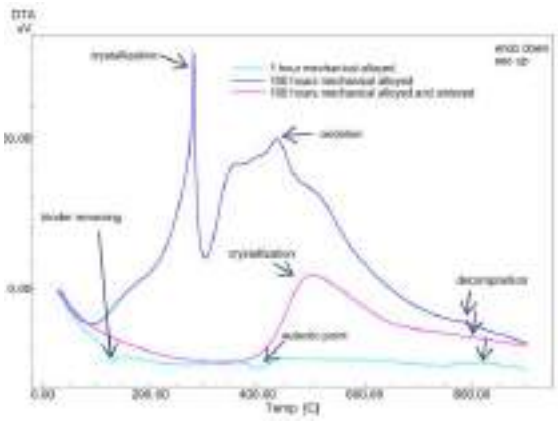

Fig. 4. DTA analysis of the samples

In DTA the heating plots exothermic peaks generally shows crystallization, oxidation, glass transition. In endothermic peaks, spinodal decomposition, eutectic point, decomposition and melting points.

When we compare the samples, we observed two endothermic peaks for the one hour mechanical alloyed sample and there is no exothermic peak so the first endothermic peak means the binder removing from this alloy and the second peak is the eutectoid point. On the other hand the other samples exhibit a wide exothermic peak after 350 °C and this is mainly due to the oxidation mechanism occurred in the samples structure. If the elements interact between oxygen for a long time, the oxidation mechanism forms quickly. For the 100 hours mechanical alloyed sample, first exothermic peak means the crystallization in the structure. After the 700 °C, the decomposition of the 100 hours mechanical alloyed and 100 hours mechanical alloyed and sintered samples started.

Also a X-ray diffraction (XRD) analysis was carried out to determine the crystal structure using the CuKα radiation with λ=1.5405 Å at room temperature by a Rigaku device at a scanning speed of 5 deg/min.

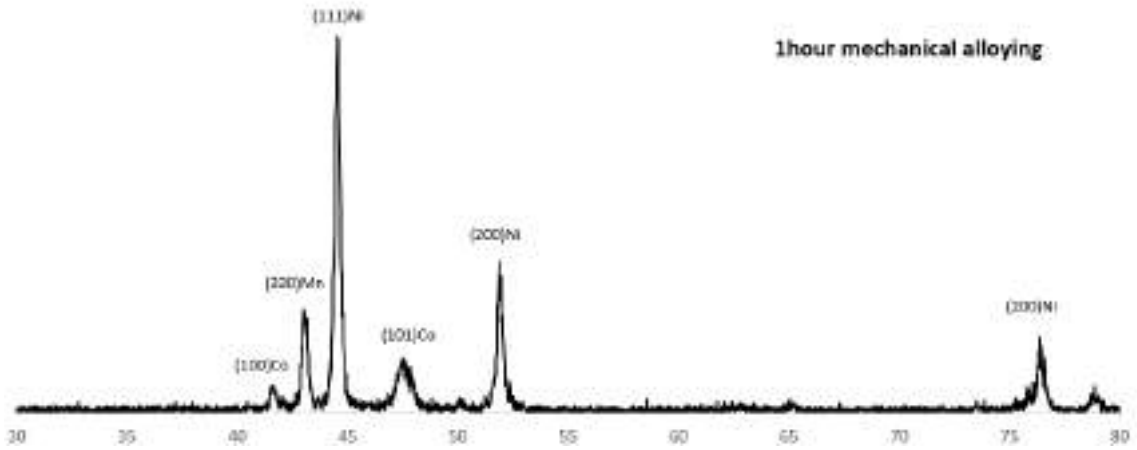

Fig. 5. XRD analysis of the samples for 1hour mechanical alloying.

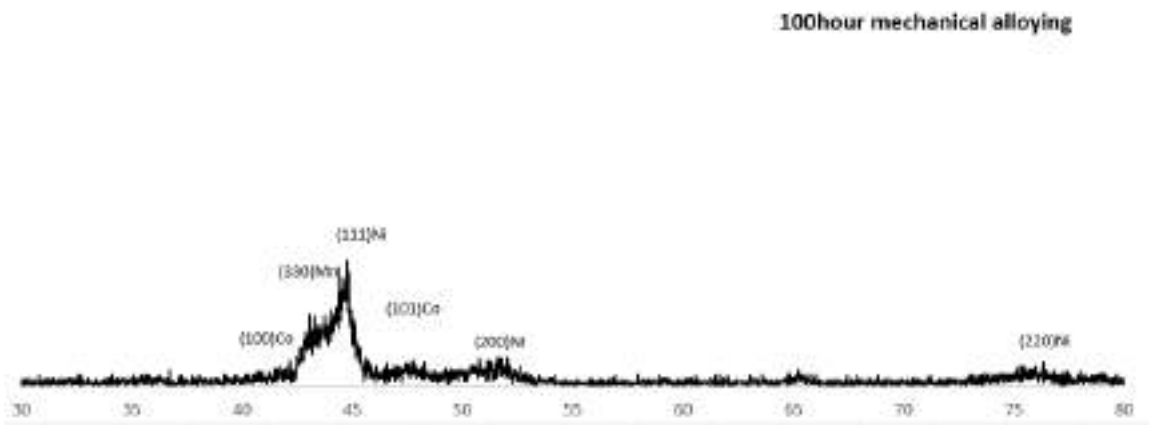

Fig. 6. XRD analysis of the samples for 100hour mechanical alloying.

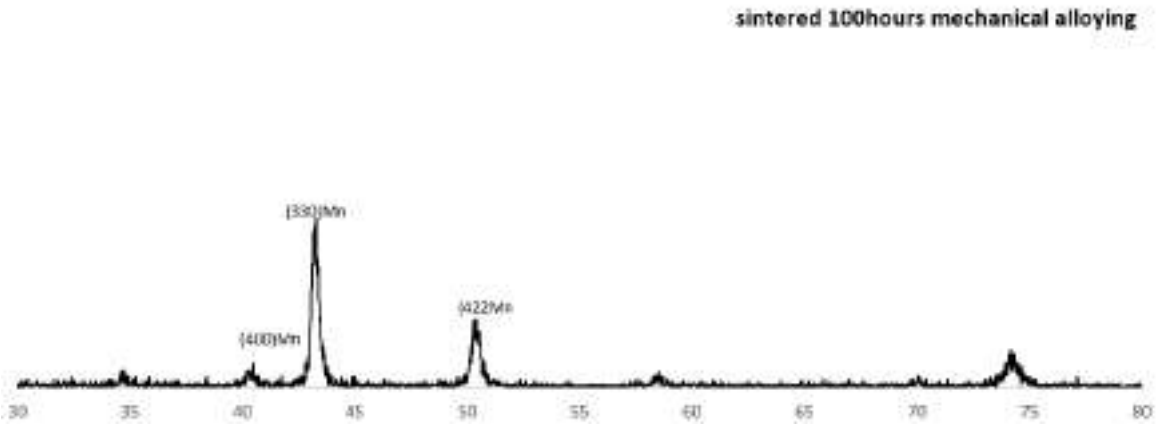

Fig. 7. XRD analysis of the samples for sintered 100hour mechanical alloying.

The Peaks in XRD pattern for 1 hour alloys are consists pure elemental peaks. However, 100 hours are clearly different peaks, differs from 1 hour alloying, and shows mechanical alloying process materialization. After sintering the peaks are show similarity with literature (Zuo *et al.* 2017; Cui *et al.* 2018).

5. CONCLUSION

In this study we have focused on synthesizing high entropy alloys which is consisted magnetocaloric elements such as iron, nickel, manganese and cobalt. These elements were prepared in same molar ratio and alloyed with mechanical alloying milling. The obtained alloys finally sintered with induction furnace under argon atmosphere. The XRD peaks have shown us the after sintering process the high entropy alloy was occurred. In following studies will focus on mechanical and magnetic properties.

REFERENCES

Cui, P., Y. Ma, L. Zhang, M. Zhang, J. Fan, W. Dong, P. Yu, G. Li and R. Liu (2018). "Effect of Ti on microstructures and mechanical properties of high entropy alloys based on CoFeMnNi system." *Materials Science and Engineering: A*, Vol. 737, No., pp. 198-204.

Diao, H., R. Feng, K. A. Dahmen and P. Liaw (2017). "Fundamental deformation behavior in high-entropy alloys: An overview." *Current Opinion in Solid State and Materials Science*, Vol. 21, No. 5, pp. 252-266.

Gali, A. and E. P. George (2013). "Tensile properties of high-and medium-entropy alloys." *Intermetallics*, Vol. 39, No., pp. 74-78.

Hume-Rothery, W. (1926). Researches on the nature, properties, and conditions of formation of intermetallic compounds, with special reference to certain compounds of tin, University of London.

Murty, B. S., J.-W. Yeh, S. Ranganathan and P. Bhattacharjee (2019). *High-entropy alloys*. Elsevier.

Yeh, J. W., S. K. Chen, S. J. Lin, J. Y. Gan, T. S. Chin, T. T. Shun, C. H. Tsau and S. Y. Chang (2004). "Nanostructured high-entropy alloys with multiple principal elements: novel alloy design concepts and outcomes." *Advanced Engineering Materials*, Vol. 6, No. 5, pp. 299-303.

Zuo, T., M. C. Gao, L. Ouyang, X. Yang, Y. Cheng, R. Feng, S. Chen, P. K. Liaw, J. A. Hawk and Y. Zhang (2017). "Tailoring magnetic behavior of CoFeMnNiX (X= Al, Cr, Ga, and Sn) high entropy alloys by metal doping." *Acta Materialia*, Vol. 130, No., pp. 10-18.

CISET - 2nd Cilicia International Symposium on Engineering and Technology
10-12 October, 2019, Mersin / TURKEY

THE IMPORTANCE OF HISTORICAL TURKISH WORK OF ARTS IN TERMS OF ENGINEERING

Cengiz Alyılmaz *[1]

[1] Uludag University, Faculty of Arts and Sciences, Department of Turkish Language and Literature, Bursa, Turkey, calyilmaz@gmail.com

ABSTRACT

The Turks, who lived in different parts of the world and always formed an important part of the world population, have had a different place and importance in the history of the world with their language, history, lifestyle, beliefs, cultural and civilization work of arts they made in the early periods. However, recent studies on Turks state that the Turks are generally horsemen and warriors, live nomadic life and have made their permanent works after leaving Asia and coming to Anatolia (especially during the Seljuk and Ottoman Periods). However, when we look at the history of the Turks, it is seen that this history does not only consist of the Seljuk and Ottoman periods, that it dates back to the older times (Saka/Scythian, Hun, Avar, [Kök]Turk, Uyghur periods, that the Turks have created unique works of language, culture, art and architecture from the early periods.

Spaces built by the Turks in history for settlement, transportation, defense, worship and training purposes (castles, towers, villages, towns, cities, architectural monuments, irrigation canals, sewerage systems, burial complexes, monuments, inscriptions, ornaments and items...) reveal that Turks adopted a sedentary life in the early periods and that these work of arts are the product of serious knowledge, background and experience.

This paper will mention the architectural structures, irrigation canals, cultural and art works that were built by the Turks in the early periods, some of which are also the first works of Turkish engineering, but which have not been researched and examined by the Turkish scientists.

Keywords: *Turks, early Turkish works, Turkish engineering history.*

*Corresponding Author

1. INTRODUCTION

The archaeological remains in different geographies of the world and the old and new sources written on the subject, especially in the Asian continent, reveal that the Turks are among the oldest known nations of human history. However, despite all the information, findings and documents about the Turks, a significant part of the domestic and foreign sources either ignore the artifacts created by the Turks, or give them to other communities and nations. According to these sources, Turks generally live on horseback and nomads;as a result of the wars they make their livelihoods with their spoils. However, Turks, like other nations, lived nomadic and settled lives in different geographies, different periods and histories; they have contributed to the history of humanity in every way of life.

It is possible to group the works that Turkish tribes and communities brought into the body in different periods, in other words, concrete cultural assets as follows: petroglyphs; sewn, stamped and depicted stones; written works (works written with different alphabets on stones, rocks, cave, monastery and temple walls, paper and various objects); kurgans, graves, cemeteries and shrines; statues, statuettes and balballs; places of worship and religious places of interest(mountain visits [oboolar], caves, temples, mosques, masjids ...); city ruins and architectural works (castles, city walls, inns, caravanserais, houses, irrigation canals ...); use and ornaments.

The place and the works on this place play an important role in the acquisition of experiences and values that constitute the collective tradition, in the integration of people with the society they live in, in the formation of nationalization and common identity. Each of the works mentioned above, which is the product of Turkish life and belief, has played a major role in the formation of the ethnic and cultural identities of Turkish tribes and communities and meeting them on a common ground.

Concrete cultural beings bear witness to the existence of nations, their experiences, coexistence, separations, achievements and frustrations in the historical process. As a matter of fact, they contain the joys and happiness of those who bring them into their bodies, as well as their sadness and unhappiness. To embody emotion, thought, joy, grief, and to make it tangible, visible, sensible with sensory organs requires a considerable experience and knowledge.

Turkish tribes and societies have moved in the early stages of history (as in other communities, peoples and nations) to survive, to be safe, to live long, healthy and peaceful; first “nomad” and then “nomad” lived. (İngilizce'de göçebe ve konargöçer eşanlamlı).http://dergiler.ankara.edu.tr/dergiler/49/1881/19769.pdf However, this lifestyle has been replaced by the “settled” system after the discovery of geographies / regions that are suitable for both themselves and their animals.

The relationship of Turkish tribes and communities with stone and tree in the mountainous and forested areas, with soil, slime and mudbrick in the flat areas played an important role in shaping the architectural structures they created for protection, shelter and worship.

Experiences and gains of Turkish tribes and communities in housing during their nomadic life; the way of life of the societies that were established before them also affected their settled lives. In order to ensure the security of the communities under their sovereignty, the Turkish khanates, gentlemen and commanders first fenced the places where they lived; then theybuilt castle cities; after the increase of the settled population, they surrounded the big cities around the city walls and placed entrance gates at certain points. There is information in the Chinese sources and the ancient Turkish inscriptions that the Turks passed the city life in the early periods, which they met with the signs of fish (~ balgat / balgas / balgasun), city (~ çent / kant / kan / ken), nation, army, province (~él).

Cities built by Turkish khan and commanders, separated as summer and winter, have become the biggest international cultural and civilization centers of their time with their architectural structures and liveliness in the fields of agriculture, commerce, religion, art and literature. Some of the cities where the Turks lived extensively in the east and west, fighting for their sake, and mentioned in the historical sources (many of which were the busiest centers of the era until the Mongol invasion) are as follows: Beş Balık, Togu Balık, Bavıl Balık, Bay Balık, Ordu Balık (Kâşgar, Kaş Balık, Ka-Şa, Sulek / Sule), Kuz Balık (Gu Balık, Kuz Ordu, Kuz Uluş, Ordu Kent, Balagasun), Can Balık, Çakuk Balık, Yengi Balık, Barçınlıg Kent, Man Kent, Öz Kent (Öz Çent, Fergana), Taş Kent (Çaç, Şaş, Terken), Tün Kent, Semiz Kent (Semerkant), Süt Kent, Yar Kent, Yegen Kent, Temir Kapıg (Temir Kapı, Demirkapı), Turfan, Bukarak (Buhara), Suğnak (Sıgnak), Karnak, Barçuk, Karaçuk, Kazvin, Kinküt, Koçungar Başı (Koçgar Başı, Koç Başı), Kuça, Argu (Argu), Aşnas, Sayram (İsbicab), Savran, Talas (Taraz, Kumi Talas, Ulug Talas), Sûyâb, Cend, Yafınç, Yafgu, Almalıg, Altun Kır, Altındağ, Altun Tepe, Çuy Tepe, Turtkul Tepe, Çardarı, Bayırkum, Balu, Barsgan, Barhan, İşkan, Kençek Sengir, Yesi, Ribâtât etc.

Fig. 1. Image of a building in the historical city of Idiku (East Turkestan; Photo: Murat YAKAR).

Fig. 2. A general view of the historic city of Por-Bajin(Toprak Kale)

1.2. Importance of Old Turkish Works in terms of Engineering

The regions where Turkish tribes and communities lived also determined their interests; enabled them to produce successful works in the fields of stone, wood and metal. Many architectural structures in the vast geography extending from Orkhon to Anatolia and the artifacts that these structures contain, reveal both the knowledge, accumulation and socio- cultural and economic levels of the Turks in these areas.

Fig. 3. An Image From Kariz Irrigation Channels (Turfan-East Turkestan; Photo; Cengiz Alyılmaz)

The works, which were built by Turkish tribes and societies and only partially existed in the old Turkish cities and other settlements(in obas, villages, towns…) mentioned above, have attracted the attention of the scientists (historians, art historians, archaeologists, linguists ...) who are generally interested in social sciences and the related studies have been done by the scientists in these fields. However, the works of ancient Turkish culture and civilization are of interest to the scientists working in the fields of basic sciences, health sciences, engineering etc. as well as these fields.

In the old Turkish cities, multi-storey architectural structures built for different purposes in the cities, their construction features, sewerage systems located in the majority of them, irrigation channels developed to meet the water needs of the inhabitants and agricultural lands (especially the Karız Irrigation Channels, which remain within the borders of East Turkestan today, most of which date back to prehistoric times and are regarded as one of the Seven Wonders of the World by many scientists), usage and ornaments made for different purposes etc. have features that require hundreds of studies on them.

Moving snow melting from the mountains thousands of kilometers away with channels excavated tens of meters below the ground keeping the freshness is not a simple experience; is a product of serious knowledge, accumulation and calculation. The Turks, of course, knew very well how to calculate and implement architectural structures as well as equipping them for future generations. As a matter of fact, many works belonging to the Old Turkish Period prove this opinion and provide the opportunity to take the history of Turkish engineering at least one thousand years ago.

Mankind has made use of different materials and mines in different sizes, religious and ritual pots, war tools etc. In order to survive, to meet their needs, to fight, to be protected, to ensure their livelihood, to look beautiful, to be decorated etc. These tools, which human beings cannot give up, have shed light on the enlightenment of many unknowns of history. Because each work is not only a simple use and ornament, but also carries deep traces from the life and belief (s) of the body (s) that brought it to the body. Use and ornaments made to be used in different areas of life allow us to obtain detailed information about the human's view of life, its development and change, and its relationship with its own species and other species. It is also possible to determine which period, to whom and to which the works belong from the construction techniques, stylistic features, materials and the graphical elements(stamp (s), painting (s), drawing (s), description (s), writing (s)) they contain. However, it is the job of engineers to determine their properties and importance in terms of engineering. The mines used by the ancient Turks, the works made from these mines, the relationship between the mines and the geography, the determination of the mines in the old Turkish geography and the places where the Turkish tribes and communities live today and making the maps of the regions they are located in are primarily concerned with the engineering field.

Fig.4. Image of the golden interrogator unearthed during the excavation at Bilge Kagan Memorial Grave

Complex (Höşöö Tsaídam - Mongolia; Photo: Cengiz ALYILMAZ)

Turks, like other communities and nations, have lived nomadic and settled lives in different periods and in different geographies. Many concrete cultural legacies of the nomadic, settled lives of the Turks have survived from the past to the present. These works, which bear deep traces of the lives and beliefs of Turkish tribes and societies, include those interested in the social sciences as well as those of engineers. However, it is an undeniable fact that Turkish scientists working in different fields of engineering do not pay enough attention to the old Turkish history, culture and adaptability, and that the studies related to the field of engineering are negligible in the regions where Turkish tribes andcommunities live.

Turkish tribes and societies, today in the territory of different countries, in the Old Turkish Period, have written inscriptions, books and written documents both with their own language and their own writings[The Köktürk Alphabet]; as well as the language and alphabets of the nations in which they have social, cultural, political, commercial, religious, military relations (Chinese, Sogdad, Tibetans, Indians, Iranians etc.). In these works, there are many words, phrases and terms related to engineering. This vocabulary is not included in any of the studies on engineering terms. The vocabulary related to engineering which is mentioned in the basic sources of Turkish language should be determined and these should be included in the related works.

Fig. 5. Photogrammetry Engineer Dr. Murat YAKAR while documenting in Yargol Caves

Scientists working in the field of engineering, by contacting scientists working in the field of social sciences and forming teams and conducting interdisciplinary studies in the Turkish world and Turkey can enlighten many unknowns of Turkish culture and civilization, as well as identify the values (information, findings and documents) of their fields and contribute to the introduction of light.

REFERENCES

http://dergiler.ankara.edu.tr/dergiler/49/1881/19769.pdf

http://dostoyanieplaneti.ru/49-por-bazhyn-uighurskaia-oziernaia-kriepost

ALYILMAZ, C. (2007). *(Kök)türk Harfli Yazıtların İzinde*. Ankara.

ALYILMAZ, C. (2012). İslamiyet Öncesi Dönemde Türklerde Konargöçerlik ve Şehircilik. *Türk Dünyası Mühendislik, Mimarlık ve Şehircilik Kurultayı Bildiriler Kitabı*, Ankara, 109-140.

ALYILMAZ, C. (2015). *İpek Yolu Kavşağının Ölümsüzlük Eserleri.* Ankara.

ALYILMAZ, C. (2019). İslamiyet Öncesi Türk Eserleri. *Ortak Türk Tarihi VI,* Ankara, 1-105.

ESİN, E. (1978). *İslamiyetten Önceki Türk Kültür Târîhi ve İslâma Giriş.* İstanbul.

MERT, O. (2009). *Ötüken Uygur Dönemi Yazıtlarından Tes – Tariat – Şine Us.* Ankara.

ÖGEL, B. (1984). *İslamiyetten Önce Türk Kültür Tarihi.* Ankara.

CISET - 2nd Cilicia International Symposium on Engineering and Technology
10-12 October, 2019, Mersin / TURKEY

ABOUT THE WORK AND MAP OF MAHMUD AL-KASHGARI

Semra ALYILMAZ [*1] and Harun ŞAHİN [2]

[1] Uludağ University, Bursa, Turkey, semraalyilmaz@uludag.edu.tr

[2] YÖK,Ankara,Turkey, harunsahin75@gmail.com

ABSTRACT

Mahmud al-Kashgari is considered by experts to be the first linguist and dictionary maker of the Turks, and his famous work Divanu Lugat'it-Turk is also considered to be the oldest known systematic and encyclopedic work of Turkish dictionary and linguistics. Divanu Lugat'it-Turk, which is a sampled and annotated work, was written in Arabic to teach Turkish to Arabs. Although it was written to teach Turkish to the Arabs, in reality the target audience of the work is Arabs in a narrow sense and the whole Islamic world in the broad sense. In this respect, the work is the first tidy source of Turkish teaching to foreigners. The material of the work was collected and gathered from the Turkish world by Mahmud al-Kashgari himself; it was published as a book in Baghdad between 1072 and 1077. In addition to being a dictionary, there is also a "world map" in the work, which includes valuable information about Turkish tribes and communities. The map, which is made in a round and colored, depicts cities, important settlements, mountains, rivers, deserts, (some geographical formations, writings and floors) in different colors. The important settlements in the world are accurately stated on the map, based on the Turkish khanate/reign center, Balasagun city. The locations and information shown on the map are largely matched with information from other sources of the period. Mahmud al-Kashgari, a noble and wise prince/tigin, traveled around the vast geography from Kasgar to Baghdad for about fifteen years and made compilation, which plays a major role in this situation. Mahmud al-Kashgari deserves the title of "Cartographer" both because of the information given by him about the geography which Turks live in and the map in his work (besides all known features). This paper mentions about Divanu Lugat-it Turk and outlines the "map of the world" in detail. Please read all information given in this template carefully before start typing.

Keywords: *Mahmud al-Kashgari, Divanu Lugat-it Turk, Map, World Map. Cartography, Turkish Cartographer.*

[*] Corresponding Author

1. KÂŞGARLI MAHMUD

Although the adjective in front of his name is K sıfşgarlı, Mahmud is not originally Kâşgarlı; He is from the city of Barsgan (which was founded by the son of Afrasiyab, Barsgan, who is in the borders of Kyrgyz Republic today) .Mahmud was known as "Kâşgarlı" / "Kudşgarlı Mahmud için because he grew up in Kâşgar and became famous.

Mahmud's grandfather, Muhammad Bughra Khan, from 1056-1057; his father Hüseyin Çağrı became the Karahanlı ruler in 1057. A noble, distinguished and respected prince / tigin, Mahmud of Kâşgarlı had to leave Kâşgar after his father was dethroned after a coup attempt (Ercilasun, 2005: 320-321).

Mahmud of Kâşgar states that he is distinguished, respected and noble in Dîvânü Lûgat'it-Türk with the following words:

'' I have studied their countries and their steppes; I learned the dialects and rhyme of Turk, Turkmen, Oguz, Cigil, Loot and Kyrgyz. I am one of the most truthful in language, the most open in expression, the most rationalist, the most rooted, the best shooter in the spear. Thus, every neck tongue found its perfect shape in me (DLT; Ercilasun and Akkoyunlu, 2014: 2).''

Based on the information in Dîvânü Lûgat'it-Türk, it would not be wrong to describe Kâşgarlı Mahmud as a linguist, lexicologist, etymologist, Turkish teacher, cultural historian, cartographer. (Apart from Dîv dışındanü Lûgat'it-Türk of Kâşgarlı Mahmud, it should be noted that there is another work called Kitabü Cevahiri'n-Nahv fi Lûgat'it-Türk and it has not been recovered until today).

2. DÎVÂNÜ LÛGAT'IT-TÜRK:1

Dîvânü Lûgat'it-Türk This is the oldest and most compact dictionary of Turkish dialects and dialects. The work was written by Kâşgarlı Mahmud between 1072-1077.

Dîvânü Lûgat'it-Türk was presented to Ebü'l-Kasım Abdullah, son of Abbasid caliph Muhammedü'l Muktedi bin Emrillah. The target audience of the work is the Arabs in the narrow sense and the whole Islamic world in the broad sense. In this respect, the book is the first tidy and systematic reference for teaching Turkish to foreigners.

The material of the work has been collected from the Turkish world; It was made a book in Baghdad. Some of the information in the work shows that Kâşgarlı also benefited from the large libraries in Baghdad.
The work contains Arabic translations of approximately 8000 Turkish words.

The words used in the work are classified on the basis of the Arabic and Arabic alphabets and the usage of the original and zaid letters. It is known that while preparing K eserşgarlı Mahmud's work, he first saw works written in this genre (especially Halilî's [Halîl b. Ahmed's book called Kitabü'l Ayn) and benefited from their system.

In Dîvânü Lûgat'it-Türk, information is given about the places where Turkish tribes and communities live, their beliefs and languages.

In this work, valuable information is given about the stamps and sacred birds of Oguz tribes. Mahmud of Kâşgarlı also mentions some Hadiths about the Turks in the book.

In this work, although the standard Turkish of the period is taken as the basis, the mouth features of different Turkish tribes and groups are also included.

Mahmud of Kâşgarlı said that he received words with a high frequency of use; he states that he does not include archaic words and special names in the work.

The work is very important in terms of being the first sampling, explanatory and comparative encyclopedic dictionary of Turkish lexicography. Expressions, sayings, proverbs, races, epic fragments ... were included in the sampling.

There is only one copy of the work which was seized by Ali Emirî Efendi in 1915; this copy is also in Istanbul Millet Library today.

Firstly published by Kilisli Muallim Rifat Bilge between 1917-19, many people (Brockelmann, Besim Atalay, Salih Muttalibov, Robert Dankoff and Ahmet B. Ercilasun - Ziyad Akkoyunlu) worked on this work.

3. DÎVÂNÜ LÛGAT'IT-TÜRK'TEKI HARITA

In the lectures of Fuat Köprülü, scientists say that if you put Dede Korkut Book in one eye of the scale, Dede Korkut Book network comes to your students.

This statement that Fuat Köprülü said to emphasize and emphasize the importance of the Book of Dede Korkut would not be wrong for Dîvânü Lûgat'it-Türk in terms of our "language ve and" lexicography ". One of the things that makes such a valuable work even more is that a "world map yer is included in the work.

The presence of a map; Turkish tribes living in that period and giving information about some nations increases the importance of the work.

First of all, it should be noted that the map of Kâşgarlı Mahmud, which was prepared to teach Turkish to foreigners and which is essentially a dictionary, was prepared to show the readers the regions where the Turks live. In other words, although the map is a "world map bilgiler, the information given on the map is outlined in accordance with the reason of the work. Settlements are shown on the map as small yellow circles, 3 of which are not mentioned. This suggests that Kâşgarlı Mahmud put it before he could complete the map; It may also be thought that what they have shown is sufficient for the target audience. However, even today, language, dialect and lexical studies based on field studies are not included in the maps of the working regions, but it is first and foremost to include such a map in the conditions of that day.

The fact that Mahmud of Kâşgarlı has given the name of many geographic units, regions, nations and countries outside the Turkish homeland that is included in the research field in her map shows her knowledge, knowledge and far-sightedness. In the works written on the subject, while preparing the map that Kâşgarlı Mahmud put in his work, there is information that he had benefited from the maps and works prepared by himself (especially Bîrûnî [Abu Reyhan Muhammed bin Ahmed al-Birûnî (d. 1038)] and the map. 4 There is nothing natural about it. As a matter of fact, it is unthinkable that a linguist and cultural historian like Klışgarlı Mahmud could not see and benefit from the works on the subject. All this in no way diminishes the significance of Kâşgarlı's work.

Kâşgarlı Mahmud, based on the map he put in his work based on the city of Balasagun; other settlements accordingly. Balasagun, the centuries-old administrative center of the Western Köktürk Khaganate, has a very important strategic position in the middle of Central Asia and is located on one of the central points of the Silk Road. Balasagun, the city of culture and civilization, which is in ruins today, has hosted many civilizations. It is therefore very meaningful that Kâşgarlı Mahmud put Balasagun at the center of the map.

Names and drawings on the Balasagun-based world map extend to the Russian borders in the west, the Idil (Volga) river in the south, from the Egyptian borders in the south to Ethiopia and India, and to China and Japan in the east. Balasagun, Barsgan, Kuca, Bârmân, Uc, Koçgarbaşı, Cürcan, Hotan, Yarkent, Kâşgar, Kümi-Talas, İkögüz, Yefnüc, Nazal, Taraz / Talas, İsbicâb, Şaş, Sulmi, Kocu, Kashmir, Kâsân, Özcend, Merginan, Hocend, Samarkand, Harezm, Cend are read as settlement names. Bilâd-ı Sicistân, Bilâd-ı Kirmân, Vadi-i İrtiş, Ötüken, Mesâkin-i Kıfçak, Bilâd-ı Sind, Arzu'l-Yemen, Arzu'l-Hicâz, Arzu'ş-Şâm, Bulgarian, Russian, Vireng Various regions are marked with names such as, Pecheneg. Much more generally, the Kashgarian world map covers Central Asia, China and North Africa.

The location, height, most of the nation's names and some geographical shapes are mentioned on the map for the first time; Although their names are mentioned in the work, it is known that there are Turkish tribes whose names are not mentioned on the map. However, all this is at the discretion of the author; perhaps it may be thought that he might not have given them space in order to avoid repeating.

4.CONCLUSION AND RECOMMENDATIONS

Dîvânü Lûgat'it-Türk, written by Kâşgarlı Mahmud, is the oldest and most compact dictionary of Turkish dialects and dialects. The work also includes a world map.

- The map in Dîvânü Lûgat'it-Türk is mainly designed to show foreigners the places where Turks live, where Turkish dialects and dialects are spoken. However, many settlements, regions, nations and countries are also included in the map. The name of Japan is "Cabarka" on the map; It is interesting to note that China's name is shown as "Yecüc Mecüc Diyarı".
- The map in Dîvânü Lûgat'it-Türk has many aspects to be criticized in terms of Surveying Engineering. But the criticism "is not by a map engineer of the map; language, dictionary scientist, cultural historian, who want to learn Turkish to foreigners prepared to show the region where Turks live "should be made with the consideration.
- When talking about Turkish cartography in the related faculties and departments of our universities, genelde Piri Reis Map genelde usually comes to mind and information is given about this map.As the map of Kâşgarlı Mahmud's unique work Dîvânü Lûgat'it-Türk is mentioned, it will take the history of Turkish cartography to an earlier age; this work and the information contained in the map will be instrumental in learning and teaching.

REFERENCES

AKALIN, Ş. (2008). Bin Yıl Önce Bin Yıl Sonra Kâşgarlı Mahmud ve Dîvânü Lûgat'it-Türk.
Ankara.
ALYILMAZ, C. (1994). Sözlükbilim ve Dîvânü Lûgat'it-Türk. Türkologiya, 1, 12-16.
ALYILMAZ, C. (2015). İpek Yolu Kavşağının Ölümsüzlük Eserleri. Ankara.
ATALAY, B. (1985, 1986). Kâşgarlı Mahmud Divanü Lûgat-it Türk Tercümesi C I-IV. Ankara.
BOZKURT, F. (2012). Kâşgarlı Mahmud Divanü Lûgat-it Türk Türk Dili Divanı. Konya.
ERCİLASUN, A. B. (2004). Başlangıçtan Yirminci Yüzyıla Türk Dili Tarihi. Ankara.
ERCİLASUN, A. B. ve AKKOYUNLU, Z. (2014). Dîvânu Lûgat'it-Türk Giriş - Metin - Çeviri - Notlar. Ankara.
GENÇ, R. (1997). Kaşgarlı Mahmud'a Göre XI. Yüzyılda Türk Dünyası. Ankara.
SARİCAOĞLU, F. (2008). Kâşgarlı Mahmud: İlk Türk Haritacısı. Kâşgarlı Mahmûd Kitabı.
Ankara, 121-132, ed. F. S. BRUTCU ÖZÖNDER.
ÜLKÜTAŞIR, M. Ş. ÜLKÜTAŞIR (1946). Büyük Türk Dilcisi Kâşgarlı Mahmut Hayatı – Şahsiyeti – Divanü Lûgatı. İstanbul.

CISET - 2nd Cilicia International Symposium on Engineering and Technology
10-12 October, 2019, Mersin / TURKEY

SOME APPLICATIONS OF FIBONACCI NUMBERS IN APARTMENTS MODELLING

Orhan Dişkaya*[1] and Hamza Menken[2]

[1] Mersin University Science and Letters Faculty Mathematics Department Ciftlikkoy, 33343 Mersin TURKEY, orhandiskaya@mersin.edu.tr

[2] Mersin University Science and Letters Faculty Mathematics Department Ciftlikkoy, 33343 Mersin TURKEY, hmenken@mersin.edu.tr

ABSTRACT
In this paper, we give some models for apartments whose sizes are Fibonacci numbers. We give some relations and identities about the sizes of these apartments. Also, we obtain the golden ration of the apartments and their cells.
Keywords: *Fibonacci numbers, Binet Formula, Fibonacci Illustrations. Fibonacci draws*

* Corresponding Author

1. INTRODUCTION

The Fibonacci sequence is named after Leonardo Fibonacci and the sequence 1, 2, 3, 5, 8... is the Fibonacci sequence. These numbers contain numerous and fascinating applications to a wide spectrum of disciplines and endeavors. They include art, architecture, biology, chemistry, chess, electrical engineering, geometry, graph theory, music, origami, poetry, physics, physiology, neurophysiology, sewage, water treatment, snow plowing, stock market trading, and trigonometry. For more information, we refer the book of (Koshy, 2019). The Fibonacci sequence F_n is defined by a second-order recurrence;

$$F_{n+2} = F_{n+1} + F_n \ , \quad n \geq 0$$

With the different initial conditions $F_0 = 0$, and $F_1 = 1$. The first few members of this sequence is given as follow;

Table 1. A few the Fibonacci numbers

n	0	1	2	3	4	5	6	7	…
F_n	0	1	1	2	3	5	8	13	…

The golden ratio is the limit of the ratios of successive terms of the Fibonacci numbers that is (Dunlap, 1997),

$$\phi = \lim_{n\to\infty} \frac{F_{n+1}}{F_n}.$$

By the Fibonacci recurrence, we have,

$$\frac{F_{n+1}}{F_n} = \frac{F_n + F_{n-1}}{F_n} = 1 + \frac{1}{\frac{F_n}{F_{n-1}}}$$

$$\lim_{x\to\infty} \frac{F_{n+1}}{F_n} = 1 + \lim_{x\to\infty} \frac{1}{\frac{F_n}{F_{n-1}}}$$

$$\phi = 1 + \frac{1}{\phi}$$

Recurrence involve the characteristic equation,

$$x^2 - x - 1 = 0$$

If its roots are denoted by (golden ratio) $\alpha = \frac{1+\sqrt{5}}{2} = 1,61803398875... = \phi$ and $\beta = \frac{1-\sqrt{5}}{2}$ then the following equalities can be derived;

$$\alpha + \beta = 1$$

$$\alpha - \beta = \sqrt{5}$$

$$\alpha.\beta = -1$$

Moreover, the Binet formula for the Fibonacci sequence is

$$F_n = \frac{\alpha^n - \beta^n}{\alpha - \beta} \qquad (1)$$

1.1. Example

In [3, 4], illustration of $F_{n+1}^2 = 4F_nF_{n-1} + F_{n-2}^2$ identity is as following,

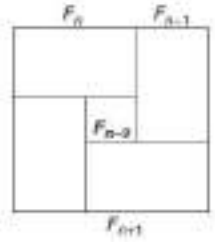

Figure 1: $F_{n+1}^2 = 4F_nF_{n-1} + F_{n-2}^2$

So, draw a $F_{n+1}F_{n+1}$ square. Since $F_{n+2} = F_{n+1} + F_n$, we divide the square into four F_nF_{n-1} rectangles with one at each corner, and a $F_{n-2}F_{n-2}$ square in the middle; see Figure 1. Adding the five areas we get $F_{n+1}^2 = 4F_nF_{n-1} + F_{n-2}^2$.

2. MAIN RESULTS

In this section, we obtain 1+1, 2+1, 3+1 and 4+1 apartment illustrations by means of Binet formula using Fibonacci identities. We can illustrate geometrically apartments using some Fibonacci identities. Similar investigations were given in (Brousseau, 1972) and (Ollerton, 2008).

2.1. Example

We consider the apartment having 2 rooms, wc+bathroom, kitchen and corridor of the 1+1 apartment with width F_{n+5}, height F_{n+4}.

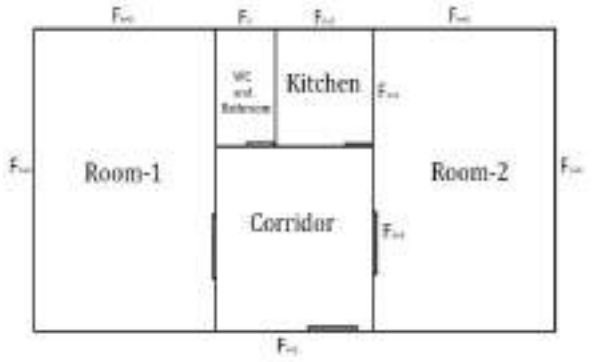

Figure 2: The 1+1 Apartment

We can find the circumference of the above apartment as following

$$\begin{aligned}\text{Circumference} &= 2F_{n+4} + 4F_{n+3} + F_{n+2} + F_{n+1} + F_n \\ &= 2\left(F_{n+4} + F_{n+3}\right) + 2F_{n+3} + F_{n+2} + \left(F_{n+1} + F_n\right) \\ &= 2F_{n+5} + 2\left(F_{n+3} + F_{n+2}\right) \\ &= 2\underbrace{F_{n+5}}_{width} + 2\underbrace{F_{n+4}}_{height}\end{aligned}$$

We also can prove the identity of above by using Binet formula. In fact we write that

$$\begin{aligned}2F_{n+5} + 2F_{n+4} &= 2F_{n+4} + 4F_{n+3} + F_{n+2} + F_{n+1} + F_n \\ &= 2\frac{\alpha^{n+4} - \beta^{n+4}}{\alpha - \beta} + 4\frac{\alpha^{n+3} - \beta^{n+3}}{\alpha - \beta} + \frac{\alpha^{n+2} - \beta^{n+2}}{\alpha - \beta} \\ &\quad + \frac{\alpha^{n+1} - \beta^{n+1}}{\alpha - \beta} + \frac{\alpha^{n} - \beta^{n}}{\alpha - \beta} \\ &= 2\frac{\alpha^{n+3}(\alpha+1) - \beta^{n+3}(\beta+1)}{\alpha - \beta} + 2\frac{\alpha^{n+3} - \beta^{n+3}}{\alpha - \beta} \\ &\quad + \frac{\alpha^{n+2} - \beta^{n+2}}{\alpha - \beta} + \frac{\alpha^{n}(\alpha+1) - \beta^{n}(\beta+1)}{\alpha - \beta} \\ &= 2\frac{\alpha^{n+3}(\alpha^2) - \beta^{n+3}(\beta^2)}{\alpha - \beta} + 2\frac{\alpha^{n+3} - \beta^{n+3}}{\alpha - \beta} \\ &\quad + \frac{\alpha^{n+2} - \beta^{n+2}}{\alpha - \beta} + \frac{\alpha^{n}(\alpha^2) - \beta^{n}(\beta^2)}{\alpha - \beta} \\ &= 2\frac{\alpha^{n+5} - \beta^{n+5}}{\alpha - \beta} + 2\frac{\alpha^{n+2}(\alpha+1) - \beta^{n+2}(\beta+1)}{\alpha - \beta} \\ &= 2\frac{\alpha^{n+5} - \beta^{n+5}}{\alpha - \beta} + 2\frac{\alpha^{n+4} - \beta^{n+4}}{\alpha - \beta}\end{aligned}$$

We can find the area of the above apartment as following

$$\begin{aligned}F_{n+5}F_{n+4} &= \left(F_{n+4} + F_{n+3}\right)F_{n+4} \\ &= F_{n+4}F_{n+4} + F_{n+3}F_{n+4} \\ &= F_{n+4}\left(F_{n+3} + F_{n+2}\right) + F_{n+4}F_{n+3} \\ &= 2F_{n+4}F_{n+3} + \left(F_{n+3} + F_{n+2}\right)F_{n+2} \\ &= 2F_{n+4}F_{n+3} + F_{n+3}F_{n+2} + F_{n+2}F_{n+2} \\ &= 2\underbrace{F_{n+4}F_{n+3}}_{Rooms} + \underbrace{F_{n+3}F_{n+2}}_{Corridor} + \underbrace{F_{n+2}F_{n+1}}_{Kitchen} + \underbrace{F_{n+2}F_{n}}_{WC}\end{aligned}$$

Likewise, we can prove that above equality is achieved with the Binet formula. Hence, we obtain a 1+1 apartment that each its cell has the golden ratio

$$\text{Apartment ratio} = \lim_{x\to\infty}\frac{F_{n+5}}{F_{n+4}} = \phi$$

$$\text{Rooms ratio} = \lim_{x\to\infty}\frac{F_{n+4}}{F_{n+3}} = \phi$$

$$\text{Corridor ratio} = \lim_{x\to\infty}\frac{F_{n+3}}{F_{n+2}} = \phi$$

$$\text{Kitchen ratio} = \lim_{x\to\infty}\frac{F_{n+2}}{F_{n+1}} = \phi$$

$$\text{WC ratio} = \lim_{x\to\infty}\frac{F_{n+2}}{F_{n}} = 1 + \phi$$

The areas of such apartments are given as the following

Table 2. The areas of the 1+1 apartments

Areas	*n=1*	*n=2*	*n=3*	...
Room-1	$15m^2$	$40m^2$	$104m^2$	...
Room-2	$15m^2$	$40m^2$	$104m^2$	...
Kitchen	$2m^2$	$6m^2$	$15m^2$	...
Corridor	$6m^2$	$15m^2$	$40m^2$	...
WC-Bathroom	$2m^2$	$3m^2$	$10m^2$	...
Apartment(sum)	$40m^2$	$104m^2$	$273m^2$	...

As seen above, we can draw the apartments, which their areas and circumference are satisfying the identities above according to values of *n*. Therefore, we can construct new buildings which have the golden ratio that provides aesthetic appearance.

2.2. Example

We consider the apartment having 3 rooms, wc, bathroom, kitchen and corridor of the *2+1* apartment with width F_{n+5}, height F_{n+4}. We can find the circumference of the above apartment as following

$$2F_{n+5} + 2F_{n+4} = 5F_{n+3} + 5F_{n+2} + F_{n+1}$$

We also can prove the identity of above by using Binet formula. We can find the area of the above apartment as following

$$F_{n+5}F_{n+4} = 5\underbrace{F_{n+3}F_{n+2}}_{\substack{Rooms\\Kitchen\\Bathroom}} + 2\underbrace{F_{n+3}F_{n+1}}_{Corridor} + \underbrace{F_{n+2}^2}_{WC}$$

Figure 3: The 2+1 Apartment

We also can prove the identity of above by using Binet formula. Hence, we obtain a 2+1 apartment that each its cell has the golden ratio

$$\text{Apartment ratio} = \lim_{x\to\infty}\frac{F_{n+5}}{F_{n+4}} = \phi$$

$$\text{Rooms ratio} = \lim_{x\to\infty}\frac{F_{n+3}}{F_{n+2}} = \phi$$

$$\text{Corridor ratio} = \lim_{x\to\infty}\frac{2F_{n+3}}{F_{n+1}} = 2+2\phi$$

$$\text{Kitchen ratio} = \lim_{x\to\infty}\frac{F_{n+3}}{F_{n+2}} = \phi$$

$$\text{Bathroom ratio} = \lim_{x\to\infty}\frac{F_{n+3}}{F_{n+2}} = \phi$$

$$\text{WC ratio} = \lim_{x\to\infty}\frac{F_{n+2}}{F_{n+2}} = 1$$

The areas of such apartments are given as the following

Table 3. The areas of the 2+1 apartments

Areas	*n=1*	*n=2*	*n=3*	...
Room-1	$6m^2$	$15m^2$	$40m^2$	...
Room-2	$6m^2$	$15m^2$	$40m^2$	...
Room-3	$6m^2$	$15m^2$	$40m^2$	...
Kitchen	$6m^2$	$15m^2$	$40m^2$	...
Corridor	$6m^2$	$20m^2$	$48m^2$	...
Bathroom	$6m^2$	$15m^2$	$40m^2$	...
WC	$4m^2$	$9m^2$	$25m^2$	...
Apartment(sum)	$40m^2$	$104m^2$	$273m^2$	...

2.3. Example

We consider the apartment having 4 rooms, WC, bathroom, kitchen and corridor of the 3+1 apartment with width F_{n+5}, height F_{n+5}.

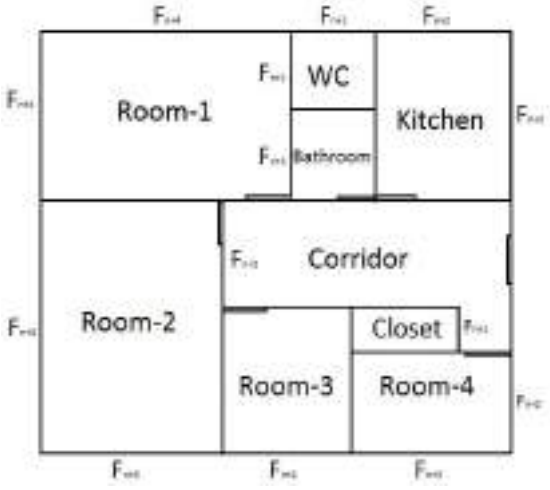

Figure 4: The 3+1 Apartment

We can find the circumference of the above apartment as following

$$4F_{n+5} = 2F_{n+4} + 5F_{n+3} + 3F_{n+2} + F_{n+1}$$

We also can prove the identity of above by using Binet formula. We can find the area of the above apartment as following

$$F_{n+5}^2 = 2\underbrace{F_{n+4}F_{n+3}}_{Rooms} + 4\underbrace{F_{n+3}F_{n+2}}_{\substack{Rooms\\Kitchen\\Bathroom}} + \underbrace{F_{n+4}F_{n+2} + F_{n+1}^2}_{Corridor}$$

$$+\underbrace{F_{n+2}F_{n+1}}_{Closet} + \underbrace{F_{n+1}^2}_{WC}$$

We can prove that above equality is achieved with the Binet formula. Hence, we obtain a 3+1 apartment that each its cell has the golden ratio

$$\text{Apartment ratio} = \lim_{x\to\infty}\frac{F_{n+5}}{F_{n+5}} = 1$$

$$\text{Rooms ratio} = \lim_{x\to\infty}\frac{F_{n+4}}{F_{n+3}} = \lim_{x\to\infty}\frac{F_{n+3}}{F_{n+2}} = \phi$$

$$\text{Closet ratio} = \lim_{x\to\infty}\frac{F_{n+2}}{F_{n+1}} = \phi$$

$$\text{Kitchen ratio} = \lim_{x\to\infty}\frac{F_{n+3}}{F_{n+2}} = \phi$$

$$\text{Bathroom ratio} = \lim_{x\to\infty}\frac{F_{n+3}}{F_{n+2}} = \phi$$

$$\text{WC ratio} = \lim_{x\to\infty}\frac{F_{n+1}}{F_{n+1}} = 1$$

The areas of such apartments are given as the following

Table 4. The areas of the 3+1 apartments

Areas	*n=1*	*n=2*	*n=3*	...
Room-1	$15m^2$	$40m^2$	$104m^2$	...
Room-2	$15m^2$	$40m^2$	$104m^2$	...
Room-3	$6m^2$	$15m^2$	$40m^2$	...
Room-4	$6m^2$	$15m^2$	$40m^2$	...
Kitchen	$6m^2$	$15m^2$	$40m^2$	...
Corridor	$1m^2$	$28m^2$	$74m^2$	...
Bathroom	$2m^2$	$6m^2$	$15m^2$	...
WC	$1m^2$	$4m^2$	$9m^2$	...
Closet	$2m^2$	$6m^2$	$15m^2$	...
Apartment(sum)	$64m^2$	$169m^2$	$441m^2$	...

2.4. Example

We consider the apartment having 4 rooms, WC, bathroom, kitchen and corridor of the 4+1 apartment with width F_{n+6}, height F_{n+5}.

We can find the circumference of the above apartment as following

$$2F_{n+6}+2F_{n+5}=4F_{n+4}+4F_{n+3}+4F_{n+2}+2F_{n+1}.$$

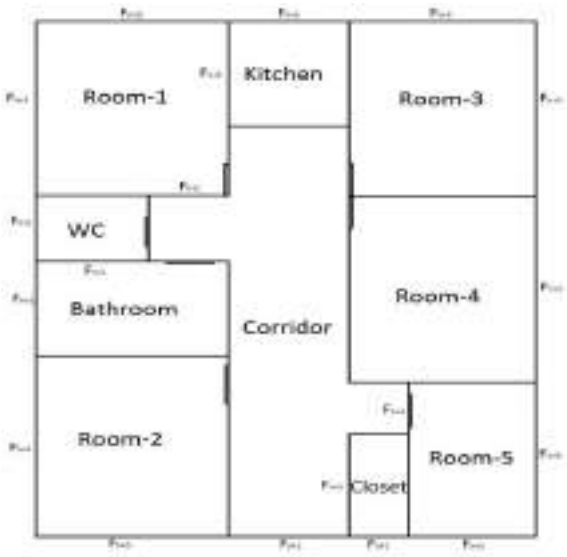

Figure 5: The 4+1 Apartment

We also can prove the identity of above by using Binet formula. We can find the area of the above apartment as following

$$F_{n+6}F_{n+5}=4\underbrace{F_{n+4}F_{n+3}}_{Rooms}+4\underbrace{F_{n+3}F_{n+2}}_{Rooms\ Kitchen}+\underbrace{2F_{n+4}F_{n+2}+2F_{n+1}^{2}}_{Corridor}$$

$$+\underbrace{F_{n+2}F_{n+1}}_{Closet}+\underbrace{F_{n+2}F_{n+1}}_{WC}.$$

We can prove that above equality is achieved with the Binet formula. Hence, we obtain a 4+1 apartment that each its cell has the golden ratio

$$\text{Apartment ratio}=\lim_{x\to\infty}\frac{F_{n+6}}{F_{n+5}}=\phi$$

$$\text{Rooms ratio}=\lim_{x\to\infty}\frac{F_{n+4}}{F_{n+3}}=\lim_{x\to\infty}\frac{F_{n+3}}{F_{n+2}}=\phi$$

$$\text{Closet ratio}=\lim_{x\to\infty}\frac{F_{n+2}}{F_{n+1}}=\phi$$

$$\text{Kitchen ratio}=\lim_{x\to\infty}\frac{F_{n+3}}{F_{n+2}}=\phi$$

$$\text{Bathroom ratio}=\lim_{x\to\infty}\frac{F_{n+3}}{F_{n+2}}=\phi$$

$$\text{WC ratio}=\lim_{x\to\infty}\frac{F_{n+2}}{F_{n+1}}=\phi$$

The areas of such apartments are given as the following

Table 5. The areas of the 4+1 apartments

Areas	*n=1*	*n=2*	*n=3*	...
Room-1	$15m^2$	$40m^2$	$104m^2$	...
Room-2	$15m^2$	$40m^2$	$104m^2$	...
Room-3	$15m^2$	$40m^2$	$104m^2$	...
Room-4	$15m^2$	$40m^2$	$104m^2$	...
Room-5	$6m^2$	$15m^2$	$40m^2$	...
Kitchen	$6m^2$	$15m^2$	$40m^2$	...
Corridor	$22m^2$	$56m^2$	$148m^2$	...
Bathroom	$6m^2$	$15m^2$	$40m^2$	...
WC	$2m^2$	$6m^2$	$15m^2$	...
Closet	$2m^2$	$6m^2$	$15m^2$	...
Apartment(sum)	$104m^2$	$273m^2$	$714m^2$	...

3. CONCLUSION

The results explained in the previous sections show that we are built various apartments using the Fibonacci numbers and identities. They also can be built the school, the hospital, the mosque, the churches and the various buildings according to the golden ratio using these numbers and identities.

REFERENCES

Koshy, T. (2019). “Fibonacci and Lucas numbers with applications.” *Wiley*.

Dunlap, R. A. (1997). “The golden ratio and Fibonacci numbers.” *World Scienti c*.

Brousseau, A. (1972). “Fibonacci Numbers and Geometry.” *Fibonacci Quarterly*, 10, 303 318, 323.

Ollerton, R.L. (2008). “Proof Without Words: Fibonacci Tiles.” *Mathematics Magazine*, 81, 302.

CISET - 2nd Cilicia International Symposium on Engineering and Technology
10-12 October, 2019, Mersin / TURKEY

THE CLASSICAL AES-LIKE CRYPTOLOGY VIA THE FIBONACCI POLYNOMİAL MATRİX

Orhan Dişkaya*[1], Erdinç Avaroğlu[2] and Hamza Menken[3]

[1] Mersin University, Graduate School of Natural and Applied Sciences, Ciftlikkoy, Mersin, TURKEY, orhandiskaya@mersin.edu.tr

[2] Mersin University, Computer Engineering Department, Ciftlikkoy, Mersin, TURKEY, eavaroglu@mersin.edu.tr

[3] Mersin University, Department of Mathematics Ciftlikkoy, Mersin, TURKEY, hmenken@mersin.edu.tr

ABSTRACT
In this paper, we consider the polynomial operations on the Galois fields, the Fibonacci polynomial sequences. Using a certain irreducible polynomial, we redefine the elements of Fibonacci polynomial sequences to use in our cryptology algorithm. So, we find the classical AES-like cryptology via the Fibonacci polynomial matrix.
Keywords: *Fibonacci numbers, Fibonacci polynomial numbers, Cassini identity, Fibonacci matrix, Galois field*

* Corresponding Author

1. INTRODUCTION

The Advanced Encryption Standard (AES), also known by its original name Rijndael (Daemen and Rijmen, 2003), is a specification for the encryption of electronic data established by the U.S. National Institute of Standards and Technology (NIST) in 2001. The AES block encryption algorithm is used for the algorithmic part of the developed system. AES is the applicable block encryption standard developed by J. Daemen and V. Rijmen in 1997 and adopted as a standard in 2000. AES is an iterative block cipher based on a design principle known as a substitution-permutation network (SPN). AES operates on a 4×4 column-major order matrixof bytes, called the state. Matrix calculations are done in a special finite field. AES supports 128-, 192-, 256- bit keys. The number of cycles of repetition for 128-bit, 192-bit, and 256-bit keys are 10, 12, and 14, respectively. These stages include key addition, byte substitution, ShiftRow, and MixColumn (Avaroğlu, Koyuncu, Özer and Türk, 2015). We too created a new encryption algorithm (known as AES-like) by using the AES algorithm. In AES-like, Galois field arithmetic is used in most layers, especially in matrix operations. We give an introduction to Galois fields as needed for this purpose before we introduced with the algorithm. A background on Galois fields is not needed for a basic understanding of AES-like. So, we will obtain a basic entrance to Galois fields (Paar and Pelzl, 2009; Stewart, 1990). Information on the following classical cryptology benefit in (Klima, and Sigmon, 2012).

1.1. Definition : In (Paar and Pelzl, 2009). A field F is a set of elements with the following features:

1. All elements of F form an additive group with the group operation + and the neutral element 0.
2. All elements of F except 0 form a multiplicative group with the group operation × and the neutral element 1.
3. When the two group operations are mixed, the distributive law holds, i.e., for all $a,b,c \in F$:

$$a(b+c) = ab + ac .$$

In extension fields $GF(2^m)$ elements are not represented as integers but as polynomials with coefficients in $GF(2)$. However, we take $m = 5$ for the next process. In AES-like the finite field contains 32 elements and is denoted as $GF(2^5)$. In the field, $GF(2^5)$, which is used in AES-like, each element $A \in GF(2^5)$ is thus represented as:

$$A(x) = a_4x^4 + a_3x^3 + a_2x^2 + a_1x + a_0,$$
$$\{a_i\} \in GF(2) = \{0,1\}$$

Note that there are exactly $32 = 2^5$ such polynomials. The set of these 32 polynomials is the finite field $GF(2^5)$. Each elements of this polynomial correspond to one letter of the alphabet.

1.2. Definition : (Addition and subtraction in $GF(2^5)$).

In (Paar and Pelzl, 2009). Let $A(x), B(x) \in GF(2^5)$. The sum and the subtraction of the two elements are then computed according to:

$$A(x) \pm B(x) = (a_4 \pm b_4)x^4 + (a_3 \pm b_3)x^3 + (a_2 \pm b_2)x^2 + (a_1 \pm b_1)x + (a_0 \pm b_0),$$
$$(a_i \pm b_i) \bmod 2 \text{ for } i \in \{0,1,2,3,4\}$$

1.1. Example: For $A(x) = x^4 + x^2 + x$ and $A(x) = x^4 + x^3 + x^2 + 1$, the sum $A(x) + B(x)$ of two elements from $GF(2^5)$ is computed:

$$A(x) + B(x) = x^3 + x + 1.$$

1.3. Definition: (Multiplication in $GF(2^5)$). In (Paar and Pelzl, 2009). Let $A(x), B(x) \in GF(2^5)$ and let

$$P(x) = p_0 + p_1x + p_2x^2 + p_3x^3 + p_4x^4 + p_5x^5,$$
$$p_i \in GF(2^5)$$

be an irreducible polynomial. Multiplication of the two elements $A(x), B(x)$ is performed as

$$A(x).B(x) \bmod P(x).$$

The irreducible polynomials of $GF(2^5)$ are as follows,

$x^5 + x^2 + 1,$

$x^5 + x^3 + 1,$

$x^5 + x^3 + x^2 + x + 1,$

$x^5 + x^4 + x^3 + x + 1,$

$x^5 + x^4 + x^3 + x^2 + 1,$

$x^5 + x^4 + x^2 + x + 1.$

For AES, the irreducible polynomial

$$P(x) = x^8 + x^4 + x^3 + x + 1$$

is used. It is part of the AES specification. For AES-like, we consider the irreducible polynomials as following,

$$P(x) = x^5 + x^2 + 1.$$

1.2. Example: For $A(x) = x^4 + x^2 + 1$ and $B(x) = x^3 + x$ in the field $GF(2^5)$, the multiplication $A(x).B(x)$ according to the irreducible polynomial

$P(x) = x^5 + x^2 + 1$ is

$A(x).B(x) = x^7 + x = x^2(x^2 + 1) + x = x^4 + x^2 + x.$

Especially, we are concerned with software implementations of the Galois fields. Hence, we know

$$A(x) = x^4 + x^2 + 1 = (10101)_2 = 21_{10}$$

$$B(x) = x^3 + x = (01010)_2 = 10_{10}.$$

The field elements, are normally stored as bit vectors in the computers. If we look at the multiplication from the previous example, the following very atypical operation is being performed on the bit level:

$$A(x).B(x) = (x^4 + x^2 + 1)(x^3 + x) = x^4 + x^2 + x$$

$$(10101)(01010) = (10110)$$

This computation is not identical to integer arithmetic. The result would have been $(01101)_2 = 13_{10}$, which is clearly not the same as the Galois field multiplication product. Inversion in $GF(2^5)$ is the core operation to decrypt of the matrix polynomial.

1.4. Definition: In (Paar and Pelzl, 2009). For a given field $GF(2^5)$ and the corresponding irreducible reduction polynomial $P(x)$, the inverse A^{-1} of a nonzero element $A \in GF(2^5)$ is defined as:

$$A^{-1}(x)A(x) = 1 \bmod P(x).$$

1.5. Definition: In (Koshy, 2018; 2019). The Fibonacci sequence $\{F_n\}_{n\geq 0}$ is

$$F_0 = 0,\ F_1 = 1 \text{ and } F_{n+2} = F_{n+1} + F_n.$$

Here, F_n is the nth Fibonacci number. The first few members of this sequence is given as follow;

Table 1. A few the Fibonacci numbers

n	0	1	2	3	4	5	6	7	8	...
F_n	0	1	1	2	3	5	8	13	21	...

1.6. Definition: In (Koshy, 2018; 2019). The Fibonacci Polynomial sequence $\{f_n(x)\}_{n\geq 0}$ is

$$f_0(x) = 0,\ f_1(x) = 1 \text{ and } f_{n+2}(x) = xf_{n+1}(x) + f_n(x).$$

The first few members of this sequence is given as follow;

Table 2. A few the Fibonacci polynomial numbers

n	0	1	2	3	4	5	...
$f_n(x)$	0	1	x	x^2+1	x^3+2x	x^4+3x^2+1	...

According to irreducible polynomial $P(x)$ the Fibonacci polynomials $f_n(x)$ are as follows;

Table 3. A few the irreducible polynomial numbers

n	$f_n(x)$	Z_2
0	0	mod 2
1	1	mod 2
2	x	mod 2
3	$x^2 + 1$	mod 2
4	x^3	mod 2
5	$x^4 + x^2 + 1$	mod 2
6	$x^2 + x + 1$	mod 2
7	$x^4 + x^3 + x + 1$	mod 2
8	$x^4 + x^2$	mod 2
9	$x^4 + x^2 + x$	mod 2
10	$x^4 + x^3 + x^2 + 1$	mod 2
11	$x^3 + 1$	mod 2
12	$x^3 + x^2 + x + 1$	mod 2
...	...	...

The following identity is non-zero, which tells us that Fibonacci polynomial matrix can be reversed,

1.1. Theorem (Cassini Identity): In (Koshy, 2018; 2019). Let $f_n(x)$ denote the n *th* Fibonacci polynomial sequence. Then,

$$f_{n+1}(x)\, f_{n-1}(x) - f_n^2(x) = (-1)^n, \quad n \geq 1.$$

1.2. Theorem (Fibonacci Polynomial Matrix): In (Koshy, 2018; 2019). Let,

$$Q(x) = \begin{pmatrix} x & 1 \\ 1 & 0 \end{pmatrix}$$

It then follows by PMI that,

$$Q^n(x) = \begin{pmatrix} f_{n+1}(x) & f_n(x) \\ f_n(x) & f_{n-1}(x) \end{pmatrix}$$

where $n \geq 1$. $Q^n(x)$ is called the Fibonacci polynomial matrix.

1.3. Theorem (Inverse of a 2x2 Matrix): Let $Q^n(x)$ be a Fibonacci Polynomial Matrix. Let $Q^n(x)$ be the Fibonacci polynomial matrix. Then, the determinant of $Q^n(x)$ is

$$\left|Q^n(x)\right| = f_{n+1}(x)\, f_{n-1}(x) - f_n^2(x) = 1.$$

and inverse of $Q^n(x)$ is given by

$$Q^n(x)^{-1} = \begin{pmatrix} f_{n-1}(x) & f_n(x) \\ f_n(x) & f_{n+1}(x) \end{pmatrix}.$$

Polynomials of the Galois field are equivalent of each alphabet is as following,

Table 4.The polynomials are equivalent of each alphabet

No	Bit	Polynom	Alphabet
0	00000	0	A
1	00001	1	B
2	00010	x	C
3	00011	$x + 1$	Ç
4	00100	x^2	D
5	00101	$x^2 + 1$	E
6	00110	$x^2 + x$	F

7	00111	x^2+x+1	G
8	01000	x^3	Ğ
9	01001	x^3+1	H
10	01010	x^3+x	I
11	01011	x^3+x+1	İ
12	01100	x^3+x^2	J
13	01101	x^3+x^2+1	K
14	01110	x^3+x^2+x	L
15	01111	x^3+x^2+x+1	M
16	10000	x^4	N
17	10001	x^4+1	O
18	10010	x^4+x	Ö
19	10011	x^4+x+1	P
20	10100	x^4+x^2	R
21	10101	x^4+x^2+1	S
22	10110	x^4+x^2+x	Ş
23	10111	x^4+x^2+x+1	T
24	11000	x^4+x^3	U
25	11001	x^4+x^3+1	Ü
26	11010	x^4+x^3+x	V
27	11011	x^4+x^3+x+1	W
28	11100	$x^4+x^3+x^2$	X
29	11101	$x^4+x^3+x^2+1$	Y
30	11110	$x^4+x^3+x^2+x$	Z
31	11111	$x^4+x^3+x^2+x+1$	Q

2. MAIN RESULTS

In the present work, we consider a message text in ns lengths (called the n-letter). Then, this messaging creates a cryptology algorithm using certain mathematical rules (Fibonacci polynomial matrix). We obtain a decryption algorithm by applying inversely of the stated mathematical rules. Similar investigations on the following algorithm were given in (Uçar, Taş, and Özgür, 2017).

2.1. The Fibonacci Blocking Algorithm

The Coding Algorithm

Step 1. Consider a text of length n and assume that each letter represents one length.

Step 2. Divide the text into 2s blocks and transform it into 2×1 type matrices. 2×1 type matrices are multiplied by the *n-th* Fibonacci polynomial matrix in 2×2 type. If there is an ascending letter in the text that is converted into 2s block, its letters are multiplied $f_n(x)$.

Step 3. Divide the latest created text into 3s blocks and transform it into 3×1 type matrices. 3×1 type matrices are multiplied by the key matrix in 3×3 type:

$$\text{Key matrix} = \begin{pmatrix} B & B & C \\ Ç & E & Ğ \\ K & E & Y \end{pmatrix} = \begin{pmatrix} 1 & 1 & 2 \\ 3 & 5 & 8 \\ 13 & 5 & 30 \end{pmatrix}$$

If there is an ascending 2 letter in the text that is converted into 3s block, it letters is multiplied by 2.key matrix in 2×2 type:

$$2.\text{Key Matrix} = \begin{pmatrix} E & A \\ O & D \end{pmatrix} = \begin{pmatrix} 5 & 0 \\ 17 & 4 \end{pmatrix}$$

If there is an ascending letter in the text that is converted into 3-block, its letters are multiplied by polynomial *"F"*.

Step 4. New text created in step 3 is addition by Fibonacci polynomial numbers $\sum_{i=1}^{n} f_i(x)$ respectively by starting from the left.

$$\sum_{i=1}^{n} f_i(x) = f_1(x) + f_2(x) + f_3(x) + \ldots + f_n(x).$$

The Decoding Algorithm

In the decryption algorithm, we can reach by applying in order of the reverse process in steps.

3. CONCLUSION

Rijndael found the AES (Advanced Encryption Standard) with the help of polynomials in Galois fields. We too created a new encryption algorithm with the help of Fibonacci polynomials and polynomials in Galois _elds and this algorithm is called Classical AES-like Cryptology via Fibonacci Polynomial Matrix. First, we present the mathematical basis necessary for understanding the specifications followed by the design rationale and the description itself. Subsequently, the implementation aspects of the cipher and its inverse are treated.

REFERENCES

Uçar, S , Taş, N., and Özgür, N. (2019). "A New Application to Coding Theory via Fibonacci and Lucas Numbers". *MSAEN 7: 62-70.*

Paar, C., and Pelzl, J. (2009). "Understanding cryptography: a textbook for students and practitioners." *Springer Science, Business Media*.

Koshy, T. (2018). "Fibonacci and Lucas Numbers with Applications." Volume 1, *John Wiley & Sons, New Jersey.*

Koshy, T. (2019). "Fibonacci and Lucas Numbers with Applications." Volume 2, *John Wiley & Sons, New Jersey.*

Stewart, I. (1990). "Galois theory." *Chapman and Hall/CRC.*

Klima, R. E., and Sigmon, N. P. (2012). “Cryptology: classical and modern with maplets.” *Chapman and Hall/CRC*.

Daemen,, J., and Rijmen, V. (2003). "AES Proposal: Rijndael". National Institute of Standards and Technology. p. 1. *Archived* from the original on 5 March 2013. *Retrieved 21 February 2013*.

Avaroğlu, E., Koyuncu, I., Özer, A. B., and Türk, M. (2015). “Hybrid pseudo-random number generator for cryptographic systems.” *Nonlinear Dynamics*, *82*(1-2), 239-248.

WASTE MINERAL OILS RE-REFINING WITH PHYSICOCHEMICAL METHODS

Ufuk Sancar Vural *

Seda Kauçuk, Plastik, Maden, Kimya, Enerji İhr.İth. San. Tic. Ltd. Şti. Yeni Mh. Emirdağ Bulvarı, 358/B, Emirdağ, Afyonkarahisar,, Turkey. usvural@gmail.com

ABSTRACT
Please read all information given in this template carefully before start typing. Please use Times New Roman 9 Font size. Abstract must contain "Problem statement, Approach, Results and Conclusions". Length of the abstract must be a maximum of 250 words. Please use this document as a template. Attach .DOC format and .PDF format during the Final Submission. Visit website for any update. Please double check that 9 Font size throughout the paper except the main title which is 12 Font size.

Keywords: Four or Five Keywords (First Characters of Each Word are in Capital/Uppercase Letters), Italic

* Ufuk Sancar Vural

1. INTRODUCTION

Waste mineral oil is any industrial oil that has become unsuitable for the use to which it was initially assigned. These especially include used oils from combustion engines, transmission systems, turbines and hydraulic systems, the different sectors of the car industry and industrial shipping activities.

Mineral oils are petroleum origin and synthetic lubricants used in generators and other machines, especially in automotive engines. It is one of the most dangerous sources of pollution. Engine oil is not clean after draining from a motor because it collects dirt particles and other chemicals while the engine is running. Used, out-of-service lubricating oils are defined as waste oil, waste engine oil, waste lubricating oil or used lubricating oil depending on where it is used. The United States Environmental Protection Agency defines waste oils (used oils) as lubricating oils obtained from refinery or synthetic methods of crude oil contaminated with physical and chemical impurities.(Zitte 2016).

Used lube oil normally tends to have a high concentration of potentially harmful pollutant materials and heavy metals which could be dangerous to both living and non-living things on the earth. Used lube oil may cause damage to environment when dumped into ground or into water streams including sewers. This may result in ground water and soil contamination (Hopmans 1974). Therefore, development of environmentally safe, sustainable and cost-effective solution is required for recycling of used lubricant (Stehlik 2009). Nowadays due to different treatment and finishing methods, there are currently available many new Technologies (Bridjanian 2006).

The direct effects that these types of oil can have on health include the following: Irritation of lung tissue due to the presence of gases that contain aldehydes, ketone, aromatic compounds, etc. The presence of chemical elements such as Cl (chlorine), NO_2 (nitrogen dioxide), H_2S (hydrogen sulphide), Sb (antimony), Cr (chrome), Ni (nickel), Cd (cadmium), and Cu (copper) that affect the upper respiratory tract and lung tissue. They produce asphyxiating effects that prevent oxygen transportation due to their content of carbon monoxide, halide solvents, hydrogen sulphide, etc. Carcinogenic effects on the prostate and lungs due to the presence of metals such as lead, cadmium, manganese, etc. (web 1). Direct effects on the environment that stand out include the following: The pollution of soils, rivers and the sea due to their low biodegradability. On coming into contact with water, they produce a film that prevents oxygen circulation. Uncontrolled combustion can lead to the emission of chlorine, lead and other gas elements into the atmosphere, with the corresponding effects (web 1).

It is also understood that used engine oil contains some components which mix with the oil when the engine is worn. These include iron, steel, copper, lead, zinc, barium, cadmium, sulfur, water and ash. Used waste engine oil contains hazardous pollutant chemicals, so it is more harmful to the environment than crude oil (Zitte, 2016), which can cause both short-term and long-term adverse environmental effects (Zitte, 2016). Only one ton of used waste oil makes one million tons of clean water unusable (US EPA, 1996). Even in sewage treatment, 50-100 ppm oil remains in water without disposal (US.EPA, 1996). In general, it has been found that five liters of oil can cover a small lake (Zitte 2016). The oil film formed on the water surface causes the BOD value to decrease and causes toxic effects. As a result, drinking water sources are polluted, dead plants and animals are observed (Zitte 2016). Diran (1997) reported that oil in surface water seriously disrupts water's life support capacity. The oil prevents sunlight and oxygen from entering the water, making it difficult for fish to breathe and photosynthesis in aquatic plants. Thus, it kills plants and fish in aqueous environments. Toxic substances in used oil can also kill small organisms that support the rest of the food chain (Diran 1997, Arner 1992). Lubricant consumption is 5.3 million tons in Europe and 39 million tons in the world (Giovanna 2003). The uses of oils are shown in Figure 1 (Diphare 2015).

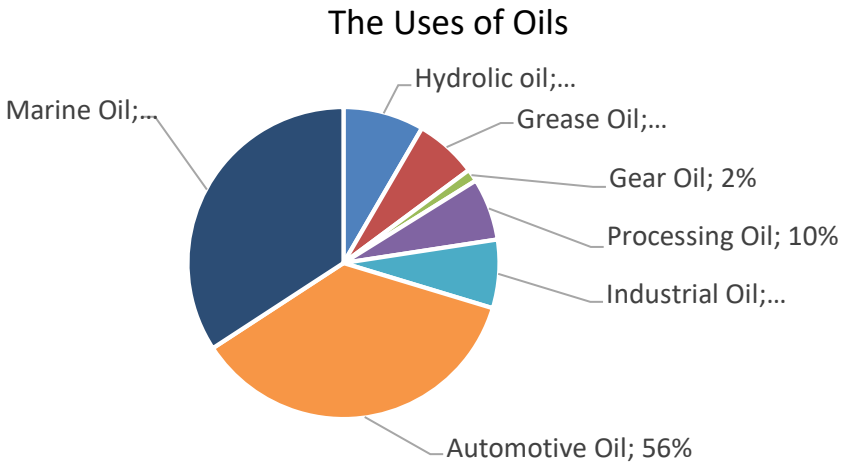

Figure 1 Application areas of oils

After understanding the pollutant effects of waste oils, intensive studies have been carried out worldwide for the disposal and recovery of waste oils. The recovery and disposal of waste oils is possible by three methods (Figure 2). These methods are reprocessing, re-refining or direct destruction (Diphare 2015).

Reprocessing: It is the production of fuel by separating water and sediments in the waste oil. For this purpose, the water and contaminated components in the waste oils are removed by precipitation, adsorption and filtration; sometimes distillation and thermal cracking (pyrolysis) are applied before filtration.

Re-Refining: After some pretreatments, fractional distillation methods are applied to obtain base oil. Lubricating oils can be produced by adding additives to the base oils.

Disposal: Especially waste oils containing PCB (polychlorobenzenes) are disposed of directly by incineration without any pretreatment.

The refining of waste oils is possible by using highly advanced technology. In this study, by refining the waste oils with physicochemical methods, it is tried to determine the more economical alternative to distillation methods.

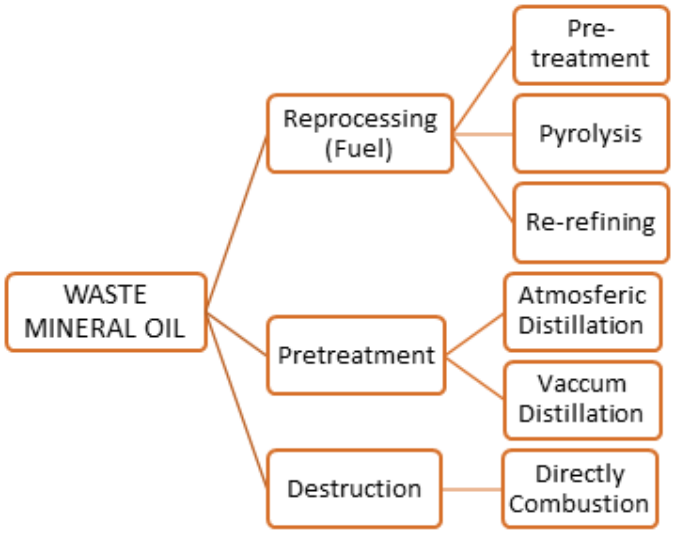

Figure 2. Waste mine oil recovery and disposal methods

2. MATERYAL VE METOD

The waste oils used in the experiments were obtained from the auto services that change the oil. The viscosity measurements of waste oils and obtained oils were determined by Shanghai God NDJ-55 rotary viscometer, density measurements by Anton Paar DMA35 densimeter, flash point measurements by Teknosem Tan-400 device and color measurement by X-RITE SP 62 device. Metal measurements were determined by the Merlab GBC Avanta model atomic absorption device. Aluminum oxide (Al2O3), sodium silicate, tetraethylenepentamine (TEPA) used in the experiments were obtained from Merck.

Physicochemical refining stages of pre-analyzed waste mineral oils are as follows.

Pretreatment (Dewatering and Dematilization): It can be defined as dewatering step. To this end, 1 liter of waste oil was added to a 2 liter beaker, 10 mL of 20% diammonium phosphate solution was added and heated at 120 ° C for 120 minutes with careful stirring. The mixture was then allowed to cool. After 8 hours, a viscous mixture was formed as a precipitate at the bottom of beaker. The supernatant was carefully transferred to another beaker so that no precipitate was contaminated.

Chemical Refining: The supernatant transferred to another beaker was stirred with heating to 30 ° C. 1.5% ethylene glycol was added, stirring for 5 minutes to reduce the viscosity of the oil. Then 1% sodium silicate was added and stirred at 30 ° C for 10 minutes. Subsequently, 2% Al 2 O 3 was added thereto and heating was continued with stirring to 50 ° C. 1% tetraethylenepentamine was added and stirred at constant temperature for 15 minutes. Subsequently, stirring was continued by careful addition of about 8-10% acid active bentonite to 160 ° C. Occasionally, the waste oil was sampled and dripped onto the filter paper to control the color. When the color was sufficiently lightened, the addition of bentonite was stopped and stirred for a further 10 minutes. The mixture was allowed to cool and filtered under vacuum at 60 ° C. The obtained oil was analyzed.

3. RESULT AND DISCUSSION

During the prolonged use of lubricating oils, black viscous structures are formed as a result of interactions between additives and metals in the oil, carbonation and polymerization reactions. Saturated hydrocarbons (30 to 70%), aromatic hydrocarbons polyaromatic (20 to 40%), polar compounds (5 to 25%) and asphalt based (0 to 10%). Waste oil also contains metal toxic metal pollutants (Pb, Hg, Zn, Cd, As and persistent organic pollutants PCB, PCT (Ouffoue 2013, Boadu, 2019). In our country, waste

oils are recovered according to the Regulation on Control of Waste Oils published by the Ministry of Environment (Resmi gazete, 2008). Although it is aimed to produce base oils from waste oils according to the regulation criteria, due to high refining plant costs and lack of technical knowledge, many recycling companies use the reprocessing method to produce fuel in existing plants. . In the recovery of oils by reprocessing, catalytic decomposition or direct thermal decomposition at high temperatures is generally employed to obtain low viscosity fuel-equivalent products. However, the production of lubricating oil by adding some chemical additives to the base oils obtained by refining of waste oils according to the purpose of use is extremely important both in terms of commercial and national economy.

The recycling regulation applied in our country prohibits the production of fuel from waste oils. Heavy fines and even imprisonment are often applied to firms that produce fuel through the reprocessing method. Therefore, it is clearly known that companies with little experience in recycling are looking for more economical and practical methods to produce base oil from waste oils instead of fuel. The most common recovery methods of waste oils are as follows (Secretariat of the Stockholm Convention on Persistent Organic Pollutants 2007):

Acid / Clay Method: In this process, after dehydration and distillation of used lubricant oil, re-refining or reprocessing operation is done using sulfuric acid. Clay is used to remove certain impurities. The acid/clay process has minimal environmental safety. The main by-product of this process is the large amounts of acidic sludge. Based on the concentration of contaminants, the type of lubricant oil and the regenerated oil quality, this process can be as a reprocessing or regenerative method. These two methods are different in terms of the heating rate (distillation unit) and the generated by-products. this method has many disadvantages: It also produces large quantity of pollutants, is unable to treat modern multigrade oils and it's difficult to remove asphaltic impurities. To reduce these hazardous contaminants from this method, the acid treatment stage of the process can be done under the atmospheric pressure to remove the acidic products, oxidized polar compounds, suspended particles and additives (Rahman *et al*. 2008, Udonne *et al*. 2013, Hamawand *et al* 2013, Abu-Elella *et al* 2015, Hani *et al*. 2011).

Vacuum Distillation: In this method, used lube oil collected is heated at a temperature of 120°C to remove the water added to the oil during combustion. Then the dehydrated oil is subjected to vacuum distilled at a temperature of 240°C and pressure 20 mmHg. This results the production of a light fuel oil (the light fuel oil can be used as fuel source for heating) and lubricating oil at 240°C. The advantages of vacuum distillation process over atmospheric pressure distillation are: Columns can be operated at lower temperatures; more economical to separate high boiling point components under vacuum distillation; avoid degradation of properties of some species at high temperatures therefore thermally sensitive substances can be processed easily. However, the remaining oil generated at this temperature (240°C) contains the dirt, degraded additives, metal wear parts and combustion products like carbon and is collected as residue. The residue is in the form similar to that of tar, which can be used as a construction material, for example, road and bitumen production. The disadvantage of this method is the high investment cost and/or the use of toxic materials such as sulphuric acid (Kanna *et al*. 2014, Havemann 1978, Puerto-Ferre *et al*. 1994).

Hydrogenation: To avoid formation of harmful products and environmental issues based on above methods, some modern processes have been used and the best one is hydrotreating (Bridjanian 2006). This method follows vacuum distillation. In this process, the distillate from vacuum distillation is hydrotreated at high pressure and temperature in the presence of catalyst for the purpose of removing chlorine, sulphur, nitrogen and organic components. The treated hydrocarbons resulted in products of improved odour, chemical properties and colour Another important aspect of this method is that, this process has many advantages: Produces of high Viscosity Index lube oil with well oxidation resistance and a good stable colour and yet having low or no discards. At the same time, it consumes bad quality feed. In addition to that, this method has advantage that all of its hydrocarbon products have good applications and product recovery is high with no (or very low) disposals. Other hydrocarbon products are: In oil refinery the light–cuts can be used as fuel in plant itself. Gas oil may be consumed after being mixed with heating gas oil and the distillation residue can be blended with bitumen and consumed as paving asphalt, because it upgrades a lot its rheological properties. Also, it can be used as a concentrated anti-corrosion liquid coating, for vehicles frames (Durrani 2014). The disadvantage of this method is that the residue resulting from the process is of high boiling range of hydrocarbon product fractionated into neutral oil products with varying viscosities which can also be used to blend lube oil.

Solvent de-asphalting process: This method has replaced acid-clay treatment as preferred method for improving oxidative stability and viscosity as well as temperature characteristics of base oils. Base oils obtained from Solvent Extraction are of good quality and contains less amounts of contaminants. In contrast to acid-clay treatment, it operates at higher pressures, requires skilled operating system and qualified personnel. The solvent selectively dissolves the undesired aromatic components (the extract), leaving desired saturated components, especially alkanes, as a separate phase (the raffinate) (Rincon *et al*. 2005). Different solvents types have been used for solvent extraction such as 2-propanol, 1-butanol, methyl ethyl ketone (MEK), ethanol, toluene, acetone, propane etc. used propane as solvent (Quang *et a*l. 1974, Rincon *et al*. 2003).. He found out that propane was capable of dissolving paraffinic or waxy material and intermediately dissolved oxygenated material. Asphaltenes which contain heavy condensed aromatic compounds and particulate matter are insoluble in liquid propane. These properties make propane ideal for recycling the used engine oil, but there are many other issues that have to be considered. Propane is hazardous and flammable therefore this process is regarded as hazardous method. In general, involves solvent losses and highly operating maintenance. Also, it occurs at pressures higher than 10 atm and requires high pressure sealing systems which makes solvent extraction plants expensive to construct, operate and the method also produces

remarkable amounts of hazardous by-products (Rincon *et al*. 2005, Hamawand *et al*. 2013, Quang *et al*. 1974, Rincon *et al*. 2003).

Modern Technologıes For Used Oıl Re-Refınıng: T Pyrolytic distillation method, pyrolysis process, thin film evaporation (TFE), including combined TFE and clay finishing, TFE and solvent finishing, TFE and hydrofinishing, thermal de-asphalting and clay finishing or hydrofinishing etc. In addition, environmentally friendly and affordable solvent extraction and adsorbents are being developed as a means of removing contaminants in used lube oil. The thin film technique is an alternative to vacuum distillation process. (Kalnes 1990, Hamed *et al*. 2005).

Thin Film Evaporation (TFE) with hydro-finishing: These methods are utilized to segregate oil and foreign components via a TFE, and purify it through hydro-finishing to prevent the secondary pollution. First, the moisture and light oil contained in the used oil are eliminated and then vacuum distillation of free components is required to permit for continuous separation of a TFE. Finally, the oil is encountered to hydro-finishing to eliminate chlorine, nitrogen, oxygen, and sulfur compounds. There is a difference between these both methods, that clay is used for absorption (Kalnes 1990).

TFE with solvent finishing: This method is used to segregate oil and foreign substances via a TFE, and request the solvent-finishing with the flow process analogous to TFE with hydro-finishing.

Solvent extraction hydro-finishing: This method combines solvent extraction and hydro-finishing by eliminating the foreign substances using the solvent and then fortifying oil quality by hydro-finishing. First, the moisture is eliminated and segregated the used oil. Then the mixture of solvent and used oil is encountered to hydro-finishing to eliminate sulfur, nitrogen and oxygen for purification purposes.

TDA with clay finishing and TDA with hydro-finishing: The dehydrated used oil is vacuum-heated at 360 ◦C. The ash remains at the bottom, and the oil is divided to 3 types, i.e. vacuum gas oil, base oil (as lubricant) and asphalt residues. Next, the base oil is encountered to hydro-finishing or clay-finishing under highpressure (107 Pa) for continuous utilization (Hamad *et al*. 2005).

Pyrolysis of waste oil: From research conducted by Arpal (Arpal et al. 2010), a fuel named as diesel-like fuel was produced by applying pyrolytic distillation method. Lam *et al*.(2012, 2016), describe pyrolysis as a thermal process that heats and decomposes substance at high temperature (300-1000°C) in an inert environment without oxygen. Pyrolysis process is not yet widespread but it has been receiving much attentions nowadays due to its potential to produce energy-dense products from materials. Examples of pyrolysis process includes microwave pyrolysis process and conventional pyrolysis process (Oladimeji, et al. 2018).

Various process combinations can be formed by configuring atmospheric distillation, vacuum distillation, solvent extraction, hydrogenation, acid / clay methods in different ways. Generally the first stage in all processes is atmospheric distillation. The cost of the recycling processes consisting of combinations of atmospheric and vacuum distillation method, distillation and solvent extraction method is quite high. Advanced processes can be considered for high capacity plants. In the waste oil recycling regulations, Category III contaminated oils are allowed to be burned only in disposal plants such as cement factories, lime quarries and Category I and II waste oils are allowed to be recycled. (Resmi Gazete 2008). Therefore, it is not possible for many licensed recycling plants to process high capacity waste oil. Due to high investment costs and high taxes, it is not feasible to establish small capacity processes.

In the oldest known acid / clay method in chemical refining, water and low boiling point components are first removed from the waste oil by atmospheric distillation. Subsequently, the waste oil is reacted with sulfuric acid at low temperature to remove carbons, asphaltenes and other sulfur compounds by precipitation from the oil, and then to be refined by treatment with various bleaching clays (Zare Kirti Bhushan 2016). The major problem in the acid /clay process is the removal of high concentrations of acid and sülfür, asphaltenes, and carbons in sediment, as well as a highly contaminated bleaching clay. Since the disposal process is very expensive and costly, waste oil recycling plants which were established primarily to prevent environmental pollution, cause greater environmental problems.. Low process efficiency (60-65%) is also a disadvantage.

The method used in this study consists of a series of physicochemical processes in which base oils are obtained from waste oils, which are less costly, without the need for high process cost distillation. In this study, carbon and metallic components in the waste oil were precipitated together with asphaltenes using coagulatory agents such as aluminum sulfate and sodium silicate instead of acid. Sulfur components, one of the biggest problems in waste oils, were removed from the oil by interacting with amine groups. Thus, acid-free sediment removed from the waste oil can be used in asphalt production, will not pose an environmental risk, and there will be no disposal problems. Active bentonite (acid active bentonite) was used as clay. The purpose of using clay is to remove polymeric materials, colloidal materials remaining in the oil phase by adsorbing with clay.

During the physicochemical refining, asphaltenes and other impurities were precipitated in waste oil with the help of coagulants at low temperatures, while the double bonds formed in the high molecular weight oxidation molecule interacted with amines to ensure oxidation stability. Thus, more stable base oils were obtained from the distillation methods without the need for hydrogenation. 85% base oil was recovered by the new method used in this study, and the acid-free precipitate amount was 10-15%. However, in the acid / clay method, the yield is as low as 60-65% and the amount of sediment is higher than 25-35%. The analysis results of the waste oil used in the experiments and the base oil obtained from the experiments are given in Table 1 and Table 2. The results were also compared with 20W50 oil.

Table 1. Physicochemical properties of waste oils, refined oil and original oil

Parameter	Waste Motor Oil	Refined Oil	20W50
Colour (ASTM D1500)	>8	3,5	4.5
Density 15 C (ASTM D1298)	0,9253	0,8870	0,8700
Viscosity 40 C (ASTM D445), CST	106,37	118	91,0
Viscosity 100 C (ASTM D445), CST	12,66	11,02	10,5
Flash Point (ASTM D97), C	210	225	230
TAN (ASTM D2896), mg KOH/g	2,74	0	0
TBN (ASTM D2896), mg KOH/g	4,66	0	0
Sulfur	>8	4	2,5

Table 2. Analysis of metals in waste oil, refined oil and the original oil

Parameter	Waste Motor Oil ppm	Refined Oil	20W50
Fe	58,6	0	0
Cr	3,2	0	0
Pb	2813	1,86	0
Cu	21,4	2,7	0
Ca	1570	9,56	543
Zn	566	4	0

As it can be seen from the results, the waste motor oils were refined in two stages without the need of hydrogenation and advanced distillation techniques and base oil was obtained again. As in the acid / clay process, it does not generate environmental waste, the processing time is much shorter, the amount of bleaching clay usage is much less, the yield is higher. In Table 3, waste mineral oil recycling methods are compared in terms of process time, recovery cost, efficiency and process setup cost.

Table 3 Comparison of waste mineral oil recycling processes

Regenerative Technologies	Energy requirement	Recycling rate (%)	Quality of regenerative oil	Economic costs	Acidic sludge	Residual oil sludge	Hazardous chemical materials
Acid/clay	Low	63	Good	Low	Much	Much	H_2SO_4
Distillation	High	50	Good	Low	Little	Much	H_2SO_4
Solvent de-asphalinting	High	70-65	API	High	Little	Much	$H_2SO_4$and Organic solvent
TFE with hydrofinishg	High	72	API	High	None	Little	None
TFE with clay finishing	High	72	API	High	None	Little	None
TFE with solvent finishing	High	72	API	High	None	Little	Orgsmic solvent
Solvent extraction hydrofinishing	High	74	API	High	None	Little	Oganic solvent
Thermal de-asphalting	High	74-77	API	High	None	Little	None
Physicochemical Regeneration	Very low	85	Good	Very low	None	Little	No

As can be seen from Table 3, chemical regeneration is the most ideal recycling method of waste mineral oil given the low process cost and high efficiency. In distillation methods, thermal cracking is inevitable because waste oils are processed at high temperatures. In recycling models containing distillation, hydrogenation is essential to produce base oil with high efficiency Otherwise, low quality base oils containing unsaturated oil molecules are obtained in distillation methods that do not contain hydrogenation. Since the unsaturated oil molecules are precipitated together with asphaltenes in chemical refining process, high quality base oils are obtained without hydrogenation.

Since the gasification rate will be increased as a result of thermal decomposition in distillation methods which do not contain hydrogenation, the base oil ratio obtained will be low. Therefore, chemical regeneration is the more preferable method if it is aimed to obtain base oil as a result of waste oil recovery. If it is desired to obtain fuel, known distillation methods by thermal decomposition at high temperature may be used. However, the law does not allow the production of fuel from waste oils.

In our country, hydrogenation-based recovery method is not available due to high process cost. In other distillation-based methods, not only base oil but also fuel-equivalent products are obtained. The Ministry of Environment emphasizes the production of base oil instead of fuel equivalent product with various regulations and measures. The way to prevent fuel production is by applying chemical regeneration, which may be an alternative to distillation methods involving thermal decomposition.

In the chemical regeneration process, it is not possible to obtain fuel, on the contrary, base oil is obtained with high efficiency. The Ministry of Environment should take steps to promote the production of base oils, which have a much higher economic value than fuel, by chemical regeneration. Products that can be produced from recovered base oils (such as grease) are included in the incentive scope and directing the recovery companies to this area will prevent the production of illegal fuel.

As a result, the consumption of lubricating oils produced from limited oil resources as fuel is a major disadvantage for the national economy and the production of base oil from waste oils is very advantageous both for the national economy and for the more conscious use of oil resources. The method determined as a result of the experiments is a method that can be preferred because of low investment costs and no environmental risk without the need for advanced technology processes.

4. REFERENCES

Abu-Elella, R., Ossman, M.E., Farouq, R., AbdElfatah, M. (2015), "Used motor oil treatment: turning waste oil into valuable products", International Journal of Chemical and Biochemical Sciences. Vol. 7, pp. 57-67.

Arner, R, (1992). "Used Oil Recycling Markets and Best Management Practice in the United States", Presented to the National Recycling Congress, Boston, USA.

Arpa, O., Yumrutas, R., Demirbas, A. (2010). "Production of diesel-like fuel from waste engine oil by pyrolytic distillation", Appl Energy, Vol. 87, pp. 122-127.

Bhushan, Z. K., Anil, S. M., Sainand, K., Shivkumar, H. (2016). "Comparison between Different Methods of Waste Oil Recovery", International Journal of Innovative Research in Science, Engineering and Technology. Vol. 5, No. 11, pp. 2001-2009.

Boadu, K. O., Joel, O. F., Essumang, D. K. and Evbuomwan, B. O., (2019). "A Review of Methods for Removal of Contaminants in Used Lubricating Oil", Chemical Science International Journal, Vol. 26, No. 4, pp. 1-11

Bridjanian, H., Sattarin, M. (2006). "Modern recovery methods in used oil rerefining", Petrol Coal Vol. 48, pp. 40–43.

Diphare, M. J., Muzenda, E., Pilusa, I. J., Mollagee, M., (2015). "A Comparison of Waste Lubricating Oil Treatment Techniques", 2nd International Conference on Environment, Agriculture and Food Sciences (ICEAFS'2013) August 25-26, Kuala Lumpur (Malaysia)

Diran, B. (1997). "The Little Adsorption Book: A Practical Guide for Engineers and Scientists". CRC Press, Boca Raton, FL, USA.

Durrani, H.A. (2014). "Re-Refining Recovery methods of used lubricating oil", International Journal of Engineering Sciences & Research Technology. Vol. 3, No. 3, pp. 1216-1220.

Giovanna, F. D., Khlebinskaia, O., Lodolo, A. and Miertus, S. (2003). "Compendium of Used Oil Regeneration Technologies", International Centre for Science and High Technology of the United Nations Industrial Development Organization (ICS-UNIDO), Trieste. 1-210

Hamad, A., Al-Zubaidya, E., Muhammad, E.F. (2005). "Used lubricating oil recycling using hydrocarbon solvents", Environ. Manage. Vol. 74, pp. 153–159.

Hamawand, I., Yusaf, T., Rafat, S. (2013), "Recycling of waste engine oils using a new washing agent", Energies. pp.1023-1049.

Hani, F. B., Al-Wedyan, H. (2011), "Regeneration of Base-Oil from Waste-Oil under Different Conditions and Variables", African Journal of Biotechnology", pp. 1150-1153.

Havemann, R. (1978), "The KTI used oil re-refining process". In Proceedings of the 3rd International Conference of Used Oil Recovery and Reuse, Houston, TX, USA, pp. 16–18.

Hegazi, S. E. F, Mohamd, Y. A., Hassan, M. I. (2017). "Recycling of waste engine oils using different acids as washing agents", International Journal of Oil, Gas and Coal Engineering, Vol(5), No.5, pp.69-74.

Kalnes, T., (1990). "Treatment and recycling of waste lubricants". A petroleum refinery integration study. In: AICHE National Meeting, San Diego, CA, pp. 19–22.

Kannan S. C., Mohan Kumar, K. S., Sakeer Hussain, M., Deepa Priya, N. K. (2014), "Studies on reuse of refined used automotive lubricant oil", Research Journal of Engineering Science. Vol. 3, No. 6, pp. 8-14.

Lam, S. S. And Chase, A. A. (2012). "A Review on Waste to Energy Processes Using Microwave Pyrolysis", Energies. Vol.5, pp. 4209-4232.

Lam, S.S., Liewa, K. K., Jusoh, A. A., Chong, C. T., Ani, F. N., Chase, H. A.(2016). "Progress in waste oil to sustainable energy, with emphasis on pyrolysis techniques". Renewable and Sustainable Energy Reviews. Vol. 53, pp. 714-753.

Oladimeji, T. E, Sonibare, J. A, Omoleye, J. A, Adegbola, A. A, Okagbue, H. I. (2018). "Data on the treatment of used lubricating oil from two different sources using solvent extraction and adsorption", Data in Brief. Vol. 19, pp. 2240- 2252.

Ouffoue, S. K, Oura, L., YAPO, K. D., Coffy A. A., (2013). "Physicochemical characterization of waste oils and analysis of the residues in contaminated soil", International Journal of Environmental Monitoring and Analysis, Vol. 1, No. 4, pp 162-166.

Puerto-Ferre, E., Kajdas, C. (1994). "Clean technology for recycling waste lubricating oils", In Proceedings of 9th International Colloquium, Ecological and Economic Aspects of Tribology, Esslingen, Germany, pp. 14–16.

Quang, D. V., Carriero, G., Schieppati, R., Comte, A., Andrews, J. W. (1974), "Propane purification of used lubricating oils". Hydrocarb. Process, Vol. 53, pp. 129–131.

Resmî gazete. (2008). "Atık yağların kontrolü yönetmeliği". Sayı: 26952.

Rincon, J., Canizares, P., Garcia, M. T. 2005), "Regeneration of used lubricating oil by polar solvent extraction". Ind. Eng. Chem. Res. Vol. 44: pp. 43-73.

Rincon, J., Canizares, P., Garcia, M. T., Gracia, I. (2003), "Regeneration of used lubricant oil by propane extraction". Ind. Eng. Chem. Res. Vol. 42, pp. 4867–4873.

Secretariat of the Stockholm Convention on Persistent Organic Pollutants, (2007). "Guidelines On Best Available Techniques And Provisional Guidance On Best Environmental Practices, Relevant to Article 5 and Annex C of the Stockholm Convention on Persistent Organic Pollutants", United Nations Environment Programme, International Environment House. Geneva, Switzerland

Udonne, J. D., Bakare, O. A. (2013),."Recycling of used lubricating oil using three samples of acids and clay as a method of treatment". International Archive of Applied Sciences and Technology. Vol. 4, No. 2, pp. 8–14.

US EPA (1996). "Managing Used Oil: Advice for Small Businesses". Report. 530EPA-F-96-004.

Web Map Tile Service, 1. http://www.cprac.org/docs/olis_eng.pdf (20.06.2019).

Zitte L. F., Awi-Waadu, G. D. B. and Okorodike, C. G, (2016). "Used-Oil Generation and Its Disposal along East-West Road, Port Harcourt Nigeria", International Journal of Waste Resources,, Vol. 6, No. 1, 1-5.

CISET - 2nd Cilicia International Symposium on Engineering and Technology
10-12 October, 2019, Mersin / TURKEY

RADAR CROSS SECTION ANALYSIS OF UNMANNED AERIAL VEHICLE USING PREDICS

Caner Özdemir [*1]

[1] Mersin University, Engineering Faculty, Department of Electrical-Electronics Engineering, Mersin, Turkey, cozdemir@mersin.edu.tr

ABSTRACT
In this study, a quantitative radar cross section (RCS) analysis of a model unmanned aerial vehicle (UAV) is accomplished by means of a series of RCS simulation. The simulations are carried out by high-frequency RCS simulation and analysis tool called Predics. To quantify the RCS features of the UAV model, both the angle-variation and frequency-variation simulations for all polarization excitations are done. The results of the simulations suggested that RCS values are dramatically changing with respect to look angle with some special angles providing the highest values of RCS values. Generally, the RCS values of the UAV model is increasing with frequency. For this particular UAV model, the RCS values can be larger than $1m^2$ for the X-band frequencies; therefore, it can easily be detected by a radar at a safe distance from the radar site.

Keywords: Radar Cross Section, Unmanned Aerial Vehicle, Radar Visibility, RCS simulation

[*] Corresponding Author

1. INTRODUCTION

For the last decade, the number of Unmanned Aerial Vehicles (UAVs) that is being used in numerous applications has been extensively increased due to growing demand from both military and civil parts (Thite *et al.*, 2012; Pieraccini *et al.*, 2017; Ananenkov, *et al.*, 2018). In a parallel manner, the need to detect such vehicles becomes really crucial for the safety on humans. In military practices, UAVs are generally used for reconnaissance, surveillance and targeted attacks (Ryapolov, *et al.*, 2014). Therefore, it is very crucial to detect and also make them ineffective before completing their missions to avoid life losses and injuries. While their military usages provide direct danger for human life, their civil usages may sometimes provide risky and hazardous situations due to accidents. For example, UAVs can be a serious
threat for the flight safety according to Aviation authorities. It is no doubt that drones and small UAVs may not be perceived by the radar of either airport's tower and/or from airplanes that are coming in or going out from the runways. Furthermore, UAVs can also be used offensive purposes such as terrorist effects. Therefore, there is a need for assessing the visibility of UAVs on the radar screen by calculating the radar cross section (RCS) of such vehicles.

In this paper, we represent a study for calculating and analyzing the RCS of a generic UAV. The RCS simulation is carried out by our recently developed RCS simulation and analysis software called Predics (Özdemir *et al*, 2014a; Özdemir *et al*, 2014b).

2. RCS SIMULATION OF UAV

2.1. UAV model

The UAV model used in Predics simulation can be seen in Fig.1. The perspective view of the UAV model is given Fig.1(a). The top and front view of the model is shared in Fig. 1(b). As it can be seen from the figure the wing extend of the UAV is 240 cm and the length is 120 cm. The side view of the UAV is plotted in Fig. 1(c).

The material of the model is assumed to be perfect electric conductor (PEC).

2.2. RCS simulation using Predics

RCS simulation of the UAV model has been accomplished by the Predics simulator (Özdemir *et al*, 2014a; Özdemir *et al*, 2014b). Predics is a fast and effective simulation tool for fast calculation of RCS from electrically large and complex-shaped platforms at high frequencies. The simulation screen of the UAV model can be seen in Fig. 2.

(a)

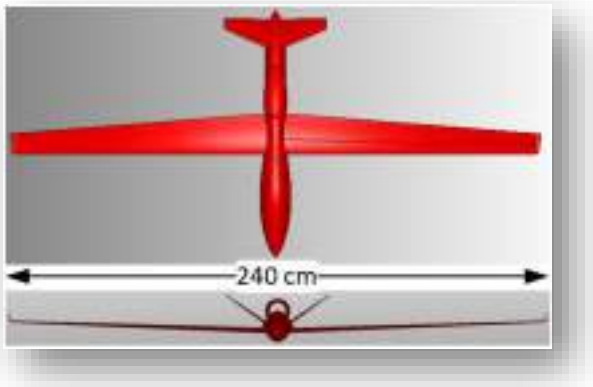

(b)

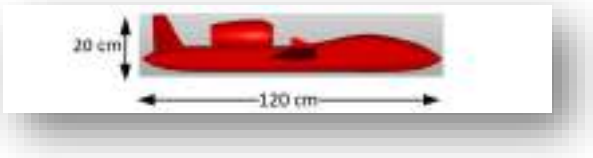

(c)

Fig. 1. Generic UAV model: (a) Perspective view, (b) Top and front view, and (c) side view

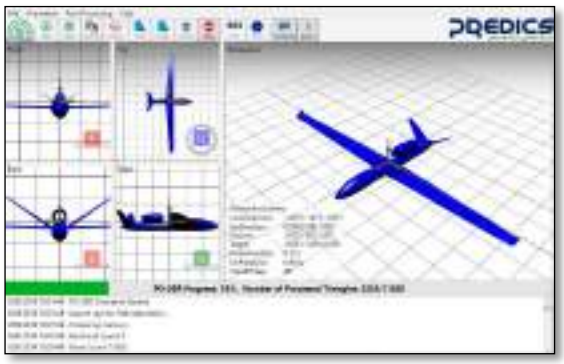

Fig. 2. Predics simulation screen for the UAV model

To characterize the RCS characteristics of the UAV model, two distinct simulation have been carried out. Firstly, angular RCS variation for a fixed frequency has been explored. Then, the frequency RCS variation for some particular look-angles has also been assessed by the help of consecutive RCS runs.

2.2.1. RCS variation over angles

In the first simulation, horizontal monostatic RCS variation for the fixed frequency of 8 GHz has been used. The detailed simulation parameters are given in Fig. 3.

Fig. 3. Simulation parameters for the horizontal angular RCS simulation

The resultant RCS variation over horizontal angles are presented for different polarization excitations in Fig. 4. In Fig 4(a) and (b), RCS variation over horizontal angles at a fixed elevation angle of 0° and the fixed frequency of 8 GHz are given for vertical-vertical (VV) and horizontal-horizontal (HH) polarizations, respectively. As obvious from the figures, RCS can be as high as 0 dBsm (i.e., 1m^2) for the look angles of 0°, 90° and 270° that corresponds to the scenarios for the nose-on case and the broad-side electromagnetic illumination cases.

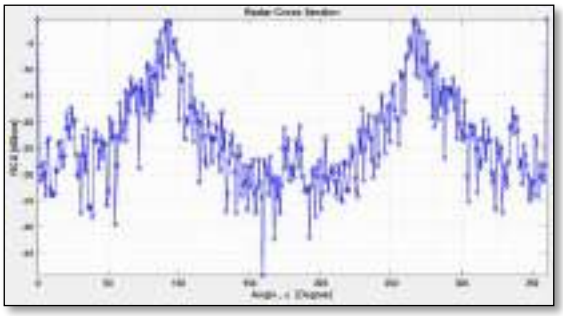

(a)

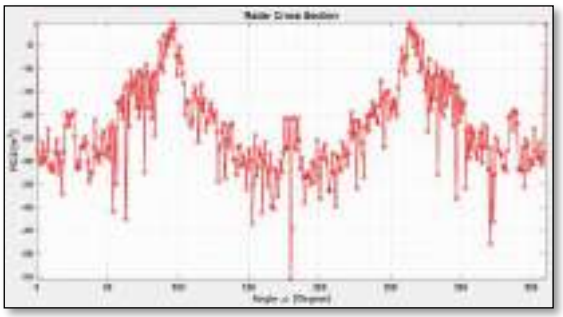

(b)

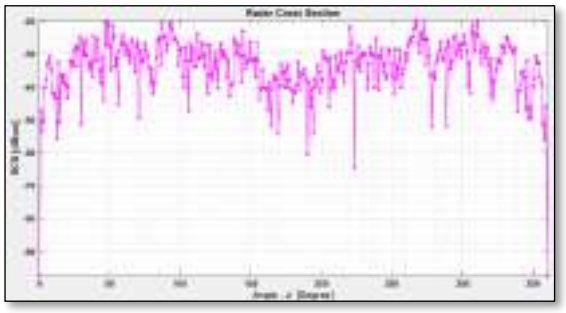

(c)

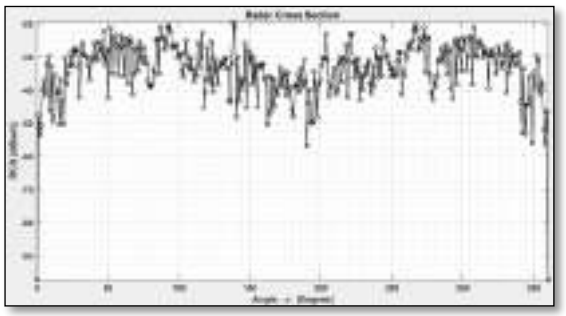

(d)

Fig. 4. Horizontal angles RCS simulation results: (a) VV, (b) HH, (c) VH, and (d) HV

In Fig 4(c) and (d), variation over horizontal angles at a fixed elevation angle of 0° and the fixed frequency of 8 GHz are given for vertical-horizontal (VH) and horizontal-vertical (HV) polarizations, respectively. In fact, cross-polarization RCS results are quite less than that of co-polarization RCS outcome. In fact, the angular RCS variation for either VH or HV polarization is always less than -20 dBsm (0.01 m^2). This is an expected result for the man-made objects. This is due to the fact that human-made targets usually experience high co-polar electromagnetic returns while providing much less cross-polar electromagnetic scatterings.

2.2.2. RCS variation over frequencies

In the second simulation, monostatic RCS variation over frequencies for the look angle of 0° elevation and 0° & 90° horizontal angles has been utilized. The detailed parameters for this particular simulation are given in Fig. 5.

As it can be seen from Fig.5, the frequency is varied from 1 GHz to 10 GHz for a total of 100 discrete frequencies. The aim of this simulation is to check if the RCS values are increasing for the higher frequencies or not. The simulation look-angles have been chosen as the look-angles that provide the highest values of RCS outcomes that were obtained in Fig. 4.

Fig. 5. Simulation parameters for the RCS simulation of frequency variation

In Fig.6 and Fig.7, RCS variation over frequencies for the fixed elevation angle of 0° and the fixed horizontal angles of 0° and 90° are given, respectively.

In Fig. 6(a), the monostatic RCS frequency variation of the UAV model and fixed elevation angle of 0° and the fixed horizontal angle of 0° is drawn. This plot is for the VV polarization. Similarly, in Fig. 6(b), the same RCS plot is provided for the HH-polarization case. As seen from both graphs, the RCS values are increased from -8.5 dB at 1 GHz to 0.5 dB at 10 GHz for both co-polarized electromagnetic waves. Since the cross-polarized RCS values are at least 20 dB less, they are not considered in this study.

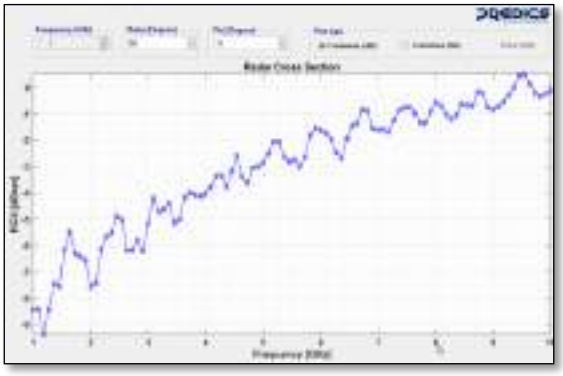

(a)

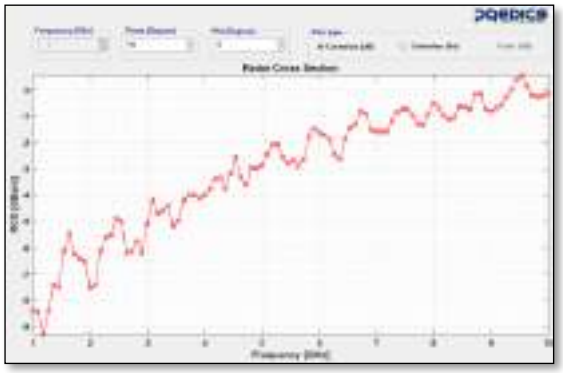

(b)

Fig. 6. RCS frequency variation for the fixed elevation angle of 0° and the fixed horizontal angles of 0°: (a) VV-polarized, (b) HH-polarized

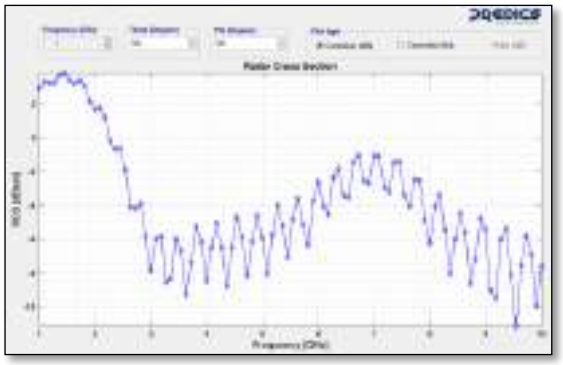

(a)

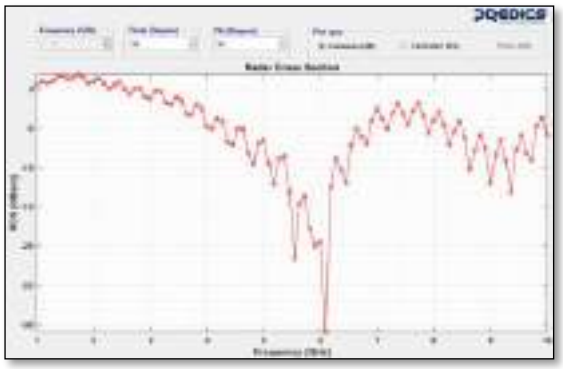

(b)

Fig. 7. RCS frequency variation for the fixed elevation angle of 0° and the fixed horizontal angles of 90°: (a) VV-polarized, (b) HH-polarized

A similar frequency variation study has been carried out for the fixed elevation angle of 0° and the fixed horizontal angles of 90° in Fig.7. In Fig. 7(a), the monostatic RCS frequency variation of the UAV model for the VV-polarization is provided; whereas, the RCS result for the HH polarization is given in Fig. 7(b). For the 90° horizontal look-angle that corresponds to the broadside illumination of the UAV model, the RCS

values are not increasing with frequency; in fact, we observe a slight decrease when the frequency is elevated from 1 GHz to 10 GHz

3. CONCLUSION

In this paper, we have represented a quantitative analysis of RCS from a model UAV to assess its visibility feature in the radar screen. We have utilized the high-frequency RCS simulator tool of Predics to perform the required RCS simulations. By the help of Predics software both the angle variation and the frequency variation monostatic RCS simulations of the mode UAV have been achieved. Results have shown that although the size of UAVs are rather small compared to manned vehicles such as aircrafts, helicopters, etc., the RCS values are not insignificant to be in the category of being low observable (stealth) by the radar. In fact, the RCS values of this model UAV are greater than $1m^2$ at 8 GHz and higher frequencies. Therefore, a hostile UAV can be detected by a radar before it reaches its targeted destination.

ACKNOWLEDGEMENTS

This work was supported by Mersin University Scientific Research Unit under Project No. 2015-TP3-1160

REFERENCES

Ananenkov, A. E., Marin, D. V., Nuzhdin, V. M., Rastorguev V. V., and Sokolov, P. V. (2018) "Possibilities to Observe Small-Size UAVs in the Prospective Airfield Radar," *2018 20th International Conference on Transparent Optical Networks (ICTON)*, Bucharest, 2018, pp. 1-6.

Özdemir, C., Yılmaz, B., and Kırık, Ö. (2014a), "pRediCS: A new GO-PO based ray launching simulator for the calculation of electromagnetic scattering and RCS from electrically large and complex structures," *Turkish Journal of Electrical Engineering & Computer Sciences,* Vol. 22, 1255 – 1269

Özdemir, C., Yılmaz, B., Kırık, Ö., Sütcüoğlu, Ö. (2014b), "A Fast and Efficient RCS Calculation and ISAR Image Formation Tool: pRediCS", *10th European Conference on Synthetic Aperture Radar* (EUSAR 2014), Berlin.

Pieraccini, M., Miccinesi, L. and Rojhani, N. (2017) "RCS measurements and ISAR images of small UAVs," in *IEEE Aerospace and Electronic Systems Magazine*, vol. 32, no. 9, pp. 28-32, September 2017.

Ryapolov, I., Sukharevsky O., and Vasilets, V. (2014) "Radar cross-section calculation for unmanned aerial vehicle," *2014 International Conference on Mathematical Methods in Electromagnetic Theory*, Dnipropetrovsk, pp. 258-261.

Thite V., and Kazi, A. Y. (2012) "Wideband VHF/UHF antennas for UAV platform with RCS approach," *2012 1st International Conference on Emerging Technology Trends in Electronics, Communication & Networking*, Gujarat, 2012, pp. 1-5.

CISET - 2nd Cilicia International Symposium on Engineering and Technology
10-12 October, 2019, Mersin / TURKEY

TREATMENT OF BARBER SALON GREY WASTE WATER BY ADSORPTION PROCESS: COMPARISON OF ACTIVATED CARBON, HUMAN HAIR, and BASALT

Hüdaverdi Arslan [1], Mohammed Saleh[*2], Mutlu Yalvaç[3]and Melis Gün[4]

[1]Mersin University, Engineering Faculty, Environmental Engineering Department, Mersin, Turkey, harslan@mersin.edu.tr

[2] Mersin University, Engineering Faculty, Environmental Engineering Department, Mersin, Turkey, muh.saleh89@gmail.com

[3] Mersin University, Engineering Faculty, Environmental Engineering Department, Mersin, Turkey, myalvac@mersin.edu.tr

[4] Mersin University, Engineering Faculty, Environmental Engineering Department, Mersin, Turkey, melis.gun.38@gmail.com

ABSTRACT

Personal care products (PCP's) are products used commonly to maintain personal hygiene. It has been found that PCP's is affecting the water bodies over the world. Conventional treatment methods are not sufficient for the treatment of PCPs. In this study, the removal of PCP's from barber salon wastewater - grey part by the adsorption process was investigated. The removal efficiency of chemical oxygen demand (COD) by different adsorbents; active carbon, raw human hair, and basalt were assessed and compared. To achieve that, 1 g of the proposed materials were added to 100 mL of the grey barber wastewater. The combinations were inserted into 250 mL beaker to prevent any unpredicted loss. The beakers were agitated at 150 rpm in an orbital shaker for 24 h at room temperature. The initial value of the COD was measured and founded to be 2400 mg/L. The COD removal efficiency by active carbon, raw human hair, and basalt was founded to be 63%, 85%, and 38.3% respectively. Since the maximum removal efficiency was obtained when basalt was used as an adsorbent, the response surface method was used to design and optimize the adsorption process onto the basalt only. When 0, 2318 g of the basalt was used, the adsorption capacity increased until 40th minute, the capacity had been constant at 721 mg/g. The use of waste material in the treatment of wastewater is a green engineering application.

Keywords: *Barber salon grey wastewater, Basalt, Adsorption, Response surface method*

[*] Corresponding Author

1. INTRODUCTION

In recent years, human life standard had been improved as a result of the development of civilization. Many materials have been produced to keep up with this development. One of these products is personal care products (PCP). PCP's are the product aiming to maintain personal hygiene (Yang et al., 2017; Rajapaksha, 2019). It can be found as neutral, anionic, cationic or zwitterion (Kummerer, 2008). Since the 1990s, the PCP's have been acknowledged as an emerging contaminant. PCP's can be discharged to the environment through Human excretion, Treatment plants, and industrial facilities (Daughton and Ternes, 1999; Chen et al., 2016).

Conventional wastewater treatment plants were established to treat urban wastewaters. However, as PCP usage has increased in recent years, its concentration in sewage water has increased. Studies have shown that PCP is present in the effluent of treatment plants. This shows that conventional purification methods are not sufficient for the treatment of PCPs (Lester et al., 2013). Previous studies have explored the presence of PCP's in water bodies and have founded more than 100 types of PCP's (Ebele et al., 2017; Archer et al., 2017; Petrie et al., 2015).

Many researchers have employed different treatments techniques to remove PCP's from water. Wang and Wang (2016) have noticed a fluctuation in the PCP's removal efficiency by activated sludge systems. In addition to that, McClellan and Halden (2010) have stated that several types of PCP's are antimicrobial agents. Many researchers have investigated the electrochemical process. They have reported a high efficiency for the degradation of PCP's (Feng et al, 2010; Boudreau, 2010; Romao et al; 2017). The main problem in this type of treatment is the possibility of production of bio-recalcitrant by-products (Sire´s and Brillas, 2012). Membranes have also shown efficacy in treated of PCP's (Sheng et al, 2016; Wang et al, 2016). The membranes efficiency depend on the diameter and the molecular weight of the PCP's, which are vary from one to another (Nghiem et al, 2004).

The using of the adsorption process to remove the PCP's was extensively investigated. The adsorption process is a simple, flexible, and economic beneficiary (Xu et al., 2017; Saleh et al, 2019a). These features made the process more favorable. The limitation in this technique is the disposal/ regeneration of the adsorbent, which can be considered as second-order contamination (Ateia et al, 2018).

Active carbon can be considered the most common adsorbent. The relatively high cost of it led the researchers to find low-cost adsorbent (Dai et al., 2012). Agricultural solid wastes (Jing et al, 2014; Chen et al., 2016), Industrial by-products (Nielsen and Bandosz, 2016), clay minerals (Styszko et al., 2015; Tsai et al, 2016), and Montmorillonite (Li et al., 2011) are some of the examples of the low-cost adsorbents which were employed to remove PCP's from liquids.

PCP is a major part of COD in real barber wastewater (Saleh et al, 2019b). In this study, a commercial active carbon was used to treat the wastewater discharged from the barber salons. Human hair as a bio-sorbent and basalt as an industrial by-product were used as a low-cost alternative. The chemical oxygen demand (COD) removal efficiencies were recorded and compared with others. The adsorbent with the maximum removal efficiency was modeled and optimized by response surface method.

2. MATERIAL AND METHOD

2.1. Material

In this study, the wastewater generated from barber salons was treated by different low cost materials (Raw clean human hair and basalt). The efficiencies of COD removal by these materials and commercial active carbon were compared. Raw clean human hair was collected from barber salon. Basalt was collected from industrial treatment sludge of a basalt processing plant in Osmaniye. The active carbon was bought without brand discrimination.

2.2. Method

To achieve the target of this research the following steps were accomplished.

2.2.1. Sample collection

The barber salon count in Mersin was obtained from the relative agencies. Water bill samples were collected from barber salons to estimate the monthly consumption. The chemical oxygen demand was measured by Closed Reflux, Titrimetric Method (5220 C) (AWWA, WEF, APHA, 1998).

2.2.2. Men barber salon load calculation

To collect sample from men barber salon, a tank was connected to the sanitary system of the salon. The tank is mounted on the outlet of the barber basin to avoid mixing with the black wastewater. It was taken into consideration that the wastewater had been generated by the different hair treatment process.

2.2.3. Batch study

In the batch study, the removal of COD by human hair, basalt, and active carbon was assessed. The initial and final COD was measured. To achieve that, 1 g of the proposed materials were added to 100 mL of the barber wastewater. The combinations were inserted into 250 mL beaker to prevent any unpredicted loss. The beakers were agitated at 150 rpm in an orbital shaker for 24 h at room temperature. The efficiencies of the COD removal were calculated by Eq. (1).

$$COD\ remocal\ \% = \frac{COD\ i - COD\ f}{COD\ i} \times 100\% \quad (1)$$

The adsorbent capacity ($mg.g^{-1}$) for each material was identified separately as shown in Eq. (2).

$$Adsorbent\ Capacity = \frac{(COD\ i - COD\ f) \times V}{M} \quad (2)$$

Where COD_i and COD_f are the initial and final COD respectively ($mg.L^{-1}$); V is the volume of the solution (L); M adsorbent mass (g).

The material that had the maximum COD removal was optimized by Response surface Method.

2.2.4. Response surface method

The COD removal efficiency was modeled by Response surface Method (RSM). In this experiment time and adsorbent mass were represented using a Central Composite Design (CCD). The experiment counts necessary to build the model were calculated using Eq. (3).

$$N = 2^n + 2n + Cp \quad (3)$$

Where N, n, Cp is the experiment runs, independent factor, and center point replicates, respectively.

The modeling process was established using Design expert v11 program. 13 experiments were accomplished.

3. RESULTS

3.1. Men barber salon wastewater load in Mersin

The barber salon wastewater load in Mersin city was calculated. The research finds there are 1119 salons for men and 1081 salon for women. This study focused on the men barber salons. Accordingly, the result in Table 1 belongs to the men salons only.

Table 1. Men barber salon wastewater load calculation

	Value	Unit
COD For men barber wastewater	2400 .0	mg/L
Monthly Average water consumption	9.0	m^3
Monthly Average wastewater consumption	7.2	m^3
Daily COD loading for each salon	0.6	Kg/d
Daily COD loading for Men Barber salons	644.5	Kg/d

3.2. Batch study

Commercial active carbon was compared with the low-cost adsorbent (raw human hair and basalt). All of the experiments were conducted in the same conditions (1g adsorbent, 24 h, 100 mL) at room temperature. At the end of the process, the changes in COD were found to be as shown in Table 2.

Table 2. COD changes and removal efficiency

	COD (mg/L)	Removal Efficiency (%)
Men barber wastewater	2400	-
Activated carbon	888	63.0
Basalt	360	85.0
Raw human hair	1480	38.3

As shown in Table 2 the maximum COD removal efficiency obtained when basalt was used as an adsorbent with 85% removal efficiency. The use of commercial active carbon had decreased the COD to 888 with a removal efficiency of 63%. Mestre et al (2007) have examined the removal efficiency for ibuprofen using active carbon. They have stated that the removal efficiency of ibuprofen exceeded 90% at pH levels from 2-4. They have also noticed that a decrease in efficiency at higher pH values. Raw human hair had decreased the COD to 1480 mg/L. Saleh et al (2019b) have obtained similar results.

3.3. Response surface method

The men barber wastewater treatment process by basalt was optimized by RSM. Basalt mass and time needed to reach the proposed efficiency and optimum capacities were modeled by Central Composite Design. The carried experiments and the results are shown in Table 3.

Table 3. Experiments Design and the result of each run

Run	Mass (g)	Time (min)	Eff. (%)	Capacity (mg/g)
1.00	0.55	30.00	76.67	334.56
2.00	0.23	11.97	43.33	448.62
3.00	1.00	30.00	83.33	199.99
4.00	0.87	11.97	71.00	196.27
5.00	0.55	30.00	76.67	334.56
6.00	0.10	30.00	46.67	1120.08
7.00	0.55	30.00	76.67	334.56
8.00	0.55	30.00	76.67	334.56
9.00	0.55	30.00	76.68	334.60
10.00	0.55	4.50	41.00	178.91
11.00	0.55	55.50	80.00	349.09
12.00	0.23	48.03	60.00	621.22
13.00	0.87	48.03	88.00	243.26

Based on the correlation coefficient (R^2 = 0.9632), the developed model was suggested to be Quadratic. Analysis of variance for the developed model was used to study the significance of the model. The model was found to be significant since F- value was 63.82 (p-value <0.0001). Table 4 shows the ANOVA test for the developed model.

Table 4. ANOVA test for the developed model

Source	Sum of squares	df	Mean	F-value	p-value	
Model	0.000874	5	0.000175	63.81528	1.09688E-05	Significant
A-mass	0.000672	1	0.000672	245.1843	1.04835E-06	Significant
B-time	9.47E-05	1	9.47E-05	34.57316	0.000611782	Significant
AB	4.45E-07	1	4.45E-07	0.16242	0.698963512	
A^2	4.29E-05	1	4.29E-05	15.65786	0.005482661	Significant

B^{2j}	5.04E-05	1	5.04 E-05	18.40406	0.0036 1071	Significant

The effects of time and basalt mass on the treatment capacity were identified separately and together. Fig. 1 shows the effect of time on the capacity.

The capacity of the modeled data increases until 40 minute. After 40 minute the capacity had been constant at capacity of 721 mg/g. The confirmation bands (green) and the prediction bands (red) gave the same phenomena.

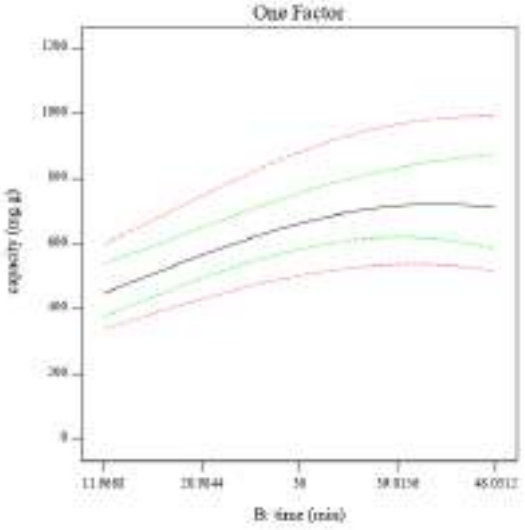

Fig. 1. The effect of time on the capacity

The mass of basalt had an inverse relationship with the capacity as shown in Fig. 2. The maximum capacity was at 0.2318 g while the minimum capacity was at 0.8982. The decrease of capacity was notice to be not linear.

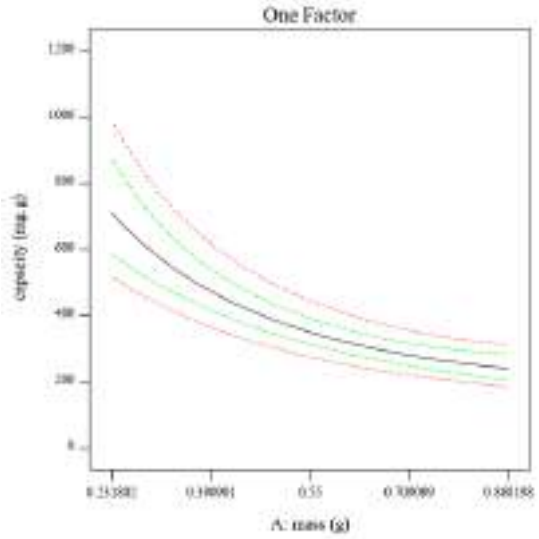

Fig. 2. Mass effects on the capacity.

The relationship between the time, the mass of basalt and the capacity of the basalt was also graphed and shown in Fig. 3. The capacity curve at low dose of adsorbent was clearer than the high dose. This means that the capacity at low dose had changed with time more than in high dose.

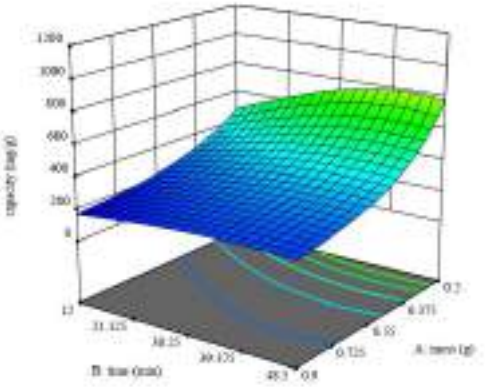

Fig. 3. Mass and time effects on the capacity

The removal of COD by basalt can be predicted by the developed model as shown in Eq. (4).

$$\frac{1}{sqrt(capacity+100)} = 0.0480 + 0.0092(mass) - 0.0034(time) + 0.0003(mass * time) - 0.0025(mass)^2 + 0.0027(time)^2 \quad (4)$$

4. CONCLUSION

Barber salons wastewater is one of the most important sources of PCPs. The COD of a normal domestic wastewater is 800 mg / L. The COD value of the gray wastewater from the barber salons was founded to be 2400 mg / L.

In this study, COD in gray wastewater was treated by adsorption method. Activated carbon, human hair and basalt were used in adsorption. The best yield was obtained from the process where basalt was used as adsorbent material.

Basalt was collected from industrial treatment sludge of a basalt processing plant. The use of a waste material in the treatment of wastewater is a green engineering application. As a result, it was found that basalt can be used effectively in the treatment of barber gray wastewater by adsorption.

ACKNOWLEDGEMENTS

The authors report no conflicts of interest. The authors alone are responsible for the content and writing of this article.

REFERENCES

Archer, E., Petrie, B., Kasprzyk-Hordern, B., Wolfaardt, G.M. (2017). "The fate of pharmaceuticals and personal care products (PPCPs), endocrine disrupting contaminants (EDCs), metabolites and illicit drugs in a WWTW and environmental waters." *Chemosphere* Vol. 174, pp. 437-446.

Ateia, M., Ceccato, M., Budi, A., Ataman, E., Yoshimura, C., Johnson, M.S. (2018). "Ozone-assisted

regeneration of magnetic carbon nanotubes for removing organic water pollutants." *Chem. Eng. J.* Vol. 335, pp. 384-391. https://doi.org/10.1016/ j.cej.2017.10.166.

Boudreau, J., Bejan, D., Li, S., Bunce, N.J. (2010). "Competition between electrochemical advanced oxidation and electrochemical hypochlorination of sulfamethoxazole at a borondoped diamond anode." *Ind. Eng. Chem. Res.* Vol. 49, pp. 2537-2542.

Chen, Y., Vymazal, J., Brezinov A., T., Kozeluh, M., Kule, L., Huang, J., Chen, Z. (2016). "Occurrence, removal and environmental risk assessment of pharmaceuticals and personal care products in rural wastewater treatment wetlands." *Sci. Total Environ.* Vol. 566, pp. 1660-1669. https://doi.org/10.1016/j.scitotenv.2016.06.069.
Closed Reflux, Titrimetric Method 5220 C (1998). *Standard Methods for the Examination of Water and Wastewater*. AWWA, WEF, APHA.

Daughton, C.G., Ternes, T.A. (1999). "Pharmaceuticals and personal care products in the environment: agents of subtle change?" *Environ. Health Perspect.* Vol. 107, pp. 907-938.

Ebele, A.J., Abou-Elwafa Abdallah, M., Harrad, S. (2017). "Pharmaceuticals and personal care products (PPCPs) in the freshwater aquatic environment." *Emerg. Contam*. Vol. 3, pp. 1-16.

Feng, Y., Wang, C., Liu, J., Zhang, Z. (2010). "Electrochemical degradation of 17-alphaethinylestradiol (EE2) and estrogenic activity changes." *J. Environ. Monit.* Vol. 12, pp. 404-408. https://doi.org/10.31127/tuje.451173

Jing, X.R., Wang, Y.Y., Liu, W.J., Wang, Y.K., Jiang, H. (2014). "Enhanced adsorption performance of tetracycline in aqueous solutions by methanol-modified biochar." *Chem. Eng. J.* Vol. 248, pp. 168-174.

Kümmerer, K. (2008). *Pharmaceuticals in the Environment*. Springer-Verlag, Berlin Heidelberg.
Lester, Y., Mamane, H., Zucker, I., Avisar, D. (2013). "Treating wastewater from a pharmaceutical formulation facility by biological process and ozone." *Water Res.* Vol. 47, pp. 4349-4356. https://doi.org/10.1016/j.watres.2013.04.059.

Li, Z., Chang, P.H., Jean, J.S., Jiang, W.T., Hong, H.(2011). "Mechanism of chlorpheniramine adsorption on Ca-montmorillonite."*Colloids Surf. Physicochem. Eng. Aspects*. Vol. 385, pp. 213-218.

McClellan, K., Halden, R.U. (2010). "Pharmaceuticals and personal care products in archived U.S. biosolids from the 2001 EPA national sewage sludge survey."*Water Res.* Vol. 44, pp. 658-668. https://doi.org/10.1016/j.watres.2009.12.032

Mestre, A.S., Pires, J., Nogueira, J.M.F., Carvalho, A.P. (2007). "Activated carbons for the adsorption of ibuprofen." *Carbon.* Vol. 45, pp. 1979-1988.

Nghiem, L.D., Sch¨afer, A.I., Elimelech, M. (2004). "Removal of natural hormones by Nano filtration membranes: measurement, modeling, and mechanisms." *Environ. Sci. Technol.* Vol. 15, pp. 1888-1896.

Nielsen, L., Bandosz, T.J. (2016). "Analysis of sulfamethoxazole and trimethoprim adsorption on sewage sludge and fish waste derived adsorbents." *Microporous Mesoporous Mater.* Vol. 220, pp. 58-72. https://doi.org/10.1016/ j.micromeso.2015.08.025

Petrie, B., Barden, R., Kasprzyk-Hordern, B. (2015)."A review on emerging contaminants in wastewaters and the environment: current knowledge, understudied areas and recommendations for future monitoring." *Water Res*. Vol. 72, pp 3-27.

Rajapaksha, A.U., Premarathna, K.S.D., Gunarathne, V., Ahmed, A., Vithanage, M. (2019). "Sorptive removal of pharmaceutical and personal care products from water and wastewater" *Pharmaceuticals and Personal Care Products Waste Management and Treatment Technology: Emerging Contaminants and Micro Pollutants*. Butterworth-Heinemann, United Kingdom, pp. 213-238. https://doi.org/10.1016/C2017-0-03544-9

Romao, J., Barata, D., Ribeiro, N., Habibovic, P., Fernandes, H., Mul, G. (2017)." High ~ throughput screening of photocatalytic conversion of pharmaceutical contaminants in water." *Environ. Pollut.* Vol. 220, pp. 1199-1207. https://doi.org/10.1016/ j.envpol.2016.11.015.

Saleh, M, Yalvaç, M, Sime, F, Mazmanci, M. (2019b). "Study the effect of hair style products on the quality of domestic wastewater- wax as case study." *Turkish Journal of Engineering*. Vol. 3, No. 2, pp. 97-101.

Saleh, M., Yalvaç, M.; Arslan, H. (2019a) "Optimization of Remazol Brilliant Blue R Adsorption onto Xanthium Italicum using the Response Surface Method." *Karbala International Journal of Modern Science*. Vol. 5, Iss. 1, Article 8.DOI: 10.33640/2405-609X.1017

Sheng, C., Nnanna, A.G.A., Liu, Y., Vargo, J.D. (2016). "Removal of trace pharmaceuticals from water using coagulation and powdered activated carbon as pretreatment to ultrafiltration membrane system." *Sci. Total Environ.* Vol. 550, pp. 1075-1083. https:// doi.org/10.1016/j.scitotenv.2016.01.179.

Sire´s, I., Brillas, E. (2012). "Remediation of water pollution caused by pharmaceutical residues based on electrochemical separation and degradation technologies: a review." *Environ. Int.* Vol. 40, pp. 212-229.

Styszko, K., Nosek, K., Motak, M., Bester, K. (2015). "Preliminary selection of clay minerals for the removal of pharmaceuticals, bisphenol A and triclosan in acidic and neutral aqueous solutions." *C.R. Chim.* Vol. 18, pp. 1134-1142.

Subedi, B., Codru, N., Dziewulski, D.M., Wilson, L.R., Xue, J., Yun, S., BraunHowland, E., Minihane, C., Kannan, K. (2014). "A pilot study on the assessment of

trace organic contaminants including pharmaceuticals and personal care products from on-site wastewater treatment systems along Skaneateles Lake in New York State, USA." *Water Res.* Vol. 72, pp. 28-39. https://doi.org/10.1016/ j.watres.2014.10.049.

Tsai, Y.L., Chang, P.H., Gao, Z.Y., Xu, X.Y., Chen, Y.H., Wang, Z.H., et al. (2016). "Amitriptyline removal using palygorskite clay." *Chemosphere*. Vol. 155, pp. 292-299.

Wang, Y., Ma, J., Zhu, J., Ye, N., Zhang, X., Huang, H. (2016). "Multi-walled carbon nanotubes with selected properties for dynamic filtration of pharmaceuticals and personal care products." *Water Res.* Vol. 92, pp. 104-112. https://doi.org/10.1016/ j.watres.2016.01.038.

Xu, Y., Liu, T., Zhang, Y., Ge, F., Steel, R.M., Sun, L. (2017). "Advances in technologies for pharmaceuticals and personal care products removal." *J. Mater. Chem. A.* Vol. 5, pp. 12001-12014.

Yang, Y., Ok, Y.S., Kim, K.-H., Kwon, E.E., Tsang, Y.F. (2017). "Occurrences and removal of pharmaceuticals and personal care products (PPCPs) in drinking water and water/sewage treatment plants: a review." *Sci. Total Environ.* Vol. 596-597, pp. 303-320. https://doi.org/10.1016/j.scitotenv.2017.04.102.

CISET - 2nd Cilicia International Symposium on Engineering and Technology
10-12 October, 2019, Mersin / TURKEY

DETERMINATION OF MARINE SELECTION CRITERIA FOR FOREIGN YACHTERS BY AHP METHOD

Volkan EFECAN [*1], İzzettin TEMIZ [2]

[1] Mersin University, Vocational School Of Maritime, Department of Transportation Services, Mersin, Turkey, volkanefecan@mersin.edu.tr

[2] Mersin University, Faculty of Maritime, Department of Maritime Business Administration, Mersin, Turkey, itemiz@mersin.edu.tr

ABSTRACT
Marine Tourism and Marina Management is developing rapidly in the global sense after the 1980s and the impact of this development is also seen in our country. Sector stakeholders are discussing the preference of foreign yachts for marinas of our country or the reasons for preferring competitor marinas. In this study, the criteria of preference of foreign yachtsmen in marinas of our country tried to be determined by using Analytic Hierarchy Process (AHP), which is one of the multi criteria decision-making methods. Security and location are the two most effective criteria compared to other criteria.

Keywords: *Marina Selection, Analytic Hierarchy Process, Tourism of Marine, Mariner.*

[*] Corresponding Author

1. INTRODUCTION

Marine tourism has made great progress in our country in recent years. Important parts of these advances are occurred by the modernization of the newly built marinas and existing marina facilities that can serve all kinds of boats by renewing their technologies. Our country has become a center of attraction especially for European (British and German) yachtsmen with its climate, sheltered bays, maritime routes suitable for yachts and cultural heritage. Marinas are spread over the Mediterranean, Marmara and Aegean coasts of our country, surrounded by inland seas and are concentrated in Istanbul, North Aegean, South Aegean and Western Mediterranean regions.

Local tourists realized the availability of yachting, which was discovered by foreign tourists in the 1960s with the intention of visiting the bays where no land transportation was available, in time, thus the marina and yachting activities in Bodrum, Marmaris gained momentum (Sezer, 2012).

According to the yacht statistics published by the Ministry of Culture and Tourism, the number of foreign private yachts coming to Bodrum Port in 2007 for example increased from 816 to 3691 in 2016 and increased by 452% (Ministry Of Culture and Tourism, 2019).

In this study, the problem of marina selection in accordance with individual expectations and boat characteristics of foreign private yacht owners who intend to visit Turkey permanently or in transit is examined.

Analytical Network Process (AHP), which is a multi-criteria decision making method, is preferred as the method. The Analytic Hierarchy Process is the decision mechanism that human beings have not been taught to, but instinctively adopts from the beginning and uses it when faced with the decision-making problem (Saaty, 2003). The instinctive mechanism is characterized by qualitative and quantitative criteria. The Analytic Hierarchy Process is difficult or impossible to deal with in most other approaches, but it is also highly applicable to many decision-making problems encountered in everyday life, since it can also address qualitative features that affect decisions.

2. AIM AND SCOPE OF RESEARCH

The aim of this study is to examine the usability of multi-criteria decision-making methods in marina selection, and to provide an alternative method for the marinas to evaluate their qualifications and handicap in a healthy way.

When the national publications in the literature are examined, it is seen that the factors that affect the service quality of marinas are determined, the application of service quality factors to marina enterprises and the choice of marina facility location are concentrated (Dikeç &Töz, 2017; Maglic, 2019; Sezer, 2012). Although the quality of service for yachtsman seems to be a very important criterion, when the occupancy rates of the marinas on our coasts are examined to include all marinas, there may be more important technical criteria.

The decision alternatives are 3 private marina enterprises located in Muğla province, all three with 5 anchors, blue flags and occupancy rate of 85% or more in summer season. The decision makers are the foreign yachtsmen in which the Ministry of Culture and Tourism deals with the status of foreign yachtsmen. Since the ranking of decision alternatives will be evaluated with a more comprehensive study, this study is not included in this study.

3. TOURISM OF YACHTING

The yachts that have a share in yacht tourism can be defined as structures where private and commercial yachts can safely approach, professional mooring services are provided, the safety of the yacht and the yacht owner are provided, and there are various boat handling and maintenance equipment, as well as social facilities and various cultural activities (Işik & Cerit, 2007). There are two basic elements of yacht tourism. These are yachts and marinas that these yachts are fastened. When we look at the official definitions of the yacht:

"It is not a cargo, passenger and fishing vessel, it has a cabin, a toilet, a sink, a kitchen, it is used commercially or non-commercially for the purpose of travel and sports, the number of passengers it carries is not more than twelve or it is limited to one hundred miles on a cabotage journey, not more than twenty miles from the nearest land. The number of passengers carried by the ship does not exceed thirty-six and the yacht is stated in the tonnage document" (Turkish Tourism Incentive Law No. 2634).

"*It is suitable for use in sea tourism trade for the purpose of travel, sport and entertainment, the number of passengers carried does not exceed twelve, differs from cargo, passenger and fishing vessels, not having the cabin, toilet and kitchen*" (Marine Tourism Regulation, 2009) found in literature.

Yachts are classified according to propulsion system, hull structure and construction methods in traditional classification. According to their functions, motor yachts, sailing yachts, sports and recreational vehicles are classified as private yachts and commercial yachts. Private yachts; refers to boats used for recreational and sporting purposes, which are limited to 12 persons. Commercial yachts mean boats that do not have the status of cargo, passenger or fishing ships, can travel up to 20 nautical miles away from the nearest land or do not make more than 100 miles in cabotage and carry more than 36 people (Kan, 2014).

The marina is defined as the facility that contains the equipment and materials that can accommodate all kinds of yachts' accommodation (TDK, 2019). The number of certified tourism businesses coastal marinas in Turkey 27, the total capacity is 11.715't. Number of yachts with tourism operation certificate is 6 and total mooring capacity is 967. The number of marinas with a tourism investment certificate is 8 and the total mooring capacity is 3530. The cruise ship port with a tourism investment certificate is 1 and the overall total of all maritime tourism facilities is 42 and the total mooring capacity is 16.212 (Marine Tourism Report, Maritime Trade Magazine, 2019).

3. METHODOLOGY

In the study, Analytical Hierarchy Process (AHP) was used to weight the criteria. The definition of the criteria which is one of the main elements of the Analytical Hierarchy Process, have been obtained through literature research. Face-to-face interviews with three academicians and a marina senior manager finalized it. The relevant expert opinion was also applied to form and weight the binary comparison matrices of the criteria. In order to score the decision alternatives for each criterion, questionnaire forms that were created for qualitative criteria were applied to marina visitors and managers. Data were collected via internet websites and e-mail for quantitative criteria. The implementation of the scoring of decision alternatives will be discussed in another more comprehensive study.

3.1. Analytic Hierarchy Process

Although the Analytic Hierarchy Process was first proposed by Myers and Alpert in 1968, Thomas Lorie Saaty developed it as a model in 1977 and made it available to decision-making processes (Yaralioglu, 2001). The Analytic Hierarchy Process allows decision makers to model problems, decision alternatives, criteria and sub-criteria, if any, and the relationship between them in a hierarchical structure. In the Analytic Hierarchy Process, the subjective interpretations and objective evaluations of the decision-maker at the decision stage are included together.

The first step in the Analytic Hierarchy Process is to establish a hierarchical model. The aim of the problem, respectively, the main criteria, if any sub-criteria, decision alternatives are listed in a hierarchical manner as in Fig. 1.

After the hierarchy table is created, in the second step, the criteria are compared between each other and sub-criteria, if any, and their importance levels and weights are determined. In binary comparison, square matrix is obtained by utilizing the scale graded 1-9 by Saaty in Table 1. The effectiveness of the 1-9 comparison scale was determined by comparisons with other scales and the use of the scale in different areas (Kuruüzüm & Atsan, 2001).

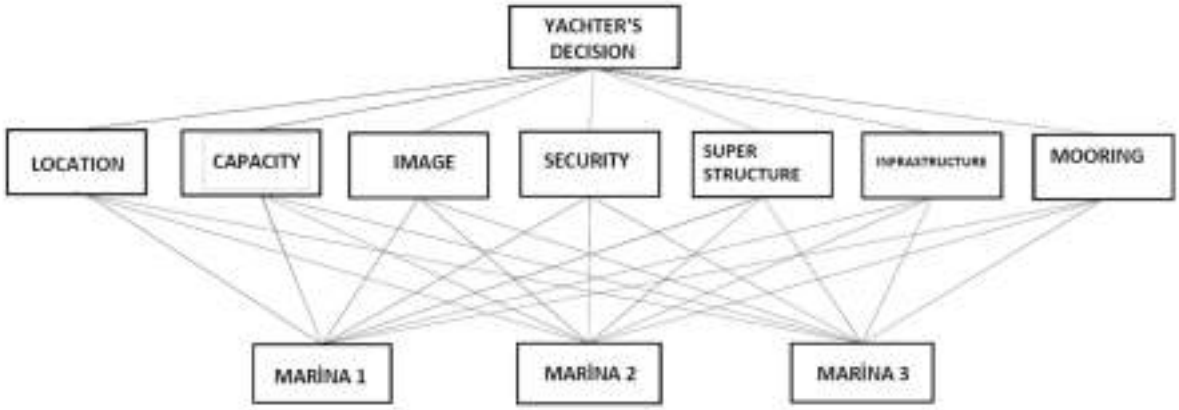

Fig. 1. Marina Selection Problem - AHP Hierarchy Model

Table 1. Thomas Saaty's 1-9 degree AHP scale (eleren, 2006).

Importance Level	Definition	Importance Level	Definition
1	Equal Importance	1	Equal Importance
3	Moderately More Important	1/3	Moderately Less Important
5	Strongly More Important	1/5	Strongly Less Important
7	Very Strongly More Important	1/7	Very Strongly Less Important
9	Extremely Strong Importance	1/9	Extremely Less Important
2-4-6-8	Intermediate Values	½,1/4, 1/6, 1/8	Intermediate Values

In step 3, the normalization of the scores in the square matrix is made and the normalized square matrix is formed. Each line is averaged to obtain a priority vector.

Normalization:

$$b_{ij} = \frac{a_{ij}}{\sum_{i=1}^{n} aij} \quad (1)$$

Definition of Priority Vector:

$$w_i = \frac{\sum_{j=1}^{n} Cij}{n} \quad (2)$$

In step 4, matrix consistency is determined. For a matrix to be consistent, its maximum eigenvalue (λmax) must be equal to the matrix size (n). To find λmax, each column element in the comparison matrix is divided by the sum of the column. Thus, the matrix is normalized. Then, each row is averaged for the priority vector calculation. The Whole Priority Matrix "is calculated by multiplying the priority vector and initial matrix. The values obtained are divided by the Priority Vector values. λmax the average of these values is determined to calculate. This is the average λmax value (Long and Kazan, 2016). This should be done after finding the value; As stated above, the consistency of the hierarchical table is determined by calculating the consistency ratio. The consistency ratio is calculated to prevent the expert from making mistakes when performing binary comparisons. If this value is greater than 0.1, the comparison should be revised. To calculate consistency, the consistency index (CI) is first calculated.

CI is calculated as follows:

$$CI = \frac{\lambda \max - n}{n-1} \quad (3)$$

Once CI is calculated, the consistency ratio (CR) is calculated by the following formula.

$$CR = \frac{CI}{RI} \quad (4)$$

RI represents the randomness indicator. The Randomness Indicator is determined by selecting the appropriate value from Table 2.

Table 2. Randomness Index

n	**1**	**2**	**3**	**4**	**5**	**6**	**7**	**8**	**9**	**10**	**11**	**12**	**13**	**14**	**15**
RI	0	0	0,58	0,90	1,12	1,24	1,32	1,41	1,45	1,49	1,51	1,48	1,56	1,57	1,59

If the obtained consistency ratio is less than 10%, the criteria weighting and/or decision-making process is consistent. The decision is applied.

4. APPLICATION

In this study, the criteria that foreign yachtsmen will take into consideration in order to determine the most suitable marina for their own yacht from the marinas in Muğla province are determined by Analytical Hierarchy Process (AHP). Questionnaire forms were created by using the scale that 1-9 graded by Saaty to be used in paired comparisons of criteria and evaluation of each alternative according to criteria.

4.1. Definition of Criteria

The criteria of the study were obtained by face-to-face interview with 3 academicians and 1 marina official after the literature research. Determined criteria are location, capacity, prestige, security, superstructure, infrastructure and mooring fee.

4.2. Determination of Criterion Weights

In weighting the criteria by pairwise comparison, expert opinion was used. Criterion weights and alternatives were evaluated by interviews with 3 academicians and 1 marina manager. In order to score the decision alternatives for each criterion, questionnaire forms created for qualitative criteria were used and data were collected via internet websites/e-mail communications for quantitative criteria.

Table 3. AHP Score / Criteria Weight

Criteria	*Ahp Scores / Criteria Weight*
Location	0,307
Capacity	0,032
Prestige	0,027
Security	0,27
Superstructure	0,086
Infrastructure	0,151
Mooring Fee	0,126

Table 4. Comparison Matrix

Criteria	Location	Capacity	Prestige	Security	Superstructure	Infrastructure	Mooring Fees
Location	1	7	9	1	5	3	3
Capacity	1/7	1	1	1/9	1/3	1/5	1/3
Prestige	1/9	1	1	1/7	1/5	1/7	1/5
Security	1	9	7	1	5	1	3
Superstructure	1/5	3	5	1/5	1	1	1/3
Infrastructure	1/3	5	7	1	1	1	1
Mooring Fees	1/3	3	5	1/3	3	1	1

Table 5. Normalized Matrix

Criteria	Location	Capacity	Prestige	Security	Superstructure	Infrastructure	Mooring Fees
Location	0,320447	0,241379	0,257143	0,2640402	0,3218	0,408560	0,338346
Capacity	0,045778	0,034483	0,028571	0,0293378	0,0214	0,027237	0,037594
Prestige	0,035605	0,034483	0,028571	0,0377200	0,0128	0,019455	0,022556
Security	0,320448	0,310345	0,200000	0,2640402	0,3218	0,136187	0,338346
Superstructure	0,064089	0,103448	0,142857	0,0528080	0,064377	0,136187	0,037594
Infrastructure	0,106816	0,172414	0,200000	0,2640402	0,064377	0,136187	0,112782
Mooring Fees	0,106816	0,103448	0,142857	0,0880134	0,193133	0,136187	0,112782

Table 6. Grading of criteria and percent consistency

%	*CA*	*Criteria*	*λmax*	*CI/RI*	*Consistency Percentage*
37%	0,95929	Location	7,4303	0,0543	%5 < %10
3,2%	0,92991	Capacity			
2,7%	0,95633	Prestige			
27%	1,02325	Security			
8,60%	1,33445	Superstructure			
15,10%	1,10837	Infrastructure			
12,60%	1,11877	Mooring Fees			

According to the above criteria weights, the criteria with the highest weight value were determined as position and safety respectively. Location and security criteria are followed by infrastructure, mooring fee, superstructure, capacity and prestige criteria.
Since the consistency indicator (CR) is determined as 5% (0.0543), it is seen that the consistency indicator is less than the upper limit of 0.1. In this case, since it is 5% <10%, it can be said that experts make comparisons consistently.

5. CONCLUSION

Marine tourism and marina management are developing day by day in the global sense and the activities in this field are increasing in our country. With increasing investments and employment in the sector, the number of scientific studies should increase day by day.

When the factors affecting the choice of foreign yachtsmen are taken from a wide perspective, location and safety are the most important factors. The criteria for infrastructure, mooring fee, superstructure, capacity and prestige that follow these two criteria are also very important. For example, it is possible to encounter interesting results between a marina operation in the Eastern Mediterranean and two marinas in the North Aegean, for example due to the large score difference in the security criteria.
It is in the interest of the sector and yachts to determine criteria, taking into account the socio-economic characteristics of each yacht, the purpose of use of the marina and the size of the yacht, and the use of Multi-Criteria Decision Making Methods, where other quantitative and qualitative criteria can be taken into account.

4. REFERENCES

Dikeç, G; Töz, A. C. (2016). Marina müşterilerinin marinalarda aldiklari hizmetlerin kalite düzeylerine yönelik algilarinin analizi. III. Ulusal Deniz Turizmi Sempozyumu.
https://doi.org/10.18872/DEU.b.UDTS.2016.0022

Eleren, A. (2006). Kuruluş yeri seçiminin analitik hiyerarşi süreci yöntemi ile belirlenmesi; deri sektörü örneği. Atatürk üniversitesi iktisadi ve idari bilimler dergisi, (2):, 20(2), 405–416

Imeak chamber of shipping, https://www.denizticaretodasi.org.tr/tr/yayinlarimiz/dergi/detay/2019/8?type=6 [accessed 12 august 2019].

Işık, D. A., & Cerit, A. G. (2007). Yacht tourism education: a study on curriculums, 585–592

Kan, N. and Nas, S. (2014). Yacht type preference in yacht purchase decision : a case study through yacht owners at ic cesme. Denizcilik Fakültesi Dergisi, 6(2), 49–69.

Kuruüzüm, A, ve Atsan, N. (2001). Analitik hiyerarşi yöntemi ve işletmecilik alanındaki uygulamaları. Akdeniz İİBF Dergisi, (1), 83–105.

Maglić, L. (2019). Multi-Criterion Decision Model for Marina Location Selection in the County of Primorje and Gorski Kotar Primjena višekriterijske analize pri izboru lokacije za izgradnju marine u Primorsko-goranskoj županiji, (April). https://doi.org/10.17818/NM/2019/1.4

Ministry, Culture and Tourism (2007). Turkey tourism strategy prevention plan 2023, action plan 2007-2013.

Ministry of culture and tourism, https://yigm.ktb.gov.tr/tr-201145/yatistatistikleri.html [accessed 15 august 2019].

Ministry of Culture and Tourism, Incentive Law, No:2634, http://www.mevzuat.gov.tr/MevzuatMetin/1.5.2634.pdf [accessed 12 august 2019].

Saaty, T. L. (2003). Decision-making with the ahp : why is the principal eigenvector necessary. European Journal of Operational Research, 145, 85–91.

Sezer, İ. (2012). In view of the effects on touristic functions and marina tourism: Didim. Eastern geographical review, 103–124.

Yaralıoğlu, K. (2001). Performans Değerlendirmede Analitik Hiyerarşi Proses. Dokuz Eylül University, Journal of İİBF, 3(5), 129–142.

CISET - 2nd Cilicia International Symposium on Engineering and Technology
10-12 October, 2019, Mersin / TURKEY

EFFECTS OF SALT ON HUMAN HEALTH AND EVALUATİON OF ROCK SALT İN TERMS OF MEDİCAL GEOLOGY

Alican ÖZTÜRK*[1], Bilgehan Yabgu HORASAN[2]

[1]Konya Technical University, Faculty of Engineering and Natural Sciences, Geological Engineering Department, Selçuklu / Konya, Turkey alicanozturktr@gmail.com
[2]Selcuk University, Sarayonu Vocational High School, Environmental Protection Technologies, Sarayonu / Konya,Turkey, bilgehanyabgu@gmail.com

ABSTRACT
Salt, which is an indispensable part of our daily life, is very important in terms of food storage, protection, cooking and taste. In recent studies, excessive salt consumption causes health problems, while insufficient or less consumption has negative effects on the balance of the body. Speleotherapy, (cave treatment) a well-known but forgotten treatment plan for thousands of years, was recognized by German scientists during the Second World War and was remembered again. As a result of researches conducted on salt caves and quarries where the salt mine is extracted, it is understood that the treatment of diseases such as asthma, bronchitis, pharyngitis, and allergy can be treated with the formation of aerosols in the cave. These salt caves and areas used for extraction of salt will make more use of the salt to be used for alternative medical center purposes.

Keywords: *Salt, Salt Caves, Speleotherapy, Rock Salt, Medical Geology*

1. INTRODUCTION

Salt, which is the type of rock that can be eaten, can be used in many fields from pharmaceutical and soap production to melting ice-holding roads and softening water. The Romans, the Chinese, the Venetians, and many states in history imposed a tax on salt for wars. One of the oldest records of salt in history BC is a document about salt production and trade of seawater produced by Xian dynasty in 800 years. The Egyptians used salt in mummification and they used salt for keeping meat and fish fresh. In addition to being used as a sign of wealth in the Renaissance period in Europe, in some cultures, salt has been used treatment for insect bites and stings. Salt, which has an important place in ancient Turkish societies, is mentioned in the Manas epic, Kutadgu Bilig, Kadı Burhanettin divan, and Yunus Emre poems (Caglar, 2015) Sodium chloride, carbonate, baking soda, salt-formed foods, and many of the foods we have encountered in our daily lives, naturally contain sodium (Besler et. al.,2015; Tayfun et.al., 2015; Baysal, 2014). Although it varies according to the sources of mineral waters, they are said to contain 10-1.300 mg / L sodium (Paplović et. al., 2015). Mineral water is used in food preparation, cooking, increasing food durability and it is used for its flavoring feature. Due to its antiseptic and moisture-absorbing properties, salt prevents the growth of bacteria that cause food spoilage. Especially the use of salt is indispensable in the production of basic food products such as bacon, sausage, cheese, olives and pickled foods (pickled and canned) (Besler et. al.,2015; Tayfun et.al., 2015). Salt, which is thought to have an important place in human life, has positive and negative effects. It has been claimed in recent years that over-consumption of salt, which is used in many areas of our daily lives, may have adverse health effects (Ozturk and Agaoglu, 2018). In this study, the current studies on the effects of salt in our daily lives, the effects of salt in excess or deficiency, as well as therapeutic properties of salt have been reviewed.

2. SALT VARİETİES İN TURKEY

According to the Turkish Food Codex Salt Communiqué; Sea salt; Salts produced from sea water in accordance with the technique, Food industry salt; Processed salt or underground source salt used in the food industry, which is produced directly or not to the end consumer, produced with or without iodine, Lake salt; Salts produced in accordance with the technique of lake water, Large brine salt; Iodine-free processed salt or underground source salt, which is used for food preservation, especially in the production of canned goods, pickles, brine and similar products offered directly to the end consumer; Sea, lake and rock salts which are produced according to human consumption and whose main substance is sodium chloride, Rock salt; Salts produced in accordance with the technique from underground salt galleries, Table salt; The finely ground, iodine-enriched, refined or untreated processed salt, delivered directly to the end consumer, is the grinding salt at the table; Crystalline, iodine added processed salt or underground source salt, presented by the consumer to the end consumer for grinding at the table; It refers to the salts obtained in accordance with the technique from water which spontaneously emerges from the ground to the earth (Turkish Food Codex Salt Communiqué, 2013). Himalayan Salt, bamboo salt and other salts, which are not published in the official newspaper is consumed from the salt brought to our country (Ozturk and Agaoglu, 2018).

3. EFFECT OF SALT ON HEALTH

Sodium in Salt has many functions within the body. Sodium is a mineral that has important functions in the body organism such as acid-base balance, fluid balance, nerve stimulation, electrolyte, blood pressure regulation, normal novelties, etc. Consumption of more salt than the body and organism needs has been reported to be related to cardiovascular diseases, cancer, obesity, lung inflammation, kidney diseases, hypertension, osteoporosis, multiple sclerosis (MS), cataract with eye disease and different diseases (Besler et. al.,2015; Tayfun et.al., 2015). Although the idea that reducing salt consumption, lowering blood pressure and reducing the risk of cardiovascular disease is gaining weight, it has been said to have negative effects when salt consumption is reduced (Ozturk and Agaoglu, 2018). In studies comparing the relationship between daily salt consumption and cardiovascular diseases, it was reported that minimum and maximum risks occur with salt consumption of 3-5 g / day and <3 g / day, respectively (Smyth et., al., 2015; O'Donnell et., al., 2015). It is said that more than the necessary salt reduction in cardiac patients also poses a risk of death (Doukky, et., al., 2016; DiNicolantonio et., al., 2016). It is also said that chlorine, which is present in salt, has important functions in body functions (DiNicolantonio et., al., 2016).

3.1. Medical Geology

Throughout human history, the natural resources that humans have applied for basic necessities have been their geological surroundings. It is understood by mankind that the geological environment is not only the source of raw materials needed, but it also has the health purpose and treatment potential (Demir, 2009). It has been said that while the geological environment sometimes provides benefits for humanity, it sometimes provides disadvantages (Demir, 2009). In the Chinese medical texts of the 3rd century BC, some elements (Pb, Zn, Cu, Au, Fe, Sb) are mentioned to cause toxic effects for human beings (Demir, 2009). It was understood that Egyptian physicians used sludge taken from the Nile river for the treatment of some diseases (Dede, 2011), salt types were used in some stages of mummification processes in ancient Egypt (Thesis, 2000), and it was understood that salt, calcium and potassium nitrate found from natural sources were among the minerals that Sumerian physicians used most when making medicines (Dede, 2000).

Medical geology is a multidisciplinary science examining the positive and negative effects of the environment on human health, animals and plants and the geographical distribution of this effect (Atabey, 2005).

3.2. Speleotherapy

Speleotherapy is generally known as cave therapy.

The origin of the word comes from the Greek meaning "spelo; cave". The main prophylaxis of bronchial asthma is said to be Speleotherapy treatment method (Khalilov, 2008). This method has been known in the world for more than two thousand years and it was used in ancient Rome and Greece, and in the beginning of the twentieth century, during the Second World War, the method of speleotherapy was brought to the agenda again with the studies of German scientists (Khalilov, et., al., 2008). Some sterile trace gases in the cave environment give bronchial expander, mucolytic, hyposensitive properties. In this context, it is accepted that asthma and salt caves have a positive effect on the treatment of respiratory diseases (Aydilek and Bozkanat, 1997).

3.3. Treatment Methods with Rock Salt Caves

According to the studies carried out in the world in recent years; It is said that 4-10% of the population is suffering from upper respiratory diseases and this rate is 10-15% in children (Dede, 2011; Thesis, 2000; Atabey, 2005; Khalilov, et., al., 2008; Aydilek and Bozkanat, 1997). Diseases observed in the respiratory tract occur due to changes in weather conditions, infection-causing factors, cigarette smoke, increased stress and allergens. At the end of these reactions, bronchitis shrinks rapidly, preventing air from passing and making breathing difficult. In addition to bronchitis spasm, swelling develops on the walls of bronchitis and frequent phlegm increases (Aydilek and Bozkanat, 1997). Speleotherapy is a supportive treatment with cave therapy in addition to drug treatment in bronchial asthma diseases. (Aydilek and Bozkanat, 1997). There are a few underground mine operation used to remove salt caves and salt in Turkey. Kırşehir, Tepesidelik rock salt cave, Çankırı rock salt cave, Gülşehir (Nevşehir), Tuzköy Rock salt cave, (Aydilek and Bozkanat, 1997), Iğdır Tuzluca and Siirt are used to extract salt mines (Yeşilova and Yeşilova, 2019). There are salt caves for clinical treatment in different parts of the world. These are Soligorsk in Belarus, Nakhchivan in Azerbaijan, Magdeburg in Germany, Chon-Salt in Kyrgyzstan, Slsbad-Salseman in Austria and Solotvine Artemovsk in Ukraine (Aydilek and Bozkanat, 1997).

After treatment in patients with 70% bronchial disease in the Rock Salt caves, patients do not have disease for 6 months to 3 years (Aydilek and Bozkanat, 1997). In natural salt materials, aerosols in the cave form microclimate and thanks to this microclimate the environment becomes stable. Chronic bronchitis, powder bronchitis, allergic patients, positive improvements have been seen after treatment. Speleotherapy reduced the effect of infection-inflammation processes on the respiratory organs. In the treatment of salt caves, the treatment process should continue for 20-30 days, at the beginning of the treatment process is said to be appropriate for patients to stay for 2-3 hours. After the adaptation process, the waiting time for treatment in rock salt caves was said to be appropriate to apply 12 hours (Aydilek and Bozkanat, 1997). Elements such as iodine, cobalt, manganese, iron, zinc, copper, selenium, which are in the salt content, have positive sides for human health (Aydilek and Bozkanat, 1997). Diseases that will be adversely affected by this treatment method; lung emphysema, diffuse pneumosclerosis, severe bronchial asthma due to hormones, third-degree breathing difficulty, pulmonary functions, tuberculosis, second-third-degree cardiovascular disease, bronchiectasis, is said to be unappropriate for such diseases (Aydilek and Bozkanat, 1997).

4. CONCLUSION

Salt, which has a very important place in human history in the period from past to present, is understood to be important in health as well as social and economic life. Salt, which is vital for the body, is understood to play a crucial role in storing, cooking and flavoring nutrients. It is said that salt in excess consumption causes many diseases from cardiovascular patients to cancer, and in less consumption it can cause blood pressure to fall and vascular diseases (Ozturk and Agaoglu, 2018). On the other hand, it is said that the treatment of asthma, bronchitis, pharyngitis and allergy can be done in the quarries and the naturally occurring salt caves (Dede, 2011; Thesis, 2000; Atabey, 2005; Khalilov, et., al., 2008; Aydilek and Bozkanat, 1997; Yeşilova and Yeşilova, 2019). In Turkey and in the world, it is widely seen that salt has many uses and if it is not consumed enough, it can negatively affect the health of the body, underground mines in operation where the same salt is removed, while the natural salt cave may also be a support in the treatment of diseases related to especially the respiratory tract. We believe that salt consumption and its usage is important for a healthy and quality life, similar to the information given in case of excessive or inadequate salt consumption, treatments should be done in salt caves with Speleotherapy, encouraging investors to use such places will be very beneficial.

REFERENCES

Atabey, E.,(2005), Medical Geology, Chamber of Geological Engineers Publications, 88, 2005.

Aydilek, R., and Bozkanat, E., (1997), "Altarnative treatments in bronchial asthma", Journal of Medical Sciences, 17, 362-364.

Baysal, A., 2014,Water and minerals, Nutrition 15th Edition, Hatiboğlu Publications; Ankara, p.114-116.

Besler, H.T., Rakicioglu, N., Ayaz A., Demirel, Z., Ozel, H., Samur, G., (2015), Salt consumption and health Specific Food and Nutrition Guide Turkey, Hacettepe University, Faculty of Health Sciences, Department of Nutrition and Dietetics.1. Printing. Ankara: Ladder Advertising Promotion; p.55-7.

Çağlar, S., 2015, https://dunyalilar.org/humanity-history-degistiren-bir-baharat-tuz.html/ [Accessed 29.07.2019].

Dede Z., (2011), Evaluation of Çankırı Salt Caves in terms of Medical Geology, Niğde University, Institute of Science and Technology, Department of Geological Engineering, 81sf, 2011.

Demir, B.M., (2009), "Therapeutic Geology", Journal of Geological Engineers, 33, 63-70.

DiNicolantonio, J,J., Chatterjee, S., O'Keefe, J,H.,(2016), "Dietary salt restriction in heart failure: where is the evidence?", Prog Cardiovasc Dis; 58 (4): 401-6.

Doukky, R., Avery, E., Mangla, A., Collado, F,M., Ibrahim, Z., Poulin, M,F., (2016), "Impact of dietary sodium restriction on heart failure outcomes", JACC Heart Fail; 4 (1): 24-35.

Khalilov, H., Yusufov, Z. E., (2008), Proc., Akhundov, Azerbaijan and Turkey salt caves and effects on health, The International Symposium on Medical Geology Participatory Book, Pg; 125-128.

O'Donnell, M., Mente, A., Yusuf, S., (2015), "Sodium in-take and cardiovascular health" Circ Res; 116 (6): 1046-57.

Paplović, L,B., Popović, M.B., Bijelović, S.V., Velicki, R.S., Torović, L,D., (2015), "Salt content in ready-to-eat food and bottled spring and mineral water re-tailed in novi sad", Srp Arh Celok Lek, 143 (5-6): 362-8.

R. Ozturk, Agaoglu M., G., (2018), "Salt Consumption and Health", Turkey Clinical Health Sci J; 3 (1): 57-65.

Smyth, A., O'Donnell, M., Mente, A., Yusuf, S., (2015), "Di-etary sodium and cardiovascular disease" Curr Hypertens Rep; 17 (6): 559.

Tayfur, M., Besler, H, T., Kiziltan, G., Yildiz, E., Ozturk, B., Turker, P, F., (2016), "Food and nutrients should be reduced consumption" T. C. Ministry of Health 1st Edition Turkey Nutrition Guide Ankara; p.68-71.

Thesis Z., (2000), History of Chemistry in Science and Industry, Nobel Publication Distribution, Ankara, 2000.

Turkish Food Codex Salt Communiqué, (2013), Official Gazette (16. 08.2013, No: 28737), Ankara Prime Ministry Printing House, p.48.

Yeşilova P., G., Yeşilova Ç., (2019), "Use of Salt Mines (Rock Salt) in Health Sector and Tourism Purposes; Sürkit Salt Plant (Tuzluca, Iğdır) and Examples from the World", Yüzüncü Yıl University Journal of the Institute of Science and Technology, Vol 24, No 1, 56-63.

CISET - 2nd Cilicia International Symposium on Engineering and Technology
10-12 October, 2019, Mersin / TURKEY

RADAR CROSS SECTION SIMULATION AND ANALYSIS OF A SMALL DRONE MODEL BY THE HELP OF PREDICS TOOL

Caner Özdemir [*1]

[1] Mersin University, Engineering Faculty, Department of Electrical-Electronics Engineering, Mersin, Turkey, cozdemir@mersin.edu.tr

ABSTRACT
In this paper, we examine the radar cross section (RCS) merits of a small drone model by simulating and assessing the RCS simulation of it by the help of reliable simulator tool of Predics. The analysis and assessment of RCS merit of the Drone model is explored via series of angle-diverse and frequency-diverse numerical RCS simulations. Also, RCS maps of the drone model is also constructed for few frequencies of interest to quickly observe the high RCS look-angles. The RCS simulation results suggest that the RCS of this drone model can reach to 2 m^2 for S-band microwave frequencies; therefore, it can easily be visible for a nominal radar at a reasonably far distance for the radar. It is also concluded from the RCS results that the RCS variation do not change dramatically for both elevation and horizontal look-angles.

Keywords: Radar Cross Section, Drone RCS calculation, Radar Visibility, RCS simulation

[*] Corresponding Author

1. INTRODUCTION

Recently, the number of different drone types that are being used in many usages have been expansively amplified due to rising demand from both military and civil institutions (Vinogradov, *et al.*, 2018). The use of drones for leisure and specialized usages may cause personal and government concerns regarding the safety of people. Furthermore, the offensive use of drones as terrorist attacks has becoming a growing concern in parallel to the increasing number of drones. So, it becomes very vital to detect and also make them useless before succeeding their missions to circumvent possible fatalities and injuries.

Many techniques have been used for the detection of drones. These include visual techniques (Rozantsev, *et al.*, 2017), acoustic techniques (Kim, *et al.*, 2017) and electromagnetic (i.e, radar) techniques (Hoffmann, *et al.*, 2016). Among them, it is no doubt that radar-based methods offer the most reliable detection performance compared to other techniques. While radar hardware can be used to detect the drones, the question becomes if the drones can be sensed at a fairly safe distance from the radar based on their radar cross section (RCS) values. Therefore, there is a quite much of interest in knowing the RCS values of drones to assess their visibility in a nominal radar.

In this work, we offer a study for calculating and examining the RCS of a drone model that is very common for personal leisure usages. The RCS calculation is performed by the recently developed RCS simulation and analysis software called Predics (Özdemir *et al*, 2014a; Özdemir *et al*, 2014b).

2. RCS SIMULATION OF THE DRONE

2.1. The Drone model

The drone model used in Predics simulation is given in Fig.1. The perspective view of the drone model is given Fig.1(a). The bottom view of the model is as viewed in Fig. 1(b). The side view of the drone model is given in Fig. 1(c). The dimensions of the model are 378 mm, 382 mm, and 165 mm in x-axis, y-axis and z-axis (height), respectively. The model's material is taken as to be perfect electric conductor (PEC).

2.2. RCS simulation by the help of Predics

RCS simulation of the drone model has been carried out by the Predics simulator (Özdemir *et al*, 2014a; Özdemir *et al*, 2014b). Predics is a fast and effective simulation tool for the reliable calculation of RCS from electrically large and complex-shaped targets at 1 GHz and beyond frequencies. The RCS simulation screen of the drone model can be observed in Fig. 2.

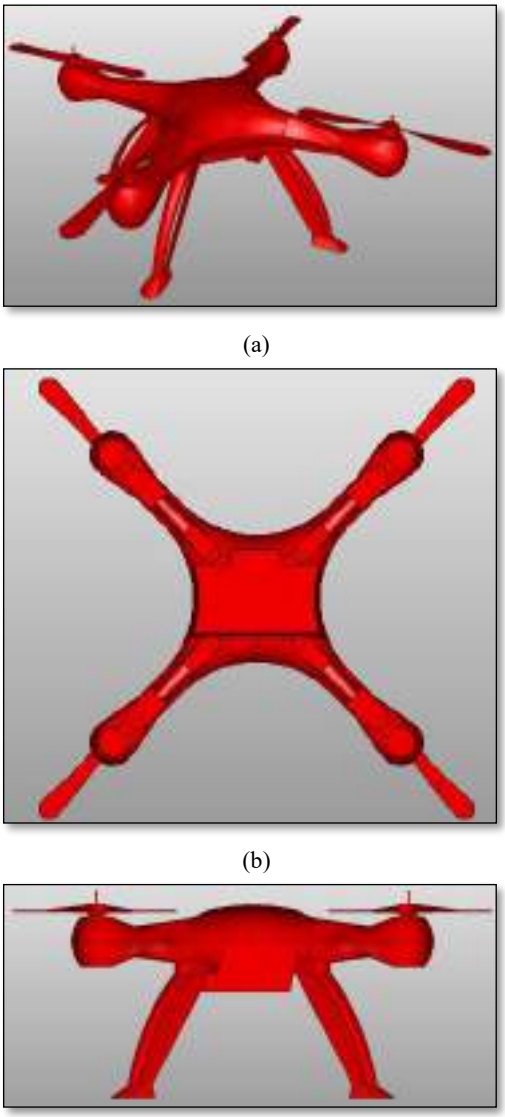

(a) (b) (c)

Fig. 1. Small drone model: (a) Perspective view, (b) Bottom view, and (c) side view

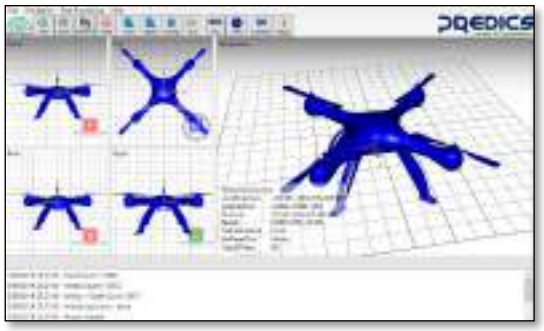

Fig. 2. Predics simulation screen for the drone model

To depict the RCS characteristics of the drone model, various simulations were performed. Firstly, angular RCS variation for a fixed frequency was done.

Then, angular RCS-map plot simulation was accomplished to see the RCS variation of the model with respect to look-angles in a single snap-shot. Furthermore, the frequency RCS variation of the drone model for some fixed look-angles were also done.

2.2.1. RCS variation over angles

In the first simulation, horizontal monostatic RCS variation for a static frequency of 10 GHz has been explored. The detailed simulation parameters are given in Fig. 3.

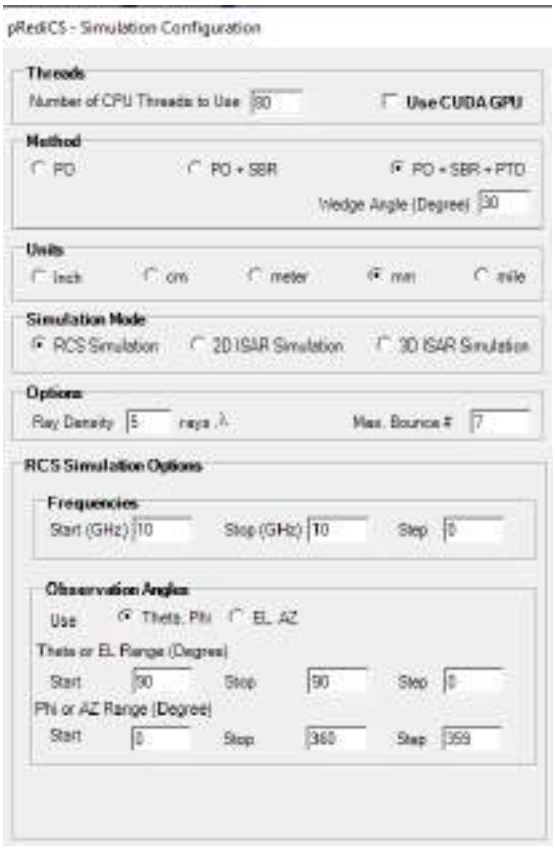

Fig. 3. Simulation parameters for the horizontal angular RCS simulation

The resultant RCS variation over horizontal angles are presented for different polarization excitations in Fig. 4. In Fig 4(a), RCS variation over horizontal angles at a fixed elevation angle of 0° and the fixed frequency of 10 GHz are given for vertical-vertical (VV) [drawn as blue] polarization. As clear from Fig. 4(a), RCS can be as much as 2.83 dBsm (i.e., 1.9 m2) for the look angle of 17° and 2.23 dBsm (i.e., 1.6 m2) for the look angle of 343°. In Fig 4(b), RCS variation over horizontal angles at a fixed elevation angle of 0° and the fixed frequency of 10 GHz are given for horizontal-horizontal (HH) [drawn as erd] polarization. As seen from Fig. 4(b), RCS can be as much as -1 dBsm (i.e., 0.78 m2) for the look angle of 17° and -1.3dBsm (i.e., 0.73 m2) for the look angle of 343°.

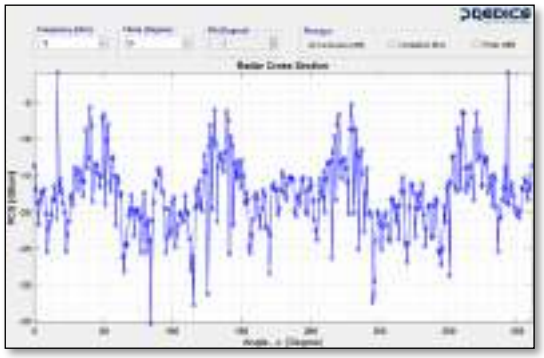

(a)

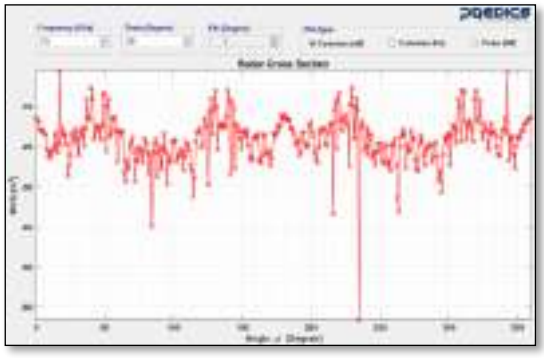

(b)

Fig. 4. Horizontal angles RCS simulation results: (a) VV, and (b) HH

2.2.2. Angular RCS MAPs of the drone

As the second simulation, two-dimensional (2D) angle simulation over horizontal and elevation angles were carried out to map the monostatic RCS variation over angles for a static frequency of 8 GHz in a single view. The detailed simulation parameters are given in Fig. 5.

The resultants 2D RCS maps for the VV and HH polarizations are plotted in Fig. 6(a) and Fig. 6(b), respectively. In can be observed from the figure that the RCS value is fluctuating over angles; but do not offer a superior peak or hollow as a whole. This is kind of expected since the geometry of the drone is somewhat a spherical-like shape.

Fig. 5. Simulation parameters for 2D angular RCS-map simulation

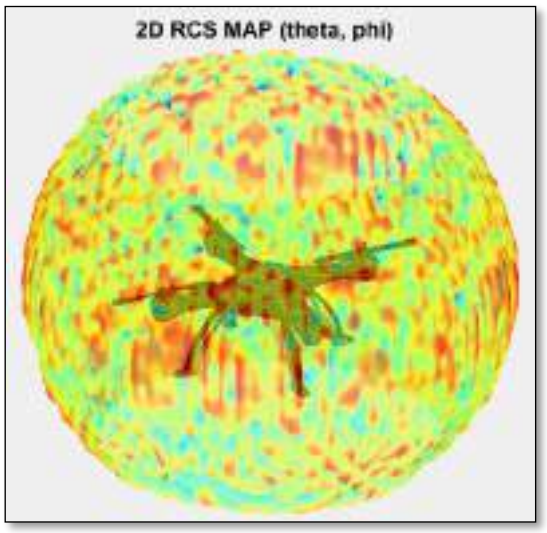

(a)

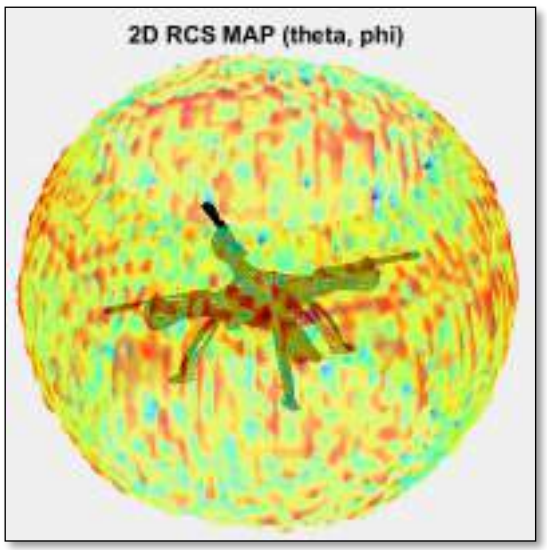

(b)

Fig. 6. 2D RCS maps at 8 GHz for (a) VV and (b) HH polarizations

2.2.2. RCS variation over frequencies

As the last study, monostatic RCS variation over frequencies for the look angle of 0° elevation and 0° & 90° horizontal angles has been tested. The detailed parameters for this particular simulation are given in Fig. 7. As obvious from Fig.7, the frequency is altered from 1 GHz to 10 GHz for a total of 100 distinct frequency values.

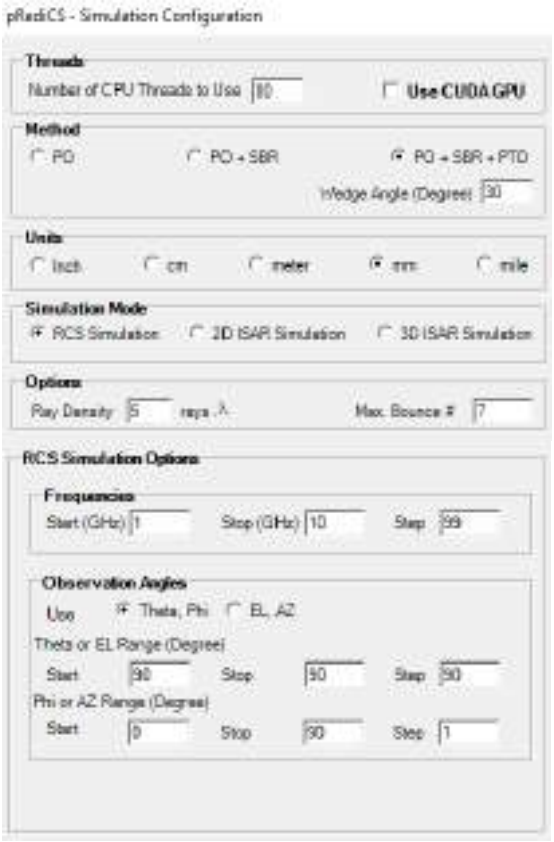

Fig. 7. Simulation parameters for the RCS simulation of frequency variation

In Fig. 8(a) and 8(b), RCS variation over frequencies for the fixed elevation angle of 0° and the fixed horizontal angles of 0° and 90° are presented, respectively. In Fig. 8(a), the monostatic RCS frequency variation of the drone model and fixed elevation angle of 0° and the fixed horizontal angle of 0° is drawn. This plot is for the VV polarization [drawn as blue] and HH polarization [drawn as red]. In an analogous manner, in Fig. 8(b), the similar RCS plots are supplied for the horizontal angle of 90°. As seen from both graphs, the RCS values are fluctuating with respect to frequency.

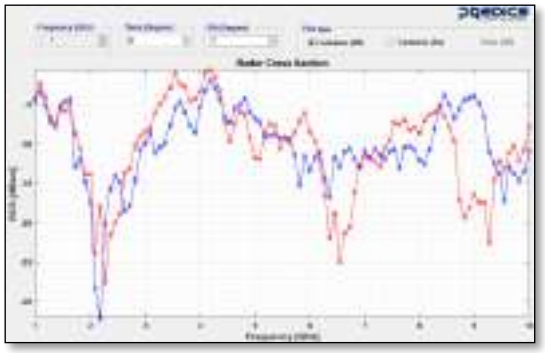

(a)

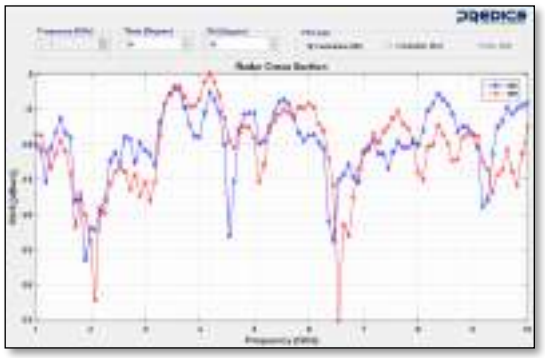

(b)

Fig. 8. RCS frequency variation for the fixed elevation angle of 0° and the fixed horizontal angles of (a) 0°, and (b) 90°: VV-polarization case [blue], (b) HH-polarization case [red]

3. CONCLUSION

In this paper, we have supplied a numerical analysis of RCS from a small drone model to evaluate its visibility feature in a nominal radar. The reliable high-frequency RCS simulator code; Predics has been exploited to perform the RCS simulation and the resultant analyses. Using the Predics tool, both the angle variation and the frequency variation monostatic RCS simulations of the drone model have been carried out. Results suggested that RCS values can reach to 2 m^2 for microwave frequencies. Therefore, this model can easily be sensed and detected by a generic radar.

ACKNOWLEDGEMENTS

This work was supported by Mersin University Scientific Research Unit under Project No. 2015-TP3-1160

REFERENCES

Hoffmann, F., Ritchie, M., Fioranelli, F., Charlish, A. and Griffiths, H. (2016) "Micro-Doppler based detection and tracking of UAVs with multistatic radar," *IEEE Radar Conference*, 1–6.

Kim, J., Park, C., Ahn, J., Ko, Y., Park, J., and Gallagher, J. C. (2017) "Real-time UAV sound detection and analysis system," *IEEE Sensors Applications Symposium*, 1–5.

Rozantsev, A., Sinha, S., Dey, D., and Fua, P. (2017) "Flight Dynamics based Recovery of a UAV Trajectory using Ground Cameras," *CVPR17*, 2482-2491.

Özdemir, C., Yılmaz, B., and Kırık, Ö. (2014a), "pRediCS: A new GO-PO based ray launching simulator for the calculation of electromagnetic scattering and RCS from electrically large and complex structures," *Turkish Journal of Electrical Engineering & Computer Sciences,* Vol. 22, 1255 – 1269

Özdemir, C., Yılmaz, B., Kırık, Ö., Sütcüoğlu, Ö. (2014b), "A Fast and Efficient RCS Calculation and ISAR Image Formation Tool: pRediCS", *10th European Conference on Synthetic Aperture Radar* (EUSAR 2014), Berlin.

Vinogradov, E, . Kovalev, D.A. and Pollin, S. (2018) "Simulation and Detection Performance Evaluation of a UAV-mounted Passive Radar", *The 29th Annual IEEE International Symposium on Personal, Indoor and Mobile Radio Communications (IEEE PIMRC 2018),* Bologna, 1185-1191.

CURVATURE OF THE TRİAXİAL ELLİPSOİD

Sebahattin Bektas

Ondokuz Mayis University, Faculty of Engineering, Geomatics Engineering, Samsun, Turkey, e-mail: sbektas@omu.edu.tr

Abstract
This study aims to show how to obtain the curvature of the ellipsoid depending on azimuth angle. The curvature topic is quite popular at an interdisciplinary level. It can be to the friends of geometry, geodesy, satellite orbits in space, in studying all sorts of elliptical motions (e.g., planetary motions), curvature of surfaces and concerning eye-related radio-therapy treatment, for example the anterior surface of the cornea is often represented as ellipsoidal in form. On the calculation of the curvature, there is a famous Euler formula for rotating ellipsoid that everyone knows. I wonder how can a formula for a triaxial ellipsoid? so we started to work. And we finally found the formula for the triaxial ellipsoid.

Keywords: *Triaxial Ellipsoid, Normal Section Curve, Principal Curvatures, Gaussian Curvature, Mean Curvature -ellipsoid-and-a-plane*

The parameter lines *(u,v)* and geodetic (planetographic) coordinates (Φ, λ) are orthogonal on rotational ellipsoid but are not orthogonal on triaxial ellipsoid.

In this parametrization, the coefficients of the first fundamental form are

$E=[b^2\cos^2 u + a^2\sin^2 u]\sin^2 v$ (5)

$F=(b^2-a^2)\cos u \sin u \cos v \sin v$ (6)

$G=[a^2\cos^2 u + b^2\sin^2 u]\cos^2 v + c^2\sin^2 v$ (7)

I. fundamental form

$$\mathrm{I} = E.du^2 + 2.F.du.dv + G.dv^2 \quad (8)$$

and of the second fundamental form are

$$e = \frac{a.b.c.\sin^2 v}{\sqrt{(a.b.\cos v)^2 + c^2(b^2\cos^2 u + a^2\sin^2 u)\sin^2 v}} \quad (9)$$

$f = 0$ (10)

$$g = \frac{a.b.c}{\sqrt{(a.b.\cos v)^2 + c^2(b^2\cos^2 u + a^2\sin^2 u)\sin^2 v}} \quad (11)$$

II. fundamental form

$$\mathrm{II} = e.du^2 + 2.f.du.dv + g.dv^2 \quad (12)$$

Also in this parametrization, the Gaussian curvature is

$$K = \left[\frac{a.b.c}{(a.b.\cos v)^2 + c^2(b^2\cos^2 u + a^2\sin^2 u)\sin^2 v}\right]^2 \quad (13)$$

and the Mean curvature is

$$H = \frac{a.b.c.[3(a^2+b^2) + 2c^2 + (a^2+b^2-2c^2)\cos 2v - 2(a^2-b^2)\cos 2u.\sin^2 v]}{8[(a^2b^2\cos^2 v + c^2(b^2\cos^2 u + a^2\sin^2 u)\sin^2 v]^{3/2}} \quad (14)$$

The Gaussian curvature and Mean curvature can be calculated from Cartesian coordinates given below formulas Lipschutz 1969, Zhang and Feng 2006

$$K = \frac{1}{\left(\mathrm{a.b.c.}\left(\frac{\mathrm{x}^2}{\mathrm{a}^4} + \frac{\mathrm{y}^2}{\mathrm{b}^4} + \frac{\mathrm{z}^2}{\mathrm{c}^4}\right)\right)^2} \quad (15)$$

$$H = \frac{\left|x^2 + y^2 + z^2 - a^2 - b^2 - c^2\right|}{2(a.b.c)^2\left(\frac{\mathrm{x}^2}{\mathrm{a}^4} + \frac{\mathrm{y}^2}{\mathrm{b}^4} + \frac{\mathrm{z}^2}{\mathrm{c}^4}\right)^{3/2}} \quad (16)$$

We will compute H and K in terms of the first and the second fundamental form.

$$K = \frac{e.g - f^2}{E.G - F^2} = \frac{\mathrm{II}}{\mathrm{I}} \quad (17)$$

$$H = \frac{G.e - 2F.f + E.g}{2(E.G - F^2)} \quad (18)$$

2.2 Principal Curvatures, Gaussian Curvature, Mean Curvature

We will now study how the normal curvature at a point varies when a unit tangent vector varies. In general, we will see that the normal curvature has a minimum value κ_1 and a maximum value κ_2,. This was shown by Euler in 1760. The quantity

$K = \kappa_1.\kappa_2$ called the Gaussian curvature (19)

and the quantity

$H = (\kappa_1 + \kappa_2)/2$ called the mean curvature, (20)

play a very important role in the theory of surfaces.

$$R_1 = \frac{1}{\kappa_1} = \frac{1}{H - \sqrt{H^2 - K}}$$

Maximum radii of curvature (21)

$$R_2 = \frac{1}{\kappa_2} = \frac{1}{H + \sqrt{H^2 - K}}$$

Minimum radii of curvature (22)

The formula for the radius of curvature at arbitrary azimuth points up that the fact that the fundamental mathematical quantity is the inverse of these radii, which are simply called curvatures

2.3 Normal section of a surface

Let us construct a normal to a surface at a point P_o. Then the curve that is described on the surface by any plane passing through the normal (i.e. containing the normal) is called a **normal section** of the surface (Fig.1). In other words a normal section is a plane section formed by a plane containing a normal to the surface Lipschutz (1969),James 1992,Aleksandrov et al 1999.

2.4 Curvature of a surface at a point

Let us construct a unit normal $\overline{n}$ and a tangent plane at given point P_o on surface and consider the curves that are formed on the surface by planes passing through P_o containing the normal i.e. the various normal sections passing through point P_o. Each normal section passing through P_o possesses a particular curvature at point P_o. We can specify a particular normal section by use of a polar coordinate system constructed on the tangent plane, origin at point P_o, polar axis as some arbitrarily chosen initial ray in the tangent plane, and an angle α measured clockwise from the polar axis to the plane of the normal section (Fig.2). The curvature at point P_o in direction α is thus given as the function κ_n (α). For each value of α there is a curvature associated with that particular normal section. This curvature κ_n (α) is called the **normal curvature** of the surface at point P_o in the direction α.

Then the normal curvature at point P_o is given by

$$\kappa_n(du, dv) = \frac{e.du^2 + 2.f.du.dv + g.dv^2}{E.du^2 + 2.F.du.dv + G.dv^2} \quad (23)$$

where E, F, G, e, f, g are the fundamental coefficients of the first and second order.

Formula (39) above can be re-written in the following way

$$\kappa_n\left(\frac{dv}{du}\right) = \frac{e + 2.f.\left(\frac{dv}{du}\right) + g.\left(\frac{dv}{du}\right)^2}{E + 2.F.\left(\frac{dv}{du}\right) + G.\left(\frac{dv}{du}\right)^2} \quad (24)$$

simply by dividing the numerator and denominator by du^2. In this form it is obvious that κ_n is a function of the ratio dv/du. If we let $\cot \alpha = dv / du$ then (24) becomes

$$\kappa_n(\alpha) = \frac{e + 2.f.\cot\alpha + g.\cot^2\alpha}{E + 2.F.\cot\alpha + G.\cot^2\alpha} \quad (25)$$

where

$$\cot\alpha = \frac{E + F\tan\theta}{W\tan\theta} \quad (26)$$

A surface may be curved in many ways and consequently one might think that the dependence of the curvature κ on the angle α might be arbitrary. In fact this is not so. The following theorem is due to Euler.

2.5 Euler's theorem

Let θ be the angle, in the tangent plane, measured clockwise from the direction of minimum curvature κ_1 . Then the normal curvature $\kappa_n(\theta)$ in direction θ is given by

$$\kappa_n(\theta) = \kappa_1 \cos^2\theta + \kappa_2 \sin^2\theta = \kappa_1 + (\kappa_2 - \kappa_1)\cos^2\theta \quad (27)$$

$\kappa_n(\theta)$ curvature at azimuth θ

For spheroid (rotational ellipsoid):

$$N = R_1 = \frac{1}{\kappa_1}$$ Radius of Curvature in Prime Vertical (Max. radii of curvature) (28)

$$M = R_2 = \frac{1}{\kappa_2}$$ Radius of Curvature in Meridian (Min. radii of curvature) (29)

N, M can be easily calculated the latitude of point P_o as below

$N = c_p / V$, $M = c_p / V^3$, $c_p = a^2/c$, $V^2 = 1 + e_x^2 \cos^2\Phi_o$

$$\kappa_n(\theta) = \frac{N.\cos^2\theta + M.\sin^2\theta}{N.M} \quad (30)$$

same as Eq.26

$$\cot\alpha = \sqrt{\frac{E}{G}}\cot\theta \qquad (31)$$

2.6 Computing the principal directions and curvatures at a point P_o

Given a point P_o on a surface ***S***, the directions at which the normal curvature at P_o attains its minimum and maximum values can be computed as follows. Let the normal curvature at P_o be given as

$$\kappa_n(\lambda) = \frac{e + 2.f.\lambda + g.\lambda^2}{E + 2.F.\lambda + G.\lambda^2} \qquad (32)$$

where $\lambda = dv/du$. We wish to find those values of λ at which the function $\kappa_n(\lambda)$ has its minimum and maximum values. We are thus faced with a problem of finding the maxima and minima of a function. A necessary condition for the function $\kappa_n(\lambda)$ to have a maxima or minima at a point is that at that point $d\kappa_n(\lambda)/d\lambda = 0$. Using the usual formula for computing the derivative of a quotient we obtain

The directions corresponding to the minimum and maximum values of curvature are called the **principal directions** of the surface. The values κ_1 and κ_2 are called the **principal curvatures** of the surface James 1992,Aleksandrov et al 1999.

$$(E + 2F\lambda + G\lambda^2)(f + g\lambda) - (e + 2f\lambda + g\lambda^2)(F + G\lambda) = 0 \qquad (33)$$

Upon expansion f=0 and rearrangement (33) becomes

$$(F\,g)\lambda^2 + (E\,g - G\,e)\lambda - F\,e = 0 \qquad (34)$$

One can then solve (34) obtaining the two principal directions λ_1 and λ_2. One can then substitute the two values λ_1 and λ_2 into (32) to obtain the principal curvatures κ_1 and κ_2 . The principal directions

$$r_{max} = \arctan(\lambda_1) \qquad (35)$$

$$r_{min} = \arctan(\lambda_2) \qquad (36)$$

2.7 The Curvature of the Ellipsoid With Cartesian Coordinates

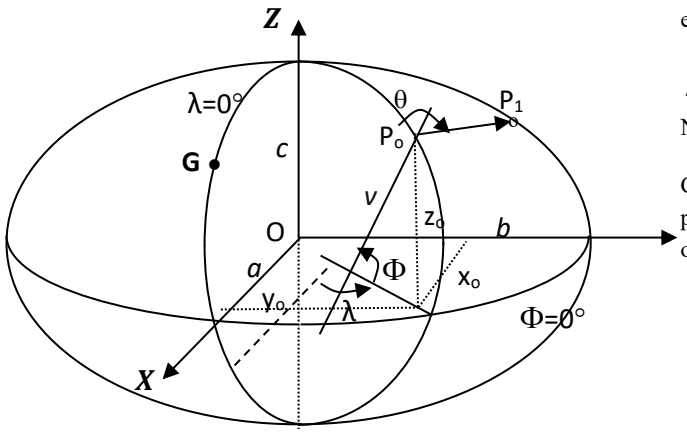

Figure-2 (X,Y,Z) Cartesian and (Φ, λ, h) Geodetic coordinates on Triaxial ellipsoid

First, we need to find the azimuth angle between the two points known as the Cartesian coordinates. Let's assume that θ is between azimuth angle of P_o and P_1 points. For this we need the P_o geodetic coordinates (Φ,λ). We may obtain the P_o geodetic coordinates (Φ,λ) from its Cartesian coordinates (x_o,y_o,z_o). Formulas related the geodetic and Cartesian coordinates conversion on a triaxial ellipsoid were expressed on Feltens (2009), Ligas (2012) and Bektas (2014). For detailed information on this subject please refer to Bektas (2014). The following link can be used for the conversion of Cartesian coordinates to geodetic coordinates on triaxial ellipsoid (URL-1).

$\Delta x = x_1 - x_O$ $\quad$ $\Delta y = y_1 - y_O$ $\quad$ $\Delta z = z_1 - z_O$

The azimuth angle of (P_o-P_1) from Cartesian coordinates. Moritz,1980

$$\theta = \mathbf{(P_o\text{-}P_1)} = \arctan\left(\frac{-\Delta x\sin\lambda + \Delta y\cos\lambda}{-\Delta x\sin\Phi\cos\lambda - \Delta y\sin\lambda\sin\Phi + \Delta z\cos\Phi}\right) \qquad (37)$$

P_o geodetic coordinates (Φ,λ) calculated from its (x_o,y_o,z_o) Cartesian coordinates (URL-1).

In order to calculation for the curvature, we need to add the reduction of the direction of r_{min} to the angle θ

Let's assume that r is the reduction of the direction of minimum curvature r_{min}

$$r = \arctan\left(\frac{W\tan(r_{min})}{E + F\tan(r_{min})}\right) \qquad (38)$$

For spheroid r_{min} and r becomes zero

And we give a new formula for the curvature calculation depending on the θ angle of the azimuth on the triaxial ellipsoid

$$\kappa_n(\theta) = \kappa_1 + (\kappa_2 - \kappa_1)\cos^2(\theta - r)$$

New Formula (39)

Curvature calculation can also be made as follows: First a plane's equation is determined which contains P_o surface of normal and passes P_1 point. And then we find elliptical

equation the intersection of the plane and the ellipsoid Grey 1997, Klein 2012, Ferguson 1979, URL-2. The curvature can be calculated at point P_o on the elliptical equation.

3. Conclusion

This study aims to show how to obtain the curvature of the ellipsoid depending on azimuth angle. We have developed an algorithm to obtain the curvature of the ellipsoid depending on azimuth angle. The efficiency of the new approaches is demonstrated through a numerical example. The presented algorithm can be applied easily for spheroid, sphere and also other quadratic surface, such as paraboloid and hyperboloid. Today, backward and forward problem between the two points on the triaxial ellipsoid with geodetic coordinates could not be a clear solution. Our future work will be on this unsolvable problem. I hope, the result of this study will contribute to the solution of the above problem.

4. Numerical Example

Find the curvature of normal section curve at P_o point which contains P_o surface of normal and passes P_1 point on a triaxial ellipsoid

θ Angle is a azimuth angle P_o-P_1 direction and Cartesian coordinates of P_o and P_1 point are given below

$$\frac{x^2}{25}+\frac{y^2}{16}+\frac{z^2}{9}-1=0$$ (Ellipsoid equation)

(a= 5, b= 4, c= 3) semi-axis

Cartesian coordinates (*x,y,z*)

P_o(3.000 2.500 1.4981) P_1(2.6189 2.4125 1.8047)

Geodetic coordinates (URL-1)

Φ_o = 40.194814370 º λ_o = 52.47573738º h_o = 0

u, v surface parameters on P_o point Eq.(4)

u = 46.1691393 *v* = 60.0413669

E, F, G, e, f, g are the Fundamental Coefficients of the First and Second Order evaluated at P point. Eqs.(5-12)
E= 15.52562500 F= -1.94530956 G= 11.82202800

e=2.91030887 f= 0 g= 3.87718085

Gaussian Curvature, Mean Curvature

From fundamental coefficients of the first and second order.

K- Gauss= 0.06277139

H-Mean Curve= 0.26313232 (Eqs.17-18)

Main radii of curvatures

$$R_1=\frac{1}{\kappa_1}=\frac{1}{H-\sqrt{H^2-K}}$$ =5.4730575

maximum radii of curvature (Eq.21)

$$R_2=\frac{1}{\kappa_2}=\frac{1}{H+\sqrt{H^2-K}}$$ = 2.9107724

minimum radii of curvature Eq.(22)

Principal Curvatures
κ_1 = 0.182713 minimum curvature

κ_2 = 0.343551 maximum curvature

Principal directions Eq.(34)

$-7.54231697\,\lambda^2 + 25.7899\,\lambda + 5.66145 = 0$

λ_1 = 3.62635252

λ_2 = -0.20699173

r_{max} =arc tan(λ_1) = 74.583317 º

r_{min} =arc tan(λ_2)= -11.694599 º

Azimuth angle (P_o-P_1) from Eq.(37)
θ = **(P_o-P_1)** = 30.136633 º

$$r=\arctan\left(\frac{W\tan(r_{\min})}{E+F\tan(r_{\min})}\right)$$ ➔

r = –9.88360428º

θ - r =30.136633º – (-9.88360428º) = 40.02023728º

and curvature

$$\kappa_n(\theta)=\kappa_1+(\kappa_2-\kappa_1)\cos^2(\theta-r)$$ = 0.277041

Control

Equation of plane which contains P_o surface of normal and passes P_1 point

$0.3125\,x - 0.50134\,y + 0.245316\,z - 0.051655 = 0$

Intersection ellipse's equation URL- 2

$$\frac{x^2}{\eta^2}+\frac{y^2}{\xi^2}=1 \quad \Longrightarrow \quad y=\xi\sqrt{1-\frac{x^2}{\eta^2}}$$

$\eta = 4.65998$ $\xi = 3.11078$

Transformed coordinates of P_o point in intersection's plane

$x_o = -3.7331$ $y_o = -1.8619$

$y_o' = 0.89347$ $y_o'' = -0.66809$

and curvature

$$K = \frac{1}{R} = \frac{y_o''}{(1+y_o'^2)^{3/2}} = 0.2770411$$

5. References

Aleksandrov A.D., Kolmogorov A. N., Lavrent'ev M. A., Mathematics: Its Content, Methods and Meaning, Dover Publications, ISBN: 9780486409163,1999

Barbero, S. "The concept of geodesic curvature applied to optical surfaces", Ophthalmic Physiol Opt 2015 . doi: 10.1111/ opo.12216

Bektas, S, "Orthogonal Distance From An Ellipsoid", Boletim de Ciencias Geodesicas, Vol. 20, No. 4 ISSN 1982-2170 , http://dx.doi.org/10.1590/S1982-21702014000400053 , 2014

Bektas, S, " Least squares fitting of ellipsoid using orthogonal distances", Boletim de Ciencias Geodesicas, Vol. 21, No. 2 ISSN 1982-2170 , http://dx.doi.org/10.1590/S1982-21702015000200019, 2015a

Bektas, S, Geodetic Computations on Triaxial Ellipsoid, International Journal of Mining Science (IJMS) Volume 1, Issue 1, June 2015b, PP 25-34 www.arcjournals.org ©ARC Page | 25

Benett,A.G., Aspherical and continuous curve contact lenses, Part Three, Optom. Today 28, 238-242,1988

C. C. Ferguson, "Intersections of Ellipsoids and Planes of Arbitrary Orientation and Position," Mathematical Geology, Vol. 11, No. 3, pp. 329-336. doi:10.1007/BF01034997, 1979

Douthwaite, W.A.,Pardhan,S., Surface tilt measured with the EyeSys Videokeratoscope: influence on corneal asymmetry,Invest.Ophthalmol.,1998, Vis. Sci 39,1727-1737

Feltens J., Vector method to compute the Cartesian (*X*, *Y* , *Z*) to geodetic (φ, *λ*, *h*) transformation on a triaxial ellipsoid. J Geod 83:129–137, 2009.

Gray, A. "The Ellipsoid" and "The Stereographic Ellipsoid." §13.2 and 13.3 in *Modern Differential Geometry of Curves and Surfaces with Mathematica, 2nd ed.* Boca Raton, FL: CRC Press, pp. 301-303, 1997.

Harris W. F. Curvature of ellipsoids and other surfaces. Ophthalmic Physiol Opt 2006; 26: 497–501

James R.C., Mathematics Dictionary,5th Edition Number,Springer Netherlands, ISBN 978-0-412-99041-0,1992

Klein, P., "On the Ellipsoid and Plane Intersection Equation," *Applied Mathematics*, Vol. 3 No. 11, pp. 1634-1640. doi: 10.4236/am.2012.311226, 2012

Lipschutz M, Schaum's Outlines – Differential Geometry, Schaum's/McGraw-Hill, 1969, ISBN 0–07–037985–8

Ligas M., Cartesian to geodetic coordinates conversion on a triaxial ellipsoid, J. Geod., 86, 249-256. 2012

Moritz, H., Advanced Physical Geodesy, Herbert Wichmann Verlag Karlsruhe. 1980

Zhang Hongxin, Feng Jieqing, Preliminary Mathematics of Geometric Modeling (4), State Key Lab of CAD&CG, http://www.cad.zju.edu.cn/home/zhx/GM/003/00-sg.pdf, 2006

URL-1 http://www.mathworks.com/matlabcentral/fileexchange/46248-converter-cartesian-coordinates-to-geodetic-coordinates

URL-2 http://www.mathworks.com/matlabcentral/fileexchange/52958-intersection-ellipsoid-and-a-plane

CISET - 2nd Cilicia International Symposium on Engineering and Technology
10-12 October, 2019, Mersin / TURKEY

FORWARD AND BACKWARD PROBLEM ON TRIAXIAL ELLIPSOID

Sebahattin BEKTAŞ[1]

[1] Ondokuz Mayis University, Faculty of Engineering Geomatics Engineering Department, Samsun, TURKEY, sbektas@omu.edu.tr

ABSTRACT

In this paper, we aim to show how to generalization of the Forward and Backward (First and Invers) problem on triaxial ellipsoid. When we look at the studies related to the subject, it seems that the solution of the direct and invers geodetic problems with geographical coordinates on the triaxial ellipsoid is very difficult. In order to overcome this difficulty, in this work, we made the direct and invers problem with Cartesian coordinates instead of geographical coordinates. We will also use slope length that directly connects two points instead of the geodesic curve length. We think that our choice is also meaningful at the same time. This is because the geodesic curve lengths can not be measured with the measuring instruments and can not be applied to the ground, while the slope lengths can easily be measured with modern measuring instruments and can applied to the surface.In addition to we will see how to solve the conversion between the geographical coordinates with Cartesian coordinates or vice versa on triaxial ellipsoid.

Keywords: *Forward and Backward problem, Triaxial ellipsoid, Coordinate transformation, Geographical coordinates, Cartesian coordinates.*

1. INTRODUCTION

Rotational ellipsoid generally used in geodetic computations. Triaxial ellipsoid surface although a more general so far has not been used in geodetic applications and, the reason for this is not provided as a practical benefit in the calculations. We think this traditional thought ought to be revised again. Today increasing GPS and satellite measurement precision will allow us to determine more realistic earth ellipsoid. Several studies have shown that the Earth, other planets, natural satellites, asteroids and comets can be modeled as triaxial ellipsoids.

It is possible to reduce the most geodesic problems into one of two types. The two geodesic problems usually considered are:

1. the direct geodesic problem or first geodesic problem, it is also called coordinate transportation problem. The geographical coordinates of a P1 point (B1, L1), the S12 geodesic curve length connecting points P1 and P2 on the triaxial ellipsoid, and α12 azimuth on P1 at this edge are known. The geographical coordinates of point P2 (B2, L2) and the azimuth towards α21 are desired,

2. the inverse geodesic problem or second geodesic problem, It is also called the problem of finding the edge and angle (azimuth). In this basic task, the geographical coordinates of points P1 and P2 (B1, L1) and (B2, L2) are known, the length of the S12 geodesic curve connecting the points P1 and P2 on the triaxial ellipsoid and azimuths α12 and α21 are desired.

Because of symmetry, the solution of basic geodetic problems on the rotational ellipsoid is relatively simple in mathematical terms. The solution of the basic geodetic problems on the triaxial ellipsoid was a difficult "unsolved" problem in the first half of the 19th century, due to the fact that the motion of the geodesics was not a definite constant. In Jacobi's (1839) work he solved this problem by discovering a constant that allowed this problem to be reduced to a quadratic form. (URL-1, URL-2) (Panou, 2013) presents a method for solving the second problem on the triaxial ellipsoid by directly integrating the ordinary differential equation system for geodesics without using Jacobi's solution.

When we look at the studies related to the subject, it seems that the solution of the direct and invers geodetic problems with geographical coordinates on the triaxial ellipsoid is very difficult. In order to overcome this difficulty, in this work, we made the direct and invers problem with Cartesian coordinates instead of geographical coordinates. We will also use d_{12} slope length that directly connects two points instead of the S_{12} geodesic curve length. We think that our choice is also meaningful at the same time. This is because the S_{12} geodesic curve lengths can not be measured with the measuring instruments and can not be applied to the ground, while the slope lengths can easily be measured with modern measuring instruments and can applied to the surface.

So we have a relatively easy solution to the problem. On the other hand, the ability to perform transformation calculations between Cartesian coordinates and geographical coordinates gives us the ability to find the direct and invers geodetic problems results on the triaxial ellipsoid in geographical coordinates from the the direct and invers geodetic problems calculations we have made with Cartesian coordinates.

Although Triaxial ellipsoid equation is quite simple and smooth but geodetic computations are quite difficult on the Triaxial ellipsoid. The main reason for this difficulty is the lack of symmetry. Triaxial ellipsoid generally not used in geodetic applications. Rotational ellipsoid is frequently used in geodetic applications. Triaxial ellipsoid is although a more general surface so far but has not been used in geodetic applications. The reason for this is not provided as a practical benefit in the calculations. We think this traditional thought ought to be revised again.

Geodetic research has traditionally been motivated by the need to approximate closer and closer the physical reality. Several investigations have shown that the Earth is approximated better by a triaxial ellipsoid rather than a biaxial one (Bektaş, 2015a).

2. WHICH REFERENCE SURFACE?

Geodesic studies need to accept a model for the earth. This model can not be the intersection of the atmosphere with the earth. The oceans show a partial regularity, but we can not talk of such a scheme on land. The reference surface for the earth to be selected according to the actual shape of the earth, measurement and calculation must be easy to connect with it. The most suitable physical model for the earth is geoid. But geoid is not a suitable surface for geodetic computations. Because geoid has undulating shape, has no symmetry and can not be described as math. Therefore reference surface is selected as appropriate geometric surfaces to Earth. Selection of the reference surface depends on the size of the region study and desired accuracy.

The size of the working area and the desired accuracy level determines the reference surface. Triaxial ellipsoid can be evaluated as a more appropriate geometric approach to the geoid according to the rotational ellipsoid. largest semi-axis of a triaxial ellipsoid to be referred to for the Earth is on 345 ° longitude and the difference between the equatorial semi-axis is approximately 70 m. (Muller 1991), (Bursa 1995). This 70m difference is not a size that can be ignored in a geodetic sense. On the other hand, there are objections against taking the triaxial ellipsoid as a reference surface physically:
(Torge 2001) The use of triaxial ellipsoid does not significantly reduce the deviations between the geoid and the level ellipsoid. Calculations on these surfaces make the gravitational fields more complex. Finally, they are not suitable as physical normal numbers. For example, although the triaxial rotational ellipsoids are available as equilibrium shapes (homogeneous ellipsoids of Jacobi), such an ellipsoid gives an entirely unnatural form when the actual values are used for the angular velocity and mass of the earth.

Although the triaxial ellipsoid model is not used in geodetic applications in the world today, it is hoped that triaxial ellipsoid or more developed models will be used in the near future modeling of other celestial objects, satellites, astreoids and comets, as well as applications such as image processing, face recognition, computer games etc (Iz et al 2011), (Nyrtsov, et al., 2005). The reference surfaces that can be selected for the earth are simply ordered towards complexity: Plane (tangential), Sphere, Rotational Ellipsoid and Triaxial ellipsoid (figure-1)

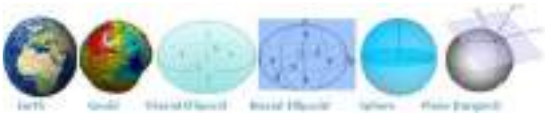

Fig. 1. Reference surfaces that can be selected for the Earth

The reference ellipsoids are used as a preferred surface on which geodetic network computations are performed and point coordinates such as latitude, longitude, and elevation are defined.The reference surfaces can be selected for the Earth from simple to complex: Plane(tangent),Sphere,Ellipsoid (biaxial) and Triaxial ellipsoid

If we think of asking a question about the above ranking accuracy computations will be difficult. If desire to simplify on the computational, the accuracy will be reduced. Considering today's computing facilities can not talk about the difficulty computing.

In addition, triaxial ellipsoid surface is most suitable reference surface for Earth and triaxial ellipsoid is more general surface than the rotational ellipsoid. Triaxial ellipsoid formulas are quite useful, because obtaining the rotational ellipsoid formula from triaxial ellipsoid formula is easy. For this, equatorial semi-axis are accepted equal to each other ($a_x=a_y=a$) which is sufficient on triaxial ellipsoid formula. Similarly to obtain sphere formula from rotational ellipsoid formula it is sufficient to take as (a = b= R). And to obtain plain formula from sphere Formula it is sufficient to take as (R= ∞) is sufficient (Bektas 2016).

Geodetic applications in the near future will be used for triaxial ellipsoid or more advanced surfaces are expected. Today, even if triaxial ellipsoid is not use for the Earth, we think it will be use for other celestial bodies and other aplications such as; image processing, face recognition, computer games etc. The celestial bodies whose shapes are different from a sphere or ellipsoid it is possible to use the well known triaxial ellipsoid as a reference surface which is mathematically calculated and shows the elongated figure of a body. Many small bodies such as satellites, asteroids or nuclei of comets have more complex figures than a triaxial ellipsoid can show. In accordance of investigations of Academician Lyapunov A.N. "The celestial bodies have most stable shapes close to triaxial ellipsoid". Traditionally most non-spherical bodies are approximated by a triaxial ellipsoid which is mathematically calculated and shows the non-spherical figure of the body (Nyrtsov, et al., 2005).

2.1. Triaxial Elipsoid (Elipsoid)

An ellipsoid is a closed quadric surface that is analogue of an ellipse. Ellipsoid has three different axes ($a_x>a_y>b$) as shown in Fig.2. Mathematical literature often uses "ellipsoid" in place of "Triaxial ellipsoid or general ellipsoid". Scientific literature (particularly geodesy) often uses "ellipsoid" in place of "biaxial ellipsoid,rotational ellipsoid or ellipsoid revolution". Older literature uses 'spheroid' in place of rotational ellipsoid. The standart equation of an ellipsoid centered at the origin of a cartesian coordinate system and aligned with the axes.

$$\frac{x^2}{a_x^2}+\frac{y^2}{a_y^2}+\frac{z^2}{b^2}=1 \qquad (1)$$

The following definitions will be used.
a_x = equatorial semimajor axis of the ellipsoid
a_y = equatorial semiminor axis of the ellipsoid
b = polar semi-minor axis of the ellipsoid
L = geodetic longitude
B = geodetic latitude
h = *ellipsoid height*
$e_x^2 = (a_x^2-b^2)/a_x^2$ first polar eccentricity
$e_e^2 = (a_x^2-a_y^2)/a_x^2$ first equatorial eccentricity

In the Triaxial ellipsoid, the geographical coordinates of a point (B, L, h) are determined the surface normal at that point, just as it is in the rotational ellipsoid. The angle between the equatorial plane and Po surface normal is called the ellipsoidal latitude (B), the angle between the meridian plane containing the surface normal at the Po point and the initial (Greenwich) meridian plane is called the ellipsoidal longitude (L) and the distance between the P landmark and its projection Po point is the ellipsoidal height . The triaxial ellipsoidal surface normals every time do not cut the Z axis unlike the rotation ellipsoid.

The local polar measurements (t,□,d) are showing respectively horizontal direction (bearing angle), vertical angle, and slope length measurements between P and Q point.

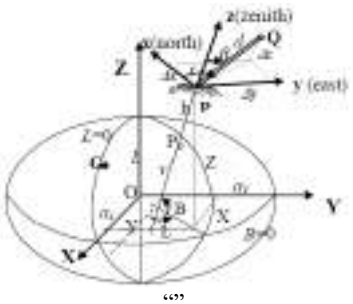

Fig. 2. (**X Y Z)** Cartesian (Global), (**B L h)** Geographical coordinate , (**x y z)** Local three-dimensional coordinate system and (**t β d)** local polar coordinate system

2.2. Triaxial Elipsoid (Elipsoid)

The problem of coordinate transformation is one of the most important issues in the geodetic calculations on the triaxial ellipsoid. The problem of the transformation from Cartesian to geodetic coordinates on triaxial ellipsoid were discussed by several authors ; The problem has been recently discussed by (Feltens, 2009), (Ligas, 2012)

In this study, The details of the Transformation between Cartesian and Geographic Coordinates will not be entered on the Triaxial ellipsoid. For Transformation details (Bektaş, 2014), (Feltens, 2009), (Ligas, 2012) sources can be seen. For example, the Cartesian

coordinates from Geographical coordinates are relatively easy and can be performed as follows (Figure-2).

(B, L, h) → (X, Y, Z)

$$X = (v + h) \cos B \cos L \quad (2)$$

$$Y = (v.\ (1 - e_{e^2}) + h) \cos B \sin L \quad (3)$$

$$Z = (v.\ (1 - e_{x^2}) + h.\ \text{Sin}\ B \quad (4)$$

$$v = \frac{a_y}{\sqrt{1 - e_x^2 \sin^2 B - e_y^2 \cos^2 B \sin^2 L}} \quad (5)$$

v = radius of main curvature

The following link can be used for calculations http://www.mathworks.com/matlabcentral/fileexchange/46239-converter-geodetic-coordinates-to-cartesian-coordinates

(X,Y,Z) → (B, L, h) transformation shown in the referenrces section, to make transformation calculations on the triaxial ellipsoid between the Cartesian coordinates and the geographical coordinates.

The following link can be used for calculations http://www.mathworks.com/matlabcentral/fileexchange/46248-converter-cartesian-coordinates-to-geodetic-coordinates

3. THREE-DIMENSIONAL COORDINATE TRANSFORMATION

As it is known, 7 transformations (datum) parameters must be known in order to convert between two three dimensional coordinate systems. The 7 datum parameters are: 3 shifted parameters (tx, ty, tz), 3 rotation parameters (εx, εy, εz) and 1 scale (k) parameters. These parameters are determined as coordinates of at least 2 points in both coordinate systems and only one coordinate of the other point is known. If the coordinates of three or more points are known in both systems, the transformations parameters are determined by adjustement (Bektaş, 2005).

We can do similarity transformation between two three-dimensional Cartesian coordinate systems (XYZ and xyz) without scale factor as follows. R_{3x3} rotation matrix (Eq.6);

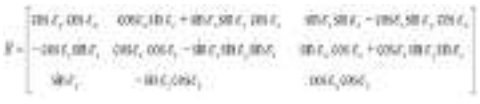

(6)

(7)

Three-Dimensional Coordinate Transformation **w**ith T The expanded transformation matrix can be easily transformed from xyz to XYZ or vice versa as in (Eq.7) (Bektas, 2015a).

3.1. Transformations Between Global (XYZ) and Local Vertical Coordinate System (xyz)

Three dimensional (3D) geodesy naturally uses three dimensional coordinate systems. From these coordinate systems, the three-dimensional local coordinate system xyz and the global coordinate system (geocentric) system XYZ are widely used. As it is known, the three dimensional local coordinate system (x, y, z) can be used in areas where the work area is not very large. The center point of the system is usually chosen in the middle of the study area (Öztürk and Şerbetçi 1989).

The xyz local (topocentric) system used here is a three-dimensional model coordinate system, the z-axis is containing ellipsoid's surface normal on P point. However, the coordinate system in which the measurements are made is the toposentric coordinate system at point P, which coincides with the tangent to the geoid normal of the plumb curve passing through the z-axis P land point. Making the measurements in the natural system and the calculations in the model system will cause the fault. In this case there are two operations that need to be done. The first one is to accept the error, that is, to assume that the ellipsoid normal coincides with the geoid normal (the plumb line) at that point. The second and, in fact, the reduction of the *t* horizontal direction (bearing angle) and *β* vertical angle measurements made at point P to the model system with the help of the plumb line components at point P. In other words, to convert the measurements from the geoid normal to the ellipsoid normal (Moritz, 1980). The direction of the x axis is towards the Z axis (north pole point) and is called north. y axis was oriented to the east and formed a left-handed system (figure-3). The XYZ global coordinate system (figure-2) is a right-handed system.

We know that seven datum parameters are needed to convert the similarity between two three dimensional coordinate systems. If there is no scale difference between XYZ and xyz, the required number of conversion parameters is six. If we know the coordinates of the origin (P point) of the local orthogonal coordinate system, We have determined three shift parameters required for the transformation. The rotation parameter (εx ,εy ,εz) three around the x, y, z axes to be determined is easily obtained from the geographical coordinates of the origin point P(εx=0 ,εy=90o-B ,εz=180o-L). In summary, only the Cartesian (XYZ) or (BLh) geographical coordinates of the P origin point are sufficient to transformation between XYZ and xyz coordinate systems.

Transformations xyz local, XYZ global coordinates are performed from the following equations on between P and Q points (Öztürk and Şerbetçi 1989).

$$x = \begin{bmatrix} x_Q - x_P \\ y_Q - y_P \\ z_Q - z_P \end{bmatrix} \quad X = \begin{bmatrix} X_Q - X_P \\ Y_Q - Y_P \\ Z_Q - Z_P \end{bmatrix} \quad (8)$$

x Local coordinate differences, X global coordinate differences

The R_{3x3} transformation matrix is obtained from the geographical coordinates of the origin point as follows**.**

$$R^T = \begin{bmatrix} -\sin B_p \cos L_p & -\sin B_p \sin L_p & \cos B_p \\ -\sin L_p & \cos L_p & 0 \\ \cos B_p \cos L_p & \cos B_p \sin L_p & \sin B_p \end{bmatrix} \quad (9)$$

R ortogonal transformation matrix ($R^T = R^{-1}$)

Local coordinate differences from global coordinate differences
Using the orthogonal transformation matrix ($R^T = R^{-1}$)

• Local coordinate differences from global coordinate differences
$x = R^T . X$,
• Global coordinate differences from local coordinate differences
$X = R . x$.

4. GEODETIC COMPUTATIONS WITH THREE-DIMENSIONAL (3D) CARTESIAN COORDINATES

The direct and inverse problem calculations that can be done on the plane, sphere and ellipsoid surface can also be performed on 3D Cartesian coordinates. Nowadays, we see that applications of positioning and surveying with GPS receivers are increasing day by day. We know that GPS receivers also produce Cartesian coordinates as raw, and other coordinate types (geographical, UTM, etc.) are derived from these Cartesian coordinates. It is clear that errors resulting from the transformation during the derivation phase will also affect the coordinates. Therefore, it is evaluated that working with raw Cartesian coordinates is more appropriate in terms of accuracy. On the other hand, we will be able to find the direct and invers problem calculations from the ellipsoid and sphere surface with Geographical coordinates from the direct and invers problem calculations that we will do with Cartesian coordinates.

4.1. Transformations Between Local Polar Coordinates (t, β, d) and Local Orthogonal Coordinates (x, y, z)

Δx, Δy and Δz are showing coordinate differences between the two points. These coordinate differences are obtained from the polar coordinate (t, β, d) following equations (Figure-3).

$\Delta x = d \sin\beta \cos t$ $d = (\Delta x^2 + \Delta y^2 + \Delta z^2)^{1/2}$: slope distance
$\Delta y = d \sin\beta \sin t$ $t = \arctan(\Delta y / \Delta x)$: bearings (horizontal direction) (10)
$\Delta z = d \cos\beta$ $\beta = \arccos(\Delta z / d)$: vertical angle

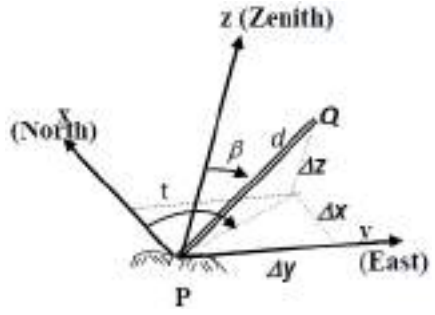

Fig. 3. Polar coordinates (t, β, d) and local orthogonal coordinates (x, y, z)

4.2. The Polar Coordinates From The Global Coordinates

The Polar coordinates (t, β,d) between the two points are obtained from the transformation matrix R as follows. ΔX, ΔY ve ΔZ are showing the global orthogonal coordinate differences between two points

$$d = \sqrt{\Delta X^2 + \Delta Y^2 + \Delta Z^2} \quad (11)$$

$$t = \arctan\left(\frac{-\Delta X \sin\Lambda + \Delta Y \cos\Lambda}{-\Delta X \sin\Phi\cos\Lambda - \Delta Y \sin\Lambda \sin\Phi + \Delta Z \cos\Phi}\right) \quad (12)$$

$$\beta = \arccos\left(\frac{\Delta X \cos\Phi\cos\Lambda + \Delta Y \cos\Phi \sin\Lambda + \Delta Z \sin\Phi}{\sqrt{\Delta X^2 + \Delta Y^2 + \Delta Z^2}}\right) \quad (13)$$

In these formulas, the values Φ, Λ are the astronomical latitude and longitude values of the P origin point. However, it is difficult to obtain these values. For this reason, instead of Φ, Λ approximately ellipsoidal B, L values are used in practice. If the components of the plumb line deviation (ζ, η) are known at point P.

$$\Phi = B + \zeta \quad (14)$$
$$\Lambda = L + \eta \sec B \quad (15)$$

Therefore above equation can be used (Moritz, 1980). How to calculate the ellipsoidal B, L values from the point of the global (XYZ) coordinates has already been mentioned in section 2.2.

4.3. Direct Problem with 3D Cartesian Coordinates On Triaxial Ellipsoid

Given: Cartesian coordinates of P_1 (X_1, Y_1, Z_1) and Polar coordinates t_{12} bearing angle , β_{12} vertical angle and d_{12} slope distance to P_2 point.

Requirements: Cartesian coordinates of P_2(X_2, Y_2, Z_2)

Solution of Problem: The local orthogonal coordinate differences between P_1 and P_2 are found from the given polar coordinates,

$$\Delta x = d \sin\beta \cos t$$
$$\Delta y = d \sin\beta \sin t \quad (16)$$
$$\Delta z = d \cos\beta$$

From these differences the global coordinate differences (ΔX, ΔY, ΔZ) are found through the R transformation matrix. Where the transformation matrix R is directly dependent the geographical (B, L) coordinates of the P origin point.
The geographical coordinates depend on the normal of the surface, so the reference surface (Triaxial, Rotational ellipsoid, Sphere) to be used in solving the problem will change the geographical coordinates of the point.

$$X = \begin{bmatrix} \Delta X \\ \Delta Y \\ \Delta Z \end{bmatrix} \qquad x = \begin{bmatrix} \Delta x \\ \Delta y \\ \Delta z \end{bmatrix} \quad (17)$$

$$\mathbf{X}=\mathbf{R}\,\mathbf{x} \rightarrow \begin{bmatrix}\Delta X\\ \Delta Y\\ \Delta Z\end{bmatrix} = \mathbf{R}\begin{bmatrix}\Delta x\\ \Delta y\\ \Delta z\end{bmatrix} \tag{18}$$

The calculated global coordinate differences are added to the coordinates of point P_1 (X_1, Y_1, Z_1) to find the coordinates of point P_2(X_2, Y_2, Z_2)

$$\begin{aligned} X_2 &= X_1 + \Delta X \\ Y_2 &= Y_1 + \Delta Y \\ Z_2 &= Z_1 + \Delta Z \end{aligned} \tag{19}$$

Numerical Example-1: Cartesian coordinates of P_1 point (X_{P1}=4235882.4602 Y_{P1}=3554249.4108 Z_{P1}= 3171030.2321m) and Polar coordinates t_{12} =30° bearing angle , β_{12}=87° vertical angle and d_{12}=3500m slope distance to P_2 point.

Solve the problem and find the Cartesian coordinates of P_2(X_2,Y_2,Z_2) separately on the triaxial ellipsoid surfaces. Use surfaces parameters below

For Triaxial elipsoid (a_x=6378388m; a_y=6378318m; b=6356911.9461m)

First the local orthogonal coordinate differences between P_1 and P_2 are found from the given polar coordinates,

$\Delta x = d \sin\beta \cos t$ =3026.9349m
$\Delta y = d \sin\beta \sin t$ =1747.6017m
$\Delta z = d \cos\beta$ =183.1758m

The calculation of the geographic coordinates of point P_1 from the cartesian coordinates, this step depends on the reference surface selected (URL-1)

Use of MATLAB function

[Geo] = cartesian_geodetic([XP1 YP1 ZP1], [ax ay b])
For triaxial ellipsoid
B_1 = 30° ve L_1 = 40° h_1= 1200.0000

From these geographical coordinates, the R transformation matrix is established as follows (9) and the Global orthogonal coordinate differences;
For triaxial ellipsoid;

$$R^T=\begin{bmatrix}-0.38302 & -0.32139 & 0.86602\\ -0.64278 & 0.76604 & 0\\ 0.66341 & 0.55667 & 0.5000\end{bmatrix}$$

$$[\Delta X\ \ \Delta Y\ \ \Delta Z]^T = R\,[\Delta x\ \ \Delta y\ \ \Delta z]^T = \begin{bmatrix}-2161.1980 & 467.8710 & 2712.9905\end{bmatrix}^T$$

Cartesian coordinates of P_2(X_2,Y_2,Z_2)

$$\begin{aligned} X_2 &= X_1 + \Delta X \\ Y_2 &= Y_1 + \Delta Y \\ Z_2 &= Z_1 + \Delta Z \end{aligned}$$

XP_2= 4233721.2616m YP_2= 3554717.2818 ZP_2= 3173743.2226

İf desired the geographic coordinates of P_2(B_2,L_2,h_2) from(URL-1)

[Geo] = cartesian_geodetic([XP2 YP2 ZP2], [ax ay b])

B_2 = 30° 01'38.2729" L_2 = 40° 01'5.2057" h_2= 1384.1361

The results of the direct problem on the surface of the rotation ellipsoid and sphere are given in Table 1 below.

Table 1. The results of the direct problem on triaxial ellipsoid, rotational ellipsoid and sphere.

	B_1,L_1,h_1	X_2,Y_2,Z_2	B_2,L_2,h_2
Triaxial ellipsoid	B1= 30° L1 = 40° h1=1200	X2=4233721.2616 Y2=3554717.2818 Z2=3173743.2226	B_2 =30°01' 38.2729" L_2 = 40° 01' 5.2057" h2= 1384.1361

4.4. Inverse problem with 3D Cartesian Coordinates On Triaxial Ellipsoid

Given: Cartesian coordinates of P_1 (X_1, Y_1, Z_1) and P_2 (X_2, Y_2, Z_2) are given.

Requirements: Polar coordinates t_{12} bearing angle, β_{12} vertical angle and d_{12} slope distance between P_1 and P_2 point

Solution: First the geographical coordinates of point P_1(B,L) are found from the Cartesian coordinates of P_1 (X_1, Y_1, Z_1) by (URL-1)

After that Global Cartesian coordinate differences are found as below

$\Delta X = X_2 - X_1$ $\Delta Y = Y_2 - Y_1$ $\Delta Z = Z_2 - Z_1$

The desired polar coordinates (t_{12} bearing angle , β_{12} vertical angle and d_{12} slope distance) between P_1 and P_2 point are found from equations (11), (12), (13).

Numerical Example-2:

Given: Cartesian coordinates of P_1 (X_1, Y_1, Z_1) and P_2(X_2,Y_2,Z_2)
XP_1=4235882.4602
YP_1= 3554249.4108
ZP_1= 3171030.2321

XP_2= 4233721.2616
YP_2=3554717.2818
ZP_2= 3173743.2226

Requirements: Polar coordinates t_{12} bearing angle , β_{12} vertical angle and d_{12} slope distance between P_1 and P_2 point

Solution: First the geographical coordinates of point P_1(B_1,L_1) are found from the Cartesian coordinates P_1 (X_1, Y_1, Z_1) by (URL-1)

[Geo]=cartesian_geodetic([XP1 YP1 ZP1], [ax ay b])
B_1 = 30° ve L_1 = 40° h_1= 1200.0000
After that Global Cartesian coordinate differences are found as below

$\Delta X = X_2 - X_1 = -2161.1986$
$\Delta Y = Y_2 - Y_1 = 67.8710$
$\Delta Z = Z_2 - Z_1 = 2712.9905$

The desired polar coordinates (t_{12} bearing angle, β_{12} vertical angle and d_{12} slope distance) between P_1 and P_2 point are found from equations (11), (12), (13).

$$d = \sqrt{\Delta X^2 + \Delta Y^2 + \Delta Z^2} = 3500\text{m}$$

$$t = \arctan\left(\frac{-\Delta X \sin\Lambda + \Delta Y \cos\Lambda}{-\Delta X \sin\Phi\cos\Lambda - \Delta Y \sin\Lambda \sin\Phi + \Delta Z \cos\Phi}\right) = 30^\circ$$

$$\beta = \arccos\left(\frac{\Delta X \cos\Phi\cos\Lambda + \Delta Y \cos\Phi \sin\Lambda + \Delta Z \sin\Phi}{\sqrt{\Delta X^2 + \Delta Y^2 + \Delta Z^2}}\right) = 87^\circ$$

The results of the Invers problem are given in Table 2 below.

Table 2. The results of the invers problem on the surface of the triaxial ellipsoid, rotation ellipsoid and sphere

	B_1, L_1, h_1	B_2, L_2, h_2	$t12, \beta_{12}, d_{12}$
Triaxial ellipsoid	B1= 30° L1 = 40° h1=1200	B_2 =30°01' 38.2729" L_2 = 40° 01' 5.2057" h2= 1384.1361	t_{12} = 30° β_{12}=87° d_{12} = 3500.0000 m

4.5. Interpretation Of Application Results

In this paper, it is shown numerically how to perform modified direct and Invers problem calculations with Cartesian coordinates on triaxial ellipsoid. In addition, the same Direct and Invers problem calculations have been made possible to solve both the rotational ellipsoid and the spherical surface and compare the results. It is very normal to obtain different results on different reference surfaces. Naturally, if the triaxial ellipsoid's equatorial half-axes approach each other; triaxial ellipsoid results will approach the results of Rotational ellipsoid. Likewise, the rotational ellipsoid results will approach the global results as far as the rotational ellipsoid flattening is approaching zero.

5. CONCLUSION

In this study, how to solve the basic geodetic problems (modified direct and invers problem) on the triaxial ellipsoid is discussed. The triaxial ellipsoid is a more general surface than the sphere and rotational ellipsoid surfaces from which the reference surface can be obtained for the Earth. For this reason, Direct and invers problem on the spherical ellipsoid and sphere surfaces were also obtained numerically from the relations of the Direct and invers problem excluded for the triaxial ellipsoid.

The algorithm used for direct and invers problem calculations made on Cartesian coordinates on the triaxial ellipsoid can also be used to make direct and invers problem calculations with geographical coordinates. The only way to do this is to convert the given geographic coordinates into Cartesian coordinates.

REFERENCES

Bektas, S,(2016), Pratik Jeodezi- Ölçme Bilgisi, OMÜ yayınları, Samsun

Bektas, S,(2014), Orthogonal Distance From An Ellipsoid, Boletim de Ciencias Geodesicas, Vol. 20, No. 4 ISSN 1982-2170 , 2014

Bektaş,S.(2015), Geodetic Computations on Triaxial Ellipsoid , International Journal of Mining Science (IJMS) Volume 1, Issue 1, June 2015, PP 25-34

Feltens J.(2009), Vector method to compute the Cartesian (X,Y,Z) to geodetic (β, λ, h) transformation on a triaxial ellipsoid, J Geod 83:129–137.

İz H. B., Ding X. L., Dai C. L. and Shum C. K.(2011), Polyaxial figures of the Moon, J. Geod. Sci., 1, 348-35

Jacobi C. G. J., (1839) Note von der geodätischen linie auf einem ellipsoid und den verschiedenen anwendungen einer merkwürdigen analytischen substitution, J. Crelle, 19, 309-313.

Ligas M.(2012), Cartesian to geodetic coordinates conversion on a triaxial ellipsoid, J. Geod., 86, 249-256.
Moritz, H.(1980), Advanced Physical Geodesy, Herbert Wichmann Verlag Karlsruhe. 1980

Müller B.(1991), Kartenprojektionen des dreiachsigen Ellipsoids, Diploma thesis, supervisor EW Grafarend, http://www.uni-stuttgart.de/ gi/education/ diplomarbeiten/ bmueller.pdf,61 pp (in German)

Nyrtsov M.V.,Bugaevsky L.M.,Stooke, P. J.(2005), The Multiple Axis Ellipsoids As Reference Surfaces For Mapping Of Small Celestial Bodies, Lev M. Bugaevsky, Moscow State University of Geodesy and Cartography (MIIGAiK), Moscow, Russia

Panou (2013), The geodesic boundary value problem and its solution on a triaxial ellipsoid, Journal of Geodetic Science, • 3(3) • 2013 • 240-249 DOI: 10.2478/jogs-2013-0028

Torge W. (2001) Geodesy. Third completely revised and extended edition. Walter de Gruyter · Berlin · New York

URL-1:
http://geographiclib.sourceforge.net/html/triaxial.html

URL-2: http://sci.fgt.bme.hu/gtoth/ge/geodesy2.pdf

URL-3:
http://www.mathworks.com/matlabcentral/fileexchange/46248-converter-cartesian-coordinate-to-geodetic-coordinate (Erişim 02 Mart 2016)

URL-4:
http://www.mathworks.com/matlabcentral/fileexchange/46239-converter-geodetic-coordinates-to-cartesian-coordinates (Erişim 02 Mart 2016)

CISET - 2nd Cilicia International Symposium on Engineering and Technology
10-12 October, 2019, Mersin / TURKEY

AN ANALYSIS OF THE EFFECTS OF ENVIRONMENTAL FACTORS ON VEHICLE SALES IN TURKEY USING MACHINE LEARNING METHODS

Serkan Karakız [a], Çiğdem Acı [b]

[a] Mersin University, Faculty of Engineering, Computer Engineering Department, Mersin, Turkey, 1802010171007@mersin.edu.tr
[b] Mersin University, Faculty of Engineering, Computer Engineering Department, Mersin, Turkey, caci@mersin.edu.tr

ABSTRACT

Recently, many car brands produce vehicles. The tendency of these manufactured car brands over the years and the estimation of their sales are important for the automobile industry. The production of the sub-industry branches of the vehicles produced is also affected in this direction. In our study, the increasing trend of investment in the motor vehicle industry will be examined and the future trend of the motor vehicle industry will be predicted. Rather, we will analyze which field of motor vehicle we need. In many previous studies, the effect of selling values such as the dollar rate has been discussed. In our study, it is aimed to take environmental factors into consideration such as geographical situation, weather, and gender. Recurrent Neural Network (RNN) and Long Short Term Memory (LSTM) deep networks will be used as prediction methods. It is aimed to estimate future sales with the help of Keras, Numpy, Scikit Learn libraries which will be included in Python language on the Turkish Statistical Institute (TUIK) data. The training was conducted with 70% of TUIK Data and the test data will be randomly selected at a rate of 30% especially from outside the training data. It is aimed to test cross-validation and compare RNN and LSTM performance.

***Keywords**: RNN (Recurrent Neural Network), LSTM (Long Short Term Memory Networks), Deep Learning, Vehicle Sales Prediction*

1. INTRODUCTION

Recently, many car brands produce vehicles. These vehicles, which have been in traffic by years, need to be estimated in the production line for the future. Model, brand, fuel types, usage, the income level of individuals, geographical characteristics, gender, number of sales by provinces and reasons for preferring these vehicles are among the factors affecting these vehicles by years. The distribution of vehicle use according to the objectives and in which area more sales will be predicted in the future. Accordingly, the demand for this tool in the following years will be determined. It will be determined which factor is the most important factor affecting vehicle sales. In this paper, tests and results of Recurrent Neural Network (RNN) and Long Short Term Memory (LSTM) algorithms will be evaluated to be used in estimating the sales of vehicles. Turkish Statistical Institute (TUIK) data will be combined and factors that affect vehicle sales will be examined. The performance differences between RNN and LSTM methods will be compared.

Through product sales forecasting, firms can create a plan for marketing, sales management, production, procurement, logistics and so on to improve their economic benefits and reduce losses caused by weaknesses in the production plan (Zhi-Ping,F., Yu-Jie,C., Zhen-Yu C. , 2017).

Long-term forecasting of car sales plays an important role in the automobile industry. Accurate predictions allow firms to improve market performance, minimize profit losses and plan to manufacture processes and marketing policies more efficiently (Fantazzini, D. , Toktamysova, Z., 2015).

According to the demand curve calculated regardless of automobile origin, demand was flexible according to price. A 10% drop in prices leads to a 12% increase in sales (Alper, C. E. , Ayşe, M., 2000)

Made a number of motor vehicles per 1,000 people in Turkey research show that while the European Union average is 473 units. Along with the improvements in national income, automobile sales increased by 76.60% in the first quarter of 2011 (Karaatlı, M., Helvacıoğlu, Ö. C., Ömürbek, N., Tokgöz, G., 2012).

Factors affecting the decision-making process of consumers buying a car in Turkey are grouped under four headings. These;

1. Input Variables: brand, product, quality, price, availability, service, etc. Various stimulants such as
2. External Variables Affecting Purchasing Behavior: Family, reference groups, personality, social class, culture, roles, the financial situation.
3. Buyer's Knowledge and Decision Process: Learning time, internal variables
4. Output Variables: Attention, perception, attitude, intent, purchase (Arslan, K., 2003).

The European continent, which was the leader in the automotive market in the early 2000s, has now retreated to third place after Asia-Oceania and America. Among the leading automotive manufacturers in Europe, Volkswagen takes the first place in the world, Fiat is the second and Renault is the third. Apart from these three brands, the other important European automotive industry organizations are as follows: bmw, peugeut, citroen, audi, mercedes-benz,…Although not as much as the other three brands in these brands are selling both in Europe and in different parts of the world

Since 2005, it has become one of the major manufacturers in Europe with over 1 million production (Tüzüntürk, S., Sert Eteman , F., Sezen , H. K., 2016).

In order to reach 4 million production, 3 million export and 75 billion dollars export revenue targeted in the domestic automotive sector for 2023, it was realized in order to model the demand of strategically important domestic cars (Akyurt , İ.Z., 2015).

Industry published by the Chamber of "Turkey's Top 500 Industrial Board" When the study examined 500 large oven in the share of sales from the production of the automotive industry in 2008,% 12.7, while the share of exports reached 25% is observed (Kaba ,G., Başaran Şen, A.,2009).

Chinese automobile industry achieved great accomplishment through the development in the past 50 years. In 2004, sale proceeds of Chinese automobile industry broke through RMB 1 trillion and the contribution of automobile industry to GDP was the fifth in all industries of China. The domestic automobile production reached 5.7 million and ranked the fourth in the word in 2005. (Daoping ,C., 2011).

Based on an exhaustive research of sales data for various popular brand cars in Pakistan following findings could be established:

a) The customers preferred cars with dual fuel options such as petrol as well as CNG.

b) In both the observed years, the CNG models sold more for all the types of cars by the specific manufacturer.

c) Even among CNG models, the air-conditioned cars and vans sold in more numbers as compared to their counter parts.

d) The present analysis could be used as a reference for identifying the sales trends of any car models throughout the years.

e) The results of such a study could be used a s a reference by the customers as well as sellers for either predicting the future price increase or the number of units sold in a business period.

f) Data mining and decision analysis could be successfully used to establish the future trends of cars sales (Shahid , S., Manarvi , İ., 2009).

2. DEEP LEARNING AND MACHINE LEARNING

In order to define a model with classical machine learning techniques or to establish a machine learning system, the feature vector must first be extracted. In order to extract the feature vector, those skilled in the art are needed. These processes take a lot of time and occupy the expert. Therefore, these techniques cannot process raw data without preprocessing and without expert assistance. Deep Learning has made great progress by eliminating this problem, which has been working for many years in the field of machine learning. Because deep networks, unlike traditional machine learning and image processing techniques, the learning process is done on raw data. While processing raw data, it obtains the necessary information through the representations it has formed in different layers (Ülker, E., İnik, Ö. 2017).

2.1. Recurrent Neural Networks (RNN)

RNNs are networks in which the connections between the units form a directed loop. It is allowed to exhibit dynamic temporal behavior with RNN. Unlike feedforward neural networks, RNNs can use their input memory to process inputs. This attribute makes RNNs a useful method of handwriting recognition and speech recognition (Recurrent Neural Network, 2018).

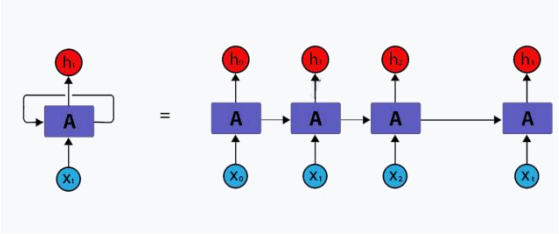

Figure.1.RNN Algorithms

2.2. Long Short Term Memory (LSTM)

LSTM is a special type of RNN that can learn long-term dependencies. Remembering information for a long time is in practice the default behavior, not something they are trying to learn. All repetitive neural networks are in the form of repetitive neural network module chains. In the standard RNN, this repeating module will have a very simple structure like a single *tanh* layer. LSTM is clearly designed to avoid the problem of long-term dependence (Long Short-Term Memory, 2018).

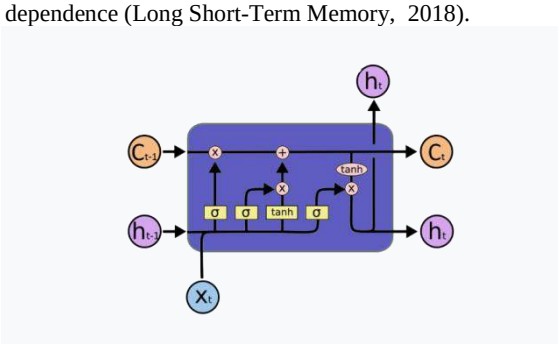

Figure.2.LSTM Algorithms

2.3. MATERIAL AND METHOD

Step 1: The RNN algorithm is set to apply to the entire dataset. The dataset is divided into two datasets such as train and test.

Step 2: In this step, the data that the RNN has learned incorrectly is re-included in the dataset. The number of elements of the new dataset is the same as the original dataset.

Step 3: Incorrect learning in the dataset is accepted if it is below the tolerance value. If not, the test is repeated.

Step 4: The data in RNN is tested with LSTM this time. Once again, the dataset is divided into the dataset to be tested, the test dataset and the control dataset.

Step 5: Incorrect data is included in the dataset and the dataset, test dataset and control dataset to be tested are reconstructed.

Step 6: Learning is complete if the data that has been subjected to cross-validation is below an acceptable error value.

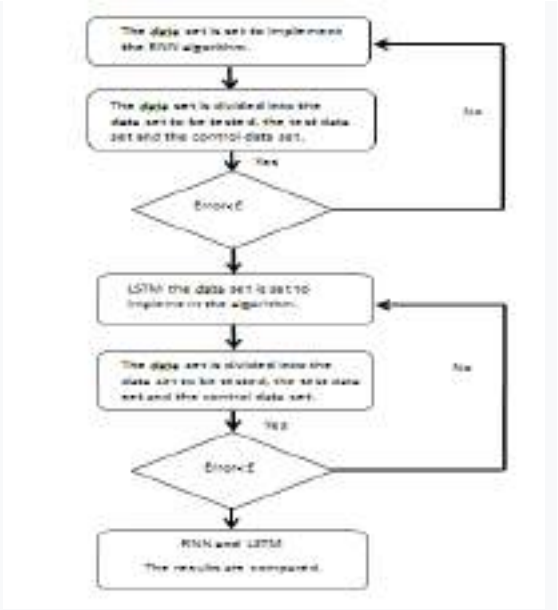

Figure.3. The Flow Chart of Algorithms

Python language will be used as the programming language. The data will be taken from TUIK records. The data will be analyzed in Python using Keras, Numpy, Scikit Learn libraries. A sample of data is shown in Figure 4.

TRAFİĞE KAYITLI ARAÇLAR, 2004-2018

			cinsadi								
	yil	TOPLAM	OTOMOBİL	MİNİBÜS	OTOBÜS	KAMYONET	KAMYON	TOSİKLET	EL AMACLI	TRAKTÖR
TÜRKİYE	2004	10 236 357	5 400 440	318 954	152 712	1 259 867	647 420	1 218 677	28 004	1 210 283
	2005	11 145 826	5 772 745	338 539	163 390	1 475 057	676 929	1 441 066	30 333	1 247 767
	2006	12 227 393	6 140 992	357 523	175 949	1 695 624	709 535	1 822 831	34 260	1 290 679
	2007	13 022 945	6 472 156	372 601	189 128	1 890 459	729 202	2 003 492	38 573	1 327 334
	2008	13 765 395	6 796 629	383 548	199 934	2 066 007	744 217	2 181 383	35 100	1 358 577
	2009	14 316 700	7 093 964	384 053	201 033	2 204 951	727 302	2 303 261	34 104	1 368 032
	2010	15 095 603	7 544 871	386 973	208 510	2 399 038	726 359	2 389 488	35 492	1 404 872
	2011	16 089 528	8 113 111	389 435	219 906	2 611 104	728 458	2 527 190	34 116	1 466 208
	2012	17 033 413	8 648 875	396 119	235 949	2 794 606	751 650	2 657 722	33 071	1 515 421
	2013	17 939 447	9 283 923	421 848	219 885	2 933 050	755 950	2 722 826	36 148	1 565 817
	2014	18 828 721	9 857 915	427 264	211 200	3 062 479	773 728	2 828 466	40 731	1 626 938
	2015	19 994 472	10 589 337	449 213	217 056	3 255 299	804 319	2 938 364	45 732	1 695 152
	2016	21 090 424	11 317 998	463 933	220 361	3 442 483	825 334	3 003 733	50 818	1 765 764
	2017	22 218 945	12 035 978	478 618	221 885	3 642 625	838 718	3 102 800	60 099	1 838 222
	2018	22 865 921	12 398 190	487 527	218 523	3 755 580	845 462	3 211 328	63 359	1 885 952

Figure.4. A sample of TUIK's Data

3. CONCLUSIONS

The purpose of this paper is to determine the characteristics of the motor vehicles being sold, what are the features of the motor vehicles to be sold, and to determine the interest of motor vehicles in the future, and to plan the production of the vehicles in that area. It is aimed to create the right supply against consumer demand by producing vehicles that can meet these demands in the future.

REFERENCES

Akyurt, İ. Z. (2015). "Modeling Demand Forecasting with Artificial Neural Networks: The Case of Domestic Cars" *Istanbul University Faculty of Economics Journal of Econometrics and Statistics*, Vol. 23, pp. 147-157.

Arslan, K. (2003). "Consumer In Car Purchase Factors Affecting Behavior " *Istanbul Commerce University Journal*, pp. 83-103.

Daoping, C. (2011). "Chinese Automobile Demand Prediction Based on ARIMA Model." *International Conference on Biomedical Engineering and Informatics* , Chongqing, China , pp.2197-2201.

Fantazzini, D., Toktamysova, Z. (2015). "Forecasting German car sales using Google data and multivariate models" *International Journal of Production Economics*, Vol. 170, pp. 97-135.

Kaba, G., Başaran Şen, A. (2009) " The Effects Of Using Leading Economic Indicators In Increasing Forecast Accuracy:An Analyses On The Turkish Automotive Sector" *I.I.B.F Journal*, Vol. 27, No.2, pp. 397-411.

Karaatlı, M., Helvacıoğlu, Ö. C., Ömürbek, N., Tokgöz, G. (2012). "An Artificial Neural Network Based Automobile Sales Forecasting" *International Journal of Management Economics and Business*, Vol.8, No.17.

Long Short-Term Memory https://Devhunteryz.Wordpress.Com/2018/07/14/Uzun-Kisa-Sureli-Bellek-Long-Short-Term-Memory/. [Accessed 28 Aug 2019].

Ülker, E., İnik, Ö. (2017). "Deep Learning and Deep Learning Models Used in Image Analysis"*Journal of Gaziosmanpasa Scientific Research*, Vol. 7, No. 14, pp. 85-104.

Recurrent Neural Network http://elitcenkalp.blogspot.com/2018/04/recurrent-neural-network.html [Accessed 28 Aug 2019].

Shahid, S. , Manarvi, İ. (2009) "A Methodology of Predicting Automotive Sales Trends through Data Mining*" 2009 International Conference on Computers & Industrial Engineering*, Taxila, Islamabad, Pakistan, pp.1464-1469.

Tüzüntürk, S., Sert Eteman, F., Sezen, H. K. (2016). "Estimation Of The Sales Amounts Of The Dispenser Size Water With Artificial Neural Network Method ", *Akademik Bakiş Dergisi,* Vol. 56, pp. 147-157.

Zhi-Ping, F., Yu-Jie, C., Zhen-Yu C. (2017). "Product sales forecasting using online reviews and historical sales data: A method combining the Bass model and sentiment analysis " *Journal of Business Research*, Vol. 74, pp. 90-100.

CISET - 2nd Cilicia International Symposium on Engineering and Technology
10-12 October, 2019, Mersin / TURKEY

MECHANICAL PROPERTIES OF TIC REINFORCED METAL MATRIX COMPOSITES FABRICATED BY SAND CASTING

Suleyman Cinar Cagan [*1], Recep Dabak[1] and Berat Baris Buldum[1]

[1] Mersin University, Engineering Faculty, Mechanical Engineering Department, Mersin, Turkey,
cinarcagan@mersin.edu.tr

ABSTRACT

Composite materials are widely used in transportation industry (automotive, aerospace and aerospace) because of their properties such as heat resistance, chemical resistance, stiffness and strength. In addition, composite materials are corrosion resistant to many chemicals and have very large production possibilities and are lighter than metals and alloys. In this way, fuel consumption, which is the most important problem in the transportation sector, will be minimized. In this study, metal matrix composite material was produced by using sand mold casting method. Al2014 aluminum alloy was used as the matrix material and titanium carbide in different proportions (3%, 5%, 7%) was used as reinforcing element. The mechanical tests (hardness and tensile tests) of the metal matrix composite material produced were performed. In addition, scanning electron microscopy analysis were investigated. In the tensile test, it was determined that the tensile strength increased up to a certain reinforcement ratio and then decreased. In the hardness test, it was determined that the hardness values increased with increasing reinforcement ratio. In SEM examination, it was determined that ceramic powders provide homogeneity at certain points. As a result, the mechanical and structural effects of reinforced ceramic powders in composite material production are observed.

Keywords: *Metal matrix composites, tensile strength, microhardness, titanium carbide.*

[*] Corresponding Author

1. INTRODUCTION

In our age has been increasing needs which are different and new materials with technological developments (Clyne *et al.* 2019). These materials are required in parallel with the various requirements for enhancing mechanical properties. In this context, features not found in a single material are obtained by combining multiple materials with different methods (Marchi *et al.* 2003; Clyne and Hull 2019).

Composite materials have been found in widespread and wide areas today (Mavhungu *et al.* 2017). They were spearheaded by various industrial fields such as space, automotive, aerospace, textiles, defense, and armor systems (Kara *et al.*). Materials with superior properties obtained by combining two or more materials are referred to as composites. They are two separate parts, matrix and reinforcing elements, which allow the formation of composite materials (Bhattacharya *et al.* 2017).

Composites are generally used as reinforcements to matrices such as ceramics, metals, plastics, fibers, particles, whiskers and so on. reinforcing elements (Baradeswaran *et al.* 2014). Metal Matrix Composite materials (MMC) have shown significant improvements in reinforcement elements in recent years (Rezayat *et al.* 2016; Jawalkar *et al.* 2017; Padmavathi *et al.* 2019). In addition to this, obtaining new mechanical properties with new low costs in production techniques also enables the change in the physical structure of the material with the difference in the amount of reinforcement. Among MMCs, aluminum matrix composites (AMCs) are often preferred for low density, high specific strength, and toughness, high elevated temperature, low thermal coefficient of thermal expansion, good resistance and machinability, especially in automotive and aerospace applications such as engine blocks and aircraft bodies (Mahesh *et al.* 2017; Mahesh *et al.* 2018). Consequently, aluminum attracts attention because of its low density among metal matrix composite materials. Reinforced materials such as SiC, TiC, Al2O3, B4C, and MgO are generally used in aluminum matrix composites (Bains *et al.* 2016).

Ensuring the desired performance for the production of composite material is primarily determined by the fact that the matrix material can provide wettability of the reinforcing element and facilitate adhesion for bond formation (Casati *et al.* 2014). The production stage of the metal matrix composites is difficult to produce, even today because it is costly and the wettability between the matrix and the reinforcement is not strong. During the production of composite materials, the reinforcement and matrix phases must not dissolve between them. However, the dissolution of the matrix and reinforcement at a very small rate contributes positively to the formation of a strong bond between these two.

The matrixes have many features such as ensuring the unity of various reinforcing elements and helping to hold them (Rao *et al.* 2016). By means of the matrix, the loads acting on the composites are conveyed to the reinforcing elements, furthermore, the crack formed in one fiber prevents the fibers from spreading to each other and prevents them from spreading to other fibers. Most of the composite materials have not been determined with many mechanical properties, but matrix material and reinforcing elements are preferred according to the technical properties planned in production. For this reason, matrices that do not show the same features in terms of technical properties are determined and preferred with great care. Aluminum is more preferred than different metals due to its high wettability and strong interface bond (Moona *et al.* 2018).

This study aims to determine the effects on the structural and mechanical properties of homogeneous distribution of ceramic powders in the 2014 aluminum matrix composites by sand casting method. Mixtures of TiC ceramic powders in three different contents were provided. The composite samples obtained were subjected to tensile test, microhardness measurement, and metallographic preparation procedures and then microstructural examinations were performed. structural and physical properties of composite materials.

2. MATERIALS AND METHODS

2.1. Fabrication Process

In this study, Al 2014 aluminum alloy was employed as the matrix material. The chemical content of Al 2014 is exhibited in Table 1. TiC (minimum purity 99.5%) ceramic powders from Alfa Aesar were used as reinforcement ceramic material during the experiments.

Table 1. The chemical content of Al 2014 aluminum alloy (wt. %)

Element	Content % in Al 2014
Cr	0.03
Cu	4.06
Fe	0.47
Mg	0.56
Mn	0.57
Si	0.61
Ti	0.01
Zn	0.10
Al	Balance

Two pieces of Al2014 aluminum alloy with 10x30x80mm dimensions are thrown into the crucible and melted in the oven at 900℃. In the molten Al2014 aluminum alloy, different amounts of TiC powders were added. The mixture was subjected to stirring by mechanical stirrer to form a fine vortex. TiC particles and Mg were introduced at a constant feed rate into the vortex. Mg has been used to improve the wettability between Al2014 aluminum alloy and TiC particles. The process parameters carried out during the process are depicted in Table 2. The molten mixtures were mixed thoroughly and transferred to a ladle. From the ladle, the liquid alloy was poured into sand (cylindrical shape dies) mould and solidified. The same fabrication procedure is repeated for fabricating different weight percentages of (3, 5, and 7) the Al2014 aluminum alloy. Different metal matrix composites made of Al2014 reinforced with 3, 5 and 7% TiC by weight are manufactured in the form of cylindrical rods of 20 mm diameter and 200 mm length.

2.2. Mechanical Tests

Tensile tests were applied to cylindrical specimens produced as casting according to ASTMB557:2006 standard. The samples used in the tensile test are shown

in figure 1. Samples produced by sand mold casting method were processed by lathe and brought to suitable dimensions for stretching. In addition, each sample was subjected to sanding and subsequent polishing to remove imperfections on the surface.

Fig. 1. Samples for Tensile strength test

Vickers microhardness values of certain materials obtained from composite material samples to determine the change in the proportions of titanium carbide ceramic powders (3%, 5% and 7%) mixed into aluminum matrix were obtained by taking three different measurements from each sample. It was calculated. The surface of the sample was sanded in the first stage and then the peak angle 136° diamond pyramid tip was used (Fig. 2.). The microhardness values were calculated by means of these square traces.

Fig. 2. Vickers microhardness tester

2.3. Scanning electron microscopy (SEM)

Scanning electron microscopy (SEM) (Supra 55, Zeiss) was used to examine the structures of TiC ceramic powders in the surface structure of the obtained metal matrix composite material samples. The SEM device used in the analyzes is presented in Fig. 3. SEM analysis (3%, 5% and 7%) titanium carbide ceramic powders microstructure was investigated.

Fig. 3. Scanning electron microscope

3. RESULTS AND DISCUSSION

Tensile test results of metal matrix composite material samples produced at different rates (3.5 and 7% TiC) with ceramic powder reinforced are presented in the Fig. 4. The tensile strength of Al2014 aluminum alloy with no added ceramic powder was found to be 92 MPa. The tensile strength of 3, 5, 7% TiC reinforced aluminum matrix composite material was measured as 123, 138 and 129 MPa, respectively.

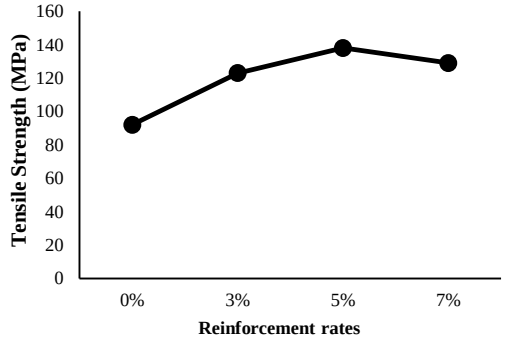

Fig.4. Tensile strength values of TiC powders at different reinforcement rates

Vickers microhardness tests of composite samples were carried out after the sanding operations were carried out on the sample surfaces at the first stage. A square trace was created by applying load to the samples for 15 seconds. Figure 5 shows the Vickers microhardness values of TiC powders at different reinforcement rates.

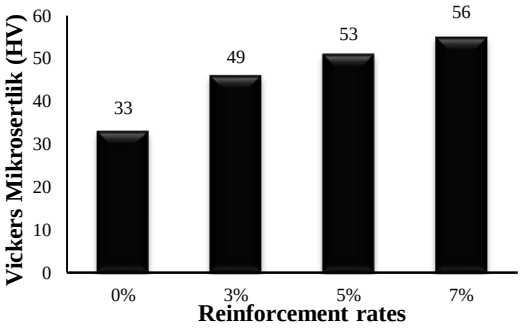

Fig.5. Vickers microhardness values of TiC powders at different reinforcement rates.

SEM images of composite material samples composed of titanium carbide ceramic powders produced in different reinforcement ratios are shown in Fig. 6. It has been determined that ceramic reinforced powders provide homogeneity and no agglomeration in the composite material samples with increasing amount of reinforcement.

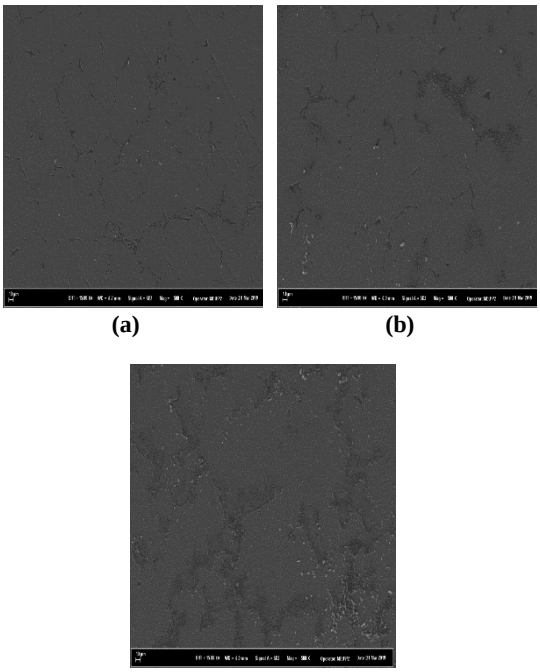

(a) **(b)**

(c)

Fig.6. SEM images of (a) 3%, (b) 5%, (c) 7% composite materials reinforced with aluminum matrix titanium carbide

4. CONCLUSION

In this study, Al2014 aluminum alloy was preferred as the matrix material in order to investigate the structural and mechanical effects of the composite materials. As reinforcing elements, composite materials were obtained by sand casting of titanium carbide (3%, 5%, 7%) ceramic powders. The melting of the matrix material was carried out in the ash furnace in the graphite crucible, the mixing of the melting matrix material and the ceramic powders was carried out and finally the casting of the mold was performed. Following these procedures, tensile test, microhardness test and SEM examination were performed; mechanical properties of composite materials with different reinforcement ratios and their effects on the structure were determined.

It was observed that tensile strength increased in samples with 3% and 5% reinforcement ratio in titanium carbide ceramic reinforcement powders. However, it is determined that tensile strength of 7% reinforcement ratio decreases the tensile strength between reinforcement and matrix due to the high volume of ceramic reinforcements in the matrix.

In the Vickers microhardness test performed at different reinforcement ratios and different ceramic powders, it was determined that composite material samples increased the hardness values of the composite material samples according to the hardness value of the non-reinforced matrix material.

The increase in reinforcement ratio increases the tensile strength up to a certain ratio, but after 5% reinforcement ratio, the powders are not able to provide a homogeneous distribution due to their high volume in the matrix, causing the tensile strength to decrease.

ACKNOWLEDGEMENTS

This project with the code 2018-1-TP2-2754 is supported for financial by Mersin University Scientific Research Projects unit.

REFERENCES

Bains, P. S., S. S. Sidhu and H. Payal (2016). "Fabrication and machining of metal matrix composites: a review." *Materials and Manufacturing Processes*, Vol. 31, No. 5, pp. 553-573.

Baradeswaran, A., S. Vettivel, A. E. Perumal, N. Selvakumar and R. F. Issac (2014). "Experimental investigation on mechanical behaviour, modelling and optimization of wear parameters of B4C and graphite reinforced aluminium hybrid composites." *Materials & Design*, Vol. 63, No., pp. 620-632.

Bhattacharya, S. and A. T. Alpas (2017). Tribology of aluminum and aluminum matrix composite materials for automotive components. Lightweight and Sustainable Materials for Automotive Applications, CRC Press: 303-328.

Casati, R. and M. Vedani (2014). "Metal matrix composites reinforced by nano-particles—a review." *Metals*, Vol. 4, No. 1, pp. 65-83.

Clyne, T. and D. Hull (2019). *An introduction to composite materials*. Cambridge university press.

Jawalkar, C., A. S. Verma and N. Suri (2017). "Fabrication of aluminium metal matrix composites with particulate reinforcement: a review." *Materials Today: Proceedings*, Vol. 4, No. 2, pp. 2927-2936.

Kara, M., M. Kirici and S. C. Cagan "Effects of the Number of Fatigue Cycles on the Hoop Tensile Strength of Glass Fiber/Epoxy Composite Pipes." *Journal of Failure Analysis and Prevention*, Vol., No., pp. 1-6.

Mahesh, L., J. S. Reddy and P. Mukunda (2017). "A Study of Microstructure and Wear Behaviour of Titanium Carbide Reinforced Aluminium Metal Matrix Composites." *International Journal of Advances in Scientific Research and Engineering*, Vol. 3, No.

Mahesh, L., M. Vinyas, J. S. Reddy and B. Muralidhara (2018). "Investigation of the microstructure and wear behaviour of titanium compounds reinforced aluminium metal matrix composites." *Materials Research Express*, Vol. 6, No. 2, pp. 026516.

Marchi, C. S., A. Mortensen and A. Evans (2003). Metal matrix composites in industry: an introductionand a survey, Springer.

Mavhungu, S., E. Akinlabi, M. Onitiri and F. Varachia (2017). "Aluminum matrix composites for industrial use: advances and trends." *Procedia Manufacturing*, Vol. 7, No., pp. 178-182.

Moona, G., R. Walia, V. Rastogi and R. Sharma (2018). "Aluminium metal matrix composites: A retrospective investigation." *Indian Journal of Pure & Applied Physics (IJPAP)*, Vol. 56, No. 2, pp. 164-175.

Padmavathi, K., R. Ramakrishnan and K. Palanikumar (2019). "Wear properties of SiCp and TiO2p reinforced aluminium metal matrix composites." Vol., No.

Rao, V. R., N. Ramanaiah and M. Sarcar (2016). "Tribological properties of aluminium metal matrix composites-AA7075 reinforced with titanium carbide (TiC) particles." *International Journal of Advanced Science and Technology*, Vol. 88, No., pp. 13-26.

Rezayat, M., M. Bahremand, M. Parsa, H. Mirzadeh and J. Cabrera (2016). "Modification of As-cast Al-Mg/B4C composite by addition of Zr." *Journal of Alloys and Compounds*, Vol. 685, No., pp. 70-77.

CISET - 2nd Cilicia International Symposium on Engineering and Technology
10-12 October, 2019, Mersin / TURKEY

PRODUCTION OF CERAMIC REINFORCED ALUMINUM ALLOY COMPOSITE MATERIALS: A REVIEW

Suleyman Cinar Cagan[1], Recep Dabak[1] and Berat Baris Buldum[*1]

[1] Mersin University, Engineering Faculty, Mechanical Engineering Department, Mersin, Turkey
barisbuldum@mersin.edu.tr

ABSTRACT
In recent years, with the development of the manufacturing industry depending on the technology, the need for materials with superior properties is increasing. The scientists are studying on new and superior material production to meet the needs. The composites at the beginning of these studies have become one of the important elements of developing technology due to their high strength, high elastic modulus and low thermal expansion properties. High temperature resistance, high chemical resistance, rigidity and high strength composite materials are widely used in the transportation industry, aerospace industry and daily and commercial life. Aluminum matrix and ceramic reinforced composite materials were produced in different types such as microstructure, machinability properties, tensile tests in the literature and different analyzes were conducted and the results were compared.

Keywords: *Aluminum Matrix, Ceramic Reinforcement, Composite Materials, Microstructure Analysis*

* Corresponding Author

1. INTRODUCTION

With the development of the manufacturing industry depending on technology, the need for materials with superior properties increases. In order to meet these needs, scientists are studying on the production of new and superior materials. Since traditional materials cannot meet the requirements of technology, production of different types of materials has become mandatory. Composite materials have been used for many years in many fields of engineering (Kara *et al.* ; Kara *et al.* 2018; Padmavathi *et al.* 2019). The main disadvantage of classical materials compared to composite materials is that composites are not lightweight enough and have high strength (Padmavathi, Ramakrishnan and Palanikumar 2019). The disadvantage of composite materials is that their production is expensive and difficult, as well as lack of recycling and insufficient surface quality (Baradeswaran *et al.* 2014).

The formation of such materials consists of reinforcing elements and matrix materials surrounding the reinforcing elements. The main function of the reinforcement elements is to control the stresses in the material by holding them in the matrix. In addition, matrices are to strengthen the stiffness and strength. Therefore, if the desired conditions of the composite materials are met during the production stage, the strength of the light alloys may be increased, their densities may be increased and their resistance to high temperatures may be increased (Ma *et al.* 2015).

In addition, reinforcing elements improve properties such as corrosion and abrasion resistance other than stiffness and strength. Reinforcement elements are generally in the form of fiber, particle and whisker (Hensher 2016).

The studies for the production and mechanical properties of composite materials increased gradually towards the middle of the 18th century. There are many different kinds of composite materials and production methods and new technologies are included in these. Metal matrix composites (MMC) are also one of these composite materials (Shirvanimoghaddam *et al.* 2017).

It has superior properties when compared with materials such as metal matrix composites (MMCs), monolithic materials and polymer matrix composites (PMCs) (Shirvanimoghaddam, Hamim, Akbari, Fakhrhoseini, Khayyam, Pakseresht, Ghasali, Zabet, Munir and Jia 2017).

Metal matrix composites have recently been an important research topic in engineering applications due to their low density and high strength ratio. Metal matrix composite materials are engineering materials with higher wear resistance, strength/weight ratio than traditional materials (Clyne *et al.* 2019). For the aerospace industry, metal matrix composite materials are preferred in the material group because of their high specific strength and rigidity. Particle reinforced MMC materials are also lower in cost compared to continuous fiber reinforced composite materials. In general, Al, Mg, Ti, Ni, Fe, Cu, Ag, Co, Nb are used as matrix materials [8]. Furthermore, metal matrix composites are formed by the combination of two different materials reinforced with ceramic, such as continuous fiber, particulate SiC, TiC, B_4C and Al_2O_3 (Jawalkar *et al.* 2017; Clyne and Hull 2019).

Recently, aluminum matrix composites have been widely researched and found their place in industrial applications. Due to its corrosion resistance, low electrical resistance and excellent mechanical properties, metal matrices are an important choice for the production of such materials (Bhattacharya *et al.* 2017; Mavhungu *et al.* 2017).

Aluminum matrix materials have also started to occupy an important place in many fields from electronics to sports equipment, defense and armor systems (Bhattacharya and Alpas 2017; Mavhungu, Akinlabi, Onitiri and Varachia 2017).

2. COMPOSITE MATERIALS

More than fifty thousand varieties of materials are used in engineering applications. While some materials have been used for centuries, some of them have been used by integrating the materials at hand (Clyne and Hull 2019). Composite materials are formed by the combination of two or more materials. Composites are high-tech materials because their superior properties are better than pure materials (Khan *et al.* 2017). They consist of a matrix material and reinforcing materials surrounding and holding this matrix together (Gibson 2016).

Advantages of composite materials compared to other materials (Vasiliev 2017);

a) High strength, even though their density is not high,

b) Load sharing of the materials they are formed,

c) Easy production in various formations according to the desired mechanical properties

d) Demonstrate stronger properties than conventional materials and show fatigue, electrical conductivity, toughness, stability at high temperatures and creep.

In order to call any material composite:

•Production is made by human

•At least two materials come together and have different chemical components.

•Properties should have properties that matrix and reinforcement elements cannot show alone.

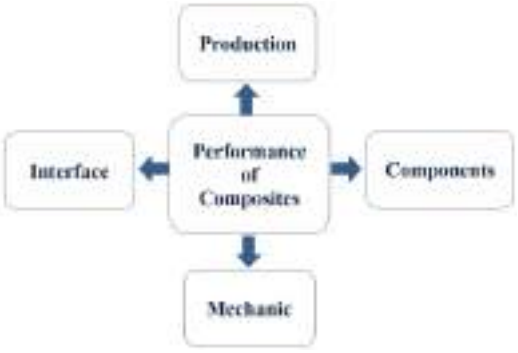

Fig. 1. Factors affecting composite performance (Ghazali *et al.* 2016).

According to the matrix material used, composite materials are divided into three main classes:

1. Metal Matrix Composite Materials (MMC)
2. Ceramic Matrix Composite Materials
3. Polymer Matrix Composite Materials (Clyne and Hull 2019).

2.1. Metal Matrix Composite Materials

Although Metal matrix composites have been used in many areas since the mid-1900s, they are mostly high-strength composites produced using reinforcement elements ceramic (Garg *et al.* 2010).

Metal matrix composites are generally divided into three (Garg, Singh, Sachdeva, Sharma, Ojha and Singh 2010);
• Particle reinforced
• Short fiber or whisker reinforced
• Continuous fiber or sheet reinforced

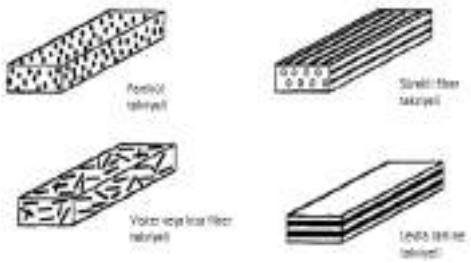

Fig. 2. Metal matrix composite material types (Gupta *et al.* 2014)

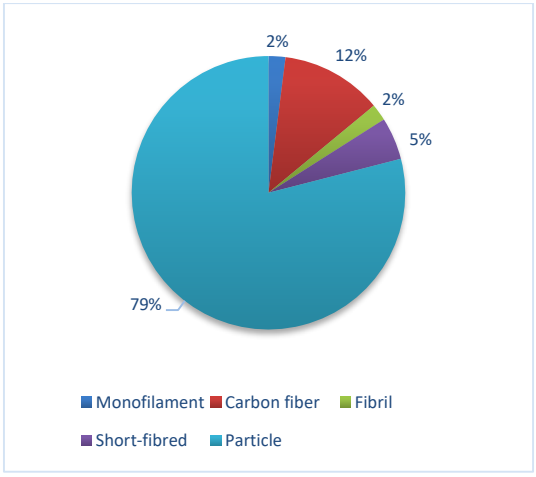

Fig. 3. Reinforcing element preference of firms producing MMC materials (Marchi *et al.* 2003)

2.2. Aluminum Matrix Composite Materials

As matrix material reinforced with aluminum and ceramic materials as reinforcements usually tensile, impact, those materials formed by increasing the various physical properties such as bending strength and abrasion resistance (Mondolfo 2013). Aluminum is one of the most preferred metals although it was discovered late among non-ferrous metals (Mondolfo 2013). Aluminum alloys are used extensively in automotive and aerospace fields due to their low density, excellent strength and toughness and high corrosion resistance (Cagan *et al.* 2018). Aluminum is generally preferred because high electrical and thermal conductivity is important (Cagan and Buldum 2018). Zn, Cu, Si, Mn and Mg are used as additional elements in aluminum alloys. These elements are preferred by many because they form a sedimentation hardening mechanism (Miao *et al.* 1999). Among aluminum alloys, 2xxx, 5xxx, 6xxx and 7xxx series are the most commonly used materials in transport industry (Mondolfo 2013).

Table 1. Physical properties of Aluminum

Density	2.7 g/cm^3
Density (liquid form)	2.375 g /cm^3
Melting point	660.32 ^{o}C
Boiling point	2519 ^{o}C
Fusion heat	10.71 kJ/mol
Heat of evaporation	294 kJ/mol
Heat capacity	24.2 J/mol.K (25 ^{o}C)

Table 2. Symbolic sequence of aluminum process alloys

Matrices	**Basic Alloying Element**
1xxx	-
2xxx	Copper (Cu)
3xxx	Manganese (Mn)
4xxx	Silicon (Si)
5xxx	Magnesium (Mg)
6xxx	Magnesium + Silicon
7xxx	Zinc (Zn)
8xxx	Other elements

2.3. Ceramic Reinforcements

Due to its good abrasion, corrosion, hardness and thermal resistance properties, ceramic materials are preferred in the industry. In addition to being used directly in industry, ceramic materials are also used as reinforcing elements in composite materials with metals. In order to achieve the desired properties, it is necessary to have the physical and chemical compatibility between the main structure and the material used as reinforcing element in order to obtain the expected properties in the composites. Due to their high melting temperatures and hardness, ceramic materials are preferred as reinforcing phase in metal matrix composites. The reasons for preference are (Singh *et al.* 2016):

a) Low density,
b) Mechanical compatibility,
c) Chemical compatibility,
d) High chemical stability,
e) High modulus of elasticity,
f) High tensile and compressive strength,
g) Usually cheaper than metals.

In this study aluminum matrix composites produced by various methods in the literature review and analysis methods to compile the data obtained are reported were tabulated and analyzed. These studies are presented in Table 3 (Miracle *et al.* 2001).

Table 3. Properties of major reinforcing materials (Miracle and Donaldson 2001)

Materials	Reinforcing form	Modulus of elasticity (GPa)	Density (g/cm^3)	Thermal conductivity (W/mk)	Thermal coefficient of expansion ($x10^{-6}/K$)
SiC	Particle	448	3.21	120	3.4
SiC	Short-fibred	400-700	3.21	32	3.4
SiC	Fiber	450	3.46	-	-
Al_2O_3	Particle	410	3.9	25	8.3
AIN	Particle	350	3.25	10	6.0
B4C	Particle	450	2.52	29	5.0-6.0
TiB_2	Particle	370	4.5	27	7.4
TİC	Particle	320	4.93	29	7.4
BN	Particle	90	2.25	25	3.8
Al_2O_3	Short-fibred (Saffil)	300	3.29	-	-

Table 4. Investigation of different aluminum matrix composites in literature

Ref. no	Furnace	Methods	Materials and reinforcements	Analysis
1	Resistance	Stir casting	Al6061 Matrix phase TiB_2 (0,4,8,12 %wt.)	Tensile, Hardness, Wear, SEM, EDS
2	Resistance	Liquid metallurgy	Al4147 Matrix phase B4C (10,15,20 %wt.) SiC (20 %wt.)	SEM, Wear, Surface roughness
3	Resistance	Stir casting	Al (%99.81 purity) Matrix phase Zr/B_4C (0,0.05,0.1 %wt.)	Tensile, SEM, EDS, XRD
4	Induction	Stir casting	Al 1100 Matrix phase B_4C (15,31 %wt.)	Tensile, SEM, XRF, XRD
5	Resistance	Stir casting	Al5Ti5Cr Matrix phase SiC (0,2,4,6,8,10 %wt.), Al5Ti5Cr Matrix phase B_4C (0,2,4,6,8,10 %wt.)	Surface roughness, SEM, EDS FTIR, AFM XRD
6	Resistance	Stir casting	Al 6061 Matrix phase B_4C (6,8,10,12 %wt.)	Tensile, Hardness, XRD
7	Resistance	Stir casting	Al-Si12Cu Matrix phase B_4C (2,4,6,8,10 %wt.)	Tensile, Hardness,
8	Resistance	Stir casting	AA 7075 Matrix phase TiO_2 (5,10,15,20 %wt.)	Tensile, Hardness, SEM, XRD
9	Resistance	Stir casting	Al 7075 Matrix phase TiO_2 (10 %wt.), Graphene oxide (0.5,0.75,1%wt.)	Tensile, Hardness,
10	Resistance	Ultrasonic casting	Al 2024 Matrix phase SiC (4,8,12 %wt.), Graphene (0.5%wt.)	Tensile, Hardness,
11	Resistance	Stir casting	Al2024 Matrix phase B_4C (2.5,5,7 %wt.)	Tensile, Hardness, SEM, XRD

In study 1, there is an increase in the hardness of aluminum with TiB_2 reinforcement. It increases the microhardness of aluminum. As a result, it is understood that the increase in the amount of TiB_2 will definitely increase the strength of aluminum (Suresh *et al.* 2013).

In study 2, the change in abrasion value of composites changed as B_4C content increased above 15%. For SiC particle 4147 it has more effect on wear resistance (Ipek 2005).

In study 3, zirconium as an alloying element was incorporated into aluminum. The addition of Zr during mixing casting to improve the bonding of boron carbide particles increases the particle yield during manufacture. The addition of Zr resulted in an 8% increase in tensile strength. The strength and elongation of the composite increased by about 30% (Rezayat *et al.* 2016).

In study 4, the ultimate tensile strength value of AA6061-31% B_4C composite was developed with 340 MPa, 112.5% (Yu *et al.* 2016).

In study 5, Al5Ti5Cr composite was prepared from

liquid metallurgical methods by changing the percentage of silicon carbide (SiC) and boron carbide (B_4C). As the volume fraction of B_4C and SiC in the matrix increased, ultimate tensile strength, 0.2% PS and VHN increased. Finally, the increased content of the hard phase in the matrix promotes different types of inter-metallic formation by aluminum reaction such as $AlTi_3$, SiC, Al_4C. As the SiC content increases, both the stress and the modulus of pressure increase, but as the B_4C content increases, the compressive strength decreases and a slight increase is observed (Ahmed *et al.* 2017).

In study 6, the highest hardness (121.31 VHN) for aluminum matrix composites was found to be 12%. The tensile strength of AMCs should be maximum (176.37 MPa) for the weight percentage of 8% by weight (Gopal Krishna *et al.* 2012).

In study 7, by increasing the weight% of the B4C particles in the aluminum matrix, the stiffness of the composites increases more than the alloy due to resistance to plastic deformation by the reinforcing particles. The tensile strength of the composites increases up to 8% by weight of the reinforcement, after which the level of increase in tensile strength decreases due to aggregation of the reinforcing particles (Raviteja *et al.* 2014).

In study 8, when the mass fraction changes from 5% to 20%, compressive strength increases by 60% due to the metal-matrix behavior in the intermediate phase, and the hardness increases by 27% and is greatly affected by shear and normal stresses caused by the ground composite (Murali *et al.* 2014).

In study 9, the tensile properties of treated composites improved with an increase in reinforcement addition. The final tensile stress for AA7075-10% TiO_2-1.0 Graphene oxide composite is 112.7MPa. Improvement in tensile properties may be due to resistance to crack propagation through reinforcement. On-disc wear test results showed that wear load increased as load applied to sample increased. Wear loss was reduced for AA7075-10% TiO_2-1.0% Graphene oxide in both load conditions (Narwate *et al.* 2016).

In study 10, the addition of SiC (0.0-12.0% Wt.), Graphene (0.5% by weight) and encapsulation provide significant improvements in hardness and flexibility. The coefficient of friction observed due to graphene and SiC content, as well as the increased coefficient of friction SiC in the composite, leads to further improvement in tribological properties (Kumar *et al.* 2017).

In study 11, uniform distribution of boron carbide particles in matrix phase was obtained. The hardness of the composites increased and the density decreased as the amount of boron carbide in the matrix phase increased. Increasing the amount of boron carbide particles in the composites resulted in an increase in the final compaction force (Rao *et al.* 2012).

4. CONCLUSION

In our study, it is known that aluminum element and its alloy are used in many fields. It has been reported in our study that the alloy gains different properties by making the aluminum alloy a composite material with the contribution of an innovative reinforcement element. In general, it is seen that the ceramic based reinforcement material added between 5%-10% shows a good fit for the aluminum matrix and adds positive gains to the physical properties of the alloy.

ACKNOWLEDGEMENTS

This project with the code 2018-1-TP2-2754 is supported for financial by Mersin University Scientific Research Projects unit.

REFERENCES

Ahmed, F., S. Srivastava and A. B. Agarwal (2017). "Synthesis & Characterization of Al-Ti-Cr MMC as friction material for disc brakes application." *Materials Today: Proceedings*, Vol. 4, No. 2, pp. 405-414.

Baradeswaran, A., S. Vettivel, A. E. Perumal, N. Selvakumar and R. F. Issac (2014). "Experimental investigation on mechanical behaviour, modelling and optimization of wear parameters of B4C and graphite reinforced aluminium hybrid composites." *Materials & Design*, Vol. 63, No., pp. 620-632.

Bhattacharya, S. and A. T. Alpas (2017). Tribology of aluminum and aluminum matrix composite materials for automotive components. Lightweight and Sustainable Materials for Automotive Applications, CRC Press: 303-328.

Cagan, S. C. and B. B. Buldum (2018). "Investigation of the Effect of Different Working Mediums on Turning Al7075-T6 Alloy." Vol., No.

Clyne, T. and D. Hull (2019). *An introduction to composite materials*. Cambridge university press.

Garg, R., K. Singh, A. Sachdeva, V. S. Sharma, K. Ojha and S. Singh (2010). "Review of research work in sinking EDM and WEDM on metal matrix composite materials." *The International Journal of Advanced Manufacturing Technology*, Vol. 50, No. 5-8, pp. 611-624.

Ghazali, M. and A. Efendy (2016). Bio-composites materials from engineered natural fibres for structural applications, University of Waikato.

Gibson, R. F. (2016). *Principles of composite material mechanics*. CRC press.

Gopal Krishna, U., K. Sreenivas Rao and B. Vasudeva (2012). "Effect of percentage reinforcement of B4C on the tensile property of aluminium matrix composites." *International journal of Mechanical Engineering and Robotics Research*, Vol. 1, No. 3, pp. 290-295.

Gupta, N. and P. K. Rohatgi (2014). *Metal matrix syntactic foams: processing, microstructure, properties and applications*. DEStech Publications, Inc.

Hensher, D. A. (2016). *Fiber-reinforced-plastic (FRP) reinforcement for concrete structures: properties and applications*. Elsevier.

Ipek, R. (2005). "Adhesive wear behaviour of B4C and SiC reinforced 4147 Al matrix composites (Al/B4C–Al/SiC)." *Journal of Materials Processing Technology*, Vol. 162, No., pp. 71-75.

Jawalkar, C., A. S. Verma and N. Suri (2017). "Fabrication of aluminium metal matrix composites with particulate reinforcement: a review." *Materials Today: Proceedings*, Vol. 4, No. 2, pp. 2927-2936.

Kara, M., M. Kirici and S. C. Cagan "Effects of the Number of Fatigue Cycles on the Hoop Tensile Strength of Glass Fiber/Epoxy Composite Pipes." *Journal of Failure Analysis and Prevention*, Vol., No., pp. 1-6.

Kara, M., M. Kırıcı, A. C. Tatar and A. Avcı (2018). "Impact behavior of carbon fiber/epoxy composite tubes reinforced with multi-walled carbon nanotubes at cryogenic environment." *Composites Part B: Engineering*, Vol. 145, No., pp. 145-154.

Khan, A., P. Savi, S. Quaranta, M. Rovere, M. Giorcelli, A. Tagliaferro, C. Rosso and C. Jia (2017). "Low-cost carbon fillers to improve mechanical properties and conductivity of epoxy composites." *Polymers*, Vol. 9, No. 12, pp. 642.

Kumar, H. P. and M. A. Xavior (2017). "Assessment of mechanical and tribological properties of Al 2024-SiC-graphene hybrid composites." *Procedia engineering*, Vol. 174, No., pp. 992-999.

Ma, Q., R. Guo, Z. Zhao, Z. Lin and K. He (2015). "Mechanical properties of concrete at high temperature—A review." *Construction and Building Materials*, Vol. 93, No., pp. 371-383.

Marchi, C. S., A. Mortensen and A. Evans (2003). Metal matrix composites in industry: an introductionand a survey, Springer.

Mavhungu, S., E. Akinlabi, M. Onitiri and F. Varachia (2017). "Aluminum matrix composites for industrial use: advances and trends." *Procedia Manufacturing*, Vol. 7, No., pp. 178-182.

Miao, W. and D. Laughlin (1999). "Precipitation hardening in aluminum alloy 6022." *Scripta Materialia*, Vol. 40, No. 7, pp. 873-878.

Miracle, D. B. and S. L. Donaldson (2001). "Introduction to composites." *ASM handbook*, Vol. 21, No., pp. 3-17.

Mondolfo, L. F. (2013). *Aluminum alloys: structure and properties*. Elsevier.

Murali, M., M. Sambathkumar and M. S. Saravanan (2014). "Micro structural and mechanical properties of AA 7075/TiO 2 in situ composites." *Universal Journal of Materials Science*, Vol. 2, No. 3, pp. 49-53.

Narwate, M. M. and K. Mohandas (2016). "A Study on Mechanical and Tribological Properties of Aluminum Metal Matrix Composite Reinforced With TiO2 and Graphene Oxide." *International Journal*, Vol. 4, No. 4, pp. 729-732.

Padmavathi, K., R. Ramakrishnan and K. Palanikumar (2019). "Wear properties of SiCp and TiO2p reinforced aluminium metal matrix composites." Vol., No.

Rao, S. R. and G. Padmanabhan (2012). "Fabrication and mechanical properties of aluminium-boron carbide composites." *International journal of materials and biomaterials applications*, Vol. 2, No. 3, pp. 15-18.

Raviteja, T., N. Radhika and R. Raghu (2014). "Fabrication and mechanical properties of stir cast Al-Si12Cu/B4C composites." *International Journal of Research in Engineering and Technology*, Vol. 3, No. 07, pp. 343-346.

Rezayat, M., M. Bahremand, M. Parsa, H. Mirzadeh and J. Cabrera (2016). "Modification of As-cast Al-Mg/B4C composite by addition of Zr." *Journal of Alloys and Compounds*, Vol. 685, No., pp. 70-77.

Shirvanimoghaddam, K., S. U. Hamim, M. K. Akbari, S. M. Fakhrhoseini, H. Khayyam, A. H. Pakseresht, E. Ghasali, M. Zabet, K. S. Munir and S. Jia (2017). "Carbon fiber reinforced metal matrix composites: Fabrication processes and properties." *Composites Part A: Applied Science and Manufacturing*, Vol. 92, No., pp. 70-96.

Singh, J. and A. Chauhan (2016). "Characterization of hybrid aluminum matrix composites for advanced applications–A review." *Journal of Materials Research and Technology*, Vol. 5, No. 2, pp. 159-169.

Suresh, S. and N. S. V. Moorthi (2013). "Process development in stir casting and investigation on microstructures and wear behavior of TiB2 on Al6061 MMC." *Procedia Engineering*, Vol. 64, No., pp. 1183-1190.

Vasiliev, V. V. (2017). *Mechanics of composite structures*. CRC Press.

Yu, L., Q.-L. Li, L. Dong, L. Wei and G.-G. Shu (2016). "Fabrication and characterization of stir casting AA6061—31% B4C composite." *Transactions of Nonferrous Metals Society of China*, Vol. 26, No. 9, pp. 2304-2312.

CISET - 2nd Cilicia International Symposium on Engineering and Technology
10-12 October, 2019, Mersin / TURKEY

Kinetic Characteristic Analysis of Elasto Caloric Copper Based Alloy

Mehmet Ali KURGUN *[1], Ece KALAY[2], İskender ÖZKUL[3] and Canan AKSU CANBAY[4]

[1] Mersin University, Engineering Faculty, Mechanical Engineering Department, Mersin, Turkey, mehmetalikurgun@gmail.com

[2] Mersin University, Engineering Faculty, Mechanical Engineering Department, Mersin, Turkey, eecekalay@gmail.com

[3] Mersin University, Engineering Faculty, Mechanical Engineering Department, Mersin, Turkey, iskender@mersin.edu.tr

[4] Fırat University, Faculty of Science, Department of Physics, Elazığ, Turkey, caksu@firat.edu.tr

ABSTRACT
Nowadays, when the technology is developing rapidly, the value of materials science and materials with different behaviors has increased considerably. Important examples for the shape memory alloys are also mentioned in the materials have different behaviors remarkable work done and continues to do. Shape memory alloys lose their shape with effects such as force, temperature and magnetically induced. They are defined as exhibiting memory behavior by regaining their lost forms by removing these effects. NiTi alloy, Cu-based alloys and Fe-based alloys can be shown as alloy with shape memory effect. In this study, Cu-based shape memory alloy was used, which is more cost-effective compared to NiTi alloy and is more resistant to corrosion than Fe-based alloy. The CuAlMnFe quaternary shape memory alloy was subjected to the cooling process at room temperature by standing in muffle furnace at 350 ° C for different periods. Aging of the material is aimed with this process. Differential scanning calorimeter was used to obtain the solid-state phase transformation temperatures of the material after the aging process and the results were evaluated.

Keywords: *Shape memory alloys, Cu based shape memory alloys, martensitic transformation, enthalpy, entropi, activation energy*

* Corresponding Author

1. INTRODUCTION

Nowadays, when the technology is developing rapidly, the value of materials science and materials with different behaviours has increased considerably. Important examples for the shape memory alloys are also mentioned in the materials have different behaviours remarkable work done and continues to do. Shape memory alloys lose their shape with effects such as force, temperature and magnetic. They are defined as exhibiting memory behaviour by regaining their lost forms by removing these effects.

In shape memory alloys (SMA) which react to stimuli such as temperature, transformations called phase transitions to result in phenomena such as shape memory effect and superelasticity.

The Shape Memory Effect (SME) is realized using solid-state phase transformation without diffusion in the material. These phase transformations are generally provided by the temperature or magnetic effect between the phases known as austenite (main phase) and martensite (product phase). Before the transformation, the austenite phase of the solid-state transformation to the martensite phase by shifting the crystal structure with external effects such as temperature. The internal structure of martensite contains the most twins of structural defects (Boyd *et al.* 1996; Kumar *et al.* 2008). The transformation of the martensite phase into the austenite phase in the SMA is generally described as a thermodynamic cycle and it also exhibits a reversible structure. During the transformation between phases, the release of chemical-free energy creates the driving force under the shape recovery. This force creates the Shape Memory Effect. Although the displacement amounts of the atoms in phase transformation are very small, this movement is carried out in the same direction and causes large scale changes in the material. Crystal structure changes in the alloy provide high-quality properties such as Shape Memory Effect and superelasticity (Otsuka *et al.* 1976; Porter *et al.* 2009). The temperature at which the martensite phase starts during phase transformation is expressed as M_s, while the temperature value at which the phase transformation is completely terminated is expressed as M_f. These abbreviations are used in the literature as A_s and A_f for the starting and ending temperature values of the austenite phase (Brinson 1993; Khovailo *et al.* 2003).

Martensitic transformations, which are sensitive to temperature differences, are also sensitive to phase transformation and stress differences, and therefore carry mechanical properties. This type of behaviour which is not observed in traditional materials gives thermodynamic properties to phase transformations. Using these properties, some theories have been developed to express the behaviour of shape memory alloys by thermodynamic laws. For example, equilibrium thermodynamics theory developed by Wollants, et al. (Acar *et al.*).

The basis of this theory is the idea that the effects of stress and temperature, which are the driving forces that perform thermo-elastic martensitic phase transformation, are equal to the phase transformation. These effects are represented schematically in Figure 1. According to this statement, energy balance is mentioned, with uniaxial force F, deformation is observed in the material. The number of deformations increases from L to L + ΔL due to martensitic transformation. In this case, the free energy balance of the system is expressed by the following formula.

$$\Delta G = \Delta H - T\Delta S - F\Delta L$$

In the formula, ΔH refers to enthalpy energy, TΔS temperature-entropy energy, and FΔL'mechanical energy. The right side of the equation contains all the free energy terms related to the deformation-transformation process (Acar and Aydın).

Fig. 1. Deformation by martensitic transformation as a result of external load (Wollants *et al.* 1980)

2. EXPERIMENTAL DETAILS

CuAlMnFe shape memory alloy was obtained by using high purity elements melting furnace. The usage rates of the elements are given in Table 1. CuAlMnFe alloy formed in arc melting furnace was homogenized in the muffle furnace at 900°C for 1 hour, to eliminate the stresses in material structure. The CuAlMnFe shape memory alloy was divided into six equal samples (S1-S2-S3-S4-S5-S6). S6 is the untreated reference sample. The aging process was applied to each sample at 350°C for different times as shown in Table 2. After the aging process, a differential scanning calorimetry (DSC) device was used to obtain the solid-state phase transformation temperatures at heating speeds of 15°C/min, of the material and results, was evaluated. Thermal analysis results from the DSC device are shown in Table 3. Enthalpy and entropy changes and activation energies of the samples were examined.

Table 1. Usage ratio of elements

Elements	wt.%	at. %
Cu	82.76	70.84
Al	11.81	23.8
Mn	4.18	4.14
Fe	1.25	1.22

The activation energy value is required for the definition of the phase transformations for both phases. Also, it indicates crystallization behavior of the alloy (Canbay *et al.* 2019). The amount of heat a system receives or delivers during a certain time or temperature range is called enthalpy. The relationship between activation energy and enthalpy is shown in Figure 2. The formula for kinetic activation energy parameter, which is given by Kissenger method (1) (Kissinger 1957) is presented below;

$$\frac{d[In(\emptyset A_{max}^2)]}{d(1/A_{max})} = -\frac{E}{R} \quad (1)$$

where; $\emptyset$ is the heating/cooling rate, A_{max} is

maximum austenite peak temperature on DSC curve, R is the universal gas constant (R= 8.314 J mol^{-1}. K). The plots of $\ln(\emptyset/A_{max}^2)$ versus $1000/A_{max}$ was presented for six samples in Figure 3-8. The activation energy of the samples was calculated and presented in Table 3.

Table 2. Heat treatment scenario

Samples	Aging temperature	Aging time	Cooling method
s1	**350°c**	**1h**	Room temperature
s2	**350°c**	**2h**	Room temperature
s3	**350°c**	**3h**	Room temperature
s4	**350°c**	**4h**	Room temperature
s5	**350°c**	**5h**	Room temperature
*s6	-	-	Room temperature

*S6 is the untreated reference sample.

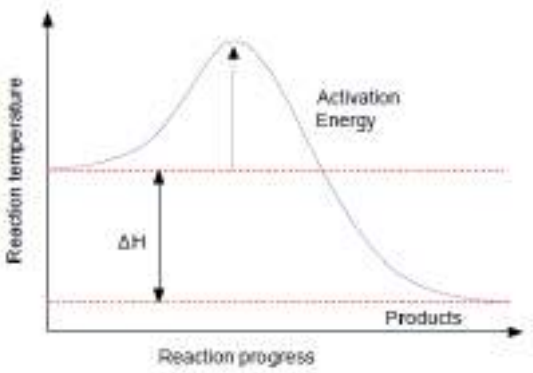

Fig. 2. Activation Energy

Table 3. Shape memory Amax values at heating/cooling rates

S1	A_{max} (°C)	S2	A_{max} (°C)	S3	A_{max} (°C)	S4	A_{max} (°C)	S5	A_{max} (°C)	Rerefence (S6)	A_{max} (°C)
5 °C/Min	118.11	5 °C/Min	120.06	5 °C/Min	126.48	5 °C/Min	131.13	5 °C/Min	123.44	5 °C/Min	123.14
15 °C/Min	122.5	15 °C/Min	124.56	15 °C/Min	128.42	15 °C/Min	133.55	15 °C/Min	126.63	15 °C/Min	131.65
25 °C/Min	126.16	25 °C/Min	126.85	25 °C/Min	130.05	25 °C/Min	134.25	25 °C/Min	129.37	25 °C/Min	148.88
35 °C/Min	130.6	35 °C/Min	129.46	35 °C/Min	130.99	35 °C/Min	135.79	35 °C/Min	132.44	35 °C/Min	132.51
45 °C/Min	144.5	45 °C/Min	129.56	45 °C/Min	132.31	45 °C/Min	140.41	45 °C/Min	149.08	45 °C/Min	141.52

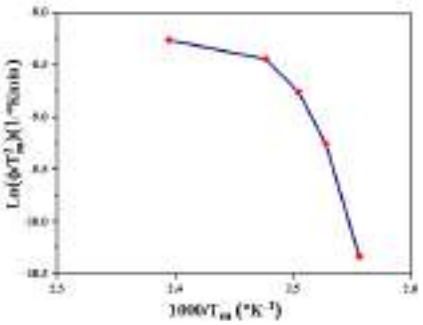

Fig. 3. The plot of activation energy changes of the S1 sample versus the maximum peak temperature of austenite transformation

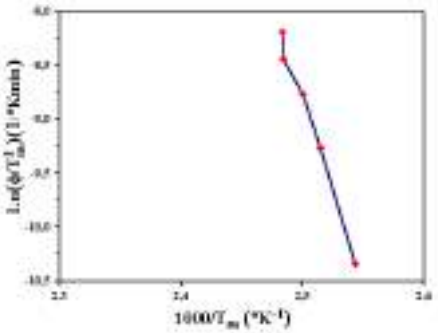

Fig. 4. The plot of activation energy changes of the S2 sample versus the maximum peak temperature of austenite transformation

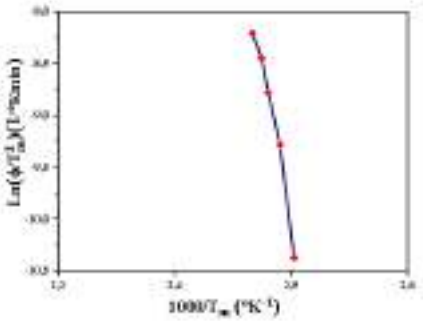

Fig. 5. The plot of activation energy changes of the S3 sample versus the maximum peak temperature of austenite transformation

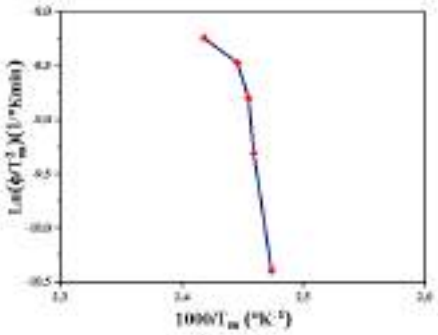

Fig. 6. The plot of activation energy changes of the S4 sample versus the maximum peak temperature of austenite transformation

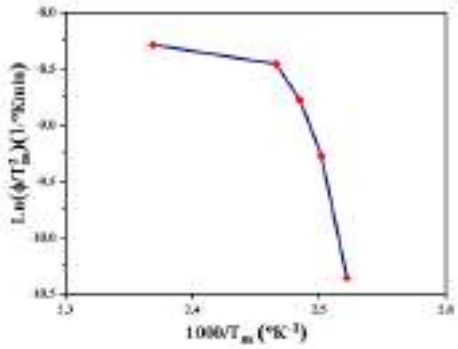

Fig. 7. The plot of activation energy changes of the S5 sample versus the maximum peak temperature of austenite transformation

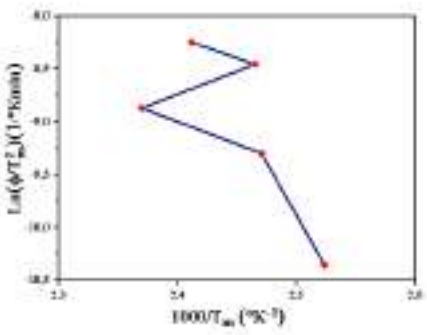

Fig. 8. The plot of activation energy changes of the S6 sample versus the maximum peak temperature of austenite transformation

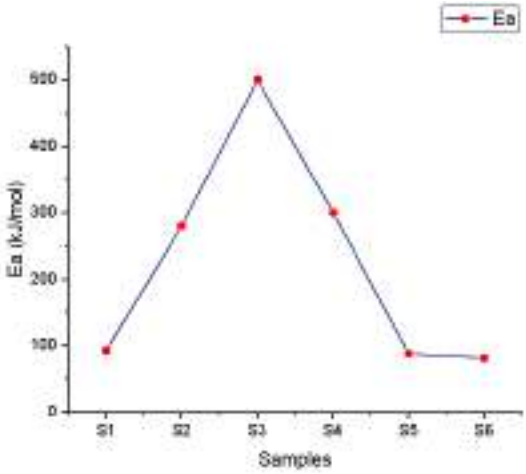

Fig. 9. Activation energy of samples

In Fig. 9, the activation energy of sample was calculated regarding equation 1. The necessary energy for solid state phase transformation values were increased till S4 sample. From 1 hour to 3 hours increased the activation energy level. However, after the 4 hours and 5 hours waiting at 350°C were make reduction in activation energy almost same level with reference sample which is S6. That's indicate that the aging medium increased precipitation and dislocation pinning effects in micro structure and it was released after 4 hours waiting.

3. CONCLUSIONS

The aging effect on any material changes the thermal, mechanical, electrical or magnetic properties. That properties can be useful or harmful for last users. In this study activation energy shifts were investigated for CuAlMnFe shape memory alloy. The five different aging time subjected the CuAlMnFe alloys. The obtained materials martensitic transformation temperatures were measured by DSC at different cooling/heating rates. The obtained values were used to calculate the activation energy which is necessary to solid-state transformation. The plotted graphs showed the between 1-3 hours waiting at 350° increased the activation energy. After the four-hour materials activation energy level began to reduce and this shows that the reaction occurrence speed is high.

4. REFERENCES

Acar, E. and M. Aydın "Şekil hafıza davranışlarının termodinamiği." *Politeknik Dergisi*, Vol. 21, No. 1, pp. 201-211.

Boyd, J. G. and D. C. Lagoudas (1996). "A thermodynamical constitutive model for shape memory materials. Part I. The monolithic shape memory alloy." *International Journal of Plasticity*, Vol. 12, No. 6, pp. 805-842.

Brinson, L. C. (1993). "One-dimensional constitutive behavior of shape memory alloys: thermomechanical derivation with non-constant material functions and

redefined martensite internal variable." *Journal of intelligent material systems and structures*, Vol. 4, No. 2, pp. 229-242.

Canbay, C. A., O. Karaduman and İ. Özkul (2019). "Investigation of varied quenching media effects on the thermodynamical and structural features of a thermally aged CuAlFeMn HTSMA." *Physica B: Condensed Matter*, Vol. 557, No., pp. 117-125.

Khovailo, V., K. Oikawa, T. Abe and T. Takagi (2003). "Entropy change at the martensitic transformation in ferromagnetic shape memory alloys Ni 2+ x Mn 1− x Ga." *Journal of applied physics*, Vol. 93, No. 10, pp. 8483-8485.

Kissinger, H. E. (1957). "Reaction kinetics in differential thermal analysis." *Analytical chemistry*, Vol. 29, No. 11, pp. 1702-1706.

Kumar, P. and D. Lagoudas (2008). Introduction to shape memory alloys. Shape memory alloys, Springer: 1-51.

Otsuka, K., C. Wayman, K. Nakai, H. Sakamoto and K. Shimizu (1976). "Superelasticity effects and stress-induced martensitic transformations in Cu Al Ni alloys." *Acta Metallurgica*, Vol. 24, No. 3, pp. 207-226.

Porter, D. A., K. E. Easterling and M. Sherif (2009). *Phase Transformations in Metals and Alloys, (Revised Reprint)*, CRC press.

Wollants, P., J. Roos and L. Delaey (1980). "On the stress-dependence of the latent-heat of transformation as related to the efficiency of a work performing cycle of a memory engine." *Scripta metallurgica*, Vol. 14, No. 11, pp. 1217-1223.

CISET - 2nd Cilicia International Symposium on Engineering and Technology
10-12 October, 2019, Mersin / TURKEY

AN INVESTIGATION OF WATER QUALITY IN PARADENİZ LAKE; GÖKSU DELTA

Olcay GÜLÇİÇEK UYSAL

[1] Mersin University, Engineering Faculty, Environmental Engineering Department, Mersin, Turkey, olcay.gulcicek@gmail.com

ABSTRACT
The nutrient level of surface water has increased significantly in the last 50 years due to the agricultural activities and uncontrolled discharge of domestic wastewater into environments. Paradeniz Lake, which is connected with the Mediterranean Sea, is located on the coast of Göksu Delta, one of the most important wetlands of the Eastern Mediterranean. It is known that as a result of intensive agricultural activities the used pesticide/chemical fertilizers and domestic wastewater leaking from the septic tanks in the study area adversely affect the delta surface waters. In this study, the changes in water quality of Paradeniz Lake, which is one of the important surface waters of the delta and separated from the sea by sand wall, were investigated depending on years (2006-2012). For the purpose samples were taken 11 times from lake and sea, and pH, temperature, electrical conductivity(EC), salinity (Sal) and dissolved oxygen (DO), nitrate nitrogen, nitrite nitrogen, ammonium nitrogen, iron and total phosphorus were analyzed. The results of the analysis were compared with the limit values of "Surface Water Quality Regulation Annex-5", and the changes in water quality were examined depending on time. The relationship between dissolved oxygen and other parameters (nitrate, ammonium, phosphorus, temperature, pH and electrical conductivity), which is an important parameter to evaluate the water quality of lakes; The relationship between phosphorus, which is the limiting nutrient in lakes, pH and iron ion was explained by regression analysis.
Keywords: *Paradeniz lake, Regression Analysis, Water Quality*

1. INTRODUCTION

Coastal lagoons are water bodies that are partially separated from the sea to which they are connected by a barrier but still receive water flow from that sea (Barnes 2011). Ecologically important wetlands and lagoons are the most productive coastal habitats in the world. However, they are considered to be extremely vulnerable to human influence and future climate change. (Gonenc and Wolflin, 2005; Acarlı ve ark., 2009).

Delta constitutes an important value in terms of its biological diversity. (Keçer ve Duman, 2007). The Göksu delta, which is formed by sediments of clay, silt, sand and gravel size carried by Göksu River, covers a total area of 15000 hectares in Mersin-Silifke district located on the Mediterranean coastline. (Demirel ve ark 2011, Ozer 2014). 17 km^2 of the 155 km^2 in the delta area consist of wetlands (lakes, rivers and rivers). The delta's coastal length is approximately 35 km.

The Göksu delta has a polygonal geometry whose base edge is connected to the mainland (Keçer ve Duman 2007: Kılar and Cicek 2018). One of the most important water resources in the delta is the Göksu River which provides the formation and development of the delta. Akgöl Lagoon (1,200 ha) and Paradeniz Lagoon (400 ha) are the second largest water source of the delta (Demirel ve ark 2011, Özer 2014). The Paradeniz lake is in direct contact with the sea and is salty, while Akgöl has the character of a freshwater lake. Both lakes are quite shallow. The maximum depth is 1 m in Akgöl and 1.5 m in Paradeniz Lagoon. Paradeniz Lake is recharged by Mediterranean, Akgöl and groundwater. The delta has a typical Mediterranean climate.

Approximately two-thirds of the bird species identified in Turkey Göksu delta was observed (Özer, 2014; ÖÇKKB 2009). The Delta system is home to many endangered bird species worldwide, and thousands of migratory birds spend the winter here in the lagoons. Göksu delta has various protection status due to its ecological and biological values (Karabulut, 2015 Delta chronologically; In 1989 Wildlife Protection Area (YHKS), in 1990 Special Environmental Protection Area (SEPA), in 1994 Ramsar area, in 1996 the first degree natural site was declared. Delta was also defined as Important Plant Area (IPA), Important Nature Area (INA) and Important Bird Area (IBA) within the scope of various international projects (Meriç ve Kavruk, 2007; Karabulut 2015).

The results of studies in Delta conducted have shown that their protection status was not sufficient to protect the delta. In the Göksu delta, chemical fertilizers/ pesticides used in agricultural activities, wastewater leaking from septic tanks have an important share in the contamination of surface and groundwater (Beyhan ve Kaçıkoç, 2009; Karabulut 2015; Özer 2014; Özer 2008; Gülçiçek 2018). As the lakes may interact with the drainage waters and surface / ground waters in the vicinity, they are in constant interaction with the land. With this interaction, pollutants are easily transported to the lake and adversely affect water quality. The interaction between lake and land is determined by the geographical structure of the lake and climatic conditions (Ünlü ve ark., 2008). Dissolved oxygen and temperature are among the most important parameters affecting the water quality of lakes. The amount of dissolved oxygen in water is an important indicator of overall lake quality. Knowing the dissolved oxygen and temperature regimes in a lake is important to develop appropriate management plans. Oxygen and temperature of a lake affect not only the physical and chemical properties of the lake, but also the sources and quantities of phosphorus and the species of fish and animal populations. Researches on delta surface water quality were revealed that agricultural activities and domestic wastewater adversely affect Paradeniz and Akgöl lake water quality (Başıbüyük ve Evliya 1993; Özer, 2008; Özer 2015; Kumbur ve ark. 2004, Gülçiçek ve Demirel 2019).

Better understanding of coastal lagoons characteristics allows implement policies, legislation and management practices leading to suitable use of coastal lagoons for economic gains while preserving their biodiversity. In this study, seasonal change of physicochemical parameters has been evaluated in Paradeniz Lake. The results would be useful for future management practices of the lake environment.

.

2. MATERIALS AND METHODS

In this study, water samples were taken from the Paradeniz Lake and Mediterranean Sea (Figure 1) between 2006 and 2012 in accordance with “Sampling and Analysis Methods of Water Pollution Control Regulation” for determine the change of water quality in lake (WPCR-SMA, 2009) and were stored 4^{o}C in the refrigerator.

Figure 1. The location map of the study area.

Electrical Conductivity (EC), Salinity (Sal), Temperature (T) and pH parameters were measured using a WTW 340i pH/Cond meter. Ammonium, nitrate, nitrite, iron and phosphate ions analyses with Hanna C200 multi parameter photometer were carried out at the Mersin University Environmental Engineering Laboratory. The goal of regression analysis is to describe and predict the relationship between two variables. The regression analysis was performed by the Microsoft Excel software to evaluate the relationship between DO and other parameters.

.

3. RESULTS AND DISCUSSION

Table 1 shows the results of the analysis of samples taken from the Paradeniz Lake and the Mediterranean Sea.

Lake	pH	T (C)	EC (uS/cm)	DO (mg/L)	NO3-N (mg/L)	NH4-N (mg/L)	Total P (mg/L)	Fe (mg/L)
June 06	8,32	8,32	45300	4,9	5,9	10	1,2	5,5
December 06	7,5	12,1	32500	8,5	0,2	0,1	0,2	0,3
July 07	8,25	29,1	48000	5,4	4,3	8,75	1,11	4,85
January 07	7,7	10,9	37000	8,9	0,1	0,08	0,25	0,05
January 08	7,9	11,1	33900	9,2	0	0,01	0,16	0,08
April 08	8,01	22,7	35200	8,1	0,1	0,1	0,3	2,5
June 08	8,29	32	46000	5,3	4,1	7,7	1,21	4,92
February 11	7,8	16,7	51800	8,2	0,2	0,02	0,15	0,108
July11	8,28	30	34400	5	4,2	7,9	1,15	4,45
September 12	8,18	28,4	42000	5,01	3,9	7,39	1,01	3,68
February 12	7,8	15,9	52000	8,1	0,1	0,09	0,28	2,6

Sea	pH	T (°C)	EC(uS/cm)	ÇO (mg/L)	NO3-N (mg/L)	NH4-N (mg/L)	Total P (mg/L)	Fe (mg/L)
June 06	8,3	8,3	53500	4,7	5,96	7,2	0,7	0,06
December 06	7,68	14,02	55000	8,5	0,1	0,1	0,28	0,01
July 07	8,2	27	52100	4,5	6,6	11,9	0,45	0,7
January 07	8,01	12,2	56000	7,9	0,5	0,07	0,17	0,02
January 08	7,84	15,3	58000	8,1	0,3	0,1	0,2	0,21
April 08	8	20	54000	8,9	0	0,02	0,2	0,03
June 08	8,35	33	57300	4,9	4,4	9,2	0,33	0,6
February 11	7,9	18,7	56600	8,6	0,1	0,01	0,04	0,167
July11	8,21	30	56000	5,04	4,3	7,89	0	2,07
September 12	8,01	29	60200	4,8	5,8	7,19	0,01	0,03
February 12	8,1	17,3	56000	8,6	0,3	0,01	0,01	1,01

The results of the analysis were graphed by using Microsoft Excel program to compare with the limit values (WQR, 2016).

pH

pH is indicative of hydrogen ion concentration in water. Hydrogen ions greatly affect flora and fauna in the water. pH, is a very important parameter in water chemistry studies and the main factor affecting the useful form conversion of nutrients to plants and animals in the aquatic environment. The most suitable pH value range for living organisms is between 6-9 (Campbell and Wildberger 1992, Radke 2000). The highest pH value was measured as the 8.32 in June 2006 and the lowest pH value was measured as the 7.5 in December 2006 in the Paradeniz lake water (Figure 2). In the samples taken from the Mediterranean Sea, the highest pH value was measured as the 8.35 in June 2008 and the lowest pH value was measured as the 7.68 in December 2006.
The aquatic plants and phytoplankton use carbon dioxide in water during photosynthesis. In summer, due to the increase in photosynthesis activity, the amount of carbon dioxide in the water decreases and the pH value increases (Ünlü et al. 2008; Sönmez et al 2008). Paradeniz and sea water pH values did not exceed the limit values in the sampling period. But, in the summer periods high pH values were detected in Paradeniz and sea water.

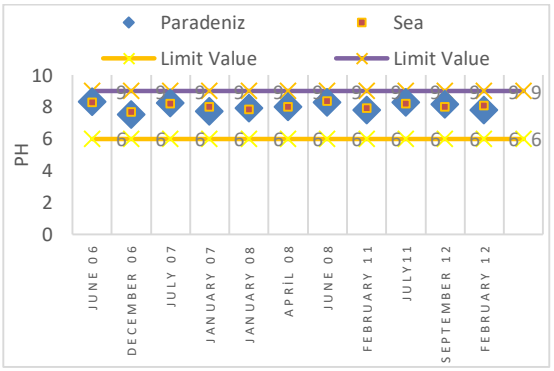

Figure 2. The change of pH values for Paradeniz Lake and Mediterranean Sea

Temperature

The study area is dominated by a typical Mediterranean climate that is the dry summers and mild and rainy winters. In the Göksu Delta, rains start in October, and continue till mid-April. In recent studies, it has been determined that temperature is an important parameter affecting the water quality of shallow lakes (Xu et al. 2012; Spears et al 2008; Xia and Zhang 2008). Temperature is effective in changing the concentration of many parameters in water. Irrigation water flows from the drainage channels to Paradeniz. Therefore, the lake water is constantly in motion. In Paradeniz Lake, the water level is the highest between May and September, when the maximum period of irrigation. The decrease in water level due to excessive evaporation during the summer months leads to the water transition from Akgöl to Paradeniz (Özer, 2014). All these events explain the change in Paradeniz lake water temperature.

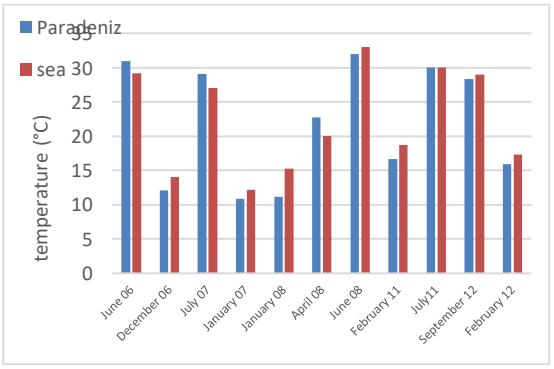

Figure 3. The change of temperature values for Paradeniz Lake and Mediterranean Sea

Electrical Conductivity (EC)

The common method for evaluating the total salt content in water is by measuring the electrical conductivity of water (EC) at 25°C. Electrical Conductivity is a parameter that indicates the ability of water to conduct electrical current and is expressed in mmhoS / cm (mS / cm) (Phocaides 2000; Özer 2014). The previous studies in Paradeniz lake water, were determined that the Na-Cl dominant ions and it was directly affected by the sea (Özer 2008; Özer 2015; Gülçiçek ve Demirel

2016). The high EC values were showed that Paradeniz Lake was affected by sea water mixing.

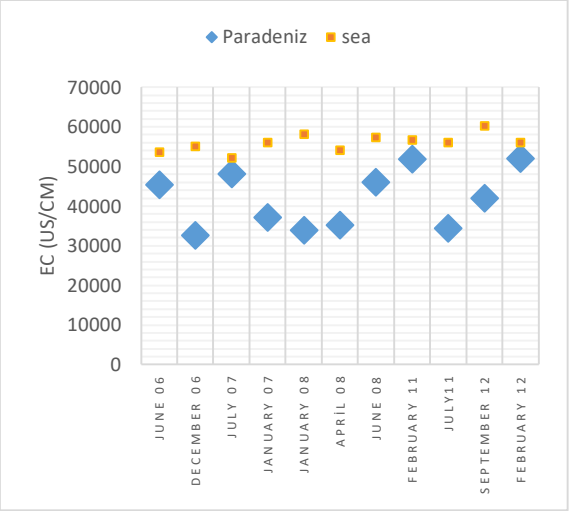

Figure 4. The change of EC values for Paradeniz Lake and Mediterranean Sea

In the Paradeniz lake water, the highest Electrical Conductivity value was measured as the 52000 µS/cm in February 2012 and the lowest Electrical Conductivity value was measured as the 32500 µS/cm in December 2006 (Şekil). In Delta, floods are observed between January and June, caused by the hard storms that occur in Ermenek and Gökçay branches of the basin (Özer 2015). These floods increase the interaction of the lake with the sea and changes the EC value of the lake water.

Dissolved Oxygen

Dissolved oxygen is a measure of the amount of oxygen dissolved in water. Dissolved Oxygen (DO) concentration provides information about living things in the water system. The dissolved oxygen (DO) concentration describes to water pollution, the concentration of organic matter in the water and the water's self-cleaning capacity (Ünlü ve ark. 2008). The low dissolved oxygen concentration (0-8 mg / L) is an indication of the high oxygen demand in water resulting from a high biological or chemical oxygen demand (BOD or COD). 8-12 mg / L dissolved oxygen concentration are generally indicative of a healthy system (Sallam ve Elsayed, 2018; Kock ve ark. 2009). The dissolved oxygen content of natural waters varies according to temperature, salinity, turbulence, photosynthetic activity of algae and plant. (EPA.1999).

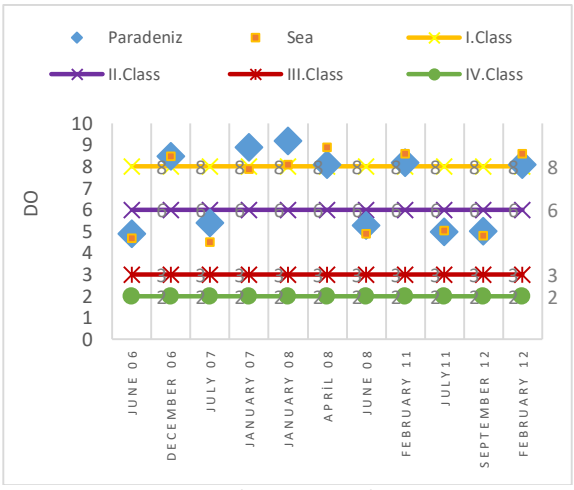

Figure 5. The change of DO values for Paradeniz Lake and Mediterranean Sea

The highest Dissolved oxygen (DO) value was measured as the 9,2 mg/L in January 2008 and the lowest Dissolved oxygen (DO) value was measured as the 4,9 mg/L in June 2006 in the Paradeniz lake water.

In the Sea water, the highest Dissolved oxygen (DO) value was measured as the 8,9 mg/L in April 2008 and the lowest Dissolved oxygen (DO) value was measured as the 4,7 mg/L in June 2006. The reason for the decrease of dissolved oxygen in the summer is due to decreased water level, increased chlorophyll-a (algae population) concentration and increased biological activity during this season. The lake water is regained dissolved oxygen the winter months, due to the increase in the stringency of rain and wind, the circulation of water in the lake and the increase in the nutrition of the lake (Singh ve ark. 2008).

Nitrogen and total phosphorus

Phosphorus (P) and nitrogen (N) are the limiting nutrients in lakes. N and P compounds increase in water are the most primary factors to cause of eutrophication. N and P are the two elements that have the least rate in the molecular formula of algae. In particular, P is the main limiting factor for controlling algae growth in water (Mainstone andParr, 2002). Nitrogen element is essential to the production of cell. It is used primarily by living organism to synthesize protein. Sources of common nitrogen compounds in lakes include septic systems, animal feeds, agricultural fertilizers, industrial wastewater, and landfills (Minnesota Pollution Control Agency 2008).

Phosphorus is the most basic element that cause of eutrophication in lake water. According to (Thomann and Mueller, 1987), the lake is oligotrophic when the total amount of phosphorus is less than 0.01 mg/l, mesotrophic when this amount is 0.01–0.02 µg/l, and eutrophic when this amount is greater than 0.02 µg/l. There are many sources of phosphorus. These include soil and rocks, wastewater treatment plants, runoff from agricultural area, septic systems, wild landfill (Spellman 2014).

Due to soil and climate characteristics, agriculture is carried out in the Göksu Delta for twelve months of the

year. The agriculture is the first degree livelihood of 80% of the inhabitants in the Göksu delta. Citrus, strawberry, horticultural crops and greenhouse are widely grown in the delta. (Özer 2015). Due to unconscious agricultural activities applied in the delta and waste water leaking from the septic tanks, water resources are very rich in nitrogen compounds (Özer 2015; Demirel ve ark 2011; Gülçiçek and Demirel 2019). The highest ammonium nitrogen value was measured as the 10 mg/L in June 2006 and the lowest ammonium nitrogen value was measured as the 0, 1 mg/L in December 2006 in the Paradeniz lake water (Figure). In the sea water, the highest ammonium nitrogen value was measured as the 11,9 mg/L in July 2007 and the lowest ammonium nitrogen value was measured as the 0, 1 mg/L in February 2011.

The highest nitrate nitrogen value was measured as the 5,9 mg/L in June 2006 and the lowest nitrate nitrogen value was measured as the 0,00 mg/L in January 2008 in the Paradeniz lake water (Figure 6). In the sea water, the highest nitrate nitrogen value was measured as the 6,69 mg/L in July 2007 and the lowest nitrate nitrogen value was measured as the 0,00 mg/L in April 2008.

The highest phosphorus value was measured as the 1,21 mg/L in June 2008 and the lowest phosphorus value was measured as the 0,15 mg/L in February 2011 in the Paradeniz lake water (Figure 8).

Phosphorus has been shown as the main limiting nutrient for the primary production of phytoplankton in many freshwater environments (Phlips, 2002). Phosphorus concentrations are generally known to be higher in summer (Søndegaard et al., 2001). The highest phosphorus value was measured as the 1,21 mg/L in June 2008 and the lowest phosphorus value was measured as the 0,15 mg/L in February 2011 in the Paradeniz lake water (Figure). In the sea water, the highest phosphorus value was measured as the 0,7 mg/L in June 2006 and the lowest phosphorus value was measured as the 0,00 mg/L in February 2011.

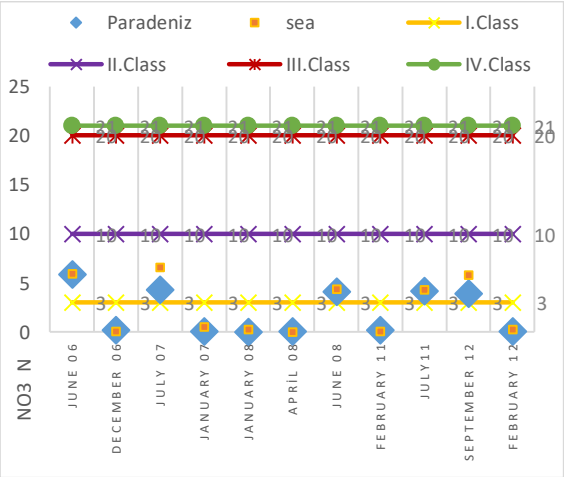

Figure 5. The change of NO_3-N values for Paradeniz Lake and Mediterranean Sea

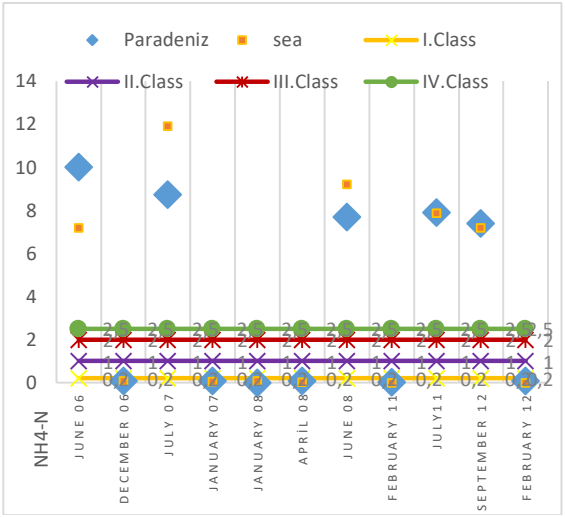

Figure 6. The change of NH_4-N values for Paradeniz Lake and Mediterranean Sea

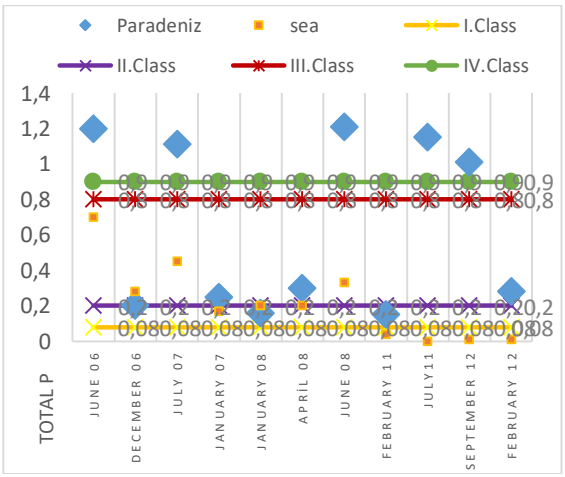

Figure 7. The change of Total P values for Paradeniz Lake and Mediterranean Sea

When the analysis results were compared with limit values;

- In the Paradeniz lake, EC results were not shown any significant variation during the sampling period; It was found to have high values due to being connected with sea water,
- When DO results were examined, it was found that the values ranged from 4.9-9 mg/L and that it was the 2nd class water category.
- When the nitrate-nitrogen results were examined, it was determined that six times were in the first class category and at the other times lake water was in the second class category in terms of nitrate nitrogen.
- When the results of ammonium nitrogen were examined, it was found that lake water was generally in the fourth class water category.
- Total phosphorus results were variable in the sampling period and it was generally found in the fourth class water category. It has been

determined that lake water is prone to eutrophication in terms of phosphorus values.

As a result of the analysis, it was determined that there is continuous nutrient input to the lake. The presence of these compounds at the same time in the sea water sample shows that the pollution on land reaches the sea via of the Paradeniz lake.

Analysis of the sea water sample which was taken from the coast of the lake is made in order to shed light on the interaction of the water quality of Paradeniz lake with the sea and it is not sufficient to predict for the pollution at sea.

Regression analysis is used to determine the relationship between variables and make predictions about the subject. In this study dissolved oxygen, which is the most important parameter in determining the quality and pollution level of lake waters, was accepted as a dependent variable. The relationship between dissolved oxygen and pH, temperature, EC, nitrate nitrogen, ammonium nitrogen and total phosphorus concentration was explained by linear regression analysis. In addition, the relationship between phosphorus, which is an important parameter in lake water quality, and iron, pH was also examined by the linear regression analysis.

According to simple linear regression analysis, the dissolved oxygen change described;

- 78% of the change in pH (R^2=0,782). There is a strong negative correlation between two parameters (r= -0,82) and this relationship was found to be "a high statistical significance"(0,001< p < 0,01) (Figure 8) .
- 91% of the change in the temperature (R^2=0,9159). There is a very strong negative correlation between the two parameters (r = -0,9518) and this relationship was found to be "a very high statistical significance significant " (p<0,001) (Figure 9) .
- 6 % of the electrical conductivity (R^2 = 0,06). There is a weak correlation between the two parameters (r =0,20) and this relationship was found to be statistically insignificant (p>0,1) (Figure 10)
- 93% of the change in the nitrate-nitrogen concentration (R^2 = 0,93). There is a very strong negative correlation between two parameters (r =-0,9580) and this relationship was found to be "a very high statistical significance" (p<0,001) (Figure 11).
- 94% of the change in the ammonium-nitrogen concentration (R^2 = 0,94). There is a very strong negative correlation between two parameters (r =-0,9654) and this relationship was found to be "a very high statistical significance"(p<0,001) (Figure 12)
- 95% of the change in the total phosphorus concentration (R^2 = 0,95). There is a very strong negative correlation between two parameters (r =-0,9791) and this relationship was found to be "a very high statistical significance"(p<0,001) (Figure 13)

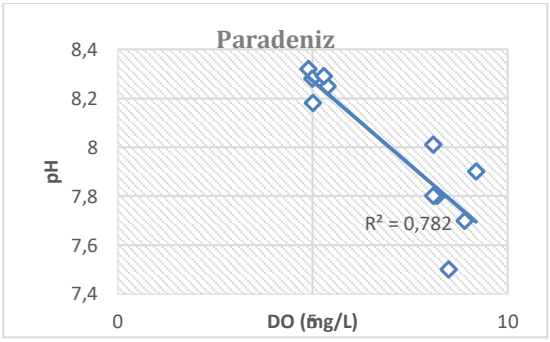

Figure 8. The relationship between of dissolved oxygen - pH

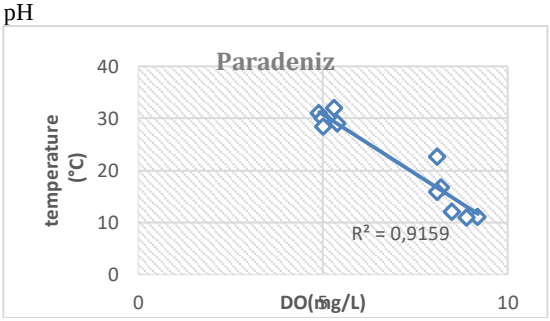

Figure 9. The relationship between of dissolved oxygen - temperature

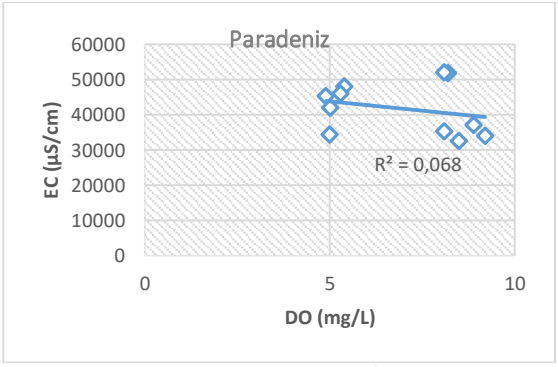

Figure 10. The relationship between of dissolved oxygen - EC

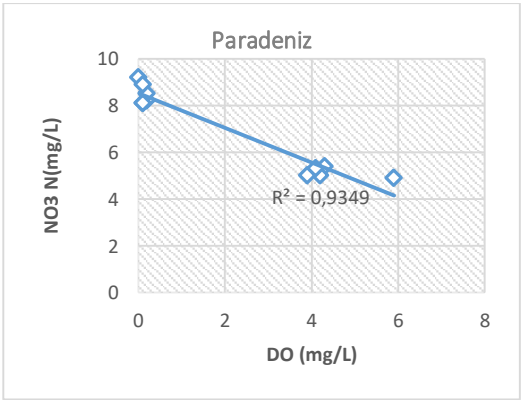

Figure 11. The relationship between of dissolved oxygen – NO_3-N

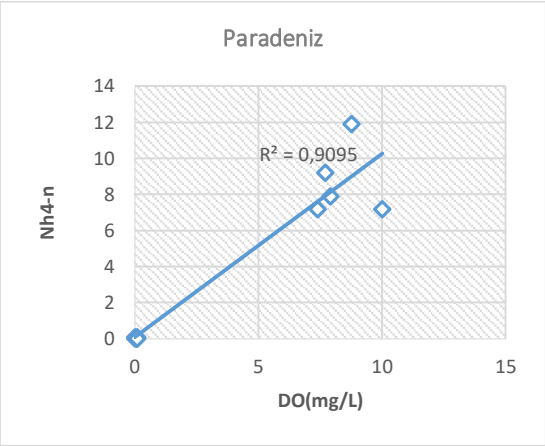

Figure 12. The relationship between of dissolved oxygen – NH_4-N

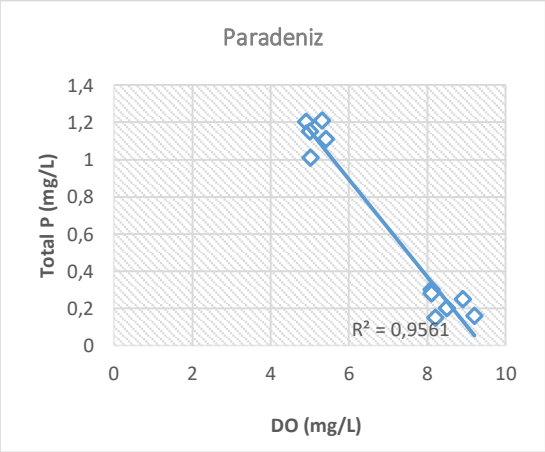

Figure 13. The relationship between of dissolved oxygen – TotalP

Nitrogen and total phosphorus concentration results, which provide information about nutrient level in Paradeniz lake were found to have a strong negative relationship with the change of dissolved oxygen concentration. This results show that nutrients contribute greatly to the dissolved oxygen exchange of the Paradeniz lake.

According to simple linear regression analysis, the total phosphorus concentration change described;

- 90% of the change in the iron concentration (R^2 =0,90). There is a very strong positive correlation between two parameters (r = 0,9374) and this relationship was found to be "a very high statistical significance"(p<0,001) (Figure 14)
- 86% of the change in the pH (R^2 = 0,86). There is a strong positive correlation between two parameters (r = 0,84214) and this relationship was found to be "a very high statistical significance"(p<0,001) (Figure 15)

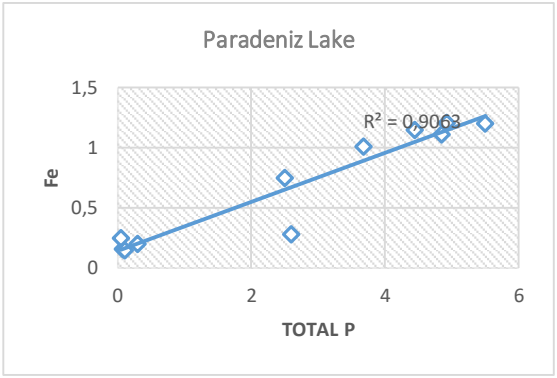

Figure 14. The relationship between of TotalP- Fe ions

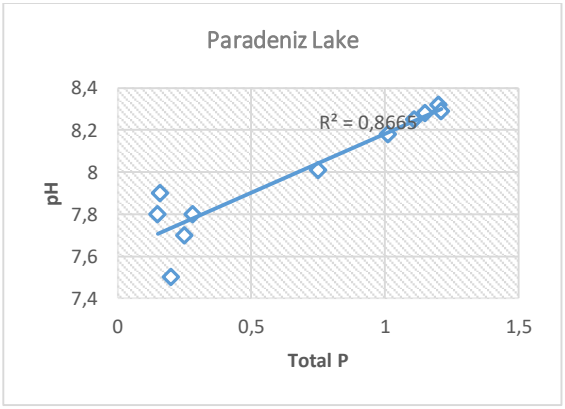

Figure 15. The relationship between of TotalP- pH ions

The seasonal change of the lake phosphorus level is a result of the phosphorus accumulation in sediment. In many shallow lakes, phosphorus is retained in the sediment throughout the winter and is released from the sediment into the lake water with increased biological activity in the spring (Sondergaard et al. 2007). The reason for the increase in phosphorus concentrations in shallow lakes, especially during the summer, is the result of phosphorus loading from sediment (Marsden 1989, Kleeberg and Kozerski 1997, Kisand 2005). It has been reported that phosphorus concentration at sediment-water interface is affected by various factors such as pH, redox potential (Eh), microbial activities and seasonal changes (Eckert et al. 2003, Clavero et al. 1999, Maassen et al. 2003, Topçu 2006).

Iron ions abundance in sediment of aquatic environments is an important factor preventing and controlling phosphorus release from sediment to water. It has been reported that pH is important parameter in lake sediment for interaction between iron and phosphorus. At the high pH values, phosphate bound to Fe (III) hydroxides is released into lake water (Sondergaard 1989, Montigny and Prairie 1993, Eckert et al. 1997). It has been reported that the release of nutrients from the sediment is significantly affected by the pH and the amount released is significantly increased especially if the pH is higher than 8.5-10 values (Moss 1988, Mc Dugall and Ho 1991).

The high pH values were observed in Paradeniz lake in summer. As mentioned in the literature, the high positive relationship between iron and phosphorus can be

explained by the passage of phosphorus retained in iron hydroxides at high pH to water.

4. CONCLUSION

In this study, the water quality change of Paradeniz was investigated depending on years. Especially the change between the years and knowing the reasons of this change will be very effective in making decisions about these areas. For this purpose, water samples were taken 11 times from 2006-2012 in the same place from Lake and Mediternian sea. In the samples; pH, temperature, electrical conductivity (EC), salinity (Sal) and dissolved oxygen(DO), nitrate nitrogen, nitrite nitrogen, ammonium nitrogen, total phosphorus and iron ion were analyzed. The analysis results were compared with limit values (The Surface Water Quality Regulation Annex-5). When the nitrogen and phosphorus results were evaluated, it was found that they exceeded the fourth class water limit values frequently. When the results were examined, it is revealed that water quality decreases generally during the summer months when irrigation is high. This shows that the water quality of Paradeniz Lake is easily affected by agricultural activities and drainage waters.

The statistical studies were determined that was a "very strong negative correlation" between dissolved oxygen and temperature / nitrogen compounds / pH / total P in the Paradeniz Lake. Also, it was determined that was a "a very strong positive correlation" between total phosphorus and pH/ iron ions. The relationship between these parameters and dissolved oxygen/ total phosphorus were determined to be "a very high statistical significance" ($p<0,001$).

The amount of dissolved oxygen and phosphorus in water is very important in determining the water quality and trophic class of the lakes. It is important to know the relationship between these important parameters and other parameters since the Paradeniz lake is in an area that is constantly exposed to pollution. This study contains the data that prepare the ground for determining the trophic class and water quality of the lake. In the future, detailed analysis should be made with samples taken from different points of the lake.

REFERENCES

Acarlı, D., Kara, A., Bayhan, B., Çoker, T. (2009). "Homa Lagünü'nden (İzmir Körfezi, Ege Denizi) Yakalanan Türlerin Av Kompozisyonu ve Av Verimi". *E.Ü. Su Ürünleri Dergisi*, Vol 26, No 1, pp. 39-47.

Barnes R.S.K. (2001). *Lagoon*s, *Encyclopedia of Ocean Sciences* (Second Edition), Editor. Steve J.S., Turekian T. K., Elsevier, Amsterdam

Başıbüyük, M., Evliya, H.(1993)."Göksu Deltası Su Kirlilik Düzeyi Ve Su Kalitesinin Belirlenmesi". *Çukurova Üniversitesi Fen Bilimleri Enstitüsü Ve Mühendislik Bilimleri Dergisi*, Adana, 15.

Beyhan, Mehmet Kacıkoç, Meltem (2009). "Göl Kirliliği ve Su Kalite Modelleri, Su Tüketimi, Arıtma", *Türkiye Sulak Alanlar Kongresi*, Bursa, pp.17-25, 22-23.

Clavero, V., Izquierdo, J.J. Fernandez, J.A. and Niell, F.X. (1999). Influence of bacterial density on the exchange of phosphate between sediment and overlying water. *Hydrobiologia*, 392: 55-63.

Demirel, Z., Özer, Z., Özer O. (2011). "Investıgatıon And Modeling Of Water Quality Of Göksu River (Cleadnos) In An International Protected Area By Using GIS". *Journal Of Geographical Sciences*, vol 21, No.3, pp. 429-440.

Eckert, W., Didenko, J., Uri, E. and Eldar, D. (2003). "Spatial and temporal variability of particulate phosphorus fractions in seston and sediments of Lake Kinneret under changing loading scenario". *Hydrobiologia*, 494: 223-229.

EPA. (1999). *Guidance manual for compliance with the interim enhanced surface water treatment rule*. United States, Environmental Protection Agency, Office of Water (4607) publishing, EPA-815- R-99-010; 201p.

Gonenc, I. E. and Wolflin, J. P.(2005*). Coastal Lagoons: Ecosystem Processes and Modeling for Sustainable Use and Development*.CRC Press, Boca Raton, FL, USA.

Gülçiçek, O. (2018). "Investigation of Water Quality of Akgöl Lake in the Göksu Delta". *Advances in Ecological And Environmental Research* . 4, pp. 1-10.

Gülçiçek, O., Demirel, Z. (2019). "Applying Isotope Techniques and Modeling to Identify the Nitrogen Source in Göksu Delta". *Polish Journal Of Environmental Studies*, 28, 1-17

Gülçiçek, O., Demirel, Z., (2016). "Yüzey ve Yeraltı Sularının Kimyasal Fasiyesinin (Tipinin) Belirlenmesi, Mekâna Bağlı Değişiminin Haritalanması; Göksu Deltası, Türkiye". *International Conference on Natural Science and Engineering* (ICNASE'16), 2016-03-19, 2016-03-20, Kilis, Türkiye.

Karabulut, M. (2015). "Farklı Uzaktan Algılama Teknikleri Kullanılarak Göksu Deltası Göllerinde Zamansal Değişimlerin İncelenmesi". *Uluslararası Sosyal Araştırmalar Dergisi*, **8** (37).

Keçer, M. Duman, Y. T. (2007) "Yapay Etkilerin Göksu Deltası Gelişimine Etkisi, Mersin-Türkiye", *MTA Dergisi*, 134, 17-26.

Kılar H., Çiçek İ.(2018), "Shoreline Change Analysis in Göksu Delta by Using DSAS", *CBD*, 16 (1), pp. 89- 104 .

Kisand, A. (2005). "Distribution of sediment phosphorus fractions in hypertrophic strongly stratified Lake Verevi". *Hydrobiologia*. 547,pp. 33-39.

Kleeberg, A. and Kozerski, H.P. (1997). "Phosphorus release in Lake Graβer Müggelsee and its implications for lake restoration". *Hydrobiologia*, 342/343.pp 9-26.

Kock Rasmussen E, Svenstrup Petersen O, Thompson JR, Flower RJ, Ahmed MH. (2009). "Hydrodynamic-ecological model analyses of the water quality of Lake Manzala (Nile Delta, Northern Egypt". *J Hydrobiol*, 622(1). Pp.195–220

Kumbur, H., Özer, Z., Özsoy H.D. (2004). *Göksu Deltası Özel Çevre Koruma Bölgesinde Su Kalitesinin İzlenmesi Projesi*. Mersin Üniversitesi, Mühendislik Fakültesi Çevre Mühendisliği Bölümü – Silifke Özel Çevre Koruma Müdürlüğü, Mersin, 76 s.

Maassen, S., Röske, I. and Uhlmann, D. (2003). "Chemical and Microbial Composition of sediments in reservoirs with different trophic state". *Internat. Rev. Hydrobiol*, 88(5),pp. 508-518.

Mainstone, C.P., Parr, W., (2002). "Phosphorus in rivers-ecology and management". *The Science of the Total Environment*, 282-283(1-3),pp.25-47.

Marsden, Martin W. (1989). "Lake restoration by reducing external phosphorus loading: the influence of sediment phosphorus release". *Freshwater Biology*, 21 pp. 139-162.

Meriç, Sibel, Kavruk, Seçkin A. (2007). "Göksu deltası Kıyı Yönetiminin Dünü ve Bugünü", *6. Ulusal Kıyı Mühendisliği Sempozyumu*, İzmir-Türkiye.

Minnesota Pollution Control Agency, (2008). *Nutrients: Phosphorus, Nitrogen Sources, Impact on Water Quality – A General Overview*.

ÖÇKK (2009). *Göksu Deltası Özel Çevre Koruma Bölgesi II. Dönem Yönetim Planı*, Ankara: Çevre ve Orman Bakanlığı Özel Çevre Koruma Kurumu.

Özer, O. (2014). Göksu Deltası Yeraltı Suyu Kirliliğinin Belirlenmesi, Modellenmesi Ve Kirletici Kaynakların İzotop Yöntemleri İle Araştırılması, Coğrafi Bilgi Sistemi Oluşturulması, Doktora Tezi, Mersin Üniversitesi.

Phlips, E.J., (2002). *Algae and Eutrophication. In: Bitton, G.(Ed.), Encyclopedia of Environmental Microbiology*. John Wiley and Sons, New York.

Phocaides A. (2000). *Water quality for irrigation, in Technical Handbook on Pressurized Irrigation Techniques* Ch. 7. Rome: FAO;. pp. 79–97.

Sallam G. A., H. , Elsayed, E.A. (2018). "Estimating relations between temperature, relative humidity as independed variables and selected water quality parameters in Lake Manzala, Egypt". *Ain Shams Engineering Journal*, 9(1). Pp.1-14

Singh, A.P., Srivastava P.C., Srivastava, P. (2008). "Relationships of Heavy Metals in Natural Lake Waters with Physico-chemical Characteristics of Waters and Different Chemical Fractions of Metals in Sediments". *Water Air Soil Pollut*. 188 pp. 181-193.

SKKY *Water Pollution Control Regulations, the Sampling, and Methods of Analysis*(WPCR-SMA). (2009). Ministry of Environment and Forestry, Ankara.

Søndergaard, M., Jeppesen, E., Lauridsen, T.L., Skov, C., vanNes, E.H., Roijackers, R., Lammens, E., Portielje, R.,(2007). "Lake restoration: Successes, failures and long-termeffects". *Journal of Applied Ecology*, 44(6):1095-1105

Sönmez, A.Y., Hisar, O., Karataş, M., Arslan, G. and Aras, M.S. (2008). *Sular Bilgisi*. Nobel Yayın Dağıtım A.Ş. Ankara.

Spears, B.M., Carvalho, L., Perkins, R. (2008). "Effects of light on sediment nutrient flux and water column nutrient stoichiometry in a shallow lake". *Water Research* 42 (4–5), pp. 977–986.

Spellman (2014). *Handbook of water and wastewater treatment plant operations, 3rd edn*. Taylor and Francis group, ISBN: 978-1-4665-5385-5

Thomann, R.V., Mueller, J.A. (1987). *Principle of surface water quality modelling and control*. Harper and Row Publishers. 644. New York.

Topçu A.(2006). Mogan Gölü Litoral Sedimentte Fosforun Mevsimsel ve Yersel Değişimi ile Göle Salınım Potansiyelinin Araştırılması. Doktora Tezi, Ankara Üniversitesi Fen Bilimleri Enstitüsü Su Ürünleri Anabilim Dalı.

Ünlü, A., Çoban, F.,Tunç, M. S., (2008). "Hazar Gölü Su Kalitesinin Fiziksel Kimyasal Parametreler Açısından İncelenmesi". *Gazi Üniversitesi Müh.Mm. Fak. Der*. vol:23 No:1,pp. 119-127.

Xia, J., Zhang, Y.Y. (2008). "Water security in North China and countermeasure to climate change and human activities". *Physics and Chemistry of the Earth* **33**, 359–363.

Xu, L., Hua Li, Xinqiang L., Yuxin Y., Li Z., Xinyi C. (2012). "Water quality parameters response to temperature change in small shallow lakes". *Physics and Chemistry of the Earth* 47–48, pp.128–134.

Yerüstü Su Kalitesi Yönetmeliği (Surface Water Quality Regulation), (2016). Orman Ve Su İşleri Bakanlığı, Resmi gazete sayı 29797.

CISET - 2nd Cilicia International Symposium on Engineering and Technology
10-12 October, 2019, Mersin / TURKEY

A CRITICAL LOOK TOWARDS DESIGN OF ANCHORED RETAINING WALLS IN ACCORDANCE WITH TURKEY'S NEW EARTHQUAKE DESIGN CODE

Özgür L. ERTUĞRUL[*1],Fatma DÜLGER CANOGULLARI[2]

[1] Assoc, Prof.Dr., Mersin University, Faculty of Eng., Dept. of Civil Eng., Mersin, Turkey, ertugrul@mersin.edu.tr

[2] Grad. Student, Mersin University, Faculty of Eng., Dept. of Civil Eng., Mersin, Turkey, fatma.dulger@toros.edu.tr

ABSTRACT

Earthquakes can be considered as one of the most devastating natural hazards causing widespread damage in our country as well as in the world. Worldwide earthquake resistant building and design codes have been periodically revised and updated depending on improvements in the field of earthquake engineering. In recent years earthquake design code of Turkey have taken comprehensive revisions and updated version has become effective at the beginning of 2018. Within this study, design aspects of earth retaining walls according to new design code were critically reviewed in the light of numerical analysis results. The calculation methods of the anchored retaining structures proposed in the Turkey's Earthquake Code are investigated and compared with the outputs of analyses performed by Plaxis finite element modeling software for soil analyses.

Keywords: *Earthquake design code, Anchored retaining structures, finite element modeling*

[*] Corresponding Author

1. INTRODUCTION

According to Turkey's earthquake design code, limit balance (collapse) and service conditions should be considered in the design of the retaining structures under seismic effects. Retaining structures should be designed in such a way as to allow displacements in proportions that do not harm the design objectives after the earthquake. The calculations are performed based on the seismic soil pressure approach. Seismic thrust acting on a specific retaining structure is calculated using the methodology proposed by Mononobe-Okabe in 1929. Total thrust is expressed as the combination of the active static and seismic incremental thrust acting during an earthquake event. Horizontal and vertical seismic earthquake coefficients are determined considering the short spectrum displacement (S_{ds}) values for a given site combined with a coefficient (r) indicating the type of the retaining wall and the allowable displacement level. Within the scope of this study, seismic thrust values are calculated for an anchored retaining wall based on new earthquake code and results were compared with the outputs of numerical analyses performed with Plaxis 2D.

2. EARTHQUAKE HAZARD MAPS

Updated earthquake hazard map of Turkey is given in Fig.1. The new map is prepared with massive and detailed data considering the most recent earthquake source parameters, earthquake catalogs and new generation mathematical methods. Unlike the previous map, the new map shows the largest ground acceleration values rather than earthquake zones and replaces the "earthquake zone" concept. The new map was prepared as a part of project entitled "Update of Turkey's Seismic Hazard Map" supported by the AFAD National Earthquake Research Program (UDAP) and carried out in cooperation with public and private universities. The interactive version of the earthquake hazard map is available in AFAD's website.

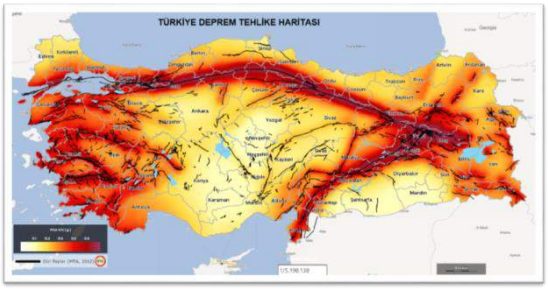

Figure 1. Turkey's Earthquake Hazard Maps

Earthquake ground motion levels in recent Earthquake Code is shown in Table 1.

Table 1. The elevations of earthquake ground motion

Earthquake Ground Motion Levels(EGM)	Probability of exceedance in 50 years	Return Period	Occurrence Probability
Level-1	2%	2475 years	very rare
Level-2	10%	475 years	rare
Level 3	50%	72 years	often
Level 4	68%	43 years	very often

3. NEW SOIL CLASSES IN TURKEY'S EARTHQUAKE CODE

The local soil classes to be used in the identification of earthquake design spectra is shown in Table 2.

Table 2. Local Soil Classes in Turkey's Earthquake Code (simplified)

Local Soil Classes	Average at the top 30 meters $(V_s)_{30}$[m/s]	$(N_{60})_{30}$	$(c_u)_{30}$
ZA	>1500	-	-
ZB	760-1500	-	-
ZC		>50	>250
ZD		15-50	70-250
ZE	<180	>15	>70
ZF	Requires site-specific investigations		

The average shear wave velocity at the top 30 meters, the average number of standard penetration impacts and the average undrained shear strength will be calculated by Eq. (1), Eq. (2) and Eq. (3):

$$(V_s)_{30} = \frac{30}{\sum_i^N (\frac{h_i}{V_{s,i}})} \quad (1)$$

$$N_{60})_{30} = \frac{30}{\sum_i^N (\frac{h_i}{N_{60,i}})} \quad (2)$$

$$(c_u)_{30} = \frac{30}{\sum_i^N (\frac{h_i}{c_{u,i}})} \quad (3)$$

where h_i is the thickness of layer [m], $(V_s)_{30}$, $(N_{60})_{30}$ and $(c_u)_{30}$, respectively, the shear wave velocity of the same layer [m / s], standard penetration test shows the number of impacts [impact / 30 cm] and undrained shear strength [kPa].

4. STANDARD EARTHQUAKE GROUND MOTION SPECTRA

Earthquake ground motion spectra are defined for a 5% damping rate based on a given earthquake ground motion level.

4.1. Location based Spectral Acceleration and Design Spectral Acceleration Coefficients

Location based spectral acceleration coefficient for short period; S_s, spectral acceleration coefficient for one second period; S_1 and the design spectral acceleration coefficients S_{DS} and S_{D1} are calculated by Eqs. (4) and (5) respectively:

$$S_{DS}=S_S F_S \quad (4)$$

$$S_{D1}=S_1 F_1 \quad (5)$$

where F_S and F_1 are coefficients of local site conditions that are shown in Tables 3 and 4.

Table 3. Local site correction coefficient for short period; F_S

Local Site Classes	Local site coefficients for short period; F_S					
	$S_S \leq 0.25$	$S_S = 0.50$	$S_S = 0.75$	$S_S = 1.00$	$S_S = 1.25$	$S_S \geq 1.50$
ZA	0.8	0.8	0.8	0.8	0.8	0.8
ZB	0.9	0.9	0.9	0.9	0.9	0.9
ZC	1.3	1.3	1.2	1.2	1.2	1.2
ZD	1.6	1.4	1.2	1.1	1.0	1.0
ZE	2.4	1.7	1.3	1.1	0.9	0.8

ZF	Site specific soil behavior analysis required.

Table 4. Local site correction coefficient for one second period; F_1

Local Site Classes	local ground effect coefficient for 1.0 second period; F_1					
	$S_1 \leq 0.10$	$S_1 = 0.20$	$S_1 = 0.30$	$S_1 = 0.40$	$S_1 = 0.50$	$S_1 \geq 0.60$
ZA	0.8	0.8	0.8	0.8	0.8	0.8
ZB	0.8	0.8	0.8	0.8	0.8	0.8
ZC	1.5	1.5	1.5	1.5	1.5	1.4
ZD	2.4	2.2	2.0	1.9	1.8	1.7
ZE	4.2	3.3	2.8	2.4	2.2	2.0
ZF	Site specific soil behavior analysis required.					

4.2. Horizontal Elastic Design Spectrum

The horizontal elastic design spectral accelerations, which are the ordinates of the horizontal elastic design acceleration spectrum, are defined in Eqs. (6), (7), (8) and (9) in gravitational acceleration (g) unit depending on the natural vibration period (T).

$$S_{ae}(T) = \left(0.4 + 0.6\frac{T}{T_A}\right) S_{DS} \qquad (0 \leq T \leq T_A) \qquad (6)$$

$$S_{ae}(T) = S_{DS} \qquad (T_A \leq T \leq T_B) \qquad (7)$$

$$S_{ae}(T) = \frac{S_{D1}}{T} \qquad (T_B \leq T \leq T_L) \qquad (8)$$

$$S_{ae}(T) = \frac{S_{D1}T_L}{T^2} \qquad (T_L \leq T) \qquad (9)$$

where A and B are design spectral acceleration coefficients, T is the natural vibration period.

T_A and T_B are calculated using Eqs. (10) and (11):

$$T_A = 0.2\ \frac{S_{D1}}{S_{DS}} \qquad (10)$$

$$T_B = \frac{S_{D1}}{S_{DS}} \qquad (11)$$

The transition period to the fixed displacement zone is taken as T_L = 6 s.

5. RETAINING STRUCTURES

Limit balance (collapse) and service conditions should be considered in the design of the retaining structures under seismic effects. Retaining structures should be designed in such a way as to allow displacements in proportions that do not harm the design objectives after the earthquake.

5.1. Stability of Retaining Structures

For the stability of the retaining structures, safety condition against overturning moment must be satisfied according to Eq.12:

$$E_{dev} \leq \frac{R_{dev}}{\gamma_{Rdev}} \qquad (12)$$

where E_{dev} is the overturning moment, R_{dev} is the resisting moments against overturning and γ_{Rdev} is the factor of safety against overturning. The factor of safety against overturning should be greater than or equal to 1.3 according to the Earthquake Code.

Bearing capacity and sliding stability controls of retaining wall foundations are performed similarly with those of the shallow foundations.

5.2. Bearing Capacity Control for the Foundations of Retaining Structures

In shallow foundations, equality which calculated by Eq. (13) should be ensured in static and earthquake conditions.

$$q_0 \leq q_t \qquad (13)$$

where q_0 is vertical load affecting at foundation levels (base pressure of foundation), q_t is design strength.

$$q_t = \frac{q_k}{\gamma_{Rv}} \qquad (14)$$

where γ_{Rv} is strength coefficient of foundation bearing capacity. Characteristic strength of foundation bearing capacity (q_k) and coefficients of bearing capacity (N_q, N_c, N_γ) are calculated by Eqs. (15), (16) and (17);

$$q_k = cN_c s_c d_c i_c g_c b_c + qN_q s_q d_q i_q g_q b_q + 0.5\gamma B' N_\gamma s_\gamma d_\gamma i_\gamma g_\gamma b_\gamma \qquad (15)$$

$$N_q = e^{\pi \tan\Phi'} \tan^2\left(45 + \frac{\Phi'}{2}\right)\ ;\ N_c = (N_q - 1)\cot\Phi' \qquad (16)$$

$$N_\gamma = 2(N_q - 1)\tan\Phi' \qquad (17)$$

where s_c, s_q, s_γ are shape coefficients; d_c,d_q,d_γ are depth coefficients; i_c,i_q,i_γ are load inclination coefficients; g_c,g_q,g_γ are foundation ground coefficients; b_c,b_q,b_γ are foundation base coefficients.

The presence of varying layers and discontinuities in the effective foundation depth shall be considered in the bearing capacity calculations. Displacements under the foundation will remain within allowable limits. Therefore; displacements will be calculated by using generally accepted geotechnical engineering approaches considering the increase of pore water pressure under cyclic loading and possible strength and stiffness loss in soft clays and saturated loose-medium dense cohesionless soils under earthquake impact. Residual deformations will be calculated by taking into account the nonlinear soil behavior that may occur under shallow foundations in the soil of high rise buildings which except ZA and ZB soil classes and the soil of other buildings with Earthquake Design Class=1,1a,2,2a which except ZA, ZB, ZC soil classes.

5.3. Horizontal Sliding of Shallow Foundations

For a combination of static and seismic loads Eq. (18) should be satisfied:

$$V_{th} \leq R_{th} + 0.3R_{pt} \qquad (18)$$

where V_{th} is design horizontal force affecting on the foundation base, R_{th} is design friction resistance and R_{pt} is design passive resistance.

Design friction resistance in drained soil conditions is calculated by Eq. (19):

$$R_{th} = \frac{P_{tv} \tan\delta}{\gamma_{Rh}} \quad (19)$$

where P_{tv} is design vertical pressure force acting on the foundation base, δ is friction angle between the foundation base and the soil and γ_{Rh} is strength reduction coefficient for friction resistance.

The coefficient of friction (tan δ) should not be greater than the values given in Table 5, unless otherwise determined by field tests.

Table 5. The coefficient of friction (tan δ)

Interface of friction	tan δ
in-situ concrete- Pressed Foundation base ground	0.6
precast reinforced concrete - Pressed Foundation base ground	0.4
in-situ concrete- concrete	0.5
concrete- base rock	0.5

Design friction resistance of cohesive soils at undrained conditions is calculated by Eq. (20):

$$R_{th} = \frac{A_c C_u}{\gamma_{Rh}} \quad (20)$$

where A_c is total contact area under foundation where compressive stresses occur. The design passive resistance (R_{pt}) shall be calculated by dividing the characteristic passive resistance (R_{pk}) by the strength reduction coefficient of passive resistance(γ_{Rp}):

$$R_{pt} = \frac{R_{pk}}{\gamma_{Rp}} \quad (21)$$

For foundations below ground water level, the design friction resistance in seismic conditions will be calculated based on the undrained shear strength of the ground.

5.4. Earth Pressures

Horizontal and vertical static-equivalent earthquake coefficients (k_h and k_v) to be used in the calculation of earth pressures are defined in Eq.(22).

$$k_h = \frac{0.4 S_{DS}}{r} \quad ; \quad k_v = 0.5 k_h \quad (22)$$

where r is the coefficient given in Table 6 for different retaining structures.

Table 6. The coefficient, r

Type of retaining structure	r
gravity retaining walls which have been allowed to displace up to $120S_{DS}$ (mm)	2.0
gravity retaining walls which have been allowed to displace up to $80S_{DS}$ (mm)	1.5
anchored retaining walls, gravity retaining walls which have been not allowed to displace	1.0

Total earth pressure (static+dynamic) is calculated as:

$$P_t = K(1 \mp k_v)\left(\frac{1}{2}\gamma^* H^2 + qH\right) + P_{su} + \Delta P_{su} \quad (23)$$

Where K is the coefficient of total earth pressure (static+dynamic), γ^* is the typical unit weight of soil, H is the wall depth, q is the surcharge load, P_{su} and ΔP_{su} are resultant static and dynamic water pressures.

Total active pressure coefficient will be calculated by Eq. (23) and Eq. (24):

- if $\beta \leq \varphi_{d'} - \theta$ is;

$$K_a = \frac{sin^2(\psi + \phi'_d - \theta)}{cos\theta\, sin^2\psi \sin(\psi - \theta - \delta_d)\left[1 + \sqrt{\frac{\sin(\phi'_d + \delta_d)\sin(\phi'_d - \beta - \theta)}{\sin(\psi - \theta - \delta_d)\sin(\psi + \beta)}}\right]^2} \quad (23)$$

- if $\beta > \varphi_{d'} - \theta$ is;

$$K_a = \frac{sin^2(\psi + \phi'_d - \theta)}{cos\theta sin^2\psi \sin(\psi - \theta - \delta_d)} \quad (24)$$

assuming that there is no friction between the base soil and the wall foundation, the total passive pressure coefficient will be calculated by Eq. (25):

$$K_p = \frac{sin^2(\psi + \phi'_d - \theta)}{cos\theta\, sin^2\psi \sin(\psi + \theta)\left[1 - \sqrt{\frac{\sin\phi'_d \sin(\phi'_d + \beta - \theta)}{\sin(\psi + \theta)\sin(\psi + \beta)}}\right]^2} \quad (25)$$

where ϕ'_d is the design angle of shearing resistance of soil, δ_d is the soil-wall frictional angle, β is the slope angle of backfill to horizontal, ψ is the angle of wall stem to horizontal. θ and γ^* values varies depending on whether there is water behind the retaining structure.

In static conditions θ is regarded as 0. Seismic earth pressure coefficient will be obtained by subtracting the static pressure coefficient from the total pressure coefficient.

5.5. Effect of Water Level Behind Retaining Structure

Drainage conditions play an important role in design of retaining structures. There should not be groundwater in the backfill. However, if there is water table, this should be considered in the calculations.

Unit weight of the soils should be modified when groundwater exists. Following conditions should be addressed in the design. If water table is below the foundation base then:

$$\theta = tan^{-1}\left[\frac{k_h}{1 \mp k_v}\right] \quad ; \quad \gamma^* = \gamma \quad (26)$$

If the water table is above foundation level and For backfill permeability coefficient is less than $5x10^{-4}$ m/s and $\Delta P_{su} = 0$:

$$\theta = tan^{-1}\left[\frac{\gamma_d}{\gamma_d - \gamma_{su}}\frac{k_h}{1 \mp k_v}\right] \quad ; \quad \gamma^* = \gamma_d - \gamma_{su} \quad (27)$$

Where γ_d is saturated unit weight of soil. If the water level is above the base level and the floor is dynamically permeable:

$$\theta = tan^{-1}\left[\frac{\gamma}{\gamma_d - \gamma_{su}}\frac{k_h}{1 \mp k_v}\right] \quad ; \quad \gamma^* = \gamma_d - \gamma_{su} \quad (28)$$

Static-equivalent dynamic water force and depth of resultant force from water surface are calculated as:

$$\Delta_{p_{su}} = \frac{7}{12}(0.4S_{DS})\gamma_{su}d_{su}^2 \quad ; \quad z^- = 0.6d_{su} \qquad (29)$$

Where d_{su} is the height of the wall under water and γ_{su} is unit weight of water.

6.ANALYSIS OF RETAINING STRUCTURES

The calculation methods of the anchored retaining structures proposed in the Turkey's Earthquake Code are investigated and compared with the outputs of analyses performed by PLAXIS finite element modeling software for soil analyses.

6.1. Numerical Modeling

In this study, anchored retaining structures modeled by using PLAXIS (2D)**.** Soil, plate and anchor parameters are given in the Tables 7, 8 and 9.

Table 7. Soil properties

Parameter	value
γ_{unsat}	18.7 kN/m³
γ_{sat}	18.7 kN/m³
E_{ref}	$2.5x10^4$ kN/m²
ν	0.400
c_{ref}	0.0171 kN/cm²
φ	36°
YASS	1.5 m

Table 8. Plate properties

Parameter	value
EA	$1.94x10^7$ kN/m
EI	$4.77x10^5$ kN/m²
υ	0,2
Distributed load	10 kN/m²

Table 9. Anchor properties

Parameter	value
EA	$1.46x10^8$ kN
L spacing	1,20 m
Material type	Elastic

For the analyses, soil class is considered as ZD and EGM level is taken as 2. Model geometry in Plaxis is given in Figure 2.

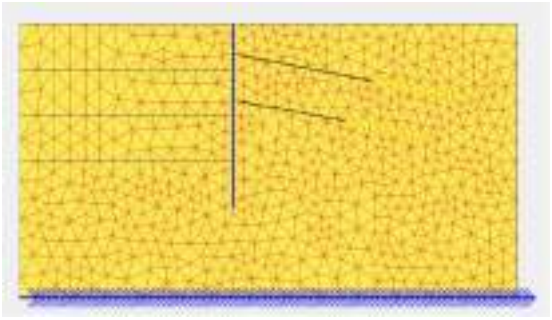

Figure 2. Model geometry

Adana Ceyhan 1998 Earthquake acceleration (east-west direction) record is used as the base input motion (Figure 3). Adana Ceyhan acceleration time history was obtained from AFAD's website.

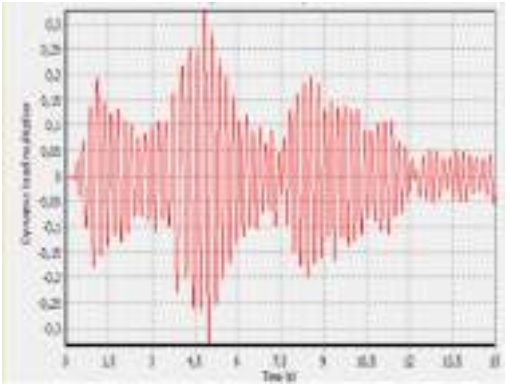

Figure 3. Adana Ceyhan acceleration time history

Equivalent force, shear force and bending moment graphs obtained from the dynamic analyses are given in Figs. 4, 5 and 6.

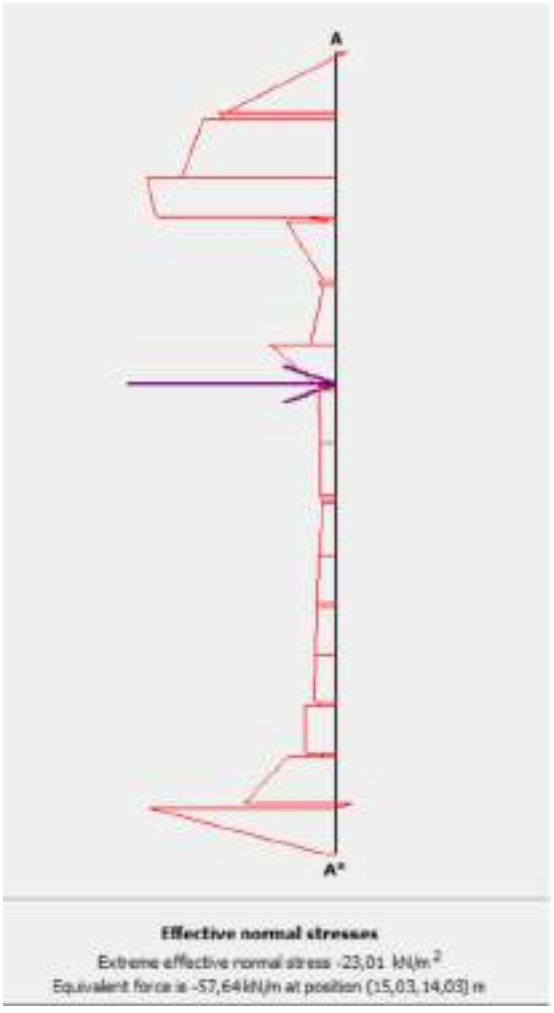

Figure 4. Equivalent force graph

According to numerical analyses results, equivalent force, shear force and bending moment values are determined as 57.64 kN/m, 23.15 kN/m and 48.66 kNm/m .

Figure 5. Envelope of shear forces

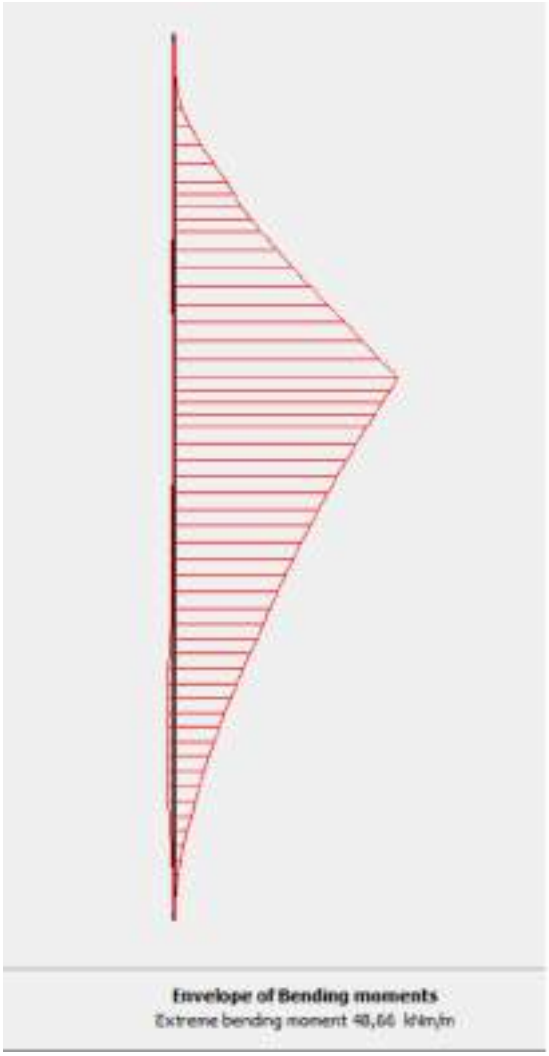

Figure 6. Envelope of bending moment

6.1. Design Approach Based on Turkey's Earthquake Code.

The preliminary design of the retaining wall is performed based on the formulations given in Turkish Earthquake Code. The input parameters used in the calculations are provided in Table 10.

Table 10. Parameters of Turkey's Earthquake Code

Parameter	Values
S_{DS}	0.45
kv	0.18
kh	0.09
r	1.0
θ	23.03°
Ka	0.64
Psu	281.25 kN/m
Pa	589.83 kN/m

When the results are compared for the numerical analyses and calculations based on earthquake code, it was observed that equivalent force value is higher than the value obtained from numerical analyses. Since formulations in the earthquake code are based on a pseudo-static approach, calculations are made considering constant acceleration coefficient. On the other hand, with Plaxis software, real time dynamic analyses are performed by using a selected acceleration time history. Application of a constant lateral earthquake force causes higher lateral earth loads.

4. CONCLUSION

In the design of retaining walls to be constructed in earthquake zones, dynamic soil pressures should be taken into consideration as well as static soil pressures. In this study, the design methodology of anchored retaining structures under seismic effects were investigated for the Turkey's new Earthquake Code and results were compared with the predictions made by numerical analyses performed by Plaxis software. It was observed that the design methodology suggested in the Turkish Earthquake Code is conservative and may lead to uneconomical design in some cases. Additional numerical analyses should be performed for the final design of anchored retaining walls.

REFERENCES

Örnek, M., Laman, M., Yıldız, A., Demir, A. and Tekinsoy, M.A. Numerical Analyses of Anchored Shoring Systems. http://www.imo.org.tr/resimler/ekutuphane/pdf/1518.pdf [Accessed 20 August 2019].

Plaxis (2D), Version 8, The Netherlands.

Silva, J.M. (2010). "Diaphragm Walls Seismic Design According to the Eurocodes" *Fifth International Conference on Recent Advances in Geotechnical Earthquake Engineering and Soil Dynamics*, San Diego, California, pp.1-3.

TDY (2018) *Rules for Design of Retaining Structures on Earthquake Impact* ,Turkish Standard Institute, Ankara, Turkey.

Turkey's Earthquake Hazard Maps, https://tdth.afad.gov.tr/ [Accessed 15 August 2019].

CISET - 2nd Cilicia International Symposium on Engineering and Technology
10-12 October, 2019, Mersin / TURKEY

AN INVESTIGATION ON THE GEOMECHANICAL PROPERTIES OF FIBER REINFORCED COHESIVE SOILS

Özgür L. ERTUĞRUL[*1],Fatma DÜLGER CANOGULLARI[2]

[1] Assoc, Prof.Dr., Mersin University, Faculty of Eng., Dept. of Civil Eng., Mersin, Turkey, ertugrul@mersin.edu.tr

[2] Grad. Student, Mersin University, Faculty of Eng., Dept. of Civil Eng., Mersin, Turkey, fatma.dulger@toros.edu.tr

ABSTRACT

In recent years, the use of fiber in soil improvement has become widespread. Easy to use and low cost fibers have been the subject of many geotechnical researches. In this study, results of experiments on fiber - added cohesive soils were reviewed in a systematical approach. Based on the data derived from the experimental studies in the literature, it has been observed that the strength of the soil and various soil properties have increased with increasing density of the fibers. The percentage of added fiber has a significant effect on improving soil properties. Simple correlation relationships were suggested based on the investigated test database.

Keywords: *Fiber, Soil improvement, Cohesive soil*

[*] Corresponding Author

1. INTRODUCTION

In recent years, soil reinforcement with synthetic and natural fibers are gaining importance. The use of natural fibers, such as bamboo, jute and coir as soil reinforcing materials has been prevalent for a long time in several South Asian nations. Synthetic fibers such as polypropylene, polyester, polyethylene and glass fibers have also been used for soil reinforcement (Mali and Singh,2014).

Since the fibers have higher tensile strengths than natural cohesive soils, fiber-ground mixtures can achieve much greater shear strength values than fiber-free soils. Fibers are thought to be efficient, especially on soils close to the surface where effective tensile and shear strength is low.

2. GENERAL PROPERTIES OF FIBERS

Fibers, which have been used for soil reinforcement, have many advantages (Darvishi, 2014):

- Mixing fibers with the ground is as easy as mixing other materials such as cement and lime used for stabilization.
- If homogeneous mixing is achieved, the fibers provide isotropic strength in the ground.
- Environment conditions have a low impact on fiber reinforced soils.

2.1. General Properties of Polypropylene Fibers

Polypropylene fibers are low cost products having good impact resistance. They have low friction coefficients and provide very good electrical insulation. Besides, polypropylene fibers have good chemical resistance. Although polypropylene fibers melt at 160-170°C, they maintain most of their mechanical properties. Polypropylene fibers are resistant to strong acids and bases. They retain their rigidity even after many bends. On the other side, polypropylene has some disadvantages such as low UV resistance, high thermal expansion, low weather resistance and oxidation susceptibility.

3. LITERATURE REVIEW

Maher and Ho (1994) reported results for randomly mixed fibers with kaolinite clay tested using unconfined compression. The results provided evidence that fibers increased the compressive strength of the soil, as well as the ductility (the amount of deformation before failure) and toughness of the soil.

Nataraj and McManis (1997) investigated the strength and deformation characteristics of soils reinforced with randomly distributed fibrillated fibers. The laboratory tests were conducted on a cohesive soil. The main properties of the sand tested in this study are shown in Table 1.

Table 1. Properties of the clay

Properties of the clay					
Liquid limit (%)	Plastic limit (%)	Plasticity index (%)	c (kPa)	ϕ (°)	w_{opt} (%)
44	18	26	84	19.5	17.9

The fibers used in this study are 25 mm long and are produced by American Synthetic Industry Corporation. In many studies, the diameter, strength or type of fiber was considered, but in this study, same type of fibers were used throughout the experimental study. Fibers were mixed into the soil by hand or by mechanical mixer. In this study, the mixture of soil and fibers was taken to a large metal pan and uniformly mixed by adding a certain amount of water. Fiber density was examined as 0.1%, 0.2% and 0.3% of dry soil weight.

In the compaction tests, the relationship between dry unit weight and moisture density was investigated by comparing fiber reinforced and non-reinforced soils. The increase in fiber density increased the dry unit volume weight slightly and decreased the moisture density. The clay specimens were compacted with a 178 N tamp in 3 layers using 30 blows per layer.

Clay specimens were prepared at maximum dry unit weight and optimum moisture ratio and they were subjected to unconfined compression tests. Three different size specimens were tested (33mmx72 mm, 70 mm x 140 mm, and 100 mm x 117 mm).

The strength of all reinforced clay specimens increases with increasing moisture content. The strength of clay samples with a fiber content of 0.2% and 0.3% is significantly higher than that of a sample with a fiber content of 0.1%.

Clay specimens with and without fibers were subjected to direct shear tests in 64 mm and 100 mm cutting boxes. The specimens were prepared at maximum dry unit weight and optimum moisture content. The clay specimens which have 0.3% fiber content reached higher shear stress values than the other specimens. California Bearing Ratio tests were conducted on reinforced and unreinforced clay specimens at maximum dry densities and moisture contents (ASTM D 698).

The CBR value for the unreinforced clay specimen increased from 8.44 to approximately 12.6 for specimens with a 0.3% fiber content.

Puppala and Musenda (2000) conducted unconfined compressive tests using Irving (PI = 55) and San Antonio (PI = 46) clays. The results indicated increased strength and ductility of the soil with increasing fiber content. The effect of fiber length was also evaluated and it was found that as the length of the fibers was increased from 1 inch to 2 inches, the strength and axial strain at failure also increased.

Abdi *et al*. (2008) studied the consolidation settlement and swelling characteristics of clays with inclusion of 5, 10, and 15 mm polypropylene fibers at fiber content of 1%, 2%, 4% and 8% by weight of dry soil. They concluded that addition of randomly distributed polypropylene fibers resulted in reducing the consolidation settlement of the clay soil. Length of fibers had an insignificant effect on this soil characteristic, whereas fiber contents proved more influential and effective. Inclusion of polypropylene fibers to the clay soil resulted in reducing the amount of swelling

after unloading. The effect was proportional to the fiber content. But at constant fiber contents, the amount of swelling was not significantly affected by increasing fiber length.

Mahmood et al investigated the effect of fibers on the consolidation settlement, swelling, hydraulic conductivity, shrinkage limit and cracking properties of cohesive soils. The soil had a liquid limit of 110%, plastic limit of 29%, plasticity index of 81%, shrinkage limit of 21% and specific gravity of 2.68. The fibers used in this research are 5, 10 and 15 mm long and have a density of 1, 2, 4 and 8% of dry unit weight. Consolidation settlement of the specimen was calculated before fiber addition. This value was accepted as the reference value (2,6 mm – 7,5 mm). Consolidation settlements in the clay specimen depend on fiber length, density and consolidation pressure. It has been found that fiber length does not have much effect on swelling property, but increasing fiber density reduces swelling amount. According to this study, it can be said that an increase in fiber length increases hydraulic conductivity. Besides, hydraulic conductivity increases with increasing fiber density at fixed length.

The shrinkage limit calculated before the fiber addition is 21%. The shrinkage limit of 15 mm fiber length and 4% fiber density was calculated as 33%. Therefore, less volume change is expected due to drying.

Jiang *et al*. (2010) performed tests on a cylindirical clayey soil sample of 61.8 mm diameter. Fibers of 0.02-0.05 mm diameter and 15,20 and 25 mm length were mixed at 0%-0.4% densities and a series of shear strength experiments were performed. At the end of the experiments, it was observed that the cohesion value and the internal friction angle increased with increasing fiber density and length.

Test data obtained from many experimental studies available in the literature were compiled in Table 2 and graphs were presented with a series of regression equations. In the regression equations LL denotes the liquid limit of the soil and d_f denotes the fiber density in percent.

Table 2. Test results from recent studies

LL/PL ratio	Fiber density (%)	c (kPa)	ϕ(°)
36.4/18.6	0	75,5	27,5
Study-1	0.05	95,9	28,2
	0.15	103	29,7
	0.25	115,6	31,6
44/18	0	84	19,5
Study-2	0.3	122,5	32
50/21	0	40	26
Study-3	0.1	90	30.1
	0.2	90	40.9
	0.3	95	44.1
	0.4	96	44.4
	0.5	50	52
65/27.6	0	97	27.3
Study-4	1	105	34.2
	2	109.9	36.3
	3	103.7	37.1
	4	100.6	37.3
72/29.9	0	160.9	20.3
Study-5	1	163.2	25.6
	2	168	27.4
	3	163	28.1
	4	149	28.5
78.58/31.5	0	185	17.4
Study-6	1	190.4	22.5
	2	194	24
	3	190	24.7
	4	188	25.3
52.9/27.5	0	59	5.5
Study-7	0.2	70	18.65
	0.5	76	26.58
	1	64	23.65
	1.5	62	13.69
26.93/20.19	0	49.16	34.07
Study-8	0.1	94.01	35.71
	0.2	138.29	36.36
	0.3	228.35	35.95

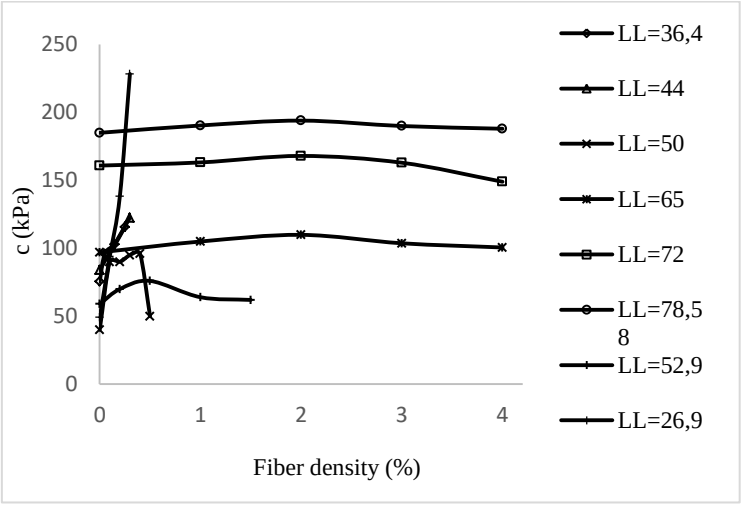

Figure 1. Effect of soil – fiber density on cohesion

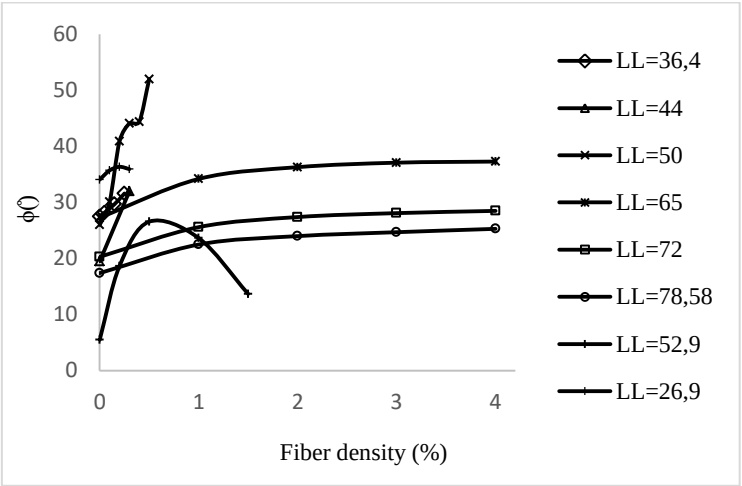

Figure 2. Effect of the soil – fiber density on the friction angle

Considering the data for the effect of fiber density on the cohesion, following regression model was fitted:

$$c = \alpha + \beta*(LL) + \gamma*(d_f) + \varepsilon*(LL)^2 + \lambda*(LL)*(d_f) + \delta*(d_f)^2 \quad (1)$$

Coefficients (with 95% confidence bounds):

α= -1825 (-2313, -1337)
β = 48.82 (35.18, 62.45)
γ= 9.617 (-9.954, 29.19)
ε = -0.2957 (-0.3906, -0.2007)
λ = -0.01199 (-0.2748, 0.2508)
δ = -2.26 (-3.492, -1.029)

On behalf of the goodness of fit, R-square value is found as 0.9943.

Considering the data for the effect of fiber density on the internal friction angle of soil, following regression model was fitted:

$$\Phi = \zeta + \eta*(LL) + \theta*y + \xi*(LL)^2 + \psi*(LL)*(d_f) + \omega*(d_f)^2 \quad (2)$$

Coefficients (with 95% confidence bounds):

ζ = 351.6 (235.3, 467.9)
η = -8.434 (-11.68, -5.185)
θ = 7.841 (3.179, 12.5)
ξ = 0.05324 (0.03063, 0.07586)
ψ = -0.03508 (-0.09769, 0.02754)
ω = -0.8338 (-1.127, -0.5404)

On behalf of the goodness of fit, R-square value is found as 0.9877.

4. CONCLUSION

Clays are known for their high compressibility and low shear strength. Previous studies have mainly evaluated the effects of additives such as sand, cement and lime on these properties of clay and the results have shown that soil properties have improved. In recent years, the use of fiber in soil improvement has become widespread. Easy to use and low cost fibers have been the subject of many geotechnical researches. Since the fibers have higher tensile strengths than natural cohesive soils, fiber-ground mixtures can achieve much greater shear strength values than fiber-free soils. The over-all effects of random fiber inclusion on clays observed, suggests potential applications of fiber reinforced soils in shallow foundations, embankments over soft soils, liners, covers and other earthworks that may suffer excessive deformations.

In this study, results of experiments on fiber - added cohesive soils are investigated. Test data obtained from many previous studies available in the literature were compiled within the scope of this study and graphs were presented with a series of regression equations. According to the performed analyses, it was been observed that the consolidation settlement of clayey soils mixed with polypropylene fibers were decreased considerably. Fiber length has a small effect on this soil property, while fiber density has been observed to be quite effective on the mechanical and consolidation characteristics of the untreated soil.

REFERENCES

Abdi, M.R., Parsapajouh, A. and Arjomand, M.A. (2008). "Effects of Random Fiber Inclusion on Consolidation, Hydraulic Conductivity, Swelling, Shrinkage Limit and Desiccation Cracking of Clays" *International Journal of Civil Engineering*, Vol.6, No.4, pp.284-292.

Cetinkaya M. (2012)Polipropilen Liflerin Uçucu Kül Zemin Karışımlarında Geoteknik Özelliklere Etkisi,MSc Thesis, İstanbul Tecnical University, Istanbul, Turkey.

Freilich, B. J., Li, C., and Zornberg, J. G. (2010) "Effective Shear Strength of Fiber-Reinforced Clays " *9th International Conference on Geosynthetics*, Brazil, pp. 1997-2000.

Girija, K.M. (2013). "Behaviour Of Randomly Distributed Fiber-Reinforced Soil" *International Journal of Research in Engineering and Technology*, pp.456-458.

Kar, K.R., Pradhan, P.K. and Naik, A. (2012). "Consolidation Characteristics of Fiber Reinforced Cohesive Soil" *The Electronic Journal of Geotechnical Engineering* , Vol. 17, pp. 3861-3874.

Li , J. , Tang, C., Wang D., Pei , X. and Shi, B. (2014) "Effect of discrete fibre reinforcement on soil tensile strength" *Journal of Rock Mechanics and Geotechnical Engineering*, Vol.6,pp. 133-137.

Mali, S. and Singh, B. (2014). "Strength Behaviour of Cohesive Soils Reinforced with Fibers." *International Journal of Civil Engineering Research*, Vol. 5, No. 4, pp.353-360.

Naeini, S.A., Sadjadi S. M. (2008). "Effect of Waste Polymer Materials onShear Strength of Unsaturated Clays" *The Electronic Journal of Geotechnical Engineering*, vol.13, pp.1-12.

Nataraj, M.S. and McManis, K.L. (1997) "Strength and Deformation Properties of Soil Reinforced With Fibrillated Fibers" , *Geosynthetics International*, Vol.4, No.1, pp. 65-79.

Soundara, B, Kumar, K. P. (2015). "Effect of Fibers on Properties of Clay." *International Journal of Engineering and Applied Sciences* , Vol. 2, No. 5, pp.123-128.

Zaimoglu, A.S., Yetimoglu, T. (2012). "Strength Behavior of Fine Grained Soil Reinforced with Randomly Distributed Polypropylene Fibers." *Geotechnical and Geological Engineering*, Vol.30, pp.197-203.

POTENTIOMETRIC DETERMINATION OF ACID DISSOCIATION CONSTANTS OF 2-IMINOTHIAZOLES

Müge Gemili [1], Hasan Atabey [2] and Yahya Nural [*3,4]

[1] Mersin University, Faculty of Pharmacy, Department of Analytical Chemistry, Mersin, Turkey, e-mail: muge.gemili@gmail.com

[2] Mersin National Education Directorate, Department of Analytical Chemistry, Mersin, Turkey, e-mail: hasatabey@gmail.com

[3] Mersin University, Faculty of Pharmacy, Department of Analytical Chemistry, Mersin, Turkey, e-mail: yahyanural@mersin.edu.tr ; ynural1805@yahoo.com

[4] Mersin University, Advanced Technology, Research and Application Center, Mersin, Turkey

ABSTRACT

In this study, acid dissociation constants of 2-iminothiazoles, consisting of 1,4-naphthoquinone moiety, were determined in 40% (v/v) dimethyl sulfoxide-water hydro-organic solvent system by potentiometric titration method at 25 ± 0.1 °C, at an ionic background of 0.1 mol / L of NaCl using the HYPERQUAD computer program. Under the conditions mentioned above, four acid dissociation constants were determined for each compound. We suggest that the pK_{a1} value is related to the protonated imine group, the pK_{a2} value is related to the protonated amine group, the pK_{a3} value is related to the tertiary amine, which is formed during the protonation of the nitrogen atom of the thiazole ring, and the pK_{a4} value is related to the OH groups of naphthoquinone.

Keywords: *Potentiometric titration, Acid dissociation constant, 2-Iminothiazoles, HYPERQUAD computer program*

1. INTRODUCTION

Thiazole moiety is one of the most important pharmacophore groups which is considered as having potential high bioactivity in pharmaceutical chemistry studies (Nural, *et al*., 2018a, 2018b; Das, *et al*., 2016). The 2-iminothiazole core is also a privileged heterocyclic structure because it is present in the molecular structure of a variety of biologically important compounds (Gemili, *et al*., 2019; Saeed, *et al*., 2016). It is known that 2-iminothiazole derivatives can exhibit a wide range of bioactivity such as antimicrobial (Gemili, *et al*., 2019; Dawood and Abu-Deif, 2014), antiviral (Turan-Zitouni, *et al*., 2011) and anticancer (Ibrar, *et al*., 2015) activity as well as alkaline phosphatase (Ibrar, *et al*., 2015) inhibitor activity.

The acid dissociation constant is a very important data to estimate the properties of a compound in pharmaceutical research studies. The acid dissociation constant provides many critical information, such as the acidity, solubility and hydrogen binding capacity of the compounds, which play a very important role in pharmaceutical research studies to be performed with both conventional and molecular modelling (Nural, 2017; Gemili, *et al*., 2017; Ersen, *et al*., 2017; Gözel, et al., 2014; Atabey, *et al*., 2012; Narin, *et al*., 2010). Furthermore, acid dissociation constant is a useful data used in a variety of the scientific disciplines such as pharmacy, medicine, chemistry and chemical engineering modeling (Mapes Jr, *et al*., 2019; Gemili, *et al*., 2017; Subirats, *et al*., 2015; Yuan, *et al*., 2015; Atabey and Sari, 2011).

In the previous work (Gemili, *et al*., 2019), we have reported the synthesis, photophysical properties and antimicrobial activity of the novel 1,4-naphthoquinone 2-iminothiazole hybrids. In this study, the determination of acid dissociation constants of ten of these compounds in 40% (v/v) dimethyl sulfoxide (DMSO) - water hydro-organic solvent system by potentiometric titration method are reported.

2. MATERIALS AND METHODS

2.1. Apparatus and Materials

The compounds were prepared according to our previous study (Scheme 1) (Gemili, *et al*., 2019). All reagents had analytical grade and were used without further purification. The compound solutions were prepared as 1.10^{-3} mol / L in DMSO and the 0.025 mol / L NaOH solution which was used as titrant, was prepared by dilution of standard 1 mol / L NaOH solution (Titrisol, Sodium hydroxide solution, Merck 1.09956.0001). The 0.1 mol / L HCl solution prepared for acidity of the medium was prepared by diluting 1 mol / L standard HCl solution (Titrisol, standard hydrochloric acid solution, Merck 1.09970.0001). The 1.0 mol / L NaCl (Merck 1.06404.1000) stock solution was prepared to kept the ionic strength of the medium at 0.1. The using deionized water was obtained by Ultra water purification system (Milli-Q Gradient) with a resistance of 18.2 MΩ.cm.

Titration was performed by using a set of the SI Analytics TitroLine 7000 pH-mV-meter, having an automatic micro burette which is controlled by a PC computer. During titrations, the temperature was kept at 25.0 ± 0.1 ° C in a double-walled glass titration vessel using a thermostat (Buchi, Recirculating Cooler F-105) and the vessel solution was stirred. The electrode was calibrated at three points at pH 4.01, pH 7.00 and pH 10.01 using reference solutions. All of the titration process was carried out under nitrogen (99.9%) atmosphere. The HYPERQUAD computer program, which is one of the best computer program for determination of acid dissociation constants with high precision and accuracy (Gans, *et al*., 1996), was used to calculate the acid dissociation constants from potentiometric data.

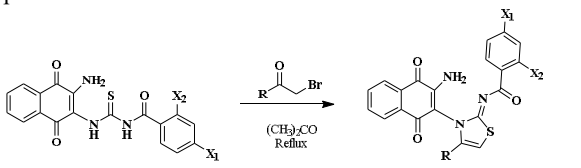

1

1a: X_1= CH_3 X_2= H
1b: X_1= $C(CH_3)_3$ X_2= H
1c: X_1= OCH_3 X_2= H
1d: X_1= Cl X_2= H
1e: X_1= Cl X_2= Cl

2

2a: R= 4-CNPh X_1= CH_3 X_2= H
2b: R= 4-CNPh X_1= $C(CH_3)_3$ X_2= H
2c: R= 4-CNPh X_1= OCH_3 X_2= H
2d: R= 4-CNPh X_1= Cl X_2= H
2e: R= 4-CNPh X_1= Cl X_2= Cl
2f: R= Coumarin-3-yl X_1= CH_3 X_2= H
2g: R= Coumarin-3-yl X_1= $C(CH_3)_3$ X_2= H
2h: R= Coumarin-3-yl X_1= OCH_3 X_2= H
2i: R= Coumarin-3-yl X_1= Cl X_2= H
2j: R= Coumarin-3-yl X_1= Cl X_2= Cl

Scheme 1. Synthesis of 2-iminothiazole derivatives **2a–j** (Gemili, *et al*., 2019)

2.2. Titration Procedure

The double-wall glass titration vessel which has a lid containing three holes, was rinsed and dried before and after each titration process and the lids were capped during titration process. Using a syringe needle, continuous nitrogen gas was introduced into the medium through one of the holes**.** Before dropwise addition of the alkali solution, air bubbles were removed. Potentiometric procedure was performed according to a literature (Nural, *et al*., 2018c). To determine of the pK_a values of 1,4-naphthoquinone 2-iminothiazole derivatives **2a–j** in 40% (v/v) DMSO-water hydro-organic solvent, added 10 mL of the ligand solution, 10 mL of DMSO, 0.2 mL of the HCl solution and 5 mL of the NaCl solution from previously prepared their stock solutions to the titration cell. After that, the titration cell was filled to 50.00 mL with deionized water to obtained the 2.10^{-4} mol / L ligand solution.

3. RESULTS AND DISCUSSION

Potentiometric determination of acid dissociation constants of 1,4-naphthoquinone 2-iminothiazole derivatives **2a–j** were determined in a 40 % (v/v) DMSO-water hydro-organic solvent system in acidic media at 25.0 ± 0.1 ºC at an ionic background of 0.1 mol/L of NaCl. As a result of the calculations using HYPERQUAD computer program, four different pK_a values were found for each ligand. pK_{a1}, pK_{a2}, pK_{a3} and pK_{a4} values were obtained in a range of 3.12 ± 0.03 – 3.91 ± 0.01, 3.85 ± 0.03 – 4.76 ± 0.02, 10.59 ± 0.02 – 11.60 ± 0.01 and 11.34 ± 0.01 – 12.02 ± 0.02, respectively (Table 1 and Table 2).

The pK_a values were obtained from protonation of some functional groups of **2a–j** derivatives in acidic medium (Scheme 2). Titration curves obtained from titrations are given in Fig. 1 and Fig. 3.

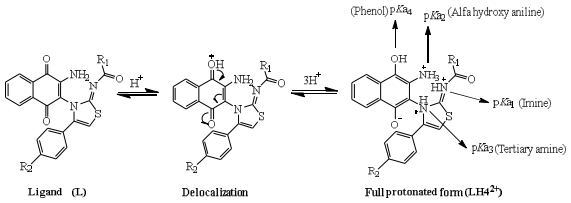

Scheme 2. Proposed mechanism for protonation of **2a–j** in acidic media

We suggest that the pK_{a1} value is related to the imine group (-C=NH$^+$-), the pK_{a2} value is related to the protonated amine group (-NH$_3^+$), the pK_{a3} value is related to the tertiary amine, which is formed during the protonation of the nitrogen atom of the thiazole ring, and the pK_{a4} value is related to the OH groups of naphthoquinone.

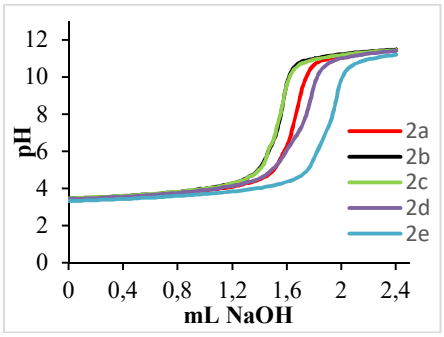

Figure 1. Potentiometric titration curves of **2a–e** in a 40% (v/v) DMSO–water mixture

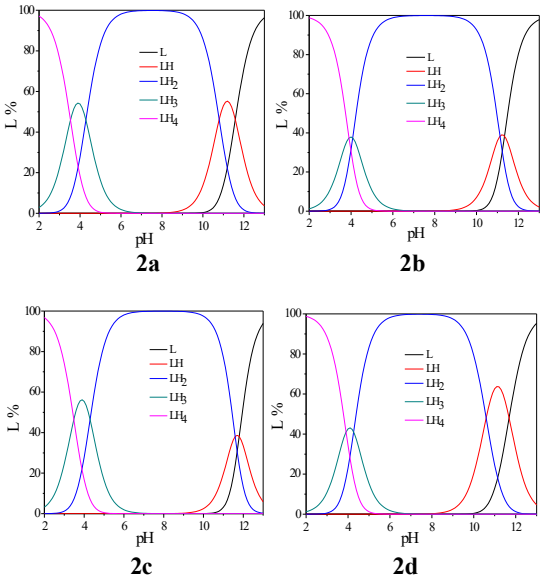

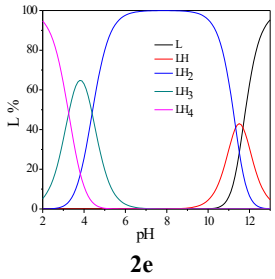

Figure 2. Distribution curves of **2a–e**

Table 1. Dissociation constants of **2a-e** (298K, I=0.1 mol dm^{-3} NaCl, 40/60 DMSO/Water)

Ligand	Species	pK_a values
	LH_4	3.53 ± 0.01
	LH_3	4.29 ± 0.01
2a	LH_2	10.80 ± 0.02
	LH	11.58 ± 0.02
	LH_4	3.91 ± 0.01
	LH_3	4.08 ± 0.01
2b	LH_2	11.12 ± 0.02
	LH	11.34 ± 0.01
	LH_4	3.48 ± 0.01
	LH_3	4.30 ± 0.02
2c	LH_2	11.60 ± 0.01
	LH	11.79 ± 0.01
	LH_4	3.91 ± 0.01
	LH_3	4.27 ± 0.02
2d	LH_2	10.59 ± 0.02
	LH	11.69 ± 0.01
	LH_4	3.46 ± 0.03
	LH_3	4.39 ± 0.04
2e	LH_2	11.33 ± 0.01
	LH	11.69 ± 0.02

The compounds **2a–d** contain CH_3, $C(CH_3)$, OCH_3, Cl as substituent X_1 and H as substituent X_2. The compound **2e** contains Cl atom as substituent X_1 and X_2. In addition, all of the compounds **2a–e** contain 4-cyanophenyl as substituent R. When compared pK_a values of compounds **2a–e** with each other, the pK_a values of **2e** are expected to be more acidic since it contains two chlorine atoms in its molecular structure as substituted groups. Although the pK_{a1} value was found to be the lowest, the other pK_a values for **2e** were not the lowest. The pK_{a2} and pK_{a4} values were found to be the lowest for **2b**, which contains $C(CH_3)$ group as the X_1 substituent, with a value of 4.08 ± 0.01 and 11.34 ± 0.01, respectively. Furthermore, the pK_{a3} value was found to be the lowest for **2d**, which contains Cl atom as the X_1 substituent, with a value of 10.59 ± 0.02.

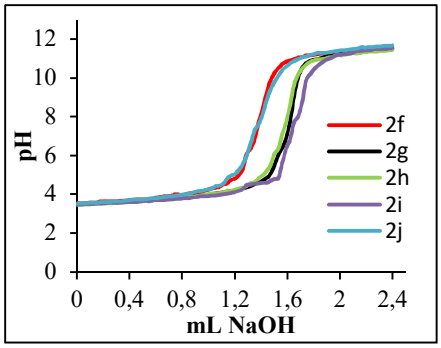

Figure 3. Potentiometric titration curves of **2f–j** in a 40% (v/v) DMSO–water mixture

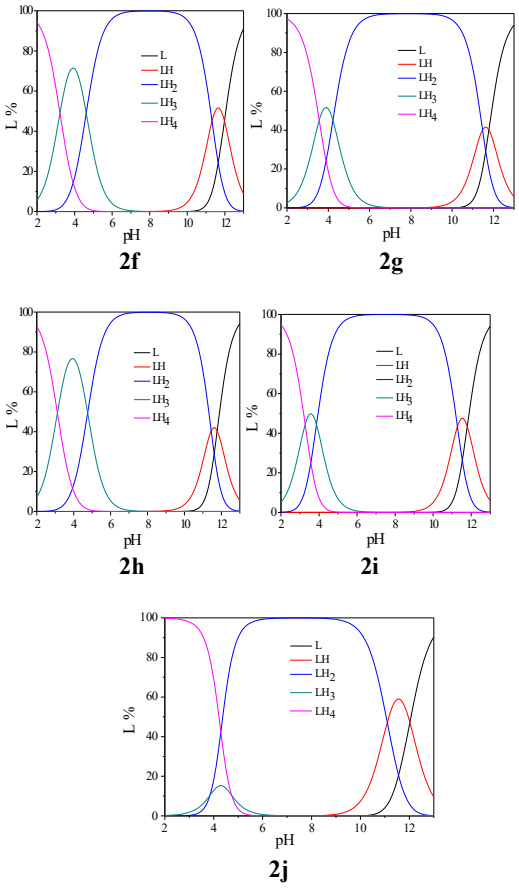

Figure 4. Distribution curves of **2f–j**

Table 2. Dissociation constants of **2f-j** (298K, *I*=0.1 mol dm^{-3} NaCl, 40/60 DMSO/Water)

Ligand	Species	pK_a values
	LH_4	3.22 ± 0.04
	LH_3	4.46 ± 0.04
2f	LH_2	11.32 ± 0.02
	LH	11.98 ± 0.03
	LH_4	3.56 ± 0.01
	LH_3	4.23 ± 0.02
2g	LH_2	11.44 ± 0.01
	LH	11.78 ± 0.01
	LH_4	3.12 ± 0.03
	LH_3	4.76 ± 0.02
2h	LH_2	11.45 ± 0.01
	LH	11.78 ± 0.03
	LH_4	3.27 ± 0.01
	LH_3	3.87 ± 0.02
2i	LH_2	11.28 ± 0.02
	LH	11.80 ± 0.02
	LH_4	3.73 ± 0.03
	LH_3	3.85 ± 0.03
2j	LH_2	11.10 ± 0.01
	LH	12.02 ± 0.02

The compounds **2f–i** contain CH_3, $C(CH_3)$, OCH_3, Cl as substituent X_1 and H as substituent X_2. The compound **2j** contains Cl atom as substituent X_1 and X_2. All of the compounds **2f–j** contain coumarin-3-yl as substituent R. When compared pK_a values of compounds **2f–j** with each other, the pK_a values of **2j** are expected to be more acidic because it contains two chlorine atoms in its molecular structure as X_1 and X_2 substituted groups. Although the pK_{a2} and the pK_{a3} value were found to be the lowest with a value of 3.85 ± 0.03 and 11.10 ± 0.01, respectively, the pK_{a1} and pK_{a4} values for **2j** were not the lowest. The pK_{a1} value was found to be the lowest for **2h**, which contains OCH_3 group as the X_1 substituent, with a value of 3.12 ± 0.03. Furthermore, the pK_{a4} value was found to be the lowest for **2g** and **2h** with a value of 11.78. It can be said that the delocalization in the molecule, solvent effect and molecular / intermolecular interactions plays a critical role in acid dissociation constants of 1,4-naphthoquinone 2-iminothiazole derivatives.

Potentiometric data obtained from three individual measurements were used to calculate the pK_a values with HYPERQUAD computer program. Four deprotonated species formulated as LH_4, LH_3, LH_2 and LH were determined using HYPERQUAD computer program. The deprotonation equilibrium for the ligands is given in the following Eq. (1) (charges are omitted for simplicity) (Sarigul, et al., 2017).

$$LH_n \rightleftharpoons LH_{n-1} + H \qquad (1)$$

and the deprotonation constants (K_n) were given by equation 2 (Sarigul, *et al.,* 2017);

$$K_n = [LH_{n-1}]\,[H] / [LH_n] \qquad (2)$$

While increasing pH, the protonated ligand lost its protons and converted into another species of the ligand. The titration curves of **2a-j** and the distribution curves of species H were given in Fig. 2 and Fig. 4.

4. CONCLUSION

In summary, we have described potentiometric determination the acid dissociation constants, which play a critical role in understanding the nature of the compounds and in the studies to be performed on such these compounds, of 1,4-naphthoquinone 2-iminothiazole derivatives. Four pK_a values were determined for each compound under the experimental

conditions described. These data will make significant contributions to both the literature and the studies to be performed on such compounds.

ACKNOWLEDGEMENTS

This work is a part of Müge Gemili's PhD thesis and we are thankful to Mersin University (project grant 2018-1-TP3-2899) for financial support.

REFERENCES

Atabey, H., Sari, H. (2011). "Potentiometric, theoretical, and thermodynamic studies on equilibrium constants of aurintricarboxylic acid and determination of stability constants of its complexes with Cu^{2+}, Ni^{2+}, Zn^{2+}, Co^{2+}, Hg^{2+}, and Pb^{2+} metal ions in aqueous solution." *Journal of Chemical & Engineering Data,* Vol. 56, No. 10, pp. 3866-3872.

Atabey, H., Sari, H., Al-Obaidi, F. N. (2012). "Protonation equilibria of carminic acid and stability constants of its complexes with some divalent metal ions in aqueous solution." *Journal of Solution Chemistry*, Vol. 41, No. 5, 793-803.

Das, D., Sikdar, P., Bairagi, M. (2016). "Recent developments of 2-aminothiazoles in medicinal chemistry." *European Journal of Medicinal Chemistry*, Vol. 109, pp. 89-98.

Dawood, K. M., Abu-Deif, H. K. A. (2014). "Synthesis and antimicrobial evaluation of some new 1,2-bis-(2-(*N*-arylimino)-1,3-thiazolidin-3-yl)ethane derivatives." *Chemical and Pharmaceutical Bulletin*, Vol. 62, No. 5, pp. 439-445.

Ersen, D., Gemili, M., Sarı, H., Nural, Y. (2017). "Acid dissociation constants of 5,5-diphenylpyrrolidine *N*-aroylthioureas and stability constants of their Pt (II) and Ni (II) complexes in acetonitrile-water hydroorganic solvent." *CBÜ Fen Bil Dergi*, Vol. 13, No. 1, pp. 125-138.

Gans, P., Sabatini, A., Vacca, A. (1996). "Investigation of equilibria in solution. Determination of equilibrium constants with the HYPERQUAD suite of programs." *Talanta*, Vol. 43, No. 10, pp. 1739-1753.

Gemili, M., Nural, Y., Keleş, E., Aydıner, B., Seferoğlu, N., Ülger, M., Şahin, E., Erat, S., Seferoğlu, Z. (2019). "Novel highly functionalized 1,4-naphthoquinone 2-iminothiazole hybrids: Synthesis, photophysical properties, crystal structure, DFT studies, and anti (myco) bacterial/antifungal activity." *Journal of Molecular Structure*, vol. 1196, pp. 536-546.

Gemili, M., Sari, H., Ulger, M., Sahin, E., Nural, Y. (2017). "Pt (II) and Ni (II) complexes of octahydropyrrolo [3,4-c] pyrrole *N*-benzoylthiourea derivatives: Synthesis, characterization, physical parameters and biological activity." *Inorganica Chimica Acta*, Vol. 463, pp. 88-96.

Gözel, A., Kose, M., Karakaş, D., Atabey, H., McKee, V., Kurtoglu, M. (2014). "Spectral, structural and quantum chemical computational and dissociation constant studies of a novel azo-enamine tautomer." *Journal of Molecular Structure*, Vol. 1074, pp. 449-456.

Ibrar, A., Zaib, S., Khan, I., Jabeen, F., Iqbal, J., Saeed, A. (2015). "Facile and expedient access to bis-coumarin–iminothiazole hybrids by molecular hybridization approach: synthesis, molecular modelling and assessment of alkaline phosphatase inhibition, anticancer and antileishmanial potential." *RSC Advances*, Vol. 5, No. 109, pp. 89919-89931.

Mapes Jr, N. J., Rodriguez, C., Chowriappa, P., Dua, S. (2019). "Residue Adjacency Matrix Based Feature Engineering for Predicting Cysteine Reactivity in Proteins." *Computational and Structural Biotechnology Journal*, Vol. 17, pp. 90-100.

Narin, I., Sarioglan, S., Anilanmert, B., Sari, H. (2010). "pK_a determinations for montelukast sodium and levodropropizine." *Journal of Solution Chemistry*, Vol. 39, No. 10, pp. 1582-1588.

Nural, Y. (2017). "Synthesis and Determination of Acid Dissociation Constants in Dimethyl Sulfoxide–Water Hydroorganic Solvent of 5, 5-Diphenylpyrrolidine *N*-Aroylthiourea Derivatives." *Journal of the Turkish Chemical Society, Section A: Chemistry*, Vol. 4, No. 3, pp. 841-854.

Nural, Y. (2018a). "Synthesis, antimycobacterial activity, and acid dissociation constants of polyfunctionalized 3-[2-(pyrrolidin-1-yl)thiazole-5-carbonyl]-2*H*-chromen-2-one derivatives." *Monatshefte für Chemie-Chemical Monthly*, Vol. 149, No. 10, pp.1905-1918.

Nural, Y., Gemili, M., Ulger, M., Sari, H., De Coen, L. M., Sahin, E. (2018b). "Synthesis, antimicrobial activity and acid dissociation constants of methyl 5,5-diphenyl-1-(thiazol-2-yl)pyrrolidine-2-carboxylate derivatives." *Bioorganic & Medicinal Chemistry Letters*, Vol. 28, No. 5, pp. 942-946.

Nural, Y., Gemili, M., Seferoglu, N., Sahin, E., Ulger, M., Sari, H. (2018c). "Synthesis, crystal structure, DFT studies, acid dissociation constant, and antimicrobial activity of methyl 2-(4-chlorophenyl)-7a-((4-chlorophenyl)carbamothioyl)-1-oxo-5,5-diphenyl-3-thioxo-hexahydro-1H-pyrrolo[1,2-e]imidazole-6-carboxylate." *Journal of Molecular Structure*, Vol. 1160, pp. 375-382.

Saeed, A., Mahmood, S. U., Rafiq, M., Ashraf, Z., Jabeen, F., Seo, S-Y. (2016). "Iminothiazoline-Sulfonamide Hybrids as Jack Bean Urease Inhibitors; Synthesis, Kinetic Mechanism and Computational Molecular Modeling." *Chemical Biology & Drug Design*, Vol. 87, No. 3, pp. 434-443.

Sarigul, M., Kariper, S. E., Deveci, P., Atabey, H., Karakas, D., Kurtoglu, M. (2017). "Multi-properties of a new azo-Schiff base and its binuclear copper (II) chelate: Preparation, spectral characterization, electrochemical, potentiometric and modeling studies." *Journal of Molecular Structure*, Vol. 1149, pp. 520-529.

Subirats, X., Fuguet, E., Rosés, M., Bosch, E., Ràfols, C.

(2015). "Methods for pK_a Determination (I): Potentiometry, Spectrophotometry, and Capillary Electrophoresis." *Reference Module in Chemistry, Molecular Sciences and Chemical Engineering*, pp. 1-10.

Turan-Zitouni, G., Özdemir, A., Kaplancıklı, Z. A. (2011). "Synthesis and antiviral activity of some (3,4-diaryl-3H-thiazol-2-ylidene)pyrimidin-2-yl amine derivatives." *Phosphorus, Sulfur, and Silicon*, Vol. 186, No. 2, pp. 233-239.

Yuan, X., Goswami, N., Mathews, I., Yu, Y., Xie, J. (2015). "Enhancing stability through ligand-shell engineering: a case study with $Au_{25}(SR)_{18}$ nanoclusters." *Nano Research*, Vol. 8, No. 11, pp. 3488-3495.

CISET - 2nd Cilicia International Symposium on Engineering and Technology
10-12 October, 2019, Mersin / TURKEY

PM EMISSION FROM DIESEL ENGINES AND DPF TECHNOLOGY

Ibrahim Aslan RESITOGLU

Mersin University, Vocational School of Technical Sciences, Automotive Technology, Mersin, Turkey,
aslanresitoglu@gmail.com

ABSTRACT
Diesel engines are among the most widely used power supplies in both transportation and industrial/energy fields. High durability, high efficiency, low fuel consumption are the features that make diesel engines advantageous. However, in addition to these superior properties, they contain high levels of Nitrogen Oxide (NOx) and Particulate Matter (PM) emissions in the exhaust contents, which cause great environmental problems. Diesel engines are one of the leading sources of air pollution and global warming due to their pollutant emissions (especially NOx and PM). This study deals with PM emissions generated by diesel engines and Diesel Particulate Filter (DPF) technology used to eliminate these emissions. In this study, formation of PM emissions, negative effects on human health and environment, DPF technology, history of DPF technology and recent developments in DPF technology have been examined in detail. The results are showed that diesel engines have a significant contribution to the formation of PM emissions, PM emissions cause serious damage on human health and environment, the elimination of PM emissions is a necessity, various policies and standards are developed to prevent PM emissions. DPF technology is clearly the most effective method for removing of PM emissions and PM emissions can be eliminated at very high rates thanks to DPF technology.

Keywords: *Air Pollution, Particulate Matter, Pollutant emissions, Diesel Engine, Diesel Particulate Filter*

1. INTRODUCTION

Air pollution is one of the major problems on the agenda of many countries. Because of the air pollution, both the human health and environment are under great danger. The heavy consequences of air pollution have become undeniable. According to the report prepared by the World Health Organization, approximately 7 million people die every year due to air pollution (World Health Organization, 2014). There has also been an increase in natural events (tsunamis, floods, heat waves, storms, tornadoes, etc.) around the world.

PM emissions are one of the most important pollutant emissions causing air pollution. PM emissions directly or indirectly affect air visibility adversely, short the visibility, cause acidification, and even threat the human health by accelerating virus transfer. It is widely known that these carcinogenic emissions cause premature deaths. Air pollution caused by pollutant emissions, particularly PM emissions, has been reported to cause an average of 3.3 million premature deaths annually worldwide (Lelieveld et al., 2015). Heart failure, lung cancer, respiratory distress, respiratory diseases are important health problems caused by PM emissions (Smith et al., 2019; Pope et al., 2006;). At the same time, significant evidence has been obtained that PM emissions are associated with Type 2 diabetes and that obesity, systemic inflammation and Alzheimer's disease occur in people with Type 2 diabetes (European Environment Agency, 2018). Although many efforts are being made to reduce PM emissions worldwide, it is obvious that many people are exposed to these emissions at a high level.

The economic impact of PM emissions on countries has also reached considerable levels. The loss of work caused by premature deaths, the treatment of health problems caused by PM emissions, and the elimination of environmental damage are consuming a large part of the budget of the country (European Environment Agency, 2018).

The majority of PM emissions are generated from energy production. Diesel engines, which are widely used in the transportation and other sectors (industry, energy, agriculture etc), are the leading sources of PM emissions.

As the negative effects of PM and other pollutant emissions become widespread day by day and can be noticed by everyone, high efforts are being made to control these emissions. Many research and development (R&D) activities have been carried out in order to reduce these emissions in many areas, especially in the transportation sector, policies have been established and various limitations and standards have been promulgated. Research and development activities to ensure the elimination of pollutant emissions from vehicles have focused on aftertreatment emission control technologies. Diesel Oxidation Catalyst (DOC) for CO and HC emissions, Selective Catalytic Reduction (SCR) for NOx emissions and Diesel Particulate Filter (DPF) for PM emissions were developed and adapted to vehicles.

In this study, the formation and effects of PM emissions from diesel engines, the factors affecting the formation of PM emissions, DPF technology used to control PM emissions and the latest developments in DPF technology are explained in detail.

2. PM EMISSIONS FROM DIESEL ENGINES

High efficiency and durability compared to gasoline engines have made diesel engines usable in many sectors. However, PM emissions from diesel engines are one of the most important problems that may prevent the use of diesel engines (Maricq, 2007). Diesel engines emit higher PM emissions compared to gasoline engines. Certainly, diesel engines are among the top sources of PM emissions.

PM emissions with complex microstructures are composed of element and organic carbons, sulphate, ash, nitrate, water, metal oxides and other components (Sharma et al., 2012). In an experimental study, the particulate matter content of a diesel engine used in a heavy-duty vehicle was determined as 41% carbon, 7% unburned fuel, 25% unburned oil, 14% sulfate and water, 13% ash and other components (Kittelson, 1998). The chemical structure of PM emissions plays an important role in human health and the environment.

Diesel particulate matter generally consists of 15-40 nm spheres and approximately 90% of the particulate matter is less than 1 μm in diameter. The formation of PM emissions varies depending on many parameters such as combustion and expansion time, fuel quality (sulfur and ash content), quality and consumption of lubricating oil, combustion temperature and exhaust gas temperature.

Standards are set for PM emissions from diesel engines. These standards are tightened with each passing time and the permissible PM emission values in the exhaust gas content are lowered. Figure 1 presents the Euro Standard values for PM emissions for heavy duty vehicles. Euro standards first came into force in 1993 and a limit of 0.61 g/kwh was imposed on PM emissions. In the Euro VI standard which has been in force since 2013, this value is determined as 0.01 g/kWh. This situation shows that the accepted value of PM emissions decreased by 98.36% in 20 years.

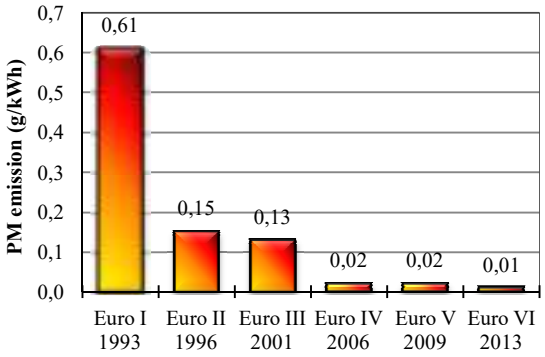

Fig. 1. Euro standards of PM emission for heavy-duty vehicles (Delphi, 2019)

The serious tightening of Euro standards for PM emissions has led many researchers, especially automotive manufacturers, to produce alternative solutions. Although significant reductions in PM emissions have been achieved with engine modifications, the development of electronically controlled fuel injection systems, improved fuel properties, and the use of alternative fuels such as biodiesel and alcohols, the desired PM emission values have not been achieved

(Vaughan et al., 2019; Fiebig et al., 2014). Thanks to the DPF technology developed as a result of the ongoing research, the values determined by the standards have been reached and the damage caused by PM emissions from diesel engine has been prevented to a great extent. DPF technology has become the center of attention especially with the Euro V standard effectuated in 2009 (Tzamkiozis et al., 2010).

3. DIESEL PARTICULATE FILTER (DPF)

DPF technology, one of the aftertreatment emission control systems, is widely used in today's diesel vehicles. Thanks to DPF, PM emissions can be eliminated at very high rates (over 90%) (Maricq, 2007). DPF on the exhaust system, which is usually made of Silicon Carbide material, acts as a filter to trap PMs in the exhaust gas content. Although the first foundation of the DPF was laid in 1969 and developed in 1978-1994, its application to vehicles was realized in the 2000s (Dittler, 2017). DPF technology was developed by tightening the restrictions on PM emissions in Euro standards.

High temperature resistance, extreme resistance to thermal stresses, corrosion resistance and mechanical strength characteristics are the factors that are considered in the selection of DPF materials. DPF is generally produced in silicon carbide (SiC), cordierite ($2MgO\text{-}2Al_2O_3\text{-}5SiO_2$) or metal structure which can provide these properties. Among these structures, SiC is most commonly used.

DPF generally has a high number of porous and parallel channels with square geometry. The channel wall thickness is generally in the range of 300 to 400 μm. Channel dimensions are determined by the number of pores. The number of pores commonly used in these filters varies between 100-300 cpsi.

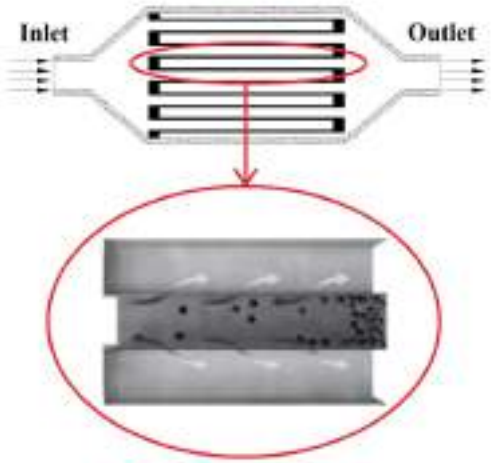

Fig. 2. The structure of Diesel Particulate Filter (DPF)

Figure 2 presents the structure of the DPF visually. DPF simply consists of several monolithic pores whose inputs and outputs are mutually closed. Since the pore outlet of the exhaust gas entering the pore is closed, it provides a flow from the pore walls to the other pores around it. During the flow through the pore walls, PM emissions are filtered in these walls. This filtering continues until the DPF filtering capacity is full. After the DPF is filled with PM emissions and clogged and an increase in pressure occurs in the exhaust system, regeneration is carried out to remove PM emissions on the DPF. Regeneration is the most emphasized process in DPF technology and many research and development activities are currently being conducted on this process (Ko et al., 2016; Dwyer et al., 2010).

The regeneration process is the combustion of the PM emissions absorbed in the DPF. Combustion is carried out by oxidation of PM emissions. Compared to O_2, the oxidation process carried out with NO_2 in the exhaust gas content reduces the combustion temperature of PM emissions and increases the regeneration efficiency. Although the temperature required for the combustion of PM emissions is above 500 ^oC, this value can be lowered depending on the amount of NO_2 contained in the exhaust content. Thanks to a Diesel Oxidation Catalyst used downstream DPF, a significant proportion of NO in exhaust gas content are converted to NO_2 (Lizarraga et al., 2011). The exhaust gas from the diesel engine reaches DPF after passing through the DOC. In the meantime, NO in the exhaust gas content is converted to NO_2 and is directed to DPF. The higher NO_2 content in exhaust gas content lower the PM ignition temperature (Jiao et al., 2017). At the same time, the exhaust gas content, the exhaust flow, the fuel used and the physical and chemical properties of the PM emissions affect the regeneration efficiency (Rodriguez et al., 2017).

Regeneration process is realized in two different ways as active and passive. The temperature increase in active regeneration is provided by an extra energy source. This energy source is generally a fuel produced specifically for this process. Fuel is burned by spraying on the exhaust at the inlet of the DPF and the temperature of the DPF is increased accordingly to ensure the combustion of PM emissions (Chen et al., 2014). Apart from the additional fuel injection, the energy source required can be provided by electric heaters or microwave beams (Pallavkar et al., 2009). Active regeneration is carried out in vehicles between 300-800 km intervals (Beatrice et al., 2017).

In the passive regeneration process, no external energy source is needed. The increase of the DPF temperature is achieved by loading the engine. When a blockage is detected in the DPF system, the engine is operated at high speeds and load to increase the exhaust gas temperature, thereby increasing the DPF temperature and burning PM emissions to the outside. Passive regeneration prevents the burning of extra fuel and extends the life of the DPF (Soltani et al., 2018). Thanks to DOC used before DPF, the formation of NO_2 which provide oxidation of PM emissions is provided. Thanks to DOC, which converts the NO emissions to the NO_2, oxidation temperatures of PM emissions can be reduced.

The most important issue in DPF technologies is the proper regeneration process. Failure to perform the regeneration process causes problems in the engine and exhaust system. Engine traction may drop and even the engine may stop due to excessive pressure increase in the exhaust system. For this reason, regeneration must be carried out regularly. The quality of the fuel used is one of the most important parameters affecting the regeneration. Fuel that does not comply with the

standards can lead to serious damage to both the DPF and the engine.

4. CONCLUSION

It is obvious that PM emissions cause very serious damage to the environment and human health. Diesel engines, which are used in many different sectors, especially in the transportation sector, are one of the most important sources in the formation of PM emissions. In order to prevent PM emissions from diesel engines, many regulations and standards are put into force. The PM emissions allowed by these standards can be achieved through DPF technology, which is one of the most widely used aftertreatment emission control technologies in diesel engines. Thanks to DPF, PM emissions can be eliminated at very high rates. Regeneration is the most important process in DPF technologies. Regeneration process can be active or passive. Passive regeneration offers significant advantages compared to active regeneration. Research on DPF technology will continue. Particularly, thanks to the nowadays catalyst-containing DPF technology, higher conversion performances can be achieved by increasing the DPF efficiency. At the same time, the use of alternative fuels with DPF can be an effective method of achieving the desired PM emission values.

REFERENCES

Agarwal, A. K., Singh, A. P., Gupta, T., Agarwal, R. A., Sharma, N., Rajput, P., et al. (2018). "Mutagenicity and cytotoxicity of particulate matter emitted from biodiesel-fueled engines." *Environ Sci Technol*, Vol. 52, pp. 14496–14507.

Beatrice, C., Costagliola, M. A., Guido, C., Napolitano, P., Prati, M. V. (2017). "How Much Regeneration Events Influence Particle Emissions of DPF-Equipped Vehicles?." *SAE International*, Vol. 24, pp. 144.

Chen, P., Ibrahim, U., Wang, J. (2014). "Experimental investigation of diesel and biodiesel post injections during active diesel particulate filter regenerations." *Fuel*, Vol. 130, pp. 286–295.

Delphi. (2019). "Worldwide Emissions Standards Heavy Duty and Off- Highway Vehicles."

Dittler, A. (2017). "The Application of Diesel Particle Filters—From Past to Present and Beyond." *Top Catal*, Vol. 60, pp. 342–347.

Dwyer, H., Ayala, A., Zhang, S., Collins, J. et al. (2010). "Emissions from a diesel car during regeneration of an active diesel particulate filter." *Journal of Aerosol Science*, Vol. 41, pp. 541–552.

European Environment Agency. (2018). "Air quality in Europe − 2018 report." *EEA*, pp. 83.

Fiebig, M., Wiartalla, A., Holderbaum, B., Kiesow, S. (2014). "Particulate emissions from diesel engines: correlation between engine technology and emissions." *Journal of Occupational Medicine and Toxicology*, Vol. 9, No 6, pp. 1-18.

Ko, J., Si. W., Jin, D., Myung, C. L., Park, S. (2016). "Effect of active regeneration on time-resolved characteristics of gaseous emissions and size-resolved particle emissions from light-duty diesel engine." *Journal of Aerosol Science*, Vol. 91, pp. 62–77.

Jiao, P., Li, Z., Shen, B., Zhang, W., Kong, X., Jiang, R. (2017). "Research of DPF regeneration with NOx-PM coupled chemical reaction." *Applied Thermal Engineering*, Vol. 110, pp. 737-745.

Kittelson, D. B. (1998). "Engines and nanoparticles: A review." *Journal of Aerosol Science*, Vol. 29, No: 5-6, pp. 575-588.

Lelieveld, J., Evans, J. S., Fnais, M., Giannadaki, D., Pozzer, A. (2015). "The contribution of outdoor air pollution sources to premature mortality on a global scale." *Nature,* Vol. 525, pp. 367-371.

Lizarraga, L., Souentie, S., Boreave, A., George, C. Et al. (2011). "Effect of Diesel Oxidation Catalysts on the Diesel Particulate Filter Regeneration Process." *Environ. Sci. Technol.*, Vol. 45, pp. 10591–10597.

Maricq, M. M. (2007). "Chemical characterization of particulate emissions fromdiesel engines: A review." *Aerosol Science*, Vol. 38, pp. 1079‑1118.

Pallavkar, S., Kim T., Rutman, D., Lin, J., Ho, T. (2009). "Active Regeneration of Diesel Particulate Filter Employing Microwave Heating." *Ind. Eng. Chem. Res.*, Vol. 48, pp. 69–79.

Pope III, C. A., Dockery, D. W. (2006). "Health effects of fine particulate air pollution: lines that connect." *Journal of the Air & Waste Management Association*, Vol. 56, pp. 709–742.

Rodriguez-Fernandez, J., Lapuerta, M., Sanchez-Valdepenas, J. (2017). "Regeneration of diesel particulate filters: Effect of renewable fuels." *Renewable Energy*, Vol. 104, 30-39.

Sharma, H. N., Pahalagedara, L., Joshi, A. et al. (2012). "Experimental study of carbon black and diesel engine soot oxidation kinetics using thermogravimetric analysis." *Energy Fuels*, Vol. 26, pp. 5613‑5625.

Smith, J. D., Ruehl C., Burnitzki, M. et al. (2019). "Real-time particulate emissions rates from active and passive heavy-duty diesel particulate filter regeneration." *Science of the Total Environment*, Vol. 680, pp. 132–139.

Soltani, S., Andersson, R., Andersson, B. (2018). "The effect of exhaust gas composition on the kinetics of soot oxidation and diesel particulate filter regeneration." *Fuel*, Vol. 220, pp. 453–463.

Tzamkiozis, T., Ntziachristos, L., Samaras, Z. (2010). "Diesel passenger car PM emissions: From Euro 1 to Euro 4 with particle filter." *Atmospheric Environment*,

Vol. 44, 909-916.

Vaughan, A., Stevonic, S., Jafari, M., Bowman, V. et al. (2019). "Primary human bronchial epithelial cell responses to diesel and biodiesel emissions at an air-liquid interface." *Toxicology in Vitro*, Vol. 57, 67‑75.

World Health Organization. (2014). "Public Health, Environmental and Social Determinants of Health (PHE)." *WHO*, Vol. 63.

CISET - 2nd Cilicia International Symposium on Engineering and Technology
10-12 October, 2019, Mersin / TURKEY

ANECHOIC CHAMBER MEASUREMENTS FOR CIRCULAR ISAR IMAGING AT MERSIN UNIVERSITY'S MEATRC LAB

Sevket Demirci [1*], and Caner Özdemir [2]

[1] Mersin University, Engineering Faculty, Electrical and Electronic Engineering Department, Mersin, Turkey, sdemirci@mersin.edu.tr
[2] Mersin University, Engineering Faculty, Electrical and Electronic Engineering Department, Mersin, Turkey, cozdemir@mersin.edu.tr

ABSTRACT
Inverse synthetic aperture radar (ISAR) imaging is a reliable detection and classification technique for targets at near and far-field regions. In this study, we examine the near-field circular ISAR imaging by conducting some real measurement experiments that were performed in microwave anechoic chamber. The focusing of the collected raw data are accomplished by applying the back-projection migration algorithm. The resultant circular ISAR images exhibit successful detection and classification of the targets with good fidelity. These experiments clearly construct a feasibility study for concealed object detection technology for security applications in airports and/or other checkpoints.

Keywords: Inverse synthetic aperture radar (ISAR), *Circular ISAR, Anechoic chamber measurement, Image reconstruction*

[*] Corresponding Author

1. INTRODUCTION

Inverse synthetic aperture radar (ISAR) is a powerful signal processing technique for imaging moving targets in range and cross-range domain for detecting the usually military targets such as airplanes, tanks and helicopters (Özdemir, 2012). An ISAR image has the ability of successfully exhibiting the leading scattering regions. These regions of hot points on the target are called as scattering centers in radar terminology. Two dimensional (2D) ISAR image is nothing but an image that displays the range profile in one axis and the cross-range profile in the other axis (Özdemir, 2012).

Circular SAR/ISAR imaging offers better resolution in cross-range domain if the sampling along the circular path is good enough (Soumekh, 1999). The key task in obstructing a successful Circular SAR image production is usually encountered while constructing 2D representations of three-dimensional (3D) large and complex-shaped objects. Therefore, the scene's extent is an important portion of the ISAR's circular path radius which may result in a huge variation of the depression angle across the scene. This causes the target's radar signature to differ spatially, which means that the same target can be displayed pretty unlike when imaged at different orientation angles and different spatial translations (Dungan et al., 2009)

In this work, we aimed to successfully apply the circular ISAR imaging theory on the data collected from real measurement experiments. The ISAR measurements were conducted in an anechoic chamber in Mersin University facilities. Here, we present two different experiments of various targets to demonstrate the success that we got in reconstructing circular ISAR images of selected objects.

.

2. THEORY

2.1. ISAR Imaging Theory

ISAR imaging procedure is based on the geometry given in Fig.1. The detailed formulation of ISAR can be found in (Özdemir, 2012) and will not be repeated here. Only the final ISAR imaging formula for narrow bandwidth small angle approximation is given as below

$$ISAR(x,y) = \iint_{-\infty}^{\infty} \{E_s(k,\emptyset)\} \cdot \mathrm{e}^{j2\pi kx} \mathrm{e}^{j2k_c\emptyset \cdot y}\, dk\, d\emptyset \quad (1)$$

Here, E_s is the collected scattered electric field, k is the wavenumber and $\emptyset$ is the look-angle of the radar towards the target. Therefore, ISAR image can be regarded as nothing but the the 2D inverse Fourier transform (IFT) of the scattered electric field from the target.

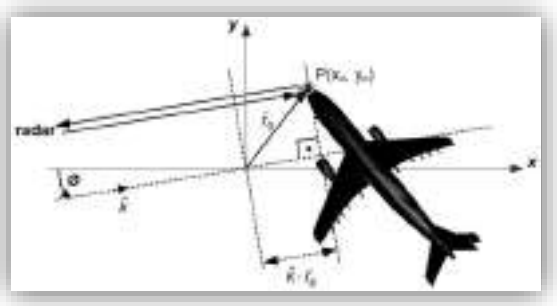

Fig. 1. The geometry of ISAR imaging

2.2. Circular ISAR imaging

The range resolution in ISAR imaging is as the same as a conventional radar as

$$\Delta r = \frac{c}{2B} \quad (2)$$

where B is the frequency bandwidth and c is the speed of light. The cross-range resolution in ISAR imaging for the geometry in Fig.1

$$\Delta y = \frac{\lambda_c}{2\Omega} \quad (3)$$

where Ω is the look-angle width and λ_c is the wavelength that corresponds to the center frequency of operation.

In the case of circular ISAR imaging, the geometry can be illustrated as given in Fig. 2.

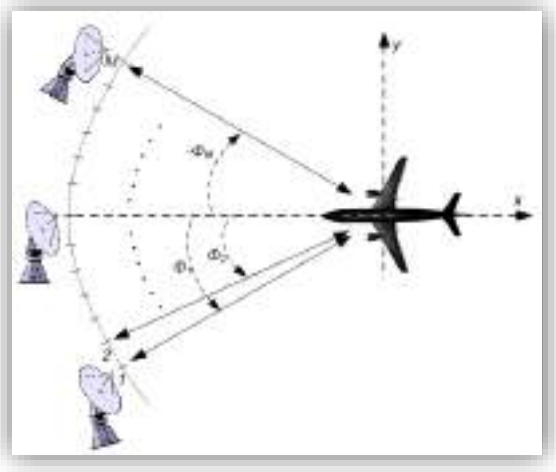

Fig. 2. The geometry for circular ISAR imaging

While range resolution is the same as conventional ISAR imaging, the cross-range resolution is mainly dependent on the angular sampling while collecting the circular ISAR data set.

3. ISAR MEASUREMENT EXPERIMENTS

3.1. Anechoic chamber and the measurement set-up

Circular ISAR imaging measurements were completed in Mersin University's Advanced Technology Education Research and Application Center (MEATRC). The anechoic chamber is pictured in Fig.3 where an ISAR measurement scene can be seen.

In this set-up, the target is put about 2 m away from the radar that works in monostatic operation. The target is put on a circular turn-table that have a sensitivity of 0.01°. Turn table is fully automated with a computer language (Matlab, 2015) script that synchronously controls the Vector Network Analyzer (VNA) [Agilent ENA5071B] that generates, transmits and receives the radar signal. During the experiments, horn a horn antenna that can opera between 4 GHz and 8.5 GHz has been used.

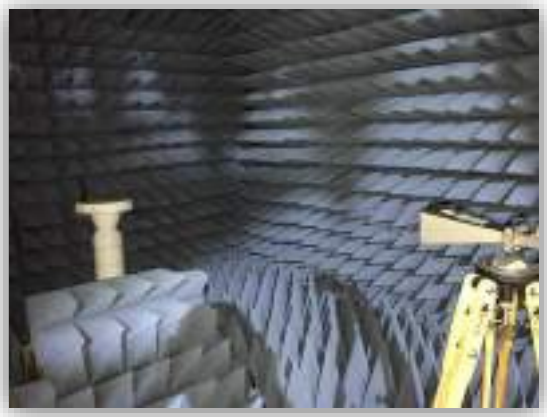

Fig. 3. ISAR measurement in anechoic chamber of MEATRC

3.2. Imaging Small Cylinders

For the first experiment, we have selected two small metal (cupper) cylinders that have diameters of 2 cm and lengths of 15 cm as seen in Fig. 4(a). The experimental set-up that was explained as in section 3.1 was used to collect the back-scattered electric field data for ISAR processing. For this particular measurement, frequency of the VNA has been altered between 4.5 GHz and 8.5 GHz for a total of 501 distinct frequencies. Angular extend of back-scattering measurements was chosen as 180° with 1° angular increments such that we have backscattering matrix of size 501 frequencies and 181 angles.

After processing the raw data-set by the help of back-projection focusing algorithm (BPA) (Demirci *et al.,* 2013, 2015), we have obtained the circular ISAR image as depicted in Fig. 4(b) where images of two cylinders were correctly mapped onto 2D range cross-range ISAR image display. It is also noteworthy that no noise energy is seen for the dynamic range of 20 dB thanks to anechoic chamber.

(a)

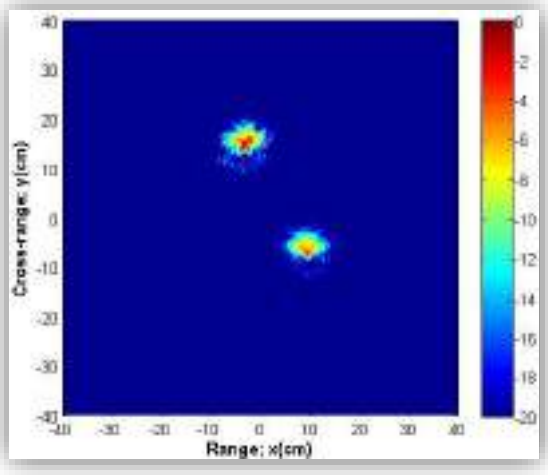

(b)

Fig. 4. (a) Two small cylinders as targets during the ISAR experiment, (b) Constructed circular ISAR images

3.3. Imaging a Screw Wrench

As the second experiment, a more complex object that is screw wrench that has a length of 36 cm was chosen. In Fig. 5(a), the picture of screw wrench is provided. In Fig. 5(b), a photograph from the experiment can be seen.

During the experiment, the same measurement set-up with similar measurement merits have been used. The only difference from the previous experiment was that the different angular look extends had been used for constructing the circular ISAR images. The constructed images are given in Fig 5(c) and Fig. 5(d) for different angular look angles of 90° and 360°, respectively. As easily seen from both figures that when the angular look angle extent increases, the resolution in the ISAR image also increases. We also observe some ghost image outlines occur around the correct location of the target due to massive summation of sub-images for every look angle. Therefore, there should be a tradeoff to be made for getting a better visual image and better resolved image.

(a)

(b)

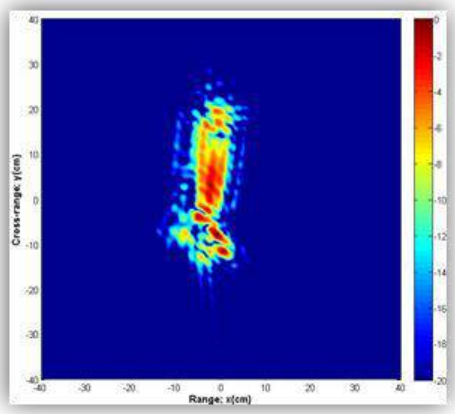

(c)

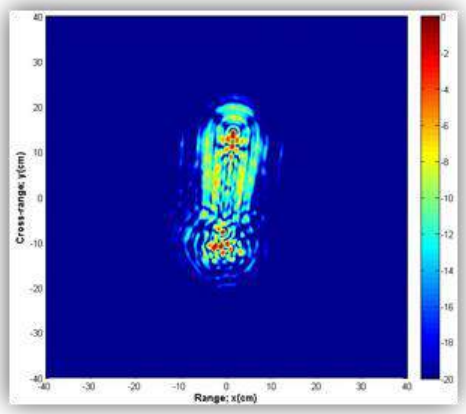

(d)

Fig. 5. (a) Picture of screw wrench target, (b) scene from the experiment Circular ISAR images for angular look extend of (c) 90°, and (d) 360°

4. CONCLUSION

In this work, we have presented our recent studies on near-field circular ISAR imaging concept. Real measurements have been conducted for real targets at anechoic chamber at Mersin University's MEATRC. Two different measurement experiments have been presented in this work. We have demonstrated that successful near-field circular ISAR images of selected targets have obtained in C-band of frequencies with the help of BPA. Such a tool can be useful for remotely sensing and detecting concealed objects in checkpoints such as airports.

ACKNOWLEDGEMENTS

This work was supported by Mersin University Scientific Research Unit under Project No. 2015-TP3-1160

REFERENCES

Demirci, Ş., Yiğit, E., Özdemir, C. (2013). "Wide-field circular SAR imaging: 2D imaging results for simulation data", *6th International Conference on Recent Advances in Space (RAST 2013*), İstanbul,

Demirci, Ş, Yiğit, E., Özdemir, C., (2015) "Wide-field circular SAR imaging: An empirical assessment of layover effects," *Microwave Opt. Tech. Letters,* Vol. 57, No.2, 489-497,

Dungan K. E., Potter L. C., (2009) "Classifying civilian vehicles using a wide-field circular SAR," *Algorithms for Synthetic Aperture Radar Imagery XVI, Proc. SPIE*, E. G. Zelnio and F. D. Garber, Eds., Vol. 7337.,

Matlab (2015), MathWorks Inc., Natick, MA, R2015a.

Ozdemir, C. (2012). *Inverse Synthetic Aperture Radar Imaging With MATLAB Algorithms*, Wiley Series in Microwave and Optical Engineering, Wiley, NJ, USA.

Soumekh, M. (1999), *Synthetic Aperture Radar Signal Processing with MATLAB Algorithms*, Wiley, New York,USA.

CISET - 2nd Cilicia International Symposium on Engineering and Technology
10-12 October, 2019, Mersin / TURKEY

STUDY OF SCATTERING MECHANISMS USING SIMULATED POLARIMETRIC ISAR IMAGING

Sevket Demirci [*1], Ozkan Kirik [2] and Caner Ozdemir [3]

[1] Mersin University, Engineering Faculty, Electrical and Electronic Engineering Department, Mersin, Turkey, sdemirci@mersin.edu.tr
[2] Mersin University, Engineering Faculty, Electrical and Electronic Engineering Department, Mersin, Turkey, cozdemir@mersin.edu.tr
[3] Mersin University, Engineering Faculty, Electrical and Electronic Engineering Department, Mersin, Turkey, ozkan@mersin.edu.tr

ABSTRACT
Inverse synthetic aperture radar (ISAR) imaging has significance to radar cross section (RCS) applications for improving target recognition. In this study, an X-band, full-polarimetric simulation investigation of ISAR is made for a realistic target model. The linear polarization backscattering data from a backhoe vehicle were generated by using our recently developed high-frequency RCS simulator tool Predics. First, the scattering matrix elements are directly utilized to evaluate the data quality and characterize the target features in amplitude domain. Then, the Pauli decomposition scheme is implemented to identify the complex scattering mechanisms occurring at target pixels. The results demonstrate that identifiable target forms are successfully captured as single, double and multi-bounce scattering mechanisms at expected locations.

Keywords: *Polarimetric ISAR, RCS imaging, Pauli decomposition, Feature extraction*

[*] Corresponding Author

1. INTRODUCTION

Inverse synthetic aperture radar (ISAR) is a microwave imaging tool for identifying the maneuvering targets such as aircrafts, ships and vehicles (Ozdemir, 2012). In high frequency approximation, the backscatter signal from such complex targets is dominated by local scattering centers on the target. Also the scattering mechanisms occurring at these target regions tend to be highly complex due to the complicated target structures. This arises from the coherent addition of contributions from single-bounce, double-bounce, and triple- and higher-order bounce scattering mechanisms from various target forms. In these situations, the physical interpretation of the resultant image becomes more difficult, especially for the single-polarization case.

Nevertheless, polarimetric ISAR can be utilized for resolving this overlapping of scattering mechanisms. Amongst the various techniques, the target decompositions have proven to be an effective tool for this task. The objective of target decompositions is to break down the total scattering into combination of the simpler (canonical) responses (Lee *et al*., 2009). This provides a better understanding of the scattering mechanisms and reduces some of the problems related to interpretation of the target's structural characteristics.

Recently, a few studies have dealt with combining target decompositions with ISAR or radar cross section (RCS) imaging. The usefulness of the Cameron (Cameron *et al*., 1990), the Huynen-Euler, (Dallmann *et al*., 2014) and the Pauli (Martorella *et al*., 2011) decompositions is tested by means of anechoic chamber measurements and scale-model targets. One possible problem within these experiments could be the errors introduced in calibration. Moreover, utilizing scale-model implementations may not always be representative of a practical situation. Using simulation models can avoid each of these difficulties and also supplement real measurements.

The problem is, therefore, approached in this study from highly accurate simulation studies. A numerical test were run for a realistic complex target and using a high-frequency RCS simulator, namely the Predics (Ozdemir *et al*., 2014). The perspective images in amplitude domain and the Pauli decomposition image are analyzed to assess the performance of polarimetric ISAR imaging in discriminating elementary scatterers.

2. THEORY

2.1. Scattering matrix

Polarimetric radars often operate in linear horizontal (H) and linear vertical (V) polarizations, measuring up to four channels, i.e., HH, VV, HV and VH with the first and second letters represent transmit and receive polarizations, respectively. The backscattering properties of a target can be completely described by a 2×2 *scattering (or Sinclair) matrix [S]*

$$[S] = \begin{bmatrix} S_{HH} & S_{HV} \\ S_{VH} & S_{VV} \end{bmatrix} \quad (1)$$

The four elements of $[S]$ are the complex scattering amplitudes which are measured by the corresponding channels of the radar. They are dependent only on the target characteristics, for a fixed viewing geometry (i.e., azimuth angle ϕ, elevation angle θ) and frequency. The diagonal and off-diagonal elements are named as co-pol and cross-pol terms, respectively. In monostatic radars, $[S]$ becomes symmetric, i.e., $S_{HV} = S_{VH} = S_{XX}$ for all targets that reciprocity property holds. Table 1 shows the theoretical scattering matrices of various canonical objects in linear polarization basis.

Manmade targets, such as those of ISAR targets, yield completely polarized scattered waves, and therefore termed as coherent targets. For such targets, the elements of $[S]$ can be directly exploited in the so-called coherent decomposition techniques, to distinguish between different types of scattering mechanisms. One of the most basic and efficient coherent decomposition is the Pauli decomposition which has been extensively utilized in polarimetric radar imaging applications. This study focuses on the Pauli decomposition, and thus a brief explanation of the method is given in the following.

2.2. Pauli decomposition

In radar polarimetry, the Pauli spin matrices for the monostatic case (i.e., $S_{HV} = S_{VH}$) is given by the following three $2x2$ matrices

$$\Psi_{P3} = \{[S]_a, [S]_b, [S]_c\} = \left\{\sqrt{2}\begin{bmatrix} 1 & 0 \\ 0 & 1 \end{bmatrix}, \sqrt{2}\begin{bmatrix} 1 & 0 \\ 0 & -1 \end{bmatrix}, \sqrt{2}\begin{bmatrix} 0 & 1 \\ 1 & 0 \end{bmatrix}\right\} \quad (2)$$

The Pauli decomposition expresses $[S]$ using this basis as

$$[S] = \begin{bmatrix} S_{HH} & S_{HV} \\ S_{HV} & S_{VV} \end{bmatrix} = k_1[S]_a + k_2[S]_b + k_3[S]_c \quad (3)$$

where

$$k_1 = \frac{S_{HH}+S_{VV}}{\sqrt{2}},\ k_2 = \frac{S_{HH}-S_{VV}}{\sqrt{2}},\ k_3 = \sqrt{2}S_{HV} \quad (4)$$

are the complex coefficients representing the weights of the associated basis matrix.

Note that that each basis matrix is closely linked with the physics of wave backscattering and also represents isotropic scattering mechanisms which means $|S_{HH}| = |S_{VV}|$. The first matrix $[S]_a$ with $S_{HH} = S_{VV}$ and $S_{HV} = S_{VH} = 0$ can be thought as the scattering matrix of an "odd-bounce" scatterer such as resulted by spheres, flat surfaces and trihedral corner reflectors (TCRs). Therefore, k_1 and $|k_1|^2$, for instance, represents the amount of the contributions of such scatterers in the measured data, in voltage and power terms, respectively.

The second matrix $[S]_b$ includes $180°$ phase difference between the co-pol terms which matches with the scattering matrix of a dihedral rotated at 0° about the line-of-sight (LOS). "Double bounce" or "even bounce" scattering such as caused from dihedral (or diplane) structures are represented with this component.

The last matrix $[S]_c$ corresponds to the scattering matrix of a dihedral rotated 45° about the LOS. Noting that this matrix is defined with respect to LP basis, it indicates a scatterer that transforms the incident polarization into its orthogonal state, and thereby being a representative of a loss of symmetry in $[S]$.

Finally, the information in $[S]$ is usually displayed

and interpreted in a single RGB image, by assigning blue, red and green colors to the amplitudes of the first, second and third components, respectively.

Table 1. Scattering matrices of various canonical objects in linear polarization basis.

Target	*Linear Polarization* $\begin{bmatrix} S_{HH} & S_{HV} \\ S_{VH} & S_{VV} \end{bmatrix}$
Sphere, flat plate, trihedral	$\begin{bmatrix} 1 & 0 \\ 0 & 1 \end{bmatrix}$
Vertical dihedral	$\begin{bmatrix} -1 & 0 \\ 0 & 1 \end{bmatrix}$
Vertical pole	$\begin{bmatrix} 0 & 0 \\ 0 & 1 \end{bmatrix}$
45° inclined pole	$\frac{1}{2}\begin{bmatrix} 1 & 1 \\ 1 & 1 \end{bmatrix}$

3. SIMULATION EXPERIMENT

3.1. Simulator

A full-polarimetric RCS/ISAR simulation experiment in linear polarization basis has been carried by our recently developed high-frequency physical electromagnetic simulator tool called Predics (Ozdemir *et al*., 2014). Predics is based on shooting-and-bouncing ray (SBR) technique that utilizes ray launching with geometric optics (GO) theory and the application of the physical optics (PO) theory together with physical theory of diffraction (PTD) afterwards. The detailed theoretical derivation about Predics and its accuracy validation studies in predicting the electromagnetic scattering and/or radar RCS from benchmark targets can be reached from (Ozdemir *et al*., 2014).

3.2. Experiment description

As seen from Fig. 1 a realistic CAD model of a generic tank platform was selected as a test object. The scattering mechanisms from such a target would be expected to be highly complex due to the complicated target structures. The X-band (9.37 to 10.615 GHz) and narrow angle ($\Delta\phi^i = 9.3°$) data were acquired with the geometry shown in Fig. 1(c) and for the look direction $(\theta^i, \phi^i) = (75°, -30°)$. The sampling points in frequency and azimuth angle ϕ were both set to 100. A Hanning window and a zero-padding with a factor of 4 were applied to the gathered far-field electric field data.

3.3. Results

The collected electric-field data represent radial samples of the target's 2D spatial frequency response. These data samples can well be assumed to span a rectangular grid on the spatial plane, because of the small angular bandwidth $\Delta\phi^i$ and far-field operation. Thus, the ISAR image formation was directly obtained by taking the 2D Fourier transform of this data.

Fig. 2 shows these reconstructed amplitude images for all polarimetric channels. As it can be seen from the images, the target's rear and right sides are clearly visualized owing to the illumination direction of the radar and also to the complex structures such as wheels that give rise to backscattering. Besides, the co-polar signatures at these locations are seen to have much more energy levels than those of the cross-polar channels, as expected for this kind of a deterministic target. The $|S_{HV}|$and $|S_{VH}|$ images are seen to be almost identical because of the monostatic operation and reciprocal target case. The cross-polar contributions can be attributed to the scattering from oriented structures (see Table 1), multipath scattering mechanisms and edge diffraction. A hot spot is seen in co-polar images which can be explained by a possible trihedral corner structure.

To obtain more information about the physical scattering mechanisms occurring at the target, the Pauli decomposition was applied to the scattering matrices of image pixels. The obtained Pauli image with RGB color coding is shown in Fig. 3. The resulted color of the RGB image can be interpreted in terms of the scattering mechanisms by noting that blue, red and green colors represent odd-, even- and multi-bounce (random) scatterings, respectively.

The red tones seen over the target area are indicative of even (or double) bounce scattering mechanisms. For example, the hot spot shown up in magenta (blue + red) indicates combination of specular (odd) and dihedral (even) type scattering. The radar signatures of the wheel section shows highly complex scattering characteristics, as evident from the large variation in color tones. The green regions are supposed to be resulted from the higher-order bounce scatterings occurred within the very complicated wheel structure. It can also be produced by tilted metal sticks. The results demonstrate that the Pauli image can provide a sufficient information on physical scattering mechanisms.

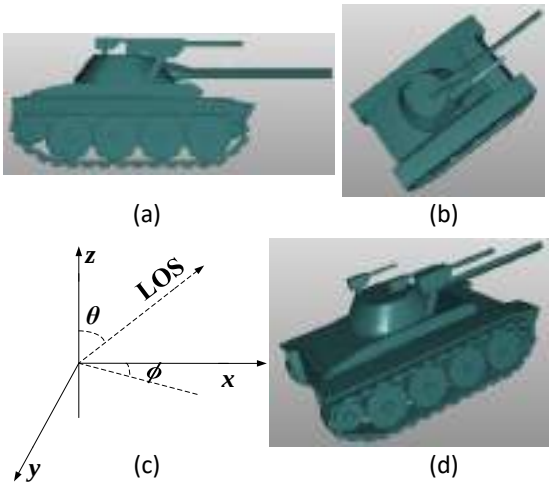

Fig. 1. 'Generic tank model' (a) side (b) top view. (c) Monostatic RCS/ISAR data collection geometry used in the simulation. LOS is towards the radar look direction of $(\theta, \emptyset)$. (d) Targets's aspect for $(\theta^i, \phi^i) = (75°, -30°)$ as seen by the radar location.

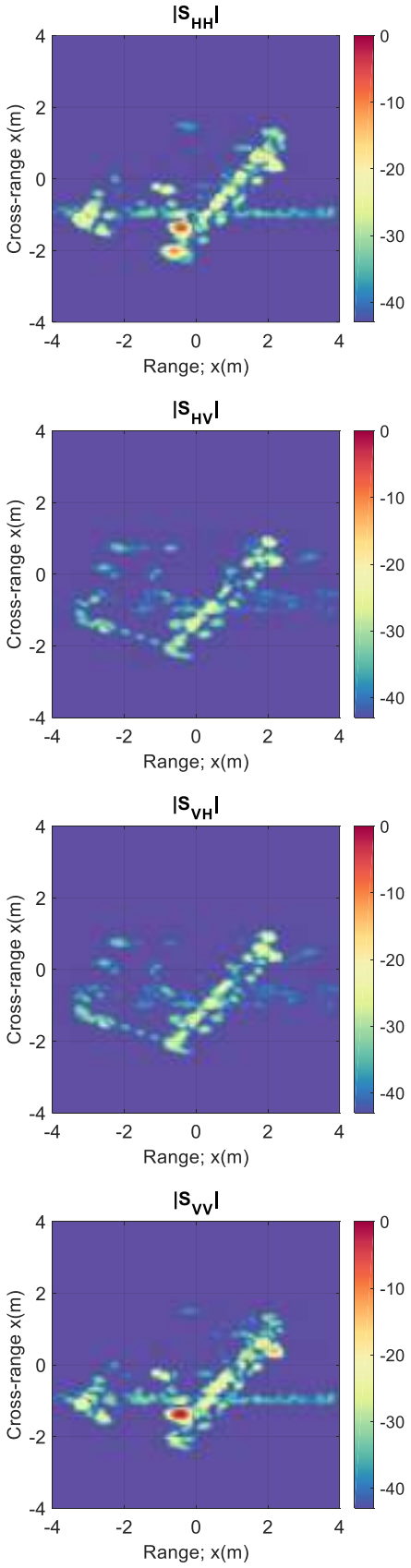

Fig. 2. X-band Polarimetric ISAR images of a 'tank model' for the radar look direction $(\theta^i, \phi^i) = (75°, -30°)$. The 2D amplitude images are produced in the xy plane.

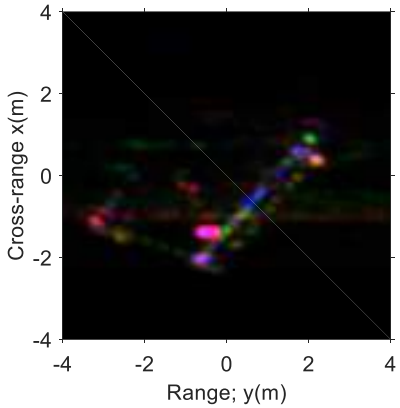

Fig. 3. Pauli image of the tank target.

4. CONCLUSION

In this study, an X-band polarimetric ISAR simulation was implemented to investigate the linearly polarized microwave backscattering of a complex tank vehicle. First, the amplitude images were analyzed and were shown to be consistent with the expected responses of various target regions. Then, the Pauli decomposition was employed to assess its performance in representing the polarimetric information of a manmade complex target. The resulted Pauli image provided useful target information by distinguishing between different scattering mechanisms, especially between odd-bounce and even-bounce mechanisms.

REFERENCES

Cameron, W. and Leung, L. (1990). "Feature motivated polarization scattering matrix decomposition." *Proc., IEEE Radar Conference*, Arlington, VA, USA, pp. 549–557.

Dallmann, T. and Heberling, D. (2014). "Discrimination of scattering mechanisms via polarimetric RCS imaging." *IEEE Antennas and Propagation Magazine*, Vol. 56, No. 3, pp. 154–165.

Lee, J. and Pottier, E. (2009). *Polarimetric Radar Imaging: From Basics to Applications*, Taylor & Francis, UK.

Martorella, M. Giusti, E., Demi, L., Zhou, Z., Cacciamano, A., Berizzi, F. and Bates, B. (2011). "Target recognition by means of polarimetric ISAR images." *IEEE Transactions on Aerospace and Electronic Systems*, Vol. 47, No. 1, pp. 225-239.

Ozdemir, C. (2012). *Inverse Synthetic Aperture Radar Imaging With MATLAB Algorithms*, Wiley Series in Microwave and Optical Engineering, Wiley, NJ, USA.

Ozdemir, C., Yilmaz, B. And Kirik, O. (2014). "pRediCS: A new GO-PO–based ray launching simulator for the calculation of electromagnetic scattering and RCS from electrically large and complex structures." *Turkish Journal of Electrical Engineering & Computer Sciences*, Vol. 22, pp. 1255-1269.

CISET - 2nd Cilicia International Symposium on Engineering and Technology
10-12 October, 2019, Mersin / TURKEY

EFFECT OF STEEL FIBER ADDITION ON ABRASION RESISTANCE OF GEOPOLYMER MORTARS

Cahit Bilim [*1], İlker Fatih Kara [2], Fatih Özcan [3] and Yunus Emre Akkaş [4]

[1] Mersin University, Faculty of Engineering, Department of Civil Engineering, Mersin, Turkey
cbilim@mersin.edu.tr

[2] Mersin University, Faculty of Engineering, Department of Civil Engineering, Mersin, Turkey
ifkara@mersin.edu.tr

[3] Mersin University, Faculty of Engineering, Department of Civil Engineering, Mersin, Turkey
fatihozcan@mersin.edu.tr

[4] Mersin University, Faculty of Engineering, Department of Civil Engineering, Mersin, Turkey
yunusemreakkas@mersin.edu.tr

ABSTRACT
In the present study, the effects of using steel fiber on Bohme abrasion resistance of geopolymer mortars were investigated. Mortar mixtures containing 0%, 0.5%, 1% and 1.5% steel fiber were produced on volume basis. The mortar mixtures had a water / binder ratio of 0.50 and a sand / binder ratio of 3. Abrasion tests were performed on cube samples measuring 71 x 71 x 71 mm after 28 days of water curing. According to the findings obtained from the experimental study, it was observed that the addition of steel fiber in the mixture improved the abrasion resistance of the mortars and the increase in the steel fiber in the mixture reduced the wear losses measured on the cube samples. In addition, it has been found that geopolymer mortars perform better in terms of abrasion resistance than mortars containing normal Portland cement.

Keywords: *Steel Fiber, Geopolymer, Abrasion, Slag*

[*] Corresponding Author

1. INTRODUCTION

In the production of concrete, the manufacturing of alternative binder material and the efficient recovery of various wastes in the cement industry are both economically and ecologically important. For this reason, geopolymer materials without cement obtained by activating the amorphous materials of natural and artificial origin containing Al_2O_3, SiO_2 and CaO in their structure attracts attention in this sense. One of the most important advantages of geopolymer materials is that CO_2 emissions are much lower than conventional Portland cement (Juenger *et al.*, 2011). The main reason for this is that a high-temperature calcination process has not been applied as in Portland cement production (Provis and Deventer, 2014).

Various studies have been carried out in order to fully understand the chemical and engineering properties of geopolymers as a sustainable building material. In these studies, it was stated that geopolymer concretes showed higher strength at early and final ages compared to normal concretes produced using traditional Portland cement, they were highly resistant to chemical attacks and freeze-thaw cycles and had low carbonation rates (Wang *et al.*, 1995; Pacheco-Torgal *et al.*, 2007).At the same time, it was stated in the previous studies that geopolymer mortars and concretes have a brittle structure similar to those produced by using Portland cement and they are sensitive to crack formation (Dias and Thaumaturgo, 2005; Savastano *et al.*, 2003). For these reasons, the idea of using fiber reinforcements with different properties has been developed to improve ductility by improving brittle fracture behavior in geopolymer mortars and concretes. However, the studies investigating the performance and properties of these new types of materials are not sufficient in addition to the studies on traditional fiber reinforced cement bonded composites.

In the literature, it has been found that the researches on the resistance of geopolymer materials to abrasion effects are limited and no study has been reached to investigate the abrasion resistance of geopolymer mortars containing fiber additives. Therefore, in this study, the effects of steel fiber additive on corrosion resistance of slag added geopolymer mortars using alkaline solution were investigated.

2. EXPERIMENTAL PROGRAM

In the mortars, the ground granulated blast furnace slag (GGBFS) whose chemical and physical properties are given in Table 1, and CEM I 42.5 R ordinary Portland cement (OPC) according to TS EN 197-1 (2012) were used. Water / binder ratio was selected as 0.50 and sand / binder ratio was selected as 3.0 in the mortar mixtures where standard sand was used as fine aggregate in compliance with TS EN 196-1 (2009). In the production of the mortars, RC 65/60 BN type, which has a length of 60 mm, a diameter of 0.90 mm and a fineness (length / diameter) of 65, was used with two ends of hooks, uncoated and low carbon steel fiber. The steel fibers were incorporated into mortar mixtures at a rate of 0% (control), 0.5%, 1.0% and 1.5% by volume.

Table 1 – Chemical and physical properties of OPC and GGBS

Composition (%)	OPC	GGBFS
SiO_2	14.38	35.40
Al_2O_3	3.33	11.20
Fe_2O_3	2.85	0.96
CaO	67.36	41.50
MgO	1.60	6.14
Na_2O	0.41	0.28
K_2O	1.09	0.81
SO_3	4.51	1.49
Cl^-	0.35	0.079
Blaine value (cm^2/g)	3250	4300
Specific gravity	3.15	2.64

In the activation of the slag, sodium hydroxide + sodium silicate solution having a modulus value (Ms = SiO_2 / Na_2O) of 1.0 having a dosage of 6% and 8% Na according to the amount of slag was used. The notations of the mixtures used in the study are shown in Table 2.

Table 2 – Mixture notations

Mixture	OPC	GGBFS	Dosage	Steel Fiber
0ÇLPÇ	100%	-	-	0%
0ÇL6Na	-	100%	6%Na	0%
0ÇL8Na	-	100%	8%Na	0%
0.5ÇLPÇ	100%	-	-	0.5%
0.5ÇL6Na	-	100%	6%Na	0.5%
0.5ÇL8Na	-	100%	8%Na	0.5%
1.0ÇLPÇ	100%	-	-	1.0%
1.0ÇL6Na	-	100%	6%Na	1.0%
1.0ÇL8Na	-	100%	8%Na	1.0%
1.5ÇLPÇ	100%	-	-	1.5%
1.5ÇL6Na	-	100%	6%Na	1.5%
1.5ÇL8Na	-	100%	8%Na	1.5%

In order to investigate the effect of steel fiber on the abrasion resistance of geopolymer mortars, cube samples having dimensions of 71x71x71 mm were produced. Samples removed from the molds 24 hours after casting were cured in water at 21 ± 1 °C for 28 days. Bohme tester was used to determine the wear losses of these samples. TS 2824 EN 1338 (2005) in the measurements made in accordance with the standard, the cube samples each of 22 cycles of a total period of 16 periods of wear test**,** the volumetric wear losses of the samples were determined as percentage.

3. RESULTS AND DISCUSSION

Wear losses of mortar samples obtained from Bohme test are given in Fig. 1, Fig. 2 and Fig. 3.

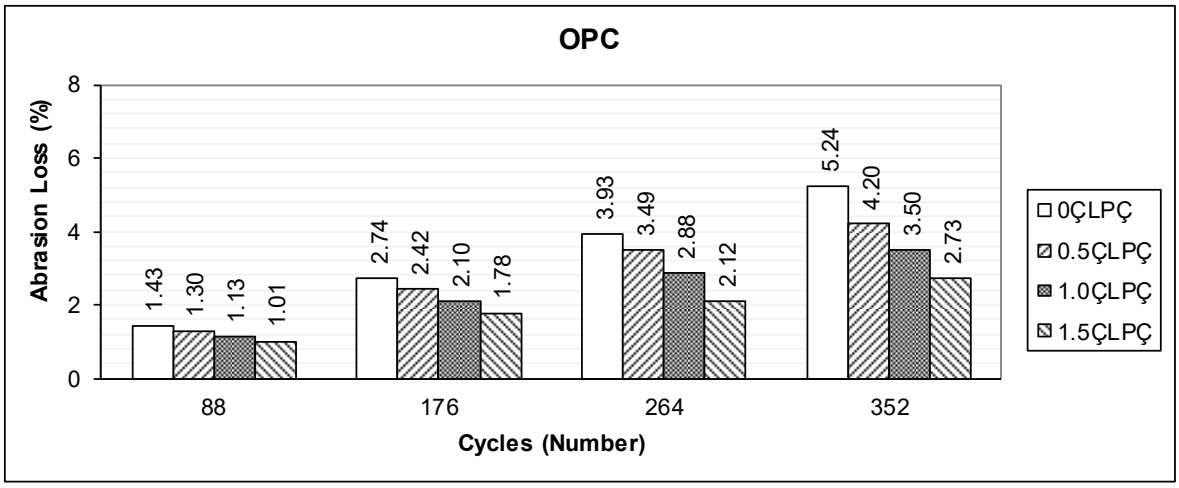

Fig. 1. Abrasion losses of OPC mortar

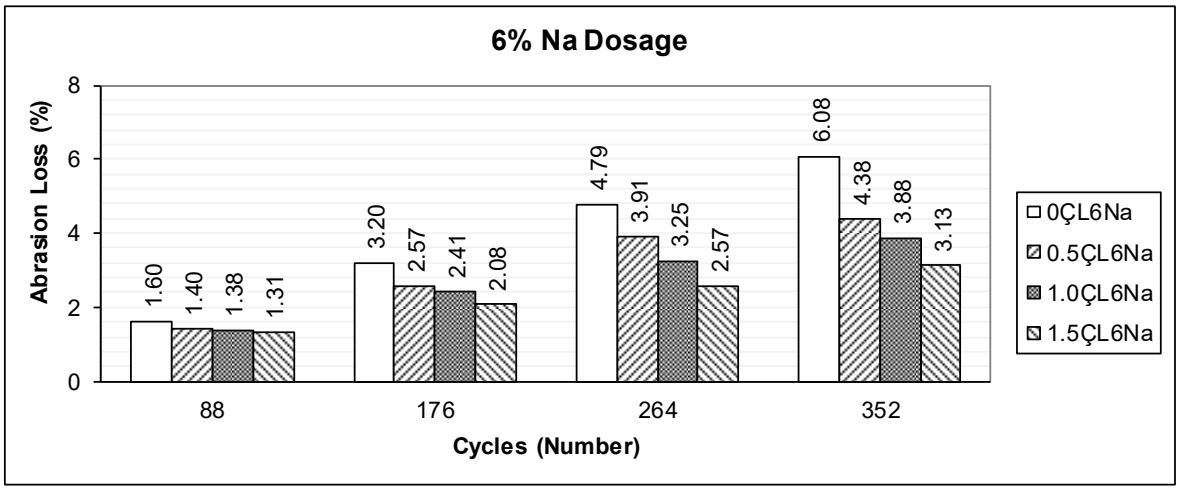

Fig. 2. Abrasion losses of geopolymer mortar containing 6% Na

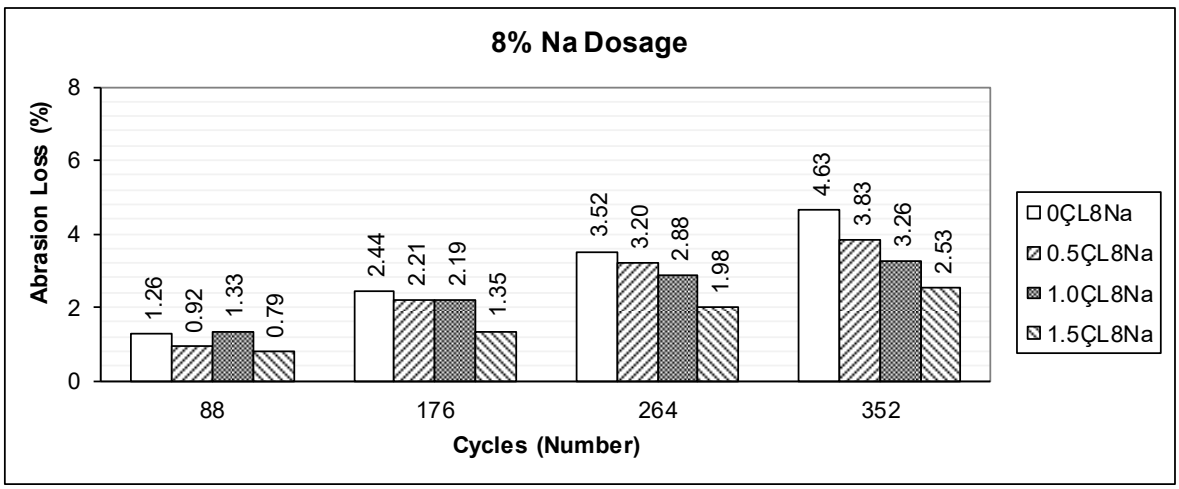

Fig. 3. Abrasion losses of geopolymer mortar containing 8% Na

According to Fig. 1, the wear loss values of the steel fiber-free OPC mortar after 88, 176, 264 and 352 cycles were 1.43%, 2.74%, 3.93% and 5.24%, while the wear losses of the steel fiber added mortars after 88 cycles were 1.01% to 1.01%. 1.30%; Wear losses after 176 cycles of 1.78% to 2.42%; Wear losses after 264 cycles from 2.12% to 3.49%; The wear losses after 352 cycles were between 2.73% and 4.20%. According to Fig. 2, where the wear losses of the 6% Na activated slag mortar are given, the end-cycle wear losses of the 88, 176, 264 and 352 cycle of the steel-free geopolymer mortar were 1.60%, 3.20%, 4.79% and 6.08% wear losses of geopolymer mortars after 88 cycles of 1.31% to 1.40%; Wear losses after 176 cycles of 2.08% to 2.57%; Wear losses after 264 cycles of 2.57 to 3.91%; The wear losses after 352 cycles ranged from 3.13% to 4.38%. In Fig. 3, the wear losses of the 8% Na activated slag mortar are given, whereas the end-cycle wear losses of 88, 176, 264 and 352 cycles of steel-free geopolymer mortar are 1.26%, 2.44%, 3.52% and 4.63%, while steel fiber is added. wear losses of geopolymer mortars after 88 cycles of 0.79 to 1.33%; Wear losses after 176 cycles of 1.35 to 2.21%; Wear losses after 264 cycles from 1.98% to 3.20%; Wear losses after 352 cycles were between 2.53% and 3.83%.

5. CONCLUSION

According to the findings obtained from this study, due to the increasing exposure of Al_2O_3 powder to the corrosive effect, the volumetric losses in mortar samples increased with the increase in the number of revolutions. On the other hand, the increase in the dosage of steel fiber in the mixture increased the abrasion resistance of the mortars, and the abrasion resistance of the steel fiber added mortars was higher than that of the steel fiber-free mixture, since it resists fragmentation from the surface by friction. In addition, while the abrasion resistance of the geopolymer mortar was slightly lower than the OPC mortar for the 6% Na dosage, the abrasion resistance of the geopolymer mortar containing 8% Na was higher than all. Therefore, the use of alkali-activated slag as binder material in the mixture instead of cement has provided a significant increase in the abrasion resistance of the mortars.

When these results are taken into consideration, it is said that, in eliminating environmental problems caused by industrial wastes and providing technical benefit, slag can be activated with alkali solutions and used as binder material on surfaces exposed to abrasion in construction sector.

REFERENCES

Dias D.P., Thaumaturgo C. (2005). "Fracture toughness of geopolymeric concretes reinforced with basalt fibers". Cement and Concrete Composites, 27(1), 49-54.

Juenger, M.C.G., Winnefeld, F., Provis, J.L. and Ideker, J. (2011). "Advances in alternative cementitious binders", Cement and Concrete Research 41 (12), 1232–1243.

Pacheco-Torgal, F., Castro-Gomes, J., Jalali, S. (2007).Investigations about the effect of aggregates on strength and microstructure of geopolymeric mine waste mud binders, Cement and concrete research 37 (6), 933-941.

Provis, J.L. and van Deventer, J. (2014). "Alkali Activated Materials", RILEM State of The Art Reports.

Savastano Jr, H., Warden, P.G., Coutts, R.S.P. (2003). Potential of alternative fibre cements as building materials for developing areas, Cement and Concrete composites 25 (6), 585-592.

TS EN 196-1. (2009). "Methods of Testing Cement - Part 1: Determination of Strength", Turkish Standards Institution, Ankara, Turkey.

TS EN 197-1. (2012). "Cement- Part 1: Compositions and Conformity Criteria for Common Cements", Turkish Standards Institution, Ankara, Turkey.

TS 2824 EN 1338. (2005). "Concrete Paving Blocks - Requirements and Test Methods", Turkish Standards Institution, Ankara, Turkey.

Wang, S.D., Pu, X.C., Scrivener, K.L., Pratt, P.L. (1995). Alkali Activated Slag Cement and Concrete: A Review of Properties and Problems. Advances in Cement Research, Vol. 7, No. 27, pp. 93–102.

CISET - 2nd Cilicia International Symposium on Engineering and Technology
10-12 October, 2019, Mersin / TURKEY

INFLUENCE OF STEEL FIBER ADDITION ON DRYING SHRINKAGE OF ALKALI-ACTIVATED SLAG MORTARS

Cahit Bilim [*1], İlker Fatih Kara [2], Fatih Özcan [3] and Yunus Emre Akkaş [4]

[1] Mersin University, Faculty of Engineering, Department of Civil Engineering, Mersin, Turkey
cbilim@mersin.edu.tr

[2] Mersin University, Faculty of Engineering, Department of Civil Engineering, Mersin, Turkey
ifkara@mersin.edu.tr

[3] Mersin University, Faculty of Engineering, Department of Civil Engineering, Mersin, Turkey
fatihozcan@mersin.edu.tr

[4] Mersin University, Faculty of Engineering, Department of Civil Engineering, Mersin, Turkey
yunusemreakkas@mersin.edu.tr

ABSTRACT
In this study, the effects of steel fiber addition on the solution of high drying shrinkage problem in alkali-activated slag binders were investigated. Mortar mixtures containing 0%, 0.5%, 1% and 1.5% steel fiber were produced on volume basis. The sand / binder ratio of the mortar mixtures was 3 and the water / binder ratio was 0.50. Drying shrinkage measurements were performed on prism samples of 25 x 25 x 285 mm for 28 days. According to the results obtained from the experimental study, the drying shrinkage of alkali-activated slag mortars is higher than the drying shrinkage of normal Portland cement mortar, but it is useful to determine the addition of steel fiber into the mixture to reduce the drying shrinkage values of alkali-activated slag mortars.

Keywords: *Drying Shrinkage, Mortar, Steel Fiber, Alkali-Activated Slag*

[*] Corresponding Author

1. INTRODUCTION

In today's construction industry, inorganic materials with superior properties, which can be an alternative to Portland cement requiring large amounts of energy for production and that has an important place in environmental pollution with carbon dioxide emitted to the atmosphere, are needed, and many comprehensive researches are conducted on this subject. Alkali-activated slag binders obtained by using activator and 100% slag without adding any cement are of particular interest in that they require lower energy consumption compared to Portland cements and thus produce less carbon dioxide. Various applications on alkali-activated slag binders, which are the main application areas are the repair and precast components, show that these binders exhibit higher strength and performance under aggressive ambient conditions than normal Portland cements. However, these new types of fasteners have some problems such as fast setting and high drying shrinkage, and these problems prevent for the widespread use of such fasteners, and need to be solved first in order to use these materials commercially.

In the studies carried out, it has been reported that sodium silicate is a highly effective activator in terms of strength in the activation of slag systems, but slag mortars activated with sodium silicate solution exhibit high shrinkage values at high alkali concentrations (Bakharev *et al.*, 1999). In another study that investigated the machinability and mechanical properties of alkali activated slag concretes, it was stated that activated slag concretes showed higher drying shrinkage compared to normal Portland cement concrete (Collins and Sanjayan, 1999a). In another study, it was reported that the complete replacement of water saturated blast furnace slag aggregate with coarse aggregate of normal weight resulted in a significant reduction in drying shrinkage of 40% (Collins and Sanjayan, 1999b). Collins and Sanjayan (2000) indicated that alkali-activated slag concretes showed higher drying shrinkage compared to normal Portland cement concrete, and reported that the capillary tensile forces generated during drying were highly effective on the drying shrinkage of alkali-activated slag concretes. Kutti *et al*. (1992) investigated alkali-activated slag concrete exposed to 59% relative humidity by examining the 12-month shrinkage values. They reported that slag concretes 1.83 times more shrinkage than Portland cement. Jang *et al*. (2014) investigated the properties of alkali activated fly ash / slag paste containing superplasticizer. They activated the UK / YFC ratio by selecting 0, 30%, 50%, 70% and 100% with NaOH and Na_2SiO_3. They observed a high rate of autogenous shrinkage in mixtures containing 70% and 100% slag. On the other hand, Bilim *et al. (2015)* investigated the different curing conditions and chemical additives to examine the shrinkage properties of alkali-activated slag mortars and they reported that hot curing and especially shrinkage reducing chemical additive is beneficial in reducing shrinkage.

Increasing the use of alkali-activated slag binders in the construction sector depends on the technical knowledge to be obtained from the researches. Therefore, in this study, the effects of steel fiber addition on drying shrinkage of geopolymer mortars containing slag activated by using alkaline solution were investigated and it was aimed to contribute to the current knowledge level in the literature.

2. EXPERIMENTAL PROGRAM

In the produced mortars, the ground granulated blast furnace slag (GGBFS) whose chemical and physical properties are given in Table 1 and CEM I 42.5 R ordinary Portland cement (OPC) according to TS EN 197-1 (2012) were used. Water / binder ratio was selected as 0.50 and sand / binder ratio was selected as 3.0 in the mortar mixtures where standard sand was used as fine aggregate in compliance with TS EN 196-1 (2009). In the production of the mortars, RC 65/60 BN type, which has a length of 60 mm, a diameter of 0.90 mm and a fineness (length / diameter) of 65, was used with two ends of hooks, uncoated and low carbon steel fiber. The steel fibers were incorporated into mortar mixtures at 0%, 0.5%, 1.0% and 1.5% by volume.

Table 1 – Chemical and physical properties of OPC and GGBS

Composition (%)	OPC	GGBFS
SiO_2	14.38	35.40
Al_2O_3	3.33	11.20
Fe_2O_3	2.85	0.96
CaO	67.36	41.50
MgO	1.60	6.14
Na_2O	0.41	0.28
K_2O	1.09	0.81
SO_3	4.51	1.49
Cl^-	0.35	0.079
Blaine value (cm^2/g)	3250	4300
Specific gravity	3.15	2.64

Sodium activation + sodium silicate solution with a modulus value (Ms = SiO_2 / Na_2O) of 1.0 with a dosage of 8% Na based on the amount of slag by weight was used in the activation of the slag. The notations of the mixtures are shown in Table 2.

Table 2 – Mixture notations

Mixture	OPC	GGBFS	Dosage	Steel Fiber
0ÇLPÇ	100%	-	-	0%
0.5ÇLPÇ	100%	-	-	0.5%
1.0ÇLPÇ	100%	-	-	1.0%
1.5ÇLPÇ	100%	-	-	1.5%
0ÇL8Na	-	100%	8% Na	0%
0.5ÇL8Na	-	100%	8% Na	0.5%
1.0ÇL8Na	-	100%	8% Na	1.0%
1.5ÇL8Na	-	100%	8%Na	1.5%

Prismatic samples with dimensions of 25x25x285 mm were produced within the scope of the study in order to investigate the effect of steel fiber on drying shrinkage of geopolymer mortars. 24 hours after casting, these prismatic samples were taken out of their molds and kept in the laboratory for 28 days according to ASTM C157/C157M (2017).

3. RESULTS AND DISCUSSION

Experimental results of drying shrinkage obtained from prismatic samples produced from mortar mixtures are given in Fig. 1 and Fig. 2.

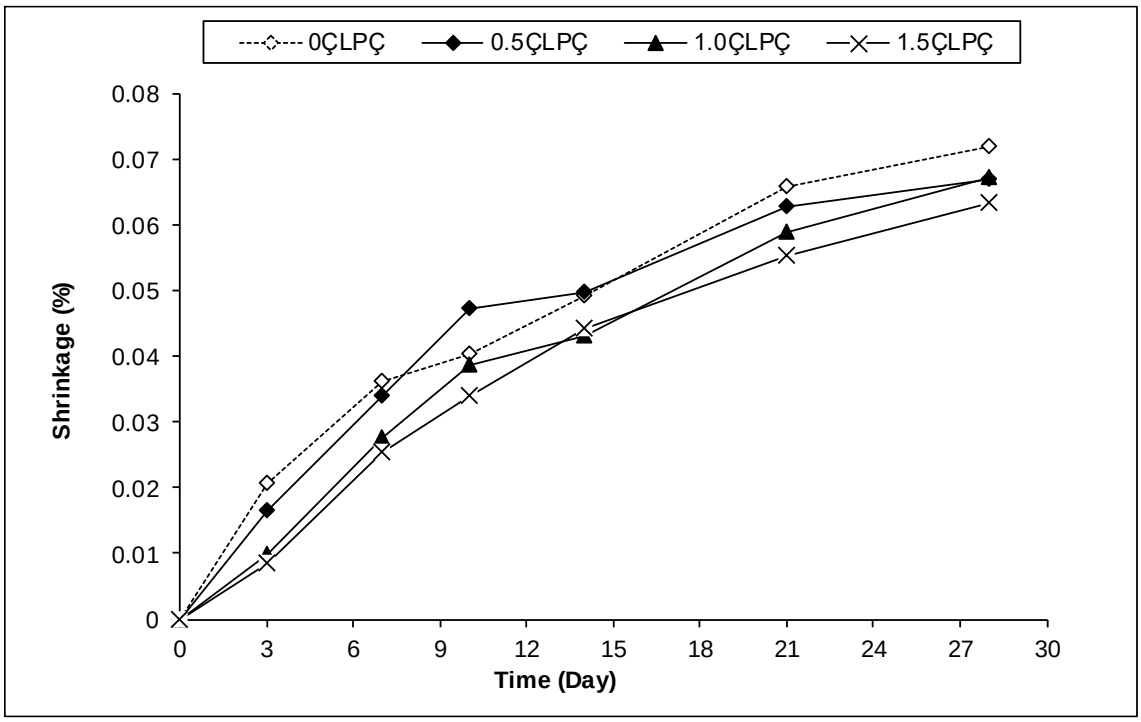

Fig. 1. Effects of steel fiber addition on drying shrinkage of OPC mortar

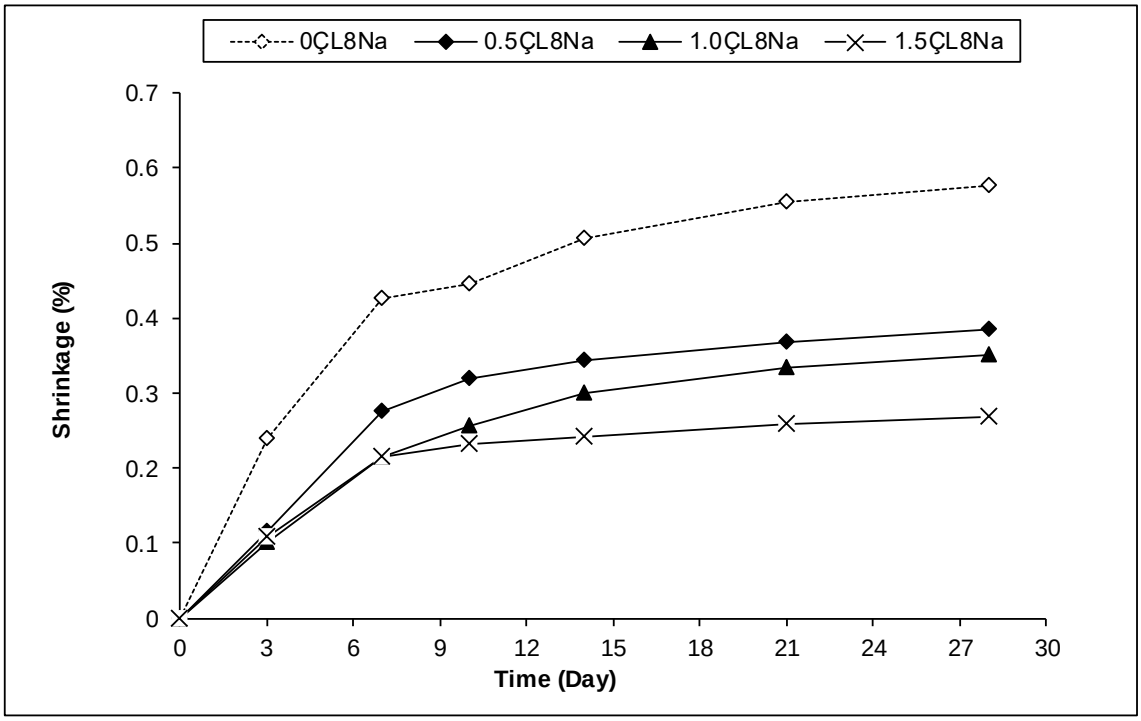

Fig. 2. Effects of steel fiber addition on drying shrinkage of geopolymer mortar with 8% Na

According to Fig. 1, the drying shrinkage value of the OPC mortar without steel fiber was 0.07% at the end of 28 days, while the drying shrinkage values of the steel fiber added mortars were 0.067% for 0.5QPP, 0.067% for 1.0QPPP and 0.064% for 1.5QPPP. On the other hand, according to Fig. 2, in which the drying shrinkage values of 8% Na activated slag mortar are found, 28 days post-drying shrinkage value of the steel fiber-free geopolymer mortar is 0.576%, while the drying shrinkage value of the steel fiber added geopolymer mortars is 0.5% for 0.5ÇL8Na. 0.385 was 0.351% for 1.0CL8Na and 0.267% for 1.5CL8Na.

As can be seen from Figs. 1 and 2, the drying shrinkage values of alkali activated slag slurries are significantly higher than the drying shrinkage values of normal Portland cement mortar. However, the addition of steel fiber into both normal Portland cement and geopolymer mortars is beneficial in reducing the drying shrinkage by reducing the drying shrinkage values. This beneficial effect is thought to result from the high deformation resistance of the steel fibers against the tensile forces during drying.

5. CONCLUSION

According to the results of the experimental study, the use of alkali activated slag as a binding material instead of cement in the mixture led to a significant increase in the drying shrinkage values of the mortars. However, it has been found that the addition of steel fibers into the mixture is particularly beneficial in reducing high drying shrinkage values in alkali activated slag slurries. In this regard, due to the magnitude of shrinkage unit deformations, it is considered appropriate to investigate the effectiveness of hot curing applications and shrinkage reducing chemical additives in combination with the use of steel fibers to reduce shrinkage problems encountered in alkaline activated slag binders.

REFERENCES

ASTM C157/C157M-17, Standard Test Method for Length Change of Hardened Hydraulic-Cement Mortar and Concrete. American Society for Testing and Material, 2017.

Bakharev, T., Sanjayan, J.G., Cheng, Y.B., (1999). Alkali Activation of Australian Slag Cements, Cement and Concrete Research, 29, 113–120.

Bilim, C., Karahan, O., Atiş, C. D., İlkentapar, S. (2015). "Effects of chemical admixtures and curing conditions on some properties of alkali-activated cementless slag mixtures", KSCE Journal of Civil Engineering, 19 (3) 733-741.

Collins, F.G., Sanjayan, J.G. (1999a). Workability and Mechanical Properties of Alkali Activated Slag Concrete, Cement and Concrete Research, 29, 455–458.

Collins, F., Sanjayan, J.G. (1999b). Strength and Shrinkage Properties of Alkali-activated Slag Concrete Containing Porous Coarse Aggregate, Cement and Concrete Research, 29, 607–610.

Collins, F., Sanjayan, J.G. (2000). Effect of Pore Size Distribution on Drying Shrinkage of Alkali-Activated Slag Concrete, Cement and Concrete Research, 30, 1401–1406.

Jang, J. G., Lee, N. K., Lee, H. K., 2014. Fresh and hardened properties of alkali-activated fly ash/slag pastes with superplasticizers. Construction and Building Materials, Vol. 50, pp. 169-176.

Kutti, T., Berntsson, L., Chandra, S. (1992). Shrinkage of Cements with High Content of Blast Furnace Slag. İstanbul, American Concrete Institute, Farmington Hills, pp. 615-625.

TS EN 196-1. (2009). "Methods of Testing Cement - Part 1: Determination of Strength", Turkish Standards Institution, Ankara, Turkey.

TS EN 197-1. (2012). "Cement- Part 1: Compositions and Conformity Criteria for Common Cements", Turkish Standards Institution, Ankara, Turkey.

CISET - 2nd Cilicia International Symposium on Engineering and Technology
10-12 October, 2019, Mersin / TURKEY

ELEVATED TEMPERATURE EFFECT ON BOND STRENGTH OF GEOPOLYMER CONCRETES

Müzeyyen Balçıkanlı Bankir [*1], Umur Korkut Sevim [2]

[1] Iskenderun Technical University, Engineering and Natural Sciences Faculty, Civil Engineering, Hatay, Turkey, muzeyyen.balcikanli@iste.edu.tr
[2] Iskenderun Technical University, Engineering and Natural Sciences Faculty, Civil Engineering, Hatay, Turkey, ukorkut.sevim@iste.edu.tr

ABSTRACT
With the development of technology, environmental problems are increasing today. Cement is the most preferred material in the construction sector and it brings many economic damages and pollution. To reduce these, it is essential to reduce the use of cement. Therefore, in this study, 3 different concretes were produced by replacing 15% by weight with GBFS, FA and SF with cement and control group concrete (without any additive) was produced. Using concrete and reinforcement in buildings also necessitates the examination of the compatibility with each other in daily life. In this study, the flexural and compressive strength of the concrete under elevated temperatures, as well as how the adherence of reinforcement is affected by high temperatures were investigated. According to the results of the experiment, it was determined that the use of mineral admixtures can be effective on reducing the strength loss ratio and not be affected from high temperatures as much as plain cement concrete.

Keywords: *Slag, Fly Ash, Silica Fume, Elevated Temperature, Adherence*

[*] Corresponding Author

1. INTRODUCTION

Concrete is the most used and expensive building material in the construction sector. Considering the country's economy, geography, natural resources and habits, it is not possible to end the consumption of concrete. Since it is not possible to reduce the amount of usage, the unit cost of the concrete should be reduced. For this purpose, different concrete admixtures are used in the researches. Granulated Blast Furnace Slag (GBFS), Fly Ash (FA) and Silica Fume (SF) are commonly used additives. Since these additives are less expensive than cement and they also have storage problems, allowing them to produce concrete with better performance than the desired effect.

Additive materials can affect many properties of concrete in a positive way. Especially in reinforced concrete structures, the behavior of the reinforcement and the concrete directly affects the performance of the concrete. In environmental events such as fire, the separation time of reinforcement and concrete is important to ensure life safety. Depending on the exposed temperature level, both the strength loss of the concrete occurs and the adherence decreases. Studies to investigate this effect are available in the literature. Yang et al. (2018) investigated the performance of concrete-reinforcement bond under elevated temperature by embedding rusted reinforcement with a mass loss of less than 2%. Embedded reinforcements with 5 different corrosion levels were exposed to 4 different high temperatures. When the exposure temperature reaches 600 degrees, it is stated that the strength of the concrete and the bond between the concrete and the reinforcement are significantly reduced due to the different thermal expansion levels. Majhi and Nayak (2019) investigated the effect of replacement GBFS with cement and recycled aggregate with normal aggregate. The GBFS replacement ratio was 0%, 40% and 60%; recycled aggregate replacement ratio was 50% and 100 %. They determined the bond strength change according to replacement ratio. It is indicated that strength values decreased with the increase in GBFS content, the high volume GGBFS can be utilized in the production of sustainable concrete.

Tanyıldızı (2009), searched the bond strength with replacement 10% silica fume and it is reported an increase of 30% in the bond strength of concrete. When 10% silica fume was used as partial cement replacement it is resulted as improvement was attributed to the high pozzolanic activity of silica fume. Tanyildizi also utilized fly ash and used at a cement replacement level of 15% in concrete. The bond strength was lower compared to the concrete with silica fume; however, the presence of fly ash still contributed to the increase of about 15% in the bond strength compared to the control concrete without any mineral admixtures. Robins and Standish (1986), indiceted an increase of up to 50% in the bond strength of concrete through the use of 20% silica fume.

When the literature studies were examined, the performance of the additives at different rates was examined, but no study could be found by the authors investigating the performance of the different materials under the same conditions. In this study, three different pozzolan additives were replaced with cement at the same ratio and four different concrete was produced with a control sample. It is known that GBFS, FA and SF contribute to concrete strength, but it has not been predicted how much the structural elements can maintain adherence with reinforcement after exposure to high temperature effect and which additive has a better resistance to high temperature. So the bond strength between different concretes and reinforcement was investigated.

2. MATERIALS AND METHOD

2.1. Materials

The specific gravities were 2.89 g / cm^3, 2.2 g / cm^3 and 2.25 g / cm^3 for GBFS, SF and FA, respectively. Blaine finenesses of GBFS, SF and FA were 5400 cm^2 / g, 210800 cm^2 / g, 2870 cm^2 / g, respectively. CEM I 42.5 R Portland cement was used. The characteristics for GBFS, FA and SF are given in Table 1 and the properties of cement are given in Table 2. Limestone based sand with the largest grain size of 4 mm and crushed stone aggregate with the largest grain size of 12 mm were used. Iskenderun city water was used as mixing water.

Table 1. Characteristics of GBFS, FA and SF

Analysis	GBFS	FA	SF
SiO_2 (%)	43.1	56.2	90.3
Al_2O_3 (%)	11.3	20.1	0.7
Fe_2O_3 (%)	0.7	6.7	1.3
CaO (%)	36.2	4.2	0.5
MgO (%)	6.1	1.9	0.0
SO_3 (%)	0.6	0.5	0.4
Loss of ignition (%)	0.0	1.7	3.1

Table 2. Characteristics of CEM I 42.5 R

Analysis	Result
Initial setting (min)	200
Final setting (min)	240
Specific gravity (g/cm^3)	3.15
Blaine fineness (cm^2/g)	3880
SO_3 (%)	2.48
MgO (%)	0.85
Loss of ignition (%)	2

2.2. Methods

GBFS, FA, and SF were replaced 15% by weight with cement. Binder dosage 400 kg / m^3 and b / w were selected as 0.5 to produce four different concretes. Mixture details are given in Table 3. Flexural strength was determined according to ASTM C78 on 100x100x500 mm beam sample. The compressive strength of the produced concrete samples was determined on 100x100x100 mm cube samples after 28 days. The samples exposed to laboratory conditions (23 °C), 250, 500 and 750 °C for 2 hours with an elevated temperature oven that rises the temperature 10 °C in a minute, according to ASTM C39.

Table 3. Mix design and test procedures

Temperature (°C)	Mix No	GBFS (%)	FA (%)	SF (%)
23 °C	B1	0.0	0.0	0.0
	B2	15	0.0	0.0
	B3	0.0	15	0.0
	B4	0.0	0.0	15
250 °C	B1	0.0	0.0	0.0
	B2	15	0.0	0.0
	B3	0.0	15	0.0
	B4	0.0	0.0	15
500 °C	B1	0.0	0.0	0.0
	B2	15	0.0	0.0
	B3	0.0	15	0.0
	B4	0.0	0.0	15
750 °C	B1	0.0	0.0	0.0
	B2	15	0.0	0.0
	B3	0.0	15	0.0
	B4	0.0	0.0	15

In order to determine the adherence (pull out) of the reinforcement with concrete, a □100 / 200 mm cylinder concrete specimen was produced and □14 mm reinforcement was embedded to top-down. After 24 hours, the samples were removed from the mold and cured in water for 28 days. After samples returned to laboratory conditions, they were exposed to temperatures of 250, 500 and 750 °C and then the pull-out test was performed. The schematic representation of the pullout test apparatus is shown in Figure 1. As seen in the experimental setup, the pump, hydraulic system, load cell, pulling load was applied to the reinforcement by using the grips to grasp the reinforcement firmly and a suitable computer program was used to record the applied load. Adherence properties were compared according to the amount of load read against the stress that the reinforcement showed when stripping from concrete. Each experiment was repeated on three samples.

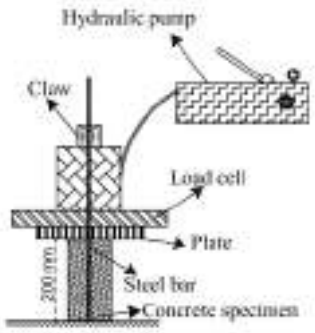

Fig. 1. Schematic representation of pull out set up

3. RESULTS AND DISCUSSIONS

Produced specimens by replacement of GGBS, FA and SF with cement and exposed different levels of elevated temperatures, were tested. The test results are presented and discussed below.

3.1. Flexural Strength

100x100x500 mm beam samples were subjected to three point bending test according to related standard. Results of the test are shown in Figure 2.

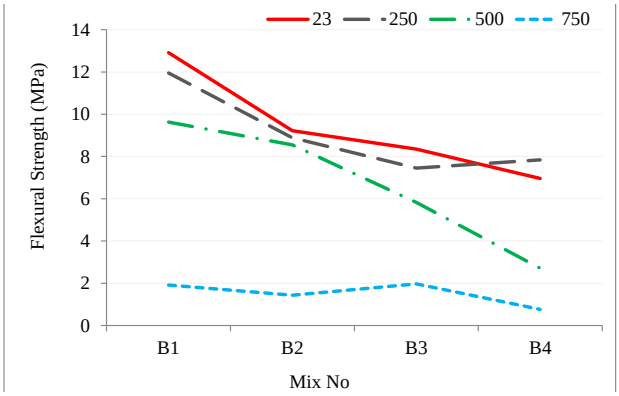

Fig. 2. Flexural strength of beam specimens according to different elevated temperatures

It has been observed that there are significant changes in the flexural strength of the samples taken from 3 different concrete containing 15% different additives (GBFS, FA, SF) and control concrete without any additives. It was observed that as the temperature value increased, the flexural strength decreased with the formation of small cracks as a result of the micro-size water coming through out of the concrete. When the additives that were used are compared with each other, it was found that GBFS was more resistant than FA and FA was more resistant than SF. After exposing 750 ° C, the flexural strength decreased by 85% in the control sample but 76% reduction in the mixture containing FA was determined. This shows that the use of additive material has a positive effect on crack behavior.

3.2. Compressive Strength

100x100x100 mm cube specimens were subjected to uniaxial compressive strength test according to related standard. Results of the test are shown in Figure 3.

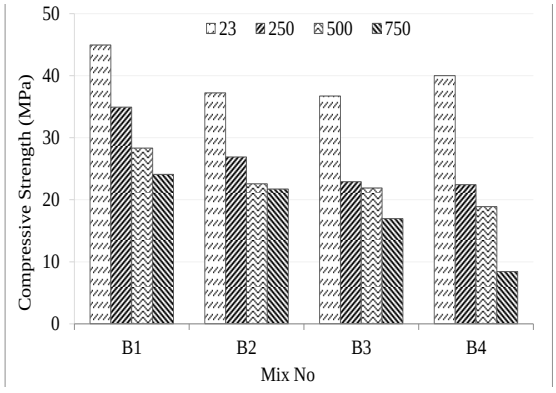

Fig. 3. Compressive strength of cube specimens according to different elevated temperatures

The performance of different concretes exposed to high temperatures changed depending on the temperature. Without exception, all samples lost strength under high temperature. It is also seen that the strength of the concrete containing SF at 23 °C is almost the same as the control concrete. As seen in Figure 3, B1 concrete lost 22% of its initial strength at 250 °C, while 37% at 500 °C and 46% at 750 °C. After exposure to 250 °C, 500 °C and 750 °C; B2 concrete 27%, 39% and 41%; B3 concrete 37%, 40% and 53%; B4 concrete 43%, 52% and 78% lost their own initial strength respectively. As in the flexural strength, it was found that GBFS was more resistant than FA and FA was more resistant than SF on compressive strength.

3.3. Pull Out Capacity

14 mm reinforcement embedded ϕ100 / 200 mm cylinder concrete specimen was subjected to pull out test and compared with each other. Results of the test are shown in Figure 4.

High temperature application adversely affected reinforcement adherence as well as flexural and compressive strength. Due to the temperature increase, it is easier to peel the reinforcement from the concrete. Since at lower slip values the bond strength is mainly governed by the adhesion force between the concrete and reinforcing bar, the bond stress at these low slip values could be taken as the indication of the adhesion strength and thus the bond stiffness. Bingöl and Gül (2009) indicated that it is known that there is a linear relationship between compressive strength and adherence properties of concrete. Figure 4 shows that the adherence between reinforcement and concrete is directly proportional to the compressive strength. B1 concrete carries 124 kg at 23 °C, while it is 89.95 kg after exposure to 250 °C, 77.96 after exposure to 500 °C, and 4.52 kg after exposure to 750 °C. Adherence loss ratio between 23 °C and 750 °C for B1, B2, B3 and B4 are 62%, 86%, 88% and 93%, respectively.

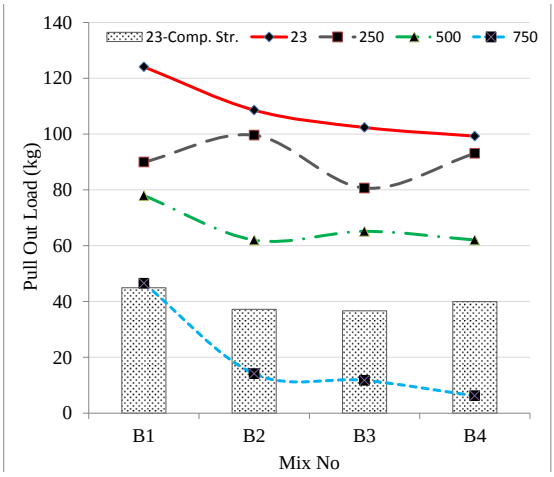

Fig. 4. Pull out capacity of cylinder specimens and compressive strength according to different elevated temperatures

4. CONCLUSION

Samples taken from 3 different concrete produced by the replacement of GBFS, SF and FA with cement and from control concrete were subjected to flexural strength, compressive strength and adherence (pull out) tests.

Although the use of mineral admixture had a negative effect on the flexural strength of the concrete for 28 days, it was observed that it decreased the strength loss rate under high temperature effect compared to the first case. GBFS addition made the concrete more resistant than FA and FA addition made the concrete more resistant than SF on compressive strength. It has been found that there is not a very significant decrease in the concrete adherence with reinforcement up to 250 °C and that the samples can maintain approximately half of the initial value after exceeding 250 °C and lost 80% - 90% of the initial value at 750 °C.

REFERENCE

ASTM International: Standart Test Method for Compressive Strength of Cylindirical Concrete Specimens, ASTM C39/C39M-10, 2010.

ASTM International: Standart Test Method for Flexural Strength of Concrete (Using Simple Beam with Third-Point Loading), ASTM C78/C78M-10, 2010.

Bingöl A. F. and Gül, R. (2009). "Donatı-Beton Aderansı, Yüksek Sıcaklıkların Beton Dayanımına ve Aderansa Etkileri Konusunda Bir Derleme," Tübav Bilim Dergisi, Vol. 2, pp. 211-230.

Majhi, R. K., and Nayak, A. N. (2019). "Bond, durability and microstructural characteristics of ground granulated blast furnace slag based recycled aggregate concrete." Construction and Building Materials, Vol. 212, pp. 578-595.

Mo, K. H., Alengaram, U. J., and Jumaat, M. Z. (2016). "Bond properties of lightweight concrete–a review." Construction and Building Materials, Vol. 112, pp. 478-496.

Robins P. J., Austin S. A. (1986). "Bond of lightweight aggregate concrete incorporating condensed silica fume." ACI Special Pub. Vol. 2, pp. 941–958.

Tanyildizi, H. (2009). "Fuzzy logic model for the prediction of bond strength of high strength lightweight concrete."Adv. Eng. Softw. Vol. 40, No. 3, pp. 161–169.

Yang, O., Zhang, B., Yan, G., and Chen, J. (2018). "Bond Performance between Slightly Corroded Steel Bar and Concrete after Exposure to High Temperature." Journal of Structural Engineering, Vol. 144, No. 11. 04018209.

CISET - 2nd Cilicia International Symposium on Engineering and Technology
10-12 October, 2019, Mersin / TURKEY

INVESTIGATION OF FULLY ENVIRONMENTALLY FRIENDLY WASTE AGGREGATED ALKALI ACTIVATED MORTARS

Müzeyyen Balçıkanlı Bankir [*1], Umur Korkut Sevim [2]

[1] Iskenderun Technical University, Engineering and Natural Sciences Faculty, Civil Engineering, Hatay, Turkey, muzeyyen.balcikanli@iste.edu.tr
[2] Iskenderun Technical University, Engineering and Natural Sciences Faculty, Civil Engineering, Hatay, Turkey, ukorkut.sevim@iste.edu.tr

ABSTRACT
Cement is one of the most widely used materials in construction. By reducing cement production, both natural resource consumption and energy savings are possible. For this reason, in order to investigate the usability of Electric Arc Furnace Slag, Basic Oxygen Furnace Slag and Blast Furnace Slag as aggregate in structures, environmentally friendly mortar was produced in this study without using any cement. As the binder, BFS was activated with sodium hydroxide and sodium silicate. In order to investigate the workability of the produced mortars in fresh state, flow table; flexural and compressive strength tests were performed to determine their strength in hardened state. According to the experimental results, it is concluded that these by-products can be a good alternative to natural aggregates.

Keywords: *Slag, Aggregate, Alkali Activation, Flow Diameter, Mortar*

[*] Corresponding Author

1. INTRODUCTION

In the production of concrete, a significant amount of natural raw material and cement, which is one of its main components, requires a lot of energy. During the production of cement, a large amount of CO_2 is emitted into the atmosphere and natural resource consumption is increasing. Therefore, in order to minimize the use of such materials that harm the environment, the search for a new generation of alternative, environmentally friendly materials has become the basic need of the sector. In addition, some industrial by-products cause long-term stocking problems and create extra costs. Basic Oxygen Furnace Slag (BOFS), Electric Arc Furnace Slag (EAFS), Blast Furnace Slag (BFS) can be used effectively to solve these problems. EAFS is generally considered as aggregate in road pavements as foundation-subbase or aggregate in concrete (Pellegrino vd., 2013; Pasetto and Baldo, 2010) Hainin et al. (2012), indicated BFS has some advantageous properties for use as an ideal aggregate. It has high impact and crush strength compared to natural aggregates. Based on high friction and abrasion resistance, steel slag is widely used on industrial roads and in places where abrasion should be low. Motz and Geiseler (2001), indicated that the physical properties of SS aggregates are superior to crushed limestone aggregates. BFS is high in terms of engineering applications is suitable for the expressed. Sorlini et al. (2012), examined the physical, geometric, mechanical and chemical properties of EAFS by performing various experiments. According to the test results, they found that EAFS has comparable wear resistance and water absorption values with the values obtained from natural aggregates. They stated that all harmful elements in the EAFS are below the boundary limits. Vasanthi (2014) tested the bending behavior of slabs containing SS by replacing steel slag with natural aggregate at 0, 30, 60 and 100% as partial replacement of 20 mm natural rough aggregate with respect to normal concrete. The use of 60% SS instead of coarse aggregate in concrete has been stated to achieve better workability and strength. (Yuksel, 2017),

EAFS, GBFS and BOFS were used instead of natural aggregates in this study in order to solve all problems encountered in the literature. As a binder, GBFS is activated with alkalis in order to avoid cement consumption. In other words, completely green eco-friendly mortars (GEM) are produced. In order to determine the processability of the produced mortar samples in fresh state, spreading diameter, bending and compressive tests were performed to determine their strength in hardened state.

2. MATERIALS AND METHOD

2.1. Materials

Blast Furnace Slag (BFS) which is used as binder in the study is Adana Çimento Sanayi T.A.Ş. / Iskenderun facilities. The BFS has a specific gravity of 2.89 g / cm^3 and a Blaine fineness of 540 m^2 / kg. The chemical composition of BFS is given in Table 1. The alkaline solution of NaOH and Na_2SiO_3 was used to give the binding properties of the BFS. The physical and chemical properties of these materials are given in Table 2 and Table 3. Mortar was produced by using EAFC, BOFC and GBFS aggregate with maximum grain size diameter of 4 mm. The densities of the EAFC, BOFC and GBFS are 3.57 g/cm^3, 2.87 g/cm^3 and 2.89 g/cm^3, respectively. In order to compare the performance of the EAFS, BOFS and BFS with control samples were produced using limestone-based crushed stone of the same size. Iskenderun city water is used in the production.

Table 1. Chemical composition of GBFS

Fe_2O_3	SiO_2	CaO	Al_2O_3	MgO	K_2O	Na_2O
0.74	35	36.25	11.34	6.10	0.75	0.28

Table 2. Physical and chemical properties of Na_2SiO_3

Properties	Result
SiO_2/Na_2O	3.19
Density (20 °C g/cm^3)	1.37
Na_2O (%)	8.52
SiO_2 (%)	27.09
Viscosity (at 20 °C)	202

Table 3. Chemical properties of NaOH

Properties	Analysis (%)
NaOH (g/kg)	≥ 990
Na2CO3 (g/kg)	≤ 4
Na2SO4 (mg/kg)	≤80
NaCl (mg/kg)	≤ 200
Fe (mg/kg)	≤ 10
As (mg/kg)	≤ 1
Sb mg/kg	≤ 5

2.2. Method

In the production of GEM activated by alkalis (AA), the ratio of binder (BFS): aggregate: alkali solution in accordance with ASTM C109 / C109M (2016) was chosen as 1: 2.75: 0.485 by weight, respectively.

Table 4. Mix design of mortars

NaOH (%)	Agg. type	NaOH (g)	Na_2SiO_3 (g)	Water (g)	Agg. (g)	Binder BFS
4%	EAFS	33	350	365	3310	1200
	BFS	22	237	250	2250	820
	BOFS	29	311	327	2965	1077
	Nat.	27	288	305	2750	1000
6%	EAFS	50	522	256	3310	1200
	BFS	33	355	175	2250	820
	BOFS	44	467	230	2965	1077
	Nat.	41	435	212	2750	1000
8%	EAFS	65	695	147	3310	1203
	BFS	45	473	100	2250	820
	BOFS	58	623	130	2965	1077
	Nat.	54	577	122	2750	1000

The silicate modulus (SiO_2 / Na_2O) of the activation

solution of all EAFC, BOFS and BFS mortars activated by alkalis was kept constant as 1,5. Details of the mortar design are given in Table 4.

The prepared mortar was poured into 40x40x160 mm molds and removed after 24 hours. The extruded samples were cured at 60 ° C for 8 hours and allowed to return to ambient temperature. Mortar samples with the same proportions were also produced as the control sample (Natural) to compare mortar samples produced by using EAFC, BOFS and BFS instead of crushed stone aggregate and using BFS instead of cement.

Flow diameter of fresh mortars produced was placed in a mold with a truncated cone shape and the surface was smoothed, the mold was lifted smoothly. The test was carried out in accordance with ASTM C230 / C230M-14. In order to determine the flexural strength, 3-point flexural test was performed on 40x40x160 mm3 samples in accordance with ASTM C348-02 (2002). After the flexural test, the compressive strength test was carried out in accordance with ASTM C349-02 (2002) using samples divided into 2 parts.

3. RESULTS AND DISCUSSIONS

Produced specimens by replacement of BFS, EAFS and BOFS with limestone based aggregate and the binder system is occurred with alkali activation of BFS. The specimens were tested for fresh and hardened properties of GEM. The test results are presented and discussed below.

3.1. Flow Diameter

The effect of EAFS, BOFS and BFS aggregates on the workability of the mortars and the effect of the change of alkaline concentration in the binding paste on the workability of the mortars were investigated by the test method mentioned above. As can be seen from Figure 1, the workability of the mortars having both the binder and the aggregate BFS is the lowest and the mortars having the aggregate BOFS are the highest. This is thought to result from both the geometric shapes of the aggregates and the fact that the water contained in the paste is not absorbed by the aggregates.

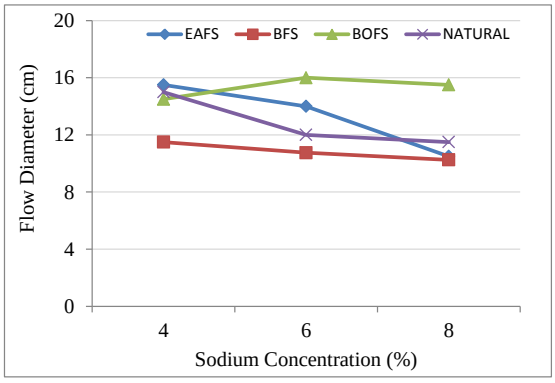

Fig. 1. Flow diameter of AA BFS mortars depending on aggregate type and sodium concentration

It has been found that as the sodium concentration increases, the workability of the mortars prepared by activating with alkalis in all mortars is generally decreased. This is thought to be due to the acceleration of reactions between BFS and alkali solution and acceleration of the setting with the rise of the alkaline medium. It was also found that the workability of mortars in which EAFS and BOFS were used as aggregate was better than the control mortars prepared with natural aggregate and it is shown in Figure 1.

3.2. Flexural Strength

The effect of EAFS, BOFS and BFS aggregates on the flexural strength of the mortars and the effect of the change of alkaline concentration in the binding system on the flexural strength of the mortars were investigated by the test method mentioned above.

Changes in flexural strength due to sodium concentration are shown in Figure 2. When the literature studies are examined, it is supported the experimental results of the study where there is a decrease in strength after a certain threshold value. Ya-min et al. (2015) stated that tensile strength is lower due to temperature curing due to the high number of micro cracks in the chemical shrinkage and matrix as reactions develop rapidly in slag concretes activated by alkalis cured at high temperatures. They stated that although the matrices of hardened slag and cement slurries became tighter as time progressed, these cracks progressed. As can be seen from Figure 2, the flexural strength decreased after the sodium concentration exceeded 6%. Depending on the type of aggregate, either both the shape and structure of the aggregates or the content of aggregate are affected the flexural strength.

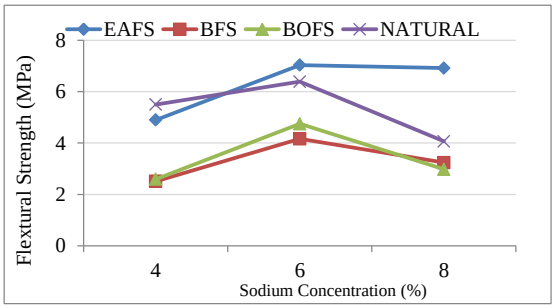

Fig. 2. Flexural strength of AA BFS mortars depending on aggregate type and sodium concentration

According to the results of the experiment, it is understood that the flexural strength of the mortars with EAFS is higher and the BOFS mortar and BFS is lower than that of the control sample. Since it is a known fact that flexural strength is directly affected by aggregate strength, it can be concluded that EAFS aggregate strength is close to or higher than natural aggregate. However, it can be concluded that the surface of aggregate dough may have been stronger in alkali activation in the EAFS aggregate mortar specimens.

3.3. Compressive Strength

The effect of EAFS, BOFS and BFS aggregates on the compressive strength of the mortars and the effect of alkaline concentration on the compressive strength of the mortars were investigated by the test method

mentioned above.

As seen in Figure 3, the compressive strength of EAFS aggregate mortars is higher than that of the control sample. It was found that the compressive strength increased due to the increase in sodium concentration.

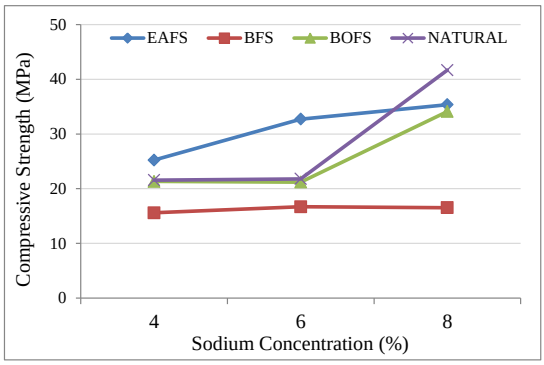

Fig. 3. Compressive strength of AA BFS mortars depending on aggregate type and sodium concentration

As well as flexural strength, compressive strength is directly affected by the strength of the aggregate. According to the test results, the compressive strength of the mortar samples with aggregate EAFS was higher than that of the control sample. It can be concluded that the strength of the EAFS aggregate is close to or higher than that of the limestone-based natural aggregate.

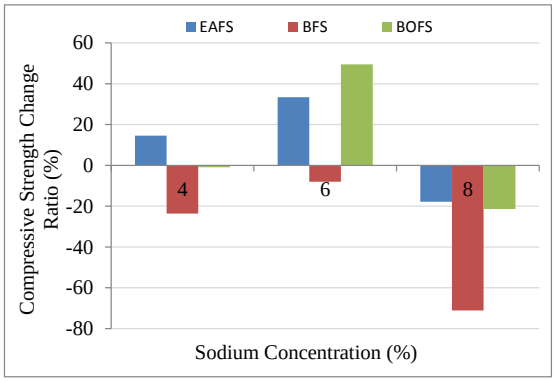

Fig. 4. Compressive strength change ratio according to control sample

Figure 4 shows the change in compressive strength relative to that of the control sample in percent, depending on aggregate type and alkali concentration. It was found that the compressive strength of the samples with alkaline concentration of 4% and 6% was 15% and 35% higher than the control sample, respectively. Compressive strength was below the control sample by 17% after exceeding the 6% alkaline concentration which is accepted as the threshold value for EAFS aggregate specimens.

5. CONCLUSION

Samples taken from 3 different mortar produced by the replacement of BFS, EAFS and BOFS with natural aggregate are subjected to fresh and hardened form tests as flow diameter, flexural and compressive strength. According to the experimental data, the following results were obtained:

It has been found that as the sodium concentration increases, the workability of the mortars prepared by activating with alkalis in all mortars is generally decreased. The workability of the mortars having both the binder and the aggregate BFS is the lowest and the mortars having the aggregate BOFS are the highest.

Flexural strength decreased after the sodium concentration exceeded 6%. Depending on the type of aggregate, either both the shape and structure of the aggregates or the content of aggregate are affected the flexural strength.

Compressive strength of the mortar samples with aggregate EAFS was higher than that of the control sample. It can be concluded that the strength of the EAFS aggregate is close to or higher than that of the limestone-based natural aggregate

REFERENCES

References should be listed in alphabetical order in the reference section.

ASTM C109/C109M. (2016). "Standard Test Method for Compressive Strength of Hydraulic Cement Mortars (Using 2-in. or [50-mm] Cube Specimens)." ASTM International, West Conshohocken, PA, http://www.astm.org,

ASTM C230 / C230M-14. "Standard Specification for Flow Table for Use in Tests of Hydraulic Cement." ASTM International, West Conshohocken, PA, 2014, www.astm.org

ASTM C348-02. "Standard Test Method for Flexural Strength of Hydraulic-Cement Mortars." ASTM International, West Conshohocken, PA, 2002, www.astm.org

ASTM C349-02. "Standard Test Method for Compressive Strength of Hydraulic-Cement Mortars (Using Portions of Prisms Broken in Flexure)." ASTM International, West Conshohocken, PA, 2002, www.astm.org

Hainin, M. R., Yusoff, N. I. M., Sabri, M. F. M., Aziz, M. A. A., Hameed, M. A. S., and Reshi, W. F. (2012). "Steel slag as an aggregate replacement in Malaysian hot mix asphalt." ISRN Civil Engineering, Article ID 459016.

Motz, H., and Geiseler, J. (2001). "Products of steel slags an opportunity to save natural resources." Waste Management, Vol.21, No. 3, pp. 285–293.

Pasetto, M., and Baldo, N. (2010). "Experimental evaluation of high performance base course and road base asphalt concrete with electric arc furnace steel slags."Journal of hazardous materials, Vol. 181, No.1-3, pp. 938-948.

Pellegrino, C., Cavagnis, P., Faleschini, F., and Brunelli, K. (2013). "Properties of concretes with black/oxidizing electric arc furnace slag aggregate." Cement and Concrete Composites, Vol. 37, pp. 232-240.

Sorlini, S., Sanzeni, A., and Rondi, L. (2012). "Reuse of steel slag in bituminous paving mixtures." Journal of Hazardous Materials, Vol. 209–210, pp. 84–91.

Vasanthi, P. (2014). "Flexural behavior of reinforced concrete slabs using steel slag as coarse aggregate replacement." IJRET: International Journal of Research in Engineering and Technology, Vol.3, No.9, pp. 141–146.

Ya-min G., Yong-hao F., Duo Y., Yong-fan G. ve Chen-hui Z., (2015). "Properties and microstructure of alkali-activated slag cement cured at below-and about-normal temperature." Construction and Building Materials, Vol. 79: pp. 1-8.

Yüksel, İ. (2017). "A review of steel slag usage in construction industry for sustainable development." Environment, development and sustainability, Vol. 19, No. 2, pp. 369-384.

CISET - 2nd Cilicia International Symposium on Engineering and Technology
10-12 October, 2019, Mersin / TURKEY

PRODUCTION OF PVA/CHITOSAN MEMBRANES AS TISSUE ENGINEERING SCAFFOLDS

Seda Ceylan*[1] and Didem Demir[2]

[1]Adana Alparslan Türkeş Science and Technology University, Department of Bioengineering, Adana, Turkey

[2]Mersin University, Department of Chemical Engineering, Mersin, Turkey

ABSTRACT

Tissue engineering is the use of a combination of cells, engineering methods, and suitable biochemical and physicochemical factors to improve or replace the biological tissues. Tissue engineering involves the use of a scaffold for the formation of new viable tissues for medical applications. Polymeric scaffolds have been used in tissue engineering applications because of their advantages such as biocompatibility and bioavailability. The main goal of this research is to produce suitable polyvinyl alcohol/chitosan (PVA-CHI) membrane scaffolds for skin tissue engineering applications. Chemically crosslinked membranes were synthesized using glutaraldehyde (GA) and genipin (GP) as the crosslinking agents. Chemical structure and pore morphology were demonstrated by Fourier transform infrared spectroscopy (FTIR) and scanning electron microscopy (SEM). Contact angle measurements and swelling ratio of the scaffolds were also determined. The overall results demonstrated that PVA-CHI membranes could have potentially appealing application as scaffolds for tissue engineering applications and crosslinking agents affect the architecture and characteristic properties of the membranes.

Keywords: *PVA, Chitosan, Membrane, Scaffold, Tissue engineering*

* Corresponding Author: sceylan@atu.edu.tr

1. INTRODUCTION

Tissue or organ failure is one of the most major problems in the world. Every year, due to diseases or accidents, millions of patients suffer from the loss or failure of organs (Lee and Mooney, 2001). Tissue engineering principles were developed to overcome clinical limitations including infection, donor availability, poor integration, and potential rejection of the grafts (Fallahiarezoudar et al., 2015; Gualandi, 2011).

Both natural and synthetic polymers have been extensively utilized in medicine and tissue engineering applications during the last decades (Cao et al., 2014; Hsieh and Liau, 2013). Synthetic polymers have predictable properties and can be tailored easily. On the other hand, natural polymers are bioabsorbent, biocompatible and do not induce an immune reaction or inflammation (Zhang et al., 2016). The main goal of blending synthetic and natural polymers is to obtain ideal scaffolds for tissue engineering applications

In this work, polyvinyl alcohol (PVA) and chitosan polymers were used to fabricate membrane scaffolds by using hydrogelation method. PVA is a water-soluble, non-toxic, flexible and biodegradable synthetic polymer. In addition to this, PVA has the unique capability of being chemically affine both to natural and synthetic polymers (Tocchio et al., 2015). Among the natural polymers, chitosan has also been widely used in the biomedical applications because of its highly hydrophilic nature, biodegradability and biocompatibility (Ali Akbari Ghavimi et al., 2015). Up to this time, for improving the mechanical properties and biocompatibility of scaffolds, natural and synthetic polymer blends are prepared using solution casting, freeze-thawing, and electrospinning methods (Dias et al., 2018; Gomes et al., 2001; Râpă et al., 2014).

In this study, the effect of polymer concentration and the type of crosslinking agent on the characteristics of PVA/CHI membrane scaffolds was analyzed with different physiochemical analyzes.

2. EXPERIMENTAL

PVA with a molecular weight 89.000-98.000 g/mol (99% hydrolyzed) and chitosan with low molecular weight were purchased from Sigma Aldrich, USA. Glacial acetic acid (100%) and GA (25%, aqueous) were obtained from Merck, Germany. GP was purchased from Sigma Aldrich, USA. Distilled water was used in all experimental steps.

2.1. Preparation of PVA/CHI membrane scaffolds

In this experiment, PVA with two different concentrations (5.0% and 7.5%, w/v) was prepared by dissolving the calculated amount of polymer in distilled water. The PVA solution was mixed at 90°C for 3 hours. Chitosan solution (1%, w/v) was dissolved in acetic acid solution (3%, v/v) for 3 hours under continuous stirring.

After that, in order to obtain the homogenous mixtures of PVA and chitosan, the polymer mixtures in equal volume were stirred continuously at room temperature. After that, the constant amount of glycerol (10µl) was added to the prepared polymer solutions. In this experiment, 25% (v/v) GA and 0.025% (w/v) GP solutions were used as crosslinking agents. These crosslinking agents was added immediately to the polymer mixtures (Table 1) and then the crosslinking agents added PVA-CHI solutions were cast in Polytetrafluoroethylene (PTFE) molds and let to crosslink for a period of 24 h at 40 °C in an incubator. Finally, four types of membranes were obtained using this procedure and characterization properties of membranes analyzed with chemical, physical and gravimetric analyzes.

Table 1. Quantities of polymers and type of crosslinking agents used in the preparation of PVA-CHI membranes.

PVA, %	Chitosan, %	GA	GP
5.0	1	+	-
7.5	1	+	-
5.0	1	-	+
7.5	1	-	+

2.2. FTIR

FTIR spectroscopy was performed (Perkin Elmer, FTIR/FIR/NIR Spectrometer Frontier-ATR, USA) to investigate the chemical groups in the synthesized membranes, within the range of 400-4000 cm^{-1}.

2.3. SEM analysis

SEM (SEM, FE-SEM Zeiss/Supra55, Quanta 400F Field Emission, USA) was used to analyze the morphology of the synthesized membranes. The samples were coated with a thin layer of platinum before analysis. SEM was operated at the acceleration of 5 kV and the magnification was 1000x.

2.4. Swelling ratio tests

To determine the swelling behavior of PVA-CHI membranes, the samples were dried at room temperature to a constant weight (WD). Then, dried samples were immersed in distilled water to obtain the swollen membranes. The excess water on the surface of the membranes was removed using a filter paper and the samples were weighed (WS). Swelling ratio percent (SR%) was calculated by the following equation:

$$SR\% = [(WS - WD) / (WD)]*100 \quad (1)$$

2.5. Contact angle measurement

Water contact angle measurements of PVA-CHI membranes were also analyzed by the sessile drop method. Three separate measurements were made on each sample at different locations.

3. RESULTS AND DISCUSSION

In this study, we demonstrate the fabrication of PVA and chitosan based membrane scaffolds by GA and GP crosslinking; and evaluate the resulting effect of these methods on the morphology and characteristic properties of the scaffolds. Figure 1 shows samples of the GP

crosslinked membranes.

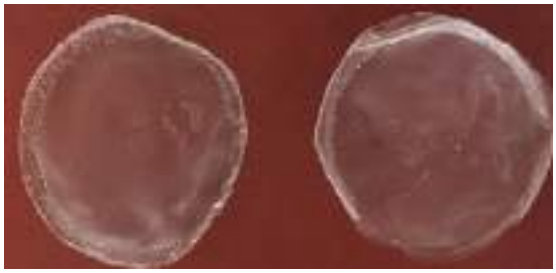

Fig.1. GP crosslinked PVA-CHI membranes

The FTIR spectrum of membranes crosslinked with GP and GA are presented in Figure 2. Using GA to crosslink the membranes causes the main absorption peak at 1646 cm^{-1} (imine bonds N=C) (Nazemi et al., 2014). The peak at 2936 cm^{-1} corresponds to C-H stretching vibration frequency. In addition, the peak at 1100 cm^{-1} shows the aliphatic amino groups (Demir et al., 2016). The peaks between 900-1000 cm^{-1} shows cross-linked PVA-CHI scaffolds indicated formation of intermolecular and intra crosslinking bonds by the formation of heterocyclic structure of GP with primary amine groups.

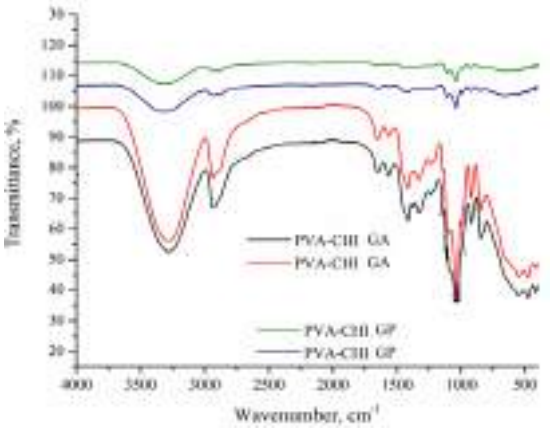

Fig. 2. FTIR spectra of membranes

The total polymer concentration and type of crosslinking agent were altered and the morphology of the membranes was analyzed by SEM (Figure 3). A smooth surface structure was observed for all membranes.

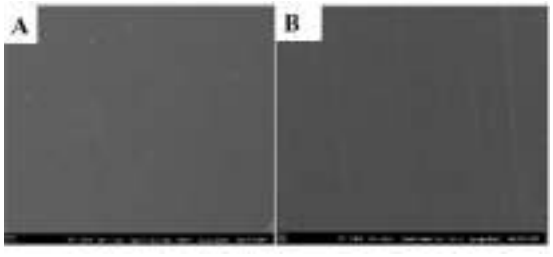

Fig. 3. SEM images of membranes, A) GA crosslinked PVA-CHI (5.0%) membrane (1000x), B) GP crosslinked PVA-CHI (5.0%) membrane (1000x).

Figure 4A and B shows the swelling ratio of crosslinked membranes with GP and GA. It was observed that when the PVA (or total polymer) concentration decreased swelling ratio of membranes increased. After 24 minutes, the swelling ratio of GA crosslinked PVA-CHI (5.0%) and GP crosslinked PVA-CHI (5.0%) membranes were around 275% and 250%, respectively.

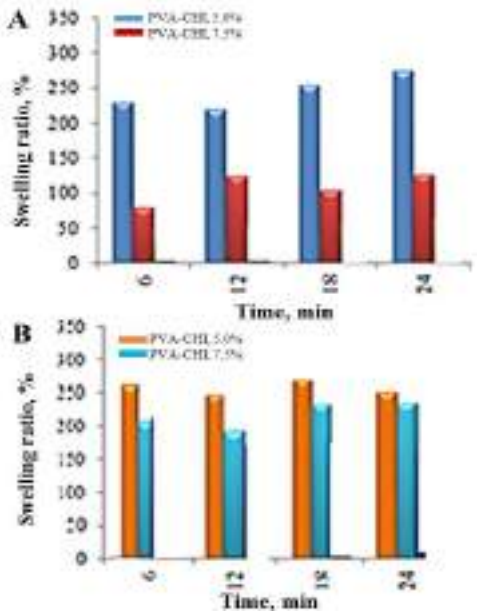

Fig. 4. Swelling ratio of membranes, A) GA crosslinked membranes, B) GP crosslinked membranes

Figure 5 shows that GA and GP crosslinked PVA-CHI scaffolds presented hydrophilic behavior; however, GP crosslinked scaffolds presented a larger contact angle than GA crosslinked.

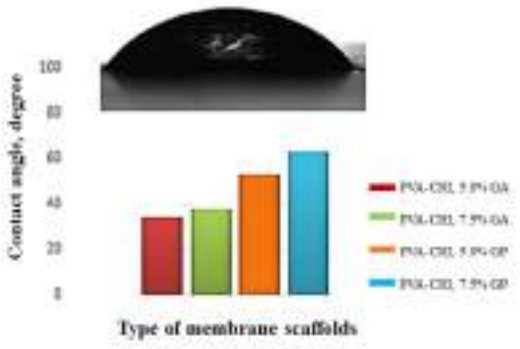

Fig. 5. Water contact angle of PVA-CHI membranes

5. CONCLUSION

PVA-CHI membranes were fabricated crosslinking at room temperature with two different types of crosslinking agents. The effect of total polymer concentration and type of crosslinking agent on characteristics of membrane scaffolds was investigated. PVA based membranes with tunable properties can be potential candidates as scaffolds for tissue engineering applications.

ACKNOWLEDGEMENT

This work was supported by The Scientific Research Projects Unit of Adana Alparslan Türkeş Science and Technology University (BAP-18103033).

REFERENCES

Ali Akbari Ghavimi, S., Ebrahimzadeh, M. H., Shokrgozar, M. A., Solati-Hashjin, M., and Abu Osman, N. A. (2015). "Effect of starch content on the biodegradation of polycaprolactone/starch composite for fabricating in situ pore-forming scaffolds." *Polym. Test.*, vol.43, pp. 94–102.

Cao, L., Wang, J., Hou, J., Xing, W., and Liu, C. (2014). "Vascularization and bone regeneration in a critical sized defect using 2-N,6-O-sulfated chitosan nanoparticles incorporating BMP-2." *Biomaterials*, vol.35, pp.684–698.

Demir, D., Öfkeli, F., Ceylan, S., and Bölgen, N. (2016). "Extraction and Characterization of Chitin and Chitosan from Blue Crab and Synthesis of Chitosan Cryogel Scaffolds." *J. Turkish Chem. Soc. Sect. A Chem.*, vol.3, pp.131–144.

Dias, J. R., Baptista-Silva, S., Sousa, A., Oliveira, A. L., Bártolo, P. J., and Granja, P. L. (2018). "Biomechanical performance of hybrid electrospun structures for skin regeneration." *Mater. Sci. Eng. C*, vol.93, pp.816–827.

Fallahiarezoudar, E., Ahmadipourroudposht, M., Idris, A., and Mohd Yusof, N. (2015). "A review of: Application of synthetic scaffold in tissue engineering heart valves.", *Mater. Sci. Eng. C*, vol.48, pp. 556–565.

Gomes, M. E., Ribeiro, A. S., Malafaya, P. B., Reis, R. L., and Cunha, A. M. (2001). "A new approach based on injection moulding to produce biodegradable starch-based polymeric scaffolds : morphology , mechanical and degradation behaviour." *Biomaterials*,vol.22, pp.883-889.

Gualandi, C. (2011). "*Porous Polymeric Bioresorbable Scaffolds for Tissue Engineering*." University Of Bologna, Italy.

Hsieh, W.-C., and Liau, J.-J. (2013). "Cell culture and characterization of cross-linked poly (vinyl alcohol)-g-starch 3D scaffold for tissue engineering." *Carbohydr. Polym.*, vol.98, pp. 574–580.

Lee, K. Y., and Mooney, D. J. (2001). "Hydrogels for tissue engineering." *Chem. Rev.*, vol.101, pp. 1869–1880.

Nazemi, K., Moztarzadeh, F., Jalali, N., Asgari, S., and Mozafari, M. (2014). "Synthesis and characterization of poly (lactic-co-glycolic) acid nanoparticles-loaded chitosan/bioactive glass scaffolds as a localized delivery system in the bone defects.", *Biomed Res. Int.*,pp.1-9.

Râpă, M., Grosu, E., Andreica, M., and Hetvary, M. (2014). "Journal of Environmental Research and Protection Polyvinyl alcohol and starch blends : properties and biodegradation behavior." ,*J. Environ. Res. Prot.*, vol.11, pp. 34–42.

Tocchio, A., Tamplenizza, M., Martello, F., Gerges, I., Rossi, E., Argentiere, S., Rodighiero, S., et al. (2015). "Versatile fabrication of vascularizable scaffolds for large tissue engineering in bioreactor." *Biomaterials*, vol. 45, pp. 124–131.

Zhang, W., Ren, G., Xu, H., Zhang, J., Liu, H., Mu, S., Cai, X., et al. (2016). "Genipin cross-linked chitosan hydrogel for the controlled release of tetracycline with controlled release property, lower cytotoxicity, and long-term bioactivity." ,*J. Polym. Res.*,vol.9, pp.419-429.

CISET - 2nd Cilicia International Symposium on Engineering and Technology
10-12 October, 2019, Mersin / TURKEY

Optimizing the efficiency and electricity production of an internal engine CHP plant

Daniel Dragomir-Stanciu[1*], Seyed Mahdi Saghebian[2], Gelu Ianuș[3]

[1]Faculty of Engineering, University of Medicine, Pharmacy, Science and Technology, Târgu Mureș, România,
Email: daniel.dragomir-stanciu@umfst.ro
[2]Department of Civil Engineering, Ahar Branch, Islamic Azad University – Ahar, Iran
Email: smsaghebian@iau-ahar.ac.ir; smsaghebian@gmail.com
[3]Faculty of Mechanical Engineering, Technical University "Gheorghe Asachi", Iași, România
Email: gianus2000@yahoo.com

ABSTRACT
The efficiency of CHP plants coupled with district heating is influenced by heat demand. The paper analyses the methods for increasing of overall efficiency of an internal engines CHP plant in summer period, when heat demand is low. Were analyzed the influence of buildings cooling in summer and using an ORC system that converts into electricity the difference between the maximum heat that can be recovered from piston engines and the heat sent to the centralized heating system. Overall annual efficiency increases by 10% in summer months, for the same amount of electrical energy produced. Results indicate that annual electricity production may significant increase, up to 22%, maintaining the efficiency over 75%. This qualify energy productin for "high efficiency cogeneration".

Keywords: *CHP, Heat Demand, Efficiency, Optimizing*

1. INTRODUCTION

A high efficiency and reducing emissions in energy production, are priorities in power and heat generation.

Cogeneration or Combined Heat and Power (CHP) represents today one of the most used technology in energy production, because it contributes to saving primary energy and reducing greenhouse gas emissions. (Chico *and* Mancarella, 2008). Therefore, energy strategies and energy legislation in different countries encourages and recommends the promotion of cogeneration.

Current regulations define cogeneration as simultaneous generation, in one process, of thermal energy and electrical or mechanical energy, using the same fuel energy. The heat produced in a cogeneration process must satisfy an economically justifiable demand for heat or cooling, being used the term "useful heat".

The overall efficiency of cogeneration depends on factors as: cogeneration technology, load curves, fuel type, unit power, heat demand (Morvay *et.al*. 2008).

Recommended minimum values for overall efficiency of cogeneration plants are: 75% for steam backpressure turbine, gas turbine, internal engine, Stirling engine, fuel cells technologies and 80% for combined cycles gas turbine with heat recovery, steam condensing extraction turbine.

"High efficiency cogeneration" is defined as cogeneration process with more than 10% energy savings obtained by combined production instead of separate production of heat and electricity.

The heat produced in cogeneration plants is widely used in district heating systems (Korpela *et.al*. 2017). The centralized heat supply systems deliver to domestic and non-domestic consumers thermal energy for heating and hot water. For such cogeneration plants located in areas where there are large temperature differences between winter and summer, a major problem is the big difference between winter and summer heat demand. Low heat demand during the summer has the effect of lowering the overall efficiency and decreasing the amount of electricity produced.

In this paper possible methods and ways of increasing of efficiency and electricity produced for an internal engines CHP plant are analyzed, in conditions of low heat demand in the warm period of the year. Decreasing of efficiency is accentuated by disconnecting from centralized heat system of a part of households, who opted for individual heating systems.

2. THE ANALYZED CHP PLANT

CHP plant has two identical cogeneration units, each deserved by a natural gas fueled internal combustion engine. The maximum electrical power of each unit is by 6,81 MW and maximum thermal power by 11,13 MW. For summer conditions, CHP plant was designed for an overall electrical power of 12 MW and 10 MW thermal power. In winter season can be used additionally two hot water boilers. Thermal energy is delivered as hot water in final heat exchangers at a temperature of 90°C and mass flow of 450 m^3/h (at nominal conditions). It is recovered waste heat from cooling water of engine, intake air, and flue gases.

The CHP plant was designed to deliver electricity to power grid and heat for centralized heating system of the city. A great disadvantage is that from 18,900 individual houses and apartments connected to district heating system in 2010, only 11,300 remained connected in 2018. Heat demand of domestic consumers decreased by 45%. The heat demand of non-domestic consumers, like public buildings, tertiary sector, industry, represents now 18,9% from total heat demand of centralized heating system. The most difficult period of the year is between the months of May to September, when there is no demand for heating, thermal energy being delivered only for hot water.

Decreasing of heat demand influenced the operation conditions for cogeneration power plant. To adapt at lower heat demand in summer months, the power plant was operated less than 24 hours per day, often in partial loads. The result was a low efficiency and a smaller amount of produced electricity in summer months.

In Fig. 1 is presented the number of hours of operating of cogeneration units in the past year.

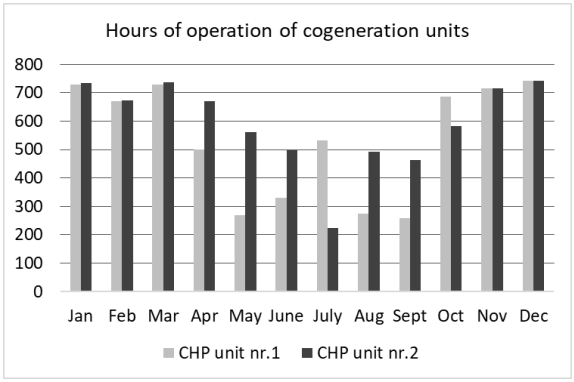

Fig. 1. Monthly hours of operation of cogeneration units

Can be seen that in the winter months the maximum number of hours of operation for both CHP units is 1484, in the summer months reach only 722 hours.

Monthly energy production (electricity and heat) and fuel energy is presented in Fig.1

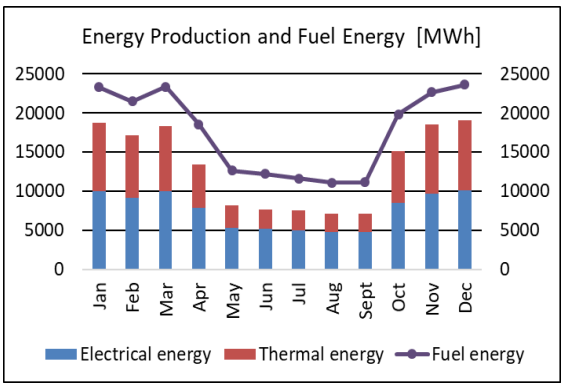

Fig.2. Electrical and thermal energy production and fuel energy

Lowest energy production is in the months from May to September. In these months the ratio electricity/heat has great values, the effect is a small efficiency. CHP was operated in this regime because it was high demand for electricity in the energy market.

Overall efficiency of a CHP plant means the sum of electricity production and useful heat output divided by the fuel input used for heat produced in a cogeneration process; is calculated with Eq. (1).

$$\eta_{CHP} = \frac{E_{CHP} + H_{CHP}}{F_{CHP}} \quad (1)$$

where: E_{CHP} – amount of electrical energy generated in CHP units;
H_{CHP} – useful thermal energy generated by CHP units;
F_{CHP} – fuel energy.

The values of overall efficiency are presented in Tabel 1.

Table 1. Overall efficiency of CHP plant

Month	η_{CHP}
Jan.	0.802
Feb.	0.797
Mar.	0.785
Apr.	0.721
May	0.648
Jun.	0.630
Jul.	0.647
Aug.	0.637
Sept.	0.638
Oct.	0.762
Nov	0.819
Dec.	0.804

Annual overall efficiency of CHP plant is 0,746. This value is under the accepted value in regulations by 0,75.

3. OPTIMIZING THE EFFICIENCY AND ELECTRICITY PRODUCTION

The low annual efficiency is due to lower demand for heat during the summer months. In these months, although there is demand for electricity in energy market, CHP plant can't produce more electricity to not further reduce annual efficiency.

Presently solutions to optimize CHP plant operation are

- heat storage
- building cooling in summer
- using an organic Rankine cycle (ORC) to recover heat that is not required by consumers. These solutions will be further analyzed.

3.1. Heat storage

Low and nonlinear heat demand generates operating of internal engines in partial loads, at a lower efficiency. Using heat storage to store the surplus heat produced by the CHP units is a solution to keep power plant functioning at a high efficiency (Abdollahi *et.al*., 2014; Nuytten *et.al*., 2013).

CHP plant should be operated at maximum efficiency for number of hours. The surplus heat is stored in a reservoir. When heat storage reservoir is at full capacity, the CHP units stop. The next start will be when the heat stored was consumed. CHP units will have intermittent functioning, with long pause periods. The hours of operating will drop.

Because the total amount of heat required by consumers is unchanged, the amount of electricity produced remains the same. that minimizes the cost of heat (

3.2. Building cooling

The second way of increasing the efficiency of the cogeneration system is further transformation in a trigeneration system, which is mentioned in literature (Xavier *et.al*., 2015). This may be achieved by cooling the building during the summer using absorption chillers, especially for non-domestic consumers: public buildings, tertiary sector, industrial consumers, etc. It is difficult to apply for individual houses and apartments. The non-domestic consumers now account for 18.9% of total consumption of centralized heating system. This solution involves installing chillers, driven by hot water from district heating system, at user's location.

Currently exist on the market simple effect chillers, driven by hot water at 80-90°C, with COP 0.7-0.75.

The cooling demand of buildings is lower than heating demand, in terms of thermal power.

Cooling buildings for non-domestic consumers would increase heat demand in months May to September.

Efficiency increases due supplementary heat demand for cooling, Eq. (2).

$$\eta_{TRIGEN} = \frac{E_{CHP} + H_{CHP+COOLING}}{F_{CHP}} \quad (2)$$

Increasing of efficiency is presented in Table2.

Table 2. Increasing of CHP efficiency by buildings cooling

Month	η_{CHP}	$\eta_{CHP+cooling}$
May	0.648	0.688
Jun.	0.630	0.712
Jul.	0.647	0.734
Aug.	0.637	0.726
Sept.	0.638	0.683

Overall efficiency for all year becomes 0,765. There is not a big increase, but above the limit of 0,75 of high efficiency cogeneration. This solution does not lead to increase production of electricity during the summer months.

3.3. Using an ORC system as bottoming cycle

An ORC system can be used as bottoming cycle for internal engines CHP. This ORC system will produce an additional amount of electrical energy using heat that is not required by consumers. Heat recovery of the internal combustion engine in an organic Rankine cycle is presented as a feasible solution, because the high exergy level of engine exhaust heat allows more efficient heat recovery (Vaja *and* Gambarrota, 2010). The advantages

of using ORC as bottoming cycle for recovering heat from internal combustion engines are also presented in literature papers (Quilin *et.al*., 2013; Invernizzi *and* Sheikh, 2018).

Heat source for vaporizing the organic fluid is hot water produced by the heat recovery in piston engines, with a temperature of 90°C and mass flow of 129,57 kg/s. Suitable for this application is an ORC with R600a as working fluid (Dragomir-Stanciu, 2018). The overall efficiency of ORC can reach value of 0,136.

Available heat for ORC is the difference between the maximum heat that can be recovered from piston engines and the heat sent to the centralized heating system. Using this heat difference, the electric generator of ORC produces an amount of electric power E_{ORC}.

The system internal engine–ORC is in fact a combine cycle, whose efficiency can be calculated with Eq. (3):

$$\eta_{CHP+ORC} = \frac{E_{CHP} + H_{CHP} + E_{ORC}}{F_{CHP}} \quad (3)$$

Electric power produced by ORC is calculated with Eq. (4):

$$E_{ORC} = \left(\frac{E_{CHP}}{C} - H_{CHP}\right) \cdot \eta_{ORC} \quad (4)$$

where: C – power to heat ratio, considered C=1.05;
η_{ORC}= efficiency of ORC system.

Efficiency monthly values are presented in Fig.4. Annual efficiency is 0,759 which is in domain of high efficiency cogeneration.

ORC produces an additional amount of electric power by 2860 MWh.

3.3. Simultaneous using of building cooling and ORC

Simultaneous use of buildings cooling in summer and of ORC for recovery the heat produced by CHP units but unused by consumers leads to increase of overall efficiency. The scheme is presented in Fig.3.

Efficiency can be calculated with Eq. (2),

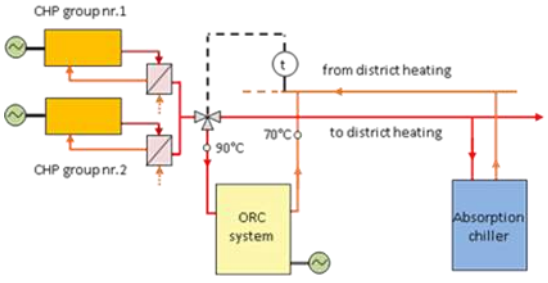

Fig. 3. Scheme of simultaneous using of CHP, building cooling and ORC

For thus case, overall efficiency of system is given by Eq. (5):

$$\eta_{TRIGEN+ORC} = \frac{E_{CHP} + H_{CHP+COOLING} + E_{ORC}}{F_{CHP}} \quad (5)$$

Monthly overall efficiency is represented in Fig.4.

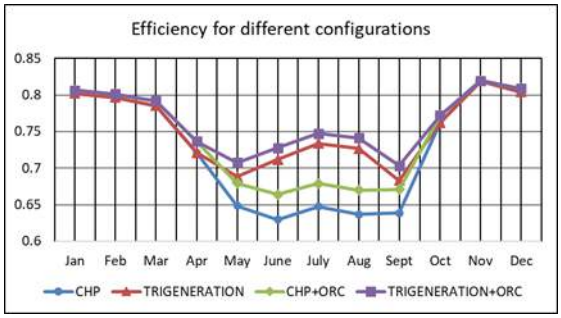

Fig.4. Overall efficiency for studied configurations

By combining CHP and ORC becomes possible to increase the amount of electricity produced by CHP units for the same heat demand of consumers. Eq. (6) allows to calculate the overall efficiency when amount of electrical energy produced increases with ratio x :

$$\eta^{x}_{TRIGEN+ORC} = \frac{(1+x)E_{CHP} + H_{CHP+COOLING} + E^{x}_{ORC}}{y(1+x)E_{CHP}} \quad (6)$$

The terms represent:

E_{CHP} – initial amount of electrical energy generated in CHP units;

E^{x}_{ORC} – amount of electrical energy produced by ORC for CHP electrical energy increased with ratio x;

y – fuel specific consumption

Electrical energy produced by ORC is calculated wit Eq. (7):

$$E^{x}_{ORC} = \left(\frac{(1+x)E_{CHP}}{C} - H_{CHP+COOLING}\right) \cdot \eta_{ORC} \quad (7)$$

For cold season months (October to April) was increased electricity production to 13,65 MW (maximum power of CHP generator), adopting an engines availability of 0.988. For May to September months the electricity production was increased with ratio x, compared to the initial production, for the same amount of heat required by consumers. Results of electricity production are presented in Fig.5.

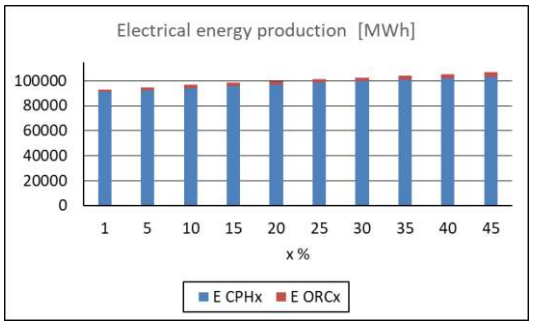

Fig.5. Electrical energy production in dependence by x ratio

The maximum value for x is that value at which efficiency reaches 0,75. This value is x = 0,45.

The initial amount of electricity was 89953,57

MWh; the amount of electrical energy using building cooling and ORC is 106862.3 MWh, for x = 0.45. Increasing percentage is 22,13 %.

In Fig.6 is presented Overall efficiency of combine Trigeneration-ORC system, in dependence by x ratio.

Fig.6. Overall efficiency of combine Trigeneration-ORC system, in dependence by x ratio

4. CONCLUSIONS

Using buildings cooling in summer and organic Rankine cycle as bottoming cycle for internal engine CHP leads to increase of efficiency and the amount of electrical energy produced.

For analyzed CHP plant, overall annual efficiency increases by 10% in summer months, for the same amount of electrical energy produced. Annual efficiency increases from 0,746 to 0,774.

The amount of produced electrical energy can be increased up to 22,13 %, maintaining the efficiency over 75 %. A bigger electrical energy production will have a positive effect on financial balance of power plant.

The overall efficiency is influenced by efficiency of ORC. Future research should focus on finding working fluids for ORC with greater heat storage capacity at low temperatures.

REFERENCES

Abdollahi, E., Wang, H., Rinne, S., Lahdelma, R. (2014) "Optimization of energy production of a CHP plant with heat storage". *IEEE Green Energy and Systems Conference* (IGESC 2014), pp.30-34.

Chico, G., Mancarella. P., (2008). "Assessment of the greenhouse gas emissions from cogeneration and trigeneration systems. Part I: Models and indicators" *Energy*, 33(3), pp.410-417.

Dragomir-Stanciu, D., (2018). "Improving the Energy Efficiency of an Internal Combustion Engine Cogeneration System Using ORC as Bottoming Cycle" *Procedia Manufacturing*, Vol. 22, pp. 691-694.

Invernizzi, C. M., Sheikh, N.A., (2018). "High-Efficiency Small-Scale Combined Heat and Power Organic Binary Rankine Cycles", *Energies*, 11, pp.1-15.

Korpela, T., Kaivosoj, J., Majannea, Y., Laakkonen L., Nurmoranta, M. and Vilkko, M. (2017). "Utilization of District Heating Networks to Provide Flexibility in CHP Production". Energy Procedia, Vol.116, pp.310-319.

Morvay, Z., Gvozdenac, D. (2008). *Applied Industrial Energy and Environmental Managemen*t, IEEE Press, John Wiley & Sons, London, United Kingdom.

Nuytten, T., Claessens, B., Paredis, K., Van Bael, J., Six, D., (2013)."Flexibility of a combined heat and power system with thermal energy storage for district heating" *Appl. Energy*, 104 (2013), pp. 583-591.

Quoilin, S., Van Den Broek, M., Declaye, S., Dewalle, P., Lemort, V., (2013). "Techno-economic survey of Organic Rankine Cycle (ORC) systems", *Renewable and Sustainable Energy Reviews*, 22, pp. 168–186.

Vaja, I., Gambarotta A., (2010). "Internal Combustion Engine (ICE) bottoming with Organic Rankine Cycles (ORCs)", *Energy*, Vol: 35, Issue: 2, pp. 1084-1093.

Velez, F., Segovia, J.J., Martin., M.C., Antolin, G., Chejne, F., Quijano, A., (2012). A technical, economical and market review of organic rankine cycles for the conversion of low-grade heat for power generation. *Renewable and Sustainable Energy Reviews*, 16, pp.4175-4189.

Wang, H., Yin, W., Abdollahi, E., Lahdelma, R., Jiao, W., (2015). "Modelling and optimization of CHP based district heating system with renewable energy production and energy storage" *Appl. Energy*, 159 (2015), pp. 401-421.

Xavier, B.H., Tuna, E.C., Mayworm, F.H., Luz Silveira, A.J., (2015). "Cogeneration with internal combustion engine and absorption refrigeration system operating with natural gas". *Technical, economical and environmental Issue*, 23 ABCM International Congress, Dec.6-11, Rio de Janeiro, Brazil.

CISET - 2nd Cilicia International Symposium on Engineering and Technology
10-12 October, 2019, Mersin / TURKEY

ANALYTICAL AND NUMERICAL MODELING OF HEAT, FLUID AND MASS TRANSFER IN *Acetobacter aceti* LIQUID STATE CULTIVATION BIOREACTOR INTEGRATED WITH GROUND SOURCE HEAT PUMP SYSTEM

Yakup Ermurat [*1], Ömer ÖZYURT[2]

[1] Bolu Abant İzzet Baysal University, Department of Environmental Engineering, Bolu, Turkey

[2] Bolu Abant İzzet Baysal University, Department of Mechanical Engineering, Bolu, Turkey

ABSTRACT
Analytical and numerical modeling of heat, fluid and mass transfer in *Acetobacter aceti* cultivation process integrated with ground source heat pump at different air flow rate is studied in this research. The calculation approaches are numerically developed to reach operative conditions for amount of the cultivation essentials heat and air blown into the cultivation water abundantly adapted for the growth of *A. aceti.* The temperature and mass profile differences in the water for quasi steady state growth circumstances of the *A. aceti* are elucidated iteratively at each time steps.

Keywords: *Analytical and numerical modeling, heat transfer, Ground source heat pump, Acetobacter aceti cultivation process*

Corresponding Author

1. INTRODUCTION

Establishing an effective combined assembly for a laboratory scale fermentation system ables to set up a functioning industrial cultivation process. The system requires main heating, aeration and agitation operations which need a considerable extent of energy. *Acetobacter aceti* fermentation process needs those similar operations and energy which can be supplied from a heat pump system. ground source heat pump (GSHP) system is acknowledged as the best competent heating and cooling equipment which use ground heat energy through circulating water antifreeze solution that absorbs heat from the ground and discharges to refrigerant gas coils air is blown across by an air fan. (Benli, 2013; Camdali and Tuncel 2010; Lucia, 2013; Nagano et al, 2006; Ozyurt and Ekinci, 2011; Zeng et al, 2093). The heated air can be used to provide the fermentation process operation needs. and aerate the liquid state A. aceti incubation media Determining the Reynolds number of the air flow in water can be used to find the relation between the Reynolds number and temperature increase.
A. aceti is among the most widely used industrial microorganisms, used for acetic acid production in larger scale. A. aceti incubation needs regular growth temperature of 30-42 ºC which is rather provided from conservational GSHP device. The heated air of GSHP system having temperature up to 55 ºC is blown into the *A. aceti* cultivation water tank through 5 pipes with 5 mm Ø for heating, aeration and mixing.

Analytical and numerical analysis methods are used to model heating of the *A. aceti* cultivation water by application of heat, fluid and mass transfer covering equations.

The heat equations can be applied to every steps of the heat transfer in the system. The heat energy balance equations can be written for each step of the heat transfer.

Heat gained by water antifreeze solution(was)in the ground:

$$\boldsymbol{Q_{soil}} = \dot{Q}_{\boldsymbol{was}}$$

$$\dot{m}_{was} c_{p_{was}} (T_{in} - T_{out})_{was} / (t_2 - t_1) = \dot{m}_{was} c_{p_{was}} (T_{out} - T_{in})_{was}$$

Heat gained by refrigerant gas (rg) in the evaporator:

$$\dot{Q}_{\boldsymbol{was}} = \dot{Q}_{\boldsymbol{rg}}$$

$$\dot{m}_{\boldsymbol{was}} \boldsymbol{c_{p_{was}}} (\boldsymbol{T_{out}} - \boldsymbol{T_{in}})_{\boldsymbol{was}} = \dot{m}_{\boldsymbol{rg}} (\boldsymbol{h_2} - \boldsymbol{h_1})_{\boldsymbol{rg}}$$

Heat gained by refrigerant gas in compressor:

$$\boldsymbol{Q_{rg}} = \dot{m}_{\boldsymbol{rg}} (\boldsymbol{h_2} - \boldsymbol{h_1})_{\boldsymbol{rg}}$$

Heat gained by fan air (fa) in condenser:

$$\dot{Q}_{\boldsymbol{rg}} = \dot{Q}_{\boldsymbol{fa}}$$

$$\dot{m}_{\boldsymbol{rg}} \boldsymbol{c_{p_{rg}}} (\boldsymbol{T_{out}} - \boldsymbol{T_{in}})_{\boldsymbol{rg}} = \dot{m}_{\boldsymbol{fa}} \boldsymbol{c_{p_{fa}}} (\boldsymbol{T_{out}} - \boldsymbol{T_{in}})_{\boldsymbol{fa}}$$

Heat gained by room air (ra):

$$\dot{Q}_{\boldsymbol{fa}} = \boldsymbol{Q_{ra}}$$

$$\dot{m}_{\boldsymbol{fa}} \boldsymbol{c_{p_{fa}}} (\boldsymbol{T_{in}} - \boldsymbol{T_{out}})_{\boldsymbol{fa}} = \boldsymbol{m_{ra}} \boldsymbol{c_{p_{ar}}} (\boldsymbol{T_{out}} - \boldsymbol{T_{in}})_{\boldsymbol{ra}} / (\boldsymbol{t_2} - \boldsymbol{t_1})$$

Heat gained by incubation water:

$$\dot{Q}_{\boldsymbol{fa}} = \boldsymbol{Q_{iw}}$$

$$\dot{m}_{\boldsymbol{fa}} \boldsymbol{c_{p_{fa}}} (\boldsymbol{T_{in}} - \boldsymbol{T_{out}})_{\boldsymbol{fa}} = \boldsymbol{m_{iw}} \boldsymbol{c_{p_{water}}} (\boldsymbol{T_{out}} - \boldsymbol{T_{in}})_{\boldsymbol{iw}} / (\boldsymbol{t_2} - \boldsymbol{t_1})$$

The heat equations can be written in balanced heat equation:

$$[mc_p(\frac{dT}{dt})]_{fa} = -[hA(T - T_0)]_{iw}$$

The analytical solution of this equation is used to assess modelling and determination of heat transfer coefficient of the cultivation water (*cw*):

$$\boldsymbol{T_t} = (\boldsymbol{T} - \boldsymbol{T_0})_{\boldsymbol{iw}} [(\frac{\boldsymbol{hA}}{\boldsymbol{mc_p}})\boldsymbol{t}]_{\boldsymbol{fa}} + \boldsymbol{T}$$

Determining the Reynolds number of the air flow in water can be used to find the relation between the Reynolds number and temperature increase using the Nusselt functions. The functional relationships of fluid and heat investigation for forced convection among dimensionless *Nu, Re and Pr* numbers (*Nu=f(Re,Pr)*) are demonstrated by establishing a power law.

- $Nu=C(Re)^k(Pr)^m$
  Where *C*, *k* and *m* are the constants.
- $Re=(\rho\ v\ l)/\mu$
- $Pr=(c_p\ \mu)/k$

Where *l* is the length, *h* is heat transfer coefficient, *k* is thermal conductivity, *v* is velocity of fluid, c_p is specific heat, μ is viscosity, and ρ is fluid density.

The grid scheme of the incubation tank temperature allows to establish implicit governing differential equation for conductive heat transfer. Figure 1 shows the grid scheme of the incubation tank temperature.

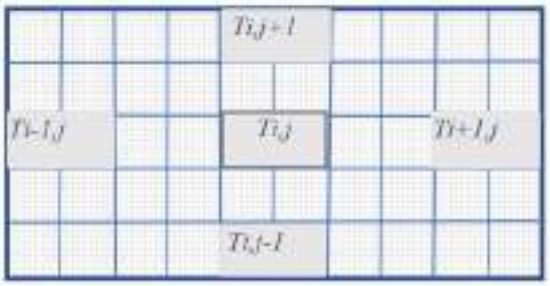

Fig. 1. The grid scheme of the incubation tank temperature.

The numerical solution of the implicit difference equation is solved as following:

$$T_{i,j} = \left(\frac{T_{i+1,j} + T_{i-1,j} + a^2 \, (T_{i,j+1} + T_{i-1,j} - 1)}{2(1 - a^2)} \right)$$

$$a = (\Delta y / \Delta x)$$

2. MATERIALS PROCEDURE

A. aceti strains used in cultivation were supplied from traditional vinegar making sources and incubated according to *Acetobacter* growth procedures. The GSHP system is designed to produce heated air which is applicable for experimental tests of *A. aceti* cultivation. The ground heat energy is absorbed by circulating water antifreeze solution in U shaped horizontal pipes that the heat is discharged to refrigerant gas in coils. The room air is blown across coils by an air fan producing heated air with various air speed.

MATLAB is used for the calculations, graphing and modeling.

3. RESULT AND DISCUSSION

Temperature of the room air min 18°C was increased up to 55°C while passing the fan unit. Heated air flow into the water increasing the water temperature up to 45°C during the incubation. The heat energy transferred to the water is calculated for each fluid speed of the system. Figure 2 shows the fluctuating temperature of the heated air at 5 min time interval.

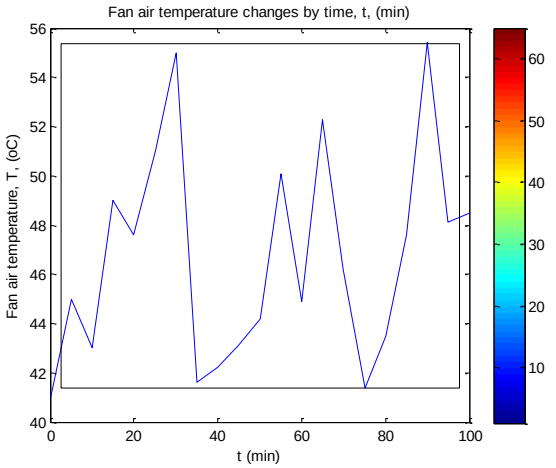

Fig. 2. The heated air temperature increase by time.

The 3D graph of the heat generated in the fan air against fluctuating temperature of the air presented in Figure 3.

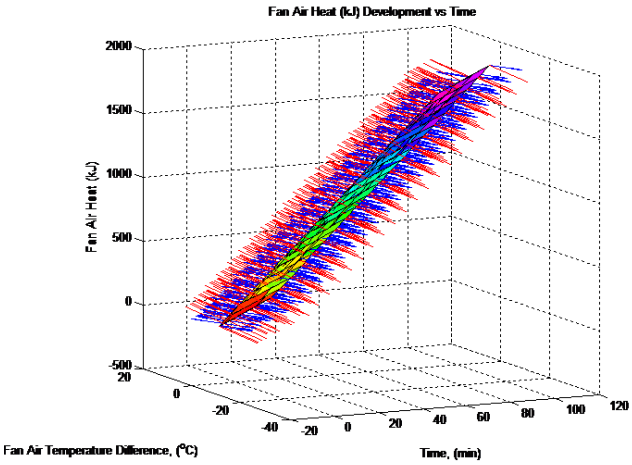

Figure 3. Graph of the heat generation in fan air.

Figure 4 shows the 3D graph of heat generated in the fan air and in the incubation water.

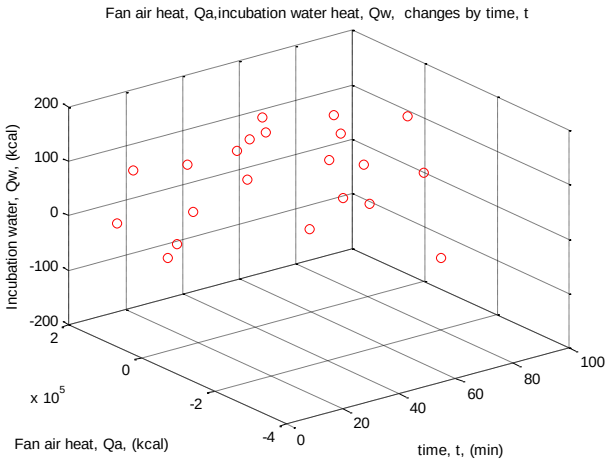

Fig. 4. Graph of the heat generation in fan air.

Modeling of temperature increases in the fan air and in incubation water is calculated and presented in figures 5 and 6.

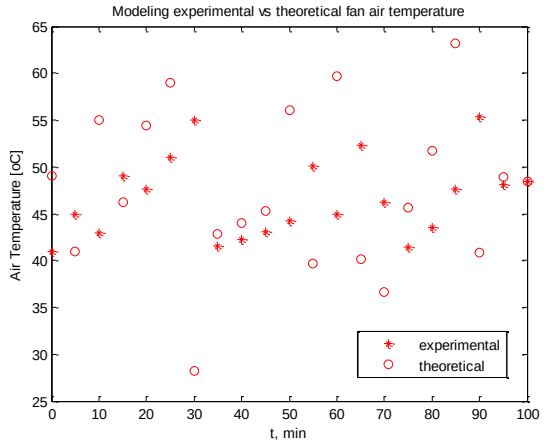

Fig. 5. Modeling the fan air temperature increase.

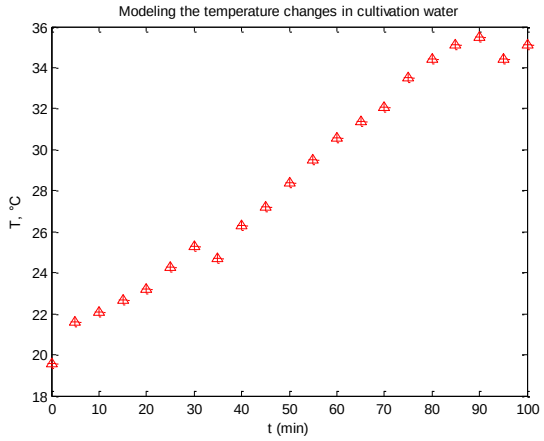

Fig. 6. Modeling the incubation water temperature increase.

Modeling results estimated from the numerical difference equation were shown in graph of Figure 7 to evaluate the numerical and experimental results.

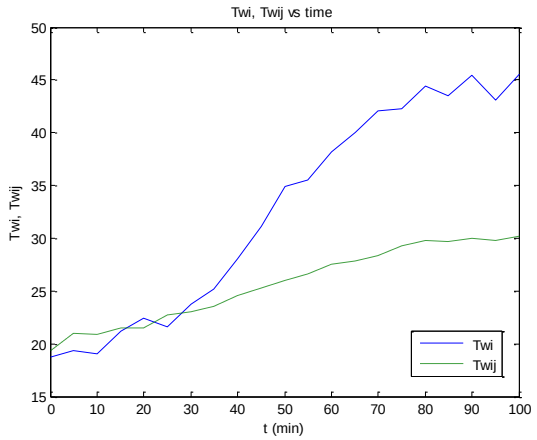

Fig. 7. Graph of the numerical and experimental results.

The fan air heat transfer coefficient, h (W m−2 °C−1) is determined using the analytical solution of the heat equation which is used to draw a graph of calculated *Re* number values as shown in graph of Figure 8.

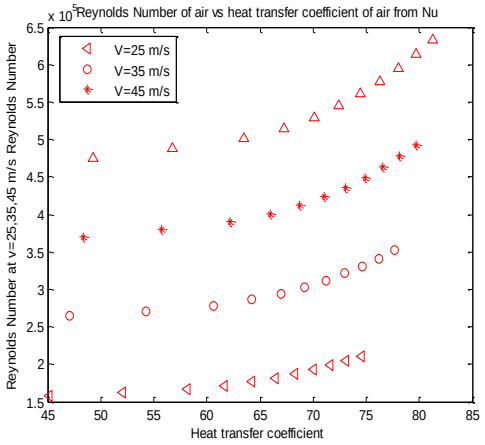

Fig. 8. The heat transfer coefficient vs Re number values.

CONCLUSION

Analytical and numerical modeling of heat, fluid and mass transfer is successfully applied to evaluate and improve an *Acetobacter aceti* incubation process integrated with a ground source heat pump (GSHP) system.

Analytical and numerical analysis methods are used to model heating of the A. aceti cultivation process which can be applied to the larger scale cultivation.

REFERENCES

Camdali U, Tuncel E. System analysis of ground source heat pumps (Gshps) for Bolu: an economical approach. Eng Mach 2010;51(604):22e35.

H. Benli. A performance comparison between a source and a vertical source heat pump systems for a greenhouse heating in the mild climate Elazig, Turkey. Appl. Therm. Eng., 50 (2013), pp. 197-206

O. Ozyurt, D. Arif Ekinci. Experimental study of vertical ground-source heat pump performance evaluation for cold climate in Turkey. Appl. Energy, 88 (2011), pp. 1257-1265.

Nagano K, Katsura T, Takeda S. Development of a design and performance prediction tool for the ground source heat pump system. Appl Therm Eng 2006;26(14–15):1578–92.

Umberto Lucia, Marco Simonetti, Giacomo Chiesa, Giulia Grisolia. Ground-source pump system for heating and cooling: Review and thermodynamic approach. Renewable and Sustainable Energy Reviews 70 (2017) 867–874.

CISET - 2nd Cilicia International Symposium on Engineering and Technology
10-12October, 2019, Mersin / TURKEY

DESIGN AND COST ANALYSIS OF SOLAR TOWER WITH THE CAPACITY OF 20 MW IN MUT DISTRICT OF MERSIN PROVINCE BY USING SAM PROGRAM

Bengi GÖZMEN ŞANLI*[1], Elif TURNA DİLSEL[2], Ahmet ÇALIK[3]

[1, 2, 3] Mersin University, Faculty of Engineering, Mechanical Engineering, Mersin, Turkey

[1]bengigozmen@gmail.com
[2]elif.turna@windowslive.com
[3]ac@mersin.edu.tr

ABSTRACT

In present study, technical performance and cost of the solar tower system with the capacity of 20 MW for Mut district of Mersin were investigated. The solar tower system with the capacity of 20 MW was designed by using SAM (System advisor Model) program theoretically. For SAM program analysis, TMY3 solar radiation data of Mut district of Mersin located at the coordinates of 33.4° E 36.7° N was used. The energy generated by this system is determined as 48.532 MWh /year and the cost of solar tower system is calculated as 123537228.72$. For this system, the number of heliostats is determined as 1115 and the layout plan of heliostat is generated.

Keywords: Solar tower, SAM (systemadvisor model), Meteonorm, Renewable energy

*bengigozmen@gmail.com

1. INTRODUCTION

One of the most important renewable energy sources is solar energy. The solar energy is widely used for many different subjects such as wristwatch, calculator, cooling systems and electric power generation. Many different systems such as photovoltaic systems are used especially for the production of electrical energy. One of them is solar tower system. Solar tower systems convert thermal energy into electrical energy by concentrating the sun's rays to the receiver mounted on the top of the tower. In these systems, a large number of mirrors called as heliostat are used to reflect and concentrate the sun's rays to the central receiver. The energy generated by the sun's rays coming to the receiver is absorbed by the working fluid used in the system. The heat collected during the absorption process is used to product steam. Electrical energy is generated by using the obtained steam in the steam power cycle in the system (Şenol et al., 2011). Due to the advantages of solar tower systems, there are many theoretical and practical studies on these systems all over the world. Yaglı et al. (2011) designed a solar tower system for a location on the sea in İskenderun by using EBSILON software and performed thermodynamic analyzes for every point of the system. Agan et al. (2016) designed a solar tower system with the capacity of 10 MW for Ceylanpınar district with SAM (System Advisor Model) program. They determined the amount of energy production, number of heliostats and heliostat placement and the cost of the system. Selbas et al. (2003) generated electricity by using solar tower system and they carried out both technical and cost analyses. Xu et al. (2011) modeled a solar tower system with the capacity of 1 MW and analyzed the system theoretically. Benammar et al. (2014) performed a mathematical model to perform energy analysis of a solar tower system. They performed the analysis by dividing the whole system into four parts. Gottschalk et al. (2018) designed solar tower systems with a capacity of 100 MW by using the Sam program for different geographical regions of the world such as China, Germany and the Mediterranean countries. Carrizosa et al. (2015) aimed to reduce the cost of the solar tower system and they optimized the system in order to reduce the cost of heat energy obtained from the solar tower system consisting of many receivers. Çevik (2018) designed a solar tower system for İskenderun by using the EBSILON program and performed the energy-exergy analysis of this system. The net power of the system was 48059.238 kW at 1000 ° C in July and 9601.60 kW at 500 ° C in December. Hekim (2017) designed a solar tower system having the capacity of 10 MW with SAM program for Birecik district of Urfa. The technical performance of the system and efficiency of the system were determined.

In present study, technical performance and cost of the solar tower system with the capacity of 20 MW for Mut district of Mersin were investigated. The solar tower system with the capacity of 20 MW was designed by using SAM (System advisor Model) program. By SAM program, technical performance of the system and heliostat placement were determined. Moreover, the cost of the solar power system was calculated, too.

2. MATERIAL VE METHOD

In this study, Mut district of Mersin province has been especially preferred in terms of having high solar energy potential and suitable geographical conditions. The average annual sunshine duration of this region is over 8.27 hours. Mut has a warm climate with an average annual temperature of 17.4 °C and the average annual rainfall is about 758 mm (tr.climate-data.org). July is the warmest month of the year with an average annual temperature of 27.9 ° C and January is the coldest month of the year with 7.0 ° C. The average annual global radiation value is more than 4.28 KWh / m^2-day (YEGM).

Fig. 1. Solar map of Mersin province (www.enerjiatlasi.com).

2.1. Solar Tower Systems

The solar energy is a clean and renewable energy source. Recently, new methods have been developed to provide energy production by utilizing solar energy. One of these new methods is the solar tower system. The solar tower system designed by J. Schlaich at the first time in the 1980s was widely used in Russia, Italy, Spain, Japan, France and the United States. The working principle of solar tower system is same with the working principle of wind turbine system (Metin, 2006). The schematic representation of the solar tower systems is shown in Figure 2. Solar tower systems consist of a tower where the receiver is located on and mirrors positioned around the tower to reflect the sun's rays (Karaman, 2016).

Fig. 2. The schematic representation of a solar tower system (https://shiftdelete.net/)

The advantages of the solar tower systems can be listed as follows (SCHLAICH, 2002):
•Solar tower systems are reliable systems and the possibility of failure and the cost of the systems are lower than that of other systems.
• Solar tower systems do not need cooling water.

•Solar tower systems can generate energy at night by collecting sun's ray at the receiver
•The materials required for building of solar tower systems are easily accessible.
• These systems are easily applicable since the installation of these systems does not need high technology.

2.1.1. Elements of Solar Power Systems

2.1.1.1. Receiver

Receiver located at the top of a high tower is the element where the sun's rays are concentrated on by using heliostats. An example of receiver is depicted in Figure 3. The receiver absorbs the concentrated sun's rays and the receiver is a kind of heat exchanger that converts sun's rays to the heat energy (Hekim, 2017; www.watermill.com). The receivers expose to the sun's rays directly or indirectly depending on types and quality of materials (Pişirir, 2014).

Fig. 3. Receiver (www.watermill.com)

2.1.1.2. Heliostat

Heliostats are used to reflect and concentrate the sun's rays to the central receiver. They are a kind of two-dimensional mirrors tracking the sun's rays by an open loop control system (Pişirir, 2014). The heliostat the most important element of the solar power system consists of heliostat frame, heliostat lever and heliostat support as indicated in Figure 4.

Fig. 4. Heliostat (Cauble, 2013).

2.1.2. Operation principles of Solar Power Systems

Solar tower systems convert thermal energy into electrical energy by concentrating the sun's rays to the receiver mounted on the top of the tower. In these systems, a large number of mirrors called as heliostat are used to reflect and concentrate the sun's rays to the central receiver (Metin, 2006). The energy generated by the sun's rays coming to the receiver is absorbed by the working fluid used in the system. The molten salt is used as the working fluid in the Rankine cycle. The concentrated rays onto the central receiver result in high temperature of the receiver which is used to heat the molten salt. Then the heated molten salt passes through the heat exchangers and transfers the thermal energy to the water flowing through the heat exchangers. After passing through the steam generator, water is heated from subcooled liquid to superheated steam, which is fed to the steam turbine for electricity generation. (XU, 2011)

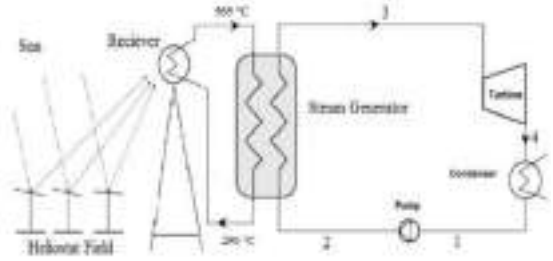

Fig. 5. Operation principles of solar power systems (Tiryaki, 2017).

2.2. System Advisor Model (SAM)

The System Advisor Model (SAM) is a free techno-economic software model that technical and cost analyses of projects on generation of power from renewable energy sources are performed by SAM program. The models of the systems generating power from renewable energy sources are created by SAM program. To analyze system performance and the cost of the system, design parameters and meteorological datas named Typical Meteorological Year (TMY3) with csv extensions, which belong METEONORM firm, are used. The modules of SAM program used in this study are defined in Table 1 (NREL, 2013).

Table 1. The modules of SAM program (NREL, 2013).

Modules of Program	Description
Location and Resource	This is the module that meteorological datas and geograpical datas are inputed to SAM program
Heliostat Field	This is the module that the required area for heliostat and the number of heliostat are determined
Tower Receiver	This is the module that height and diameter of recevier and chemical properties of molten salt are determined.
Power Cycle	This is the module that the capacity of system and power generated by system are determined.

Thermal Storage	This is the module that the number of storage tank and storage time are determined
Tower System Costs	This is the module that cost of system elements and cost of overall system are calculated

3. RESULTS and DISCUSSION

In present study, technical performance and cost of the solar tower system with the capacity of 20 MW for Mut district of Mersin were investigated. The solar tower system with the capacity of 20 MW was designed by using SAM (System advisor Model) program and the layout plan of heliostats was obtained. The design parameters used in the analyses of SAM program are indicated in Table 2.The technical datas of system were obtained by using the design parameters.

Table 2. Design parameters of Solar Tower System

Parameters	amount
Width of Heliostat	12.3 m
Height of Heliostat	9.75 m
Receiver height	6 m
Diameter of receiver	8 m
The number of storage tank	2 piece
Storage time of storage tank	10 h
Input temperature of molten salt	290 °C
Output temperature of molten salt	565 °C
Min temperature for operating the system	500 °C
Pressure of steam	10 MPa
Pressure of condenser	200 kPa
Temperature of reference (dead state)	25 °C
Pressure of reference (dead state)	100 kPa
Turbine efficieny	0.87
Pump efficiency	0.82
Optical efficiency	0.92
Receiver efficiency	0.83
Wind velocity	5 m/s

To get the correct results, meteorological datas named Typical Meteorological Year (TMY3) in csv format, which belong METEONORM firm, are used. The location information and weather data information of Mut district of Mersin are shown in Figure 6.

Fig. 6. Location information and weather data information of Mut district of Mersin

After determining of design parameters shown in table 2, the system analyses were performed and the tower height was calculated as 71.11 m. Moreover, the heliostat with the height of 9.75 m and the width of 12.3 m was needed and the number of required heliostat was determined as 1115 for this system and the layout plan of heliostat is shown in Figure 7.

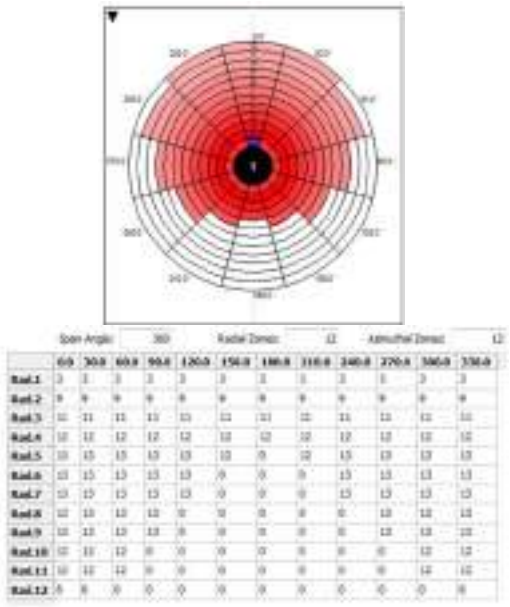

Fig. 7. Layout plan of heliostat

The net power generated by the solar power system designed with the capacity of 20 MW theoretically was determined as 17 MW due to the loss in the system. According to the layout plan of heliostat, the area required for this system was calculated as 149 decares and annual thermal energy was determined as 48.532 MWh by SAM program. In addition to these, the storage capacities of hot and cold tanks were calculated as 677.52 m^3 and 1580.89 m^3, respectively.

The cost calculation of the system was carried out and the total cost of the system was calculated as 123537228.72$ and the details of cost analyses were depicted in Table 3.

Table 3. The details of cost analyses for the solar tower system

Type of cost	cost ($)
Heliostat	$23346879.08
Storage	$13106796.12
Tower	$6817939.42
Alıcı	$22968114.05
Other expenses	$57297500.05
Total of cost	$123537228.72

4. CONCLUSION

In this study, the solar tower system with the capacity of 20 MW was designed by using SAM (System advisor Model) program theoretically. For SAM program analysis, TMY3 solar radiation data of Mut district of Mersin located at the coordinates of 33.4° E 36.7° N was used. The net power generated by the solar power system designed with the capacity of 20 MW was theoretically determined as 17 MW due to the loss in the system. The number of required heliostat was

determined as 1115 for this system and the layout plan of heliostat was created. The tower height was calculated as 71.11 m. The area required for this system was calculated as 149 decares and annual thermal energy was determined as 48.532 MWh by SAM program. Finally, to setup this solar power system, the required cost was calculated as 123537228.72$.

5. REFERENCES

Ağan, C. ve Topçu, S. (2016).“Ceylanpınar için sam simulasyon program ile güneş kulesi tasarımı.”*10. Uluslararası Temiz Enerji Sempozyumu UTES’16*, s. 531-540.

Anonim. https://tr.climate-data.org/asya/tuerkiye/mersin/mut-18656/. (Erişim Tarihi: 24.03.2019).

Anonim.http://www.enerjiatlasi.com/gunes-enerjisi-haritasi/mersin.(Erişim Tarihi: 24.03.2019).

Anonim. https://shiftdelete.net/dunyanin-en-uzun-gunes-kulesi-85196. (Erişim Tarihi: 24.03.2019).

Anonim. (2013). *Fine tubes helps sener achieve results in solar power with the gemasolar power plant*. http://www.watermill.com/fine-tubes-helps-sener-achieve-results-in-solar-power-with-the-gemasolar-power-plant/. (Erişim Tarihi: 16.03.2019).

Benammara, S., Kjellaf A. and Mohammedi, K. (2014).“Contribution to the modeling and simulation of solar power tower plants using energy analysis.” *Energy Conversion and Management,* Vol.78, pp. 923-930.

Carrizosa, E., Dominguez-Bravo, C., Fernandez-Cara, E. and Quero, M. (2015).“Optimization of multiple receivers solar power tower systems.”*Energy*, Vol. 90, pp. 2085-2093.

Cauble, A. (2013). *Brightsource’s Heliostat Technology*. http://www.brightsourceenergy.com/brightsource%E2%80%99s-heliostat-technology#.XOqgi4gzbIU (Erişim Tarihi: 20.03.2019).

Çevik, M. (2018). Akdeniz bölgesinde kurulacak olan güneş kulesinin enerji ve ekserji analizi,Yüksek Lisans Tezi, Mühendislik ve Fen Bilimleri Enstitüsü, İskenderun Teknik Üniversitesi, İskenderun, Türkiye.

Gottschalka, A. and Ramamoorthia, U. (2018). “Parametric simulation and economic estimation of thermal energy storage in solar power tower.” *Materials Today: Proceedings,* vol. 5 pp. 1571-1577.

Hekim, M. (2017). Merkezialıcısistemli (MAS) güneş güç santrali birecik uygulaması. Yüksek Lisans Tezi, HacettepeÜniversitesi, Ankara, Türkiye.

Karaman, R. (2016). Kombine organik rankine ve kompresörlü soğutma çevriminin termodinamik analizi, Yüksek Lisans Tezi, Fen Bilimleri Enstitüsü, Süleyman Demirel Üniversitesi, Isparta, Türkiye.

Metin, İ. (2006). Elektrik enerjisi üretiminde kullanılan güneş kulesi içindeki doğal konveksiyonun sayısal olarak incelenmesi, Yüksek Lisans Tezi, Fen Bilimleri Enstitüsü, Gazi Üniversitesi.

NREL. (2013). *System Advisor Model (SAM) Version 2013.1.15 Manual.*

Pişirir, O. M. (2014). Güneşgüçkuleleriiçinendüstriyelpc tabanlı heliostat kontrolü. YüksekLisansTezi, SüleymanDemirelÜniversitesi, Isparta, Türkiye.

Schlaich, J. (2002). *The Solar chimney*, http:/www.sbp.de.

Selbaş, R., Yakut, A.K. ve Şencan, A. (2003).“Güneş kulesi modeli ile elektrik enerjisi üretimi için bir uygulama.” *Pamukkale Üniversitesi Mühendislik Bilimleri Dergisi*, Vol. 9, No.2, s. 179-184.

Şenol, R., Üçgül İ., Koyun, A. veAcar, M. (2011).“10 mw’lık sdü güneşgüçkulesitesistasarımı.”*Gazi ÜniversitesiMühendislikMimarlıkFakültesiDergisi*, Vol. 26, No.4, s. 813-821.

Tiryaki, G. (2017). Energy and exergy analysis and performance optimization of a solar power tower system, Yüksek Lisans Tezi, Yıldırım Beyazıt Üniversitesi, Ankara, Türkiye.

Yağlı, H., Koç, A., Koç, Y. ve Mumcu, A.G. (2014). “Güneş kulesinin deniz üzerinde tasarımı ve ekserji analizi.” *ISITES’14*, s.906-915.

YEGM, http://www.yegm.gov.tr/MyCalculator/pages/33.aspx (Erişim Tarihi: 26.03.2019).

Xu, E., Yu, Q., Wang, Z. and Yang, C. (2011).“Modeling and simulation of 1 MW DAHAN solar thermal power tower plant.”*Renewable Energy*, Vol. 36, No. 2, s. 848–857.

CISET - 2nd Cilicia International Symposium on Engineering and Technology
10-12 October, 2019, Mersin / TURKEY

EXACT SOLUTIONS OF KLEIN-GORDON EQUATION WITH POSITION DEPENDENT MASS AND MAGNETIC FIELD

Hasan Fatih Kisoglu [*1], Kenan Sogut [2]

[1] Mersin University, Faculty of Maritime, Department of Basic Sciences, Mersin, Turkey, hasanfatihk@mersin.edu.tr

[2] Mersin University, Faculty of Science and Letters, Department of Physics, Mersin, Turkey, kenansogut@gmail.com

ABSTRACT
In this study, a system consisting of a scalar particle moving in an external magnetic field exponentially connected to the position is examined in relativistic quantum mechanics. For this purpose, Klein-Gordon equation is considered and the system's wave-function and analytical energy eigenvalues are obtained. The study also assumes that the mass of the particle varies depending on the position, as opposed to generally being considered constant.

Keywords: *Klein-Gordon Equation, External Fields, Exact Solutions, Position-Dependent Mass*

[*] Corresponding Author

1. INTRODUCTION

Studies on physical systems in external electromagnetic fields have been in high demand in recent years due to their wide use in technological fields. The studies cited in (Flügge, 1999; Greiner, 2000; Sogut, 2017; Villalba, 2001; Dehyar, 2016) are only a few examples. In order to examine the relevant systems, it is necessary to obtain the wavefunctions and energy eigenvalues that determine their behavior. This kind of physical examination can be done in quantum mechanics in two ways: relativistic quantum mechanics and non-relativistic quantum mechanics. In non-relativistic quantum mechanics, the Schrödinger equation, the cornerstone of quantum mechanics, is constructed and solved for a certain interaction in the system, which is represented by a potential function.

In order to examine a system under consideration with a more realistic quantum mechanical approach, it is necessary to consider the relativistic effects. Because it is possible to approach experimental data only with such an approach. The more the effects in the real system are considered, the closer the theoretical results to the experimental data can be obtained. For this purpose, Klein-Gordon equation, which is the most basic equation used in relativistic quantum mechanics, considers the effect of mass on the system, unlike the classical Schrödinger equation (Sever, 2008). In Dirac equation, which makes a more realistic approach than Klein-Gordon equation, electron spin is also taken into consideration in addition to mass (Kisoglu, 2019). Thus, the energy eigenvalues obtained from the Dirac equation are closer to the experimental data.

In this study, we construct the Klein-Gordon equation for a free particle moving in an external magnetic field, which is exponentially varies with the position, and find the wavefunction of the system. In addition, we obtain the energy eigenvalues for the relevant system in an analytical form. In the study, however, it is assumed that the mass of the particle is not constant, but changes in position.

The order of the study is as follows: In Part 2, the system's analytical wavefunction and energy eigenvalues are obtained. In Section 3, the results are interpreted.

2. CONSTRUCTING AND ANALYTICALY SOLVING THE PROBLEM

The time-dependent Klein-Gordon equation for a free particle under an external electromagnetic field effect is given as follows (Greiner, 2000)

$$\left[\left(\vec{p}-q\vec{A}\right)^2+m^2\right]\psi(\vec{r},t)=(p_0-qA_0)^2\psi(\vec{r},t) \qquad (1)$$

where $p_\mu=(p_0,\vec{p})$ and $A_\mu=(A_0,\vec{A})$ four-vector momentum and electromagnetic four-vector potential, respectively, while m is the mass and q is the electrical charge of the particle. In Eq. (1), t represents the time, whereas $\vec{r}$ is the position vector in three-dimensional cartesian coordinates.

Let us assume the particle to be subjected an external magnetic field in the form of

$$\vec{B}=\frac{aA'e^{-ax}}{(1-q'e^{ax})^2}\,\hat{k} \qquad (2)$$

where a, A' and q' are arbitrary constants. If the particle has a position-dependent mass given as

$$m(x)=m_0\left[1+\frac{\alpha e^{-ax}}{1-q'e^{ax}}\right] \qquad (3)$$

the Klein-Gordon equation is yielded as follows

$$\left\{\frac{d^2}{dx^2}-\left(\frac{q'A'e^{ax}}{1-q'e^{ax}}\right)^2+\left(\frac{2qk_yA'e^{ax}}{1-q'e^{ax}}\right)-\left[\frac{m_0+m_0(\alpha-q')e^{ax}}{1-q'e^{ax}}\right]^2+\varepsilon^2\right\}\varphi(x)=0 \qquad (4)$$

taking the wavefunction as $\psi(\vec{r},t)=e^{i(yk_y+zk_z-\mathcal{E}t)}\varphi(x)$ in which k_y and k_z constants are momentums of the particle on y and z-axis, respectively.

If a new variable is defined as $q'e^{ax}=u$ and write $\varphi(u)=u^{-\frac{1}{2}}f(u)$, Eq. (4) is turned into

$$\frac{d^2f(u)}{du^2}+\left(\frac{\tilde{A}}{u(1-u)}+\frac{\tilde{B}}{u(1-u)^2}-\frac{\tilde{C}}{(1-u)^2}-\frac{\frac{m_0^2}{a^2}}{u^2(1-u)^2}-\left(\frac{\mathcal{E}^2}{a^2}-\frac{1}{4}\right)\frac{1}{u^2}\right)f(u)=0 \qquad (5)$$

where

$$\tilde{A}=\frac{2qk_yA'}{a^2q'}$$
$$\tilde{B}=\frac{2m_0\left(1-\frac{\alpha}{q'}\right)+2\alpha m_0^2-A'}{a^2} \qquad (6)$$
$$\tilde{C}=\frac{m_0^2\left(\frac{\alpha^2}{(q')^2}+1\right)}{a^2}$$

By choosing $f(u)=u^{s+1}(1-u)^\mu g(u)$, following differential equation is obtained

$$\frac{d^2g(u)}{du^2}+\frac{2(s+1)-2(s+\mu+1)u}{u(1-u)}\frac{dg}{du}-\frac{2\mu(s+1)-\tilde{A}}{u(1-u)}\,g(u)=0 \qquad (7)$$

where $s(s+1)=\theta$, $\mu(\mu-1)=\tilde{C}-\tilde{B}$ and $\theta=\frac{m_0^2}{a^2}+$

$\frac{\varepsilon^2}{a^2} - \frac{1}{4}$.

Eq. (7) is in the form of hypergeometric differential equation given as follows (Abromowitz, 1965)

$$z(1-z)\frac{d^2w(z)}{dz^2} + [c-(a+b+1)z]\frac{dw(z)}{du} - a.b\,w(z) = 0 \quad (8)$$

The solutions of Eq. (8) about the z=0, z=1 singular points are given as (Abromowitz, 1965)

$$w(z=0) = (N_1)\,{}_2F_1(a,b;c;z) + (N_2 z^{1-c})\,{}_2F_1(a-c+1,b-c+1;2-c;z)$$
$$w(z=1) = (N_3)\,{}_2F_1(a,b;a+b+1-c;1-z) + (N_4(1-z)^{c-a-b})\,{}_2F_1(c-b, c-a;c-a-b+1;1-z)$$

where N_1, N_2, N_3 and N_4 arbitrary normalization constants, and ${}_2F_1(a,b;c;z)$ is hypergeometric function.

If Eq. (7) and Eq. (8) are compared, we have

$$\begin{aligned} c &\equiv 2(s+1) \\ a+b+1 &\equiv 2s+2\mu+2 \\ a\cdot b &\equiv 2\mu s + 2\mu - \tilde{A} \end{aligned} \quad (9)$$

By using these equations, one can easily obtain the below given results

$$\begin{aligned} a &\equiv \mu + s + \frac{1}{2}\left\{1 \pm \sqrt{4\left[\mu(\mu-1)+\tilde{A}\right] + (2s+1)^2}\right\} \\ b &\equiv \mu + s + \frac{1}{2}\left\{1 \mp \sqrt{4\left[\mu(\mu-1)+\tilde{A}\right] + (2s+1)^2}\right\} \end{aligned} \quad (10)$$

So, one solution about u=0 for Eq. (7) can be yielded as

$$g(u) = (N_1){}_2F_1(a,b;c;u) \quad (11)$$

via Eq. (9) and Eq. (10), where N_1 is normalization constant.

In order for the solution given by Eq.(11) is to be convergent, the parameter b should satisfy the following condition (Abromowitz, 1965)

$$b = -n$$

where n=0, 1, 2, 3, …etc. By using this condition, we can achieve the analytic energy equation as

$$\mu + s + \frac{1}{2}\left\{1 \mp \sqrt{4\left[\mu(\mu-1)+\tilde{A}\right] + (2s+1)^2}\right\} = -n \quad (12)$$

Note in Eq. (12) that the ε, which represents the energy eigenvalues, is embedded in the s parameter. If one wants to get numerical eigenvalues of the system, the analytical energy equation given in Eq. (12) can be used.

3. CONCLUSION

We have investigated a system consisting of a free spinless sub-atomic particle subjected to an external magnetic field by way of finding out the analytical eigenfunctions and eigenvalues of Klein-Gordon equation. For this survey, we have assumed the magnetic field and the mass of the particle to be varied as functions of position. The position dependent mass (or "effective mass") attracts attention for the studies in high-energy physics, nuclear physics, …etc. which require to take into account the relativistic effects for the quantum mechanical examination.

In the study, we have achieved the analytical wavefunction and energy equation of the system. As it is seen from Eq. (11) the wavefunction of the system is given as hypergeometric functions. Besides, analytical energy equation has been obtained by using the quantization condition of the hypergeometric functions (see in Eq. (12)). One can achieve the numerical energy eigenvalues of the system by using this equation for given set of the constant parameters such as a, A', q', α and m_0. In the next step for the study, analytical solutions of the system will be found out for different forms of the external field and the mass.

REFERENCES

Abromowitz, M. and Stegun, I. A. (1965). *Handbook of mathematical functions: with formulas, graphs and mathematical tables*, Dover Publications, New York, USA.

Dehyar, A., Rezaei, G. and Zamani, A. (2016). "Electronic structure of a spherical quantum dot: effects of the Kratzer potential, hydrogenic impurity, external electric and magnetic fields." *Physica E: Low-Dimensional Systems and Nanostructures*, Vol. 84, pp. 175-181.

Flügge, S. (1999). *Practical quantum mechanics*, Springer-Verlag Berlin Heidelberg, Berlin, Germany.

Greiner, W. (2000). *Relativistic quantum mechanics*, Springer-Verlag Berlin Heidelberg, Berlin, Germany.

Kisoglu, H. F., Yanar, H. et al. (2019). "Relativistic spectral bounds for the general molecular potential: application to a diatomic molecule." *Journal of Molecular Modelling*, Vol. 25, pp. 143-153.

Sever, R. and Tezcan, C. (2008). "Exact solution of Schrödinger equation for the modified Kratzer's molecular potential with position-dependent mass." *International Jurnal of Modern Physics E*, Vol. 17, pp.

1327-1334.

Sogut, K., Yanar, H. and Havare, A. (2017). "Production of Dirac particles in external electromagnetic fields." *Acta Physica Polonica B*, Vol. 48, No. 9, pp. 1493-1505.

Villalba, V. M. and Pino, R. (2001). "Energy spectrum of a relativistic two-dimensional hydrogen-like atom in a constant magnetic field of arbitrary strength." *Physica E: Low-Dimensional Systems and Nanostructures*, Vol. 10, No. 4, Arcticle ID: 561568.

CISET - 2nd Cilicia International Symposium on Engineering and Technology
10-12 October, 2019, Mersin / TURKEY

GEOCHEMİCAL PROPERTİES OF SALT DEPOSİTS AROUND DELİCE (KIRIKKALE)

Bilgehan Yabgu Horasan [*1], Alican Ozturk [2]

[1] Selcuk University, Sarayonu Vocational High School, Environmental Protection Technologies, Sarayonu / Konya,Turkey, bilgehanyabgu@gmail.com

[2] Konya Technical University, Faculty of Engineering and Natural Sciences, Geological Engineering Department, Selçuklu / Konya, Turkey alicanozturktr@gmail.com

ABSTRACT
Salt, which is the main nutrient, is a very important raw material in the life of living organisms and industry. Salt production and consumption have improved and increased due to technological developments and industrialization. Salt has been used in the world and in our country since very ancient times. In addition to sea, lake and spring salts, Turkey has very rich rock salt reserves. Tertiary old Çankırı-Çorum Basin is one of the important basins where evaporitic formations are seen in the Central Anatolia region. Geochemical properties were determined using XRD on samples from Oligocene aged units observed in the Delice (Kırıkkale) region. Halite (NaCl), Gypsum ($CaSO_4$), Anhydrite ($CaSO_4.2H_2O$), Globerit ($CaNa_2(SO_4)_2$), Tenardit (Na_2SO_4), magnesite ($MgCO_3$) minerals were identified according to the results of XRD.

Keywords: *Rock Salt, XRD, Delice, Kırıkkale*

* Bilgehan Yabgu Horasan

1. INTRODUCTION

Salt, which is known to have been used for different purposes by civilizations in human history, continues to be used by humanity today without losing its importance. The world's largest producer of salt, China, USA and India, meet a significant portion of salt demand. Among the salt producing countries on the European continent, Germany leads, followed by Turkey, France, Spain and Poland. Especially during the harsh winter months, the amount of production is increasing, and most of the salt needed by the European continent is met by these countries (USGS, 2018). Rock salt (halite), an odorless, water soluble, easily friable material, consists of Na^+ and Cl^- ions and crystallizes in the cubic system. Although it is colorless in its pure form, it can be in different colors (green, gray, yellow) depending on the environment. Operable salt sources are divided into solid and liquid. The areas where liquid production is carried out are oceans, seas, lakes and water sources containing salt. The areas where solid production is carried out are buried salt deposits. In this context, the rock salt deposits observed in the area on the I31 B3 sheet in the Delice District of Kırıkkale (Figure 1) province were investigated and their geochemical properties were investigated.

2. GEOLOGICAL SETTINGS

The tertiary old Çankırı-Çorum Basin, located in the Anatolid tectonic Union. (Figure 1). Traces of old and young tectonics are seen in the area. For this reason, the stratigraphy of the underlying rocks is complex. Basin by many researchers (Reckamp and Özbey, 1960; Dellaloğlu, 1973; Birgili et., al.,1975; Seymen, 1981; Ünalan and Harput, 1983; Kara and Dönmez, 1990; Tüysüz and Dellaloğlu, 1992; Erdoğan and et.al., 1996; Seyitoğlu and et. al., 1997; Karadenizli, 1999; Karadenizli and et., al., 2004) have been studied for various purposes. The main units of the basin are Kırşehir Continent, Sakarya Continent and İzmir-Ankara-Yozgat suture belt. Tertiary aged Çankırı-Çorum Basin units are located on this foundation. The basal sedimentary units of Çankırı-Çorum Basin are Maastrichtian and Paleocene turbidites (Karadenizli, 2011; Norman, 1972; Kazancı and Varol, 1990). The Paleogene part of the deposit in the basin is composed of marine clastic and the Neogene part consists of terrestrial, clastic and evaporitic rocks. The facies' different and thick successions of this deposit are of Eocene and Oligocene (Birgili et al. 1975). Oligocene aged İncik formation, which contains salt deposits, includes massive-bedded conglomerates, parallel and cross-bedded sandstones, layered siltstones and massive mudstones (Karadenizli, 2011).

2.1. İncik Formation (Toi)

The unit outcrops in large areas in the field and consists of evaporite, red, brown and gray colored, parallel cross-layered, low-cornered round grained, medium-well, loosely affixed terrestrial conglomerate, sandstone and mudstone intercalations. The formation is composed of clastic rocks (Birgili et al. 1975) is called as İncik formation. The lower parts of the İncik formation are intercalated with thin-medium-thick parallel-bedded sandstones, interbedded with medium-well bonded sandstones, gypsum and anhydrite mudstones, and the middle and upper levels are intercalated with mudstones and increasing upwards, cross-layered conglomerate and sandstone (Özgüner and Kızıldağ, 2015).

. 2.2. Sekili Formation (Tois)

The red, brown, gray, light green, white and variegated colored, medium-thick evaporite, mudstone and sandstone intercalation of the İncik formation is named as Sekili evaporite member by Kara (1991). The unit outcrops in the middle and northwest of the Kırşehir-I31 and I32 section. The shaped evaporite member is generally composed of anhydrite and gypsum and contains sandstone, and marl intermediate bands and mudstone upward. Gypsum and anhydrides are white and yellowish-white in color, medium-thick bedded, generally pure and crystalline and occasionally lumpy. It is observed that gypsum and anhydrides are thinner in the lateral direction and mudstones thicken. Sandstone and mud stones are generally thin to medium in thickness and have red-brown, light green and variegated appearance in green colors (Dönmez and et. al., 2005).

Figure 1. Geological map of the study area and its environs (taken from Dönmez et al., 2005 reports).

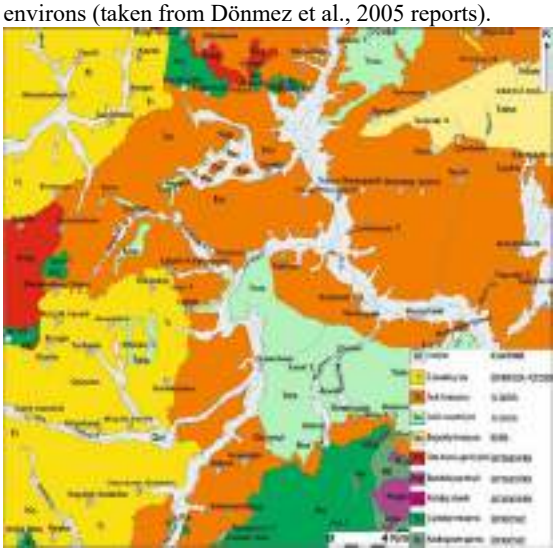

3. MATERIALS AND METHODS

In this study, salt formations observed in the Delice district of Kırıkkale province were investigated. The geology of the study area was examined and mapped by using the previous studies. A total of 2 samples were collected during the field studies and X-RD studies were performed. The analyzes were carried out in Selçuk University İLTEK.

3.1. Evaluation of XRD Results

Halite (NaCl), Gypsum ($CaSO_4$), Anhydride ($CaSO_4.2H_2O$), Globerite ($CaNa_2(SO_4)_2$), Tenardite (Na_2SO_4) minerals were determined in the study (Figure 2). In addition, formation of anhydrite / gypsum, magnesite ($MgCO_3$), dolomite ($CaMg(CO_3)_2$) in rock salt (Halite) were determined. It was thought that magnesium formed by alteration of the ophiolitic rocks at the bottom of the basin was carried to the environment by surface and ground waters and increased Mg^{+2} / Ca^{+2} ratio and as a result magnesite and dolomite precipitated in lake water. Halite mineral is both individually crystallized and located within the matrix in sabkha environment (Sönmez, 2014).

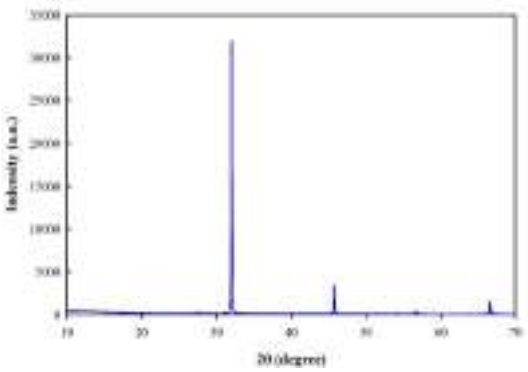

Figure 2. XRD diffractogram of samples taken from the Sekili formation

4. CONCLUSION

It was observed during the field studies that the Upper Eocene-Oligocene aged red colored sandstones and claystones contain small sized anhydrite and rock salt lenses, Oligocene aged rock salt deposits over this unit and these rock salts are under a gypsum-clay alternation. Halite (NaCl), Gypsum ($CaSO_4$), Anhydride ($CaSO_4.2H_2O$), Globerite ($CaNa_2(SO_4)_2$), Tenardite (Na_2SO_4) minerals were determined. In the analyzes, there is a highly mixed mineral aggregate, magnesite ($MgCO_3$), dolomite ($CaMg(CO_3)_2$) and other minerals observed in evaporitic environment. Magnesium formed by alteration of the ophiolitic rocks at the bottom of the basin was carried to the environment by surface and ground waters and increased Mg^{+2} / Ca^{+2} ratio and as a result magnesite and dolomite precipitated in lake water. Halite mineral is both individually crystallized and located within the matrix in sabkha environment

REFERENCES

Birgili, Ş., Yoldaş, R., Ünalan, G., (1975), "Geology and petroleum opportunities of Çankırı-Çorum basin", MTA Raporu, no: 5621.

Dellaloğlu, A, A., (1973), "Detail geology and oil possibilities of Iskilip mercury and its south and southwest", MTA Raporu, no: 6132.

Dönmez, M., Bilgin, Z. R., Akçay, A.E., Kara, H., Yergök, A. F., Esentürk, K. (2005), "1/100.000 ölçekli Türkiye Jeoloji Haritaları serisi. Kırşehir - İ31-İ32 paftası: No: 46-47", Maden Tetkik ve Arama Genel Müdürlüğü yayını.

Erdoğan, B., Akay, E., Uğur, M, S., (1996), "Geology ofthe Yozgat Region and evolution of the collisional Çankırı Basin", International Geology Review, 38; 788-806.

Helvacı, C., (2002), "Evaporit Jeolojisi Ve Türkiye Borat Yatakları Kurs Notları", Jeoloji Mühendisleri Odası Yayını, Page; 35, Ankara.

Kara, H., (1991), "MTA 1/100 000 Ölçekli açınsama nitelikli Türkiye Jeoloji Haritaları Serisi, Kırşehir - G 18 paftası", Maden Tetkik ve Arama Genel Müdürlüğü,Ankara.

Kara, H., and Dönmez, M., (1990), "1 \ 100000 scale geological map of Turkey qualified SICH up series Kırşehir-G 17 paftası", MTA yayını.

Karadenizli, L., (1999), "Sedimentology of Middle Eocene-Early Miocene Sediments in Çankırı-Çorum Basin", Doktora Tezi, Ankara Üniversites Fen Bilimleri Enst., Ankara.

Karadenizli, L., (2011), "Oligocene to Pliocene palaeogeographic evolution of the Çankırı-Çorum Basin, Central Anatolia, Turkey", Sedimentary Geology, 237, 1-29.

Karadenizli, L., Saraç, G., Şen, Ş., Seyitoğlu, G., Antoine, P, O., Kazancı, N., Varol, B., Alçiçek, M, C., Gül, A., Erten, H., Esat, K., Özcan, F., Savaşçı, D., Antoine, A., Filoreau, X., Hervet, S., Bouvrain, G., De Bonis, L., Hakyemez, H, Y., (2004), "Oligo-Miocene biostratigraphy and filling evolution based on mammalian fossils of the western and southern parts of Çankırı-Çorum basin", MTA report no:10706.

Kazancı, N., and Varol, B., (1990), "Development of a mass flow-dominated fan-delta complex and associated carbonate reefs within a transgressive Paleocene succession, Central Anatolia, Turkey", Sedimentary Geology, 68, 261–278.

Norman, T., (1972), "Stratigraphy of Upper Cretaceous-Lower Tertiary sequence in Ankara-Yahşıhan region", TJK, 15, 180–276.

Özgüner, A, M., and Kızıldağ, İ., (2015), "Kırıkkale-Sekili Evaporit Havzasındaki Kiaş Kaya Tuzu Yatağının Jeolojik Etüdü Ve Doğalgaz Depolama İmkanlarının Araştırılması", KİAŞ Teknik Rapor.

Reckamp, J,V., Özbey, S., (1960), "Complementary report on oil facilities of Çankırı field", Pet.İş.Gn.Md., AR/TGOfil; 471-472.

Seyitoğlu, G., Kazancı, N., Karakuş, K., Fodor, L., Araz, H., Karadenizli, L., (1997), "Does continuous compressive tectonic regime exist during Late Palaeogene to Late Neogene in NW Central Anatolia, Turkey? Preliminary observations", Turkish Joumal ofEarth Sciences, 6; 77-83.

Seymen, İ., (1981), "Stratigraphy and metamorphism of the Kırşehir massif around Kaman (Kırşehir)", TJK Bülteni, 24 (2); 7-14.

Sönmez, İ., (2014), "Glauberıte-Halıte Associatıon In Bozkır Formatıon (Pliocene, Çank›r›-Çorum Basin, Central Anatolia, Turkey)", MTA Dergisi, 149: 155-177.

Tüysüz, O., and Dellaloğlu, A, A., (1992), "Tectonic units of Çankırı basin and geological evolution of the basin", Türkiye 9.Petrol Kongresi Bildirileri, 180.

U.S. Geological Survey, 2018, Mineral commodity summaries 2018: U.S. Geological Survey, 200 p., https://doi.org/10.3133/70194932.

Ünalan, G., Harput, B., (1983), "Source rock investigations in the Late Cretaceous and Early Tertiary sediments on the western edge of the Çankırı basin" TJK Bülteni, 26; 177-186.

CISET - 2nd Cilicia International Symposium on Engineering and Technology
10-12 October, 2019, Mersin / TURKEY

TREATMENT OF SLAUGHTERHOUSE WASTEWATERS BY FENTON PROCESS

Nazım GÖREN[1] and Aydeniz DEMİR DELİL[2]

[1] Mersin University, Engineering Faculty, Environmental Engineering Department, Mersin, TURKEY, nazimgoren1@gmail.com

[2] Mersin University, Engineering Faculty, Environmental Engineering Department, Mersin, TURKEY, demiraydeniz@gmail.com

ABSTRACT
In this study, the treatability of real slaughterhouse wastewater which contains a high amount of organic pollutants was investigated with the Fenton process. Fenton process is one of the advanced oxidation processes commonly used in recent years. The removal efficiencies of chemical oxygen demand (COD) and the color parameter by the Fenton process were investigated. The initial COD and color concentrations of wastewater were 5600 mg/L and 1780 mg/L (Pt-Co), respectively. The effects of pH, Fe^{+2} and H_2O_2 on wastewater treatment in the Fenton process were investigated. The optimum working conditions were determined. In this study, the pH, Fe^{+2} and H_2O_2 working ranges were (2-2.5-3-3.5-4), (20, 40, 60 and 80 mg/L), (300, 600, 900 and 1200 mg/L), respectively. The working time was 2 h. At the end of the reaction period, the optimum conditions were found to be pH 2, 60 mg/L Fe^{+2} and 600 mg/L H_2O_2 concentrations. A maximum of 84% COD and 92% color removal efficiency were achieved under optimum conditions.

Keywords: *Fenton process, Slaughterhouse wastewaters, COD, Color*

1. INTRODUCTION

The food industries one of the most developed industries in our country. Slaughterhouse industry has an important place in the food industry in terms of creating adequate and balanced nutrition and creating employment (T.C. Kalkınma Bakanlığı 2001).

The meat processing sector consumes 24% of the freshwater used in the food industry (Gerbens et al., 2013). 2.5 to 40 m3 of water is consumed per ton in a slaughterhouse facility (World Bank Group Environmental 2007). Because of this high water consumption in the slaughterhouse industry, approximately 10-25 m3 of wastewater is produced per ton (Bustillo et al., 2016).

In the slaughterhouse industry, wastewater originates from paddocks, slaughterhouses and rendering facilities. These wastewaters have high BOD and COD (chemical oxygen demand) values depending on the amount of blood, protein, carbohydrate, and fat (Kaftan 2010).

To treat slaughterhouses wastewater, many processes are applied. physical treatment is generally used as pre-treatment in terms of reducing pollution load by processes such as pre-settling, sand-oil trap. Aerobic and anaerobic methods are mostly used in biological treatment. Coagulation, flocculation, and electrocoagulation are preferred for chemical growth. In addition to these methods, membrane technologies and advanced oxidation processes have been used in recent years. The Fenton process is one of these advanced oxidation processes and has been preferred in industrial wastewater growth in recent years (Bustillo et al., 2016). Fenton oxidation produces the hydroxyl radicals (OH) by decomposition of H_2O_2 in the presence of Fe^{+2} ion under acidic conditions (Benatti 2012).

$$Fe^{+2} + H_2O_2 \rightarrow Fe^{+3}OH^{-} + {}^{\bullet}OH \quad (1)$$

$$Fe^{+2} + {}^{\bullet}OH \rightarrow Fe^{+3} + OH^{-} \quad (2)$$

Fenton oxidation is a process where a mixture of H2O2 and Fe+2 salts is added directly to the wastewater. This mixture leads to the catalytic decomposition of H_2O_2 to form hydroxyl radicals and to make the organic pollutants more safely. In Fenton oxidation, Fe^{+2}, which is oxidized to Fe^{+3}, reacts with H2O2 and turns into Fe^{+2} and starts the reaction again. This increases the efficiency of the Fenton process. However, the intensive use of chemicals such as H_2O_2 and Fe^{+2} increases the cost and reduces the use of the system in industrial areas (Bianco 2011).

In the study conducted in 2010, Tezcan investigated the efficiency of COD and phenol removal of olive oil industry wastewater by Fenton process. As a result of optimization studies, optimum pH 4.5, 1500 mg / L $FeSO_4$, 1750mg / L H_2O_2 doses of 82.3% COD and 62% phenol removal efficiency was obtained (Tezcan 2010). Odabaşı et al (2017) aimed to remove aspirin from wastewater by using Fenton and photo-Fenton processes. They obtained 83.91% COD and 57.52% TOC removal (Odabaşı et al., 2017).

This study aimed to investigate the COD and color removal efficiencies from highly polluted slaughterhouse wastewater by Fenton oxidation process.

2. MATERIALS AND METHODS

2.1.Material

The wastewater used in the study was obtained from a slaughterhouse near Mersin. The wastewater was stored in the refrigerator at +40C to avoid any change in its structure. All chemicals used in the study are of analytical purity.

2.2.Fenton experiments

In the Fenton process, The H_2O_2 / Fe^{+2} ratio should be determined. If the added amount of Fe^{+2} is more than H2O2 amount, the process is chemical coagulation, not oxidation. Hence, determining the H2O2 / Fe^{+2} ratio is the most important step of the Fenton process. Therefore, H2O2 (300-1200 mg/L) and Fe^{+2} (20-80 mg/L) COD and color removal efficiencies were investigated at different concentrations. A volume of

500 mL of wastewater was inserted into 600 mL borosilicate beakers and agitated at a speed of 90 rpm on the jar tester. Firstly, pH of wastewater was adjusted to acidic conditions with 1 M H_2SO_4 After that, Fe^{+2} and H_2O_2 was sequence added in known concentrations. By reagents addition, 2 h oxidation process started. Samples were taken at certain times. The pH's of the collected samples were adjusted with 1M NaOH to be 9-10. To form iron hydroxide Fe (OH) 3 flocks, the samples were allowed to precipitate for 2 h. Finally, samples were taken from the clear phase formed on top and COD and color analyzes were performed.

2.3.Analytical procedure

Over the study, COD was analyzed by Closed Reflux method 5220B HACH DR 6000 spectrophotometer was used to analyze color using Pt-Co method 2120C (Standart Methods for the Examination of Water and Wastewater 1998.) The samples were filtered with Whatman 0.42 nm before the analyzes. COD and color removal efficiencies were calculated from the difference between the initial concentrations (C0) and post-treatment concentrations (Ct) of the wastewater.

$$\text{Removal Efficiency (\%)} = \frac{C0 - Ct}{C0} \, x \, 100 \quad (3)$$

3. RESULTS AND DISCUSSION

3.1. Wastewater Characterization

Table 1. Wastewater characters

Parameters	Value
Chemical oxygen demand (COD), mg/L	5600
Color (Pt-Co) mg/L	1780
pH	6.21
Conductivity, mS/cm	2.08

The Fenton process removal efficiency is extremely affected by pH parameter. At Low pH's, the removal

efficiency of the Fenton process increases because of the high oxidation ability of hydroxyl radicals (Gogate and Pandit 2004). In this study, the treatments of slaughterhouse wastewater by Fenton process were carried out at acidic condition (pH 2-4). The effect of pH on COD and color removal efficiencies were examined and the results are shown in Figure 1. and Figure 2.

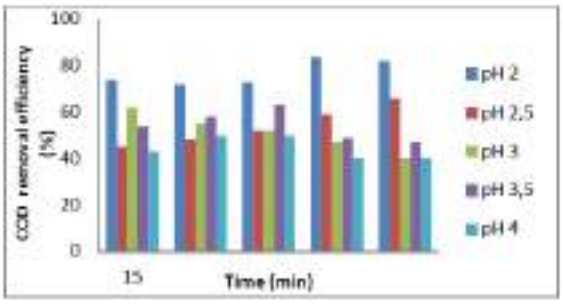

Fig. 1. Effect of pH on COD removal (H_2O_2 concentration: 600 mg / L, Fe^{+2} concentration: 60 mg / L)

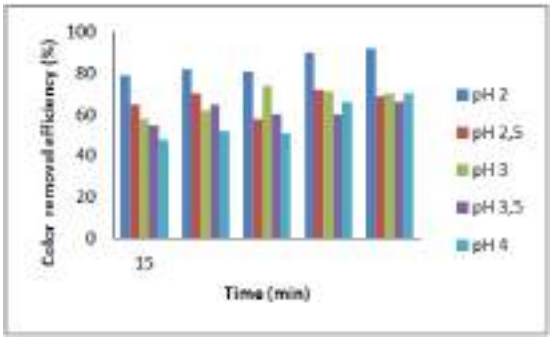

Fig. 2. Effect of pH on color removal (H_2O_2 concentration: 600 mg / L, Fe^{+2} concentration: 60 mg / L)

In the optimization of pH, the pH of the wastewater was carried out in acidic conditions (2-2.5-3-3.5-4) at 60 mg/ L Fe^{+2} and 600 mg / L H_2O_2 concentrations. At pH 2, COD removal efficiency reached 85% after 60 min. COD removal efficiency was 70% at pH 2.5. For pH 3-3.5-4, the removal efficiency of COD has been varied between 40% and 63%. Color removal efficiencies reached 92% at pH 2 and did not exceed 74% at other pH values. In the study, optimum pH was 2. This shows that the Fenton process is effective at low pH ranges and is consistent with previous Fenton studies. Duman (2006) has shown that the pH range of the Fenton process is effective between 2-3.5 (Duman, 2006).

The high removal efficiency of the Fenton process at low pH is explained by the loss of catalytic activity of Fe^{+2} ions into Fe^{+3} flocks (Sahinkaya et al., 2008). Fe + 2 and H_2O_2 are more stable if the pH is less than 3.5. When the pH is higher than 3.5, Fe^{+2} and H_2O_2 become unstable since Fe^{+2} iron forms hydroxyl groups and H_2O_2, becomes unstable due to its reduction of oxidation capacity (Benitez et al., 2001).

3.1. Effect of Fe^{+2} Concentration

The effect of Fe^{+2} concentration on COD and color removal efficiencies were examined and the results are shown in Figure 3. and Figure 4.

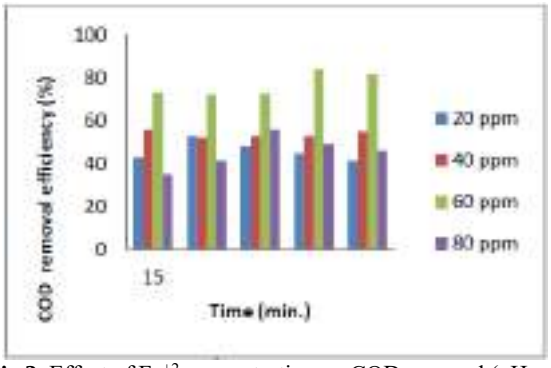

Fig.3. Effect of Fe^{+2} concentration on COD removal (pH: 2, H_2O_2 concentration: 600 mg / L)

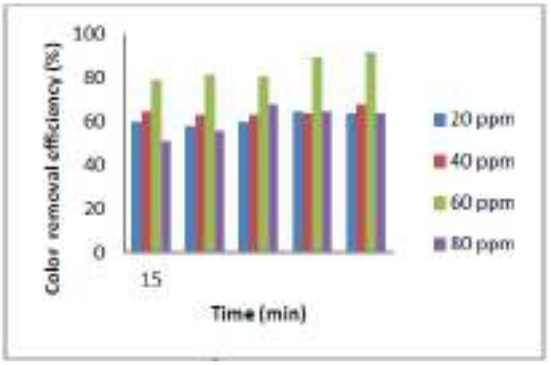

Fig.4. Effect of Fe^{+2} concentration on color removal (pH: 2, H_2O_2 concentration: 600 mg / L)

The effect of Fe + 2 concentration on COD and color removal efficiency was investigated in this study at pH 2 and 600 mg / L H_2O_2 concentration and within 20-80 mg/L Fe^{+2} concentrations. At the end of 2 h reaction, the COD removal efficiencies at Fe^{+2} concentration of 20, 40, 60 and 80 mg/L were 42%, 58%, 84%, and 50%, respectively. For the same concentrations sequences, Color removal efficiencies were 65%, 70%, 92% and 64% respectively. As shown in the results, the efficiencies of COD and color removal were increased up to 60 mg / L Fe^{+2} concentration and decreased at 80 mg/L. The reason for this decrease is due to redox reactions at 60 mg/L Fe^{+2} in wastewater and the completion of the coagulation process. Therefore, optimum Fe^{+2} concentration was determined as 60 mg/L.

3.2. Efect Of H_2O_2 Concentration

The effect of H_2O_2 concentration on COD and color removal efficiencies were examined and the results are shown in Figure 5. and Figure 6.

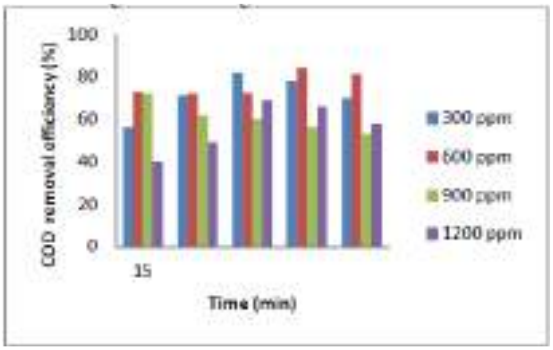

Fig.5. Effect of H_2O_2 concentration on COD removal (pH: 2, Fe^{+2} concentration: 60 mg / L)

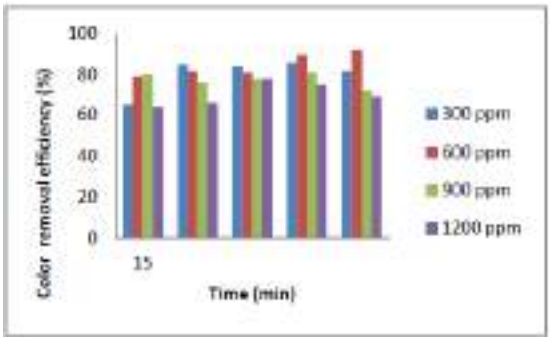

Fig.6. Effect of H_2O_2 concentration on Color removal (pH: 2, Fe^{+2} concentration: 60 mg / L)

The effect of H_2O_2 concentration on COD and color removal efficiency was investigated in this study at pH 2 and 60 mg/L Fe^{+2} concentration and 300-1200 mg/L H_2O_2 concentrations. At the end of 2 h reaction, the COD removal efficiencies at H_2O_2 concentration of 300, 600, 900 and 1200 mg/L were 70%, 84%, 55%, and 60%, respectively. For the same concentrations sequences, Color removal efficiencies were 82%, 92%, 72% and 70% respectively. As H_2O_2 concentration increases, the rate of decomposition of pollutants and affects COD removal efficiency increase. However, after a point, excess H_2O_2 reacts with hydroxyl radicals which negatively affects the oxidation efficiency (Bouasla et al., 2010). In the study, H_2O_2 showed an increase in COD and color removal up to 600 mg / L and a decrease in 900 and 1200 mg/L concentrations.

When COD and color removal efficiencies were examined, the concentration of 600 mg / L H_2O_2 was determined as optimum.

4. CONCLUSION

In this study, treatment possibility of slaughterhouse wastewater by Fenton process was investigated. Three parameters; pH, Fe^{+2} and H_2O_2 were optimized. At the end of the 2 h reaction period, the optimum conditions were pH 2, 60 mg / L Fe^{+2} and 600 mg / L H_2O_2. Under the optimum conditions, maximum COD and color removal efficiencies were 84% and 92% respectıvely. Although the color parameter in the wastewater meets the discharge criteria specified in the regulation, the COD parameter does not meet the discharge criteria. As shown in this study, The Fenton process alone was not sufficient for slaughterhouse wastewater treatment. It is possible to achieve discharge standards by means of a Fenton process by pre-treatment.

REFERENCES

Benatti, C.T., Tavares, C.R.G. Organic Pollutants Ten Years After the Stockholm Convention Environmental and Analytical Update. Puzyn, D.T. (ed), p. 247, In Tech. 2012.

Benitez, F. J., Acero, J. L., Real, F. J., Rubio, F. J., Leal, A. I., "The role of hydroxyl radicals for the decomposition of p-hydroxy phenylacetic acid in aqueous solutions", Water Research, 35(5), s. 1338-1343, 2001.

Bianco, B., De Michelis, I., Veglio, F. Fenton treatment of complex industrial wastewater: Optimization of process conditions by surface response method. Journal of Hazardous Materials, 186(2-3): 1733-1738. 2011.

Bouasla, C., Samar, M. E. H., Ismail, F., " Degradation of methyl violet 6B dye by the Fenton process." Desalination, 254(1-3), s. 35-41, 2010.

Bustillo-Lecompte, C. F., Ghofoorib, S., Mehrvar, M. Photochemical degradation of an actual slaughterhouse wastewater by continuousUV/H_2O_2 photoreactor with recycle, journal of Environmental Chemical Engineering, 4: 719-732. 2016.

Closed Reflux, Titrimetric Method 5220 C (1998). Standart Methods fort he Examination of Water and Wastewater. AWWA, WEF, APHA.

Duman, E., "İlaç Endüstrisi Atıksularının Fenton Oksidasyonu İle Arıtılabilirliğinin Araştırılması. Hacettepe Üniversitesi Çevre Müh. ABD, "Yüksek Lisans Tezi, Ankara, 2006.

Gerbens-Leenes, P.W., Mekonnen, M.M., Hoekstra A.Y. The water footprint of poultry, pork and beef: a comparative study in different countries and production systems Water Resour. Ind., 1–2 (2013), pp. 25-36.

Gogate, P. R., Pandit, A. B., "A review of imperative technologies for wastewater treatment II: hybrid methods." Advances in Environmental Research, 8(3-4), s. 553-597, 2004.

Kaftan, A. Entegre Et Tesislerinde Atık Suyun Yeniden Kullanımı. Ondokuz Mayıs Üniversitesi Gıda Mühendisliği Bölümü. Samsun 2010.

Odabaşı, S., Maryam, B., Büyükgüngör, H. Fenton ve Fotofenton Prosesleri ile Atıksudaki Aspirinin Giderim Verimliliğinin Karşılaştırılması. Nevşehir Bilim ve Teknoloji Dergisi Cilt 6(ICOCEE 2017 Özel Sayı) 326-332. 2017.

Oğuz, M. İnternational Journal of Environmental Studies. 1993. 44, 39-44.

Tezcan, H. Zeytinyağı Atık sularının Fenton Prosesi İle Arıtılması. Selçuk Üniversitesi Fen Bilimleri Enstitüsü Yüksek Lisans Tezi Konya 2010.

T.C. Kalkınma Bakanlığı. Sekizinci Beş Yıllık Kalkınma Planı. Gıda Sanayi Özel İhtisas Komisyonu Raporu. Et ve et ürünleri sanayi alt komisyon raporu. 2001.

World Bank GroupEnvironmental, Health and Safety (EHS) Guidelines for Meat Processing. General EHS Guidelines: Environmental Wastewater and Ambient Water Quality, 2007.

CISET - 2nd Cilicia International Symposium on Engineering and Technology
10-12 October, 2019, Mersin / TURKEY

INVESTIGATION OF SOIL PROPERTIES IN THE WEST OF ERDEMLI (MERSIN) DISTRICT CENTER

Barış Başeren[1], T. Fikret Kurnaz[2]

[1] Mersin Metropolitan Municipality, General Directorate of Meski, Department of Investment and Construction, Mersin, Turkey, baris.baseren@gmail.com

[2] Mersin University, Vocational School of Technical Sciences, Department of Transportation Services, Mersin, Turkey, fkurnaz@mersin.edu.tr

ABSTRACT

In this study, the ground investigation based on field and laboratory research studies have been conducted to evaluate the settlement suitability of the region located west of Erdemli district center. In this context, the results of the soil drilling studies representing the region and the test results on the soil samples were utilized. The findings of the soil profile in the region, especially in the southern part showed that very loose. It was found that there was a relative improvement in soil properties due to the presence of limestone as it went north.

Keywords: *Erdemli, Ground Survey, Settlement Suitability*

1. INTRODUCTION

Local ground conditions play an important role in the planning of residential areas. Variation of soil properties in a region, even at short distances, may cause differences in structural damage that may occur. Therefore, detailed investigation of local soil conditions, especially in areas with high earthquake risk, is of great importance in terms of development of earthquake resistant structure design and minimizing the damages that may occur.

Urban planning sets short, medium and long term targets for data collection, analysis and synthesis methods for current and expected problem solutions and defines applicable methods to achieve these goals (Lobo et al., 1997; Sengezer 1998). The main constraints that may affect site selection in urban planning are topography, geological structure, climatic conditions, seismology, hydrogeological characteristics, building materials, soil quality, mineralogical and geochemical properties. Urban planning has an important place in the planning and mapping of the geological environments of cities all over the world.

In this study, the soil properties of the region located to the west of the Erdemli district center of Mersin were investigated. The region is located within the borders of Koyuncu quarter and covers an area of approximately 800.000 m2 (Figure 1). The study area was examined with the results of geological and geotechnical methods and the suitability of the region to the settlement was investigated. In this respect, the results of the laboratory tests applied to the disturbed and undisturbed soil samples were investigated in detail by 5 drilling works in the region.

Figure 1. Location Map

2. GENERAL GEOLOGY

Mersin is a port city in the south of Turkey. 87% of the land is mountainous. Central Taurus Mountains stretching to the rocky hill, Bolkar Medetsiz Mountain Peak (3,584) is the province's highest peak, and has opened a few important transitions to mid Anatolia. These transition points are Sertavul and Gülek defiles. The Taurus Mountains are the mountain range that extends for approximately 560 km parallel to the coast on the Mediterranean coast and forms the southern border of the Anatolian plateau. There are high meadows and small plains between 700 and 1500m. The province has 321 km of coastline, mostly sandy. Tarsus and Mersin are the continuation of Çukurova Region and are wide plains. Although the largest rivers are Göksu and Tarsus, there are many small streams flowing towards the lake or the Mediterranean Sea.

Tarsus-Mersin Coastal aquifer system and the geological units in the drainage area of this aquifer system are located in the southeastern part of the Ecemiş Fault of the Taurus Mountain formation Belt and have the geological characteristics of this belt.

Palaeozoic aged metamorphics (marble, schist, quartzite), ophiolitic mélange settled during the Upper Cretaceous, terrestrial, transitional and marine environment deposits (limestone-sandstone-claystone-conglomerate-marl-gypsum), Quaternary aged terrestrial and transitional sediments and morphological units are common in the eastern and southern parts of the region. The surface spread of the units from old to young is generally from north to south (Alfa 2018). The geological map of the region is presented in Figure 2.

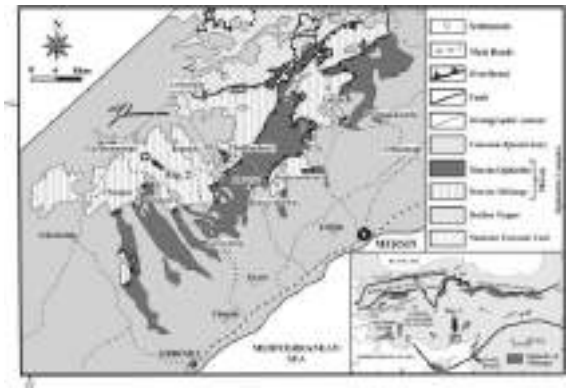

Figure 2. The Geology Map of Mersin (Senel 2002; Alan et al., 2007)

3. FIELD AND LABORATORY STUDIES

3.1. Field Studies

Within the scope of field studies, 5 drilling works with depths of 15 m were used to obtain the disturbed and undisturbed samples and to determine the soil conditions in the study area. (Figure 3).

In order to determine the horizontal and vertical soil profile and soil properties in the investigated land, 5 boreholes were drilled by taking into consideration the characteristics of the existing structures.

No.1 Borehole; there is a fill layer of 0.40 m thickness from the ground surface. Below the fill layer, there is a gray colored clay unit up to 2.50 m. There is a sand layer

up to 10.00 m beneath the gray clay unit. The clay layer continues up to 15.00 m under the sand layer.

No.2 Borehole; there is a fill layer of 0.35 m thickness from the ground surface. Below the fill layer there is a gray colored clay unit up to 3.00 m. There is a sand layer up to 10.50 m beneath the gray clay unit. The clay layer continues up to 15.00 m under the sand layer.

No.3 Borehole; there is a fill layer of 0.40 m thickness from the ground surface. Below the fill layer there is a gray colored clay unit up to 3.00 m. There is a sand layer up to 10.50 m beneath the gray clay unit. The clay layer continues up to 15.00 m under the sand layer.

No.4 Borehole; there is a 1.50 m thick filling layer from the ground surface. There is a clay layer up to 4.50 m below the fill layer. Under the clay layer, limestone layer continues up to 15.00 m.

No.5 Borehole; there is a 1.00 m thick filling layer from the ground surface. Limestone layer continues up to 15.00 m below the fill layer.

Figure 3. Satellite Image of Study Area

When the ground water level is examined, it is observed that the ground water level is between 0.75 meters and 1.25 meters in drilling zones 1, 2 and 3, while it is between 2.80 and 10.00 meters in drilling zones 4 and 5. As a result of the standard penetration test carried out on the samples taken from the field to a depth of 3.50 meters, it was found that the survey area had very loose ground as a result of the number of 4 ~ 5 drops in all drilling regions.

3.2. Laboratory Tests and Analyzes

According to the Atterberg limit test results on the samples taken from the drillings no. 1, 2 and 3, the clay units in the field were found to be NON PLASTIC. However, the soil class was determined to be clayey sand (SC). In the researches on the samples taken from the drillings no. 4 and 5; Liquid Limit (LL) is 73.03% and Plastic Limit is between 14.20% - 17.96% were determined. In addition, the Plasticity Index value was found to be 48.48%. Soil class was determined as high plasticity clay (CH).

The cohesion was found to be 0.05kg / cm2 and the internal friction angle was 14 degrees in the cut-box test on the sample taken from drilling 1 in the south of the study area. The cohesion was calculated as 1.085kg / cm2, qu = 2.17 kg / cm2 by the free pressure test on the sample taken from the drilling 4 in the north of the study area.

4. CONCLUSION

In this study, the soil characteristics of the region located west of Erdemli district center were investigated by geological and geotechnical methods and the suitability of the region to the settlement was investigated. According to the findings, alluvium units are dominant throughout the study area but limestone is encountered in the northern parts. According to the results of the SPT test during the drillings, the soil in the region was found to be very loose especially in the southern parts. Due to the limestone levels observed in the north of the region, the soil properties are relatively improved as move from south to north. Since the southern sections are 200 m away from the coast, the loose sediments in these sections carry a risk in terms of construction. It is useful to take measures such as choosing the suitable foundation type and soil improvement while going to construction in these sections.

REFERENCES

Alan, I., Sahin, S., Keskin, H., Altun I., Bakirhan, B., Balci, V., B€oke, N., Sacli, L., Pehlivan, S., Kop, A., Hanilci, N. & Celik, € O. F. (2007). Geodynamic evolution of central Tauride- Eregli (Konya)-Ulukisla (Nigde)-Karsanti (Adana)- Namrun (Icel) region. General Directorate of Mineral Research and Exploration, Department of Geological Investigation, Report No: 245. [Unpublished, in Turkish.]

Alfa Construction and Soil Mechanics Laboratory (2018), Mersin Province Erdemli District Kocahasanlı Neighborhood Geology Soil and Foundation Survey Report, Mersin.

Costa Lobo, M., Mesones, J., Dal Cin, A., Franchini, T. and Lourenzo, J. (1997) "Risk in planning a new paradigm. Risk Assesment and Management: Planning for Uncertain Future", *33rd World Planning Cong*, September, Ogaki, Japan, pp. 17-18.pp. 103-107.

Senel, M. (2002). 1/500.000 scale Turkish geological maps, Adana Quadrangle. General Directorate of Mineral Research and Exploration, Ankara.

Şengezer, B. S. (1998) "Importance and Role of Disaster Mitigation Target in Planning", *Urbanization and Geology Symposium*, 19-20 November, Istanbul, pp. 17-26

CISET - 2nd Cilicia International Symposium on Engineering and Technology
10-12 October, 2019, Mersin / TURKEY

INVESTIGATION OF SOIL PROPERTIES IN OLD MEZITLI LOCATION OF MEZITLI (MERSIN) DISTRICT

Barış Başeren[1], T. Fikret Kurnaz[2]

[1] Mersin Metropolitan Municipality, General Directorate of Meski, Department of Investment and Construction, Mersin, Turkey, baris.baseren@gmail.com

[2] Mersin University, Vocational School of Technical Sciences, Department of Transportation Services, Mersin, Turkey, fkurnaz@mersin.edu.tr

ABSTRACT

In this study, in order to evaluate the settlement suitability of the region located in the Old Mezitli location of Mezitli district (Mersin), a soil survey based on field and laboratory studies was conducted. In this context, soil drilling studies representing the region and test results on soil samples were utilized. Based on the findings, the soil profile in the region is composed of softpan gravel limestone blocks with limestone gravels. It was determined that the region was suitable for the settlement in terms of engineering properties.

Keywords: *Mezitli, Ground Survey, Settlement Suitability*

1. INTRODUCTION

Geological and geotechnical investigations made according to the zoning plan are important in the planning of urban areas. Identifying risky and safe areas in terms of soil characteristics will help prevent structural damage caused by natural disasters. In this way, it is possible to develop earthquake resistant structure design and minimize the damages that may occur especially in areas with high earthquake risk.

In the field surveys for land planning, it is necessary to determine the changes in the parameters explaining the local soil conditions in the region and to combine the data layers obtained as a result of the analysis of these parameters to understand the relationships between them. Urban planning sets short, medium and long term targets for data collection, analysis and synthesis methods for current and expected problem solutions and defines applicable methods to achieve these goals (Lobo et al., 1997; Sengezer 1998). The main constraints that may affect site selection in urban planning are topography, geological structure, climatic conditions, seismology, hydrogeological characteristics, building materials, soil quality, mineralogical and geochemical properties. Urban planning has an important place in the planning and mapping of the geological environments of cities all over the world.

In this study, soil properties of the region located in Old Mezitli of Mezitli district of Mersin were investigated. The region is located within the borders of the Akdeniz quarter and covers an area of approximately 100,000 m2 (Figure 1). The study area was examined with the results of geological and geotechnical methods and the suitability of the region to the settlement was investigated. In this respect, the results of the laboratory tests applied to the disturbed and undisturbed soil samples that have been traumatized by 4 drilling works carried out in the region have been examined in detail.

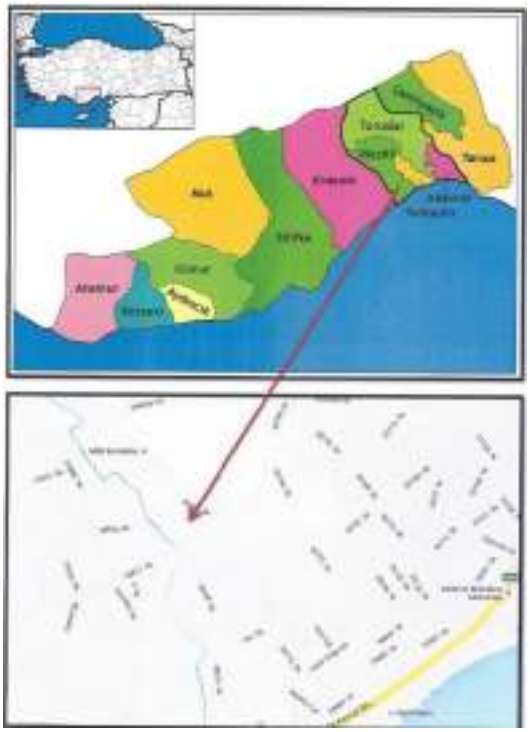

Figure 1. Location Map

2. GENERAL GEOLOGY

Mersin is a port city in the south of Turkey. 87% of the land is mountainous. Central Taurus Mountains stretching to the rocky hill, Bolkar Medetsiz Mountain Peak (3,584) is the province's highest peak, and has opened a few important transitions to mid Anatolia. These transition points are Sertavul and Gülek defiles. The Taurus Mountains are the mountain range that extends for approximately 560 km parallel to the coast on the Mediterranean coast and forms the southern border of the Anatolian plateau. There are high meadows and small plains between 700 and 1500m. The province has 321 km of coastline, mostly sandy. Tarsus and Mersin are the continuation of Çukurova Region and are wide plains. Although the largest rivers are Göksu and Tarsus, there are many small streams flowing towards the lake or the Mediterranean Sea.

Tarsus-Mersin Coastal aquifer system and the geological units in the drainage area of this aquifer system are located in the southeastern part of the Ecemiş Fault of the Taurus Mountain formation Belt and have the geological characteristics of this belt.

Palaeozoic aged metamorphics (marble, schist, quartzite), ophiolitic mélange settled during the Upper Cretaceous, terrestrial, transitional and marine environment deposits (limestone-sandstone-claystone-conglomerate-marl-gypsum), Quaternary aged terrestrial and transitional sediments and morphological units are common in the eastern and southern parts of the region. The surface spread of the units from old to young is generally from north to South (Zemka 2016). The geological map of the region is presented in Figure 2.

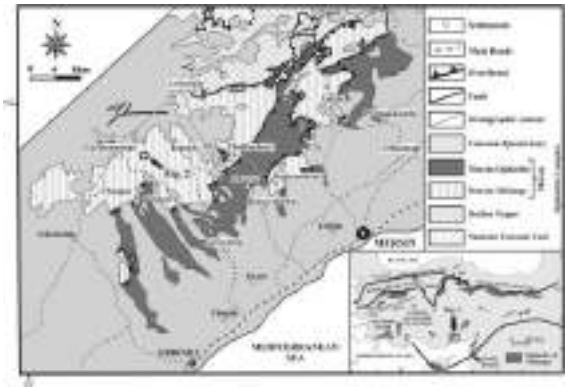

Figure 2. The Geology Map of Mersin (Senel 2002; Alan et al., 2007)

3. FIELD AND LABORATORY STUDIES

3.1. Field Studies

Within the scope of field studies, 4 drilling works with depths of 10 meters were used to obtain the disturbed and undisturbed samples and to determine the soil conditions in the study area (Figure 3).

In order to determine the horizontal and vertical soil profile and soil properties of the investigated land, 4 boreholes were drilled by taking into account the characteristics of the existing structures.

No.1 Borehole; It has been determined that from the ground surface up to about 0.50 meters of filling soil, from this level up to 3.00 meters of weak rock-resistant

carbonate shells called hardpan caliche, up to 3.00 meters of 10.00 meters limestone gravels formed by block gravel softpan caliche continues.

No.2 Borehole; It has been determined that from the ground surface up to about 0.50 meters of filling soil, from this level up to 3.00 meters of weak rock-resistant carbonate shells called hardpan caliche, up to 3.00 meters of 10.00 metes limestone gravels formed by block gravel softpan caliche continues.

No.3 Borehole; It has been determined that from the ground surface up to about 0.80 meters of filling soil, from this level up to 2.50 meters of weak rock-resistant carbonate shells called hardpan caliche, up to 2.50 meters of 10.00 metes limestone gravels formed by block gravel softpan caliche continues.

No.4 Borehole; It has been determined that from the ground surface up to about 0.70 meters of filling soil, from this level up to 2.00 meters of weak rock-resistant carbonate shells called hardpan caliche, up to 2.00 meters of 10.00 metes limestone gravels formed by block gravel softpan caliche continues.

Figure 3. Satellite Image of Study Area

When the groundwater level was examined, no groundwater was found in the boreholes.

3.2. Laboratory Tests and Analyzes

It was determined that the water content of the soil ranged from 12.4% to 18.2% by testing on samples taken from 4 boreholes. The natural unit volume weight for the soil was determined in the range of 2.089-2.111 tons/m3 and the dry unit volume weight was determined in the range of 1.781-1.878 tons/m3.

According to the Atterberg limits determined for the ground in the depth range of 6.00 - 10.00 meters in drilling operations, the Liquid Limit (LL) is in the range of 38,00-41,90, the Plastic Limit (PL) is in the range of 18,50-22,70 and the Plasticity Index (PI) is 19,50. -21,60. For the same depth range, grain size distribution was found as 57.10% - 61.40% Gravel, 7.50% - 14.70% Sand, 23.9% - 35.40% Clay-Silt.

The cohesion test performed on the sample taken from the drilling study no. 1 was found to be 0.06 kg/cm2 with an internal friction angle of 17.70; the cohesion test performed on the sample taken from the drilling study no. 2 was found to be 0.04 kg/cm2 with an internal friction angle of 18.20; the cohesion test performed on the sample taken from the drilling study no. 3 was found to be 0.01 kg/cm2 with an internal friction angle of 20.30; the cohesion test performed on the sample taken from the drilling study no. 4 was found to be 0.02 kg/cm2 with an internal friction angle of 19.50.

Considering the results of the drilling works, the experiments on the samples taken from the boreholes and the field observations, it was determined that the soil dominated by the block gravel softpan caliche formed by limestone gravels is clayey gravels (GC) according to the soil class.

4. CONCLUSION

In this study, the soil characteristics of the region located in the Old Mezitli location of Mezitli district (Mersin) were investigated by geological and geotechnical methods and the suitability of the region to the settlement was investigated. According to the findings, quaternary aged caliche unit is dominant throughout the study area. Considering the results of the drilling works, the experiments on the samples taken from the boreholes and the field observations, it was determined that the soil dominated by the block gravel softpan caliche formed by limestone gravels is clayey gravels (GC) according to the soil class.

REFERENCES

Alan, I., Sahin, S., Keskin, H., Altun I., Bakirhan, B., Balci, V., B€oke, N., Sacli, L., Pehlivan, S., Kop, A., Hanilci, N. & Celik, € O. F. (2007). Geodynamic evolution of central Tauride- Eregli (Konya)-Ulukisla (Nigde)-Karsanti (Adana)- Namrun (Icel) region. General Directorate of Mineral Research and Exploration, Department of Geological Investigation, Report No: 245. [Unpublished, in Turkish.]

Costa Lobo, M., Mesones, J., Dal Cin, A., Franchini, T. and Lourenzo, J. (1997) "Risk in planning a new paradigm. Risk Assesment and Management: Planning for Uncertain Future", *33rd World Planning Cong*, September, Ogaki, Japan, pp. 17-18.pp. 103-107.

Senel, M. (2002). 1/500.000 scale Turkish geological maps, Adana Quadrangle. General Directorate of Mineral Research and Exploration, Ankara.

Şengezer, B. S. (1998) "Importance and Role of Disaster Mitigation Target in Planning", *Urbanization and Geology Symposium*, 19-20 November, Istanbul, pp. 17-26

Zemka Soil Research Laboratory (2016), Mersin Province Mezitli District Mersin Wastewater Plant Project 2745 Parcel Geology, Soil and Foundation Survey Report, Mersin

CISET - 2nd Cilicia International Symposium on Engineering and Technology
10-12 October, 2019, Mersin / TURKEY

ANALYSIS OF STATIC OUTPUT MEASUREMENTS FOR TOMOTHERAPY HDA

Songul BARLAZ US

Mersin University, School of Medicine, Department of Radiation Oncology, Mersin, Turkey, barlaz@gmail.com

ABSTRACT
Helical tomotherapy is a relatively new modality with integrated treatment planning and delivery hardware for radiotherapy. The output of the tomotherapy is measured in dose per unit time. In this study, It was aimed to analysis the change of static output values of the device. Ion chamber and cheese phantom were used for static output measurement. Output changes, once a week and and 10 weeks, calculated. According to results, maximum difference was 2.161% and minimum difference was 0 %. These differences were within a 3% window.

Keywords: *radiotherapy, tomotherapy, static output, ion chamber, cheese phantom*

INTRODUCTION

The helical tomotherapy is a technologically advanced radiation dose delivery system designed to perform intensity-modulated radiation therapy (IMRT). It is characterized by radiation delivery in which the patient is constantly translated through a continuously rotating radiation beam mounted on a slip-ring gantry (Balog and Soisson, 2008, Saw *et al*, 2018).

Output is defined the dose per unit of time. The monitor unit (MU) readings that are displayed on the operator screen are derived from the monitor chamber signals. One MU represents the machine output expressed in cGy/min measured at a depth of 1.5 cm with an SAD of 85 cm and a 5x40 cm^2 static field (NCS Report 27, 2017). Output should be check and difference should be within the tolerance window.

In this study, the changes of static output value of the tomotherapy were analyzed.

METHOD AND MATERIALS

In this study, Exradin A1SL ion chamber and cheese phantom were used for Tomotherapy HDA's output checks (Figure 1).

Figure 1. Measurement set

Output measured once a week. Dose values read by ion chamber were compared with dose values obtained from treatment planning. The difference was calculated as a percentage and these differences were evaluated for 10 weeks.

RESULTS

For 10 weeks, the difference between the calculated output values and treatment planning is shown in the figure 1.

According to results, maximum difference was 2.161% and minimum difference was 0%. All difference values were within a 2% window except three values.

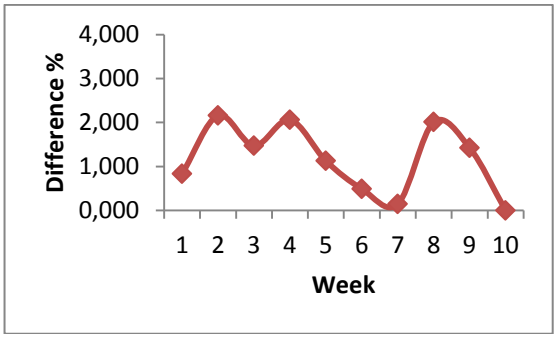

Figure 1. Changes of static output

CONCLUSION

Static output is a valuable part f the tomotherapy quality assurence. Recommendation and tolerance limit is %2 for static output according to AAPM Task Group 148 (Langen *et al*, 2010). When the output value exceeds 2%, it is set by the technical service engineer to be within the limit values.

REFERENCES

Balog J and Soisson E. (2008). "Helical Tomotherapy Quality Assurance." *Int. J. Radiation Oncology Biol. Phys*, Vol. 71, No. 1, Supplement, pp. S113–S117.

Langen KM, Papanikolaou N, Balog J, Crilly R et al (2010). "QA for helical tomotherapy: Report of the AAPM Task Group 148." *Med. Phys.* V. 37 No.9, p. 4817-4853.

Report 27 of the Netherlands Commission on Radiation Dosimetry (2017), Quality Assurance for Tomotherapy Systems, Nederlandse Commissie Voor Stralingsdosimetrie.

Saw CB, Katz L, Gillette C, Koutcher L. (2018). "3D treatment planning on helical tomotherapy delivery system." *Med Dosim.* Vol. 43 No. 2, pp.159-167.

CISET - 2nd Cilicia International Symposium on Engineering and Technology
10-12 October, 2019, Mersin / TURKEY

DESIGN AND PROTOTYPE OF A SLOTTED WAVEGUIDE ARRAY ANTENNA FOR MARINE RADAR APPLICATIONS

Hakan Işıker [1], and Caner Özdemir [*2]

[1] Mersin University, Engineering Faculty, Electrical and Electronic Engineering Department, Mersin, Turkey, Hakan hakan.isiker@mersin.edu.tr
[2] Mersin University, Engineering Faculty, Electrical and Electronic Engineering Department, Mersin, Turkey, cozdemir@mersin.edu.tr

ABSTRACT
In this work, a practical antenna, in the form of slotted waveguide array, is first designed and then produced to be used in marine radar applications. The design steps of the slotted waveguide array antenna were performed by the help of CST Microwave Studio simulation software. After optimizing the antenna for reflection coefficient, the required frequency bandwidth of operation and other antenna parameters, the design has been prepared for manufacturing. The prototyping process has been completed with an industry firm in Mersin area. Comparison of the antenna parameters of the design and the prototyped antenna shows a very good agreement that fairly demonstrated the success of the design. The manufactured slotted waveguide array antenna is ready to be used especially for marine radar applications.

Keywords: *Antenna design, computer aided design, slotted waveguide array antenna, antenna manufacturing*

[*] Corresponding Author

1. INTRODUCTION

In marine radar applications, horizontally polarized antennas are usually preferred since the civil and military sea vessels are in the form of a long platforms (Parsa, *et al.*, 2012). This is due to the fact that the horizontal radar cross section signatures of ships are relatively higher than that of vertical ones. One of the most preferable antennas is the slotted waveguide array antenna (SWAA) that has fair advantages of design simplicity, light-weight, compactness, high-power handling, good directivity, and high efficiency. (Sekretarov *et al.,* 2010). One challenge in SWAA's can be its moderate bandwidth feature that needs to be optimized for the selection of the application (El Misilmani *et al.,* 2015).

In this study, we aim to design and prototype a horizontally polarized antenna that can operate at the center frequency of 3 GHz with a bandwidth goal of 100 MHz. The radiation pattern is needed to be Omni such that the antenna can provide the same power for all horizontal angles. For the design of the SWAA, CST Microwave Studio software has been used (Hirtenfelder, F., *et al.,* 2007). Then, the design is optimized for the above-mentioned antenna parameters. The designed antenna was manufactured by an aluminum production firm in Mersin area. The optimized design and the prototyped SWAA produce almost the same antenna reflection coefficient that clearly demonstrates the success of our antenna design.

2. CST SIMULATION

The SWAA antenna is needed to be operated around 3 GHz achieving a 100 MHz bandwidth. For the design, we assume a total of four vertical slots in each side of the waveguide to be able to achieve a vertical -3dB beam-width around 20°-25°. The antenna has to be fed by a coaxial line of 50Ω line-impedance. The gain of the antenna was aimed to be around 8 dBi or better. Taken into account these design goals, CST Microwave Studio software is used to design the antenna. After the preliminary design, optimization of the antenna parameters was also accomplished by CST for the best fit of the antenna design goals. The optimized parameters are listed in Table 1.

Table 1. Optimized parameters for SWAA

Parameter	*Value*
waveguide length (inner)	274.90 mm
waveguide width (inner)	78.14 mm
waveguide height (inner)	17.01 mm
slot length	47.5 mm
slot width	7 mm
coax excitation location	30. 51 mm from the bottom of the antenna

The resultant designed SWAA can be seen in Fig. 1. The perspective, side, front, and top view of the designed SWAA are provided in Fig. 1(a), (b), (c), and (d), respectively.

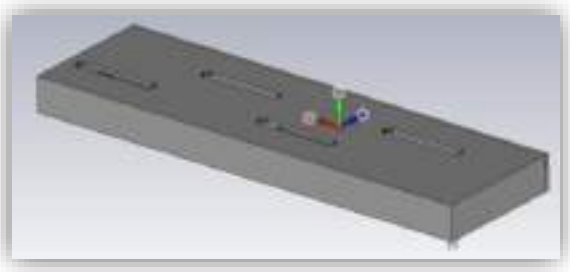

(a)

(b)

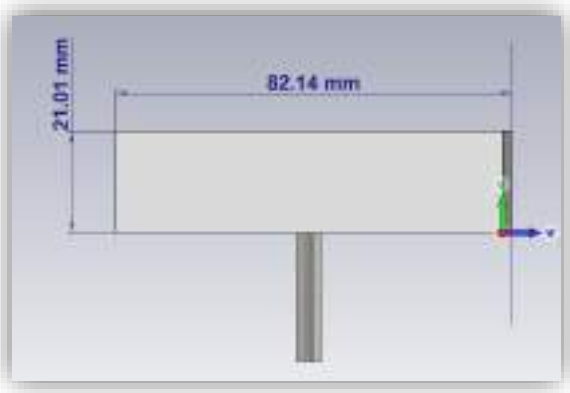

(c)

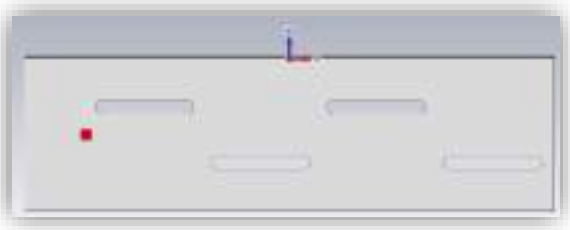

(d)

Fig. 1. Designed slotted waveguide array antenna with dimensions: (a) perspective (b) side, (c) front, and (d) top view.

The antenna parameter analysis of the designed SWAA was also be done with the help of CST. The reflection coefficient (or S_{11}) is as obtained in Fig. 2. As seen from the figure, the antenna's center frequency of operation is 3 GHz with a -10 dB band ranging from 2.94 GHz to 3.05 GHz achieving a 110 MHz of bandwidth. The return loss is -24 dB at the center frequency.

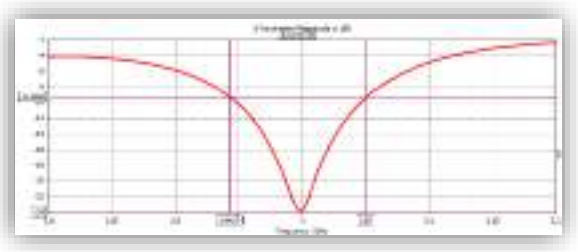

Fig. 2. S_{11} simulation performance of the designed SWAA

The antenna pattern of the designed SWAA at 3 GHz is given in Fig. 3(a). The horizontal pattern is plotted in Fig. 3(b) in which almost an omni pattern is achieved. The vertical pattern can be observed from Fig. 3(c). The -3dB beam-width of the vertical beam is 20.6°. Also, the directivity of the antenna pattern is 9.13 dBi and the gain is 9.16 dBi.

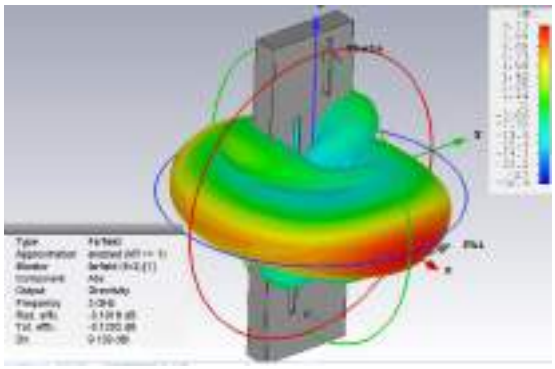

(a)

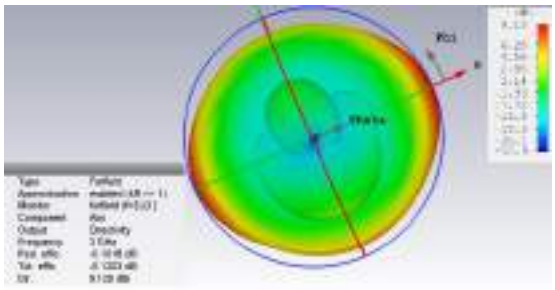

(b)

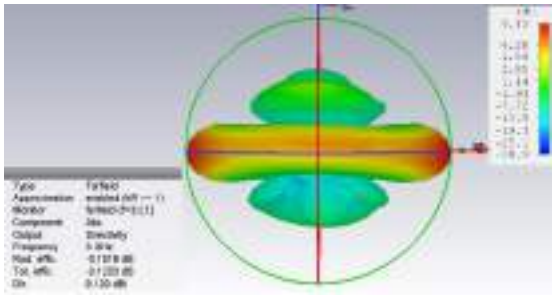

(c)

Fig. 3. Antenna radiation pattern of the designed SWAA: (a) perspective view, (b) top view, and (c) side view.

Looking at Fig.2 and Fig.3, all the design goals including center frequency of operation, frequency bandwidth, radiation pattern metrics (gain, directivity, beam-width, omni pattern in horizontal direction and -3dB merit along the elevation pattern, etc.) have been successfully achieved in the CST simulation.

3. PROTOTYPED SWAA

The designed antenna has been produced at an industrial firm that is specialized in aluminum materials production in Mersin area. The model is fully produced with aluminum material as the manufactured antenna can be viewed in Fig. 4.

Fig. 4. Manufactured SWAA

After prototyping the SWAA, its reflection coefficient performance was measured at anechoic chamber facility in Mersin University Advanced Technology Education Research and Application Center (MEATRC). The measurement was done by the help of the vector network analyzer device [*Agilent Technologies ENA series ENA 5071B*].

The measured S_{11} performance of the manufactured SWAA is as shared in Fig. 5 where the screen-shot of the vector network analyzer's screen during the measurement can be observed. As it can be clearly read from the figure, the antenna has an operational center frequency of 2.991352 GHz with -10 dB band ranging from 2.94 GHz to 3.03 GHz that is almost a very good agreement with the designed SWAA in CST simulation.

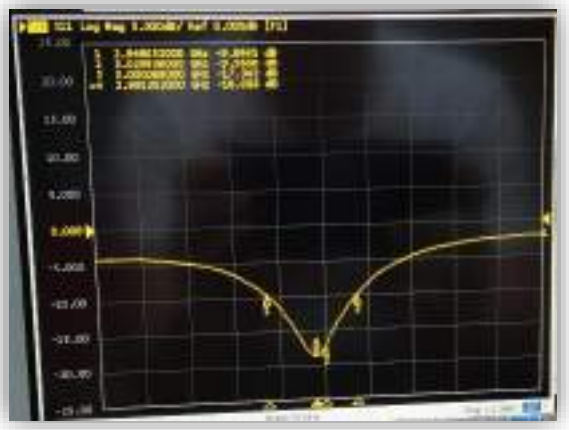

Fig. 5. Measured S_{11} performance of the manufactured SWAA

4. CONCLUSION

In this study, we have designed and manufactured an S-band slotted waveguide array antenna for marine radar applications. The design goals of the antenna were used in the CST simulation. The optimization of the pre-design has been accomplished and a designed antenna that fulfilled all the design goals have been achieved. The designed antenna has the precious feature of being horizontally polarized with an OMNI pattern along the horizontal direction and a 20° beam-width in vertical direction. The gain of the antenna is just lower than 10 dBi and has an operational frequency bandwidth of about 100 MHz. The manufacture of the design clearly demonstrates the success of the design and the good production work while prototyping the SWAA.

REFERENCES

El Misilmani, H. M., Al-Husseini, M., and Kabalan, K. Y. (2015) "Design of Slotted Waveguide Antennas with Low Sidelobes for High Power Microwave Applications" *Progress in Electromagnetics Research C,* Vol. 56, 15–28

Hirtenfelder, F. (2007) "Effective Antenna Simulations using CST MICROWAVE STUDIO®," *2007 2nd International ITG Conference on Antennas*, Munich, 239-239.

Parsa, A. and Hansen, N. H. (2012) "Comparison of vertically and horizontally polarized radar antennas for target detection in sea clutter - An experimental study," *2012 IEEE Radar Conference, Atlanta,* GA, 653-658.

Sekretarov, S. S. and Vavriv, D. M. (2010) "A Wideband Slotted Waveguide Antenna Array for Sar Systems" *Progress in Electromagnetics Research M,* Vol. 11, 165–176

CISET - 2nd Cilicia International Symposium on Engineering and Technology
10-12 October, 2019, Mersin / TURKEY

THE MICROPLASTIC DEBRIS SINK, LAKES; A REVIEW

Olcay GÜLÇİÇEK UYSAL

Mersin University, Engineering Faculty, Environmental Engineering Department, Mersin, Turkey,
olcay.gulcicek@gmail.com

ABSTRACT

In the last decade, microplastic contamination in the environment has attracted more and more attention and is currently a developing subject of research.
While many studies have focused on determining the amount of micro plastic in the marine environment, there is little interest in the amount of micro plastic in the freshwater environment.
The main source of microplastics reaching the marine environment is terrestrial resources. They are rivers that move within the terrestrial resources and form a channel towards the sea. The lakes, which are another fresh water source, constitute a point source with a high concentration in terms of being stationary and holding the pollutant in it for a long time.
In this review, a general information about the models related to the location, determination, source and transport of lakes in microplastic pollution is not compiled. The aim of this study is to emphasize that microplastics, which is a current pollutant, should be investigated in lakes**.**
Key Word;
.

Keywords: *Lake, Microplastic pollution,*

1. INTRODUCTION

Plastic is a general term that refers to a family of organic polymers derived from petroleum sources (polyvinylchloride (PVC), nylon, polyethylene (PE), polystyrene (PS), and polypropylene (PP)) (Vert et al., 2012). Plastic materials are widely used as they are light, resistant, durable and cost effective (Hammer et al., 2012; Ivleva et al., 2017).

Therefore, pollution from microplastic waste in the world has raised global concerns.The first synthetic plastic, Bakelite, was produced in 1907. However, global plastic production did not grow rapidly until the 1950s. The annual global production of plastic product in 2016 alone was around 322 million tonnes (Europe, 2016).This is roughly equivalent to the mass of two-thirds of the world population.

However, plastic debris has raised global concerns over its wide distribution and associated environmental consequences.

To understand the entry of plastics into the natural environment and aquatic ecosystems in the world, we must understand the various elements of the production, distribution and waste management chain. This is very important to us not only in understanding the magnitude of the problem, but also in applying the most effective interventions to reduce the problem.

Microplastics (MP) are commonly described as synthetic polymers and <5 mm in size (Thompson et al., 2009). They can be categorized as primary microplastics and secondary microplastics. Due to the plastic's resistance to disintegration and its permanence in the aquatic environment the microplastics, that observed for the first time in the 1970s, have regularly accumulated. So that microplastics have became a pollutant found in all aquatic environments of the world (Sivan, 2011;Barnes ve diğerleri, 2009;).

Primary microplastics are plastics with a size smaller than 5 mm and often found in textiles, pharmaceuticals and personal care products (Cole et al., 2011; Browne, 2015). These primary microplastics are transported to marine and freshwater environments by discharge from wastewater treatment plants, rivers, drainage systems, runoff from agricultural land, erosion by wind and currents (Gall and Thompson, 2015; Zalasiewicz et al 2016; Murphy et al 2016).

Secondary microplastics are obtained by disintegrating large plastic wastes by processes such as photo-disintegration, physical, chemical and biological interactions (Galgani et al 2013). Sources of secondary microplastics include fishing nets, industrial resin pellets, household items and other disposed plastic waste (Eerkes-Medrano et al., 2015).

Microplastics have two main sources, land and oceans (Hammer et al., 2012). Ocean-based resources are total plastic waste from the marine environment due to commercial fishing, ships and other marine activities (Andrady, 2011). And ocean-based microplastic wastes account for only 20% of pollution. Microplastics from terrestrial sources contribute to the remaining 80%. Terrestrial resources include personal products, improperly placed plastics, and substances from leaks in landfills (Cole et al., 2011; Gallo et al 2018). When terrestrial microplastics are released into natural water systems, most will be transported to oceans by rivers, while others will remain in freshwater environments, including isolated water systems such as lakes (Browne et al., 2010; Free; et al., 2014). Rivers, that provide an important conduit for microplastics between inland terrestrial inputs and marine environments, are depositional sites as well as major transport pathways for microplastics and macroplastics (Lechner et al., 2014; Rech et al., 2014; Zhao et al., 2014; Corcoran et al., 2015).

The global presence of microplastics has been recognized in recent years and has raised concerns about its presence and durability in aquatic environments. From horizontal perspective, microplastics were reportedly found in tropical areas (Ng and Obbard, 2006; Nor and Obbard, 2014); they were even seen in the polar waters of Antarctica and Arctic (Barnes et al., 2010; Bergmann et al., 2015). When one looks at vertical distribution, microplastics exist in benthic zone of water bodies, water columns, surface waters and beaches.

Most of efforts on the microplastics research, we significant amount of information was obtained on this pollutant in marine environments. Although rivers and terrestrial environments are known to be the major source of marine microplastics, less than 4% of studies on microplastics are reported to be associated with lakes and rivers (Dris et al2015; Chen et al 2017; Lambert and Wagner, 2018).

Freshwater ecosystems, such as lakes and reservoirs, may serve as sinks for microplastic pollutants, given the long detention time of pollutants in these environments. The aim of this review paper is to reveal the current knowledge about microplastics in lake waters for a better understanding of microplastics contamination and potential risks.

2. ENVİRONMENTAL FATE AND BEHAVİOUR

Plastics consist of different polymers that can be buoyant or sink, depending upon composition, density, and shape of the plastic. Materials whose specific density is less than that of water may be buoyant, or whose a specific density greater than that of water may be sink. The PP and PE are typically low-density plastics that are expected to be relatively buoyant, while PVC, PS, polyester, and polyamide are considered high-density plastics that are more likely to sink (Anderson et al 2016).

The plastics with a density less than water accumulate at the sediment, while plastics with a density greater than water buoyant on the water surface can be detected.

Plastics may be subjected to various degradations: biological, photo, thermal, mechanical, thermal oxidative and hydrolysis (Browne et al., 2007, Andrady, 2011) and as a result of degradation, it may be micro or potentially nano-sized (dimensions in nanometers) (Galgani et al. 2010, Cole et al., 2011).

The decomposition of plastic waste into smaller pieces allows more widespread distribution. The smaller the size, the higher the surface area and the more adsorption of pollutants. The high molecular weight of plastics made of synthetic polymers makes them resistant to biodegradation (Ballent 2016).

It is estimated that the time required for the complete mineralization of plastics is between hundreds and thousands of years (Barnes et al., 2009). Some types of plastics (eg cellophane) are biodegradable in the environment (Byrdson, 1999), but they are not the most commonly used plastics today (Ballent 2016).

3. ENVIRONMENTAL IMPACTS

Microplastic pollution is a serious hazard due to its negative effects on ecosystems and organisms. Many studies to date have shown that plastic particles are taken up by aquatic organisms and transferred to the food chain (Wagner et al 2014; Wright et al 2013)

Microplastics are made of polymeric compounds that can cause some health effects. For example, polystyrene (PS), which is resistant to biological degradation, accumulates in the fish stomach (Carpenter et al., 1972) and can be displaced through the bloodstream (Chen et al., 2006).Various additives are added to improve the physical properties such as durability and hardness during the production of plastics. Some of these chemicals are known as endocrine disrupting compounds and are expected to accumulate in the human body through bioaccumulation. Some studies have confirmed the presence of additives such as bisphenol A, polybrominated diphenyl ethers, tetrabromobisphenol A and phthalates in humans (Talsness et al., 2009).

In addition, some heavy metal-containing compounds such as chromium, cadmium and lead are often used in the manufacture of colorants, stabilizers and plasticizers (Murphy et al 2016)

4.MICROPLASTICS IN LAKE SYSTEMS

It is important to collect data on the microplastic contents of rivers and lakes, which constitute the main source of microplastics in the marin ecosystem (Anderson et al 2016).

To date, studies in lake waters revealed that microplastic particles were not evenly distributed in lake sediments and that concentrations vary greatly between studies. Imhof et al. (2013) argues that this distribution is mainly a result of wind, lake morphology and dominant currents. Because the lake basins are stable, they provide a semi-closed system with variable hydrographic conditions. In freshwater lakes, the mixture is modeled differently than in oceans and coastal areas. These models depend on the size, depth of the lake and prevailing wind systems. (Eriksen et al., 2013; Imhof et al., 2013; Zbyszewski and Corcoran, 2011). In addition, geographic location (latitude and hence climate) will cause seasonal lake temperature-density stratification and affect the inter-layer mixture (Boehrer and Schultze, 2008).

Some researchers have investigated the vertical velocity, wind force, breaking waves of microplastics within the water column, depending on the density, size and shape of the polymer. They found that after storms and strong winds, the concentration of microplastics in the surface layer was reduced and the mixture occurred in the vertical direction (Ballent et al., 2012; Brunner et al., 2015; Enders et al., 2015;, Kukulka et al., 2012, 2016; Kukulka and Brunner, 2015; Reisser et al., 2015).

As a central aspect of vertical plastic distribution within the water column, the buoyancy of plastic particles with varying densities in freshwater (with a mean density of 1.00 g/cm 3) has also be taken into account. Compared to marine ecosystems with a mean density of 1.02 g/cm 3 , the proportion of floating versus sinking polymer particles within freshwater lakes is significantly smaller (Fischer.et al 2016).

Various studies have been reported on microplastic contamination of aquatic systems in Europe, North and South America and Asia on lake shore, lake bottom and river bank sediment samples. In the study of Garda Lake lakeshore sediments (Italy), were reported that the northern shore contained 1.108 ± 983 microplastic particles.m^{-2}, whereas only 108 ± 55 microplastic particles.m^{-2} were observed on the southern shore (Imhof et al. 2013). Spatial distribution of microplastics, dominant wind, lake morphology and strong currents indicate that responsible. In another study, microplastic contamination of sediments along the lake shore along Lake Geneva (Switzerland) was evaluated (Faure et al., 2012). The dominant polymer was PS. The reported amounts are, for example, 48,146 particles / km2 surface water in Lake Geneva (Faure et al. 2012) and 43,159 particles / km2 in Laurentian Great Lakes (Eriksen et al. 2013b). Microplastics in a remote lake in Mongolia have also been reported to have an average density of 20,264 particles / km² (Free et al. 2014).

Quantities, proximity to densely populated areas, wind and water circulation have been shown to be affected. Measurements in Swedish lakes (Kärrman et al. 2016; Landbecker 2012) show similar particle counts compared to seawater

Investigation of microplastic debris in lakeside sediments were investigated in the Great Lake Huron Lake (Zbyszewski and Corcoran, 2011), in the Lake Geneva in Switzerland (Faure et al. 2012), in the Lake Garda in Italy (Imhof et al., 2013), in the Great Lakes Lake Erie and Saint Clair (Zbyszewski et al., 2014), in the Great Lakes Lake Michigan (Hoellein et al., 2014; Hoellein et al., 2015) and in the Lake Great Lakes in Ontario. (Corcoran) et al., 2015).

Free et al. (2014), in their microplastic study in Hovsgol Lake in Mongolia, pointed out a very high microplastic load (average 20,264 particles km^{-1}) due to the long retention time calculated between 500 and 600 years. However, the retention time varies between lakes. For example, the Laurentian Great Lakes are considered to be a potential source of microplastics for the North Atlantic Ocean (Eriksen et al., 2013) and this has been linked to lower residence times: Lake Erie (2 years), Lake Michigan (38) years, and Lake Ontario (20 years)(Quinn 1992). Dynamic environments (eg streams, rivers and estuaries) have a lower residence time than stagnant water

environments (Soballe and Kimmel, 1987), so their role as microplastic pollutant sources needs to be considered.

5. MICROPLASTICS IDENTIFICATION AND QUANTIFICATION

Although there have been studies on microplastics, a complete sampling method, pretreatment method, quantification and identification standard has not been established yet. Findings from the reported studies are highly variable and cannot be easily compared.

In the first stage, visual sorting is performed in microplastic water samples. This sorting is commonly used to select suspicious microplastics (Rochman, 2015; Qiu et al., 2016). However, the presence of particles such as clay and algae in water in the visual sorting technique may not provide precise information about microplastics. Additional approaches such as spectroscopic approaches are required. They can be used as a more reliable technical tool for the identification of plastic particles, rather than relying on visual observations that will make large differences in results.

Quantitative and qualitative research of microplastics; Raman spectroscopy (Imhof et al., 2016; Qiu et al., 2016; Zhao et al., 2017); liquid chromatography (Hintersteiner et al., 2015; Elert et al., 2017); pyrolysis gas chromatography coupled to mass spectrometry (Nuelle et al., 2014); Fourier-transform infrared (FT-IR) spectroscopy (Besseling et al., 2015; Qiu et al., 2016); and the most recently reported labeling method (Shim et al., 2016).

6. FATE AND TRANSPORT MODELS OF MICROPLASTICS IN FRESHWATER SYSTEMS

Four main model types of microplastics in fresh water modeling are discussed. These are emission based mass balance modeling, global modeling, multimedia modeling and spatial modeling. Models are vary according to their purpose, scale, level of detail and verification status.

Emission-based mass flow / mass balance models have been used for chemicals . These models have recently been applied to nanoparticles as well (Gottschalk et al 2013; Gottschalk et al 2009; Keller et al 2014). The emission of microplastic particles can also be modeled in air, soil, water and sediment sections assuming that they behave like nanoparticles [45]. In the model, it is assumed that the particle mixes homogeneously in the environment [45, 98]. Similar mass flow model applications that calculate the environmental concentration of plastic waste in all environments (air, soil, water and sediment) have not yet been published. The essence of this approach, however, has been used to estimate the concentrations of microplastics from cosmetics in wastewater treatment plants effluents (Gouin et al 2015) in the Netherlands and mass emissions of microplastics from cosmetics from Europe to the North Sea (Van et al 2015).

River pollution is a worldwide problem and canal for transporting microplastics from land to oceans. There are many global river pollution models. One is the Global NEWS model (Mayorga et al 2010; Seitzinger et al 2010). Global NEWS is a model that calculates the transfer of nutrients in the river from land to sea as a function of human activity. Global NEWS includes more than 6,000 river basins using hydrology in the water balance model (Fekete et al 2010). It has been used to simulate river pollution trends for the 1970-2050 period, taking into account changes in land use, food production, urbanization and hydrology (Fekete et al 2010; Van et al 2009). The results show that over time, most rivers around the world are more polluted. Transport patterns of pollutants in rivers such as Global NEWS have been under development for more than 20 years. With this model, plastic debris can also be considered as pollutants and simulation can be made about transport.

Multimedia models are used for chemicals. Calculates the transport paths between the environmental compartmants to be modeled and creates a mass balance equation for each partition. The flow is calculated according to the first order kinetic parameters and concentration. Model equations are generally solved by simple matrix algebra under steady state conditions. To date, the most widely used multimedia models for nanoparticle particles are MendNano (Liu and Cohen 2014)and SimpleBox4Nano (SB4N) (Meesters et al 2014; Meesters et al 2016). These models calculate their concentration under steady state conditions in the atmosphere, surface waters, soil and sediment. First microplastic application was made by using SB4N model. SB4N models the partitioning between dissolved and particulate forms of the chemical as nonequilibrium colloidal behavior (Meesters et al 2013).

To date, two models have been presented that can simulate the spatial and temporal transport of plastic debris in freshwater systems (Besseling et al 2014; Nizzetto et al 2016). Both models were limited by the authors as theoretical models, ie they were expected to be valid according to design criteria and to be in harmony with the existing theory. However, it has not yet been validated against the measured data for plastic debris.
Besseling et al. [Besseling et al 2014; Besseling et al 2017) is the first model to simulate the fate of macroplastic particles in a river (Koelmans et al 2015). The model is based on the NanoDUFLOW hydrological model (Klein et al 2016; Quik et al 2016) and includes advective transport of particles, their homo and heterogeneous aggregations, biofouling, sedimentation / resuspension, disintegration of plastic, and sedimentation. (UK) Nizzetto et al. They used a spatial dispersion model applied to the Thames River basin (Nizzetto et al 2016). The study is theoretically limited to data on microplastic emissions and concentrations. This model is based on an existing hydro-geochemical multimedia model, INCAcontaminants (Nizzetto et al 2016), a sediment transport module (Lazar 2010), a precipitation flow module (Futter et al 2014), and the possibility to add direct wastewater effluent from WWTPs, for example. It is a model that assumes homogeneous precipitation and temperature distribution.

DUFLOW and INCA-Plastic models design criteria and working purposes are compared; The NanoDUFLOW model is particularly useful in modeling sub-micron particles as it involves the aggregation process (Praetorius

et al 2012; Quik et al 2012). Besseling et al. (Besseling et al 2014; Besseling et al 2017) have also considered biological contamination that affects the deposition behavior of plastic particles. However, Besseling et al. they did not provide long-term simulations explaining the effects of weather conditions. In principle, however, DUFLOW considers pollutants from spot and dispersed sources such as wastewater treatment plants, river tributaries (Klein et al 2016).

Both models agree on the significant effect of particle size on retention and on high retention for particles> 0.2 mm. However, the INCA-Plastic model accepts that smaller particles will be retained less in the river and thus exported to the sea. In the NanoDUFLOW model, it is recognized that there is an increased retention for particles smaller than 5 um. The results of both studies depend on the variability of the modeled scenario and parameters. In addition, laboratory experiments have shown that processes such as biofouling and aggregation (Lagarde et al 2016; Fazey and Ryan 2016; Long et al 2015) and particle properties such as density, size and shape (Isachenko 2016; Kowalski et al 2016) significantly affect particle fate.

7. CONCLUSIONS

The recognition of microplastics, a current and global pollutant around the world, and the recognition of their serious negative impact on environmental pollution have recently occurred. We still do not have detailed information about the determination and risk assessment of this pollutant whose presence is very old. It has been shown that lakes, have been adversely affected by microplastics with limited studies conducted to date. The existence of many parameters affecting the water quality of these non-flowing systems creates confusion in predicting the behavior of microplastics. In this review, we provide a brief overview of MP, sources, determination methods, entry and behavior into lake water systems, transport modeling.

Studies in the literature have shown that there is no standard method for the determination of microplastics in lakes and fresh water resources. Combining or rearranging the different techniques would be good to avoid future problems.

It is difficult to quantify and characterize microplastics from complex environmental samples using a single analytical method. Therefore, the combination of multiple methods depending on the size of the microplastics is preferred. In addition to these methods, emerging microplastic modeling can be used to make predictions.

Contamination of the fresh water environment with plastic waste of all sizes has received increasing attention. In this review, it has been found that plastic pollutants and their sources can be used to make an appropriate risk assessment and to make predictions given the lack of data. Through the literature research, we found that it was difficult to use a single method for quantitation and quantification of microplastics from freshwater samples. The combination of different techniques can greatly improve our understanding of this new environmental problem and more reliable data for environmental risk assessment and preparation/enforcement of rules and regulations in the future.

Especially lake sediments (shorelines, lake bottom), as well as inputs and exports via receiving streams and effluents and airborne inputs, should be included in further analyses to enable the calculation of catchment based budgets of plastic contamination.

REFERENCES

Anderson J. C., Bradley J. Park, Vince P. (2016). “Palace, Microplastics in aquatic environments: Implications for Canadian ecosystems”, Environmental Pollution, Volume 218, ,pp 269-280,

Andrady A.L. (2011)”Microplastics in the marine environment” Mar. Pollut. Bull., 62 , pp. 1596-1605

Ballent, A. M., (2016). "Anthropogenic particles in natural sediment sinks: Microplastics accumulation in tributary, beach and lake bottom sediments of Lake Ontario, North America" Electronic Thesis and Dissertation Repository. 3941.

Ballent, A., Purser, A., de Jesus Mendes, P., Pando, S., Thomsen, L., (2012). “Physical transport properties of marine microplastic pollution”. Biogeosci. Discuss. 9, 18755-18798

Barnes, D.K.A., Galgani, F., Thompson, R.C., Barlaz, M., (2009). “Accumulation and fragmentation of plastic debris in global environments”. Philos. Trans. R. Soc. Lond B: Biol. Sci. 364, 1985–1998.

Besseling E, Quik JTK, Koelmans AA (2014) “Modeling the fate of nano- and microplastics in freshwater systems. SETAC Annual Meeting”, Basel, Switzerland.

Besseling E, Quik JTK, Sun M, Koelmans AA (2017)” Fate of nano- and microplastic in freshwater systems: a modeling study”. Environ Pollut 220:540–548

Besseling, E., Foekema, E., Van Franeker, J., Leopold, M.F., Kühn, S., Rebolledo, E.B., Heße, E., Mielke, L., IJzer, J., Kamminga, P., (2015). “Microplastic in a macro filter feeder: humpback whale Megaptera novaeangliae”. Mar. Pollut. Bull. 95 (1), 248-252.

Boehrer, B., Schultze, M., (2008). “Stratification of lakes. Rev”. Geophys. 46.

Browne M.A. , T. Galloway, R. Thompson (2007)”Microplastic - an emerging contaminant of potential concern”, Integr. Environ. Assess. Manage., 3 , pp. 559-566

Browne, M.A., Galloway, T.S., Thompson, R.C., (2010).” Spatial patterns of plastic debris along Estuarine shorelines”. Environ. Sci. Technol. 44 (9), 3404-3409.

Browne, M.A.,(2015). In: Bergmann, M., Gutow, L., Klages, M. (Eds.), *Marine Anthropogenic Litter*. Springer International Publishing, Cham, pp. 229-244.

Brunner, K., Kukulka, T., Proskurowski, G., Law, K.L., (2015). “Passive buoyant tracers in the ocean surface boundary layer: II, Observations Simul. Microplastic Mar. Debris”. J. Geophys. Res. Oceans 120, 7559-7573

Carpenter, E.J., Anderson, S.J., Harvey, G.R., Miklas, H.P., Peck, B.B., (1972). “Polystyrene spherules in coastal waters”. Science 178 (4062), 749-750.

Chen, J., Tan, M., Nemmar, A., Song, W., Dong, M., Zhang, G., Li, Y.,(2006). “Quantification of extrapulmonary translocation of intratracheal-instilled

particles in vivo in rats: effect of lipopolysaccharide". Toxicology 222 (3), 195-201.

Chen, Q., Gundlach, M., Yang, S., Jiang, J., Velki, M., Yin, D., Hollert, H., (2017). "Quantitative investigation of the mechanisms of microplastics and nanoplastics toward zebrafish larvae locomotor activity". Sci. Total Environ. 584, 1022–1031

Cole, M., Lindeque, P., Halsband, C., Galloway, T.S., (2011). "Microplastics as contaminants in the marine environment: a review". Mar. Pollut. Bull. 62 (12), 2588-2597.

Corcoran, P. L., Norris, T., Ceccanese, T., Walzak, M. J., Helm, P. A., & Marvin, C. H. (2015). "Hidden plastics of Lake Ontario, Canada and their potential preservation in the sediment record". Environmental Pollution, 204, 17–25.

Corcoran, P.L., Norris, T., Ceccanese, T., Walzak, M.J., Helm, P.A., and Marvin, C.H. (2015). "Hidden plastics of Lake Ontario, Canada and their potential preservation in the sediment record". Environ. Pollut. 204, 17–25

Derraik, J.G.B., (2002). "The pollution of the marine environment by plastic debris: a review". Mar. Pollut. Bull. 44 (9), 842-852

Dris, R., Imhof, H., Sanchez, W., Gasperi, J., Galgani, F., Tassin, B., and Laforsch, C. (2015). "Beyond the ocean: Contamination of freshwater ecosystems with (micro-) plastic particles". Environ. Chem. 12, 539-550

Eerkes-Medrano, D., Thompson, R.C., Aldridge, D.C., (2015). "Microplastics in fresh- water systems: a review of the emerging threats, identification of knowledge gaps and prioritisation of research needs". Water Res. 75, 63-82

Elert, A.M., Becker, R., Duemichen, E., Eisentraut, P., Falkenhagen, J., Sturm, H., Braun, U., (2017). "Comparison of different methods for MP detection: what can we learn from them, and why asking the right question before measurements matters" Environ. Pollut. 231, 1256-1264.

Enders, K., Lenz, R., Stedmon, C.A., Nielsen, T.G., (2015). "Abundance, size and polymer composition of marine microplastics 10 m in the Atlantic Ocean and their modelled vertical distribution". Mar. Pollut. Bull. 100, 70-81

Eriksen, M., Mason, S., Wilson, S., Box, C., Zellers, A., Edwards, W., Farley, H., Amato, S.,(2013). "Microplastic pollution in the surface waters of the Laurentian Great Lakes". Mar. Pollut. Bull. 77, 177-182.

Europe, P., (2016). Plasticsdthe Facts 2016 an Analysis of European Plastics Production, Demand and Waste Data. Association of Plastic Manufacturers, Brussels.

F. Galgani, D. Fleet, J. VanFraneker, S.Katsanevakis, T. Maes, J. Mouat, L.Oosterbaan, I. Pitou, G. Hanke, R.T hompson, E. Amata, A. Birkun, C. Janss n(2010) *Marine Strategy Framework Directive: Task Group 10 Report*, Marine Litter European Commission Joint Research Centre Scientific and Technical Report. 57 pp

Faure, F., Corbaz, M., Baecher, H., de Alencastro, L., (2012). "Pollution due to plastics and microplastics in Lake Geneva and in the Mediterranean Sea". Arch. Sci. 65, 157-164.

Fekete BM, Wisser D, Kroeze C et al (2010) "Millennium ecosystem assessment scenario drivers (1970–2050): climate and hydrological alterations". Global Biogeochem Cycles 24(4).

Fischer E. K., Paglialonga L., Czech E., Tamminga M., (2016), "Microplastic pollution in lakes and lake shoreline sediments – A case study on Lake Bolsena and Lake Chiusi (central Italy)", Environmental Pollution, V 213, Pp 648-657

Free, C.M., Jensen, O.P., Mason, S.A., Eriksen, M., Williamson, N.J., Boldgiv, B., (2014). "High-levels of microplastic pollution in a large, remote, mountain lake". Mar. Pollut. Bull. 85 (1), 156-163.

Futter MN, Erlandsson MA, Butterfield D et al (2014) "PERSiST: a flexible rainfall-runoff modelling toolkit for use with the INCA family of models". Hydrol Earth Syst Sci 18:855–873

Galgani, F., Hanke, G., Werner, S., De Vrees, L., (2013). "Marine litter within the European marine strategy framework directive." ICES J. Mar. Sci. 70

Gall, S.C., Thompson, R.C., (2015). "The impact of debris on marine life". Mar. Pollut. Bull. 92 (1e2), 170-179.

Gallo F., Fossi C., Weber R., Santillo D., Sousa J., Ingram I., Nadal A., Romano D. (2018) "Marine litter plastics and microplastics and their toxic chemicals components: the need for urgent preventive measures" Environ Sci Eur. ; 30(1): 13.

Gottschalk F, Sonderer T, Scholz RW, Nowack B (2009) "Modeled environmental concentrations of engineered nanomaterials (TiO2, ZnO, Ag, CNT, fullerenes) for different regions". Environ Sci Technol 43:9216–9222

Gottschalk F, Sun T, Nowack B (2013) "Environmental concentrations of engineered nanomaterials: review of modeling and analytical studies". Environ Pollut 181:287–300

Gouin T, Avalos J, Brunning I (2015)" Use of micro-plastic beads in cosmetic products in Europe and their estimated emissions to the North Sea environment". SOFW-J 141:40–46

Hammer, J., Kraak, M.H.S., Parsons, J.R., (2012). In: Whitacre, D.M. (Ed.), *Reviews of Environmental Contamination and Toxicology*. Springer New York, New York, NY, pp. 1-44.

Hammer, J., Kraak, M.H.S., Parsons, J.R.,(2012). In: Whitacre, D.M. (Ed.), *Reviews of Environmental Contamination and Toxicology*. Springer New York, New York, NY, pp. 1-44.

Hintersteiner, I., Himmelsbach, M., Buchberger, W.W., (2015). "Characterization and quantitation of polyolefin microplastics in personal-care products using high- temperature gel-permeation chromatography". Anal. Bioanal. Chem. 407 (4), 1253-1259

Imhof, H.K., Ivleva, N.P., Schmid, J., Niessner, R., Laforsch, C., (2013). "Contamination of beach sediments of a subalpine lake with microplastic particles". Curr. Biol. 23, R867-R868.

Ivleva, N.P., Wiesheu, A.C., Niessner, R., (2017). "Microplastic in aquatic ecosystems". Angew. Chem. Int. Ed. 56 (7), 1720-1739.

Kärrman A, Vigren D, Karlsson C, van Bavel B. (2016). "Pilot study on the occurence and disposition of microplastics in lake Vättern. Report to Vätternvårdsförbundet". In preparation.

Keller AA, Vosti W, Wang H, Lazareva A (2014) "Release of engineered nanomaterials from personal care products throughout their life cycle." J Nanopart Res 16:1–10

Klein JJM, Quik JTK, Ba¨uerlein PS, Koelmans AA (2016) "Towards validation of the NanoDUFLOW nanoparticle fate model for the river Dommel, The Netherlands". Environ Sci Nano 3:434–441

Koelmans AA, Besseling E, Shim WJ (2015)" *Nanoplastics in the aquatic environment. Critical review. In: Marine anthropogenic litter*". Springer, Berlin, pp 325–340

Kukulka, T., Law, K.L., Proskurowski, G., (2016). "Evidence for the influence of surface heat fluxes on turbulent mixing of microplastic marine debris". J. Phys. Oceanogr. 46 (3)

Kukulka, T., Proskurowski, G., Moret-Ferguson, S., Meyer, D.W., Law, K.L., (2012). "The effect of wind mixing on the vertical distribution of buoyant plastic debris: wind effects on plastic marine debris". Geophys. Res. Lett. 39

Kowalski N, Reichardt AM, Waniek JJ (2016) "Sinking rates of microplastics and potential implications of their alteration by physical, biological, and chemical factors". Mar Pollut Bull 109(1):310–319

Lambert, S., Wagner, M., (2018). *Freshwater Microplastics*. Springer, pp. 1-23.

Landbecker D. (2012). Anthropogenic particles in lake mälaren. Bachelor thesis. Uppsala University

Lazar AN, Butterfield D, Futter MN et al (2010) "An assessment of the fine sediment dynamics in an upland river system: INCA-Sed modifications and implications for fisheries". Sci Total Environ 408:2555–2566

Lechner, A., Keckeis, H., Lumesberger-Loisl, F., Zens, B., Krusch, R., Tritthart, M., Glas, M., Schludermann, E. (2014). "The Danube so colourful: A potpourri of plastic litter outnumbers fish larvae in Europe's second largest river". Environmental Pollution, 188, 177–181.

Liu HH, Cohen Y (2014) "Multimedia environmental distribution of engineered nanomaterials". Environ Sci Technol 48:3281–3292

Long M, Moriceau B, Gallinari M et al (2015) "Interactions between microplastics and phytoplankton aggregates: impact on their respective fates". Mar Chem 175:39–46.

Mayorga E, Seitzinger SP, Harrison JA (2010) "Global nutrient export from WaterSheds 2 (NEWS 2): model development and implementation". Environ Model Softw 25:837–853

Meesters JAJ, Koelmans AA, Quik JTK et al (2014)" Multimedia modeling of engineered nanoparticles with simpleBox4nano: model definition and evaluation". Environ Sci Technol 48:5726–5736. doi:10.1021/es500548h

Meesters JAJ, Quik JTK, Koelmans AA et al (2016) "Multimedia environmental fate and speciation of engineered nanoparticles: a probabilistic modeling approach". Environ Sci Nano 3:715–727

Meesters JAJ, Veltman K, Hendriks AJ, van de Meent D (2013) "Environmental exposure assessment of engineered nanoparticles: why REACH needs adjustment". Integr Environ Assess Manag 9:e15–e26

Murphy F., C. Ewins, F. Carbonnier, B. Quinn, (2016) "Wastewater treatment Works (WwTW) as a source of microplastics in the aquatic environment", Environ. Sci. Technol. 50 5800-5808.

Murphy, F., Ewins, C., Carbonnier, F., Quinn, B., (2016). Wastewater treatment Works (WwTW) as a source of microplastics in the aquatic environment. Environ. Sci. Technol. 50 (11), 5800-5808.

Nizzetto L, Bussi G, Futter MN et al (2016)" A theoretical assessment of microplastic transport in river catchments and their retention by soils and river sediments". Environ Sci Process Impacts 18:1050–1059

Nizzetto L, Butterfield D, Futter M et al (2016) "Assessment of contaminant fate in catchments using a novel integrated hydrobiogeochemical-multimedia fate model". Sci Total Environ 544:553–563

Nuelle, M.T., Dekiff, J.H., Remy, D., Fries, E., (2014). "A new analytical approach for monitoring microplastics in marine sediments". Environ. Pollut. 184, 161-169.

Olivier F, O, Zanella M et al (2016) "Microplastic interactions with freshwater microalgae: hetero-aggregation and changes in plastic density appear strongly dependent on polymer type". Environ Pollut 215:331–339

Praetorius A, Scheringer M, Hungerbühler K (2012) "Development of environmental fate models for engineered nanoparticles- a case study of TiO2 nanoparticles in the Rhine river". Environ Sci Technol 46:6705–6713

Qiu, Q., Tan, Z., Wang, J., Peng, J., Li, M., Zhan, Z., (2016). "Extraction, enumeration and identification methods for monitoring microplastics in the environment". Estuar. Coast Shelf Sci. 176, 102-109.

Quik JTK, de Klein JJM, Koelmans AA (2015)" Spatially explicit fate modelling of nanomaterials in natural waters". Water Res 80:200–208

Quinn, F.H., (1992). "Hydraulic residence times for the Laurentian Great Lakes". J. Great Lakes Res. 18, 22–28.

Rech, S., Macaya-Caquilpán, V., Pantoja, J. F., Rivadeneira, M. M., Jofre Madariaga, D., and Thiel, M. (2014). "Rivers as a source of marine litter--a study from the SE Pacific". Marine Pollution Bulletin, 82(1-2), 66–75.

Reisser, J., Slat, B., Noble, K., du Plessis, K., Epp, M., Proietti, M., de Sonneville, J., Becker, T., Pattiaratchi, C., (2015). "The vertical distribution of buoyant plastics at sea: an observational study in the North Atlantic Gyre". Biogeosciences 12, 1249-1256

Rochman, C.M., Kross, S.M., Armstrong, J.B., Bogan, M.T., Darling, E.S., Green, S.J., Smyth, A.R., Veríssimo, D.,(2015). *Scientific Evidence Supports a Ban on Microbeads*. ACS Publications.

Seitzinger SP, Mayorga E, Bouwman AF et al (2010) "Global river nutrient export: a scenario analysis of past and future trends". Global Biogeochem Cycles 24:GB0A08

Shim, W.J., Song, Y.K., Hong, S.H., Jang, M., (2016). "Identification and quantification of microplastics using Nile Red staining". Mar. Pollut. Bull. 113 (1-2), 469-476.

Sivan, A., (2011). "New perspectives in plastic biodegradation". Curr. Opin. Biotechnol.22, 422–426.

Soballe, D.M., Kimmel, B.L, (1987)." A large-scale comparison of factors influencing phyto- plankton abundance in rivers, lakes, and impoundments". Ecol. 68, 1943–1954.

Talsness, C.E., Andrade, A.J., Kuriyama, S.N., Taylor, J.A., vom Saal, F.S., (2009). Components of plastic: experimental studies in animals and relevance for

human health. Philos. Trans. R. Soc. Lond. B Biol. Sci. 364 (1526), 2079-2096.

Thompson, R.C., Moore, C.J., vom Saal, F.S., Swan, S.H., (2009). "Plastics, the environment and human health: current consensus and future trends". Philos. Trans. R.Soc. Lond. B Biol. Sci. 364 (1526), 2153-2166.

Van Drecht G, Bouwman AF, Harrison J, Knoop JM (2009) "Global nitrogen and phosphate in urban wastewater for the period 1970 to 2050". Global Biogeochem Cycles 23(4).

Van Wezel A, Caris I, Kools S (2015) "Release of primary microplastics from consumer products to wastewater in The Netherlands". Environ Toxicol Chem 35:1627–1631

Vert, M. Doi, Y. Hellwich K.-H. , Hess M. , Hodge P., Kubisa P. , Rinaudo M. , Schue F. (2012), "Terminology for biorelated polymers and applications *(IUPAC Recommendations 2012)"* Pure Appl. Chem., 84 pp. 377-410

Wagner, M., Scherer, C., Alvarez-Mu ~ noz, D., Brennholt, N., Bourrain, X., Buchinger, S., Fries, E., Grosbois, C., Klasmeier, J., Marti, T., (2014). "Microplastics in freshwater ecosystems: what we know and what we need to know". Environ. Sci. Eur. 26 (12)

Wright, S.L., Thompson, R.C., Galloway, T.S.,(2013). " The physical impacts of micro- plastics on marine organisms: a review". Environ. Pollut. 178, 483-492

Zalasiewicz J., C.N. Waters, J.A. Ivar do Sul, P.L. Corcoran, A.D. Barnosky, A. Cearreta, M. Edgeworth, A. Gałuszka, C. Jeandel, R. Leinfelder, J.R. McNeill,W. Steffen, C. Summerhayes, M. Wagreich, M. Williams, A.P. Wolfe, Y. Yonan, (2016)

Zbyszewski, M., Corcoran, P.L., and Hockin, A. (2014). "Comparison of the distribution and degradation of plastic debris along shorelines of the Great Lakes, North America". J. Gt. Lakes Res. 40, 288–299.

Zbyszewski, M., Corcoran, P.L.,(2011). "Distribution and degradation of fresh water plastic particles along the beaches of Lake Huron, Canada". Water, Air, & Soil Pollut. 220, 365-372.

Zhao, S., Danley, M., Ward, J.E., Li, D., Mincer, T.J., (2017). "An approach for extraction, characterization and quantitation of microplastic in natural marine snow using Raman microscopy". Anal. Methods 9 (9), 1470-1478

Zhao, S., Zhu, L., Wang, T., & Li, D. (2014). "Suspended microplastics in the surface water of the Yangtze Estuary System, China: First observations on occurrence, distribution". Marine Pollution Bulletin, 0–6

CISET - 2nd Cilicia International Symposium on Engineering and Technology
10-12 October, 2019, Mersin / TURKEY

CLASSIFICATION OF VEHICLE MODELS USİNG DEEP CONVOLUTIONAL NEURAL NETWORK AND TRANSFER LEARNING METHODS

Begüm Kılıç*[1], Ali Akdağlı [2] , Çiğdem ACI [3]

[1] Mersin University, Engineering Faculty, Electrical and Electronics Engineering Department, Mersin, Turkey, kilicbgm@gmail.com

[2] Mersin University, Engineering Faculty, Electrical and Electronics Engineering Department, Mersin, Turkey, akdagli@mersin.edu.tr

[3] Mersin University, Engineering Faculty, Electrical and Electronics Engineering Department, Mersin, Turkey, caci@mersin.edu.tr

ABSTRACT
Machine learning applications are obtained from a specific dataset and analyzed. The performance of the method used greatly influences from extracted features. Feature extraction is a matter that requires expertise. Algorithms are needed to automatically extract feature and classification from applications with large amounts of data. Deep learning methods, which perform these two processes together and automatically, should be utilized. However, since deep learning algorithms require large amounts of data and time, transfer learning is proposed. Transfer learning is the transfer of deep learning method that provides high performance to the solution of the designer's problem. In this process, all parameters of the selected deep learning model are assigend as the initial parameter in the designer's problem. Afterwards, training and test procedures are carried out. In this study, 169 different vehicle models obtained using mobese camera were determined by transfer learning method. The proposed models for transfer learning are AlexNet, GoogleNet and ResNet-50. Softmax and Support Vector Machine are used as classifier in these models. The results obtained are presented as a comparative analysis.

Keywords: *Deep Learning, Transfer Learning, Vehicle Classification, Recognition of Vehicle Models, Convolutional Neural Networks, Softmax, Support Vector Machine*

* Begüm KILIÇ

1. INTRODUCTION

Automated car model analysis, particularly well classified automobile categorization and verification can be used for numerous purposes, including regulation, identification and indexing in the intelligent transport system. For example, depending on different rates for different vehicle types, car categorization can be used to cheaply automate and speed up toll booths. It helps track a car over multiple camera networks when the car verification or license plate recognition from view fails in video surveillance applications. Car model analysis also has a significant value in personal car choice. Other applications, such as estimating the popularity of a car based on its appearance and recommending cars of similar styles, might be useful for both manufacturers and consumers.

Within the scope of machine learning, certain features are obtained from the existing data and these features are analyzed with learning algorithms. The success of the algorithms realized depends on the quality of the data obtained. Due to the fact that feature determination requires expertise and high the number of tool images used in this study, deep learning algorithms were used for feature determination and classification operations. The CompCars data set used in the application was obtained from internet and surveillance based scenarios. In addition, identification of vehicle models was performed by using different Convolutional Neural Networks models on 169 different vehicle model images. Separation of training and test data sets was made from image data consisting of many classes on different models. Alexnet, Googlenet and Resnet were used for network training and transfer learning. Afterwards, comparative analysis of softmax and support vector machine classifiers were performed.

High accuracy rates were obtained with the method used in this study and feature determination processes were used to train deep learning network automatically. Thus, the error in the vehicle classification problem is minimized. At the same time, it has been observed that the performance of the classification process increases with transfer learning in the networks designed under the recommended method.

2. ARTIFICIAL NEURAL NETWORKS

An artificial nerve receives the signals as an input, processes it, and sends it to the other nerve as an output through the axon. Each nerve pathway is dynamically strengthened or weakened depending on the frequency of use. Artificial nerve models are used to translate information into computer language by imitating biological nerves.

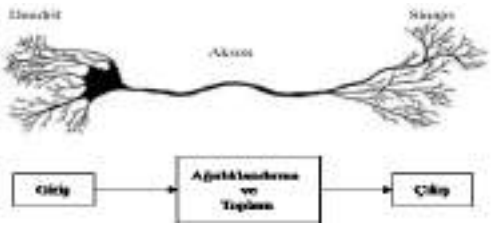

Fig.1. Real vs Artificial Neural Models

In figure 1, [w1, w2,… wn] the input information and weights [x1, x2,… xn] are multiplied and are functionally linearized activated by functions in neuron units. In the linearization process, the selection of the activation function sigmoid, ReLU or Tanh varies depending on the problem. Weighted data is passed through one of these activation functions. The output result can be obtained by adding bias values in the formula below, as well as performing vector products of properties and weights.

$$y = w.x + b \tag{1}$$

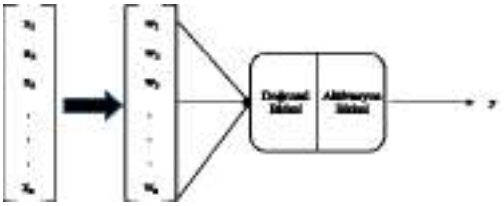

Fig.2. Artificial Neural Model

2.1. Convolutional Neural Networks

Convolutional Neural Networks (CNN) is often used for computer vision tasks and consists of various operations. In the structure of convolutional neural networks, there are different layers such as convolution, pooling and ReLU. Fig.3 shows the architecture of LeNet, known as the first CNN model. (LeCun et al. 1998. The input shape is shown as 28 × 28 × 6. In this illustration, the first value indicates the width of the filter, the second value indicates the height of the filter and the third value indicates the depth, which means the filter number.)

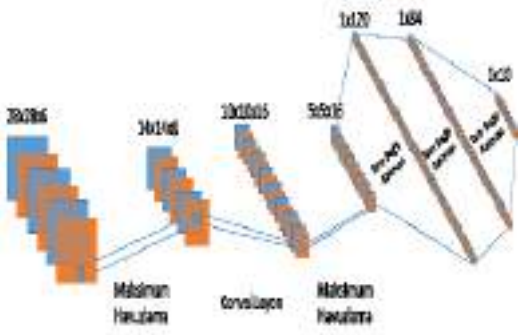

Fig.3. Architecture of LeNet

A CNN model has two important advantages. The first one of these is to reduce the size of the parameters of the filters which must be learned considerably. The second main advantage is that the parameters learned with the CNN are shared as input to the next layer. In this way, subsequent layers can learn more complex features and patterns.

Recent research has shown that a person's preferences can be recognized by deep neural networks. Likewise, face recognition has the potential to solve problems that these algorithms cannot reach even in the future. In addition, deep neural networks have been used for the detection of cancer cells.

2.1.1. AlexNet

Krizhevsky et al. they performed object recognition with the CNN model they proposed. The model, named AlexNet, was trained with the ILSVRC 2012 ImageNet dataset. AlexNet has shown quite high performance for object recognition problems. More training data is needed to achieve higher accuracy rate.

2.1.2. GoogleNet

GoogleNet contains 12 times less parameters than Alexnet architecture.

The GoogleNet model processes the input image at 224x224x3. 1x1 filters are used for size reduction. However, the ReLU activation function is used to eliminate linearities in the network. 70% dropout is applied to overcome the excessive consistence problem. As classifier, the softmax structure is used.

2.1.3. ResNet

The creation of deep CNN structures requires higher-quality hardware during the training process. Residual block structures are used to reduce the number of parameters. Some convolution layers can also be ignored with shortcut links. 1x1 and 2x2 filters are used in ResNet structure. 1000 properties are obtained at the end of the network and the Softmax classifier is trained. Different models of ResNet structures are available.

2.2. Classifiers

2.2.3. Softmax

Mathematical expression of the softmax function, which is frequently used for classification, is given in Equation 1.1.

$$\sigma(z) = \frac{1}{\sum_{j=1}^{n} \exp(\lambda z_j)} \begin{bmatrix} \exp(\lambda z_1) \\ \cdot \\ \cdot \\ \exp(\lambda z_n) \end{bmatrix}, \quad \lambda > 0 \tag{1}$$

2.2.3.Support Vector Machines (SVM)

In the classification process, Support Vector Machines (SVM) can separate the data with the help of planes. The SVM algorithm can be used in nonlinear planes as well as linear planes for classification. The kernel functions are exploited in the SVM algorithm, which includes nonlinear planes. The kernel functions may be radial, sigmoid or polynomal. In SVM classification, the error is tried to be minimized as much as possible.

2.3. Transfer Learning

The use of pre-trained models as a starting parameter for a different task is called transfer learning. Transfer learning is basically divided into three main groups: inductive, transducer and unsupervised. When this distinction was made, attention was paid to the task to be solved and whether the data was labeled or not. Transfer learning is a research problem in machine learning that focuses on storing the information obtained while solving a problem and then applying it to a different problem of interest. For example, the knowledge acquired while learning to recognize cars can be applied when trying to recognize trucks. With the transfer learning method applied, the designers had the opportunity to obtain high accuracy rates while saving time. It is very difficult to provide data and design complex models in different image processing problems. With the recommended transfer learning it is possible to achieve higher performance with less data.

3. CLASSIFICATION OF VEHICLE MODELS BY CONVOLUTION NEURAL NETWORKS

The CompCars data set used in the applications made in this study consists of internet and surveillance based scenarios. Internet-based images are provided by search engines and open-access websites. Surveillance based scenarios are obtained from mobese cameras. A total of 1716 vehicle model images were recorded with the support of Internet-based scenarios. The number of images obtained is over 136 thousand. The number of images obtained from surveillance based scenarios is around 45 thousand.

Taking into account the number of images in the classes, a number of adjustments have been made in the CompCars dataset. In the data set, there are approximately 15 thousand images in total and 169 vehicle models.

In this study, three different architectures such as AlexNet, GoogleNet and ResNet50 are used as a deep learning model. The depth, number of filters, filter sizes and configuration of each model are different. Besides, the effect of three different types of CNN models used in the comparative analysis was examined to see it's effect to the general performance by changing the classifiers which are the last layer. Softmax regression and SVM were used as classifiers.

3.1. MATLAB Application Result and Graphs

MATLAB 2017 software was used in all image processing and classification studies. Three different CNN structures were trained using Transfer Learning technique and CompCars data set. The CNN structures used are AlexNet, GoogleNet and ResNet-50 models. Within the scope of the comparative analysis, test data accuracy rates and training periods were evaluated. Gradient descent algorithm was used as the optimization algorithm. The learning rate was chosen as 10^{-3}.

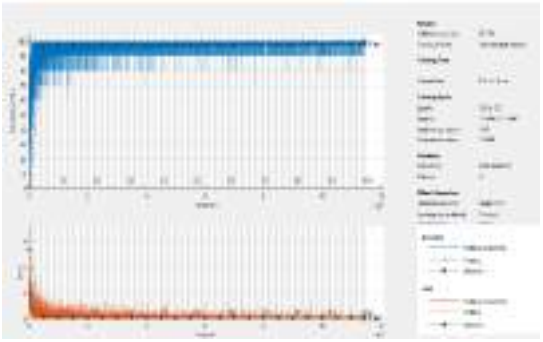

Fig.4 . AlexNet Training Graphic

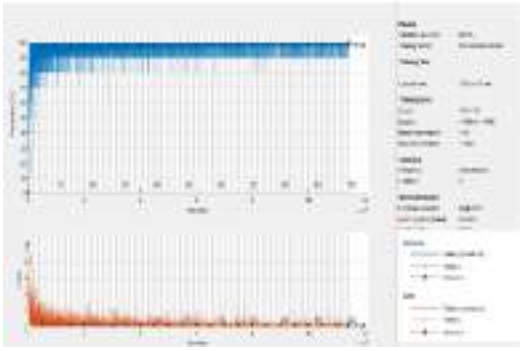

Fig.5 . GoogleNet Training Graphic

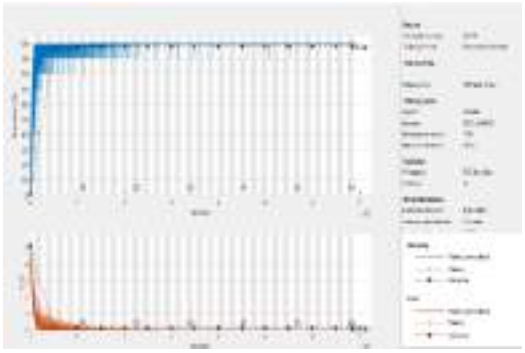

Fig.6 . ResNet50 Training Graphic

In the graphs obtained as a result of training of CNN structures, blue curves show the performance of the training data. The black lines in the accuracy metric show the performance of the network during training at certain iteration values of the test data. When the loss graphs are examined, the red curves show error rates for the training data. Black curves represent the amount of error calculated by the use of test data. Table 1 gives the accuracy rates and training times of the CNN models used.

Table 1. Comparative Analysis Results

CNN Models	Accuracy Rates Of Tests (%)		Training Duration (Minute)
	Softmax	SVM	
AlexNet	98.71	98.51	412
GoogleNet	98.73	97.62	1282
ResNet50	98.21	97.92	1878

When Table 1 is analyzed, the highest test accuracy rate CNN model is GoogleNet + softmax model. The success of classification is 98.73%. Secondly, the AlexNet + Softmax model has a 98.71% ratio. Lastly, ResNet50 + Softmax has the lowest performance with 98.21% accuracy. When the effect of classifiers is examined, it can be seen that Softmax classifier generally has higher performance than SVM classifier. The SVM classifier achieved the highest performance with the AlexNet model at 98.51%. The lowest performance was seen in the GoogleNet model with 97.62%. In terms of training times, the AlexNet model is the shortest-trained architecture with 412 minutes. Secondly, GoogleNet comes with 1282 minutes. ResNet50 has the longest training time with 1878 minutes. Figure 7 shows the classification results and percentages obtained with GoogleNet + Softmax model according to different colors and models.

Fig.7 . Googlenet + Softmax Test Results

4. CONCLUSION

In this study, transfer learning has been used to solve the problems of recognition of vehicle models. Within the proposed method, real vehicle images containing large amounts of data were analyzed. The high diversity of the data set makes it stand out compared to other data sets. These characteristics of the data set increase the performance of transfer learning models.

This study is expected to be successful in detecting forgery in plate in real-time. The performance of the application depends on how accurate and fast the detection and forecasting is performed. It is very difficult to detect an unauthorized vehicle when the license plates cannot be read. However, security providers easily improve their chances of detecting unauthorized cars by filtering them in relation to their brands and models. The application can be more robust and reliable for use in the real world, especially after accessing data from surveillance cameras recording from highways.

It is possible to use the recommended transfer learning method to reach the vehicle models of interest to the users. In addition, it may be possible to establish relationships between the vehicles and the images of the different vehicle parts contained in the data set. In this study, higher performance and a more meaningful classification process can be performed with three different CNN models proposed. It is possible to train CNN models of different structures by further diversifying and expanding the data set. Within the framework of the obtained results, GoogleNet + Softmax model, one of the CNN structures that have been completed training, can define 169 different vehicle models with 98.73% performance. The range of data sets can be increased by contacting the online vehicle markets for future studies. Moreover, different experiments can be performed using different CNN models.

REFERENCES

Buduma, N. and Locascio, N. (2017) Deep Learning.

De Schutter, E. (2018) 'Deep Learning and Computational Neuroscience', Neuroinformatics. Neuroinformatics, 16(1), pp. 1–2. doi: 10.1007/s12021-018-9360-6.

He, K. M., Zhang, X. Y., Ren, S. Q. ve Sun, J., (2016) Deep Residual Learning for Image Recognition, 2016 IEEE Conference on Computer Vision and Pattern Recognition (CVPR), 770-778.

Krizhevsky, A., Sutskever, I. ve Hinton, G. E., (2017) ImageNet Classification with Deep Convolutional Neural Networks, Communications of the ACM, 60 (6), 84-90.

Nahid, A.-A., Mehrabi, M. A. and Kong, Y. (2018) 'Histopathological Breast Cancer Image Classification by Deep Neural Network Techniques Guided by Local Clustering', BioMed Research International. Hindawi, 2018, pp. 1–20. doi: 10.1155/2018/2362108.

Pan, S. J. ve Yang, Q. A., (2010). A Survey on Transfer Learning, IEEE Transactions on Knowledge and Data Engineering, 22 (10), 1345-1359.

Szegedy, C., Liu, W., Jia, Y. Q., Sermanet, P., Reed, S., Anguelov, D., Erhan, D., Vanhoucke, V. ve Rabinovich, A., (2015). Going Deeper with Convolutions, 2015 IEEE Conference on Computer Vision and Pattern Recognition (CVPR), 1-9.

Torrey, L., Shavlik, J., Walker, T. ve Maclin, R., (2008), Relational macros for transfer in reinforcement learning, Inductive Logic Programming, 4894.

CISET - 2nd Cilicia International Symposium on Engineering and Technology
10-12 October, 2019, Mersin / TURKEY

COMPARISION OF EFFECT OF ABSORBER- REFRIGERANT MIXTURE FOR COOLING A HOTEL IN MERSİN PROVINCE BY USING A SOLAR POWERED ABSORPTION REFRIGERATION SYSTEM

Bengi GÖZMEN ŞANLI[1*], Elif TURNA DİLSEL[2]

[1,2] Mersin University, Faculty of Engineering, Mechanical Engineering, Mersin, Turkey

[1] bengigozmen@gmail.com
[2] elif.turna@windowslive.com

ABSTRACT

In this study, cooling of a hotel having 40 rooms in Mersin by using solar-assisted single effect absorption refrigeration machine, which uses ammonia-water (NH_3-H_2O) mixture, has been evaluated. The main aim of this study is to compare the effect of absorber- refrigerant couple for cooling a hotel in Mersin province by using a solar powered absorption refrigeration system. Design of the solar-assisted single effect absorption refrigeration system using NH_3-H_2O mixture has been carried out according to data of August the warmest month in the cooling season. The cooling load of hotel building and the heat given to generator have been calculated. To provide the heat given to generator which is used to supply hotel's cooling energy demand, required collector surface area has been determined by considering different types of collectors (flat plate and evacuated tube collectors). it has been understood that the usage of evacuated tube collectors are suitable for this cooling system. The COP of the single effect absorption refrigeration system using NH_3-H_2O mixture has been calculated as %74. This value is %3,1 lower than that of the single effect absorption refrigeration machine using H_2O-LiBr mixture.

Keywords: *Absorption Refrigeration, solar power, solar collector, NH3-H2O mixture*

1. INTRODUCTION

Energy requirement increases with development of technology and population growth. Due to the reduction of fossil fuel consumption and harmful emissions into the environment, new energy sources have been researched like solar energy. The reason of preference of renewable energy is harmless and endless. Turkey is one of the favorable countries in terms of solar energy potential and Turkey has taken place in the region called as sun belt (Daşkın et al., 2014). Southeastern Anatolia region and Mediterranean region are two regions having the highest solar energy potential. At these regions, the cooling of areas is an important requirement to provide thermal comfort. Solar powered absorption refrigeration system discovered by Ferdinand Carre (Dinçer et al., 1993) is preferred for cooling in summer season. The usage of these systems decreases the cooling cost significantly (Büyükalaca et al., 2003). Moreover, absorption refrigeration systems work effectively at the high temperature of ambient air. (Pastakkaya et al., 2008). The absorption refrigeration systems are widely used in several areas owing to their advantages mentioned above (Ali et al. (2008), Ramesh et al. (2014). Öztürk (2006), designed a SPAR system working with NH3-H2O fluid pair and thermodynamic analysis was performed theoretically. Sayadi et al. (2013), carried out simulations by EES and TRNSYS programs of single effect absorption refrigeration machine using H_2O-LiBr and economic performance was investigated. Özay (2008), designed a solar powered absorption refrigeration system by using a parabolic solar collector for july in Isparta province. The COP and usability of the system were investigated. The performance analysis of a SPAR system used in Mersin province was investigated by Şahin et al. (2016). They designed a NH_3-H_2O SPAR system using vacuum tube solar collectors and analyzed the system. Xu et al. (2009), performed a study on a new solar powered absorption refrigeration (SPAR) system with advanced energy storage technology. The results of this study indicated that the COP of this system can increase to 0.7525. Bozkaya et al. (2011), designed a single acting SPAR system using NH_3-H_2O in order to provide the required cooling load of İzmir province at a summer season. To supply heat given to generator, proper collector area and collector type were determined. The collector area was calculated as 56 m^2. Şanlı and Dilsel (2018) carried out a study on a SPAR system working with H_2O-LiBr to cool a hotel placed in Mersin. In order to provide the cooling load, the area of vacuum tube solar collectors was calculated as 359.5 m^2.

In present study, a solar powered absorption refrigeration (SPAR) system working with a NH_3-H_2O is designed to cool a hotel having five floors and analyzed theoretically. The main aim of this study is to compare the results of this study with the results of study on providing the cooling load of same hotel via a SPAR system using H_2O-LiBr mixture. The effect of absorber- refrigerant couple on the coefficient of performance of the system is investigated.

2. MATERIAL and METHOD

2.1. Absorption Refrigeration System and Working Principle

At absorption refrigeration systems, a refrigerant is used to transfer the heat equal to the cooling load from the house to outdoor by the evaporator and an absorbent provides to transport the refrigerant (Yamankaradeniz et al., 2002). The refrigerant-absorbent pairs (LiBr-H_2O) are selected by considering both chemical and physical properties of fluids. The refrigerant-absorbent pairs H_2O-LiBr and NH_3-H_2O are used most commonly. At the H_2O-LiBr mixture, H_2O is used as refrigerant while NH_3 is preferred as refrigerant at NH_3-H_2O mixture (Goralı 2007). With the absorption refrigeration system working with NH_3-H_2O mixture, the cooling is performed up to -10 C°. On the other hand, the evaporator temperature of the SPAR system working with H_2O-LiBr is about -4 C° due to freezing risk of the water. A schematic presentation of a single effect solar powered absorption refrigeration (SPAR) system using NH_3-H_2O mixture is indicated in Figure 1. The absorption refrigeration system using ammonia-water (NH_3-H_2O) mixture consists of generator, deflagmator, condenser, evaporator, absorber, heat exchanger and a pump (Goralı 2007).

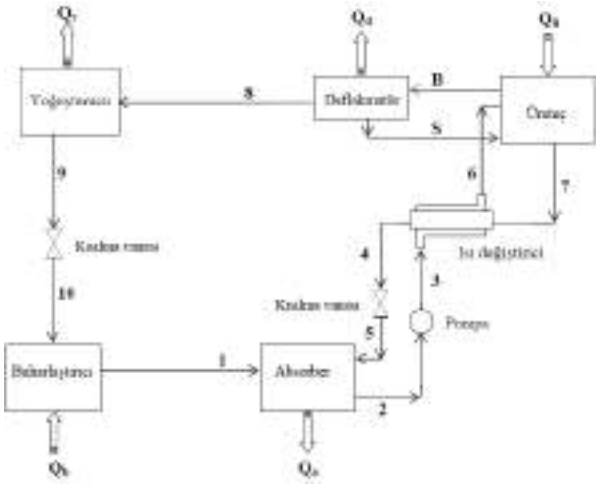

Fig. 1. Effect Solar Powered Absorption Refrigeration (SPAR) System Using NH_3-H_2O Mixture (Goralı, 2007).

The useful heat Q_b is obtained by the evaporator of the system and the refrigerant is evaporated by absorbing the heat from the cooled place. The vapour of the refrigerant coming from the evaporator is absorbed by the weak solution. During this process, the heat energy releases. The heat of Q_a released during the absorber process should be removed from the absorber since the absorber capacity of the water decreases with the increase in the temperature. This rich solution is pressured by a pump. The heat exchanger placed between absorber and deflagmator decreases the heat demand in the deflagmator. Therefore, the cooling process can be more effective and economic. In the generator, the NH_3-H_2O mixture evoparates by absorbing the heat from the

generator and moves away from the generator. The water vapour leaves from the NH_3-H_2O mixture in the deflagmator. Then, the NH_3 vapour condenses in the condenser. The heat of Qy generated during the condensation process is transfered to the coolant. The coolant condensed in the condenser passes through an expansion valve and reaches to the evaporator. (Öztürk et al. 1998, Can 1998, Eicker 2003, Goralı, 2007).

2.2. Calculation of Cooling Load for a Hotel

In order to cool a hotel having 40 rooms and five floors in Mersin province via a solar powered ammonia-water (NH3-H2O) absorption refrigeration system, the cooling load of the hotel should be determined. In this study, the considered hotel is located on a longitude of 34,63° and 36,8° latitude. To use at the calculation of cooling load, the meteorological datas of cooling season for Mersin province are presented in Table 1. At this study, the meteorological data of august was used for the calculation of cooling load since the cooling load is maximum in august for Mersin province.

Table 1. Meteorological data for Mersin province (MGM 2018, YEGM 2018).

Month	Average Temperature(°C)	H_Y (mJ/m^2. gün)
May	21,2	26,9
June	25,0	28,6
July	27,8	27,9
August	28,3	26,2
September	25,8	21,7

The hotel has five floors. The ground floor is earth-contacted, each floor area is about 200 m^2 and the hotel has a flat roof. The heat transfer coefficients of the building elements are 1.03 W/m^{2}K for the outer wall, 2.6 W/m^{2}K for the double-glazed window, 4.0 W/m^{2}K for the outer door, 0.58 W/m^{2}K for the floor and 0.44 W / m^{2}K for the ceiling (Kent et al., 2009). The hotel is facing to South and there is no obstacle on any sides of the hotel. The hotel is well insulated, and it has the normal glass light color shade. The internal design temperature was assumed as 25°C while the external design temperature was assumed as 35 °C and the calculation of cooling load of the house was performed. The cooling load was calculated for August. The floor plan of this hotel is shown in Figure 2.

Fig.2. Floor plan this hotel

While calculating the total cooling load; heat gain from people, lighting and devices, heat gain from neighboring walls, floors and ceilings, heat gain coming from windows by convection and radiation were considered. The total cooling load was calculated using the following formulas (Canovete energy, 2018);

The cooling load for human;

$$Q_H = numberofperson \times propertiesofthehouse \quad (1)$$

The cooling load for fresh air;

$$Q_{TH} = freshairperson \times numberofperson \times roomfactor \quad (2)$$

Cooling load for lightings and electrical devices;

$$Q_{lighting} = roomarea \times propertiesofroom \quad (3)$$

$$Q_{devices} = numberofdevices \times devicesproperties \quad (4)$$

Cooling load from radiation;

$$Q_{radiation} = windowsproperties \times windowarea \times windowsshabdingfactor \quad (5)$$

Cooling load for convection and conduction;

$$Q_{convection,conduction} = 8-12 \ percent \ of \ total \ of \ cooling \ load \ of \ human, fresh \ air, lightings, electrical \ devices \ and \ radiation. \quad (6)$$

Total cooling load;

$$Q_{total} = Q_H + Q_{IH} + Q_L + Q_E + Q_R + Q_{C,C} \quad (7)$$

For Mersin, the total cooling load is multiplied with 1.24 as the correction factor.

2.3. Thermodynamic Analysis of Absorption Refrigeration System

The equations of energy conservation and mass conservation demonstrated in Table 2 is used at the thermodynamic analysis of the SPAR system indicated in Figure 1.

Tablo 2. The equations of energy conservation and mass conservation used at the design of the SPAR system (Goralı,2007).

Parameter	Value
Evaporator temperature	5°C
Absorber temperature	30°C
Condenser temperature	30°C
Generator temperature	75°C
Concentration of amonia	0,999
Concentration of vapour	0,975
Efficiency of heat exchanger	0,8
Pompa Efficiency	0,75

The evaporator heat capacity is determined by calculating total cooling load of the house. The thermodynamic calculations of this SPAR system were performed by using evaporator heat capacity and other design parameters shown in Table 3.

Table 3. Design Parameters of Solar-Powered Absorption Refrigeration System

System eguipments	Mass conservation	Amonia conservation	Energy conservation
Evaporator	$\dot{m}_1=\dot{m}_{10}$	$\dot{m}_{10}X_{10}=\dot{m}_1X_1$	$\dot{m}_{10}h_{10}+Q_b=\dot{m}_1h_1$
Absorber	$\dot{m}_2=\dot{m}_1+\dot{m}_5$	$\dot{m}_2X_2=\dot{m}_1X_1+\dot{m}_5X_5$	$\dot{m}_2h_2+Q_a=\dot{m}_1h_1+\dot{m}_5h_5$
Heat exchanger	$\dot{m}_3+\dot{m}_7=\dot{m}_4+\dot{m}_6$	$\dot{m}_3X_3+\dot{m}_7X_7=\dot{m}_4X_4+\dot{m}_6X_6$	$\dot{m}_3h_3+\dot{m}_7h_7=\dot{m}_4h_4+\dot{m}_6h_6$
Deflagmator	$\dot{m}_B=\dot{m}_8+\dot{m}_S$	$\dot{m}_BX_B=\dot{m}_SX_S+m_8X_8$	$\dot{m}_Bh_B-Q_d=\dot{m}_8h_8+\dot{m}_Sh_S$
Generator	$\dot{m}_6=\dot{m}_7+\dot{m}_8$	$\dot{m}_6X_6=\dot{m}_7X_7+m_8X_8$	$\dot{m}_6h_6+Q_ü=\dot{m}_8h_8+\dot{m}_7h_7+Q_d$
Condenser	$\dot{m}_8=\dot{m}_9$	$\dot{m}_8X_8=\dot{m}_9X_9$	$\dot{m}_9h_9+Q_y=\dot{m}_8h_8$

2.4. Monthly Average of Solar Radiation Reaching to surface of inclined collector and Defination of Collector Area

The surface area of collector is determined after the generator heat capacity is calculated by the thermodynamic analysis of the SPAR system. While the surface area of collector is defined, the first step is calculation of declination angle. The declination angle is used in order to determine the optimum inclination of plane where the collectors are placed on. Total daily solar radiation reaching to collector surface is assessed by using the monthly average solar radiation (Hy) for Mersin Province. The collector efficiency based on collector type is calculated and the required collector area is determined. The corresponding equations are given below (Goralı, 2007):

Declination angle is calculated by the equation (8):

$$\delta = 23,45° \times \sin(360 \times \frac{n+284}{365}) \quad (8)$$

n means the day of which data is used in a year. The tilt angle of collector is defined as

$$s_0 = e - 1,5 \times \delta - \frac{|\delta| \times e}{180} \quad (9)$$

Here, e is the latitude angle. Total daily solar radiation reaching to collector surface (H_t) is calculated by;

$$\bar{R} = \frac{H_t}{H_y} \quad (10)$$

In the equation above, Hy is the mountly average solar radiation (H_y) for Mersin Province. The equation 11 is used to calculate the coefficient $\bar{R}$;

$$\bar{R} = \frac{\cos(e-s)\times\cos\delta\times\sin H_g + \frac{\pi}{180}\times\sin(e-s)\times\sin\delta}{\cos e\times\cos\delta\times\sin H + \frac{\pi}{180}\times\sin e\times\sin\delta} \quad (11)$$

Here, H is the defined as the angle of sunrise and sunset and it is determined by the equation (12);

$$H = \arccos(-\tan\delta\times\tan e) \quad (12)$$

Moreover, H_g is calculated by the equation (13);

$$H_g = \min\left[\arccos(-\tan e\times\tan\delta), \arccos(-\tan(e-s)\times\tan\delta)\right] \quad (13)$$

With the equation (14), the day length is assessed.

$$t_0 = \frac{2}{15}\times H = \frac{2}{15}\times\arccos(-\tan\delta\times\tan e) \quad (14)$$

Daily average solar radiation reaching to surface of inclined collector (I_e) is defined as;

$$I_e = \frac{H_t}{t_0} \quad (15)$$

After I_e is calculated, the surface area of collector (A_c) is determined by the equation (16). Here, Q_g is the generator heat capacity, η is the efficiency of the collector system.

$$A_C = \frac{Q_j}{\eta \times I_e} \quad (16)$$

This efficiency (η) is determined as shown below;

$$\eta = c_0 - c_1 \times x - c_2 \times x^2 \times I_e \quad (17)$$

$$x = \frac{\Delta T}{I_e} \quad (18)$$

$$\Delta T = T_{ort} - T_{ç} \quad (19)$$

The useful energy acquired by the selected collector is calculated by the following equation;

$$Q_f = \eta \times A_c \times I_e \quad (20)$$

Some refrigerant systems are designed that the required energy is only obtained from solar energy. On the other hand, some of these systems use both solar energy and electrical energy as supplement energy in order to supply the required energy for SPAR systems. At these systems, the solar fraction (SF) is determined by the equation;

$$SF = 1 - \frac{Q_{ek}}{Q_g} \quad (21)$$

The supplement energy for a month (Q_{sp}) can be assessed as indicated below;

$$Q_{sp} = \Delta Q = Q_f - Q_g \quad (22)$$

For the SPAR systems using only solar energy, the SF is equal to 100% (Goralı, 2007). The performance coefficient (COP) of the SPAR systems is defined as;

$$COP = \frac{Q_e}{Q_g} \quad (23)$$

While determining the collector area for solar powered absorption refrigeration (SPAR) system, the month datas of which cooling loads are high are used. (Henning,2004).

3. RESULTS and Dıscussıon

In this study, a solar-powered absorption refrigeration system (SPAR) using NH_3-H_2O was designed and analyzed theoretically to cool a hotel having 40 rooms in Mersin Province. The required energy for this SPAR system was supplied by solar energy. The cooling load of the house for august was calculated as 84,6 kW and details for calculation of cooling load are demonstrated in Table 4.

Table 4. Details of cooling load

Type of cooling load	Capacity(W)
Heat gain due to person	16100
Heat gain due to fresh air	25200
Heat gain due to electrical devices and lighting	29100
Heat gain due to Radiation	6500
Heat gain due to convection and conduction	7700
Total cooling load (total heat gain)	84600

The required cooling load for the hotel is equal to absorbed heat from the house by the evaporator. The equations of energy conservation and mass conservation shown in Table 2 were used every equipment of the SPAR system. The cooling performance coefficient (COP) of the SPAR systems designed in this study was calculated as 0.74 and the heat capacities of all equipments are given in Table 5a. These results were compared with the results of SPAR system using H_2O-LiBr shown in table 5b (Şanlı and Dilsel 2018) and it is understood that the corresponding equipment capacities are different from each other and the capacity of SPAR systems using NH_3-H_2O is %3,1 higher than that of the SPAR system using H_2O-LiBr.

Table 5a. The equipment capacity of solar-powered absorption refrigeration system using NH_3-H_2O

Parameter	Capacity
Evaporator capacity	84,6 kW
Absorber capacity	111,45 kW
Generator capacity	113,743 kW
Deflagmator capacity	18,93 kW
Condenser capacity	87,18 kW
Pump work	0,288 kW
Performance coefficient (COP)	0,741

Table 5b. The equipment capacity of solar-powered absorption refrigeration system using H_2O-LiBr (Şanlı and Dilsel 2018**)**

Parameter	Capacity
Evaporator capacity	84,6kW
Pump work	0,214kW
Absorber capacity	10,513kW
Generator capacity	119,413kW
Condenser capacity	28,927kW
Heat exchanger	27,216kW
Performance coefficient COP)	0,71

The required heat for the generator of SPAR system (Q_g) was calculated as 113,743 kW by the thermodynamic analyses. The inclination of plane that the collectors were placed on was determined as 16. 33°.Table 6 displays total daily solar radiation reaching to collector surface (H_t), day length and daily average solar radiation reaching to surface of inclined collector (I_e).

Table 6. Total daily solar radiation reaching to collector surface (H_t), day length (t_0) and daily average solar radiation reaching to surface of inclined collector (I_e)

Month	H_t(MJ/m^2.gün)	t_o(h)	I_e(W/m^2)
May	26,72	13,97	531,30
June	28,32	14,45	544,41
July	27,62	14,21	539,92
August	25,94	13,34	540,15
September	21,48	12,22	488,28

The collector surface area was determined and the results were shown in Table 7. This table presents collector efficiency (η), solar fraction (SF) and collector surface area. In order to provide the cooling load of this hotel, the required surface area for the vacuum tube collectors was calculated to be 359,5 m^2 while it was found to be 690,1 m^2 for the flat plate collectors. These values were same with results of the SPAR system using H_2O-LiBr since the solar fraction given with the equation 21 was same with that of the SPAR system using NH_3-H_2O in spite of the difference in the generator capacity.

Table 7. Type of collectors analyzed in this study

Type of collector	η	SF	Area(m^2)
Viessmann Vitesol300T Vacuumtube collector Optical performance: 0.809 k1:1.37 W/m2K k2:0.0068 W/m2K	0,615	1	359,5
Viessmann Vitesol300F flat plate collector Optical performance 0.834 k1:3.66 W/m2K k2:0.0169 W/m2K	0,320	1	690,1

4. CONCLUSION

In this study, cooling of a hotel having 40 rooms in Mersin by using solar-assisted single effect absorption refrigeration machine, which uses ammonia-water (NH_3-H_2O) mixture, has been evaluated. The main aim of this study is to compare the analysis results of the solar-powered single effect absorption refrigeration system using NH_3-H_2O with the SPAR system using H_2O-LiBr in order to reveal the effect of absorber- refrigerant couple. Design of the solar-assisted single effect absorption refrigeration system using NH_3-H_2O mixture has been carried out according to data of August. The cooling load of the hotel was calculated as 84,6 kW and the heat required for the generator in order to provide the cooling load of the hotel was determined as 113,743 kW, and the required collector surface area was determined by considering different types of collectors (flat plate and vacuum tube) to meet this heat capacity. The required surface area for the vacuum tube collectors was calculated to be 359,5 m^2 as it was found to be 690,1 m^2 for the flat plate collectors. When these results were compared with the results of SPAR system using H_2O-LiBr, it is understood that the performance coefficient (COP) of the SPAR system working with NH_3-H_2O is %3,1 higher than that of the SPAR system using H_2O-LiBr.

5. REFERENCES

Ali, A.H.H., Noeres, P. and Pollerberg, C. (2008). "Performance assessment of an integrated free cooling and solar powered single-effect lithium bromide-water absorption chiller." *Solar Energy,* Vol.82, pp. 1021-1030.

Bozkaya, B. ve Akdemir, Ö. (2011). "Güneş enerjili nh3-h2o absorpsiyonlu soğutma sisteminin izmir ili için incelenmesi." *X. Ulusal Tesisat Mühendisliği Kongresi Soğutma Teknolojileri Sempozyumu*, s. 1405-1413.

Büyükalaca, O. ve Yılmaz, T. (2003). "Güneş enerjisi ile soğutma teknolojilerine genel bir bakış." *Tesisat Mühendisliği Dergisi,* Vol. 3, s. 45-56.

Can, A. (1998). "Güneş enerjisiyle soğutma ve ekstrem şartlar." *Güneş Günü Sempozyumu ve Fuarı Bildiri Kitabı,* İzmir, Türkiye, s. 57-62.

Anonim, http://portal.canovateenerji.com/trTR/sogutma-yuku-hesabi/ (Erişim Tarihi:25.04.2018).

Daşkın, M. ve Aksoy, İ.G. (2014). "İklimlendirme amaçlı güneş enerjisi destekli bir absorpsiyonlu soğutma sisteminin simülasyonu." *Batman Üniversitesi Yaşam Bilimleri Dergisi,* Vol. 4, No. 1, s. 52-65.

Dinçer, İ. ve Erdallı, Y. (1993). "Absorpsiyonlu soğutma sistemlerinin rolü ve etkinliği." *Termodinamik Dergisi,* vol. 5, s. 31-37.

Eicker, U. (2003). *Solar Technologies for Buildings*, Wiley, İngiltere.

Goralı, E. (2007). Güneş enerjili absorpsiyonlu soğutma sistemi, Yüksek Lisans Tezi, İstanbul Teknik Üniversitesi, Enerji Enstitüsü, İstanbul, Türkiye.

Henning, H. M. (2004). *Solar-Assisted Air-Conditioning in Buildings,* Springer Press, Viyana.

Kent, E.F. ve Kaptan İ.N. (2009). "İzmir ilindeki elli yataklı bir otel için güneş enerjisi destekli ısıtma ve absorbsiyonlu soğutma sisteminin teorik incelenmesi." *IX. Ulusal Tesisat Mühendisliği Kongresi,* İzmir, Türkiye, s.163-170.

MGM, https://www.mgm.gov.tr/?il=Mersin, (Erişim Tarihi: 25.04.2018).

Özay, İ. F. (2008). NH_3-H_2O absorbsiyon soğutma sisteminin güneş enerjisi ile çalıştırılması ve verimlilik analizi, Yüksek Lisans Tezi, Süleyman Demirel Üniversitesi Fen Bilimleri Enstitüsü, Isparta, Türkiye.

Öztürk, A. ve Kılıç, A. (1998). *Çözümlü problemlerle termodinamik,* Çağlayan Kitabevi, İstanbul.

Öztürk, İ.T. (2006). "Güneş enerjisinden absorpsiyon teknolojisi yardımı ile güç üretimi." *Mühendis ve Makine*, Vol. 563, No. 47 s. 17-23.

Pastakkaya, B., Ünlü K. ve Yamankaradeniz R. (2008). "Isıtma ve soğutma uygulamalarında güneş enerjisi kaynaklı absorpsiyonlu sistemler." *TTMD Dergisi*, Vol. 57, s. 25-32.

Ramesh, R, Murugesan S.N., Narendran, C. and Saravanan, R. (2015). "Cascaded energy plant using amonia absorption refrigeration system for combined cooling and heating applications." *Science And Technology For The Built Environment,* Vol. 21, pp. 290-299.

Sayadi, Z., Bourois M., and Bellagi A. (2013). "Technical and economic analysis of a solar-assistedair-conditioning system," *Int. J. Renewable Energy Technology,* Vol.4, No.1, pp:65-85.

Şahin B., Bilgili M., Çetingöz A. ve Kurtulmuş N. (2016). "Performance analysis of solar powered absorptionrefrigerationsystemfor mersin province." *Çukurova Üniversitesi Mühendislik Mimarlık Fakültesi Dergisi,* Adana, Vol. 31, No.1 pp: 371-379.

Şanlı, B. ve Dilsel T. E. (2018). "Mersin ilindeki bir otelin soğutulması için güneş enerjisi destekli absorbsiyonlu soğutma sistemi tasarımı ve teorik analizleri." *BEÜ Fen Bilimleri Dergisi,* Vol. 7 No. 2 s. 301-310.

Yamankaradeniz R., Horuz İ. ve Coşkun S. (2002). *Soğutma tekniği ve uygulamaları,* Vipaş, Bursa.

YEGM.http://www.yegm.gov.tr/MyCalculator/pages/33.aspx, (Erişim Tarihi: 25.04.2018).

Xu S.M., Huang X.D., Du R. (2011). "An investion of solar powered absorbtion refrigeration System with advanced energy storage technology." *Solar Energy*, Vol.85, pp. 1794-1804.

CISET - 2nd Cilicia International Symposium on Engineering and Technology
10-12 October, 2019, Mersin / TURKEY

REMOVAL OF MANGANESE FROM DRINKING WATER WITH HYDROXYAPATITE OBTAINED FROM FISH BONESBY USING RESPONSE SURFACE METHODOLOGY

Pınar Belibağlı[1], BehsatOzanEskikaya[1] and Yağmur Uysal*[1]

[1] Mersin University, Engineering Faculty, Environment Engineering Department, Mersin, Turkey,
yuysal@mersin.edu.tr

ABSTRACT

Heavy metal pollution is one of the most important environmental problems in the world. Most of the heavy metals such as chromium (Cr), copper (Cu), lead (Pb), cadmium (Cd), nickel (Ni), manganese (Mn) and zinc (Zn) are widely used in industries, and because of their high toxicity to living things are classified as environmental priority pollutants. Among the heavy metals, manganese is a very common contaminant of wastewater and ground water. The presence of manganese (II) in drinking water can cause to its bioaccumulation in human body, and this particularly affects the nervous system. Various techniques have been used for the removal of manganese ions from water and wastewater. In this study,the removal of Mn (II) ions from drinking water was investigated by adsorption technology with an adsorbent material of hydroxyapatite (HAp) that produced from biowastes (fish bones) by using Response Surface Methodology (RSM). In order to determine the adsorption mechanism of HAp particles, adsorption isotherms and kinetics were also calculated. The results showed that Mn (II) adsorption byHAp particles was more suitable for Harkins-Jura isotherm and pseudo-second kinetic model. The maximum adsorption efficiency of Mn (II) (80 %) was obtained in 73 mg/L initial concentration, at contact time of 75 min, pH 7.4 and adsorbent dosage of 10 g/L.

Keywords: *Adsorption, Fish Bone, Hydroxyapatite, Manganese, Removal*

1. INTRODUCTION

Heavy metals threaten the environment and public health due to their various properties such as non-biodegradability, toxic effects even at low concentrations and persistence in nature. (Baptista et al., 2000; Asasian et al., 2012). Thus, it is essential to remove them effectively from water and wastewater by using suitable treatment technologies (Elmi et al., 2017). Inefficient methods for the management of heavy metals in urban run-off may cause direct or indirect long-term risks for the ecosystem as well as human beings.

Manganese (Mn), a reddish-gray metal is the twelfth most abundant element with 0.095% estimated concentration in the Earth's crust. Manganese has an atomic number of 25 with atomic weight of 54.938 (Patnaik 2002). Mn (II) is gradually oxidized in chlorinated water distribution systems and results in aesthetic and operating problems, including discoloration of water, metallic taste and odor, and staining of the plumbing fixtures as well as scaling and clogging of pipes (Kenari et al., 2019). The excessive usage of manganese containing products lead to environmental pollution. Although it is essential for human life at exceeding level of 0.1 mg/L, the presence of manganese (II) in drinking water may lead to its bioaccumulation. (Patnaik et al., 2002). The health-based value of 0.4 mg/L for manganese is higher than this acceptability threshold level of 0.1 mg/L. According to European Community Directive 98/83/EC Annex 1 Part C-indicator parameters, parametric value for Mn is 50mg/L (WHO, 2011). US Environmental Protection Agency and the EU Directive have established 0.005 mg/L as the maximum manganese concentration level in domestic water supplies (USEPA, 2004).

Compared to particulate Mn oxides that could be easily separated from liquids by the water treatment plant, the removal of soluble Mn (II) ions is much more difficult (Hamilton et al., 2013). The primary target of manganese (II) toxicity is the nervous system, and common symptoms of toxic exposure include ataxia, dementia, anxiety, a 'mask-like' face, and manganism that a syndrome similar to Parkinson's disease (USEPA, 2003; USEPA, 2004; Aschner et al., 2007; Nadaska et al., 2015).

Adsorption technology is considered as an economic and effective technique for the removal of metal ions from water and wastewater. The common utilized adsorbents primarily include activated carbons, zeolites, clays, biomass and polymeric materials (Ali et al., 2016).

Calcium phosphates form a privileged class of biomaterials because of their good biocompatibility, their possibility of biodegradability and their possible bioactivity. (Ibrahim et al., 2020). Hydroxyapatite ($Ca_{10}(PO4)_6(OH)_2$) is calcium phosphate mineral phase that can be found in natural bone and is a well known bioceramic material which is widely used in various medical applications as a promising material for healing damaged bones, due to itsbiocompatibility and bioactivity as well as its inorganic compositionsimilar to that of natural bone (Oliviera et al., 2017). In water treatment applications, HAp is a perfect material for handling long-term pollutants because of its high adsorption capacity for contaminants, high effectiveness, low price, and high stability under redox conditions (Pandi et al., 2014; Pandi et al., 2015). Generally, their small size and high surface area make the HAP nanoparticles them especially reactive sorbent materials toward metal ions contaminants from polluted water (El Kady et al., 2016).

Response surface methodology (RSM) is a method in which statistical and mathematical techniques are used to compare theoretical and experimental data by optimizing dependent variables with various independent variables (Ecer et al., 2018; Taheri et al., 2012). In this study, Mn (II) adsorption potential of HAp particles from water was determined by using RSM. This method was used to determine the optimum conditions of the adsorption process variables including pH, time, adsorbent dose and initial Mn(II) concentration. According to statistical results, a predictive model equation for the adsorption process was generated. Isotherm and kinetic evaluation of the adsorption process were also made by using several kinetic and isotherm models.

2. MATERIAL AND METHOD

2.1.Reagents

Manganese(II) sulfate (Sigma-Aldrich) was used to prepare stock metal solutions. Hexane (n-Hexane, Merck) was used to wash all the fishbones for our study.Different pHvaluesof the solutions were adjusted with HCl and NaOH.

2.2.Preparation of the adsorbent material

In this study, seabreams (*Sparusaurata*) were taken from the fish restaurant.As in the study of Zhang et al. (2019), the fishes were put into boiling water for 1 h, andwashed three times with tap water in order to remove the organic substances and grease attached to the surface of the fish bones. The treated fish bones were dried in anoven at 60°C for 20–30 min to remove residual moisture, then were washed with hexane and distilled water.The fish bones were sintered in muffle furnace at 700°C for 1 h for calcination. After that, the calcined fish bones were ground using mortar.Finally, the resultant powder was sieved with the mesh about 212 μm as shown in Fig. 1.

Fig. 1. Hydroxyapatite synthesis from fish bones

2.3. Adsorption experiments

The effects of adsorbent dose, pH, contact time and initial Mn^{+2}concentration on the adsorption process were investigated in batch mode. Mn^{2+}ions were prepared by solving $MnSO_4.H_2O$ in tap water and used as stock metal solution. Batch adsorption studies were performed in flasks with 100 mL sample volumes.Metal ion solutions with concentrations of 10-100 mg/L were added to flasks.The effect of sorbate to sorbent ratio for the percentage unit metal sorbate sorption capacity of the fish bones was determined by varying the solid mass phase in the range of 0.5 g-1.0 g of fish bones. The contents of all erlenmeyer flasks were mixed thoroughly using orbital shaker with a fixed constant speed. The samples were shaken at 150 rpm speed, at 25°C constant room temperature. Then suspension was separated by centrifugation at 4000 rpm for 5 min, and the remaining concentrations of Mn^{+2}in the solutions were determined by spectrophotometer (Hach-Lange DR 3900). The effect of initial pH on the metal sorption by fish bones was evaluated in the range of 6-8. The factors influencing the conditions of the adsorption process were studied as percentage (%)of Mn^{2+}removal, and calculated using the following Eq. (1):

$$\%\ Mn^{2+}ions\ removal = ((C_o-C_e)/C_o)x100 \quad (1)$$

where C_0 (mg/L) and C_e (mg/L) are the concentrations of Mn^{2+}ions at initial and time of *t*, respectively.

For the effectiveness and accuracy in results, all the adsorption experiments were conducted in duplicate and average values were reported in this study.

2.4. RSM-CCD model

The experimental data was analyzed and fitted by Response Surface Method (RSM) using Design Expert 12 software.RSM is an efficient technique for process optimization in a minimal experimental run and which is used to explain the combined effects of all the factors. The effect of different operating parameters such as adsorbent dose, contact time, pHand Mn^{2+}concentrations, and the interactions between them required full factorial designwhen the central compositedesign (CCD) was used to obtain the experimental design matrix. The number of factors *"n"* increases the number of runs for a complete replicate of the design which is given in Eq. (2):

$$N = 2^n + 2n + n_c \quad (2)$$

The CCD consists of a 2^n factorial runs with $2n$ axial runs and $n_c$center runs. A five-level CCD with four factor (reaction time, amount of adsorbent, pH and initial Mn^{2+}ions concentrations) was used to investigate the effects of parameters. The ranges of the independent variables were shown in Table 1.

Table 1. All variables factors in CCD.

Factors	Term.	Unit	Low	High
pH	A	-	6.0	8.0
Adsorbent dose	B	g	0.5	1.0
Reaction time	C	min	30	180
Mn^{2+}con.	D	mg/L	10	100

The connection amongst independent and dependent variables was worked in CCD utilizing the second order polynomial model. The recovery percentage was calculated through Eq. (3):

$$Y = \beta_0 + \sum_{i=1}^{k}\beta_i x_i \sum_{i=1}^{k}\beta_{ii} x_i^2 + \sum_{i=1}^{k}\sum_{j=1}^{k}\beta_{ij} x_i x_j + \varepsilon \quad (3)$$

Where β_o is the offset term; $\beta_i$and β_{ii} are the linear and quadratic effects of input factor of X_i; β_{ij} is thelinear effectbetween the independent factor for X_i and X_j; and ε isthe error (Roosta*et al.*, 2014).

3. RESULT AND DISCUSSION

3.1.Adsorption experiments

3.1.1. Effect of pH on Mn^{+2}removal efficiency

The pH of the solution is one of the most important variables that affect the metal sorption on the sorbent. pH value of drinking water is generally between 6.5-9.0 in Turkish Standards Institute (TSE 226, 2005). Therefore, in this part of the study, the initial pH of the manganese solution was adjusted to 6.0-8.0 range. Fig. 2 shows effect ofdifferent pH valuesonMn^{2+}removalwithHAp.

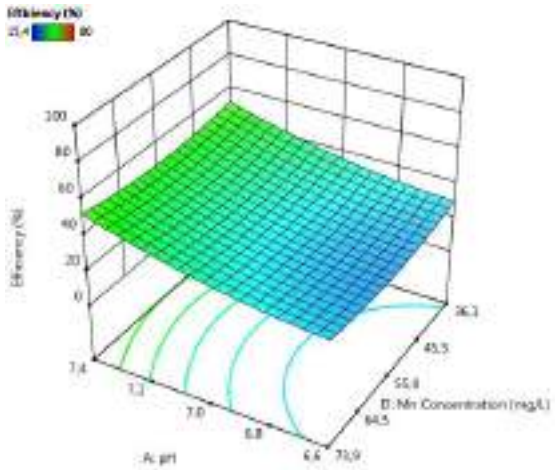

Fig. 2. The effect of pH on the efficiency of Mn^{2+}removal

Manganese removal increases when pH value increases, and complete precipitation was obtained at high pH values(≥10)(Sayilgan et al., 2010).Similarly, it was observed that manganese removal increased with increasing of pH(Fig. 2).

3.1.2. Effect of adsorbent dose on Mn^{2+} removal efficiency

The effect of the adsorbent concentration on Mn^{2+} removal efficiency was studied at different adsorbent concentrations of 0.5-1.0 g.The relationship between HApdosage and adsorption of Mn^{2+} was shown in Fig. 3. According to Fig. 3,it was shown that Mn^{2+} removal efficiency increased from 17% to 78%with increasing of adsorbent dosages. This is due to the fact that greater surface area and more adsorption sites create by increasing adsorbent doses.

3.1.3. Effect of contact time on Mn^{+2} removal efficiency

Contact time is another important parameter affecting to adsorption dynamics. The effect of contact time on the adsorption capacity of HAp for Mn^{+2} ions was studied at different time intervals ranging from 30 to 180 minto design and optimize the adsorption process. Fig. 4a shows the sorption of Mn^{+2} ions on HAp under different time intervals.The results showed that increasing of time had a positive effect on Mn^{2+} removalfrom water.

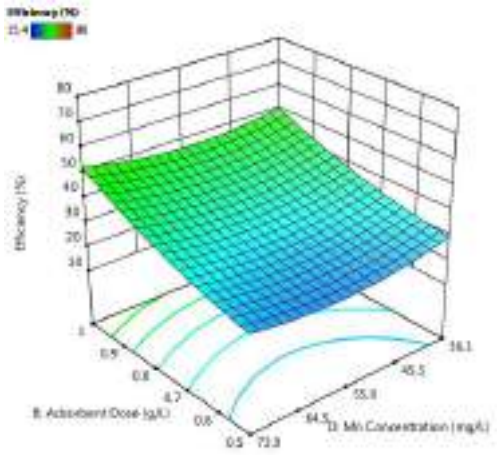

Fig. 3. The effect of adsorbent dosage on the efficiency of Mn^{2+} removal.

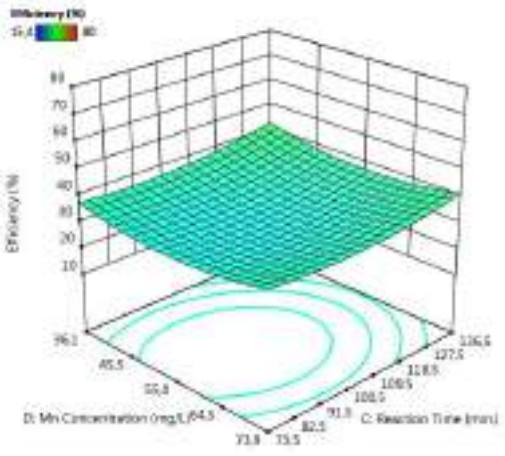

Fig. 4a. The effect of contact time on the efficiency of Mn^{2+}removal

Two experiments (Run 6 and Run 20) which has different reaction times under the same conditions are examined, and the removal efficiencies increased from 32% to 68.5% when the reaction time was increased from 30 to 105 min. These experiment showed the effect of contact time on the batch adsorption of metal solution containing 55 ppm of Mn^{2+}(25°C, 0.75 g adsorbent dose, 150 rpm and pH 7.0). As the contact time increases, adsorption decreases depending on the behavior of the surface (Adeleke et al., 2017).

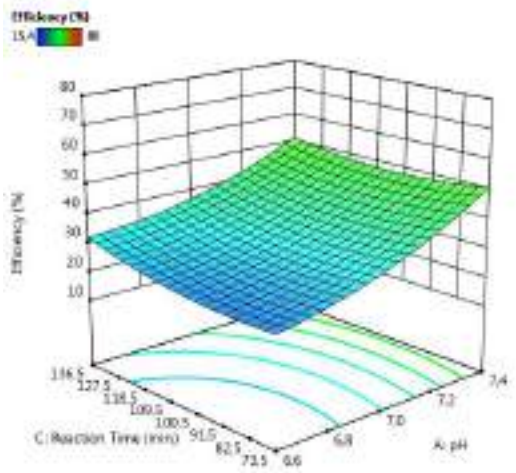

Fig. 4b. The effect of between pH and contact time

At the same time, it has been observed that pH has an effect on the reaction time due to the precipitation of Mn^{2+} ions at high pH values in experiments having the same reaction times (105 min) but different pH values. This effect between pH and contact time was given in Fig. 4b.However, it was observed that Mn^{2+} removal efficiency increased from 30% to 80% when pH increased.

3.1.4. Effect of initial concentration on Mn^{2+} removal efficiency

The effect of the initial concentration of Mn^{2+} ions on adsorption process was found to be crucial because it had overwhelmed the mass transfer constraints of Mn^{2+} ions between the solution and the solid phases. Effect of initial Mn^{2+} concentration on adsorption process was shown in Fig. 5.Metal ions were initially fixed on the active sites of HAp but further increasing initial Mn^{2+} concentration caused to decrease of Mn^{2+} removal due to the saturated active sites on adsorbent. It was clear to see that the q values increase with the increase of initial Mn^{2+} concentrations. The adsorption capacity was calculated using mass balanceshown inEq. (4):

$$q = \frac{(C_0 - C_e) \times M}{V} \qquad (4)$$

where C_0 (mg/L) is the initial and and C_e (mg/L) is the equilibrium concentrations of Mn^{+2},respectively.M (g) is the mass of HAp, V (L) is the volume of solution.

As expected, the removal efficiencies decreased with increasing of initial concentrations of Mn^{2+} (Elmi et al.,

2017). The adsorption capacity of the adsorbents increased up to 73 ppm and its effect began to decrease with increasing Mn^{2+}concentrations.

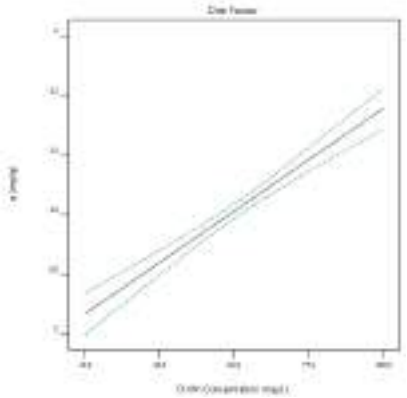

Fig. 5. The effect of initial Mn^{2+}concentrations on adsorption capacity

3.1.5. Modeling and Statistical Analysis

All experiments of this study were created using the Response Surface Method (RSM) on Desing Expert 12 software. Initial Mn^{2+}concentration, pH, adsorbent dosage and contact time are the most important parameters which affect the efficiency of Mn^{+2} ions by HApmaterials. RSM design was used for exploring different combined parameters and for evaluating the combined effects of those factors. In the present work, linear, two factor interaction (2FI), quadratic and cubic models were used to analysis experimental data in order to obtain the regression equations.The model equation representing efficiency (%) was expressed as functions of pH (A), adsorbent dose (B), reaction time (C) and Mn^{+2} concentration (D) for coded units as given belowEq. (5):

$$\textit{Efficiency (\%)}=983{,}44 - 288{,}97A + 68{,}04B + 0{,}41C - 1{,}95D - 16{,}71\,A*B - 0{,}14A*C + 0{,}05A*D + 0{,}02B*C + 0{,}27B*D - 0{,}0006C*D + 23{,}58A^2 + 47{,}18B^2 + 0{,}0030C^2 + 0{,}01D^2 \quad (5)$$

The adequacy of the selected model and statistical significance of the regression coefficients were tested using the analysis of variance (ANOVA). ANOVA is a statistical technique that subdivides the total variation in a set of data into component parts associated with specific sources of variation for the purpose of testing hypotheses on the parameters of the model.Data were also analyzed to check the normality of the residuals, as shown in Fig. 6.

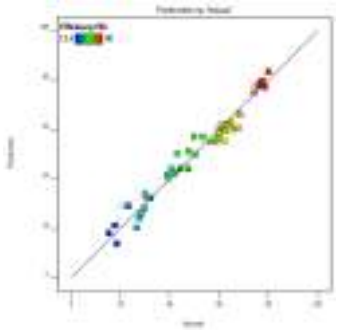

Fig. 6. Predicted and actual values for Mn^{2+} ionsremoval by HAp.

Itcan be seen from Fig. 6 that the data on this plot were reasonably close to a straight line (R^2= 0.9445).Hence, the results suggest that the developed model was adequate in predicting the response variables for the experimental because residual results were distributed near the diagonal line.

3.1.6. Adsorption isotherms

Kinetics study was necessary to determination the removal efficiency and to control the residual time of the total sorption process (Shokry et al., 2016). Sorption experiments were carried out using a solution of manganese with different manganese initial concentrations ranging from 10 to 100 ppm. A series of isotherm models of Langmuir, Freundlichand Harkins-Jura, and Dubinin–Radushkevich were applied to data sets to calculate kinetics. Later, the series of isotherm models were applied to data sets to calculate all kinetic parameters.

Adsorption parameters attained by well-known equation of traditionally known isotherms give useful information about mechanism and properties of adsorption, and tendency of adsorbent toward manganese. The constant parameters of the isotherm equations for this adsorption process and the correlation coefficients (R^2) for conventional isotherms were summarized in Fig. 7.

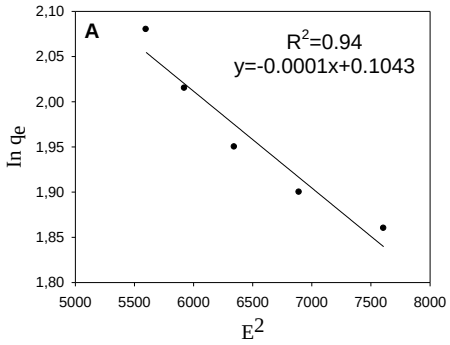

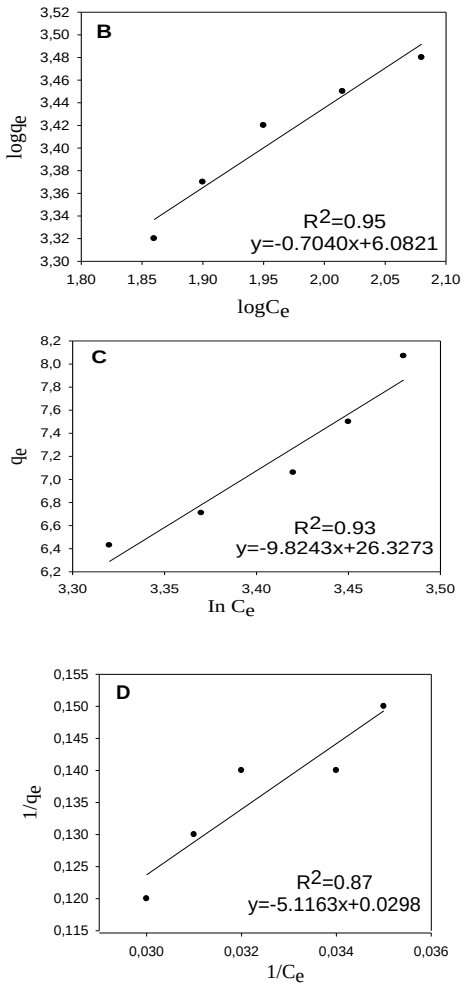

Fig. 7. The isotherm modeling results of Mn^{+2}adsorption with HAp; (A) Dubinin–Radushkevich Isotherm Model, (B) Freundlich Isotherm Model, (C) Harkins-Jura Isotherm Model, (D) Langmuir Isotherm Model.

The constant parameters of the isotherm equations for this adsorption process were calculated by regression using linear form of the isotherm equations. The calculated kinetics parameters of Langmuir, Freundlich, Harkins-Jura, Scartchard and Dubinin–Radushkevich (D-R) Isotherm modelswere given in Table 2.

Table 2. The parameters of isotherm models

Langmuir Isotherm Model		Freundlich Isotherm Model	
$\frac{1}{q_e}=\frac{1}{bq_mC_e}+\frac{1}{q_m}$		$\ln q_e=\ln K_f+\frac{1}{n}\ln C_e$	
q_e (mg/g)	0.20	K_f(mg/g)(L/mg$^{1/n}$)	106.51
b (L/mg)	167.78	n	1.42
R_L	$7.74*10^{-5}$	R^2	0.95
R^2	0.87		
Dubinin–RadushkevichIsotherm Model		Harkins-Jura Isotherm Model	
$\ell n q_e=\ell n Q_s-B\varepsilon^2$		$\frac{1}{q_e^2}=\left(\frac{B}{A}\right)-\left(\frac{1}{A}\right)\log C_e$	
Q_s	14.01	A	5.94
B	0.0001	B	3.76
R^2	0.94	R_2	0.97

Where q_e: amount of adsorbed material, b: Langmuir constant, C_e: equilibrium concentration q_m: monolayer adsorption capacity, K_f and n: Freundlich constants, R: constantand A and B: Harkins-Jura constants, ε =Dubinin–Radushkevich isotherm constant, Q_s = theoretical isotherm saturation capacity (mg/g), K_s = Dubinin–Radushkevich isotherm constant.

According to constant parameters shown in the Table 2, it was observed that the values of n and R_L were all less than 1.0 indicating that adsorption Mn^{+2} was unfavorable. The results show that the degree of fit for the Harkins-Hura model is higher than that for the Freundlich model.

3.1.7. Adsorption kinetics

Kinetic analyses based on well-known models give good and deep knowledge about the rate and mechanism of an adsorption process. The pseudo-first-order, the pseudo second order and intraparticle diffusion models were used to evaluate the fits of the obtained data. The constant parameters and correlation coefficients (R) are summarized in Table 3 and and Fig. 8.

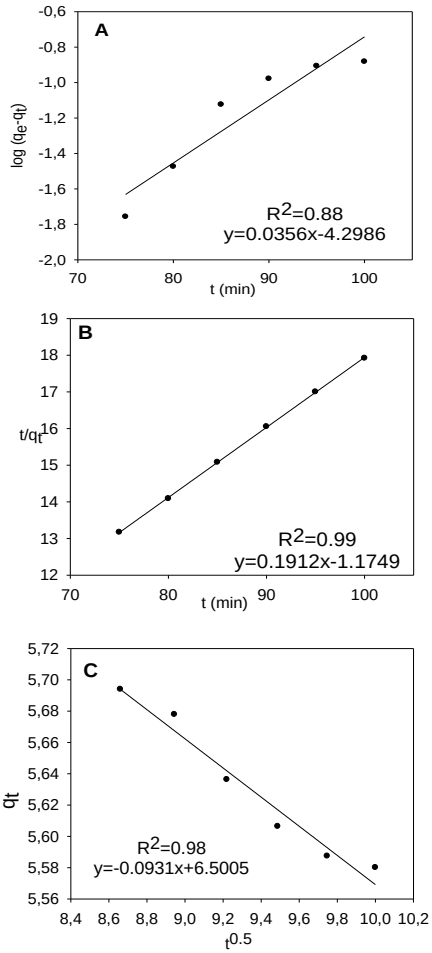

Fig. 8. The kinetic modeling results of PO_4^{3-} adsorption with HAp; (A) Pseudo-first-order kinetic model, (B) Pseudo-second-order kinetic model, (C) Intraparticle diffusion model.

As can be seen from Table 3 that correlation coefficient for pseudo-second-order model is larger than correlation coefficients for pseudo-first order and intraparticle diffusion models.

Table 3. The parameter of kinetic models

Pseudo-First Order Kinetic Model	
$\log(q_e - q_t) = logq_e - \frac{k_1}{2.303} * t$	
k_1 (l/min)	0.08
qe (mg/g)	0.6
R^2	0.88
Pseudo-Second Order Kinetic Model	
$\frac{1}{q_t} = \left[\frac{1}{k_2 * q_e^2}\right] + \frac{1}{q_e} * t$	
k_2(l/min)	0.03
qe (mg/g)	5.23
R^2	0.99
Intraparticle Diffusion Model	
$q_e = k_p t^{0.5} + C$	
k_p(g.dk$^{0.5}$)	0.09
C (mg/g)	6.5
R^2	0.98

Where; k_1: the pseudo first-order rate constant, k_2: the pseudo second-order rate constant, k_p: intra-particle diffusion rate constant, C: boundary layer thickness.

Pseudo-second-order model for Mn^{2+} adsorption demonstrates the chemisorption may be the rate-limiting step.

4. CONCLUSION

Although manganese is an essential element for human life, its concentration above a certain level in the environment can pose danger. The objective of the study was to investigate the application of the composite adsorbent for the removal of manganese from drinking water with HAp using the response surface methodology. The influences of experimental parameters on the removal percentage were investigated using CCD combined with RSM.

The variations of pH values showed that the governing factors affecting at low pH values; maximum adsorption has reached at pH 8. As it was cleared that the amount of pH value was increased from 6 g to 8, removal efficiency of the Mn^{2+} ion increased from 30% to 80%, respectively. Although magnesium removal is high at pH 8 in drinking water, pH 7.40 is accepted as the optimum pH value considering the pH values of drinking water.

The removal of Mn significantly increased in the HAp. The removal efficiency of 73 mg/L initial Mn^{+2} ions concentration increased from 17,82% to 68.53% when the dose of HAp was increased from 0.15 to 0.75 g in same pH value at 105 min.

Under the optimized conditions of a 73 mg/L Mn^{+2} ions concentration, 1 g HAp, a pH value of 7.40 and at 75 min, the degradation efficiency of heavy metal approached almost 80%.

REFERENCES

Adeleke, A. O., Al-Gheethi, A. A., and Daud, Z. (2017). "Optimization of operating parameters of novel composite adsorbent for organic pollutants removal from POME using response surface methodology." *Chemosphere*, Vol.174, pp. 232-242.

Ali, R. M., Hamad, H. A., Hussein, M. M., and Malash, G. F. (2016). "Potential of using green adsorbent of heavy metal removal from aqueous solutions: adsorption kinetics, isotherm, thermodynamic, mechanism and economic analysis." *Ecological Engineering*, Vol.91, pp.317-332.

Arulkumar M., Sathishkumar P., and Palvannan T. (2011). "Optimization of orange G dye adsorption by activated carbon of thespesiapopulnea pods using response surface methodology." *Journal of Hazardous Materials*, pp. 186 - 827.

Asasian, N., Kaghazchi, T., and Soleimani, M. (2012). "Elimination of mercury by adsorption onto activated carbon prepared from the biomass material." *Journal of Industrial and Engineering Chemistry*, Vol.18, No. 1, pp.283-289.

Aschner, M., Guilarte, T.R., Schneider, J.S., and Zheng W., (2007). "Contemporary issues in manganese: recent advances in understanding its transport and neurotoxicity," *Toxicol. Appl. Pharmacol.*, Vol.221 pp.131–147.

Baptista, J.N., Smith, B.J., and McAllister, J.J. (2000). "Heavy metal concentrations in surface sediments in a nearshore environment, Jurujuba Sound, Southeast Brazil." *Environmental Pollution*, Vol. 109, No. 1, pp. 1-9.

Ecer, Ü. and Sahan, T. (2018). "A response surface approach for optimization of Pb(II) biosorption conditions from aqueous environment with Polyporussquamosus fungi as a new biosorbent and kinetic, equilibrium and thermodynamic studies." *Desalin. Water Treat.*, Vol.102, pp. 229-240.

Elmi, F., Chenarian-Nakhaei, R., and Alinezhad, H. (2018). "Conversion of fisheries waste as magnetic hydroxyapatite bionanocomposite for the removal of heavy metals from groundwater." *Water Science and Technology: Water Supply*, Vol. 18 No. 4, pp. 1406-1419.

Ghosh, A., Das, P., and Sinha, K. (2015). "Modeling of biosorption of Cu(II) by alkali-modified spent tea leaves using response surface methodology (RSM) and artificial neuralnetwork (ANN)." *Appl.Water Sci.* Vol.5, pp.191–9.

Hamilton, G., Chiswell, B., Terry, J., Dixon, D., and Sly, L., (2013). "Filtration and manganese removal." *Journal of Water Supply: Research and Technology-AQUA*, Vol.62, No. 7, pp.417-425.

Ibrahim, M., Labaki, M., Giraudon, J.M., and Lamonier, J.F., (2020). "Hydroxyapatite, a multifunctional material for air, water and soil pollution control: A review."

Journal of Hazardous Materials, Vol. 389, pp. 1-18.

Kausar, A. and Ashraf, A. (2017). "Batch versus column modes for the adsorption of radioactive metal onto rice husk waste conditions optimization through response surface methodology." *Water Science Technology*, Vol.76, pp. 1035-1043.

Karri, R.R. and Sahu, J.N. (2018). "Modeling and optimization by particle swarm embedded neural network for adsorption of zinc (II) by palm kernel shell based activated carbon from aqueous environment." *Journal of Environmental Management.,* Vol. 206, pp.178-191.

Kenari, S.L.D., Shabanian, J., and Barbeau, B. (2019). "Dynamic modeling of manganese removal in a pyrolusite fluidized bed contactor." *Water Research*, Vol.154, pp. 125-135.

Krestou, A., Xenidis, A., and Panias, D. (2004). "Mechanism of aqueous uranium (VI) uptake by hydroxyapatite." *Minerals Engineering*,Vol.17, No. 3, pp.373-381.

Li, G., Ding, Y., Xu, H., Jin, J., and Shi, B., (2018). "Characterization and release profile of (Mn, Al)-bearing deposits in drinking water distribution systems." *Chemosphere*, Vol.197, pp. 73-80.

Nadaska, G., Lesny, J., Michalik, I., (2015). "Environmental aspect of manganese chemistry." *HEJ ENV*, 100702-A.

Oliveira, H.L., Da Rosa, W.L.O., and Cuevas-Suárez, C.E., (2017). "Histological evaluation of bone repair with hydroxyapatite: a systematic review." *Calcif. Tissue Int.* Vol. 101 (4), pp. 341–354.

Pandi K., and Viswanathan, N., (2014). "Synthesis of alginate bioencapsulated nano-hydroxyapatite composite for selective fluoride sorption." *Carbohydr. Polym.* Vol. 112, pp. 662–667.

Pandi, K., and Viswanathan, N., (2015). "In situ precipitation of nano-hydroxyapatite in gelatin polymatrix towards specific fluoride sorption, I*nt. J. Biol. Macromol*. Vol. 74, pp. 351–359.

Patil, D. S., Chavan, S. M., and Oubagaranadin, J. U. K. (2016). "A review of technologies for manganese removal from wastewaters." *Journal of Environmental Chemical Engineering*, 4 (1), 468-487.

Patnaik, P. (2002), *Handbook of Inorganic Chemicals*, McGraw-Hill, New York, pp. 538–540.

Roosta, M., Ghaedi, M., Daneshfar, A., and Sahraei, R. (2014). "Experimental design based response surface methodology optimization of ultrasonic assisted adsorption of safaranin O by tin sulfide nanoparticle loaded on activated carbon." *SpectrochimicaActa Part A: Molecular and Biomolecular Spectroscopy*, Vol. 122, pp. 223-231.

Sayilgan, E., Kukrer, T., Yigit, N. O., Civelekoglu, G., and Kitis, M. (2010). "Acidic leaching and precipitation of zinc and manganese from spent battery powders using various reductants." *Journal of Hazardous Materials*, Vol. 173, No.1-3, pp. 137-143.

Shokry, H., and Hamad, H. (2016). "Effect of superparamagnetic nanoparticles on the physicochemical properties of nano hydroxyapatite for groundwater treatment: adsorption mechanism of Fe (II) and Mn (II)." *RSC Advances*, Vol. 6, No. 85, pp. 82244-82259.

Singh K.P., Gupta S., Singh A.K., and Sinha S. (2011). "A Kinetic study of anaerobic biodegradation of food and fruit residues during biogas generation using initial rate method." *Journal of Hazardous Materials*, Vol. 186, pp. 1462-1470.

Sly, L., Hodgkinson, M., and Arunpairojana, V., (1990). "Deposition of manganese in a drinking water distribution system." Application. *Environment. Microbiology*, Vol.56,No. 3, pp. 628-639.

Taheri, M., Moghaddam, M.R.A. and Arami, M. (2012). "Optimization of acid black 172 decolorization by electrocoagulation using response surface methodology." *Iranian J.Environ.HealthSci.Eng.* pp. 923-31.

TSE-266. (2005). "İnsanitüketimamaçlısular. TürkİçmeSuyuStandartları TS 266 sayılıstandart - TürkStandartlarıEnstitüsü." Ankara, Turkey.

TS EN 196-1 (2009). *Methods of testing cement-Part 1: Determination of strength*, Turkish Standard Institute, Ankara, Turkey.

USEPA. (2003) Health Effects Support Document for Manganese, *U.S. Environmental Protection Agency Office of Water*, Washington, DC EPA 822-R-03-003.

USEPA. (2004), Drinking Water Health Advisory for Manganese, *U.S. Environmental Protection Agency Office of Water*, Washington, DC EPA-822-R-04-003.

Xu, Y., Schwartz, F. W., and Traina, S. J. (1994). "Sorption of Zn^{2+} and Cd^{2+} on hydroxyapatite surfaces." *Environmental Science and Technology*, Vol.28, No. 8, pp. 1472-1480.

World Health Organization(2011). *Guidelines for drinking water quality*, p. 226.

Zendehdel, M., Shoshtari-Yeganeh, B., Khanmohamadi, H., and Cruciani, G. (2017). "Removal of fluoride from aqueous solution by adsorption on NaP: HAp nanocomposite using response surface methodology." *Process Safety and Environmental Protection*, Vol. 109, pp. 172-191.

Zhang, L., Zhang, C., Zhang, R., Jiang, D., Zhu, Q., and Wang, S. (2019). "Extraction and characterization of HA/β-TCP biphasic calcium phosphate from marine fish." *Materials Letters*, Vol. 236, pp. 680-682.

CISET - 2nd Cilicia International Symposium on Engineering and Technology
10-12 October, 2019, Mersin / TURKEY

PHOSPHATE REMOVAL FROM WATER WITH HYDROXYAPATITE SYNTHESIZED FROM FISH BONE USING RESPONSE SURFACE METHODOLOGY

Behsat Ozan Eskikaya [1], Buşra Nur Çiftci [1] and Yağmur Uysal [*1]

[1] Mersin University, Faculty of Engineering, Environmental Engineering, Mersin, Turkey, yuysal@mersin.edu.tr

ABSTRACT

Phosphate (PO_4^{3-}) is one of the major nutrients contributing in the increased eutrophication of lakes and natural waters. Many methods have been developed to remove phosphate ions from aquatic environment. A new method of phosphate removal by hydroxyapatite (HAp) has gained increasing interest as the need for the implementation of clean technology. Seed material used for the experiment was prepared by the calcination of fish bones. In this study, the effects of initial phosphate concentration, pH, reaction time and adsorbent dosage were examined for drinking water by batch experiment. The experiment procedures were prepared from fish bones at optimized conditions by employing Central Composite Design (CCD) under Response Surface Methodology (RSM) whereby a model was built to examine the effects of the different parameters. The software gave fifty (50) runs experiment within the conditions. The yield percentages were determined and a standard method of pore size estimation phosphate was used to estimate the adsorption capacity of the calcined fish bones. The results of this study showed that the sorption of phosphate ions was rapid, and the percentage of phosphate sorption was approximately 90% which confirms close to RSM results. The experimental results showed that a good phosphate removal could be achieved by HAp.

Keywords: *Adsorption, Hydroxyapatite, Nanocomposite, Phosphate removal, Response surface methodology*

[*] Corresponding Author

1. INTRODUCTION

Contaminants found in drinking water cover a broad range of physical, inorganic chemical, organic chemical, bacteriological, and radioactive parameters. Principally, many of the same pollutants that play a role in surface water pollution may also be found in polluted groundwater, although their respective importance may differ. Table 1 shows quality classification of surface waters.

Table 1. Quality classification of surface waters (MEB, 2011)

Pollutants	I	II	III	IV
pH	6.5-9.5	6.5-9.5	6-9	6-9
Dissolved Oxygen (mg/L)	8	6	3	< 3
Total Phosphate (mg/L)	0.02	0.16	0.65	> 0.65
NO_2^- - N (mg/L)	5	10	20	> 20
Sodium (mg/L)	125	125	250	> 250
Arsenic (µg/L)	20	50	100	> 100
Manganese (µg/L)	100	500	3000	> 3000

For more than a century, agricultural activities have considerably increased their consumption of phytosanitary and fertilizers products. unfortunately, these are often a source of drinking water pollution, especially for the more soluble ones, namely nitrates and phosphates (Borggaard et al., 2004; Serio et al., 2018). The principal phosphorus compounds in wastewater are generally orthophosphate forms together with smaller amounts of organic phosphate. These phosphorus compounds, dissolved in surface, ground or drinking water, are responsible for the eutrophication in closed water systems, especially in lakes and enclosed bays where the water is almost stagnant (Irdemez et al., 2006). However, many open water sources such as lakes, streams, oceans and reservoirs, are currently experiencing excess of phosphorus from human activities, which can speed up eutrophication in aquatic system and cause water quality impairment, aquatic species biodiversity decrease, adverse human health impacts, and increase the cost of water treatment, etc. (Chislock et al., 2013; Wilkinson, 2017). Phosphate (PO_4^{3-}) ion is an important nutrient for the growth of organisms and it is not categorised as a harmful or toxic element for mankind at low concentrations (Hasim et al., 2019).

Several technologies for the removal of phosphorus from water, including physical adsorption, chemical precipitation, biological decomposition, membrane separation, ion-exchange adsorptions have been reported (Guaya et al., 2015; Lalley et al., 2016; Su et al., 2015; Zhang et al., 2011; He et al., 2018). Several scientists indicated that the biological decomposition is exhibited the high proficiency, but it is costly (Awual et al., 2012; Awual and Jyo, 2009, 2011).

Adsorption is a low cost and effective separation operation that can be used to improve the water quality. In particular, it can be applied as tertiary process to mitigate and remediate the water contamination via the reduction of the concentrations of a variety of micro-pollutants that are present in concentrations from ng to mg per liter (Sholl et al., 2016). The adsorbents directly affect the adsorption efficiency. So far, various types of adsorbents such as activated carbon, clay minerals, chelating materials, hydroxyapatite, biosorbents, or natural zeolites have been developed as adsorbents to eliminate toxins from aqueous solution (Zandipak et al., 2016). Stoichiometric hydroxyapatite ($Ca_{10}(PO_4)_6(OH)_2$) (HAp) is crystallographically similar to the calcium deficient heavily substituted apatites that dominate the composition of the main mineral component of bones and teeth (Teixeira et al., 2009; L. Guo et al., 2003). HAp is a calcium phosphate ceramic with an hexagonal structure and a stoichiometric Ca/P ratio of 1.67 (Kalita et al., 2007; Mostafa et al., 2007). Nano-hydroxyapatite (nHAP) has a large surface area and also Ca on the surface could be easily replaced by heavy metals. Therefore nHAP shows better adsorption performance in the removal of heavy metal for water treatment (Wang et al., 2014; Yang et al., 2016).

2. MATERIAL AND METHOD

2.1. Reagents

Phosphate (PO_4^{3-}, Riedel-de Haën) was used to prepare stock phosphate solutions. Hexane (n-Hexane, Merck) was used to wash all the fish for our study. Different pH values of the solution were adjusted with HCl and NaOH.

2.2. Preparation of adsorbent

In this study, seabreams (*Sparus aurata*) were taken from the fish restaurant in Mersin. As in the study of Zhang et al. (2019), the fish was put into boiling water for 1 h, washed three times with tap water, in order to remove the organic substance and grease attached to the surface of the fish bones. The treated fish bones were dried in an oven at 60°C for 20–30 min to remove residual moisture, then were washed with hexane and distilled water. The fish bones were sintered in muffle furnace at 700 °C for 1 h for calcination. After that, the calcined fish bones were ground using mortar. Finally, the resultant powder was sieved with the mesh about 212 µm as shown in Fig. 1.

2.3. Adsorption experiments

The effects of adsorbent dose, pH, contact time and initial PO_4^{3-} concentration on the adsorption were investigated in batch mode. PO_4^{3-} ions were prepared by solving $NaH_2PO_4.2H_2O$ in tap water and used as stock phosphate solution. Batch adsorption studies were performed in flasks with 100 mL sample volumes. Phosphate solutions with concentrations of 5-70 mg/L were added to flasks. The effect of sorbate to sorbent ratio for the percentage unit phosphate sorbate sorption capacity of the fish bones was determined by varying the solid mass phase in the range of 0.5 g-1.0 g of fish bones. The contents of all erlenmeyer flasks were mixed thoroughly using orbital shaker with a fixed constant speed. The samples were shaked at 150 rpm speed, at 25°C constant room temperature. Then suspension was

separated by centrifugation at 4000 rpm for 5 min, and the remaining concentration of PO_4^{3-} in the solution was determined by spectrophotometer (Hach-Lange DR 3900).

Fig. 1. Synthesis of fish bones adsorbent

The effect of pH on the phosphate sorption by fish bones was evaluated in the range of 6-8. The initial pH of the phosphate solution was adjusted to the desired pH value using 0.1 M HCl or 0.1 M NaOH. This experiment was carried out by determining the amount of the adsorbates adsorbed at various reaction times, ranging from 30 min to 180 min. The factors influencing the conditions of the adsorption process were studied as percentage (%) of PO_4^{3-} removal, and calculated using the following Eq. (1):

$$\% PO_4^{3-} \text{ removal} = ((C_o-C_e)/C_o) \times 100 \quad (1)$$

where C_0 (mg/L) and C_e (mg/L) is the concentration of target at initial and after time *t* respectively.

For the effectiveness and accuracy in results, all the adsorption experiments were conducted in duplicate and average values were reported in this study.

2.4. RSM-CCD model

The experimental data was analyzed and fitted by Response Surface Method (RSM) using Design Expert 12 software. RSM is an efficient technique for process optimization in a minimal experimental runs and which is used to explain the combined effects of all the factors. The effect of different operating parameters such as adsorbent dose, contact time, pH and PO_4^{3-} concentrations, and the interactions between them required full factorial design when the central composite design (CCD) was used to obtain the experimental design matrix. The number of factors *"n"* increases the number of runs for a complete replicate of the design which is given in Eq. (2):

$$N = 2^n + 2n + n_c \quad (2)$$

The CCD consists of a 2^n factorial runs with $2n$ axial runs and n_c center runs. A five-level CCD with four factor (reaction time, amount of adsorbent, pH and initial PO_4^{3-} concentrations) was used to investigate the effects of parameters. The ranges of the independent variables are shown in Table 2.

Table 2. All variables factors in CCD.

Factors	Term.	Unit	Low	High
pH	A	-	6	8
Adsorbent dose	B	g	0.5	1.0
Reaction time	C	min.	30	180
PO_4^{3-} Con.	D	mg/L	5	70

The connection amongst independent and dependent variables was worked in CCD utilizing the second order polynomial model. The recovery percentage was calculated through Eq. (3):

$$Y = \beta_0 + \sum_{i=1}^{k} \beta_i \chi_i \sum_{i=1}^{k} \beta_{ii} \chi_i^2 + \sum_{i=1}^{k} \sum_{j=1}^{k} \beta_{ij} \chi_i \chi_j + \varepsilon \quad (3)$$

where βo is the offset term; βi and βii are the linear and quadratic effects of input factor X_i; βij is the linear effect between the independent factor X_i and X_j; and ε is the error (Roosta *et al.*, 2014).

3. RESULT AND DISCUSSION

3.1. Adsorption studies

3.1.1. Effect of pH on PO_4^{3-} removal

The pH of the solution is one of the most important variables that affect the phosphate sorption on the sorbent. pH value of drinking water is generally between 6.5-9 in Turkish Standards Institute (TSE 226, 2005). Therefore, in this part of the study, the initial pH of the phosphate solution was adjusted from 6 to 8 Fig. 2 shows effect of different pH values on PO_4^{3-} removal with HAp.

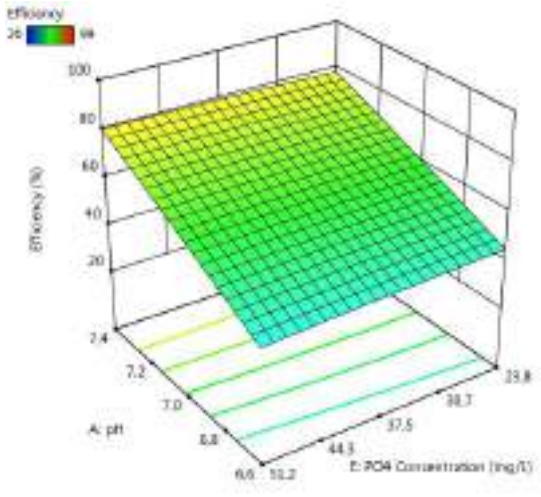

Fig. 2. The effect of adsorbent dosage on the efficiency of PO_4^{3-} removal.

Experimental results show that when the initial pH value of the wastewater increases, the same rate of phosphate removal is observed. A higher pH is more suitable for precipitation of phosphate with calcium as apatite and hydroxyapatite (Irdemez et al., 2006). In literature, phosphate removal increases at high pH values. In the experimental study, pH was considered to be a strong effect, but in this experiment it accounted for approximately 23% of the total effect (Zhang et al., 2014). When the Fig. 2 was examined, phosphate removal increased from 20 to 90% when the pH of drinking water increased from 6 to 8 under the same conditions.

3.1.2. Effect of adsorbent dose and contact time on PO_4^{3-} removal

The relationship between HAp dosage and reaction time was shown in Fig. 3. The removal percentage of phosphate was studied by varying the adsorbent dose between 0.5 and 1 g. The rate of metal sorption by fish bones was determined by analysing the residual phosphate in the supernatant after contact durations of 30 min and 180 min.

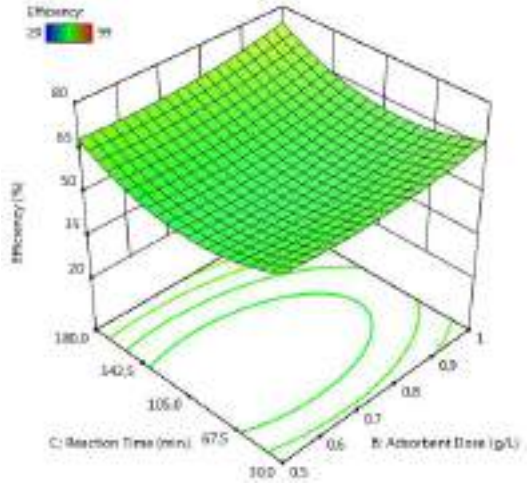

Fig. 3. Effect of fish bones adsorbent dose on the removal of PO_4^{3-} at different reaction time.

The data shows that increasing the adsorbent dose will enhance the adsorption of PO_4^{3-} since the number of phosphate binding sites increase as well at 150 rpm speed on orbital shaker.

Longer contact time provides sufficient duration for the adsorption process to take place and thus enhance the phosphate uptake from the solution onto the phosphate binding sites of the adsorbent. In experiments carried out at the same initial pH value (pH:7), adsorbent dose amount (0,75 g), phosphate concentration (37,5 mg/L), it was observed that the phosphate removal efficiency increased from 50% to 85% when the reaction time was increased from 75 min to 105 min.

3.1.3. Effect of Initial Concentration on PO_4^{3-} Removal

The effect of the initial concentration of PO_4^{3-} was found to be crucial because it had overwhelmed the mass transfer constraints of PO_4^{3-} between the solution and the solid phases. Effect of initial PO_4^{3-} concentration on adsorption process was shown in Fig. 4. Phosphate were initially fixed on the active sites of HAp but further increasing initial PO_4^{3-} concentration caused to decrease of PO_4^{3-} removal due to the saturated active sites on adsorbent. It was clear to see that the q values increase with the increase in the initial PO_4^{3-} concentrations. The adsorption capacity was calculated using mass balance Eq. (4) written as:

$$q = \frac{(C_0 - C_e) \times M}{V} \quad (4)$$

where C_0 (mg/L) is the initial and and C_e (mg/L) is the equilibrium concentrations of PO_4^{3-} concentration**,** respectively. M (g) is the weight of HAp, V (L) is the volume of solution.

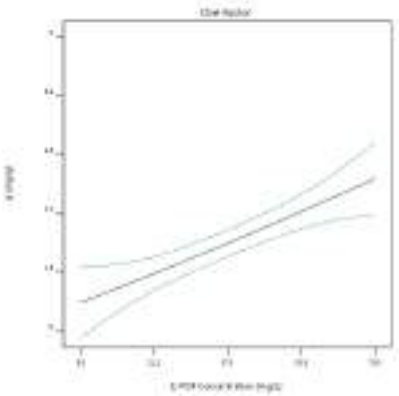

Fig. 4. The effect of between q and PO_4^{3-} concentration

The adsorption capacity of the adsorbents increased up to 50 ppm and its effect began to decrease with increasing phosphate concentrations.

3.1.4. Modeling and Statistical Analysis

All experiments of this study were created using the Response Surface Method (RSM) on Desing Expert 12 software. Initial concentration, pH, adsorbent dosage and contact time are the most important parameters which affect the efficiency of PO_4^{3-} ion by HAp nanomaterials. RSM design was used for exploring different combined parameters and for evaluating the combined effects of those factors. In the present work, linear, two factor interaction (2FI), quadratic and cubic models were used to analysis experimental data in order to obtain the regression equations. The model equation representing efficiency (%) was expressed as functions of pH (A), adsorbent dose (B), reaction time (C) and PO_4^{3-} concentration (D) for coded units as given below Eq. (5):

$$\textbf{\textit{Efficiency (\%) = -401.34 + 82.86 A + 83.98 B + 0.07 C -1.17 D – 20.81 A*B – 0.04 A*C + 0.25 A*D – 0.04 B*C + 0.13 B*D – 0.002 C*D – 2.24 A² + 42.42 B² + 0.001C²-0.001D²}} \quad (5)$$

The adequacy of the selected model and statistical significance of the regression coefficients were tested using the analysis of variance (ANOVA). ANOVA is a

statistical technique that subdivides the total variation in a set of data into component parts associated with specific sources of variation for the purpose of testing hypotheses on the parameters of the model. Data were also analyzed to check the normality of the residuals, as shown in Fig. 5.

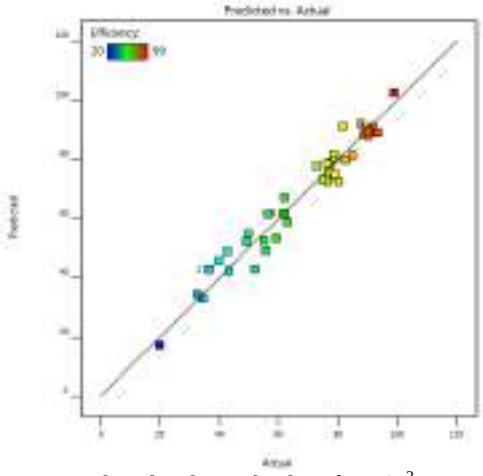

Fig. 5. Predicted and actual values for PO_4^{3-} removal by HAp.

It can be seen from Fig. 5 that the data on this plot were reasonably close to a straight line (R^2= 0.9649). Hence, the results suggest that the developed model was adequate in predicting the response variables for the experimental because residual results were distributed near the diagonal line.

3.1.5. Adsorption isotherms

Kinetics study which was necessary for determination the efficiency and control the residual time of the total sorption process (Shokry et al., 2016). Sorption experiments were carried out using a solution of phosphate with different phosphate initial concentrations ranging from 5 to 70 ppm. A series of isotherm models of Langmuir, Freundlich and Harkins-Jura and Scartchard were applied to data sets to calculate kinetics. Later, the series of isotherm models were applied to data sets to calculate all kinetics parameters.

Adsorption parameters attained by well-known equation of traditionally known isotherms give useful information about mechanism and properties and tendency of adsorbent toward phosphate. The constant parameters of the isotherm equations for this adsorption process and the correlation coefficient (R^2) for conventional isotherms based on known equation and requirement are summarized in Fig. 6.

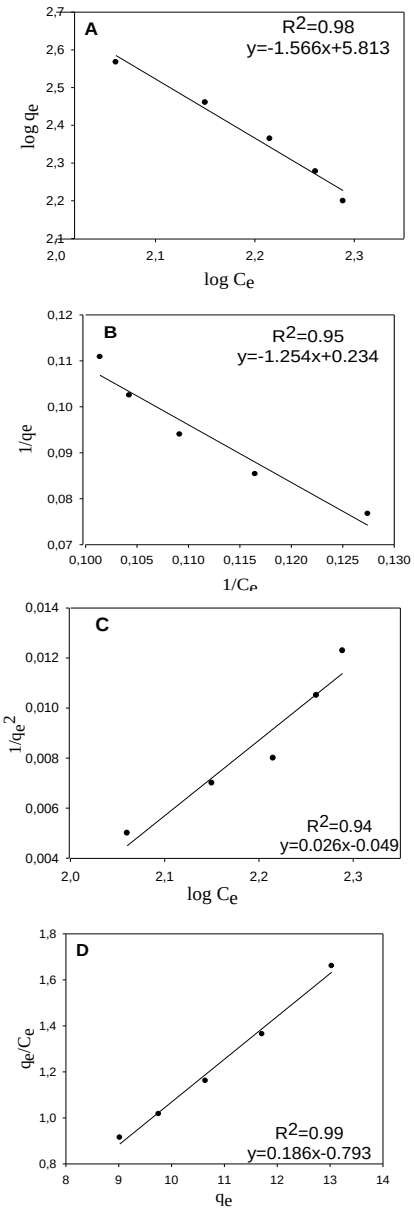

Fig. 6. The isotherm modeling results of PO_4^{3-} adsorption with HAp; (A) Freundlich Isotherm Model, (B) Langmuir Isotherm Model, (C) Harkins-Jura Isotherm Model, (D) Scartchard Isotherm Model

The constant parameters of the isotherm equations for this adsorption process were calculated by regression using linear form of the isotherm equations. Models the calculated kinetics parameters using Langmuir, Freundlich, Harkins-Jura and Scartchard for HAp is given in Table 3.

Table 3. The parameters of isotherm models

Langmuir Isotherm Model		Freundlich Isotherm Model	
$\frac{1}{q_e}=\frac{1}{bq_mC_e}+\frac{1}{q_m}$		$Inq_e = InK_f + \frac{1}{n}InC_e$	
q_e (mg/g)	0.80	K_f (mg/g)(L/mg$^{1/n}$)	650
b (L/mg)	5.34	n	0.63

R_L	$3.73*10^{-3}$	R^2	0.98
R^2	0.95		

Scartchard Isotherm Model		Harkins-Jura Isotherm Model	
$\frac{q_e}{C_e} = Q_s . K_s - q_e . K_s$		$\frac{1}{q_e^2} = \left(\frac{B}{A}\right) - \left(\frac{1}{A}\right) \log C_e$	
Q_s	4.26	A	38.46
K_s	0.186	B	1.88
R^2	0.99	R_2	0.94

Where q_e: amount of adsorbed material, b: Langmuir constant, C_e: equilibrium concentration q_m: monolayer adsorption capacity, K_f and n: Freundlich constants, R: constant, A and B: Harkins-Jura constants, Q_s = theoretical isotherm saturation capacity (mg/g),.

According to constant parameters shown in the Table 2, it was observed that the values of n and R_L were all less than 1.0 indicating that adsorption PO_4^{3-} was unfavorable. The results show that the degree of fit for the Scartchard isotherm model is higher than that for the Freundlich and Langmuir isotherm model.

3.1.6. Adsorption kinetics

Kinetic analyses based on well-known models give good and deep knowledge about the rate and mechanism of an adsorption process. The pseudo-first-order, the pseudo second order and intraparticle diffusion models were used to evaluate the fits of the obtained data. The constant parameters and correlation coefficients (R) are summarized in Table 4 and Fig. 7.

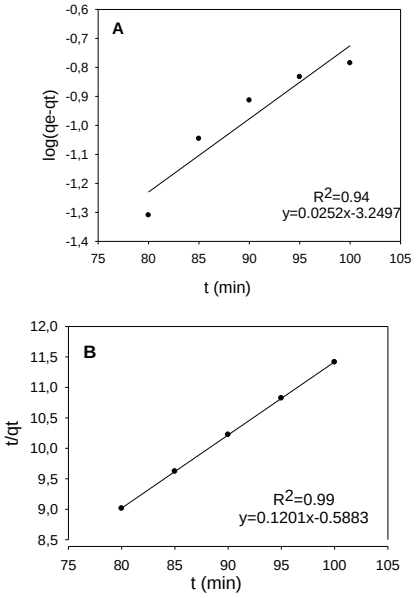

Fig. 7. The kinetic modeling results of PO_4^{3-} adsorption with HAp; (A) Pseudo-first-order kinetic model, (B) Pseudo-second-order kinetic model

As can be seen from Table 4 that correlation coefficient for pseudo-second-order model is larger than correlation coefficients for pseudo-first order and intraparticle diffusion models.

Table 4. The parameter of kinetic models

Pseudo-First Order Kinetic Model	
$\log(q_e - q_t) = log q_e - \frac{k_1}{2.303} * t$	
k_1 (l/min)	0.05
qe (mg/g)	0.46
R^2	0.94

Pseudo-Second Order Kinetic Model	
$\frac{1}{q_t} = \left[\frac{1}{k_2 * {q_e}^2}\right] + \frac{1}{q_e} * t$	
k_2 (l/min)	0.025
qe (mg/g)	8.32
R^2	0.99

Where; k_1: the pseudo first-order rate constant, k_2: the pseudo second-order rate constant, k_p: intra-particle diffusion rate constant, C: boundary layer thickness.

Pseudo-second-order model for PO_4^{3-} adsorption demonstrates the chemisorption may be the rate-limiting step.

4. CONCLUSION

The objective of this study is to explore using CCD combined with response surface methodology (RSM) to model phosphate removal from drinking water by the nanocomposite adsorbent as HAp.

The variations of pH values showed that the governing factors affecting at low pH values; maximum adsorption has reached at pH 8. As it was cleared that the amount of pH value was increased from 6 g to 8, removal efficiency of the PO_4^{3-} increased from 20% to 90%, respectively.

When the effect of the adsorbent dose on phosphate removal is considered, the increase in the adsorbent dose increased the phosphate binding capacity in drinking water. Increasing the amount of adsorbent dose in drinking water did not cause a significant increase in phosphate removal under the same experimental conditions. However, the effect of the reaction time on the increased adsorbent dose is avoided in addition to the effect of the adsorbent dose. Phosphate removal increased with increasing reaction time was approximately 40%. However, in real scale studies, the optimum reaction time was determined as 75 minutes considering the acceptable efficiency amount, since no working conditions were desired at high minutes in terms of cost. When all efficiency values were examined, the optimum adsorbent dose was 0.5 g and the reaction time was 75 minutes.

Under the optimized conditions of a 50 mg/L PO_4^{3-} concentration, 0.5 g HAp, a pH value of 7.40 and at 75 min, the degradation efficiency of phosphate removal approached almost 90%.

REFERENCES

Awual, M. R. and Jyo, A. (2009). "Rapid column-mode removal of arsenate from water by crosslinked poly(allylamine) resin." *Water Res.* Vol.43, pp. 1229-1236.

Awual, M.R. and Jyo, A. (2011). "Assessing of phosphorus removal by polymeric anion exchangers." *Desalination,* Vol. 281, pp. 111-117.

Borggaard, O. K., Szilas, C., Gimsing, A. L., and Rasmussen, L. H. (2004). "Estimation of soil phosphate adsorption capacity by means of a pedotransfer function." *Geoderma*, Vol. 118 No. 1-2, pp. 55-61.

Chislock, M. F., Doster, E., Zitomer, R. A., and Wilson, A. E. (2013). "Eutrophication: causes, consequences, and controls in aquatic ecosystems." *Nature Education Knowledge*, Vol. 4, No. 4, pp.10.

Guaya, D., Valderrama, C., Farran, A., Armijos, C., and Cortina, J. L. (2015). "Simultaneous phosphate and ammonium removal from aqueous solution by a hydrated aluminum oxide modified natural zeolite." *Chemical Engineering Journal,* Vol. 271, pp. 204-213.

Guo, L., Huang, M. and Zhang, X. (2003). "Effects of sintering temperature on structure of hydroxyapatite studied with Rietveld method." *Journal of Materials Science: Materials in Medicine,* Vol. 14, No. 9, pp. 817-822.

Hashim, K. S., Al Khaddar, R., Jasim, N., Shaw, A., Phipps, D., Kot, P., and Alawsh, R. (2019). Electrocoagulation as a green technology for phosphate removal from River water. Separation and Purification Technology, Vol. 210, pp. 135-144.

He, Y., Lin, H., Dong, Y., Li, B., Wang, L., Chu, S. and Liu, J. (2018). "Zeolite supported Fe/Ni bimetallic nanoparticles for simultaneous removal of nitrate and phosphate: synergistic effect and mechanism." *Chemical Engineering Journal,* Vol. 347, pp. 669-681.

Irdemez, Ş., Demircioğlu, N. and Yildiz, Y. Ş. (2006). "The effects of pH on phosphate removal from wastewater by electrocoagulation with iron plate electrodes." *Journal of hazardous materials*, Vol. 137, No. 2, pp. 1231-1235.

Kalita, S.J., Bhardwaj, A. and Bhatt, H.A. (2007). ''Nanocrystalline calcium phosphate ceramics in biomedical engineering, Mater.'' *Sci. Eng.* Vol. 27, No. 3, pp. 441–449.

Lalley, J., Han, C., Li, X., Dionysiou, D. D. and Nadagouda, M. N. (2016). "Phosphate adsorption using modified iron oxide-based sorbents in lake water: kinetics, equilibrium, and column tests." *Chemical Engineering Journal,* Vol. 284, pp. 1386-1396.

MEB. (2011). *Çevre Sağlığı-Suların Analiz Parametreleri,* Ankara.

Mostafa, N. Y. and Brown, P. W. (2007). ''Computer simulation of stoichiometric hydroxyapatite: structure and substitutions, J. Phys.'' *Chem. Solids*, Vol. 68, No. 3, pp. 431–437.

Roosta, M., Ghaedi, M., Daneshfar, A. and Sahraei, R. (2014). "Experimental design based response surface methodology optimization of ultrasonic assisted adsorption of safaranin O by tin sulfide nanoparticle loaded on activated carbon." *Spectrochimica Acta Part A: Molecular and Biomolecular Spectroscopy*, Vol. 122, pp. 223-231.

Serio, F., Miglietta, P.P., Lamastra, L., Ficocelli, S., Intini, F., De Leo, F. and De Donno, A. (2018). ''Groundwater Nitrate Contamination And Agricultural Land Use: A Grey Water Footprint Perspective In Southern Apulia Region (Italy).'' *Sci. Total Environ.* Vol. 645, pp. 1425–1431.

Shokry, H. and Hamad, H. (2016). "Effect of superparamagnetic nanoparticles on the physicochemical properties of nano hydroxyapatite for groundwater treatment: adsorption mechanism of Fe (II) and Mn (II)." *RSC Advances*, Vol. 6, No. 85, pp. 82244-82259.

Sholl, D. S. and Lively, R. P. (2016). ''Seven Chemical Separations to Change the World.'' *Nature* Vol. 532, pp. 435–437.

Su, Y., Yang, W., Sun, W., Li, Q. and Shang, J.K. (2015). ''Synthesis of mesoporous ceriumezirconium binary oxide nanoadsorbents by a solvothermal process and their effective adsorption of phosphate from water.'' *Chem. Eng*. J. Vol. 268, pp. 270-279.

TSE-266. (2005). *İnsani tüketim amaçlı sular. Türk İçme Suyu Standartları TS 266 sayılı standart -Türk Standartları Enstitüsü.* Ankara, Turkey.

Yang, Z., Fang, Z., Zheng, L., Cheng, W., Tsang, P.E., Fang, J. and Zhao, D. (2016). ''Remediation of lead contaminated soil by biochar-supported nano-hydroxyapatite.'' *Ecotoxicol. Environ. Saf.* Vol. 132, pp. 224-230.

Wang, L., Li, Y., Li, H., Liao, X., Wei, B., Ye, B., Zhang, F., Yang, L., Wang, W. and Krafft, T. (2014). ''Stabilize lead and cadmium in contaminated soils using hydroxyapatite and potassium chloride.'' *Environ. Monit. Assess.* Vol. 186, No. 12, pp. 9041-9050.

Zandipak R. and Sobhanardakani S. (2016). ''Synthesis of $NiFe_2O_4$ nanoparticles for removal of an ionic dyes from aqueous solution.'' *Desalin Water Treat.* Vol. 57, No. 24, pp. 11348–60

Zhang, L., Zhang, C., Zhang, R., Jiang, D., Zhu, Q. and Wang, S. (2019). "Extraction and characterization of HA/β-TCP biphasic calcium phosphate from marine fish." *Materials Letters*, Vol. 236, pp. 680-682.

Zhang, J., Shen, Z., Shan, W., Mei, Z. and Wang, W. (2011). "Adsorption behavior of phosphate on lanthanum (III)-coordinated diamino-functionalized 3D hybrid mesoporous silicates material." *J. Hazard Mater.* Vol. 186, pp. 76-83.

Zhang, Y. and Pan, B. (2014). "Modeling batch and column phosphate removal by hydrated ferric oxide-based nanocomposite using response surface methodology and artificial neural network." *Chemical Engineering Journal*, Vol. 249, pp. 111-120.

Treatment of Wastewater resulted from Printing Processes in Corrugated Cardboard Production

Diğdem YAR[1], Fatma DENİZ[2] and Mehmet Ali MAZMANCI[3]

[1] Mersin University, Engineering Faculty, Environmental Engineering Department, Mersin, TURKEY
e-mail: digdemyar@outlook.com

[2] Mersin University, Engineering Faculty, Environmental Engineering Department, Mersin, TURKEY
e-mail: fatmadeniz@mersin.edu.tr

[3]Mersin University, Engineering Faculty, Environmental Engineering Department, Mersin, TURKEY
e-mail: mazmanci@mersin.edu.tr

ABSTRACT

Corrugated cardboard factories produce in order to meet the packaging needs of many sectors. Production consists of two stages: gluing and printing. As a result of gluing processes, wastewater with starch content and as a result of printing processes with dye content is formed. In this study, treatment of raw wastewater (RW) caused by printing processes by coagulation method was investigated. In the study, coagulant type ($FeCl_3$, $FeSO_4$, $Al_2(SO_4)_3$), coagulant ratio (1, 2, 3, 5%), pH (6.0, 6.5, 7.0, 7.5), mixing speed (30, 60, 90, 120, 150 rpm), mixing time (3, 5, 7 min) and settling time (15, 30, 45 min) parameters were optimized.

High rate of treatment was obtained by adding $Al_2(SO_4)_3$ to waste water. Optimum working conditions were determined as original pH (7.3), 30 rpm mixing speed, 5 minutes mixing time and 15 minutes settling time. In optimum conditions, 87, 98 and 99% removal of COD, color and phenol were achieved respectively.

Keywords:*Corrugated board, coagulation, optimization, treatment, COD, color, phenol*

1. INTRODUCTION

Today, cardboard packaging is used in many sectors (food, electronic goods, etc.) to protect its products. These packages are mostly corrugated types. Starch based adhesives are used in their production. During the production of corrugated board, wastewater with high pollution load is formed in the preparation of starch pulp, in forming the corrugated shape and in combining them into corrugated board. In the same way, it is seen that colored wastewater is formed due to the printing of corrugated cardboard produced on demand of the customers. As a result, in the production of corrugated cardboard, wastewater consists of two main sources: *Bonding* and *Printing* (Tezakıl, 2013). The wastewater generated after production is brought together and treated (Gengeç, 2017; Karabacakoğlu and Tezakıl, 2012; Renault et al., 2009; Pozzi et al., 2014; Mansour and Kesentini, 2008). In this study, coagulation treatment of wastewater resulting from printing processes was studied.

2. MATERIAL VE METHODS

In this study, wastewater formed during printing processes of corrugated board production was used as material from Ova Oluklu Mukavva Ambalaj Sanayi ve Ticaret A.Ş. in Tarsus.

Optimization studies (coagulant type, coagulant ratio, pH, mixing time, mixing speed and settling time) were investigated (Table 1).Stock solutions at 50 g / L concentration were prepared for each coagulant and final ratios of coagulants in raw wastewater (RW) were showed in Table 1. 200 mL samples were used in the experiments.

Table 1. Optimized parameters

Coagulant Type	$Al_2(SO_4)_3$, $FeCI_3$, $FeSO_4$
Coagulant Ratio(%)*	1-2-3-5
pH	6,0-6,5-7,0-**7,3****-7,5
Mixing Time(min)	3, 5, 7
Mixing Speed(rpm)	30-60-90-120-150
Settling Time (min)	15-30-45

*: Final ratios in RW; **:The value of original pH of RW

pH, conductivity, COD (Standard Methods Closed Reflux, Colorimetric Method, 5220 D), color (Standard Methods 204 B) and phenol (Folin and Ciocalteu, 1927) analyses were performed during the study.

The removal efficiency was calculated using the following formula (COD values; COD_0initial andCOD_aafter processing)

$$\text{Removal efficiency}(\%)=\frac{COD_0-COD_a}{COD_0}*100$$

3. RESULTS AND DISCUSSION

The pH, conductivity, COD, color and phenol analysis results of the original wastewater from printing processes are given in Table 2.

Table 2. Characteristics of Raw Wastewater (RW)

Parameters	Values
pH	7.30
Conductivity	2.50mS/cm
COD	5.520mg/L
Color	16.000pt-Co mg/L
Phenol	1.180mg/L

3.1. OPTIMIZATION of COAGULATING TYPE

The original pH value of the raw wastewater was used and the coagulant ratio is set to1% for each coagulant. It was stirred at 30 rpm for 5 minutes and allowed to settle for 15 minutes.

Flock formation was observed in alum treated wastewater. In COD removal, removal efficiencies were found 31, 17 and 28% for alum, $FeSO_4$, $FeCl_3$, respectively. High yields from color and phenol removal were achieved with alum (Figures 1a and b). In the studies using alum, high removal efficiencies were observed in color and phenol removal.

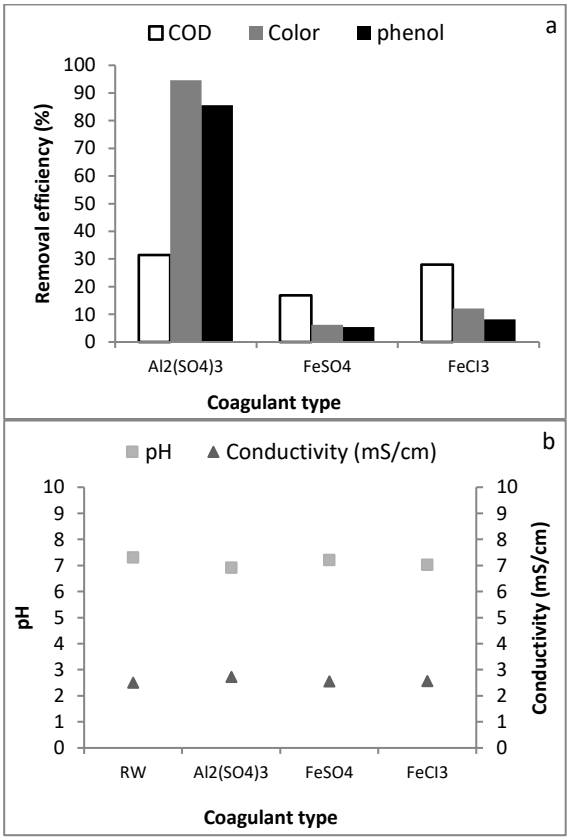

Figure 1.Effect of coagulant type on COD, color and phenol removal (a) and pH, conductivity (b)

Flock formation was observed in alum treated wastewater. In COD removal, removal efficiencies were found 31, 17 and 28% for alum, FeSO4, FeCl3, respectively. High yields from color and phenol removal were achieved with alum (Figures 1a and b). In the

studies using alum, high removal efficiencies were observed in color and phenol removal.

In the optimization of coagulant type, the highest removal efficiency was obtained with alum which was 31, 94 and 85% removal of COD, color and phenol, respectively.

3.2. OPTIMIZATION of COAGULATION RATIO

Coagulant ratio optimization studies were performed by alum because of obtaining the highest removal efficiency. The original pH value of the raw wastewater was used. Alum was added (final ratio as 1, 2, 3 and 5%), then experimental sets were mixed for 5 minutes at 30 rpm, allowed to settle for 15 minutes (Figure 2).

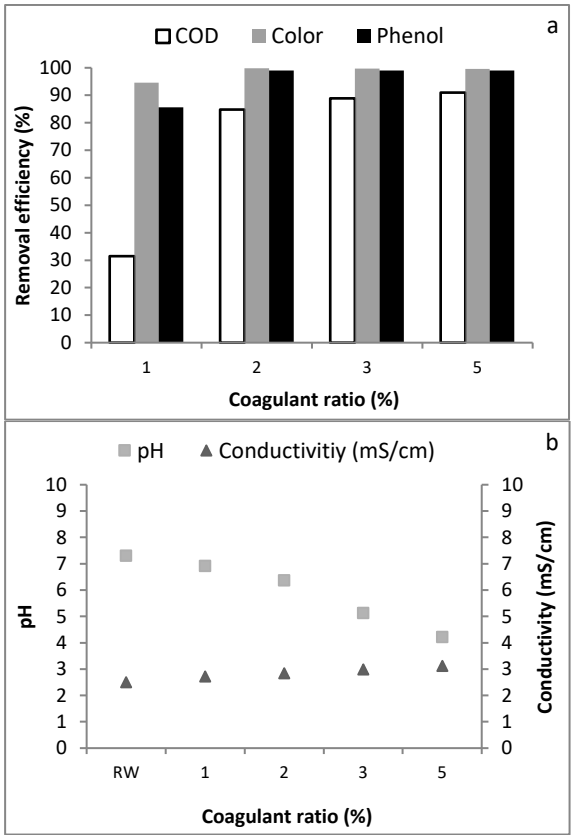

Figure 2. Effect of coagulant ratio on COD, color, phenol removal (a) and pH, conductivity (b)

In this experiment where different ratios of alum (1, 2, 3 and 5%) were used, 31, 85, 89 and 91% COD removal was obtained respectively (Figure 2a). Removal efficiency was obtained 95-99% for color removal and 85-99% for phenol removal. It was observed that pH decreased with increasing amount of alum added to raw wastewater, in contrast, the conductivity value increased (Figure 2b).

The results showed that 2% alum ratio was the optimum ratio for COD, color and phenol removal and this ratio was used for followed experiments.

3.3. pH OPTIMIZATION

In pH optimization (6.0, 6.5, 7.0, 7.3 and 7.5), alum was added to the raw wastewater, the wastewater was stirred for 5 minutes at 30 rpm and allowed to settle for 15 minutes (Figure 3).

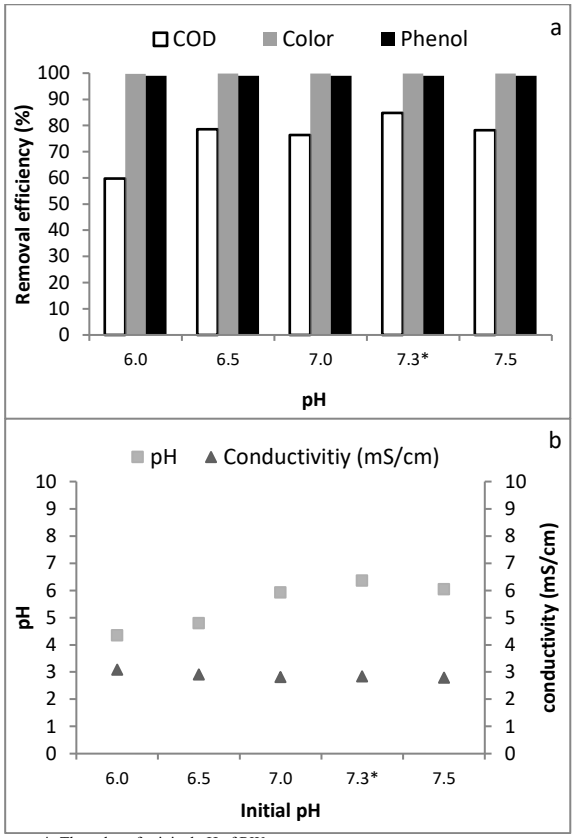

*: The value of original pH of RW

Figure 3. Effect of pH on COD, color, phenol removal (a) and pH, conductivity (b) in wastewater treatment

85% COD removal was achieved in the experiment carried out at the original pH of the raw wastewater. However, COD removal efficiency decreased to 60% in wastewater with pH lower than original pH. Color and phenol removal efficiency reached 99% at all pH values (Figure 3a).The initial pH value of the wastewater was reduced by the addition of coagulant (Figure 3b).

Optimum pH for treatment was found to be the original pH of the raw wastewater.

3.4. OPTIMIZATION of MIXING TIME

Mixing time optimization experiments were performed by adding alum to the raw wastewater (pH 7.3). The mixture was then stirred at 30 rpm for 3, 5 and 7 minutes, then allowed to settle for 15 minutes (Figure 4).

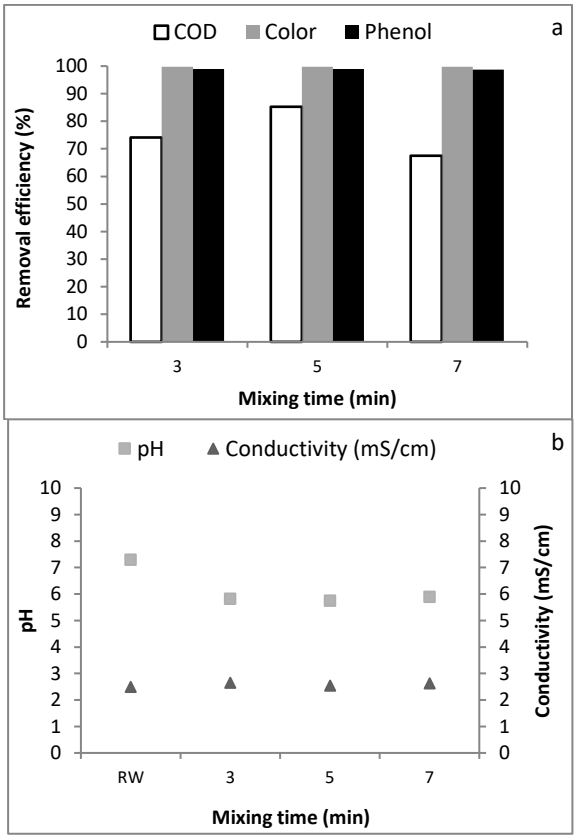

Figure 4. Effect of mixing time on COD, color, phenol removal (a) and pH, conductivity (b)

The mixing times of 3, 5 and 7 minutes resulted in 74, 85 and 67% COD removal, respectively. It was observed that strong flocks were formed at 5 minutes, but the flock structures were dispersed with increasing time.In all experiments, removal efficiency reached 99% for color and phenol (Figure 4a).The mixing time was found to have no effect on pH and conductivity (Figure 4b).

3.5. OPTIMIZATION of MIXING SPEED

It was stirred for 5 minutes at 30, 60, 90, 120 and 150 rpm and allowed to settle for 15 minutes, after addition of alum to the raw wastewater (Figure 5).

85, 76, 87, 86 and 78% COD removal was achieved with a mixing speed of 30, 60, 90, 120 and 150 rpm, respectively. Dispersion of the flock structures at 150 rpm caused a decrease in COD removal. 99% removal of color and phenol was obtained (Figure 5a).The pH and conductivity values showed a similar trend with previous experiments (Figure 5b).The lowest speed was considered optimum because the removal efficiencies were close to each other at different mixing speeds.

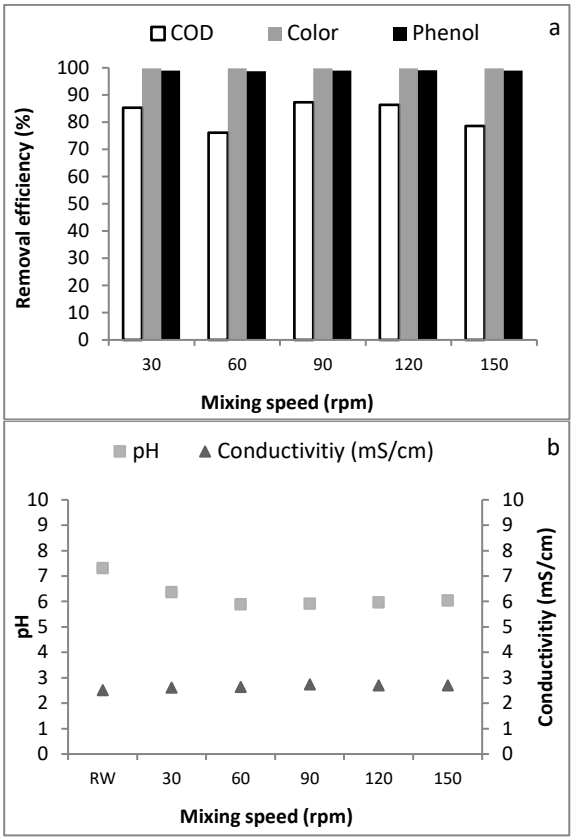

Figure 5. Effect of mixing speed on COD, color, phenol removal (a) and pH, conductivity (b)

3.6. OPTIMIZATION of SETTLING TIME

Settling time optimization experiments were performed with alum at the original pH. The wastewater was mixed at 30 rpm for 5 minutes, allowing 15, 30 and 45 minutes to settle (Figure 6).

Settling times of 15, 30 and 45 minutes resulted in 87, 85 and 88% COD removal, respectively. It was determined that the settling time had no effect on the removal efficiency. 99% yield was obtained in color and phenol removal (Figure 6a). There was no change in conductivity and pH levels (Figure 6b).

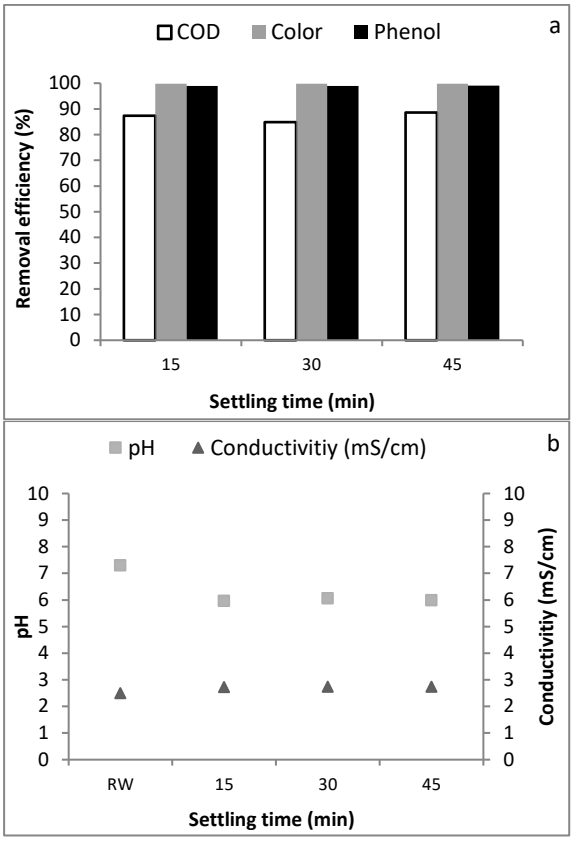

Figure 6. Effect of settling time on COD, color and phenol removal (a) and pH, conductivity (b)

Studies on the treatment of wastewater generated from gluing and printing processes have focused on the treatment of both wastewaters together (Table 3).

Tablo 3. Earlier Studies

	Methods	COD %	Renk %	Fenol %
Mansour ve Kesenti, 2008	Coagulation + Electroflotation	96,5	-	-
Karabacakoğlu ve Tezakıl, 2012	Electrocoagulation	90	-	-
Pozzive ark. 2014	AeratedMicrobial Thermophilic Reactor	88	-	-
Gengec,2017	Electrocoagulation + Electrooxidation	85,3	-	-
Inthisstudy	**Coagulation**	**87,3**	**99,8**	**98,9**

Mansour and Kesenti reported that COD was removed by 96.5% when they applied coagulation and electrophlotation in 2008.90% of the COD removal was reported by applying electrocoagulation (Karabacakoglu and Tezakil, 2012).In another study using electrocoagulation and electrooxidation, COD removal was found to be 85.3% (Gengec,2017). Pozzi and colleagues (2014) showed that 88% COD removal by Aerated Microbial Thermophilic Reactor (Table 3).

4. CONCLUSION

In this study, coagulation method was used for the treatment of corrugated cardboard waste water. Coagulant type ($FeCl_3$, $FeSO_4$, $Al_2(SO_4)_3$), coagulant ratio (1, 2, 3 and 5%), pH (6.0, 6.5, 7.0, 7.5) mixing time (3, 5, 7), mixing speed (30, 60, 90, 120, 150 rpm) and settling time (15, 30, 45 min) were optimized. Optimum conditions were obtained by adding 2% alum to the original pH (7.3) and mixing for 5 minutes at 30 rpm for 15 minutes. When optimum conditions were applied, 87% COD, 99% color and 98% phenol removal were performed.

5. ACKNOWLEDGEMENT

This project is supported by Çukurova Development Agency within the scope of the Financial Support Program for Small Scale Infrastructure Program for Production in 2018 (Project number: TR/62/18/0036).

6. REFERENCES

Gengec, E. (2017). Treatment of highly toxic cardboard plant wastewater by a combination of electrocoagulation and electrooxidation processes. Ecotoxicology and Environmental Safety, 145, 184-192.

Karabacakoğlu, B.,Tezakıl, F. (2012). "Oluklu mukavva kutu üretimi atıksuyunun elektrokoagülasyon yöntemi ile arıtımı.'' BAÜ Fen Bil. Enst. Dergisi, 14 (1), 34-39.

Mansour, L. B.,Kesentini, I. (2008). "Treatment of effluents from cardboard industry by coagulation–electroflotation." Journal of Hazardous Materials, 153 (3), 1067-1070.

Pozzi, E., Megda, C. R., Caldas, A. E. V., Domianovic, M., Pires, C. E. (2014)."Microbial population in an aerated thermophilic reactor that treats recycled cardboard plant wastewater." Journal of Water Process Engineering, 4, 74-81.

Renault, F., Sancey, B., Charles, J., Morin-Crini, N., Badot, P. M., Winterton, P., Crini, G. (2009). "Chitosan flocculation of cardboard-mill secondary biological wastewater.''Chemical Engineering Journal, 155 (3), 775-783.

Tezakıl, F. (2013). Oluklu mukavva endüstrisi boya-baskı işlemlerinden kaynaklanan atıksuların farklı yöntemlerle arıtılabilirliği, Doktora Tezi, Eskişehir Osmangazi Üniversitesi, Eskişehir.

CISET - 2nd Cilicia International Symposium on Engineering and Technology
10-12 October, 2019, Mersin / TURKEY

INVESTIGATION OF THE ACTIVITY AND KINETIC OF RECOMBINANT BILE SALT HYDROLASE OBTAINED BY TRANSFERRING BSH GENE FROM LACTOBACILLUS PLANTARUM TO ESCHERICHIA COLI

Yakup Ermurat*[1], Mehmet Öztürk[2], Cansu Önal[2] and Zekiye Kılıçsaymaz[2]

[1] Bolu Abant Izzet Baysal University, Engineering Faculty, Department of Chemical Engineering, Bolu, Turkey
[2] Bolu Abant Izzet Baysal University, Science and Literature Faculty, Department of Biology, Bolu, Turkey

ABSTRACT
Variations in six bile salt substrate concentrations were tested with wild pCON2 mutant F18L and Y24L BSH enzymes which were specified competent efficiencies on hydrolyzing both the glycine and taurine conjugated bile salt substrates. Kinetic constant values, μ_{max} and K_m of the wild and mutant BSH enzymes used for hydrolysis of six glycine and taurine conjugated bile salt substrates were determined using the Michaelis-Menten equation. The wild pCON2 and mutant Y24L enzymes were presented maximal activity for GDCA at pH 4 and the mutant enzyme F18L was effectively exhibited a varied range of pH preferences.

Keywords: *Lactobacillus plantarum, Escherichia coli, recombinant bile salt hydrolase, bioreaction kinetics, hydrolysis activity*

* Corresponding Author: Yakup Ermurat (yakupermurat@ibu.edu.tr)

1. INTRODUCTION

The BSHs, usually an intracellular enzyme, are found commonly in the intestinal microbiota of bacteria which classified as probiotics such as *Lactobacillus, Clostridium, Bacteroides* and *Bifidobacterium*, catalyze the hydrolysis of glycine or taurine-conjugated bile acids into the amino acid residues and the bile acids. Bile salt deconjugation by hydrolase enzyme controls hypercholesterolemia in humans which has received amplified focus and several studies were accomplished to realize the hydrolyzing effect of hydrolase enzyme (Gilliland et al., 1985; De Smet et al., 1995; Gill and Guarner, 2004; Jones et al., 2004; Degireloma et al., 2012; Moschetta 2012; Choi et al., 2015; Ridlon et al., 2016; Kaya et al., 2017; Öztürk et al., 2018).

Recent experimental studies with bile salt hydrolase enzymes characterized by *Lactobacillus rhamnosus* E9, the most common probiotic strain for the detection of BSHs activity, showed a slight preference for tauro-conjugated bile salts against conjugated glycine at pH 6 and 45°C temperature. It's stated that the detection of substrate specific amino acids of the enzymes was responsible for occurrence of secondary toxic metabolites by repetition of studies with one or more directed mutagenesis (Kaya et al., 2017).

The eight major human bile salts including both primary and secondary bile acids and both glyco and tauro conjugated bile salts were tested with rBSH enzymes for the substrate specificity evaluations and the BSH A exhibited greater reactivity with tauro-conjugated bile salts and the BSH C displayed greater hydrolyzing activity with glyco-conjugated bile salts (De Smet et al., 1995).

Two BSHs (BSH1 and BSH2) from *Lactobacillus salivarius* were expressed and purified in a heterologous manner and BSH1 showed a wide optimum pH range of 5.5 to 7.0, while a narrower pH range of 5.5 to 6.0 was determined for BSH2. The kinetic curves of BSH1 and BSH2 were found to be similar to the hyperbolic forms of Michaelis-Menten kinetics in the presence of dithiothreitol (DTT) (Bi et al., 2013). The results of the obtained Michaelis-Menten kinetics constant K_m were found to be significant at pH (6.0) and temperature (37°C) conditions and also at pH (6.0) and (37-45°C) temperature conditions.

Protein molecule structured enzymes have an outstanding ability to accelerate the rates of biochemical reactions so that they are recognized as the primary biological catalysts. Enzymes specifically bind the transition state more strongly than the reactant state, consequently lowering the free energy of activation. The mechanisms of enzyme reactions are needed further comprehended researches at the atomistic level at transition and reactant states using the three-dimensional structures of enzymes and enzyme–substrate complexes simulation methods (Robinson, 2015).

The general kinetic equation for an enzyme reaction occurred by enzyme (*E*) and substrate (*S*) binding reversibly to an enzyme with k_1 forward and k_{-1} backward kinetic constants to form enzyme-substrate (*ES*) complexes at transition state than a product (*P*) occurs at reactant state with k_2 forward and k_{-2} backward kinetic constants, releasing the free ready to reuse enzyme (*E*) catalyst.

$$E + S \underset{k_{-1}}{\overset{k_1}{\rightleftharpoons}} ES \underset{k_{-2}}{\overset{k_2}{\rightleftharpoons}} E + P$$

The Michaelis-Menten equation, used to model the obtained transformation data, is based on the maximum reaction rate μ_{max} and reaction constant (K_m) of the consumed substrate (*S*). It is possible to equate the derivatives of the polynomial equations obtained from the graphical curves of the consumed substrate (*S*) experimental data to the Michaelis-Menten equation. The Michaelis-Menten equation is linearized to obtain μ_{max} and K_m constants using the Eadie-Hofstee linearization approach, one of the most commonly used linearization methods.

With the Eadie-Hofstee linearization method, the linearized Michaelis-Menten equation is rearranged as follows:

$$\mu = \mu max - K_m \frac{\mu}{S}$$

According to the Eadie-Hofstee approximation equation, the linear equation is obtained by plotting the graph according to μ vs (μ/S). In this graph, the intersection point of the y axis gives μ_{max} and the intersection point of x axis gives (μ_{max}/K_m).

Determination of the kinetic constants through Michaelis-Menten enzyme analysis function is further used for the advance of rational enzyme design and controlled enzyme catalytic activity which support high yielded enzyme reactions. Pant et al. suggested procedures of two techniques for the optimal determination of μmax and K_m values which were used for efficient determination of the accurate values for a set of six enzymes (Pant et al., 2008). Study of Öztürk et al. stated that biochemical and the in-silico analysis presented the bsh1 enzyme is a member of the bsh family while bsh2-4 enzymes are members of the PVA family (Öztürk et al., 2018).

2. METHODOLOGY

The substrate specificities of the BSHs were experimented using the six primary and secondary bile acids and glyco-conjugated and tauro-conjugated bile salts. The bile acid standards, glycocholic acid (GCA), glycodeoxycholic acid (GDCA), glycochenodeoxycholic acid (GCDCA), taurocholic acid (TCA), taurodeoxycholic acid (TDCA) and taurochenodeoxycholic acid (TCDCA), were obtained from Sigma-Aldrich and Calbiochem (San Diego, USA). The ninhydrin assay method is applied for the evaluation of the substrate specificities of the BSHs using the six bile acid standards. The U-1900 spectrophotometer (Hitachi, Tokyo, Japan) is used for the determination of the released amino acid amounts by measuring the absorbance of the mixture at 570 nm. The obtained absorbance values have been converted into relative activities.

3. RESULTS AND DISCUSSION

In this research, the biocatalytic activities of human-sourced wild-type and mutant BSHs cloned from the Lb. plantarum B14 strains were studied through the kinetic analysis using the six conjugated bile salts as the substrates.

In order to investigate the hydrolysis activity and kinetic performance of the enzymes on the substrate specificities, the GCA, GDCA, GCDCA, TCA, TDCA and TCDCA bile salts found in bile secretion, were treated with negative control without enzyme (pet22b), wild type enzyme positive control (pCON2) and mutant enzymes (F18L and Y24L) at 3.0, 4.0, 5.0, 7.0 pH values and at 37 °C temperature conditions, according to previously studied experimental trials. The obtained substrate (S) transformation data were plotted against the experimental pH parameter. The polynomial equations of the graph lines were obtained showing the variation of each curve. Table 1 presents the determined polynomial equations of the graph lines.

Table 1. The polynomial equations of the substrate hydrolysis.

pCON2	pH T=37°C
GCA	y = - 0.00012*x^{2} + 0.0019*x + 0.58
GDCA	y = - 0.14*x^{2} + 1.5*x - 3.2
GCDCA	y = - 0.098*x^{2} + 1.1*x - 2.2
TCA	y = - 0.015*x^{2} + 0.16*x - 0.34
TDCA	y = - 0.013*x^{2} + 0.16*x - 0.31
TCDCA	y = - 0.016*x^{2} + 0.16*x - 0.5
F18L	pH T=37°C
GCA	y = - 0.015*x^{2} + 0.22*x - 0.15
GDCA	y = - 0.026*x^{2} + 0.32*x - 0.72
GCDCA	y = - 0.021*x^{2} + 0.22*x - 0.46
TCA	y = - 0.052*x^{2} + 0.062*x - 0.14
TDCA	y = - 0.016*x^{2} + 0.17*x - 0.71
TCDCA	y = - 0.0049*x^{2} + 0.046*x - 0.077
Y24L	pH T=37°C
GCA	y = - 0.057*x^{2} + 0.68*x - 1.4
GDCA	y = - 0.15*x^{2} + 1.7*x - 3.5
GCDCA	y = - 0.12*x^{2} + 1.2*x - 2.5
TCA	y = - 0.027*x^{2} + 0.28*x - 0.59
TDCA	y = - 0.016*x^{2} + 0.17*x - 0.34
TCDCA	y = - 0.013*x^{2} + 0.13*x - 0.26

The Michaelis-Menten reaction constant, rate of binding of substrate to the enzyme (K_m) and the maximum reaction rate (μ_{max}) were estimated using the data obtained from the biochemical treatment of the six bile salt substrates with the enzymes by applying Eadie-Hofstee linearization approach as seen in Figure 1.

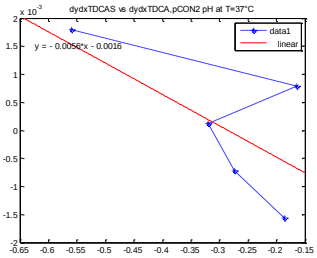

Figure 1. Eadie-Hofstee linearization tactic of TDCA substrate

The approximated K_m values were given in Table 2.

Table 2. Estimated μ_{max} and K_m values

pCON2	pH T=37°C		
	ymax= μ_{max}	xmax= μ_{max} / Km	Km= μ_{max} / xmax
GCA	0.39	5132,00000	0,07600
GDCA	0.66	10,48000	0,06300
GCDCA	0.512	6564,00000	0,07800
TCA	0.07	5833,00000	0,01200
TDCA	0.082	11,47000	0,00710
TCDCA	0.064	2286,00000	0,02800
F18L	pH T=37°C		
	ymax= μ_{max}	xmax= μ_{max} / Km	Km= μ_{max} / xmax
GCA	0.13	32.5	0,00400
GDCA	0.164	41,00000	0,00400
GCDCA	0.094	8545,00000	0,01100
TCA	-0.25	-11,17000	0,02200
TDCA	0.0166	4815,00000	0,03440
TCDCA	0.064	3048,00000	0,02100
Y24L	pH T=37°C		
	ymax= μ_{max}	xmax= μ_{max} / Km	Km= μ_{max} / xmax
GCA	0.13	2,88900	0,04500
GDCA	0.164	16,40000	0,01000
GCDCA	0.094	5222,00000	0,01800
TCA	-0.25	-3,02600	0,08300
TDCA	0.0166	4815,00000	0,00370
TCDCA	0.064	3048,00000	0,02100

The relative activity % was estimated for each of the six substrates to evaluate the performance of the substrate specificities of the rBSH enzymes at different pH values. Figure 2 shows the relative activity (%) which was performed by using the ratios of the mutant enzymes the wild-type control enzyme pCON2, and mutants F18L and Y24L for the six major bile salts.

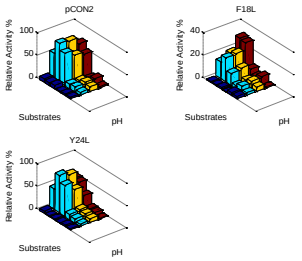

Figure 2. Relative activity % of wild and mutant enzymes

DISCUSSION

The experimental research results were indicated that the biochemical characteristics of the human-sourced wild type positive control enzyme (pCON2)) and mutant enzymes (F18L and Y24L) cloned from the *Lb. plantarum* B14 strains were found proficiently effective on the bile salt substrates (GCA, GDCA, GCDCA, TCA, TDCA and TCDCA) and able to hydrolyze both the glycine and taurine conjugated bile salt substrates at 3.0, 4.0, 5.0, 7.0 pH and at 37 °C temperature conditions as revealed in Figure 1.

The activity of the wild type positive control enzyme (pCON2) and the mutant enzyme (Y24L) are specified the highest enzyme activity effectiveness at pH 4, then presented decreasing activity on the glycine-conjugated GCA, GDCA, and GCDCA substrates, especially on GDCA substrate.

The Michaelis-Menten constants μ_{max} and K_m by the Eadie Hofstee linearization are used to evaluate the biocatalytic performances of the enzymes on the specific substrates. The assessed μ_{max} and K_m values of the BSHs showed remarkable activity of F18L compared to the other BSH.

The relative activity (%) was estimated for each of the six substrates to compare and evaluate the performance of the substrate specificities of the wild and mutant BSH enzymes at different pH values. Associating with the conducted studies, mutant enzymes (F18L and Y24L) over the wild-type control enzyme (pCON2) clearly declared a notable preference to the glyco-conjugated bile salts. As the most BSH enzymes display more effective activity on the hydrolysis of the glyco-conjugated bile salts, the wild-type control and mutant enzymes showed similar results.

4. CONCLUSION

The estimated Michaelis-Menten constants μmax and Km values of the BSHs showed an expectable diverse order of F18L>Y24L>pCON2 and the mutant BSHs results were found remarkable in some folds compared over wild-type BSH. The relative activity (%) evaluations of the wild-type and the mutant BSH enzymes for each of the six substrates were anticipated a notable preference to the glyco-conjugated bile salts.

ACKNOWLEDGEMENTS: This study is supported as a scientific research project by Bolu Abant İzzet Baysal University.

REFERENCES

Bi J., Fang F., Lu S., Du G. & Chen J. (2013) New insight into the catalytic properties of bile salt hydrolase. Journal of Molecular Catalysis B: Enzymatic 96 46– 51.

Choi S.B., Lew L.C., Yeo S.K., Nair P.S. & Liong M.T. (2015) Probiotics and the BSH-related cholesterol lowering mechanism: a Jekyll and Hyde scenario. Crit. Rev. Biotechnol. 35(3) 392-401.

Degireloma C., Modica S., Palasciano G. & Moschetta A. (2012) Bile acids and colon cancer: Solving the puzzle with nuclear receptors. Trends in Molecular Medicine 17(10) 564-572.

De Smet I., Van Hoorde L., De Saeyer N., Woestyne M.V. & Verstraete W. (1994). In vitro study of bile salt hydrolase (BSH) activity of BSH isogenic *Lactobacillus plantarum* 80 strains and estimation of cholesterol lowering through enhanced BSH activity. Microb. Ecol. Health Dis. 73 15–329.

Gill, H.S., & Guarner F. (2004) Probiotics and human health: a clinical perspective. Postgrad. Med. J. 80516-526.

Gilliland S.E., Nelson C.R. & Maxwell C. (1985) Assimilation of cholesterol by *Lactobacillus acidophilus*. Appl. Environ. Microbiol. 49 377–381

Jones M.L., Chen H., Ouyang W., Metz, T. & Prakash, S. (2004) Microencapsulated genetically engineered *Lactobacillus plantarum* 80 (pCBH1) for bile acid deconjugation and its implication in lowering cholesterol. Journal of Biomedicine and Biotechnology (1) 61-69.

Kaya Y., Kök M.Ş. & Öztürk, M. (2017) Molecular cloning, expression and characterization of bile salt hydrolase from *Lactobacillus rhamnosus* E9 strain. Food biotechnology 31(2) 128-140.

Pant M., Sharma P., Radha T., Sangwan R.S. & Roy U. (2008). Nonlinear Optimization of Enzyme Kinetic Parameters. Journal of Biological Sciences 8 1322-1327. doi:10.3923/jbs.2008.1322.1327.

Ridlon J.M., Wolf P.G. & Gaskins H.R. (2016) Taurocholic Acid Metabolism by Gut Microbes and Colon Cancer. Gut Microbiota Metabolites in Health and Disease 7 201-15.

Robinson P.K. (2015) Enzymes: principles and biotechnological applications. Essays Biochem. 59 1–41. doi: 10.1042/bse0590001.

Öztürk H., Aydin Y., Kiliçsaymaz Y., Önal C. & Ba N. (2018) Molecular Cloning, Characterization, and Comparison of Four Bile Salt Hydrolase-Related Enzymes from Lactobacillus plantarum GD2 of Human Origin. Food Biotechnology 32(3) 191–205. https://doi.org/10.1080/08905436.2018.1507911.

CISET - 2nd Cilicia International Symposium on Engineering and Technology
10-12 October, 2019, Mersin / TURKEY

COMPARATIVE STUDY OF THE USE OF TWO IRRIGATION SYSTEMS; SPRINKLING AND DRIP ON SOIL MOISTURE AND QUINOA PRODUCTION IN OUARGLA REGION- ALGERIA

Mohamed Abdelmalek Khemgani*[1], Afaf Allali[2] and Nour Elhouda Hati [2]

[1] Kasdi Merbah University, Laboratory of Bio- geo- chemistry of arid regions, Ouargla 30000, Algeria, malek.khemgani@yahoo.com

[2] Kasdi Merbah University, 511, Ouargla 30000, Algeria

ABSTRACT
The study highlights the evolution of cultivated soil moisture under two different irrigation systems: sprinkling and drip in Ouargla region. The approach adopted consists of the area prospection and then choose of the study site. This study focused mainly on an assessment of irrigation water quality, characterization of irrigation parameters and soil characterization in situ and in laboratory, and survey of some stages and the yield of Quinoa, for each irrigation system. Soil samples were collected before and after each irrigation for each system and at different depth levels (10, 15, 20, 25, 30 and 35 cm), with a control sample of bare soil (non-irrigated and uncultivated). The water and soil study showed that irrigation water is highly saline with basic pH, and has a sulphate sodium and chloride chemical facies. The soil is slightly calcareous, slightly gypsum, with a low organic matter content, slightly alkaline, not very salty, and has a silty sandy texture. Soil moisture increases with depth under spray system, and decreases under drip. The complete random block tracking of some stage of Quinoa showed that there is no significant difference between the two systems. The statistical test indicates that drip system presents the best system compared to the spray one.

Keywords: *Sprinkling, Drip, Soil Moisture, Quinoa, Ouargla.*

* malek.khemgani@yahoo.com

1. INTRODUCTION

Arid environments are characterized by extreme climatic conditions (winds, high temperatures, etc.) and specific edaphic conditions (coarse texture, low organic matter content, etc.), which can cause water stress for crops and influence their growth and production thereafter. For that, it is necessary to take in consideration when cultivating these soils to ensure sufficient moisture in the root zone to avoid any water stress that can have a negative impact on yield (KOULL, 2003). The liquid phase consists mainly of water and elements such as salts in solution. It occupies a portion of the void space, the water contained in the soil is described by moisture (CHENIN et al, 1972).

Soil moisture plays an important role in the maintenance of life on earth. Its first use is to allow the growth of vegetation, and also conditioning the establishment of plant stands (LUCIE, 2001). Quinoa "Chenepodium quinoa willd", is a species native to South America; the Andean region and more particularly to the Bolivian and Peruvian highlands (WILSON, 1990). Quinoa cultivation has enjoyed a great commercial success for some fifteen years, and its production can contribute to food security, especially in the Mediterranean regions. It can be used in several areas, such as a feed for cattle, their leaves, stems and grains are used.

2. MATERIAL AND METHODS

The objective of our work is to study the water profile of the soil as well as to evaluate quinoa production through a comparative analysis of the two irrigation systems: sprinkling and drip at Hassi ben Abdallah region. We have adopted the following approach: The approach that we adopted during this research begins with a prospecting phase on the ground. This is a preliminary phase of finding and choosing the work site (ITDAS - Hassi ben Abdallah station), followed by an experimental phase from which we have irrigation water, soil and for medicinal purposes (CAUDA, 1998). In fact, water is one of the ecological factors that most determines crop growth and development, and its deficit plays a very important role in the imbibition of yields (TAHRI & al, 2011). But on the other hand, the choice of irrigation system that will bring this water plays a key role in ensuring adequate and sustainable productivity (ALDESUQUYl et al, 2014). In this context, localized irrigation may be an irrigation technique capable of increasing production while respecting the environment: Drip irrigation is one of the localized irrigation systems while sprinkling is to reproduce on the ground the natural phenomenon of rain, with the control of the intensity and the height of the downpour (NITIEU, 2009). Our work was undertaken at ITDAS (Technical Institute for the Development of Saharan Agriculture) farm in Hassi Ben Abdallah, Ouargla region. It's a soil moisture study, as well as evaluation quinoa production through a comparative analysis of two irrigation systems: sprinkler and drip. It is more specifically to evaluate the agronomic yield relative to soil moisture for each system. The supported questions are: How to evaluate the soil moisture profile under these two irrigation systems? and therefore, What is the best system that can give us a good quinoa production ? the plant as the main material of study. The irrigation water and soil were sampled for chemical, physicochemical and physical analyzes at laboratory. For plant material, we worked on the quinoa species, by following some phynological stages and the evaluation of agronomic yield after statistical analysis.

2.1. Location and description of the study area

Our experiment was carried out in palm plantation of ITDAS farm, which measures 21 ha, and located at Hassi Ben Abdallah region, in the North-East of Ouargla city, in the south of Algeria (Figure 01), between latitudes 32 ° 02 '0.487' ' N and 5 ° 28' 32.34 " E, and at 156 m of altitude.

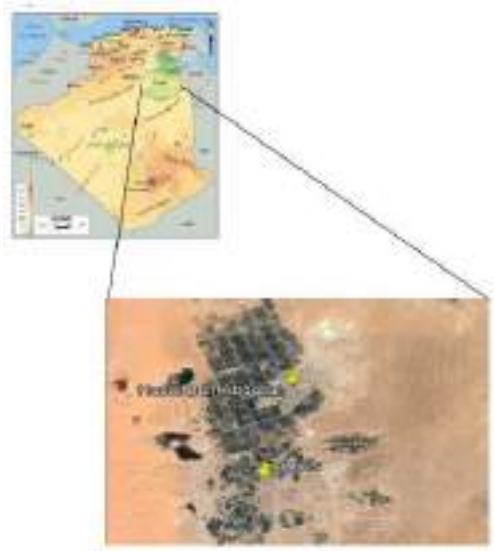

Fig. 1. Location of study area

Hydrological context: The hydrographic network of Ouargla basin (Figure 02) consists essentially of M'ya, N'sa and M'Zab valey (DPAT, 2010). According to (DUBIEF, 1953), M'ya valey basin covers 19800 km2, and considered as fossil. N'Sa and M'Zab valey are functional, unlike M'ya, they can have one or two floods per year. They reach the bowl of Ouargla, sebkhat Safioune, only when the flood is important.

Hydrogeological context: According to NESSOUN (1975); DHW (1993); In BENMAHCEN et al (1994); ANRH (2003); REMAUX (2003), the geological formations of this region contain two large sets of aquifer formations, called Intercalary Continental (IC) or Albian at the base and at the top Terminal Complex (TC). A third formation, of more modest importance, is added to the two previous ones: the shallow groundwater.

Pedological context

Ouargla basin is characterized by soils that the majority of them are grouped into the less evolved alluvial and windy soils classes and halomorphic and hydromorphic soils classes(LEGER, 2003). The region is characterized by light, predominantly sandy soils with a particulate structure. They are characterized by low levels of organic matter, alkaline pH, low biological activity, high salinity and good aeration (LEGER, 2003). According to the denomination of soils, we find the following five soil landscapes from West to East:

On the plateau, soils have a gravelly surface, gravel reg, or stony reg, and windy soils. This surface horizon

overcomes a dolomite limestone crust, very hard, 30 cm thick. Then there is a calcareous, nodular, less hard and cracked horizon, between 35 and 60 cm and then, beyond 60 cm, a petrogypsic horizon with 57% of gypsum. The electrical conductivity (EC) is low (1.97 to 3.4 dS / m), the pH is neutral. It is a Hamada petrocalcaric lithosol with gypsum encrustation at depth (BURRI, 2004).

* On the glacis, at 140 m of altitude, the soil consists of a loose material, exclusively detrital, inherited from the alteration of the red sandstone of the Mio-pliocene. It is the poorest soil in gypsum in the region; up to 8 m deep, it has no level of encrustation; the maximum of EC is 22.05 of / m between 25 and 75 cm of depth. It is a sandy soil with gravel and salic soil. (REMAUX 2001).

* In the chott, the surface horizon is a thick or polygonal gypsum crust, whitish, partially covered with gypso-siliceous windy sands and Sebkhas associated with gypso-halophilic vegetation with Zygophyllum album. At 15-20 cm thick, or found a powdery, homogeneous gypsum encrustation, of a very light reddish yellow color. Below, there is an indurated gypsum encrustation 40 cm thick, less rich in gypsum than the previous horizon. The non-calcareous soil has a decreasing gypsum content of 68.6% in the polygonal crust at 43%. The EC ranges from 17.2 to 54.6 dS / m, the pH is 7.8. It is a sali-sol sulfated chloride with a gypsum and petrogypsic surface horizon (REMAUX, 2001).

- The dunes are rego-soils. There are also dune cords. Finally, in the thalwegs and on the rocky slopes, we find on the surface outcrops of red sandstone from Mio-pliocene (HAMDI-AISSA, 2001).

The quinoa crop in Ouargla region:Quinoa was introduced in 2014 in Ouargla region by I.T.D.S institute - Hassi ben Abdallah. The leader of this project reports that an experiment of different periods of sowing of quinoa, multiplication of seeds, and production of this crop under different irrigation system (the case of our study).Today, 17 quinoa varieties are known in Ouargla region.

2.2. Methodology

The experimental set-up adopted is a completely random block (Figure 02), consisting of 2 treatments that are the two irrigation modes: spraying (T1) and drip (T0) with 3 repetitions per treatment. Each block of 51m2 is a repetition for both plots (the two irrigation systems), resulting in an experimental area of 238 m2. The two parcels are separated by a distance of 11 m and cultivated in the same variety of quinoa (Chenopodium quinoa wild).

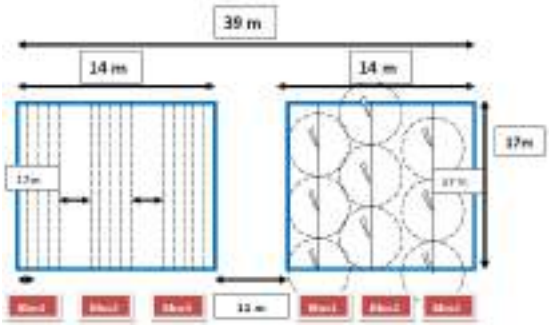

Fig. 2 Schemes of the experimental setup

The survey was conducted by a first step of consultation of available basic documents that could give some information on the study area. The second step is of prospecting-recognition, which consists of a recognition survey of the field, to have a general idea of the study area. At this stage we choosed the location of sites, realization of soil profiles and sampling of water and soil.Taking a sample of water irrigation in order to characterize the quality of this water. This operation is done using a plastic sampler during the irrigation period (October-March). This step is accompanied by a measurement of the irrigation parameters. Temperature, pH and electrical conductivity are measured using a multi-field meter.

- Cl-: by titration with silver nitrate: MOHR method;
- SO42-: by BC1 gravimetric method;
- HCO3- and CO3: titrimetric method with H2SO4;
- Na+ and K+ are determined by flame spectrophotometer; and Ca2+ and Mg2+ by atomic absorption.

Soil sampling is done randomly using a biological auger 20 to 120 cm deep. (MATHIEU and PIELTAIN, 2003). It consists of digging six (06) profiles (auger sampling) before and after irrigation, and at 06 levels of depth: 0_10 cm, 10_15 cm, 15_20 cm, 20_25 cm, 25_30 cm and 30_35 cm (following the rooting of culture).The sampling took place during the period, from October 2017 to March 2018, in all 123 soil samples were studied. To characterize the cultivated soil of the studied part, we carried out field surveys, because of a good characterization of the depths and their contents in the different irrigations systems, with a control (bare soil; not worked and not irrigated).

3. RESULTS AND DISCUSSIONS

Table 1. Irrigation water quality

Characteristics		Value	Unit
EC at 25°C		2,5	dS/m
Dry residue at 105°C		1.6	mg/l
Water temperature		58	°C
pH		8.41	/
Salt content	Cations		meq/l
	NA+	21.92	
	K+	1.69	
	Ca+2	8.41	
	Mg+2	6.95	
	Anions		
	HCO-3	1.65	
	Cl-	11.76	
	SO-4	11.2	
	Co	00	
SAR	6.35		/

The pH varies between 7.5 and 8.7 so, it is basic according to pH scale of the water given by BAISE (2000) . According to SEEE (2007) the pH is acceptable, it belongs to class A according to HÉBERT (1997). According to the dry residue scale given by DURAND (1958) in CHEDALA and MOULATI (2008), our water

has a high salinity whose dry residue varies between 0.75 and 2.25 which it is the case of our soil. According to Reverside classification used to evaluate the quality of irrigation water according to their salinities and the danger of alkalinization which may occur in the soil (RICHARDS, 1954), and modified by DURAND (1983), our irrigation water belongs to the class C4, it is very delicate in use, it requires very permeable and well drained soils, which is the case of our study area. The characterization of the water salinity according to F.A.O classification in GANA (2002), it belongs to the category of waters which have an average salinity (0.75 <EC <3 dS / m).The cationic facies are sodium and that of the anionic one is chlorinated sulphated, giving a global facies Sodium sulphate chloride (Table 01).For the degree of alkalization and according to the scale given by SERVANT et al (1966) in BENZAHI (1994), this water has a low alkalization (4 <SAR <8).

3.1. Soil characterization

From the grain size analyzes conducted on the soil of this operation we found a notable dominance of coarse sand with a considerable proportion of fine and coarse silt and low clay percentages for all layers. HAMDI-AISSA (2001) reports that this area is a vast alluvial, coarse sand glacis which is consistent with our present results. The projection of these data on the textural triangle shows that the soil is sandy loamy.

Table 2. Results of physical and chemical analyzes of soil (profile A)

Horizons	Depth (cm)	pH	EC (dS/m)	Anions (meq/l)				Cations (meq/l)			
				Cl	SO_4^{2-}	HCO_3	CO_3^{2-}	Na^+	K^+	Ca^{+2}	Mg^{+2}
AP	00-44	7.71	0.01	3	51.30	7	0	1.08	0.10	14.00	11.8
C	44-120	7.84	0.72	4	51.35	7	0	2.08	0.11	11.23	9

3.2. Variation of the water profile

The results of monitoring analyzes of soil moisture evolution during the growing season of the crop, between October 2017 and March 2018 are presented in the following graphs.

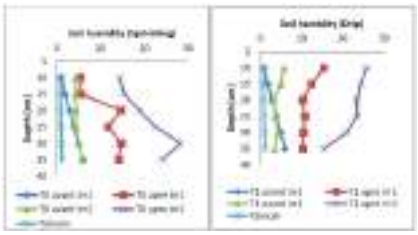

Fig. 3. Soil moisture profile change in November

From the results shown in the graphs (Figures 03 and 04), the numerical values of control soil moisture ranged from 0.92% to 1.22%, usually with low soil levels. water supply to cultivated soils and irrigated by both systems.

The figure 03 shows the state of soil moisture in November 2017. An increase in the soil moisture content in the irrigated plot by drip is observed at depths either before or after irrigation, with a rate of significant humidity at 20 to 30 cm, which subsequently decreases in the other depths. On the other hand, for soil irrigated by sprinkling, the humidity decreases with depth.

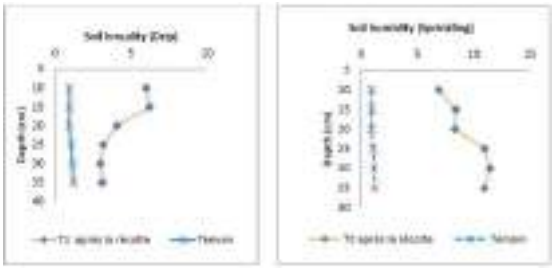

Fig. 4. Soil moisture profile change after harvest (March 2018)

After harvest (March 2018), soil moisture monitoring showed a significant reduction in water content of soil irrigated by sprinkling, and for the drip irrigated soil we noticed a small decrease in moisture content, but it should be noted that the moistening of this soil remains permanent for long term. According to a study conducted by HADEF (2005) on the soil of this farm shows that soil has a very low moisture content which was confirmed by the results of our study. Finally, we find that either before or after irrigation, the soil water profile varies according to an increasing gradient of the surface downwards for the soil irrigated by drip, while the soil irrigated by spraying whose water profile varies according to a gradient descending from the surface to bottom.

3.3. Crop monitoring phenological stages

The following-table (03) shows some phenological stages during the vegetative cycle of the cultivated variety (Q102), from sowing to the physiological maturity of the plant.

Table 3. Phenological stages of the crop

Stages	T0	T1
Sowing	17/10/2017	17/10/2017
Emergence	26/10/2017	26/10/2017
2 leaves	03/11/2017	03/11/2017
Branching	04/11/2017	04/11/2017
Early panicle formation	11/12/2017	11/12/2017
Panicle	21/12/2017	21/12/2017
Early flowering	03/01/2018	03/01/2018
Flowering	20/01/2018	20/01/2018
Maturity	12/03/2018	12/03/2018
Number of days	145	145

T0: Sprinkling parcel.
T1: Drip parcel.

After 8 days of sowing we notice the exit of the seedlings in all the blocks of the plots experimented. According to the scale described by MUJICA and CANAHUA (1989), the cotyledonary leaves of this plant are deployed between 7 and 10 days after sowing, which confirms the case of our crop. The complete appearance of two true leaves was noticed on the 16th day after sowing for both treatments. According to the scale given by MUJICA and CANAHUA (1989), quinoa assures its stage from the 15th to the 20th day of their sowing, which has been confirmed by our observations. At the 48th day of sowing, leaf branching was observed on the plant stem for both treatments. The same observations were recorded

for other stages, namely the stage of branching (45 to 50 days after sowing), the inflorescence (55 to 60 days after sowing), The complete formation of the panicle was observed after 65 th day of sowing, as well as at the 77 th day of sowing, we noticed the opening of the first flowers at the level of the plots experimented. While the opening of 50% of the flowers of the inflorescence was noted in the 93rd of sowing. This is the same case for the panicle stage, where the beginning of flowering and the flowering stage for Chenopodium quinoa willd will also be visible after 65 to 70, 75 to 80 and 90 th or 100 th day respectively after sowing, which was the case for our culture.

The harvest was carried out on 12/03/2018, after the physiological maturity of the plant for both plots (145 days after sowing). While the standards of MUJICA and CANAHUA (1989) report that quinoa has a vegetative cycle of 160 to 190 days after sowing. A comparison of our results with the standards indicated by MUJICA and CANAHUA (1989) reveals that there is a significant reduction in vegetative cycle of 15 to 35 days of this plant. This early maturity can be referential to the physical conditions of the environment, hydro-edaphic properties and the cultural requirements of the plant as well as the varietal properties of the crop. There is no significant difference between the two irrigation systems because both reach at harvest in the same time frame.

3.4. Yield evaluation Number of plants / m^2

From the results recorded in Figure 05 and although the seeding density is identical for the whole (200 seeds / m²), we find that the emergence rate or the number of plants / m² is variable between the blocks and between the two irrigation systems. The values recorded for the drip (T0) range between 57 and 100 plants / m² with an average of 78.66 plants / m², an average emergence rate of 39.33%, while sprinkling (T1) has higher values than the first case, with a minimum of 135 plants / m² in the 3rd block while the maximum is 159 plants in the 1st block. The average value of the density of emerged plants / m² is 145.33, ie a rate of emergence of 72.66%.

Fig. 5. Plant emergence rate

During field observations, we found a poor distribution of water in the T0 block due to the malfunction of some drippers (clogging).

3.5. Total weight of plants (kg / m2)

The results on total plant weight indicate that the sprinkler system has higher values of plant weight relative to drip, the minimum value of which is 3.465 kg / m2 and a maximum of 6.145 kg / m2 with an average of 4.992 kg / m2 or 499.2 q/ ha for sprinkling, while the drip presents weights vary between 4.450 kg / m2 and 5.315 kg / m2 with an average of 4,855 kg / m2 or 4852 kg / m2 , 5 q/ ha, which gave us a difference of 0.137 kg / m2 or 13.7 q/ ha..

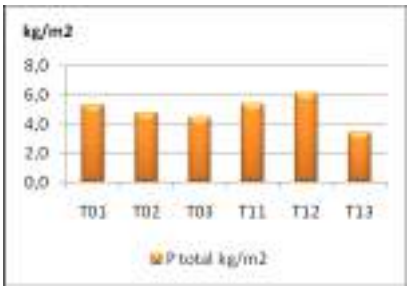

Fig. 6. Total weight of plants / m^2

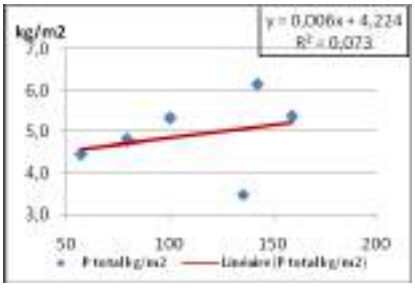

Fig. 7. Total weight of plants / number of plants

The Figure 6 shows a positive correlation between the number of plants and their total weights, this correlation is strongly significant at the 5% threshold, it indicates that the increase or decrease in number of plants / m² (density) proportionally affects the total weight of these plants. As a result, the difference between the total weights under both systems can be explained by the difference in the number of plants / m² or the density of the emergence. We can see that sprinkling is the best system that can give us a good production in plant biomass.

3.6. Height of plants

The results obtained on the height of plants show that plants under the drip system are shorter compared to those under the spray. In fact, the drip plants have heights varying between 86.5 and 112.1 cm with an average of 97.87 cm while the minimum height of the plants irrigated by sprinkling is 86 cm with a maximum height reached. of 114 cm and an average of 100.37 cm.This indicates that sprinkling is the best system that can give us a good development in plant height as the system drips.

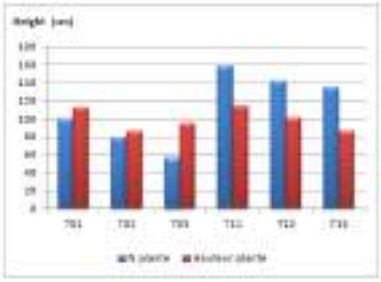

Fig. 8. Average plant height (cm)

A comparison between the height and the number of plants indicates a positive correlation between them on the one hand. On the other hand, according to field observations, we note that under sprinkler irrigation the distribution of water is of variable heights, this position of the sprinklers can cause competition between the plants of the plot (T1) which causes upward development of plants (in height), while water in the case of drip irrigation is located at the bottom of plants (it can not cause this phenomenon).

3.7. Total grain weight

We note a significant difference in grain yield between the two systems whose minimum value is 0.753 kg / m2 and a maximum of 0.83 kg / m2 with an average of 0.7803 kg / m2 is 78.03 q/ ha for drip, while the maximum value under sprinkling is about 0.8 kg / m2 and a minimum of 8.505 kg / ha with an average of 0.71 kg / m2 is 71 q/ ha or a difference of 7 q/ ha. In fact, these results reveal that drip is the best system that can give us a good grain yield A comparison between the main panicle weight and the number of secondary panicles with the total grain weight shows the existence of a positive correlation, which reveals that the increase or decrease of these two parameters varies proportionally with the total weight of grains on the one hand. On the other hand, it can be said that the total weight of the grains also comes from the main panicle filling and the secondary panicles in grain. We note that the correlation between the main pp and the total weight in grains and strongly significant at the threshold of 5% , which gives drip a significant grain yield than sprinkling.

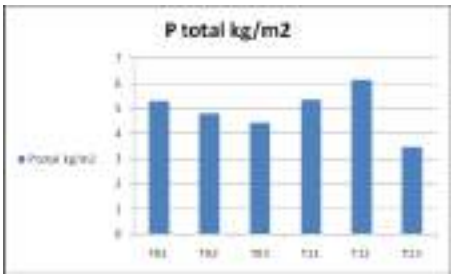

Fig. 9. Total grain weight

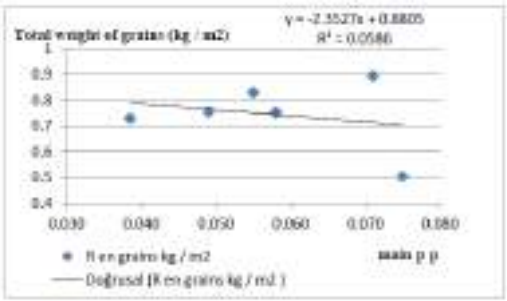

Fig. 10. Relationship between main panicle weights and total grain weight

3.8. Weight of 1000 grains

ERCHIDI et al (2003) report that the grain yield is not only represented by the total weight of these grains, it can also be expressed by two other components, the number of grains per unit area and the weight of a thousand grains like our case. From the results obtained on the weight of 1000 grains (Figure 09) under both systems, we note that these weights vary from about 3 to 5 g / 1000 seeds. However, drip irrigation still remains the best system compared to sprinkling with averages of 4.29 and 4.09 g / m2 respectively for drip and spray.

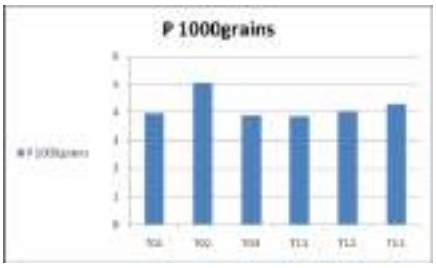

Fig. 11. Weight of 1000 grains

3.9. Summary of the results

The seeding density is identical for both systems, the differences observed in the rate of emergence is explicable by the irrigation system itself since the spraying allows a spatial distribution of water in the soil wider than the drop to drop that feeds the soil in concentrated spots. The differences observed within each system can be explained by the sometimes heterogeneous distribution of water following the problems of clogging drippers in the case of drip or the effect of wind direction in the case of sprinkle. Mujica (2001) mentioned that the water requirement of quinoa is around 200 and 300 m3, which reveals that the drip system provides the plant with the requirements, while the spray exceeds the standards, which leads to development and production. important in the height of the plants and the number of branches, but what interests us is much more agronomic grain yield. In other words, the parameters studied can be classified into two groups as follows: The rate of emergence or the number of plants / m², the number of branches, the weight of the plants / m² and the height of the plants which evolve together in positive relationship and whose increase causes an increase in the plant production of the plant. And this case is favored by sprinkler irrigation.

The number of total or secondary panicles, panicle head weight, and grain yield are also positively correlated together and inversely proportional to other parameters. Increasing the values of this group of parameters have a positive influence on the overall grain yield of the crop. And this case is favored by drip irrigation. Finally, we will conclude that the drip system is the best system that can give us a good quinoa production

4. CONCLUSION

The optimization of irrigations and the prediction of agricultural production require information on the soil water status and on these variations, soil moisture is therefore an important factor in the analysis of these soils and the setting in place of cultures.This work focuses on the comparative study on the use of two irrigation systems: sprinkling and drip irrigation, soil moisture and quinoa production in the Hassi ben Abdallah, Ouargla region. The study of the water characteristics shows that the water used in irrigation which comes from the aquifer

of interbedded complex (albian), has a basic pH, their dry and highly salted residue of which their chemical facies is sulphate sodium chloride. The study of some irrigation parameters indicates that sprinkler irrigation uses about 1.80 times water compared to the drip system, and this allows a water saving of 55% compared to sprinkling.The comparative analysis of the doses and the quantities of water distributed to the plant indicate that the drip system ensures the quinoa water requirements, whereas the amount of water used by the sprinkler system is greater than that indicated. in the bibliography.The study of the edaphic characteristics indicates that the soil of the plots studied is slightly calcareous, slightly gypsum, low in organic matter, slightly alkaline, not very salty to unsalted. The texture of this soil is sandy-loamy which has given us a good natural drainage of water. Graphical representations of soil water profiles under both irrigation systems from October 2017 to March 2018 revealed that:

• the evolution of soil moisture is variable over time.

• the climatic conditions of the environment (temperature, evaporation, rain, wind speed) are factors limiting soil moisture.

• crustal crust formations cause a reduction in the penetration and infiltration of water into the soil.

• the water profile of the soil varies according to an increasing gradient from top to bottom for the drip system on the other hand the soil water profile under the spray varies according to a decreasing gradient from top to bottom.

The follow-up of a few phenological stages under a complete random block shows that:

• The vegetative cycle of quinoa is short compared to that indicated in the bibliography (early maturity of the plant).

• but, there is no significant difference between the two irrigation systems; that is to say that both systems have ensured the physiological maturity of the plant within the same period.

Statistical analyzes of agronomic yield reveal that:

• There are positive and negative effects between the performance indicator parameters,

• Sprinkler irrigation has allowed good seed germination.

• Excess water causes significant vegetative growth in height and number of branches for plants.

• The main panicle weight and the number of secondary panicles are variables determining the average weight of a plant and the grain yield.

The comparative study of the use of two irrigation systems indicates that the drip system is the best system that has yielded good quinoa production.

References

Burri Jm., Burri Jp.,(2004). Études D'assainissement Des Eaux Résiduaires Pluviales Et D'irrigation: Mesure De Lutte Contre La Remonté Dee La Nappe. Mission Ii Rapport Final,<<Investigations,Essais De Pompage Et Bilans D'eau, Établissement Des Cartes Piézométriques, Diagnostic Edes Captages D'eau Et Mesures Des Réhabilitation, De Protection Des Ressources En Eau>>, Bg, Laucane,19p.

Erchidi A E, Benbella M, Talouizte A., (2003). Croissance Su Grain Chez Neuf Cultivars De Blé Dur. Zaragoza: Ciham- Iamz,2000,Pp 137_140. Série A.

Gandarillas H., (1979). La Quinoa (Chenopodium Quinoa Willd): Génética Y Origen. Un: Tapia Et Al., Eds. La Quinua Y La Kaniwa Cultivés Andinos. Bogota. Ciid-Iica,Pop:20_44.

Hadef D., (2005). Effet De Date De Semis Sur La Productivité De Colza Dans La Région De Ouargla Cas De Hassi Ben Abdallah, Mem Ing, Univ De Ouargla,60p.

Hamdi-Aissa B., (2001) - Le Fonctionnement Actuel Et Passé De Sols Du Nord Sahara (Cuvette De Ouargla). Approches Micromorphologique, Géochimique, Minéralogique Et Organisation Spatiale.Thèse Doct.I.N.A Paris-Grignon, Paris,315p.

Leger C., (2003). Études D'assainissement Des Eaux Résiduaires Et Pluviales Et D'irrigation: Mesure De Lutte Contre La Remonté De La Nappe: Volet Étude D'impact Sur L'envirennement, Mission Iib: <<Caractérisation Environnementale De La Situation Actuelle>>,Rapport,Bg,, Laucane,Pop:5,11,12,15,16.

UTILIZATION OF FOOD WASTE

Bihter İşyaran[1], Sedat Sayar[1]

[1]Mersin University, Department of Food Engineering, Mersin, Turkey, bihter.isyaran@gmail.com, ssayar@mersin.edu.tr

Abstract

Food wastes consist of the production surplus and wastes generated as a result of production which are not consumed by people and disposed of directly in to the garbage. In this study, a review has been made about the utilization methods and usage areas of food waste. Besides, statistical data by sectors and countries are indicated. The assessment of food waste provides significant benefits for environmental pollution, human nutrition, and the economy. Therefore, in recent years, a lot of studies have been done on the evaluation of food waste and adapted to new technology.

Keywords: *Food waste, utilization, waste in groups*

1. FOOD WASTE AND IT'S FORMED

Food has an important place in the life cycle as the basic need of humans. The need for food increases with the population increase. As a result, there is a rapid increase in the amount of waste generation in both household and industrial terms. Concurrently, the amount of waste increased as a result of the rapid increase in production with the transition to the industrial economy in the world between 1985 and 1990.

Generally, most of the food wastes are produced as the residual amounts from human consumption. Besides, food waste is produced as a result of production facilities in food factories. Most of these are exterminated or transformed into low-cost products by using low-cost technologies.

The problem of waste generation also increases in parallel with the increasing population in the world. The effective use of food waste is of great importance not only for the prevention of environmental pollution but also for product diversification and contribution to the economy. Therefore, the evaluation and recovery of food waste has been the subject of many studies and new technologies.

2. FOOD WASTE BY SECTORS IN THE WORLD

Every year, around one-third (1.3 billion tons) of food produced for human consumption is wasted in the world. While food waste is 680 billion dollars compared to 670 million tons of consumption in industrialized countries, it is 310 billion dollars against 630 million tons of consumption in developing countries. Food demand is expected to increase by 70% by 2050. In this context, food losses and wastes are increasing day by day [FAO, 2009].

Every year, consumers in rich countries waste much of Africa's food production (222 million tons), which is about 230 million tons. Food production per capita for annual consumption in the rich countries is 900 kg, while in low-income countries it is 460 kg. Consumption of waste per capita is between 95-115 kg per year in Europe and North America, while 6-11 kg per year in Africa, south and Southeast Asia [1].

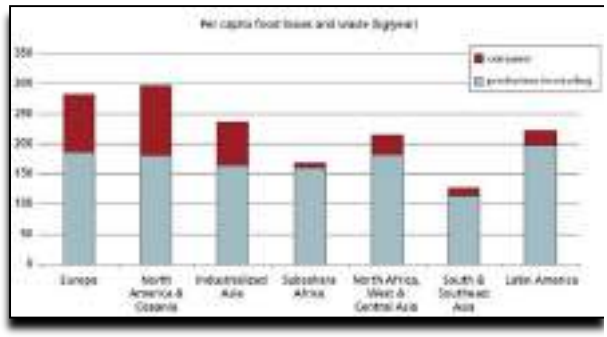

Fig 1: Food loss and waste percentages per person in different regions, consumption and pre-consumption stages [FAO, 2013].

When the waste food percentages are evaluated according to sectors, they constitute 71% household wastes, 17% industrial wastes, 9% service area wastes, 1% garbage and 2% wholesale and retail wastes.

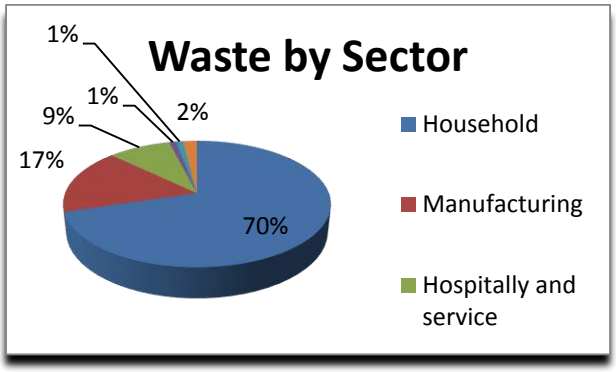

Fig 2: Food waste percentages [2].

Food wastes by industry;

- Fruits, vegetables, roots and tubers,
- Olive and olive oil,
- Sugar, starch, and confectionery,
- Cereals and oilseeds,
- Distilled spirits, breweries, and winemaking,
- Meat and meat products, eggs,
- Fish and seafood,
- Milk and milk products. It can be classified as it [3].

Fruits and vegetables, as well as roots and tubers, have the highest wastage rate in the food industry. Annual global food loss and wastes are around 30% in cereals, 40-50% in root crops, fruits and vegetables, 20% in oilseeds, 20% in meat and dairy products, and 35% in the fishing industry [4]. The amount of food lost or wasted each year is equal to more than half of the world's annual produced grain products (2.3 billion tons). In developing countries, more than 40% of wastes occur during post-harvest and processing, while in industrialized countries more than 40% of wastes occur during retail and consumption [5].

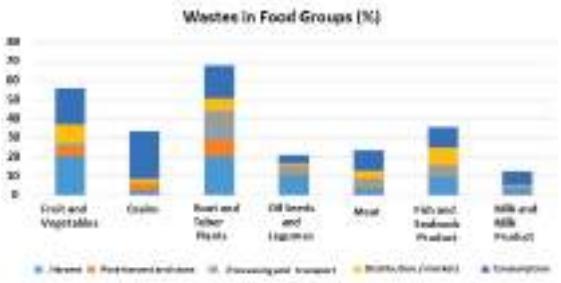

Fig 3: Waste percentages in food groups [6]

Food wastes also cause a major disintegration of resources such as water, soil, energy, labor, and capital, and generate unnecessary greenhouse gas emissions, leading to global warming and climate change.

3. FOOD WASTE BY SECTORS IN TURKEY

When compared to population growth, Turkey is situated in the front row at the World. Therefore, waste amounts are also increasing with increasing production and consumption of food products in Turkey. As a result, the amount of waste in Turkey is no different from developed countries.

According to resource results, there are about 24,000 food businesses in Turkey. 56% of the food sector is flour and bakery products, 18% is milk and dairy products, 12% is fruit and vegetable processing, 4% is vegetable oil and margarine, 3% is sugar products, 2.5% is meat products and 4.5% of non-alcoholic beverages, seafood, and other food production enterprises. Types of waste caused by the food business in Turkey are not different from the type of waste in developed countries. Only 20% of these wastes can be disposed of. Considering the utilization of food industry wastes, the composition of wastes and the presence of toxic components, the availability of waste, recyclability, price, and economy have to be taken into consideration [7].

4. IMPORTANCE OF UTILIZATION OF FOOD WASTES

The efficient use of wastes generated during food production and consumption is important not only for the prevention of environmental pollution but also for the creation of added value and diversification of products. The increase in the number of food processing factories along with the increasing population in the world causes the amount of food waste and consequently waste problems. Therefore, the collection of wastes and their use in the production of new products are important for human health, environmental pollution, and the national economy.

5. ACTIVITIES RELATED TO WASTE PROBLEM IN THE WORLD

5.1. Activities of State Institutions and Enterprises

England is one of the main country which is active about trying to reduce food waste. The Love Food Hate Waste charity, developed by the waste and resource action program (WRAP), worked with the government to reduce food waste by 20%. This study saved about 7.5 billion Euros in food purchases. WRAP also developed a 5-5-5 approach to help businesses deal with food waste [8].

Throughout the European Union, food waste innovation projects are also underway, with the PUReOPE project run by the UK within the framework of the EU eco-innovation fund, providing an innovative methodology for obtaining high-value polyphenols from process wastes. It is expected that high-value polyphenols will be produced instead of synthetically derived products. It is also aimed at reducing the energy required to treat processing waste in food sectors [9].

The Whey2value project, developed within the EU framework, aimed to obtain microbial mass enriched with vitamin B12 from whey. It aims to develop an innovative technology using acid whey to produce as the key ingredient in this process [10].

Research by the University of Aberdeen (Scotland) shows that when food prices are increased, the average amount of food consumed remains constant and food waste is reduced [2].

5.2. Market Activities

Large businesses and the retail sector around the world want to avoid the problem of waste reduction. Especially, businesses such as Pret a Manger, Starbucks, and Aldi are working on waste problems by using brand awareness and making various discounts.

Sainsbury, the UK's second-largest supermarket chain, has invested £ 1 million in a particular area of the UK to develop new technology to reduce household waste by 50%. In a survey of 2051 shoppers in and around the UK, 22% said they wanted smartphone applications to help them with food waste.

In Scotland, the ‘Too Good To Go’ attempt encourages to restaurants a take-home service for leftovers [2].

5.3. Start-up and Applications

5.3.1. Chicp

A founder in England says that 40% of British products are rejected due to their shape and size, 600,000 tons of food is wasted in restaurants and 300,000 tons of food is wasted annually by supermarkets. In order to evaluate the waste foods consisting of healthy foods, especially in this research, it has produced especially sauce and humus production and offered it for sale in the market [11].

5.3.2. Food Cloud

More than 9100 volunteer charity groups can get more food in Ireland and the United Kingdom, thanks to the technological application to reduce food waste in Ireland and England. The application informs the aid organizations that excess food that is not sold in the stores is available and is can be collected for evaluation [12].

5.3.3. Cuan Tec

The Scottish company is engaged in biotechnological studies for the good use of waste generated in the fisheries sector. With chitosan obtained from wastes, it produces degradable bio-plastic packages to reduce plastic waste in nature [13].

5.4. Renewable Energy

Food waste can be recovered in different ways, such as energy, anaerobic digestion, and combustion. Renewable energy companies such as ReFood have established anaerobic digestion facilities in and around the UK. The company has recently reduced total food waste by up to 50% by reducing its carbon footprint. Besides, the new technology creates an anaerobic treatment plant and builds bio-fertilizers if we load the nutrient content. Similarly, companies such as Bavaria, Ben, Jerrys, and Lamb Weston produce biogas from wastewater that is fed back into the electricity grid [14].

6. Products Obtained from Food Waste and Their Usage Areas

In fruit and vegetable wastes, there is a loss of many beneficial substances such as dietary fiber, antioxidants, pectin, essential fatty acids and vitamins which are important for nutrition. One of the fruit wastes grape seed and peel have rich anthocyanin and other phenolic substances, apple pulp has polyphenols and citrus pulp are very important sources of antioxidants due to their flavonoid and phenolic acids. Besides, tomatoes are an important source of lycopene and lycopene production is carried out from tomato pulp [15].

The grain industry has an important place in the food industry. The wastes of this industry are generally starch-containing. Ethyl alcohol, single-cell protein, lactic acid can be produced biotechnologically from these wastes [6].

One of the important products in the grain industry is sub-semolina flour. Semolina flour is a by-product obtained by combining low quality blended flours during the processing of durum wheat or produced during grinding of wheat. Sub-semolina flour has higher ash content than semolina, which is the main product but constitutes about 13-16% of ground wheat. Nowadays, sub-semolina flour is generally used in bakery products as an additive to increase the gluten content of cereals with low gluten content such as rye and oats [15].

Olive oil production wastes are sub-products of olive as blackwater, prina, and pruning waste. The pomace wastes are used as fertilizer, fuel, and feed for cattle. Blackwater contains in its structure sugars, organic acids, polyalcohols, pectins, colloids, tannins, and lipids. Biogas, fertilizer, single-cell protein, lipase production, is used in the production of biosurfactants [16].

Chitin and chitosan, which are natural, non-toxic biopolymers in the seafood industry, are produced from crab and shrimp shell residues. These polymers are used in the food industry as antimicrobial agents and additives (as acidifiers in beverages, emulsifiers, and stabilizers, color stabilizers). They are also used in many areas such as single-cell protein production [17].

Lactose, nitrogenous substances, and mineral substances are present in the whey which makes up approximately 70-90% of milk processed in milk production [18]. Whey is generally made into whey powder and is used as an additive in the biscuit, chocolate and ice cream industry [19]. Due to its high emulsion stability and capacity, it is stated that whey proteins can be used in creams with high-fat content, mayonnaise, cream cheese, meat sauces, and salad dressings.

In the regions where animal husbandry is concentrated, the waste generated by livestock in the enterprises where livestock activities are carried out, as well as the waste and by-products generated after slaughtering these animals, are important for economic, social and environmental sustainability. After slaughter, all animal by-products except carcass; food, paint, and chemical industry, as well as the use of animal waste in the plant without causing environmental pollution, especially solid and liquid separation and processing contribute to the economy [20].

In sugar factories, syrups that do not crystallize during sugar production from molasses. Molasses is one of the most important wastes of sugar factories molasses sugar content is 60% and the pure sugar amount is 1.32 kg. Light-colored molasses is generally used in confectionery and dark-colored molasses is used in animal feed. Molasses remaining as waste in sugar factories; ethanol can be used in the production of bread yeast, in the production of single-cell protein and lactic acid. Ethyl alcohol can be produced in biotechnologically from molasses. Molasses do not crystallize, are inexpensive, always available and suitable for industrial ethyl alcohol production. *Saccharomyces cerevisiae* is widely used in the production of ethyl alcohol from molasses [21].

7. Results and Discussion

Awareness has been raised in the food industry about environmental pollution caused by process wastes and the loss of valuable nutrients. For this reason, studies are carried out in different fields to turn the negative effects of waste into valuable products. The resulting wastes have led to the development of favorable properties both in the food industry and in the production of other products in general.

In developing countries, food waste and losses are mainly seen in the early stages of the food production chain. Supporting farmers in the supply chain can help reduce food loss and waste, strengthening investments in infrastructure, transport, and expansion of the food and packaging industry.

In middle and high-income countries, it is wasted and lost in later stages of the food supply chain. Unlike situations in developing countries, consumer behavior plays a major role in industrialized countries. The deficiency of coordination between rings in the supply chain is an important factor. Agreements between the farmer and the buyer can help to increase the level of coordination. Besides, it is important to raise awareness among industries, retailers, and consumers and to find new ways of use for waste foods, to reduce the amount of waste and waste.

New researches and studies and methods developed will be beneficial for the food industry and environment. Food production increases parallel to the rapid increase in consumption in the world. The amount and problem of waste also increases rapidly with production increases. If waste is not recovered, it poses a major threat to the environment. In addition to preventing environmental pollution by alternative ways of evaluating food wastes, an additional benefit to human health and nutrition can be provided by obtaining economic gains and valuable foods [22].

8. Acknowledgments

This study was supported by Mersin University Scientific Research Projects Coordination Unit as 2019-2-TP2-3597 project.

9. References

[1]. http://www.fao.org/save-food/resources/keyfindings/en/ [Accessed 10 Sept 2019]

[2]. https://www.nottingham.ac.uk/biosciences/documents/business/food-innovation centre/food-waste-utilisation-nov-2017/food-waste-untilization.pdf [Accessed 10 Sept 2019]

[3]. http://foodwaste.tripod.com/id12.html [Accessed 10 Sept 2019]

[4]. Otles, S., Despoudi, S., Bucatariu. C. and Kartal, C. (2015). ''*Food Waste Management, Valorization, And Sustainability In The Food Industry.''* Processing Technologies and Industrial Techniques, Academic Press, London, Chapter 1, pp. 3-24.

[5]. http://www.fao.org/save-food/resources/keyfindings/en/ [Accessed 10 Sept 2019]

[6]. Anonym, (2018). Gıda Zincirindeki Hasat Sonrası Kayıpları Azaltmak İçin Yenilikçi Yaklaşımlar, *Central Research Institute of Food and Feed Control*, Bursa, Turkey.

[7]. Sener, A. and Unal, U.M. (2008). ''Gıda Sanayisi Atıklarının Biyoteknolojik Yöntemlerle Değerlendirilmesi.''Turkey *10th Congress of Food*, Erzurum, Turkey

[8]. https://www.lovefoodhatewaste.com/about-us [Accessed 10 Sept 2019]

[9]. https://ec.europa.eu/environment/eco-innovation/projects/en/projects/pureope [Accessed 10 Sept 2019]

[10]. http://www.whey2value.com/index.html [Accessed 11 Sept 2019]

[11]. https://www.chicp.co.uk/ethos [Accessed 11 Sept 2019]

[12]. https://food.cloud/how-foodcloud-works/ [Accessed 11 Sept 2019]

[13]. https://www.cuantec.com/who-we-are/the-company [Accessed 11 Sept 2019]

[14]. https://refood.co.uk/about-refood/ [Accessed 11 Sept 2019]

[15]. Yagcı, S., Altan, A., Gögüş, F. and Maskan, M. (2006). ''Gıda Atıklarının Alternatif Kullanım Alanları.'' *Turkey 9th Food Congress*, University of Gaziantep, Gaziantep, Turkey.

[16]. Baskan, A.E. (2010). ''Zeytinyagı Isletmelerinin Atiklari Ve Değerlendirme Yollari.'' *T.C. Güney Ege Kalkınma Ajansı, GEKA,* Denizli, Turkey.

[17]. Caklı, S. and Kılınc, B. (2004). ''Kabuklu Su Urünleri Isleme Atıklarının Endüstriyel alanda değerlendirilmesi.'' *Ege Journal of Fisheries and Aquatic Sciences*, Vol. 21, pp. 145-152.

[18]. Kurultay, S., Simsek, O. and Kaptan, B. (2000). ''Fermente edilmis ve edilmemis peyniraltı sularından meyve aromalı içecek yapımı üzerine bir arastırma.'' *The Journal of Food,* Vol. 7, pp. 79-85.

[19]. Kavas, G. and Karagözlü, C. (2001). ''Süt ürünlerinin gıda sanayinde kullanılabilirliği hakkında bir görüş.'' ''Turkey *10th Congress of Food*, Vol.2, pp. 90-92.

[20]. Türkten, H., Yıldırım, Ç., Ceylan, V. and Gündüz, O. (2016) '' Samsun ilinde sığır besiciliği faaliyetlerinden ortaya çıkan atık ve yan ürünlerin değerlendirilmesi ve yönetimi'' *Anadolu Journal of Agricultural Science*, Vol. 31, pp. 353-359.

[21]. Aylanganı, A. (2008). Hayvansal Gıda Sanayisi Yan Ürünleri Kullanılarak Protein Hidrolizatları Üretimi.'' *Turkey 10th Congress of Food*, Erzurum, Turkey.

[22]. Tatlıdil, F.F., Dellal,İ. and Bayramoğlu, Z. (2013). ''Food *Losses and Waste in Turkey, Country Report, Food and Agriculture Organization of the United Nations*.''

CISET - 2nd Cilicia International Symposium on Engineering and Technology
10-12 October, 2019, Mersin / TURKEY

EFFECTS OF FAT CONTENT ON THE TEXTURAL ATTRIBUTES OF STARCH PASTE PREPARED IN MILK

Ayşegül Bilgiç*[1], Sedat Sayar[2]

[1] Mersin Univercity, Engineering Faculty, Food Engineering, Mersin, Turkey, aysegul_bilgic@windowslive.com

[2] Mersin University, Engineering Faculty, Food Engineering, Mersin, Turkey, ssayar@mersin.edu.tr

ABSTRACT
Starch is an important source of carbohydrate that is highly abundant in human nutrition and is a natural component that is largely present in most plants. Different types of starch are used with dairy products that may have different amounts of fat. Starch plays an important role in the consistency of the final product, especially when used with milk. For this purpose, it is aimed to increase the quality of the final product by looking at the textural properties of the gels obtained from starch/milk mixture with different fat ratios. In the study, 5 different types of starch and whole (3% fat), reduced fat (1.5% fat) and skimmed (less than 0.15% fat) milk were used as material. The hardness, viscosity and consistency of the starch gels were determined by the Texture Analyzer (TA -XT2i Texture Analyzer, Stable Micro Systems Ltd, Surrey, UK). As a result of the study, the highest hardness value was seen in corn starch, while the lowest hardness value was found in rice starch. On the other hand, tapioca starch gave the lowest adhesion and consistency value. Thanks to these data obtained from the study, different formulas will be developed according to the desired properties in the products that will be used in different types of starch in the food industry, and predictions will be provided about the raw materials to be used.

Keywords: *Starch, Milk, Texsture.*

* Corresponding Author

1. INTRODUCTION

Starch is a major source of carbohydrate in human nutrition (Ratnayake et al.,2008). It can be obtained from corn, wheat, rice, tapioca, potatoes and some other sources (BeMiller et al.,2009). Although cereals are the main source of starch production, tubers and root crops also have an important place in starch production (Burrell et al.,2003). Wheat as a raw material constitutes 8% of the world starch production whereas corn, potato and tapioca constitutes 73%, 4%, and 14%, respectively (Bemiller et al.,2009,Marshall et al.,1993).

Starch consists two different polymers of D-glucose, amylose and amylopectin (Smith,2001). Amylose consists of approximately 500–2000 glucose units connected in a straight chain by α- (Ratnayake et al.,2008,Marshall et al.,1993) glycosidic bonds. Unlike amylose, amylopectin has a branching similar to grape bunches. Each branch is composed of 20–30 glucose units and α- (Ratnayake et al.,2008, Horie,2010) glycosidic bonds and glucose units are connected to each other at branching points (Horie,2010, Elgün et al.,2003, Ertugay et al.,1988, Karaoğlu, 2005). Amylose and amylopectin create 98-99% of dry matter in natural starch. The remainder contains low amounts of proteins, fats, phosphates and minerals. These ratio changes according to the source of starch. The amylose-amylopectin ratio in starch structure is very important because it affects the functional properties, granule structure and gelatinization of starch in food (Sharma et al.,2008).

Starch granules undergo a structural change under the influence of water and temperature to form a suspension and thicken. As the temperature increases, the amylose is separated from the amylopectin and the amylose passes from the granule into the solution. After cooling, the amylose molecules form H + bonds with other amylose and amylopectin. Gelling occurs when water is trapped between this reticulated structure of amylose and amylopectin. In general, the control of these structural changes of starch granules under the influence of water and temperature is the most important factor in starch functionality (Tester et al.,2004, Dennis et al.,2000, Singh et al.,2005).

Starch is a food consumed mainly in human nutrition as well as a basic raw material for the food industry, textile, paper and many other industrial areas. Factors such as the molecular structure of amylose and amylopectin in starch, granular structure and shape of starch, amylose-amylopectin ratio, lipid, protein and phosphate amount play an important role in determining the functional properties of starch. For example; amylose-free starches are preferred in frozen products, whereas high amylose-containing starches are preferred in desserts and fried products. Thus, the idea of the use of starch in the industrial field is obtained (Köksel, 2005).

Milky desserts are the most important field of the utilization of starch in the food industry. Different types of starch are used in dairy products, which may have different fat content. Starch plays an important role in the consistency of the final product, especially when used with milk. The functional properties of starch include gel structure, specific viscosity, freeze-thaw stability, crystallinity, clarity, swelling and swelling resistance, color. Starch due to its significant contribution on the textural properties of the foodstuff to which it is incorporated in its composition; colloidal stabilizer, gelling agent, thickener, bulking agent, and adhesive are used in water applications as water trap (Kahraman et al., 2006, Karaoğlu, 1998). Starch and milk proteins coexist in a large number of milk-based products. Starch is added to dairy products to increase gel strength and viscosity. Despite their industrial importance and the intensive research of starch and milk proteins individually, studies on their interactions are relatively small compared to mixtures of milk proteins with other biopolymers. Accordingly, the aim of this study is to improve the quality of the end product by determining the properties of starch gels prepared in milk with different fat ratios (Doublier et al.,2008, Keogh et al.,1998, Mounsey et al.,2008).

2. MATERIAL AND METHOD

2.1. Material

Starch samples (potato, rice, wheat, corn and tapioca starch) supplied from a local company (Tito, Turkey). Whole (3% fat), reduced fat (1.5% fat) and skimmed (less than 0.15% fat) milk were also bought from a local distributor (Migros A.Ş.). All fat sample were the same brand and prepared from the same raw material.

2.2. Method

The starch samples (3 g) mixed with the milk sample (27 mL) and pasted in the rapid visco-analyser instrument (RVA 4500, Perten Instruments, Australia) by using the standard RVA procedure. The gel formed in the RVA canister after RVA analysis was wrapped with parafilm and placed in the refrigerator for 18 h. Analysis of textual properties was performed on a TA-XT2i Texture Analyzer (Stable Micro Systems Ltd., Surrey, UK) equipped with Texture Expert software. Each starch gel sample in the RVA canister was pressed to a distance of 10 mm (trigger force = 3.0 g) with a cylinder probe 5 mm in diameter at the speed of 1.0 mm/s during two repeated runs, the pre-speed and post-speed were both set at 2.0 mm/s and the obtain rate was 10.0 pps. Hardness (HD, N), adhesiveness (ADH, g s) and cohesiveness (COH) were obtained from the instrument software.

3. RESULTS AND DISCUSSION

Textural properties such as hardness (HD, N), adhesion (ADH, g s) and cohesiveness (COH) were derived from texture profile analysis. In Texture Profile Analysis (TPA), various parameters were obtained by simulating human chewing motion, exposing the sample to a compression deformation (first bite) followed by a relaxation followed by a second deformation (second bite). In these parameters, significant differences were observed between starch gels prepared with meats having 3 different fat ratios.

Table 1. Texture profile analysis results of starch in water or milk. (RS, CS, TS, WS and PS is rice, corn, tapioca, wheat and potato starch, respectively; W: water, SM: skimmed milk, RFM: reduced fat milk, WM: whole milk)

Sample	Hardness (N)	Adhesiveness (g s)	Cohesiveness
RS+W	0.31	-67.07	0.50

RS+SM	0.26	-73.11	0.47
RS+RFM	0.24	-47.32	0.41
RS+WM	0.27	-49.56	0.39
CS+W	0.42	-80.47	0.46
CS+SM	0.40	-98.52	0.52
CS+RFM	0.39	-100.39	0.56
CS+WM	0.39	-118.46	0.59
TS+W	0.25	-18.16	0.33
TS+SM	0.35	-3.36	0.54
TS+RFM	0.39	-5.58	0.36
TS+WM	0.46	-19.88	0.53
WS+W	0.43	-94.12	0.51
WS+SM	0.32	-106.55	0.56
WS+RFM	0.31	-96.66	0.54
WS+WM	0.29	-105.59	0.55
PS+W	0.34	-35.84	0.47
PS+SM	0.29	-35.92	0.41
PS+RFM	0.31	-31.83	0.39
PS+WM	0.36	-38.89	0.42

According to the data obtained as a result of the analysis, the highest hardness was observed in corn starch as shown in Table 1. In their study, Mir and Bosco (Mir et al.,2014), found that this stiffness was due to the high amylose content found in corn starch. Amylose is thought to cause hardness due to its ability to crystallize in a short time. The lowest hardness values were seen in samples prepared from rice starches, followed by potato, tapioca, and wheat starch. This low stiffness is due to the fact that it has shorter amylopectin chains and again has a low amylose content (Wang et al.,2002).

In this study to the data obtained in the study, no significant difference was observed in the adhesiveness values, but the highest stickiness value was found in wheat starch. Adhesion values in wheat starches may be due to their higher amylose content. Linehan and Hughes (Linehan et al.,1969) observed a correlation between the intercellular adhesion and the amylose content during their studies on the tissue of starch gels. With the increase in temperature, the amylose structure is weakened, thereby increasing the intercellular adhesion. While the least viscosity is determined in tapioca starch, it is thought that the reasons for these differences are due to the thin structure of amylose and amylopectin (Hanashiro et al., 1998).

The cohesiveness value of the prepared gels, which is an indicator of their structure, was the highest in corn starch and the lowest was in potato starch. The relationship between the texture tissue of the gels obtained from these starches is thought to be due to the presence of impurities such as fats and proteins in the structure of the starch (Whittenberger et al., 1948).

It was found that the different textural properties observed were caused by different starches and also the fat ratios of the milk where the gels were prepared were effective. Collison (Collison, 1968), determined that the factors such as protein content and fat content of the material prepared by the gels affect the textural properties. According to the results, the increase of fat in milk has a negative effect on the hardness of rice, corn and wheat starches; hardness of potatoes and tapioca starch caused an increase in value. It is thought that the presence of casein micelles, soluble milk minerals and lactose in milk may provide more binding sites for the intermolecular coupling of the amylose network, which in turn affects the textural properties (Gunaratne et al., 2007).

In this study, it was determined that different types of starches affect the textural properties by affecting the fat ratios of the milk. Thus, different formulas can be developed according to the desired properties in the products that will be used in different types of starch in the food industry and predictability can be provided about the raw material to be used.

ACKNOWLEDGEMENTS

This study was supported by Mersin University Scientific Research Projects Coordination Unit as 2019-1-TP2-3447 project.

REFERENCES

BeMiller, J.N., Whistler, R., (2009). “Wheat Starch: Production , properties, modification and uses.” Starch chemistry and Technology, Academic Press, New York, pp. 441.

Burrell, M. M. (2003). “Starch: the need for improved quality or quantitiy-an overview. “ Journal of Experimental Botany, Vol. 54 No. 382, pp. 451-456.

Collison, R., (1968). “Swelling and gelation of starch.” Starch and its derivatives, In J. A. Radley, Ed., London: Chapman & Hall, pp. 168–193.

Dennis, D.T. and Blakeley, S.D., (2000). “Carbohydrate metabolism.” In Biochemisty & Molecular Biology of Plants, Bob B. Buchanan, Wilhelm Gruissem and Russell L. Jones, Ed., American Society of Plant Biology, pp. 630-675.

Doublier J. L., Durand S., (2008). “ A rheological characterization of semi-solid dairy systems.” Food Chem., pp.1169– 1175.

Elgün, A., Ertugay, Z., (2003). “Tahıl İşleme Teknolojisi.” Atatürk Üniv. Yayınları, No.718, pp.376.

Ertugay, Z., Kotancılar, G., (1988). “Nişastanın bazı fizikokimyasal özellikleri ile ekmek içi sertliği arasındaki ilişkiler.” Gıda, No. 13, pp. 115-121.

Gunaratne, A., Ranaweera, S., and Corke, H., (2007). “Thermal, pasting, and gelling properties of wheat and potato starches in the presence of sucrose, glucose, glycerol, and hydroxypropyl β-cyclodextrin.” Carbohydrate Polymers, Vol. 70, No. 1, pp. 112–122.

Hanashiro, I., & Takeda, Y., (1998). “Examination of number-average degree of polymerization and molar-based distribution of amylose by fluorescent labeling with 2-aminopyridine.” Carbohydrate Research, No. 306, pp. 421–426.

Horie, V. (2010). “Materials for Conservation : Organic Consalidants.” Adhesives and Coatings, 1th Ed., London, pp. 504.

Kahraman, K., Köksel, H.,(2006). “Enzime dirençli nişasta üretimi ve fonksiyonel özelliklerinin incelenmesi.” Hububat Ürünleri Tekn. Kong., 7-8 September,

Gaziantep.

Karaoğlu, M.M., (2005). "Nişasta retrogradasyonu: 1. Nişasta retrogradasyonu ve Gıda endüstrisi için önemi." Unlu Mamuller Tekn., No. 67, pp. 52-65.

Karaoğlu, M.M., (1998). "Farklı yöntemler uygulanarak elde edilmiş modifiye nişastaların kek kalitesi üzerin etkileri." Atatürk Üniv. Fen Bil. Ens. (Yüksek Lisans Tezi), Erzurum.

Keogh M. K., O'Kennedy B. T., (1998). "Rheology of stirred yogurt as affected by added milk fat, protein and hydrocolloids." J. Food Sci., No. 63, pp. 108–112.

Köksel, H., (2005). "Karbonhidratlar." Gıda Kimyası, 3. Baskı. Ankara: Hacettepe Üniversitesi Yayınları, pp. 49–132.

Linehan, D. J., & Hughes, J. C. (1969). "Texture of cooked potatoes." I. Introduction. Journal of Science and Food Agriculture, No. 2, pp. 110–112.

Marshall, W.E., Wadsworth, J.I., Verma, L.R., Velupillai, L., (1993). "Determination the degree of gelatinization in parboiled rice: Comparison of a subjective and an objective method." Cereal Chem., Vol. 70, No. 2, pp. 226–230.

Mir, S. A., and Bosco, S. J. D., (2014). "Cultivar difference in physicochemical properties of starches and flours from temperate rice of Indian Himalayas." Food Chemistry, No. 157, pp. 448–456.

Mounsey J. S., Oriordan E. D.,(2008). " Influence of pre-gelatinised maize starch on the rheology, microstructure and processing of imitation cheese." J. Food Eng., No. 84, pp. 57–64.

Ratnayake, W. S., Jackson, D. S. (2008). "Thermal behavior of resistant starches RS 2, RS 3, and RS 4." Journal of Food Science, Vol. 73, No. 5, pp. 356–366.

Sharma, A., Yadav, B. S. ve Ritika, B. (2008). "Resistant starch: Physiological roles and food applications." Food Reviews International, No.24, pp. 193–234.

Singh, N., Sandhu, K.S. and Kaur, M., (2005). "Physicochemical properties ıncluding granular morphology, amylose content, swelling and solubility, thermal and pasting properties of starches from normal, waxy, high amylose and sugary corn." Progress in Food Biopolymer Research, No. 1, pp. 44-54.

Smith, A.M. (2001). "The Biosynthesis of starch granules." Biomacromolecules, Vol. 2, pp. 335-341.

Tester, R.F., Karkalas, J. and QI, X., (2004). "Starch structure and digestibility Enzyme-Substrate relationship." World's Poultry Science Journal, No. 60, pp. 186-195.

Wang, Y. J.; Wang, L. F.; Shephard, D., Wang, F. D.; (2002). "Patindol, J. Properties and structures of flours and starches from whole, broken, and yellowed rice kernels in a model study." Cereal Chem., No. 79, pp. 383-386.

Whittenberger, R. T., & Nutting, G. C., (1948). "Potato starch gels." Indian Engineering Chemistry, No. 40, pp. 1407.

Roughness coefficient of circular channels with smooth and rigid beds via evolutionary algorithm

Kiyoumars Roushangar[1, 2*] Roghayeh Ghasempour[1]

[1] Department of Water Resource Engineering, Faculty of Civil Engineering, University of Tabriz, Tabriz, Iran

[2] Center of Excellence in Hydroinformatics, University of Tabriz, Tabriz, Iran

Email: kroshangar@yahoo.com

ABSTRACT

The prediction of roughness coefficient in circular channels such as sewer pipes is an important issue in hydraulic engineering due to its importance in the design and management of water resources projects. The current study, applies Gene Expression Programming (GEP) as an evolutionary model to simulate the roughness coefficient of circular channels in limit of deposition state. Therefore, two types of channels bed conditions were considered: smooth bed and rough bed. For models developing, different input combinations were considered based on hydraulic and sediment characteristics The results proved the capability of the applied technique in prediction of the roughness coefficient and it was found that both hydraulic and sediment characteristics had impact on prediction process. Also, the sensitivity analysis results showed that Dimensionless particle number parameter is the most influential variable for roughness coefficient prediction in both smooth and rough bed channels.

Key words: *Circular channel, GEP, Limit of deposition, Roughness coefficient .*

1. Introduction

Sewer systems are important hydraulic structures which are used for carrying runoff and sewage. The presence of sediment and formation of bedforms can affect the performance of a sewer pipe and decrease the sediment carrying capacity by changing the hydraulic conditions by increasing the overall hydraulic roughness of the pipe. Decreases in the sediment carrying capacity in turn lead to blockage, surcharging, and local flooding. Therefore, estimation of the roughness coefficient in sewer pipes is an important issue for hydraulic engineers and researchers. However, accurate prediction of this parameter is difficult due to the multitude of factors influencing roughness such as bed material and bedforms. Numerous of classic friction factor models have been developed, which describe the complex phenomenon of the flow resistance. Ackers et al. (1964) reported the presence of permanently deposited sediment in sewers while studying the hydraulic roughness in sewers. Henderson (1984) drew attention to the importance of sewer roughness in relation to sewer performance. Henderson's (1984) studies showed that the sewer hydraulic roughness is influenced not only by the sewer materials but also the jointing of the pipe sections, pipe sliming, pipe ageing, and the presence of sediment deposits. Kleijwegt (1992) did experiments over loose beds in a 152 mm diameter pipe running full and part-full. May (2003) studied the sediment transport and roughness coefficient in horizontal pipes and developed a design method. Romanova et al. (2011) developed a novel, noninvasive, and in situ acoustic method and instrumentation to measure the water surface pattern, and, hence, determine the resistance and then the pipe wall roughness. Seifollahi et al. (2013) investigated the effects of pipe roughness uncertainty on water distribution network performance during an operational period. Due to the complexity and uncertainty of the roughness coefficient phenomenon, the results of the classical models are not general and under variable conditions do not yield the same results. Therefore, it is essential to use other methods with greater accuracy in predicting the roughness coefficient within the pipes under varied hydraulic and bed conditions.

In recent years artificial intelligence approaches [e.g., Artificial Neural Networks (ANNs), Neuro-Fuzzy models (NF), Genetic Programming (GP), Gene Expression Programming (GEP), Support Vector Machine (SVM), and Gaussian Process Regression (GPR)] have been used for the assessment of the accuracy of complex hydraulic and hydrologic phenomena, such as real-time flood forecasting (Ren et al., 2010), estimation of hydraulic jump characteristics

(Roushangar et al., 2018; Roushangar and Ghasempour, 2018), predicting bedload transport in sewer pipes (Roushangar & Ghasempour, 2017), and forecasting monthly and seasonal streamflow (Zhu et al., 2018). Urban storm sewer pipes have an important role in runoff and wastewater system management, therefore, the current study aimed to assess the capability of the GEP method in modeling roughness coefficient in circular pipes with smooth and rough beds. The hydraulic and sediment characteristics were used for modeling. Also, sensitivity analysis were done to determine the most important parameters in roughness coefficient modeling.

2. Materials and Methods

2.1. Used Data Sets

The data sets of laboratory experiments collected by May et al. (1989) and Ghani (1993) were used for modeling the roughness coefficient in pipes carrying storm water. May et al. (1989) did experiments on a pipe, sized 300 mm in diameter and 20 m in length. Thirty eight tests under part-full flow conditions were done out with non-cohesive sediment with median diameter, d50, of 0.72 mm and a specific gravity of 2.62, and the flow velocity was in the range $0.082 < V < 1.5$ m/s in a limit of deposition state. Ghani (1993) studied sediment transport and flow resistance in smooth and rough beds under part-full flow conditions. Two hundred fifty four experiments on flow resistance in the rigid bed state were done in sewer pipes with diameter, D, of 154, 305, and 450 mm and a length of 20.5 m. The ranges of some parameters used in the experiments are listed in Table 1 in which S_0, y/D, d_{50}, D, V, Cv, and Re represent pipe slope, proportional flow depth, particle median diameter, pipe diameter, flow velocity, sediment concentration, and flow Reynolds, number respectively. Also, k_0 indicates the bed roughness.

Table 1. The range of experimental data used in this study.

Channel bed	Researcher	Parameters				
		D(mm)	V(m/s)	**y**/D	d_{50} (mm)	C_v
Smooth bed	Ghani (1993)	154	0.24 - 0.862	0.153 - 0.756	0.93 - 5.7	38 – 145
		305	0.395 - 1.2	0.210 - 0.8	0.46 - 8.30	1- 1280
		450	0.502 - 1.2	0.50 - 0.75	0.72	2- 37
	May et al. (1989)	300	0.082-1.5	0.37-0.75	0.72	0.31-443
Rough bed	Ghani (1993)	305 Roughness 1 (k_0=0.53 mm)	0.411 – 1	0.18- 0.77	0.97 - 8.30	1- 923
		305 Roughness 2 (k_0=1.34 mm)	0.56 - 0.827	0.243 - 0.764	2.00 - 8.30	7- 403

2.2. Gene Expression Programming (GEP)

Gene expression programming (GEP) was developed by Ferreira (2001) using fundamental principles of the Genetic Algorithms (GA) and Genetic Programming (GP). Genetic Algorithms are the heuristic search and optimization techniques that mimic the process of natural evolution. Thus genetic algorithms implement the optimization strategies by simulating evolution of species through natural selection. GAs use populations of individuals (chromosomes), select them according to fitness, and introduce genetic variation using one or more genetic operators. In fact GA's are uniquely distinguished by having a parallel-population based search with stochastic selection of many individual solutions, stochastic crossover and mutation. GP, a branch of the genetic algorithm (GA), is a method for learning the most "fit" computer programs by means of artificial evolution and GEP is an extension to GP that evolves computer programs of different sizes and shapes encoded in linear chromosomes of fixed length. The fundamental difference between the three algorithms resides in the nature of the individuals: in GAs the individuals are symbolic strings of fixed length (chromosomes); in GP the individuals are non-linear entities of different sizes and shapes (parse trees); and in GEP the individuals are encoded as symbolic strings of fixed length (chromosomes) which are then expressed as non-linear entities of different sizes and shapes (expression trees). GEP as GA, mimics the biological evolution to create a computer program for simulating a specified phenomenon. The problems are encoded in linear chromosomes of fixed-length as a computer program (Ferreira, 2001) which are then expressed or translated into expression trees (ETs). GEP algorithm begins by selecting the five elements such as the function set, terminal set, fitness function, control parameters, and stop condition. There is comparison between predicted values and actual values in subsequent step. When desired results in accord with error criteria initially selected are found, the GEP process is terminated. If desired error criteria could not be found, some chromosomes are chosen by method called roulette wheel sampling and they are mutated to obtain new chromosomes. After desired fitness score is found, this process terminates and then the chromosomes are decoded for the best solution of the problem.

In the current study, the model's performance was evaluated using three statistical parameters: Correlation Coefficient (R), Determination Coefficient (DC), and Root Mean Square Errors (RSME), as depicted in equation (1).

$$DC = 1 - \frac{\sum_{i=1}^{N}(l_o - l_p)^2}{\sum_{i=1}^{N}(l_o - \overline{l_p})^2}$$

$$R = \frac{\sum_{i=1}^{N}(l_o - \overline{l_o}) \times (l_p - \overline{l_p})}{\sqrt{\sum_{i=1}^{N}(l_o - \overline{l_o})^2 \times (l_p - \overline{l_p})^2}} \quad (1)$$

$$RMSE = \sqrt{\sum_{i=1}^{N}\frac{(l_o - l_p)^2}{N}}$$

where l_o , l_p , $\overline{l_o}$, $\overline{l_p}$, N respectively are: the measured values, predicted values, mean measured values, mean predicted values and number of data samples.

Using non-normalized data in estimation of the intended parameter may lead to undesirable accuracy; therefore, all datasets were normalized before modeling. This will increase the capability of the SVM model. The equation (2) was used to normalize the data utilized in this study:

$$x_n = 0.1 + 0.7 \times \left(\frac{x - x_{min}}{x_{max} - x_{min}} \right) \quad (2)$$

Where x_n, x, x_{max}, x_{min} respectively are: the normalized value of variable x, the original value, the maximum and minimum of variable x.

3. Simulation and models development

3.1. Input variables

Appropriate selection of input parameters is an important step in modeling process using an intelligent technique. According to the experimental studies by May et al. (1989), Ghani (1993), and Vongvisessomjai et al. (2010) flow resistance in sewer pipes can be affected by following parameters:

V, Dgr, d_{50}, D, y or R, F_{rm}, C_v

where R is hydraulic radius, Dgr is Dimensionless particle number, and F_{rm} is Modified Froude number. Tree states were considered for models developing. State 1 based on hydraulic characteristics, state 2 based on both hydraulic and particle characteristics without using Cv, and state 3 based on hydraulic and particle characteristics considering Cv as an input parameter. In the current study, Manning's roughness coefficient, n, was considered as the output parameter. Table 2 lists the models developed for assessing the roughness coefficient in sewer pipes with different bed conditions. In Table 2 Fr is flow Froude number.

Table 2. Developed Models for predicting n.

State	Model	Input variables
1	(I)	Re
	(II)	F_r
	(III)	Re, y/D
	(IV)	F_r, y/D
2	R(I)	F_{rm}, D_{gr},d_{50}/D
	R(II)	F_{rm}, D_{gr}, y/d_{50}
	R(III)	F_{rm}, D_{gr}, d_{50}/y
3	CR(I)	F_{rm}, D_{gr}, C_v
	CR(II)	F_{rm}, D_{gr}, y/d_{50}, C_v

4. Results and Discussion

4.1. State 1 for roughness coefficient modeling

State 1 was developed based on hydraulic features. For assessing the roughness coefficient modeling in circular channels using only hydraulic characteristics as input parameters four models were developed for smooth and rough rigid beds. The results of the GEP models are presented in Table 3 and Fig 1. From the obtained results, it can be stated that the estimated and observed values of the state 1 are not in good agreement. For this state, model (III) with parameters Re and y/D led to more accurate outcomes than the other models. As it can be seen in Table 3, the developed models for a smooth bed led to better prediction than for a rough bed.

Table 3. Statistical parameters of the GEP models; sate 1.

Models	Performance criteria					
		Train			Test	
Smooth bed	R	NSE	RMSE	R	NSE	RMSE
(I)	0.905	0.814	0.059	0.921	0.768	0.069
(II)	0.463	0.289	0.115	0.331	0.129	0.096
(III)	0.919	0.844	0.048	0.914	0.815	0.066
(IV)	0.907	0.847	0.048	0.932	0.752	0.070
Rough bed						
(I)	0.734	0.513	0.106	0.721	0.455	0.163
(II)	0.449	0.166	0.135	0.432	0.119	0.096
(III)	0.858	0.734	0.075	0.871	0.727	0.115
(IV)	0.843	0.714	0.077	0.823	0.620	0.134

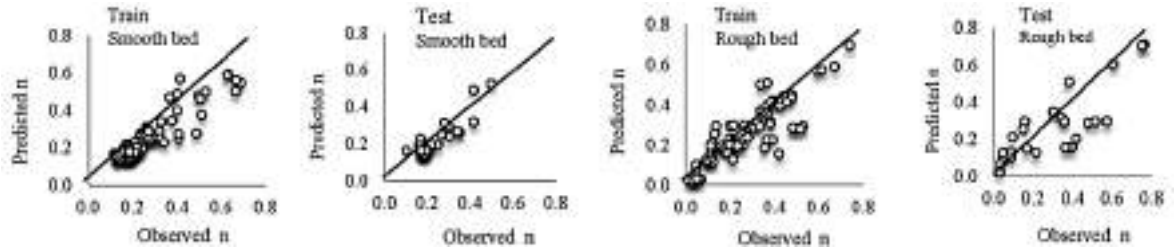

Fig. 1. Comparison of observed and predicted roughness coefficient for superior model of sate 1.

4.2. State 2 for roughness coefficient modeling

In state 2 for modeling the roughness coefficient in circular channels with different bed conditions several models were developed based on the flow and sediment characteristics without considering the Cv as an input parameter. The obtained results from the GEP models are listed in Table 4 and shown in Fig. 2(a). From the obtained results of the statistical parameters, it can be stated that model R(II) with input parameters F_{rm}, Dgr, and y/d_{50} led to more accurate results for the state of smooth and rough beds. It can be inferred that in modeling the roughness coefficient in pipes, state 2 which took advantage of both flow and sediment characteristics as input, performed better than sate 1.

4.3. State 3 for roughness coefficient modeling

In state 3 the models were developed based on the flow and sediment characteristics considering the Cv as an input parameter. The results obtained for Scenario 3 are listed in Table 4 and shown in Fig. 2(b). According to the Table 4, it can be seen that in the state of rigid beds for smooth and rough pipes the model CR(II) with input parameters Cv, F_{rm}, Dgr, and y/d_{50} led to a more accurate outcome. It can be deduced that using parameter y/d50 increased the model's accuracy. With comparing the results of sates 2 and 3, it can be deduced that in modeling the roughness coefficient, sate 3 performed better than state 2 and using Cv increased the model's efficiency.

Table 4. Statistical parameters of the GEP; sates 2 and 3.

State	Model	Performance criteria					
		Train			Test		
		R	NSE	RMSE	R	NSE	RMSE
2	Smooth bed						
	R(I)	0.911	0.834	0.056	0.914	0.750	0.077
	R(II)	0.955	0.909	0.044	0.964	0.873	0.056
	R(III)	0.951	0.912	0.047	0.935	0.814	0.061
	Rough bed						
	R(I)	0.722	0.571	0.016	0.664	0.371	0.184
	R(II)	0.933	0.821	0.062	0.852	0.787	0.016
	R(III)	0.932	0.913	0.042	0.892	0.761	0.108
3	Smooth bed						
	CR(I)	0.981	0.883	0.047	0.921	0.771	0.079
	CR(II)	0.988	0.957	0.015	0.915	0.893	0.027
	Rough bed						
	CR(I)	0.763	0.664	0.051	0.736	0.594	0.057
	CR(II)	0.994	0.968	0.042	0.852	0.805	0.013

(a)

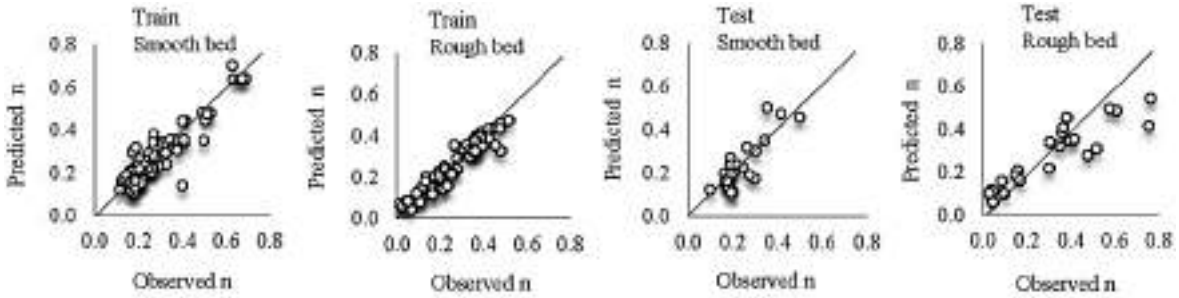

(b)

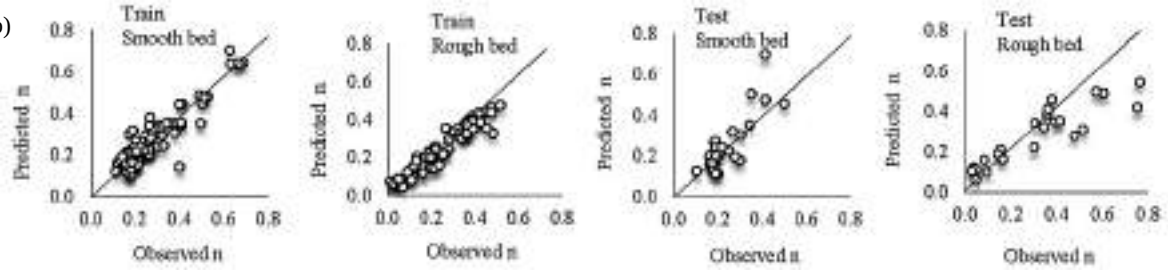

Fig. 2. Comparison of observed and predicted roughness coefficient for superior model of (a): sate 2 and (b): state 3.

4.4. Sensitivity analysis

Sensitivity analysis is used to evaluate the effect of different variables on the roughness coefficient in sewer pipes. For evaluating the impact of each independent parameter, the best GEP model (sate 3) was run with all input parameters and then, one of the input parameters was eliminated and the GPR model was re-run. The change in the RMSE error criteria (ΔRMSE) which represents the percentages of the added values to the error criteria for each eliminated parameter, was used as an indication of the significance of each parameter. Figure 3 shows the sensitivity analysis results. According to the Fig. 3, it can be deduced` that variable Dgr for smooth and rough rigid beds had the most significant impact on the modeling.

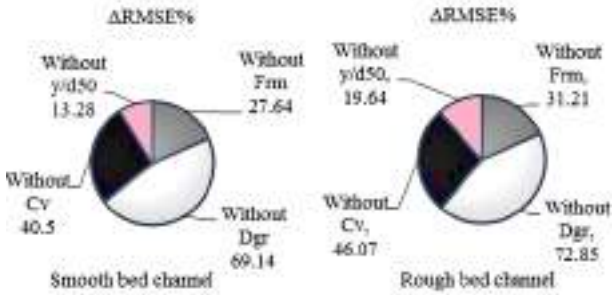

Fig. 3. Statistical parameters of the GEP models for smooth channels.

5. Conclusion

In this study, the capability of GEP model was assessed for predicting the roughness coefficient in circular channels with smooth and rough beds. Different models based on flow and sediment characteristics were developed under three states. The obtained results showed that in predicting of the roughness coefficient, modeling based on both flow and sediment characteristics performed better than modeling based on only flow characteristics. Also, adding variable Cv as an input parameter (state 3) improved the models' efficiency. The results showed that the best performance for smooth and rough bed pipes was the model with inputs parameters C_v, F_{rm}, Dgr, and y/d_{50}. It was found that the developed models for smooth beds yielded better prediction than rough beds and using parameter y/d_{50} increased the models' accuracy. Sensitivity analysis showed that variable Dgr had the most significant impact on the modeling.

REFERENCES

Ackers, P., Crickmore, M. J., & Holmes, D. W. (1964). Effects of use on the hydraulic resistance of drainage conduits. *Proceedings of the Institution of Civil Engineers*, *28*, 339-360.

Ferreria, C. (2001). Gene expression programming: a new adaptive algorithm for solving problems. *Complex Syst*, 13(2), 87–129.

Ghani, A. A. (1993). *Sediment transport in sewers (Ph.D. dissertation)*. Department of Civil Engineering, University of Newcastle Upon Tyne, England.

Henderson, R. J. (1984). *A guide to hydraulic roughness in sewers*. External Report E, WRc Engineering, Swindon, England.

Kleijwegt, R. A. (1992) Sewer sediment models and basic knowledge. *Water Science and Technology*, *25*(8), 123-130.

May, R. W. P., Brown, P. M., Hare, G. R., & Jones, K. D. (1989). *Self-cleansing conditions for sewers carrying sediment, Report SR 221*. Hydraulics Research Ltd., Wallingford, England.

May, R.W.P. (2003). Preventing sediment deposition in inverted sewer siphons. *Journal of hydraulic* Engineering, *129*(4), 283-290.

Ren, M., Wang,, B., Liang, Q., & Fu, G. (2010). Classified real-time flood forecasting by coupling fuzzy clustering and neural network. *International Journal of Sediment Research*, *25*(2), 134-148.

Richardson, E. V., &Simons, D. B. (1967). Resistance to flow in sand channels. *Proceedings, 12th IAHR Congress,* Vol. 1, (pp. 141-148).

Roushangar, K., & Ghasempour, R. (2017). Estimation of bedload discharge in sewer pipes with different boundary conditions using an

evolutionary algorithm. *International Journal of Sediment Research*, *32*(4),564-574.

Roushangar, K., R. Ghasempour, and R. Valizadeh. (2018). "Effect of Channel Boundary Conditions in Predicting Hydraulic Jump Characteristics using an ANFIS-Based Approach." *Journal of Applied Fluid Mechanics*, 11(3).

Roushangar, Kiyoumars, and Roghayeh Ghasempour. (2018). "Evaluation of the impact of channel geometry and rough elements arrangement in hydraulic jump energy dissipation via SVM." *Journal of Hydroinformatics* 21(1), 92-103.

Seifollahi, S., Haddad, O.B., Omid, M.H., & Mariño, M.A. (2013). Effects of pipe roughness uncertainty on water distribution network performance during its operational period. *Water Resources management*, *27*(5), 1581-1599.

Vongvisessomjai, N., Tingsanchali, T., & Babel, M. S. (2010). Non-deposition design criteria for sewers with part-full flow. *Urban Water Journal*, *7*(1), 61-77.

Zhu, S., Luo, X., Xu, Z., & Ye, L. (2018). Seasonal streamflow forecasts using mixture-kernel GPR and advanced methods of input variable selection. *Hydrology Research*, nh2018023.

CISET - 2nd Cilicia International Symposium on Engineering and Technology
10-12 October, 2019, Mersin / TURKEY

DRYING OF SLUDGE BY HEAT, CASE STUDY

Hüdaverdi Arslan[1], Mutlu Yalvaç[2]

[1]Mersin University, Engineering Faculty,Environmental Engineering Department, Mersin, Turkey,
harslan@mersin.edu.tr

[2]Mersin University, Engineering Faculty,Environmental Engineering Department, Mersin, Turkey,
myalvac@mersin.edu.tr

ABSTRACT
Significant amounts of treatment sludge are formed at the end of domestic and industrial wastewater treatment plants. Sewage sludge contains concentrated chemical and biologically pollutant. For sludge disposal, procedures are carried out within the framework of the relevant legislation issued within the scope of environmental law in our country. Among these issues, the Waste Management Regulation and the Regulation on the Use of Domestic and Urban Treatment Sludges limited the using of this in Soil. However, sludge can be used as an alternative fuel in cement plants. The limiting parameter in their use is the moisture content.
Thıs study has investigated the potentiality of using the after dried sludge generated from the domestic and industrial wastewater treatment plant in Mersin province. In the study, a drying system with a capacity of 96 tons/day was established in Mersin. The system can reduce the sludge moisture content from 80% to reach 10%. The dried sludge has a thermal value of 2000-2500 kcal/kg. The dried sludge is proposed to be used as an alternative fuel in licensed facilities.

Keywords: *Sewage sludge, heat drying, reuse*

1. INTRODUCTION

The protection of the natural environment is one of the most important issues all over the world. In recent years, studies on the development of technologies that do not generate waste or where waste is least produced are rapidly increasing. Many old and widely used treatment technologies cause secondary waste while treating primary waste. Domestic and industrial wastewater treatment plants are widely used. However, sewage sludge from these plants constitutes secondary wastes harmful to the environment. Treatment sludge is formed in all physical, chemical and biological processes. Treatment of this sludge brings additional investment and costs. For example, activated sludge treatment is still a widely used method in the treatment of waste water. Organic pollutants with activated sludge process can be treated in an efficient and economical way cleaved by microbial activities. However, large amounts of sewage sludge are produced at the end of this process (Chung et al., 2009). Industrial and domestic sludge are often considered useless biological waste due to the high concentration of heavy metals, the presence of pathogens and other harmful substances. In the disposal of this sludge, traditional methods such as soil filling, pumping to the ocean and incineration are used worldwide (He et al., 2014). However, these methods are no longer recommended because they constitute a secondary source of pollutants in the soil, sea and atmosphere, and because of the new environmental regulations for solid waste (Laurent et al., 2011). Treatment and disposal of sewage sludge amounts to 25-65% of the total operating cost of a wastewater treatment plant (Pérez-Elvira et al., 2006; Wilson and Novak, 2009). In recent years, useful applications such as composting and fermentation of sewage sludge and fertilizer and biogas production have been carried out. However, it is not possible to obtain good yields from these methods for each treatment sludge (Baati et al., 2018; Li et al., 2017; Oh and Lee, 2018; Zhang et al., 2017).

Heat treatment of treatment sludge is an appropriate commercial option to obtain heat and energy. As a result of heat treatment, all pathogens die and the sludge volume is reduced (Magdziarz and Werle, 2014). However, the high water content (> 95%) of the sludge can limit the effective and economic application of conventional heat treatments (Chung et al., 2009; Strong et al., 2011; Wang and Li, 2015). Hydrothermal treatment, which uses water as a reactant and solvent as a special thermal method for the treatment of sewage sludge, has received increasing attention in recent years (Hii et al., 2014; Kim et al., 2015; Wu et al., 2018). Hydrothermal carbonization was used to recover solid carbon fuel (hydrochar) (Danso-Boateng et al., 2015; Yang et al., 2018). The main purpose of these processes is to produce gas, liquid and solid energy products from the previously dewatered treatment sludge. Drying of sludge prior to these processes requires significant costs (Park, M. et al., 2019).

2. MATERIAL AND METHOD

2.1.Material

Waste sludge from domestic and industrial treatment systems will be used.

2.1.1. Working Area

This study was conducted in Hazardous and Non-Hazardous Waste Recycling Facility which is being established in Akdeniz District of Mersin City. In this plant, high-humidity sewage sludge and solid wastes with thermal value will be dried.

2.2.Method

Sewage sludge is separated by waste producers according to waste codes and collected in temporary waste storage. These wastes are brought to licensed facilities by licensed transportation vehicles. Wastes coming to the facility are weighed and accepted wastes are taken to appropriate temporary storage area according to waste codes. Wastes are stored in a closed area of 1500 m^2 temporary storage area in sealed concrete structure in a way not to exceed 4 m height. Wastes in the facility are transported from the temporary stock area by appropriate methods to the drying unit. The feeding unit will be fed 24 times a day from the drying unit. Drying will be done with rotary drum drying unit. In the project, it is planned to install one rotary drum with a capacity of 96 tons / day. The front and rear parts of the rotary drum where the drying takes place is fixed and the raw material will be dried by the rotation process. The dried raw material shall be stored in a sealed material reinforced concrete structure of 500 m^2 dry material storage area not exceeding 4 m height. Wood pellet or charcoal will be used for drying. Wood pellets or coal will be used for the realization of a drying process. Before starting the drying process, the furnace will be burned with wood pellet or coal and sludge will be fed when it reaches the desired temperature. The outside of the rotating drum will be surrounded by glass wool and the inside by brick to maintain the desired temperature. The sludge from the feed line to the drying unit will be dried to approximately 90% dryness. It is planned to reach the desired dryness in approximately 1 hour by subjecting 4 tons of sludge drying to each charge. Dried sludge will be transported to licensed Hazardous Waste Recycling or Hazardous Waste Disposal Facility by licensed vehicles. The subject of the project is sludge drying. There is no incineration process in this process. Drying system consists of cooker, firebrick, rotary suction cyclones and suction fans.

1) Hearth section of the dryer; According to the capacity needed to produce calories. This section is covered with refractory material operating at a temperature of 1500 ^oC, it is called hell.

2) Wet raw material is conveyed to the feeding section on the drying system with the help of spiral carrier.

3) In the rotary dryer section, the heated air and the raw material move together.

4) Steam separated from the raw material by high temperature; Thanks to the air flow inside, it moves

faster than the raw material which is drying and it is thrown out of the chimney as water vapor by means of high suction fans.

5) The raw material which is moved 150 cm by force in the dryer is brought back by force by 50 cm.

6) Moisture extracted from the raw material is absorbed by the fans and thrown out. This prevents the agglomeration and re-adherence of the steam to the raw material. The efficiency of the system is also increased.

7) The raw material, which is reduced to the desired moisture content, that is drying, is discharged from the drying system by means of the outlet screw and elevator.

8) Dryer is made of 6341 boiler sheet. This material is high temperature resistant.

The temperature of the air used in the system is maximum 1500 ºC. Hot air is mixed with cold air in certain proportions so that the raw material does not burn. During the process, the temperature of the air is kept under control between 200 - 1250 ºC.

3. RESULTS AND CONCLUSION

Many technologies have been developed for the disposal of sewage sludges. The first step of these technologies is drying. Before the sludge is used for any other purpose, the bound or free water contained in it must be substantially reduced. In all domestic or industrial wastewater treatment plants, after sludge treatment, treatment sludge is formed as a secondary source of pollution. In the installation described above, the sludge will be dried before final disposal of the treatment sludge. The advantages of the drying process can be listed as follows.

1. The volume of sewage sludge will be reduced by an average of 80%.

2. If it is not to be used for any other purpose, the space it occupies in the landfills, which are the final disposal, will be reduced.

3. One of the most important problems of sewage sludge is odor problem. The odor problem of the dried sludges will be greatly reduced.

4. Dried sewage sludge has an average thermal value of 2000 kcal / kg. This will allow the use of the dried material as an alternative fuel. This can be considered as renewable energy by using it in energy production.

5. Depending on the content of dried sludge, it will gain economic value as there will be soil healing material within the scope of the legislation.

6. In this way, a waste that requires cost disposal will gain economic value.

ACKNOWLEDGEMENTS

The authors report no conflicts of interest. The authors alone are responsible for the content and writing of this article.

REFERENCES

Baati, S., Benyoucef, F., Makan, A., El Bouadilli, A., El Ghmari, A., 2018. Influence of hydraulic retention time on biogas production during leachate treatment. Environ. Eng. Res. 23 (3), 288–293.

Chung, J., Lee, M., Ahn, J., Bae, W., Lee, Y.W., Shim, H., 2009. Effects of operational conditions on sludge degradation and organic acids formation in low-critical wet air oxidation. J. Hazard Mater. 162 (1), 10–16.

Danso-Boateng, E., Shama, G., Wheatley, A.D., Martin, S.J., Holdich, R.G., 2015. Hydrothermal carbonisation of sewage sludge: effect of process conditions on product characteristics and methane production. Bioresour. Technol. 177, 318–327.

He, C., Chen, C.L., Giannis, A., Yang, Y., Wang, J.Y., 2014. Hydrothermal gasification of sewage sludge and model compounds for renewable hydrogen production: a review. Renew. Sustain. Energy Rev. 39, 1127–1142.

Hii, K., Baroutian, S., Parthasarathy, R., Gapes, D.J., Eshtiaghi, N., 2014. A review of wet air oxidation and thermal hydrolysis technologies in sludge treatment. Bioresour. Technol. 155, 289–299.

Kim, D., Lee, K., Park, K.Y., 2015. Enhancement of biogas production from anaerobic digestion of waste activated sludge by hydrothermal pre-treatment. Int. Biodeterior. Biodegrad. 101, 42–46.

Laurent, J., Casellas, M., Carrere, H., Dagot, C., 2011. Effects of thermal hydrolysis on activated sludge solubilization, surface properties and heavy metals biosorption. Chem. Eng. J. 166 (3), 841–849.

Li, Y., Zhai, Y., Zhu, Y., Peng, C., Wang, T., Zeng, G., Wu, D., Zhao, X., 2017. Distribution and conversion of polycyclic aromatic hydrocarbons during the hydrothermal treatment of sewage sludge. Energy Fuels 31 (9), 9542–9549

Magdziarz, A., Werle, S., 2014. Analysis of the combustion and pyrolysis of dried sewage sludge by TGA and MS. Waste Manag. 34 (1), 174–179.

Oh, J., Lee, H., 2018. Exploring a zero food waste system for sustainable residential buildings in urban areas. Environ. Eng. Res. 23 (1), 46–53.

Park, M., Kim, N., Lee, S., Yeon, S., Seo, J.,H., Park, D., 2019. A study of solubilization of sewage sludge by hydrothermal treatment. Journal of Environmental Management 250, 109490

Pérez-Elvira, S.I., Nieto Diez, P., Fdz-Polanco, F., 2006. Sludge minimisation technologies. Rev. Environ. Sci. Biotechnol. 5 (4), 375–398.

Strong, P.J., McDonald, B., Gapes, D.J., 2011. Combined thermochemical and fermentative destruction of municipal biosolids: a comparison between thermal hydrolysis and wet oxidative pre-treatment. Bioresour. Technol. 102 (9), 5520–5527.

Wang, L.P., Li, A.M., 2015. Hydrothermal treatment coupled with mechanical expression at increased temperature for excess sludge dewatering: the dewatering performance and the characteristics of products. Water Res. 68, 291–303.

Wilson, C.A., Novak, J.T., 2009. Hydrolysis of macromolecular components of primary and secondary wastewater sludge by thermal hydrolytic pretreatment. Water Res. 43 (18), 4489–4498.

Wu, K., Zhang, X., Yuan, Q., 2018. Effects of process parameters on the distribution characteristics of inorganic nutrients from hydrothermal carbonization of cattle manure. J. Environ. Manag. 209, 328–335.

Yang, S.K., Kim, D., Han, S.K., Kim, H., Park, S., 2018. Conversion of organic resdue from solid-state anaerobic digestion of livestock waste to produce the solid fuel through hydrothermal carbonization. Environ. Eng. Res. 23 (4), 456–461.

Zhang, Q., Hu, J., Lee, D.J., Chang, Y., Lee, Y.J., 2017. Sludge treatment: current research trends. Bioresour. Technol. 243, 1159–1172.

CISET - 2nd Cilicia International Symposium on Engineering and Technology
10-12 October, 2019, Mersin / TURKEY

CLASSIFICATION PERFORMANCE COMPARISONS OF DEEP LEARNING MODELS IN PNEUMONIA DIAGNOSIS USING CHEST X-RAY IMAGES

Osman Doğuş Gülgün [*1] and Hamza Erol [2]

[1] Mersin University, Engineering Faculty, Computer Engineering Department, Mersin, Turkey, dogusgulgun@gmail.com

[2] Mersin University, Engineering Faculty, Computer Engineering Department, Mersin, Turkey, herol@mersin.edu.tr

ABSTRACT
Data set containing 5840 x-ray images of individuals was classified into two categories which are pneumonia and healthy person using deep learning models convolutional neural network, convolutional neural network with data augmentation and transfer learning. For the three deep learning models used in the classification; loss and classification accuracy values were compared. In comparison of three different deep learning models with two different performance values, 5216 chest x-ray images in the data set were used to train the deep learning model and the remaining 624 were used to test the model.

Keywords: *Classification, Deep Learning, Medical Diagnosis, Data Augmentation, Convolutional Neural Network*

[*] Corresponding Author

1. INTRODUCTION

The dataset containing chest x-ray images consists of image data from two classes [1]. Two classes in the data set; refers to people with pneumonia and healthy people. The data set was obtained from x-ray images of children aged one to five years from Guangzhou Women's and Children's Medical Center. Chest x-ray images of 5840 individuals are included in the data set. 5216 images in the data set were used to train the deep learning model and the remaining 624 images were used to test this model [1]. An exemplary chest x-ray image in the data set is given in Figure 1.

Fig. 1. An exemplary chest x-ray image in the data set.

2. METHOD

In this section, classification of the dataset consisting of 5840 x-ray images of 5840 individuals into two categories as: people with pneumonia and healthy people using deep learning models: convolutional neural network, convolutional neural network with data augmentation and transfer learning will be explained.

In the comparison of three different deep learning models with two different performance values, 5216 chest x-ray images in the data set were used to train the deep learning model and the remaining 624 were used to test this model.

For the three deep learning models used in the classification; loss and classification accuracy values were calculated with the software prepared in python programming language. As a result of the calculations, graphs of performance values were created for deep learning models.

2.1. Classification Using Convolutional Neural Network Model

In order to diagnose pneumonia from the image data, convolutional neural network deep learning model was used first. In the design of convolutional neural network model, keras library was used in software. In the models used in the study, the image matrices of the images in the data set are obtained primarily in the size of 64x64. The resulting image matrices are first transformed with 3x3 filters to extract feature maps from the images. In this way, it is provided to determine the desired parts in the images and find the desired features [2].

The image matrices are then transferred by the model to the pooling layer. This layer reduces the image size and reduces the number of pixels [3]. In this way, the performance and speed of the model is increased and the problem of overfitting, which results in excessive adaptation of the model to the training set during the learning stage, is also avoided. In the convolutional neural network model used in the study, image matrices are passed through convolution and pooling layers two more times, respectively. Thus, it is provided that the model can detect the desired parts in the image and the classification performance of the model is increased.

In the model used in this stage, 32 filters were used in the first convolution layer and 64 filters were used in the second and third convolution layers. The image matrices are then transferred to the fully connected layer. The data is processed in the artificial neural network, first the model is trained with the training data and then the performance of this model is tested by using the test data. In the artificial neural network, sigmoid function was used in the software. In addition, dropout technique was used in the software. With this technique, half of the neurons are disabled in different iterations with different possibilities during data processing in the artificial neural network [4]. Dropout technique is also useful for avoiding the problem of overfitting. By using this technique, the classification performance of the model is improved.

2.1.1. Calculation of Classification Performance Values of Convolutional Neural Network Model

Classification performance values of convolutional neural network model: loss and classification accuracy values were calculated with the software prepared in python programming language.

2.1.1.1. Loss Value

The graph of the loss performance values generated as a result of the application of convolutional neural network model is shown in Figure 2.

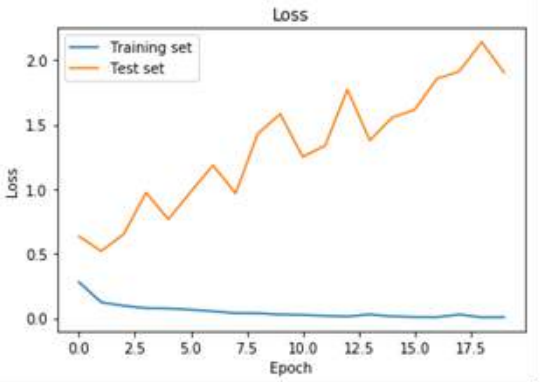

Fig. 2. Graph of loss performance values generated by the application of convolutional neural network model.

2.1.1.2. Classification Accuracy Values

The graph of the classification accuracy performance values generated by the application of the convolutional neural network model is shown in Figure 3.

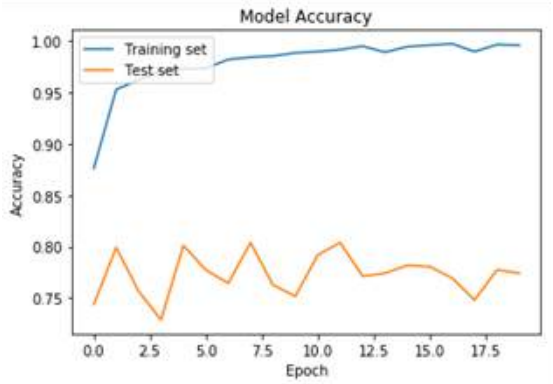

Fig. 3. Graph of classification accuracy performance values generated by the application of the convolutional neural network model.

2.1.1.3. Performance Evaluation

It is seen that the percentage of correct classification of test data at the test stage of the trained model with this data set is 75-80%. The best classification performance of the model is 80.4% accuracy at the 12th iteration. It is understood from the results that the convolutional neural network model used in this stage shows a successful classification performance and it is suitable for the diagnosis of the disease, however, in this model, when the data augmentation technique is used, it is seen that the model gives better results in the next stage results.

2.2. Classification Using Convolutional Neural Network Model with Data Augmentation

In order to diagnose pneumonia from the image data, a convolutional neural network model similar to the previous step was used. However, in the convolutional neural network model used in this stage, the classification performance is improved by using data augmentation technique. Using this technique, images are shown again at different angles and at different distances to the model [5]. In this way, the model learns better from the trainig data and the classification performance of the model is improved. Although the model used in this stage is the same as the model in the first stage, the effect of data augmentation technique applied to the model in this stage on the classification performance of the model was observed.

2.2.1. Calculation of Classification Performance Values of Convolutional Neural Network Model with Data Augmentation

.

The classification performance values of the convolutional neural network model with data augmentation: loss, and classification accuracy values were calculated with the software prepared in python programming language. Graphs of the values obtained as a result of the calculation are given.

2.2.1.1. Loss Value

The graph of loss performance values generated as results of the application of the convolutional neural network model with data augmentation is shown in Figure 4.

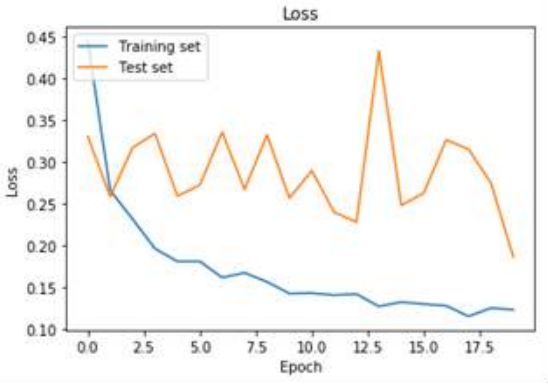

Fig. 4. Graph of loss performance values generated as results of the application of the convolutional neural network model with data augmentation.

2.2.1.2. Classification Accuracy Values

The graph of the classification accuracy values generated by the application of the convolutional neural network model with data augmentation is shown in Figure 5.

Fig. 5. Graph of classification accuracy values generated by the application of the convolutional neural network model with data augmentation.

2.2.1.3. Performance Evaluation

When the results obtained from the model are examined, it is seen that the model has reached the lowest loss value in the 20th iteration and this value is 0.1864. It is seen that the percentage of accurate classification of test data during the test phase of the trained model is 89-93%. The best classification performance of the model is 93.4% accuracy rate in the 20 th iteration. Therefore, the model was able to accurately predict the class of 93.4% of the test data. At this stage, it can be seen that the data augmentation technique used in convolutional neural network model increases the model success and classification performance.

As a result of the data augmentation technique used in the model, the model has succeeded in extracting the disease-related features more successfully from images that vary in terms of size, angle and proximity. Thus, the model showed a higher classification performance compared to the previous stage. It can be seen from the results that the model created at this stage is suitable for

use in providing diagnosis of disease through medical images.

2.3. Classification Using Transfer Learning Model

Transfer learning technique was used in the creation of the third model to be used for the diagnosis of pneumonia from the image data. At this stage, weights of the VGG16 neural network, which was previously trained using a data set containing 1000 classes, will be used in the model to be used in the classification of image data [6]. The output layer of the VGG16 model has been changed and adapted to solve this problem which includes 2 classes. The most important advantage of this technique and this model is that it has been optimally trained by a multidimensional dataset. Therefore, the feature map of the model is highly developed. The classification results obtained from the model used in this section are given in the results section.

2.3.1. Calculation of Classification Performance Values of Transfer Learning Model

The classification performance values of the transfer learning model: loss, and classification accuracy values were calculated with the software prepared in python programming language. The values obtained from the calculation are given.

2.3.1.1. Loss Value

When the results obtained from the model were examined, it was observed that the loss value calculated after the test with the test data of the model was 0,17.

2.3.1.2. Classification Accuracy Values

When the results were examined, it was seen that the accuracy percentage of the test classification of the model was 85,6%. The results obtained from the model using the python programming language are shown in Figure 6.

```
Found 5216 images belonging to 2 classes.
Found 624 images belonging to 2 classes.
165/165 [==============================] - 19694s 119s/step - loss:
0.1679 - acc: 0.9311 - val_loss: 0.3984 - val_acc: 0.8564
```

Fig. 6. The results obtained from the model using the python programming language

3. CONCLUSIONS AND SUGGESTIONS

When the results of the models used in this study were examined, it was observed that the correct classification rate of the convolutional neural network model, which is the first model, reached 80.4%. The second neural network model, which was formed by applying data augmentation technique to convolutional neural network model, showed that accurate classification rate of test data reached up to 93.4%. Therefore, when the results are examined, it is understood that the data augmentation technique improves the classification performance of the convolutional neural network model. The last model used in this study was obtained by using the structure of VGG16 model, which has been obtained by training with a data set containing 1000 classes, by using transfer learning technique. The output layer of this model was rearranged in accordance with the two-class classification problem in the study. According to the results, the model succeeded in classifying the test data with an accuracy rate of 85.6%.

When the performance of three different deep learning models is considered, it is seen that the most successful classification results are obtained by convoltional neural network model with data augmantation. Therefore, it is understood from the results that deep learning techniques such as data augmentation and dropout used in convoluted neural networks have a positive effect on the diagnostic classification performance of the model. In addition, these techniques help to avoid the problem of overfitting in deep learning models, that is, the model's misinterpretation of the classes of new samples due to excessive adaptation to training data. In deep learning neural network models, it is thought that increasing the filter size and number of filter parameters used in convolution process will increase the model performance and increase the classification success.

REFERENCES

[1] Kermany, Daniel; Zhang, Kang; Goldbaum, Michael (2018), “Labeled Optical Coherence Tomography (OCT) and Chest X-Ray Images for Classification”, Mendeley Data, v2

[2] Springenberg, J. T., Dosovitskiy, A., Brox, T., & Riedmiller, M. (2014). Striving for simplicity: The all convolutional net. arXiv preprint arXiv:1412.6806.

[3] Krizhevsky, A., Sutskever, I., & Hinton, G. E. (2012). Imagenet classification with deep convolutional neural networks. In Advances in neural information processing systems (pp. 1097-1105).

[4] Srivastava, N., Hinton, G., Krizhevsky, A., Sutskever, I., & Salakhutdinov, R. (2014). Dropout: a simple way to prevent neural networks from overfitting. The journal of machine learning research, 15(1), 1929-1958.

[5] Wong, S. C., Gatt, A., Stamatescu, V., & McDonnell, M. D. (2016, November). Understanding data augmentation for classification: when to warp?. In 2016 international conference on digital image computing: techniques and applications (DICTA) (pp. 1-6). IEEE.

[6] Molchanov, P., Tyree, S., Karras, T., Aila, T., & Kautz, J. (2016). Pruning convolutional neural networks for resource efficient transfer learning. arXiv preprint arXiv:1611.06440, 3.

CISET - 2nd Cilicia International Symposium on Engineering and Technology
10-12 October, 2019, Mersin / TURKEY

EFFECT OF SEAWATER AGEING ON THE HARDNESS PROPERTIES OF GFRP COMPOSITE PIPES

Alper Gunoz [*1], Yusuf Kepir [2], Memduh Kara [3]

[1] Mersin University, Faculty of Engineering, Department of Mechanical Engineering, Mersin, Turkey, alpergunoz@mersin.edu.tr

[2] Mersin University, Faculty of Engineering, Department of Mechanical Engineering, Mersin, Turkey, yusufkepir94@gmail.com

[3] Mersin University, Faculty of Engineering, Department of Mechanical Engineering, Mersin, Turkey, memduhkara@mersin.edu.tr

ABSTRACT
Glass reinforced plastic (GFRP) composite pipes have many superior properties such as resistance to corrosion and adverse weather conditions caused by chemicals and long life. GFRP composite pipes are used in submarine oil and natural gas transmission lines and transmission lines of chemical fluids. The changes in the mechanical properties of composite pipes used in submarine applications are of great importance in terms of the service life of the material. Some of these mechanical properties are hardness and density value. In this study, the changes in the hardness and density values of GFRP composite pipes which were kept in seawater for one month were investigated. According to this study, it has been determined and evaluated that the mechanical properties of the sample have been changed with the effect of seawater.

Keywords: *GFRP composite pipe, seawater effect, hardness properties, density properties*

[*] Corresponding Author

1. INTRODUCTION

Glass fiber reinforced plastic materials (GFRP) are composite materials produced by incorporating glass fibers as reinforcement material into the resin. The glass fibers may be present in the composite material in a continuous or discontinuous phase. Many studies have been carried out to investigate the mechanical properties of glass fiber pipes due to the rapid increase in their usage. Glass fiber reinforced polymer (GFRP) composites are recommended for use in marine infrastructures. These materials, due to their excellent corrosion resistance and light weight property have gathered tremendous attention in marine sectors for applications in ship building industry, water storage vessels, desalination plants, manufacture of leisure boats etc (Gellert and Turley, 1999; Kara, 2012; Kootsookos et al., 2001). It is also widely used in sectors such as civil defense and aerospace due to its many advantages such as long lifetime and low cost (Schutte, 1994).

Irreversible changes in mechanical properties occur when the composite materials are exposed to environmental conditions such as temperature and humidity for a long time. This change in the properties of composite materials is called ageing. The change in mechanical properties of materials under environmental conditions such as temperature, humidity, pure water, salt water and ultraviolet radiation should be well known in order to determine the strength and service life of composite materials at the places of use (Doğan, 2014). Many polymer materials absorb water when they remain in water for a long time, and this absorbed water changes the properties of the polymers. Absorbed water softens the material so it increases the distance between the polymer chains (Baschek et al., 1998). The stresses caused by the water in the material cause expansion. Consequently, the damage tolerance and structural strength of the material is reduced. Water absorption creates reversible and irreversible interactions in the mechanical properties of polymer composites. Plasticization and swelling are unwanted formations caused by water absorption. The plastification causes plastic deformation and it reduces the glass transition temperature (Tg) of the material. The water absorbed into the material forms expansion forces and the polymer chains are forced under the influence of these forces (Lee et al., 1993). Glass reinforced plastic materials when they remain in the water for a long time, the damage caused by the water creates a significant change in the creep, tension and fatigue properties of the materials (Liao et al., 1998). The matrix properties and the fiber/matrix interface region play an important role in controlling the performance of glass reinforced plastic materials in the fluid medium (Schutte, 1994). The fibers are also susceptible to water and moisture degradation (Chu et al., 2004).

Researchers reported that water absorption of polymer matrix composite materials takes place in accordance with Fick's law (Ferreira et al., 2007; Pavan et al., 2001; Zhang et al., 2000; Mouzakis, 2008). Other researchers consider that the process to be non-Fickian, because of factors such as the viscoelastic nature of polymers and resulting cracks (Shen and Springer, 1976; Pritchard and Speake, 1987; Carter and Kibler, 1978).

Filament winding, which is one of the composite material production methods, is used to produce cylindrical parts such as pressure vessels, water tanks and pipes. Composite pipes with circular cross-section generally used in applications where fluids are transported, have high specific strength, good fatigue and corrosion resistance as well as high hardness properties (Alderson and Evans, 1992). In the production with filament winding, glass fibers are generally preferred as reinforcing material. The most widely used material as a matrix material in polymer composites is epoxy resin. The reasons why epoxy resin is preferred are high tensile, impact resistance and abrasion strength, high electrical and chemical resistance properties.

In the literature, there are many studies examining the effect of seawater on the mechanical properties of GFRP composite materials (Gellert and Turley, 1999; Visco et al., 2011; Pal et al., 2012; Davies and Rajapakse, 2014). Seawater causes deterioration of mechanical properties in composite materials (Shenoi and Wellicome, 1993). Degradation in mechanical properties of carbon/fiber and glass fiber/epoxy composites was observed by Buehler and Seferis (2000) as a result of water absorption. Kawagoe et al. (2001) observed that seawater molecules exist in clusters at the resin–glass fiber interface where hydrolysis reactions take place causing interfacial fracture. Dehkordi et al. (2010) produced glass/epoxy and basalt/epoxy composites in their studies and exposed the produced composites to seawater corrosion. They determined waiting time of composite pipes in the water as 10, 20, 30 and 50 days. They found a significant decrease in the strength of composites over a period of 10 days. Wei et al. (2011) maintained glass fiber reinforced and basalt fiber-reinforced composites in seawater. They observed a rapid decrease in mechanical properties in the seawater environment for the first 30 days. Summerscales (2013) found the durability of epoxy and vinyl ester resins as a function of immersion time and temperature. Chakravarty et al. (2015) performed experiments on glass fiber polymer composites material to understand the effect of marine environment on glass transition temperature and weight of the composites. The influence of water absorption on the mechanical and thermo-mechanical behavior of carbon nanofiber (CNF) doped epoxy composites was investigated by Saha and Bal (2018). The results demonstrated a general reduction in flexural modulus, strength, hardness, storage modulus and glass transition temperature (Tg) for seawater exposed specimens due to absorption of seawater as compared to their unexposed specimens.

In this study, the GFRP composite pipes subjected to ageing in seawater for 1 month and then the hardness and density properties of the aged and non-aged composite pipes were compared.

2. MATERIAL AND METHOD

2.1. Production of GFRP Composite Pipes

In this study, E-glass/epoxy composite pipes with a winding angle of ± 55° were used. The fiber material used in the pipes was Vetrotex 1200 tex E-glass with 17 μm diameters, whereas the matrix material was Bisphenol A, Epoxy CY 225. The mechanical properties of the fiber and matrix used are given in Table 1 (Kara, 2012).

Table 1. Mechanical properties of fiber and matrix used in this study (Kara, 2012)

	E(GPa)	σ_t(MPa)	ρ(g/cm^3)	$\varepsilon_{rupture}$ (%)
E-glass	73	2400	2.6	1.5-2
Epoxy	3.4	50-60	1.2	4-5

2.2. Seawater Ageing

In this study, Mediterranean water was used for ageing process. The fact that the salinity of the Mediterranean water is between the high salinity seas is suitable for the corrosive environment conditions of the composites. The salinity rate of Mediterranean water is 3.8%. In addition, high amounts of NaCl, MgCl, $MgSO_4$, $CaSO_4$, K_2SO_4, $CaCo_3$, $MgBr_7$ salts are present in the Mediterranean water. The minerals found in the Mediterranean water are shown in Table 2 (Demirci, 2017). The GFRP composite pipes subjected to ageing in seawater for 1 month are shown in Fig. 1.

Table 2. Percentage of elements in Mediterranean water (Demirci, 2017)

Element	Rate	Element	Rate
Oxygen	85.84	Sulfur	0.091
Hydrogen	10.82	Calcium	0.04
Chlorine	1.94	Potassium	0.04
Sodium	1.08	Bromine	0.0067
Magnesium	0.1292	Carbon	0.0028

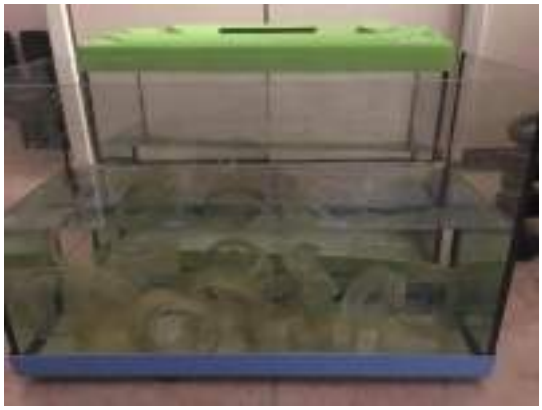

Fig. 1. Samples exposed to seawater ageing

2.3. Hardness Test

The hardness of samples was measured using Rockwell hardness testing machine is shown in Fig. 2.

Fig. 2. Digital Rockwell hardness tester

Test specimens (Fig. 3.) were made according to the ASTM D 785. The diameter of the ball indenter used was 0.25 inches and the maximum load applied was 60 kg as per the standard L-scale of the tester. The testing was carried out at room temperature for all the samples. All the readings were taken 10 s after the indenter made firm contact with the specimen. The hardness was measured at three different locations of the specimen and the average value was calculated.

Fig. 3. Samples for hardness test

2.4. Density Measurement Method

The density of the samples was calculated according to the Archimedes principle is given Eq. (1). In this equation, ρ is the density (g/cm^3) of GFRP sample, ρ_{water} is the density (g/cm^3) of water, W_{air} is the weight (g) of sample in air and W_{water} is the weight (g) of sample in water. Firstly, the sample was weighed in air as shown in Fig. 4a and then the sample was placed in a pot as shown in Fig. 4b and weighed in water at 25 ± 4 ºC.

$$\rho = \frac{W_{air}}{W_{air} - W_{water}} \rho_{water} \quad (1)$$

(a)

(b)

Fig. 4. a) Dry and b) wet weighing of the composite specimen with precision scales

3. RESULTS AND DISCUSSION

The exposure time of composite test specimens to seawater was determined according to the literature support. Wei et al. (2011) studied the mechanical properties of basalt and glass fiber reinforced epoxy composites in seawater. In their studies, they stated that the first 30 days were very effective in the change of mechanical properties and that after 30 days the change took constant values. They stated that the composite samples absorb water molecules in the seawater environment within 30 days and the molecules enter the sample and cause the mass increase.

In this study, it has been observed that there is a change in the hardness values depending on the seawater molecules entering the sample. Hardness tests were determined according to the Rockwell method. Rockwell hardness measurement gives a clear indication of the stability of aged specimens. 1 month of exposure of composites to the marine environment reduced hardness value by 4.6%. The hardness values of aged and dry specimens are given in Table 3.

Table 3. Average Rockwell hardness value

Ageing period in month	Rockwell hardness (HRL)
0	107.4
1	102.5

Due to the corrosive effect of the saline water entering the sample, epoxy resin, one of the structures forming the composite, will undergo wear (Wei et al. 2011). The hardness value is expected to increase as the fiber volume ratio of the sample increases due to the abrasion of the epoxy. Because the hardness value of glass fiber is much higher than epoxy. When the hardness values of the samples exposed to and not exposed to seawater are examined, it is seen that the hardness value of the sample which is kept in sea water is lower. The reason is the epoxy cavities dissolved by the abrasive effect of saltwater reduce the hardness of

the samples. Density values of composite samples exposed and unexposed to saline water are given in Fig. 5. When the figure is examined, it is seen that waiting in saltwater increases the density of the composite sample by 6.9 %. The reason for this is that the saltwater erodes the epoxy, therefore, it can be considered as an increase in the fiber volume ratio of the sample. The density of the fiber is much higher than the epoxy. Density increase was realized with increasing fiber volume ratio.

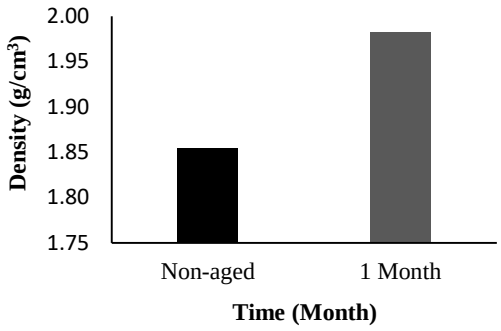

Fig. 5. Average density value of composite samples exposed to and unexposed to seawater

4. CONCLUSION

In this study, the effect of ageing process in sea water on the hardness and density values of GFRP composite pipes were investigated. As a result of working;

• Hardness values of samples exposed to seawater decreased.

• It was determined that the density value of the samples exposed to seawater increased due to the change in fiber volume ratio.

REFERENCES

Alderson, K. L. and Evans, K. E. (1992). "Low velocity transverse impact of filament-wound pipes: Part 1. Damage due to static and impact loads." *Composite structures*, 20(1), 37-45.

ASTM D 785 (1993), "Rockwell Hardness of Plastics and Electrical Insulating Materials. American Society for Testing and Materials," ASTM International, West Conshohocken, PA, 2006, www.astm.org.

Baschek, G., Hartwig, G. and Zahradnik, F. (1998). "Effect of water absorption in polymers at low and high temperatures." *Polymer,* 40, 3433-3441.

Buehler, F. U. and Seferis, J. C. (2000). "Effect of reinforcement and solvent content on moisture absorption in epoxy composite materials." *Composites Part A: Applied Science and Manufacturing*, 31(7), 741-748.

Carter, H. G. and Kibler, K. G. (1978). "Langmuir-type model for anomalous moisture diffusion in composite resins." *Journal of Composite Materials*, 12(2), 118-131.

Chakraverty, A. P., Mohanty, U. K., Mishra, S. C. and Satapathy, A. (2015). "Sea water ageing of GFRP composites and the dissolved salts." In IOP conference series: materials science and engineering (Vol. 75, No. 1, p. 012029). IOP Publishing.

Chu, W., Wu, L. and Karbhari, V. M. (2004). "Durability evaluation of moderate temperature cured E-glass/vinylester systems." *Composite Structures*, 66(1-4), 367-376.

Davies, P. and Rajapakse, Y. D. (2014). *Durability of composites in a marine environment (Vol. 208)*. Springer, Berlin, Germany.

Dehkordi, M. T., Nosraty, H., Shokrieh, M. M., Minak, G. and Ghelli, D. (2010). "Low velocity impact properties of intra-ply hybrid composites based on basalt and nylon woven fabrics." *Materials and Design*, 31(8), 3835-3844.

Demirci, I. (2017). ÇDKT ve Silika Katkılı Bazalt/Epoksi Hibrit Nanokompozitlerin Korozif Ortamda Darbe Davranışları, M.Sc. Thesis, Selçuk University, Konya, Turkey.

Doğan, A. (2014). Farklı çevresel koşullara maruz kompozitlerin mekanik davranışları, M.Sc. Thesis, Dokuz Eylül University, Izmir, Turkey.

Ferreira, J. M., Pires, J. T. B., Costa, J. D., Errajhi, O. A. and Richardson, M. (2007). "Fatigue damage and environment interaction of polyester aluminized glass fiber composites." *Composite structures*, 78(3), 397-401.

Kara, M. (2012). Düşük hızlı darbe sonrası yama ile tamir edilmiş filaman sarım CTP boruların iç basınç altındaki hasar davranışı, PhD Thesis, Selçuk University, Konya, Turkey.

Kawagoe, M., Doi, Y., Fuwa, N., Yasuda, T. and Takata, K. (2001). "Effects of absorbed water on the interfacial fracture between two layers of unsaturated polyester and glass." *Journal of materials science*, 36(21), 5161-5167.

Kootsookos, A., Mourotz, A. P. and St John, N. A. (2001). "Comparison of the seawater durability of carbon and glass polymer composites." Proceedings of the 13th International Conference on Composite Materials, ID-1200, Proceedings of ICCM-13, Beijing.

Lee, T. H. Y. C., Freddy and Loh, N. L. (1993). "Characterization of a fibre-reinforced PPS composite by dynamic mechanical analysis: effect of aspect ratio and static stres." *Composite science and technology*, 49, 217-223.

Liao, K., Schultesiz, C. R., Hunston, D. L. and Brinson, L. C. (1998). "Long-term durability of fiber-reinforced polymer-matrix composite materials for infrastructure applications: a review." *Journal of advanced materials*, 30(4):3–40.

Mouzakis, D. E., Zoga, H. and Galiotis, C. (2008). "Accelerated environmental ageing study of polyester/glass fiber reinforced composites (GFRPCs)." *Composites part B: engineering*, 39(3), 467-475.

Pal, R., Murthy, H. N., Sreejith, M., Mahesh, K. V., Krishna, M. and Sharma, S. C. (2012). "Effect of laminate thickness on moisture diffusion of polymer matrix composites in artificial seawater ageing." *Frontiers of Materials Science*, 6(3), 225-235.

Pavan, R. M., Saravanan, V., Dinesh, A. R., Rao, Y. J., Srihari, S. and Revathi, A. (2001). "Hygrothermal effects on painted and unpainted glass/epoxy composites—Part A: moisture absorption characteristics." *Journal of reinforced plastics and composites*, 20(12), 1036-1047.

Pritchard, G. and Speake, S. D. (1987). "The use of water absorption kinetic data to predict laminate property changes." *Composites*, 18(3), 227-232.

Saha, S. and Bal, S. (2018). "Long term hydrothermal effect on the mechanical and thermo-mechanical properties of carbon nanofiber doped epoxy composites." *Journal of Polymer Engineering*, 38(3), 251-261.

Schutte, C. L. (1994). "Environmental durability of glass-fiber composites." *Materials Science and Engineering: R: Reports*, 13(7), 265-323.

Shen, C. H. and Springer, G. S. (1976). "Moisture absorption and desorption of composite materials." *Journal of composite materials*, 10(1), 2-20.

Shenoi, R. A. and Wellicome, J. F. (1993). *Composite Materials in Maritime Structures*: *Fundamental Aspects (Vol. 1)*. Cambridge University Press, England.

Summerscales, J. (2013). "Durability of composites in the marine environment." Solid Mechanics and Its Applications,Vol 208, no. 3, pp. 1–13.

Wei, B., Cao, H. and Song, S. (2011). "Degradation of basalt fibre and glass fibre/epoxy resin composites in seawater." *Corrosion Science*, 53(1), 426-431.

Visco, A. M., Campo, N. and Cianciafara, P. (2011). "Comparison of seawater absorption properties of thermoset resins based composites." *Composites Part A: Applied Science and Manufacturing*, 42(2), 123-130.

Zhang, S., Karbhari, V. M., Mai, L. Y. and Mai, Y. W. (2000). "Evaluation of property retention in E-glass/vinylester composites after exposure to salt solution and natural weathering." *Journal of reinforced plastics and composites*, 19(9), 704-731.

CLUSTERING NETWORK TRAFFIC RECORDS WITH K-MEANS ALGORITHM

Yusuf Turhan Tekin[1], Erdinç Avaroğlu[2], Musa Gül[3]

[1]Mersin University, Faculty of Engineering, Department of Computer Engineering, Mersin, Turkey, turhantekin@gmail.com

[2] Mersin University, Faculty of Engineering, Department of Computer Engineering, Mersin, Turkey, eavaroglu@gmail.com

[3]Mersin University, Faculty of Engineering, Department of Computer Engineering, Mersin, Turkey, csemusagul@gmail.com

ABSTRACT

Intrusion detection systems use the signatures of the known intrusions that are recorded. But with only signature based intrusion detection new intrusions cannot be detected. To identify the unknown intrusions machine learning techniques are becoming widespread day by day.
Machine learning algorithm are sub-grouped into two main groups as supervised learning and unsupervised learning. In this study K-Means which is a supervised learning algorithm is used for clustering the KDD Cup 199 dataset. The results of the clustering showed high success.

Keywords: *Machine learning,Clustering, K-Means, Intrusion Detection System*

* Corresponding Author

INTRODUCTION

The increasing number and types of cyber attacks necessitates the support of traditional signature based systems with intelligent intrusion detection systems. In general, intrusion detection systems are divided into two groups as signature-based and anomaly-based.

Intrusion detection systems detect violations and attacks by scanning traffic flowing through the computer network. For detected violations, network administrators are prompted to make corrections. Conventional intrusion detection systems detect attacks by looking at the signatures of previous attacks.

In signature-based intrusion detection, the system searches for malicious bytes or packets in network traffic to detect threats and compares them with predetermined attack signatures [1]. The working logic of signature-based attack systems is based on the basic classification problem. They detect known types of attacks with high success. However, as with anti-virus software, they cannot detect new attacks.

New types of attacks that are emerging day by day make the work of intrusion detection systems increasingly difficult. Data mining and machine learning approaches have been widely used to identify new attacks that are not yet registered in the databases, which are described as zero-day attacks.

Machine learning algorithms generally fall into two types, supervised learning and unsupervised learning. Supervised learning or controlled learning is to learn a function to obtain the desired Y output set from the given X input set [2]. In the case of unsupervised learning, there are no outputs of labeled data. The data is uploaded to the system in an unlabeled manner, separated by algorithms and in this way meaningful inferences are made from the data. In supervised learning, data is classified by assigning to known classes. In case of unsupervised learning, no causal relationship is defined to the system. Data is assigned to clusters based on similar properties. Data are classified in supervised learning, while data are clustered in unsupervised learning.

Since signature-based detection systems may be preferred for known attack types, unattended learning techniques from machine learning techniques can yield more effective results for new attack types when the goal is to detect unknown, emerging attacks. In this study, using the k-means algorithm, one of the unsupervised learning algorithms, the data contained in the kdd cup 1999 data set will be clustered and the results will be evaluated.

2. METHODOLOGY

In this section, general information about the data set, clustering algorithms and K-Means model will be given.

2.1. Dataset Used

KDDcup1999 used in this study is a widely used and free data set which is available to the public. This data set is a data set that simulates many network attacks and violations. It was collected with TCP dump data from the local network for nine weeks. There are 38 properties in the data set and records of 22 types of attacks. These 22 attack types are attack types in 4 main categories:

1) Denial of Service Attack (DoS): In this type of attack, an attacker can deplete the resources of the attacked system, rendering them inoperable.
2) User To Root-U2R: In this type of attack, a user who connects to the system with a less authoritative account tries to upgrade the account to the administrator account using system vulnerabilities [5].
3) Remote local network logon (Remote to Local-R2L): In this kind of attack the user who does not have any authority on the target system sends some packets to the target system to gain access to the computer as a user [1].
4) Probing Attack: Information scanning attacks known as probing attacks are the scanning of information such as user account information, ip, port of computers in the network [1].

Attack Class	Attack Tool
DOS (Denial Of Service)	Back, Land, Neptune,pod, smurf, Teardrop,
U2R (User To Rott)	Buffer_overflow, loadmodule, perl, rootkit
R2L (Remote To Local)	ftp_write, guess_passwd, imap, multihop, phf, spy,warezlient, warezmaster
Probe (Bilgi Toplama)	IPsweep,nmap, satan,portsweep

Table 1: Attacks simulated in KDD Cup 99 dataset

#	Özellik	#	Özellik
1	duration	22	is_guest_login
2	protocol_type	23	Count
3	service	24	srv_count
4	flag	25	serror_rate
5	src_bytes	26	srv_serror_rate
6	dst_bytes	27	rerror_rate
7	land	28	srv_rerror_rate
8	wrong_fragment	29	same_srv_rate
9	urgent	30	diff_srv_rate
10	hot	31	srv_diff_host_rate
11	num_failed_logins	32	dst_host_count
12	logged_in	33	dst_host_srv_count
13	num_compromised	34	dst_host_same_srv_rate
14	root_shell	35	dst_host_diff_srv_rate
15	su_attempted	36	dst_host_same_src_port_rate
16	num_root	37	dst_host_srv_diff_host_rate
17	num_file_creations	38	dst_host_serror_rate
18	num_shells	39	dst_host_srv_serror_rate
19	num_access_files	40	dst_host_rerror_rate
20	num_outbound_cmds	41	dst_host_srv_rerror_rate
21	is_host_login		

Table 2: Features included in KDD 99 dataset

2.2. Clustering and K-Means Algorithm

Clustering is an unsupervised method of machine learning. It is a method of analyzing data. The purpose of clustering is to collect data according to similar characteristics and to collect data with different characteristics into different areas [3, 4]. The most commonly used clustering methods are K-Means and hierarchical clustering methods. In this study, k-means clustering model will be emphasized.

In the K-Means algorithm, first of all, the number of sets of data in the data set is specified. The K value determines how many clusters the data will be divided into. The K value is entered as a parameter to the function. After determining the K value, K numbers of center points are randomly determined. These values are initially determined randomly. The distances between the data and the selected center points are calculated and the data is assigned to the center point with the minimum distance.

The K-Means algorithm uses the Euclidean distance. Euclidean distance is the linear distance between two points. The number of cluster centers is calculated so that the sum of the squares of distances to the center of each cluster is minimum.

The distance calculation according to Euclidean calculation is done as shown in formula 1.

$$d(\mathbf{p},\mathbf{q}) = \sqrt{\sum_{i=1}^{n}(p_i - q_i)^2}$$

Formula 1: Euclidean Distance Formula

General steps of K-Means algorithm is described below:

1. Determination of the number of clusters
2. Assignment of gravity centers for each cluster.
3. Each object is assigned to the cluster which has nearest center of gravity..
4. The average value of each cluster is assigned to the cluster as the new center of gravity.
5. Step 3 is repeated until there is no data to cluster.

In general, the flow diagram of the k-means algorithm is as in figure 1.

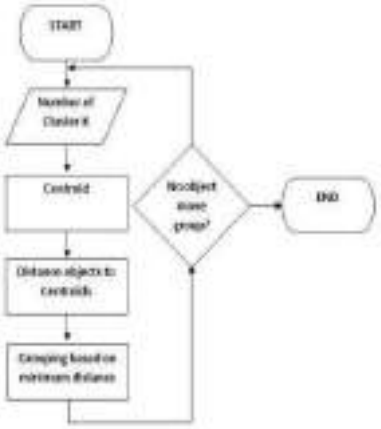

Figure 1: The flow diagram of k-means algorithm

3. DISCUSSION

When detecting intruders, data sets containing a large number of meaningless data and numerous features can occur. This results in a very large feature vector. This increases computational time and leads to excessive compatibility between the data. It is very important to determine the number of clusters and to select the appropriate number of features in the clustering.

When the data set is examined, it is seen that some properties have a value of 0 or 1 indicating the presence or absence of a condition, such as the su_attempted property in column 15. Some properties specify the number of times a state occurs, such as in the num_file_creations property. Some features also indicate the bytes sent or received.

Determining the number of features and clusters are the research topics that are the most emphasized and algorithm development areas.

3.1. Initial Test

When the data set is examined, since there are 22 different attack types and normal traffic records, there are 23 different types of traffic. In this respect, it can be assumed that the K value should be at least 23. Most of the time, as here, we cannot know how many different types of data will be, since the data is unlabeled. In this regard, the first job should be to determine a good value for K. For this purpose, the data set was tested with different K values.

For clustering testing with K-Means, Apache Spark and MLLib libraries were used in Python programming language. Apache Spark libraries in Python can be used in applications by including the pyspark library. Using Apache Spark, large data can be run in parallel, calculations and feature extraction can be performed.

First of all, 3 categorical features in the data set were removed. And 3 variables with the highest distribution among the numerical properties were determined. These properties were duration, src_bytes, and dst_bytes. For these 3 properties, clustering was performed using 1% of the data set. Extreme values were discarded from the data set before this operation.

The distribution of clustered data was then graphically shown in Figure 2 using the numpy and matplotlib libraries in the Jupyter Notebook program development environment in Python. As can be seen, there is not much data in cluster 0. The data in Cluster 1 is located too far from the center of gravity. In order to be balanced for the clustering process, the data in each cluster must be close to the center of gravity of its own cluster and the mean distance of the data from different clusters to the center should be close to each other. As a result, the clustering process was unstable. No successful results have been achieved. A good result could not be obtained by defining K value as 2.

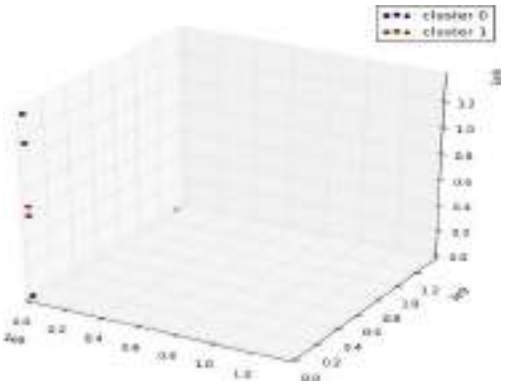

Figure 2: The Distribution Of Two Clustered data

The success of clustering process is judged by the fact that each data point is as close as possible to its center of gravity. One of the most commonly used methods for evaluating the developed model is to calculate Mean of Squared Errors for all data points.

3.3. Normalizing Features And Testing The K Values

The K-means clustering takes into account all directions and dimensions equally in space. If we do not balance the distribution of variance, the variables with more distribution will make the distribution within the clusters more discrete. This is avoided if the values of the data are collected within certain ranges by normalizing the variables.

In the second stage of the experiment, the categorical variables that were ignored in the first stage were added to the data set. In our first experiment, the number of clusters was only 2. It is necessary to increase this value for better results, but finding the correct k value is not an easy process.

Silhouette analysis was used to determine the number of clusters. It is expected that the distance of the data with the cluster center of gravity will decrease as the K value increases. In the Silhouette analysis, 1% of the data was used instead of the whole data to determine the K value at a faster time. K value was increased in a loop and optimum k value was determined. At the end of the Silhouette analysis, a value called Silhouette score returns. At the end of the Silhouette analysis, a value called Silhouette score returns.

As a result, attack types were clustered with 99% accuracy using 35 properties and 23 clusters.

4. CONCLUSION

In this study, k-means algorithm which is an unsupervised learning method is used to make a clustering study on on KDD cup 1999 data set which is a frequently preferred data set in scientific studies. Machine learning techniques are becoming more and more important in intrusion detection systems and machine learning in intrusion detection is a wide field of research for researchers.

For this study it was seen that the categorical features of the connection records on this data set were found to be more effective in determining the attack types. There were lots of numerical feature but among the numerical features some are important, some should be eliminated.

In the study, the data set which was first tried to be grouped into 2 clusters, and then the Silhouette and Entropy analyzes, the number of clusters and the number of properties were optimized.

In this study, Silhouette and Entropy methods are used for clustering and feature selection. Much research is being done on these subjects.

5. REFERENCES

[1] K. Kendall, Database of Computer Attacks for the Evaluation of Intrusion Detection Systems, MIT Department of Electrical Engineering and Computer Science, 1999.

[2] Alpaydın, Ethem (2010). Introduction to Machine Learning. Londra: The MIT Press. s. 8. ISBN 978-0- 262-01243-0.

[3] K. Lee, S. Jung, T. Lee, and J. Choe, "Use of Clustered Covariance and Selective Measurement Data in Ensemble Smoother for Three-Dimensional Reservoir Characterization," J. Energy Resour. Technol, vol. 2016;139(2), 2017.

[4] V. Sucasas, A. Radwan, H. Marques, J. Rodriguez, S. Vahid, and R. Tafazolli, "A survey on clustering techniques for cooperative wireless networks," Ad Hoc Networks, vol. 47 (2016), pp. 53–81, 2016.

CISET - 2nd Cilicia International Symposium on Engineering and Technology
10-12 October, 2019, Mersin / TURKEY

EFFECT OF SEAWATER AGEING ON THE MECHANICAL PROPERTIES OF E-GLASS EPOXY COMPOSITE PIPES

Alper Gunoz [*1], Yusuf Kepir [2], Memduh Kara [3]

[1*] Mersin University, Faculty of Engineering, Department of Mechanical Engineering, Mersin, Turkey, alpergunoz@mersin.edu.tr

[2] Mersin University, Faculty of Engineering, Department of Mechanical Engineering, Mersin, Turkey, yusufkepir94@gmail.com

[3] Mersin University, Faculty of Engineering, Department of Mechanical Engineering, Mersin, Turkey, memduhkara@mersin.edu.tr

ABSTRACT
Mechanical and thermal resistance capabilities of composite pipes are of great importance depending on different usage purposes. In this study, the effect of seawater ageing on tangential tensile strength of E-glass fiber reinforced epoxy pipes was investigated. E-glass epoxy composite pipes are used in submarine applications, natural gas, and oil transportation lines, transfer of chemical liquids. Especially in the transport of pressurized fluids, changes in the strength of the pipe are important. The corrosive effect of seawater has an impact on the mechanical properties of the composite material. In particular, the change in hoop tensile strength is one of the issues to be investigated. In this study, the strength values of the composite pipes changed due to the waiting in seawater.

Keywords: *Composite pipes, seawater effect, mechanical properties, hoop strength*

[*] Corresponding Author

1. INTRODUCTION

Composite materials are materials formed by combining these materials at the micro and macro levels in order to gather the best properties of two or more same or different groups of materials together or to form new material having different properties. There are many production methods of composite materials such as filament winding, resin transfer, spraying and hand lay-up. The production method is chosen according to the application area where the material will be used. In applications where fluid is transported, such as gas, oil and water transmission lines, composite pipes with circular cross-section are generally used (Kara, 2012). Composite pipes have high specific strength and hardness properties, as well as good fatigue and corrosion resistance. Therefore, it is widely used in many engineering applications. It is preferred by filament winding for the production of pipe-like parts (Alderson and Evans, 1992). In the production with filament winding, glass fibers are generally preferred as reinforcing material. The most widely used material as a matrix material in polymer composites is epoxy resin. Glass fiber reinforced polymer (GFRP) composites are frequently used in marine vessels due to their low cost, light weight, high strength and excellent corrosion resistance. Many vessels, such as mine hunting, patrol boats, skis, canoes, and fishing boats, are made of glass-fiber-reinforced polymer composites (Kootsookos et al., 2001).

GFRP composite pipes may be exposed to environmental conditions such as seawater, rain water, sun and wind which cause deterioration of material properties (Kayıran, 2018). In order to determine the effect of different environmental conditions on composite pipes and to prevent or minimize the deformation of this effect on the material, it is necessary to know the mechanical properties of the pipes under different environmental conditions.

Seawater creates two macroscopic effects in the form of deterioration of mechanical properties in composite materials and weight gain of the material (Shenoi and Wellicome, 1993). Generally, composites perform water absorption in the presence of water due to their hydrophilicity behaviour (Chow, 2007). This absorbed water causes the material to swell and permanently deform. Thus, the mechanical properties of the material are weakened (Barkoula et al., 2009).

In the literature, there are many studies examining the effect of seawater on the mechanical properties of GFRP composite materials (Gellert and Turley, 1999; Visco et al., 2011; Pal et al., 2012; Davies and Rajapakse, 2014; Bazli, 2016). Kootsookos and Mouritz (2004) have investigated experimentally the resistance of glass and carbon fiber reinforced polymer composites to seawater. They exposed the materials to aging in seawater at 30 ° C for two years. They observed that the mechanical properties of glass fiber reinforced composites deteriorated more than carbon fiber reinforced composites after aging in seawater. Gu (2009) in his study, observed the change in the mechanical properties of glass fiber reinforced polymer composites exposed to the seawater. It was found that the deterioration of the matrix and interface surfaces of the composite material increased as the seawater exposure time increased. Sarı (2010) investigated the effect of seawater on fatigue behavior of GFRP composite pipes subjected to impact damage. It observed a slight increase in impact and blasting strength of GFRP composite pipes exposed to seawater for three months. Örçen and Gür (2011) investigated the effect of seawater on glass fiber reinforced epoxy composite materials. The samples were exposed to seawater for three and six months. The mechanical properties of non-aged and seawater aged specimens were examined and found that the non-aged specimen had the highest modulus of elasticity. They also found that as the residence time of the samples increased in seawater, the modulus of elasticity decreased. Karakuzu et al. (2017) investigated the effect of seawater on the impact behavior of glass fiber epoxy composite plates. Composite samples were exposed to seawater for 1, 3, 6 and 9 months and impact tests were then performed on the samples. At the end of the study, they determined that salt of seawater, impact energy and impact mass have a significant effect on impact behavior of composite plates. José-Trujillo et al. (2018) investigated the effect of seawater aging on the mechanical properties of glass/epoxy, glass/vinyl ester, glass/polyester, carbon/epoxy and carbon/vinyl ester composite materials. As a result of their studies, they observed that seawater caused the decrease in mechanical properties of glass fiber epoxy composites at most.

In this study, GFRP composite pipes produced by filament winding method were exposed to aging in seawater for 1 month and then mechanical properties of non-aged and aged composite pipes were compared.

2. MATERIAL AND METHOD

2.1. Production of GFRP Composite Pipes

E-glass/epoxy composite pipes with a winding angle of ± 55° were used in this study. Vetrotex 1200 tex E-glass with a diameter of 17 μm diameters was used as glass fiber and Ciba Geigy, Bisphenol A, Epoxy CY 225 was used as the matrix material. Composite pipes have a length of 300 mm and an inner diameter of 72 mm. The wall thickness is 2.25 mm. The mechanical properties of the fiber and matrix used are given in Table 1 (Kara, 2012) and the geometry of the GFRP pipes is given in Fig. 1 (Kara and Kırıcı, 2017).

Fig. 1. Geometry of GFRP pipes (Kara and Kırıcı, 2017)

Table 1. Mechanical properties of fiber and matrix used in composite pipe production (Kara, 2012)

	E (GPa)	$\sigma_ç$(MPa)	ρ(g/cm3)	ε_{kop} (%)
E-glass	73	2400	2.6	1.5-2
Epoxy	3.4	50-60	1.2	4-5

2.2. Seawater Ageing

Mediterranean water, which has a high salinity (3.8 %), has an abrasive effect on the matrix of composite pipes. There are high amounts of NaCl, MgCl, $MgSO_4$, $CaSO_4$, K_2SO_4, $CaCo_3$, $MgBr_7$ salts in Mediterranean water (Demirci, 2017). The GFRP composite pipes subjected to ageing in seawater for 1 month are shown in Fig. 2.

Fig. 2. Samples exposed to seawater ageing

2.3. Hoop Tensile Strength Test

Hoop tensile strength test was performed according to ASTM D 2290 Procedure A. The test method given in this standard covers the work of determining the comparative tensile strength of many plastic products under certain prerequisites such as temperature, humidity and test speed using a split disk or ring part. Test specimens were prepared from six-layered GFRP composite pipes in accordance with the measurements given in Fig. 3. According to Procedure A, notching on both sides of the sample is left to the user's preference. In the hoop tensile test, conditions such as tensile speed, humidity, temperature and specimen thickness of the test machine jaw were taken into consideration. The standard laboratory ambient temperature is 25 °C ± 0.5 °C; humidity, %50 ± 5. The test speed is at least 0.1 inch/min. The hoop tensile test is shown in the Fig. 4.

By applying this test, the stress value could be determined by the following equation (Eq. 1). In this equation, σ_T is the apparent yield or tensile strength value (MPa) of the sample, P_b is the maximum load value (N), A_m is the minimum cross-sectional area (mm^2) of two measurements (d x b), and d and b represent the thickness (mm) and width (mm) in the reduced area.

$$\sigma_T = \frac{P_b}{2A_m} \quad (1)$$

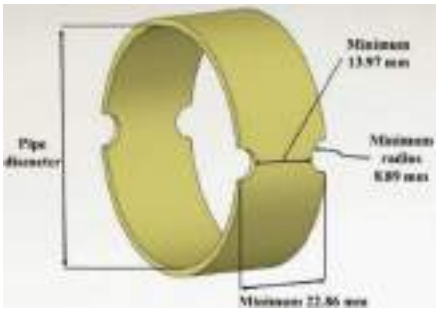

Fig. 3. Reduced section specimens for Procedure A

Fig. 4. Hoop tensile test instrument

3. RESULTS AND DISCUSSION

As stated in the literature, the mechanical properties of GFRP pipes exposed to seawater are changed after 30 days of aging. Composite pipes absorb water molecules in seawater environment within 30 days. Water molecules enter the specimen and cause weight increase (Wei et al., 2011).

Hoop tensile tests were performed according to ASTM D 2290 Procedure A. Each experiment was continued until the sample ruptured. The hoop tensile strength values were determined by using Eq. 1., which is the largest tensile strength value obtained from hoop tensile tests. Experiments were repeated 3 times for each case and the mean values were determined. Hoop tensile strength values of samples exposed to seawater and unexposed to seawater are given in Fig. 5. When the Fig. 5. is examined, it is seen that the strength value of composite pipe samples decreases as a result of exposure to seawater. Composite test specimens absorb water molecules while remaining in seawater. The absorbed seawater molecules are corrosive to the epoxy forming the composite structure. Epoxy abrasion results in weakening of the bond between the fiber and the matrix. The weakening of the bonds between the fiber and the matrix reduces the strength of the composite structure. The bonds between the fiber and the matrix are the most important bonds in terms of the stability of the composite structure.

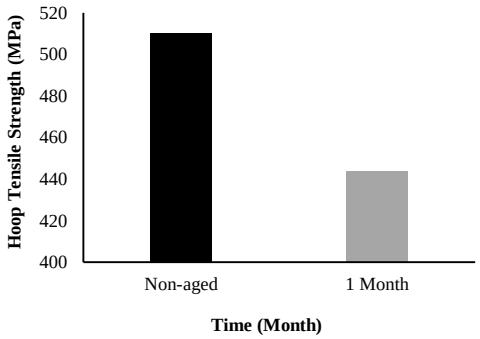

Fig. 5. Hoop tensile strength of the composite pipes unexposed to and exposed to seawater

The damage to the six-layered composite pipes a) unexposed to and b) exposed to seawater as a result of the hoop tensile test is shown in Fig. 6.

When the hoop tensile strength value was reached in both samples, fibers were ruptured and the specimens were splitted from the notch region. It is seen in all samples that the split is in the direction of the winding angle of ± 55 °.

(a) **(b)**

Fig. 6. (a) Non-aged (b) 1 month aged GFRP composite pipes

4. CONCLUSION

In this study, changes in hoop tensile strength of E-glass epoxy composite pipes exposed to seawater were investigated.

- It has been determined that the strength values of the samples waiting in seawater decreased due to abrasion in epoxy.
- In the damage images of the composite test specimens, it is seen that the rupture of the specimens occurs in the direction of the winding angle.

REFERENCES

ASTM D 2290-12 (2013), "Standard Test Method for Apparent Hoop Tensile Strength of Plastic or Reinforced Plastic Pipe. American Society for Testing and Materials," ASTM International, West Conshohocken, PA, 2006, www.astm.org.

Alderson, K. L. and Evans, K. E. (1992). "Low velocity transverse impact of filament-wound pipes: Part 1. Damage due to static and impact loads." *Composite structures,* 20(1), 37-45.

Barkoula, N. M., Paipetis, A., Matikas, T., Vavouliotis, A., Karapappas, P. and Kostopoulos, V. (2009). "Environmental degradation of carbon nanotube-modified composite laminates: a study of electrical resistivity." *Mechanics of Composite Materials,* 45(1), 21-32.

Bazli, M., Ashrafi, H. and Oskouei, A. V. (2016). "Effect of harsh environments on mechanical properties of GFRP pultruded profiles." *Composites Part B: Engineering,* 99, 203-215.

Chow, W. S. (2007). "Water absorption of epoxy/glass fiber/organo-montmorillonite nanocomposites." *Express Polymer Letters,* 1(2), 104-108.

Davies, P. and Rajapakse, Y. D. (2014). *Durability of composites in a marine environment (Vol. 208)*. Springer, Berlin, Germany.

Demirci, I. (2017). ÇDKT ve Silika Katkılı Bazalt/Epoksi Hibrit Nanokompozitlerin Korozif Ortamda Darbe Davranışları, M.Sc. Thesis, Selçuk University, Konya, Turkey.

Gellert, E. P. and Turley, D. M. (1999). "Seawater immersion ageing of glass-fibre reinforced polymer laminates for marine applications." *Composites Part A: Applied Science and Manufacturing,* 30(11), 1259-1265.

Gu, H. (2009). "Behaviours of glass fiber-unsaturated polyester composites under seawater environment." *Materials and Design,* 30(4), 1337-1340.

José-Trujillo, E., Rubio-González, C. and Rodríguez-González, J. A. (2018). "Seawater ageing effect on the mechanical properties of composites with different fiber and matrix types." *Journal of Composite Materials,* 0021998318811514.

Karakuzu, R., Çalık, İ.C. and Deniz, M.E. (2017). "Tabakalı kompozit plakaların darbe davranışı üzerine deniz suyu etkisinin araştırılması." *Batman Üniversitesi Yaşam Bilimleri Dergisi,* 7 (2/2), 1-12.

Kara, M. (2012). Düşük hızlı darbe sonrası yama ile tamir edilmiş filaman sarım CTP boruların iç basınç altındaki hasar davranışı, PhD Thesis, Selçuk Universtiy, Konya, Turkey.

Kara, M. and Kırıcı, M. (2017). "Effects of the number of fatigue cycles on the impact behavior of glass fiber/epoxy composite tubes." *Composites Part B: Engineering,* 123, 55-63.

Kayıran, H. F. (2018). Farklı ortam koşullarına maruz hibrit kompozit plakalarda burkulma davranışının incelenmesi, PhD Thesis, Süleyman Demirel Universtiy,

Isparta, Turkey.

Kootsookos, A., Mourotz, A. P. and St John, N. A. (2001). "Comparison of the seawater durability of carbon and glass polymer composites." *Proceedings of the 13th International Conference on Composite Materials*, ID-1200, Proceedings of ICCM-13, Beijing.

Kootsookos, A. and Mouritz, A. P. (2004). "Seawater durability of glass-and carbon-polymer composites." *Composites Science and Technology*, 64(10-11), 1503-1511.

Örçen, G. and Gür, M. (2011). "Cam fiber takviyeli dokuma epoksi kompozit prepreglerin mekanik özellikleri üzerinde çevre şartlarının etkisi." *18.Ulusal Mekanik Kongresi*, Fırat University, Elazığ, 1-10.

Pal, R., Murthy, H. N., Sreejith, M., Mahesh, K. V., Krishna, M. and Sharma, S. C. (2012). "Effect of laminate thickness on moisture diffusion of polymer matrix composites in artificial seawater ageing." *Frontiers of Materials Science*, 6(3), 225-235.

Sarı, M. (2010). Seawater effect on composite pipes subjected to impact loading, M.Sc. Thesis, Dokuz Eylül University, Izmir, Turkey.

Shenoi, R. A. and Wellicome, J. F. (1993). *Composite Materials in Maritime Structures*: *Fundamental Aspects (Vol. 1)*. Cambridge University Press, England.

Wei, B., Cao, H. and Song, S. (2011). "Degradation of basalt fibre and glass fibre/epoxy resin composites in seawater." *Corrosion Science*, 53(1), 426-431.

Visco, A. M., Campo, N. and Cianciafara, P. (2011). "Comparison of seawater absorption properties of thermoset resins based composites." *Composites Part A: Applied Science and Manufacturing*, 42(2), 123-130.

CISET - 2nd Cilicia International Symposium on Engineering and Technology
10-12 October, 2019, Mersin / TURKEY

THE EFFECT OF LA (LANTANIUM) ON THE MICROSTRUCTURE AND MECHANICAL PROPERTIES OF THE HIGH-PRESSURE DIE CAST Mg-4Sb MAGNESIUM ALLOY

L. CENK KUMRUOĞLU[1], GÜVEN YARKADAŞ[2]

[1]Sivas Cumhuriyet University, Enginering Faculty, Dept of Metallurgy and Materials Eng, Sivas, Turkey, lkumru@cumhuriyet.edu.tr

[2]Mersin University, Enginering Faculty, Dept of Metallurgy and Materials Eng. Mersin, Turkey, guvenyarkadas@gmail.com

ABSTRACT

In this work, the effect of addition of La (Lanthanum) element (%wt. 0.5, 1, 2) on Mg-4Sb alloy was examined. As a casting process, high pressure die casting method was used. The specimens were produced directly as tensile and impact samples and represent semi-industrial pilot sized samples. In order to determine the mechanical properties of the produced samples, tensile tests, hardness tests, metallographic examination studies were carried out to determine the metallurgical relationship. Depending on the added La ratio, the mechanical properties increased. LaSb, $Mg_{12}La$ and Mg_3Sb_2 intermetallics were found in the grain boundaries. The yield strength increased continuously due to the added La ratio and the tensile strength increased to the highest strength as 147 MPa with the addition of 1% La. On the other hand, elongation was 0.5% to 1% La and 11.1% and 11.8% respectively. LaSb, $Mg_{12}La$ and Mg_3Sb_2 intermetallics which accumulate in the grain boundaries, increased the tensile strength by preventing dislocation movement and forming a fine-grained structure. La added to Mg-4Sb alloy showed grain refining effect up to 1%. When it is added to the ratio of 2%, it has accumulated as a result of eutectic decomposition at the grain boundaries and has reduced elongation and tensile strength.

Keywords: *High pressure die casting, Mg-4Sb-XLa, Alloy, Mechanical Properties, Lanthanum*

1. INTRODUCTION

Magnesium alloys are of great potential in the electronic, computer, medical, structural and automotive applications owing to their high specific strength [1-3]. The magnesium alloy is lighter than that of the other light metals such as Titanium and Aluminum. The use of magnesium alloy as a structure material for vehicles is could reduce driving energy consumption. [1,2]. Mg alloys are usually manufactured by different casting processes. The most common techniques are high-pressure die casting (HPDC) using metal mold and gravity casting using sand mold [4]. HPDC magnesium components are increasingly used due to their excellent casting capabilities and faster production capability in mass production. The HPDC process of thin-walled components is particularly suitable because of the excellent flow properties of liquid magnesium alloys [5]. Grain size is one of the most important factors that determine the engineering performance of metal alloys produced by casting. The casting size can be manipulated by varying various casting parameters such as grain size, cooling rate, or by adding alloying elements and nucleating agents before or during the casting process. Magnesium alloys with added rare earth elements increase the strength / density ratio and make them important materials for applications such as automotive, aerospace, where weight reduction is important [5,6]. The effect of rare earth metals on the mechanical properties of magnesium is a result of the different solubility of RE in solid magnesium, which varies regularly with respect to the size of the atomic radius. It is well known that the RE of the yttrium group has a higher solubility in solid magnesium than the RE of the cerium group. The properties of magnesium alloys used for structures can be enhanced by using rare earth metals in various combinations [6].

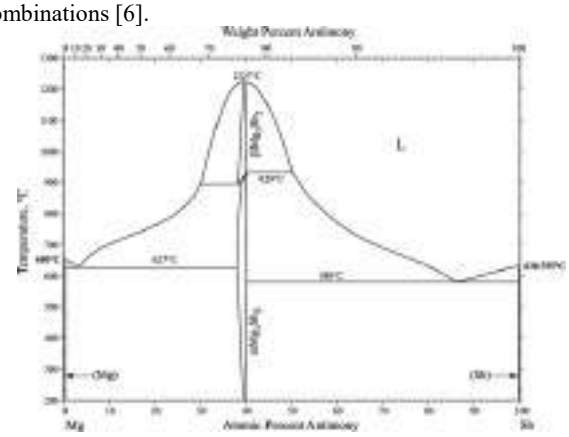

Fig. 1 Mg-Sb phase diagram [8]

Sb is one of the metals added to magnesium as an alloying element. Sb is a surface-active element which has effect as grain refinement in Mg alloys and formed intermetallic components at grain boundaries. The Mg-Sb phase diagram shows the high temperature allotropy of the single compound Mg_3Sb_2. Despite a suitable size factor (atomic radius ratio (Sb / Mg), 1.09, hence the atomic size difference is less than 15%), Sb in (Mg) or solid in Mg (Sb) do not have a solubility [7] The Mg-Sb phase diagram is shown in Fig.1 [8].

Although the addition of Sb has a grain refining effect, it has been reported that Sb does not contribute sufficiently to plasticity and ductility [9]. It is known that RE metals enhance the engineering properties of Mg alloys, so it will be possible for a RE metal to be added to the Mg-Sb system to increase the mechanical properties and elongation by showing synergistic effect. In addition, because of the lack of sufficient studies to discuss the effect of the addition of La to Mg-Sb alloy on the mechanical properties in the literature, La (Lanthanum) was selected as the RE element to be added.

2. EXPERIMENTAL STUDIES

The compositions were prepared from commercially pure magnesium, antimony and of Mg-%30 La master alloy. Produced alloys were (Mg-4Sb, Mg-4Sb-0,5La, Mg-4Sb-1La and Mg-4Sb-2La), listed in Table 1. All alloys were melted in a ZrO_2 coated graphite crucible, using an induction heating. Melting was carried out with a typical shielding gas mixture, 96% CO 2 - 4% SF 6. The melt temperature was kept at roughly 760 °C and no modifiers were used. Using a SiC impeller the melt was mixed and homogenized. The alloys were maintained at a casting temperature of 750 ° C for 15 minutes, immediately poured into the preheated mold (Fig.3.) using a cold chamber high pressure casting machine with a squeeze of 100k and an injection force of 76 kN.

Table 1. Elemental analysis of HPDC alloys (wt %)

Alloy	Mg (wt. %)	Sb (wt.%)	La (wt.%)
Mg-4Sb	Balance	4.04	–
Mg-4Sb-1La	Balance	4.01	0.51
Mg-4Sb-2La	Balance	4.06	1.04
Mg-4Sb-4La	Balance	4.00	2.06

The grain size measurements were performed using image analysis software (Clemex). Tensile tests were performed on the RAAGEN universal drawing machine. Four samples were used to calculate the stress and strain values. Tensile tests were performed at room temperature and with a tensile velocity of 3.3 x 10^{-3} mm/s.


Fig. 2. Macrograph of experimental alloy cast.

3. RESULTS AND DISCUSSION

Optical microscope images of Mg-4Sb alloy taken at

10x and 50x magnification are given in Figure 3. As a result of solidification due to out of equilibrium solidification conditions, (αMg) phase and Mg_3Sb_2 eutectic phase which is mainly distributed along grain boundaries were formed. Since Sb has no solubility in magnesium, formation of the intermetallic Mg_3Sb_2 phase along the grain boundary is an expected result. It is obvious that Sb acts as a grain refiner. The grain size of Mg-4Sb alloy ranges between 8 and 41 microns. The average was measured as 20 micrometers.

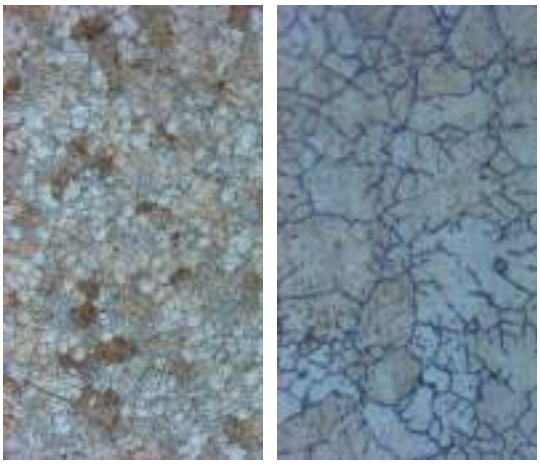

Fig.3. Microstructure of high-pressure die-casting Mg-4Sb alloy

The grain size of the Mg-4Sb-0.5La alloy ranges from 3 to 33 microns. The average grain size was measured as 17 micrometers. Depending on the addition of 0.5% La, LaMg12 phase was formed in dark-spherical form with an average of 5 micro diameter in the grain(Fig.4.).

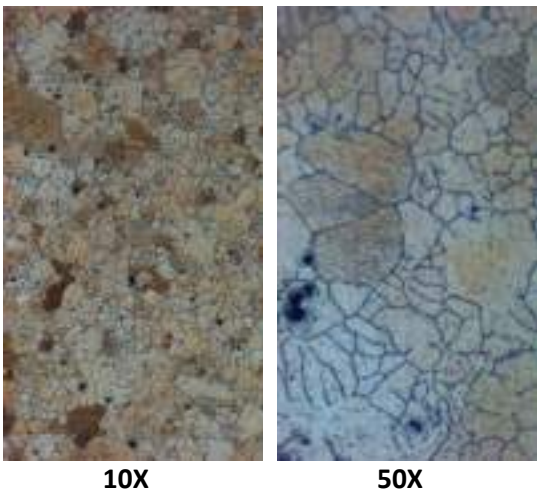

Fig.4. Microstructure of high-pressure die-casting Mg-4Sb-0.5La alloy

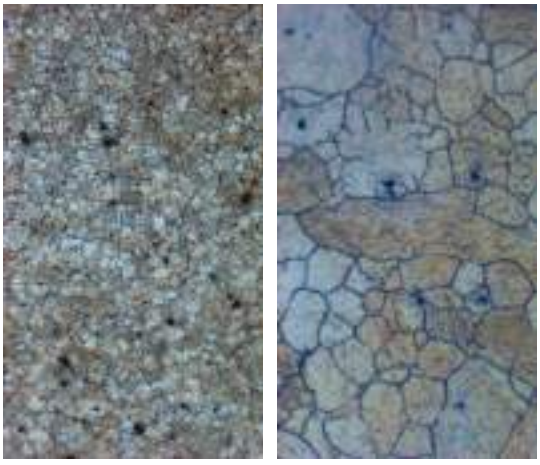

Fig.5. Microstructure of high-pressure die-casting Mg-4Sb-1 La alloy

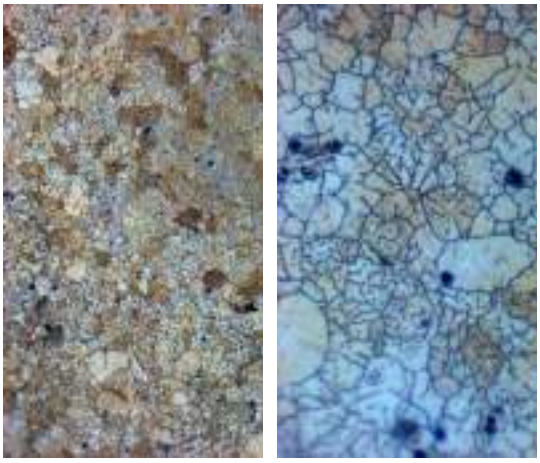

Fig.6. Microstructure of high-pressure die-casting Mg-4Sb-1 La alloy

It was observed that 1% La was added to Mg-4Sb alloy and the dendritic network structure decreased, the dendrites formed in a more rounded shape and grains were formed in more spherical form. The average grain size is 10 microns. The grain size of LaSb phase formed in round form at the grain boundaries was measured as 5 microns. However, it is understood that the spherical SbLa phase in the alloy containing 1% La is homogeneously dispersed over a larger area compared to the alloy with 0.5% La added. Mg-4Sb alloy with 2% La addition was observed to be very effective in fine-grained microstructure. The average grain size is 10 microns or less. Dendritic network structure was reduced, LaSb phase formed in round form at the grain boundaries, and the grain size of these spherical phases was measured as 8 microns. However, the spherical phase in the microstructure was measured as 18 microns and accumulated at the grain boundaries. (Fig.6).

Tensile testing is used to evaluate the mechanical behavior of alloys. The yield and tensile strength and elongation of the main alloy and modified alloys are shown in Fig. 7. As observed in Fig. 7, the yield, tensile strength and elongation values of the Mg-4Sb alloy increased, respectively, from 80 to 95 MPa, from 127 to

147 MPa and from 6 to 11.8, with the addition of La up to 1% wt. However, the tensile strength and elongation decreased with the addition of 2 % wt of La while the yield strength remained unchanged. In addition, the hardness value of theMg-4Sb alloy increased with the addition of La.

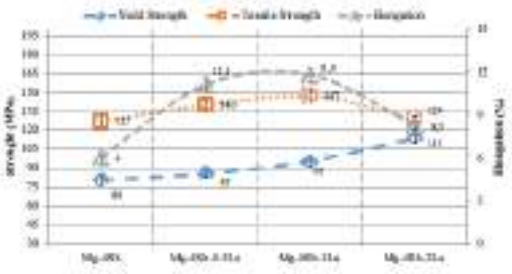

Fig. 7. The yield strength, tensile strength, elongation and hardness graphs of Mg-Sb-La alloys at room temperature

The increase in yield and tensile strength and elongation and hardness value of the Mg-4Sb alloy could be attributed to the combined effect of grain refinement strengthening, and the formation of additional intermetallic phases. These factors are known to increase strength by preventing dislocation movement. Therefore, the mechanical properties of the Mg-4Sb alloy were improved. However, with the addition of 2 wt% La of the formed intermetallic phases, the irregular phases in the microstructure of an average size of 18 microns reduced the tensile strength and elongation of the Mg-4Sb-2La alloy.

4. CONCLUSION

In this study, the main alloy (Mg-4Sb) and modified alloys (Mg-4Sb-0.5La, Mg-4Sb-1La and Mg-4Sb-2La) are successfully produced using HPDC technique. Our results of microstructure show that the addition of La to the Mg-4Sb alloy reduced the grain size of the main alloy and the two new intermetallic phases like MgSbLa and LaSb has formed. The addition of La up to 1% wt increased the yield and tensile strength and elongation value of the Mg-4Sb alloy. However, the tensile strength and elongation value decreased with the addition of 2% wt. The hardness value of the Mg-4Sn alloy increased with the addition of La.

REFERENCES

1. ASM Specialty Handbook. (1999). Magnesium and Magnesium Alloys, ASM International Handbook Committee, United States of America.

2. Zeytin, H.K. (1999). “Magnezyum Alaşımları: Otomotiv Endüstrisinde Uygulaması ve Geleceği”, Marmara Araştırma Merkezi, Kocaeli.

3. Friedrich, H.E. ve Mordike, B.L. (2006). Magnesium Technology (Metallurgy, Design Data, Applications), Springer, Berlin

4. ASM Handbook Volume 2 (1996), Properties and Selection: Nonferrous Alloys and Special Purpose Materials, ASM International Handbook Committee, United States of America.

5. Mg-Al-RE Magnesium Alloys for High-Pressure Die-Casting K.N. Braszczyńska-Malik, ARCHIVES o f FOUNDRY ENGINEERING DOI: 10.2478/afe-2014-0035

6. Effect of Lanthanum Addition on Microstructures of Mg –4Al Alloys, January 2009, Conference: First Scientific Conference on Nanotechnology, University of Technology, Baghdad IraqAt: University of Technology, Baghdad IraqVolume: Eng.& Tech.Journal,Vol.27,No.B,2009, Ahmed Moosa, Ahmed Moosa Saba. Al- Huseen. Alrazaq Saba A. Al- Huseen. Alrazaq

7. Wang, Q., Zhu, Y., Chen, W. et al. Metall. and Mat. Trans. A (2001) 32: 787. https://doi.org/10.1007/s11661-001-0094-x

8. Okamoto, H. J. Phase Equilib. Diffus. (2010) 31: 574. https://doi.org/10.1007/s11669-010-9784-7

9. E.L. Lavernia, E. Gomez, and N.J. Grant: Mater. Sci. Eng., 1987,

CISET - 2nd Cilicia International Symposium on Engineering and Technology
10-12 October, 2019, Mersin / TURKEY

COMPARISON OF REGRESSION LEARNER METHODS FOR DAILY DEMAND PREDICTION IN MASS MEAL PRODUCTION

Derya Yergök [*1], Mehmet Acı [2]

[1] Mersin University, Engineering Faculty, Computer Engineering Department, Mersin, Turkey, deryayergok@gmail.com

[2] Mersin University, Engineering Faculty, Computer Engineering Department, Mersin, Turkey, maci@mersin.edu.tr

ABSTRACT
In this study, it is aimed to minimize the cost and waste by estimating the number of people who eat food in places where mass food is produced. In this study, support vector machines, one of the regression methods, were used and the results were compared with the regression methods used in the previous studies. Used data set was obtained from the university refectory. The data set was trained and tested with the support vector machine method and the number of people eating was estimated. In the study, prediction models, linear, quadratic, cubic, fine gaussian, medium gaussian and coarse gaussian support vector machine models were used. When these models and other regression models used previously were compared, the best results were obtained in the fine gaussion support vector machine model.

Keywords: *Food Demand Forecast, Support Vector Regression, Food Production, Regression.*

[*] Derya Yergök

1. INTRODUCTION

Today, the food sector; with the developing industry, the globalizing world, the growth of large and small enterprises, the opening of various educational institutions and new shopping spaces, it is growing day by day. With this growth, food companies are gaining momentum. In continuous works and organizations catering companies, in shopping centers restaurants and in schools and workplaces refectories come to the forefront. As the food market continues to develop, cost is the most important problem affecting companies. Every company that produces food wants to minimize its cost. In this case, the most important role in the costs is to determine the exact number of people eating. With the error in the number of people who eat food, there may be an increase in costs and wastes, as well as problems such as lack of food.

The aim of this study is to estimate the number of people who will eat that day according to the meal to be prepared by using data from the university refectory. Accordingly, it is aimed to prevent the problems that may arise if too much or less food is produced. Various regression methods were used to solve the problem. Data were trained with support vector regression (SVR) models for estimation using supervised machine learning with the Regression Learner App in MATLAB's statistics and machine learning toolbox.

Support vector machines (SVM); are training algorithms used for learning, classification, clustering, prediction and finally generating regression rules from data. The theoretical foundations of the SVM were first laid by V. Vapnik in the 1960s and then proposed for classification (Çomak, 2004).

The SVM-based model is called SVR for regression. SVR uses the principle of minimizing structural risk, which is aimed at reducing not only the experimental measurement error, but also the upper limit of the generalization error, compared to conventional supervised learning methods of neural networks (Karal, 2018).

Basically, a SVM creates a hyperplane or a series of hyperplanes in a high or infinitely dimensional field to solve classification or regression problems. With the help of the hyperplane located between the maximum distance to the nearest data points of each class, the given data set is distinguished (Demren, 2011).

SVMs have become a subject of intense work. It has been successfully applied to classification tasks and more recently as regression (Müller et al., 1997).

In theory, SVM is a learning algorithm based on statistical learning theory suitable for small sample. Converts the problem of solving optimal classification margin to the problem of optimal hyperplane research between two classes (Zhiwei et al., 2009).

The basic idea in the SVM regression method is that there is a linear differential function that reflects the character of the educational data at hand as close to reality as possible and fits the statistical learning theory. Similar to classification, the kernel functions are used to process nonlinear states in regression. With the use of kernel functions, SVM becomes a linear model in high dimensional attribute space. Since all the necessary calculations are performed in the input space, the mapping to the higher dimensional property space from the input space does not impose an additional computational burden on the SVM training process. Therefore, SVM can perform its tasks with a simple learning algorithm even in the most complex nonlinear learning processes (Çomak, 2008).

The data set used in the research was divided into two groups as test and training data sets, and after the model was trained with training data estimates were obtained with test data. These operations were performed in MATLAB software environment.

Six different SVR models were designed in this study. These are Linear SVR, Quadratic SVR, Cubic SVR, Fine Gaussian SVR, Medium Gaussian SVR and Coarse Gaussian SVR models.

2. DATASET AND MODELS

2.1. Dataset

The data set consists of 241 rows and 9 columns. Before these values were used, the text in it was converted to numeric values. In addition, a grouping operation was performed for similar data. In this way, the learning ability of the network is increased. The dataset has 9 properties. 8 of them are input data (weekdays, salary days, soups, main course, side meal, Ramadan, holiday and exam week) and 1 (number of people) output data. Table 1 shows an example of the attribute content. An example of a dataset converted to numeric values is given in Table 2.

Table 1. A sample of dataset content

Attribute	Range	Description
Days of the Week (A)	1-5	Monday,Tuesday, etc.
Salary Day (B)	0-1	Salary day or not
Soups (C)	0-9	Chicken, Lentil, etc.
Main Courses (D)	0-14	Beef meal, Chicken meal, etc.
Side Meal (E)	0-5	Rice, pasta with sauce, etc.
Ramadan (F)	0-1	Ramadan or not
Holiday (G)	0-1	Holiday or not
Exam Week (H)	0-1	Exam week or not
Number of People (I)	0-9	Number of people eating at the dining hall

Table 2. A sample of dataset

A	B	C	D	E	F	G	H	I
3	0	3	3	1	0	1	0	1
4	0	3	12	0	0	1	0	2
5	0	5	2	4	0	1	0	2
1	0	0	5	4	1	1	1	0
2	0	3	10	1	1	1	1	0
3	0	3	5	1	1	1	1	0
4	0	5	14	5	1	1	1	0
5	0	3	3	2	1	1	1	0
1	0	3	8	1	1	1	0	0
3	1	3	2	1	1	1	0	0

2.2. Regression Learner

The concept of regression was first introduced by a British statistician named Francis Galton in the 19th century, during a biological study. Francis Galton

developed regression as a concept and method during these researches. Karl Pearson, R.A. Fisher and Udny Yüle developed this method by adapting it to more general statistical fields. The Least Squares Method, which was found by Adrien Marie Legendre in 1805, is the first form of regression method. Then in 1809 C.F. Gauss explained the same method. These two scientists discovered the Least Squares method while making astronomical observations to determine the orbits of the satellites around the Sun. Regression Analysis; is a method used to investigate the numerical relationship between dependent and independent variables. The dependent variable (the variable described, the response variable, also called the result variable) is the variable that is considered to be affected by the independent variable. The independent variable (descriptive variable, also called the active variable) is the variable that is thought to affect the dependent variable. In Regression Analysis; if there is one dependent and one independent variable, Simple Regression Analysis method is applied. If there is one dependent variable and more than one independent variable multiple regression analysis method is applied. If there is more than one dependent variable, Multivariate Regression analysis method is applied. If the relationship between the variables is linear, it is called Linear Regression Analysis, otherwise it is called Curvilinear Regression Analysis (Deniz and Koç, 2019).

The Regression Learner application included in MATLAB's toolbox contains many models. These models train the data appropriate to the problem, put it into the test process and perform estimation. It gives the user the results of the transaction in the form of graphs and error rates. It is possible to reduce error rates and improve performance due to its advanced features.

2.2.1. Support vector regression

SVM is an educated learning method developed by Vapnik and is used for classification and regression. This method is much better in performance and ability to solve nonlinear problems compared to other traditional learning methods. The adaptation of SVM for regression, commonly used for classification problems, was proposed by Smola et al. This method is called SVR (Aci et al., 2017).

2.2.2. Gaussian process regression

Gaussian process regression (GPR) models are non-parametric kernel-based probability models with a limited collection of multivariate random variables. Each linear combination is evenly distributed. Gaussian processes are named after Carl Friedrich Gauss because Gaussian distribution is based on the notion that multivariate normal distributions are an infinite dimensional generalization. Gaussian processes are used for statistical modeling, regression to multiple target values, and higher dimensional analysis of mapping (Zhang et al., 2018). GPR are non-parametric kernel based probability techniques with infinite dimensional generalization of multivariate normal distributions. Gaussian processes are used in statistical modeling, regression to multiple target values, and higher dimensional analysis of mapping. There are four different models with different cores (Zhang and Leatham, 2018). Gaussian processes are a family of stochastic processes that provide a flexible nonparametric tool for data modeling. In the most basic setting, a Gaussian process models a hidden function based on a limited set of observations. The Gaussian process can be seen as extending a multivariate Gaussian distribution to an infinite number of dimensions, where any combination of finite dimensions leads to a multivariate Gaussian distribution that fully specifies the mean and covariance functions. The selection of the mean and covariance function (also known as the kernel) applies uniformity assumptions to the latent function of interest, and determines the correlation between the Y output observations as a function of X Euclidean distance between the respective observation data points (Fairbrother et al., 2018).

2.2.3. Regression tree

Tree-structured classification and regression are non-parametric, computationally intensive methods that have greatly increased in popularity in recent years. It can be applied to data sets that contain both multiple cases and multiple data. They are highly resistant to variables and outliers (Sutton, 2005).

The classification and regression tree method is referred to by different names according to the characteristics of the analyzed data. If the dependent variable is categorical, the Classification Tree is used and in case of continuous variable, the Regression Tree is used (Kayri and Boysan, 2008).

Decision trees (DT) form classification and regression models as a tree structure according to the structure of the data sets that constitute a problem. The comprehensibility of the decision rules used in the construction of these tree structures made the use of the method widespread. DT performs a simple decision making process by transforming complex data into a staged state with a multi-step and sequential approach in solving the classification and regression problem. If the target attributes to be predicted as a result of classification or regression process by DT method consists of discrete data or certain categories, the model called as classification tree. If the attribute data consists of continuous variables, the model is called as regression tree (Kavzoğlu et al., 2012).

Regression trees are a special type of decision tree that deals with a continuous target variable. These methods perform induction through an efficient recursive partitioning algorithm. The test selection in each node of the tree is usually guided by the least squares error criterion. Binary trees think that each tree node has a two-way division (Torgo, 1997).

DT forms a classification and regression model as a tree structure depending on the structure of a given problem. Tree structures consist of rules. The fact that the rules are understandable makes the use of the method easy and practical. DT, in solving a problem, performs a simple decision-making process after multi-stage and sequential processes. While the attributes to be estimated in the classification tree consist of discrete data, the attribute data in the regression tree consist of continuous variables. A simple regression tree structure is shown in Figure 1. In this structure, each attribute is represented by a node. The top part of the tree structure consists of roots

and the bottom part consists of leaves; relations between roots, leaves and nodes are defined as branches. While constructing DT structure, decision rules are formed by asking some questions to the data. Questions are asked at the root node, branching of the tree continues until the leaves (Şengür and Tekin, 2013).

3. RESULTS AND DISCUSSIONS

All prediction models were evaluated in terms of three performances measured, (1) R value is used for measuring the correlation between target and predicted values, (2) MSE measures the average of the squares of the errors, (3) MAE measures the closeness of the predictions to the target values (Witten and Frank, 2005). Equations of these performance measures are given in equations (1), (2) and (3), respectively.

$$\boldsymbol{R} = \sqrt{\mathbf{1} - \frac{\sum_{i=1}^{n}(\boldsymbol{O_i}-\boldsymbol{P_i})^2}{\sum_{i=1}^{n}(\boldsymbol{O_i}-\boldsymbol{O_m})^2}} \quad (1)$$

$$\boldsymbol{MSE} = \frac{\mathbf{1}}{\boldsymbol{n}}[\sum_{\boldsymbol{i}=\mathbf{1}}^{\boldsymbol{n}}(\boldsymbol{O_i} - \boldsymbol{P_i})^2] \quad (2)$$

$$\boldsymbol{MAE} = \frac{\mathbf{1}}{\boldsymbol{n}}\sum_{\boldsymbol{i}=\mathbf{1}}^{\boldsymbol{n}}|\boldsymbol{O_i} - \boldsymbol{P_i}| \quad (3)$$

where n is the number of data points used for testing, P_i is the predicted value, O_i is the observed value and O_m is the average of the observed values.

According to the results given in Table 3, 4 and 5, the following results are obtained:

- In the SVR model, the best results were obtained with Fine Gaussian SVR. MSE was calculated as 0.7082, MAE was calculated as 0.5590 and R was calculated as 0.9433.
- The best results were achieved with Exponential GPR. In this model, 1.2613 value was obtained for MSE, 0.8772 for MAE, and 0.90 for R.
- In Regression Tree model, the best result was achieved with Fine Tree. The values for MSE, MAE and R were calculated as 1.0664, 0.7348 and 0.9165, respectively.
- According to all results, SVR is the most successful model among the regression models used.

Table 3. The results obtained with the SVR model.

Models	MSE	MAE	R
Linear SVR	2.2707	1.1765	0.8124
Quadratic SVR	1.8078	1.0279	0.8544
Cubic SVR	1.5947	0.8802	0.8717
Fine Gaussian SVR	**0.7082**	**0.5590**	**0.9433**
Medium Gaussian SVR	1.0607	0.9396	0.8717
Coarse Gaussian SVR	2.2172	1.1702	0.8124

Table 4. The results obtained with the GPR model.

Models	MSE	MAE	R
Rational Quadratic GPR	1.8657	1.0723	0.8485
Squared Exponential GPR	1.8657	1.0723	0.8485
Matern 5/2 GPR	1.8464	1.0680	0.8485
Exponential GPR	**1.2613**	**0.8772**	**0.90**

Table 5. The results obtained with the Regression Tress model.

Models	MSE	MAE	R
Fine Tree	**1.0664**	**0.7348**	**0.9165**
Medium Tree	1.2196	0.8162	0.90
Coarse Tree	1.6752	0.9326	0.8660

Figure 1-13 shows the performance graphs of SVR, GPR and regression tree models. The X-axis of the graph shows all data consisting of 241 rows, and the Y-axis represents the result data. The fields shown in black represent the actual values and the fields shown in gray represent the estimated values. Fine Gaussian SVR, Exponential GPR and Fine Tree models achieved the best performance results.

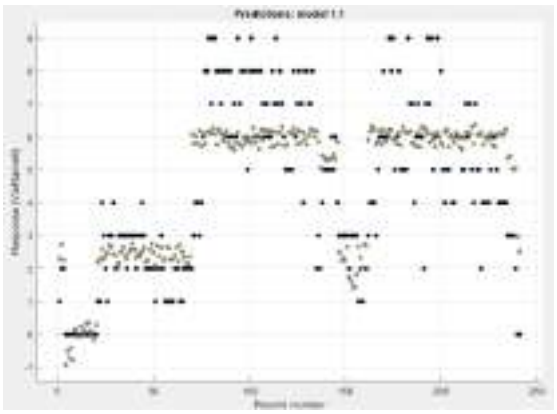

Fig. 1. Response graph of linear SVR model

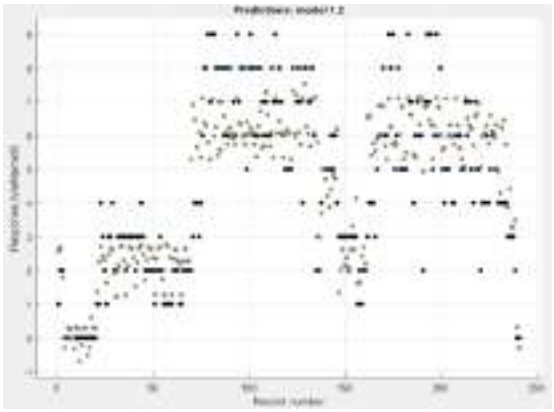

Fig. 2. Response graph of quadratic SVR model

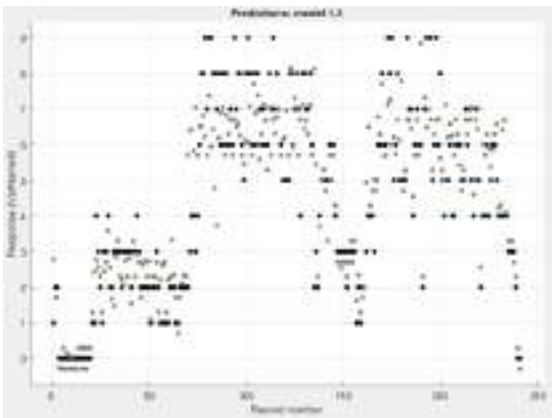

Fig. 3. Response graph of cubic SVR model

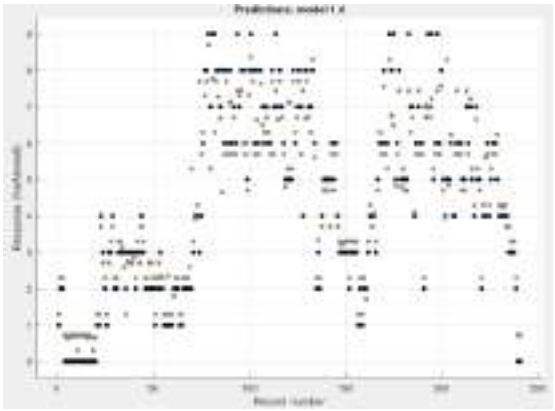

Fig. 4. Response graph of fine gaussian SVR model

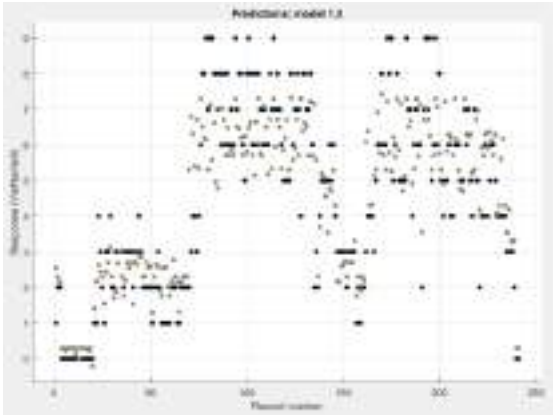

Fig. 5. Response graph of medium gaussian SVR model

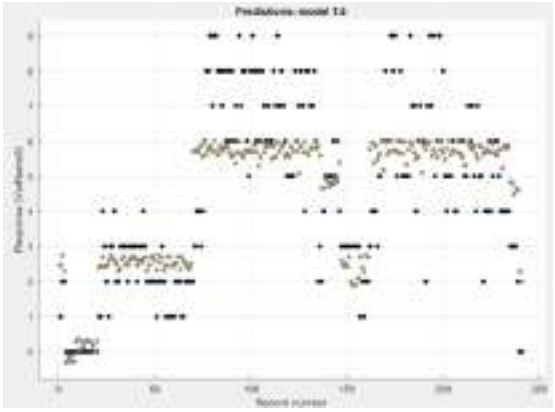

Fig. 6. Response graph of coarse gaussian SVR model

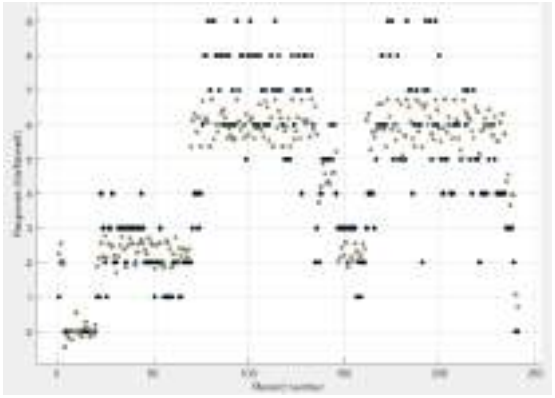

Fig. 7. Response graph of rational quadratic GPR model

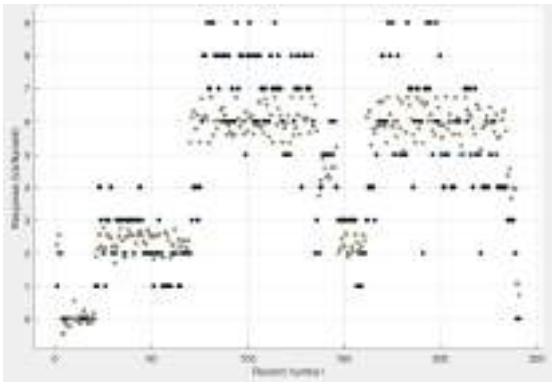

Fig. 8. Response graph of squared exponential GPR model

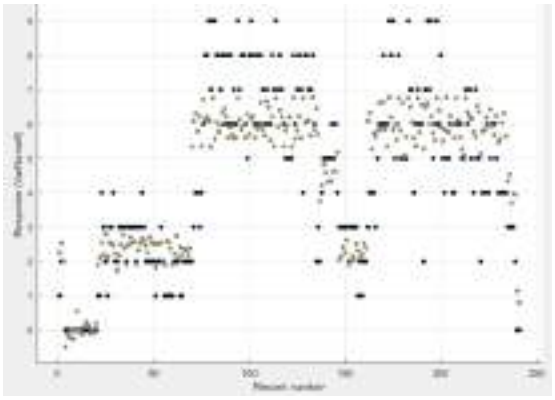

Fig. 9. Response graph of matern 5/2 GPR model

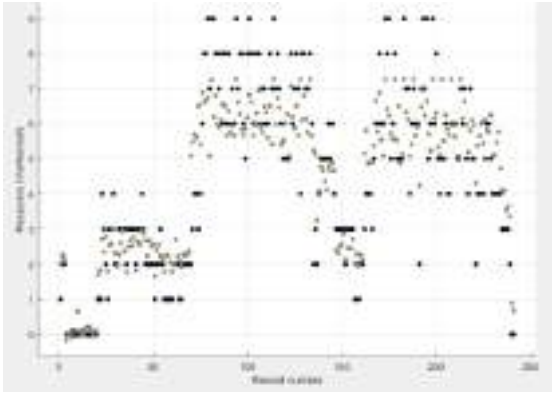

Fig. 10. Response graph of exponential GPR model

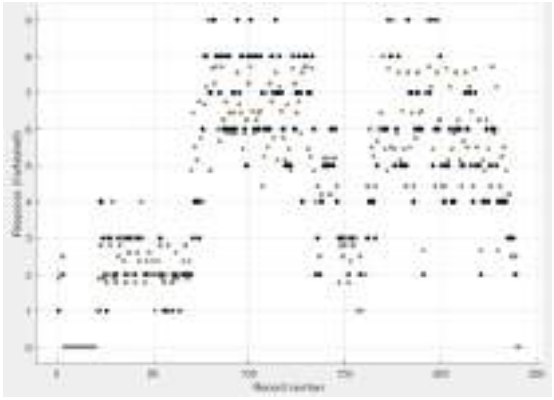

Fig. 11. Response graph of fine tree regression model

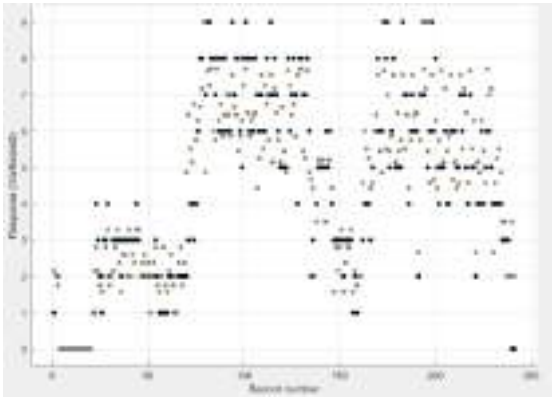

Fig. 12. Response graph of medium tree regression model

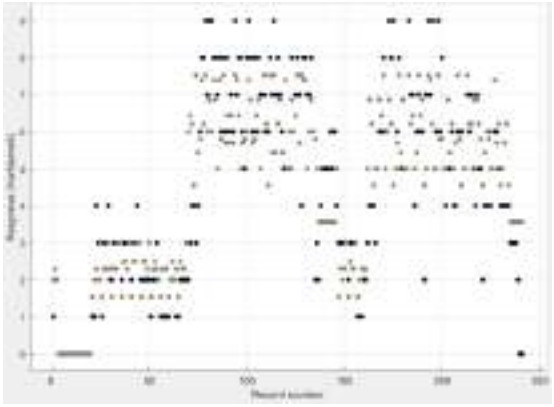

Fig. 13. Response graph of coarse tree regression model

4. CONCLUSION

In this study, different regression models were designed to predict the number of people who eat according to the food to be prepared using the data obtained from the university refectory and the results were compared. It has been concluded that exponential GSR, fine tree and fine gaussian SVR methods are more successful than the other methods among the three models and a total of 13 methods. Among the regression models, the support vector regression model was found to be the best model. Successful results show that existing methods can be improved and better results can be obtained by using different methods / models.

ACKNOWLEDGEMENTS

This study was supported by Mersin University Scientific Research Projects Unit with Project Number 2019-1-TP2-3215.

REFERENCES

Acı, M., Avcı, M. and Acı, Ç. (2017). "Reducing simulation duration of carbon nanotube using support vector regression method." *Journal of the Faculty of Engineering and Architecture of Gazi University*, Vol.32, No.3, pp.901-907.

Çomak, E.(2004). Proposals to solve support vector machines multiclass problems, MSc Thesis, Selcuk University, Konya, Turkey.

Çomak, E.(2008). New approaches for effective training of support vector machines, PhD Thesis, Selcuk University, Konya, Turkey.

Demren, D.(2011). Electrical load demand forecasting application using support vector machines, MSc Thesis, Istanbul Technical University, Istanbul, Turkey.

Deniz, G. and Koç, S.(2019). "The relationship between economic growth and some macro variables in turkey : multiple linear regression model analysis." *Journal of Business Research,* Vol.11 No.1, pp.101-113.

Fairbrother, J., Nemeth, C., Rischard, M. and Brea, J.

(2018). GaussianProcesses. jl: A nonparametric bayes package for the Julia Language. *arXiv preprint arXiv:1812.09064*.

Karal, Ö.(2018). "Compression of ECG data by support vector regression method." *Journal of the Faculty of Engineering & Architecture of Gazi University*, Vol.33, No.2, pp.746-747.

Kayri, M. and Boysan, M.(2008). "Assessment of relation between cognitive vulnerability and depressions level by using classification and regression treeanalysis." *H.U. Journal of Education*, Vol.34, No.34, pp.168-177.

Kavzoğlu, T., Şahin, E. K. and Çölkesen, İ.(2012). "Assessment of landslide susceptibility using regression trees: the case of trabzon province." *Journal of Map*, Vol.147, No.3, pp. 21-33.

Müller, R. K., Smola, A. J., Ratsch, G., Scholkopf, B., Kohlmorgen, J. and Vapnik, V. (1997). "Predicting time series with support vector machines." *Proc., International Conference On Artificial Neural Networks*, ICANN, Berlin, Germany, pp.1327.

Şengür, D. and Tekin, A.(2013). "Prediction of student's grade point average by using the data mining methods." *Journal of Information Technologies*, Vol. *6 No.*3, pp.7-16.

Torgo, L. (1997). "Functional models for regression Tree leaves." In *ICML,* Porto, Portugal, pp. 385-393.

Witten, I. H., Frank, E., Hall, M. A. and Pal, C. J. (2016). *Data Mining: Practical Machine Learning Tools and Techniques*, Morgan Kaufmann, Burlingon, USA.

Zhiwei, G. and Guangchen, B. (2009). "Application of least squares support vector machine for regression to reliability analysis." *Chinese Journal of Aeronautics,* Vol.22, No.2, pp.160-166.

Zhang, N., Xiong, J., Zhong, J. and Leatham, K. (2018). "Gaussian process regression method for classification for high- dimensional data with limited samples." In *2018 Eighth International Conference on Information Science and Technology (ICIST)*, pp. 358-363.

Zhang, N. and Leatham, K.(2018). "Neurodynamics-Based nonnegative matrix factorization for classification." In *International Conference on Neural Information Processing,* Washington, USA, pp. 519-529.

CISET - 2nd Cilicia International Symposium on Engineering and Technology
10-12 October, 2019, Mersin / TURKEY

DAILY DEMAND PREDICTION IN MASS FOOD PRODUCTION WITH ENSEMBLES OF TREES MODEL

Derya Yergök [*1], Mehmet Acı [2]

[1] Mersin University, Engineering Faculty, Computer Engineering Department, Mersin, Turkey, deryayergok@gmail.com

[2] Mersin University, Engineering Faculty, Computer Engineering Department, Mersin, Turkey, maci@mersin.edu.tr

ABSTRACT
In this study, it is aimed to minimize the cost and waste by estimating the number of people who eat food in places where mass food is produced. In this study, one of the regression methods, the tree ensemble model, was applied to the data obtained from the university refectory. The data set was trained and tested by the tree ensemble method and the number of people eating was estimated. The tree community regression model used includes two different models, boosted tree and bagged tree. When these models are compared, the best result is achieved in the boosted tree model.

Keywords: *Regression, Food Demand Forecast, Prediction, Ensembles of Trees.*

[*] Derya Yergök

1. INTRODUCTION

Mass food production is seen and important in many establishments such as refectories of universities, restaurants, cafes and hotels. The list of meals in such establishments, although it is clear how much food will come out every day, it is not possible to reach the exact number. An average number of meals comes out. This results in lack of food or too much food. Therefore, cost is the most important problem affecting companies. Every company that produces food wants to minimize its cost. In this case, the most important role in the costs is to determine the exact number of people eating. Accurate estimates of the number of people who eat will result in a reduction in cost and waste, while will greatly benefit businesses.

The aim of this study is to estimate the number of people who will eat that day according to the meal to be prepared by using the data of the university refectory. Accordingly, it is aimed to prevent the problems that may arise if too much or less food is produced. Various regression methods were used to solve the problem. MATLAB's statistics and machine learning tools are trained with tree community models to predict data using supervised machine learning with the Regression Learner App in the toolbox.

Community methods combine several decision tree classifiers to provide better predictive performance than a single decision tree classifier. The main principle behind the community model is that a group of weak learners come together to form a strong learner, thereby enhancing the accuracy of the model. When we try to estimate the target variable using any machine learning technique, the main reasons for the difference in actual and predicted values are noise, variance and bias. The community helps to reduce these factors (excluding noise, which is an irreducible error). Another way of thinking about community learning is the tales of blind men and elephants. All blind men had their own elephant identification. Although each definition was correct, it would have been better to come together and discuss their meaning before concluding. This story perfectly describes the community learning method (Shubham, 2018).

In classification, clustering and regression problems, the concept of community learning has been proposed to increase the stability and predictive accuracy of a single learning algorithm. A community learning-based model combines individually trained models and produces a single final estimate (Kapucu and Çubukçu, 2019).

Community-based tree models are better compared to single tree models. Bagging and reinforcement are the two most popular learning methods of tree communities (Panda et al., 2009).

Using techniques such as bagging and reinforcement helps reduce variance and increases the robustness of the model. Combinations of multiple classifiers reduce variance, especially in the case of unstable classifiers, and can produce a more reliable classification than a single classifier (Shubham, 2018).

Bagging creates different classifiers, only if the basic learning algorithm is unstable. The ambiguity in the basic learning algorithm means that minor changes to the training set cause major changes in the learned classifier. Breiman (1996) explores the causes of imbalance in learning algorithms and discusses a way to reduce or eliminate it.

Bagging (and to a lesser extent reinforcement) can be seen as ways to use this instability to improve classification accuracy (Dietterich, 2000).

Reinforcement is one of several techniques that aims to improve the performance of many models by adapting them to a single model and combining them for forecasting. Reinforcement is a method used to improve model accuracy. Rather than finding a single and highly accurate prediction rule, it is based on the idea that very difficult rules are easier to find (Elith et al., 2008).

The data set used in the research was divided into two groups as test and training data set. After the model was trained with training data, test data and estimates were obtained. These operations were performed in MATLAB software environment. The Regression Learner App, available in MATLAB's statistics and machine learning toolbox, proposes regression models for predicting data using supervised machine learning.

In this study, two different tree communities were designed. Principal component analysis (PCA) was used in both of the designed models. PCA is a multivariate technique that analyzes a data table in which observations are defined by several quantitative dependent variables associated with each other. Its purpose is to extract important information from the table, to show it as a new set of orthogonal variables called fundamental components, and to show the similarity model between the observations and the scores on the maps (Abdi and Williams, 2010). Among the methods, the best results were obtained with boosted trees.

The accuracy of the proposed models; Mean Square Error (MSE), Mean Absolute Error (MAE) and Multiple Correlation Coefficient (R) were determined.

2. DATASET AND MODELS

2.1. Dataset

The data set consists of 249 rows and 11 columns. Before these values were used, the text in it was converted to numeric values. In addition, a grouping operation was performed for similar data. In this way, the learning ability of the network is increased. The data set contains 11 properties. 10 of these are input data (weekdays, salary days, soups, main course, side meal, complementary meal, calories, meat amount, Ramadan, lesson / exam / holiday period) and 1 output data (number of people). Table 1 shows an example of the attribute content. An example of a dataset that is converted to numerical values is given in Table 2.

Table 1. A sample of dataset content

Attribute	Range	Description
Days of the Week (A)	1-5	Monday,Tuesday, etc.
Salary Day (B)	0-1	Salary day or not
Soups (C)	1-5	Chicken/beef, vegetables, legumes, yoghurt, pastry.
Main Courses (D)	1-5	Beef ,chicken, fish, vegetables, legumes.
Side Meal (E)	1-3	Rice, pastry, legumes.
Complementary Meal (F)	1-5	Yoghurt, fruit, salad, sugary,drink
Calorie (G)	1-3	Calories of food

Amount of Meat (H)	1-4	How many grams of meat
Ramadan (I)	0-1	Ramadan or not
Lesson/ Exam/Holiday (J)	1-3	Semester or exam week or holiday
Number of People (K)	1-9	Number of people eating at the dining hall

Table 2. A sample of dataset

A	B	C	D	E	F	G	H	I	J	K
2	0	3	1	1	1	3	3	0	3	1
3	0	4	2	1	2	3	4	0	3	1
4	0	5	1	2	3	1	2	0	3	1
5	0	3	1	1	1	2	2	0	3	1
1	0	3	1	1	2	2	2	0	2	3
2	0	1	2	1	1	3	4	0	2	3
3	0	1	1	2	1	2	1	0	2	2
4	0	4	1	1	4	3	3	0	2	2
5	0	4	2	3	1	2	4	0	2	2
1	1	3	5	1	1	3	1	0	3	1

2.2. Ensembles of Trees

Community learning is a machine learning paradigm in which multiple students are trained to solve the same problem. Unlike ordinary machine learning approaches that attempt to learn a hypothesis from educational data, community methods attempt to form a series of hypotheses and combine them to use them (Zhou, 2015). Tree communities are one of the community learning models in which more than one regression tree is combined and found the most appropriate result. A simple tree ensemble structure is shown in Fig.1.

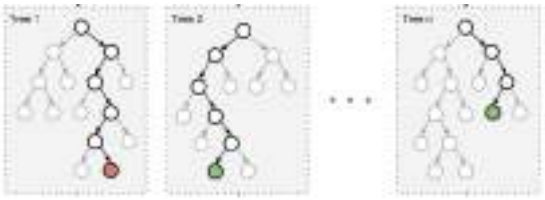

Fig. 1. Ensembles of trees model (Smolyakov,2017)

2.2.1. Boosted trees

Empowerment refers to a group of algorithms that use weighted averages to make weak learners more powerful learners. Unlike bagging, which allows each model to function independently, it then collects the outputs without preferring any model. Empowerment is all about "teamwork". Each working model determines which features the next model will focus on (Shubham, 2018).

2.2.2. Bagged trees

Bagging is a simple and very powerful community method. Bagging is the application of the Bootstrap procedure to a high-variability machine learning algorithm, typically decision trees (Shubham, 2018).

Ensembles of trees model is recommended by L. Breiman. It is a method of retraining the basic learner by deriving new sets of training from an existing training set. Replacement is done by sampling. The training set is produced by randomly selecting a training set with n samples from bagging. Each selected sample is put back into the training set. Some examples are not included in the new training set, while others take place more than once (Güzel, 2018).

3. RESULTS AND DISCUSSIONS

All prediction models were evaluated in terms of three performances measured, (1) R value is used for measuring the correlation between target and predicted values, (2) MSE measures the average of the squares of the errors, (3) MAE measures the closeness of the predictions to the target values (Witten and Frank, 2005). Equations of these performance measures are given in equations (1), (2) and (3), respectively.

$$\boldsymbol{R} = \sqrt{\mathbf{1} - \frac{\sum_{i=1}^{n}(\boldsymbol{O_i}-\boldsymbol{P_i})^2}{\sum_{i=1}^{n}(\boldsymbol{O_i}-\boldsymbol{O_m})^2}} \quad (1)$$

$$\boldsymbol{MSE} = \frac{\mathbf{1}}{\boldsymbol{n}}[\sum_{\boldsymbol{i}=\mathbf{1}}^{\boldsymbol{n}}(\boldsymbol{O_i}-\boldsymbol{P_i})^2] \quad (2)$$

$$\boldsymbol{MAE} = \frac{\mathbf{1}}{\boldsymbol{n}}\sum_{\boldsymbol{i}=\mathbf{1}}^{\boldsymbol{n}}|\boldsymbol{O_i}-\boldsymbol{P_i}| \quad (3)$$

where n is the number of data points used for testing, P_i is the predicted value, O_i is the observed value and O_m is the average of the observed values.

According to the results given in Table 3, the following results are obtained: In the Ensembles of Trees model, the best result was achieved with Boosted Trees. For MSE 0.5103, for MAE 0.5036 and for R 0.9591 values are achieved.

Table 3. The results obtained with the Ensembles of Trees model.

Models	MSE	MAE	R
Boosted Trees	**0.5103**	**0.5036**	**0.9591**
Bagged Trees	1.0147	0.7630	0.9165

The dataset consists of 249 rows and 11 columns. Column 11 is the result column, which contains the estimated values of the number of people who eat. Figures 2 and 3 show the performance graphs of the boosted tree and bagged tree models. The X-axis of the graph shows all data consisting of 249 lines, and the Y-axis represents the result data. The fields shown in black represent the actual values and the fields shown in gray represent the estimated values. Both methods yielded good results and boosted tree model showed better results than bagged tree model.

For the methods in the tree community model, MATLAB's current parameter values were played and high results were obtained. It was found that the parameters of the models were changed in accordance with the data set and the problem. In both methods, PCA was activated and the current value of 95 was 100. At the same time, advanced settings have been changed for both methods. For boosted tree model; the minimum leaf size was 8, the number of learners was 30, the learning rate was 0.25. For the bagged tree model; the minimum leaf size was 1, the number of learners was 23. With these settings, error rates decreased and R value increased.

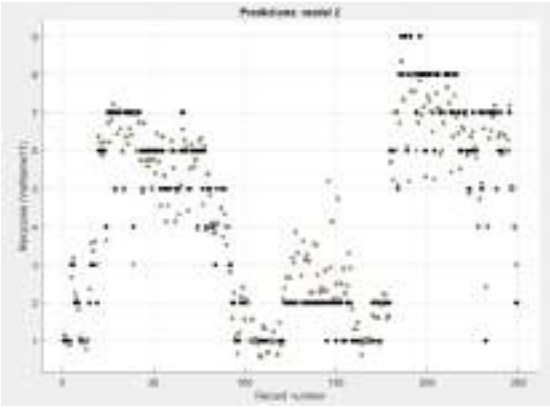

Fig. 2. Response graph of boosted tree model

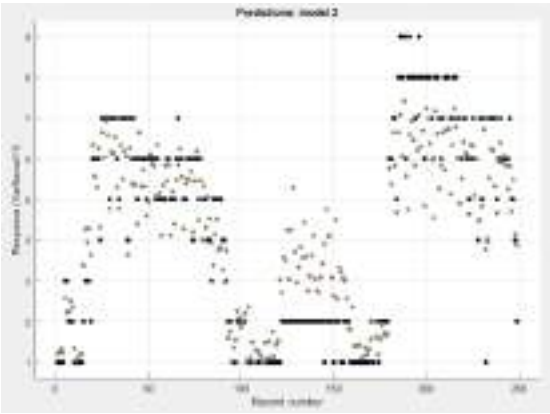

Fig. 3. Response graph of bagged tree model

4. CONCLUSION

In this study, using the data obtained from the university refectory, a regression model of the tree community was designed to predict the number of people eating food according to the food to be prepared and successful results were obtained. Two methods were modeled in the study and boosted tree model was found to reach better results than bagged tree model.

Successful results show that existing methods can be improved and better results can be obtained by using different methods and models.

ACKNOWLEDGEMENTS

This study was supported by Mersin University Scientific Research Projects Unit with Project Number 2019-1-TP2-3215.

REFERENCES

Abdi, H., and Williams, L. J. (2010). "Principal component analysis." *Wiley interdisciplinary reviews: computational statistics*, Vol.*2,* No.4, pp.433-459.

Breiman, L. (1996). "Bagging predictors." *Machine learning,* Vol.24, No.2, pp.123-140.

Dietterich, T. G. (2000). "An experimental comparison of three methods for constructing ensembles of decision trees: Bagging, boosting, and randomization." Machine learning, Vol.40, No.2, pp. 139-157.

Elith, J., Leathwick, J. R., and Hastie, T. (2008). "A working guide to boosted regression trees." Journal of Animal Ecology, Vol.77, No.4, pp.802-813.

Güzel, K. (2018). Kolektif Öğrenme (Ensemble Learning) ve Bagging Algoritması https://medium.com/@billmuhh/kolektif-öğrenme-ve-bagging-algoritması-e8ea3d932b72 [Accessed 22 Aug 2019]

Kapucu, C. and Çubukçu, M. (2019). "Fotovoltaik Sistemlerde Topluluk Öğrenmesi Temelli Hata Tespiti." Bilişim Teknolojileri Dergisi, Vol.12, No.2, pp.83-91.

Panda, B., Herbach, J. S., Basu, S., and Bayardo, R. J. (2009). "Planet: massively parallel learning of tree ensembles with mapreduce." Proceedings of the VLDB Endowment, pp.1426-1437.

Shubham, J.(2018). Ensemble Learning Bagging and Boosting https://becominghuman.ai/ensemble-learning-bagging-and-boosting-d20f38be9b1e [Accessed 22 Aug 2019]

Smolyakov, V.(2017). Ensemble Learning to Improve Machine Learning Results https://blog.statsbot.co/ensemble-learning-d1dcd548e936 [Accessed 22 Aug 2019]

Witten, I. H., Frank, E., Hall, M. A. and Pal, C. J. (2016). Data Mining: Practical Machine Learning Tools and Techniques, Morgan Kaufmann, Burlingon, USA.

Zhou, Z. H. (2015). "Ensemble learning. "*Encyclopedia of biometrics*, pp.411-416.

CISET - 2nd Cilicia International Symposium on Engineering and Technology
10-12 October, 2019, Mersin / TURKEY

APPROACHES TO BLOCK VPN APPLICATIONS

Musa GÜL [1], Dr. Erdinç AVAROĞLU [2] and Yusuf Turhan TEKİN [3]

[1] Mersin University, Computer Engineering, Mersin, Turkey, csemusagul@gmail.com

[2] Mersin University, Computer Engineering, Mersin, Turkey, eavaroglu@mersin.edu.tr

[3] Mersin University, Computer Engineering, Mersin, Turkey, turhantekin@gmail.com

ABSTRACT
Today, Usage of Virtual Private Networks are increasing. Using virtual private networks, users can indirectly access the points that their service providers restrict or block access to. In this study, three basic methods used to prevent such accesses have been examined and the method which gives stable and definite results has been determined.

Keywords: *VPN, 5651, Software Prohibition, Virtual Private Networks, ISP*

1. INTRODUCTION

Some places where people want to access the internet have been restricted by service providers in line with legal obligations. These restrictions are stated within the framework of Law no 5651 due to the inappropriate content. Users can access these points by overcoming this restriction process supported by law with VPN Applications.

Turkey's VPN usage rates, according to the reports GeoSurf and GO-Globe 2019 is 32%. Turkey is ranked 3rd in the world in after these rates; VPN Applications Usage in Indonesia 38% and India 38%. [1]

Within the framework of Law No. 5651, service providers, institutions, organizations and enterprises are obliged to block VPN Applications. In the near future, the studies carried out in the ministry regarding the use of these practices will be subject to criminal proceedings are on the agenda. In order to meet this obligation, Active Directory Application Blocking, Firewall Application Blocking and Third Party Software Application Blocking methods used to block VPN Applications are used in this study.

When examining the Approaches to Block VPN Applications, 5 different VPN Applications have been selected and these applications; It is named VPN1, VPN2, VPN3, VPN4, and VPN5.

In the Data Set Creation step, all the information required for the blocking methods was collected from 5 different vpn applications. These datas were processed on the platforms prepared for the blocking method in the Processing of Data to Environments step before testing.

In the test and conclusion step, applications were forced to run contrary to the working structure of the blocking methods. More stable and accurate results were obtained when applications were blocked only by hash or hash values instead of the ports they used, according to the application path and name values. The study consists of Data Set Creation in which the data of the applications are collected, Processing of the Data in which the blocking methods are created, Testing in which the blocking situation is observed, and the Conclusion section where the judgments obtained as a result of the observations are explained.

2. DESCRIPTION OF METHODS

In Active Directory Application Blocking, applications are blocked according to Microsoft Software Restriction Policies according to hash values or names. Software Restriction Policies (SRP) is a Group Policybased feature that identifisses and controls the ability of software programs running on computers in a domain. Software restriction policies are part of the Microsoft security and management strategy to help businesses improve the reliability, integrity, and manageability of their computers. [2]

The most common method of blocking VPN Applications using Firewall Policies is port prohibition. Ports used by most common VPN applications, such as PPTP or L2TP to establish connections and transfer datas can be closed by system administrators to prevent them from being used on specific networks. [3]

With this process, it is seen that when applications want to use these ports in order to provide communication, they are blocked over the firewall.

Anti-Executable, the Faronics product, was used in the Application Blocking Method with Third Party Software. The program is a software program that prevents unauthorized applications from running on a machine. Depending on the selected security level, even low-level drives can be prevented from operating. Anti-Executable works on the “whitelist” principle. When installed on a machine, AntiExecutable scans all executable applications installed on the machine and whitelists them at the first stage: a list of programs authorized to run. [4]

Any program added to the blacklist by the system administrator is considered unauthorized and will not be installed or run.

3. Creating Data Sets

When creating Data Sets, the identified blocking methods were examined in order and the requirements required for these methods were determined according to the study structures. In Active Directory Application Blocking, since the applications are blocked according to Microsoft Software Restriction Policies according to their hash values or names, the application names and hash values for 5 separate vpn applications have been collected and shown in Table 1.

Table 1: Application hash values in md5 format for VPN applications

Name	Application Hash Value (MD5)
VPN1	460c9d10270b3257b6975ee3a3b2
VPN2	fcee51840a0b57d6db77bdf835df6
VPN3	c94444f8c94437af1d40d19672666
VPN4	3ba6af15da2394798b471c481c5fc
VPN5	121d8884e64583ce07910b467f33

The port informations that 5 separate vpn applications are using is entered in the data set for the Block VPN Applications action through Firewall Policies. Udp ports and Tcp ports are shown in Table 2 and Table 3, respectively.

Table 2: Udp port information

Name	Udp Ports
VPN1	1194, 1197, 1198, 9201
VPN2	500, 1701, 4500
VPN3	500
VPN4	-
VPN5	1194, 1204

Table 3: Tcp port information

Name	Tcp Ports
VPN1	502,501,110
VPN2	-
VPN3	-
VPN4	1723, 47
VPN5	-

In order to implement Anti-Executable, which is the Application Blocking method using Third Party Software, hash values of 5 different vpn applications are entered in the data set and shown in Table 4.

Table 4: Application hash values in md5 format for vpn applications

Name	Application Hash Value (MD5)
VPN1	460c9d10270b3257b6975ee3a3b2fd66
VPN2	fcee51840a0b57d6db77bdf835df6b32
VPN3	c94444f8c94437af1d40d19672666a50
VPN4	3ba6af15da2394798b471c481c5fc191
VPN5	121d8884e64583ce07910b467f33e079

4. PROCESSING DATAS TO ENVIRONMENTS

In this step, the testing environment created for approaches to block VPN Applications was identified as the Windows platform. This determination stems from the fact that the Windows operating system is the most widely used desktop operating system in the world. [5] These datas were shown in Statistics 1.

Statistics 1: World Operating System Usage Rates

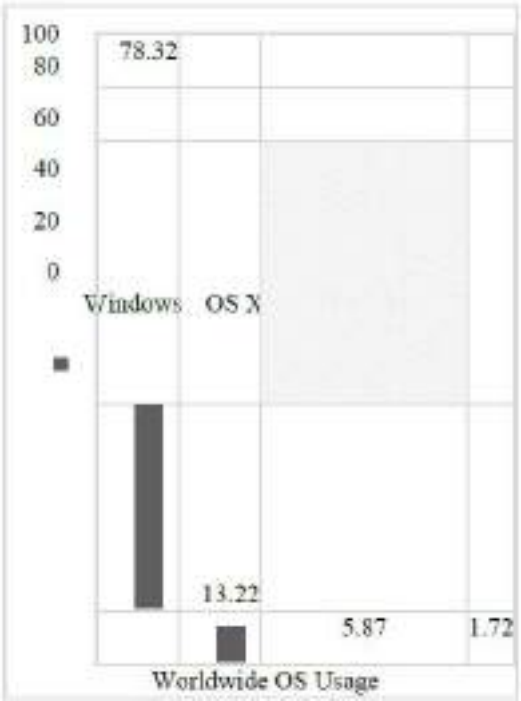

3 independent Windows 10 operating systems were installed. These operating systems are named as W1, W2, W3 respectively. The devices are connected to a network configured with initial settings. Only 5 different VPN applications have been installed on the devices. The necessary update procedures have been completed on the devices.

Active Directory was installed on one Windows Server 2012 R2 and made ready with basic configurations and named as S1. One FreeBSD operating system was named S2 by installing pFSense Firewall on this operating system, basic configurations were made operational. The FreeBSD operating system, which was preferred at this stage, had no effect on the results, and pFSense Firewall, which is also preferred as a Firewall, did not have a positive or negative effect on the results due to the fact that the basic operating principles of the Firewall were the same for all other security products.
Application hash values of 5 different vpn applications are made ready to be recorded in order to prohibit the use of these applications by means of group policies on Active Directory located on S1. The W1 environment is included in the domain on S1 for the application HASH value and the blocking method to be used in the Blocking Applications using Active Directory method.

Information about 5 different vpn applications were entered on pFSense Firewall on S2 as Standard Firewall Rules. These rules are UDP and TCP port information for 5 different vpn applications. The rules are configured to block all incoming and outgoing packets over these ports in network traffic and were left passively. It has been confirmed that the standard gateway information for the W2 environment is pFSense Firewall and that the network traffic for all applications to be used in that environment passes through the pFSense Firewall. Anti-Executable software was downloaded and installed on W3. After the installation, Anti-Executable has whitened all the software on the device with its internal browser. Anti-Executable is left passive without any rule definition for use in the test step**.**

5. Test

It has been confirmed that 5 different VPN applications are installed in W1, W2 and W3 environments and the environments are equivalent to each other in order to create definite values on the results of the operational actions performed in the test step. It has been checked that the S1 and S2 platforms are associated with the W1, W2 and W3 platforms. A table was created in which the data of the test action can be entered and the criteria of speed, precision and sustainability of the methods can be entered. With the hash value on Active Directory installed in S1 environment, the rule to block vpn applications has been activated. Port blocking rules on pFSense Firewall in S2 environment have been activated. Anti- Executable software in W3 environment has been configured to block vpn applications.

5 different vpn applications which were present in W1, W2 and W3 environment were run and observed simultaneously for effective results on the results. At this stage, the speed criterion of the blocking action was checked. This process was repeated several times and the accuracy criterion was checked as a result of long-term

use and attempts to reach different addresses. The application names of 5 different vpn applications were changed, the port information was changed from within the application and the sustainability criterion was checked. At this stage, 5 different vpn applications were updated and its impact on sustainability criteria was controlled. The score table created as a result of the controls is given in Table 5 and the speed according to the blocking speed over 5 points, the accuracy according to the functionality of the functions and the sustainability criteria according to the continuity of the blocking process as a result of the new version updates are scored.

Table numbers and labels should be placed on top of the table, and left- and right-justified. Number the tables consecutively and locate them after and close to where they are first referenced. Leave one line between the table, label and the text. Tables should be auto-fit to window and no vertical lines or borders are needed.

Table 1. This is the example for table formatting

Items	x	y	z
a	5	2	5
b	6	1	6
c	8	3	9
d	1	2	7
e	3	4	1

Note: should be placed under the table leaving no space in-between; 9-pt font; and left- and right-justified.

6. Conclusion

VPN Applications have different practices and methods to prevent these applications from being a type of application that should be prohibited by service providers within the framework of Law No. 5651. In this study, the most stable and precise method was determined than the blocking methods used by Active Directory Application Blocking, Application Blocking Through Firewall and Application Blocking Using Third Party Software from these environments.

The score table created for the tests, practices and methods that was done. When the applications were blocked by closing the ports over the firewall, it was observed that the methods and methods were negatively affected by the accuracy and sustainability items by communicating over VPN 3 and VPN 4 different ports from 5 different VPN applications.

The Anti-Executable application used in Third Party Software Application Blocking Method hash value and blocking method has definite results on the existing installed versions of VPN Applications, but hash effect on sustainability by changing the hash values as a result of updating the applications.

It was found that the update operation could not be performed depending on the group policy rules entered, because applications were blocked by showing the hash value, name and path when applying the Application Blocking Method with Active Directory. The method of Blocking VPN applications with Active Directory has yielded the most stable and precise results compared to other ways and methods in terms of speed, accuracy and sustainability.

REFERENCES

[1] Go-Globe “The State Of Vpn Usage – Statistics and Trends [Infographic]” https://www.goglobe.com/vpn-usage-statistics/
Geosurf “Vpn Usage Statistics” https:// www.geosurf.com/blog/vpn-usage-statistics/
[2] Microsoft (2016), “Software Restriction Policies” https://docs.microsoft.com/tr-tr/windows-server/identity/software-restriction-policies/softwarerestriction-policies
[3] Wikipedia, “Vpn Blocking” https://en.wikipedia. org/wiki/VPN_blocking [4] Faronics, Anti-Executable “Getting Started” https://www.antiexecutable.com.au/download/FA EEnt_GettingStarted.pdf
[5] Desktop OperatingSystem Market Share Worldwide (08/2019) https://gs.statcounter.com/ os-market- share/desktop/worldwide

Table 5: Test scores.

Enviroment	Method	Speed	Precision	Sustainability	Total
Blocking with Active Directory	Application Hash Value and Application Spesifics(Name & Path)	5	5	5	15
Blocking by pFSense Firewall	Application Port Informations	4	5	1	10
Blocking by AntiExecutable	Application Hash Value	5	5	1	11

CISET - 2nd Cilicia International Symposium on Engineering and Technology
10-12 October, 2019, Mersin / TURKEY

High Pressure Processing of Foods

Eda Adal [*1], Tugba Aktar [2]

[1] Gaziantep University, Faculty of Engineering, Food Engineering Department, Gaziantep, TURKEY;
adal@gantep.edu.tr

[2] Alanya Alaaddin Keykubat University, Faculty of Engineering, Food Engineering Department, Antalya, TURKEY;
tugba.aktar@alanya.edu.tr

ABSTRACT
High pressure processing is an emerging non-thermal unit operation that is mainly used for preservation and sometimes for process aid operations. Basically it provides a microbiologic protection by inactivation and causes advantages especially during the storage and extended shell life. However, HPP effects on the food quality are still a controversial topic, due to showing decreased quality parameters for specific food groups. In this symposium, under the title of High Pressure Processing, the unit operation parameters and properties will be discussed along with its effect on the microbiologic structure, sensory features (color, texture and flavor), and nutritional value. Additionally methodological approaches with its advantages and limitations as well as comparison with the other similar conventional methods will be provided along with the examples of HPP applications on specific and vulnerable food groups including seafood, fishery products and dairy products..

Keywords: *High pressure, Food processing, Unit operation, Pressure*

[*] Corresponding Author

1. INTRODUCTION

High Pressure Processing (HPP, Fig. 1) is generally a non-thermal unit operation for the food products preservation. Indeed, it enables to inactivate spoilage and pathogenic microorganisms, and thus extend the shelf life of the product without degrading its nutritional and sensory qualities. This technique does not require the utilization of heat and it is based on the application of high hydrostatic pressure.

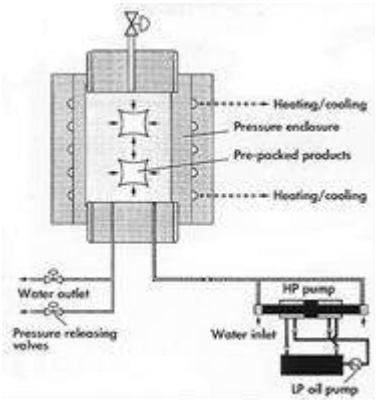

Figure 1: A typical HPP system for treating pre-packaged foods (FAO, 2001)

For the process the food product is placed in the treatment chamber, which is able to keep the high pressure level constant for a period of time. Following the product loading, pressure transmitting agent fills the chamber and pressure is generated by a pump. The hydrostatic pressure inside the chamber is uniformly transmitted to all sides of the product which enables homogenous pressure distribution throughout the product.

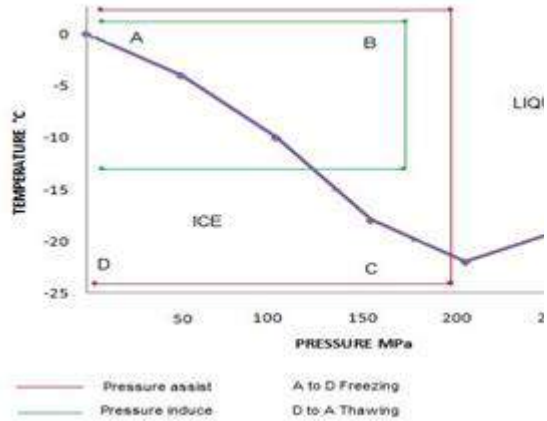

Figure 2: High pressure modeling with freezing and thawing (Reynaud, 2009)

Some studies show that high pressure technique can be applied with; heat treatment, antimicrobials, ultrasound, ionizing radiation to be more efficient for the inactivation of microorganisms and enzymes. For instance as illustrated at Fig.2 HPP can be used with heat applications for food treatments such as; freezing and thawing operation. In this case HPP can either assist (state change is provided by temperature variation instead of pressure variation) or induce (state change is provided by variation of pressure) freezing or thawing operation (Barbosa-Cánovas et al. 2005).

One important factor for HPP applications is the chamber and equipment itself. The equipment must be strong enough to handle the high pressure. The vessel must be 'prestressed' to avoid fatigue which is the expansion of the vessel due to the repeated forces. Tensions are applied layer by layer on the press by reducing the diameter of the cylinder until a point where the dilatation of the cylinder does not exceed the diameter of the original material. In order to have a regular distribution of the product, the vessel has to be circular and avoid any possible dead space. The vessel also must not have any irregularities that could initiate cracks. The HPP method uses a medium as a pressure driving agent. Generally this medium is water which can be mixed with minerals and vegetable oil for lubrication with anticorrosive aims. Some experiments have been conducted with glycol, oil or emulsions as a pressure medium. Even if they are easier to pump and do not drive corrosion, they grease foods and make the cleaning of the equipment difficult (Barbosa-Cánovas et al 2005). For HPP high pressure is described as a pressure value varying between 100 and 1000 MPa. In the case of an industrial production, the hold time must be as short as possible to avoid any delay or breaks of the production line. An increasing pressure usually reduces the required hold time at full pressure. Hence, the general principle of the process is the increasing of the pressure gradually for the efficiency. Furthermore, the pressure must be isostatic for a uniform pressure application on the entire product. On the other hand, temperature has to be controlled especially for the adiabatic heat is added to the heating temperature. The temperature increases naturally when the pressure goes up; for instance increase of every 100 MPa, the water at 20 °C gains 3 °C of temperature. Therefore, selected temperature value depends on what we want to focalize, like safety, quality etc.

2. HPP APPLICATIONS

For HPP applications there are two main approaches; batch process and continuous process.

2.1. Batch HPP Application

Batch process is generally used for pre-packed foodstuffs. In this process a high pressure is applied directly on the package. The packing material must be flexible to bear high pressure such as pouches, cups or large bulk bags. Dead space amount in the package depends on the product, for instance, if it is flexible with some liquid or viscous content in it, the space will easily be fulfilled with the pressure applications. With batch press, the package provides a safe environment by avoiding contamination of the food during the process. Illustration of the batch HPP process can be seen on Fig. 3. The figure shows an Avure technology for HPP batch process application where the pressure vessels can have capacities from 35 liters to 700 liters and 600 MPa operation pressure depending on the food sample.

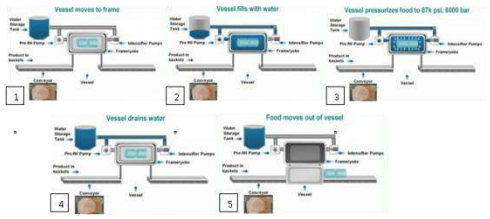

Figure 3: Explanation of the batch process principle by Avure high pressure processing (2009)

2.2. Continuous HPP Application

On the other hand for the continuous process a pumpable food such as liquids is necessary. Fig. 4 shows the illustration of continuous HPP application with 4 steps of the process. The initial step is the feeding of the foodstuff and pumping of the fluid food into the line. Second step involves pumping of the water at the lower closure and a movable divider separates the water from the juice, like a piston. After the second stage a pressure application starts and after holding the full pressure during a short period, some water is released to decrease the pressure. Lastly, more water is pumped into the system but this time with higher pressure to push up the piston to reach to the top of the cylinder and liquid is ejected from the cylinder.

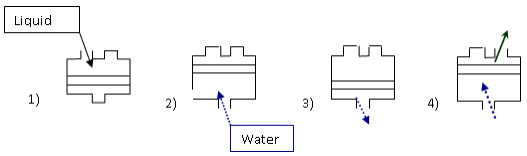

Figure 4: Principle of the High Pressure Process, Falque, (2009)

In the continuous HPP applications with at least three vessels (one for filling, one for holding and other for emptying the product) there is almost a continuous output of juice with always one cylinder to fulfill. The volume of high-pressed product is larger with the continuous press. However, a damage of large or sensitive particles can always occur especially while passing of the food with pumps and narrow valves.

3. EFFECTS OF HPP

3.1. Microbiologic Effects

There are different levels of high pressure, which are mainly divided into equivalents of pasteurization and sterilization levels of damaging microorganisms. Both are effective in inactivating most pathogenic and spoilage causing microorganisms. Pasteurization treatments lead to inactivate bacteria, yeasts and moulds but do not have any effect on spores and enzymes. The sterilisation is also a heating process, which is accelerated by a high-pressure application. As a result of these applications foods are free of bacterial spores, spoilage spore and enzymes. Noteworthy, non-proteolytic type B spores are the most common pressure-resistant pathogenic spore and they may be critically important for HPP design in food processing.

The inactivation involves proteins denaturation with the pressure breaking the cell walls, and releasing of the proteins. The proper denaturation occurs in 3 phases; unfolding–aggregation–gelation. Therefore, it inhibits enzymatic activities, destroys the vital intracellular organelles, and damages the membrane structure. It can also cause chemical reactions taking part in inactivation. Despite the type and the state (growth, stationary phase, and spore) of the microorganisms, the high-pressure efficiency on inactivating vegetative bacteria and spores depends on several factors, notably the pressure level, the temperature and the duration of the treatment. In the pressure-thermal treatments, nonlinear models describe these parameters effect on inactivation kinetics of various microbes.

The composition (for example salt, sugar and low-water content) of the dispersion medium is also significant for the protection of the microorganisms from inactivation (baroprotective effect). A good example is sugars where, sugars in the surface of the treated food bind some water around it, which provides a protector film. However, the pH of the medium seems not to have a significant effect on high-pressure treatment efficiency.

Pros and cons of the high-pressure are still not well controlled, so that research is still needed on various fields such as pressure-thermal resistance of microorganisms, spore physiology, mechanisms for inactivation of food toxins, role of the food matrix, pH and etc.

The mode of inactivation of viruses by high pressure (HP) has not been fully elucidated. It is known that HP causes macromolecules to dissociate and much of the published data concerns the use of HP as a tool to investigate virus assembly. HP induced dissociation of viruses may be fully reversible or irreversible, depending on the virus and treatment conditions and typically more extreme treatments lead to irreversible changes in virus conformation (Gaspar et al., 1997 and Silva & Weber, 1988). For example, feline calicivirus, a norovirus surrogate, is inactivated by treatment at 275 MPa during 5 min (Kingsley et al., 2002). In contrast, poliovirus is very resistant to HPP, with no significant reductions in infectivity reported after relatively severe treatments, such as 600 MPa at 20 °C for 60 min (Wilkinson et al., 2001). The reason for the disparate resistance of viruses to HPP is still unknown. It has been suggested that the resistance of viruses may be related to the size and shape of the virus (Wilkinson et al., 2001) or its high thermodynamic stability (Oliveira et al., 1999).

3.2. Sensorial Effects

The sensorial qualities include color, texture and flavor. They can be measured or evaluated by a trained panel if possible. Each product is affected by high pressure in different ways and the following topics summarize these effects.

3.2.1. Color

For most of fruits and vegetables, high pressure does not affect the color. However, some of them suffer a change of the brightness and the intensity of the color. For example, for avocado puree, the intensity of color decreases during the shelf storage because of the activity of residual polyphenoloxidase (López-Malo et al., 1998). On the other hand in case of meat treatments, high pressure increases the lightness and reduces redness. Meat discoloration through pressure processing may result from a whitening effect especially between 200–350 MPa pressure due to globin denaturation and/or to heme displacement or release, and initiation of the oxidation of ferrous myoglobin to ferric metmyoglobin at 400 MPa. Only the latter phenomenon is prevented by total oxygen removal or prior formation of nitrosomyoglobin. (Anne-Carlez, et al., 1994).

3.2.2. Texture

The effect of high pressure treatment on texture depends of the pressure intensity and the sensibility of the product. Process design and product selection is very important for the texture, for instance on the HP application causes permanent loss of firmness on fruits and vegetables. On the other hand, for meat and fish, high pressure usually increases the muscle firmness due to protein denaturation and softness after cooking. Fig 5. shows the effect of pressure level and time on the firmness of some fruits. From the figure it is obvious that the fruit texture is significantly affected from a HPP applications and the magnitude of the effect depends on the fruit type.

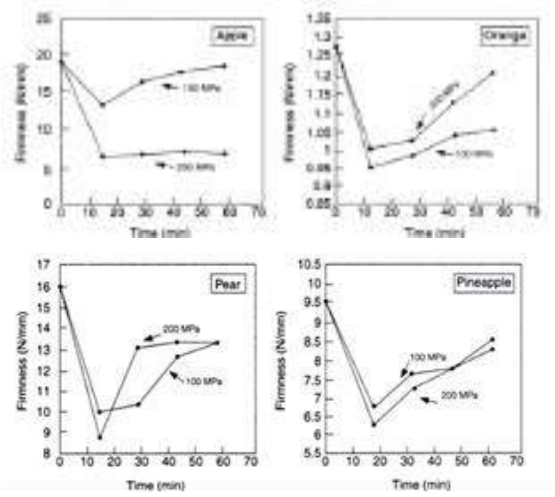

Figure 5: Effect of HPP on the firmness of fruits (Marc and Dietrich, 2002)

3.2.3. Flavor

HP treatment can denature some molecules and causes some change on the flavor. For example, in tomato juice, HPP decreases the amount of hexanol and increases the amount of trans-2-hexanal and n-hexanal. These molecules are responsible of rancid flavor at higher concentration. However, some food products do not show any alterations caused from the HPP applications, while others showing dramatic changes on the flavor profiles during the storage (Marc and Dietrich, 2002).

3.3. Nutritional Effects

Vitamin content of the fruits and vegetables are not significantly affected by high pressure treatments (Butz, et al., 2003). A study showed that about 95% of vitamin C in strawberries is conserved by high pressure treatment of strawberry jam, which is 1.7 times more than in heat treatment. The decrease of the nutritive value during the storage is the same as the product which was heated.

4. HPP VS. OTHER PROCESSES

Table 1. Advantages and limitations of the HPP method

Advantages	Limitations
Inactivates vegetative bacteria and spores	Cannot ensure a certain inactivation of microbial
Retains the main sensorial quality closer to the raw food	Little effect on enzyme
Reduction of the use of preservatives	Equipment is expensive and complex
Not harmful for Human Health	Serve limited number of packages at a time
Requires less time	Cannot be applied to food with a small percentage of free water (less than 40%) for anti-microbial effect
Can be applied after packaging	
Treats the product uniformly	
Extend shelf-life	6Affect a little bit the color of meat and vegetables

HP applications could replace conventional heat treatments such as sterilization, pasteurization and blanching methods. Sterilization by heating is a process which uses temperature higher than 100 °C, whereas pasteurization does not exceed 100 °C. On the other hand, HPP enables to pasteurize milk to produce cheese, citric beverages, juices etc. with lower heat treatments (Guamis, et al., 2005). Blanching inhibits enzymes between 70 and 100 °C. HPP can be an alternative method for vegetable blanching due to its permitting color changes (Welti-Chanes, et al., 2005). Also, for protein containing products heat causes denaturation of the proteins and some microorganisms can be inactivated which also causes nutritional and sensorial quality loss on the product. (Hjelmqwist, 2005). Therefore, product type and chemical structure are determinant for the selection of the unit operation.

5. HPP APPLICATION ON SPECIFIC FOOD PRODUCTS

5.1. Fishery Products (e.g. capaccio)

Carpaccios are very thin slices of fish, and are usually consumed fresh with herbs. Consumption of raw and minimally processed food is a growing concern and in case of fishery products due to risk of contamination and health. HPP application on; salmon (Salmon salar), tuna (Thunnus alalunga), desalted bacalao (dried salted cod fish) causes loss of physicochemical and sensorial quality on salmon and tuna whereas no significant effect on the desalted bacalao (Gómez-Estaca, et al., 2009). On the other hand the pressurization level has significant effect on the appearance of fish muscles. At surrounding temperature, the more the pressure increase, the more opaque and whiter muscles obtain. So, high pressure treatment is a suitable process to obtain high quality fish carpaccios and thus acquired new sensory features and high scores of acceptability (Gómez-Estaca et al., 2009).

5.2. 2.Seafood (e.g. oysters)

Oysters are the most common harvested shell-fish in the world. At present, health risk associated to the consumption of oyster meat is one of the growing concerns for the oyster industry. Post harvested treatments are applied to remove pathogenic bacteria and reduce spoilage causing microorganisms. Especially, high pressure inactivates Vibrio parahaemolyticus and Vibrio vulnificus, which are the momentous oyster-borne pathogens. These pathogens can be inactivated under high pressure in phosphate buffer saline (PBS). As a result of that, shelf life of the product can be increase and freshness and quality can be maintained (Prapaiwong et al., 2009). Moreover, high pressure treatment is used for oyster shucking procedure to adduct oyster muscle from the shell. Shucking process needs different range (250 to 310 MPa) of pressure depending on variety of oyster species. This process eases the shell opening of the oyster which is not a simple task for untrained consumer. Koo et al. (2006) reported that the flavor of these oysters remain unchanged when they were treated under 400 Mpa for 10 minutes at 7 °C and the product obtained with better quality.

5.2.3. Dairy products (e.g. curd cheese)

High pressure treatment can produce the intended result as an implement to extend shelf-life while maintaining the quality belonging to the product. One of the main advantages of high pressure treatment is that the components, which are responsible for the sensorial and nutritional quality of foods, are not damaged by high pressure treatment as much as they are with traditional methods. For the commercial production of curd cheese from pasteurized bovine milk, the use of starter bacteria (Lactococcus) is a well-known production method. High pressure treatment of cheese was carried out by taking vacuum packaging of samples in plastic pouches. After completion of pressurization, feasible amount of Lactococcus bacteria were reduced. High pressure treatment of fresh lactic curd cheese at over 300 MPa produces the intended result of removing spoilage yeast and lengthens the shelf-life of the product for up to 8 weeks without adding any preservatives. But Treatment under pressure of 200 MPa did not affect significantly to prevent the growth of yeasts, but effectively controlled for 6 to 8 weeks when the samples were subjected to pressure above 300 MPa (Daryaei, 2007).

REFERENCES

Hendrickx, M. E. G. and Knorr, D. W. 2002. Ultra high pressure treatments of foods. In the book: Heremans, K. Springer publication (ed). The effects of high pressure on biomaterials. Food Engineering Series. Pages 167-180.

Avure Technologies. 2007. Advertisement for the QFP 35L–600 High Pressure Food Processing. (http://www.youtube.com/watch?v=dEiS8ODzGI8)

Balasubramaniam V.M and D. Farkas. 2008. High-pressure Food Processing. Food Science and Technology International. Vol. 14, No. 5: 413-418.

Barbosa-Cánovas G. V., Tapia M. S., Pilar Cano M. 2005. Novel Food Processing Technologies. In the book: Hjelmqwist, J. illustrated (ed). Commercial High pressure equipment. CRC Press.

Butz, P., García, A. F., Lindauer, R., Dieterich, S., Bognar, A., & Tauscher, B. (2003). Influence of ultra-high pressure processing on fruit and vegetable products. Journal of Food Engineering, 56(2-3), 233-236.

Daryaei, H., Conventry, M.J., Versteeg, C. and Sherkat, F. 2007. Effect of high pressure treatment on starter bacteria and spoilage yeasts in fresh lactic curd cheese of bovine milk. Innovative Food Science and Emerging Technologies, 9:201-205.

FAO. 2001. Technical elements of new and emerging non-thermal food technologies. Part I: Technical elements. Rome, Italy. [Available at: http://www.fao.org/Ag/ags/Agsi/Nonthermal/nonthermal_1.htm accessed on 26/03/09].

Fellows, P.J. 2000. Food Processing Technology: Principles and practice. Second Edition, Woodhead publishing limited, Cambridge, England, p. 212.

Gómez-Estaca, J., López-Caballero, M.E., Gómez-Guillén. M.C., López de Lacey, A. and Montero, P. 2009. High pressure technology as a tool to obtain high quality carpaccio and carpaccio-like products from fish. Innovative Food Science and Emerging Technologies, 10:148-154.

Gudmundsson M. and H. Hafsteinsson. 2006 Minimal processing in practice: seafood. Minimal processing technologies in the food industry. Technological Institute of Iceland (MATRA), Reykjavik.

Koo, J., Jahncke, M.L., Reno, P.W., Hu, X. and Mallikarkjunan, P. 2006. Inactivation of Vibrio parahaemolyticus and Vibrio vulnificus in phosphate-buffered saline and inoculated whole oysters by high pressure processing. J. Food Prot., 69:596-601.

López-Malo, A., Palou, E., Barbosa-Canovas, G. V., Welti-Chanes, J., & Swanson, B. G. (1998). Polyphenoloxidase activity and color changes during storage of high hydrostatic pressure treated avocado puree. Food Research International, 31(8), 549-556.

Polydera, A. C., Stoforos, N. G., Taoukis, P. S. 2003. Comparative shelf life study and vitamin C loss kinetics

in pasteurised and high pressure processed reconstituted orange juice. Journal of Food Engineering, 60:21-29.

Prapaiwong, N., Wallace, R.K. and Arias, C.R. 2008. Bacterial loads and microbial composition in high pressure treated oysters during storage. International Journal of Food Microbiology, in press.

Wolbang, C.M. Concepción SM, Rosana L, Begoña de A. and Pilar C. 2008. Onion high-pressure processing: Flavonol content and antioxidant activity. Innovative Food Science and Emerging Technologies. 9. 196–200.

MAGNETRON SPUTTERED Cu_2SnS_3 THIN FILMS

Yusuf Selim OCAK[1]

[1] Smart-Lab, Dicle University, Diyarbakır, Turkey E-mail: yusufselim@gmail.com

ABSTRACT

Cu_2SnS_3 (CTS) is a ternary p-type semiconductor is one of the most exiting materials for the formation of solar cells. CTS contains low lost and earth abundant materials. The control of physical parameters of thin films is very important to obtain high efficient devices. In this study, Cu_2SnS_3 thin films were deposited on soda lime glasses (SLGs) by magnetron sputtering method. The sputtered thin films were annealed in a quartz tube furnace in H_2S atmosphere. The morphological, structural and optical properties of CTS thin films by scanning electron microscopy (SEM), x-ray diffraction (XRD), Raman spectroscopy and uv-vis data. It was seen that the thin films of the sputtered and H_2S annealed thin films shows CTS characteristics without any other secondary phases.

Keywords: *Cu_2SnS_3, Thin Film, Sputtering*

1. INTRODUCTION

The demand on energy increases every day. Fossil fuels is the main energy source used all over the world. Fossil fuels based contaminations is accepted as the main environmental problem. Therefore alternative energy sources have a great importance. Solar energy is one of the most important renewable energy sources.

Si based solar cells are the dominant in the market. But development of Si based solar cells needs expensive and difficult processes. Therefore, alternative materials are needed to fabrication of low cost and easy processable solar cells. $Cu(InGe)Se_2$ (CIGS) thin films have been used as absorber layers for the fabrication of thin films solar cells. The toxicity and the cost of the elements (CIGS) directed scientists to the development of new materials.

Cu_2SnS_3 (CTS) is a ternary p-type semiconductor with high absorption constant. CTS is composed of earth abundant, non-toxic, and inexpensive elements such as Cu, Sn and S. It has a tunable band gap (0.9-1.4 eV). Koike et al (2012) fabricated a thin film solar cell by sulfurizing Cu–Sn precursors deposited by co-electrodeposition technique with a structure glass/Mo/ CTS/CdS/ZnO:Al/Al were fabricated from the films. The best cell had an efficiency of 2.84%. A relatively high conversion efficiency was obtained from films with Cu/Sn≤2.

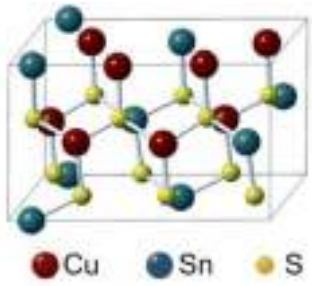

Fig. 1. Crystal structure of monoclinic CTS

In this study, CTS thin films were deposited on soda lime glass (SLG) substrates by sputtering method. The film annealed in H_2S atmosphere. The physical parameters of the thin films were analyzed by spectroscopic methods.

2. EXPERIMENTAL PROCEDURES

In this study, high purity Cu and Sn targets bought from Lesker Company were used. Firstly Cu and Sn targets sputtered separately to understand the deposition rate of the targets. Then, Cu and Sn layers were deposited on SLG. The films were annealed in a quartz furnace in H_2S atmosphere. The scanning electron microscopy (SEM) images were taken by FEI Quanta 250 SEM, X-ray diffraction patterns were taken by Bruker D8 diffraction system, Raman spectroscopy measurements were taken using SNOM Raman Spectroscopy with 532 nm excitation wavelength. Finally, the optical properties of thin films were determined by Shimadzu UV-3600 spectrophotometer.

3. RESULTS AND DISCUSSION

The SEM image of the sputtered and annealed CTS thin film is presented in Figure 2. As seen from the figure, the CTS surface is very homogenous and can be used in the fabrication of planar solar cells.

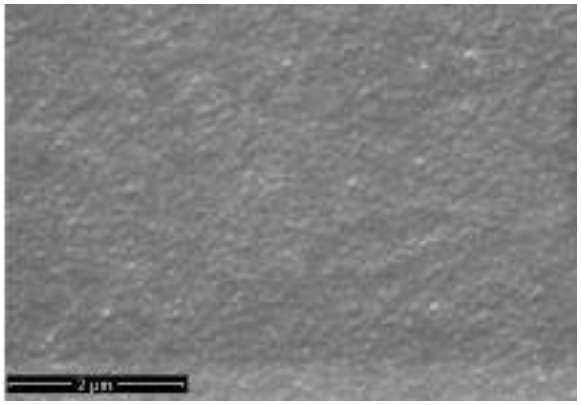

Fig.2. SEM images of CTS film

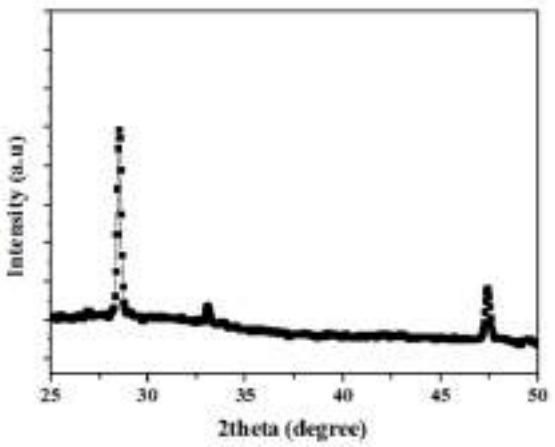

Fig.3. XRD pattern of CTS film

The crystal structures of the thin films were examined at the limit values of $20° \leq 2\theta \leq 60°$ by using the Bruker D8 DISCOVER x-ray device with λ=1.5413Å wavelength light. Figure 3 shows the XRD pattern of CTS thin film between 10 and 60 degrees. The XRD pattern fit to ICDD ref no 01-089-2877 (Chantana, 2017). Raman spectroscopy of the the film is also presented in Figure 4. Raman spectra showed peaks at 290 and 350 cm^{-1} which can be assigned to the Ao symmetry vibrational modes of monoclinic CTS as reported, which is in agreement with the XRD results (Mathews, 2013).

The band gap of a film can be determined using the equation ^{m}

$$\alpha h\nu = B(h\nu - E_g) \quad (1)$$

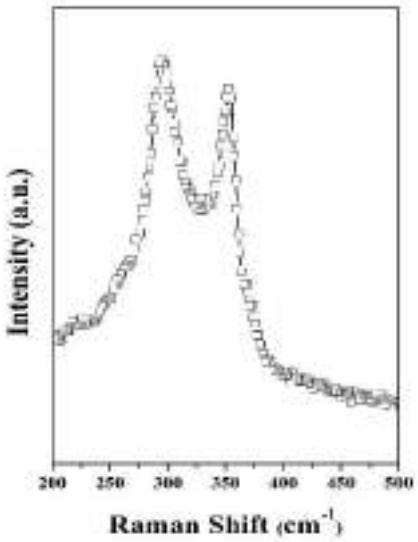

Fig.4. Raman spectroscopy of CTS thin film

Where α is the absorption coefficient, B is a constant and h is the plank constant. The exponent m depends on the nature of the transition, m = 1/2, 2, 3/2, or 3 for allowed direct, allowed nondirect, forbidden direct, or forbidden nondirect transitions, respectively. It is well known that CTS has an allowed direct band gap and m = 1/2 was used for the band gap calculation. $(\alpha h\nu)^2$–hν curve of CTS thin film on glass was calculated according to Eq. (1). The E_g of CTS thin film was determined as 0.96 eV by extrapolating the straight line of the graph to intercept the photon energy axis

4. CONCLUSION

In the present study, CTS thin films were deposited by sputtering of Cu and Sn targets and annealing in H_2S atmosphere. The morphological, structural and optical properties of the films analyzed by SEM, XRD, Raman and uv-vis data.

REFERENCES

Chantana, J., Suzuki, K., & Minemoto, T. (2017). Introduction of Na into Cu2SnS3 thin film for improvement of its photovoltaic performances. *Solar Energy Materials and Solar Cells*, *168*, 207-213.

Koike, J., Chino, K., Aihara, N., Araki, H., Nakamura, R., Jimbo, K., & Katagiri, H. (2012). Cu2SnS3 thin-film solar cells from electroplated precursors. *Japanese Journal of Applied Physics*, *51*(10S), 10NC34.

Mathews, N. R., Benítez, J. T., Paraguay-Delgado, F., Pal, M., & Huerta, L. (2013). Formation of Cu 2 SnS 3 thin film by the heat treatment of electrodeposited SnS–Cu layers. *Journal of Materials Science: Materials in Electronics*, *24*(10), 4060-4067.

PHOTOELECTRICAL PROPERTIES OF Mo/n-Si METAL SEMICONDUCTOR CONTACTS

Yusuf Selim OCAK[1]

[1] Smart-Lab, Dicle University, Diyarbakır, Turkey E-mail: yusufselim@gmail.com

ABSTRACT

Metal-semiconductor (MS) contacts are one of the main components of modern electronic and optoelectronic industry. In this study, Mo/n-Si MS rectifying diode was fabricated by DC sputtering of Mo target on n-Si semiconductor. The current-voltage (I-V) measurements of the junction were executed in dark and under a solar simulator with various light intensities. It was seen that the MS contact had excellent rectifying property and behaves as a Schottky rectifying diode. The main electrical parameters including ideality factor and barrier height. The I-V measurements of the Mo/n-Si contact under the solar simulator showed that the reverse bias current increases with the increase in light intensity. The results showed that the device had also a photodiode properties.

Keywords: *Molybdenum, MS contact, n-Si semiconductor, photoelectrical properties*

1. INTRODUCTION

Metal-semiconductor (MS) contacts have been one of the main part of all semiconductor electronic and optoelectronic devices. Because of its technological importance, the studies are still the focus of interest. Silicon (Si) is the dominant semiconductor materials in modern technology especially for the fabrication of integrated circuits, chips, light emitting diode and solar cells.

Many studies have been performed to understand electrical properties of MS contacts. For instance, Karataş et al (2007) evaporated Sn metal on p-Si semiconductor to obtain rectifying MS contact and determined temperature dependent electrical properties of Sn/p-Si MS contact between 150 and 400 K. It was seen that the ideality factor and series resistance decreased and barrier height values increased with the increase in temperature. Ocak et al (2010) fabricated Ta/*n*-Si and Ta/*p*-Si Schottky barrier diodes obtained by sputtering of tantalum (Ta) metal on semiconductors. The characteristic parameters of these contacts like barrier height, ideality factor and series resistance have been calculated using current voltage (*I–V*) measurements. They showed that the sum of calculated barrier heights (1.21 eV) for Ta/*n*-Si and Ta/*p*-Si is higher than the band gap of the Si (1.12 eV) because of the native oxide layer on semiconductor surface.

Sputtering is a common method to deposit both refractory metals and ceramics. The evaporation of Mo metal is not easy because of its high evaporation point. Therefore, sputtering is a suitable method for the formation of Mo thin films.

In this study, Mo/n-Si MS diode was fabricated by sputtering of Mo metal on n-Si semiconductor. The electrical and optoelectronic properties of Mo/n-Si MS diode were analyzed by means of its current-voltage measurements in dark and under a solar simulator with various intensities.

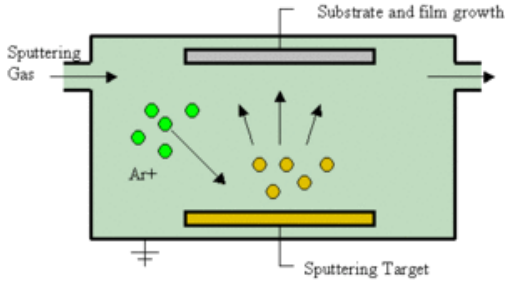

Figure 1. Sputtering process

2. EXPERIMENTAL PROCEDURES

In this study, an n-type Si wafer with (100) orientation and 1-10 Ωcm resistivity, high purity Mo target were used. The Si wafer was cleaned by putting it in boiling

trichloroethylene for 5 min and ultrasonically vibrated in acetone and ethanol for 5 min. The wafer was immersed into diluted HF solution to remove native oxide layer on the surfaces. Between each step the wafer washed with deionized water. Before formation of ohmic contact to p-Si wafer, it is dried under N_2 atmosphere. Au metal was evaporated on unpolished side of the wafer in high vacuum and annealed at 420 °C for 3 min in N_2 atmosphere. Mo metal was sputtered at 10 mTorr and room temperature. 100 W DC power was applied to target and the sputtering process continued for 10 min. The electrical properties of the diode were analyzed using current-voltage measurements by Keithley 2400 source meter in dark and under a solar simulator with AM1.5 global filter.

3. RESULTS AND DISCUSSION

Current-voltage (*I-V*) measurements of Mo/n-Si MS contact is presented in Figure 2. As seen from the figure, the device had excellent rectification property. When a MS contact is considered the *I-V* relationship can be written as (Rhoderick, 1988)

$$I = I_0 \exp\left(\frac{q(V - IR_S)}{nkT}\right) \qquad 1$$

where I_0 is the saturation current which is expressed as

$$I_0 = SA^*T^2 \exp\left(\frac{q\phi_b}{kT}\right) \qquad 2$$

q is the electronic charge, R_S is the series resistance, n is the ideality factor, k is the Boltzmann constant and T is the absolute temperature**.** S is the diode area, A^* is Richardson constant and ϕ_b is the barrier height. The

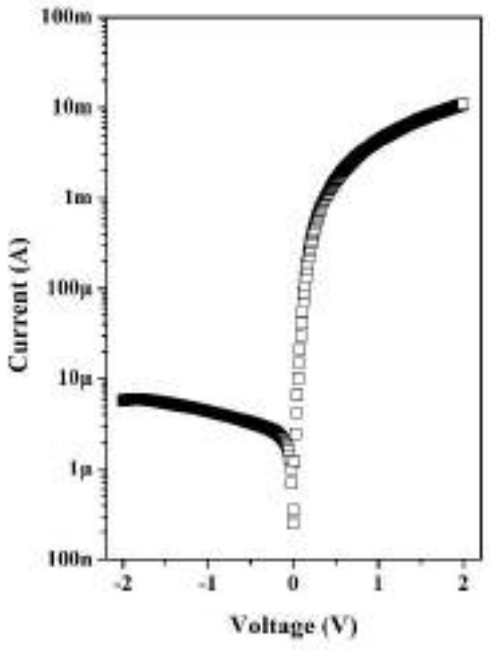

Figure 2. I-V measurements of Mo/n-Si MS contact in dark

ideality factor values of a MS diode the can be calculated using the slope values of ln*I-V* plots by the help of the equation

$$n = \frac{q}{kT}\frac{dV}{d\ln(I)} \qquad 3$$

The ideality factor and barrier height values calculated as 1.05 and 0.65 eV. The ideality factor of the diode should be unity. The ideality of the Mo/n-Si MS junction nearly ideal. A small deviation from ideality can be attributed the fabrication induced native oxide layeron n-Si substrate and interface states between Mo and n-Si.

Furthermore, Current-voltage (*I-V*) measurements of Mo/n-Si MS diode were repeated under a solar simulator from 40 to 100 mW/cm^2 and the semilog I-V plots are given in Figure 3. As seen from the figure the reverse bias current increases with the increase in light intensity. This situation shows us the formation of electron-hole pairs by incident photons (Ocak 2012).

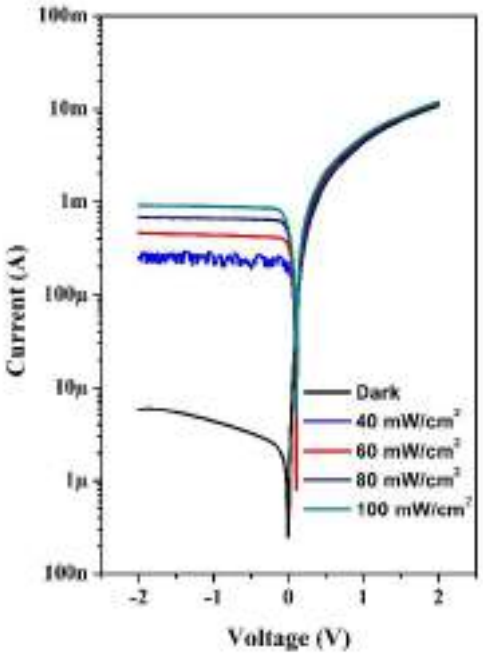

Figure 3. Light intensity dependent I-V measurements of Mo/n-Si MS diode.

4. CONCLUSION

Mo/n-Si MS contacts were fabricated by DC sputtering of high purity Mo target. The electrical properties of the diode were determined by its current-voltage measurements. It was seen that the structure had excellent rectification behavior. In addition the photo-induced current-voltage properties of the diode were analyzed. It was seen that the device can be used as a photodiode.

REFERENCES

Karataş, Ş., Altındal, Ş., Türüt, A., & Cakar, M. (2007). Electrical transport characteristics of Sn/p-Si schottky contacts revealed from I–V–T and C–V–T measurements. *Physica B: Condensed Matter*, *392*(1-2), 43-50.

Ocak, Y. S. (2012). Electrical characterization of DC sputtered ZnO/p-Si heterojunction. *Journal of Alloys and Compounds*, *513*, 130-134.

Ocak, Y. S., Genisel, M. F., & Kılıçoğlu, T. (2010). Ta/Si Schottky diodes fabricated by magnetron sputtering technique. *Microelectronic Engineering*, *87*(11), 2338-2342.

Rhoderick, E. H., & Williams, R. H. (1988). Metal-Semiconductor Contacts. 1988. Clarendon.

CISET - 2nd Cilicia International Symposium on Engineering and Technology
10-12 October, 2019, Mersin / TURKEY

TEMPERATURE DEPENDENT ELECTRICAL PROPERTIES OF ZnO/p-Si HETEROJUNCTION WITH CdS BUFFER LAYER

Yusuf Selim OCAK[1]

[1] Smart-Lab, Dicle University, Diyarbakır, Turkey E-mail: yusufselim@gmail.com

ABSTRACT

ZnO is one of most common materials for the fabrication of electrical and optoelectronic devices. In this study ZnO/p-Si heterojunction device was obtained with a thin CdS buffer layer. Both CdS and ZnO thin films were deposited by sputtering method. Ag metal was evaporated on ZnO thin films as front contact. Electrical properties of the junction were analyzed by current-voltage (I-V) measurements in dark between 77 and 500 K. The electrical parameters of the junction including ideality factor, barrier height and series resistance were determined using I-V data. It was seen that while barrier height values increased, the ideality factor and series resistance values decreased with the increase in temperature.

Keywords: ZnO, CdS, Heterojunction, Buffer Layer, Electrical Properties

1. INTRODUCTION

Zinc oxide (ZnO) is an n-type semiconductor with a 3.37 eV band gap. It has been used in various applications including piezoelectric transducers, varistors and solar cells (Tian, 2003). Cadmium Sulphide (CdS) is naturally an n-type material with an optical band gap of 2.4 eV (Tak, 2009). It is as an important material due to its applications in photovoltaic cells. For instance, CdS is used as buffer layer in the fabrication of Cu2(InGe)Ss2 and Cu2ZnSnS4 based solar cells (Tanaka 2009).

Many methods have been used to deposit thin films of the materials including spin coating, thermal evaporation, successive ionic layer adsorption and reaction (SILAR) and chemical bath deposition methods. Sputtering method is preferred to deposit thin films of refractory metals and ceramics. It is used especially for large area applications (Ocak, 2010).

Some studies have been performed to understand electrical and optoelectrical properties of n-ZnO/p-Si heterojunction devices. In this study, n-ZnO/p-Si heterojunction device was fabricated with CdS buffer layer by sputtering of CdS and ZnO thin films. Then its electrical properties of the device were analyzed by means of current-voltage measurements in dark between 77 and 500 K.

2. EXPERIMENTAL PROCEDURES

In this study, a p-type Si wafer with (100) orientation and 1-10 □cm resistivity, high purity CdS and ZnO targets were used. The Si wafer was cleaned by putting it in boiling trichloroethylene for 5 min and ultrasonically vibrated in acetone and ethanol for 5 min. The wafer was immersed into diluted HF solution to remove native oxide layer on the surfaces. Between each step the wafer washed with deionized water. Before formation of ohmic contact to p-Si wafer, it is dried under N2 atmosphere. Al metal was evaporated on unpolished side of the wafer in high vacuum and annealed at 570 °C for 3 min in N2 atmosphere. Then, CdS and ZnO thin films were deposited on p-Si semiconductor by radio frequency (RF) sputtering of the targets. After formation of CdS and ZnO thin films, Ag metal was evaporated as front contact. The obtained structure of the junction is presented in Figure 2. The electrical properties of the junction were analyzed using current-voltage measurements in dark between 77 and 500 K using Keithley 2400 source meter and Janis VPF-100 Cryostats with Lake Shore 335 temperature controller.

Fig. 1. The vacuum system used in the study

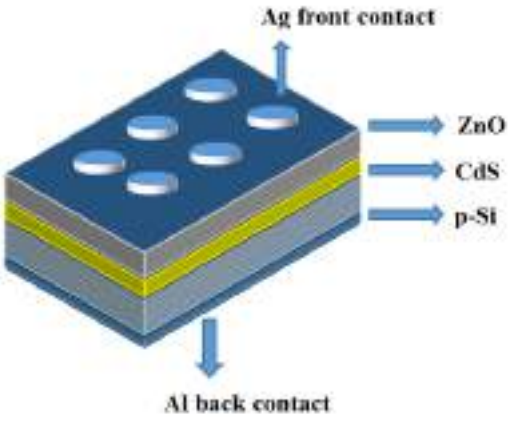

Fig. 2. The ZnO/p-Si heterojunction with CdS thin films

3. RESULTS AND DISCUSSION

Current-voltage (I-V) measurements of Ag/ZnO/p-Si heterojunction with CdS buffer layer between 77 and 500 K is presented in Figure 3. As seen from the figure, the device had excellent rectification property. While the reverse bias remains constant, the exponential increase in forward bias is expressed as rectification property. The I-V relationship of a rectifying junction can be expressed as (Rhoderick, 1988)

$$I = I_0 \exp\left(\frac{q(V - IR_s)}{nkT}\right) \quad (1)$$

where I_0 is the saturation current, q is the electronic charge, R_S is the series resistance, n is the ideality factor, k is the Boltzmann constant and T is the absolute temperature. The I_0 saturation current can be written as

$$I_0 = SA^*T^2 \exp\left(\frac{q\phi_b}{kT}\right) \quad (2)$$

where S is the diode area, A^* is Richardson constant and ϕ_b is the barrier height. The ideality factor values of the Ag/MoO_3/p-Si diode were calculated using the slope values of ln$I$-V plots by the help of the equation

$$\mathrm{n} = \frac{\mathrm{q}}{\mathrm{kT}} \frac{dV}{d\ln(I)} \quad (3)$$

The ideality factor of the device decreased from 3.396 to 1.12 with the increase of measurement temperature between 77 and 500 K. The ideality factor value for the room temperature was calculated as 1.8. The ideality factor greater than unity shows the deviation from ideal diode behavior. This deviation can be attributed the influence of the interface layer, series resistance.

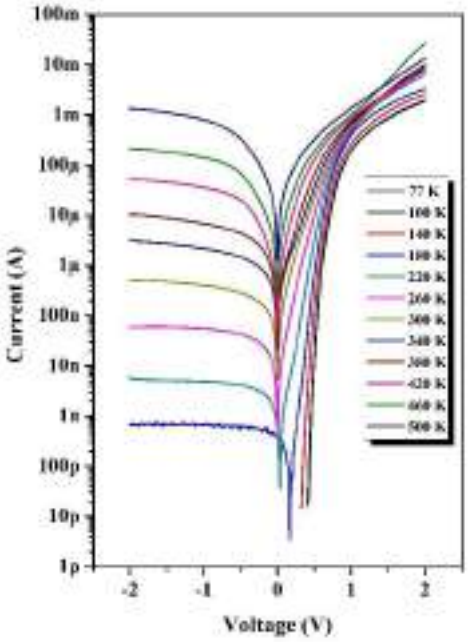

Fig. 3. The I-V measurements of ZnO/p-Si heterojunction with CdS thin films

Furthermore, the barrier height value increased from 0.235 to 0.805 eV from 77 to 500 K. Similar results have been reported in literature. For instance, Kocyigit et al (2017) obtained Au/ZnO/n-Si device by deposition of ZnO thin layer by atomic layer deposition technique and obtained *I-V* relationship between 100 and 380 K. They have reported that the ideality factor of the junction decreased from 4.34 to 2.4. They also showed that the barrier height value increased from 0.29 to 0.89 eV.

The deviation from linearity at forward bias current-voltage plot is caused by the series resistance effect. There are several methods to calculate series resistance of the junctions. In this study, the Norde method was used to calculate series resistance of the junction. Norde functions can be expressed as (Norde 1979)

$$F(V) = \frac{V}{\gamma} - \frac{kT}{q}\left(\frac{I(V)}{SAT^2}\right) \quad (4)$$

where γ is the first integer greater than ideality factor and $I(V)$ is the current executed from current-voltage measurements. The series resistance values of the diode are defined using the equation

$$RS = \frac{kT(\gamma - n)}{qI_{\min}} \quad (5)$$

where I_{min} the corresponding current value at V_0. Series resistance values the device decreased from 3120 to 243 Ω with the temperature.

4. Conclusion

Ag/ZnO/p-Si heterojunction device with CdS buffer layer was fabricated by RF sputtering of CdS and ZnO thin films. The temperature dependent electrical properties of the device were calculated by current-voltage measurements between 77 and 500 K.

REFERENCES

Kocyigit, A., Orak, I., Çaldıran, Z., & Turut, A. (2017). Current–voltage characteristics of Au/ZnO/n-Si device in a wide range temperature. Journal of Materials Science: Materials in Electronics, 28(22), 17177-17184.

Norde, H. (1979). A modified forward I‐V plot for Schottky diodes with high series resistance. Journal of Applied Physics, 50(7), 5052-5053.

Ocak, Y. S., Genisel, M. F., & Kılıçoğlu, T. (2010). Ta/Si Schottky diodes fabricated by magnetron sputtering technique. Microelectronic Engineering, 87(11), 2338-2342.

Rhoderick, E. H., & Williams, R. H. (1988). Metal-Semiconductor Contacts. 1988. Clarendon.

Tak, Y., Hong, S. J., Lee, J. S., & Yong, K. (2009).
Fabrication of ZnO/CdS core/shell nanowire arrays for efficient solar energy conversion. Journal of Materials Chemistry, 19(33), 5945-5951.

Tanaka, K., Oonuki, M., Moritake, N., & Uchiki, H. (2009). Cu2ZnSnS4 thin film solar cells prepared by non-vacuum processing. Solar Energy Materials and Solar Cells, 93(5), 583-587.

Tian, Z. R., Voigt, J. A., Liu, J., Mckenzie, B.,
Mcdermott, M. J., Rodriguez, M. A., ... & Xu, H. (2003). Complex and oriented ZnO nanostructures. Nature materials, 2(12), 821.

CISET - 2nd Cilicia International Symposium on Engineering and Technology
10-12 October, 2019, Mersin / TURKEY

WAVE ENERGY: A GLOBAL OVERVIEW OF THE CURRENT STATE OF ESTABLISHED COMPANIES

Emre Kaygusuz [1], Ali Magdi Sayed Soliman [2] and Huseyin Mutlu [*3]

[1] Mersin University, Engineering Faculty, Mechanical Engineering Department, Mersin, Turkey, emrekaygusuz@mersin.edu.tr

[2] Mersin University, Engineering Faculty, Mechanical Engineering Department, Mersin, Turkey, ali.magdi.sarhan@gmail.com

[3] Mersin University, Engineering Faculty, Mechanical Engineering Department, Mersin, Turkey, hmutlu@mersin.edu.tr

ABSTRACT
R&D in the field of wave energy is still ongoing; however, the governments should subsidize the new startups in this technology to minimize the fossil energy risks in our environment. In the past years, many companies have declared bankruptcy and closed down since the demand for fossil energy in the market is still abundant. Also, many companies are still in the testing process. In this paper, we provide a brief introduction to wave energy converter systems as well as an update to the existing wave energy companies established around the world. In conclusion, we want to shed light on the need for our governments' subsidies to save our planet from global warming and air pollution.

Keywords: *Wave Energy Converter (WEC), Wave Energy, Renewable Energy, Marine Renewable Energy, Current State*

[*] Corresponding Author

1. INTRODUCTION

Renewable energy is a source of energy that is renewed on its own and never ends with time, such as solar energy, wind energy, or wave energy. Recently, the global interest has tended to use clean and renewable energy since consumption of fossil energy has been the foremost cause of the current environmental problems such as acid rain, air pollution, and global warming, that might be the reason of death to the next generations. Wave energy is one of the renewable water energies that we can capture from water motion (Chen *et al.*, 2013). When winds blow across the oceans, they create waves that travel across the ocean's surfaces fast to long distances. As known, the earth is a watery planet as it has five oceans in total, where the waves exist: the Arctic, Atlantic, Pacific, Indian, and the Antarctic. The world ocean is 361 million square kilometers out of 510 million square kilometers, the total area of the earth (Fang *et al.*, 2018). Therefore, the oceans cover nearly 71 percent of the entire land on our planet, and thus the availability of energy that can be captured from waves in the oceans is so high. The global wave energy reserve is estimated to be about 2.5 billion kW (Fang *et al.*, 2018), and this energy has many advantages that make it very appropriate as a source of renewable energy. One of these advantages is that It can be produced 90 percent of the whole day, unlike the sun and wind energy that can be obtained only 20 ~ 30 percent of the day (Drew *et al.*, 2009). Additionally, using waves to create energy means that no vast agricultural lands are needed. Also, no waste or even noise is produced.

For obtaining energy from the waves, technologies have been developed to create Wave Energy Converter systems that transfer the wave energy into electricity. The history of wave energy research extends for 220 years as the first patent in wave energy came from Frenchman Pierre Simon in 1799 (Titah-Benbouzid et al., 2015). In Japan, North America, and Europe, more than a thousand wave energy conversion techniques have been patented until 2009 (Drew et al., 2009). However, this technology is still young in its initial levels. And because of the ongoing subsidize to fossil energy and lack of demand for wave energy, many companies have failed. Therefore, governments must support the startups in this area; otherwise, it will be so difficult for these companies to cope with the immense demand for fossil energy. In this paper, we firstly give a brief introduction to wave energy generation, and then we present information about the current state of established companies in wave energy.

2. CLASSIFICATION OF WAVE ENERGY CONVERTER SYSTEMS

There are two different classifications of Wave Energy Converter (WEC) systems based on location and working principle.

2.1. Based on the Location

In terms of location, WEC systems can be classified, depending on the depth of the water, into three types: onshore, nearshore, and offshore systems (Nezhad *et al.*, 2018). As depicted in Fig. 1, onshore WEC systems are located so near to the utility network, while nearshore systems are located in shallow water of 10 to 25 meters deep, and offshore systems are located in so deep water, more than 40 meters deep.

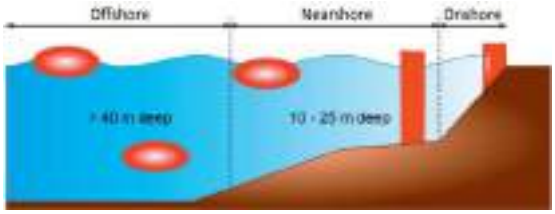

Figure 1: WECs types according to the location (Titah-Benbouzid *et al.*, 2015)

The installation and maintenance of onshore systems are much easier than offshore or nearshore systems as well as the required electrical transmission cables are much less in length thus the system's cost is cheaper (Fadaeenejad *et al.*, 2013). Besides, onshore systems are located far from storm areas and big sea animals. However, onshore systems have a bad visual impact since they occupy the coastal area. In addition, the behavior of shallow water wave is sometimes unstable and can be dangerous to the build systems because of the possibility of a wave breaking force (Poullikkas *et al.*, 2014). Furthermore, onshore systems operate in the presence of less powerful wave energy compared to offshore and nearshore systems as, for example, if an offshore system produces 70 kW/m, the same waves onshore can produce just 20 kW/m, (Poullikkas *et al.*, 2014).

2.2. Based on the Working Principle

Many different types of Wave Energy Converter systems exist under this classification.

2.2.1. Attenuator

Attenuator is a mode of operation in which the WEC device floats parallel to the wave direction and rides the waves (EMEC, accessed 19 Sep 2019). While the wave passes, the energy is captured from the relative motion between the right and left arms. As an example of these systems, Pelamis WEC is shown in Fig. 2

Figure 2: Pelamis Wave Energy Converter system (Solar Thermal, accessed 19 Sep 2019)

2.2.2. Point absorber

Point absorber is a mode of operation in which the WEC device moves up and down due to the buoyant body on the water surface. The device converts this movement to electricity (Koca *et al.*, 2013). In Fig. 3, the PowerBuoy device built by the company of Ocean Power Technologies is shown (EMEC, accessed 19 Sep 2019).

Figure 3: A point absorber WEC system called PowerBuoy (Power, accessed 19 Sep 2019)

Another example of this type is the Wave Star Machine, as shown in Fig. 4, which consists of multiple half-submerged floats that rise and fall as the waves pass. And from this motion electrical power is achieved.

Figure 4: A multi-point absorber system called The Wave Star Machine (wavestarenergy, accessed 19 Sep 2019)

2.2.3. Oscillating Wave Surge (OWS) converter

Oscillating wave surge WEC devices are anchored perpendicular to the wave direction around a pivoted joint; hence, they oscillate like a pendulum in response to the back and force movement of water driven by waves' surges. As waves pass overhead, the paddle moves with the surges; thus, energy is captured to transfer it to electricity (WaveRoller, accessed 19 Sep 2019). The wave roller Wave Energy Converter made by AW-Energy Oy is an example of this type, as shown in Fig. 5.

Figure 5: The Oscillating Wave Surge WEC system made by WaveRoller (WaveRoller, accessed 19 Sep 2019)

2.2.4. Oscillating Water Column (OWC) converter

Oscillating Water Column WEC is a system that harnesses energy from the oscillating water inside a partially submerged chamber or hollow column. As shown in Fig. 6, waves act like a piston inside the chamber. When the air is compressed inside the chamber, it flows through the turbine. The continuous movement of the column (up and down) and the changing status of the air (compressed and decompressed) help the turbine to stay rotating and therefore the electricity can be generated.

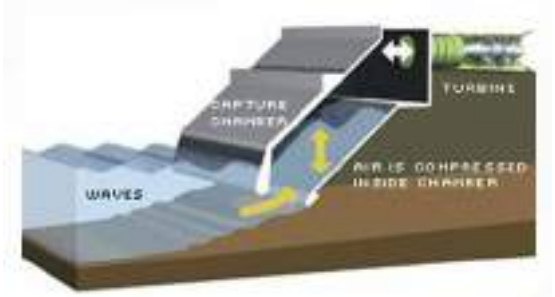

Figure 6: Pictorial representation of the Limpet Oscillating Water Column WEC system (Poullikkas, 2014)

2.2.5. Overtopping

Overtopping devices are based on the principle of hydropower production. When the sea waves break into the system, they rise to a high elevated reservoir, and when the seawater recedes, the sea water is returned to the sea through the existing water turbines to generate electricity, as shown in Fig. 7 (EMEC, accessed 19 Sep 2019).

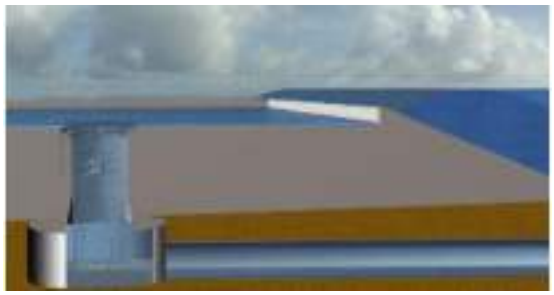

Figure 7: Overtopping system (EMEC, accessed 19 Sep 2019).

An example of this system is the Wave Dragon built by Wave Dragon company.

Figure 8: Wave Dragon's WEC system (Maritime Journal, accessed 19 Sep 2019)

There is another shape of overtopping systems, as shown in Fig. 10. This system has a tapered channel gradually narrowing and at the end of it, an elevated reservoir exists. The channel works to concentrate the waves and let them enter from the wide end to the narrow end where the reservoir is. Power is then generated using the conventional hydroelectric power plant. Eventually, the collected water is allowed back into the sea.

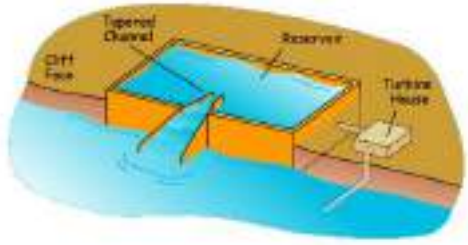

Figure 9: Tapchan WEC system (Tapered Channel Wave Energy, accessed 19 Sep 2019)

2.2.6. Submerged pressure differential

Submerged pressure differential systems are built to be attached to the seabed. The motion of waves causes changes in the pressure on these devices; therefore, the devices move up and down. An example of this type is the Archimedes Waveswing (Fig. 10) built by AWS Ocean Energy.

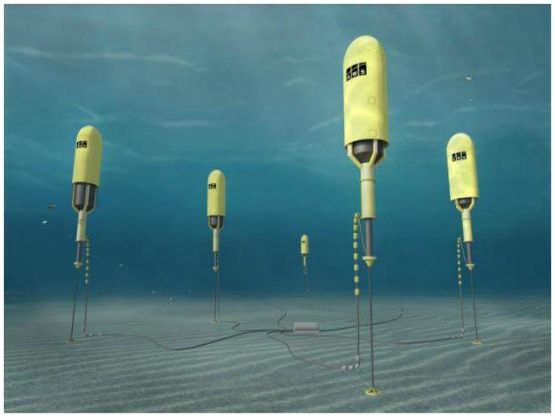

Figure 10: The Archimedes Waveswing submerged wave power buoy (AWS Ocean Energy, accessed 19 Sep 2019)

2.2.7. Bulge wave

In this WEC system, a long rubber tube is filled with water under low pressure moored to the seabed and floating parallel to the wave direction. When the sea wave passes along with the tube, pressure variations along the tube are created thus the tube flexes, compressing the water inside and a bulge wave is excited. While the running bulge travels through the tube in a speed determined by the geometry, it is getting bigger, gathering energy that can be converted into electrical power (Sustainable Energy Research Group, accessed 19 Sep 2019; EMEC, accessed 19 Sep 2019). The Anaconda Bulge Wave (Fig. 11) is an example of this type built by Checkmate Sea Energy.

Figure 11: The Anaconda Bulge Wave WEC system made by Checkmate Sea Energy (Koca *et al.*, 2013)

2.2.8. Rotating mass

Rotational mass is another method of action that can be used to obtain power from the waves. As shown in Fig. 19, the floating device shows heaving and swaying motions due to the waves (EMEC, accessed 19 Sep 2019). As a result of that, the mass or gyroscope, inside the device, rotates by gravity and thus the circular motion generated is converted into electrical power.

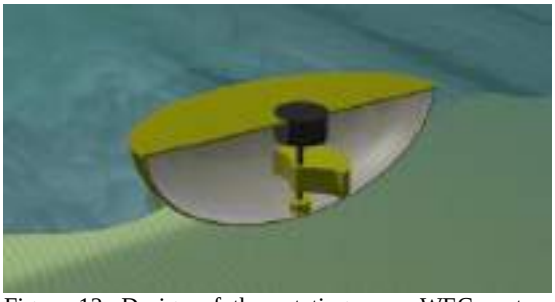

Figure 12: Design of the rotating mass WEC system (EMEC, accessed 19 Sep 2019).

The Penguin, patented by Wello Oy, is an example of this system, as shown in Fig. 13. The Penguin has no contact with the sea water, no hydraulics or joints, and no audible disturbance (Wello Oy, accessed 19 Sep 2019). This offshore system floats like a small boat in deep water away from the wave-breaking zone.

Figure 13: The Penguin Rotating Mass WEC system built by Wello Oy (Wello Oy, accessed 19 Sep 2019)

2.2.9. Others

There are other designs like the one developed by Bombora Wave Power. This Bombora device uses a flexible low-cost membrane that changes its shape/volume thus compress the air inside the device to generate electricity (Koca *et al.*, 2013).

3. DEVELOPERS OF WAVE ENERGY CONVERTER SYSTEMS

Over many years, a lot of companies have been established in the field of wave energy. However, few of them managed to commercialize. The established companies of onshore, nearshore, and offshore WEC systems are shown in Tables 1-3, respectively. The used WEC device type, the mode of operation, and the development phase are given.

Table 1: Established companies of onshore WEC systems

Developer	WEC	Mode of Operation	Development phase	Reference
Wavegen	Limpet	Oscillating Wave Column	Production	(Poullikkas, 2014)
Wavegen	Osprey	Oscillating Wave Column	Abandoned	(Poullikkas, 2014)
WaveEnergy	Seawave Slot-cone Generator	Overtopping	Testing	(Margheritini *et al.*, 2010)
S.D.E Energy	Onshore Wave Absorber	Line Absorber	Testing/early production	(offshorewind, accessed 20 Sep 2019)
Pico Power Plant	Pico Oscillating Water Column	Oscilatting Wave Column	Closed	(Pico-OWC, accessed 20 Sep 2019)
OceanEnergy	Tapchan	Overtopping	Unknown	(Joubert *et al.*, 2013)
-	WECA	Oscilatting Wave Column	Unknown	(Joubert *et al.*, 2013)
-	Wave Energy Machine	Point absorber	Unknown	(Joubert *et al.*, 2013)

Table 2: Established companies of nearshore WEC systems

Developer	WEC	Mode of Operation	Development phase	Reference
WPP A/S	WavePlane	Overtopping	Unknown	(Joubert et al., 2013)
Aquamarine Power	Oyster	Oscillating Wave Surge	Testing	www.aquamarinepower.com/
AW-Energy Oy	WaveRoller	Oscillating Wave Surge	Production	aw-energy.com/
Bombora Wave Power	Bombora	-	Production	www.bomborawave.com/
Neptune Equipment Corp.	Neptune Wave Engine	Multiple Point Absorbers	Testing	www.neptunewave.ca/business
S.D.E Energy	SDE Sea Waves Power Plant	Buoy	Closed	www.offshorewind.biz/2012/02/28/sde-energy-world-no-1-in-sea-wave-energy-technologies-israel/
Wavepiston ApS	Wavepiston	Oscillating wave surge converter	Testing	wavepiston.dk/#aau
SINN Power GmbH | Wave Energy	SINN Power wave energy converter	Buoy	Production	www.sinnpower.com/
Alvin Smith (Dartmouth Wave Energy) \Ecotricity	SeaRaser	Buoy	Testing	(Babajani et al., 2018)
Seatricity Ltd	Oceanus 2	Buoy	Production	marineenergy.biz/category/news-by-topic/
Oceanlinx	Oceanlinx	Oscillating wave Column	Sold Patents to Hong Kong developer	www.oceanlinx.com/
Atmocean Inc.	Atmocean	Point Absorber array	Testing	atmocean.com/
Zyba Renewables	CCell	Oscillating wave surge	Production	www.ccell.co.uk/
Seapower Ltd.	Sea Power	Surface-following attenuator	Testing	www.seapower.ie/
Eco Wave Power	Gibraltar	Buoy	Production	www.ecowavepower.com/

Table 3: Established companies of offshore WEC systems

Developer	WEC	Mode of Operation	Development phase	Reference
Ocean Power Technologies	PowerBuoy	Point Absorber	Production	www.oceanpowertechnologies.com
Pelamis Wave Power	Pelamis Wave Energy Converter	Attenuator	Closed	www.emec.org.uk/about-us/wave-clients/pelamis-wave-power
Langlee Wave Power	Langlee Robusto	Oscillating Wave Surge	Closed	www.langleewp.com
Erik Friis-Madsen, Wave Dragon	Wave Dragon	Overtopping	Testing	www.wavedragon.net
AWS Ocean Energy	AWS-III	Submerged Pressure Differential	Testing	www.awsocean.com
Carnegie Clean Energy	CETO	Fully submerged point absorber	Production	www.carnegiece.com
ALBATERN	WaveNET Series-6	Point Absorber	Production	albatern.co.uk
Northwest Energy Innovations	Azura	Point Absorber	Testing	azurawave.com
FORTUM Power	Sotenas	Point Absorber	Production	www.fortum.com
Wave Star	WaveStar Machine	Floating Buoy	Testing	wavestarenergy.com
Checkmate SeaEnergy	Anaconda Wave Energy Converter	Surface-following attenuator	Testing	www.checkmateukseaenergy.com
Finavera Wind Energy, later SSE Renewables Limited	AquaBuOY	Buoy	Closed	www.theregister.co.uk/2007/11/09/aquabuoy_wave_power_renewable_sinks/
Crestwing ApS	Crestwing	Surface-following attenuator	Testing	crestwing.dk
Atargis Energy Corporation	Cycloidal Wave Energy Converter	Fully Submerged Wave Termination Device	Testing	atargis.com
-	Energen Wave Power	Attenuating Wave Device	Closed	(Joubert et al., 2013)
FlanSea	FlanSea (Flanders Electricity from the Sea)	Buoy	Testing	www.flanderstoday.eu/innovation/buoys-ride-north-seas-waves-generate-power
Uppsala University	Swedish Buoy (Lysekil)	Buoy	Testing	(Poullikkas, 2014)
University of Groningen	Ocean Grazer	Buoy	Testing	www.rug.nl/research/ape/ocean-grazer-project
Ocean Energy	OE Buoy	Buoy	Production	www.oceanenergy.ie
Ocean Wave Energy Ltd	OWEL	Wave Surge Converter	Testing	www.renewableenergyfocus.com/view/18008/owel-to-test-wave-energy-converter/
Wello Oy	Penguin Wave Energy Converter	Rotating mass	Production	wello.eu
40South Energy	R38/50 kW, R115/150 kW	Underwater attenuator	Production	marineenergy.biz/2015/08/04/marina-di-pisa-project-to-make-waves-off-italy/
Seabased AB.	Seabased	Buoy	Production	www.seabased.com
SRI International	Unnamed Ocean Wave-Powered Generator	Buoy	Production	www.sri.com
Wavebob	Wavebob	Buoy	Closed	www.irishtimes.com/business/ocean-energy-developer-wavebob-set-to-go-under-1.1347036
Waves4Power	WaveEL	Buoy	Unknown	(Joubert et al., 2013)
WPP A/S	Waveplane	Overtopping	Testing	www.waveplane.com
Seatricity Ltd	Oceanus 2	Buoy	Production	marineenergy.biz/category/news-by-topic/

Oceanlinx	blueWAVE	Oscillating Wave Column	Production	(Poullikkas, 2014)
Atmocean Inc.	OSCAR	Point Absorber array	Testing	atmocean.com
Zyba Renewables	CCell	Oscillating Wave Surge	Production	www.ccell.co.uk
JAMSTC	Mighty Whale	Oscillating Wave Column	Testing	www.jamstec.go.jp
Seapower Ltd.	Sea Power	Surface-following attenuator	Testing	www.seapower.ie

4- CONCLUSION

Waves in seas and oceans are a colossal energy reservoir that can be obtained and used as a clean and renewable energy source using wave energy converter systems. Many companies started building their wave energy converter systems, but after a short time, they stopped and declared bankruptcy due to their inability to stand peer against the immense demand for fossil energy. If the governments do not promote these companies against fossil energy companies, dangerous problems due to global warming and air pollution could occur to future generations. Hence, in this paper, we wanted to give a global overview of the wave energy companies and shed light on the number of companies that have started but still not commercialized because of the lack of support. Universities also have to always fund the research labs for developing new wave energy technologies and new wave energy converters in order to make our planet safe and clean.

REFERENCES

AWS Ocean Energy, http://www.awsocean.com/archimedes-waveswing.html [Accessed 19 Sep 2019].

Babajani, A., Jafari, M., Hafezisefat, P., Mirhosseini, M., Rezaniakolaei, A. and Rosendahl, L. (2018). Parametric Study of a Wave Energy Converter (Searaser) for Caspian Sea. *Energy Procedia*. 10.1016/j.egypro.2018.07.101.

Chen, Z., Haitao, Y., Minqiang, H., Gaojun, M. and Cheng, W. (2013) "A Review of Offshore Wave Energy Extraction System.", *Advances in Mechanical Engineering*. http://dx.doi.org/10.1155/2013/623020.

Drew, B., Plummer, A.B. and Sahinkaya, MN (2009) "A review of wave energy converter technology." *Journal of Power and Energy*. 10.1243/09576509JPE782.

Joubert, J. R., Niekerk, J. L., Reinecke, J. and Meyer, I. (2013). "Wave Energy Converters (WECs)" *Center for Renewable and Sustainable Energy Studies.*

Maritime Journal, https://www.maritimejournal.com/news101/industrynews/denmarks_wave_dragon_delivers_power_to_the_grid [Accessed 19 Sep 2019].

Margheritini, L., Vicinanza, D. and Kofoed, J. P. (2010). "Overtopping performance of Sea wave Slot cone Generator" *ICE Virtual Library*. 10.1680/cmsb.41301.0066

Offshorewind, https://www.offshorewind.biz/2012/02/28/sde-energy-world-no-1-in-sea-wave-energy-technologies-israel/ [Accessed 20 Sep 2019].

Pico-OWC, http://www.pico-owc.net/news.php?cat=89&newid=346&wnsid=ffaedab643e41be91f9eecf88f429ee8 [Accessed 20 Sep 2019].

Tapered Channel Wave Energy, https://taperedchannelwaveenergy.weebly.com/how-does-it-work.html [Accessed 19 Sep 2019].

The European Marine Energy Center (EMEC), http://www.emec.org.uk/marine-energy/wave-devices/ [Accessed 09 Sep 2019].

Fadaeenejad, M., Shamsipour, R., Rokni, S. D. and Gomes, C. (2013) "New approaches in harnessing wave energy: With special attention to small islands." *Renewable and Sustainable Energy Reviews*. https://doi.org/10.1016/j.rser.2013.08.077.

Fang, H. W., Feng, Y. Z. and Li, G. P. (2018) "Optimization of Wave Energy Converter Arrays by an Improved Differential Evolution Algorithm." *Energies*. 10.3390/en11123522.

Koca, K., Kortenhaus, A., Oumeraci, H., Zanuttigh, B., Angelelli, E., Cantu, M., Suffredini, R., Franceschi, G. (2013) "Recent Advances in the Development of Wave Energy Converters" *The 10th European Wave and Tidal Energy Conference (EWTEC 2013).*

Kramer, M., Marquis, L. and Frigaard, P. (2010) "Performance Evaluation of the Wavestar Prototype." *EWTEC 2011 conference in Southampton.* http://wavestarenergy.com/sites/default/files/EWTEC2011_2011-09-06.pdf [Accessed 19 Sep 2019].

Patel, S. (2016). "Power, Ocean Power Technologies Deploys Commercial PowerBuoy with Energy Storage." *Power*. https://www.powermag.com/ocean-power-technologies-deploys-commercial-powerbuoy-energy-storage/ [Accessed 19 Sep 2019].

Poullikkas, A. (2014). "Technology prospects of wave power systems." *Electronic Journal of Energy & Environment*. 10.7770/ejee-V2N1-art662

Solar Thermal Magazine Clean Energy Technology,

https://solarthermalmagazine.com/wave-energy-scotland-receives-funding-to-award-first-contract-to-pelamis-wave-power/ [Accessed 19 Sep 2019].

Sustainable Energy Research Group (SERG), http://www.energy.soton.ac.uk/anaconda-wave-energy-converter-concept/ [Accessed 19 Sep 2019].

Titah-Benbouzid, H. and Benbouzid, M. (2015). "An Up-to-Date Technologies Review and Evaluation of Wave Energy Converters" *International Review of Electrical Engineering-IREE.* 10.15866/iree.v10i1.5159.

Wave Devices, http://www.emec.org.uk/marine-energy/wave-devices/ [Accessed 19 Sep 2019].

WaveRoller, https://aw-energy.com/waveroller/ [Accessed 09 Sep 2019].

Wello Oy, https://wello.eu/ [Accessed 19 Sep 2019].

ZINC AND LEAD RECOVERY FROM ZINC EXTRACTION RESIDUE BY TWO-STAGE SELECTIVE HIGH TEMPERATURE-PRESSURE LEACHING

Mehmet ŞAHİN*[1] and Mehmet ERDEM[1]

Department of Environmental Engineering, Fırat University, 23279 Elazığ, Turkiye

ABSTRACT

In the combined hydrometallurgical zinc production systems consist of roasting-leaching-electro-winning, huge quantities of solid leaching residues containing different metallic compounds such as lead, cadmium, silver, zinc are continuously generated around the world. Due to increasing demand of metals and the depletion of high grade natural resources, these types of wastes are gaining great importance in the metallurgical industries. In this study, zinc and lead recovery from the zinc extraction residue containing 7.98 % Zn in the form of franklinite and 19 % Pb in the form of anglesite were investigated by high temperature-pressure sequential H_2SO_4 and NaOH leaching. For this purpose; the effects of H2SO4 concentration, contact time and temperature on the zinc leaching and the effect of NaOH concentration on the lead leaching from ZER were investigated in high temperature-pressure conditions. Leaching results showed that 98.6 % Zn under the conditions of 2 M H_2SO_4 concentration, 60 min contact time and 100°C temperature, and 99.65 % Pb under the conditions of 17.5 % NaOH concentration, 60 min contact time and 100°C temperature could be recovered from the ZER.

Keywords: *Zinc extraction residue; Lead recovery; Pressure leaching; Metallurgical waste*

* Corresponding Author

1. INTRODUCTION

The increasing demand for metals and alloys has led to the rapid depletion of raw material resources worldwide. In order to meet the expected needs, manufacturers and researchers have been making intensive efforts to find alternative sources of raw materials for a long time. For this purpose, it is seen that intensive research has been done on the reusability of metal containing residues and wastes such as scrap, slag, furnace and flue dusts. Among these alternatives, sometimes the waste of a process can be the raw material of an another process.

Lots of studies have been carried out on the recovery of precious metals from different kinds of wastes such as red mud generated in aluminum production (Fe, Al, Ti, Si, Sc)(Pepper, Couperthwaite et al. 2016, Zhou, Teng et al. 2018), power plant fly ashes (different metals) (Meawad, Bojinova et al. 2010), iron and steel blast furnace dusts (Zn, Ni, Pb) (Strobos and Friend 2004, Dutra, Paiva et al. 2006), copper smelter slags and converter slags (Cu, Co, Zn, V, Fe and Ti)(Arslan and Arslan 2002, Xiang, Huang et al. 2017). Depending on the related researches, it can be stated that the hydrometallurgical processes are the most convenient recovery techniques for the metal recovery. In these processes, different lixiviants such as sulphuric acid (Zeydabadi, Mowla et al. 1997, Basir and Rabah 1999, Nagib and Inoue 2000, Huang, Li et al. 2007, Karakaya, Kükrer et al. 2007, Kul and Topkaya 2008, Ruşen, Sunkar et al. 2008, Li, Wei et al. 2010), hydrochloric acid (Basir and Rabah 1999, Nagib and Inoue 2000), nitric acid (Basir and Rabah 1999, Zárate-Gutiérrez, Lapidus et al. 2010), caustic soda (Xia and Pickles 1999a, Xia and Pickles 1999b, Nagib and Inoue 2000, Xia and Picklesi 2000, Youcai and Stanforth 2000a, Youcai and Stanforth 2000b) , brine solution (Raghavan, Mohanan et al. 1998, Andrews, Raychaudhuri et al. 2000, Raghavan, Mohanan et al. 2000, Turan, Altundoğan et al. 2004, Guo, Pan et al. 2010), ammonia, ammonium carbonate, ammonium chloride, some carboxylic acids (Nagib and Inoue 2000) are used depending on the characteristics and mineralogical form of metal to be recover.

Zinc extraction residues (ZER) generated in zinc production are of particular importance due to valuable components such as lead, cobalt, cadmium, silver, germanium, as well as non-extractable zinc. Considering that zinc is one of the most commonly used metals, it can also be realized how important it is in terms of quantity and content of the extraction wastes released.

Zinc is mainly produced from sulphides, carbonates and partly from various secondaries and wastes containing zinc such as electric arc furnace dusts, zinc ash, zinc dross, scraps, slags by hydrometallurgical, pyrometallurgical or their combination processes (Nagib and Inoue 2000). The combined systems consist of roasting-leaching-electrowinning processes are employed in many countries. In these processes, ZnO-rich calcine is first produced from the concentrates and then zinc in the calcine is leached with hot sulphuric acid solution. A pregnant solution and a solid leach residue are obtained after liquid-solid separation by rotary filter. Pregnant zinc solution is purified and zinc is won by electrolysis. The leach residue contains significant amount of lead and unextractable zinc along with some minor constituents such as cadmium, silver and germanium. In this study, it is aimed to recover lead and zinc which are major components of waste. Mineralogical analyzes showed that the zinc in the waste was in the form of franklinite crystal structure ($ZnFe_2O_4$) and lead was in the form of anglesite ($PbSO_4$) due to sulfuric acid leaching (Özverdi and Erdem 2010, Şahin and Erdem 2015). The amphoteric properties of both metals make it difficult to selectively recovery from the ZER. However, the difference in the crystal structure of each metal indicates that zinc can first be leached in H_2SO_4 solution, while in the remaining residue, the enriched lead can be extracted with NaOH solution. In our previous atmospheric pressure leaching study for the same purpose, it was found that zinc leaching efficiency increased with the increasing temperature and it reached at 84.61% at 80°C. But, lead could not be leached in H_2SO_4 solution. It was determined that the increase in kinetic energy of the components in the solution with the effect of high temperature created a driving force for mass transfer and thus leaching efficiencies increased with effective contact of reactants. (Şahin 2014). This result suggested that it would be advantageous to try higher temperatures to obtain higher zinc leaching efficiencies. Starting from these findings, in this study, the effects of H_2SO_4 concentration, contact time and temperature on the zinc leaching and the effect of NaOH concentration on the lead leaching from ZER were investigated in high temperature-pressure conditions.

2. MATERIALS AND METHODS

2.1. Materials

As described in our previous papers, the zinc leaching residue (ZER) used in the study was obtained from Çinkur Plant located in Kayseri, Turkey. It was dried at room temperature for ten days and then subjected to sieve analysis. Sieve analysis showed that about 76 % of the ZER was smaller than 150 µm (-100 mesh). The sample was sieved to obtain particles smaller than 75 µm (-200 mesh) prior to use. The chemical and mineralogical compositions of the residue were determined. Chemical analysis shows that the ZER contains 19.02 % Pb, 12.25 % S, 7.98 % Zn, 6.19 % Ca, 6.74 % Si, 5.44 % Fe and 1.85 % Al as major elements. The major mineralogical phases in the residue were determined to be gypsum [$CaSO_4.2H_2O$], anglesite [$PbSO_4$], massicot [PbO], quartz [SiO_2], maghemite [Fe_2O_3], hercynite [Al_2FeO_4] and franklinite [$ZnFe_2O_4$]. Some other properties and analytical methods related characterization of the ZER can be seen in the our previous studies (Özverdi and Erdem 2010).

H_2SO_4 (Sigma-Aldrich 339741) and NaOH (Merck 106462) solutions having different concentrations were used as leaching reagents in the study. Analytical reagent grade chemicals were used. All aqueous solutions were prepared using distilled water.

2.2. Leaching experiments

In order to recover of zinc and lead from the ZER by leaching, H_2SO_4 and NaOH solutions were selected as leaching reagents and two stage leaching procedure were applied. The conditions of zinc recovery in the first stage

by H_2SO_4 and lead recovery in the second stage by NaOH were investigated. Leaching experiments were conducted in a 500 ml stainless steel high pressure reactor (Berghof BR 500). The reactor is equipped with a PTFE insert, thermal sensor with immersion tube, manometer, vent valve and stirrer. All sides of the reactor are lined with PTFE. The temperature and stirring speed were controlled with a PID controller. About 40 g of the ZER was mixed 200 ml of leaching solution having desired concentration in the PTFE insert prior to each experiment and then it was placed in the reactor. The reactor content agitated continuously at a 700 rpm constant speed was heated up to predetermined temperature. After achieving the desired temperature, the required reaction time was started. After the reaction was completed, the reactor was removed from the heater mount and was rapidly water-cooled to 70ºC. The reactor content was filtered by vacuum filtration. The leach residue was then washed three times with 50 ml 50ºC distilled water and then the wash solutions were added to main pregnant leach solution. The solutions were analyzed for lead, zinc, iron and calcium by using Perkin Elmer AAnalyst 800 atomic absorption spectrophotometer.

3. RESULTS AND DISCUSSION

3.1. Recovery of zinc by high temperature H_2SO_4 leaching

In our previous atmospheric pressure leaching study for the same purpose, it was found that zinc leaching efficiency increased with the increasing temperature and it reached at 84.61% at 80°C. It was determined that the increase in kinetic energy of the components in the solution with the effect of high temperature created a driving force for mass transfer and thus leaching efficiencies increased with effective contact of reactants (Şahin 2014). This result suggested that it would be advantageous to try higher temperatures to obtain higher zinc leaching efficiencies. For this purpose, in this study, the effects of acid concentration, contact time and temperature on the lead and zinc leaching from ZER were investigated in high temperature-pressure reactor. The results obtained are given as sub-headings below.

3.1.1. Effect of H_2SO_4 Concentration

The mineralogical composition of the zinc extraction waste shows that the zinc is in the franklinite and zinc oxide crystal structure in the extraction waste. The reactions of these compounds with H_2SO_4 under high temperature-pressure are given as follows:

$$ZnO + H_2SO_{4\,(aq)} \rightarrow ZnSO_{4\,(aq)} + H_2O \quad (1)$$

$$ZnFe_2O_4 + 4H_2SO_{4\,(aq)} \rightarrow ZnSO_{4\,(aq)} + Fe_2(SO_4)_3 + 4H_2O \quad (2)$$

$$ZnFe_2O_4 + H_2SO_{4\,(aq)} \rightarrow ZnSO_{4\,(aq)} + Fe_2O_3 + H_2O \quad (3)$$

As can be seen from the equations, the acid concentration is the most important parameter on the zinc leaching. Starting from this point, effect of the acid concentration was investigated in the H_2SO_4 solutions having the concentration range of 0.5 to 2.0 M depending on the contact time at constant temperature by taking into account other components that can dissolve in acid. The results obtained are presented in Fig. 1.

The results obtained confirm that the acid concentration is an effective parameter on metal leaching except for lead. Leaching yields of zinc increased from 68.1% to 98.6 % with increasing H_2SO_4 concentration from 0.5 M to 2 M. Zinc extraction yield reach a satisfactory value in 2 M. Therefore, 2 M H_2SO_4 concentration is sufficient for the maximum recovery of zinc.

Fig. 1 also shows the effect of contact time as a function of acid concentration. As can be seen, significant amounts of the metals in the waste dissolved in the first 15 min and the extraction yields increased up to contact time of 60 min in a low rate. But, they remained almost constant after 60 min. Since the main purpose is to provide high zinc extraction from the waste, it can be said that 60 min is the best contact time to obtain satisfactory zinc extraction efficiency. Under these conditions, it was determined that the 19.24 % calcium and 21.57 % of iron together with zinc were dissolved. The lead present in the form of anglesite [$PbSO_4$] in the waste did not dissolve in H_2SO_4 and thus released into the solution in very small quantities. Due to these solubilities in the waste, insoluble components are concentrated in the solid leach residue from H_2SO_4 leaching. Particularly, insoluble lead is very important due to its high content in the waste. The leach residue was subjected to mineralogical and chemical analysis to investigate this situation. As a result of the analysis, it was determined that the acid dissolving components were significantly separated from the waste and thus the lead content of the leach residue increased from 15.14% to 22.29% and the lead content of the waste was enriched. This can be seen more clearly than the XRD patterns showing the mineralogical composition of the leach residue given in Fig. 2. XRD patterns showed that iron and zinc compounds were disappeared by dissolving in H_2SO_4, but lead insoluble in H_2SO_4 concentrated in the residue in the form of anglesite crystal structure.

Consequently, compared with leaching yields at atmospheric conditions, it has been determined that increasing the temperature to 100°C significantly increases the zinc leaching efficiency depending on the acid concentration.

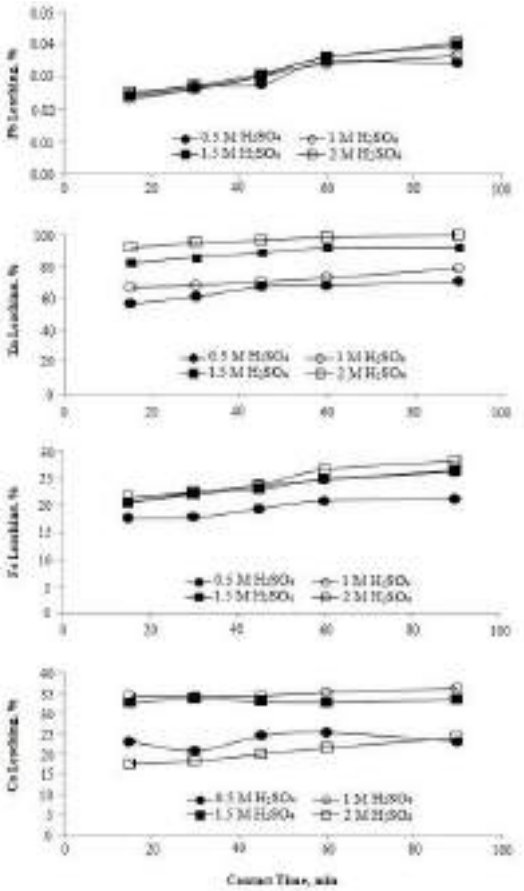

Fig 1. Effect of H_2SO_4 concentration on zinc, iron, lead and calcium extraction from the waste (liquid/solid:5, stirring speed: 700 rpm, temperature: 100°C)

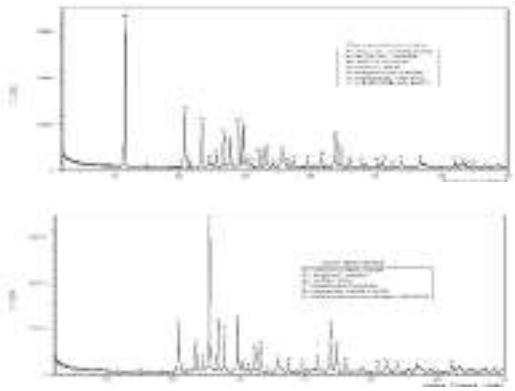

Fig 2. XRD patterns of the zinc extraction waste and leach residue from H2SO4 leaching

3.1.2. Effects of temperature and contact time

Effect of the temperature on the zinc extraction from the waste was investigated in the range of 100-175°C depending on contact time. Fig 3 shows the results obtained.

It has been determined that increased temperature and contact time cause a slight increase in zinc extraction yields. However, when compared with energy requirements, it can be said that the increase in leaching rates with the temperature has remained on the order of negligible level. For example; while zinc extraction yield was increased about 1% with the increasing temperature from 100°C to 175 °C, it was increased about 6% with the increasing contact time from 30 to 90 min. Therefore, it can be said that the optimum temperature and contact time at which satisfactory zinc extraction yields is obtained are 100°C and 60 min, respectively.

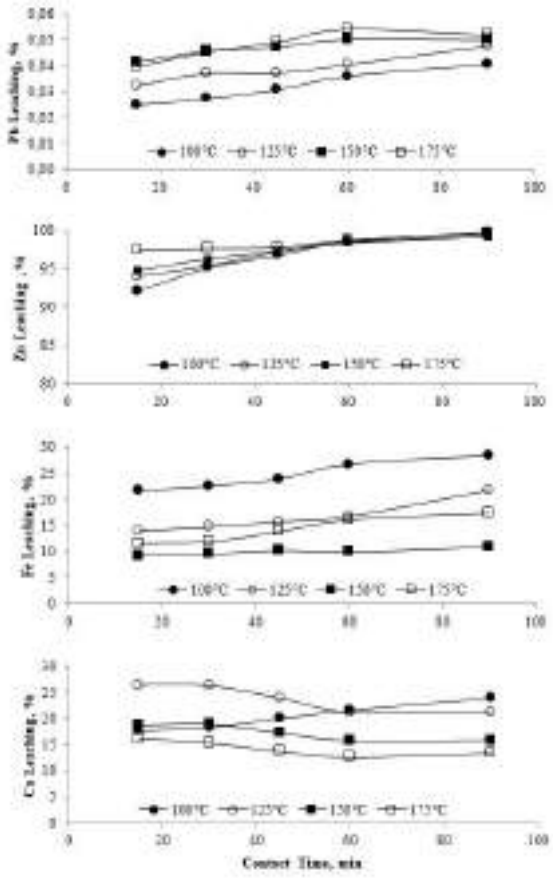

Fig 3. Effect of temperature on zinc, iron, lead and calcium extraction from the waste depending on contact time (liquid/solid:5, H_2SO_4 concen.:2 M, stirring speed: 700 rpm,)

Under the conditions investigated, lead in the waste was found to be dissolved in less than 0.05 %. However, leaching yields of iron and calcium decreased depending on the increasing temperature. It can be said that the decrease of iron extraction yields depending on the increasing temperature is caused by the jarosite formation. Iron ions precipitates in the form of $XFe_3(SO_4)_2(OH)_6$ at pH 1 in aqueous solutions by forming jarosite. Since leaching conditions are suitable for jarosite formation, the iron ions releasing into the solution possibly precipitates by forming jarosite according to the Eq 5 reported by Li et al. (2010) (Li, Wei et al. 2010) and Shanming et al. (2010)(He, Wang et al. 2010). The decrease in the calcium extraction yields is due to the precipitation of calcium in the form of calcium sulphate. Calcium sulfate peaks in the XRD pattern confirm this situation (Fig 2). Havlik et al. have also observed that the calcium sulphate is formed at the high temperature conditions and it precipitate by crystallization (Havlik, Laubertova et al. 2005).

$3Fe^{3+} + 2SO_4^{2-} + (Na, K)^+ + 6\ H_2O \leftrightarrow (Na, K)Fe_3(SO_4)_2(OH)_6 + 6\ H^+$ (4)

3.2. Recovery of Lead from Leach Residue of H_2SO_4 Leaching by High Temperature NaOH Leaching

It was determined that the remaining secondary waste from the high temperature H_2SO_4 leaching carried out at 100°C for 60 min with 2 M H_2SO_4 contained 22.29 % Pb. In order to obtain lead from this secondary waste, which is very economically important due to its high lead content, selective high temperature NaOH leaching was applied to obtain a relatively pure leach solution. For this purpose, batch leaching experiments were carried out at liquid/solid ratio of 5, 100°C for 60 min in the presence of NaOH solutions having different concentrations in the range of 11%-25%. The results obtained are shown in Table 1.

99.65 % of the zinc in the secondary waste was selectively leached with 17.5 % NaOH.
In these conditions, it was found that approximately 5.91% of the zinc remaining in the residue was also dissolved in NaOH solution. The NaOH leaching applied to the ZER after the H_2SO_4 leaching has shown that two-stage leaching is a very convenient method for effectively recovering of lead and zinc from ZER. The only disadvantage of the applied process would be that the impurities in the waste release to the solution by acid leaching and make it difficult to purify the concentrated zinc solution for electrolysis. These efforts will increase the cost of zinc recovery. However, on the contrary, it can be said that it is a great advantage to break down the high temperature lead sulfate structure with NaOH leaching to obtain a high concentration and very clean lead leaching solution.

Table 1. Recovery of lead from leach residue of H_2SO_4 leaching by high temperature NaOH leaching (contact time: 60 min; temperature: 100°C; liquid/solid: 5)

NaOH Concentration, %	Pb Extraction Yield, %	Zn Extraction Yield, %
11	82.16	5.27
15	89.40	5.53
17.5	99.65	5.91
20	99.68	6.17
22.5	99.63	5.91
25	99.81	6.28

CONCLUSIONS

In the present study, the recovery of Pb and Zn from the zinc extraction residue by sequential H_2SO_4 and NaOH leaching was investigated by taking into consideration the parameters of H_2SO_4 and NaOH concentration, contact time and temperature. It was found that the recovery yields of Pb and Zn were strongly dependent on leaching reagents concentration. The optimum leaching conditions were found to be H_2SO_4 concentration: 2 M, contact time: 60 min and temperature: 100°C for Zn recovery, and NaOH concentration: 17.5 %, contact time: 60 min and temperature: 100°C for Pb recovery. Under the optimized conditions, it has been determined that the 98.6 % Zn and 99.65 % Pb could be recovered from the ZER.

ACKNOWLEDGEMENTS

This study was financed by the Scientific and Technological Research Council of Turkey (TUBITAK) under the project number of 109Y262.

REFERENCES

Andrews, D., A. Raychaudhuri and C. Frias (2000). "Environmentally sound technologies for recycling secondary lead." *Journal of Power Sources* Vol. 88, No. 1, pp. 124-129.

Arslan, C. and F. Arslan (2002). "Recovery of copper, cobalt, and zinc from copper smelter and converter slags." *Hydrometallurgy* Vol. 67, No. 1-3, pp. 1-7.

Basir, S. A. and M. A. Rabah (1999). "Hydrometallurgical recovery of metal values from brass melting slag." *Hydrometallurgy* Vol. 53, No. 1, pp. 31-44.

Dutra, A., P. Paiva and L. Tavares (2006). "Alkaline leaching of zinc from electric arc furnace steel dust." *Minerals engineering* Vol. 19, No. 5, pp. 478-485.

Guo, Z.-H., F.-K. Pan, X.-Y. Xiao, L. Zhang and K.-Q. Jiang (2010). "Optimization of brine leaching of metals from hydrometallurgical residue." *Transactions of Nonferrous Metals Society of China* Vol. 20, No. 10, pp. 2000-2005.

Havlik, T., M. Laubertova, A. Miskufova, J. Kondas and F. Vranka (2005). "Extraction of copper, zinc, nickel and cobalt in acid oxidative leaching of chalcopyrite at the presence of deep-sea manganese nodules as oxidant." *Hydrometallurgy* Vol. 77, No. 1-2, pp. 51-59.

He, S., J. Wang and J. Yan (2010). "Pressure leaching of high silica Pb–Zn oxide ore in sulfuric acid medium." *Hydrometallurgy* Vol. 104, No. 2, pp. 235-240.

Huang, K., Q.-w. Li and J. Chen (2007). "Recovery of copper, nickel and cobalt from acidic pressure leaching solutions of low-grade sulfide flotation concentrates." *Minerals engineering* Vol. 20, No. 7, pp. 722-728.

Karakaya, E., T. Kükrer, F. Veglio, A. Akçıl and M. Kitis (2007). "Atık alkali ve çinko-karbon pillerden mangan ve çinko geri kazanımı-inorganik ve organik asitlerle liç testleri." *Yedinci Ulusal Çevre Mühendisliği Kongresi* Vol., No., pp.

Kul, M. and Y. Topkaya (2008). "Recovery of germanium and other valuable metals from zinc plant residues." *Hydrometallurgy* Vol. 92, No. 3-4, pp. 87-94.

Li, C., C. Wei, H.-s. Xu, M. Li, X. Li, Z. Deng and G. Fan (2010). "Oxidative pressure leaching of sphalerite concentrate with high indium and iron content in sulfuric acid medium." *Hydrometallurgy* Vol. 102, No. 1-4, pp. 91-94.

Meawad, A. S., D. Y. Bojinova and Y. G. Pelovski (2010). "An overview of metals recovery from thermal power plant solid wastes." *Waste management* Vol. 30, No. 12, pp. 2548-2559.

Nagib, S. and K. Inoue (2000). "Recovery of lead and zinc from fly ash generated from municipal incineration plants by means of acid and/or alkaline leaching." *Hydrometallurgy* Vol. 56, No. 3, pp. 269-292.

Özverdi, A. and M. Erdem (2010). "Environmental risk assessment and stabilization/solidification of zinc extraction residue: I. Environmental risk assessment." *Hydrometallurgy* Vol. 100, No. 3-4, pp. 103-109.

Pepper, R. A., S. J. Couperthwaite and G. J. Millar (2016). "Comprehensive examination of acid leaching behaviour of mineral phases from red mud: Recovery of Fe, Al, Ti, and Si." *Minerals engineering* Vol. 99, No., pp. 8-18.

Raghavan, R., P. Mohanan and S. Patnaik (1998). "Innovative processing technique to produce zinc concentrate from zinc leach residue with simultaneous recovery of lead and silver." *Hydrometallurgy* Vol. 48, No. 2, pp. 225-237.

Raghavan, R., P. Mohanan and S. Swarnkar (2000). "Hydrometallurgical processing of lead-bearing materials for the recovery of lead and silver as lead concentrate and lead metal." *Hydrometallurgy* Vol. 58, No. 2, pp. 103-116.

Ruşen, A., A. Sunkar and Y. Topkaya (2008). "Zinc and lead extraction from Çinkur leach residues by using hydrometallurgical method." *Hydrometallurgy* Vol. 93, No. 1-2, pp. 45-50.

Strobos, J. G. and J. Friend (2004). "Zinc recovery from baghouse dust generated at ferrochrome foundries." *Hydrometallurgy* Vol. 74, No. 1-2, pp. 165-171.

Şahin, M. (2014). Çinko Ekstraksİyon Atiği Döner Filtre Kekinden Yüksek Sicaklik-Basinç Şartlarinda Çinko-Kurşun Kazanimi. Fen Bilimleri Enstitüsü, Fırat Üniversitesi.

Şahin, M. and M. Erdem (2015). "Cleaning of high lead-bearing zinc leaching residue by recovery of lead with alkaline leaching." *Hydrometallurgy* Vol. 153, No., pp. 170-178.

Turan, M. D., H. S. Altundoğan and F. Tümen (2004). "Recovery of zinc and lead from zinc plant residue." *Hydrometallurgy* Vol. 75, No. 1-4, pp. 169-176.

Xia, D. and C. Pickles (1999a). "Kinetics of zinc ferrite leaching in caustic media in the deceleratory period." *Minerals engineering* Vol. 12, No. 6, pp. 693-700.

Xia, D. and C. Pickles (1999b). "Caustic roasting and leaching of electric arc furnace dust." *Canadian metallurgical quarterly* Vol. 38, No. 3, pp. 175-186.

Xia, D. and C. Picklesi (2000). "Microwave caustic leaching of electric arc furnace dust." *Minerals engineering* Vol. 13, No. 1, pp. 79-94.

Xiang, J., Q. Huang, X. Lv and C. Bai (2017). "Multistage utilization process for the gradient-recovery of V, Fe, and Ti from vanadium-bearing converter slag." *Journal of hazardous materials* Vol. 336, No., pp. 1-7.

Youcai, Z. and R. Stanforth (2000a). "Extraction of zinc from zinc ferrites by fusion with caustic soda." *Minerals engineering* Vol. 13, No. 13, pp. 1417-1421.

Youcai, Z. and R. Stanforth (2000b). "Integrated hydrometallurgical process for production of zinc from electric arc furnace dust in alkaline medium." *Journal of hazardous materials* Vol. 80, No. 1-3, pp. 223-240.

Zárate-Gutiérrez, R., G. Lapidus and R. Morales (2010). "Pressure leaching of a lead–zinc–silver concentrate with nitric acid at moderate temperatures between 130 and 170 C." *Hydrometallurgy* Vol. 104, No. 1, pp. 8-13.

Zeydabadi, B. A., D. Mowla, M. Shariat and J. F. Kalajahi (1997). "Zinc recovery from blast furnace flue dust." *Hydrometallurgy* Vol. 47, No. 1, pp. 113-125.

Zhou, K., C. Teng, X. Zhang, C. Peng and W. Chen (2018). "Enhanced selective leaching of scandium from red mud." *Hydrometallurgy* Vol. 182, No., pp. 57-63.

CISET - 2nd Cilicia International Symposium on Engineering and Technology
10-12 October, 2019, Mersin / TURKEY

A SMART HOME SYSTEM DEVELOPED USING ARTIFICIAL NEURAL NETWORK ON RASPBERRY PI

Cevdet Tamer GÜVEN [*1], Mehmet ACI [2]

[1] Mersin University, Engineering Faculty, Computer Engineering Department, Mersin, Turkey, ctamerguven@gmail.com

[2] Mersin University, Engineering Faculty, Computer Engineering Department, Mersin, Turkey, maci@mersin.edu.tr

ABSTRACT
In this study, a smart home system based on artificial intelligence on raspberry pi and various sensors has been developed. Multilayer perceptron classifier (MLP Classifier) model of artificial neural networks (ANN) was used as an artificial intelligence method. The aim of the study is to record the activities of the residents in their homes every day in the data format by means of sensors and then teach these records to the system with MLP to ensure that the system performs some activities autonomously for the benefit of the residents. The developed system can also be controlled as mobile via GSM and Bluetooth. The smart home system is designed to detect and alert potential catastrophes. The results obtained in this study showed that the study can make effective decisions and develop these kinds of problems.

Keywords: *Smart Home Systems, Multilayer Perceptron Classifier, Raspberry Pi, Robotics*

[*] Cevdet Tamer GÜVEN

1. INTRODUCTION

Today, together with the developing technology, technological developments that facilitate the lives of people in every field take their place among the indispensables of our daily lives. Although these technological advances seem to make people's lives easier, they are often developed to prevent possible accidents in our daily lives. People prefer smart home systems for their intensified business life, to facilitate their work and for their safety. Nowadays, as systems consume more power and resources, their control becomes increasingly difficult. This increases the necessity of the systems that act as smart home assistants (Prakash and Kumar, 2018). Automation is a technique, method or system capable of operating or controlling a process with electronic devices that minimize human participation. The foundation of an automation system for an office or home is to increase efficiency and benefit. Automation not only ensures efficiency, but also the economic use of electricity and water and prevents waste (Tseng et al., 2014). The concept of home automation has been coming since the late 1970s. However, with the development of technology and services, people's expectations of what a house should do or how the services should be delivered at home have changed greatly over time (Jose and Malekian, 2015).

Today's smart home systems rely only on remote control or monitoring the home. The system realized in the study is a self-learning and predictable system instead of these standard activities. Learning and estimation process is performed by using the multilayer perceptron classsifier (MLP Classifier) method of artificial neural networks (ANN), which is an artificial intelligence method. The aim of artificial intelligence is to imitate human intelligence by means of computers and in this sense, to gain the ability to learn computers to a certain extent. In this way, artificial intelligence often consists of methods that attempt to model human thinking, the brain's working model, or the biological evolution of nature. Expert systems, fuzzy logic, artificial neural networks and genetic algorithms are the main methods of artificial intelligence (Tektaş et al., 2002). ANN is an artificial intelligence method used for estimating time series starting from the end of 1980s. ANN forecasting technique is widely used in many fields today. It simply simulates the way the human brain works. ANN has many important features such as learning from data, generalization and working with unlimited number of variables. ANN can provide linear and non-linear modeling without any prior knowledge between input and output variables (Ataseven, 2014). ANN has many methods and MLP is one of them. MLP is the most preferred model of artificial neural networks using back propagation algorithm. In MLP, designing the network architecture is the most important point. Lack of connection in the network structure may cause the model to become unable to resolve the network(Lins and Ludemir, 2005) . MLP model has two most commonly used methods. In this study, MLP Classifier which is a classification method is used. The concept of classification is simply to share data between the various classes defined on a dataset. Classification algorithms learn this type of sharing from the given training set and try to classify the test data in which the class is not known correctly (Şeker, 2013).

In the study, Raspberry Pi (RPi) was used as hardware infrastructure. RPi is a credit card sized computer developed in 2012 and used to teach the basics of computer science in schools (Solak et al., 2017). The RPi 3 Model B+ used in the project has an A53 / ARMv8 quad-core 64-bit processor. It has 1GB ram capacity. Through the Raspbian operating system, which is written to an external micro sd card, all operations can be performed easily on a normal computer. RPi is based on the python programming language. Python is an objective, interpretable, modular and interactive programming language. Python supports the class system and any type of data field entry (Ok et al., 2017). With the Python programming language, a data set was created with the data collected from the sensors in the system. This data set is taught to the system by ANN's MLP Classifier method and it is aimed to perform some routine operations of the system instead of the residents. At the same time, 10-fold cross-validation was applied to the data set. Cross-validation is a computer technique that uses all existing samples as training and test samples. In the K-fold cross-validation technique, the entire data set is randomly subdivided into different and almost equal sized Ks that exclude one. The classification algorithm is trained and tested K times. Each time one of the clusters is randomly taken as test data and the remaining cluster data is used for training (Barışçıl et al., 2012).

In this study, a smart home system has been developed that can perform some operations instead of residents by artificial intelligence. At the same time, the developed system detects possible disasters and sends information SMS to users. The system that detects potential hazards such as gas leakage, flooding, and high intensity sound detection can alert the people by SMS. Users can communicate with the smart home system via SMS and Bluetooth and control many operations.

2. MATERIAL AND METHOD

2.1. Hardware

In this study, RPi is used on the basis of smart home system. It works optimally with Raspbian, an operating system based on open source Debian. RPi 3 Model B+ was used in the study (Fig. 1.).

Fig. 1. Raspberry Pi 3 Model B+

Two DHT11 temperature and humidity sensors are used to measure the temperature and humidity values inside and outside the house. DHT11 is a temperature and humidity sensor with an already calibrated digital signal output. The sensor includes an NTC temperature sensor, a resistant moisture component. Featuring an 8-

bit high-performance connection, the single-chip microcontroller offers the sensor excellent quality, super-fast response, jamming capability and affordability (Zhou et al., 2012).

MQ-4 gas sensor is used to detect possible gas leaks in the house and flame sensor is used to detect fire situation.

Sound sensor is used to detect the noise inside the house when no one is in the house. The sound sensor is calibrated to inform residents by sending a warning SMS when it detects frequencies higher than the predetermined sound level. SMS sending is done by GSM module. The two basic connections of the GSM module are the TX and RX pins, which allow the microcontroller to connect to the GSM module that sends serial data. The GSM module works with a SIM card. The SIM card requires a subscription with a mobile communications provider. Based on this, the user can access the mobile network. The UART (Universal Asynchronous Transceiver) interface encodes and decodes data between parallel and serial formats. Bytes of data are received and transmitted as a bit sequence. Thus, the data can be transmitted via TX in serial mode to the microcontroller or network as an antenna (Isa and Sklavos, 2017).

The house has 2 relay modules, 1 servo motor, 1 PIR (Passive Infrared Radiation or Pyroelectric Infrared) sensor, 1 fan and 3 LEDs. All components of the smart home system are shown in Fig. 2. Component connections and circuit diagrams are shown in Fig. 3.

Fig. 2. Smart Home Components

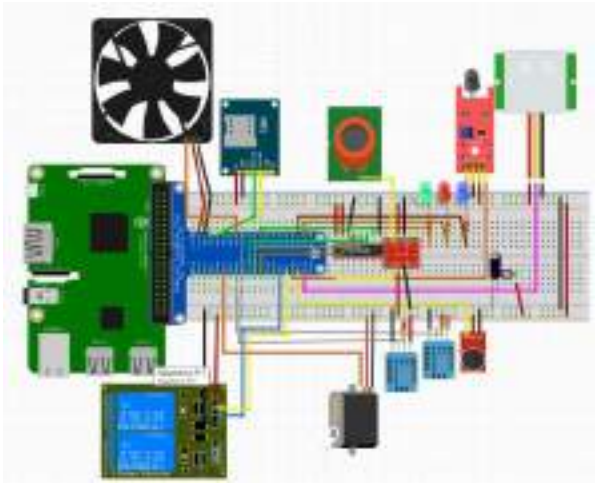

Fig. 3. Smart Home Circuits Scheme

2.2. Software

MLP is a supervised learning algorithm that learns the function $f(.): R^2 \rightarrow R^0$ by training on a dataset. Given a range of properties X = {x_1, x_2, ..., x_m} and a target y, it can learn a nonlinear function estimator for classification or regression (www.scikit-learn.org, 2019).

Advantages of MLP include non-linear models and real-time models using partial_fit. The disadvantages are that some hyperparameters, such as the number of hidden neurons, layers and number of iterations, need to be adjusted and feature is sensitive to scaling.

In this study, ANN's MLP Classifier method was used as artificial intelligence method. In the data collection process, data containing various situations were used. These situations are generally listed as follows:

- Data on actions taken by the user before leaving home
- Data from sensors based on changes when the user is not at home
- Data on actions taken by the user when he comes home
- Data from sensors according to user's activities up to sleep
- Data from the user's sleep to wake-up

When the data set reaches a certain saturation, it will be able to autonomously control some situations within the home. Depending on the user preference, the system will send a confirmation message to the user before performing the operation on its own and after the approval, the activities will be performed. In this way, human errors will be minimized and problems that seem important for a more comfortable life will be eliminated. The user will be able to control the house as he wishes by means of a mobile interface (Fig. 4.) designed to be connected to the developed system while the user is at home.

Fig. 4. Smart Home Mobile Application

Smart home system can be controlled by SMS when the user is not at home. The purpose of using the GSM module in the study is to get information about the house and to control the house easily remotely even when there is no internet connection. In case of any alarm (gas leakage, fire, etc.), the system will send SMS to the residents and prevent a possible disaster.

3. DATASET AND MODELS

3.1. Dataset

The data set consists of 4320 rows and 18 columns. The system records the data received from the sensors every half hour with the date, day and time. The data set was obtained after 3 months of learning. A grouping process was performed for similar data. In this way, the learning ability of the network is increased. Data set descriptions are shown in Table 1.

Table 1. A sample of dataset content

Attribute	Description
Date	Date when the data was saved
Day	The day the data was saved
Hour	Time of recording data
Home Status	Whether or not residents are at home
Internal Temperature	Temperature in the house
Outside Temperature	Outside temperature
Home Humidity	Humidity inside the house (%)
External Humidity	Humidity outside the house (%)
Gas Value	Flammable gas (methane) in the house
Flame Rating	Flame value in the house
Sound Value	Sound values in the house
Hall Light Condition	Whether the hall light is on or not
Bedroom Light Condition	Whether the bedroom light is on or not
Relay – 1	Whether relay-1 is open or not
Relay – 2	Whether relay-2 is open or not
Air conditioning	Whether or not the fan is on
Curtain	Whether the curtain is open
Warning	Current alert status in the system

Date, time and day information was added to the data obtained from all sensors at 30 minute intervals. Then, the data were taught to the system by ANN method of MLP and the system was able to perform some operations on its own. In the study, 10-fold cross validation was applied on the data set.

The main features of the model used in the study are listed below:

- Input – Output neurons: 18 - 1
- Hidden Layer sizes: 100
- Activation: relu
- Learning Rate: constant
- Iteration size: 200

4. RESULTS AND DISCUSSIONS

The basic concepts used in evaluating model performance are error rate (1), precision (2), sensitivity (3) and f criteria (4). The success of the model is related to the quantity of samples assigned to the correct class and the number of samples assigned to the wrong class. In the complexity matrix, the performance information of the results obtained from the test indicates the real numbers of the samples in the test set and the columns represent the estimation of the model (Coşkun and Baykal, 2011).

The success performances of the model are shown in Table 2 and the confusion matrix of the model is shown in Table 3.

$$\textbf{Error rate} = \frac{\textbf{FP+FN}}{\textbf{TP+FP+FN+TN}} \quad (1)$$

$$\textbf{Precision} = \frac{\textbf{TP}}{\textbf{TP+FP}} \quad (2)$$

$$\text{Sensitivity} = \frac{\text{TP}}{\text{TP+FN}} \quad (3)$$

$$\text{Criteria F} = 2 * \frac{\text{Sensitivity} * \text{Precision}}{\text{Sensitivity+Precision}} \quad (4)$$

TP = True Pozitif

FP = False Pozitif

FN = False Negatif

TN = True Negatif

Table 2. Classification report

X	precision	recall	F1	support
0	0.98	0.95	0.96	183
1	0.62	0.79	0.70	19
accuary			**0.94**	202
Macro avg	0.80	0.87	0.83	202
Weighted avg	0.94	0.94	0.94	202

Table 3. Confusion Matrix

		Prediction		
		0	1	**Total**
Real	0	TN 174	FP 9	183
	1	FN 4	TP 15	19
	Total	178	24	

According to these results, 174 out of 183 piece of 0 values are classified as true and 9 as incorrect. For the 19 piece of 1 values, 15 are classified as true and 4 as incorrect. The success performance of the model was found to be 0.94.

5. CONCLUSION

In this study, a smart home system which can perform some operations instead of user with artificial intelligence has been developed. At the same time, the developed system detects possible disasters and sends information SMS to users. The system detects potential hazards such as gas leakage, flooding, high intensity sound detection and can alert people by SMS. Users can communicate with the smart home system via SMS and Bluetooth and control many operations. As a method of artificial intelligence, ANN's MLP Classifier method was used. The accuracy of the model was found to be 0.94. Successful results show that the current method can be improved and better results can be obtained by using different methods.

ACKNOWLEDGEMENTS (OPTIONAL)

This study was supported by Mersin University Scientific Research Projects Unit with Project Number 2019-1-TP2-3222.

REFERENCES

Ataseven, B. (2014). Yapay sinir ağları ile öngörü modellemesi.

Başçıl, M. S, Çetin, O, Er, O, and Temurtaş, F. (2012). Olasılıksal sinir ağının (PNN) parkinson hastalığının teşhisinde kullanılması. Electronic Letters on Science and Engineering, 8(1), 1-10.

Coşkun, C., and Baykal, A. (2011). Veri madenciliğinde sınıflandırma algoritmalarının bir örnek üzerinde karşılaştırılması. Akademik Bilişim, 2011, 1-8.

Hybrid optimization algorithm for the definition of mlp neural network architectures and weights. In Fifth International Conference on Hybrid Intelligent Systems (HIS'05) (pp. 6-pp). IEEE.

Isa, E, and Sklavos, N. (2017). Smart Home Automation: GSM Security System Design and Implementation. Journal of Engineering Science and Technology Review, 10(3).

Jose, A. C., and Malekian, R. (2015). Smart home automation security: a literature review. SmartCR, 5(4), 269-285.

Lins, A. P. S., and Ludermir, T. B. (2005, November). Neural network models (supervised), https://scikit-learn.org/stable/modules/neural_networks_supervised.html#neural-networks-supervised [Accessed 28 Aug 2019]

Ok, F., Can, M., Üçgün, H., and Yüzgeç, U. (2017, October). Smart mirror applications with raspberry Pi. In 2017 International Conference on Computer Science and Engineering (UBMK) (pp. 94-98). IEEE.

Palanca, J., del Val, E., Garcia-Fornes, A., Billhardt, H., Corchado, J. M., and Julián, V. (2018). Designing a goal-oriented smart-home environment. *Information Systems Frontiers*, *20*(1), 125-142.

Solak, S., Yakut, Ö., and Bolat, E. D. (2017). Yaygın Kullanılan ARM Tabanlı Tek Kart Bilgisayar Sistemleri ve Kullanım Alanları. El-Cezeri Journal of Science and Engineering, 4(1).

Şeker Ş. E. (2013). Sınıflandırma (Classification). http://bilgisayarkavramlari.sadievrenseker.com/2013/03/31/siniflandirma-classification/ [Accessed 23 Aug 2019]

Tektaş, M., Akbaş, A., and Topuz, V. (2002). Yapay zeka tekniklerinin trafik kontrolünde kullanilmasi üzerine bir inceleme.

Tseng, S. P., Li, B. R., Pan, J. L., and Lin, C. J. (2014, September). An application of Internet of things with motion sensing on smart house. In 2014 International Conference on Orange Technologies (pp. 65-68). IEEE.

Zhou, Y, Zhou, Q, Kong, Q, and Cai, W. (2012, April). Wireless temperature and humidity monitor and control system. In 2012 2nd International Conference on Consumer Electronics, Communications and Networks (CECNet) (pp. 2246-2250). IEEE.

Witten, I. H., Frank, E., Hall, M. A. and Pal, C. J. (2016). Data Mining: Practical Machine Learning Tools and Techniques, Morgan Kaufmann, Burlingon, USA.

CISET - 2nd Cilicia International Symposium on Engineering and Technology
10-12 October, 2019, Mersin / TURKEY

DEVELOPMENT OF AN ARTIFICIAL INTELLIGENT BASED SMART HOME SYSTEM USING NAÏVE BAYES CLASSIFIER

Cevdet Tamer GÜVEN [*1], Mehmet ACI [2]

[1] Mersin University, Engineering Faculty, Computer Engineering Department, Mersin, Turkey, ctamerguven@gmail.com

[2] Mersin University, Engineering Faculty, Computer Engineering Department, Mersin, Turkey, maci@mersin.edu.tr

ABSTRACT
In this study, a smart home system based on artificial intelligence based on raspberry pi and various sensors has been developed. Two different models of naïve bayes classifier, Bernoulli Naïve Bayes (BernoulliNB) and Gaussian Naïve Bayes (GaussianNB) were used as the method. The aim of the study is to record the activities of the residents in their homes every day in the data format via sensors and then classify these records with BernoulliNB and GaussianNB to enable the system to perform some activities autonomously for the benefit of the residents. The developed system can also be controlled as mobile via GSM and Bluetooth. The smart home system is designed to detect and alert potential disaster. The best results were obtained by GaussianNB.

Keywords: *Smart Home Systems, Bernoulli Naïve Bayes, Gaussian Naïve Bayes, Raspberry Pi, Robotics*

[*] Cevdet Tamer GÜVEN

1. INTRODUCTION

Smart home systems are the application of the control systems used in the industry according to daily life and personal needs. Smart home systems are houses that can meet the needs of the residents and offer them a safer, more economical and more comfortable life. Smart home systems have become much more accessible and usable today through the development of mobile communication, the decrease in the size of technological devices and the cheapening of the technological devices. Safety and comfort are the main reasons for people preferring smart home systems. In addition, smart home systems minimize time and money losses.

In this study, a smart home system which can perform some operations instead of user with artificial intelligence has been developed. At the same time, the developed system detects possible disasters and sends information SMS to users. Gas leakage, flooding, high intensity sound detection, fire detection and so on. It can detect possible danger situations and notify people by SMS. Users can communicate with the smart home system via SMS and Bluetooth and control many operations. Bernoulli and Gaussian Naïve Bayes methods, which are the most commonly used classification algorithms, are compared.

The simple Bayesian classifiers seem to have gained popularity recently and performed surprisingly well. The Naïve Bayes model is a highly simplified Bayesian probability model. The Naïve Bayes classifier is based on a strong assumption of independence. This means that the probability of one attribute does not affect the probability of another. Given a series of n properties, the Naïve Bayes classifier is 2n! makes independent assumptions. However, the results of the Naïve Bayes classifier are often correct (Mukherjee and Sharma, 2012). In this study, two different Naïve Bayes models were used: Bernoulli Naïve Bayes (BernoulliNB) and Gaussian Naïve Bayes (GaussianNB).

BernoulliNB is a Naïve Bayes classifier for multivariable Bernoulli models. Like Multinomial Naïve Bayes (MultinominalNB), this classifier is suitable for discrete data. The difference shows that although MultinomialNB works with the number of occurrences, BernoulliNB is designed for binary / boolean properties. BernoulliNB applies pure Bayesian training and classification algorithms for data distributed according to multivariate Bernoulli distributions; that is, there may be more than one property, but each is assumed to be a binary-value (Bernoulli, boolean) variable. Therefore, this class requires that the samples be represented as divalent property vectors; otherwise, a BernoulliNB instance can binary input (depending on the binarize parameter) (www.scikit-learn.org, 2019).

A typical way to address the continuous properties in the Naive Bayes classification is to use Gaussian distributions to represent the probability of conditioned properties in classes (Bustamante et al., 2006). The GaussianNB classifier is a supervised learning algorithm that uses the Bayes theorem to classify a set of predefined observations of classes based on information provided by the determinant variables (Griffis et al., 2016).

In the study, Raspberry Pi (RPi) was used as hardware infrastructure. RPi is a credit card sized computer that was developed in 2012 and used to teach the basics of computer science in schools (Solak, Yakut, and Bolat, 2017). The RPi 3 Model B+ used in the project has an A53 / ARMv8 quad-core 64-bit processor. It has 1GB ram capacity. Thanks to the Raspbian operating system, which is written to an external micro sd card, all operations can be performed easily on a normal computer. RPi is based on the python programming language. Python is an objective, interpretable, modular and interactive programming language. Python supports the class system and any data field entry (Ok et al., 2017). With the Python programming language, a dataset is created from the data received from the sensors. The Naïve Bayes classifier models GaussianNB and BernoulliNB classification methods were applied to this data set and the classification success of the models was compared.

2. MATERIAL AND METHOD

2.1. Hardware

In this study, RPi is used on the basis of smart home system. RPi is a credit card size and cost effective development card, which is mostly used for educational purposes. It works optimally with Raspbian, an operating system based on open source Debian. RPi 3 Model B+ was used in the study (Fig. 1).

Fig. 1. Raspberry Pi 3 Model B+

Two DHT11 temperature and humidity sensors are used to measure the temperature and humidity values inside and outside the house. DHT11 is a temperature and humidity sensor with an already calibrated digital signal output. The sensor includes an NTC temperature sensor, a resistant moisture component. The single-chip microcontroller with an 8-bit high-performance connection offers the sensor excellent quality, super-fast response, jamming capability, and cost-effectiveness (Zhou et al., 2012).

MQ-4 gas sensor is used to detect possible gas leaks in the house and flame sensor is used to detect fire situation.

Sound sensor is used to detect the noise inside the house when no one is in the house. The sound sensor is calibrated to notify the user by sending a warning SMS when it detects frequencies higher than the predetermined volume level. SMS sending is done with GSM module. The two basic connections of the GSM module are the TX and RX pins, which allow the microcontroller to connect to the GSM module that sends serial data. The GSM module works with a SIM card. The SIM card requires a subscription with a mobile communications provider. Based on this, the user can

access the mobile network. The UART (Universal Asynchronous Transceiver) interface encodes and decodes data between parallel and serial formats. Bytes of data are received and transmitted as a bit sequence. Thus, data can be transmitted via serial TX to the microcontroller or network as an antenna (Isa and Sklavos, 2017).

The house has 2 relay modules, 1 servo motor, 1 PIR (Passive Infrared Radiation or Pyroelectric Infrared) sensor, 1 fan and 3 LEDs. All components of the smart home system are shown in Fig. 2. Component connections and circuit diagrams are shown in Fig. 3..

Fig. 2. Smart Home Components

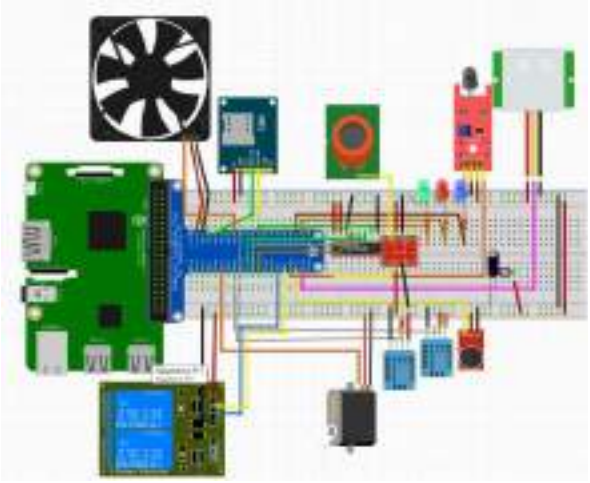

Fig. 3. Smart Home Circuits Scheme

2.2. Software

Naïve Bayes methods are a series of supervised learning algorithms based on the application of Bayes' theorem with the assumption of if "naive" conditional independence between each pair of properties given the value of the class variable.

GaussianNB applies the Gaussian Naïve Bayes algorithm for classification. The probability of properties is considered to be Gaussian (1).

$$P(x_i \mid y) = \frac{1}{\sqrt{2\pi\sigma_y^2}} \exp\left(-\frac{(x_i - \mu_y)^2}{2\sigma_y^2}\right) \quad (1)$$

BernoulliNB applies the Naïve Bayes training and classification algorithm for multivariable data; that is, there may be more than one property, but each is assumed to be a binary value (Bernoulli boolean) variable (2).

$$P(x_i \mid y) = P(i \mid y)x_i + (1 - P(i \mid y))(1 - x_i) \quad (2)$$

In the study, BernoulliNB and GaussianNB methods which are Naïve Bayes classifiers are used as artificial intelligence method. The following guidelines were used for data collection:

- Data on actions taken by the user before leaving home
- Data from sensors based on changes when the user is not at home
- Data on actions taken by the user when he comes home
- Data from sensors according to user's activities up to sleep
- Data from the user's sleep to wake up

When the data set reaches a certain saturation, it will be able to autonomously control some situations within the home. Since the project is in the process of development, activities will be performed after the system sends a confirmation message to the user before the transaction is performed on its own. In this way, human errors will be minimized and problems that seem important for a more comfortable life will be eliminated. While the user is at home, he can connect to the developed system via bluetooth and control the house as he wishes by means of the designed mobile interface (Fig. 4.).

Fig. 4. Smart Home Mobile Application

Smart home system can be controlled by SMS when users are not at home. The purpose of using the GSM module in the study is to get information about the house and to control the house easily remotely even

when there is no internet connection. In case of any alarm (gas leakage, fire, etc.), the system will send SMS to the residents and prevent a possible disaster.

3. DATASET AND MODELS

3.1. Dataset

The data set consists of 4320 rows and 18 columns. The system records the data received from the sensors every half hour with the date, day and time. The data set was obtained after 3 months of learning. A grouping process was performed for similar data. In this way, the learning ability of the network is increased. Data set descriptions are shown in Table 1.

Table 1. A sample of dataset content

Attribute	Description
Date	Date when the data was saved
Day	The day the data was saved
Hour	Time of recording data
Home Status	Whether or not residents are at home
Internal Temperature	Temperature in the house
Outside Temperature	Outside temperature
Home Humidity	Humidity inside the house (%)
External Humidity	Humidity outside the house (%)
Gas Value	Flammable gas (methane) in the house
Flame Rating	Flame value in the house
Sound Value	Sound values in the house
Hall Light Condition	Whether the hall light is on or not
Bedroom Light Condition	Whether the bedroom light is on or not
Relay – 1	Whether relay-1 is open or not
Relay – 2	Whether relay-2 is open or not
Air conditioning	Whether or not the fan is on
Curtain	Whether the curtain is open
Warning	Current alert status in the system

Date, time and day information was added to the data obtained from all sensors at 30 minute intervals.

4. RESULTS AND DISCUSSIONS

The basic concepts used in evaluating model performance are error rate (3), precision (4), sensitivity (5) and f criteria (6). The success of the model is related to the quantity of samples assigned to the correct class and the number of samples assigned to the wrong class. In the complexity matrix; the rows represent the real numbers of the samples in the test set and the columns represent the estimates of the model (Coşkun and Baykal, 2011).

The success performances of the models are shown in Table 2 and Table 3, and the complexity matrices of the models are shown in Figure 5 and Figure 6.

$$\textbf{Error rate} = \frac{\textbf{FP+FN}}{\textbf{TP+FP+FN+TN}} \quad (3)$$

$$\textbf{Precision} = \frac{\textbf{TP}}{\textbf{TP+FP}} \quad (4)$$

$$\text{Sensitivity} = \frac{\text{TP}}{\text{TP+FN}} \quad (5)$$

$$\text{Criteria F} = 2 * \frac{\text{Sensitivity} * \text{Precision}}{\text{Sensitivity+Precision}} \quad (6)$$

TP = True Pozitif

FP = False Pozitif

FN = False Negatif

TN = True Negatif

Table 2. BernoulliNB - Classification report

X	Precision	Recall	F1	Support
0	0.79	0.95	0.86	157
1	0.96	0.84	0.90	246
accuary			0.88	403
Macro avg	0.88	0.90	0.88	403
weighted avg	0.90	0.88	0.88	304

Table 3. GaussianNB - Classification report

X	Precision	Recall	F1	Support
0	0.92	0.91	0.91	157
1	0.92	0.93	0.93	246
accuary			0.92	403
Macro avg	0.92	0.92	0.92	403
weighted avg	0.92	0.92	0.92	304

Figure 5. BernoulliNB – Convolution matrix

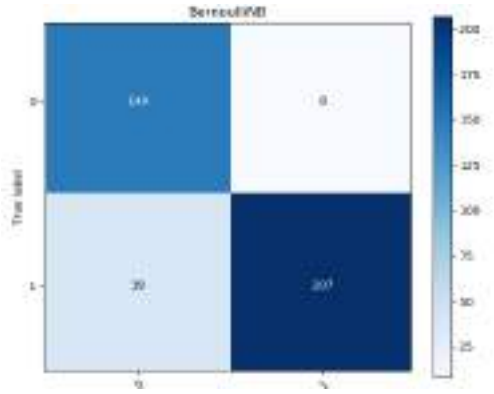

Figure 6. GaussianNB – Convolution matrix

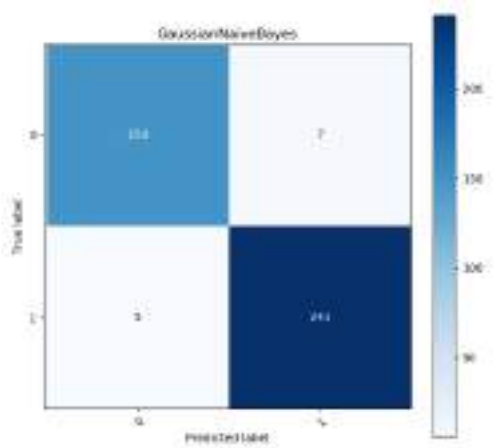

According to these results, BernoulliNB's classification success was 0.88 and GaussianNB's classification success was 0.92. According to complexity matrices, BernoulliNB classified 149 of the 157 piece of 0 values as true, 8 of them as false and 39 of the 246 piece of 1 values as wrong, 207 of them as correct. On the other hand, GaussianNB categorized 150 of 157 piece of 0 values as correct, 7 of them as false and 5 of 246 piece of 1 as incorrect, and 241 of them as correct.

5. CONCLUSION

In this study, a smart home system which can perform some operations instead of user with artificial intelligence has been developed. The BernoulliNB and GaussianNB methods of Naïve Bayes classifiers were compared as artificial intelligence method. The results showed that GaussianNB method gave more successful results than BernoulliNB method. Successful results show that the current method can be improved and better results can be obtained by using different methods.

ACKNOWLEDGEMENTS

This study was supported by Mersin University Scientific Research Projects Unit with Project Number 2019-1-TP2-3222.

REFERENCES

Bernoulli Naïve Bayes, https://scikit-learn.org/0.21/modules/naive_bayes.html#bernoulli-naive-bayes [Accessed 27 Aug 2019]

Bustamante, C., Garrido, L., and Soto, R. (2006, November). Comparing fuzzy naive bayes and gaussian naive bayes for decision making in robocup 3d. In Mexican International Conference on Artificial Intelligence (pp. 237-247). Springer, Berlin, Heidelberg.

Griffis, J. C., Allendorfer, J. B., and Szaflarski, J. P. (2016). Voxel-based Gaussian naïve Bayes classification of ischemic stroke lesions in individual T1-weighted MRI scans. Journal of neuroscience methods, 257, 97-108.

Isa, E, and Sklavos, N. (2017). Smart Home Automation: GSM Security System Design and Implementation. Journal of Engineering Science and Technology Review, 10(3).

Mukherjee, S., and Sharma, N. (2012). Intrusion detection using naive Bayes classifier with feature reduction. Procedia Technology, 4, 119-128.

Ok, F., Can, M., Üçgün, H., and Yüzgeç, U. (2017, October). Smart mirror applications with raspberry Pi. In 2017 International Conference on Computer Science and Engineering (UBMK) (pp. 94-98). IEEE.

Solak, S., Yakut, Ö., and Bolat, E. D. (2017). Yaygın Kullanılan ARM Tabanlı Tek Kart Bilgisayar Sistemleri ve Kullanım Alanları. El-Cezeri Journal of Science and Engineering, 4(1).

Zhou, Y, Zhou, Q, Kong, Q. and Cai, W. (2012, April). Wireless temperature and humidity monitor and control system. In 2012 2nd International Conference on Consumer Electronics, Communications and Networks (CECNet) (pp. 2246-2250). IEEE.

CISET - 2nd Cilicia International Symposium on Engineering and Technology
10-12 October, 2019, Mersin / TURKEY

INFLUENCE OF Mn DOPING ON OPTICAL PROPERTIES OF MgO THIN FILMS

Ömer Çelik *[1,2], Şilan Baturay[1,3], Yusuf Selim OCAK[1,4]

[1]Smart-Lab, Dicle University, Diyarbakır, Turkey
[2]Department of Physics, Faculty of Education, Dicle University, Diyarbakır, Turkey E-mail: celiko21@yahoo.com
[2]Department of Physics, Science, Dicle University, Diyarbakır, Turkey E-mail: silan@dicle.edu.tr
[4]Department of Science, Faculty of Education Dicle University, Diyarbakır, Turkey E-mail: yusufselim@gmail.com

ABSTRACT

Thin MgO films were grown by spin coating technique on soda lime glass substrates at different Mn doping concentrations (pure, 1, 2, and 3%). Optical properties of the MgO films (transmittance, absorbance and energy band gap) were investigated as a function of different Mn doping concentrations and characterized by using ultraviolet–visible (UV–vis) spectrophotometry at room temperature. Ultraviolet–visible spectroscopy measurements indicate that the transmittance and energy band gap of thin films annealed at 500 °C in air ambient are changed due to the different crystallinity. Energy band gap of films is significantly decreased from 5.35 to 3.11 eV with increasing Mn doping rate.

Keywords: *Energy band gap, thin film, spin coating*

* Corresponding Author

1. INTRODUCTION

MgO has ionic insulating crystalline structure with NaCl structure owing to its important properties such as chemical inertness, electrical insulation, optical transparency, stabilized in high temperature and very high thermal conductivity (Durusoy, 1991). MgO symmetry is cubic because of the fact that it has a lattice constant of 4.213 Å, which is close to that of several ferroelectric, perovskite ferroelectrics and superconducting materials (Hsu & Raj, 1992).

In the earlier studies, single crystal MgO thin films have obtained using electron-beam fabricated on to LiF substrates (Reichelt, 1973) and LiF substrate's (100) orientation is found in this study. Aboelfotoh showed that MgO film has preferred the (111) direction when fabricated on substrates including quartz, fused silica, (100) and (111) oriented silicon at substrate temperatures of the range of 30 and 300 °C (Aboelfotoh, Park, & Pliskin, 1977). Fu and Song indicated that the crystallinity of the MgO films was obtained after annealing over 800 °C (Fu et al., 1999). Hsu and Raj reported that growth rate and crystalline quality of epitaxial MgO films were sensitive to the substrate temperature using reactive rf planar magnetron sputtering method (Hsu & Raj, 1992). They also reported that the MgO film was not fully crystalline at lower temperature. But it was obtained highly oriented crystallinity MgO film when the substrate temperature was between 500 and 530 ºC.

MgO films have been depozited by a different methods such as pulsed laser deposition (Fork, Ponce, Tramontana, & Geballe, 1991), sol-gel technique (Ho, Xu, & Mackenzie, 1997), metalorganic chemical vapor deposition technique (Kwak, Boyd, Zhang, Erbil, & Wilkins, 1989), electrostatic spray pyrolysis (ESP) method (Kim, Kim, & Kim, 2000) and electron beam evaporation (Masuda & Nashimoto, 1994). Different from among these methods, spin coating method offers important advantages including homogeneity, various concentration control, temperature control, ease of processing and apply to different coat area.

In this paper, Mn doped MgO thin films were deposited on soda lime glass (SLG) substrates by spin coatin method. The film annealed in air atmosphere at 500 ºC. The optical parameters of the all thin films were analyzed by Ultraviolet–visible spectrophotometry. The optical properties of Mn doped MgO films were not comprehensively investigated and very little knowledge are in literature about this study. Therefore, the concentration effect on MgO film was comprehensively investigated in this study.

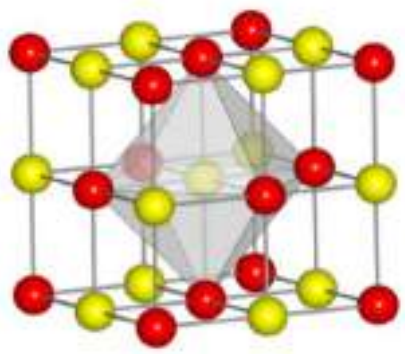

Figure 1. Crystal structure of monoclinic MnO

2. EXPERIMENTAL PROCEDURES

In this study, undoped and Mn doped MgO films with different weight ratios (1, 2 and 3 at wt% of Mn) were fabricated via spin coating technique using a solution comprising 0.1 M magnesium nitrate $Mg(NO_3)2 \cdot 6H_2O$, 0.01 M manganese (II) nitrate $Mn(NO_3)2 \bullet 4H_2O$, deposited under optimized condition. To obtain the formation of clear and homogenous solution, the magnesium nitrate and manganese (II) nitrate high purity of around 98 %. Suitable amount magnesium nitrate stirred in 50 ml of ethanol for 12 h and suitable amount manganese (II) nitrate stirred in 20 ml of ethanol for 12 h also. After this, an adequate amount of manganese (II) nitrate was slowly mixed into the magnesium nitrate solution to give various doping concentrations (i.e. 0, 1, 2 and 3 %) and then this obtained solutions were stirred at room temperature for 24 h. Before fabrication process, the soda lime glass (SLG) substrates were cleaned by boiling in sufficient quantities mixture of water, ammonia, and hydrogen peroxide at 90 °C and then in sufficient quantities mixture of water, hydrogen peroxide, and hydrogen chloride at 90 °C to remove any residual waste. Then, these substrates were cleaned in deionized water for 3 min. each and dried under N_2 gas. After obtaining these processes, the films with different weight ratios were deposited via spin coated at a rate of 3000 rpm for 60 s in air condition by layer and layer, and each layer was preheated to 240 °C for 10 min. after fabrication process, the obtained films annealed at 500 °C in furnace. The conclusion of the transmittance, absorbance and energy band gap of the all thin films were analyzed using UV-Vis spectrophotometer in the 300-1100 nm wavelength.

3. RESULTS AND DISCUSSION

The optical properties of undoped and Mn doped MgO films fabricated onto soda lime glass substrates are analyzed to observe the effect of doping on the transmittance T(λ), absorbance and energy band gap Eg(λ) using UV–visible spectrophotometry in the wavelength range from 300 to 1100 nm at room temperature. There was not seen any other peak in the UV-vis area which indicates that thin films have a good quality, clear and homogenous surface. Fig. 1 shows that the optical transmission spectra of MgO films for different concentrations at the room temperature.

Undoped MgO nanostructure film has the maksimum transmittance value compared to the other thin films. The transmittance value decreases with increasing Mn doping concentration. Tamboli et al indicated that transmittance of MgO films varied significantly with the oxidation temperatures and time by thermal oxidation of vacuum evaporated vapour chopped. They indicated that increase in optical transmittance was seen because of increasing oxidation temperature and duration (Tamboli, Patil, Kamat, Puri, & Puri, 2009).

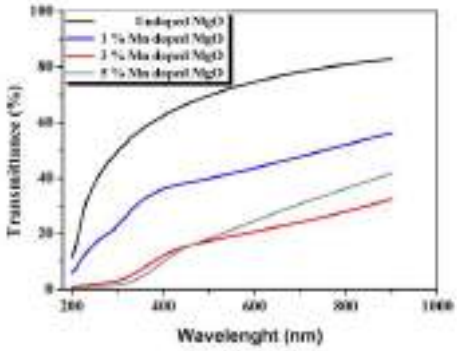

Figure 2. Tranmittance-wavelenght plots of undoped and Mn doped MgO thin films

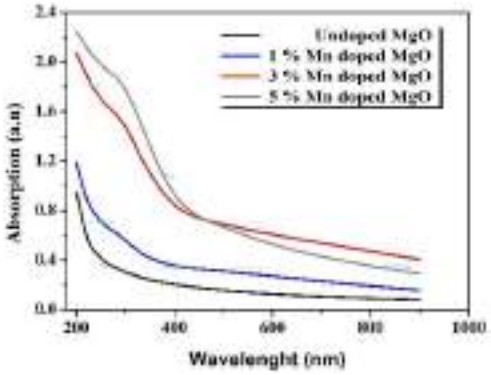

Figure 3. Absorption-wavelenght plots of undoped and Mn doped MgO thin films

Table 1 Band gap values of undoped and Mn doped MgO thin films

Sample	Band Gap (eV)
Undoped MgO	5.35
%1 Mn doped MgO	3.35
%3 Mn doped MgO	3.16
%5 Mn doped MgO	3.11

Fig. 3 shows the graph of $(\alpha h\upsilon)^2$ as a function of hυ. From the absorption data, the band gap energy was calculated using formula:

$$\alpha h\nu = B(h\nu - E_g)^m$$

where E_g is the energy band gap, α is the absorption coefficient of thin film, $h\upsilon$ is the photon energy and m is a constant. The value of m depends on the probability of the nature of the transition; it takes values as 1/2, 3/2, 2 and 3 for direct allowed, direct forbidden, indirect allowed and nondirect forbidden transition, respectively. It is known that MgO film has an allowed direct band gap and $m = 1/2$ was used for the energy band gap calculation. The calculated values of energy band gap are seen in Table 1. The variation in energy band gap values was observed owing to concentration of Mn dopant.

The calculated energy band gap of the films found from this graph were 5,35, 3.35, 3,16 and 3.11 eV for 0, 1, 2, 3 % Mn doped MgO films, respectively. Mn doped in solution has changed the energy band gap value, which shows that Mn could be used to regulate the optical band gap of MgO films. Kurth et al reported that the energy band gap of bulk magnesium oxide is 7.8 eV (Kurth & Graat, 2002) and Reichel et al. obtained energy band gap in the range 2–2.5 eV for MgO thin films (Reichel, Jeurgens, & Mittemeijer, 2008). MgO films using spray pyrolysis technique on quartz substrates also show lower energy band gap as compared to bulk (Raj, Nehru, Jayachandran, & Sanjeeviraja, 2007). It was obtained lower energy band gap in his study which may be attributed to the varied extent of non-stoichiometry of the fabrication layers. That may be due to the different lattice due to atomic interaction phenomena as a result of the ionic crystalline nature.

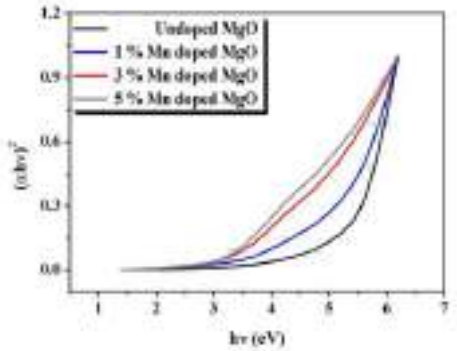

Figure 4. $(\alpha h\nu)^2$-hν plots of undoped and Mn doped MgO thin films

4. CONCLUSION

In this study, undoped and Mn doped MgO thin films with various weight ratios (1, 2 and 3 at wt% of Mn) were fabricated via spin coating technique on soda lime glass substrates. Various Mn doping concentrations on the MgO films characterized by using Ultraviolet–visible spectrophotometry at room temperature. Ultraviolet–visible spectroscopy measurements indicate that the transmittance and energy band gap of thin films annealed at 500 °C are significantly changed. Undoped MgO film has the maximum transmittance value compared to the other thin films. The transmittance value significantly reduces with increasing Mn doping concentration in solution. The calculated energy band gap of the films is found to be 5,35, 3.35, 3,16 and 3.11 eV for 0, 1, 2, 3 % Mn doped MgO films, respectively. Mn doped has decreased the energy band gap value, which indicates that Mn doping could be used to regulate the energy band gap of MgO films.

REFERENCES

Aboelfotoh, M., Park, K., & Pliskin, W. (1977). Infrared and high- energy electron diffraction analyses of electron- beam- evaporated MgO films. *Journal of Applied Physics, 48*(7), 2910-2917.

Durusoy, H. (1991). Growth structures of MgO films on Si (100) and Si (111) surfaces. *Journal of materials science letters, 10*(17), 1023-1025.

Fork, D., Ponce, F., Tramontana, J., & Geballe, T. (1991). Epitaxial MgO on Si (001) for Y- Ba- Cu- O thin-film growth by pulsed laser deposition. *Applied physics letters, 58*(20), 2294-2296.

Fu, X., Song, Z., Wu, G., Huang, J., Duo, X., & Lin, C. (1999). Preparation and characterization of MgO thin films by a novel sol-gel method. *Journal of sol-gel science and technology*, *16*(3), 277-281.

Ho, I.-C., Xu, Y., & Mackenzie, J. D. (1997). Electrical and optical properties of MgO thin film prepared by sol-gel technique. *Journal of sol-gel science and technology*, *9*(3), 295-301.

Hsu, W. Y., & Raj, R. (1992). MgO epitaxial thin films on (100) GaAs as a substrate for the growth of oriented PbTiO3. *Applied physics letters*, *60*(25), 3105-3107.

Kim, S. G., Kim, J. Y., & Kim, H. J. (2000). Deposition of MgO thin films by modified electrostatic spray pyrolysis method. *Thin Solid Films*, *376*(1-2), 110-114.

Kurth, M., & Graat, P. C. J. (2002). Quantitative analysis of the plasmon loss intensities in x-ray photoelectron spectra of magnesium. [Article]. *Surface and Interface Analysis*, *34*(1), 220-224. doi: 10.1002/sia.1287

Kwak, B., Boyd, E., Zhang, K., Erbil, A., & Wilkins, B. (1989). Metalorganic chemical vapor deposition of [100] textured MgO thin films. *Applied physics letters*, *54*(25), 2542-2544.

Masuda, A., & Nashimoto, K. (1994). Orientation of MgO thin films on Si (100) and GaAs (100) prepared by electron-beam evaporation. *Japanese journal of applied physics*, *33*(6A), L793.

Raj, A. M. E., Nehru, L. C., Jayachandran, M., & Sanjeeviraja, C. (2007). Spray pyrolysis deposition and characterization of highly (100) oriented magnesium oxide thin films. [Article]. *Crystal Research and Technology*, *42*(9), 867-875. doi: 10.1002/crat.200710918

Reichel, F., Jeurgens, L. P. H., & Mittemeijer, E. J. (2008). The thermodynamic stability of amorphous oxide overgrowths on metals. [Article]. *Acta Materialia*, *56*(3), 659-674. doi: 10.1016/j.actamat.2007.10.023

Reichelt, K. (1973). Hetero-epitaxial growth of MgO on LiF single crystal films. *Journal of Crystal Growth*, *19*(4), 258-262.

Tamboli, S. H., Patil, R. B., Kamat, S. V., Puri, V., & Puri, R. K. (2009). Modification of optical properties of MgO thin films by vapour chopping. *Journal of Alloys and Compounds*, *477*(1), 855-859. doi: https://doi.org/10.1016/j.jallcom.2008.11.011

CISET - 2nd Cilicia International Symposium on Engineering and Technology
10-12 October, 2019, Mersin / TURKEY

ELECTRICAL PROPERTIES OF Sb:ZnO/p-Si HETEROJUNCTIONS

Ömer Çelik*[1,2], Şilan Baturay [2,3] and Yusuf Selim Ocak [2,4]

[1] Department of Physics, Faculty of Education, Dicle University, Diyarbakır, Turkey E-mail: celiko21@yahoo.com

[2] Smart-Lab, Dicle University, Diyarbakır, Turkey

[3] Department of Physics, Science, Dicle University, Diyarbakır, Turkey E-mail: silan@dicle.edu.tr

[4] Department of Science, Faculty of Education Dicle University, Diyarbakır, Turkey E-mail: yusufselim@gmail.com

ABSTRACT
ZnO is one of the most exiting n-type semiconductor with 3.37 eV band gap. It has been used in the fabrication of many kinds of devices. Many studies have been performed for doping of ZnO with various metals. Doping procedures have strong influence on electrical and optical properties of ZnO thin films. These influence can directly change the electrical amd photoelectrical characteristics of obtained devices. In this study, undoped and Sb doped ZnO thin films were deposited on p-Si semiconductor by spin coating technique and Ag/ZnO/p-Si and Ag/Sb:ZnO/p-Si heterojunction devices were fabricated by evaporation of Ag metal on deposited thin films. The electrical properties of the heterojunction were analyzed using the current-voltage measurements of the devices. The results showed that the Sb doping had a strong influence on the performance of the heterojunctions.

Keywords: *Sb doping, ZnO, Heterojunction, electrical properties*

* Corresponding Author

1. INTRODUCTION

Zinc oxide (ZnO) as a compound of semiconductor have been comprehensively studied in 1912. ZnO with a band gap of 3.37 eV and an exciton binding energy of 60 meV, has been recognized as an important material for ultraviolet optical and short-wavelength as photodiodes (Mandalapu, Xiu et al. 2006) (Pearton, Norton et al. 2004). ZnO have been used for different fields such as gas sensor (Roy and Basu 2002), solar cell (Ellmer, Klein et al. 2007), optoelectronic devices (Look 2001) and transistors (Hoffman, Norris et al. 2003). Nominally pure ZnO typically shows n-type conductivity due to its the asymmetric doping limitations (Zhang, Wei et al. 2001). On the other side, many groups have successfully obtained p-type conductivity ZnO film by various doping with N (Guo, Tabata et al. 2001), Sb (Mandalapu, Xiu et al. 2006) and Li (Zeng, Ye et al. 2006).

In Recent years, a model which was proposed for large-sized-mismatched group-V dopant basen upon first principles calculation including arsenic (As) and antimony (Sb) in ZnO was given, in which an SbZn–2VZn complex was thought to be a good acceptor instead of deep SbO acceptor because of the fact that AsZn−2VZn complex may have lower formation energy (Limpijumnong, Zhang et al. 2004). Aoki et al. reported on p-type conductivity ZnO film fabricated by excimer laser irradiation doping with Sb as a dopant source (Aoki, Shimizu et al. 2002). Zhu et al reported that pure and different mole ratios Sb-doped ZnO film were synthesized using vapor condensation technique in a mixture of Ar + O_2 gas (Zhu, Xie et al. 2005). Palani et al. indicated the effect of Sb as a catalyst in the growth of two different ZnO nanostructures including nanowires and nanosheets (Palani, Nakamura et al. 2011). They also indicated that Sb ion is substituted on the Zn site without change in the ZnO structure. Mandalapu et al. have deposited homojunction photodiodes based on p type Sb doped ZnO for ultraviolet detection via molecular-beam epitaxy technique. They showed that Current-voltage measurements of p- type Sb-doped ZnO have good rectifying behavior. However, the Current-voltage measurements of Sb doped ZnO thin films grown by spin coating technique (SCT) are seldom reported.

Several film fabrication techniques, molecular-beam epitaxy (Mandalapu, Xiu et al. 2007), combining chemical vapor deposition, spin coating method (Benelmadjat, Touka et al. 2010), radio frequency magnetron sputtered (Wang, Chen et al. 2006) and hydrothermal process (Escobedo-Morales and Pal 2011) have been used to obtain Sb doped ZnO films. Among the abundant fabrication techniques, SCT is a useful method for obtaining Sb doped ZnO films owing to its low cost and large area fabrication capabilities.

In this work, we have fabricated pure and Sb doped ZnO thin films by SCT p-Si to obtain Sb:ZnO/p-Si heterojunction devices. The influence Sb doping on electrical properties of the heterojunction was investigated.

2. EXPERIMENTAL PROCEDURES

Pure and Sb-doped ZnO films were prepared by spin coating technique using p-type Si(1 0 0) wafers, which had a resistivity of 1–10 Ω cm. Before deposition process, the p-type Si wafers were boiled in trichloroethylene for 5 min, and ultrasonically cleaned in acetone to remove any organic and any residual contamination. The Si substrates were cleaned with the mixture of HF:H_2O (1:10) and then dried with N_2 gas. The back contacts were formed by evaporating a 200-nm-thick aluminum (Al) contact layer on the unpolished side of the p-type Si wafer, followed by rapid thermal annealing at 570 °C for 3 min under a N_2 atmosphere. Sb doped ZnO thin films with different weight ratios (0 and 3at wt% of Sb) were grown by spin coating technique using a zinc acetate dihydrate (Zn $(CH_3COO)_2$ $2H_2O$) and 0.01 M antimony (III) chloride ($SbCl_3$) fabricated under optimized condition. To obtain clear and homogenous white solution, the zinc acetate dihydrate and antimony (III) chloride high purity of about 98%. The zinc acetate dihydrate stirred in ethanol of 0.1M concentration for 24h and the antimony (III) chloride stirred in ethanol of 0.01M concentration for 24h also. After this process is completed, an adequate amount of antimony (III) chloride was slowly mixed into the zinc acetate dihydrate solution to give various doping concentrations (i.e. 0 and 3 at.%) and then this obtained solutions were stirred for 8h until a clear and homogeneous solution was attained.

The I–V characteristics of the structures were investigated by a source meter (model 2400; Keithley, Cleveland, OH, USA) in the dark under illumination with solar simulator at room temperature,

3. RESULTS AND DISCUSSION

The current-voltage measurements of Ag/ZnO/p-Si and Ag/Sb:ZnO/p-Si heterojunction structures are presented in Figure 1 and Figure 2. As seen from the figures, both structures had excellent rectification properties. When a rectifying heterojunction device taking into account, thermionic emission theory

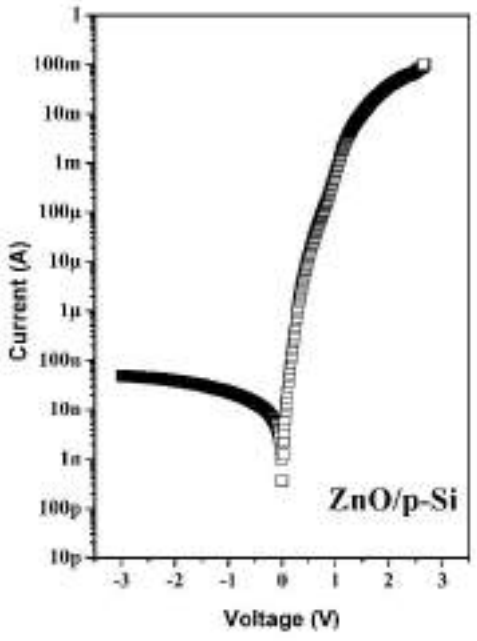

Figure 1. Current-voltage plot of ZnO/p-Si heterojunction device in dark

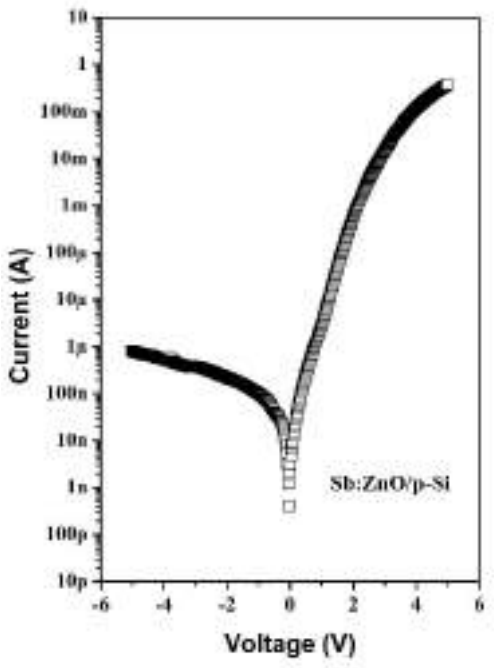

Figure 2. Current-voltage plot of 3 % Sb doped ZnO/p-Si heterojunction device in dark

can be used. In this study, the TET is used to calculate electrical properties of both Ag/ZnO/p-Si and Ag/Sb:ZnO/p-Si devices. The ideality rectification ratio, ideality factor and barrier height values of Ag/ZnO/p-Si heterojunction was calculated as $8.16x10^5$ (the ratio of current obtained -3 V to the current obtained 3 V), 1.21 and 0.782 eV, respectively. In addition, the ideality rectification ratio, ideality factor and barrier height values of Ag/ZnO/p-Si heterojunction was calculated as $4.32x10^4$ (the ratio of current obtained -3 V to the current obtained 3 V), 4.226 and 0.755 eV, respectively. The results showed that the Sb doping had a strong influence on electrical properties ZnO/p-Si heterojunction.

5. CONCLUSION

In this study, Ag/ZnO/p-Si and Ag/Sb:ZnO/p-Si heterojunction devices were obtained by spin coating technique. The electrical properties of both junctions were calculated using their current-voltage (I-V) measurements in dark. It was seen that the Sb doping had strong effects on electrical parameters of the junctions.

REFERENCES

Aoki, T., Y. Shimizu, et al. (2002). "p-type ZnO layer formation by excimer laser doping." physica status solidi (b) 229(2): 911-914.

Benelmadjat, H., N. Touka, et al. (2010). "Study of structural and optical properties of Sb doped ZnO thin films deposited by spin coating method." Optical Materials 32(7): 764-767.

Ellmer, K., A. Klein, et al. (2007). Transparent conductive zinc oxide: basics and applications in thin film solar cells, Springer Science & Business Media.

Escobedo-Morales, A. and U. Pal (2011). "Effect of In, Sb and Ga doping on the structure and vibrational modes of hydrothermally grown ZnO nanostructures." Current Applied Physics 11(3): 525-531.

Guo, X. L., H. Tabata, et al. (2001). "Pulsed laser reactive deposition of p-type ZnO film enhanced by an electron cyclotron resonance source." Journal of Crystal Growth 223(1-2): 135-139.

Hoffman, R., B. J. Norris, et al. (2003). "ZnO-based transparent thin-film transistors." Applied physics letters 82(5): 733-735.

Limpijumnong, S., S. Zhang, et al. (2004). "Doping by large-size-mismatched impurities: the microscopic origin of arsenic-or antimony-doped p-type zinc oxide." Physical review letters 92(15): 155504.

Look, D. C. (2001). "Recent advances in ZnO materials and devices." Materials Science and Engineering B: Solid-State Materials for Advanced Technology 80(1-3): 383-387.

Mandalapu, L., F. Xiu, et al. (2007). "Al/Ti contacts to Sb-doped p-type ZnO." Journal of Applied Physics 102(2): 023716.

Mandalapu, L., F. Xiu, et al. (2006). "p-type behavior from Sb-doped ZnO heterojunction photodiodes." Applied physics letters 88(11): 112108.

Palani, I. A., D. Nakamura, et al. (2011). "Influence of Sb as a catalyst in the growth of ZnO nano wires and nano sheets using Nanoparticle Assisted Pulsed Laser Deposition (NAPLD)." Materials Science and Engineering: B 176(18): 1526-1530.

Pearton, S. J., D. P. Norton, et al. (2004). "Recent advances in processing of ZnO." Journal of Vacuum Science and Technology B: Microelectronics and Nanometer Structures 22(3): 932-948.

Roy, S. and S. Basu (2002). "Improved zinc oxide film for gas sensor applications." Bulletin of Materials Science 25(6): 513-515.

Wang, P., N. Chen, et al. (2006). "p-type Zn 1− x Mg x O films with Sb doping by radio-frequency magnetron sputtering." Applied physics letters 89(20): 202102.

Zeng, Y., Z. Ye, et al. (2006). "Dopant source choice for formation of p-type ZnO: Li acceptor." Applied physics letters 88(6): 062107.

Zhang, S. B., S. H. Wei, et al. (2001). Phys. Lett. A 67: 075205.

Zhu, B. L., C. S. Xie, et al. (2005). "Investigation of gas sensitivity of Sb-doped ZnO nanoparticles." Materials Chemistry and Physics 89(1): 148-153.

CISET - 2nd Cilicia International Symposium on Engineering and Technology
10-12 October, 2019, Mersin / TURKEY

AN OVERVIEW OF TRAFFIC ACCIDENT IN TURKEY: STATISTICS OF 2018

İslam GÖKALP [*1], Volkan Emre UZ[2]

[1] AAT University of Science and Technology, Engineering Faculty, Civil Engineering, Adana, Turkey, islamgokalp@gmail.com

[2] AAT University of Science and Technology, Engineering Faculty, Civil Engineering, Adana, Turkey vemreuz@gmail.com

ABSTRACT
Traffic accidents are a set of events that affect millions of people all over the world, causing thousands of people to die and hundreds of thousands of people being injured. Traffic accidents not only cause losses in terms of human resources but also economic losses of billions of dollars. Although it has many factors, it has been revealed that the most basic factor causing traffic accidents is human. It is a known fact that the other basic factors include road geometric and structural characteristics and vehicle characteristics. However, these two non-human factors are the main factors that increase the severity of traffic accidents. When the statistics given in our country and the studies conducted in this field are examined, it can be easily seen that similar situations exist. In this study, the statistics of traffic accidents shared by Turkish Statistical Institute (TURKSTAT) for the year of 2018 are examined. In this way, it was aimed to make the main factors affecting the traffic accidents and the factors that affect the occurrence of it clear to emphasize the importance of this event which caused significant material and moral losses to our country in the light of the statistics of the year of 2018. At the same time, attract the attention of those who deal with such incidents in a traffic accident, it is in fact not just a number.

Keywords: *Traffic accident, statistics, awareness, annual report.*

[*] islamgokalp@gmail.com

1. INTRODUCTION

Transport is one of the basic human need. Transportation is a set of systems established to meet this need of human. It is a key element of not only human welfare but economic development. It may be provided with highway, railway, airway, seaway or others such as bicycle, motorcycle. Sometimes, especially for short distance, the transportation can be provided by walk or on foot (Özen et al. 2014). Among them, in Turkey, highway transportation is the most used one, with 95.2% and 76.1% for passengers and freight transportation, respectively (Keçeci, 2019). With the increase in population, the demand for transportation naturally raises and new roads are being built or rehabilitation of the existing ones to meet the demand. The new roads, too, cause an increase in the number of vehicles and people to go to traffic. With the increase in the number of vehicles on the roads and the number of people driving for different purposes, various problems arise. The most important of these problems is traffic accidents due to the negative impact on both human and economic resources (Gökalp, 2016).

Traffic accident is an internationally recognized problem causing loss of life and property. There are many causes of traffic accident. The general causes might be (1) a large increase in number of vehicles, (2) insufficient transport infrastructures and systems, (3) lack of traffic control systems, (4) lack of education for both local and non-local people. On the other hand, specific reasons also exist. There are (1) human include drivers, passengers, pedestrians, cyclist, etc. faults, (2) lack of geometrical and structural design of road, (3) climatic and environmental conditions, and (4) lack of vehicle design (Ansari, et al. 2010, Gökalp and Uz, 2017, Özen, 2018). Among all these reasons, the highest rate of human faults was reported by many authorities with about 90%.

According to the report published by World Health Organization (WHO), approximately 1.35 million people die, more than 20 million people injure each year. Traffic accidents also cause a major economic loss. The cost of traffic accident is estimated for most countries as 3% of their gross domestic product (WHO, 2019). The rate of occurrence of traffic accidents is quite low in developed countries compared to developing or non-developed ones. The rate is reported as about 7% that of occurred in the world.

Turkey is one of developing country, and traffic accident is one the major problem that must be coped with. Because, more than 1.3 million of traffic accident occurs every year and about 1.0 million of them are financially damaged whereas the rest of them are with fatal injuries. Moreover, the economic cost of it to the country is estimated to be about 40 billion Turkish Lira, approximately 5 billion USD dollars (Anonymous, 2019). Although traffic accident has many factors, it has been revealed that the most basic factor causing traffic accidents is human-based factors. The other basic factors include road geometric and structural characteristics and vehicle characteristics and these two non-human factors are the main factors that increase the severity of traffic accidents (Persson, 2008, Odero, et al. 2003). The statistics given for Turkey and the studies conducted on this task show that similar situations exist for the reason of traffic accident occurrence (TURKSTAT, 2019).

To make a clear observation about the reason of traffic accident, which occurred, it is necessary to evaluate the data shared by the competent authorities either in annual or decade base. In this study, the statistics of traffic accidents reported by Turkish Statistical Institute (TURKSTAT) for the year of 2018 were examined to make clear the main factors affecting the traffic accidents and the factors that affect the occurrence. And secondly it was aimed to emphasize the importance of traffic accident caused significant material and moral losses to Turkey in the light of the statistics of the year of 2018.

2. DATA EVALUATION

At the end of each year, the TURKSTAT shares statistical data under many headings with publicly accessible websites. In the scope of this study, the authors utilized the data shared for the traffic accident statistics for the year of 2018. The current study, in this respect, was prepared under (1) Population and vehicle statistics (2) number of traffic accidents and results, (3) people killed or injured in road traffic accidents by age groups, (4) faults causing road traffic accidents.

2.1. Population and Vehicle Statistics

The number of population of Turkey reached 82 million at the of the year of 2018. Looking for the year of 2002, the population was about 69 million. This means that approximately 20% of population has increased since 2002. Looking at the statistics of vehicles registered, it can be seen an incredible gap between the 2002 and 2018 numbers of vehicles. The number of registered vehicle is about 8.6 million in 2002, whereas the number of that of reaches about 22.9 million. As can be seen, there has been an increase of approximately 1.7 times (TURKSTAT, 2019). The types of vehicle are classified into eight group and the proportion in total is presented in the following table for the year of 2018.

Table 1. The types of vehicle for the year of 2018

Vehicles	Number of vehicle	Rate (%)
Car	12398190	54.22
Bus	218523	0.96
Minibus	487527	2.13
Truck	845462	3.70
Small Truck	3755580	16.42
Motorcycle	3211328	14.04
Other	1949311	8.53
Total	22865921	100

From Table 1, it is clear that the highest proportion of vehicles is the car, whereas the lowest is that of bus among the registered vehicles.

2.2. Number of Traffic Accidents and Results

In this part, the number of traffic accidents and the results of them in terms of killed and injured persons, and the rates of the accident occurred in the responsibility area of traffic police and gendarme that show the rate of accident in rural and urban are presented in Table 2.

Table 2. Traffic accidents statistics and results for 2018

Relevant Element	Number of Event	Rate (%)
Number of killed people	6675 (3368[1]/3307[2])	0.54
Number of injured people	307071	24.98
Responsibility area of traffic police	1184732 (4836[3]/249687[4])	96.37
Responsibility area of traffic police	44632 (1839[3]/57384[4])	3.63

[1] Number of killed people at accident scene
[2] Number of killed people at accident follow-up
[3] The number of killed people in relevant responsibility areas
[4] The number of injured people in relevant responsibility areas

Note for Table 2 that the rates are calculated with the number of relevant element divided by the number of accident in total which is 1229364.

It is obvious in table 2 that, traffic accident results with the considerable amount of killed and injured person. Although the mortality rate seemed to be low compared to the number of accidents, this result showed us that almost every accident ends with a death. The rate of accidents occurred are significantly on police-controlled roads, which means that most of accident were happened at urban areas. It can also be seen that there has been an increase or decrease in accidents caused by deaths and injuries due to the location.

Giving one more statistics about the type of the accident that not presented in Table 2 is worth indicating in this sub-title. This is the number of the accident involving materials loss and death and personal injury. 85% of total accident was recorded in the accident group of materials loss, and the rest is in that of death and personal injury.

2.3. People Killed or Injured in Road Traffic Accidents by Age Groups

This section of the current study shows us the tragedy of the traffic accident. With this section, the reality of the traffic accident will be more obvious. Since, almost all age groups of people are affected by traffic accidents. To make this situation clear, Table 3 was prepared for the year of 2018.

Table 3. People killed or injured in road traffic accidents by age groups for the year of 2018.

Age groups	Number of Killed	Rate (%)	Number of Injured	Rate (%)
0-9	309	4.64	23765	7.74
10-14	156	2.34	15524	5.05
15-17	200	2.99	16322	5.32
18-20	369	5.53	25995	8.46
21-24	490	7.34	32515	10.59
25-64	3771	56.49	172077	56.04
+65	1349	20.21	20031	6.53
Unknown	31	0.46	842	0.27
Total	6675	100	307071	100

The table 3 showed the fact of the traffic accident results on human life and health. The age groups from 0 to +65 are affected from this event. The statistics revealed that the age group of 25-64 are the most affected one by means of both killed and injured people. Following this, 21-24 and 18-20 are in order of the second and the third one that of affected by traffic accident. These three group constituted 70% of deaths and injurie people. Finally, the lowest rate after the unknowns remarked the 10-14 age group.

2.4. Faults Causing Road Traffic Accidents

By examining the records of 217898 among all of traffic accidents that occurred in 2018, the faults cause traffic accidents have been determined. Although, scholars have revealed that there are various type of faults causing the traffic accident and classified them as the faults based human, the defects of road, vehicle and harsh climatic and environmental conditions. The TURKSTAT did not take into consideration for evaluation. The faults are categorized by TURKSTAT into five group: (1) driver faults, (2) passenger faults, (3) pedestrian faults, (4) road defects, and (5) vehicle defects. The statistical information about them is given in Table 4.

Table 4. Faults causing road traffic accidents for the year of 2018.

Type of Faults	Number of Event	Rate (%)
Driver Faults	194928	89.46
Passenger Faults	1916	0.88
Pedestrian Faults	18394	8.44
Road Defects	1300	0.60
Vehicle Defects	1112	0.52
Total	217898	100

Almost all studies done on faults and/or defects causing road traffic accident implied that the human based faults are the major reason. They generally remarked the faults of driver, however, the other two elements of transportation system as given in Table 4, pedestrian and passenger, have a significant role on safety. For the case of Turkey due to the data of the year of 2018, 98.78% of faults causing traffic accident, is linked with human based faults. Although the other two defects are proportionally low, they are important in the formation of traffic accidents. Moreover, these are two important defects that determine the severity of the accident.

3. CONCLUSION

This study was established on the statistical data published by TURKSTAT for the year of 2018 about the traffic accident. In the scope of the paper, population and vehicle statistics, traffic accidents statistics and the results, people killed or injured in road traffic accidents by age groups, and finally faults causing road traffic accidents were examined. The objective was to attract the attention of people, who are likely to be exposed to such a situation, to highlight the fact that traffic accidents have important consequences and to ensure that these results are not only considered as figures. Since, traffic accidents are a set of events that can affect everyone, from infant to elderly.

The following remarks can be implied as a result of this study.

1. About 23 million of vehicle were registered and more than half of the registered vehicles was cars.
2. About 1.3 million of traffic accident were occurred throughout the year of 2018. More than 96% of them occurs where it is in the urban area.
3. As a results of traffic accident, 6675 people died, and more than 300 thousand ones injured.
4. Traffic accident is a phenomenon that affects people from all age segments of society. However, 25-64 is the age group most exposed to death and injury.
5. The humans based faults are the major factor causing traffic accident.

REFERENCES

Anonymous, (2019), https://www.itohaber.com, [Accessed 24 Sep 2019]

Ansari, S., Akhdar, F., Mandoorah, M., and Moutaery, K. (2000). Causes and effects of road traffic accidents in Saudi Arabia. *Public health*, Vol. 114 No. 1, pp.37-39.

Gökalp, İ. (2016), Laboratory investigation of the effects of aggregate's type, size and polishing level to skid resistance of surface coatings, Ms.C. Thesis, Adana Science and Technology University, Adana, Turkey.

Gökalp, İ., Uz, V. E., and Saltan, M. (2016). Testing the abrasion resistance of aggregates including by-products by using Micro Deval apparatus with different standard test methods. *Construction and Building Materials*, Vol.123, pp. 1-7.

Keçeci, A. (2019), http://www.mfa.gov.tr, [Accessed 24 Sep 2019]

Odero, W., Khayesi, M., and Heda, P. M. (2003). Road traffic injuries in Kenya: magnitude, causes and status of intervention. *Injury control and safety promotion*, Vol.10 No.1-2, pp.53-61.

Özen, E., Genc, E., and Kaya, Z. (2014). Estimation of the costs of traffic accidents in turkey: an evaluation in terms of the insurance and financial system. *Journal of Yasar University*, Vol. 9 No. 33. Pp. 5649-5673.

Özen, M. (2018). Trends in road traffic crashes in turkey, 1980-2016. *Ömer Halisdemir Üniversitesi Mühendislik Bilimleri Dergisi*, Vol. 7 No. 2, pp. 732-740.

Persson, A. (2008). Road traffic accidents in Ethiopia: magnitude, causes and possible interventions. *Advances in transportation studies*, Vol.15, pp. 5-16.

TURKSTAT, (2019), http://www.tuik.gov.tr/Start.do, [Accessed 10 Sep 2019]

Uz, V. E., and Gökalp, İ. (2017). The effect of aggregate type, size and polishing levels to skid resistance of chip seals. *Materials and Structures*, Vol.2 No. 50, pp. 1-14.

WHO, (2019), https://www.who.int/news-room/fact-sheets/detail/road-traffic-injuries, [Accessed 24 Sep 2019]

CISET - 2nd Cilicia International Symposium on Engineering and Technology
10-12 October, 2019, Mersin / TURKEY

THRESHOLDS FOR PAVEMENT SURFACE TEXTURE AND SKID RESISTANCE

İslam GÖKALP [*1], Volkan Emre UZ[2]

[1] AAT University of Science and Technology, Engineering Faculty, Civil Engineering, Adana, Turkey, islamgokalp@gmail.com

[2] AAT University of Science and Technology, Engineering Faculty, Civil Engineering, Adana, Turkey vemreuz@gmail.com

ABSTRACT
In this study, pavement surface properties in terms of skid resistance and surface texture were examined. These two properties are significantly important for road safety and comfort. Rather than comfort, the effects of these two properties on the safety element of pavement are emphasized. In this regard, the minimum criteria, in other words, the thresholds for these two parameters were searched in the light of technical specifications and earlier studies. Then, the thresholds for mentioned parameters are tried to be compared to that of recommended in Highways Technical Speciation of Turkey. Based on research, a general view was revealed that there are important shortcomings in defining minimum values, thresholds, for the road in service in our country's specifications. In this sense, some recommendations have been made as a result.

Keywords: *Pavement, Skid Resistance, Surface Texture, Macro Texture*

[*] islamgokalp@gmail.com

1. INTRODUCTION

Transportation is a key factor of not only human welfare but economic development. There are different types of mode of transportation including highway, railway, airway, seaway or others such as bicycle, motorcycle, pipelines etc. Walking is considered as one of the transportation mode that provided by foot. Moreover, telecommunications are also a kind of transportation systems that provide the "instantaneous" movement of information (Rodrigue, 2019; Özen et al. 2014).

Highway transportation is the most used mode among the mentioned ones in case of both passengers and freight transportation with 95.2% and 76.1%, respectively (Keçeci, 2019). An increase occurred in population, create a demand for transportation naturally and to meet the demand, new road infrastructure is being built, if deemed necessary and sufficient, existing ones can be rehabilitated. It is obvious that new roads networks generate its new demand and therefore the number of vehicles and people to go to traffic increases (Gökalp, 2016).

The increase in the number of vehicles on the roads and population causes various problems including administrative, operational and public problems. The most important of these problems is traffic accidents due to certain negative impacts. Traffic accident is an internationally recognized problem causing loss of life and property (Özen, 2018). According to World Health Organization, approximately 1.3 million people die, more than 20 million people injure every year. It also causes significant amount of economic loss. It is estimated for most countries about 3% of their gross domestic product (WHO, 2019). Therefore, traffic accident is one the major problem that must be coped with all around the world. For example, more than 1.3 million of traffic accident occurs every year and about 1.0 million of them are financially damaged and the rest of them are with fatal injuries in Turkey. Moreover, the economic cost of them is about 5 billion USD dollars (Anonymous, 2019).

There are many causes of traffic accident. These are as followings:

- Increase in number of vehicles,
- Insufficient transport infrastructures and systems,
- Lack of traffic control systems,
- Lack of education for both local and non-local people.
- Human based faults including those are drivers, passengers, pedestrians, cyclist.
- Lack of geometrical and structural design of road,
- Climatic and environmental conditions, and finally,
- Lack of vehicle design.

Although there are many factors linked with traffic accident, it has been revealed that the most basic factor causing traffic accidents is human-based factors. The rate more than 90% among all factors. The other factors mentioned before that as road geometric/structural characteristics and vehicle characteristics. These two non-human factors are the main factors that change the fate of the accident and the severity of losses in terms of people and property (Persson, 2008, Odero, et al. 2003).

In the scope of this paper, skid resistance and surface texture of road, which is one the road structural characteristics are examined based on traffic safety and conformability. Rather than comfortability, the effects of these two properties on the safety of pavement are concentrated. The main concern about them are the minimum criteria or threshold for bot skid resistance and surface texture are reviewed in the light of the earlier studies and guide book of the department of transportation, based on the specifications published by directorate of highways for the pavement in service.

2. THRESHOLDS FOR PAVEMENT SKID RESISTANCE

Skid resistance is referred to the friction force developed at the contact zone between tire and pavement (Mataei et al. 2016). Skid resistance is an important properties of road surface that is affected by numerous factors including texture, materials characteristics, climatic and environmental conditions, the compatibility of the works and procedures followed during the construction, rehabilitation and maintenance process to the technical standard. Skid resistance is mainly linked with micro-texture to produce good frictional resistance between the wheels and the pavement. The aggregate source directly affects the surface micro texture of pavement (Kanafi, et al. 2015). Polishing resistance of aggregate is taken into consideration while a new pavement construction, especially for wear courses. The aggregates that are first rough, then durable and tough or strength form better micro-texture, which creates surfaces with higher skid resistance. This is why the origin of aggregates is important.

There are numerous methods have been developed to assess surface texture of pavements. These methods can be grouped as portable/vehicle-mounted and static/dynamic, based on their operating and measuring principles, respectively. Dynamic Friction Tester, British Pendulum Tester and Locked-Wheel Skid Resistance Tester are only one of them used commonly (Saito et al. 1996).

The skidding resistance of the road surface, which is one of the most important parameters affecting the occurrence and severity of traffic accidents, is required to remain at a certain level both during the design phase of the road and throughout the service life of the road. Because the road surface with insufficient slip resistance causes traffic accidents due to slipping, especially on rainy days, and serious life and property losses may occur (Hall et al. 2009). It is possible to prevent a significant amount / level of slip-related traffic accidents, to determine the slip resistance of the road surface at the right time and in the right way, to perform maintenance and repair when necessary, or to re-construct where they are necessary.

To demonstrate the skip resistance performance of the pavement, to determine if it pose a risk to road safety, the minimum threshold values for the road pavement skid resistances were determined using different measuring tools. In general, minimum shear resistance thresholds are handled and used by highways administrations at two levels. These are called the **Investigatory** level and the **Intervention** level. For a road pavement with a shear

resistance value at investigatory level, regular monitoring of the road administration and the necessary preventive maintenance and repair are required. On the other hand, it is obligatory to take the necessary intervention by taking an active role in the maintenance and repair of the administration without wasting time for a road pavement with a shear resistance value at the intervention level (Fwa, 2017).

Different minimum thresholds for shear resistance have been proposed in different parts of the world, depending on both the standard test methods followed and the type of road and traffic level. The most typical example is the minimum criteria for airport pavement by the United States Department of Transportation. These are the skid resistance classification and threshold values that require for maintenance and repair planning and the expected from the newly constructed pavement (Please see, Table 1.) As can be seen that there are different thresholds were identified for different skid resistance tester/methods and for existence situation of the pavement surface. It can be said that a similar situation is observed for the road superstructure, but different values are generally proposed for different road classes with a similar device and method (Hall et al. 2001). An example of this is the values recommended by the United Kingdom (U.K.) transport department and defined depending on the class of the road (Please see, Table 2).

Table 1. Skid resistance thresholds for Airport pavement surfaces (White, 2018)

Speed		65 kph			95 kph	
Tester/Pavement Conditions	Minimum	Maintenance Planning	New Constructed	Minimum	Maintenance Planning	New Constructed
Mu meter	0.42	0.52	0.72	0.26	0.38	0.66
Dynatest	0.50	0.60	0.82	0.41	0.54	0.72
Skiddometer	0.50	0.60	0.82	0.34	0.47	0.74
Airport Skid Resistance Tester	0.50	0.60	0.82	0.34	0.47	0.74
Safegate Skid Resistance Tester	0.50	0.60	0.82	0.34	0.47	0.74
Finland Grip Tester	0.43	0.53	0.74	0.24	0.36	0.64
Tatre Skid Resistance Tester	0.48	0.57	0.76	0.42	0.52	0.67
Norsemeter Skid Resistance Tester	0.45	0.52	0.69	0.32	0.42	0.63

Table 2. UK road classes and shear resistance investigatory level thresholds (Hall et al. 2001)

Road Class	Investigatory level thresholds (50 km / h)							
	0.30	0.35	0.40	0.45	0.50	0.55	0.60	0.65
Motorway	X	X						
Double Lane Road	X	X	X					
Single Lane Road		X	X	X				
Approaches to small and large intersections, Approaches to roundabouts				X	X	X		
Approaches to pedestrian crossings and other high risk situations					X	X		
Roundabouts				X	X			
Sections with a slope of 5 to 10% longer than 50 m				X	X			
Sections longer than 50 m with a slope greater than 10%				X	X	X		
Bend radius <500 m - double lane road				X	X			
Bend radius <500 m - single lane road				X	X	X		

In addition to the situation given in Table 2, there will be seen differences in both road classification and skid resistance investigatory and intervention level values in different regions of the world. Some examples of studies for different regions, the recommended/defined intervention level values for skid resistance are given in Table 3. The information given in the table shows us the following fact.

Table 3. Intervention levels for skip resistance

Regions	Thresholds
Idaho	SN64S = 30
Kentucky	SN64R=28 (Interstate roads, motorways)
	SN64R=25 (Primary and secondary roads)
Texas	SN64R = 30 (Interstate roads, motorways)
	SN64R = 26 (Primary Roads)
	SN64R = 22 (Secondary Roads)
Ohio	SN64S = 32
	SN64R = 23
Maryland	SN64R = 30 (Undivided Roads)
	SN64R = 25 (Divided Roads)
New-Zealand	ESC = 0.30 (Highways)
England	CSC = 0.30 (low traffic highways)
	CSC = 0.35 (high traffic highways)

SN64R: Rough Wheel kph; SN64S: Smooth Wheel 64 km/s, ESC: SCRIM Equivalence coefficient, CSC: SCRIM characteristic coefficient.

1. The characteristic of the region is case that needed to be take into consideration. Since, the environmental and climatic conditions may not be the same for each.
2. The class of the road is important parameter to determine the thresholds. Because, the geometrical and structural characteristic of each road class are quite different from each other. Moreover, the traffic loads to which these roads are exposed and the traveling speeds of the vehicles passing over them are also different from each other.
3. Although the test method used and the velocity do not change, it should be taken into consideration in the changes in the measurement material used.

Many studies have been carried out on the determination of coating shear resistance thresholds other than those described above. These studies and the results obtained from these studies are listed in Table 4.

Table 4. Intervention levels for skip resistance

References	Thresholds
Runklend and Mahone (1977)	SN ≥ 30
Li et al. (2004)	SN ≥ 20
Mccullough and Hankins (1966)	SN ≥ 40
Wambold (1988)	SN ≥ 35, BPN ≥ 55
Bellopede et al. (2016).	DFT ≥ 0.30
TS EN 13036-4	54 ≥ BPN ≥ 24
Msallam et al. (2017).	45 ≥ BPN ≥ 65

The results in this chapter indicate that, the thresholds of skid resistance that increase the risk of traffic accident due to in adequate skid resistance level can vary based on the tester and the apparatus used for the same tester. The type of the pavement is also important parameter. As can be figured out that the airport pavement which is mostly constructed as rigid pavement s higher than that of the flexible pavement. The category of the pavement was also value important parameter for recommending any thresholds.

So what is the situation for our country? It is a complete mystery. The Highway Technical Specification Published by General Directorate of Highway of Turkey in 2013, that is last version, do not recommend any skid resistance performance limitations. This is really a tragic situation that the road administration should face. Although it does not have an official basis, it is a fact that managers / engineers who are aware of some of the above literature benefit from this information in the skid resistance performance evaluations. Accordingly, the decide on the reconstruction of the pavement or the improvement of the surface properties with a new layer or making the maintenance and repair.

3. THRESHOLDS FOR PAVEMENT SURFACE TEXTURE

The surface texture is significantly affect skid resistance performance during pavement lifetime span. It is basically classified into four branches depending on amplitude and/or wavelength. These are micro, macro, mega textures and unevenness or roughness. Micro-texture (with wavelengths less than or equal to 0.5 mm) which is a function of aggregate mineralogy and petrology and provides certain skid resistance at all speeds for dry and wet conditions thanks to ensuring direct wheel-pavement contact. Aggregates play an important role at the particle level in micro texture however, the size, shape, spacing and arrangement of them affect macro-texture (with wavelength from 0.5 mm to 50 mm). Macro texture provides not only quick drainage of water, but cause tyre noise over pavement surface due to the hysteresis component of the friction, particularly at high speed. The role of macro texture on the slip resistance of the coating is undeniable, although not as much as micro texture. Mega-texture (with wavelengths from 50 mm to 500 mm) describes irregularities of the road surface that may be revealed from pavement and it influences tyre/road contact that decisive on noise levels and skid resistance of the pavement. The last is unevenness or roughness (with wavelengths from 0.5 m to 50 m) is mostly be linked with faults at construction or maintenance/rehabilitation phase. It affects not only vehicle dynamics but ride quality, conformability. Therefore, all increase road and vehicle operating costs. In extreme cases, roughness can bring forth loss of contact of wheels with the surface and this raises the risk of traffic accident (Flintch, et al., 2003; Prowell and Hanson, 2005; Fisco and Sezen, 2013; Uz and Gökalp, 2017).

Likewise skid resistance measurement methods, there are many testers developed in basis of operating and measuring principles including portable/vehicle-mounted and static/dynamic. Volumetric measurement test methods, circular texture meter and vehicle mounted laser profilometer are used to evaluate texture depth of a road section (Flintch, et al., 2003).

It is generally accepted that skid resistance of pavement is controlled by the surface texture characteristics. As mentioned before that almost all texture type can be linked with skid resistance. In the scope of this study, the authors focused on macro texture depth measurement and the thresholds for it suggested or specified by scholars as well as by transportation agencies. In accordance with this perspective, literature was reviewed. The following tables (Table 5 and Table 6) are presented based on the studies and manual published the relationship between texture and accident rates.

Table 5. Recommended texture thresholds

References	Thresholds	
	SMTD	ETD
Roe, et al. (1991)	0.70	1.00
Cairney (2005)	0.40	0.70
Li et al. (2010)	0.40	0.70
Kuttesch (2004)	0.75	1.09
Chelliah et al. (2003)	0.63	0.97

SMTD: Sensor Measured Texture Depth
ETD: Estimated texture depth

Table 6. Class for texture depth and thresholds (Viner, et al 2006)

Class	Definition	Required Actions	Thresholds
1	No visible deformation	NR	> 1.1 mm
2	Some deterioration	Detailed investigations are not needed	0.8-1.1 mm
3	Moderate deterioration	Detailed investigation may be required depend on the data of condition parameters	0.4-0.8 mm
4	Severe deterioration	Intervention level of concern, which means that investigation should be carried out on each sections	< 0.4 mm

Table 5 and 6 showed that there exist different thresholds suggested by scholars and transport agency for different measurement methods, just like highlighted that of skid resistance. This is because of the selecting texturing method or establishing a threshold value for a friction related parameter that have to be taken into consideration numerous factors including climate, traffic, speed, geometry, materials etc. (Sanders and Brittain, 2014). Due to diversity conditions at individual project locations, it is not possible to offer a specific threshold.

Returning to the evaluation of this case for Tukey in basis of highway technical specification, there exist a threshold for the new road surface texture, which is 1.00 mm using sand patch methods. In practice, this test cannot be seen that use much. Instead, International Roughness Index values has accepted for criteria that used to make progress payments. It is also a shortcoming of the technical specification of Turkey, as fa as we know. Moreover, the typical used thresholds may not be available for every region of the country due to the mention factors. Therefore, it is imperative to identify a requirement based on not only different region, but also different instrument or test methods.

4. CONCLUSION

It was aimed with this study to figure out the importance of the two characteristics of pavement surface, skid resistance and surface texture (specifically macro texture) and the threshold for traffic safety in the light of extensive literature survey.

The following can be remarked at the end of this study that is there is important shortcoming in defining the thresholds for both characteristics. As a responsible public institution, General Directorate of Highway needs a certain revision in highway technical specification associated with this case. On basis of the country geographical situation, the author recommends that different minimum values should be determined based on many parameters mention in the text.

REFERENCES

Anonymous, (2019), https://www.itohaber.com, [Accessed 24 Sep 2019]

Bellopede, R., Marini, P., Karaca, Z., and Gökçe, M. V. (2016). Relationship between Slipperiness and Other Characteristics of Stones used as Flooring Slabs. *Journal of Materials in Civil Engineering*, Vol.28 No.8, 04016049.

Cairney, P. (2005). Road Surfacing Revisited–a new look at an old countermeasure. In Australasian Road Safety Research Policing Education Conference, 2005, Wellington, New Zealand.

Chelliah, T., Stephanos, P., Shah, M.G., and Smith, T. (2003). Developing a Design Policyto Improve Pavement Surface Characteristics. Presented at 82nd Transportation Research Board Annual Meeting, Washington, D.C

Fisco N. and Sezen, H. (2013) Comparison of surface macrotexture measurement methods, *Journal of Civil Engineering and Management, vol*. 19, pp. S153-S160.

Flintsch, G. Leon, E. de, McGhee, K. and AI-Qadi, I. (2003). Pavement surface macrotexture measurement and applications," Transportation Research Record: *Journal of the Transportation Research Board*, pp. 168-177,

Fwa, T. (2017). Skid resistance determination for pavement management and wet-weather road safety. *International journal of transportation science and technology*, Vol. 6 No. 3, pp. 217-227.

Gökalp, İ. (2016), Laboratory investigation of the effects of aggregate's type, size and polishing level to skid resistance of surface coatings, Ms.C. Thesis, Adana Science and Technology University, Adana, Turkey.

Hall, K. T., Correa, C. E., Carpenter, S. H., ve Elliot, R. P. (2001). Rehabilitation strategies for highway pavements. National Cooperative Highway Research Program, Web Document, 35.

Hall, J. W., Smith, K. L., Titus-Glover, L., Wambold, J. C., Yager, T. J., & Rado, Z. (2009). Guide for pavement

friction. Final Report for NCHRP Project, 1, 43.

Kanafi, M.M., Kuosmanen, A., Pellinen, T. K.,and Tuononen, A. J. (2015). Macro-and micro-texture evolution of road pavements and correlation with friction. *International Journal of Pavement Engineering*, 16(2), 168-179.

Keçeci, A. (2019), http://www.mfa.gov.tr, [Accessed 24 Sep 2019]

Kuttesch, J. S. (2004). Quantifying the relationship between skid resistance and wet weather accidents for Virginia data (Doctoral dissertation, Virginia Tech).

Li, S., Zhu, K., Noureldin, S., and Daehyeon, K. (2004). Pavement Surface Friction Test Using Standard Smooth Tire: The Indiana Experience. Paper presented at the TRB 83rd Annual Meeting, Washington, D.C

Li, H., Tang, B., Shao, D., Li, M., & Gao, J. (2010). Impact of Macro-texture Depth and Its Variation on Safety on Rainy Days. In ICCTP 2010: Integrated Transportation Systems: Green, Intelligent, Reliable pp. 484-495.

Mataei, B., Zakeri, H., Zahedi, M., and Nejad, F. M. (2016). Pavement friction and skid resistance measurement methods: a literature review. *Open J. Civ. Eng,Vol.* 6 No.4, pp.537-565.

Mccullough, B. F., and Hankins, K. D. (1966). A Study of Factors Affecting the Operation of a Locked Wheel Skid Trailer

Odero, W., Khayesi, M., and Heda, P. M. (2003). Road traffic injuries in Kenya: magnitude, causes and status of intervention. *Injury control and safety promotion*, Vol.10 No.1-2, pp.53-61.

Özen, E., Genc, E., and Kaya, Z. (2014). Estimation of the costs of traffic accidents in turkey: an evaluation in terms of the insurance and financial system. *Journal of Yasar University*, Vol. 9 No. 33. Pp. 5649-5673.

Özen, M. (2018). Trends in road traffic crashes in turkey, 1980-2016. *Ömer Halisdemir Üniversitesi Mühendislik Bilimleri Dergisi*, Vol. 7 No. 2, pp. 732-740.

Persson, A. (2008). Road traffic accidents in Ethiopia: magnitude, causes and possible interventions. *Advances in transportation studies*, Vol.15, pp. 5-16.

Prowell, B. and Hanson, D. (2005). Evaluation of circular texture meter for measuring surface texture of pavements, Transportation Research Record: *Journal of the Transportation Research Board*, pp. 88-96, 2005.

Rodrigue, JP. (2019). https://transportgeography.org. [Accessed 25 Sep 2019]

Roe, P. G., Webster, D. C., & West, G. (1991). The relation between the surface texture of roads and accidents, Transport and Road Research Laboratory (TRRL), Wokingham, Berkshire, United Kingdom

Runkle, S. N., and Mahone, D. C. (1977). Critique of Tentative Skid-Resistance Guidelines. Paper presented at the Transportation Research Board Washington, D.C.

Saito, K., Horiguchi, T., Kasahara, A., Abe, H., and Henry, J. J. (1996). Development of portable tester for measuring skid resistance and its speed dependency on pavement surfaces. *Transportation research record*, vol.1536 No.1. pp. 45-51.

Sanders, P.D. and Brittain, S. (2014), Surface treatment options for concrete roads, Published Project Report: PPR677, Transportation Research Laboratory, Wokingham, Berkshire United Kingdom.

TS EN 13036-4. (2014). Road and airfield surface Characteristics-Test Methods - Part 4: Method for measurement of slip/skid resistance of a surface: The pendulum test

Uz, V. E., and Gökalp, İ. (2017). The effect of aggregate type, size and polishing levels to skid resistance of chip seals. *Materials and Structures*, Vol.2 No. 50, pp. 1-14.
Wambold, J. C. (1988). Road characteristics and skid testing. *Transportation Research Record* (1196).

WHO, (2019), https://www.who.int/news-room/fact-sheets/detail/road-traffic-injuries, [Accessed 24 Sep 2019]

White, G. (2018). State of the art: Asphalt for airport pavement surfacing. *International Journal of Pavement Research and Technology*, Vol. 11 No.1, 77-98.

Viner, H., Abbott, P., Dunford, A., Dhillon, N., Parsley, L., & Read, C. (2006). Surface texture measurement on local roads. Published Project Report PPR148, TRL Limited, August.

CISET - 2nd Cilicia International Symposium on Engineering and Technology
10-12 October, 2019, Mersin / TURKEY

HERAKLEIA KARIA ANCIENT PORT CITY with GEOHERITAGE AREAS and URBAN GEOLOGY-LATMOS GEOPARK (BEŞPARMAK MOUNTAINS)

Aziz Cumhur KOCALAR*[1]

[1] Niğde Ömer Halisdemir University, Architecture Faculty, City and Regional Planning, Turkey,
azizcumhurkocalar@gmail.com

ABSTRACT

LATMOS (mountain range), which is a geopark, is located near Lake Bafa Nature Park on the border of Aydın and Muğla. The region has a history dating back to 500 million years and valuable natural, archaeological and geological heritage sites. In this study, the geomorphological structure of the region is examined in general terms, especially in terms of geotourism has quite interesting features. The elevations at the end point of the Büyük Menderes Basin reach up to 1900 m and have an important geostrategically important and wide viewing area. These mountains, which were considered sacred especially in the Carian period in history, have always been in an important position in terms of culture. The presence of traces of rock settlements dating to the Neolithic period in the mountains is also known today. Scattered rock paintings in the region were the most important finds. However, they have survived to the present day by being damaged. These and similar rock churches and monasteries, as well as military castles and walls, leaving many distinctive and interesting cultural traces, these mountainous areas, which are constantly inhabited, are expected to be preserved and renewed. In history, there are other ruins of the Carian State, which spread to a much larger background in the lower Aegean. The port city of Herakleia (now Kapıkırı village) is located on the shores of Lake Bafa. Massive rock formations that have undergone metamorphic changes in the process are in need of investigation in many aspects of volcanic, magnetic and mineralogical aspects. These rocks also have qualities that can be salty due to their relationship with the sea. In summary, this region is composed of mountain ranges and valleys that have an important natural park feature ans, archelogical site features also geopark for (Latmos Mountains); In addition to its interesting natural structure, rock formations and geoheritage areas, it is protected with the awareness of geotourism. It should not be forgotten that in order to transfer the traces of many different cultural settlements within the rocks to the next generations in a healthy way, the region is obliged to be carefully protected with educational, and etc. tourism as well as a conservation aimmed development plan.

Keywords: *Geopark of Latmos, Urban Geology, Geoheritage-Geotourism, Urban Geography, Cultural Heritage Conservation, City and Regional Planning*.

* Corresponding Author

1. INTRODUCTION

The aim of this study was to explore the rural development planning approaches towards geotourism potential in Turkey. The structure of geotourism makes a discussion for the possible effects on the processes of Turkey's rural development. Also, theorical approaches are cited in the inter-disciplinary areas (tourism, public management, planning, art history, etc.) about subject.

2. TOURISM FOR RURAL DEVELOPMENT

The starting point of sustainability objectives in ecological approaches are increasing with interest in the development of interdisciplinary researches of alternative-tourism related subjects. Tourism alternatives for rural economy and/or rural development can research with different dimensions. Rural legislation is also covered here.

2.1. Alternative Tourism

One of them is eco-tourism for rural development, especially cittaslow movement is interesting with festivals. Geotourism also another alternative for rural economy and/or rural development.

2.1.1. Eco-tourism and Cittaslow

Eco-tourism trends are accelerating in the world. Turkey can be created in rural development with Eco-tourism opportunities. But building pressure in rural sites with new generations also critical reason, new generations need jobs. If they are not be able to job, are migrate to big cities.

Cittaslow movement, pioneered by settlements such as Seferihisar-Izmir, draws attention to domestic products and has various potentials for eco-tourism and rural development (Bostancı, 2017).

"Developing a 'One Village-One Product (OVOP)' in Model for the Rural Economy Diversification and Intensification Program in the Final Report of the Eastern Black Sea Regional Development Plan (DOKAP) prepared by the Japanese International Cooperation Agency (JICA) in 2000 was proposed in order to have various fruits and increase the production in general by the Harşit Stream" (JICA, 2000; Yücer, 2016). Turkey also partially initiated at the local OVOP Project as Table 1 at below.

Table 1. Some sample villages and products for Cityslow OVOP practice in Turkey. (Yücer, 2016).

Year	City	Place	Products
2002	Giresun	Espiye/ İbrahimşeyh	mandarin and fruit growing.
2003	Tokat	Villages	sour cherry, walnut, peach, vegetables.
2007	Hakkari	Villages	walnut, vegetables, rugs.
2007	Kütahya	Simav Villages	fruit and vegetables

The Governorship Special Administrative Directorates and the Provincial Directorate of Agriculture were supporting with the institutions of these OVOP projects.

In the other oppurtunity for special rural areas that characterized with geotourism (geosite, geomorphocyte, geopark, geotope), are staying current conditions.

2.1.2. Geo-tourism

The initiatives of the local and/or central authorities have just stayed for tourism and the adoption of sustainability of stakeholders that owners of alternatives tourism ideas not yet been achieved in geotourism.

So geotourism can also be supported by international funding but need to coordination with national authorities again (Fig. 1).

Fig. 1. Latmos Geopark and Bafa Lake views.

2.2. Legislation

Legislation changed in last years for village management subjects. There are some critical points for the future in rural lands. This legislation is also covered below:

"Current discussion in rural development: in 2012, arrangements made with the Law No. 6360, expanding the municipal boundaries of cities in 30 provinces (these are metropolitan municipalities), changes the statue of villages to neighborhoods" (Albayrak; Eryılmaz, 2018).

The characteristics of rural settlements in the metropolitan areas are affected with these changed. These rural areas must be protected in the future.

3. HISTORICAL-NATURAL-CULTURAL STRUCTURE AND ALSO GEOLOGICAL AREAS-"LATMOS GEOPARK"

Recommended as "Latmos Geopark", the region on the shores of Bafa Lake Nature Park on the border of Aydın and Muğla is interesting with its geological history dating back 500 million years.

The geomorphological structure of the region, which has been studied in the mountainous areas and valleys, has quite different features especially in terms of geo-tourism like figures (Fig. 1, 2, 3, 4).

Fig. 2. Latmos Geopark and Bafa Lake connections.

Massive masses undergoing metamorphic changes in the process are expected to be investigated from a mineralogical and petrographical point of view. Located in the Büyük Menderes Basin, Latmos Mountain (wheel shaped at the top of it) is dominated by a wide range of elevations with elevations reaching 1375 meters.

It is understood from the historical structures of the Karia king, which is unearthed as well as the fortress and city walls where the mountains are geostrategically important in history.

3.1. The fortress city of Herakleia (Kapıkırı Village) and Urban Geology

The fortress city of Herakleia (Kapıkırı village), which is the dominant city and the coast and sea as an end port city on the borders of the Aegean Sea, has been on the shore of the lake today.

This region, which is located on the Aegean Sea borders of Caria State, which has been spread to a wide background in the lower Aegean, is an end port city. In the ancient period, the port city of Herakleia (Kapıkırı village) is a fortress-type city which is dominated by the shore and the sea (Fig. 3). Today, the city is on the shore of the lake.

Fig. 3. Herakleia findings (Kapıkırı village).

The cultivated areas like as Kapıkırı, transforming year by year for residences and/or summer houses, etc. against the rural development with conservation. (Kocalar, 2018a).

3.2. Traces of Rock Settlements and Rock Paintings (Art History)

In addition, traces of rock settlements dating to the Neolithic period were also found at different points of the area and the pictures scattered in the region were the most important findings. However, they have been damaged by external influences and vandalism.

It should not be forgotten that the skirts of the mountainous area where the ancient city and the scattered rock paintings are located, must be carefully protected together with the conservation aimed development plan.

It is of great importance that the lake is prevented from pollution. On the large scale it is necessary to complete the Büyük Menderes Basin Plan, and that it provides a unity with the conservation aimed development plan. Lastly, a holistic protection consciousness should be created in the area.

3.3. Natural Park Features

Besides, the Natural Park is suitable for use with its status and area management, while preserving its natural thresholds (Kocalar, 2018b).

In order to be able to convey the traces of many different cultural settlements within the rocks to the next generations in a healthy way, the priority should be given to the evaluation of the region for purposes of natural history education and through alternative tourism functions.

Area; Because of its natural structure, rock formations and geo-heritage areas, it must be protected within the framework of geo-tourism awareness.

3.4. Geotourism Potential in Geoheritage Areas in Latmos Mountains

These mountainous geological-archaeological sites, which have witnessed permanent settlements with their rock churches and monasteries as well as their military and commercial structures and with many distinct and interesting cultural traces, should be carefully preserved and renewed in tourism. Latmos Mountains are very near Lake at below (Fig. 4).

Fig. 4. Latmos Mountains and Bafa Lake.

5. CONCLUSION

Geo-tourism is important for this site research in the rural development of Turkey. Geological values discussed with other values in the selected site where is Latmos Mountains in the near of Bafa Lake.

Latmos Mountains and walleys are also very special natural area as geological and other cumulative characteristics in historical, archelogical, cultural, architectural, natural, sport, and educational and geotourism.

The main feature of this kind of study is to develop a marked area from the original values of special geological and natural also rural areas. Also, to determine the deterioration of the characteristics of these areas.

The most critical issue for Turkey is the villages which turned into neighborhoods by the new metropolitan law. These kinds of special lands must be protected and also can't be converted into second homes.

The cultivated areas like as Kapıkırı, transforming year by year for residences and/or summer houses, etc. against the rural development with conservation.

Additional researches should increase the database and methodological approaches to develop the theoretical and practical bases at the national level in geological sites. Local efforts should be given priority in the design and implementation of initiatives in the world for these types of sites.

ACKNOWLEDGEMENTS

Thanks for project partners that's named "Archaeological-Natural-Geological-Historical-Cultural Environment (Rivers-Basins-Lakes) Conservation Issues and Solution Proposals: "Bafa Lake Natural Park""

REFERENCES

2012 dated and Law No. 6360, *Legal Arrangements*.

Albayrak, A.N., and Eryılmaz, Y. (2018). "From Rural to Urban: Transformation of Villages at the Border of Metropolitan Cities", *CAUMME 2018: Conference of Architecture and Urbanism in the Mediterranean and the Middle East Proceedings*. Ed., Girginkaya Akdağ, S.; Soygeniş, S.; Vatan, M., Bahçeşehir University, İstanbul.

Bostancı, S.H. (2017). *Sustainable Urban Model Approaches of Local Governments in Turkey*. Management & Education/Upravlenie i Obrazovanie, 13.

JICA, Japonya Uluslararası İşbirliği Ajansı, (2000). Doğu Karadeniz Bölgesel Gelişme Planı Nihai Raporu, TC Başbakanlık Devlet Planlama Teşkilatı Yayını, Ankara.

Kocalar, Aziz Cumhur, (2018a). "Historical Environment Conservation Issues: (Karia Period) "Herakleia-Latmos"", *International Journal of Social Humanities Sciences Research (JSHSR)*, (Jshsr.com), 2018 Vol: 5 / Issue: 19 pp.654-662.

Kocalar, Aziz Cumhur. (2018b). "Archaeological-Natural-Geological-Historical-Cultural Environment (Rivers-Basins-Lakes) Conservation Issues and Solution Proposals: "Bafa Lake Natural Park", *Mimarlık, Planlama ve Tasarım Alanında Yenilikçi Yaklaşımlar*, L.G. Kaya, Ş.A. Dönmez, N. Abbasov Ed. Gece Kitaplığı Yayınevi, ISBN 978-605-288-796-7, 15. Chapter, S: 215-248.

Yücer, A.A. (2016). "Kırsal Kalkınma için Bir Köy Bir Ürün Projeleri ve Başarı Koşulları", *XII. Ulusal Tarım Ekonomisi Kongresi*,
https://www.nationmaster.com/country-info/stats/Agriculture [Accessed 26 Sept 2019].

CISET - 2nd Cilicia International Symposium on Engineering and Technology
10-12 October, 2019, Mersin / TURKEY

ESTIMATION OF VOLTAGE STABILITY IN POWER SYSTEMS USING ARTIFICIAL NEURAL NETWORKS

Hakan Açıkgöz*[1], İlhami Poyraz[2], Resul Çöteli[3] and Beşir Dandil[4]

[1]Kilis 7 Aralık University, Vocational School of Technical Sciences, Department of Electricity and Energy, Kilis, Turkey, e-mail: hakanacikgoz@kilis.edu.tr

[1]Dicle University, Vocational School of Technical Sciences, Department of Electricity and Energy, Diyarbakır, Turkey, e-mail: ilhami.poyraz@dicle.edu.tr

[3]Fırat University, Faculty of Technology, Department of Energy Systems Engineering, Elazığ, Turkey, e-mail: rcoteli@firat.edu.tr

[4]Fırat University, Faculty of Technology, Department of Mechatronics Engineering, Elazığ, Turkey, e-mail: bdandil@firat.edu.tr

ABSTRACT

For economic reasons, energy systems are operated within the limits of maximum load ability, and as a result, systems are more likely to be exposed to voltage sags. In this study, Line Stability Index (LSI), which is a measure of voltage stability in power systems, is estimated with the help of Artificial Neural Networks (ANN). For this purpose, IEEE 3-bus power system model is built in Matlab environment. The parameters of oscillation and production busbars are kept constant while obtaining LSI value. Active and reactive powers of the load busbar are increased by 0.05 unit value (pu). A total of 81 units are obtained from each; the phase angle of the production bus, the phase angle of the load busbar and the amplitude of the voltage of the load busbar. 81 LSI values obtained from IEEE 3-bus power system model parameter values are estimated by using multi-layer ANN. The input parameters of ANN are active power of the busbar, reactive power, amplitude-phase angle of the voltage and the phase angle of the production busbar. The output parameter of ANN is LSI values. From the obtained results, it has been seen that the ANN predicts the LSI with a very high performance in determining the voltage stability in IEEE 3-bus power systems.

Keywords: *Voltage Stability, Artificial Neural Networks, Line Stability Index*

* Corresponding Author

1. INTRODUCTION

Electrical energy is the most widely used type of energy today. Energy power system planners have to do all kinds of research and development for minimum cost, consumption and saving. Energy power systems are nonlinear systems operating under ever-changing conditions. In recent years, economic and environmental conditions have made it necessary to operate under the most efficient operating conditions of power systems and near operating limits. Depending on this; Voltage stability analysis, which is a nonlinear, time-varying and dynamic phenomenon, is an important criterion in the operation of power systems (Gao, et al, 1996; Kundur, 1994; Chakrabarti et al. 2010).

Voltage stability is the ability of a power system to maintain the balance between the load demand and the power generated and transmitted to the load center. The more accurate and faster the prediction of the voltage stability limit, the more accurately and faster the system operator starts the necessary control actions. There are generally two important points in voltage stability studies. The first is the assessment of voltage stability and the other is the analysis of voltage instability mechanisms. Conventional methods used to evaluate voltage stability are active power-voltage (PV) and active power-voltage (QV) curves and node analysis methods. However, in recent years, several methods have been proposed to examine the voltage stability. Many methods have been proposed in the literature to determine the voltage sag (Ramaswamy and Nayar, 2004; Saxena and Sharma, 2016; Sharma, et al. 2016; Sharma, et al. 2018; Yazdanpanah-Goharrizi and Asghari, 2007; Konar et al. 2015; Jeyasurya, 1994; Açıkgöz et al, 2019; Ahmad et al. 2004).

In this study, in an IEEE 3-bus power system, the Line Stability Index (LSI) is estimated for different load conditions using a feedforward forward propagated neural network. The power flow model is used for IEEE 3-bus power system and LSI values ware obtained by Newton Raphson method. Then, the LSI values obtained by several parameters are estimated using a multilayer Artificial Neural Network (ANN). It is aimed to estimate LSI values with ANN. In addition, the predictive performance of ANNs are examined by changing the number of cells in the hidden layer and the results obtained from ANNs with different number of intermediate cells are given.

2. VOLTAGE STABILITY

Modern power systems are highly planned, multivariable, dynamic systems. Voltage stability is actually the ability of the power system to maintain system variables in an acceptable balance after exposure to a distortion within a wide area, no matter how small or large it is. Voltage instability includes a wide range of events occurring in the system; there are different opinions for voltage stability (Kundur, 1994; Açıkgöz et al, 2019). According to the Institute of Electrical and Electronics Engineers (IEEE), voltage stability is the ability of a system to maintain its voltage.

As in Figure 1, the whole system is reduced to two busbars. In Fig. 1; busbar-1 is chosen as oscillation and busbar-2 is chosen as load busbar. In addition, V1; the voltage of the oscillating busbar, V2; the voltage of the load busbar, P1; the active power of the oscillating busbar, Q1; the reactive power of the oscillation bus, P2; active power of the load busbar, Q2; reactive power of the load busbar, S1; the apparent power of the oscillating busbar, S2; apparent power of the load busbar, I; line current, θ; phase angle of oscillation bus, δ; phase angle of the load busbar.

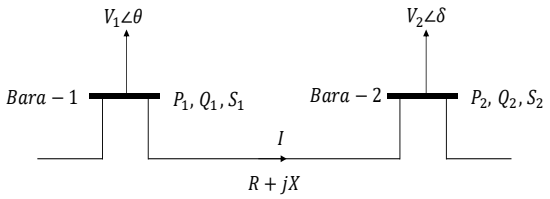

Fig. 1. Two busbar power system model

The Voltage Stability Indexes (VSI) are provided important information about the voltage collapse in a power system. These indices can be used for a weak bus or weak line identification, or can be used to evaluate the voltage stability limits of a system (Ramaswamy and Nayar, 2004; Saxena and Sharma, 2016; Sharma, et al. 2016). LSI is formulated according to the equation in (1) based on a power transmission concept in a single line.

$$LSI = \frac{4XQ_j}{\left[V_i \sin(\theta-\delta)\right]^2} \quad (1)$$

Here; X is the reactance of the line, Q_j is the final receiver reactive power, V_i is the first transmitter voltage, θ is the last receiver reactive power, and δ is the angle difference between the supply voltage and the receiver voltage. The value of the LSI should be less than 1 to protect the voltage stable system.

3. ARTIFICIAL NEURAL NETWORKS

ANN is a parallel distributed processor that can store experimental information and has a feature that makes it suitable for use. ANN is similar to the human brain in that the information is acquired by the network with the help of a learning process and that this information is stored by synaptic weights. The ANN can learn the relationship between the parameters that are controlled or not controlled by input data and the input parameters without the need for detailed information about the system. Another advantage of ANN is its ability to cope with complex and large systems with much unrelated parameters (Öztemel, 2003; Saxena and Sharma, 2016; Sharma and Saxena, 2016).

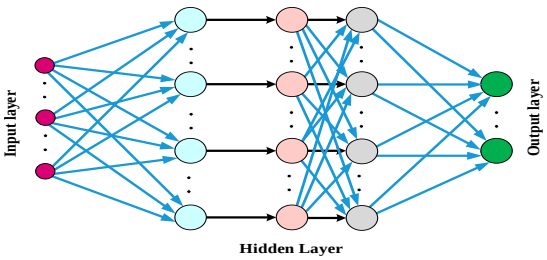

Fig. 2. ANN structure

Figure 2 schematically illustrates the multilayer

feedback feed-back network used in this study. As can be seen from the Fig. 2, a neural network consists of three layers such the input, hidden and output layers. Using the inputs given to the input of the neural network, the output of the network is calculated forward (Öztemel, 2003; Saxena and Sharma, 2016; Sharma and Saxena, 2016). The feedforward network sends signals from the input layer to the output layer via the intermediate layer.

$$Y_k^i = X_k \tag{1}$$

Where, X_k is the k*th* processing element in the input layer. X_k^i is the output of the k*th* processing element. Each process element in the hidden layer receives information from all process elements in the input layer under the influence of the link weights. For an ANN with a single hidden layer, the net input to the processing element in the intermediate layer can be calculated as follows.

$$NET_j^a = \sum_{k=1}^{n} A_j^k Y_k^i + b_j \tag{2}$$

A_j^k denotes the weighting function connecting the k*th* input layer element to j*th* hidden layer and b_j indicates the biases. The connection weights of the feedforward network are derived from the input and output examples in the training dataset by applying the general delta rule .The output of the j*th* hidden layer element is calculated as follows:

$$Y_k^i = f\left(NET_a^j\right) \tag{3}$$

The net output of ANN is given below:

$$o_i = \beta_i \times Y_k^i \tag{4}$$

Where, β_i are the weight values that connect the hidden layer to the output. The error occurring for the m*th* processing element in the output layer is as follows:

$$E_m = B_m - Y_m \tag{5}$$

Here, Y_m and B_m are the outputs produced by the network and the expected outputs of the network for the input given to the network, respectively. The Total Error (TE) for the output layer can be expressed as follows:

$$TE = \frac{1}{2}\sum_m \left(E_m\right)^2 \tag{6}$$

The most effective and popular learning algorithm in ANN is back propagation algorithm. This algorithm is a slope reduction algorithm and aims to improve the performance of the network by changing weights with slope. Back propagation training is initially done by assigning random values to weights on all nodes. The training data is always shown to the network and the activation function is calculated for each node. The training data is always sent to the network and the activation function is calculated for each node. The change of weight in the t*th* iteration is as follows:

$$\Delta A_{jm}^a\left(t\right) = \lambda \delta_m Y_j^a + \alpha \Delta A_{jm}^a\left(t-1\right) \tag{7}$$

Where, λ is the learning coefficient, α is the momentum coefficient, δ_m is indicates the error of the m*th* output unit. The error of the m*th* output unit can be expressed as:

$$\delta_m = Y_m\left(1-Y_m\right) - E_m \tag{8}$$

4. SIMULATION RESULTS

In this study, LSI which is a criterion of voltage stability in power systems is estimated by ANN. For this purpose, IEEE 3-bus power system model is built in Matlab environment. The IEEE 3-bus power system model is shown in Fig. 3 and the parameters of this model are given in Table I and busbar variables in Table II. The busbars 1, 2 and 3 shown in Fig. 3 are selected as load bus (PQ bus), production bus (PV bus) and oscillation bus respectively.

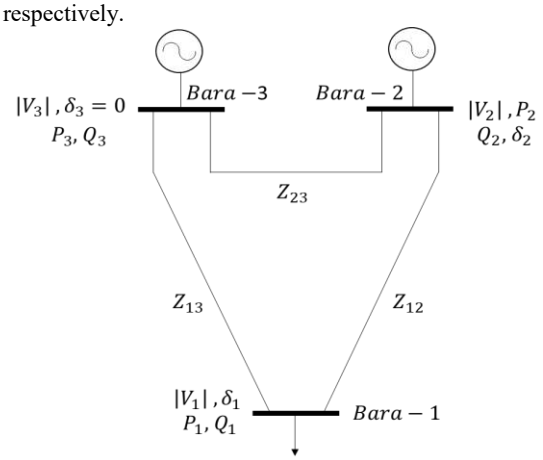

Fig. 3. IEEE 3-bus power system

Table 1. Parameters of IEEE 3-busbar power system Model

BN	P (pu)	Q (pu)	V (pu)	δ (pu)	Z (pu)
1	5	1			Z_{12}=0.0047+j0.474
2	2		1.05		Z_{13}=0.062+j0.6332
3			1	0	Z_{23}=0.0047+j0.474

Table 2. Bus Variables in IEEE 3-Busbar Power System

BN	Control Variables	State Variables	Number of Busbar
1	P_1, Q_1	$\|V_1\|, \delta_1$	1
2	$P_2, \|V_2\|$ $Q_{2min} \le Q_2 \le Q_{2max}$	Q_2, δ_2	1
3	$\|V_2\|, \delta_2$	P_2, Q_2	1

In Tables I and II; P_1; active power of the load busbar, Q_1; reactive power of the load busbar, $|V_1|$; the amplitude of the voltage of the load busbar, δ_1; phase angle of the load busbar, P_2; active power of the production busbar, Q_2; reactive power of the production busbar, $|V_2|$; the amplitude of the voltage of the production bus, δ_2; The phase angle of the production bus is the impedance of the lines between the busbars Z_{12}, Z_{13} and Z_{23}. The power flow model of IEEE 3-bus power system created in Matlab is used in this study and LSI values are obtained by Newton Raphson method. Table III shows some HCM values obtained according to the variable power values of the load busbar. The validity performance of the ANN structures is shown in Fig. 4.

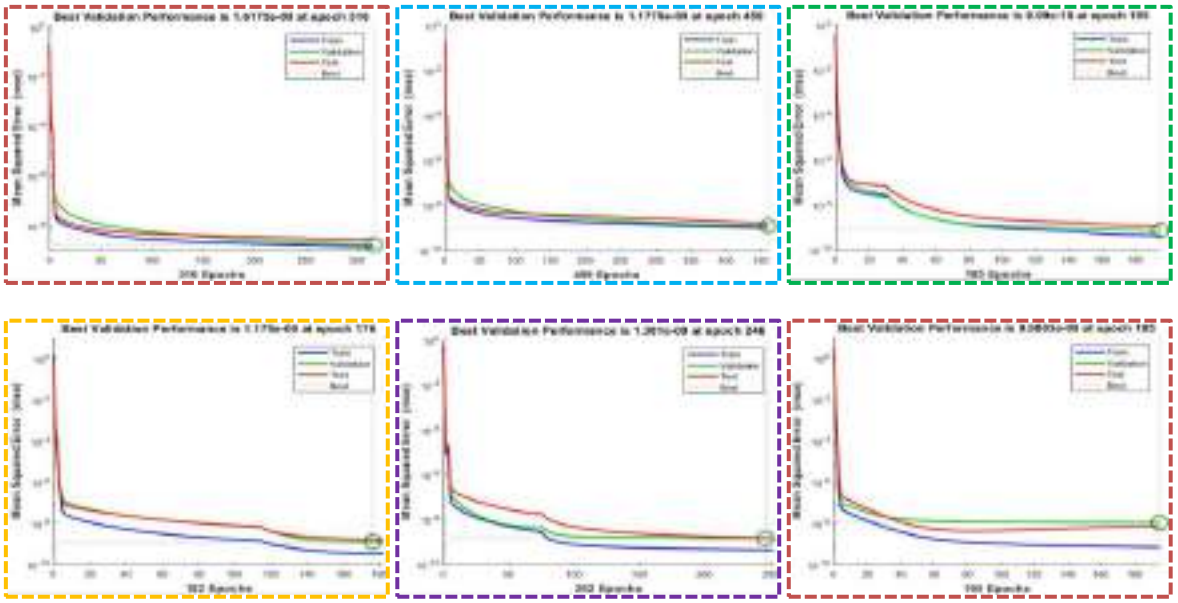

Fig. 4. Performance Graphics of ANN Structures

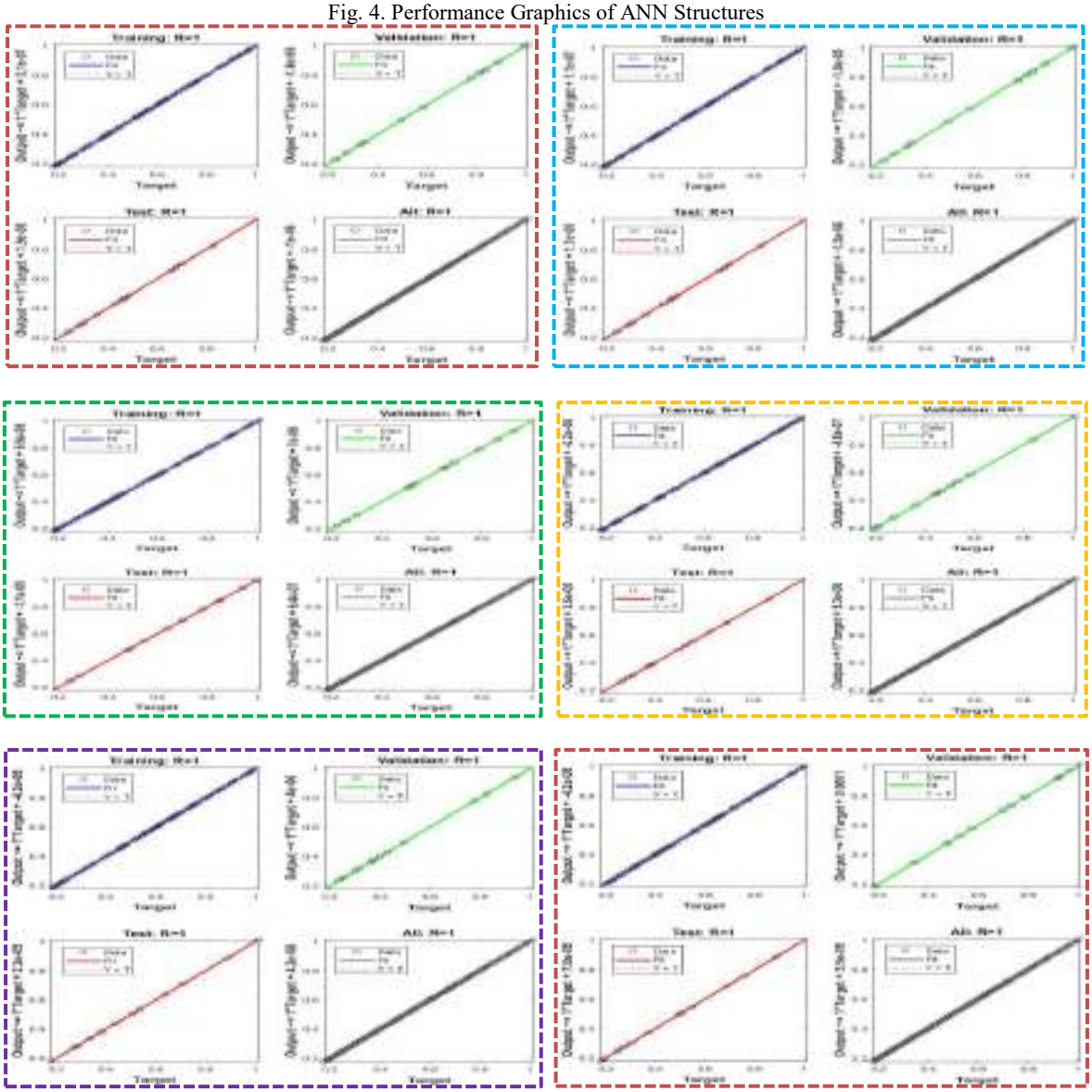

Fig. 5. Regression graphs of different ANN structures

Table 3. LSI values for different variables

P_1	Q_1	δ_2	δ_1	$\lvert V_1 \rvert$	LSI
5.00	1.00	2.0665	8.7873	0.9781	0.1734
5.05	1.05	2.1240	8.9053	0.9763	0.1822
5.10	1.10	2.1817	9.0239	0.9745	0.1910
5.15	1.15	2.2396	9.1430	0.9727	0.1998
5.20	1.20	2.2975	9.2625	0.9708	0.2086
7.90	3.90	5.6946	16.7983	0.8501	0.7321
7.95	3.95	5.7646	16.9678	0.8473	0.7433
8.00	4.00	5.835	17.1393	0.8444	0.7547
8.05	4.05	5.9057	17.3123	0.8415	0.7662
8.10	4.10	5.9768	17.4872	0.8386	0.7778
6.85	2.85	4.2982	13.5543	0.9032	0.5130
6.90	2.90	4.3620	13.6974	0.9009	0.5228
6.95	2.95	4.4261	13.8414	0.8986	0.5327
7.00	3.00	4.4904	13.9866	0.8962	0.5426
7.05	3.05	4.5549	14.1326	0.8938	0.5526
7.40	3.40	5.0139	15.1855	0.8767	0.6240
7.45	3.45	5.0805	15.3405	0.8742	0.6345
7.50	3.50	5.1475	15.4969	0.8716	0.6450
7.60	3.6	5.2823	15.8137	0.8664	0.6663
8.80	4.80	7.0235	20.1709	0.7933	0.9540
8.85	4.85	7.1027	20.3836	0.7897	0.9678
8.90	4.9	7.1826	20.5997	0.786	0.9819
8.95	4.95	7.2632	20.8196	0.7822	0.9962
9.00	5.00	7.3447	21.0433	0.7784	1.0107

Table 4. Parameters of ANN structures

	Hidden Layer	Fault tolerance	Learning Coefficient	Learning Rule	Iteration Number
1	10	1e-10	0.1	LM	1000
2	10	1e-10	0.5	LM	1000
3	20	1e-10	0.1	LM	1000
4	20	1e-10	0.5	LM	1000
5	30	1e-10	0.1	LM	1000
6	30	1e-10	0.5	LM	1000

The validation performance is used to measure the generalization of the network and to stop the training of the network if the generalization reaches the desired value. Test performance has no impact on the training of the network and therefore, it provides an independent measure of network performance during and after the training of the network. The reason why each validity is different in performance graph is that it stops training because it reaches network error tolerance value. As can be seen from the figures, according to the desired error tolerance, the sixth ANN parameters gave the best validity performance graph with 9.9803e-09 error tolerance value.

The regression graphs of the ANN structures are given in Figure 5. The regression values measure the correlation between outputs and objectives. If the value of R is close to 1 or 1, the outputs have a close relationship to the targets. If the value of R is zero, the outputs are in a random relationship with the targets. As can be seen from the figures, the R value shows that the ANN predicts the LSI values at very high performance.

5. CONCLUSION

In this study, LSI values of the system are obtained from the power flow model of IEEE 3-Bar power system created in Matlab by Newton Raphson method for different loading conditions. While these values were obtained, the active and reactive powers of the load busbar were increased by 0.05 pu. Using these parameters, 81 LSI values are calculated. The inputs of the ANN are the amplitude and phase angle of the active and reactive powers and voltage of the load busbar. LSI values are taken for the output of ANN. It has been observed how the predictive performance of ANN has changed by

changing some parameters of ANN by trial and error. For this purpose, six different ANN structures have been designed. From these results, it has been seen that ANN predicts LSI with a very high performance in determining voltage stability in IEEE 3-bus power systems.

REFERENCES

Açıkgöz, H., Poyraz, İ., Çöteli, R. (2019). "IEEE 14-Baralı Güç Sisteminde Gerilim Kararlılığının Uç Öğrenme Makinesi ile Analizi", *Gazi Üniversitesi Fen Bilimleri Dergisi Part C: Tasarım ve Teknoloji*, Vol. 7, No. 3, pp. 575-564.

Ahmad, A.S., Ghosh, P.S., Ahmad, S.S., Aljunid, S.A.K. (2004). "Assessment of ESDD on High-Voltage Insulators Using Artificial Neural Network", *Electric Power Systems Research*, 72, pp. 131–136.

Chakrabarti, A., Kothari, D.P., Mukhopadhyay, A.K., De, A. (2010). *An introduction to reactive power control and voltage stability in power transmission systems,* PHI Ltd., India.

Gao, B., Morison, G., Kundur, P. (1996). Towards the development of a systematic approach for voltage stability assessment of large-scale power systems", *IEEE Transactions on Power Systems,* vol. 11, no. 3, pp. 1314-1324.

Jeyasurya, B. (1994). "Artificial neural networks for power system steady-state voltage instability evaluation", *Electric Power Systems Research*, Vol.29, No. 2, pp. 85-90.

Konar, S., Chatterjee, D., Patra, S. (2015). "V–Q sensitivity-based index for assessment of dynamic voltage stability of power systems," *IET Generation, Transmission & Distribution*, vol. 9, no. 7, pp. 677–685.

Kundur, P. (1994). "*Power system stability and control*", McGraw-Hill, New York.

Öztemel, A. (2003). *Yapay Sinir Ağları*, Papatya Yayınları, 75-113.

Ramaswamy, M., Nayar, K.R. (2004). "On-line estimation of bus voltages based on fuzzy logic", *International Journal of Electrical Power & Energy Systems*, Vol. 26, No. 9, pp. 681-684.

Saxena, A., Sharma, A. K. (2016). "Assessment of global voltage stability margin through radial basis function neural network", *Advances in Electrical Engineering*, Vol. 2016, pp. 1-12.

Sharma, A.K., Saxena, A. and Tiwari, R. (2016). "Voltage stability assessment using GVSM and preventive control using SVC," *International Journal of Computer Applications*, Vol. 142, No. 11, pp. 23–31.

Sharma, A.K., Saxena, A., Pratap Soni, B., Gupta, V. (2018). "Voltage stability assessment using artificial neural network," *IEEMA Engineer Infinite Conference (eTechNxT)*, pp. 1–5.

Yazdanpanah-Goharrizi, A., Asghari, R. (2007). "A Novel Line Stability Index (NLSI) for Voltage Stability Assessment of Power Systems", *7th WSEAS International Conference on Power Systems*, China, pp. 15-17.

CISET - 2nd Cilicia International Symposium on Engineering and Technology
10-12 October, 2019, Mersin / TURKEY

SOLUTION OF EXAM SCHEDULING PROBLEM WITH ANT COLONY OPTIMIZATION: AN EXAMPLE OF MERSIN UNIVERSITY ENGINEERING FACULTY

Semir Aslan [*1] and Çiğdem Acı [2]

[1] Mersin University, Engineering Faculty, Computer Engineering, Mersin, Turkey, aslansemir26@gmail.com

[2] Mersin University, Engineering Faculty, Computer Engineering, Mersin, Turkey, caci@mersin.edu.tr

ABSTRACT

In universities, preparation of test schedules according to the wishes, suitability and needs of lecturers, assistants and students is very difficult, complex and time consuming. Although many improvements have been made at this point, exam schedules are still set out manually in many universities and cannot be performed according to the requests. In this study, Mersin University Faculty of Engineering final exam schedule was prepared by using Ant Colony Optimization (ACO) technique. 51 assistants, 105 faculty members, 9 departments, 24 common classrooms, 239 courses, 425 branches and 16.517 students who are required to take the exams are taken into consideration while exam scheduling. In the placement of the exams in the schedule, 4 exams can be planned in 1 day in classrooms. Minimum classroom usage-maximum lecture are targeted and the problem is provided to be adapted in ACO algorithm. Appropriate hours of assistants, faculty members and student groups are considered strict constraints. The branches of the Mersin University Faculty of Engineering's 2016-2017 Spring Semester examinations were applied to the appropriate classrooms at a rate of 99% by applying ACO technique.

Keywords: *Ant Colony Optimization, Exam Scheduling*

[*] Semir Aslan, Çiğdem Acı

1. INTRODUCTION

Scheduling problems in academic institutions have been subject to research for many years and may vary from country to country and even from different academic institutions in the same country. Exam scheduling problems, such as scheduling problems, NP is located in the class of difficult problems. Researchers have developed many algorithms in order to solve these problems. Exam scheduling problems depend on the research assistant, academic staff, the number of students who are required to take the exams, the capacity of the classrooms and the exam parameters of the department. Examination schedules are prepared by research assistants, department secretaries or administrative staff in universities. (Woumans *et al.*, 2016). The manual creation of the test schedule, while creating a timeline for the personnel who make up the schedule, limits the time it will devote to the areas where it can be productive and causes it to stop working for a while.

. In this study, ACO algorithm was applied on the spring semester exams of Mersin University Faculty of Engineering and an examination schedule was created. The availability of instructors, assistants, and students who are required to take the exam is taken into consideration. In addition to this, it is ensured that the exams of the same department do not coincide in the same time period and it is prevented from overlapping with the courses belonging to a different class of the department. Examinations were divided into 4 different time periods and rest periods were established between 2 exams.

2. ANT COLONY

Real ants are able to find the shortest path for their nest from a food source without using any visual hints. At the same time, they can accommodate themselves to changes around them; for example they can find a new path when the old path can't be practicable because of appearing of a new obstacle. Consider Fig. 1.1: there is a straight line which ants can move on it in order to connect their nest to a food source.

Pheromone trail is a well-known fact that creates and maintains the line for ants as a primary means. While the ants are walking, they save a sufficient amount of pheromone, and every ant's preference is to follow any direction that is rich in pheromone. The real ants' findings of the shortest path which reconnects a dashed line after rapid appearance of an unforeseeable obstacle that has crossed their path can be explained with this basic behavior. (Fig. 1.2) In fact, when the obstacle occurs, the ants that have the obstacle in front of them are not able to go on to follow the pheromone trail and for this reason they have to choose whether to turn right or to turn left. In this circumstances, we have expected from half of the ants to choose turning right and the other half of the ants to turn left. It has been seen nearly the same situation on the other part of the obstacle. (Fig.1.3). The ants that coincidentally choose the shorter way around the obstacle are going to reconstitute the dashed pheromone trail when compared to the ants choosing the longer path. Therefore, in larger amounts of pheromone are going to be received in the shorter path on per time unit, so many more ants start to choose the shorter way. Thanks to this positive feedback process, the shorter path will be chosen by all the ants. What makes interesting this autocatalytic process for ants is to find the shortest path that is around obstacle appears as a feature of interaction between shape of the obstacle and distributed behaviors of ants. Though all ants act at the same speed roughly and save the pheromone trail at the same rate roughly, saving the pheromone trail quicker on their shorter part than on their longer part is a fact makes it takes longer time to contour obstacles. Ants prefer higher pheromone trail and that makes this saving more quicker on their shorter path. (Dorigo, M., Socha, K. 2007).

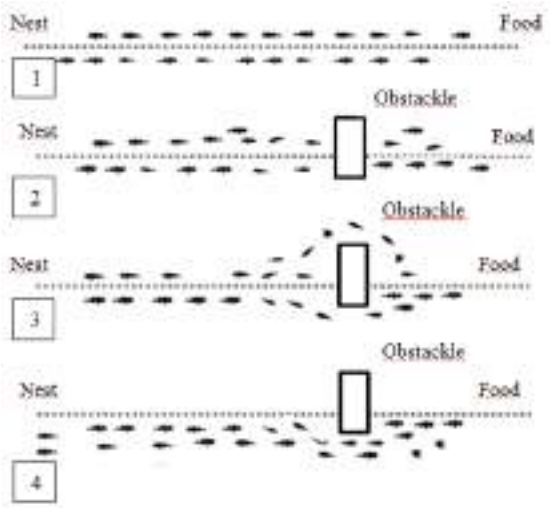

Figure 1: Ant colony food search behavior

3. ANT COLONY OPTIMIZATION ALGORITHM

ACO gets inspired from the several ants' species' behavior of foraging. These ants save pheromone on the ground so as to mark the suitable path which should be followed by colony's other members. ACO benefits from a mechanism that is similar in order to solve the problems of optimization.

Ant System (AS): Here is the first proposed ACO algorithm in the literature.
The main feature of it is to update the pheromone values, by all mants, which have given solution to the iteration itself.
The pheromone, associated with the edge joining cities *i*and*j*, is updated as follows:

$$\boldsymbol{k\tau_{ij}} \leftarrow \boldsymbol{(1-\rho)\tau_{ij}} + \boldsymbol{\sum_{c=1}^{m} \Delta\tau_{ij}^{k}} \quad (1)$$

The evaporation rate is ρ, the number of ants is m and the quantity of pheromone is $\Delta\tau_{ij}^{k}$ and it is laid on edge (***i***, j) by ant ***k***.

$$\Delta\boldsymbol{\tau_{ij}^{k}} = \begin{cases} \frac{\boldsymbol{Q}}{\boldsymbol{L_k}} & \boldsymbol{if\ used\ edge\ (i,j)in\ this\ tour,} \\ \mathbf{0} & \boldsymbol{otherwise,} \end{cases} \quad (2)$$

Where Q is a constant, and L_k is the length of the tour constructed by ant. (Li *et al*,. 2008)

In the building of a solution, ants choose the following city as being visited with a stochastic mechanism. By the time ant *k* is in city $\boldsymbol{i}$ and has built the partial solutions$^{\rho}$ until now, the possibility to go to the city $\boldsymbol{j}$ is given by:

$$\boldsymbol{P_{ij}^{k}} = \begin{cases} \frac{\tau_{ij}^{\alpha} \times \eta_{ij}^{\beta}}{\sum_{c_{il} \epsilon N(s^{\rho})} \tau_{ij}^{\alpha} \times \eta_{ij}^{\beta}} \; \boldsymbol{if\ c_{il} \in N(s^{\rho})} \\ \boldsymbol{0} \qquad\qquad \boldsymbol{otherwise} \end{cases} \quad (3)$$

Where $N(s^{\rho})$ is a set of applicable components, in other words, edges ($\boldsymbol{i}$, l) where $\boldsymbol{l}$ is a city and has not visited by the ant k. $\boldsymbol{\alpha}$ and $\boldsymbol{\beta}$ parameters control the pheromone relative importance againist to heuristic informaton, which is given by:

$$\boldsymbol{\eta_{ij}} = \frac{\boldsymbol{1}}{\boldsymbol{d_{i,j}}}, \quad (4)$$

$d_{i,j}$ is the distance between cities $\boldsymbol{i}$ and $\boldsymbol{j}$. (Dorigo *et al.*, 1997). (Brezina Jr Zuzana Čičková, I. 2011).

4. ADAPTATION OF THE ANT COLONY SYSTEM TO THE EXAM SCHEDULING PROBLEM

While applying ACO algorithm, the exam parameter, class hour parameter and exam class parameter are applied to the roulette wheel method for selection and added to the algorithm. Accordingly, the resulting formula and the meaning of the parameters according to this formula are shown below.

4.1. Choosing Exam

When modeling is done, the exam-classroom distance matrix is normalized to 0-1 (Figure 2). A random exam is selected from unselected exams. According to the selected exam, (3) is applied for classroom selection. In Equation 3, t is the classroom which is not yet visited by the ant $\boldsymbol{k}$. Appropriate classrooms are selected.

4.2. Choosing Classroom

Formula 5 is used to select classrooms up to the number of branches belonging to the selected exam. Formula 3 is used again to select the new exam. The program is terminated until all exams are placed or after the branches are tried to be placed in classrooms.

$$P_{ij}^{k} = \begin{cases} \frac{\tau_{ij}^{\alpha} \times \eta_{ij}^{\beta} \times \nu_{:h}^{\gamma}}{\sum_{c_{il} \epsilon N(s^{\rho})} \tau_{ij}^{\alpha} \times \eta_{ij}^{\beta} \times \nu_{:h}^{\gamma}} \; if\ c_{il} \in N(s^{\rho}) \\ 0 \qquad\qquad otherwise, \end{cases} \quad (5)$$

$\boldsymbol{\tau_{ij}}$: The pheromone matrix between classroom $\boldsymbol{i}$ and exam $\boldsymbol{j}$,

$\boldsymbol{\eta_{ij}}$: The visibility matrix between classroom $\boldsymbol{i}$ and exam $\boldsymbol{j}$,

$\boldsymbol{\nu_{:h}}$: Matrix of suitable classrooms in that time slot,

$\boldsymbol{\alpha}$: Relative importance of $\boldsymbol{\tau_{ij}}$

$\boldsymbol{\beta}$: Relative importance of $\boldsymbol{\eta_{ij}}$

$\boldsymbol{\gamma}$: Relative importance of the $\boldsymbol{\nu_{:h}}$

Classroom

Exam Branch

425x24 double

	1	2	3	4	5	6	7	8	9	10	11	12	13	14	15	16	17	18	19	20	21	22	23	24
1	0.8301	0.8301	0.0286	1	0.0079	0.0174	0.0174	0.0079	1	1	0.0174	0.8206	0.0206	0.0174	1	1	0.0079	0.0174	0.0206	0.0079	1	1	0.0174	0.0206
2	0.8301	0.8301	0.0286	1	0.0079	0.0174	0.0174	0.0079	1	1	0.0174	0.8206	0.0206	0.0174	1	1	0.0079	0.0174	0.0206	0.0079	1	1	0.0174	0.0206
3	0.8222	0.8222	0.0127	0.8321	1	0.0065	0.0065	1	0.8321	0.8321	0.0065	0.8127	0.0127	0.0065	0.8321	0.8321	1	0.0065	0.0127	1	0.8321	0.8321	0.0065	0.0127
4	0.8108	0.8108	0.0103	0.8207	0.0376	0.0071	0.0071	0.0376	0.8297	0.8297	0.0071	0.8103	0.0103	0.0071	0.8297	0.8297	0.0376	0.0071	0.0103	0.0376	0.8297	0.8297	0.0071	0.0103
5	0.8214	0.8214	0.0119	0.8313	0.0392	0.0087	0.0087	0.0392	0.8313	0.8313	0.0087	0.8119	0.0119	0.0087	0.8313	0.8313	0.0392	0.0087	0.0119	0.0392	0.8313	0.8313	0.0087	0.0119
6	0.8301	0.8301	0.0286	1	0.0079	0.0174	0.0174	0.0079	1	1	0.0174	0.8206	0.0206	0.0174	1	1	0.0079	0.0174	0.0206	0.0079	1	1	0.0174	0.0206
7	0.8293	0.8293	0.0188	0.8392	0.0071	0.0166	0.0166	0.0071	0.8392	0.8392	0.0166	0.8198	0.0198	0.0166	0.8392	0.8392	0.0071	0.0166	0.0198	0.0071	0.8392	0.8392	0.0166	0.0198
8	0.8293	0.8293	0.0188	0.8392	0.0071	0.0166	0.0166	0.0071	0.8392	0.8392	0.0166	0.8198	0.0198	0.0166	0.8392	0.8392	0.0071	0.0166	0.0198	0.0071	0.8392	0.8392	0.0166	0.0198
9	0.8301	0.8301	0.0286	1	0.0079	0.0174	0.0174	0.0079	1	1	0.0174	0.8206	0.0206	0.0174	1	1	0.0079	0.0174	0.0206	0.0079	1	1	0.0174	0.0206
10	0.8206	0.8206	0.0111	0.8305	0.0384	0.0079	0.0079	0.0384	0.8305	0.8305	0.0079	0.8111	0.0111	0.0079	0.8305	0.8305	0.0384	0.0079	0.0111	0.0384	0.8305	0.8305	0.0079	0.0111
11	0.8127	0.8127	0.0032	0.8226	0.0305	1	1	0.8305	0.8226	0.8226	1	0.8032	0.0032	1	0.8226	0.8226	0.8305	1	0.8032	0.8305	0.8226	0.8226	1	0.8032
12	0.8214	0.8214	0.0119	0.8313	0.0392	0.0087	0.0087	0.0392	0.8313	0.8313	0.0087	0.8119	0.0119	0.0087	0.8313	0.8313	0.0392	0.0087	0.0119	0.0392	0.8313	0.8313	0.0087	0.0119
13	0.8151	0.8151	0.0055	0.8249	0.0329	0.0024	0.0024	0.0329	0.8249	0.8249	0.0024	0.8055	0.0055	0.0024	0.8249	0.8249	0.0329	0.0024	0.0055	0.0329	0.8249	0.8249	0.0024	0.0055
14	0.8368	0.8368	0.0273	0.8467	0.0146	0.0242	0.0242	0.0146	0.8467	0.8467	0.0242	0.8273	0.0273	0.0242	0.8467	0.8467	0.0146	0.0242	0.0273	0.0146	0.8467	0.8467	0.0242	0.0273
15	0.8095	0.8095	1	0.8194	0.0273	0.0368	0.0368	0.0273	0.8194	0.8194	0.0368	1	1	0.0368	0.8194	0.8194	0.0273	0.0368	1	0.0273	0.8194	0.8194	0.0368	1
16	0.8040	0.8040	0.0345	0.8139	0.0218	0.0313	0.0313	0.0218	0.8139	0.8139	0.0313	0.8345	0.0345	0.0313	0.8139	0.8139	0.0218	0.0313	0.0345	0.0218	0.8139	0.8139	0.0313	0.0345

Figure 2: Exam Branch- Classroom Matrix

5. DATA USED IN IMPLEMENTING THE PROGRAM

The data used were taken from Mersin University Computer Center and are shown in detail below. Data are from the 2016-2017 spring semester of the Faculty Engineering.

- Mersin University
- Engineering Faculty
- 9 Department Number
- 24 Common Classrooms
- 105 Faculty Members
- 51 Assistant
- 238 Courses
- 425 Total Number Of Branches
- 16.517 Students Who Are Required To Take The Exam

6. RUNNİNG THE PROGRAM

When applying the algorithm, a random exam is selected. A random exam is selected when modeling. Placement will be made as much as the number of branches for the selected exam. The 10th and 11th time periods are reserved for History and Turkish exams, which are the common examinations of the Faculty Engineering, and no exams will be placed in these periods. The time period in which the exam will be placed is selected by random selection method. It is checked whether the department of the selected exam has another exam at the same time on the same day and whether another exam belonging to the period of the exam has another exam at the same day on the different time. The availability of the assistants from the assistant group who will supervise the examination of the department is checked. Strict constraints are created for non-available assistants so that no exams are assigned. The selection of the classrooms for the branches will be calculated according to formula 5 and the branches will be placed in the appropriate classrooms by roulette wheel method. The same procedure is carried out for another exam and continues until all exams are visited. All the ants perform this process. After all processes have finished, the best exam schedule is recorded and the global pheromone is updated. The next iteration is passed. After all of the iterations are completed, the exam schedule is saved and the program ends.

- Exams are scheduled for 2 weekdays, 10 days and 40 time periods.
- It is accepted as there will be 2 exams before noon and 2 exams in the afternoon.
- Exams are accepted as 90 minutes.
- There are at least 30 minutes between the two exams.
- Plan of week 1; 1-4 Monday, 5-8 Tuesday, 9-12 Wednesday, 13-16 Thursday, 17-20 Friday
- In the 2nd week; 21-24 Monday, 25-28 Tuesday, 29-32 Wednesday, 33-36 Thursday, 37-40 Friday
- Courses that have been placed in a classroom can be seen in Figure 4.

Figure 4. Exam İnformation- Time Slot

A sample of Engineering Faculty exam scheduling is seen in Figure 5. Exam code is written on the figure

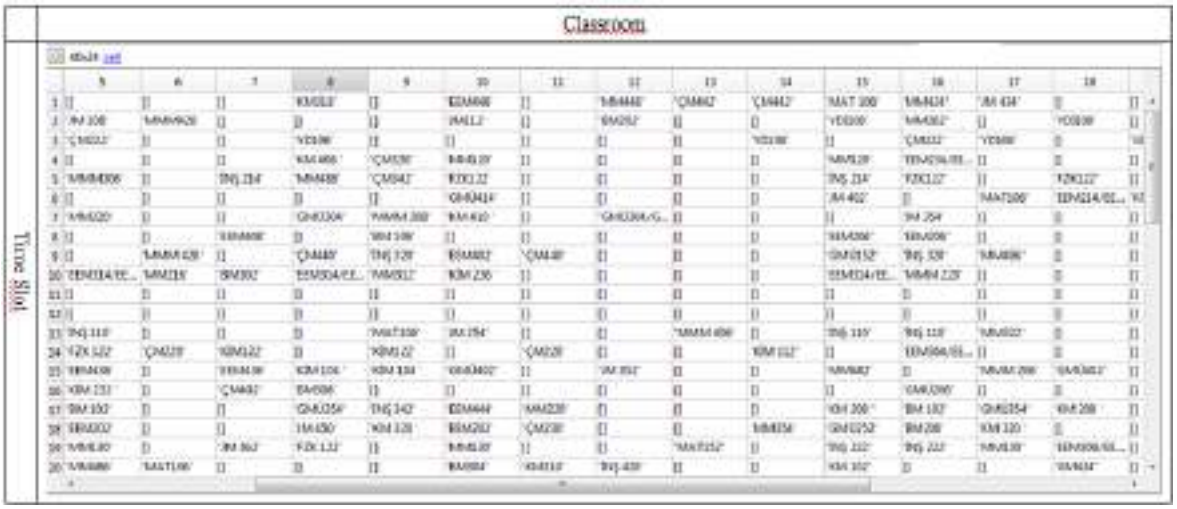

Figure 5. A sample of Engineering faculty exam schedule

6. CONCLUSION

In this study, Mersin University Faculty of Engineering exam scheduling problem is tried to be solved. ACO algorithm has been developed for the solution. The NP-hard problems, which had to be created manually each semester, were placed in appropriate classrooms in a short time with the help of the program. The maximum number of branches that will take the exam is placed in the classrooms and the availability of the assistants and faculty members, the absence of a different exam at the same time for the department and the absence of a different exam for the same day are provided to reach a solution.

The developed ACO algorithm written in MATLAB programming language has reached the desired solutions. MATLAB is a high-performance technical programming language. (Uzunoğlu 2003) In addition, it is suitable to add many parameters to the program such as scheduling the exams according to the wishes of the faculty members, placing exams in the desired classrooms, and planning exams according to the length of the exams. If these parameters are added to the function, they are open to give the best values or close to the best value according to the desired result.

ACKNOWLEDGEMENTS

We would like to thank Information Technologies Center of Mersin University for letting us use the data.

REFERENCES

Woumans, G., De Boeck, L., Beliën, J., Creemers, S. (2016). “A column generation approach for solving the examination-timetabling problem. “ *European Journal of Operational Research*, *253*(1), 178–194. doi:10.1016/J.EJOR.2016.01.046

Dorigo, M., Socha, K. (2007). “Ant Colony Optimization.” *Handbook of Approximation Algorithms and Metaheuristics*, (April 2006), 26.1--26.14.

Dorigo, M., Gambardella, L. M. (1997). “Ant colonies for the travelling salesman problem.” *Biosystems*, *43*(2), 73–81. doi:10.1016/S0303-2647(97)01708-5

Brezina Jr Zuzana Čičková, I. (2011). “Solving the Travelling Salesman Problem Using the Ant Colony Optimization.” *Management Information Systems*, *6*(4), 10–14.

Li, B., Wang, L., Song, W. (2008). “Ant Colony Optimization for the Traveling Salesman Problem Based on Ants with Memory.” In *2008 Fourth International Conference on Natural Computation* (pp. 496–501). IEEE. doi:10.1109/ICNC.2008.354

Uzunoğlu, M., Kızıl, A., Onar, Ö. Ç. (2003). “*Her Yönü ile MATLAB*.” İstanbul: Türkmen Kitabevi.

COMPARING SHORELINES OF AYDINLAR POND WITH PHOTOGRAMMERIC AND REMOTE SENSING METHODS

Fatma BUNYAN UNEL*[1], Lutfiye KUSAK [2], Mehmet Ozgur CELIK [3], Aydin ALPTEKIN [4] and Murat YAKAR [5]

[1] Mersin University, Engineering Faculty, Geomatics Engineering Department, Mersin, Turkey, fatmabunel@mersin.edu.tr

[2] Mersin University, Engineering Faculty, Geomatics Engineering Department, Mersin, Turkey, lutfiyekusak@mersin.edu.tr

[3] Mersin University, Engineering Faculty, Geomatics Engineering Department, Mersin, Turkey, mozgurcelik@mersin.edu.tr

[4] Mersin University, Engineering Faculty, Geomatics Engineering Department, Mersin, Turkey, aydinalptekin@mersin.edu.tr

[5] Mersin University, Engineering Faculty, Geomatics Engineering Department, Mersin, Turkey, myakar@mersin.edu.tr

ABSTRACT

Turkey has many natural and artificial lakes. Shoreline, which shows the maximum water elevation, shows variation in time. For sustainable soil and water management, optimum benefit should be achieved by protecting the ecosystem. For this reason, the shoreline separating the land and water should be determined and followed. Aydinlar pond, located in Erdemli district, was selected as study area. An unmanned aerial vehicle (UAV) was used to create actual orthophoto of the study area. When the 2019 and 2015 orthophotos were compared, it was found that area of the shoreline grew by 8713.83 m^2. Landsat 8 satellite images belonging to 2013, 2016 and 2019 years were taken to determine the change in water level. Image analysis was performed to measure the pond area. According to the results, the pond area was decreased 2700 m^2 in period between 2013 and 2019.

Keywords: *Shoreline, Orthophoto, Landsat, UAV*

* Corresponding Author

1. INTRODUCTION

Soil and water resources are the two most important natural resources in terms of food production for human life in the world (Yakar et al., 2019). Sustainable land and water management are taken together and the main purpose of these resources is to protect and convey these resources to future generations. Approximately two-thirds of the Earth's surface and three sides of our country are surrounded by water. In addition, there are many lakes, streams, and dams. In sustainable management, which is considered to be the optimum utilization by preserving the natural structure, maps with the actual location, height and depth information are needed.

To benefit optimum use of seas, lakes, dams and river coasts, the shoreline with water and land separation should be mapped. The coasts, which are under the rule and disposition of the state, are important attraction areas in tourism, logistics, and trade. Tourism and port activities on the coasts contribute more than 30 billion annually to the national economy (Economy, 2018). Approximately 84% of international trade in the world and our country is realized by sea (Sea Trade, 2017). Unplanned filling areas and distorted structures on the coasts disrupt the natural texture. Especially the construction of houses, holiday sites and hotels create excessive population density in coastal areas and problems of protection of coastal areas are encountered (Ünel et al., 2019).

Shoreline of sea and natural lake areas shows alteration due to geographic, geological and meteorological events. In the world and in our country, it is difficult to constantly follow the shorelines that change temporarily with natural and fillings in the ecosystem (Ünel et al., 2019).

Sea level changes are detected by monitoring the sea shoreline. Analysis of natural phenomena is important for coastal management and saving. The shoreline of natural and artificial lakes is changing due to meteorological reasons. In the summer months when the evaporation is high, the water level decreases and the area formed by the shoreline narrows; while in the spring months when the rainfall is high, the water increases and the area formed by coastal line broadens. According to the regions; this situation can cause water shortage when it gets less rain and a flood disaster when it gets too much rain. To take precautions against natural events, continuous monitoring of the constantly changing coastline is required.

Once the shoreline is passed, the determination of the coast margin line is made by the commission. The boundary formed by the coast margin line cannot be changed if land is obtained by filling (Coastal Regulation, 1990). While the shoreline is variable, the coast margin line is fixed as long as it is not extraordinary.

Ground and air photogrammetry, LIDAR systems and classical measurement techniques are used in determining the shoreline and coast margin line. It has been observed that satellite images whose sensitivity and cost vary according to the characteristics of the satellites used in remote sensing method are preferred (Ünel et al., 2019).

In literature, it was researched many topics related to the shoreline and coast margin line such as Integrated Coastal Zone Management-ICZM (Mumby et al., 1995; Rodríguez et al., 2009), coastal problems (Pala, 1975; Akyarlı et al., 2002), coast margin line determination (Uzel et al., 2014; Korkmaz et al., 2016), shoreline extraction (Erdem et al., 2018), coastal information system (Akdeniz; et al., 2013; Mayerle et al., 2016; Supriyono, 2018), shorelines changes (Oyedotun et al., 2018; Dewi and Bijker, 2019).

Casella et al., (2014) produced beach topography low-altitude aerial photogrammetry for coastal management and Darwin et al., (2014) examined the potential of unmanned aerial vehicles for large scale mapping of coastal area.

Both in the world and in our country, there are problems detecting shore-shorelines changes. To solve the problems, it requires a long time and periodic land surveying. In monitoring shore-shorelines, it is used surveying methods which are photogrammetry, lidar, GNSS, remote sensing and terrestrial surveying. These methods vary according to their accuracy. Aerial photogrammetry and lidar consist of UAV system. Darwin et al., (2014) attained that the UAV system has great potential to be used for various applications that require accurate results or products at limited time and less man power.

In this study, it was compared shorelines of Aydinlar pond in the 2019 and 2015 orthophotos and Landsat 8 satellite images belonging to 2013, 2016 and 2019 years. On 11 July 2019, aerial images were taken from ANAFI Parrot UAV by using photogrammetry method. It was monitored differences in orthophotos and Landsat 8 images in area of the shoreline. These results showed that the usage in agriculture areas increased and evaporation was very high, despite rain or snowfall.

2. MATERIAL AND METHODS

2.1. Shore and Coast Margin Line

According to the formation, lakes are divided into two; natural and artificial lakes. Natural lake occurs as result of tectonic, karstic and volcanic events. Artificial lake is a pond formed by people making obstacles in front of water. Dams and ponds are examples of artificial lakes (Geographer, 2018). Aydinlar Pond is an artificial lake that was created by taking a set in front of it.

Shore is the area between the shoreline and coast margin line. The shoreline consists of points where the water touches the land in the sea, natural and artificial and lakes. The coast margin line is the natural boundary of the sandy, gravel, rocky, stony, reeds, swamp, etc. areas where water movements are formed. The area which is horizontally at least 100 meters in width from the coast margin line is defined as coast. (Coastal Legislation, 1990).

In natural and artificial lakes, the maximum water elevation determined by the General Directorate of State Hydraulic Works determines the shoreline (Coastal Regulation, 1990). The maximum water elevation of Aydinlar Pond is 1370.19 m (SHW, 2019). The coast margin line is also determined by the commissions who are geology engineer, geologist, geomatics engineer, agriculture engineer, and architect and city planner, construction engineer.

2.2. Study Area: Aydinlar Pond

Aydinlar Pond is an artificial lake for agricultural irrigation purposes. It is located in Aydinlar Neighborhood, which is 70.1 km to the city center of Mersin and 32 km to the north of Erdemli district (Fig. 1). The water source of Aydinlar Pond is Sudokulen stream, which is in the east of the neighborhood.

Fig. 1. Location map of the study area

2.3. Landsat 8 Satellite images

Landsat 8 satellite was launch on 11 February 2013, from California, on an Atlas-V rocket. The satellite carries the Operational Land Imager (OLI) and the Thermal Infrared Sensor (TIRS). LandSat 8 Data are acquired on the Worldwide Reference System-2 (WRS-2) path/row system. Band 1-7 and 9 have 30 m resolution, but Band 8 has Panchromatic (PAN) 15 m resolution. The Landsat Data Continuity Mission (LDCM) was created in October 2002 to investigate and research options for the most feasible solution to follow the Landsat 7 mission (USGS, 2017).

2.4. Photogrammetry Method

Photogrammetry types are aerial and terrestrial Photogrammetry. In aerial Photogrammetry, it is commonly used the UAV. The UAV photogrammetry describes a photogrammetric measurement platform, which operates remotely controlled, semiautonomously, or autonomously, without a pilot sitting in the vehicle Major advantages of UAV compared to manned aircraft systems are that UAV can be used in high risk situations without endangering a human life and inaccessible areas, at low altitude and at flight profiles close to the objects where manned systems cannot be flown. However, especially low-cost UAV limit the sensor payload in weight and dimension. Therefore, small or medium format cameras are selected. In addition, these payload limitations require the use of low weight navigation units, which implies less accurate results for the orientation of the sensors (Eisenbeiss, 2009).

In this study, the shoreline of Aydinlar Pond was determined by photogrammetric method. Air photogrammetry was preferred in the method, which was divided into two as air and terrestrial photogrammetry because the area to be measured was large and the surface was covered with water. Today, UAV is generally used in applications of air photogrammetry. UAV usage is practical, easy, fast and cost-effective.

It is taken photos by means of ANAFI Parrot, which is one of UAV. ANAFI Parrot is used to survey small area. Because there are four batteries in the Anafi carrying bag. With each the battery, it is taken photos for 18 minutes (Fig. 2). A smartphones is assembled to control panel of ANAFI Parrot. To prepare flight plan, it is needed Ctrl+parrot 2 and Pix4Dcapture applications worked in operating systems of the smartphones.

Fig. 2. ANAFI Parrot

3. SHORELINE OF AYDINLAR POND

3.1. Landsat 8 Satellite Images

Landsat 8 satellite images were downloaded from USGS for 2013, 2016 and 2019, which corresponds to the July of the current flight. The necessary atmospheric and geometric corrections of the images were made with the open source code software QGIS.

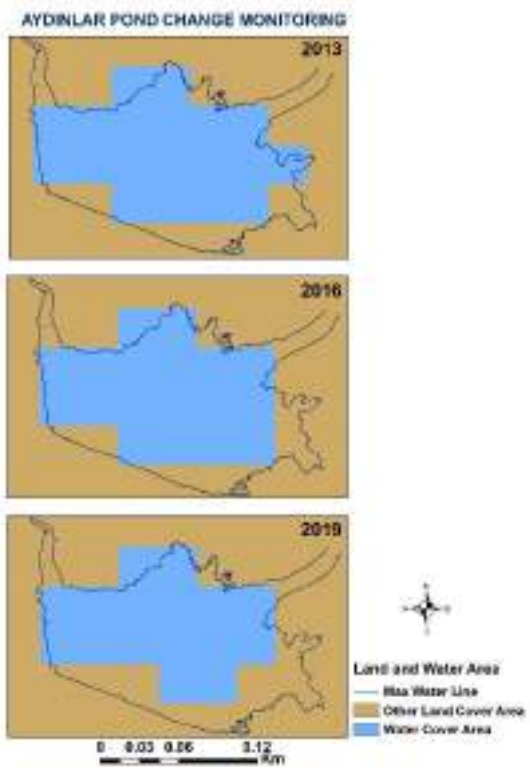

Fig. 3. Processed and classified satellite images

In ArcGIS software, it was made raster calculation by using Eq. (1) with Band 3 and Band 5 in Normalized Difference Water Index (NDWI). Land and water areas were separated from each other. NDWI is one of the most well-known multiband water indices' methods, widely used for identification of water bodies.

$$NDWI = \frac{G-NIR}{G+NIR} = \frac{Band3-Band5}{Band3+Band5} \quad (1)$$

The processed image from which were obtained water and land areas, it was classified by using the so "Iso Cluster Unsupervised Classification" method. A tool has been developed for the "Iso Cluster Unsupervised Classification" process in ArcGIS software. The classification of images is performed automatically using this tool. With the help of this tool, it was generated Fig. 3 from Landsat 8 satellite images of Aydinlar Pond belong to 2013, 2016 and 2019.

Most of the processed and classified satellite image areas remain within the maximum water elevation line. Between 2013 and 2019, it has been observed that it has decreased by 2700 m^2 (Table 1).

Table 1. Areas of processed and classified images

Date	Number of Pixels	Band Width	Area (m^2)
02.07.2013	19	30*30	17100.00
10.07.2016	18	30*30	16200.00
03.07.2019	16	30*30	14400.00

3.2. Orthophotos

The shoreline was drawn by using ArcGIS software over the orthophoto produced in 2015. Orthophoto was updated in this study.

Fig. 4. Orthophotos

On 11 July 2019, ANAFI Parrot took flight over the study area covering Aydinlar Pond. The flight plan was prepared by taking flight altitude as 50 m and UAV aerial photographs were collected. Pictures were imported into Agisoft Metashape software and orthophoto of the study area was created (Fig. 4).

The contour lines show topography of terrain. The line that passes from 1370.19 m, maximum water elevation, is the shoreline. Based on this line, the water surface covers 12906.51 m^2 less area in 2015. The water surface area of the Aydinlar Pond was found to be almost twice that of 2019 compared to 2015. Although there is a difference of 4192.68 m^2 in 2019, the occupancy rate is quite good (Table 2).

Table 2. Water surface areas in Orthophotos

Year of Orthophotos	Area (m^2)
2015	8528.33
2019 (11.07.2019)	17242.16
Max. water surface Area	21434.84

In addition, the three-dimensional (3D) digital surface model was prepared. The digital surface model is a model that consists of the elevation of natural and artificial objects such as land, home, tree etc. (Fig. 5).

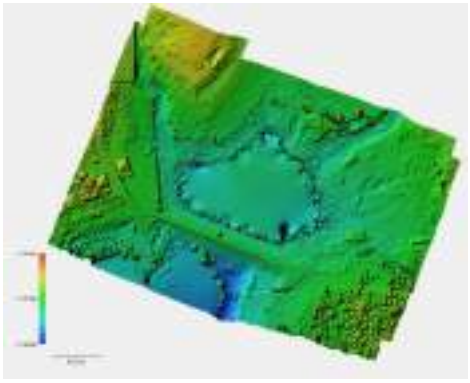

Fig. 5. The 3D digital surface model

Since Sudokulen stream, which is source feeding Aydinlar Pond has little water; the amount of rainfall is of great importance. Concordantly, the temperature that causes water to evaporate and decrease plays an important role. For this reason, temperature and precipitation rates between the years 2000-2018 were analyzed from the meteorological data. In the Mediterranean Region, it is seen that 2008 and 2013 received less rainfall than other years. According to the increase in the amount of precipitation; 2016, 2015 and 2018 are listed. In terms of temperature between the years 1940-2018 in Mersin, the highest average temperature is 23.3 ºC, the lowest average temperature is 14.8 ºC (MGM, 2018). The meteorological data and the results from image analysis showed that the usage in agriculture areas increased and evaporation was very high, despite rain or snowfall.

5. CONCLUSION

The shoreline varies according to seasons and years. Since the monitoring of the shoreline is continuous, it can be done with low cost methods in a short time with little labor. UAV photogrammetry method can be used for this aim.

Investigating the causes of global warming, taking environmental measures, determining the average sea level are possible with the monitoring of the shoreline. The monitoring of the pond shores is also determined by how many cubic meters of water volume is taken and environmental measures are taken.

The shoreline was determined according to the maximum water elevation of Aydinlar pond. Changes have been observed depending on rainfall and temperature over the years. In Landsat 8 satellite images in 2013, 2016 and 2019, the surface area of the water surface has been found to shrink gradually. The difference between the 2015 and 2019 orthophoto shorelines was found to be approximately half and increased. In addition, it has been determined that it approaches with a difference of 2842.16 m^2 between Landsat 8 and orthophoto shoreline in July 2019. This difference is thought to decrease when working in larger areas.

The lidar method can also be used to determine the shoreline. It is thought that more sensitive results can be obtained due to the fact that the water is mobile. In the next study, it is aimed to determine the shoreline of Aydinlar Pond by using the local lidar method and compare it with the orthophoto maps. The depth map of the pond should be produced by using unmanned surface tools and the water volume should be calculated. The adequacy of the use of the surrounding agricultural land will be examined.

REFERENCES

Akdeniz, Y., Bakırman, T. and Gümüşay, M.Ü. (2013). "Edremit Körfezi Kıyı Bilgi Sistemi." *TMMOB Coğrafi Bilgi Sistemleri Kongresi*, 11-13 Kasım 2013, Ankara.

Akyarlı, A., Yüksel, Y., Çevik, E., Yalçiner, A.C. and Güler, I. (2002). "Kıyı Bölgesi Yönetimi ve Sorunları." *TMH-Türkiye Mühendislik Haberleri*, No. 420-421-422 / 2002/4-5-6, pp. 65-68.

Casella, E. Rovere, A. Pedroncini, A. Mucerino, L., Casella, M. Cusati, L.A., Vacchi, M., Ferrari, M., and Firpo, M. (2014). "Study of wave runup using numerical models and low-altitude aerial photogrammetry: A tool for coastal management." *Estuarine, Coastal and Shelf Science*, Vol. 149, pp. 160-167.

Coastal Legislation, (1990). *3621 Sayılı Kıyı Kanunu*, Kabul Tarihi : 4/4/1990, Yayımlandığı Resmî Gazete : Tarih : 17/4/1990 Sayı : 20495, Yayımlandığı Düstur : Tertip : 5 Cilt : 29 Sayfa : 76.

Coastal Regulation, (1990). *Kıyı Kanununun Uygulanmasına Dair Yönetmelik*, Resmî Gazete Tarihi: 03.08.1990 Resmî Gazete Sayısı: 20594.

Darwin, N., Ahmad, A. and Zainon, O. (2014). "The Potential of Unmanned Aerial Vehicle for Large Scale Mapping of Coastal Area." *8th International Symposium of the Digital Earth (ISDE8), IOP Conf. Ser.: Earth Environ. Sci.* 18 012031.

Dewi R. S. and Bijker W. (2019). "Dynamics of shoreline changes in the coastal region of Sayung, Indonesia." *The Egyptian Journal of Remote Sensing and Space Sciences*, Article in Press.

Economy, (2018). 2018 Performans Programı, Ekonomi Bakanlığı, Strateji Geliştirme Dairesi Başkanlığı, Ankara.

Eisenbeiss, H. (2009). *UAV photogrammetry*. PhD, Diss. ETH No. 18515, Institute of Geodesy and Photogrammetry, ETH Zurich, Switzerland.

Erdem, F., Derinpınar, M.A., Nasirzadehdizaji, R., Oy, S., Şeker, D.Z. and Bayram, B. (2018). "Rastgele Orman Yöntemi Kullanılarak Kıyı Çizgisi Çıkarımı İstanbul Örneği." *Journal of Geomatics*, Vol. 3, No. 2, pp. 100-107.

Geographer, 2018, Göller Oluşumuna Göre Doğal Göller ve Yapay Göller, 2018. https://www.cografyaci.gen.tr/goller-olusumuna-gore-dogal-goller-ve-yapay-goller/ [Accessed 07 Sep 2019].

Korkmaz, H. Geçen R. and Kuşçu, V. (2016). "Asi Deltası (Samandağ) Kıyı Kenar Çizgisi." *Fırat University Journal of Social Science*, Vol. 26, No. 1, pp. 21-35, Elazığ.

Mayerle, R., Al-Subhi, A., Jaramillo, J. F., Salama, A., Bruss, G., Zubier, K., Runte, K., Turki, A., Hesse K., Jastania, H., Ladwig, N. and Mudarris, M. (2016). "Development of a coastal information system for the management of Jeddah coastal waters in Saudi Arabia." *Computers &Geosciences*, Vol. 89, pp.71–78.

MGM, (2018). Meteoroloji Genel Müdürlüğü, Ankara.https://www.mgm.gov.tr/veridegerlendirme/yillik-toplam-yagis-verileri.aspx https://www.mgm.gov.tr/veridegerlendirme/il-ve-ilceler-istatistik.aspx?k=undefined&m=MERSIN

Mumby, P.J., Raines, P.S., Gray D.A. and Gibson, J.P. (1995). "Geographic information systems: A tool for integrated coastal zone management in Belize." *Journal Coastal Management*, Vol. 23, No. 2, pp. 111-121.

Oyedotun, T. D. T., Ruiz-Luna A. and Navarro-Hernández A. G. (2018). Contemporary shoreline changes and consequences at a tropical coastal domain, Geology, Ecology, and Landscapes, Informa UK Limited.

Öz, E. (2018). "Türkiye ve dünyada deniz ticaretinin ekonomiye katkısı." https://www.dunya.com/kose-yazisi/turkiye-ve-dunyada-deniz-ticaretinin-ekonomiye-katkisi/427642

Pala, K. (1975). "Türkiye'nin Kıyı Sorunları ve Politikası." *TMMOB Harita ve Kadastro Mühendisleri Odası Dergisi*, Yıl 10, No. 33-34, pp. 3-38.

Rodríguez, I., Montoya, I., Sánchez, M.J. and Carreño, F. (2009). "Geographic Information Systems applied to Integrated Coastal Zone Management." *Geomorphology*, Vol. 107, No. 1–2, 1 June 2009, pp. 100-105.

Sea Trade, (2017). "Deniz Ticareti 2017 İstatistikleri, Ulaştırma ve Altyapı Bakanlığı." Deniz Ticareti Genel Müdürlüğü, Ankara.

SHW, (2019). Aydınlar Pond Project Plan. Devlet Su İşleri (DSİ) Müdürlüğü (The General Directorate of State Hydraulic Works-SHW), Mersin.

Supriyono, (2018). "Critical Land Detection Watershed River Bengkulu and Effect of Coastal Area using Geographic Information System." *Sumatra Journal of Disaster, Geography and Geography Education*, Vol.

2, No. 1, pp. 30-37.

USGS, (2017). Landsat 8, https://www.usgs.gov/land-resources/nli/landsat/landsat-8?qt-science_support_page_related_con=0#qt-science_support_page_related_con https://www.usgs.gov/land-resources/nli/landsat/landsat-data-continuity-mission-history?qt-science_support_page_related_con=0#qt-science_support_page_related_con [Accessed 01 Sep 2019]

Uzel, T., Eren, K. and Ürüşan, A.Y. (2014). "Kıyı Kenar Çizgilerinin Belirlenmesi ve Sahil Bilgi Sistemi Tasarımı." HKMO Mühendislik Ölçmeleri STB Komisyonu, *7. Ulusal Mühendislik Ölçmeleri Sempozyumu*, 15-17 Ekim 2014, Hitit Üniversitesi, Çorum.

Uzun, S.M. and Garipağaoğlu, N. (2014). "Kıyı Çizgisi Değişiminin Yaratacağı Riskler Açısından İzmit Körfezi Kıyılarının Değerlendirilmesi." *The Journal of International Social Research*, Vol. 7, No. 31, pp. 469-480.

Ünel, F.B., Çelik, M.Ö., Yakar, M., and Kuşak, L. (2019). "Kıyı Yönetimi için Kıyı ve Kıyı Kenar Çizgisinin Belirlenmesi ve Mersin Kıyı Bilgi Sistemi Altyapısının Araştırılması." *2. International Mediterranean Symposium*, 23-25 Mayıs 2019, Mersin.

Yakar, M., Ünel, F.B., Kuşak, L. and Doğan, Y. (2019). "Barajlarda Hidrografik Ölçme Yöntemleri ve Üretilen Haritalar." *2. International Mediterranean Symposium*, 23-25 Mayıs 2019, Mersin.

MODELLING OF A LANDSLIDE SITE WITH SATELLITE AND UAV

Lütfiye Kuşak [*1], Fatma Bünyan Ünel [2], Aydın Alptekin [3], Mehmet Özgür Çelik [4] , Murat Yakar [5]

[1]Mersin University, Engineering Faculty, Geomatics Engineering Department, Mersin, Turkey, lutfiyekusak@mersin.edu.tr

[2]Mersin University, Engineering Faculty, Geomatics Engineering Department, Mersin, Turkey, fatmabunel@mersin.edu.tr

[3] Mersin University, Engineering Faculty, Geomatics Engineering Department, Mersin, Turkey, aydinalptekin@mersin.edu.tr

[4]Mersin University, Engineering Faculty, Geomatics Engineering Department, Mersin, Turkey, mozgurcelik@mersin.edu.tr

[5]Mersin University, Engineering Faculty, Geomatics Engineering Department, Mersin, Turkey, myakar@mersin.edu.tr

ABSTRACT

Landslide, which is mostly seen natural disaster cause loss of life and property. In order to protect people from landslide, the potential disaster area needs to be analyzed, monitored and modelled in a proper way. In this study, landslide location was surveyed, analyzed and modelled by using an unmanned aerial vehicle UAV and satellite images. First of all, Sentinel-2 satellite images were used to determine the pre- and post-landslide status. Later, the previously prepared DEM with 5m resolution and the DEM data obtained with UAV were evaluated together.

Keywords: *Landslide, UAV, Sentinel-2, DEM*

[*] Corresponding Author

1. INTRODUCTION

The movement of a mass of material composed of rock, soils, artificial fills debris, or earth down a slope is defined as a landslide. These movements are classified as falling, sliding, flowing, or by their combinations (‘USGS’, 2019).

There are two main factors in the formation of landslides. The first is the preparatory factors that include the geological, topographic and environmental characteristics of the region; the second is the triggering factors consisting of earthquake, precipitation and human factor. (Gökçeoğlu & Ercanoğlu, 2001; Solís-Castillo, Mendoza, Vázquez Castro, & Bocco, 2019)

Landslide disaster is frequent news topic in the world and Turkey. Every year, there are many lives and property losses due to landslides. 55997 people died between 2004-2016 due to landslide and economic loss was also determined to be over 6 billion dollars (‘ISPRA’, 2018).

The largest landslide on Earth in recorded history occurred during the 1980 eruption of Mount St. Helens, a volcano in the Cascade Mountain Range in the State of Washington, USA (‘USGS’, 2019)

When natural disasters lived in Turkey in the past are examined, it has been observed that the landslide of 15% (Uluğ, 2014)

Landslide that occurred in Turkey between the years 1950-2008 were examined. It is observed that landslides are especially in areas such as Black Sea, Mediterranean, Eastern Anatolia where slope is high and also on active fault lines (Çan, Mazman, Tekin, & Y, 2015; ‘ÇEM’, 2019; Gökçe, Özden, & Demir, 2008).

Natural disasters such as landslides may not be predicted. However, the collection of records such as location, date, time, climatic conditions of the past landslide events, the topographical condition of the land, soil structure, and sensitive areas can be determined. Risky regions can be identified as a result of analysis. Human beings do not have the ability to prevent natural phenomena, but they can take precautions. As a result of these procedures, laws can be handled more easily (‘Afet Riski’, 2012).

In order to monitor the possible landslides in the world, historical data are recorded and databases are prepared (‘ELSUS’, 2018; ‘GLC’, 2019).

Landslides are monitored by the MTA (‘MTA’, 2018; ‘MTA’, 2019) and the AFAD in Turkey.

DEM (Cha, Hwang, & Choi, 2018), photogrammetric methods, radar images (Nikolaeva, Walter, Shirzaei, & Zschau, 2014; Qu et al., 2019) and LIDAR (Parente & Pepe, 2018; Wang et al., 2014), Landsat 8 OLI (Plank, Twele, & Martinis, 2016; Zhao et al., 2018), SPOT-5 (Tsutsui et al., 2007), Sentinel-1 (Mondini et al., 2019), Sentinel-2 (Lacroix, Bièvre, Pathier, Kniess, & Jongmans, 2018; Qin, Lu, & Li, 2018; Yang, Wang, Sun, Wang, & Ma, 2019) satellite images are preferred for data acquisition for landslide studies.

In this study, instead of determining the volume of the landslide size, it was focused on modeling the landslide area. Because, whether or not these data sets can be used in landslide regions and modeling is the main subject of the study.

The study consists of 3 stages: data acquisition, processing and modeling.

2. DATA AND METHOD

2.1. Study Area

In January 2019, landslides took place in Emirler, İnsu, Değirmençay, Uzunkaş, Turunçlu and Karahacılı neighborhoods in Mersin. Roads and farmland were damaged by landslides. The landslide area where the Karahacılı neighborhood was affected from these areas was examined in this study.

Karahacılı which is one of the neighborhoods of Yenişehir district of Mersin province. This area is located 36°.813081N and 34°.482932E. Karahacılı neighborhood has agricultural land and pomegranate, black grapes and figs are grown.

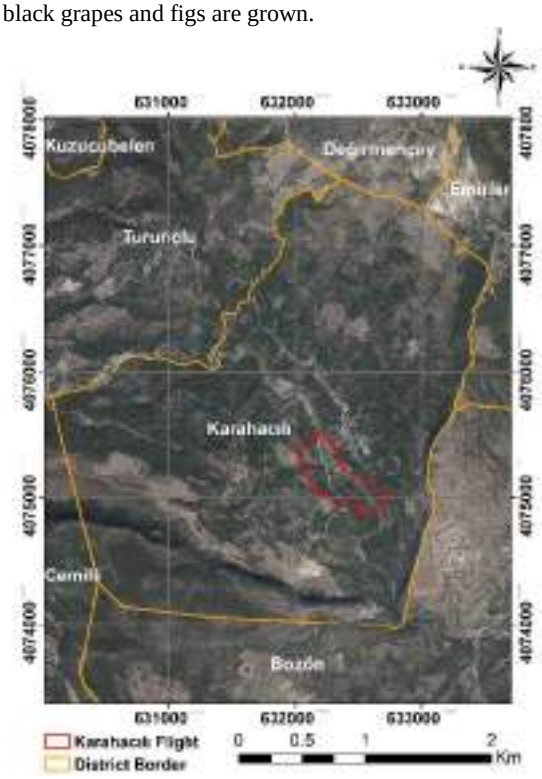

Fig. 1. Karahacılı and study area

It is surrounded by Turunçlu, Emirler, Bozön, Değirmençay and Cemilli neighborhoods. The area of Karahacili District is 7860281.36 m^2 (Fig. 1).

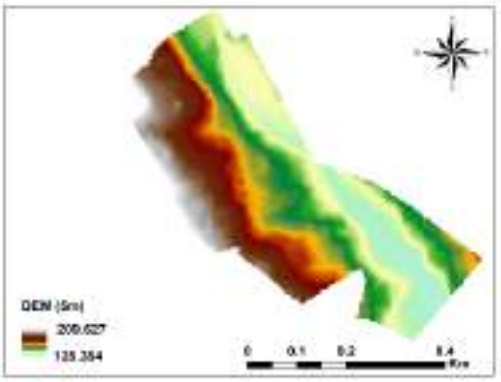

Fig. 2. Karahacılı DEM

When the DEM information is examined in the study area of Karahacılı neighborhood, it is seen that heights vary between 128.324-209.627m (Fig. 2).

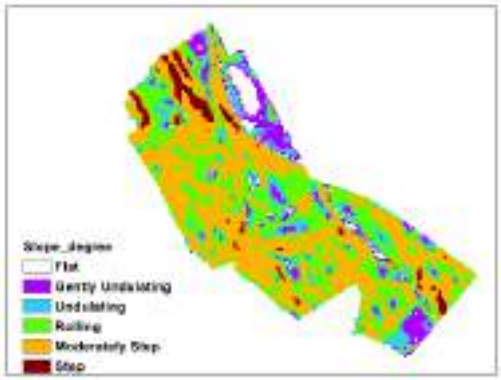

Fig. 3. Karahacılı slope analysis

In the study area, the Kaplankaya Formation, which is 60 meters thick, is observed in the Lower-Middle Miocene age. Sand and gravel, which is a type of noncohesive soil, has a sloping topography. No active fault line is observed in the immediate vicinity of the study area.

2.2. Data

In this study, three different data sets are evaluated: DEM map, satellite images and orthophoto.

The slope analysis study was carried out from DEM maps prepared for Mersin (Fig. 3). The current DEM map has a resolution of 5m and was used both for slope analysis and for the evaluation of altitude information of DEM obtained by UAV.

Sentinel satellite images were used in the study before and after landslides to determine the situation in a small scale but in a large area. The Sentinel-2 constellation have much higher spatial resolution (10 m multi-spectral) and more frequent revisit interval (5-day) in the world. NDVI was used to determine the landslide area. NDVI is one of the particularly preferred methods in such studies.

In this study, satellite images of 2018 and 2019 of Karahacılı neighborhood were utilized and orthophoto and DEM of landslide region was produced with the help of ANAFI Parrot UAV in landslide area.

2.3. Methods

In order to make the slope analysis of the region using DEM map, the classification prepared within the scope of SOTER (Soil Terrain Database) was utilized. The Slopes are classified as 0-2% Flat, 2-5% Gently undulating, 5-8% Undulating, 8-15% rolling, 15-30% Moderately stepping and 30-60% stepping ('SOTER', 2012).

Satellite images allow rapid analysis of large areas. Satellite images are used to investigate changes in the region before and after some geological (landslide) and climatic (flood) disasters.

In this study, the changes in the landslide area were determined by using Sentinel-2 satellite images. In order to reveal this change, NDVI (2.1) is used in landslide studies.

$$NDVI = \frac{NIR - RED}{NIR + RED} \qquad (2.1)$$

Although it has been 7 months since the landslide event, traces of landslides are still visible in the study area. The flight, which was performed on 28 June 2019 using Anafi Parrot, was planned with 65m height, 1.86cm / pixel GSD and 80% transverse 70% length thrust. 5 ground control points were used. The flight was completed with 447 photos. It was flown in an area of 211000m2. TUREF (ITRF96) 36-3^{o} projection system was selected for the region.

In the map, ellipsoidal heights of 1912 points were found and orthometric heights were obtained. Using the existing 5m resolution DEM map of the region, elevation information of the same points was obtained and the differences between them were compared.

3. RESULTS

It is preferred in observing risk areas because it is possible to examine much larger areas faster with the help of satellite images.

When the A and B regions were examined before and after landslides, the changes in NDVI's were noteworthy. It is seen that a part of the water area in zone A was closed as a result of sliding, and in zone B the green area was replaced by soil (Fig. 4).

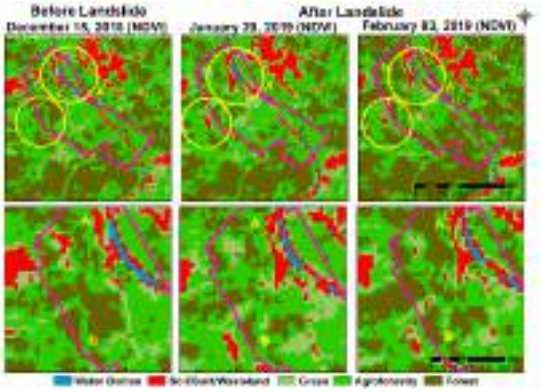

Fig. 4. NDVI results

The following Table 1 and Table 2 were generated at the end of the NDVI results. According to the results, it is seen that the land cover has changed. However, it is seen that the vegetation in the field recovered slowly in February.

Table 1. NDVI results (m^2)

	Landslide (m^2)		
	Before	After	
	12/15	29/01	02/03
Water Bodies	7400	8700	9900
Soil/Built/Wasteland	80200	85900	83200
Vegetation Area	1056300	1049300	1050800

Table 2. NDVI difference results

	Differences (m^2)	
	December-January	December-February
Soil/Built/ Wasteland	5700	3000

ANAFI Parrot UAV flight was conducted to investigate the current data of landslides detected from satellite images on site. Such measurements are very useful in situations where ground measurements are difficult. Orthophoto was created after the flight (Fig. 5).
The UAV is used for more detailed and up-to-date modeling of small areas. DEM was also produced for the region after the flight. With the DEM map obtained from the flight with UAV, the heights of 1912 randomly selected points in the previously prepared DEM map were examined. The correlation between these heights was 0.89.

Fig. 5. Orthophoto

When the heights of the randomly selected 1912 points in the DEM map prepared with the UAV and the DEM map obtained from the flight were examined, it was found that heights increased at 1416 points and decreases at 496 points (Fig. 6).

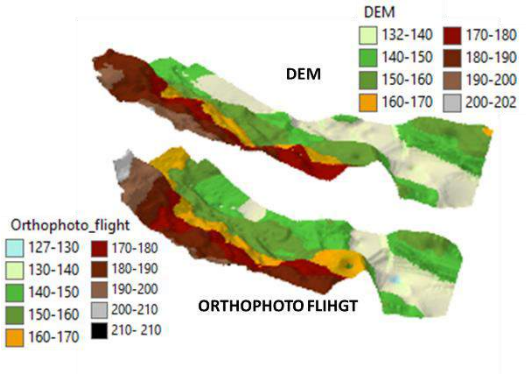

Fig. 6. DEM visualization

4. DISCUSSION

When all the data were examined, it was found that groundwater was included in the geological characteristics which are among the factors that prepare the landslide in the region.

In addition, when the region was examined in terms of topography, it was found to be quite inclined. Especially in region A, the slope is 15-30% moderately stepped and 8-15% rolling. In zone B, the slope increases up to 30-60% where there is water line.

Among all these factors, precipitation is known to be effective in triggering landslides in the region.

5. CONCLUSION

According to the results obtained, the geological structure of the study area should be examined in detail and kept under observation. Drainage procedures should be performed in the region.

The approximate volume of the landslide can be calculated using the results obtained.

With the development of a software, landslides can also be detected from the satellite imagery in places where no more people live. In this way, before and after the landslide studies can be followed easily.

With systems such as UAV, it can be used for damage detection in landslide areas where there is no upward climbing situation and in places that do not allow local measurement. In this way, these zones can be recorded and used for insurance damages.

As a result of the study, it is seen that all used data sets are complementary and can be used in landslide modeling studies and in the establishment of information systems.

REFERENCES

Afet Riski. (2012). *6306 Sayılı Afet Riski Altındaki Alanların Dönüştürülmesi Hakkında Kanun. Yayımlandığı Resmî Gazetenin Tarihi: 31/5/2012 Sayısı: 28309, Yayımlandığı Düsturun Tertibi: 5 Cildi: 52.*

Çan, T., Mazman, T., Tekin, S., & Y, D. T. (2015). Doğu Akdeniz Bölgesi Tarihsel Heyelan Envanterinin Frekans Büyüklük Dağılımlarına Göre Tamamlılık Değerlendirmesi. In *68th Geological Congress of Turkey*.

ÇEM. (2019). Retrieved 22 September 2019, from

http://www.cem.gov.tr/erozyon/Libraries/cemDocument/HEYELANLAR.sflb.ashx

Cha, D., Hwang, J., & Choi, B. (2018). Landslides detection and volume estimation in Jinbu area of Korea. *Forest Science and Technology*. https://doi.org/10.1080/21580103.2018.1446367

ELSUS. (2018). Retrieved 22 September 2019, from https://esdac.jrc.ec.europa.eu/content/european-landslide-susceptibility-map-elsus-v2

GLC. (2019). Retrieved 22 September 2019, from https://data.nasa.gov/Earth-Science/Global-Landslide-Catalog/h9d8-neg4

Gökçe, O., Özden, Ş., & Demir, A. (2008). *Türkiye'de Afetlerin Mekânsal ve İstatistiksel Dağılımı Afet Bilgileri Envanteri*. Ankara: Mülga Afet İşleri Genel Müdürlüğü Yayınları.

Gökçeoğlu, C., & Ercanoğlu, M. (2001). Heyelan duyarlilik haritalarinin hazirlanmasinda kullanilan parametrelere ilişkin belirsizlikler. *Yerbilimleri*.

ISPRA. (2018). Retrieved from http://www.isprambiente.gov.it/contentfiles/00010100/10185-second-world-landslide-forum-press-release.pdf

Lacroix, P., Bièvre, G., Pathier, E., Kniess, U., & Jongmans, D. (2018). Use of Sentinel-2 images for the detection of precursory motions before landslide failures. *Remote Sensing of Environment*. https://doi.org/10.1016/j.rse.2018.03.042

Mondini, A. C., Santangelo, M., Rocchetti, M., Rossetto, E., Manconi, A., & Monserrat, O. (2019). Sentinel-1 SAR amplitude imagery for rapid landslide detection. *Remote Sensing*. https://doi.org/10.3390/rs11070760

MTA. (2018). Retrieved 25 September 2019, from https://heysemp2018.afad.gov.tr/tr/24326/Turkiyenin-Heyelan-Tarihcesi

MTA. (2019). Retrieved 24 September 2019, from http://yerbilimleri.mta.gov.tr/anasayfa.aspx

Nikolaeva, E., Walter, T. R., Shirzaei, M., & Zschau, J. (2014). Landslide observation and volume estimation in central Georgia based on L-band InSAR. *Natural Hazards and Earth System Sciences*. https://doi.org/10.5194/nhess-14-675-2014

Parente, C., & Pepe, M. (2018). Uncertainty in landslides volume estimation using DEMs generated by Airborne Laser Scanner and Photogrammetry data. In *International Archives of the Photogrammetry, Remote Sensing and Spatial Information Sciences - ISPRS Archives*. https://doi.org/10.5194/isprs-archives-XLII-3-W4-397-2018

Plank, S., Twele, A., & Martinis, S. (2016). Landslide mapping in vegetated areas using change detection based on optical and polarimetric SAR data. *Remote Sensing*. https://doi.org/10.3390/rs8040307

Qin, Y., Lu, P., & Li, Z. (2018). Landslide inventory mapping from Bitemporal 10 m Sentinel-2 images using change detection based markov random field. In *International Archives of the Photogrammetry, Remote Sensing and Spatial Information Sciences - ISPRS Archives*. https://doi.org/10.5194/isprs-archives-XLII-3-1447-2018

Qu, T., Xu, Q., Liu, C., Li, Z., Chen, B., & Dai, K. (2019). Radar remote sensing applications in landslide monitoring with multi-platform insar observations: A case study from China. In *International Archives of the Photogrammetry, Remote Sensing and Spatial Information Sciences - ISPRS Archives*. https://doi.org/10.5194/isprs-archives-XLII-2-W13-1939-2019

Solís-Castillo, B., Mendoza, M. E., Vázquez Castro, G., & Bocco, G. (2019). Landslide inventory map of the tropical dry Sierra Costa Region, Michoacán México. *Physical Geography*. https://doi.org/10.1080/02723646.2019.1574136

SOTER. (2012). Retrieved 24 September 2019, from https://esdac.jrc.ec.europa.eu/projects/SOTER/Soter_Model.html

Tsutsui, K., Rokugawa, S., Nakagawa, H., Miyazaki, S., Cheng, C. T., Shiraishi, T., & Yang, S. Der. (2007). Detection and volume estimation of large-scale landslides based on elevation-change analysis using DEMs extracted from high-resolution satellite stereo imagery. *IEEE Transactions on Geoscience and Remote Sensing*. https://doi.org/10.1109/TGRS.2007.895209

Uluğ, A. (2014). Nasıl Bir Afet Yönetimi? In *TMMOB İzmir Kent Sempozyumu*. İzmir.

USGS. (2019). Retrieved 24 September 2019, from https://www.usgs.gov/natural-hazards/landslide-hazards

Wang, T. S., Yu, T. T., Lee, S. T., Peng, W. F., Lin, W. L., & Li, P. L. (2014). MATLAB code to estimate landslide volume from single remote sensed image using genetic algorithm and imagery similarity measurement. *Computers and Geosciences*. https://doi.org/10.1016/j.cageo.2014.06.004

Yang, W., Wang, Y., Sun, S., Wang, Y., & Ma, C. (2019). Using Sentinel-2 time series to detect slope movement before the Jinsha River landslide. *Landslides*. https://doi.org/10.1007/s10346-019-01178-8

Zhao, Y., Huang, Y., Liu, H., Wei, Y., Lin, Q., & Lu, Y. (2018). Use of the Normalized Difference Road Landside Index (NDRLI)-based method for the quick delineation of road-induced landslides. *Scientific Reports*. https://doi.org/10.1038/s41598-018-36202-9

CISET - 2nd Cilicia International Symposium on Engineering and Technology
10-12 October, 2019, Mersin / TURKEY

TRIGONOMETRIC SERIES SOLUTIONS FOR STATIC ANALYSIS OF SIMPLY SUPPORTED BEAM

Kübra ERDEM [*1], Atilla ÖZÜTOK [2*]

[1] KTO Karatay University, Engineering Faculty, Department of Civil Engineering, Konya, Turkey,
kubraerdem42@gmail.com
[2] KTO Karatay University, Engineering Faculty, Department of Civil Engineering, Konya, Turkey,
atilla .ozutok@karatay.edu.tr

ABSTRACT
In this study, static analysis of orthotropic Euler-Bernoulli beams, which have a simple support at both ends, have a uniform distributed load effect and constant cross-sectional geometry, have been performed. Equilibrium equations, kinematic equations and structural relations of beam theory were obtained by using energy principles. The obtained equations were transformed into operator form and functional including dynamic and geometric boundary conditions of beam theory were obtained with the help of Gâteaux differential method. Ritz method was used in the solution of functional. In the Ritz method, trigonometric shape functions which provide geometric and dynamic boundary conditions of the problem were chosen. The solution of the matrices is done by coding in a computer program. Numerical applications were made for static analyzsis and the results were compared with the results of similar studies in the literature and the results were found to be very close to each other.

Keywords: *Beam, Ritz method, Gâteaux differential method, Trigonometric-series solution.*

[*] Corresponding Author

1. INTRODUCTION

Today, as in many areas, the solution of the mechanical problems of the buildings is affected by the rapidly developing modern computer technology. With the rapidly developing capacity and fast computers, solutions are provided for more complex and time-consuming problems. Advances in computer technologies have enabled numerical solution methods to become more operational.

For the analysis of beams, researchers have applied beam theories such as Euler-Bernoulli Beam Theory (CLBT), Timoshenko Beam Theory (FSDT) and higher order theories. When the source research is done, it is seen that many researchers work on these theories. Trung-Kien Nyugen et al. (2016) developed a new trigonometric series solution based on high-beam theory for the analysis of static, torsional and vibration of composite beams. Ngoc-Duong Nguyen et al. (2018) proposed new Ritz functions for size-dependent analysis of randomly placed micro-layer composite beams. In his study, Zhou (2000) studyexamined the free vibrations of multi-span Timoshenko beams by Rayleigh-Ritz method. Özütok et al. (2014) examined the free vibration analysis of angled laminated composite beams. They obtained the functionalities by using the Gâteaux differential method and calculated the natural frequencies of composite beams using mixed finite element formulation on the basis of Euler-Bernoulli and Timoshenko beam theory. Aköz and Kadıoğlu (1996) in their work, under the arbitrary load on the elastic Winkler ground variable beams of circular cross-section with the analysis of mixed finite element method. They obtained the functions by Gâteaux differential method. Aköz and Uzcan (1991) presented a new functional Gâteaux differential for Reissner plates with geometric and dynamic boundary conditions. Aköz and Özütok (2000) in their work with the Gâteaux differential method obtained a new functional arbitrary shell geometry and mixed finite element method used in their solution.

In this study, static analysis of beams based on Euler-Bernoulli beam theory was performed by Ritz method. In this study, simple supported beams with uniform cross - sectional load and constant cross - sectional geometry are discussed. For the Euler-Bernoulli beam theory, EBT2 beam elements are defined, where bending moment and collapse are defined as unknown. Field equations of Euler-Bernoulli beam theory are obtained from the energy principles by using the virtual displacement principle. Dynamic and geometric boundary conditions were determined by performing variational operations, then field equations containing these boundary conditions were converted to operator form. By applying Gâteaux derivative to this operator form, continuity and potentiality checks were made and the functional of Euler-Bernoulli beam theory was obtained. Field equations and boundary conditions are reflected in this function obtained in a robust Aköz (1985, 1991, 1996, 2000) has been used by the sources published. This functional contains only first-order derivatives. Functional unknowns include bending moment and displacement. Bending moment and displacement are defined by trigonometric series. Trigonometric shape functions provide the geometric and dynamic boundary conditions of the problem. The solution of the obtained system matrices was done by coding developed in a computer program. Bending moment and displacement were obtained directly.

2. FORMULATION

For generality purposes, the displacement field in the beam may be assumed to be

$$\begin{aligned} u &= -z\left(w_{,x}\right) \\ v &= 0 \\ w &= w_0(x) \end{aligned} \tag{1}$$

where *(u,v,w).* are the displacemets of a point *(x,y,z)* along the *x,y* and *z* coordinates, respectively. *w* transverse displacement of the normal. According to the displacement statement above, the elongation ratio for Euler-Bernoulli beam theory is as follows

$$\varepsilon_x = u_{,x} = -z\, w_{,xx} \tag{2}$$

2.1. Beam Theory

The total virtual work of internal forces and the virtual work of external forces are given below using the principle of virtual displacement to derive equilibrium equations.

$$\delta U = \int_0^L \iint_A \left(\sigma_x \delta\varepsilon_x\right) dA\, dx$$

$$\delta W = -\int_0^L q\, \delta w\, dx \tag{3}$$

Virtual displacements principle when a given beam element is in balance

$$\delta U + \delta W = 0 \tag{4}$$

Euler-Lagrange equations are obtained following

$$-M_{x,xx} - q = 0 \tag{5}$$

Adoption of linear elastic isotropic material

$$\sigma_x = E\varepsilon_x \tag{6}$$

is known to be. Moment expression in Euler-Bernoulli beam theory

$$M = \int_{-h/2}^{h/2} \sigma_x\, z\, dz = \int_{-h/2}^{h/2} E\left[-z\, w_{,xx}\right] z\, dz = -EI\, w_{,xx} \tag{7}$$

Kinematic equation for Euler-Bernoulli beam obtained.

$$-\frac{M}{EI} - w_{,xx} = 0 \tag{8}$$

Dynamic boundary conditions and geometric boundary conditions of the beam in addition to Eq. (5) and Eq. (8),

$$-\mathbf{M}+\hat{\mathbf{M}}=0,\quad -\mathbf{R}+\hat{\mathbf{R}}=0$$
$$-\boldsymbol{\Omega}+\hat{\boldsymbol{\Omega}}=0,\quad -\mathbf{u}+\hat{\mathbf{u}}=0 \qquad (9)$$

can be written symbolically. Where $\hat{M}$ and $\hat{u}$ refer to the known moment and displacement vectors at the boundaries, respectively.

2.2. The Gâteaux Differantial And Functional

Field equations, including dynamic and geometric boundary conditions, can be written in the operator form.

$$\mathbf{Q=Ly-f} \qquad (10)$$

The Gâteaux differential method was used in order to find the functional of the field equations obtained for Euler-Bernoulli beam. This method is widely used and explanations (Aköz 1991, 2000) are included. Here, basic steps and definitions for simplicity will be summarized briefly. The Gâteaux derivative of the **Q** operator is defined as follows.

$$d\mathbf{Q}(\mathbf{y};\bar{\mathbf{y}})=\frac{\partial\mathbf{Q}(\mathbf{y}+\tau\bar{\mathbf{y}})}{\partial\tau}\Big|_{\tau=0} \qquad (11)$$

where τ is a scalar quantity. A required and sufficient condition for **Q** to be a potantial is

$$\left\langle d\mathbf{Q}(\mathbf{y};\bar{\mathbf{y}}),\mathbf{y}^{*}\right\rangle=\left\langle d\mathbf{Q}(\mathbf{y};\mathbf{y}^{*}),\bar{\mathbf{y}}\right\rangle \qquad (12)$$

where the parantheses indicate the inner products. If the operator **Q** potantiel, then the functional corresponding to the field equations will be given as

$$I(y)=\int_0^1\langle\mathbf{Q}(s\mathbf{y}),\mathbf{y}\rangle ds \qquad (13)$$

where s is a scalar quantity. For the Euler-Bernoulli beam, a clear expression of the $I(y)$ function of the Q operator can be written

$$I(y)=\left[M_{x,x},w_x\right]-\left[q,w\right]-\frac{\alpha}{2}\left[M_x,M_x\right]$$
$$-\left[\hat{w}_{,x},M_x\right]_{\varepsilon}-\left[w,\hat{T}\right]_{\sigma}-\left[\left(M_x-\hat{M}_x\right),w_{,x}\right]_{\sigma} \qquad (14)$$
$$+\left[\left(\hat{w}-w\right),T\right]_{\varepsilon}$$

The parantheses with the subscripts σ and ε indicate the dynamic and geometric boundary conditions, respectively. And the terms with "^" are valid if the boundary conditions are linear; otherwise, they vanish.
Where $\alpha=1/EI$.

2.3. Ritz Method

The Ritz method is one of the approximate solution methods that gives a very good approach to the differential equation where the functional of the problem is present. In the Ritz method for high accuracy, the selected interpolation function must meet the boundary conditions of the problem. In this way, an approximate solution is made for the differential equation using the selected solution functions. If the value of a_i which makes the I functional minimum is sought, the partial derivatives of the I functional with respect to a_i must be zero.

$$\frac{\partial I(y)}{\partial a_n}=0 \quad (i=1,2,3,...,n) \qquad (15)$$

The functional variables of Euler-Bernoulli beam are $w=w(x)$ and $M=M(x)$ respectively. Trigonometric shape function providing dynamic and geometric boundary conditions of a simple supported beam

$$\varphi_j(x)=sin\frac{j\pi}{L}x \quad (j=1,3,5,...,n) \qquad (16)$$

The trigonometric series expressions of displacement and moment to be used in the Ritz method are as follows.

$$w(x)=\sum_{j=1}^{n}\varphi_j(x)w_j$$
$$M(x)=\sum_{j=1}^{n}\varphi_j(x)M_j \qquad (17)$$

The trigonometric series expressions in Eq. (17) are written in place of the functional of Euler-Bernoulli beam theory. And when the Ritz method given in equation (15) is applied, it is the product of the trigonometric shape functions.

$$\left[k_1\right]=\int_0^L\varphi_i\varphi_j dx \;,\; (i,j=1,2,3,...,n)$$
$$\left[k_2\right]=\int_0^L\varphi_i'\varphi_j' dx \;,\; (i,j=1,2,3,...,n)$$
$$\left[k_4\right]=\int_0^L q\,\varphi_i' dx \;,\; (i,j=1,2,3,...,n) \qquad (18)$$

System matrix and load matrix obtained by substituting multiplication expressions,

$$\left[S\right]_{EBT2}=\begin{matrix}\\ 2n\end{matrix}\left[\begin{array}{c|c} M & w \\ \hline -\alpha\left[k_1\right] & \left[k_2\right] \\ \hline \left[k_2\right]^T & \left[0\right] \end{array}\right]^{2n} \quad \left[Y\right]_{EBT2}=\begin{matrix}\\ 2n\end{matrix}\left[\begin{array}{c} {}_n[0] \\ \hline {}_n\left[k_4\right] \end{array}\right] \qquad (19)$$

3. NUMERICAL RESULTS

In this study, a functional, Gâteaux differential method, which corresponds to the field equations of a homogeneous and isotropic Euler-Bernoulli (EBT2) beam with a simple support, constant cross-sectional area at both ends under the effect of uniformly

distributed load, is obtained. These variables are represented by trigonometric shape functions which provide the conditions of collapse and moment, geometric and dynamic boundary conditions. Ritz method was used to solve the problem. The solutions of the obtained matrices were made by coding in a computer program. The results obtained in the static analyzes were compared with the results of similar studies in the literature. Some parameters used in static calculations for beams are accepted. These accepted parameters E = 29000, b = 1, q = 10, υ = 0,3, ρ = 1. Solutions were made for different L / h ratios. The beam model given in Fig. 1 was taken into consideration in all calculations.

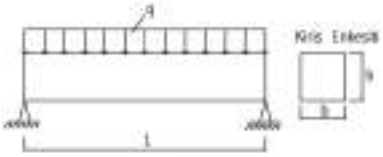

Fig. 1. Simple support beam model

Below are some of the results obtained from the analyzes.

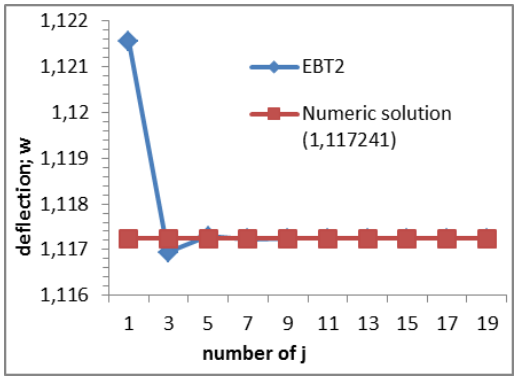

Fig. 2. Comparative approximation test for maximum collapse of EBT2 beam (L = 12, h = 1)

As shown in Figure 2, the results found for the EBT2 beam correspond to the actual results obtained by the analytical solution with the increase of the number j.

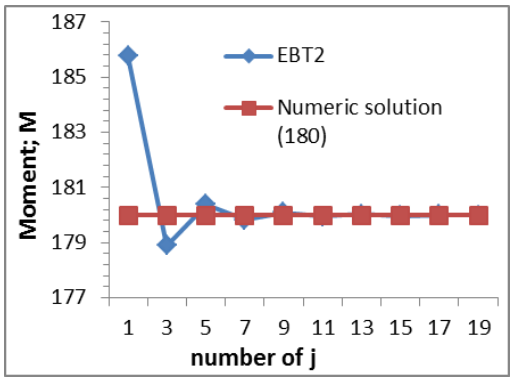

Fig. 3. Comparative approximation test for EBT2 beam maximum torque (L = 12, h = 1)

As shown in Figure 3, the maximum moment values in the middle of the beam correspond to the actual results obtained by the analytical solution with the increase of the number j. Table 1 shows the comparison of maximum displacements values in the solutions made by considering different L / h ratios for EBT2 beam.

Table 1. Maximum displacement of simple supported EBT2 beams (w)

Reference	L/h			
	12/12	40/12	80/12	160/12
EBT2	0.000647	0.07982	1.2772	20.435
Özütok, Madenci	0.000644	0.07971	1.2750	20.410
Vo, Thai	0.000647	0.07982	1.2771	20.434
Bickford	0.000647	0.07982	1.2771	20.434

3. CONCLUSIONS

In this study, static analysis of orthotropic Euler-Bernoulli beams with simple support, uniformly distributed load and fixed cross-sectional geometry were performed. Equilibrium equations, kinematic equations and structural relations of beam theory were obtained using the principle of virtual displacement. These field equations including dynamic and geometric boundary conditions were transformed into operator form by performing variational operations. The Gâteaux derivative was applied to this operator form and functional was obtained including dynamic and geometric boundary conditions of beam theory. Ritz method was used in the solution of the functional. The bending moment and displacement values, which are unknown in function and which will be obtained directly from the analysis, are expressed with trigonometric shape functions that provide geometric and dynamic boundary conditions of the problem. The solution of the obtained system matrices was done by coding in a computer program. Numerical applications were made and the results were compared with the results of similar studies in the literature and the results were found to be very close to each other.

As a continuation of this study, it is considered to continue the studies by making solutions for different bearing conditions.

REFERENCES

Aköz, A. Y. (1985). "Çubuklar için yeni enerji fonksiyonelleri ve uygulamaları." *V. Ulusal Mekanik Kongresi*, İTÜ.

Aköz, A. Y., Kadıoğlu F. (1996). "The mixed finite element solution of circular beam on elastic foundation." *Computers & Structures*, 60 (4), pp. 643-651.

Aköz A. Y., Kadıoğlu F. (1999). "The mixed finite element method for the quasi-static and dynamic analysis of viscoelastic Timoshenko beams." *International Journal For Numerical Method in Engineering*, 44, pp. 1909-1932,

Aköz A. Y., Özütok A. (2000). "A functional for shells of arbitrary geometry and a mixide finite element method for parabolic and circular cylindirical shells." *International Journal For Numerical Method in Engineering*, 47, pp. 1933-1981,

Bickford, W. B. (1982). "A consistent higher order beam theory." *Development in Theo. App. Mech*., Vol. 11, pp. 137-142.

Aköz A. Y., Uzcan N. (1992). "The new functional for Reissner plates and its application." *Computers & Structures,* Vol. 44 (5), pp. 1139-1144.

Eratlı N., Aköz A. Y. (1997). "The mixed finite element formulation for the thick plates on elastic foundations." *Computers and Structures*, 65 (4), pp. 515-529.

Heyliger P.R., Reddy J. N., Eftekhari S.A. (1988). "A higher order beam finite element for bending and vibration problems." *Journal of Sound and Vibration,* 126 (2), pp. 309-326.

Nguyen N. D., Nguyen T. K., Nguyen T. N., Thai H. T. (2018). "New Ritz-solution shape functions for analysis of thermo-mechanical buckling and vibration of laminated composite beams." *Composite Structures,* 184, pp. 452-460,
.

Nguyen N. D., Nguyen T. K., Thai H. T., Vo T. P. (2018). "A Ritz type solutions with exponential trial functions for laminated composite beams based on the modified couple stress theory", *Composite Structures,* 191, pp. 154-167.

Nguyen T. K., Nguyen N. D., Vo T. P., Thai H. T. (2017). "Trigonometric-series solution for analysis of laminated composite beams", *Composite Structures*, 160, pp. 142-151.

Özütok A., (1999). Genel kabuklara ait fonksiyonel ve parabolik silindir kabuklar için karma sonlu eleman formülasyonu, Doktora Tezi, İstanbul Teknik Üniversitesi, Fen Bilimleri Enstitüsü, İstanbul.

Özütok A., Madenci E. (2017). "Static analysis of laminated composite beams based on higher-order shear deformation theory by using mixed-type finite element method." *International Journal of Mechanical Sciences*, 130, pp. 234-243.

Özütok A., Madenci E., Kadioğlu F. (2014). "Free vibration analysis of angle-ply laminate composite beams by mixed finite element formulation using the Gâteaux differantial.", *Sci Eng Compos Mater*, 21, pp. 257-266.

Reddy J. N. (2004). *Mechanics of Laminated Composite Plates and Shells: theory and analysis*, Second Editions, CRC Press, Boca Rotan.

Vo T. P., Thai H. T. (2012). "Static behavior of composite beams using various refined shear deformation theories." *Composite Structures*, 94, pp. 2513-2522.

Zhou D. (2001) "Free vibration of multi-span Timoshenko beams using static Timoshenko beam functions." *Journal of Sound and Vibration*, 241 (4), pp. 725-734.

CISET - 2nd Cilicia International Symposium on Engineering and Technology
10-12 October, 2019, Mersin / TURKEY

FUZZY NEURAL NETWORK DC VOLTAGE CONTROLLER OF THREE PHASE SHUNT ACTIVE POWER FILTER

Resul Çöteli*[1], Hakan Açıkgöz[2] and Beşir Dandıl[3]

[1]Fırat University, Faculty of Technology, Department of Energy Systems Engineering,
Elazığ, Turkey, e-mail: rcoteli@firat.edu.tr

[2]Kilis 7 Aralık University, Vocational School of Technical Sciences, Department of Electricity and Energy,
Kilis, Turkey, e-mail: hakanacikgoz@kilis.edu.tr

[3]Fırat University, Faculty of Technology, Department of Mechatronics Engineering,
Elazığ, Turkey, e-mail: bdandil@firat.edu.tr

ABSTRACT

Shunt active power filters (SAPFs) are utilized to compensate for harmonic and reactive power caused by linear and non-linear loads in AC grid. In this paper, a three-phase SAPF with fuzzy neural network (FNN) DC voltage controller is modelled by using Matlab/Simulink software. Reference current for control of SAPF is obtained via load current, voltage of point of common coupling and output of FNN DC voltage controller. Dynamic performance of three-phase SAPF with FNN DC voltage controller is evaluated under non-linear loading condition. The simulation results are given both FNN and PI DC voltage controller. If performance of the two controllers is evaluated according to the settling time of the DC voltage, the maximum overshoot and total harmonic distortion (THD) of AC supply current, FNN controller has superior performance than PI controller.

Keywords: *Harmonic, Reactive Power, Shunt Active Power Filter, Fuzzy Neural Network Controller*

*Corresponding Author

1. INTRODUCTION

The developments in semiconductor devices and microprocessor technologies have led to widespread use of power electronics circuits. These circuits draw non-sinusoidal currents from the utility side due to their nonlinear nature. Conventionally, the power quality problems caused by non-sinusoidal currents are compensated by using the passive filter (Chaoui *et al.*, 2007). New devices based on power electronic are known as Active Power Filter (APF) or power conditioners. These devices are capable of reactive power and harmonic compensation. The active filters can be divided into three categories according to the type of connection as series, shunt and series-parallel (Akagi, 1994).

The shunt APFs (SAPFs) have been known as a feasible solution to the power quality problems caused by nonlinear loads. They can eliminate the harmonics as well as compensate fundamental reactive power by injecting reactive currents into the AC lines. Further, SAPFs are capable of keeping the power system balance even under operating conditions such as unbalanced and nonlinear loads (El-Kholy *et al.*, 2006).

It is important to keep the DC voltage at the desired value for the active filter to work properly. Conventionally, DC voltage of SAPFs has been controlled via proportional + integral + derivative (PID) controller. To design such a controller, a precise mathematical model of the system is needed. Unfortunately, it is very difficult to obtain a precise mathematical model in a system under load disturbance and parameter change (Mansour *et al.*, 2016). In addition, many different control methods have been applied to DC voltage control, such as fractional order PI **λ** control (Zhang *et al.*, 2011), auto-disturbance rejection control (Ding *et al.*, 2013), adaptive control (Sarhan *et al.*, 2014) and type-2 fuzzy controller (Acikgoz et al., 2017)

In this paper, DC voltage of SAPF is regulated by a fuzzy neural network (FNN). For this aim, a SAPF is built in Matlab/Simulink software. Reference current for control of SAPF is obtained by using instantaneous *pq* theory. Dynamic performance of SAPF with FNN DC voltage controller is investigated under non-linear loading conditions. The simulation results show that SAPF reduces the total harmonic distortion (THD) of source current and improves the power factor of the AC grid under non-linear loading conditions.

2. SHUNT ACTIVE POWER FILTER AND ITS CONTROL STRATEGY

Figure 1 depicts the SAPF system. It consists of a three-phase voltage source inverter, DC capacitor and a coupling inductance. This inverter is connected in parallel to AC supply by means of coupling inductance L_f. In Fig. 1, R_f symbol represents internal resistance of coupling inductance. The DC side of the SAPF is terminated with a DC capacitor(C_f). This capacitor provides a constant DC voltage and the real power necessary to cover the losses of the system. The inductors (El-Kholy *et al.*, 2006). The circuit equations of SAPF in the *abc* coordinates can be written as follows (Vardar, 2016):

$$L_{af}\frac{di_{af}}{dt} = e_a - R_f i_{af} - v_{af} \quad (1)$$

$$L_{bf}\frac{di_{bf}}{dt} = e_b - R_f i_{bf} - v_{bf} \quad (2)$$

$$L_{cf}\frac{di_{cf}}{dt} = e_c - R_f i_{cf} - v_{cf} \quad (3)$$

$$C_{dc}\frac{dv_{dc}}{dt} = f_a i_{af} + f_b i_{bf} + f_c i_{cf} \quad (4)$$

In Equation (4), f_a, f_b and f_c are switching functions. For control aim of SAPF, the voltages and currents in *abc* coordinates should be converted into $\alpha\beta$ frame.

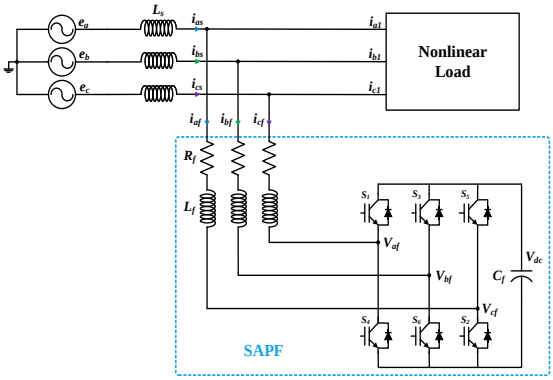

Fig. 1. Three phase SAPF system

AC supply voltages and currents in $\alpha\beta$ frame as:

$$\begin{bmatrix} v_{s\alpha} \\ v_{s\beta} \end{bmatrix} = \sqrt{\frac{2}{3}} \cdot \begin{bmatrix} 1 & -1/2 & -1/2 \\ 0 & \sqrt{3}/2 & -\sqrt{3}/2 \end{bmatrix} \cdot \begin{bmatrix} v_{sa} \\ v_{sb} \\ v_{sc} \end{bmatrix} \quad (5)$$

$$\begin{bmatrix} i_{s\alpha} \\ i_{s\beta} \end{bmatrix} = \sqrt{\frac{2}{3}} \cdot \begin{bmatrix} 1 & -1/2 & -1/2 \\ 0 & \sqrt{3}/2 & -\sqrt{3}/2 \end{bmatrix} \cdot \begin{bmatrix} i_{sa} \\ i_{sb} \\ i_{sc} \end{bmatrix} \quad (6)$$

The control algorithm of SAPF is shown in Fig. 2. Instantaneous reactive power theory is used to control of SAPF in this study. This theory requires instantaneous three-phase current and voltages to be transformed to $\alpha\beta$ coordinates from *abc* coordinates. In addition, DC voltage of SAPF is controlled by FNN controller. Instantaneous active and reactive power in $\alpha\beta$ coordinates can be calculated as follows:

$$p = v_{s\alpha} i_{s\alpha} + v_{s\beta} i_{s\beta} \quad (7)$$

$$q = v_{s\alpha} i_{s\beta} - v_{s\beta} i_{s\alpha} \quad (8)$$

Instantaneous real and imaginary powers in Eq. (7) and (8) include AC $(\tilde{p}\ and\ \tilde{q})$ and DC $(\bar{p}\ and\ \bar{q})$ components. Thus,

$$p = \tilde{p} + \bar{p} \quad (9)$$

$$q = \tilde{q} + \bar{q} \quad (10)$$

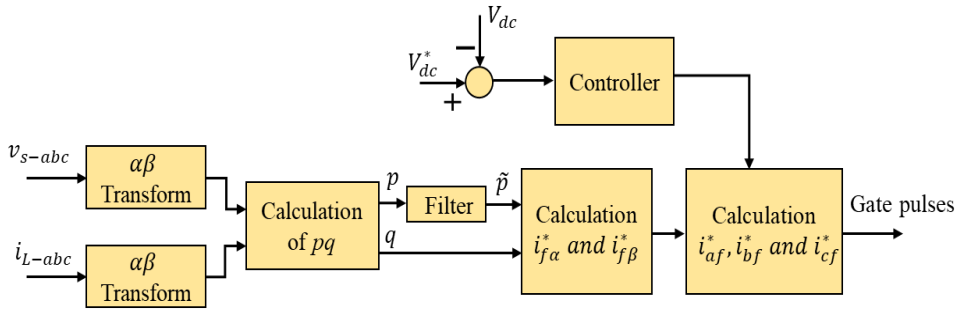

Fig. 2. Complete control schema of three-phase SAPF

Reference currents of SAPF in $\alpha\beta$ coordinates can be determined as follows:

$$\begin{bmatrix} i_{s\alpha}^{ref} \\ i_{s\beta}^{ref} \end{bmatrix} = \frac{1}{(v_{s\alpha})^2 + (v_{s\beta})^2} \begin{bmatrix} v_{s\alpha} & -v_{s\beta} \\ v_{s\beta} & v_{s\alpha} \end{bmatrix} \begin{bmatrix} \bar{q} + \bar{p}_{loss} \\ 0 \end{bmatrix} \quad (11)$$

Then, reference currents in $\alpha\beta$ coordinates are transformed into *abc* coordinates to generate gate pulses for inverter and SAPF compensates both harmonics and reactive currents caused by load. Gate pulses are generated via hysteresis band current control method (Kesler, 2009).

3. FUZZY NEURAL NETWORK

The FNN controller is a controller that combines the properties of neural network and fuzzy logic controllers. The functions of a fuzzy logic controller are performed in the same way as a neural network controller. FNN controller does not require a mathematical model of the system to be controlled. The FNN controller used in this study is of Mamdani type with two inputs and one output. It has four layer and its structure is depicted in Fig. (3). Rule set with two fuzzy IF-THEN Mamdani type FNN is given as follows (Coteli *et al.,* 2012; Abraham, 2005; Acikgoz *et al*., 2016):

$$R^l: IF\ X_1\ is\ A_1^l\ and\ X_2\ is\ A_2^l\ THEN\ y\ is\ \omega_l \quad (12)$$

Where, X_1 and X_2 are input variables, y is the output variable, A_1^l and A_2^l are linguistic terms of antecedents part with membership functions and ω_l is a real number of the consequent part. Inputs are selected as DC voltage tracking error (e) and change of this error (Δe) and they are obtained as follows (Coteli *et al.,* 2012):

$$e = V_{dc}^* - V_{dc} \quad (13)$$

$$\Delta e = e(k) - e(k-1) \quad (14)$$

Here, V_{dc}^* and V_{dc} are reference and sensed DC voltage, respectively. Layer-I transmits input signals to the Layer-II directly. Each node in Layer-II corresponds to one linguistic label to one of the input variables in Layer-I. A node in Layer-III represents the antecedent part of a rule. The output of a Layer-III represents the firing strength of the corresponding fuzzy rule. Layer-IV combines the incoming rule antecedents and determines the degree to which they belong to the output linguistic label. This node does the combination of all the rules consequents and computes the crisp output after defuzzification (Abraham, 2005).

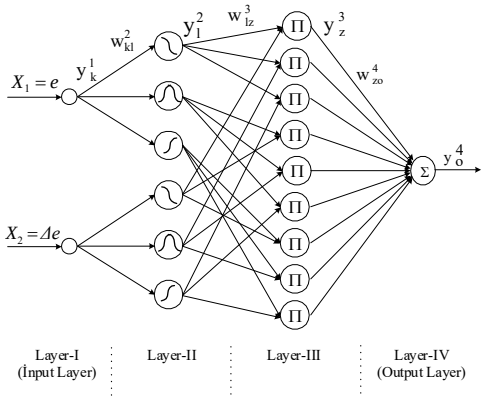

Fig. 3. Structure of FNN controller used in this study

The control parameters of the membership functions and the output weights of FNN controller are updated by using the back-propagation algorithm. The detailed information on update of parameters can be founded in (Coteli *et al.,* 2012).

4. SIMULATION RESULTS

In this study, a three-phase SAPF with FNN DC voltage controller is built in Matlab/Simulink software and its dynamic performance is evaluated operating condition with non-linear load. The Matlab/Simulink model of SAPF is shown in Fig. 4. The non-linear load is a three phase uncontrolled rectifier supplying a *RL* load. The output of FNN is integrated to eliminate the steady state error. Simulation parameters are given in Table 1.

Simulation studies were conducted for operating scenario with non-linear load. In the scenario, the nonlinear load is connected into AC supply and the SAPF is operated at 0.05s. DC voltage waveform of SAPF for this scenario is illustrated in Fig. 4 (a) for both PI and FNN controller. It is seen that DC voltage of SAPF reaches the reference value faster than the case with the PI controller.

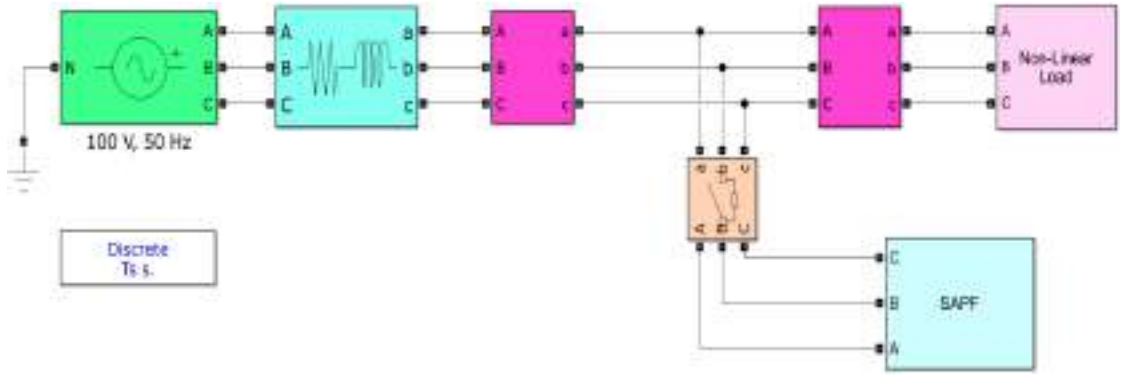

Fig. 4. Matlab/Simulink Model of SAPF

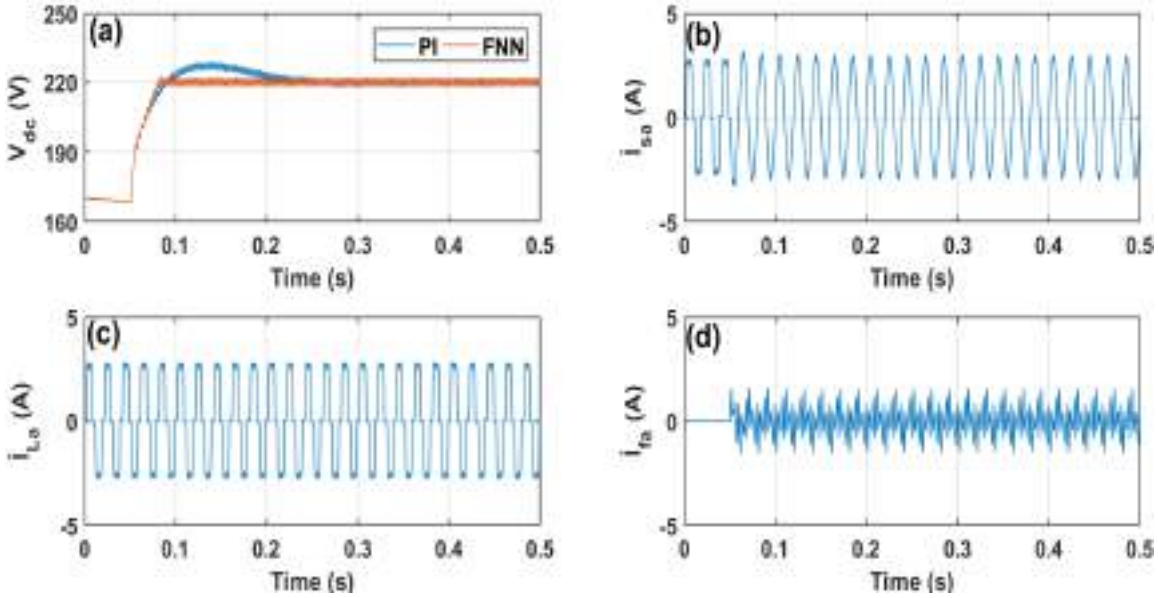

Fig. 5. Simulation results of SAPF (a) DC bus voltage (b) grid current (c) Load current (d) One phase SAPF current

As can be seen from Fig. 4, PI controller has an overshoot of 3.57% and follow the reference DC bus voltage after 181.22 ms. The proposed controller has no overshoot and reaches reference DC bus voltage after 34.21 ms. In steady state, the two controllers maintain the DC voltage at the reference value.

Table 1. Simulation parameters

Parameters	Value
AC supply voltage	100 V
AC supply frequency	50 Hz
DC voltage	220 V
DC capacitor	4.7 mF
Coupling inductance	3.5 mH
Internal resistance of coupling inductance	0.1 Ω
Non-linear load	60+j20

The load current, AC supply voltage-current and current of SAPF are shown for one phase in Fig. 5 (b-d). It is seen in this figure that the AC supply current is sinusoidal form and in phase with AC supply voltage after the SAPF was run. Figure 6 shows total harmonic distortion (THD) in AC supply current for PI and FNN controller. THD is 1.75% in case with the FNN controller whereas THD is 2.33% for PI controller.

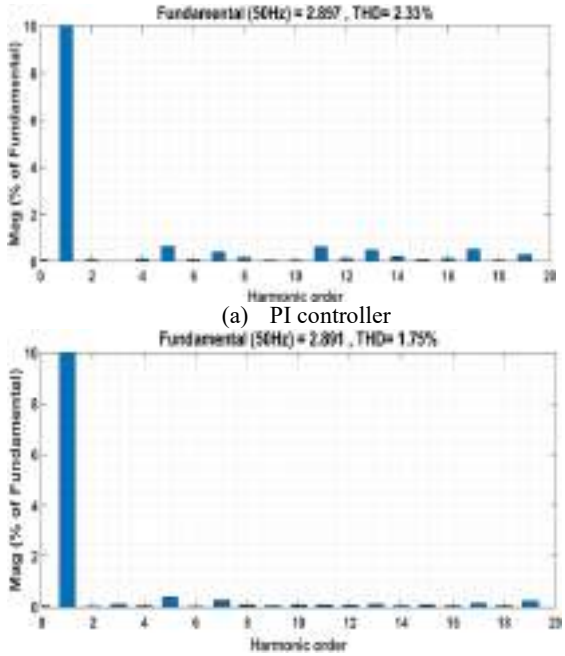

(a) PI controller

(b) FNN controller

Fig. 6. THD of AC supply current

5. CONCLUSION

This paper presents a three-phase SAPF with FNN FC voltage controller. A three-phase SAPF based on voltage source inverter is modelled in Matlab/Simulink. The model is used to eliminate harmonics and compensate for reactive power caused by nonlinear load. Three-phase uncontrolled rectifier supplying RL load is used as non-linear load. The simulation results are given for both FNN and PI controller. The performance of SAPF with FNN DC voltage controller shows superior performance than PI controller in terms of settling time of the DC voltage, the maximum overshoot and THD of AC supply current.

REFERENCES

Acikgoz, H., Kececioglu, O.F., Gani, A., Tekin, M., Sekkeli, M. (2017). "Robust Control of Shunt Active Power Filter Using Interval Type-2 Fuzzy Logic Controller For Power Quality Improvement", *Tehnički vjesnik,*Vol. 24, Suppl. 2, pp. 363-368.

Acikgoz, H., Kececioglu, O.F., Gani, A., Yildiz, C., Sekkeli, M. (2016). "Improved control configuration of PWM rectifiers based on neuro-fuzzy controller", *SpringerPlus*, Vol. 5, pp. 1-19.

Abraham, A. (2005). "Adaptation of fuzzy inference system using neural learning." *In Fuzzy systems engineering*, Springer, Berlin, Heidelberg.

Akagi, H. (1994). "Trends in active power line conditioners." *IEEE transactions on power electronics*, Vol. 9, No. 3, pp. 263-268.

Chaoui, A., Gaubert, J. P., Krim, F., & Champenois, G. (2007). "PI controlled three-phase shunt active power filter for power quality improvement." *Electric Power Components and Systems*, Vol. 35, No. 12, pp. 1331-1344.

Coteli, R., Deniz, E., Dandil, B., Tuncer, S., and Ata, F. (2012). "Phase angle control of three level inverter based D-STATCOM using neuro-fuzzy controller." *Advances in Electrical and Computer Engineering*, Vol. 12, No. 1, pp. 77-84.

Ding, Z., Liu, B., and Zhang, Y. (2013). "Optimal control for DC side voltage of active power filter based on auto-disturbance rejection control." *Power System Technology*, Vol. 37, No. 7, pp. 2030-2034.

El-Kholy, E. E., El-Sabbe, A., El-Hefnawy, A., and Mharous, H. M. (2006). "Three-phase active power filter based on current controlled voltage source inverter." *International Journal of Electrical Power & Energy Systems*, Vol. 28, No. 8, pp. 537-547.

Kesler, M. and Özdemir, E. (2009)." Operation of shunt active power filter under unbalanced and distorted load conditions." *In 2009 International Conference on Electrical and Electronics Engineering-ELECO 2009*, pp. I-92.

Mansour, B., Abdelkader, B., and Said, B. (2014). "Application of backstepping to the virtual flux direct power control of five-level three-phase shunt active power filter." *International Journal of Power Electronics and Drive Systems*, Vol. 4, No. 2, pp. 173.

Sarhan, G. M., Elkousy, A. A., Hagras, A. A., & Saad, S. M. (2010). Adaptive control of shunt active power filter using interval type-2 fuzzy logic controller. *In Proceedings of the 14th IEEE Middle East Power System Conference MEPCON'10*, (pp. 253-259).

Vardar, K. and Akpinar, E. (2016). "Linear model of a three-phase shunt active power filter with a hysteresis controller." *Turkish Journal of Electrical Engineering & Computer Sciences*, Vol. 24, No. 2, pp. 384-397.

Zhang, X. F., Wang, X. H. and Tia, L. F. *et al.,* (2011). "DC Voltage Control of Active Power Filter Based on Fractional-order PI λ Controller." *Automation of Electric Power Systems*, Vol. 37, No. 16, pp. 108-124, 2011.

ANTIMICROBIAL ACTIVITY OF *LAURUS NOBILIS* ESSENTIAL OIL ON *ESCHERICHIA COLI* ATCC 25922

Didem Erbaşcivan *[1], H.İbrahim Ekiz [1] and Esma Eser [2]

[1] Mersin University, Faculty of Engineering, Department of Food Engineering, Mersin, Turkey,

[2] Canakkale Onsekiz Mart University, Faculty of Engineering, Department of Food Engineering, Canakkale, Turkey,

ABSTRACT
In this study, the inhibitory effect of *Laurus nobilis* essential oil on *Escherichia coli* ATCC 25922 was investigated. Firstly the laurel leaves were dried at room temperature and the essential oil was obtained from the leaves using the hydrodistillation method with the Clevenger apparatus. The obtained oil samples were stored at +4° C until the analysis. In order to investigate the inhibitory effect of *L. nobilis* essential oil on *E. coli* during storage period, different amounts of essential oils(160, 200, 240, 480 and 2400 µL) were mixed with 240 µl of *E. coli* culture with the level of 10^8 CFU / ml and these mixtures with different concentrations were stored at +4° C for 6 days. Microbial analysis were performed both at the beginning (t=0) and the at first, third and sixth days of storage period. The analyzes were conducted by spreading plate method and carried out in 3 parallel. The microbial load of 160 µl essential oil -culture mixture was found less than the microbial load of the t=0 for the first storage day. This shows us that the preventive effect was observed in the samples stored in for 1 day. However, at the end of the 3rd and 6th days of the storage period of, the inhibitory effect of the essential oil was decreased. For the oil (240 µL)-culture (200 µL) mixture, it was also determined a continious inhibitory effect during the storage period.
The inhibitory effect was also determined for the mixture prepared with 480 µL of laurel essential oil 1st, and 3th days, but on the 6th day of the storage this mixture started to lose its effect. The mixture prepared from 2400 µL of essential oil was totally eliminated the microbial load. As a result, the amount of 2400 µL *Laurus nobilis* essential oil showed the maximum inhibitory effect on *Escherichia coli* ATCC 25922.

Keywords: *Laurus nobilis, Laurus nobilis essential oil, Escherichia coli ATCC 25922, inhibitor effect*

*Corresponding Author

1. INTRODUCTION

Essential oils have been used since the beginning of human history for flavored foods and beverages; they have been empirically used to disguise unpleasant odors, attract other individuals and control health problems, contributing to the welfare humans and animals, thus demonstrating the cultural and economic importance use of these products.(Andrade, 2014)Essential oils are complex mixtures obtained from the leaves, fruits, bark, and roots of plants by distillation or pressing. Essential oils are liquid at room temperature, a natural product that can easily crystallize, usually colorless or light yellow. These compounds are known to act on different types of microorganisms which are causing to food spoilage and poisoning (*Listeria monocytogenes, Enterococcus faecalis, Staphylococcus spp., Micrococcus spp., Bacillus spp., Campylobacter jejuni, Vibrio parahaemolyticus, Pseudomonas fluorescens, Shigella spp., Escherichia coli*), yeasts, and molds (*Saccharomyces cerevisiae, Aspergillus flavus, Aspergillus parasiticus*)due to their antibiotic-antimicrobial properties.(Evren, 2011)

Laurus nobilis is an evergreen shrub or tree native of the southern mediterranean region and its dried leaves and essential oil are used in the food industry as a spicy for flavoring and food preservative and are used in folk medicine.(Vilela,2016) *Laurus nobilis* leaves may vary depending on factors such as genotype, the region in which it is grown, harvest time, and contains essential oil between 0.20% and 2.51%.(Golukcu,2018) 1,8-cineole is the major laurel essential oil component with percentages ranging between 31.4 and 56%. Other compounds were present in appreciable amounts include linalool, trans Sabinene Hydrate, a-terpinyl-acetate, methyl eugenol, sabinene and eugenol. Benzene compounds present in percentages ranging Between 1 and 12%, are responsible for the spicy aroma of the leaves and are extremely important factors determining its sensory quality.(Vilela, 2016)

Laurus nobilis essential oil has shown antibacterial and antifungal properties.(Chmit, 2014)

Escherichia coli (*E.coli*) is a gram-negative, facultative anaerobe, mostly mobile, non-spore, rod-shaped bacterium of the genus *Escherichia* in the *Enterobacteriaceae* family.(Temelli, 2002) *Escherichia coli* is a foodborne pathogenic bacteria.(Harmankaya, 2013) *Escherichia coli* is found in the natural intestinal flora of humans and most warm-blooded animals. Pathogenic strains of *Escherichia coli* can cause various diseases such as diarrheal infections, urinary tract infections, meningitis and septicemia.(Degirmenci, 2017)

In this study, the inhibitory effect of *Laurus nobilis* essential oil on *Escherichia coli* ATCC 25922 was investigated.

2. MATERIAL AND METHOD

2.1. Material

The fresh *Lauris Nobilis* leaves were collected from the region of Tarsus –Mersin located in the south Turkey. *Escherichia coli* ATCC 25922 used as culture was obtained from Food Microbiology Lab., Department of Food Engineering, Mersin University.

2.2.Method

2.2.1.Extraction of *Lauris Nobilis* Essential Oil

The laurel leaves were dried at room temperature and the essential oil was obtained from the leaves using the hydrodistillation method with the Clevenger apparatus. The obtained oil samples were stored at +4° C until the analysis.(Aksoy, 2011)

2.2.2.Preparation of *Escherichia coli* ATCC 25922 Culture

Culture was taken from the stock with the help of an inoculation loop that is added to the Tryptic Soy Broth medium. Incubation was carried out at 37ºC for 18-24 hours.(Harrigan,1998)

Serial dilutions were prepared using 0.1% sterile peptone water to determine the microbial load of culture and by the spreading plate method.

2.2.3.Microbiological Analysis

240 µl *Escherichia coli* ATCC 25922 and 5 different concentrations (160, 200, 240,480 and 2400 µl) of *Laurus nobilis* essential oil were mixed. These samples were prepared for t = 0 , 1., 3., and 6. days and stored in the refrigerator at 4 ◦C until the day of the microbial analysis. The analyses were carried out in 3 parallels. Serial dilutions were prepared using 0.1% sterile casein peptone waters. Serially dilutions samples were transferred to petri dishes with the amount of 0.1 mL with the spreading plate method. Plate count agar medium (MERK: 1.05463.050 DARMSTADT, GERMANY) was used for the analysis and incubated at 37 ºC for 24 hours. At the end of this period, colonies were counted and microbial loads were calculated as CFU/ µl.

3. RESULT AND DISCUSSION

The results obtained for determinationof Antimicrobial Activity of *Laurus Nobilis* Essential Oil on *Escherichia coli* ATCC 25922 are given in Table.1.

Table.1. Antimicrobial Activity of *Laurus Nobilis* Essential Oil on *Escherichia coli* ATCC 25922

Concentration of *Laurus Nobilis* Essential Oil (µL *Laurus Nobilis* essential oil)	Initial *Escherichia coli* ATCC 25922 Number's (Log CFU/ µl)	0.Day Inhibitor Effect (Log CFU/µl)	1.Day Inhibitor Effect (Log CFU/ µl)	3.Day Inhibitor Effect (Log CFU/ µl)	6.Day Inhibitor Effect (Log CFU/ µl)
160	**8,66±0,28**	**5,64±0,11**	**4,79±1,07**	**U**	**U**
200	**7,46±0,47**	**4,32±0,30**	**6,08±0,42**	**3,86±0,80**	**4,27±0,11**
240	**7,46±0,47**	**5,04±0,55**	**3,35±0,10**	**4,33±0,28**	**4,48±0,59**

480	**8,88±0,22**	**3,77±0,26**	**3,66±0,35**	**4,53±0,57**	**U**
2400	**8,72±0,43**	-	-	-	-

U: uncounted, **(-)** : No microbial growth was observed.

The microbial load of 160 µl essential oil -culture mixture was found less than the microbial load of the t=0 for the first storage day. This shows us that the preventive effect was observed in the samples stored in for 1 day. However, at the end of the 3rd and 6th days of the storage period of, the inhibitory effect of the essential oil was decreased. For the oil (240 µL)-culture (200 µL) mixture, it was also determined a continious inhibitory effect during the storage period.

The inhibitory effect was also determined for the mixture prepared with 480 µL of laurel essential oil 1st, and 3th days, but on the 6th day of the storage this mixture started to lose its effect. The mixture prepared from 2400 µL of essential oil was totally eliminated the microbial load. As a result, the amount of 2400 µL *Laurus nobilis* essential oil showed the maximum inhibitory effect on *Escherichia coli* ATCC 25922.

Previous studies given in literatur,that *laurus nobilis* essential oil had bactericidal activity against *L.monocytogenes* (Alzoreky, 2003) and other pathogens and that 2 µl of laurel essential oil had antimicrobial effect against *E.coli*, *S.aureus* and various microorganisms.(Cenet,2006) Kara previously reported 2 microliters of *Laurus nobilis* essential oil, *Escherichia coli* bacteria, *Staphylococcus aureus, Pseudomonas pyocyaneus, Yersinia enterocolitica, Aeromonas hydrophila, Enterococcus Saccharomyces cerevisiae, fecalis* have found to create zones.(Kara, 2010)

4.CONCLUSION

Laurus nobilis essential oil has known antibacterial and antifungal properties.As a result of the experiment, it has also been found that *Laurus nobilis* essential oils peak inhibitory activity on *Escherichia coli* ATCC 25922 was at 2400 µl. It has been found that the inhibitory effect increases as the amount of *Laurus nobilis* essential oil increases. It was determined that *Laurus nobilis* essential oil continued to show inhibitory effect during the storage.

5. REFERENCES

Aksoy,A., Güven, A., Gülmez,M., (2011). The Effect of Some Plant Infusions and Hydrodistylates on Decontamination and Shelf Life of Chicken Meats, Kafkas University Journal of Veterinary Medicine, 17,40-74.

Alzoreky, NS., Nakahara,K., (2003). Antibacterialactivity of extracts from some edible plants commonly consumed in Asia, International Journal of Food Microbiology,80,223-230.

Andrade, B., Barbosa, L., Probst, I., (2014). Antimicrobial activity of essential oils, Journal of,Essential Oil Research, 26:1, 34-40.

Cenet, M., Digrak, M. ve Toroglu, S. (2006) Antimicrobial Activities of Laurus nobilis Linn and Zingiber officinale Roscoe Plant Essential Oils Consumed as Spices and Determination of In Vitro Effects on Antibiotics, Journal of Science and Engineering, 9 (1), 20-26.

Chmit, M., Kanaan, H., Habib, J., Abbass, M., (2014). Antibacterial and antibiofilm activities of polysaccharides, essential oil, and fatty oil extracted from Laurus nobilis growing in Lebanon, Asian Pacific Journal of Tropical Medicine, 7,S546-S552.

Degirmenci, I., (2017). Antimicrobial Effect Of Bitter Orange Sauce, Pomegranate Sauce, Plum Sauce, And Sumac Sauce Against Some Food Pathogens Bacteria (*Salmonella, E.Coli, , Listeria Spp., S.Aureus*), (Msc Thesis), Cukurova Universty, Adana.

Evren, M., Tekgüler, B., (2011).Antimicrobial Properties of Essential Oils, Journal of Electronic Microbiology, 9, 28-40.

Golukcu, M., Tokgoz, H., Turgut, D., (2018). Effect of Distillation Time on Essential Oil Compositions of Bay Leaf (*laurus nobılıs* l.), Food And Health,4(1), 37-42.

Harmanakaya, S., (2013).Investigation of the Effect of Rosemary and Clove Essential Oils on Shelf Life of Chicken Meat, Institute of Health Sciences, Kafkas University, Kars. (Ph.D. Thesis).

Harrigan,WF., (1998). Laboratory methods in food microbiology,Academic Pres, London.

Kara, S., (2010). The Antifungal Activity Of Some Spice Extracts On Moulds, Producing Aflatoxin, On Mazie And Wheat Grains in Different Storage Conditions, (MSc. Thesis), Namık Kemal University,Tekirdag.

Temelli, S.,(2002). Food Poisoning Agent E.coli O157:H7 and Its Importance, Uludag Universıty Journa. Faculty Veterian Medicine, 21,133-138.

Vilela, J.,Martins,D., Monteiro-Silva, F., (2016). Antimicrobial effect of essential oils of Laurus nobilis L. and Rosmarinus officinallis L. on shelf-life of minced Maronesa beef stored under different packaging conditions, Food Packaging and Shelf Life,8,71-80.

ACKNOWLEDGEMENTS (OPTIONAL)

This study was supported by Mersin University Scientific Research Projects Units as the project no: 2018-1-TP2-2914.

CISET - 2nd Cilicia International Symposium on Engineering and Technology
10-12 October, 2019, Mersin / TURKEY

SPEED CONTROL OF DIRECT TORQUE CONTROLLED INDUCTION MOTOR BASED ON TYPE-2 FUZZY LOGIC CONTROLLER WITH ELLIPTIC MEMBERSHIP FUNCTION

Hakan Açıkgöz*[1], Resul Çöteli[2] and Beşir Dandil[3]

[1]Kilis 7 Aralık University, Vocational School of Technical Sciences, Department of Electricity and Energy, Kilis, Turkey, e-mail: hakanacikgoz@kilis.edu.tr

[2]Fırat University, Faculty of Technology, Department of Energy Systems Engineering, Elazığ, Turkey, e-mail: rcoteli@firat.edu.tr

[3]Fırat University, Faculty of Technology, Department of Mechatronics Engineering, Elazığ, Turkey, e-mail: bdandil@firat.edu.tr

ABSTRACT

Induction motors are preferred in many industrial applications because of their durable structure. Today, vector and direct torque control methods are used for these motors. In this study, Type 2 Fuzzy Logic Controller (T2FLC) is proposed for speed control of a Direct Torque Controlled (DTC) induction motor. T2FLC is provided better results in nonlinear systems due to having lower and upper membership functions. In addition, Elliptic membership function is preferred for T2FLC used in this study. DTC based induction motor is designed in Matlab/Simulink environment. Conventional PI and T2FLC are applied to speed control unit of induction motor. Simulation studies are carried out under the same conditions for these controllers. Three different cases are built for simulation studies. The results obtained from these cases are examined and evaluated. According to the results of the simulation study, T2FLC has better speed response than PI controller.

Keywords: *Direct Torque Control, Type 2 Fuzzy Logic Controller, PI Controller, Elliptic Membership Function*

* Corresponding Author

1. INTRODUCTION

Today, induction motors are used in most of the applications requiring speed control. Due to the undesirable properties of DC motors, the use of induction motors has become widespread. However, the mathematical model of induction motors has a complex structure that includes nonlinear and high grade differential equations. Because of this complex structure, the control of an asynchronous motor is rather difficult than that of DC motor. As known, the control process is performed as scalar and vector in induction motors. In the scalar control method, the controlled variables are stator voltage and frequency (Dandil, 2009; Dandil et al. 2005; Sekkeli et al., 2009; Kilic et al., 2018). In the vector control, the flux and moment of induction motor are controlled independently from each other, as in a DC motor. Blaschke first investigated vector control (VC) method with analytical analyzes on the induction motor model (Blaschke, 1972). The developments in microprocessor technology and practical applications of control theory have become inevitable in the application of induction motors. As a result of these developments, vector control has become applicable to induction motors. In the years following the implementation of the vector control method, technological advances have enabled the emergence of Direct Torque Control (DTC) method. This method was introduced by Takahashi and Noguchi in 1986 (Takahashi and Noguchi, 1986). In DTC method, the actual flux and moment of the motor are controlled independently from each other within the hysteresis band. The high dynamic response, simple and durable structure are the most important features of this method. Although the implementation structures of the VC and DTC method are different, their purposes are the same (Acikgoz and Sekkeli, 2013; Acikgoz et al., 2014; Toufouti and Benalla, 2006).

PI and PID controllers which are one of the classic controller structures, are applied to control unit of induction motors due to their simple structure. However, due to the complex nature of the induction motors, the gain parameters of these controllers are difficult to find. In the application of these controllers with fixed parameters, an accurate mathematical model of the controlled drive system is required. These controllers, which require an accurate mathematical model of the system to be controlled, may be inadequate in high-performance drive applications. In this respect, intelligent controller structures that do not need a mathematical model of the system are widely used today. The one of these intelligent controller structures is the fuzzy logic controllers (FLCs) proposed by Zadeh (Zadeh, 1965). The FLC can be realized using the knowledge of the expert without the need for a mathematical model of the system to be controlled. FLCs can be divided into type-1 and type-2 (Zadeh, 1975). Type-1 FLCs have a single membership function while type-2 FLCs have a lower and upper membership functions. Type-1 FLCs may not provide the desired performance in systems with uncertainties. Type-2 FLCs have been proposed as an alternative to type-1 FLCs (Khanesar et al., 2011; Kayacan et al., 2018). With Type-2 FLCs, control of uncertainty and nonlinear systems can be performed better (Mendel and Mouzouris, 1999; Acikgoz 2018a, 2018b; Acikgoz et al., 2017).

In this study, Type-2 FLC is proposed for the speed control of DTC based induction. Elliptic membership function is preferred for type-2 FLC. The performance of the proposed controller structure is compared with the classical PI controller. Simulation studies were carried out under the same conditions. In addition, other parts of the study are as follows. The mathematical model of the DTC method is described in section-2. Section-3 provides general information about type-2 FLCs. In the section-4, simulation studies were carried out. The results are in the section-5.

2. DIRECT TORQUE CONTROL

There are many different modeling methods that are made to examine the behavior of the induction motor and to represent the motor (Dandil, 2009; Dandil et al. 2005). The dq-axis model is one of the most commonly used methods. The dq-axis model of induction motor is given in Fig. 1. The voltage equations of the induction motor are as follows.

$$v_{sabc} = R_s i_{sabc} + \frac{d\psi_{sabc}}{dt} \tag{1}$$

$$\begin{bmatrix} v_{sa} \\ v_{sb} \\ v_{sc} \end{bmatrix} = \begin{bmatrix} R_s & 0 & 0 \\ 0 & R_s & 0 \\ 0 & 0 & R_s \end{bmatrix} \begin{bmatrix} i_{sa} \\ i_{sb} \\ i_{sc} \end{bmatrix} + \frac{d}{dt} \begin{bmatrix} \psi_{sa} \\ \psi_{sb} \\ \psi_{sc} \end{bmatrix} \tag{2}$$

$$v_{rabc} = R_r i_{rabc} + \frac{d\psi_{rabc}}{dt} \tag{3}$$

$$\begin{bmatrix} v_{ra} \\ v_{rb} \\ v_{rc} \end{bmatrix} = \begin{bmatrix} R_r & 0 & 0 \\ 0 & R_r & 0 \\ 0 & 0 & R_r \end{bmatrix} \begin{bmatrix} i_{ra} \\ i_{rb} \\ i_{rc} \end{bmatrix} + \frac{d}{dt} \begin{bmatrix} \psi_{ra} \\ \psi_{rb} \\ \psi_{rc} \end{bmatrix} \tag{4}$$

Where; v_{sabc} and v_{rabc} are the stator and rotor voltages of the induction motor. R_s is the stator winding resistance. ψ_s and ψ_r are stator and rotor flux.

$$\begin{bmatrix} \psi_{sabc} \\ \psi_{rabc} \end{bmatrix} = \begin{bmatrix} L_{ssabc} & L_{srabc} \\ L_{rsabc} & L_{rrabc} \end{bmatrix} \begin{bmatrix} i_{sabc} \\ i_{rabc} \end{bmatrix} \tag{5}$$

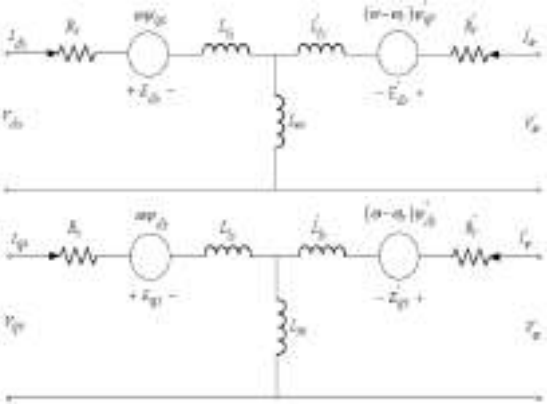

Fig. 1. dq-axis model of induction motor

The dq-axis equations of induction motors is given in Eq. (6-9).

$$v_{ds} = R_s i_{ds} + \frac{d}{dt}\psi_{ds} - \omega\psi_{qs}$$
$$v_{qs} = R_s i_{qs} + \frac{d}{dt}\psi_{qs} - \omega\psi_{ds} \quad (6)$$

The torque equation of induction motor is expressed in Eq. (7)

$$T_e = \frac{3}{2}\frac{P}{2}\frac{L_m}{\sigma L_s L_r}|\bar{\psi}_s||\bar{\psi}_r|\sin\alpha \quad (7)$$

Where, σ is the leakage factor. This value can be defined as $\sigma=1-L_m^2/L_sL_r$. Figures 3 and 4 show the hysteresis comparators used for flux and torque. Flux and torque band widths are defined in these hysteresis blocks.

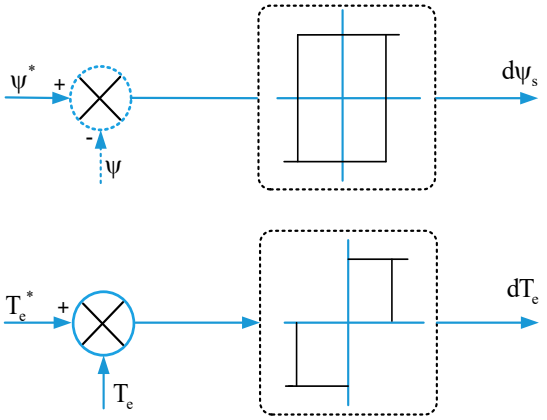

Fig. 2. Flux and torque hysteresis band block diagrams

With these bandwidths, the deviation of the calculated values of flux and torque from the reference values is determined. With the output information of the hysteresis blocks and the position information of the stator flux, the most suitable voltage vectors are selected from the switching table given in Table 1 and applied to the inverter.

Table 1. Optimum switching table

$d\psi_s$	dT_e	S_1	S_2	S_3	S_4	S_5	S_6
1	1	V2	V3	V4	V5	V6	V1
	0	V7	V0	V7	V0	V7	V0
	-1	V6	V1	V2	V3	V4	V5
0	1	V3	V4	V5	V6	V1	V2
	0	V0	V7	V0	V7	V0	V7
	-1	V5	V6	V1	V2	V3	V4

3. TYPE-2 FUZZY LOGIC CONTROLLER

Type-2 FLCs are widely preferred in many applications because they have better performance in systems with uncertainties. Type-1 FLCs cannot handle rule uncertainties directly because they use fuzzy sets with crisp value. Despite these characteristics of Type-1 FLCs, Type-2 FLCs are very useful in situations where it is difficult to determine an exact membership function (Mendel and Mouzouris, 1999; Khanesar et al., 2011; Kayacan et al., 2018). A type-2 fuzzy set B can be characterized as below:

$$\tilde{B} = \left\{\left((x,u),\mu_{\tilde{A}}(x,u)\right)\middle|\forall x \in X, \forall u \in J_x \subseteq [0,1]\right\} \quad (8)$$

$$\tilde{B} = \int_{x\in X}\int_{u\in J_x} \mu_{\tilde{B}}(x,u)/(x,u) \quad J_x \subseteq [0,1] \quad (9)$$

Where, $J_x \subseteq [0,\ 1]$ and $\int\int$ indicates the union over all admissible x and u. Also, $\mu_{\tilde{B}}(x,u)$ can be written as $0 \le \mu_{\tilde{B}}(x,u) \le 1$. As shown in the Fig. 3, Type-2 FLC consists of a fuzzifier, a rule base, fuzzy inference engine, and an output processor (Mendel and Mouzouris, 1999).

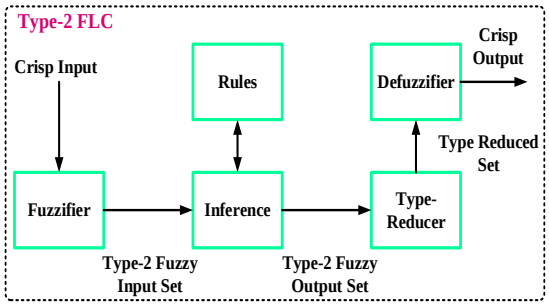

Fig. 3. Flux and torque hysteresis band block diagrams

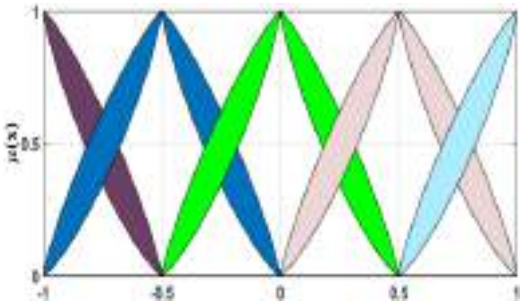

Fig. 4. Elliptic membership functions

Elliptic membership function is preferred for type-2 FLC used in this study and is given in Fig. 4. As shown in the Fig.4, Type-2 FLC have lower and upper membership functions. The region between these two membership functions is expressed as the footprint of uncertainty (FOU). The fuzzifier is used to map a crisp point. The rules used in type-2 FLC is given as below:

$$R^l : If\ \ x_1\ is\ \tilde{F}_1^l\ and\ x_p\ is\ \tilde{F}_p^l, Then\ y\ is\ \tilde{T}^l\ \ l=1,...,M. \quad (10)$$

The inference engine collects rules and provides a mapping from input type-2 fuzzy sets to output type-2 fuzzy sets.

$$\underline{f}^l(x') = \underline{\mu}_{\tilde{F}_1^l}(x_1') * ... * \underline{\mu}_{\tilde{F}_p^l}(x_p')$$
$$\overline{f}^l(x') = \overline{\mu}_{\tilde{F}_1^l}(x_1') * ... * \overline{\mu}_{\tilde{F}_p^l}(x_p') \quad (11)$$

Type reducer produces type-1 fuzzy set output and the following equation can be expressed:

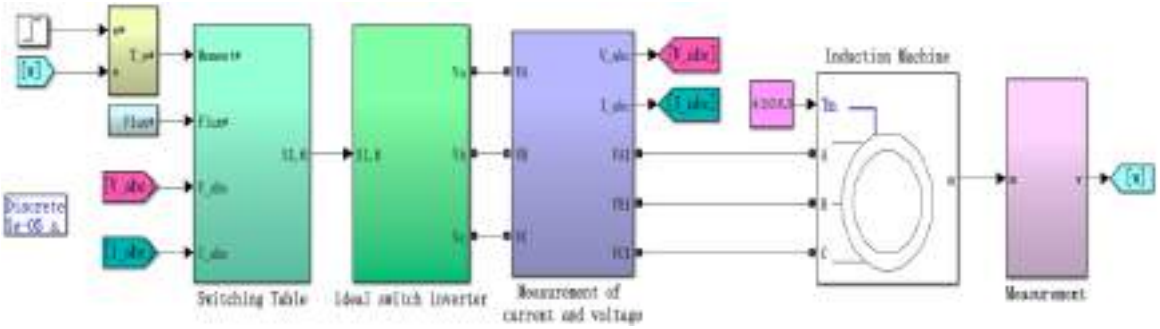

Fig. 5. Matlab/Simulink model of induction motor

$$y_l = \frac{\sum_{i=1}^{M} f_l^i y_l^i}{\sum_{i=1}^{M} f_l^i}$$
$$y_r = \frac{\sum_{i=1}^{M} f_r^i y_r^i}{\sum_{i=1}^{M} f_r^i} \quad (12)$$

The defuzzified output of type-2 FLC is given in Eq. (13).

$$y(x) = \frac{y_l + y_r}{2} \quad (13)$$

Type-2 FLC used in this study has two inputs and a single output. An anti-wind-up integrator is connected to the output of type-2 FLC. The fuzzy membership functions of type-2 FLC consist of five fuzzy sets: Negative Big (NB), Negative Small (NS), Zero (Z), Positive Small (PS) and Positive Big (PB). The rule base for FLC is given in Table 2.

Table 2. Type-2 FLC rule table

de / *e*	**NB**	**NS**	**Z**	**PS**	**PB**
NB	NB	NB	NB	NM	Z
NM	NB	NM	NM	NS	PS
NS	NB	NS	NS	Z	PM
Z	NB	NS	Z	PS	PB
PS	NM	Z	PS	PS	PB
PM	NS	PS	PM	PM	PB
PB	Z	PM	PB	PB	PB

4. SIMULATION STUDIES

In this study, T2FNN controller is proposed for speed controlling of DTC based induction motor.
For this purpose, Matlab/Simulink model of DTC based induction motor is designed in Figure 5. In addition, electrical parameters of the induction motor used in simulation studies are given in Table 1.Three different cases have been established to test the performance of the proposed controller. In case-1, the reference speed is selected as 1500 rpm. Waveforms of this case are given in Figure 6 consisting of speed, torque and grid currents.

As shown in Figure 6(a), the proposed controller has achieved the reference speed without overshoot after 54.4 ms. The PI controller has a 5% of overshoot and follows the reference speed after 95.2 ms. In Figure 6(b), it is seen that the motor speed produces torque until it reaches a reference. In the case of steady state, it is produced torque for losses. In Figure 6(c), the grid draws overcurrent at the first start-up.

In case-2, the reference controller performance of the proposed controller is tested. The waveforms obtained from this case are shown in Figure 7. The reference speed was initially set to 1000 rpm. In 0.5 seconds, the reference speed was increased to 1500 rpm. The PI controller follows after 52.4 ms, while the T2FNN controller captured the reference rate after 18.5 ms. The torque and current graphs obtained from this case are given in Figure 7(b-c).

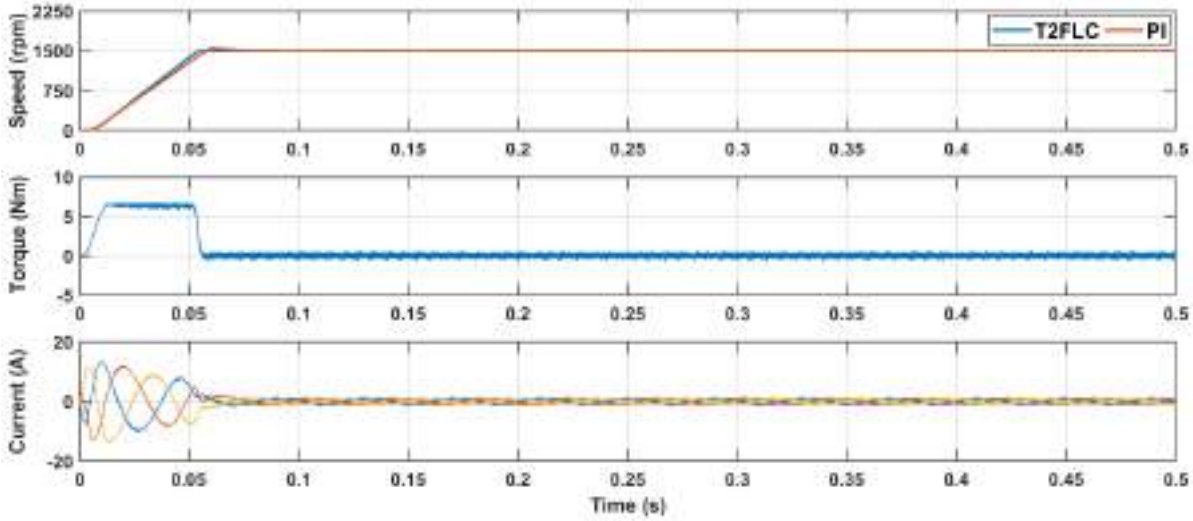

Fig. 6. The waveforms obtained from case-1

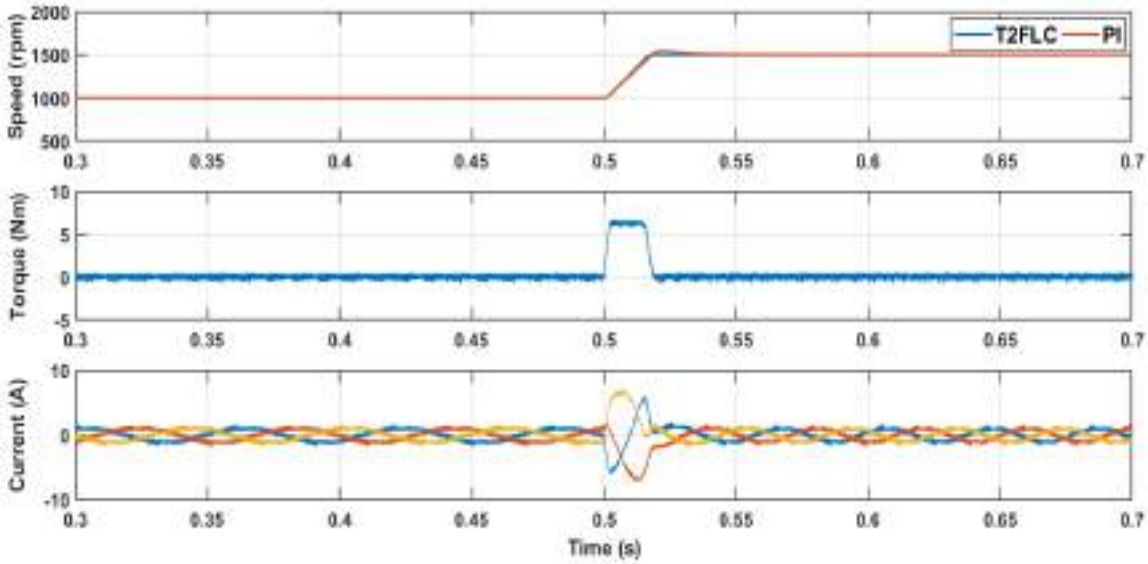

Fig. 7. The waveforms obtained from case-2

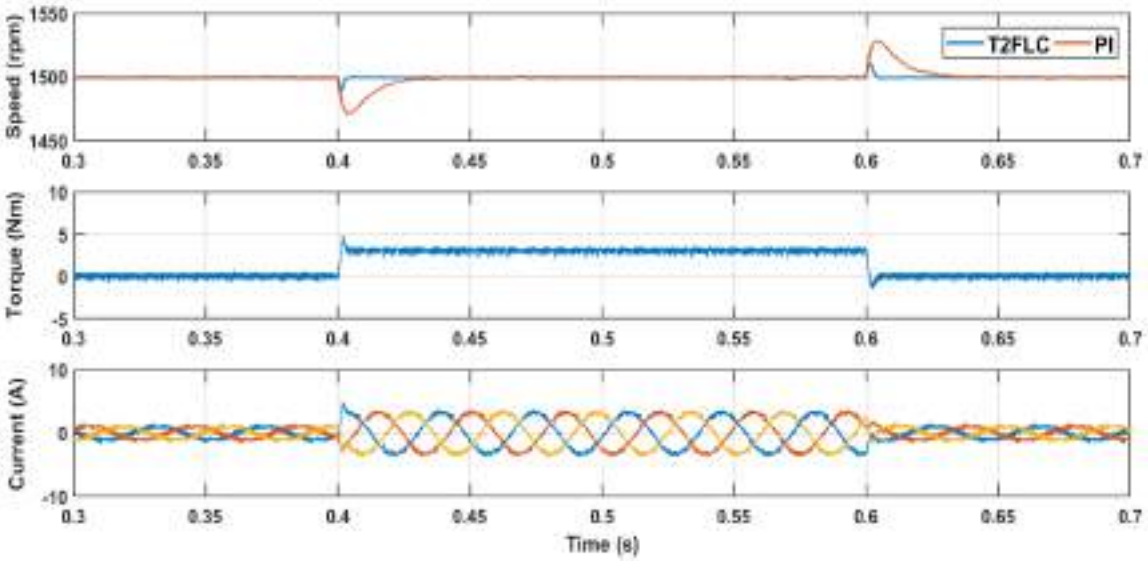

Fig. 7. The waveforms obtained from case-3

In case-3, the load was applied to the motor. The waveforms of both controllers under load are given in Figure 8. The speed of motor is set to 1500 rpm. When a load of 3.72 N.m was applied to the motor in 0.4 seconds, the T2FNN and PI controllers follow the reference speed after 6 ms and 48 ms respectively. When the load was applied to the motor, the speed responses of both controllers are decreased to 1490 rpm and 1472 rpm. When the load is removed in 0.6 seconds, the proposed controller has achieved a faster reference speed. The torque and current graphs obtained from this situation are given in Figure 8(b-c).

5. CONCLUSION

This paper presents a type-2 FLC with elliptic membership function for speed control of direct torque controlled induction motor. DTC based induction motor model is built in Matlab/Simulink. Proposed controller is compared with conventional PI controller. For fair comparison, Simulation studies is realized under same conditions. In order to investigate the performance of both controllers, three scenarios are created. These cases consist of constant speed, variable speed and load change. According to the simulation results, proposed controller has better dynamic response than PI controller in terms of overshoot, settling time and rise time.

REFERENCES

Açıkgöz, H., Şekkeli, M. (2013). "Bulanık Mantık Denetleyici ile Doğrudan Moment Denetim Yöntemi Uygulanan Asenkron Motorun Hız Denetim Performansının İncelenmesi", *Akademik Platform Mühendislik ve Fen Bilimleri Dergisi*, vol. 1, no. 2, pp. 50-57.

Acikgoz, H., Kececioglu, O.F., Gani, A., Sekkeli, M. (2014). "Speed Control of Direct Torque Controlled Induction Motor By using PI, Anti-Windup PI and Fuzzy Logic Controller", *IJISAE*, vol. 2, no. 3, pp. 58-63.

Acikgoz, H., Kececioglu, O.F., Gani, A., Tekin, M., Sekkeli, M. (2017). "Robust Control of Shunt Active Power Filter Using Interval Type-2 Fuzzy Logic Controller For Power Quality Improvement", Tehnički vjesnik,Vol. 24, Suppl. 2, pp. 363-368.

Acikgoz, H. (2018a). Üç Seviyeli D-STATKOM'un Tip-2 Bulanık Mantık Denetleyici ile Denetimi ve Performans Analizi, *Kahramanmaraş Sütçü İmam Üniversitesi Mühendislik Bilimleri Dergisi*, vol. 21 no. 4, pp. 346-357.

Acikgoz, H. (2018b). "Speed Control of DC Motor Using Interval Type-2 Fuzzy Logic Controller", *IJISAE*, vol. 6, no. 3, pp. 197-202.

Blaschke, F. (1972). "The Principle of Field Orientation as Applied to the new Transvector Closed-Loop System for Rotating-Field Machines," *Siemens Review*, Vol. 34, No. 3, pp. 217-220.

Dandil B. (2009). "Fuzzy neural network IP controller for robust position control of induction motor drive", *Expert Systems with Applications*, vol. 36, no. 3, pp. 4528-4534.

Dandil, B., Gokbulut, M. and Ata, F. (2005). "A PI Type Fuzzy-neural Network Controller for Induction Motor Drives", *Journal of Applied Sciences*, vol. 5, pp. 1286-1291.

Kayacan, E., Sarabakha, A., Coupland, S., John, R., Khanesar, M.A. (2018). "Type-2 fuzzy elliptic membership functions for modeling uncertainty," *Eng. Appl. Artif. Intell.,* vol. 170, pp. 170–183.

Khanesar, M., Kayacan, E., Teshnehlab, M. and Kaynak, O. (2011). "Analysis of the noise reduction property of type-2 fuzzy logic systems using a novel type-2 membership function," *IEEE Trans. on Systems, Man, and Cybernetics, Part B: Cybernetics*, vol. 41, pp. 1395-1406.

Kilic E., Ozcalik H.R., Sit S. (2018). Adaptive controller with RBF neural network for induction motor drive, *International Journal of Numerical Modelling: Electronic Networks, Devices and Fields*, vol. 31, no. 3, pp. 1-11.

Mendel, J.M. and Mouzouris, G.C. (1999). "Type-2 fuzzy logic systems", *IEEE Trans. Fuzzy Syst.* Vol. 7, pp. 643–658.

Sekkeli, M., Yıldız, C., Ozcalik, H.R. (2009). "Fuzzy Logic Based Intelligent Speed Control of Induction Motor Using Experimental Approach" *International Symposium on 1Nnovaitons in intelligent SysTems and Applications,* Trabzon/Turkey, June 29, July 1.

Takahashi, I. and Noguchi, T. (1986). "A new quick-response and high efficiency control strategy of an induction motor," *IEEE Transactions on Industry Application*, vol. IA, no. 5, pp. 820-827.

Toufouti, R. and Benalla, H. (2006). "Direct torque control for induction motor using fuzzy logic," *ACSE Journal*, vol 6, no. 2, 2006. pp.19-26.

Zadeh, L.A. (1965). "Fuzzy sets," *Inform Control*, Vol.8, 1965, pp.338-353.

Zadeh, L.A. (1975). "The concept of linguistic variable and its application to approximate reasoning," *Inf. Sci.,* vol.8, pp. 199-249.

CISET - 2nd Cilicia International Symposium on Engineering and Technology
10-12 October, 2019, Mersin / TURKEY

SCREEN CONFORMAL LIGHTLIKE HYPERSURFACES OF METALLIC SEMI-RIEMANNIAN MANIFOLDS

Nergiz (ÖNEN) POYRAZ [1] and Burçin DOĞAN *[2]

[1] Çukurova University, Faculty of Science and Arts, Department of Mathematics, Adana, Turkey, nonen@cu.edu.tr

[2] Mersin University, Faculty of Science and Arts, Department of Mathematics, Mersin, Turkey, bdogan@mersin.edu.tr

ABSTRACT
In this study, we introduce screen conformal lightlike hypersurfaces of metallic semi-Riemannian manifolds. We give an example for such hypersurfaces and prove some characterization theorems.

Keywords: *Lightlike hypersurface, metallic structure, screen conformal hypersurface, semi-Riemannian manifold.*

* *Corresponding Author*

1. INTRODUCTION

A submanifold M of a semi-Riemannian manifold $\bar{M}$ is called lightlike (degenerate) submanifold if the induced metric on M is degenerate. The general theory of lightlike submanifolds of a semi-Riemannian manifold has been developed by Duggal-Bejancu (Duggal, Bejancu, 1996) and Kupeli (Kupeli, 1996). Duggal and Sahin introduced and studied geometry of classes of lightlike submanifolds in indefinite Kaehler and indefinite Sasakian manifolds which is an umbrella of CR-lightlike, SCR-lightlike, screen real GCR-lightlike submanifolds (Duggal, Şahin, 2005; Duggal, Şahin, 2006).

The number ϕ, which is the real positive root of the equation

$$x^2 + x + 1 = 0$$

(thus, $\phi = \frac{1+\sqrt{5}}{2}$) is the golden proportion. Crasmareanu and Hretcanu investigated properties of the golden structure. They also defined golden Riemannian manifold (Crasmareanu, Hretcanu, 2008). Şahin and Akyol introduced golden maps between golden Riemannian manifolds, gave an example and showed that such map is harmonic (Şahin, Akyol, 2014). Poyraz and Yaşar introduced lightlike submanifolds of golden semi-Riemannian manifolds (Poyraz, Yaşar, 2019).

As a generalization of the golden mean, which contains the silver mean, the bronze mean, the copper mean, the nickel mean, etc., the metallic means family was introduced by de Spinadel in 2002 (De Spinadel, 2002). The positive solution of the equation given by

$$x^2 - px - q = 0$$

for some positive integer p and q is called a (p, q)-metallic number (De Spinadel, 1997-1999), which has the form

$$\boldsymbol{\sigma_{p,q} = \frac{p + \sqrt{p^2 + 4q}}{2}}.$$

For $p = q = 1$ and $p = 2, q = 1$, it is well known that we have the golden mean $\phi = \frac{1+\sqrt{5}}{2}$ and silver mean $\sigma_{1,2} = \frac{1+\sqrt{5}}{2}$, respectively.

The geometry of metallic Riemannian manifold was studied in (Blaga, Hretcanu, 2018; Hretcanu, Blaga, 2018). Then Acet introduced lightlike hypersurfaces of metallic semi-Riemannian manifolds (Acet, 2018) and lightlike submanifolds of metallic semi-Riemannian manifolds were studied in (Acet, et al., 2018) by Acet, Erdoğan and Perktaş. Moreover, differen tclasses of lightlike submanifolds of metallic semi-Riemannian manifolds were reported in (Erdoğan, 2018; Erdoğan, et al. 2018).

In this paper we introduce screen conformal lightlike hypersurfaces of a metallic semi-Riemannian manifold. Section 2 is devoted to preliminaries containing basic definitions for metallic semi-Riemannian manifolds and lightlike hypersurfaces. In Section 3 firstly we define screen conformal lightlike hypersurfaces of a metallic semi-Riemannian manifold and prove some characterization theorems.

2. PRELIMINARIES

For p and q positive integers, the positive solution of

$$x^2 - px - q = 0$$

is called a $(\boldsymbol{p, q})$ metallic number and the solution set is denoted by

$$\boldsymbol{\sigma_{p,q} = \frac{p + \sqrt{p^2 + 4q}}{2}}.$$

Let $(\bar{M}, \bar{g})$ be a semi-Riemannian manifold. If $\bar{J}$ satisfies

$$\bar{J}^2 = p\bar{J} + q\mathrm{I} \quad (1)$$

then $\bar{J}$ is a metallic structure on $\bar{M}$. Moreover if $\bar{g}$ is $\bar{J}$-compatible i.e.

$$\bar{g}(\bar{J}X, Y) = \bar{g}(X, \bar{J}Y) \quad (2)$$

and equivalent to

$$\bar{g}(\bar{J}X, \bar{J}Y) = p\bar{g}(X, \bar{J}Y) + \mathrm{q}\bar{g}(X, Y) \quad (3)$$

then $(\bar{M}, \bar{g}, \bar{J})$ is a metallic semi-Riemannian manifold (Hretcanu, Crasmareanu, 2013).

Let (M, g) be a hypersurface of semi-Riemannian manifold $(\bar{M}, \bar{g})$ with index v, $0 < v < r + 1$. If the induced metric g is degenerate on M and $rank(TM) = r$, then (M, g) is called a lightlike hypersurface of $(\bar{M}, \bar{g})$ (Duggal, Bejancu, 1996).

For a lightlike hypersurface, the normal space is given as

$$TM^{\perp} = \{V \in T\bar{M} : \bar{g}(U, V) = 0, \forall U \in TM\}.$$

Also, the radical distribution $Rad(TM) = TM \cap TM^{\perp}$ and there exists a complemantary screen distribution $S(TM)$ to $TM^{\perp}$ in TM.

Theorem 1. Let $(M, g, S(TM))$ be a lightlike hypersurface of a semi-Riemannian manifold $\bar{M}$. Then there exists a unique rank 1 vector subbundle $ltr(TM)$ of $(T\bar{M})$, with base space N, such that for every non-zero section E of $Rad(TM)$ on a coordinate neighbourhood $\varphi \subset M$, there exists a section N of $ltr(TM)$ on φ satisfying: $\bar{g}(N, N) = 0$, $\bar{g}(N, W) = 0$, $\bar{g}(N, E) = 1$, for $W \in \Gamma(S(TM)\,|\varphi$. $ltr(TM)$ is called the lightlike transversal vector bundle of M (Duggal, Bejancu, 1996).

From previous theorem, we can write:

$$TM = S(TM) \perp Rad(TM), \quad (4)$$

$$T\bar{M} = TM \oplus ltr(TM) = S(TM) \perp Rad(TM) \oplus ltr(TM). \quad (5)$$

Let $\omega : \Gamma(TM) \to \Gamma(S(TM))$ be the projection morphism. For $U, V \in \Gamma(TM)$, we have

$$\bar{\nabla}_U V = \nabla_U V + B(U, V)N, \quad (6)$$

$$\bar{\nabla}_U N = -\mathrm{A}_N U + \tau(U)N, \quad (7)$$

$$\nabla_U \omega V = \nabla^*_U \omega V + C(U, \omega V)E, \quad (8)$$

$$\nabla_U E = -A^*_E U - \tau(V)E. \quad (9)$$

If we describe

$$\theta(U) = \bar{g}(N, U),$$

then induced connection is calculated as

$$(\nabla_U g)(V, Z) = B(U, Z)\theta(V) + B(U, V)\theta(Z). \quad (10)$$

On the other hand, we get

$$B(U, E) = 0, \quad (11)$$

$$g(A^*_E U, PV) = B(U, PV), \; g(A^*_E U, N) = 0, \quad (12)$$

$$g(\mathrm{A}_N U, PV) = C(U, PV), \quad g(\mathrm{A}_N U, N) = 0, \quad (13)$$

$$\boldsymbol{A^*_E E = 0}. \quad (14)$$

3. SCREEN CONFORMAL LIGHTLIKE HYPERSURFACES

Let $\boldsymbol{M}$ be a lightlike hypersurface of a metallic semi-Riemannian manifold $(\bar{\boldsymbol{M}}, \bar{\boldsymbol{g}}, \bar{\boldsymbol{J}})$. Then we can write

$$\bar{\boldsymbol{J}}\boldsymbol{U} = \boldsymbol{\phi U} + \boldsymbol{u}(\boldsymbol{U})\boldsymbol{N}, \tag{15}$$

$$\bar{\boldsymbol{J}}\boldsymbol{N} = \boldsymbol{\zeta} + \boldsymbol{v}(\boldsymbol{E})\boldsymbol{N}, \tag{16}$$

where $\boldsymbol{\phi U},\ \boldsymbol{\zeta} \in \boldsymbol{\Gamma(TM)}$ and

$$\boldsymbol{u}(\boldsymbol{U}) = \boldsymbol{g}(\boldsymbol{U}, \bar{\boldsymbol{J}}\boldsymbol{E}),\ \boldsymbol{v}(\boldsymbol{U}) = \boldsymbol{g}(\boldsymbol{U}, \bar{\boldsymbol{J}}\boldsymbol{N}). \tag{17}$$

Lemma 2. (Acet, 2018) Let $\boldsymbol{M}$ be a lightlike hypersurface of $(\bar{\boldsymbol{M}}, \bar{\boldsymbol{g}}, \bar{\boldsymbol{J}})$. Then we have

$$\boldsymbol{\phi^2 U} = \boldsymbol{p\phi U} + \boldsymbol{q}(\boldsymbol{U}) - \boldsymbol{u}(\boldsymbol{U})\boldsymbol{\zeta}, \tag{18}$$

$$\boldsymbol{u}(\boldsymbol{\phi U}) = \boldsymbol{pu}(\boldsymbol{U}) - \boldsymbol{u}(\boldsymbol{U})\boldsymbol{v}(\boldsymbol{E}), \tag{19}$$

$$\boldsymbol{\phi\zeta} = \boldsymbol{p\zeta} - \boldsymbol{v}(\boldsymbol{E})\boldsymbol{\zeta}, \tag{20}$$

$$\boldsymbol{v}(\boldsymbol{E})^{\boldsymbol{2}} = \boldsymbol{pv}(\boldsymbol{E}) + \boldsymbol{q} - \boldsymbol{u}(\boldsymbol{\zeta}), \tag{21}$$

$$\boldsymbol{g}(\boldsymbol{\phi U}, \boldsymbol{V}) = \boldsymbol{g}(\boldsymbol{U}, \boldsymbol{\phi V}) + \boldsymbol{u}(\boldsymbol{V})\boldsymbol{\theta}(\boldsymbol{U}) - \boldsymbol{u}(\boldsymbol{U})\boldsymbol{\theta}(\boldsymbol{V}), \tag{22}$$

$$\boldsymbol{g}(\boldsymbol{\phi U}, \boldsymbol{\phi V}) = \boldsymbol{pg}(\boldsymbol{U}, \boldsymbol{\phi V}) + \boldsymbol{qg}(\boldsymbol{U}, \boldsymbol{V}) + \boldsymbol{pu}(\boldsymbol{V})\boldsymbol{\theta}(\boldsymbol{U}) - \boldsymbol{u}(\boldsymbol{V})\boldsymbol{g}(\boldsymbol{\phi U}, \boldsymbol{N}) - \boldsymbol{u}(\boldsymbol{U})\boldsymbol{g}(\boldsymbol{\phi V}, \boldsymbol{N}). \tag{23}$$

Definition 3. Let $\bar{J}$ be a metallic semi-Riemannian structure. If $\nabla\bar{J} = 0$, i.e., $\bar{J}$ is parallel then $\bar{J}$ is named a locally metallic structure (Acet, 2018).

Lemma 4. (Acet, 2018) Let $\boldsymbol{M}$ be a lightlike hypersurface of a locally metallic semi-Riemannian manifold $(\bar{\boldsymbol{M}}, \bar{\boldsymbol{g}}, \bar{\boldsymbol{J}})$. Then we obtain

$$(\boldsymbol{\nabla_U \phi})\boldsymbol{V} = \boldsymbol{u}(\boldsymbol{V})\boldsymbol{A_N U} + \boldsymbol{B}(\boldsymbol{U}, \boldsymbol{V})\boldsymbol{\zeta}, \tag{24}$$

$$(\boldsymbol{\nabla_U u})\boldsymbol{V} = \boldsymbol{B}(\boldsymbol{U}, \boldsymbol{V})\boldsymbol{v}(\boldsymbol{E}) - \boldsymbol{B}(\boldsymbol{U}, \boldsymbol{\phi V}) - \boldsymbol{\tau}(\boldsymbol{U})\boldsymbol{u}(\boldsymbol{V}), \tag{25}$$

$$\boldsymbol{\nabla_U \zeta} = -\boldsymbol{\phi A_N U} + \boldsymbol{\tau}(\boldsymbol{U})\boldsymbol{\zeta} + \boldsymbol{A_N U v}(\boldsymbol{E}), \tag{26}$$

$$\boldsymbol{U}\big(\boldsymbol{v}(\boldsymbol{E})\big) = -\boldsymbol{B}(\boldsymbol{U}, \boldsymbol{\zeta}) - \boldsymbol{u}(\boldsymbol{A_N U}). \tag{27}$$

Definition 5. Let M be a lightlike hypersurface of a locally metallic semi-Riemannian manifold $(\bar{M}, \bar{g}, \bar{J})$. If

$$\bar{J}\big(Rad(TM)\big) \subset S(TM), \quad \bar{J}(ltr(TM)) \subset S(TM), \tag{28}$$

then M is called a screen semi-invariant lightlike hypersurface of $\bar{M}$ (Acet, 2018).

For a screen semi invariant hypersurfaces, we can write the following decompositions:

$$S(TM) = \mu_0 \perp \{\bar{J}\big(Rad(TM)\big) \oplus \bar{J}\big(ltr(TM)\big)\}, \tag{29}$$

$$TM = \{\bar{J}\big(Rad(TM)\big) \oplus \bar{J}\big(ltr(TM)\big)\} \perp \mu_0 \perp Rad(TM), \tag{30}$$

$$T\bar{M} = \{\bar{J}\big(Rad(TM)\big) \oplus \bar{J}\big(ltr(TM)\big) \perp \mu_0 \perp \{Rad(TM) \oplus ltr(TM)\}, \tag{31}$$

where μ_0 is a non-degenerate invariant distribution.

Let we consider invariant and anti-invariant distributions in $T\bar{M}$ by $\widetilde{D} = Rad(TM) \perp \bar{J}(Rad(TM)) \perp \mu_0$ and $\widetilde{D}' = \bar{J}(ltr(TM))$ on M, respectively. Thus, we have

$$T\bar{M} = \widetilde{D} \oplus \widetilde{D}'. \tag{32}$$

Now we set local lightlike vector fields by $\zeta = \bar{J}N$ and $\psi = \bar{J}E$. If we denote the projections of TM on $\widetilde{D}$ and $\widetilde{D}'$ by Q and R, respectively, we can write

$$U = QU + RU \tag{33}$$

for any $U \in \Gamma(TM)$.

Let M be a lightlike hypersurface of a locally metallic semi-Riemannian manifold $(\bar{M}, \bar{g}, \bar{J})$. Then from Lemma 2. and Lemma 4. we get

$$\phi^2 U = p\phi U + q(U) - u(U)\zeta, \tag{34}$$

$$u(\phi U) = pu(U),\ u(\zeta) = q, \tag{35}$$

$$g(\phi U, V) = g(U, \phi V) + u(V)\theta(U) - u(U)\theta(V), \tag{36}$$

$$g(\phi U, \phi V) = pg(U, \phi V) + qg(U, V) + pu(V)\theta(U) - u(V)g(\phi U, N) - u(U)g(\phi V, N), \tag{37}$$

$$(\nabla_U \phi)V = u(V)A_N U + g(A_E^* U, V)\zeta, \tag{38}$$

$$(\nabla_U u)V = -B(U, \phi V) - u(V)\tau(U), \tag{39}$$

$$\nabla_U \zeta = -\phi A_N U + \tau(U)\zeta, \tag{40}$$

$$\nabla_U \psi = -\phi A_E^* U - \tau(U)\psi, \tag{41}$$

$$B(U, \zeta) = -C(U, \psi) \tag{42}$$

for $U, V \in \Gamma(TM)$, $\zeta \in \Gamma(\widetilde{D}')$ and $\psi \in \Gamma(\widetilde{D}$.

Definition 6. Let M be a lightlike hypersurface of a locally metallic semi-Riemannian manifold $(\bar{M}, \bar{g}, \bar{J})$. If for $\forall U, V \in \Gamma(TM)$,

$$C(U, wV) = \gamma B(U, V) \tag{43}$$

or

$$A_N = \gamma A_E^* \tag{44}$$

then M is called a screen conformal lightlike hypersurface of $\bar{M}$ where γ is a non-vanishing smooth function (Duggal, Şahin, 2010).

Particulary, M is named screen homothetic if γ is a non-zero constant (Duggal, Şahin, 2004).

From (42) and (43), we obtain

$$B(U, \zeta) = \gamma B(U, \psi).$$

Thus, from the last equation, we get

$$B(U, \zeta + \gamma\psi) = 0.$$

That is, $\{\zeta, \psi\}$ is a basis of $\Gamma(\bar{J}(Rad(TM)) \oplus \bar{J}(ltr(TM)))$. Also, if we denote $\vartheta_1 = \zeta + \gamma\psi,\ \vartheta_2 = \zeta - \gamma\psi$, then $\{\vartheta_1, \vartheta_2\}$ is a basis of $\Gamma(\bar{J}(Rad(TM)) \oplus \bar{J}(ltr(TM)))$, too.

If we denote $\lambda_1(\vartheta_1) = Sp\{\vartheta_1\}$ and $\lambda_2(\vartheta_1) = \mu_0 \perp Sp\{\vartheta_2\}$, then we have the following decomposition:

$$S(TM) = \lambda_1(\vartheta_1) \perp \lambda_2(\vartheta_1). \tag{45}$$

Thus, using (36) and (37) we derive

$$\begin{aligned}\nabla_U \vartheta_1 &= \nabla_U(\zeta - \gamma\psi)\\ &= \phi A_N U + \tau(U)\zeta\\ &\quad -\gamma(-\phi A_E^* U - \tau(U)\psi - u[\gamma]\\ &= \tau(U)\vartheta_2 - u[\gamma]\psi.\end{aligned}$$

Theorem 7. Let M be a screen conformal screen semi invariant lightlike hypersurface of a locally metallic semi-Riemannian manifold $(\bar{M}, \bar{g}, \bar{J})$. Then ϑ_1 is parallel iff M is screen homothetic and $\tau = 0$.

Proof. From (41), we know that

$$\nabla_U \vartheta_1 = \tau(U)\vartheta_2 - u[\gamma]\psi.$$

Putting ϑ_2 into the last equation, we obtain

$$\tau(U)\,\zeta + (\gamma\tau(U) - u[\gamma])\psi = 0.$$

Since

$$g(\tau(U)\,\zeta + (\gamma\tau(U) - u[\gamma])\psi, \psi) = 0,$$

then we find $\tau(U) = 0$. Similarly, since

$g(\tau(U)\,\zeta + (\gamma\tau(U) - u[\gamma])\psi, \zeta) = 0,$
we get $\gamma\tau(U) - u[\gamma] = 0$. Thus, $u[\gamma] = 0$ is obtained, that is M is screen homothetic.

Theorem 8. Let M be a screen conformal screen semi invariant lightlike hypersurface of a locally metallic semi-Riemannian manifold $(\bar{M}, \bar{g}, \bar{J})$. If ϑ_1 is parallel, then $M = R_E \times R_{\vartheta_1} \times M'$ has a locally product structure where R_E and R_{ϑ_2} are null and non-null geodesics which tangents to $Rad(TM)$ and $\lambda_2(\vartheta_1)$, respectively. Also, M' is a leaf of
$\lambda_2(\vartheta_1)$.

Proof. We assume that ϑ_1 is parallel. For $U \in \Gamma(\lambda_2(\vartheta_1))$ and $V \in \Gamma(\mu_0)$, we find
$$\mathrm{g}(\nabla_U V, \vartheta_1) = \bar{\mathrm{g}}(\overline{\nabla}_U V, \vartheta_1) = -\bar{g}(V, \overline{\nabla}_U \vartheta_1) = -g(V, \nabla_U \vartheta_1) = 0$$
and
$$\mathrm{g}(\nabla_U \vartheta_2, \vartheta_1) = \bar{\mathrm{g}}(\overline{\nabla}_U \vartheta_2, \vartheta_1) = -\bar{g}(\vartheta_2, \overline{\nabla}_U \vartheta_1) = -u[\gamma] + 2\gamma\tau(U).$$
If ϑ_1 is parallel, then $\mathrm{g}(\nabla_U V, \vartheta_1) = \bar{\mathrm{g}}(\overline{\nabla}_U \vartheta_2, \vartheta_1) = 0$. Hence $\lambda_2(\vartheta_1)$ is integrable which completes our assertion.

Theorem 9. Let M be a screen conformal screen semi invariant lightlike hypersurface of a locally metallic semi-Riemannian manifold $(\bar{M}, \bar{g}, \bar{J})$. If ϑ_1 is parallel with respect to ∇ on M, then M is locally a product manifold $C_{\vartheta_1} \times M^*$, where C_{ϑ_1} is a non-null geodesic tangent to $\lambda_1(\vartheta_1)$ and M^* is a leaf of $N(\vartheta_1) = \mu_0 \perp Sp\{E, \vartheta_2\}$.

Proof. From (4) and (45) we obtain $TM = \lambda_1(\vartheta_1) \perp N(\vartheta_1)$. For any $U \in \Gamma(N(\vartheta_1))$ and $V \in \Gamma(\mu_0)$, we obtain
$$g(\nabla_U E, \vartheta_1) = -B(U, \vartheta_1) = 0, \quad (46)$$
$$g(\nabla_U \vartheta_2, \vartheta_1) = -g(\vartheta_2, \nabla_U \vartheta_1) = 0, \quad (47)$$
$$g(\nabla_U V, \vartheta_1) = -g(\overline{\nabla}_U V, \vartheta_1) = -g(V, \nabla_U \vartheta_1) = 0. \quad (48)$$
Hence the distribution $N(\vartheta_1)$ is integrable. This completes the proof.

4. CITATION AND REFERENCE LIST

Acet, B. E. (2018). "Lightlike hypersurfaces of metallic semi-Riemannian manifolds", *Int. J. Geom. Methods Mod. Phys.*, DOI:10.1142/S0219887818502018.

Acet, B. E., Erdoğan, F. E., Perktas, S. Y. (2018). "Lightlike Submanifolds of Metallic Semi-Riemannian Manifolds", *arXiv preprint arXiv: 1811.05019v1*.

Blaga, A. M., Hretcanu, C. E. (2018). "Invariant, anti-invariant and slant submanifolds of a metallic Riemannian manifold", *arXiv preprint* arXiv:1803.01415.

Crasmareanu, M. and Hretcanu, C. E. (2008). "Golden differential geometry", *Chaos Solitons and Fractals*, Vol. 38, No. 5, pp. 1229–1238.

De Spinadel, V. W. (2002). "The metallic means family and forbidden symmetries", *Int. Math. J.*, Vol. 2, No. 3, pp. 279–288.

Duggal, K. L., Bejancu, A. (1996). *Lightlike submanifolds of semi-Riemannian manifolds and applications, Mathematics and Its Applications.* Kluwer Publisher.

Duggal, K. L. and Sahin, B. (2004). "Screen conformal half-lightlike submanifolds", *Int.. J. Math. & Math. Sci.*, Vol. 68, pp. 3737--3753.

Duggal, K. L. and Sahin, B. (2005). "Screen Cauchy Riemann Lightlike Submanifolds", *Acta Math. Hungar.*, Vol. 106, No. (1-2).

Duggal, K. L., Sahin, B. (2006). "Generalized Cauchy-Riemann lightlike submanifolds of Kaehler manifolds". *Acta Math. Hungarica*,. 112, pp. 107-130.

Duggal, K. L., Sahin, B. (2007). "Lightlike submanifolds of indefinite Sasakian manifolds". *Int. J. Math. and Math. Sci.*, Article ID:57585.

Duggal, K. L., Sahin, B. (2010). *Differential geometry of lightlike submanifolds*. Frontiers in Mathematics.

Erdoğan, F. E. (2018). "Transversal lightlike submanifolds of metallic semi-Riemannian manifolds", *Turk. J. Math.* DOI: 10.3906/mat-1804-88.

Erdoğan, F. E., Perktas, S. Y., Acet, B. E., Blaga, A. M. (2018). "Screen Transversal lightlike submanifolds of Metallic semi-Riemannian manifolds", *Accepted in Journal of Geometry and Physics*.

Hretcanu, C. E. and Crasmareanu, M. (2013). "Metallic structures on Riemannian manifolds", *Rev. Un. Mat. Argentina*, Vol. 54, No. 2, pp. 15–27.

Hretcanu, C. E., Blaga, A. M. (2018), "Submanifolds in metallic Riemannian manifolds". *Dif. Geom. Dynm. Syst.* Vol. 20, pp. 83-97.

Kupeli D. N. (1996). *Singular Semi-Riemannian Geometry*, Kluwer Academic Publishers Group, Dordrecht.

(Önen) Poyraz, N. and Yaşar, E. (2017). "Lightlike Hypersurfaces of A Golden semi-Riemannian Manifold", *Mediterr. J. Math.*, 14:204.

(Önen) Poyraz, N. and Yaşar, E. (2019). "Lightlike submanifolds of Golden semi-Riemannian Manifolds", *Journal of Geom. and Physcs*, Vol. 141, pp. 92-104.

Perktaş, S. Y., Kılıç, E. and Acet, B. E. (2014). "Lightlike Hypersurfaces of Para-Sasakian Space Form", *Gulf J. Math.* Vol. 2, No. 2, pp. 333-342.

Şahin, B. and Akyol, M. A. (2014). "Golden maps betwen Golden Riemannian manifolds and constancy of certain maps", *Math. Commun.*, Vol. 19, pp. 333-342.

Yıldırım, C. and Sahin, B. (2010) "Screen Transversal Lightlike submanifolds of indefinite Sasakian Manifolds", *An.St. Univ. Ovidius Constanta*, Vol.18, No.2, pp. 315-336.

CISET - 2nd Cilicia International Symposium on Engineering and Technology
10-12 October, 2019, Mersin / TURKEY

ON A STUDY OF SCREEN SEMI INVARIANT LIGHTLIKE HYPERSURFACES OF METALLIC SEMI-RIEMANNIAN MANIFOLDS

Burçin DOĞAN *[1], Nergiz (ÖNEN) POYRAZ [2] and Erol YAŞAR [3]

[1] Mersin University, Faculty of Science and Arts, Department of Mathematics, Mersin, Turkey, bdogan@mersin.edu.tr

[2] Çukurova University, Faculty of Science and Arts, Department of Mathematics, Adana, Turkey, nonen@cu.edu.tr

[3] Mersin University, Faculty of Science and Arts, Department of Mathematics, Mersin, Turkey, yerol@mersin.edu.tr

ABSTRACT
In this study, we introduce screen semi-invariant lightlike hypersurfaces of metallic semi-Riemannian manifolds. We give an example for such hypersurfaces and prove some characterization theorems.

Keywords: *Lightlike hypersurface, metallic structure, screen semi invariant hypersurface, semi-Riemannian manifold.*

* *Corresponding Author*

1. INTRODUCTION

Because of their applications in black hole theory, electromagnetism and general relativity, lightlike submanifolds are one of the important and interesting fields of study of differential geometry. The first studies on lightlike geometry belong to Duggal and Bejancu (Duggal-Bejancu, 1996). Later, new lightlike submanifold classes of indefinite Kaehler and indefinite Sasakian manifolds were described by Duggal and Şahin (Duggal-Şahin, 2006; Duggal-Şahin, 2007; Duggal-Şahin, 2010). For studies on lightlike submanifolds see: (Poyraz, Yaşar, 2017; Perktaş, et al. 2014; Yıldırım, Şahin, 2010).

It is well known that there are several geometric structures that facilitate the characterization of submanifolds. One of these structures is the metallic structure. Built by V. W. de Spinadel in 2002 (De Spinadel, 2002), the metallic mean is actually a generalization of the golden mean. Let p and q be positive integers; the positive solution of

$$x^2 - px - q = 0$$

is called a $(\boldsymbol{p},\boldsymbol{q})$ metallic number and the solution set is denoted by

$$\boldsymbol{\sigma_{p,q}} = \frac{\boldsymbol{p} + \sqrt{\boldsymbol{p^2} + \boldsymbol{4q}}}{\boldsymbol{2}}.$$

The term of metallic manifold has been described as inspired by the metallic mean (Hretcanu, Crasmareanu, 2013). Let $\bar{\boldsymbol{M}}$ be a manifold, $\bar{\boldsymbol{J}}$ and $\boldsymbol{I}$ be a endomorphism and identity operator on $\bar{\boldsymbol{M}}$, respectively. For $\boldsymbol{p},\boldsymbol{q}$ positive integers, if the equation

$$\bar{\boldsymbol{J}}^{\boldsymbol{2}} = \boldsymbol{p}\bar{\boldsymbol{J}} + \boldsymbol{qI}$$

is satisfied then (1,1) type tensor $\bar{\boldsymbol{J}}$ is called a metallic structure on $\bar{\boldsymbol{M}}$. Moreover, if $\bar{\boldsymbol{g}}(\bar{\boldsymbol{J}}\boldsymbol{X},\boldsymbol{Y}) = \bar{\boldsymbol{g}}(\boldsymbol{X},\bar{\boldsymbol{J}}\boldsymbol{Y})$ for $\forall\, \boldsymbol{X},\boldsymbol{Y} \in \boldsymbol{\Gamma}(\boldsymbol{T}\bar{\boldsymbol{M}})$, then the Riemannian metric $\bar{\boldsymbol{g}}$ is $\bar{\boldsymbol{J}}$-compatible and $(\bar{\boldsymbol{g}},\bar{\boldsymbol{J}})$ is named a metallic structure. A Riemannian manifold with a metallic structure is called a metallic Riemannian manifold and denoted by $(\bar{\boldsymbol{M}},\bar{\boldsymbol{g}},\bar{\boldsymbol{J}})$. It is easy to see that

$$\bar{\boldsymbol{g}}(\bar{\boldsymbol{J}}\boldsymbol{X},\bar{\boldsymbol{J}}\boldsymbol{Y}) = \boldsymbol{p}\bar{\boldsymbol{g}}(\boldsymbol{X},\bar{\boldsymbol{J}}\boldsymbol{Y}) + \mathbf{q}\bar{\boldsymbol{g}}(\boldsymbol{X},\boldsymbol{Y}).$$

The geometry of metallic Riemannian manifold was studied in (Blaga, Hretcanu, 2018; Hretcanu, Blaga, 2018). Then Acet introduced lightlike hypersurfaces of metallic semi-Riemannian manifolds (Acet, 2018) and lightlike submanifolds of metallic semi-Riemannian manifolds were studied in (Acet, et al., 2018) by Acet, Erdoğan and Perktaş. Moreover, different classes of lightlike submanifolds of metallic semi-Riemannian manifolds were reported in (Erdoğan, 2018; Erdoğan, et al. 2018).

In this paper we introduce screen semi-invariant lightlike hypersurfaces of a metallic semi-Riemannian manifold. Section 2 is devoted to preliminaries containing basic definitions for metallic semi-Riemannian manifolds and lightlike hypersurfaces. In Section 3 firstly we define screen semi invariant lightlike hypersurfaces of a metallic semi-Riemannian manifold. Then we give an example and prove some characterization theorems.

2. PRELIMINARIES

For p and q positive integers, the positive solution of

$$x^2 - px - q = 0$$

is called a $(\boldsymbol{p},\boldsymbol{q})$ metallic number and the solution set is denoted by

$$\boldsymbol{\sigma_{p,q}} = \frac{\boldsymbol{p} + \sqrt{\boldsymbol{p^2} + \boldsymbol{4q}}}{\boldsymbol{2}}.$$

Let $(\bar{M},\bar{g})$ be a semi-Riemannian manifold. If $\bar{J}$ satisfies

$$\bar{J}^2 = p\bar{J} + q\mathrm{I} \tag{1}$$

then $\bar{J}$ is a metallic structure on $\bar{M}$. Moreover if $\bar{g}$ is $\bar{J}$-compatible i.e.

$$\bar{g}(\bar{J}X,Y) = \bar{g}(X,\bar{J}Y) \tag{2}$$

and equivalent to

$$\bar{g}(\bar{J}X,\bar{J}Y) = p\bar{g}(X,\bar{J}Y) + \mathrm{q}\bar{g}(X,Y) \tag{3}$$

then $(\bar{M},\bar{g},\bar{J})$ is a metallic semi-Riemannian manifold (Hretcanu, Crasmareanu, 2013).

Let (M,g) be a hypersurface of semi-Riemannian manifold $(\bar{M},\bar{g})$ with index v, $0 < v < r+1$. If the induced metric g is degenerate on M and $rank(TM) = r$, then (M,g) is called a lightlike hypersurface of $(\bar{M},\bar{g})$ (Duggal, Bejancu, 1996).

For a lightlike hypersurface, the normal space is given as

$TM^{\perp} = \{V \in T\bar{M} : \bar{g}(U,V) = 0, \forall U \in TM\}$.

Also, the radical distribution $Rad(TM) = TM \cap TM^{\perp}$ and there exists a complemantary screen distribution $S(TM)$ to $TM^{\perp}$ in TM.

Theorem 1. Let $(M,g,S(TM))$ be a lightlike hypersurface of a semi-Riemannian manifold $\bar{M}$. Then there exists a unique rank 1 vector subbundle $ltr(TM)$ of $(T\bar{M})$, with base space N, such that for every non-zero section E of $Rad(TM)$ on a coordinate neighbourhood $\varphi \subset M$, there exists a section N of $ltr(TM)$ on φ satisfying: $\bar{g}(N,N) = 0$, $\bar{g}(N,W) = 0$, $\bar{g}(N,E) = 1$, for $W \in \Gamma(S(TM)\,|\varphi$. $ltr(TM)$ is called the lightlike transversal vector bundle of M (Duggal, Bejancu, 1996).

From previous theorem, we can write:

$$TM = S(TM) \perp Rad(TM), \tag{4}$$

$$\begin{aligned} T\bar{M} &= TM \oplus ltr(TM) \\ &= S(TM) \perp Rad(TM) \oplus ltr(TM). \end{aligned} \tag{5}$$

Let $\omega : \Gamma(TM) \to \Gamma(S(TM))$ be the projection morphism. For $U,V \in \Gamma(TM)$, we have

$$\bar{\nabla}_U V = \nabla_U V + B(U,V)N, \tag{6}$$

$$\bar{\nabla}_U N = -\mathrm{A}_N U + \tau(U)N, \tag{7}$$

$$\nabla_U \omega V = \nabla^*_U \omega V + C(U,\omega V)E, \tag{8}$$

$$\nabla_U E = -A^*_E U - \tau(V)E. \tag{9}$$

If we describe

$\theta(U) = \bar{g}(N,U)$,

then induced connection is calculated as

$$(\nabla_U g)(V,Z) = B(U,Z)\theta(V) + B(U,V)\theta(Z). \tag{10}$$

On the other hand, we get

$$B(U,E) = 0, \tag{11}$$

$$g(A^*_E U, PV) = B(U,PV), \; g(A^*_E U,N) = 0, \tag{12}$$

$$g(\mathrm{A}_N U, PV) = C(U,PV), \quad g(\mathrm{A}_N U,N) = 0, \tag{13}$$

$$\boldsymbol{A^*_E E} = \mathbf{0}. \tag{14}$$

3. SCREEN SEMI INVARIANT LIGHTLIKE HYPERSURFACES

Let $\boldsymbol{M}$ be a lightlike hypersurface of a metallic semi-Riemannian manifold $(\bar{\boldsymbol{M}},\bar{\boldsymbol{g}},\bar{\boldsymbol{J}})$. Then we can write

$$\bar{\boldsymbol{J}}\boldsymbol{U} = \boldsymbol{\phi U} + \boldsymbol{u}(\boldsymbol{U})\boldsymbol{N}, \tag{15}$$

$$\bar{\boldsymbol{J}}\boldsymbol{N} = \boldsymbol{\zeta} + \boldsymbol{v}(\boldsymbol{E})\boldsymbol{N}, \tag{16}$$

where $\boldsymbol{\phi U}$, $\boldsymbol{\zeta} \in \boldsymbol{\Gamma}(\boldsymbol{TM})$ and

$$\boldsymbol{u(U) = g(U, \bar{J}E),\ v(U) = g(U, \bar{J}N).} \quad (17)$$

Lemma 2. (Acet, 2018) Let $\boldsymbol{M}$ be a lightlike hypersurface of $(\boldsymbol{\bar{M}, \bar{g}, \bar{J}})$. Then we have

$$\boldsymbol{\phi^2 U = p\phi U + q(U) - u(U)\zeta,} \quad (18)$$
$$\boldsymbol{u(\phi U) = pu(U) - u(U)v(E),} \quad (19)$$
$$\boldsymbol{\phi\zeta = p\zeta - v(E)\zeta,} \quad (20)$$
$$\boldsymbol{v(E)^2 = pv(E) + q - u(\zeta),} \quad (21)$$
$$\boldsymbol{g(\phi U, V) = g(U, \phi V) + u(V)\theta(U) - u(U)\theta(V),} \quad (22)$$
$$\boldsymbol{g(\phi U, \phi V) = pg(U, \phi V) + qg(U, V) + pu(V)\theta(U) - u(V)g(\phi U, N) - u(U)g(\phi V, N).} \quad (23)$$

Definition 3. Let $\bar{J}$ be a metallic semi-Riemannian structure. If $\nabla\bar{J} = 0$, i.e., $\bar{J}$ is parallel then $\bar{J}$ is named a locally metallic structure (Acet, 2018).

Lemma 4. (Acet, 2018) Let $\boldsymbol{M}$ be a lightlike hypersurface of a locally metallic semi-Riemannian manifold $(\boldsymbol{\bar{M}, \bar{g}, \bar{J}})$. Then we obtain

$$\boldsymbol{(\nabla_U \phi)V = u(V)A_N U + B(U,V)\zeta,} \quad (24)$$
$$\boldsymbol{(\nabla_U u)V = B(U,V)v(E) - B(U,\phi V) - \tau(U)u(V),} \quad (25)$$
$$\boldsymbol{\nabla_U \zeta = -\phi A_N U + \tau(U)\zeta + A_N U v(E),} \quad (26)$$
$$\boldsymbol{U\big(v(E)\big) = -B(U,\zeta) - u(A_N U).} \quad (27)$$

Definition 5. Let M be a lightlike hypersurface of a locally metallic semi-Riemannian manifold $(\bar{M}, \bar{g}, \bar{J})$. If

$$\bar{J}\big(Rad(TM)\big) \subset S(TM), \quad \bar{J}(ltr(TM)) \subset S(TM), \quad (28)$$

then M is called a screen semi-invariant lightlike hypersurface of $\bar{M}$ (Acet, 2018).

For a screen semi invariant hypersurfaces, we can write the following decompositions:

$$S(TM) = \mu_0 \perp \{\bar{J}\big(Rad(TM)\big) \oplus \bar{J}\big(ltr(TM)\big)\}, \quad (29)$$
$$TM = \{\bar{J}\big(Rad(TM)\big) \oplus \bar{J}\big(ltr(TM)\big)\} \perp \mu_0 \perp Rad(TM), \quad (30)$$
$$T\bar{M} = \{\bar{J}\big(Rad(TM)\big) \oplus \bar{J}\big(ltr(TM)\big) \perp \mu_0 \perp \{Rad(TM) \oplus ltr(TM)\}, \quad (31)$$

where μ_0 is a non-degenerate invariant distribution.

Let we consider invariant and anti-invariant distributions in $T\bar{M}$ by $\widetilde{D} = Rad(TM) \perp \bar{J}(Rad(TM)) \perp \mu_0$ and $\widetilde{D}' = \bar{J}(ltr(TM))$ on M, respectively. Thus, we have

$$T\bar{M} = \widetilde{D} \oplus \widetilde{D}'. \quad (32)$$

Now we set local lightlike vector fields by $\zeta = \bar{J}N$ and $\psi = \bar{J}E$. If we denote the projections of TM on $\widetilde{D}$ and $\widetilde{D}'$ by Q and R, respectively, we can write

$$U = QU + RU \quad (33)$$

for any $U \in \Gamma(TM)$.

Let M be a lightlike hypersurface of a locally metallic semi-Riemannian manifold $(\bar{M}, \bar{g}, \bar{J})$. Then from Lemma 2. and Lemma 4. we get

$$\phi^2 U = p\phi U + q(U) - u(U)\zeta, \quad (34)$$
$$u(\phi U) = pu(U),\ u(\zeta) = q, \quad (35)$$
$$g(\phi U, V) = g(U, \phi V) + u(V)\theta(U) - u(U)\theta(V), \quad (36)$$
$$g(\phi U, \phi V) = pg(U, \phi V) + qg(U, V) + pu(V)\theta(U) - u(V)g(\phi U, N) - u(U)g(\phi V, N), \quad (37)$$
$$(\nabla_U \phi)V = u(V)A_N U + g(A_E^* U, V)\zeta, \quad (38)$$
$$(\nabla_U u)V = -B(U, \phi V) - u(V)\tau(U), \quad (39)$$
$$\nabla_U \zeta = -\phi A_N U + \tau(U)\zeta, \quad (40)$$
$$\nabla_U \psi = -\phi A_E^* U - \tau(U)\psi, \quad (41)$$
$$B(U, \zeta) = -C(U, \psi) \quad (42)$$

for $U, V \in \Gamma(TM)$, $\zeta \in \Gamma(\widetilde{D}')$ and $\psi \in \Gamma(\widetilde{D}$.

Example 6. Let $(\bar{M} = \mathbb{R}_2^7, \bar{g})$ be a 7-dimensional semi-Euclidean space with signature $(+,-,+,-,+,+,+)$ and $(x_1, x_2, x_3, x_4, x_5, x_6, x_7)$ be the standard coordinate system of $\mathbb{R}_2^7$. We define $\bar{J}$ metallic structure by

$$\bar{\mathbf{J}}(\mathbf{x_1}, \mathbf{x_2}, \mathbf{x_3}, \mathbf{x_4}, \mathbf{x_5}, \mathbf{x_6}, \mathbf{x_7}) = (\boldsymbol{\sigma}\mathbf{x_1}, \boldsymbol{\sigma}\mathbf{x_2}, (\mathbf{p} - \boldsymbol{\sigma})\mathbf{x_3}, (\mathbf{p} - \boldsymbol{\sigma})\mathbf{x_4}, \boldsymbol{\sigma}\mathbf{x_5}, \boldsymbol{\sigma}\mathbf{x_6}, \boldsymbol{\sigma}\mathbf{x_7}).$$

Let M be a lightlike hypersurface of $\mathbb{R}_2^7$ which given by

$$\mathbf{x_1} = \mathbf{u_1} + \boldsymbol{\sigma}\mathbf{u_2} + \frac{\boldsymbol{\sigma}}{\mathbf{2(p\sigma + q + 1)}}\mathbf{u_3},$$
$$\mathbf{x_2} = \mathbf{u_1} + \boldsymbol{\sigma}\mathbf{u_2} - \frac{\boldsymbol{\sigma}}{\mathbf{2(p\sigma + q + 1)}}\mathbf{u_3},$$
$$\mathbf{x_3} = \boldsymbol{\sigma}\mathbf{u_1} - \mathbf{q}\mathbf{u_2} - \frac{\mathbf{q}}{\mathbf{2(p\sigma + q + 1)}}\mathbf{u_3},$$
$$\mathbf{x_4} = \boldsymbol{\sigma}\mathbf{u_1} - \mathbf{q}\mathbf{u_2} + \frac{\mathbf{q}}{\mathbf{2(p\sigma + q + 1)}}\mathbf{u_3},$$
$$\mathbf{x_5} = \mathbf{u_4} - \mathbf{u_5}, \quad \mathbf{x_6} = \mathbf{u_4} + \mathbf{u_5}, \quad \mathbf{x_7} = \mathbf{u_6}.$$

Thus $\boldsymbol{TM} = \boldsymbol{Sp}\{\boldsymbol{U_1}, \boldsymbol{U_2}, \boldsymbol{U_3}, \boldsymbol{U_4}, \boldsymbol{U_5}\}$ where

$$\mathbf{U_1} = \frac{\boldsymbol{\partial}}{\boldsymbol{\partial}\mathbf{x_1}} + \frac{\boldsymbol{\partial}}{\boldsymbol{\partial}\mathbf{x_2}} + \boldsymbol{\sigma}\frac{\boldsymbol{\partial}}{\boldsymbol{\partial}\mathbf{x_3}} + \boldsymbol{\sigma}\frac{\boldsymbol{\partial}}{\boldsymbol{\partial}\mathbf{x_4}},$$
$$\mathbf{U_2} = \boldsymbol{\sigma}\frac{\boldsymbol{\partial}}{\boldsymbol{\partial}\mathbf{x_1}} + \boldsymbol{\sigma}\frac{\boldsymbol{\partial}}{\boldsymbol{\partial}\mathbf{x_2}} - \mathbf{q}\frac{\boldsymbol{\partial}}{\boldsymbol{\partial}\mathbf{x_3}} - \mathbf{q}\frac{\boldsymbol{\partial}}{\boldsymbol{\partial}\mathbf{x_4}},$$
$$\mathbf{U_3} = -\frac{\mathbf{1}}{\mathbf{2(p\sigma + q + 1)}}\Big(-\boldsymbol{\sigma}\frac{\boldsymbol{\partial}}{\boldsymbol{\partial}\mathbf{x_1}} + \boldsymbol{\sigma}\frac{\boldsymbol{\partial}}{\boldsymbol{\partial}\mathbf{x_2}} + \mathbf{q}\frac{\boldsymbol{\partial}}{\boldsymbol{\partial}\mathbf{x_3}} - \mathbf{q}\frac{\boldsymbol{\partial}}{\boldsymbol{\partial}\mathbf{x_4}}\Big),$$
$$\mathbf{U_4} = \frac{\boldsymbol{\partial}}{\boldsymbol{\partial}\mathbf{x_5}} + \frac{\boldsymbol{\partial}}{\boldsymbol{\partial}\mathbf{x_6}}, \quad \mathbf{U_5} = -\frac{\boldsymbol{\partial}}{\boldsymbol{\partial}\mathbf{x_5}} + \frac{\boldsymbol{\partial}}{\boldsymbol{\partial}\mathbf{x_6}}, \quad \mathbf{U_6} = \frac{\boldsymbol{\partial}}{\boldsymbol{\partial}\mathbf{x_7}}.$$

It is obvious that $\boldsymbol{Rad(TM)} = \boldsymbol{Sp}\{\boldsymbol{U_1}\}$ and $\boldsymbol{S(TM)} = \boldsymbol{Sp}\{\boldsymbol{U_2}, \boldsymbol{U_3}, \boldsymbol{U_4}, \boldsymbol{U_5}\}$. By direct calculations it is seen that lightlike transversal bundle $\boldsymbol{ltr(TM)}$ is spanned by

$$\boldsymbol{N} = -\frac{\mathbf{1}}{\boldsymbol{2(p\sigma + q + 1)}}\Big(-\frac{\boldsymbol{\partial}}{\boldsymbol{\partial x_1}} + \frac{\boldsymbol{\partial}}{\boldsymbol{\partial x_2}} - \boldsymbol{\sigma}\frac{\boldsymbol{\partial}}{\boldsymbol{\partial x_3}} - \boldsymbol{\sigma}\frac{\boldsymbol{\partial}}{\boldsymbol{\partial x_4}}\Big).$$

If we set $\boldsymbol{U_1 = E}$, we get $\boldsymbol{g(E, N) = 1}$ and $\boldsymbol{\bar{J}E = -U_2}$, $\boldsymbol{\bar{J}N = U_3}$. Also, distribution $\boldsymbol{\mu_0}$ is spanned by $\{\boldsymbol{U_4}, \boldsymbol{U_5}, \boldsymbol{U_6}\}$. Then $\boldsymbol{M}$ is a screen semi invariant lightlike hypersurfaces of $\mathbb{R}_2^7$.

Theorem 7. Let M be a screen semi invariant lightlike hypersurface of a locally metallic semi-Riemannian manifold $(\bar{M}, \bar{g}, \bar{J})$. If ϕ is parallel then $\widetilde{D}$ is parallel and $M = M_1 \times M_2$ has a locally product structure where M_1 is a tangent curve to $\bar{J}(ltr(TM))$ and M_2 is a leaf of $\widetilde{D}$.

Proof. Suppose that ϕ is parallel. Then $\forall U \in \Gamma(TM)$ and $V \in \Gamma(\mu_0)$,

$$g(\nabla_U E, \bar{J}E) = g(\nabla_U \bar{J}E, \bar{J}E) = g(\nabla_U V, \bar{J}E) = 0.$$

Thus, we get easily the following equations:

$g(\nabla_U E, \bar{J}E) = -g(E, \overline{\nabla}_U \bar{J}E) = -B(U,\psi)$,
$g(\nabla_U \bar{J}E, \bar{J}E) = 0$,
$g(\nabla_U V, \bar{J}E) = g(\bar{J}V, \overline{\nabla}_U E)$
$= -g(\bar{J}V, A^*_E U) = -B(U, \bar{J}V)$.
If we take $V = \psi = \bar{J}E$ in (38), then we get $g(A^*_E U, \psi) = 0$, that is, $B(U,\psi) = 0$.
Besides, we know that for $V \in \Gamma(\mu_0)$, $\bar{J}V \in \Gamma(\mu_0)$. So, replacing $V = \bar{J}V$ in (38), we have $B(U, \bar{J}V) = 0$. Thus, $\widetilde{D}$ is parallel and integrable, that is, M has a locally product structure.

Theorem 8. Let M be a screen semi invariant lightlike hypersurface of a locally metallic semi-Riemannian manifold $(\bar{M}, \bar{g}, \bar{J})$. Then the following assertions are equivalent:
(i) $\widetilde{D}$ is parallel.
(ii) $\widetilde{D}$ is totally geodesic.
(iii) ϕ is parallel.

Proof. We know that $\widetilde{D}$ is parallel iff $g(\nabla_U V, \psi) = 0$, for $\forall U, V \in \Gamma(\widetilde{D})$.
From (6) and (2), we derive
$g(\nabla_U V, \psi) = \bar{g}(\overline{\nabla}_U V, \bar{J}E) = \bar{g}(\overline{\nabla}_U \bar{J}V, E) = B(U, \bar{J}V)$.
Thus, i)⇔ii) is provided.
Since $u(V) = 0$, for $\forall V \in \Gamma(\widetilde{D})$, using (38) we derive
$(\nabla_U \phi)V = g(A^*_E U, V)\zeta$.
That is, ii)⇔iii) is provided which completes the proof.

Theorem 9. Let M be a screen semi invariant lightlike hypersurface of a locally metallic semi-Riemannian manifold $(\bar{M}, \bar{g}, \bar{J})$. Then $\bar{M}$ is totally geodesic iff the followings are satisfied:
(i) $(\nabla_U \phi)V = 0$,
(ii) $(\nabla_U \phi)\zeta = A_N U$
for $U \in \Gamma(TM)$, $V \in \Gamma(\widetilde{D})$.

Proof. We assume that $\bar{M}$ is totally geodesic. Then for any $V \in \Gamma(TM)$, we can write $V = V_{\widetilde{D}} + \zeta$.
If $V \in \Gamma(\widetilde{D})$ then $u(V) = 0$. Thus we get $(\nabla_U \phi)V = 0$ which satisfies (i).
If we choose $V = \xi$ then $u(\zeta) = 1$ and from this $(\nabla_U \phi)\zeta = A_N U$. Thus ii) is satisfied.
Conversely, we assume that (i) and (ii) are provided. Since for $V \in \Gamma(TM)$, $V = V_{\widetilde{D}} + \zeta$ then we write easily
$B(U,V) = B(U, V_{\widetilde{D}}) + B(U, \zeta)$.
On the other hand, for $V \in \Gamma(\widetilde{D})$, $u(V) = 0$ and from this, $B(U, V_{\widetilde{D}}) = 0$.
For $\xi \in \Gamma(\widetilde{D})$, from (ii) and (38) $B(U,\zeta) = 0$. Thus, we have $B(U,V) = 0$ which means that $\bar{M}$ is totally geodesic and the proof is completed.

4. CITATION AND REFERENCE LIST

Acet, B. E. (2018). "Lightlike hypersurfaces of metallic semi-Riemannian manifolds", *Int. J. Geom. Methods Mod. Phys.*, DOI:10.1142/S0219887818502018.

Acet, B. E., Erdoğan, F. E., Perktas, S. Y. (2018). "Lightlike Submanifolds of Metallic Semi-Riemannian Manifolds", *arXiv preprint arXiv: 1811.05019v1*.

Blaga, A. M., Hretcanu, C. E. (2018). "Invariant, anti-invariant and slant submanifolds of a metallic Riemannian manifold", *arXiv preprint* arXiv:1803.01415.

Crasmareanu, M. and Hretcanu, C. E. (2008). "Golden differential geometry", *Chaos Solitons and Fractals*, Vol. 38, No. 5, pp. 1229–1238.

De Spinadel, V. W. (2002). "The metallic means family and forbidden symmetries", *Int. Math. J.*, Vol. 2, No. 3, pp. 279–288.

Duggal, K. L., Bejancu, A. (1996). *Lightlike submanifolds of semi-Riemannian manifolds and applications, Mathematics and Its Applications.* Kluwer Publisher.

Duggal, K. L., Sahin, B. (2006). "Generalized Cauchy-Riemann lightlike submanifolds of Kaehler manifolds". *Acta Math. Hungarica*,. 112, pp. 107-130.

Duggal, K. L., Sahin, B. (2007). "Lightlike submanifolds of indefinite Sasakian manifolds". *Int. J. Math. and Math. Sci.*, Article ID:57585.

Duggal, K. L., Sahin, B. (2010). *Differential geometry of lightlike submanifolds*. Frontiers in Mathematics.

Erdoğan, F. E. (2018). "Transversal lightlike submanifolds of metallic semi-Riemannian manifolds", *Turk. J. Math.* DOI: 10.3906/mat-1804-88.

Erdoğan, F. E., Perktas, S. Y., Acet, B. E., Blaga, A. M. (2018). "Screen Transversal lightlike submanifolds of Metallic semi-Riemannian manifolds", *Accepted in Journal of Geometry and Physics*.

Hretcanu, C. E. and Crasmareanu, M. (2013). "Metallic structures on Riemannian manifolds", *Rev. Un. Mat. Argentina*, Vol. 54, No. 2, pp. 15–27.

Hretcanu, C. E., Blaga, A. M. (2018), "Submanifolds in metallic Riemannian manifolds". *Dif. Geom. Dynm. Syst.* Vol. 20, pp. 83-97.

(Önen) Poyraz, N. and Yaşar, E. (2017). "Lightlike Hypersurfaces of A Golden semi-Riemannian Manifold", *Mediterr. J. Math.*, 14:204.

Perktaş, S. Y., Kılıç, E. and Acet, B. E. (2014). "Lightlike Hypersurfaces of Para-Sasakian Space Form", *Gulf J. Math.* Vol. 2, No. 2, pp. 333-342.

Yıldırım, C. and Sahin, B. (2010) "Screen Transversal Lightlike submanifolds of indefinite Sasakian Manifolds", *An.St. Univ. Ovidius Constanta*, Vol.18, No.2, pp. 315-336.

CISET - 2nd Cilicia International Symposium on Engineering and Technology
10-12 October, 2019, Mersin / TURKEY

SOME AZOMETHINS AND OXAZOLIDINES SYNTHESIZED BASED ON 2-AMINO-4-ARYLSUBSTITUTED THIAZOLES

Sevinj Sadigova

"Gilan Textile Park" LLC, Sumgait, Azerbaijan, s_sevinj@mail.ru

ABSTRACT
The reactions of 2-amino-4-aryl-substituted thiazoles with aromatic aldehydes, as well as the reactions of synthesized azomethines with 1,2-epoxypropane, 1,2-epoxy-3-chloropropane and 1,2-epoxy-3-phenoxypropane, have been studied.

Keywords: 2-Amino-4-aryl-substituted Thiazoles, Aromatic Aldehydes, Azomethines, Oxazolidines.

1. INTRODUCTION

Nitrogen-containing heterocyclic compounds occupy one of the leading places in organic chemistry due to the wide range of their biological effects and diverse applications in various fields of human activity. In particular, derivatives of aminothiazoles can serve as the basis for numerous drugs [2,6,10], various heterocycles [5]; they are used as antioxidants of oil products [3], vulcanization accelerators [4]. Schiff bases, or azomethines, obtained on the basis of 2-amino-4-arylthiazoles [7] are of great importance in analytical chemistry and chemotherapy [8,1,9]. They are used for concentration and photometric determination of a number of transition metals.

2. HEADINGS

2.1. Synthesis of Source and Target Compounds

We have studied the reaction of 2-amino-4-aryl-substituted thiazoles (1-4) with various aromatic aldehydes - benzaldehyde, salicylic aldehyde, bromosalicylic aldehyde, 2-hydroxy-1-naphthaldehyde, 4-(N,N-dimethylamino)benzaldehyde:

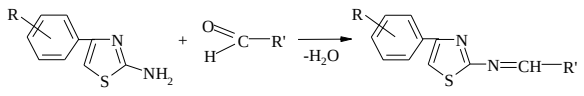

1-14

R' = C_6H_5, R = H (1), 2,5-$(CH_3O)_2$ ($_2$), 2-OH (3), 4-Cl (4);
R' = 2-HOC_6H_4, R = H (5), 2,5-$(CH_3O)_2$ (6), 2-OH (7);
R' = 2-HO-4-BrC_6H_3, R = H (8), 2,5-$(CH_3O)_2$ (9), 2-OH (10), 4-Cl (11);
R' = 2-$HOC_{10}H_6$, R = H (12);
R' = 4-$(CH_3)_2NC_6H_4$, R = H (13), 2-OH (14)

The IR spectra of azomethines (1-14) are similar to the IR spectra of thiazoles. However, have been found out the wide strip in the field of 3450 sm^{-1} in the molecules (5–14), which characterizes the intramolecular hydrogen bond between the hydroxyl group in the phenyl radical and the N=CH fragment. Absorption bands characteristic for the valent fluctuations of the primary NH_2 groups were not detected. The phenol hydroxyl proton signal in the ^1H NMR spectra of azomethines (1-14) appears in the field of 3.25 ppm, and the proton signal of the N=CH fragment has been found in the field of 7.85-7.90 ppm. The signals of four nonequivalent protons in the 2-hydroxyphenyl fragment are observed as a multiplet in the field of 7.2–7.5 ppm.

By ternary condensation of 2-benzylidenamino-4-phenylthiazole (1), acetone and ethyl alcohol has been received 4-methyl-2,6-diphenylpyrimido[1,2-b]thiazoline (15):

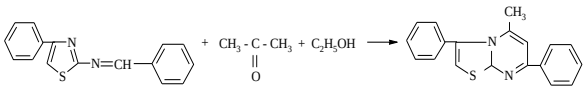

1 15

Physicochemical properties of the synthesized compounds (1-15) are shown in Table 1.

By reaction of azomethine (12) with 1,2-epoxypropane has been synthesized 2-(2′-hydroxynaphthyl)-3-(4″-phenylthiazolyl)-5-methyl-1,3-oxazolidine (16):

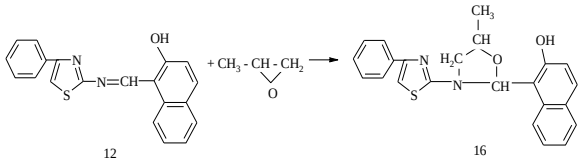

12 16

By reaction of azomethines (1) and (12) with 1,2-epoxy-3-chloropropane have been obtained substituted 5-chloromethyl-1,3-oxazolidines (17) and (18), respectively:

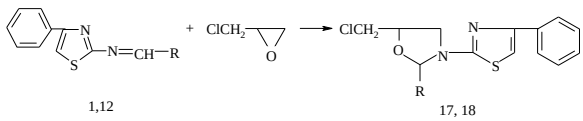

1,12 17, 18

R = C_6H_5 (17), 2-$HOC_{10}H_6$ (18)

The synthesis of 5-chloromethyl-1,3-oxazolidines based on the reaction of 1,2-epoxy-3-chloropropane with Schiff bases in the presence of tin tetrachloride proceeds via the formation of an intermediate complex. It was found that the yield of oxazolidines depends on the proper mixing of the reagents - it's important the simultaneous introduction of oxirane and azomethine into the reaction mixture during the reaction.

The reaction of azomethines (5) and (12) with 1,2-epoxy-3-phenoxypropane gave substituted 5-phenoxymethyl-1,3-oxazolidines (19) and (20), respectively:

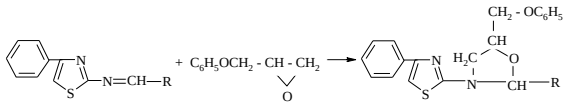

5, 12 19, 20

R = 2-HOC_6H_4 (19), 2 - $HOC_{10}H_6$ (20)

Physicochemical properties of the synthesized compounds (16-20) are shown in Table 2.

2.2. The Experimental Part

IR spectra of the compounds were recorded on a Specord IR-75 spectrophotometer in a thin layer or in liquid paraffin in the range 700-3700 sm^{-1} using KBr, NaCl, and LiF prisms. ^1H NMR spectra were recorded on a Varian VXR-400S (400 MHz) for solutions of substances in DMSO-*d*$_6$, the internal standard is TMS. TLC analysis was performed on Silufol UV-254 plates with isopropyl alcohol and heptane mixture (1:1) with the manifestation of iodine vapor.

2.2.1. Synthesis of 2-benzylidenamino-4-phenylthiazole (1)

8.8 g (0.05 mol) of 2-amino-4-phenylthiazole was added to 5.3 g (0.05 mol) of benzaldehyde and stirred vigorously for 30 min. Then the reaction mixture was poured into a glass with 15 ml of ethyl alcohol. The colorless crystalline precipitate that formed after a few minutes was filtered. Yield: 9.4 g (71%), m.p. 160-161^{0}C. Found, %: C 72.61; H

4.73; N, 10.75. S 12.02. $C_{16}H_{12}N_2S$. Anal. calcd., %: C 72.80; H 4.58; N, 10.60; S 12.12. R_f = 0.74.

2.2.2. Synthesis of 2-benzylidenamino-4-(2′,5′-dimethoxy-phenyl)thiazole (2)

11.8 g (0.05 mol) of 2-amino-4-(2′,5′-dimethoxyphenyl) thiazole was added to 5.3 g (0.05 mol) of benzaldehyde in a 50 ml three-necked flask and stirred vigorously for 30 min. Then the reaction mixture was poured into a glass with 15 ml of ethyl alcohol. The colorless crystalline precipitate that formed after a few minutes was filtered. Yield: 11 g (73%), m.p. 147-148^{0}C. Found, %: C 66.78; H 4.72; N, 8.82; S 9.76. $C_{18}H_{16}N_2O_2S$. Anal. calcd., %: C 66.65; H 4.97; N, 8.64; S 9.88.

2.2.3. Synthesis of 2-benzylidenamino-4-(2′-hydroxyphenyl) thiazole (3)

9.6 g (0.05 mol) of 2-amino-4-(2′-hydroxyphenyl) thiazole was added to 5.3 g (0.05 mol) of benzaldehyde in a 50 ml three-necked flask and stirred vigorously for 30 min. Then the reaction mixture was poured into a glass with 15 ml of ethyl alcohol. The colorless crystalline precipitate that formed after a few minutes was filtered. Yield: 10.51 g (75%), m.p. 143-144^{0}C. Found, %: C 68.73; H 4.17; N 10.16; S 11.17. $C_{16}H_{12}N_2OS$. Anal. calcd., %: C 68.55; H 4.32; N, 9.99; S 11.44.

2.2.4. Synthesis of 2-benzylidenamino-4-(4′-chlorophenyl) thiazole (4)

10.5 g (0.05 mol) of 2-amino-4-(4′-chlorophenyl)-thiazole was added to 5.3 g (0.05 mol) of benzaldehyde and stirred vigorously for 30 min. Then the reaction mixture was poured into a glass with 15 ml of ethyl alcohol. The colorless crystalline precipitate that formed after a few minutes was filtered. Yield: 10.01 g (67%), m.p. 149-150^{0}C. Found, %: C 64.57; H 3.52; N, 9.65; S 10.58. $C_{16}H_{11}N_2SCl$. Anal. calcd., %: C 64.32; H 3.71; N, 9.38; S 10.73.

2.2.5. Synthesis of 2-(2′-hydroxybenzylideneamino)-4-phenylthiazole (5)

8.8 g (0.05 mol) of 2-amino-4-phenylthiazole was added to 6.1 g (0.05 mol) of salicylic aldehyde and stirred vigorously for 30 minutes; the reaction is exothermic and the temperature of the mixture rose to 40^{0}C. The reaction mixture was poured into a beaker, then 15 ml of ethyl alcohol was added and cooled with ice. The precipitated crystalline was filtered. Yield: 11.21 g (80%), m.p. 143^{0}C. Found, %: C 68.76; H 4.13; N, 9.74; S 11.28. $C_{16}H_{12}N_2OS$. Anal. calcd., %: C 68.55; H 4.31; N, 9.99; S 11.44.

2.2.6. Synthesis of 2-(2′-hydroxybenzylideneamino)-4-(2″,5″-dimethoxyphenyl)thiazole (6)

11.8 g (0.05 mol) of 2-amino-4-(2′,5′-dimethoxyphenyl)-thiazole was added to 6.1 g (0.05 mol) of salicylic aldehyde and stirred vigorously for 30 minutes. The reaction is exothermic and the temperature of the mixture rose to 40^{0}C. The reaction mixture was poured into a beaker, then 15 ml of ethyl alcohol was added and cooled with ice. The precipitated crystalline was filtered. Yield: 11.6 g (68%), m.p. 139-140^{0}C. Found, %: C 63.29; H 4.61; N, 8.42; S 9.08. $C_{18}H_{16}N_2O_3S$. Anal. calcd., %: C 63.51; H 4.74; N, 8.23; S 9.42.

2.2.7. Synthesis of 2-(2′-hydroxybenzylideneamino)-4-(2″-hydroxyphenyl)thiazole (7)

9.6 g (0.05 mol) of 2-amino-4-(2′-hydroxyphenyl)-thiazole was added to 6.1 g (0.05 mol) of salicylic aldehyde and stirred vigorously for 30 minutes; the reaction is exothermic and the temperature of the mixture rose to 40^{0}C. The reaction mixture was poured into a beaker, then 15 ml of ethyl alcohol was added and cooled with ice. The precipitated crystalline was filtered. Yield: 11 g (74%), m.p. 189-190^{0}C. Found, %: C 64.72; H 4.19; N, 9.59; S 10.66. $C_{16}H_{12}N_2O_2S$. Anal. calcd., %: C 64.85; H 4.08; N, 9.45; S 10.82.

2.2.8. Synthesis of 2-(2′-hydroxy-4′-bromobenzyliden-amino)-4-phenylthiazole (8)

1.76 g (0.01 mol) of 2-amino-4-phenylthiazole dissolved in 10 ml of isopropyl alcohol was added to 2.01 g (0.01 mol) of bromosalicylic aldehyde and stirred vigorously for 1-2 hours. The reaction mixture was poured into a glass with 2 ml of ethyl alcohol and cooled with ice. The precipitated crystalline was filtered. Yield: 2.9 g (80%), m.p. 100-102^{0}C. Found, %: C 53.63; H 2.85; N, 7.39; S 8.49. $C_{16}H_{11}N_2OSBr$. Anal. calcd., %: C 53.49; H 3.09; N, 7.80; S 8.93.

2.2.9. Synthesis of 2-(2′-hydroxy-4′-bromobenzyliden-amino)-4-(2″,5″-dimethoxyphenyl)thiazole (9)

2.36 g (0.01 mol) of 2-amino-4-(2′,5′-dimethoxyphenyl) thiazole dissolved in 10 ml of isopropyl alcohol was added to 2.01 g (0.01 mol) of 4-bromosalicylic aldehyde, and stirred vigorously for 1-2 h. The reaction mixture was poured into a glass with 2 ml of ethyl alcohol and cooled with ice. The precipitated crystalline was filtered. Yield: 3 g (71%), m.p. 145-147^{0}C. Found, %: C 51.76; H 3.44; N, 6.37; S 6.98. $C_{18}H_{15}N_2O_3SBr$. Anal. calcd., %: C 51.56; H 3.61; N, 6.68; S 7.65.

2.2.10. Synthesis of 2-(2′-hydroxy-4′-bromobenzylidenami-no)-4-(2″-hydroxyphenyl)thiazole (10)

3.84 g (0.02 mol) of 2-amino-4-(2′-hydroxy-phenyl)thiazole dissolved in 10 ml of isopropyl alcohol was added to 4.02 g (0.02 mol) of 4-bromosalicylic aldehyde and stirred vigorously for 1-2 hours The reaction mixture was poured into a glass with 2 ml of ethyl alcohol and cooled with ice. The precipitated crystalline was filtered. Yield: 5.6 g (75%), m.p. 159-160^{0}C. Found, %: C 51.44; H 2.73; N, 7.68; S 8.32. $C_{16}H_{11}N_2O_2SBr$. Anal. calcd., %: C 51.21; H 2.98; N, 7.47; S 8.55.

2.2.11. Synthesis of 2-(2′-hydroxy-4′-bromobenzylidenamino)-4-(4″-chlorophenyl) thiazole (11)

To 2.01 g (0.01 mol) of 4-bromosalicylic aldehyde was added 2.1 g (0.01 mol) of 2-amino-4-(4-chlorophenyl) thiazole dissolved in 10 ml of isopropyl alcohol and stirred vigorously for 1-2 hours. The reaction mixture was poured into a glass with 2 ml of ethyl alcohol and cooled with ice. The precipitated crystalline was filtered. Yield: 2.7 g (68%), m.p. 121-123^{0}C. Found, %: C 48.72; H 2.19; N, 7.26; S 8.33. $C_{16}H_{10}N_2OSBrCl$. Anal. calcd., %: C 48.81; H 2.56; N, 7.12; S 8.14.

2.2.12. Synthesis of 2-(2′-hydroxynaphthylidenamino)-4-phenylthiazole (12)

To 4.3 g (0.025 mol) of 2-hydroxy-1-naphthaldehyde dissolved in 12 ml of ethyl alcohol was added 4.4 g (0.025 mol) of 2-amino-4-phenylthiazole dissolved in 15 ml of ethyl alcohol and stirred for 3 h at 75^{0}C. The reaction mixture was cooled to room temperature. The precipitated crystalline was filtered. Yield: 5.1 g (74%), m.p. 156-157^{0}C. Found, %: C 72.52; H 4.43; N, 8.78; S 9.51. $C_{20}H_{14}N_2OS$. Anal. calcd., %: C 72.70; H 4.30; N, 8.50; S 9.70.

2.2.13. Synthesis of 2-(4′-N,N-dimethylaminobenzylidenamino)-4-phenylthiazole (13)

To 3.7 g (0.025 mol) of 4-(N,N-dimethylamino)benzaldehyde was added 4.4 g (0.025 mol) of 2-amino-4-phenylthiazole dissolved in 20 ml of ethyl alcohol and stirred vigorously for 2 hours. The mixture was poured into a glass with 2 ml of ethyl alcohol and cooled with ice. The precipitated crystalline was filtered. Yield: 6.07 g (79%), m.p. 200-201^{0}C. Found, %: C 70.47; H 5.29; N 13.45; S 10.28. $C_{18}H_{17}N_3S$. Anal. calcd., %: C 70.33; H 5.57; N 13.67; S 10.43.

2.2.14. Synthesis of 2-(4′-N,N-dimethylaminobenzylidenamino)-4-hydroxyphenylthiazole (14)

To 1.5 g (0.01 mol) of 4-(N,N-dimethylamino) benzaldehyde was added 2.12 g (0.01 mol) of 2-amino-4- (2′-hydroxyphenyl)thiazole dissolved in 10 ml of ethyl alcohol and stirred vigorously within 2 hours. The reaction mixture was poured into a glass with 2 ml of ethyl alcohol and cooled with ice. The precipitated crystalline was filtered. Yield: 2.2 g (69%), m.p. 220-221^{0}C. Found, %: C 66.92; H 5.06; N, 12.73; S 10.17. $C_{18}H_{17}N_3OS$. Anal. calcd., %: C 66.85; H 5.30; N, 12.99; S 9.91.

2.2.15. Synthesis of 4-methyl-2,6-diphenylpyrimido[1,2-b]-thiazoline (15)

A reaction mixture of equimolar amounts of 0.8 g (0.003 mol) of 2-benzylidenamino-4-phenylthiazole (1) dissolved in 20 ml of nitrobenzene, 1.5 ml (0.02 mol) of acetone, 6 ml of ethyl alcohol and 0.7 ml of concentrated HCl was heated in reflux flask in a boiling water bath for 3 hours. Yield: 0.5 g (55%), m.p. 213^{0}C. Found, %: C 74.69; H 5.12; N, 9.05; S 10.74. $C_{19}H_{16}N_2S$. Anal. calcd., %: C 74.97; H 5.30; N, 9.20; S 10.53.

2.2.16. Synthesis of 2-(2′-hydroxynaphthyl)-3-(4″-phenylthiazolyl)-5-methyl-1,3-oxazolidine (16)

A solution of 0.23 ml (0.002 mol) of $SnCl_4$ in 2.4 ml of CCl_4 was added dropwise to a solution of 1.69 ml (0.022 mol) of 1,2-epoxypropane and 3.3 g (0.01 mol) of 2-(2′-hydroxynaphthylidenamino)-4-phenylthiazole (12) in 4 ml of CCl_4. The organic layer was dried with Na_2SO_4. Yield: 2.52 g (65%), m.p. 85-86^{0}C. Found, %: C 71.26; H 5.32; N, 7.43; S 8.03. $C_{23}H_{20}N_2O_2S$. Anal. calcd., %: C 71.11; H 5.19; N, 7.21; S 8.25.

2.2.17. Synthesis of 2-(2′-phenyl)-3 (4″-phenylthiazolyl)-5-chloromethyl-1,3-oxazolidine (17)

A solution of 0.23 ml (0.002 mol) of $SnCl_4$ in 5 ml of CCl_4 was added dropwise to a solution of 1.69 ml (0.022 mol) of 1,2-epoxy-3-chloropropane and 5.60 g (0.02 mol) of 2-hydroxybenzylidenamino-4-phenylthiazole (1) in 8 ml of CCl_4. The organic layer was dried with Na_2SO_4. Yield: 5.2 g (75%), m.p. 78-79^{0}C. Found, %: C 63.72; H 4.96; N, 7.68; S 8.66. $C_{19}H_{17}N_2OSCl$. Anal. calcd., %: C 63.95; H 4.80; N, 7.85; S 8.99.

2.2.18. Synthesis of 2-(2′-hydroxynaphthyl)-3-(4″-phenylthiazolyl)-5-chloromethyl-1,3-oxazolidine (18)

A solution of 0.23 ml (0.002 mol) of $SnCl_4$ in 5 ml of CCl_4 was added dropwise during 1 h to a solution of 1.69 ml (0.022 mol) of 1,2-epoxy-3-chloropropane and 6.6 g (0.02 mol) of 2-(2′-hydroxynaphthylidenamino)-4-phenylthiazole (12) in 8 ml of CCl_4. The organic layer was dried with Na_2SO_4. Yield: 5.92 g (70%), m.p. 106^{0}C. Found, %: C 65.13; H 4.72; N, 6.47; S 7.79. $C_{23}H_{19}N_2O_2SCl$. Anal. calcd., %: C 65.32; H 4.53; N, 6.62; S 7.58.

2.2.19. Synthesis of 2-(2′-hydroxyphenyl)-3-(4″-phenylthiazolyl)-5-phenoxymethyl-1,3-oxazolidine (19)

A solution of 0.23 ml (0.002 mol) of $SnCl_4$ in 5 ml of CCl_4 was added dropwise to a solution of 3.3 ml (0.022 mol) of 1,2-epoxy-3-phenoxypropane and 5.6 g (0.02 mol) of 2-(2′-hydroxybenzylideneamino)-4-phenylthiazole (5) in 8 ml of CCl_4. The organic layer was dried with Na_2SO_4. Yield: 5.76 g (67%), m.p. 128-129^{0}C. Found, %: C 69.56; H 5.37; N, 6.42; S 7.66. $C_{25}H_{22}N_2O_3S$. Anal. calcd., %: C 69.74; H 5.15; N 6.51; S 7.45.

2.2.20. Synthesis of 2-(2′-hydroxynaphthyl)-3-(4″-phenylthiazolyl)-5-phenoxymethyl-1,3-oxazolidine (20)

A solution of 0.23 ml (0.002 mol) of $SnCl_4$ in 5 ml of CCl_4 was added dropwise to a solution of 3.3 ml (0.022 mol) of 1,2-epoxy-3-phenoxypropane and 6.6 g (0.02 mol) of 2-(2′-hydroxynaphthylidenamino)-4-phenylthiazole (12) in 8 ml of CCl_4. The organic layer was dried with Na_2SO_4. Yield: 6.9 g (72%), m.p. 171-172^{0}C. Found, %: C 72.31; H 5.18; N,

5.97; S 6.79. $C_{29}H_{24}N_2O_3S$. Anal. calcd., %: C 72.48; H 5.03;
N, 5.83; S 6.67.

3. TABLES, FIGURES AND EQUATIONS

Table 1. The values of yields, melting points and data of elemental analysis of azomethines (1-15)

Comp No.	Yield, %	M.p., ^{0}C	Found, %				Formula	Anal. calcd, %			
			C	H	N	S		C	H	N	S
1	71	155-156	72.61	4.73	10.75	12.02	$C_{16}H_{12}N_2S$	72.80	4.58	10.60	12.12
2	73	147-148	66.78	4.72	8.82	9.76	$C_{18}H_{16}N_2O_2S$	66.65	4.97	8.64	9.88
3	75	143-144	68.73	4.17	10.16	11.17	$C_{16}H_{12}N_2OS$	68.55	4.32	9.99	11.44
4	67	149-150	64.57	3.52	9.65	10.58	$C_{16}H_{11}N_2SCl$	64.32	3.71	9.38	10.73
5	86	143	68.76	4.13	9.74	11.28	$C_{16}H_{12}N_2OS$	68.55	4.32	9.99	11.44
6	68	139-140	63.29	4.61	8.42	9.08	$C_{18}H_{16}N_2O_3S$	63.51	4.74	8.23	9.42
7	74	189-190	64.72	4.19	9.59	10.66	$C_{16}H_{12}N_2O_2S$	64.85	4.08	9.45	10.82
8	80	100-102	53.63	2.85	7.39	8.49	$C_{16}H_{11}N_2OSBr$	53.49	3.09	7.80	8.93
9	71	145-147	51.76	3.44	6.37	6.98	$C_{18}H_{15}N_2O_3SBr$	51.56	3.61	6.68	7.65
10	75	159-160	51.44	2.73	7.68	8.32	$C_{16}H_{11}N_2O_2SBr$	51.21	2.96	7.47	8.55
11	68	120-123	48.72	2.19	7.26	8.33	$C_{16}H_{10}N_2OSBrCl$	48.81	2.56	7.12	8.14
12	74	156-157	72.52	4.43	8.78	9.51	$C_{20}H_{14}N_2OS$	72.70	4.30	8.50	9.70
13	79	200-201	70.47	5.29	13.45	10.28	$C_{18}H_{17}N_3S$	70.33	5.57	13.67	10.43
14	69	220-221	66.92	5.06	12.73	10.17	$C_{18}H_{17}N_3OS$	66.85	5.30	12.99	9.91
15	55	213	74.69	5.12	9.05	10.74	$C_{19}H_{16}N_2S$	74.97	5.30	9.20	10.53

Table 2. The values of yields, melting points and data of elemental analysis of 5-methyl-substituted-1,3-oxazolidines (16-20)

Comp No.	Yield, %	M.p., ^{0}C	Found, %				Formula	Anal. calcd, %			
			C	H	N	S		C	H	N	S
16	65	85-86	71.26	5.32	7.43	8.03	$C_{23}H_{20}N_2O_2S$	71.11	5.19	7.21	8.25
17	75	78-79	63.72	4.96	7.68	8.66	$C_{19}H_{17}N_2OSCl$	63.95	4.80	7.85	8.99
18	70	106	65.32	4.53	6.62	7.58	$C_{23}H_{19}N_2O_2SCl$	65.32	4.53	6.62	7.58
19	67	128-129	69.56	5.37	6.42	7.66	$C_{25}H_{22}N_2O_3S$	69.74	5.15	6.51	7.45
20	72	171-172	72.31	5.18	5.97	6.79	$C_{29}H_{24}N_2O_3S$	72.48	5.03	5.83	6.67

4. CITATION AND REFERENCE LIST

1. Aptekar M.D., Traplika E, Savich I.A. Journal of General Chemistry. 1972, 42, 2555.
2. Karpov K.A., Nazarenko A.V., Pekarevsky B.V., Potekhin V.M. // Journal of Applied Chemistry. 2001.V. 74. Issue 6, p. 971-974.
3. Kelarev V.I., Gracheva O.G., Silin M.A. and others // Processes of Petrochemistry and Oil-Refining. 1997. No. 12. P. 29-32.
4. Kurtzer F. Sulfur, Selenium and Tellerium (Spesialist Periodical Reports), The Chemical Sosiety. London.: 1973. V. 2. P. 13.
5. Kuznetsov V.V, Prostakov N.S. // Chemistry of Heterocyclic Compounds. 1990. No. 1. P. 5-32.
6. Manian A.K., Khadse B.G., Kirticar P.A., Sengupta S.R. // Indian J. Pharm. Sci. 1991. V. 53. N 3. P. 102-103.
7. Sadigova S.E., Magerramov A.M., Allakhverdiyev M.A., Aliyeva R.A., Chiragov F.M., Vekilova T.M. Journal of General Chemistry. 2003, 73, 2043-2046.
8. Samus N.M., Melnik S.V., Tsapkov V.I. Journal of General Chemistry. 2000, 70, 302.
9. Samus N.M., Nausat Al-Nabgali, Shlyakhov E.N., Tsapkov V.I. Pharmaceutical Chemistry Journal. 1991, 25, 37.
10. Uchikawa Osamu, Fukatsu Kohji, Suno Masahiro et al. // Chem. and. Pharm. Bull. 1996. V. 44. N 11. P. 2070-2077.

5. CONCLUSION

1. Have been studied the reactions of 2-amino-4-aryl-substituted thiazoles with aromatic aldehydes.
2. Oxazolidines were synthesized by the reaction of azomethines with 1,2-epoxypropane, 1,2-epoxy-3-chloro-propane and 1,2-epoxy-3-phenoxypropane.